NASA/CP—2003–212931

5th Conference on Aerospace Materials, Processes, and Environmental Technology

M.B. Cook and D. Cross Stanley, Editors
Marshall Space Flight Center, Marshall Space Flight Center, Alabama

Proceedings of a conference held
in Huntsville, Alabama,
September 16–18, 2002

November 2003

NASA/CP—2003–212931

5th Conference on Aerospace Materials, Processes, and Environmental Technology

M.B. Cook and D. Cross Stanley, Editors
Marshall Space Flight Center, Marshall Space Flight Center, Alabama

Proceedings of a conference held
in Huntsville, Alabama,
September 16–18, 2002

National Aeronautics and
Space Administration

Marshall Space Flight Center • MSFC, Alabama
35812

November 2003

Available from:

NASA Center for AeroSpace Information
7121 Standard Drive
Hanover, MD 21076–1320
(301) 621–0390

National Technical Information Service
5285 Port Royal Road
Springfield, VA 22161
(703) 487–4650

The NASA STI Program Office…in Profile

Since its founding, NASA has been dedicated to the advancement of aeronautics and space science. The NASA Scientific and Technical Information (STI) Program Office plays a key part in helping NASA maintain this important role.

The NASA STI Program Office is operated by Langley Research Center, the lead center for NASA's scientific and technical information. The NASA STI Program Office provides access to the NASA STI Database, the largest collection of aeronautical and space science STI in the world. The Program Office is also NASA's institutional mechanism for disseminating the results of its research and development activities. These results are published by NASA in the NASA STI Report Series, which includes the following report types:

- TECHNICAL PUBLICATION. Reports of completed research or a major significant phase of research that present the results of NASA programs and include extensive data or theoretical analysis. Includes compilations of significant scientific and technical data and information deemed to be of continuing reference value. NASA's counterpart of peer-reviewed formal professional papers but has less stringent limitations on manuscript length and extent of graphic presentations.

- TECHNICAL MEMORANDUM. Scientific and technical findings that are preliminary or of specialized interest, e.g., quick release reports, working papers, and bibliographies that contain minimal annotation. Does not contain extensive analysis.

- CONTRACTOR REPORT. Scientific and technical findings by NASA-sponsored contractors and grantees.

- CONFERENCE PUBLICATION. Collected papers from scientific and technical conferences, symposia, seminars, or other meetings sponsored or cosponsored by NASA.

- SPECIAL PUBLICATION. Scientific, technical, or historical information from NASA programs, projects, and mission, often concerned with subjects having substantial public interest.

- TECHNICAL TRANSLATION. English-language translations of foreign scientific and technical material pertinent to NASA's mission.

Specialized services that complement the STI Program Office's diverse offerings include creating custom thesauri, building customized databases, organizing and publishing research results…even providing videos.

For more information about the NASA STI Program Office, see the following:

- Access the NASA STI Program Home Page at ***http://www.sti.nasa.gov***

- E-mail your question via the Internet to help@sti.nasa.gov

- Fax your question to the NASA Access Help Desk at (301) 621–0134

- Telephone the NASA Access Help Desk at (301) 621–0390

- Write to:
  NASA Access Help Desk
  NASA Center for AeroSpace Information
  7121 Standard Drive
  Hanover, MD 21076–1320
  (301)621–0390

The AMPET Conference would not be possible without the support of our sponsors.

Marshall Space Flight Center
http://www.msfc.nasa.gov/

NASA's Materials Replacement Technology Team

Space Shuttle Program
http://www1.msfc.nasa.gov/NEWMSFC/shuttle1.html
https://shuttleonline2.msfc.nasa.gov/sea/index.cfm

NASA's Materials and Processes Working Group

National Center for Advanced Manufacturing
http://ncam.msfc.nasa.gov/

American Institute of Aeronautics and Astronautics
http://www.aiaa.org/

ASM International
http://www.asm-intl.org/

Aerospace Industries Association
http://www.aia-aerospace.org/

Environmental Protection Agency
http://www.epa.gov/

National Center for Manufacturing Sciences
http://www.ncms.org/

University of New Orleans
http://www.uno.edu/

Proceedings of 5th Conference on Aerospace Materials, Processes and Environmental Technology (AMPET)

SESSION A

A1: Pollution Prevention Efforts

Urban Plant Potentiality for VOC Detoxification
Irene I. Patalakh

JSC Metal Finishing Waste Minimization Methods
Erica N. Sullivan (paper not available)

Design for the Environment
Gene Harm (presentation also available)

Waste Water Recycling at Space Launch Complex 6
Rhonda Cardinal (presentation also available)

Oxygen and Breathing Air Hardware Cleaning and Verification Technique at NASA's Johnson Space Center's Neutral Buoyancy Facility
Pat Hudnall

A2: Innovative Inspection Techniques

Fatigue Crack and Porosity Measurement in Composite Materials by Thermographic and Ultrasonic Methods
James L. Walker (paper not available)

Quantitative Remaining Life Assessments for Aerospace Components using Photon Induced Position Annihilation (PIPA)
Douglas W. Akers (presentation also available)

Acoustography-Based Inspection of Companies
Jas Sandhu (paper not available)

NDE of Friction Stir Welds on the Space Shuttle External Tank
David Kinchen (presentation also available)

Non-ODC Aircraft Oxygen Line Cleaning System
John Herrington (presentation also available)

A3: Advancements in Manufacturing and Repair

Hydrogen Torch Braze for SSME Nozzle Tube Repair
Jack Weeks

Evaluation of New Repair Methods for Seal Surface Defects on RSRM Hardware
Stephanie Stanley (presentation also available)

Microgravity Manufacturing
Ken Cooper (presentation also available)

Advanced Material Developments with Laser Engineered Net Shaping
Glenn Williams (paper not available)

Shuttle PRCS Thruster Fuel Valve Pilot Seal Extrusion – A Cradle-to-Grave Service History Correlation
Jess Waller (presentation also available)

SESSION B

B1: Environmental Regulatory Issues

The Puget Sound Clean Air Agency Aerospace NESHAP
John Schantz (presentation also available)

Green Purchasing Overview
Rhonda Mann (paper not available)

NASA's Principal Center for Review of Clean Air Act Regulations
Marceia Clark-Ingram (paper not available)

Protecting the Global Environment – The Role of Industrial Process Engineers
Carole LeBlanc

B2: Advanced Materials I

Metal Matrix Composite LOX Turbopump Housing via Novel Tool-less Net-Shape Pressure Infiltration Casting Technology
Sandeep Shah (paper not available)

Organic Binder Developments for Solid Freeform Fabrication
Ken Cooper (presentation also available)

Environmentally Compatible Vapor-Phase Corrosion Inhibitor for Space Shuttle Hardware
Howard Novak (presentation also available)

Evaluation of EL-Form Rhenium for Zero Erosion Materials
Richard Foedinger (presentation also available)

Syntactic Metals: A Survey of Current Technology
Ray Erikson (presentation also available)

B3: Information Tools

NASA AP2 Integrated Technology Database
David Crawford

Improving Profits with Materials Optimization in Manufacturing
Chris Nunez

NASA Materials Related Lessons Learned
Danny Garcia (presentation also available)

Colossal Tooling Design: 3D Simulation for Ergonomic Analysis
Steve Hunter (presentation also available)

SESSION C

C1: Evaluation of Solvent Substitutes

Selection of a Non-ODC Solvent for Rubber Processing Equipment Cleaning
Richard Morgan (presentation also available)

Case Study on Hazardous Chemical Replacement – Solvent Paint Strippers Replaced by Dry Media Blasting
Richard Buckholz (paper not available)

Ozone Friendly Solvent Alternatives for Aerospace Applications
Abid Merchant

Testing and Qualification of a Non-CFC Cleanliness Verification Agent
Eric Eichinger (paper not available)

C2: Advanced Materials I

Optical Properties of Thin Film Molecular Mixtures
Donald A. Jaworske (presentation also available)

Development of Lightweight Material using High Strength Fibers Against Space Debris Impacts
Makoto Tanaka

Replacement of Ablators with Phase-Change Material for Thermal Protection of STS Elements
Raj Kaul (paper not available)

Using Isothermal Microcalorimetry to Determine Compatibility of Structural Materials with High Test Hydrogen Peroxide (HTP) Propellant
Rudy Gostowski

C3: Technical Standards and Aerospace Materials

NASA Technical Standards Program
William Vaughan (presentation also available)

Standardization Efforts for Mechanical Testing and Design of Advanced Ceramic Materials and Components
Jonathan Salem (presentation also available)

Standards Development Activities at WSTF
Harold Beeson

Corrosion of Highly Specular Vapor Deposited Aluminum (VDA) on Earthshade Door Sandwich Structure
Daniel Plaskon

SESSION D

D1: Surface Cleanliness Inspections

Fluorescent Cleaning Process
Jim Deardorff

Analysis of Non-Volatile Residues with a Standard FTIR Accessory, The VSphere™
Martin Szczesniak

Use of FT-IR Analysis to Support Contamination Studies for Bonding Surfaces
Richard Boothe

A Study of Stains on Metals using Infrared Hyperspectral Imaging
G. L. Powell (paper not available)

D2: Materials Test Methods and Evaluation

Corrosion Prevention Compound Evaluation Method
Sarah J. H. Kuhlman (presentation also available)

Infrared Spectroscopy as a Chemical Fingerprinting Tool
Tim Huff (presentation also available)

Reference Material Kydex-100 Test Data Message for Flammability Testing
Carl Engel (presentation also available)

The Effects of Gravity on the Combustion Synthesis of Porous Biomaterials
Martin Castillo (presentation also available)

The Effects of Molding and Machining on the Dimensional Stability of Neoflon CTFE M400H Polychlorotrifluoroethylene Rod Stock and Valve Seats
Jess Waller (presentation also available)

D3: Advanced Manufacturing Research

Cryogenic Temperature Effects on Performance of Polymer Composites
David Hui

Toward Healing of Composite Cryogenic Tanks
Richard Patton

Prediction of Microcracking Induced Permeability of Cryogenic Composite Tanks
John Whitcomb (presentation also available)

Solid-State Friction Stir Welding
George Buchanan

Non-Autoclave Processing of Large Re-Usable Aerospace Structures
Al Loos

SESSION E

E1: Environment-Friendly Cleaning Products and Processes

Precision Chair Hardware: Maintenance of Fluid Systems Cleanliness
Michael D. Pedley (paper not available)

Novec™ Engineered Fluids
David Hesselroth (presentation also available)

Cleaning to 6 Sigma Standards
Donald Bowden

Clean Machining with New Volatile Lubricant Fluid
David Hesselroth (presentation also available)

E2: Materials Test Methods and Evaluation

Durable Surface Contamination Standards
Paul Shelley (presentation also available)

Effects of Thermal Exposure on Properties of Al-Li Alloys
Sandeep Shah (paper not available)

Hydrogen Permeability of Composite Tank Materials under Biaxial Strain
Erik Stokes

Micro-Raman Analysis of Irradiated Diamond Films
R. L. Newton (presentation also available)

E3: Development in Metallic Processes

High Strength and Wear Resistant Aluminum Alloy for High Temperature Applications
Jonathan A. Lee

Aluminum Lithium Alloys Use for Reusable Future Launcher Cryogenic Metallic Tanks
Eric Grosjean (presentation also available)

Vacuum Plasma Spray Forming of Copper Alloy Liners for Regeneratively Cooled Liquid Rocket Combustion Chamber
Frank Zimmerman

JG-PP Lead-Free Solder Project
Brian Greene (paper not available)

Friction Stir Process Mapping Methodology
Alex Kooney (paper not available)

SESSION F

F1: Synthesis of Nano Materials

Synthesis and Characterization of Carbon Nanotubes for Reinforced and Functional Applications
Shen Zhu

Synthesis and Coating of Nanoparticles
Abraham Ulman

A New Process for the Deposition of Nanostructured Thin Films Size-Classified Nanoparticles
Renato P. Camata (presentation also available)

The "Ship-in-the-Bottle Approach" to Synthesis of Nano Materials via Sonolyis
Devinder Mahajan (presentation also available)

Development of High Performance Nanocomposite Pyroelectric Detectors: A Possible Approach
A.K. Batra

F2: Composite Cryotank Processing

Rotational Molding of Thermotropic Liquid Crystal Polymers
Martin Rogers (presentation also available)

Manufacturing Process Simulation of Large-Scale Cryotanks
Steven Phillips (presentation also available)

Development of Segmented Composite Toroidal Tanks
Thomas DeLay(paper not available)

Linerless Tanks for Space Application: Design and Manufacturing Considerations
Brian Jones (presentation also available)

POSTERS

Friction Stir Weld of Tapered Thickness Welds Using an Adjustable Pin Tool
Glynn Adams

Automatic Ply Verification
Scott Blake

Standard Chemical Ignition Source Characteristics for Flammability Testing
Carl D. Engel

Flammability Testing Igniter Characteristics
Shawn Goedeke

SLI Complex Curvature Friction Stir Weld Rick Reduction Program
Paula J. Hartley

Introduction to Proton Microscopy
William A. Hollerman

Thermo-Optical and Mechanical Property Testing of Candidate Solar Sail Materials
William A. Hollerman

Composite LOX Tank Development
Michael C. McBain

Correlating Flammability of Materials with FTIR Analysis Test Results
Robins E. Moore (presentation also available)

MicroDeformation Technology
Chun Man Ng

An Evaluation of the Oxygen Compatibility of Composite Materials
Erin Richardson

Ammonia Analysis by Gas Chromatograph/Infrared Detector (GC/IRD)
Joseph P. Scott

Urban Plant Potentiality for VOC Detoxification

IRENE I. PATALAKH
Dnipropetrovsk National University
13 Naukovii by-st.
Dnipropetrovsk, Ukraine 49625
Phone: 380-562-469280
Fax: 380-562-465523
E-mail: patalakh@a-teleport.com

Plant components of artificial ecosystems may be an effective barrier for volatile organic compound (VOC) contaminants during their migration in soil, subsoil water, and partial emission in atmosphere. Most plants are able to filtrate hydrophobic compounds from the environment; the problem is in surviving and normal functioning of such "green filters." Detailed investigations to obtain complex estimations of plant states and their amortization possibilities should include these next steps:

- the determination of the "normal" state of plant population throughout the natural variance of the state parameters;
- the elucidation of the threshold and critical values for VOC contamination;
- calculation of toxic loading maximum for every plant species.

A certain integral parameter for the estimation of the leaves affection intensity by VOC (index of leaves injury) has been tested as the plant organism reaction both for air pollution and soil contamination simultaneously. Such index we found has a certain correlation with total resistance of the species, but we determined that resistant plants are not such beautiful accumulators of hydrocarbon as a rule.

Obviously, it is necessary to determinate phytoaccumulative properties corresponding to intensity of some climatic factors (light intensity, air and soil humidity and temperature). We received some preliminary results concerning plant ability to absorb and partially transform VOC from air and soil. These results we are using to measure the cleaning-up efficiency of plants for non-dangerous hydrocarbon (HC) doses.

Some practical approaches are elaborated by our scientific group for the phytoremediation of VOC:

(1) For the estimation of VOC uptake in plant organs, it is necessary to distinguish between exogenous and endogenous VOC origin. Emission rates of light HC from some crops are in the range of some 10 nanograms / gram dry weight per hour, whereas anthropogenic VOC uptake varies between some hundred ppm and ppb.

(2) Harmless accumulation of HC by leaves depends on the way of drawing xenobiotic in metabolism. This process can be realized either through breaking of aromatic rings and final oxidation to some organic acids (OA) or through spontaneous metabolic transformation into some aromatic amino acids (AA). The first way is harmful; the second one is not dangerous for plants.

(3) Predominance of the OA or AA pathway depends considerably on ambient conditions (mainly on air temperature and humidity). Some practical approaches are elaborated by our scientific group on such theoretical bases.

JSC Metal Finishing Waste Minimization Methods

Erica Sullivan
Materials Research Engineer

Materials and Processes Branch
Johnson Space Center

JSC Metal Finishing Facility Overview

- Johnson Space Center (JSC) has achieved VPP Star status and is ISO 9001 compliant
- The Structural Engineering Division in the Engineering Directorate is responsible for operating the metal finishing facility at JSC
- The Engineering Directorate is responsible for $71.4 million of space flight hardware design, fabrication and testing

JSC Metal Finishing Facility Overview

- The JSC Metal Finishing Facility processes flight hardware to support the programs in particular schedule and mission critical flight hardware
- The JSC Metal Finishing Facility is operated by Rothe Joint Venture
- The Facility provides following processes
  - Anodizing
  - Alodining
  - Passivation
  - Pickling

JSC Metal Finishing Facility Overview

- JSC Metal Finishing Facility completely rebuilt in 1998
  - Total cost of $366,000.
- All new tanks, electrical, plumbing, and ventilation installed
- Designed to meet modern safety, environmental, and quality requirements
- Designed to minimize contamination and provide the highest quality finishes

Quality In-House Metal Finishing

- In-house metal finishing has significant quality benefits:
  - Better process control
    - Eliminate cross-contamination that causes process variability
    - Metal buildup in process solutions can be verified by JSC laboratories
  - Better process performance
    - Process chemistry can be adjusted to specific requirements for aerospace materials
    - Performance verified through periodic salt spray testing
    - Process improvements can be overseen by engineers firsthand
  - Achieve consistent color and appearance on flight hardware
    - Hardware viewed by millions on international television
  - Immediate troubleshooting
    - Metal finishing process problems can be diagnosed in real time and quickly corrected

Metal Finishing Facility

Safety Facility Features

- Process tanks and main floor are completely non-metallic to prevent corrosion
- Sub-floor sealed and seamless polypropylene liner installed that extends 36 inches up the wall
- Open walkways and work areas
- Independent audit by Fuss and O Neil Consulting Engineers found facility met all OSHA safety requirements

Safety Facility Features

- Fumes pulled to back of tank and away from workers
- Hexavalent chromium used only in conversion coating process
  - No agitation or heating of tank
  - Short duration of any potential worker exposure
  - Workers are protected from hexavalent chromium

Safety Multiple Levels of Containment

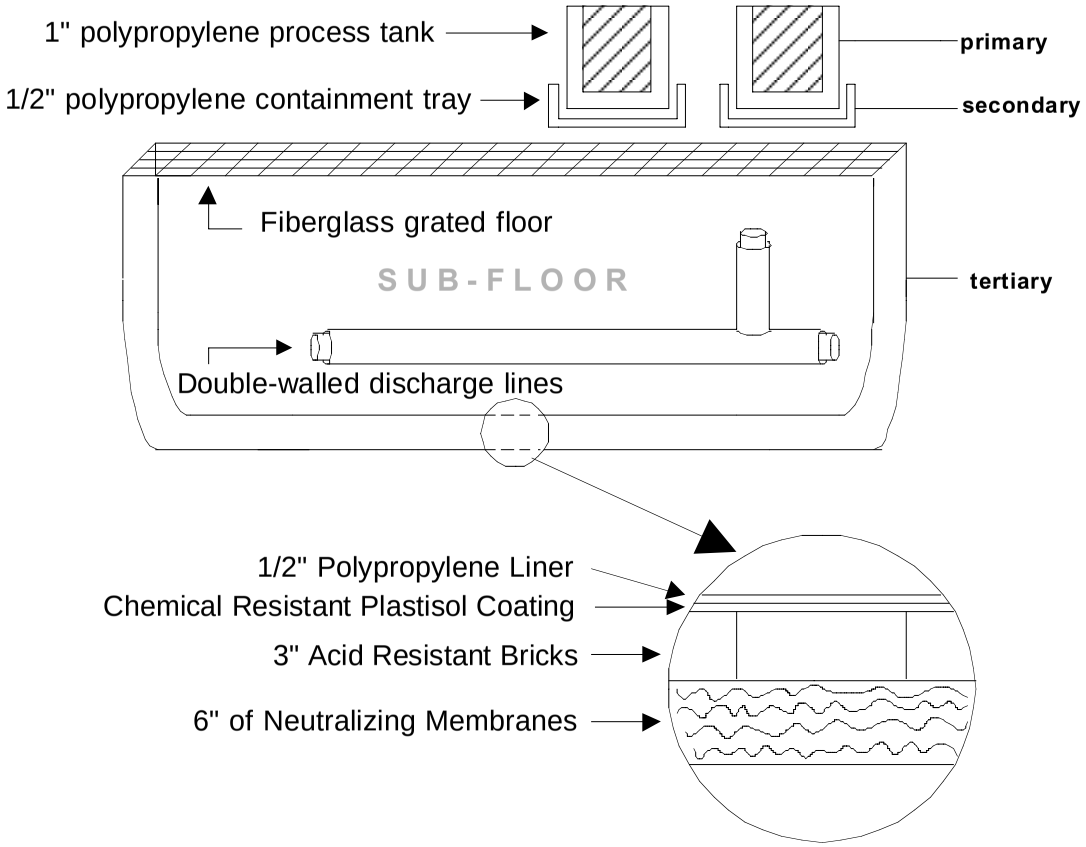

Environmental Wastewater Minimization

- A dragout rinse tank is used to capture hexavalent chromium from treated parts after conversion coating
  - Resin bed removes chromium from dragout tank
  - Counterflow rinsing is used to minimize volume of rinse water
- Conductivity of rinses are continuous monitored
  - Will detect any contamination before pretreatment

Environmental Compliance

- The JSC Environmental Office oversees the disposal practices of JSC Metal Finishing Facility
- Process chemicals are tanked and trucked to certified disposal facility
- Rinse water is treated and released to sanitary sewer
- Exhaust air is scrubbed and treated
- Zero release of hazardous metals to local environment
- JSC Metal Finishing already meets the *proposed* EPA Metal Products & Machinery (MP&M) Limits for metals in waste water
- The Federal EPA inspected the JSC Facility in 1998
  - EPA refers third parties to JSC for compliance benchmarking

Environmental Past Initiatives

TRANSITION TO NON-CHROMATED PROCESSES	
WAS	**CHANGED TO**
Chromic Deoxidizer	Non-Chromic Deoxidizer
Ferrocyanide Conversion Coatings	Ferrocyanide-Free Conversion Coatings
Chromated Pickles/Strippers	Non-Chromated Pickles
Chromic Acid Anodize	Sulfuric Acid Anodize
Chromated Anodize Seal	Non-Chromated Anodize Seal
Nitric-Chromic Acid Passivation	Nitric Acid Passivation

Memtek Facility

- A pretreatment system is used to treat the rinse waters from the Metal finishing
- The Memtek system is the chemical waste processing system used to reduce chemical waste effluent
  - After treatment, rinse water is clean enough for discharge to sanitary sewer

Memtek Facility

- Utilizes a pH adjustment followed by membrane filtration technology to remove metals prior to discharge to the sewer
- The supernatant sludge is processed through a plate and frame filter creating a dried filter cake.
- Prior to 1998, the filter cake was considered hazardous waste due the concentrations of metals contained in the waste

Environmental Current Initiatives

- **Environmental Initiatives in Progress**
  - **JSC M&P Engineering is working with the Aerospace Chromium Elimination (ACE) industry team in seeking alternatives to hexavalent chromium conversion coatings**
    - ***Non-chromated conversion coatings do not yet match performance of current conversion coatings***
  - **Working towards eliminating the need for a Hazardous Waste Permit for waste collection system**

Summary

- **Metal Finishing Lab is a state-of-the-art facility**
  - **Meets all current and *proposed* safety, environmental and quality requirements**
  - **Allows JSC to develop new replacement technologies**
- **The Metal Finishing Facility provides fast turnaround required for Space Station and Shuttle mission critical flight hardware at JSC**

Acknowledgements

- **ES Structural Engineering Division**

  -Gail Horiuchi

  -Jay Bennett

  -Leslie Schaschl

- **Rothe Joint Venture**

  -Willie Scheis

  -John Tyznik

- **JSC Environmental Office**

  -Sandra Parker

  -Rick Jones, Dyncorp

Design for the Environment

Eugene Harm

September 17, 2002

Summary Of Environmental Laws

Air Quality	Water Quality	Hazardous Waste	Toxic Substances	Cleanup & Reporting	Emergency Planning & Reporting
CAA	CWA	RCRA	TSCA	CERCLA	EPCRA

Environmental Approach

Non Compliance

Compliance

Best Management Practice

Emissions Reduction

Pollution Prevention

Sustainability

Sustainability

Hold up

and/or

Support

Closed System

Sustainable Development

- Sustainable Development meets the needs of the present without compromising the ability of future generations to meet their own needs.

- Then I say the earth belongs to each generation during its course, fully and in its own right, no generation can contract debts greater than may be paid during the course of its own existence.

  Thomas Jefferson, September 6, 1789

Moving Towards Sustainability

Pollution Control

Process Integration

Whole Facility Planning

Industrial Ecology

Sustainable Communities/ Cities/Regions

Less energy intensity per unit of product or service
Lower material intensity per unit of product or service
Lower levels of environmental toxicity and risk

Why Design for the Environment?

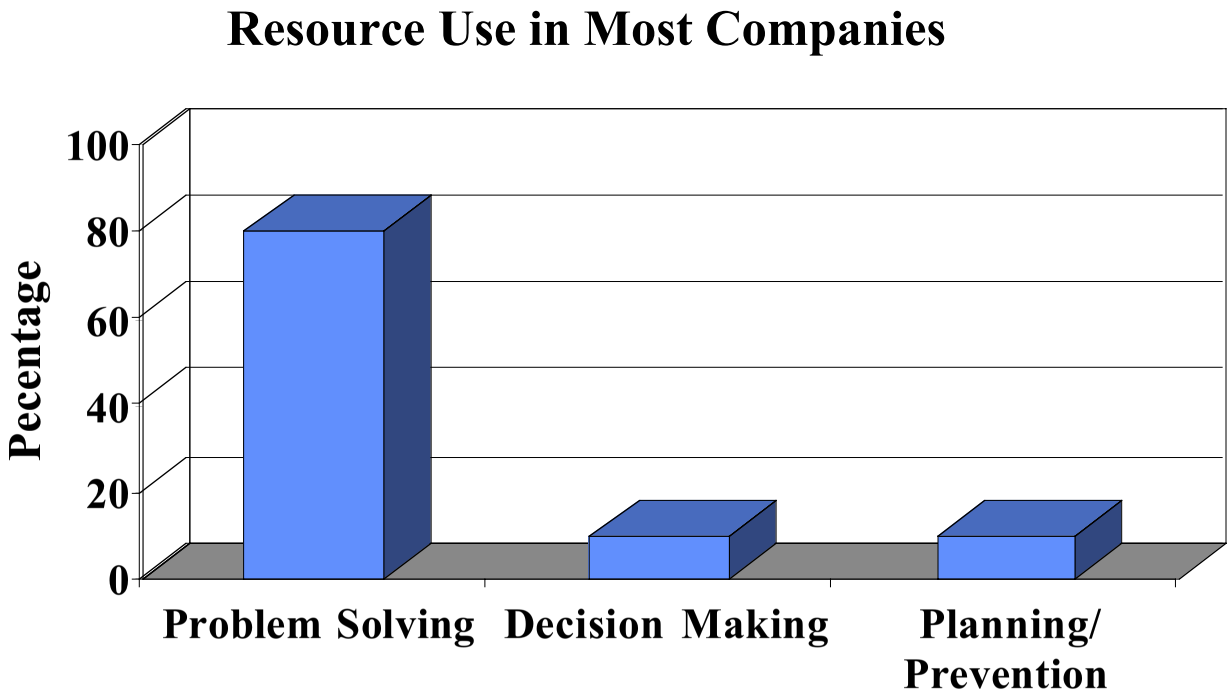

Design for the Environment

... a systematic method of integrating environment, safety and health objectives into the design process and considers impacts throughout the life cycle of the product.

Material Balances

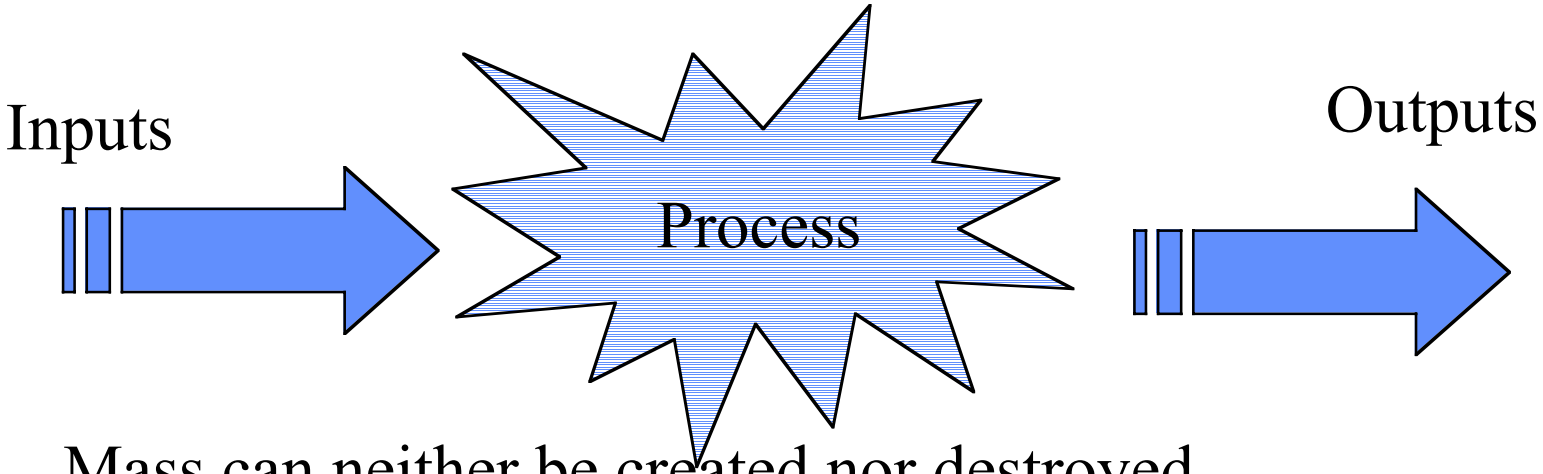

Mass can neither be created nor destroyed…

- Everything entering the system must leave the system somewhere, somehow.
- Everything leaving the system somehow got into the system in the first place.

Life Cycle Analysis

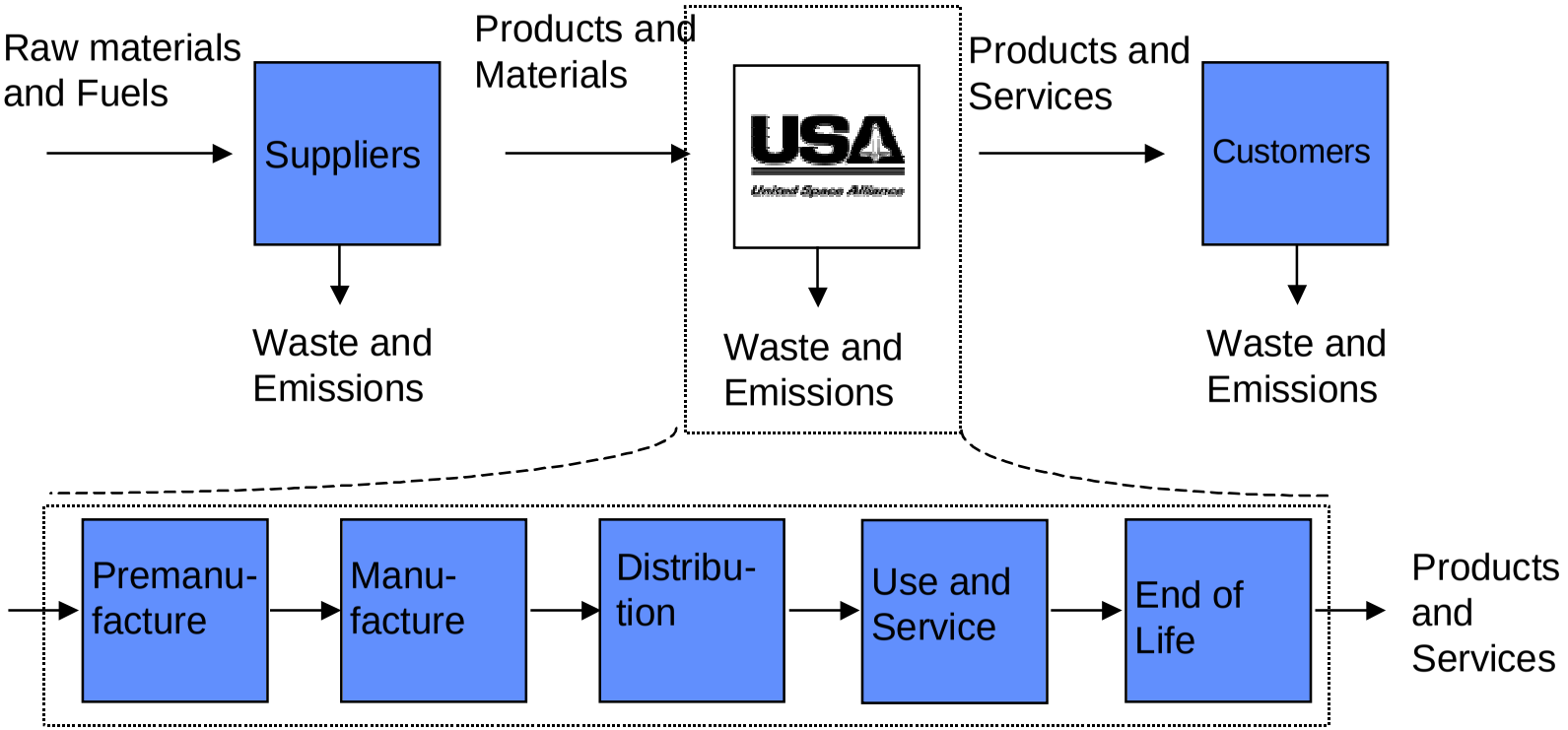

USA Environment, Safety, and Health Policy

Integrate ESH considerations into ...
- **engineering design ..... to prevent adverse impacts from company operations on employee safety and health, the environment and the community; to enhance competitiveness: and to reduce EHS costs.**

Dfe Scorecard - end of life

Pollution	
Does a disassembly,refurbishment and recycling based end-of-life option generate airborne pollution (such as NOx, SO2, or halogenated compounds)?	25 ☑
Does a disassembly and recycling based end-of-life option generate large volumes of liquid, solid, and gaseous wastes?	25 ☐
Is there a future potential liability associated with the end-of-life of the product?	50 ☑
Total	75
Conservation	
Does the design prevent the reuse or recycle of the expensive materials and components?	20 ☑
Does the product design prevent easy recovery of energy from small or inexpensive plastic parts?	20 ☐
Does the design prevent the recycling of metal materials and components?	20 ☐
Is it difficult to direct the majority of the products on the market to the preferred end-of-life option?	40 ☐
Total	20
Reset	Score

< In Service use or Flight | Safety | Pollution | Conservation

Dfe Scorecard

DfESH Scorecard

Material Properties | Refurb & Assembly | In Service use or Flight | End of Life

End Of Life Management	Score
Safety	
Are there health or safety exposure risks associated with the disposal of the product/material?	40 ☑
Are there ergonomics issues associated with product end-of-life handling or it's refurbishment?	30 ☐
Does the end of life handling require special equipment or procedures to ensure safe handling?	30 ☐
Total	40
Pollution	
Does a disassembly,refurbishment and recycling based end-of-life option generate airborne pollution (such as NOx, SO2, or halogenated compounds)?	25 ☑
Does a disassembly and recycling based end-of-life option generate large volumes of liquid, solid, and gaseous wastes?	25 ☐
Is there a future potential liability associated with the end-of-life of the product?	50 ☑
Total	75
Conservation	
Does the design prevent the reuse or recycle of the expensive materials and components?	20 ☑
Does the product design prevent easy recovery of energy from small or inexpensive plastic parts?	20 ☐
Does the design prevent the recycling of metal materials and components?	20 ☐
Is it difficult to direct the majority of the products on the market to the preferred end-of-life option?	40 ☐
Total	20
	Reset Score

< In Service use or Flight | Safety | Pollution | Conservation

Triple Bottom Line

- **Ecological Integrity**
  Consume less energy
  Avoid persistent, toxic, bio-accumulative compounds

- **Societal Responsibility**
  Educate employees, customers, suppliers, etc.

- **Economic Viability**
  Assure continuity of critical production inputs
  Develop products and services with enduring value

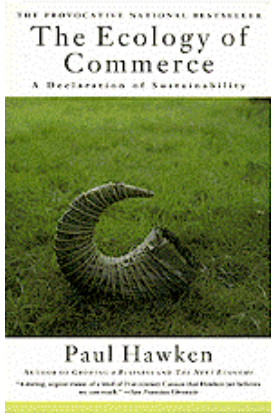

WASTEWATER RECYCLING AT SPACE LAUNCH COMPLEX 6

Rhonda Cardinal
The Boeing Company
P.O. Box 5219
Vandenberg Air Force Base, CA 93437
805-606-6340, Ext. 6566
rhonda.e.cardinal@boeing.com

INTRODUCTION

Wastewater at a launch site is typically generated through four different processes. Acoustic-suppression water has traditionally been used to dampen the effect of launch-induced sound waves on the vehicle and payload. Wash-down water after a launch involving solid rocket motors also is needed to remove corrosive particles from the launch pad and surrounding areas. Fire-suppression water is used to put out fires or cool surrounding areas. Additionally, rainwater accumulates in open containment pits.

The Space Shuttle installation at Space Launch Complex 6 (SLC-6) used approximately 400,000 gal of acoustic-suppression water per launch, released in about 30 sec. The installation at Vandenberg Air Force Base, California, included an elevated water storage tank, pumps and piping to carry water from the flame ducts to a wastewater treatment area, and pumps and piping to carry treated water back up a hill to refill the storage tank.

As part of the United States Air Force s Pollution Prevention program, a modular, portable wastewater treatment unit was developed. The unit polishes post-launch wash-down water mixed with acoustic-suppression water from the NASA Delta II launch site and recycles it back to a storage tank. This water is mildly contaminated and is not considered to be hazardous waste; however, it is too contaminated to be released to grade.

The Boeing Company Delta IV program has succeeded in obtaining permission to make use of this portable water treatment system for its operations. As part of the pad design, the unit has been incorporated into the original Shuttle water treatment installation at SLC-6. Water from post-launch wash-down and potential acoustic suppression will collect in large flame ducts located below the launch table. In the rare event of a fire, suppression water will also collect in these ducts. All water will originate from the elevated storage tank. Contaminated wash-down water will be pumped via an existing 50-gpm pump in the flame ducts to the wastewater treatment trailer. Post-treatment water will then be pumped into a new 60,000-gal holding tank. In the event that water in the flame ducts is not contaminated, it will be routed directly into the holding tank, passing through a particle filter in the bypass line to remove debris. From the 60,000-gal holding tank, water will be pumped up the hill to the storage tank via two existing 500-gpm pumps. In either case, almost all water generated during launch processes will be recycled and re-used.

Recycling launch process water reduces water consumption in the often-dry region of Central California and reduces generation of hazardous waste from the SLC-6 site.

BACKGROUND

Wastewater treatment and recycling at SLC-6 at Vandenberg Air Force Base is an evolving work in progress.

First built for the Manned Orbiting Laboratory (MOL) program in the early 1960 s, SLC-6 consisted of a mobile service tower, a concrete launch pad, a flame duct, and a launch control center. The program was canceled, and the site was decommissioned in 1969.

A Shuttle Launch and Recovery Board was formed to review possible launch and recovery sites for the Space Transportation System (STS) in April 1971. Vandenberg was selected as a launch site, along with NASA's Kennedy Space Center (KSC) in Florida. The Vandenberg site was chosen because it could support near-polar and retrograde azimuth launches that could not be achieved efficiently and safely from KSC.

A special task force established in 1974 evaluated three possible STS launch sites at Vandenberg. Cost analysis demonstrated a $100M+ cost sav-

ing using the existing MOL site (SLC-6) compared to building a new facility. The SLC-6 option was approved in 1975 and construction began in 1979.

Shuttle operations were to be conducted at several Vandenberg locations based on the availability of existing facilities. The runway; orbiter maintenance, checkout, and lifting facilities; thermal protection facility; supply warehouses; and a majority of support personnel were located at north Vandenberg. SLC-6 on south Vandenberg contained the launch control center, payload preparation room, payload changeout room, shuttle assembly building, access tower, launch mount, mobile service tower (MST), and three exhaust ducts. Approximately 12 to 15 miles separated the facilities between north and south Vandenberg.

The launch mount is a steel-framed support structure anchored to the center of the pad with openings into the flame ducts. It would have supported the Space Shuttle vehicle for the launch and provide ducting for the exhaust. To supplement the existing MOL flame ducts, 87,000 cubic yards of concrete were used to build two additional ducts, each 50 by 70 ft, with walls 9- to 12-ft thick enough concrete to build a 3-ft-wide, 4-in.-thick sidewalk from Los Angeles to San Francisco.

At liftoff, the exhaust from the solid rocket boosters and the Shuttle's main engines would be channeled underground, exiting through the three ducts at the sides of the pad. Water would flow into a deluge nozzle system into the launch mount to suppress acoustic energy that could damage the vehicle during liftoff. This sound-suppression water system was designed to release 760,000 gal onto the pad and into the exhaust ducts in less than 50 sec. A 400,000-plus-gal water tank, on a hill behind the MST, connected to a 1.25-million-gal water tank, supplied this gravity-fed system. Figure 1 shows the deluge system dumping water through the launch table.

NASA and the Air Force moved ahead with the announcement of an all-military crew for the first manned polar-orbit spaceflight and the first launch

HB2T173001.1

Figure 1. Original STS Deluge System Test (circa 1985)

from SLC-6. Mission STS-62A, commanded by veteran astronaut Robert Crippen, would be launched in mid-1986.

As SLC-6 construction efforts were rushed to completion, NASA's Space Shuttle program had a string of successful missions. That is, until 28 January 1986, the day of the *Challenger* explosion.

The *Challenger* disaster had a devastating effect on the nation's space efforts. Space Shuttle operations at Vandenberg were quickly phased out, due to increased safety concerns. On 26 December 1989, Air Force Secretary Edward "Pete" Aldridge (the "payload specialist" on the now-canceled STS-62A) terminated the Space Shuttle program at Vandenberg.

There have been some intermediate programs at SLC-6 since that time. Lockheed Martin used part of the pad capability to launch its *Athena* rocket in the mid-1990 s, but the size and scope of the site can support a much larger vehicle.

That vehicle is the Boeing Delta IV Evolved Expendable Launch Vehicle.

Boeing has been resurrecting and renovating the SLC-6 pad to accommodate the Delta IV vehicle since 1999. Figure 2, an aerial photograph, shows SLC-6 under construction in November 2001.

The MST, lowered 50 ft when the original MOL pad was reconfigured for the Shuttle, now rises to its original height. The fixed umbilical tower will double in width, to accommodate swing arms that are now 80 ft long. A fixed pad erector (PFE) pit, 70 ft long and 30 ft deep, has been carved out of the original concrete pad to accommodate the giant hydraulic cylinder that will lift the 300-ft-tall vehicle from the horizontal to vertical position. Underground tunnels, installed for the Shuttle, are being reused for Delta IV, with miles of cabling and piping snaking through the tunnels. The original hydrogen and oxygen spheres will be used again, after thorough inspection and refurbishment. The hydrogen sphere (800,000 gal) is the largest in the world.

Even the Vandenberg Harbor, first used by the U.S. Coast Guard in the 1920 s and 1930 s, later dredged and enlarged to accommodate the vessel that

HB2T173002

Figure 2. Aerial View of SLC-6 Under Construction (November 2001)

would carry the Shuttle s external tank to Vandenberg, has been resurrected. In August and September of 2001, a major re-dredging operation occurred, allowing Boeing to transport the largest component of its rocket, the common booster core (CBC) to its launch facility at SLC-6.

One major new facility has been built: the horizontal integration facility (HIF), 300 ft long, 200 ft wide and 80 ft tall. In this building, the major components of the rocket will be assembled horizontally and tested before being transported to the launch pad to be erected.

The old launch table was demolished; the new 650-ton steel launch table was delivered by barge in October 2001 and now sits astride the FPE pit. From this massive piece of ground support hardware, the largest rocket ever built will lift off, carrying payloads for government and commercial customers alike. Figure 3 is an artist s conception of the Delta IV launch vehicle lifting off from the SLC-6 pad.

In addition to the super-sized launch facilities, the Shuttle program also boasted an ambitious wastewater treatment and recycling system. Enormous quantities of water would be used for each launch 760,000 gal pouring though the launch table and surrounding areas each time a vehicle launched. This
water would be used for a combination of cooling and pulse-ignition suppression. The entire quantity was to be released in about 50 sec, a deluge of Biblical proportions. This water would come in contact with the combustion products of solid rocket motors, which are composed primarily of ammonium perchlorate. The post-launch water typically would have a low pH, converting to dilute hydrochloric acid as a result of contact with the exhaust. There would also be low levels of metal in the water, the result of charred paint from the launch pad and emissions from the vehicle. All of this water, after pouring over the launch table and surrounding areas, would drain into the flame ducts located directly below. These three flame ducts were enormous and shared a common sump. As part of the pad overall design, much of the drainage throughout

HB2T173003

Figure 3. Artist s Conception of the Delta IV Launch Vehicle Leaving the SLC-6 Pad

the facility would empty into these ducts, including seasonal rainwater. The duct walls are marked in 1-ft increments, and at the 12-ft mark, these three ducts collectively hold over 12 million gal of water. Figure 4 shows a flame duct with the 1-ft increments marked.

HB2T173004

Figure 4. Flame Duct with Water Inside, Showing Foot Increment Marks

Collected water would be too contaminated to release into the environment and thus require treatment. Additionally, due to water constraints on the Central Coast, the Air Force decided to recycle the post-treatment water back into the 400,000-gal storage tank (Figure 5) that fed the deluge system. To accomplish these goals, the Army Corps of Engineers purchased and installed a sophisticated wastewater treatment system (WWTS), as shown in Figure 6, that included capability for neutralization, metals precipitation, and a filter press. This WWTS was capable of treating 15,000,000 gal of wastewater in 7 days, operating 24-hr-per-day (approximately 1,488 gal per min)[(1)].

HB2T173005

Figure 5. Elevated 400,000-gal Water Storage Tank

HB2T173006.1

Figure 6. STS Wastewater Treatment System and 1,250,000-gal Water Storage Tank

Two pumps were housed in the common sump of the flame ducts. The smaller was a 150-gpm unit and would be used to pump uncontaminated rainwater out of the flame ducts into a series of drainage channels which, ultimately, released the water into a man-made ditch on the south side of the site. (This ditch has become overgrown with vegetation and willow trees over the last 15 years, and is now designated as a wetland.)

The other pump could move 500 gpm and would be used to move water up to the wastewater treatment system, which is located uphill and outside the fence-line of SLC-6. After treatment was complete, the water would be stored in a 1.25-million-gal storage tank located adjacent to the treatment system. From this tank, two 500-gpm Bingham pumps would push the water underground, through a 6-in. line that connected at a facility valve pit to the 10-ft-diameter line, which goes up the middle of the 400,000-gal storage tank (Figure 5). The 10-ft-diameter line accounts for approximately 10% of the overall capacity of the tank. None of this tremendous capability, ingeniously conceived, designed, and installed over 20 years ago, was ever used.

The Air Force, after discontinuing the Shuttle program, performed a low level of testing and maintenance of the WWTS over the next 15 years. Between 1990 and 1995, an Air Force contractor tested the system on three different occasions. All three tests failed, due to the under-utilization and subsequent failure of components. The wastewater treatment system was then largely abandoned. However, the Air Force still needed a place to treat water contaminated with low levels of hydrazine. This water was produced from air scrubbers that captured emissions of hydrazine to the

atmosphere during the fueling process. The Air Force used a small portion of the original treatment system, a UV/Ozone destruction system, to neutralize the hydrazine content of the water. Water classified as hazardous waste was sent off-site (from Vandenberg) for treatment. Nonhazardous wastewater was brought to the site in tank trucks and stored prior to treatment. After treatment, it was stored in the 1.25-million-gal storage tank next to the wastewater treatment pad until it was released into two lined evaporation ponds that the Air Force maintained. The Bingham pumps, although still connected to that tank, were never used as part of this process.

The Air Force also needed a way to treat metals and pH from post-launch deluge water, where solid rocket motors were employed. According to an Air Force document prepared in 1997[2], over 1,000,000 gal of nonhazardous, industrial wastewater were produced in 1996, which could not be directly discharged to grade. Because the water was nonhazardous, it was hauled to the SLC-6 location and allowed to settle in the two lined evaporation ponds. These ponds were originally built for the STS program to handle brine from the WWTS and water that could not be treated in the WWTS or the UV/Ozone system. The water in the ponds was rotated annually and the sediments removed after sufficient drying.

At the time that the 1997 water recycling report was produced, Vandenberg depended on groundwater resources for both industrial and drinking water. A concern about overdraft motivated the Air Force to look into recycling technology. Additionally, all of this water, whether treated at SLC-6 or some other location, needed to be hauled in tank trucks, which typically hold 5,000 to 10,000 gal. This resulted in 1,000 trips, averaging more than 25 miles round trip, with an estimated cost of $1,000,000 per year.

The Air Force therefore proposed, and later obtained funding for, a portable wastewater treatment unit that could remove the metals and neutralize the pH from post-launch wash-down water. The Air Force also envisioned hydrazine removal, thus replacing all of its stationary treatment facilities. However, the hydrazine removal module was later abandoned, due to concerns about permitting.

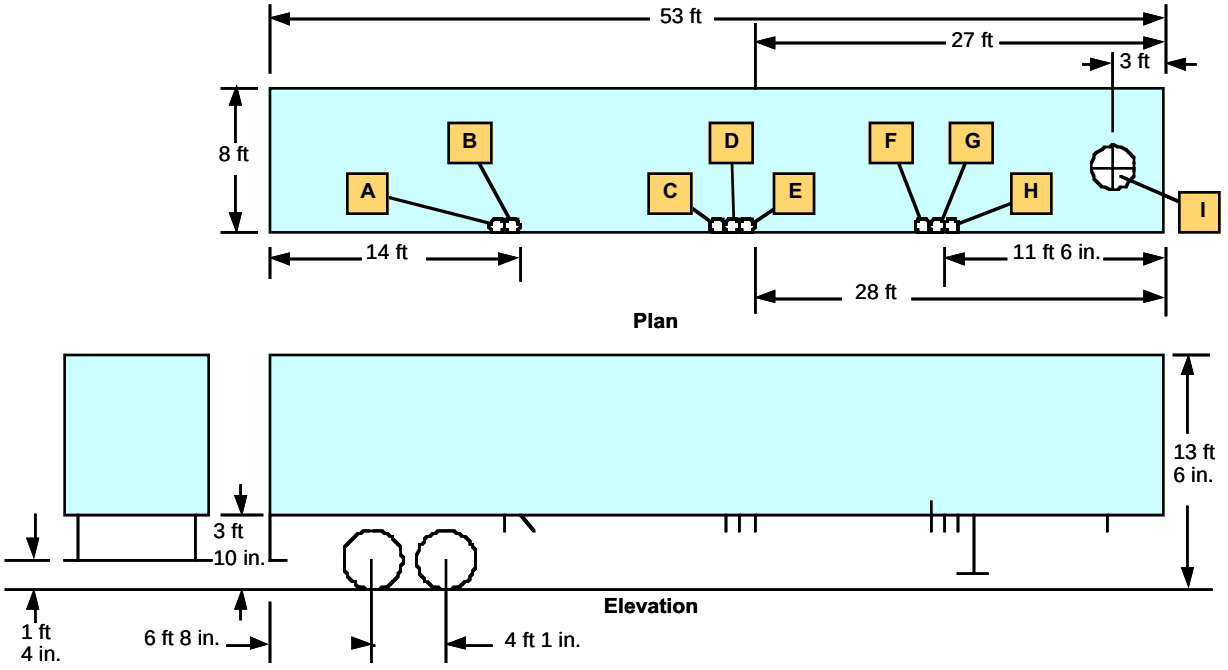

Figure 7. Launch Water Reclamation Trailer Block Diagram

A block diagram of the portable unit is shown in Figure 7. The unit would travel from launch site to launch site, polishing the nonhazardous wastewater and returning it to the various deluge water storage tanks. This approach would save the funds expended for the rental of transport trucks, air emissions from those trucks, fuel use, and also would allow the Base to recycle and thus conserve large quantities of water. All of the launch sites would require new points of connection to be installed and plumbing rerouted in order for the unit to work at each station. This proposal was viewed as a Pollution Prevention/air emission reduction initiative, and the Air Force received some credit with the local air district for implementing the program.

It was during the design and development phase of the wastewater treatment system that the Evolved Expendable Launch Vehicle (EELV) program emerged. EELV was billed as a "green" program, both by the government and by the contractors. The new Delta IV vehicle would be launched from SLC-6, home of the now-defunct Shuttle wastewater treatment system. As a Pollution Prevention initiative, Boeing requested use of the portable Launch Water Recycling System (LWRS), which was still in the development phase. For the system to be used, the trailer interface needed to be included in the design package.

The launch pad design firm working for Boeing was given instructions to integrate the LWRS into both new and existing plumbing and piping. This would prove to be an excellent opportunity to effect synergy between the equipment builder and the launch pad designer because the unit was not yet completed.

The portable wastewater treatment system is a modular unit that contains pH neutralization chemicals, an activated carbon filter, an ion-exchange resin bed, pumps, and electrical interfaces. It is intended to be operated remotely, via electrical interfaces and computer control panels. There also are inputs for a future hydrazine module, if and when the Air Force decides to include that capability. The function of this unit is to neutralize the pH and remove metals, other particulates, and trace quantities of organics to produce polished water that will meet drinking standards. The unit is capable of treating 50 gal per minute. On the inlet side, a 1000-gal water storage tank ensures a steady flow of water into the unit. Figures 8 and 9 show external and internal views of the actual trailer unit.

The task at hand was to integrate the new portable unit with existing Shuttle plumbing and piping, put in place for the larger wastewater treatment

HB2T173008

Figure 8. External View of LWRS Trailer

HB2T173009

Figure 9. Inside the LWRS Trailer

plant. Additionally, new piping had to be installed, to bypass the 1.25 million-gal storage tank, which was too big for the new launch operation. The interface between the old piping and new is shown in Figure 10.

The Shuttle used hundreds of thousands of gallons of water for ignition-pulse suppression. This water, when combined in the common sump with the pad wash-down water, became contaminated and required treatment. Because the Delta IV is a

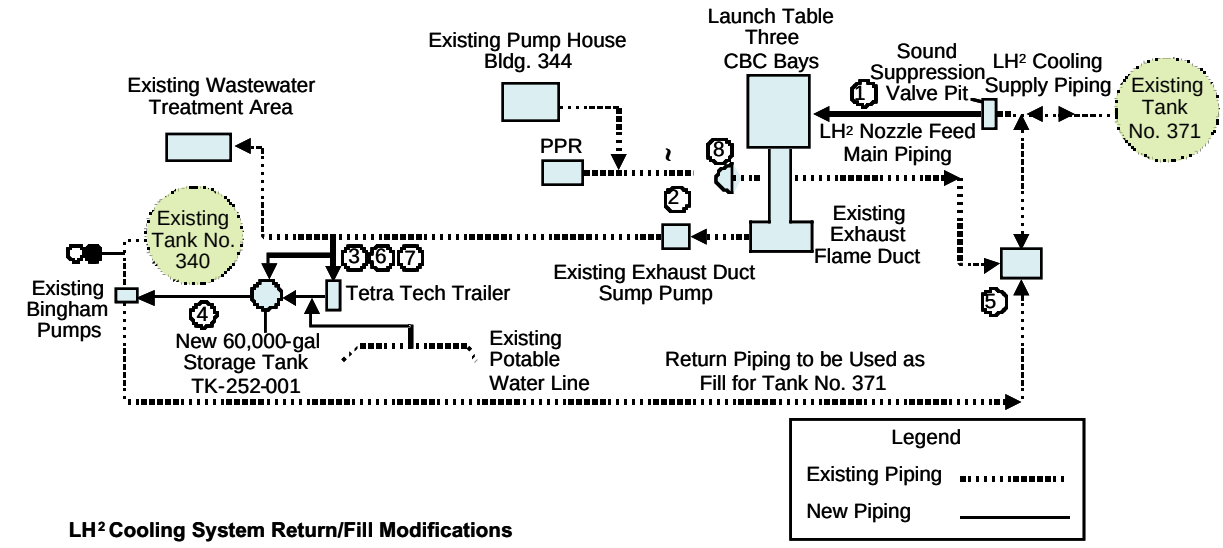

LH² Cooling System Return/Fill Modifications

(1) Valve Pit Modification: Add new control valve and feed main for LH² cooling system to launch table.
Demolition work also required for existing piping in pit.

New 10-in. feed main for LH² cooling system routed inside existing piping and extending into launch table.

New LH² cooling system discharge piping and nozzles.

(2) Modify existing 150-gpm vertical sump pump.

(7)(6)(3) Tap existing 4-in. recycle line for new feed main to Tetra Tech trailer.
New 4-in. bypass line around Tetra Tech trailer to new tank (TK-252-001).
New 4-in. tie-in for potable water supply to tank (TK-252-001).
New Tetra Tech trailer parked adjacent to waste treatment area.

(4) New 60,000-gal storage tank.
New suction line to existing Bingham pumps 550-gpm.
Isolate Tank no. 340 with blind.

(5) Valve Pit Modification: Add jumper inside valve pit for Tank 371 fill line.
Remove pressure control valve and added blinds.

(8) Isolate Pump House Bldg. 344 from system.

HB2T173010

Figure 10. Interface of Old and New Piping

"dry-launch" launch vehicle, no ignition-pulse suppression water is employed, thus greatly decreasing the overall quantity of water required per launch. The deluge system for the Shuttle consisted of five 5.0-ft-diameter pipes that branched off from the 10-ft diameter header of the 400,000-gal water storage tank (see Figure 11). Because this volume of deluge capability would not be required for the Delta IV launch, these pipes were unearthed and three were cut and capped (Figure 12).

As part of the Architect and Engineering firm s design, the LWRS unit has been incorporated into the original Shuttle water installation at SLC-6. Water from post-launch wash-down will collect below the launch mount unit in the flame ducts. In the rare event of a fire on the pad, 360,000 gal of engine-cooling water will dump at a rate of 1000 to 3000 gpm, depending on the configuration of the rocket, and will collect in the flame ducts below. It is important to note that the majority of the work outlined below for the installation of the LWRS unit is required to ensure functionality of the pad engine-cooling water system.

In addition to providing pad engine-cooling water, the 400,000-gal elevated storage tank also feeds fire suppression for the hydrogen trailer fill area. In the event of a fire at this location, the released water could not be recovered, as there is no containment available to capture the discharge.

It is estimated that 62,000 gal of wash-down water will be generated per Delta IV launch. Contaminated wash-down water will be pumped via the 150-gpm pump in the flame ducts to the wastewater treatment trailer. Post-treatment water will then be pumped into a new 60,000-gal holding tank and, following, pumped back up the hill via two existing Bingham 500-gpm pumps. In the event that the water in the flame ducts is not contaminated, it will be routed

HB2T173011

Figure 11. Original Installation of STS Deluge System Piping

directly into the holding tank, passing through a particle filter in the bypass line to remove debris. From the holding tank (Figure 13), water will be pumped up the hill to the storage tank. In either case, almost all water generated during launch processes will be
recycled and re-used. If the storage capacity is available, rainwater could also be directed to the storage tank.

The planned SLC-6 launch water recycling system is an intricate melding of old STS equipment, the Tetra Tech portable treatment unit, and the new Boeing EELV installation. At the time of this writing, plans are underway to hydrostatically test the underground piping from the Bingham pumps to the facility valve pit, and the massive 10-ft-diameter underground pipe from the center of the storage tank to the same facility valve pit. This piping has been in place for over 20 years, some of which without the full benefit of cathodic-corrosion protection. Interface controls must still be installed to make all of these components work in concert. A test of the tower wash-down system must also be completed, in part to ensure that water will be directed into the flame ducts, as was originally designed, since the launch pad has changed in some areas and drainage may be affected. Finally, the actual launch of a Delta IV in October from Cape Canaveral

HB2T173012.2

Figure 12. Deluge System Piping Modifications

Air Force Station must occur, to determine what the levels of contamination and the constituents really are. When all of this is accomplished, we will be able to prove out a complete system, which will accomplish the established goals and justify the considerable amount of effort that has gone into making this con-

HB2T173013.1

Figure 13. Post-Treatment Storage Tank for the Tetra Tech Inc. LWRS

cept a reality. Successful implementation will conserve

up to 300,000 gal of potable water per year and reduce waste-handling costs by 50%. Air emissions will also be reduced because no water-transport vehicles will be required.

The first launch of a Delta IV vehicle from Space Launch Complex 6 at Vandenberg Air Force Base is scheduled for September of 2003. If all goes well, wastewater and wash-down water from that first launch will be successfully captured, contained, treated, and recycled, becoming another Boeing pollution-prevention success story.

REFERENCES

1. Water Quality ENVVEST Initiative, Implementation Overview and request for Stakeholder Comment, prepared by the 30th Space Wing with Support from Tetra Tech, Inc., 1998.

2. Industrial Wastewater Compliance Review and Alternatives Evaluation, 30th Space Wing Environmental Services at Vandenberg Air Force Base, January, 1997.

Oxygen and Breathing Air Hardware Cleaning and Verification Technique at NASA's Johnson Space Center's Neutral Buoyancy Facility

PATRICK HUDNALL
SPACEHAB / Johnson Engineering Corp.
13000 Space Center Blvd
Houston, Texas 77059-3556
Phone: 281-792-5703
Fax: 281-792-5734
Email: phudnall@ems.jsc.nasa.gov

Paul Biesinger
SAIC
Johnson Space Center
2101 NASA Road
Houston, TX 77058
Phone: 281-244-1906
Email: paul.h.biesinger1@jsc.nasa.gov

The Neutral Buoyancy Facility has implemented an aqueous cleaning and Surface Qualilty Monitor (SQM) verification process to clean and verify its oxygen and breathing air hardware. The SQM verification process is an accepted process that was developed and implemented at the White Sands Test Facility (WSTF).

The aqueous process utilizes an environmentally acceptable method using silicated non-phosphate aqueous cleaners and a citric acid deoxidizer with a purified water rinse. The process cleans the various stainless steel / metal alloy hardware to 100 A levels. The verification method developed at the WSTF uses HFE-7100 as the verification fluid. The desirable characteristic of the process is that all waste is treatable and accepted by the Municipal Waste Facility. There is no hazardous waste generated.

Fatigue Crack and Porosity Measurement in Composite Materials by Thermographic and Ultrasonic Methods

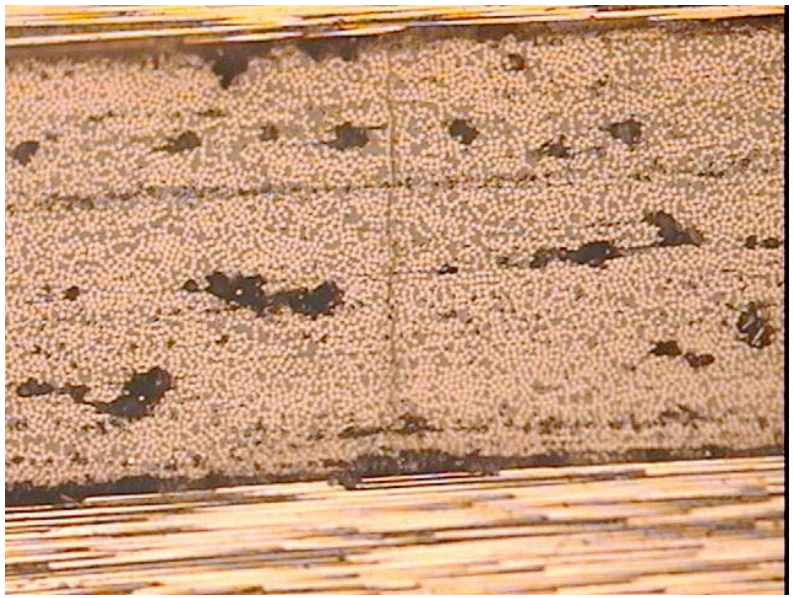

James L. Walker, Samuel S. Russell and Michael W. Suits
National Aeronautics and Space Administration
Nondestructive Evaluation Team, ED32
Marshall Space Flight Center, AL 35812
256-961-1784

Gary L. Workman
University of Alabama in Huntsville
Center for Automation and Robotics
Huntsville, AL 35899
256-824-6578

OUTLINE

- **PURPOSE**

  Detect thermo-mechanically induced intra-ply fatigue microcracking and manufactured porosity in unlined composite pressure vessels

- **DEFECT DESCRIPTIONS**

  Porosity

  Microcracking

- **THERMOGRAPHY**

  Overview of technique

  Strengths and Weaknesses

  Examples of its use for porosity detection

- **RESONANT ULTRASOUND SPECTROSCOPY**

  Overview of technique

  Strengths and Weaknesses

  Examples of its use for microcracking detection

- **CONCLUSIONS**

DEFECT DESCRIPTIONS
(Porosity)

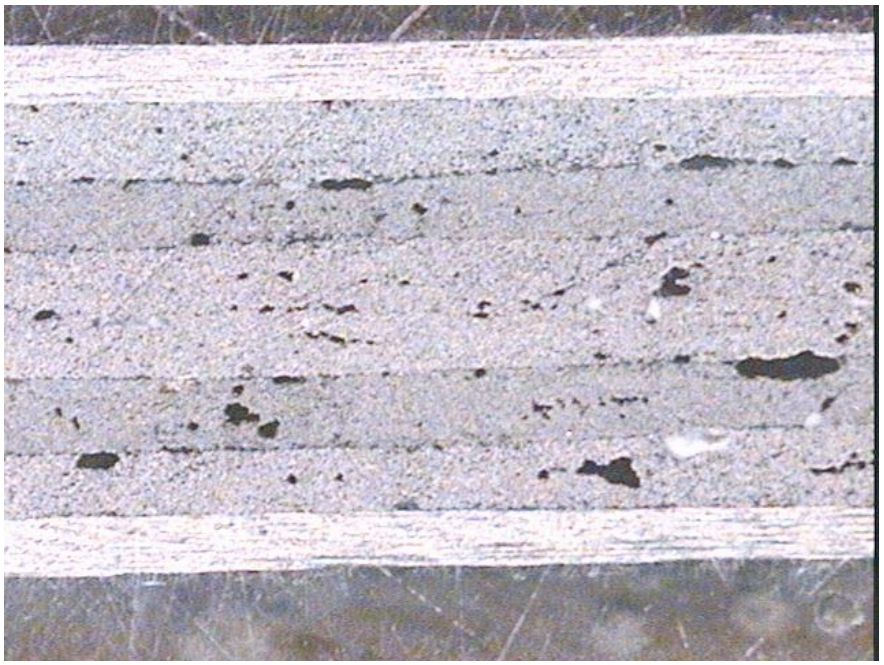

<u>Cause/Definition:</u> Voids trapped within a laminate during the curing process due to off-gassing of the resin, air trapped between plies, improper cure schedule, etc.

DEFECT DESCRIPTIONS
(Microcracking)

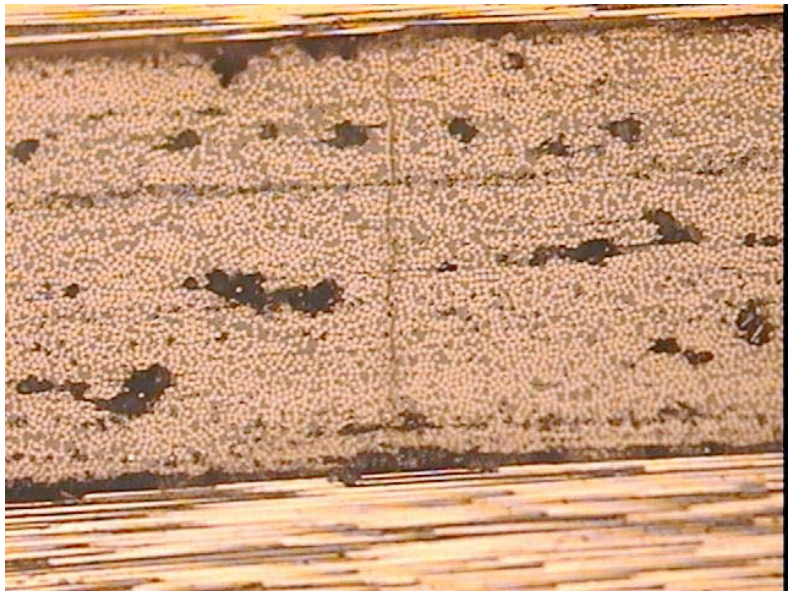

<u>Cause/Definition:</u> Cracking of the resin used to support the fibers in the laminate due to combined thermal "cryogenic" and mechanical loading.

THERMOGRAPHIC INSPECTION SYSTEM

- **Imager: Indigo Merlin Mid**
- **Detector => Indium Antimonide**
- **Detector resolution => 256 x 312**
- **Spectral Response => 3 - 5 μm**
- **Sensitivity => 0.025 °C NEΔT**
- **Software: ECHOTHERM® 32 (Thermal Wave Imaging, Inc.)**
- **Lens => 13 mm**

THERMOGRAPHIC ANALYSIS METHOD

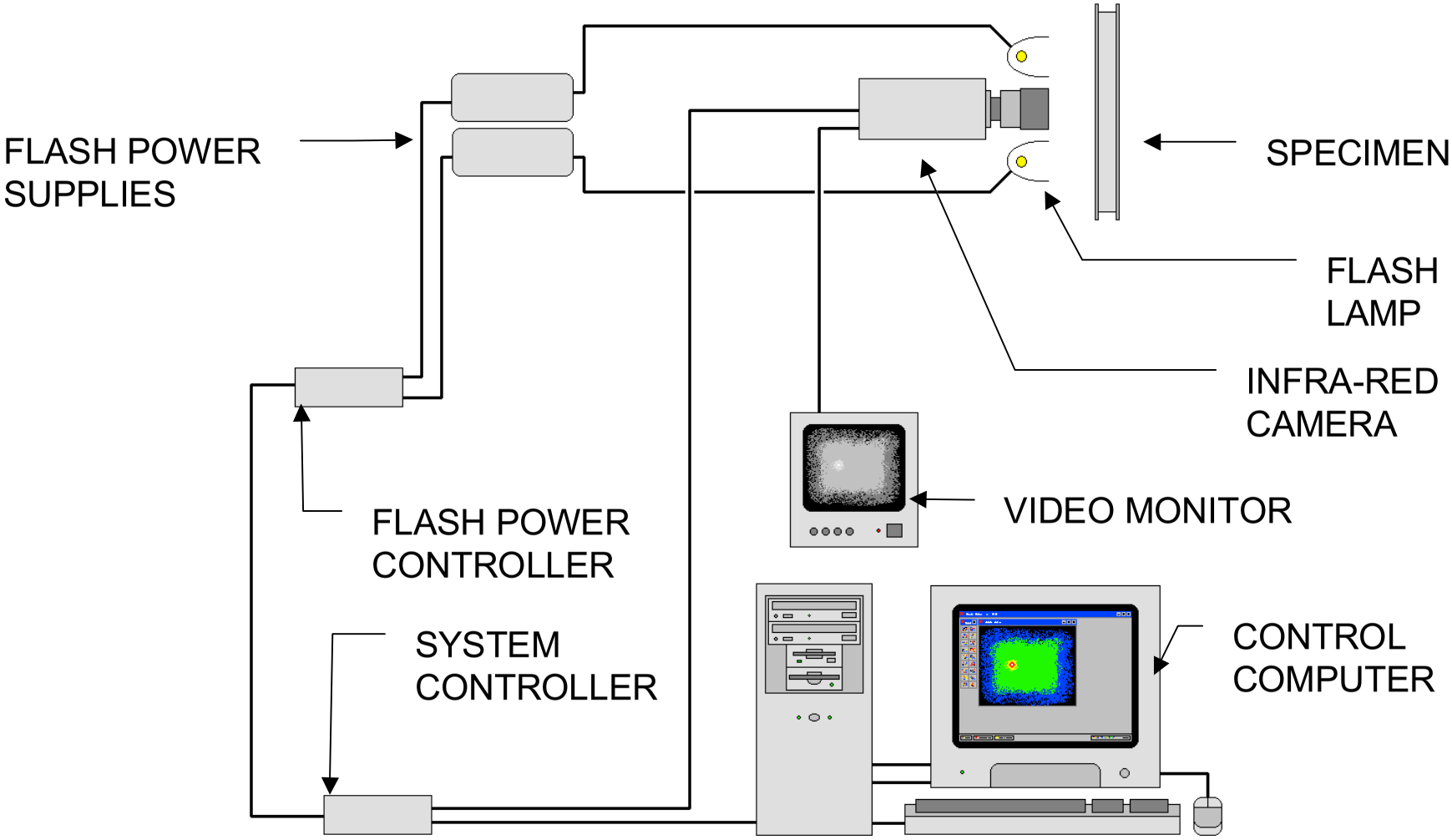

THERMOGRAPHIC ANALYSIS METHOD

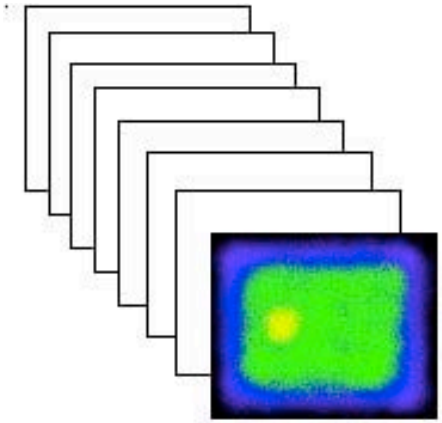

Thermography Image Sequence

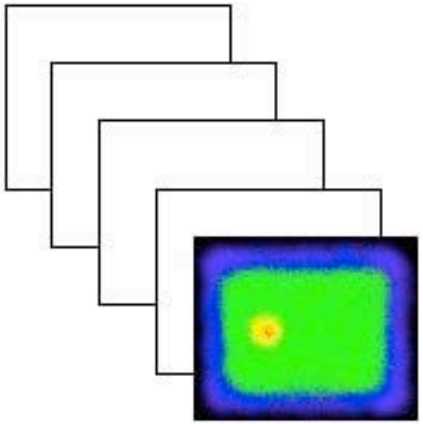

Averaged Images

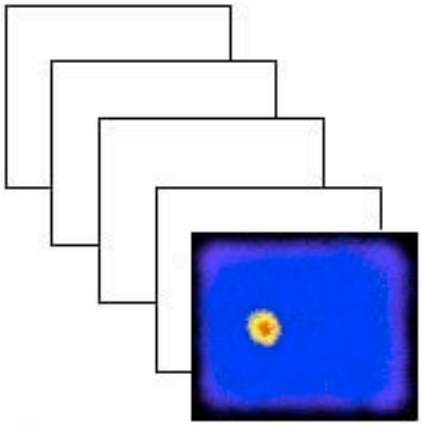

Image subtraction (Image N – Pretrigger)

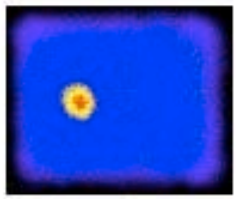

Enhanced Image

Clustered Porosity Detected Thermographically

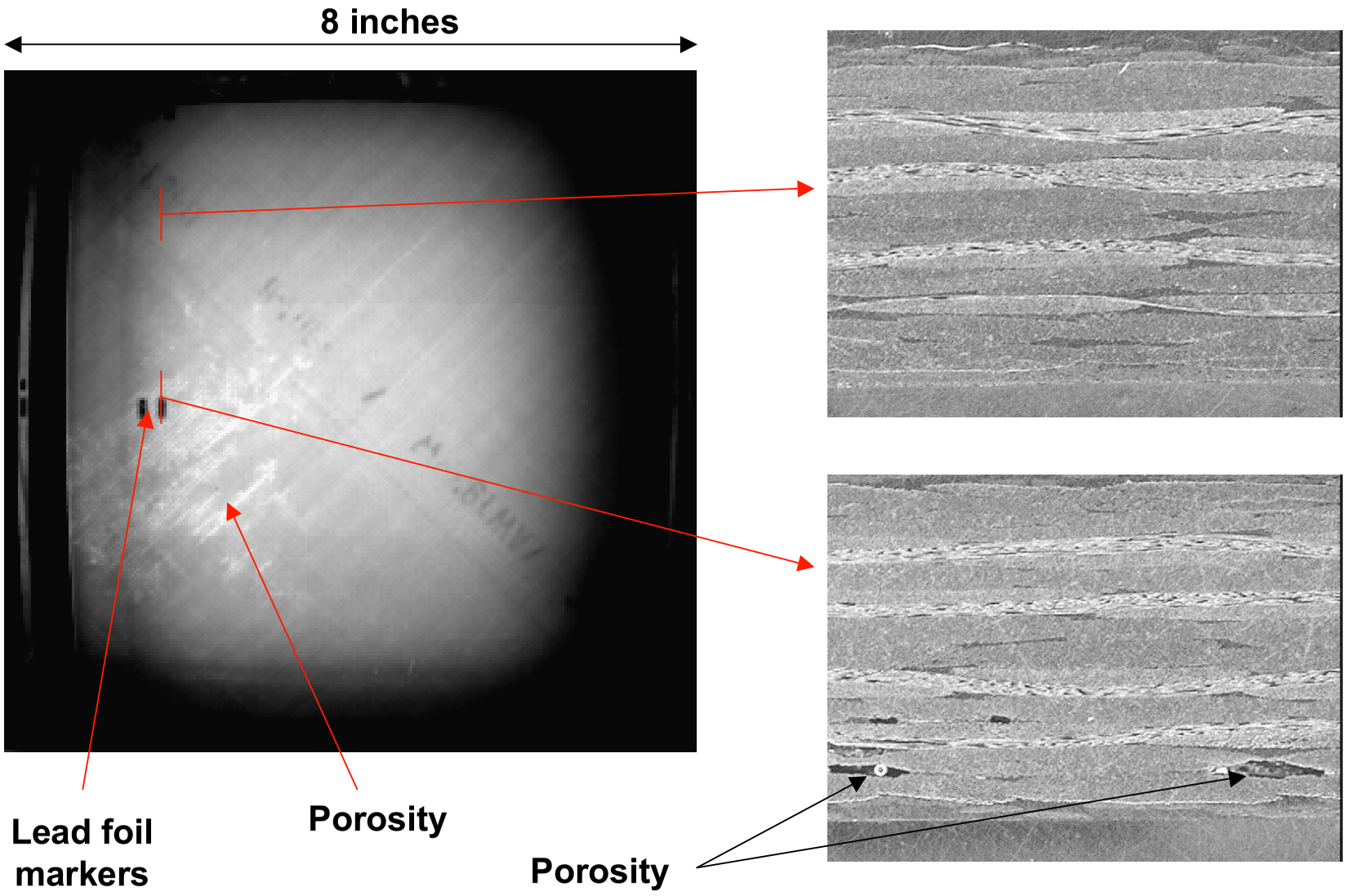

THERMOGRAPHIC MATERIAL DEGRADATION TRACKING

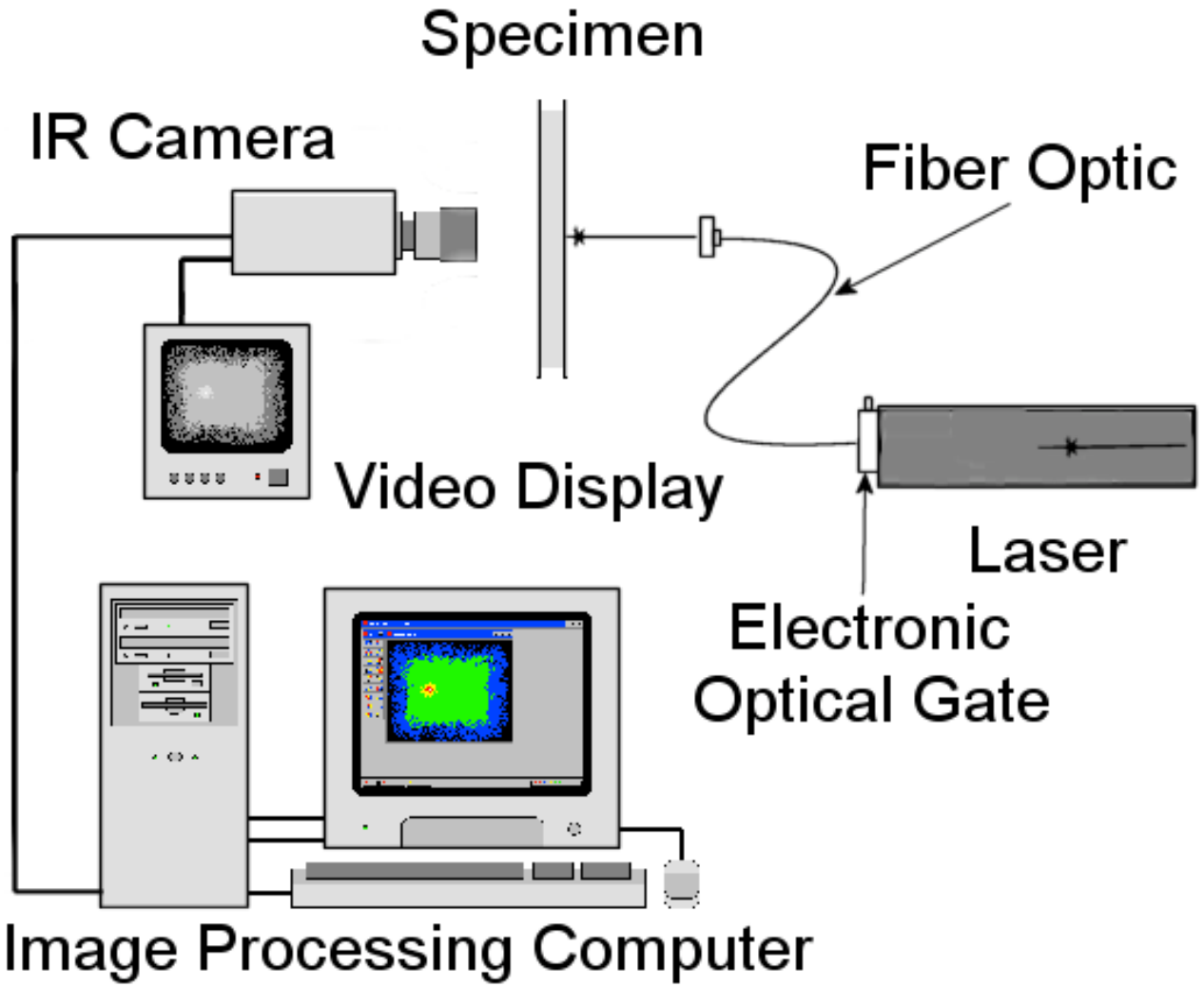

THERMOGRAPHY TREND

POROSITY IN GRAPHITE EPOXY

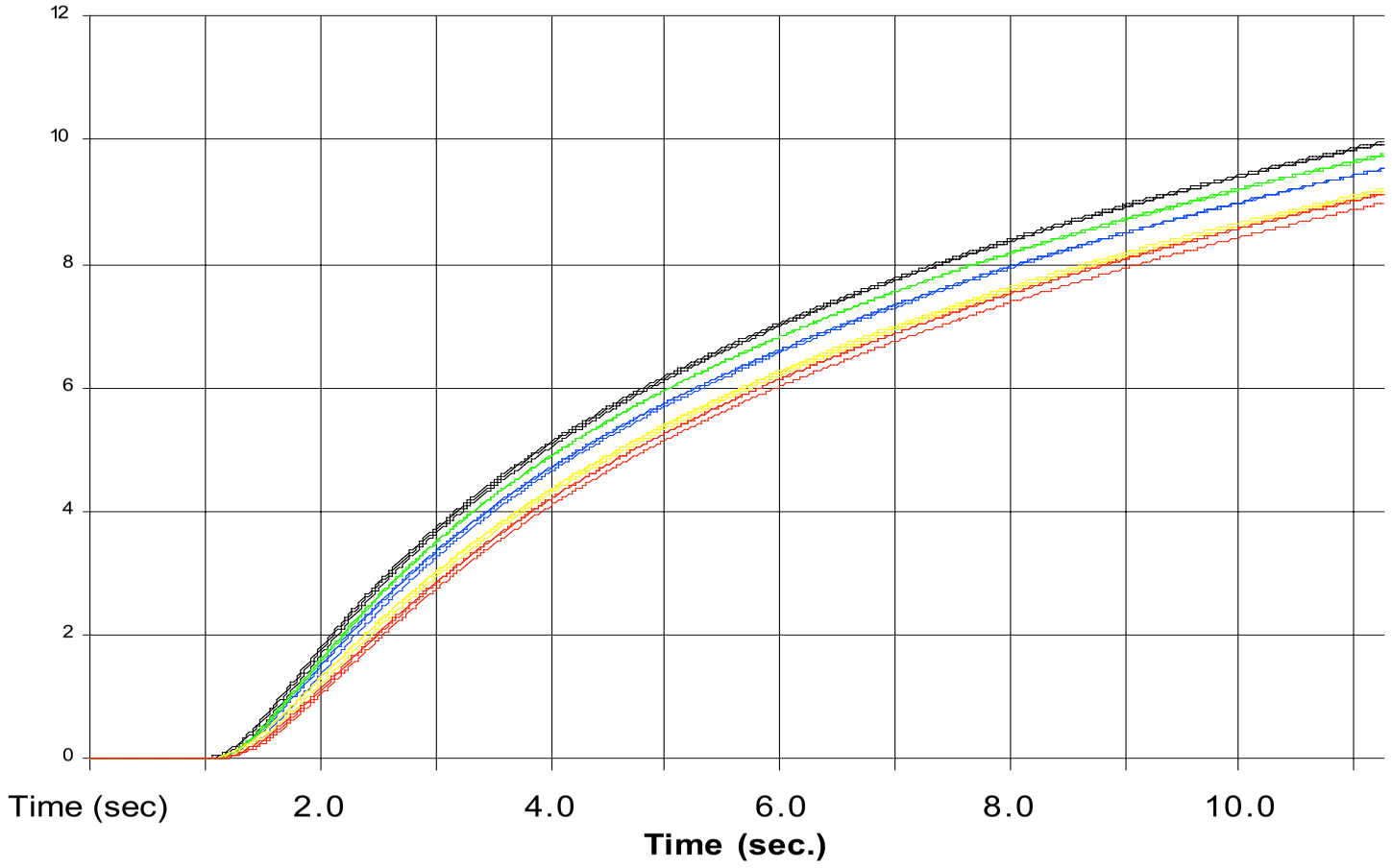

RESONANCE ULTRASOUND
(ACOUSTO-ULTRASONICS)

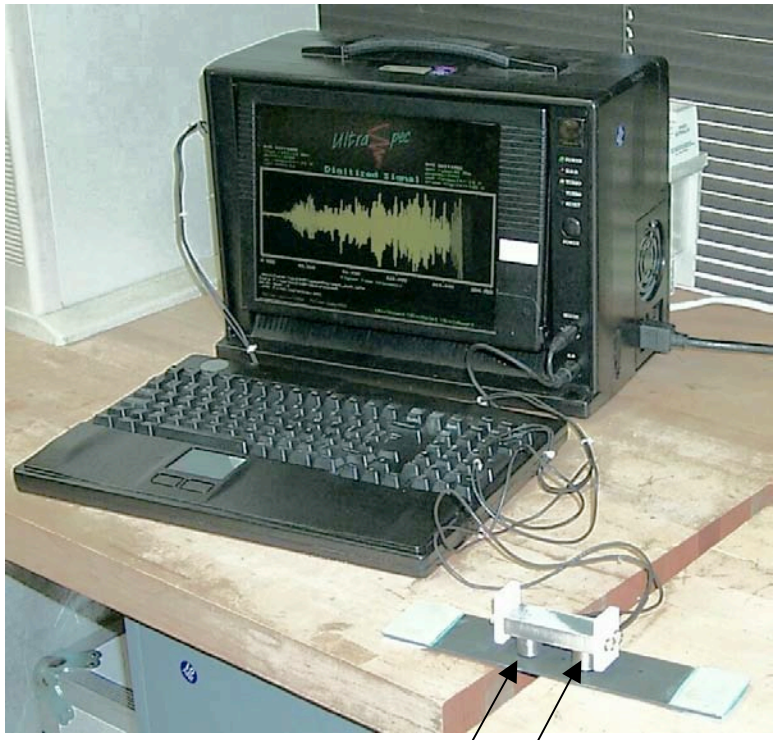

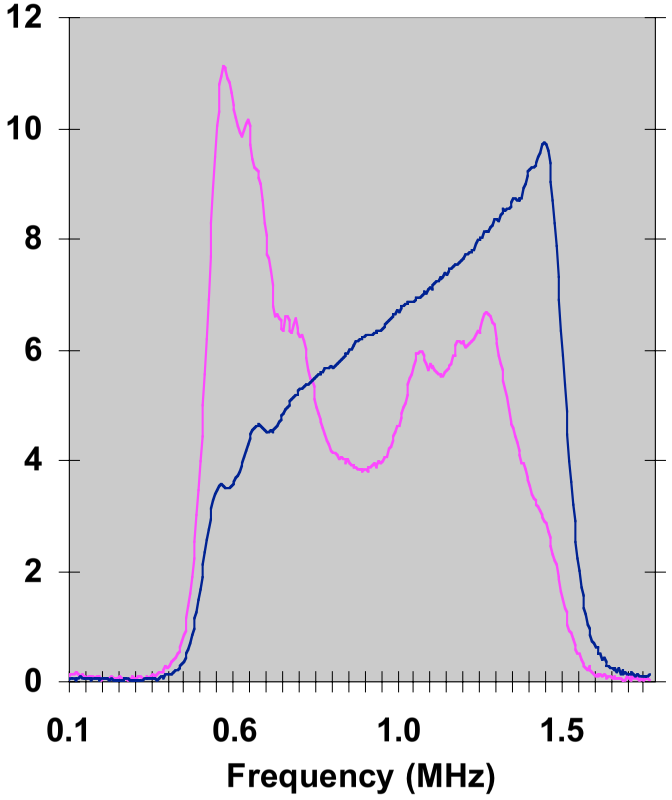

Typical Power Spectra

SAMPLE PREPARATION AND TESTING

SAMPLE PREPARATION

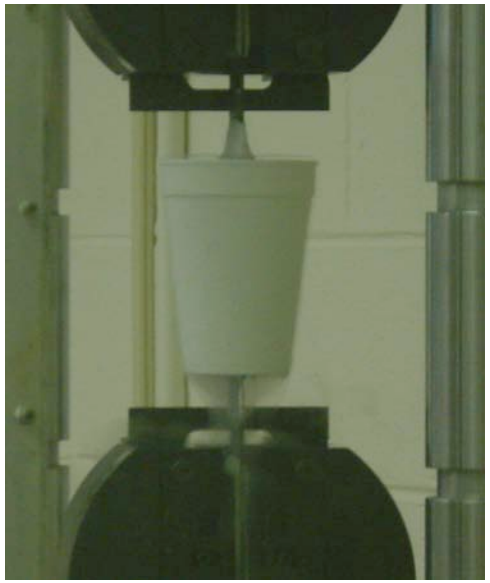

CRYOGENIC TENSILE TESTING IN
LIQUID NITROGEN

MICROCRACK COUNTING

ANALYSIS (Self Organizing Map Neural Network)

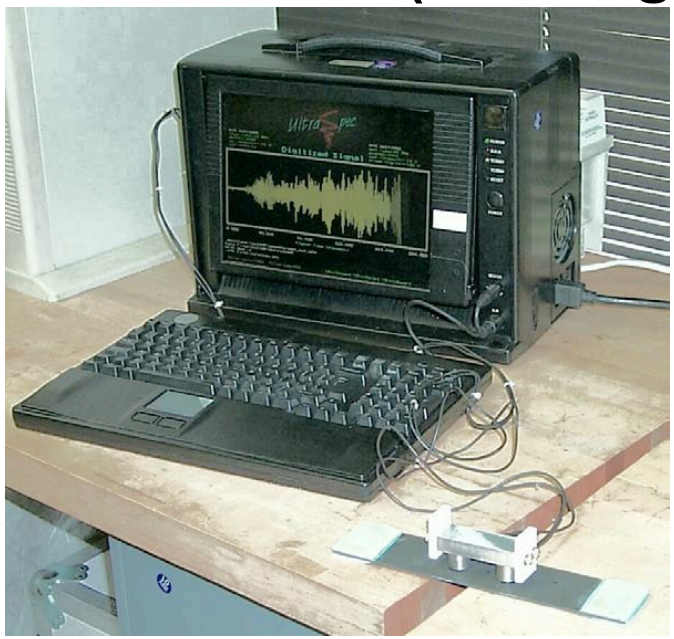

UltraSpec System

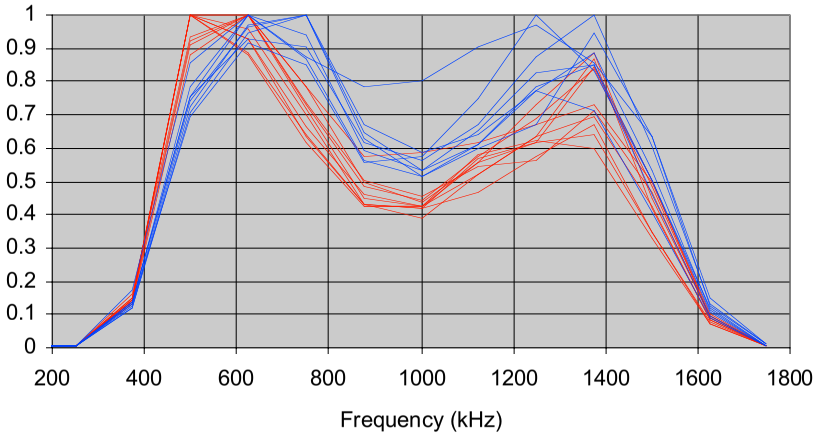

Energy distributions

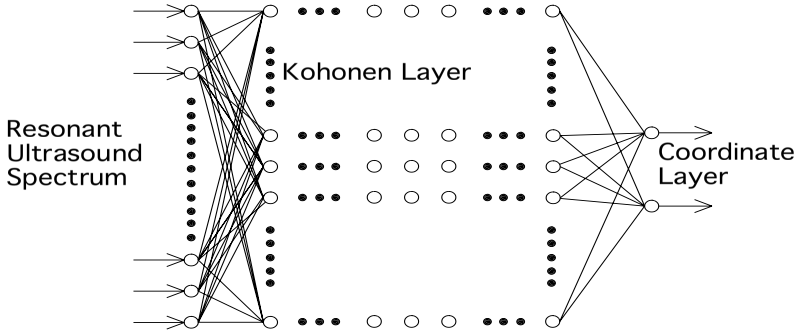

Self Organizing Map Neural Network

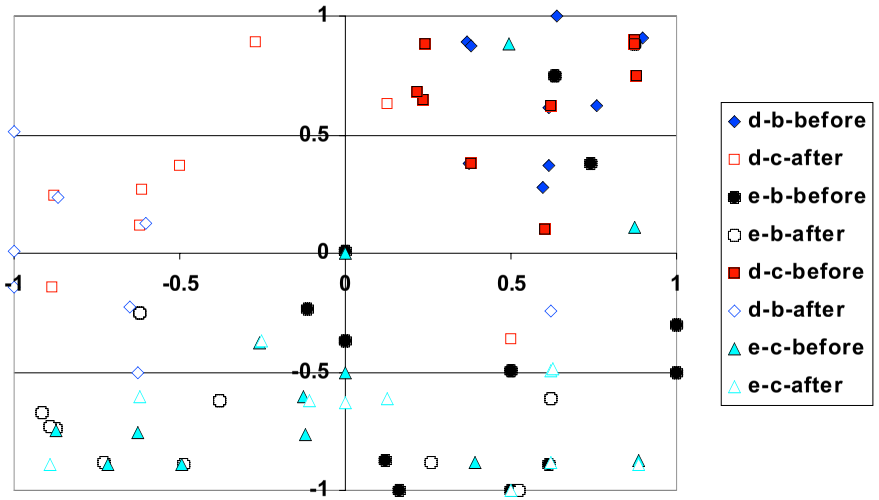

Neural Network Data Map

(0, 90, 0, 90)s SAMPLES

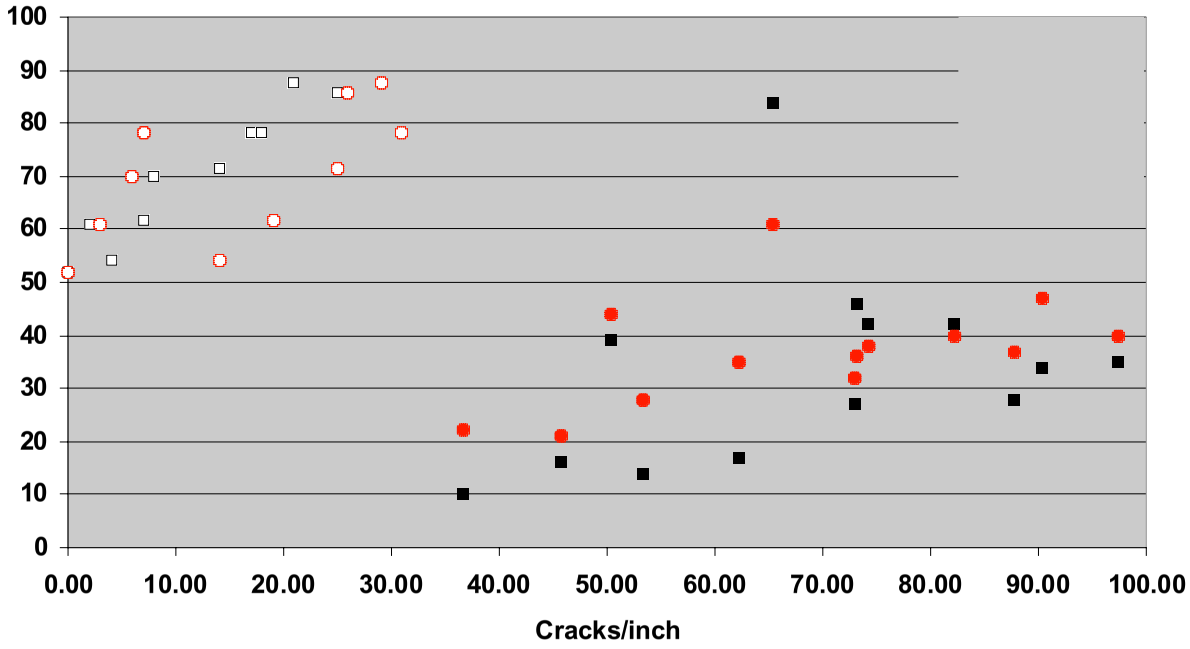

Microcrack Trend

Kohonen Map

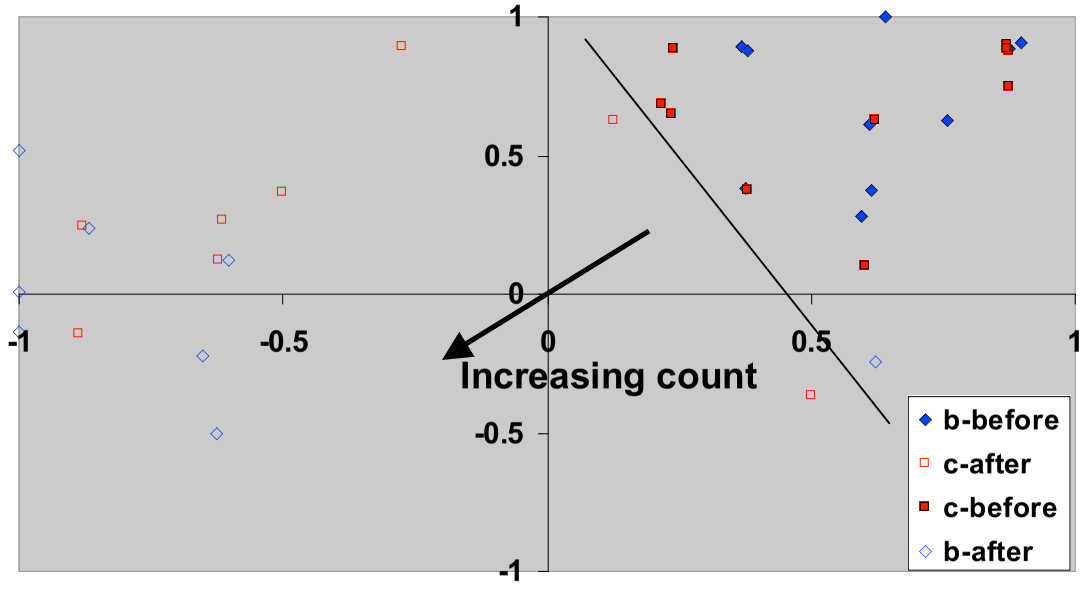

(0, 45, 0, -45)s SAMPLES

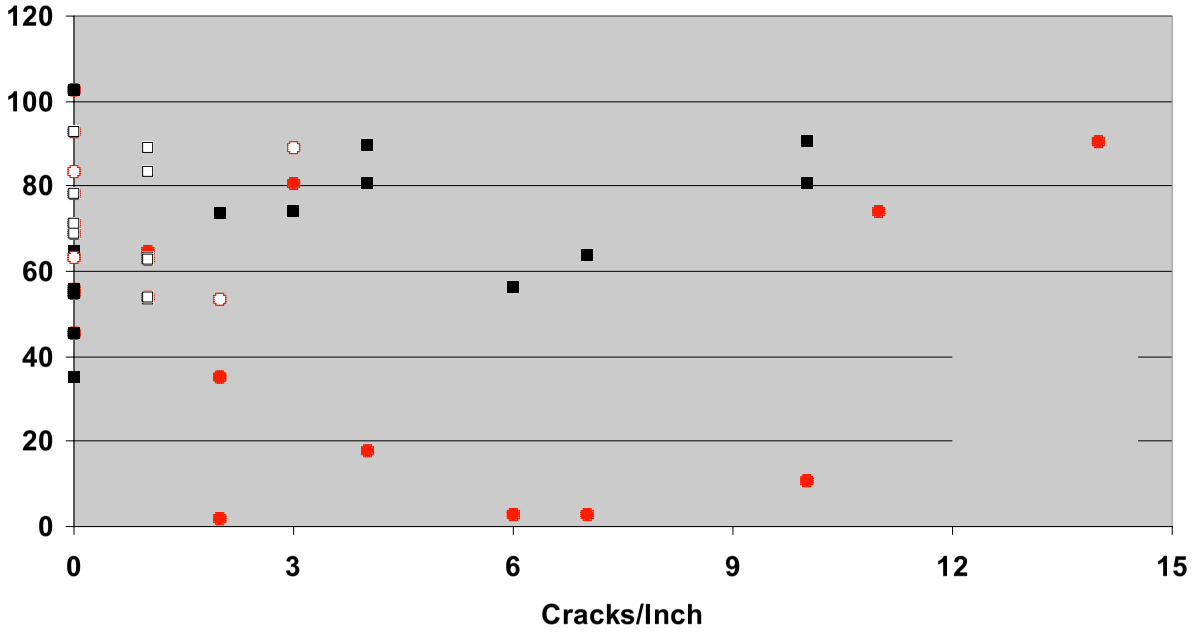

Microcrack Trend

Kohonen Map

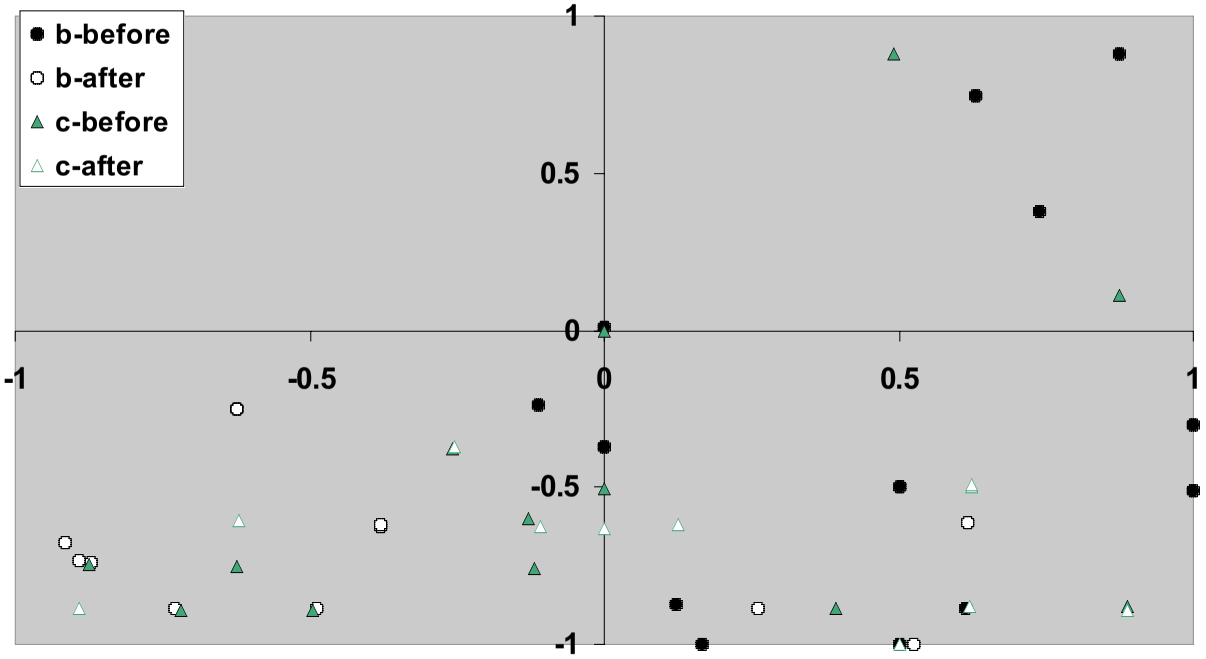

CONCLUSIONS

Thermography has been shown to be capable of detecting clustered porosity and shows promise for quantifying general porosity level

Resonance ultrasound has been shown capable of detecting the presence of microcracking

The ability to detect microcracking with resonance ultrasound is dependent upon the number of cracks present

FUTURE WORK

Validate thermographic porosity level assessment

Quantify microcrack detection

Quantitative Remaining Life Assessments for Aerospace Components Using Photon Induced Positron Annihilation (PIPA)

D. W. Akers[1], Curt Rideout[2]

[1]*Idaho National Engineering and Environmental Laboratory (INEEL), Bechtel, LLC*
P.O. Box 1625, Idaho Falls, ID 83415-2214
[2]*Positron Systems Incorporate, 6151 North Discovery Way, Boise Idaho 83713*

ABSTRACT

A new patented technology, Photon Induced Positron Annihilation (PIPA) has been developed that can be used to measure bulk fatigue and embrittlement characteristics of aerospace components beginning at <1% of fatigue life. This technology can accurately predict remaining life to within 5% based upon PIPA measurements performed on components at any stage of their fatigue life. Minimized maintenance and surveillance requirements will be possible along with highly accurate planning for system replacements.

Positron Systems PIPA technology utilizes a patented technology for implanting positrons in bulk materials and measuring the concentration and type of defects within the material. Quantitative analyses can be performed for nanodefect concentrations, defect type and following the formation of cracks, crack growth projections for various components. This technology has numerous applications in the aerospace industry from the assessment of lap splice joints on pressure hull panels to fatigue and compressive stress release assessment on aircraft jet engine fan disks and turbine blades. Portable systems can be used for in-situ NDE measurements during aircraft maintenance periods or facility-based systems can be used to assess components already removed from service for damage assessment and research.

Keywords: positron annihilation, photo-neutron excitation, metal fatigue

Introduction

A new technology, Photon Induced Positron Annihilation Analysis (PIPA) is currently being used to assess lattice structure defect damage in aircraft components composed of aluminum, titanium and super-nickel alloys. This technology, developed at the Idaho National Engineering and Environmental Laboratory and licensed to Positron Systems, Inc., provides a new approach to assessing damage in aircraft materials. It can be at any point in the life of the component material from initial fabrication through failure to assess the current damage condition of the material at varying depths in the material up to 3 inches thick in aluminum. Further, following the formation of a crack, it can be used to assess crack propagation phenomena. Specific types of damage that have

demonstrated to be detectable include low and high-cycle fatigue, thermal fatigue, corrosion-induced fatigue, creep, and composite material damage.

As has been well documented over the past several decades [1,2,3] the positron is one of the most sensitive detectors of small defects, clusters and dislocations in materials. It is now well established that there is a correspondence between the size and type of defect and the positron lifetime and/or Doppler broadening line-shape. The methods of implanting or placing the positron deep inside a material are a little less general. Investigating the bulk thickness of 1 or 2 inches of steel throughout, for example, is not trivial. Using the natural decay of positron active nuclei such as Na^{22} with the subsequent weak interaction energy spectra a small percentage of positrons will penetrate a few millimeters beyond the surface. High energy positron accelerators on the order of 2 — 3 MeV (e.g. Pelletron) have been used with success [4] and still only penetrate a few millimeters into the material and have other issues related to the production and direction of positrons in the material. Further, these positron accelerators require a dedicated laboratory facility and extensive accelerator space.

The Idaho National Engineering and Environmental Laboratory (INEEL) working in close collaboration Positron Systems and the staff at the Idaho State University Accelerator Center has been developing methods that use gamma rays to induce positrons in-situ directly in thick material. Positron Systems designs for portable systems allow this technology to be used in a field environment for aircraft and other industrial applications. Summarized below is a description of the technology followed by results from several aircraft specific applications.

Photon Induced Positron Annihilation Analysis (PIPA)

The nuclear physics associated with high-energy photon activation analysis of materials has been understood since the 60 s. The photon activation process resulted in the production of neutron deficient nuclei during the decay process over time (minutes to several hours) that decayed and, in many cases, produced positrons. Standard textbooks [5,6**]** cover the basics of these interactions. A photon (gamma ray) that carries sufficient energy to separate a particle from the nucleus (binding energy) can eject such a nucleon (proton, neutron or α-particle) from the parent nucleus. In our case a neutron is released leaving the nucleus proton rich and unstable. The proton decays into a positron (β^+) and a neutrino (ν) returning the nucleus to a stable configuration. A typical example of practical relevance is the following:

$$_{26}Fe^{54} + \gamma\,(\sim 15\ MeV) \quad {}_{26}Fe^{53} + n$$

$$_{26}Fe^{53} \quad {}_{25}Mn^{53} + \beta^+ + \nu$$

Positrons induced within material then proceed through the normal diffusion and thermalization process. Figure 1 shows the normal thermalization process along with the positron response from an annihilation in a defect location where the measured annihilation energy will be close to 511.0 keV.

The half-life of $_{26}Fe^{53}$ due to the positron emission is 8.51 minutes (the parallel process of γ-decay has a half-life of 2.6 minutes). Many of the metallic element isotopes found in today s technological materials and alloys are amenable to such in-situ positron

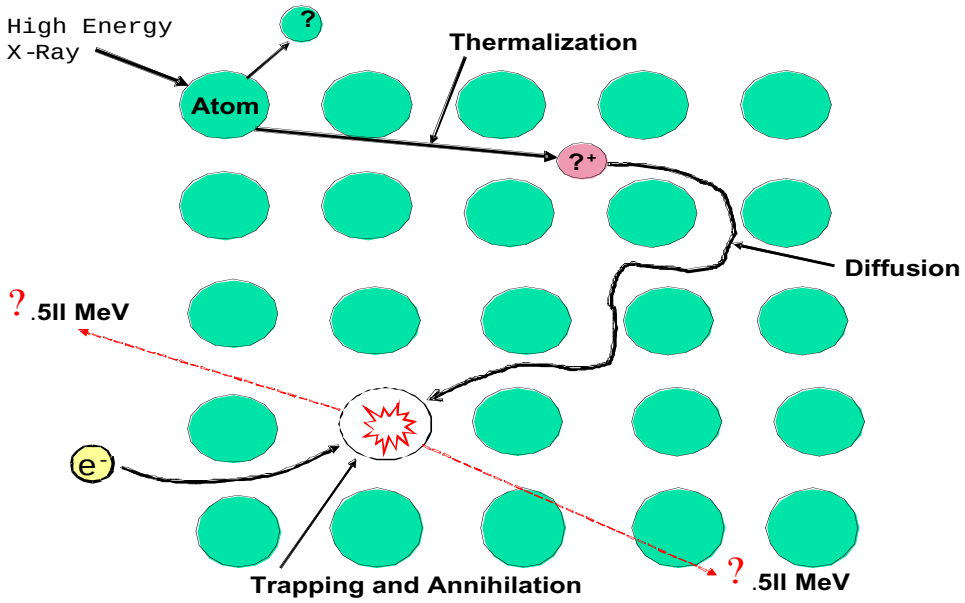

Figure 1 — Photon induction and Positron Thermalization Process

induction. Thresholds in the 10-20 MeV region are easily achievable with small electron accelerators such as those used medically for radiation therapy. Typical elements that activate easily and are relevant to the aircraft industry include copper in aluminum alloys, titanium in any alloy, iron in steel, and nickel in super-nickel alloys.

Figure 2 graphically shows the accelerator and measurement process process. Typically a sample is irradiated for several minutes to produce sufficient proton-rich nuclei in the metal for analysis. The photon beam is produced through bremsstrahlung from an accelerated electron beam that has impinged on a tungsten target. Following the nuclear excitation the sample is then examined using positron annihilation spectroscopy techniques either through lifetime measurements or Doppler broadening of the 511 keV annihilation line (one or two detector methods). Additional analysis methods suitable for field use applications have been developed through the INEEL that make it more suitable for field applications.

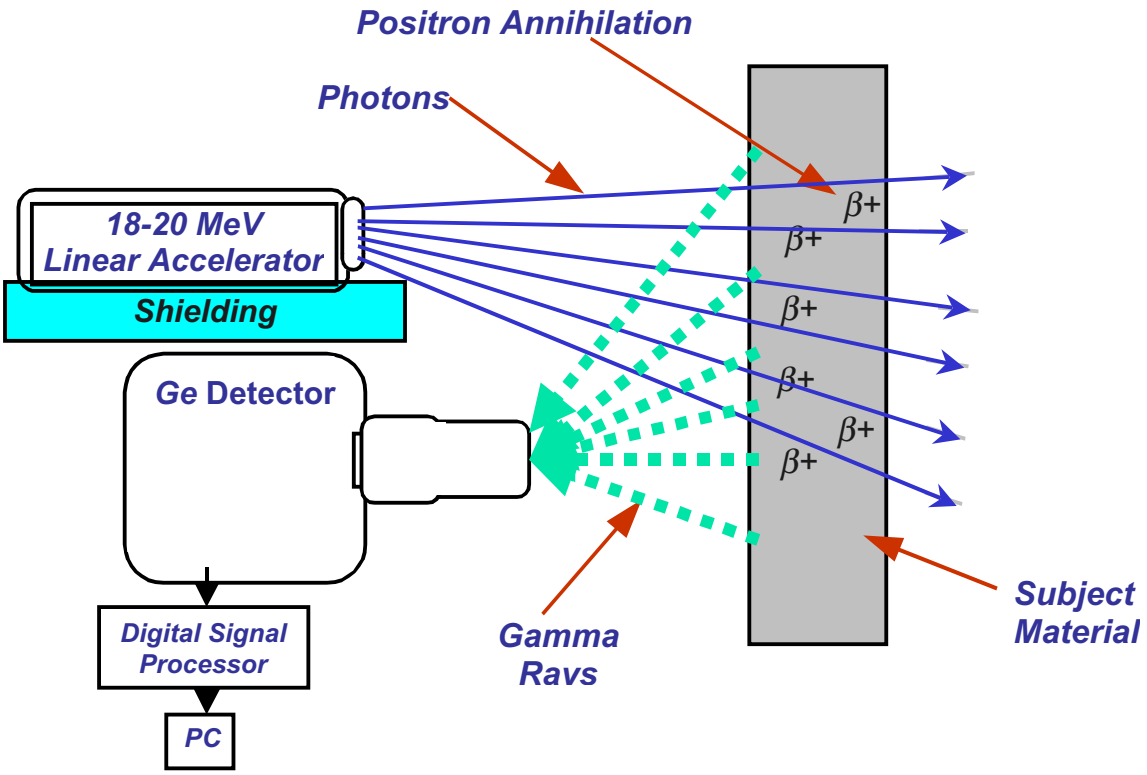

Figure 2 Basic PIPA Measurement Process

Current PIPA Aerospace Applications

Currently there are a number of aerospace applications projects underway at the Positron Systems Test and Analysis Center at the Idaho Accelerator Center. Applications research is being funded by both the military and commercial aerospace companies. Specific areas of current and potential applications development include those listed in Table 1. These applications range from fundamental alloy development through the detection of turbine blade operational damage and surface effects. Summarized below are the results for a thermal fatigue damage study in 7075-T6 aluminum, shot peening effects, and results from an assessment of second layer cracks in a wing spar.

Table 1 — Current Aerospace Applications Development Activities

- Corrosion-induced fatigue damage
- Titanium turbine blade life-cycle testing
- Reduction in lifecycle testing
- Engine parts fatigue/high cycle fatigue detection
- Composite micro cracking/fatigue/void density determination
- Oxide inclusion detection in titanium alloys
- Residual stress (shot peening) detection in surfaces
- Compressive stress impact (cold work in holes)
- New materials research to improve power to weight ratio
- Life assessment and prediction
- Failure analysis

An examination of Doppler broadening effects in heat treated aging of a high strength aluminum alloy used in the aerospace industry (Al 7075-T6) is presented. The aluminum sample contained ~1 % copper and the ^{63}Cu isotope was used to produce the positrons because of its convenient positron emitting lifetime (~ 10 minutes). After irradiation the samples were removed from the accelerator and taken into a separate room for convenient background free analysis. The positron annihilations spectrometer consisted of a single high resolution Ge detector with a well stabilized digital electronic package.

The results for the heat treated aluminum are shown in Figure 3 relating the hours in the heat aging process at 200^0C to the annihilation line widths. The positron annihilation line-shape date is plotted with the mechanical yield strength for the various treated specimens. It is known from other studies that copper precipitates form with aging from heat treatment and the formation of these is associated with the reduction in yield strength (Orowan Process). The location and type of defects are not clear at this time, however, it is known that there is a lattice mismatch between the growing Cu

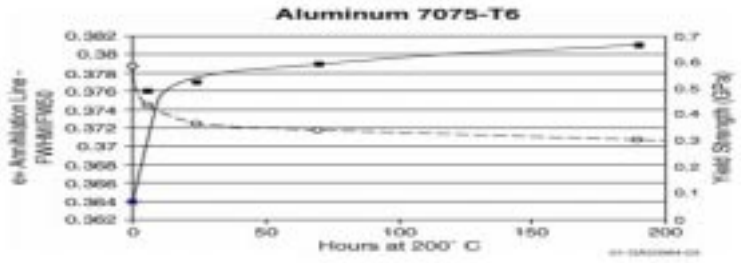

Figure 3 7075 Aluminum Thermal Damage Response

precipitates and the aluminum matrix that likely produce vacancies and associated dislocations at the interface.

Evaluations of subsurface residual stress have been performed on Almen strips to assess the capability of the PIPA technique for measuring subsurface residual stress. These data were used to assess the capability of the technique for performing damage assessments on turbine blades of various composition. The results of the turbine blade studies are not included in this paper as they are company proprietary. Figure 4 shows a blank Almen strip and a strip that was shot- peened at 100 psi. The surface of the blank strip shows surface mottling that may was likely removed from the surface of the shot-peened sample by the shot-peening process. Both bulk and surface PIPA measurements were performed on the Almen strips. The bulk measurements were performed to assess the

Figure 4 Blank and Shot Peened Specimen

effect of shot peening on the bulk Almen strip material and the surface measurements allow the fatigue damage on the surface of the strip to be measured to a depth of approximately 1 mm. As will be discussed, the difference between the bulk and surface results provide a measure of the volume of material in the strip that was affected by the shot-peening process.

Results of the PIPA bulk and surface analysis measurements for the Almen strip samples are shown in Figures 5 and 6. Both series of measurements indicate an increase in damage from the blank specimen through the 100 psi specimen indicating that the quantity of defects in the material increases with the air pressure (assumed) used to produce the shot peening. This would be expected as shot-peening would be expected to cause a higher concentration of defects near the surface of the material that goes down as

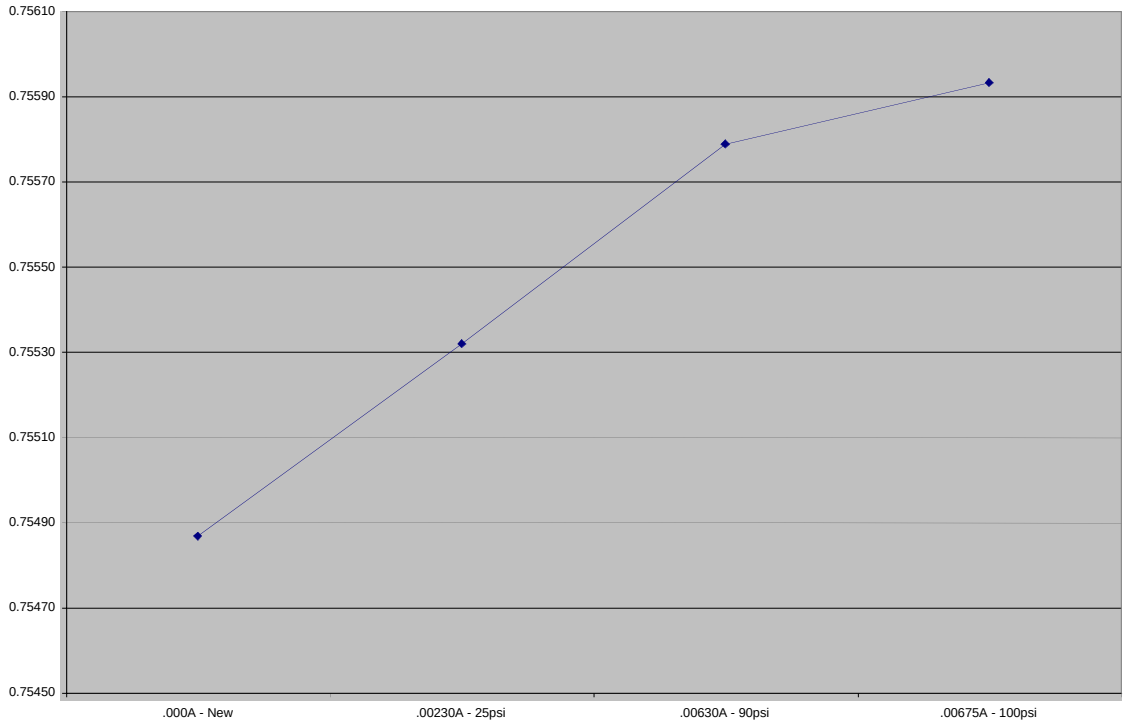

Figure 5 Bulk PIPA Analysis of Shot Peening Effects

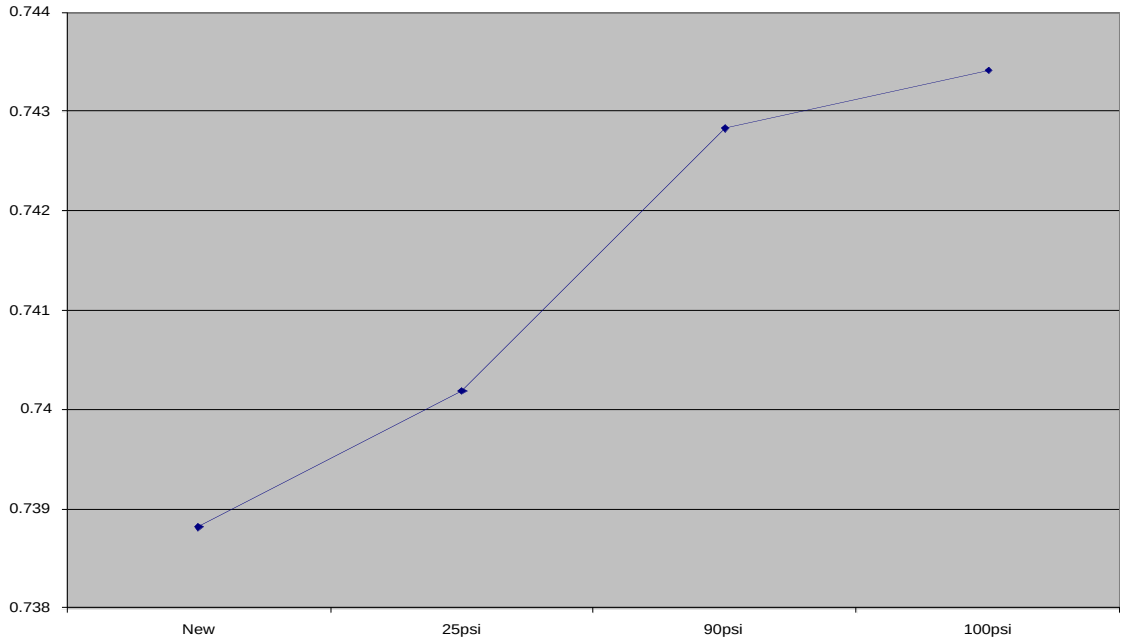

Figure 6 PIPA Surface Analysis of Shot Peening Effects

a function of the mass of material analyzed.

Figure 7 shows a case study where a second layer fatigue crack was detected through the skin of the aircraft using the PIPA technique. The fatigue crack was in the second level of the spar and was detected from the outer surface of the spar. The distinctive difference in the S parameter as compared to the undamaged locations as shown in Table 2 is due to the development of a high dislocation density around the crack location. The uncertainties associated with the data are very low as the technique is not sensitive to physical geometry, distance from the item being examined or surface effects. Systems are currently being developed by Positron Systems that will allow this examination to be performed in a field environment.

Summary

The PIPA technique (patent and patent pending) provides a new technology that can be used to assess fatigue or other types of lattice structure damage in aircraft at any point in their life. It has applications both in the early development phases of new aircraft components and engines and in the assessment of problems in aging aircraft. Because measurements can be performed at any time in the life of the component and accurate assessments of remaining life can be performed based on relatively simple calibration processes, this technology provides a way to improve new designs, increase the life of existing aircraft, and reduce surveillance and maintenance requirements. Field-portable PIPA systems are currently in the development phase and provide a means of taking this new technology to the depot level for regular assessments of existing operational

Figure 7 Exterior Surface of Wing Spar

Location	S Factor	Average —Undamaged Locations	Damaged Locations
Location #1	.6815	.6818 ± .04%	
Location #2	.682		
Location #3(Crack)	.6862		.6863 ± .02%
Location #3(Crack)	.6864		

Table 2 PIPA Response to Buried Cracks in a Titanium Wing Spar

components needed to develop new, extended surveillance requirements to the assessment of current component failures and the need for repairs.

REFERENCES

[1] P. J. Schultz, K. G. Lynn, Rev. Mod. Phys. 60 (1988) 701

[2] M. J. Puska, R. M. Nieminen, Rev. Mod. Phys. 66 (1994)

[3] R. Krause-Rehberg, H. S. Leipner, Positron Annihilation in Semiconductors: Defect Studies (Springer Series in Solid State Sciences, vol. 127) (Springer Verlag, 1991)

[4] J. H. Hartley, R. H. Howell, P. Asoka-Kumar, D. Akers, A. Denison, Proceedings of the Eighth International Conference of Slow-Positron Beam Techniques for Solids and Surfaces (SLOPOS-8), Eds. D. T. Britton, M. Harting, (Elsevier-North Holland, Amsterdam, 1999) p. 204

[5] I. Kaplan, Nuclear Physics, (Addison-Wesley, New York, 1963)

[6] W. N. Cottingham, D. A. Greenwood, An Introduction to Nuclear Physics (Cambridge University Press, 2001)

[7] B. Somieski, R. Krause-Rehberg, H. Salz, N. Meyendorf, Journal de Physique IV, 5 (1995) C1-127

[8] T. Wider, S. Hansen, U. Hozworth, K Maier, Phys. Rev. B 57 (1999) 5126

ACOUSTOGRAPHY-BASED INSPECTION OF COMPOSITES

Fifth Conference
Aerospace Materials, Processes, and Environmental Technology
September, 2002
Huntsville, AL

J. Sandhu

SANTEC SYSTEMS INC.

www.santecsystems.com

Acknowledgement

This work was supported in part by:

United States Army
Contract # DAAD17-00-C-0014

Outline

- What is Acoustography?
- Motivation
- Basic Principles
- Potential Advantages
- NDT System Development
- NDT Applications
- Summary
- Future Developments

What is Acoustography?

It is the Ultrasound analog of:

- Radiography
- Photography

Motivation

Make Ultrasonic Testing:

- Simple
- Fast
- Economical

SANTEC SYSTEMS INC.

Basic Principle – AO Sensor

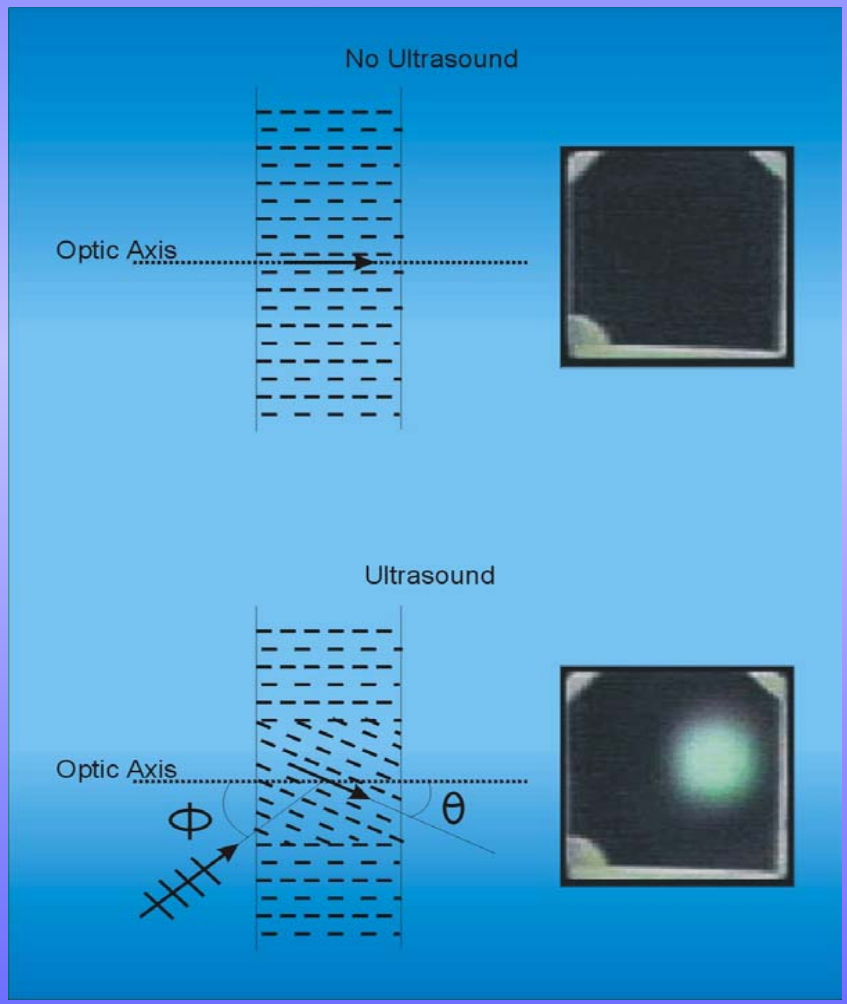

- Acousto-optic sensor contains a layer of proprietary LC material
- LC molecules reorient when exposed to ultrasound
- Ultrasonically exposed area becomes birefringent showing contrast change

SANTEC SYSTEMS INC.

Basic Principle – Image Formation

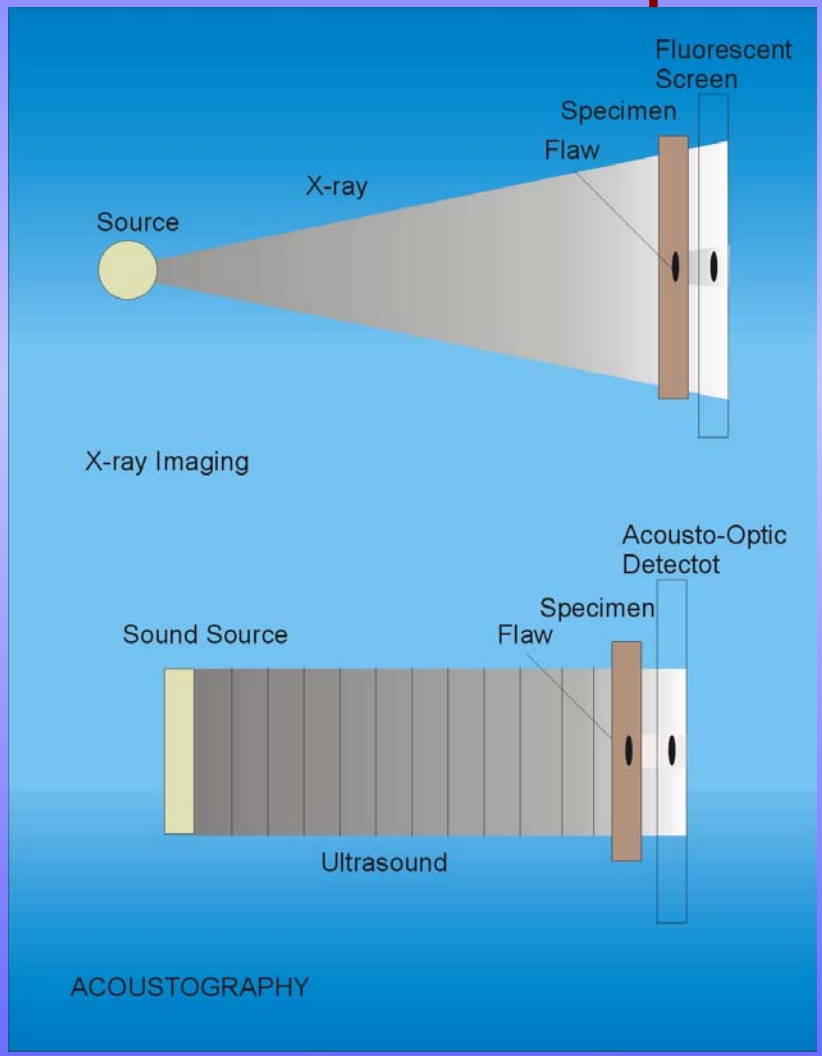

- Analogous to x-ray imaging
- AO Sensor allows near real-time visualization of ultrasound
- Resolution controlled by flaw near field length ($L \sim d^2/\lambda$)

SANTEC SYSTEMS INC.

Basic Principle – Image Formation

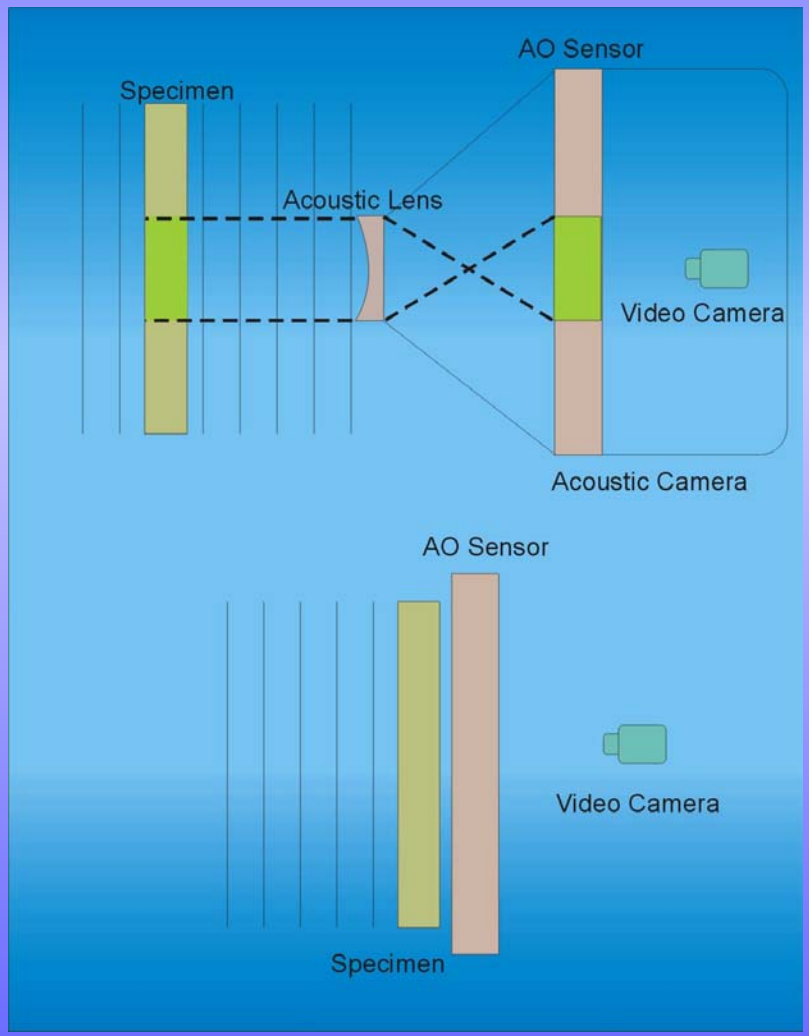

- Analogous to photography or video imaging
- Only a small portion of the specimen is imaged
- Stand-off distance needed
- Resolution diffraction limited (Rayleigh Criterion : limit of res. $1.22\lambda/2.NA$; NA~D/F)

SANTEC SYSTEMS INC.

Basic Principle – Image Formation

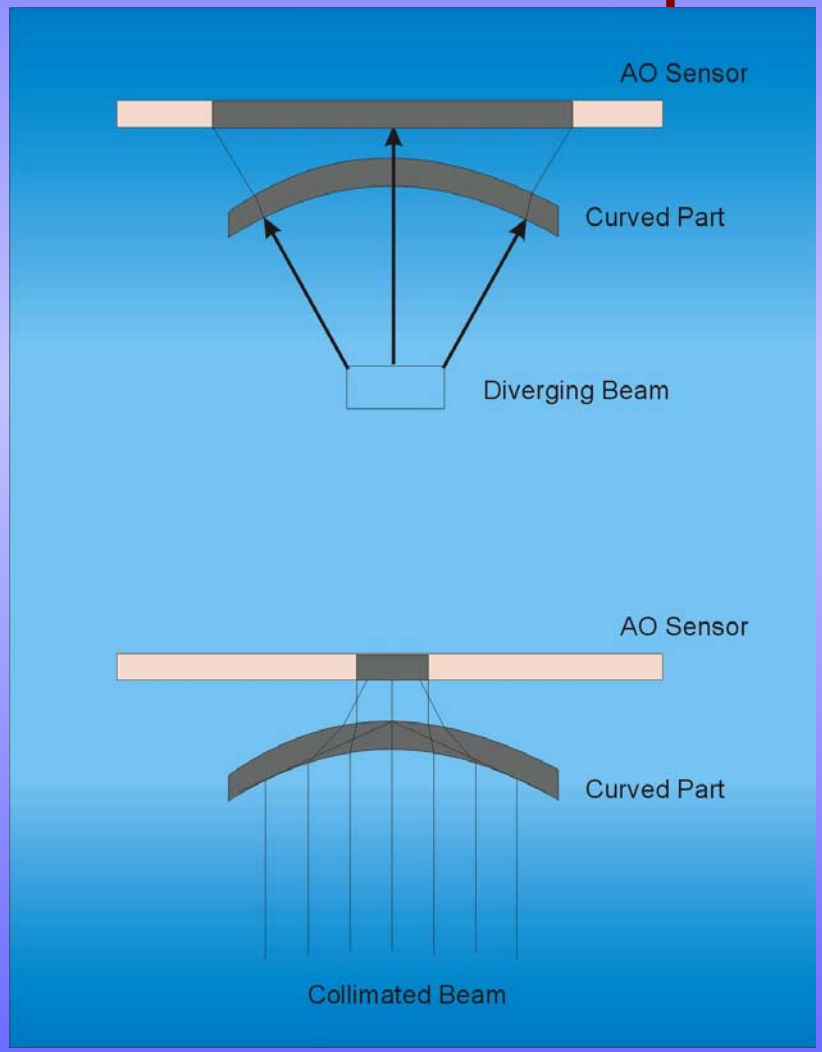

- Correct sonic illumination is important
- Refraction, mode conversion, reverberations can severely impact image quality
- Resolution controlled by ultrasound wavelength

SANTEC SYSTEMS INC.

Potential Advantages

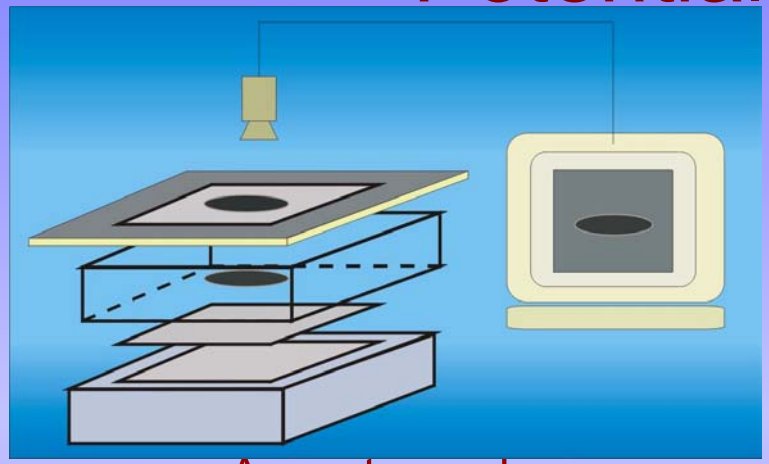

Acoustography

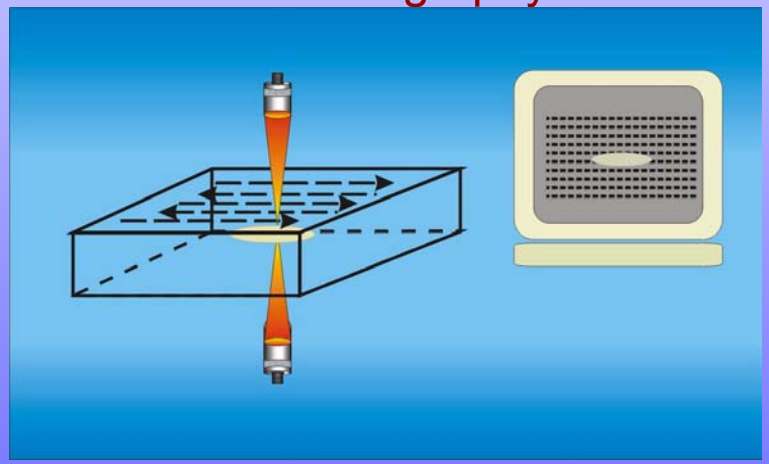

Conventional C-scan

- SIMPLE
  - -No scanning
  - -Minimal programming
- HIGH PIXEL RESOLUTION
  - -Sensing LC molecules ~20A
- FAST
  - -Full field area Inspection
  - -Instant (near real time) result
- ECONOMICAL
  - -No scanning equipment
  - -No disposables

NDT System Development

Two general concepts are being developed:

- Through Transmission Mode UT
- Single-Sided (Reflection Mode) UT

SANTEC SYSTEMS INC.

Through Transmission Mode UT

Basic Concept

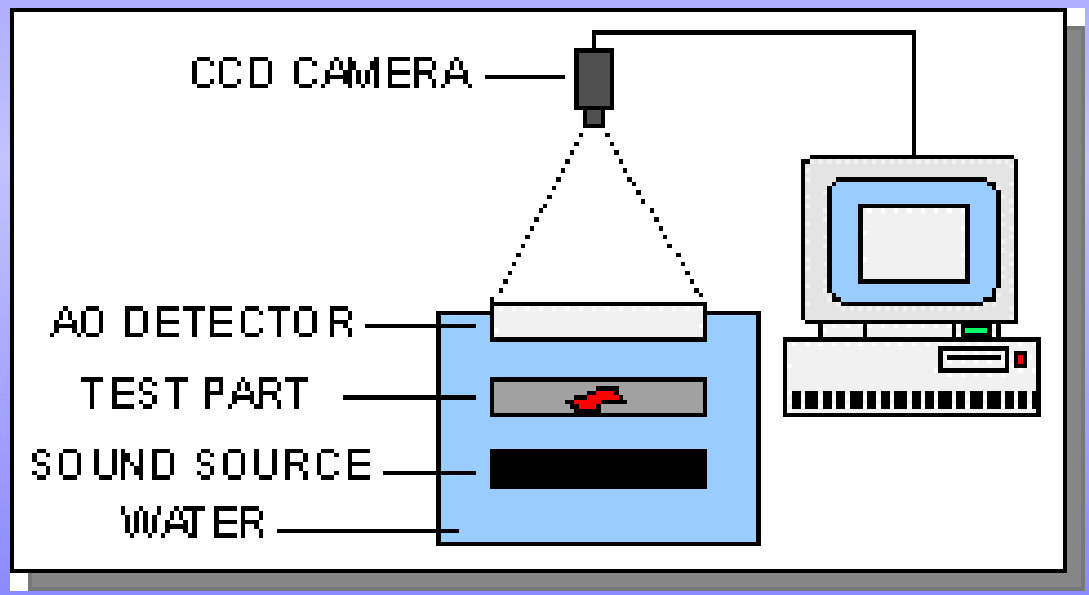

SANTEC SYSTEMS INC.

Through Transmission Mode UT

NDT System Configuration

Dedicated NDT System

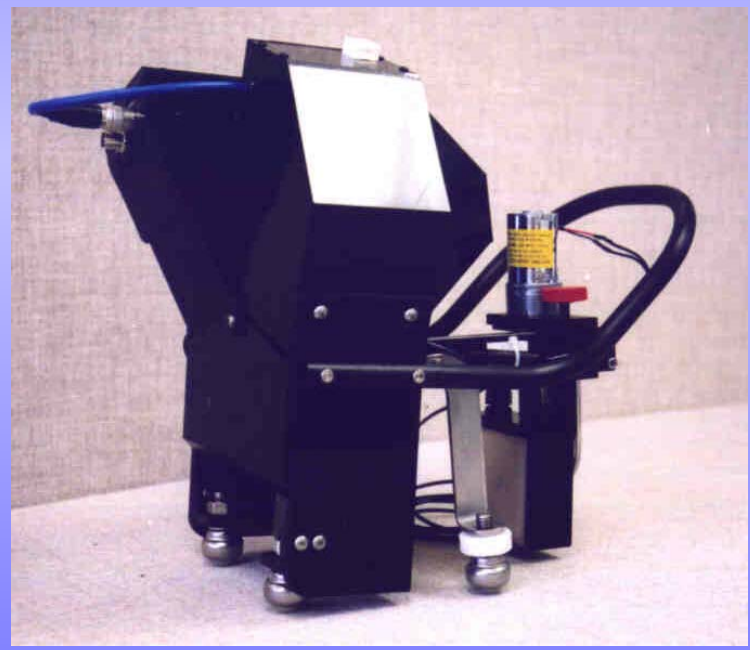

Portable NDT System

SANTEC SYSTEMS INC.

NDT Applications
Through Transmission Mode UT

Composite Standard (Inclusions)

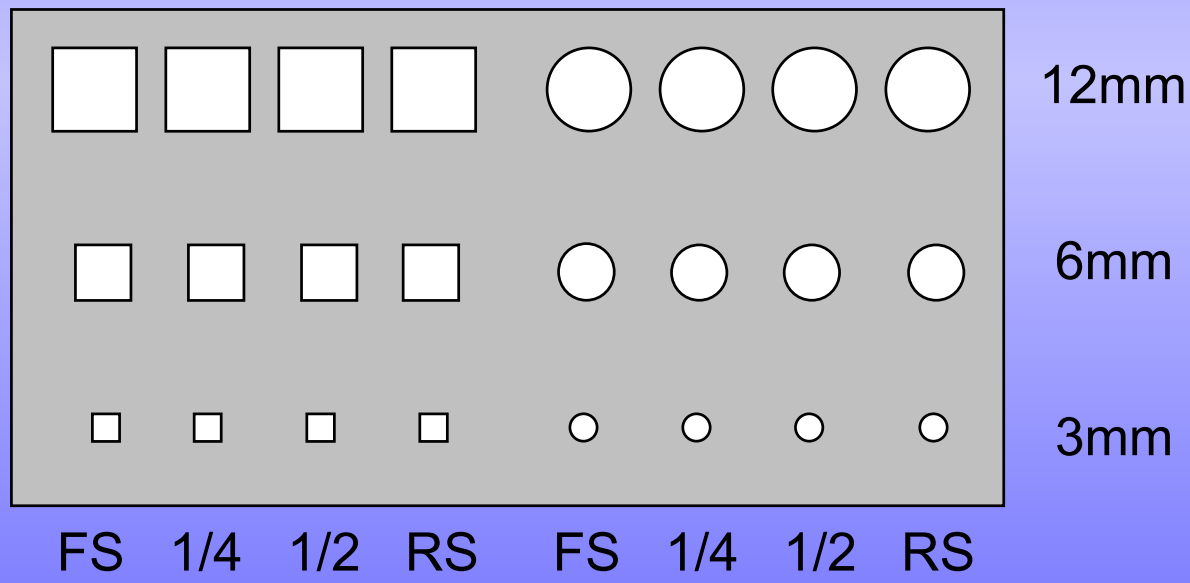

SANTEC SYSTEMS INC.

Through Transmission UT
10mm Thick Panel

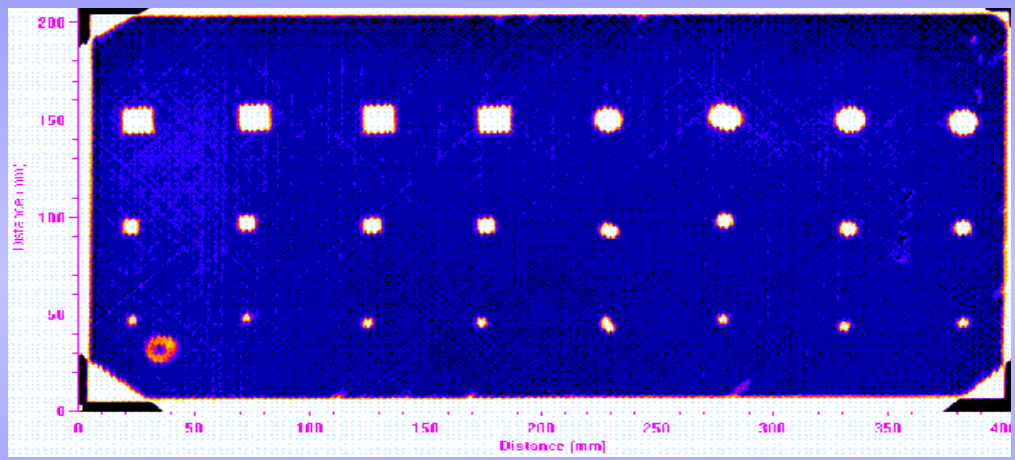

Conventional C-scan
5 MHz

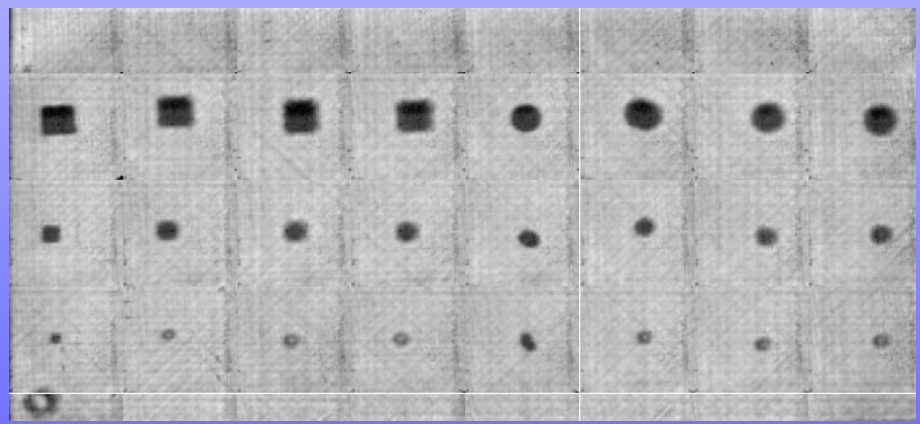

Acoustography
3.3 MHz

SANTEC SYSTEMS INC.

Through Transmission UT
40mm Thick Panel

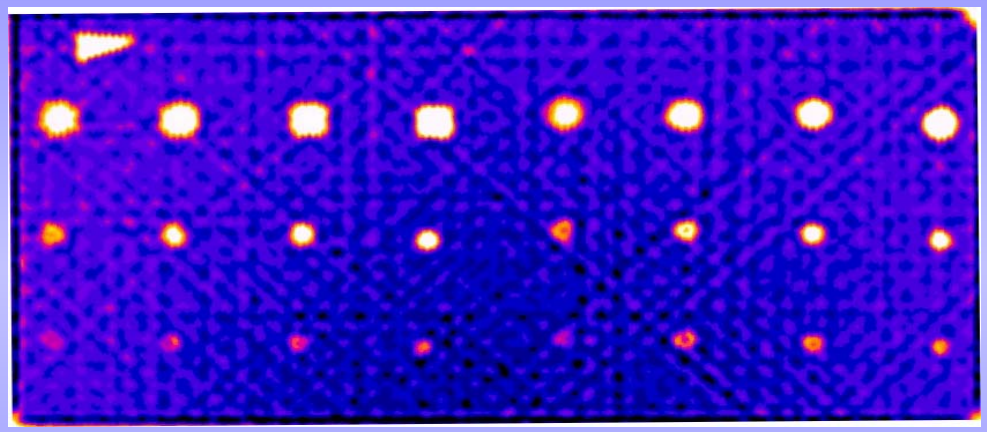

Conventional C-scan
5 MHz

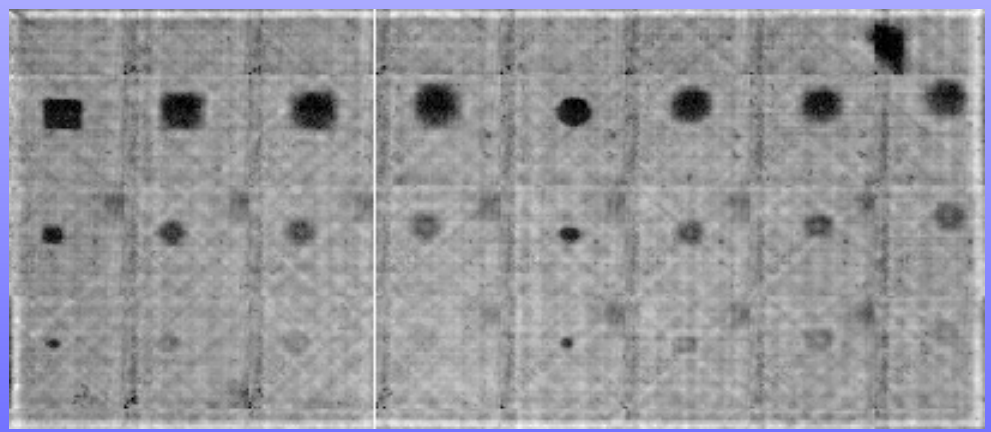

Acoustography
3.3 MHz

SANTEC SYSTEMS INC.

NDT Applications
Through Transmission Mode UT

Composite Panel (Impact Damage)

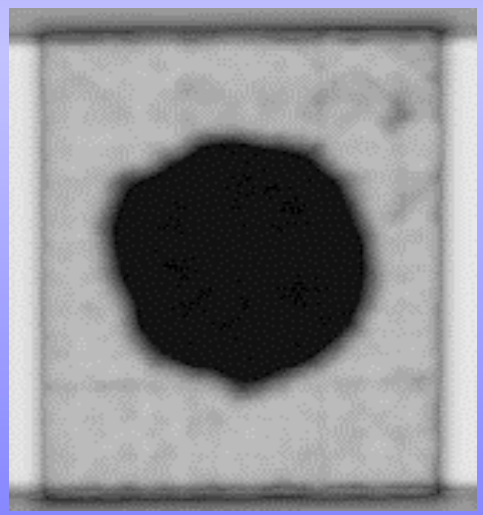

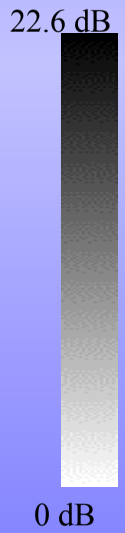

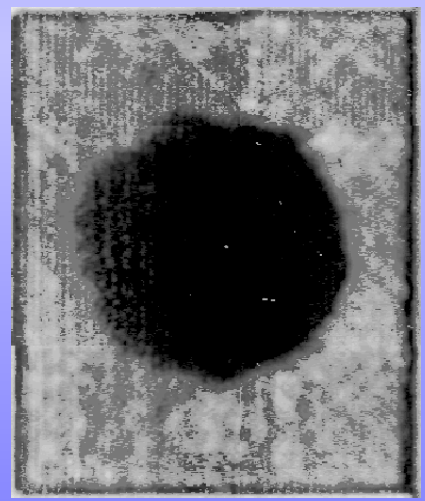

Conventional C-scan

Acoustography

SANTEC SYSTEMS INC.

NDT Applications
Through Transmission Mode UT

Tight Radii Inspection

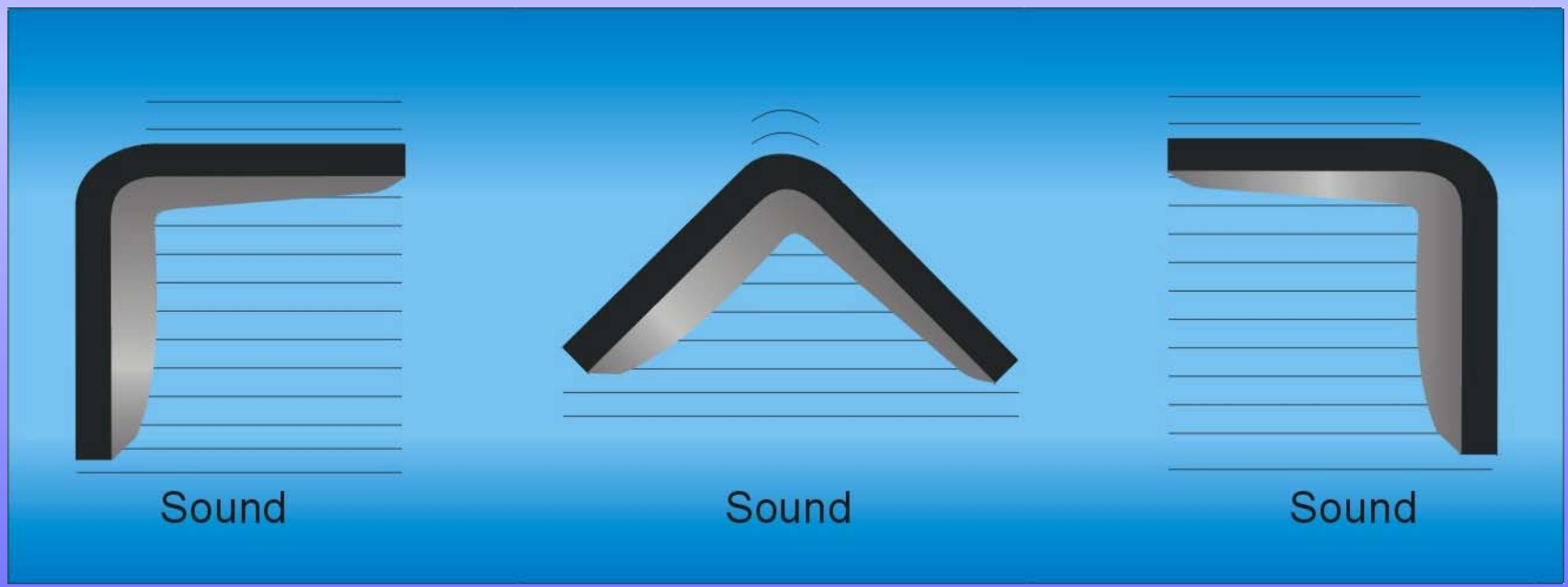

SANTEC SYSTEMS INC.

NDT Applications
Through Transmission Mode UT

Tight Radii Inspection

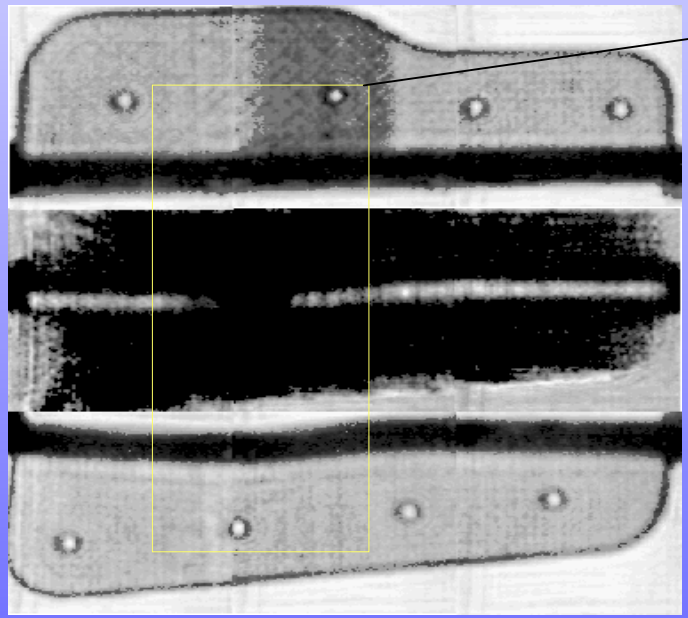

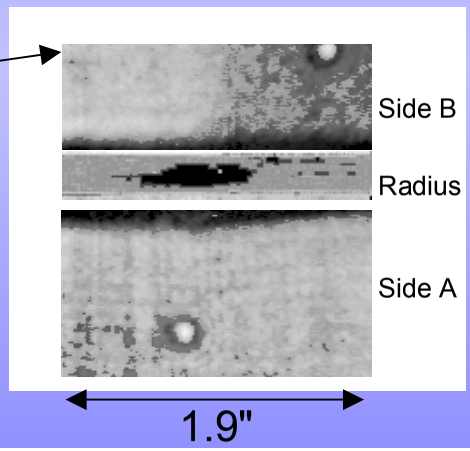

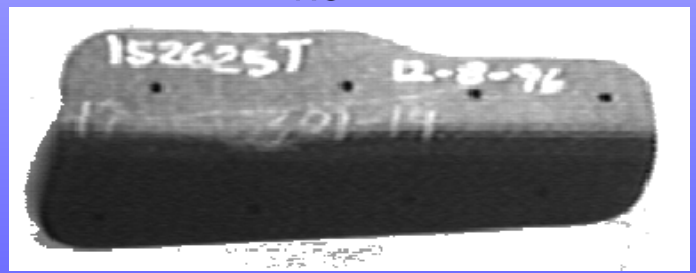

SANTEC SYSTEMS INC.

NDT Applications
Through Transmission Mode UT

Inspection of Attachments

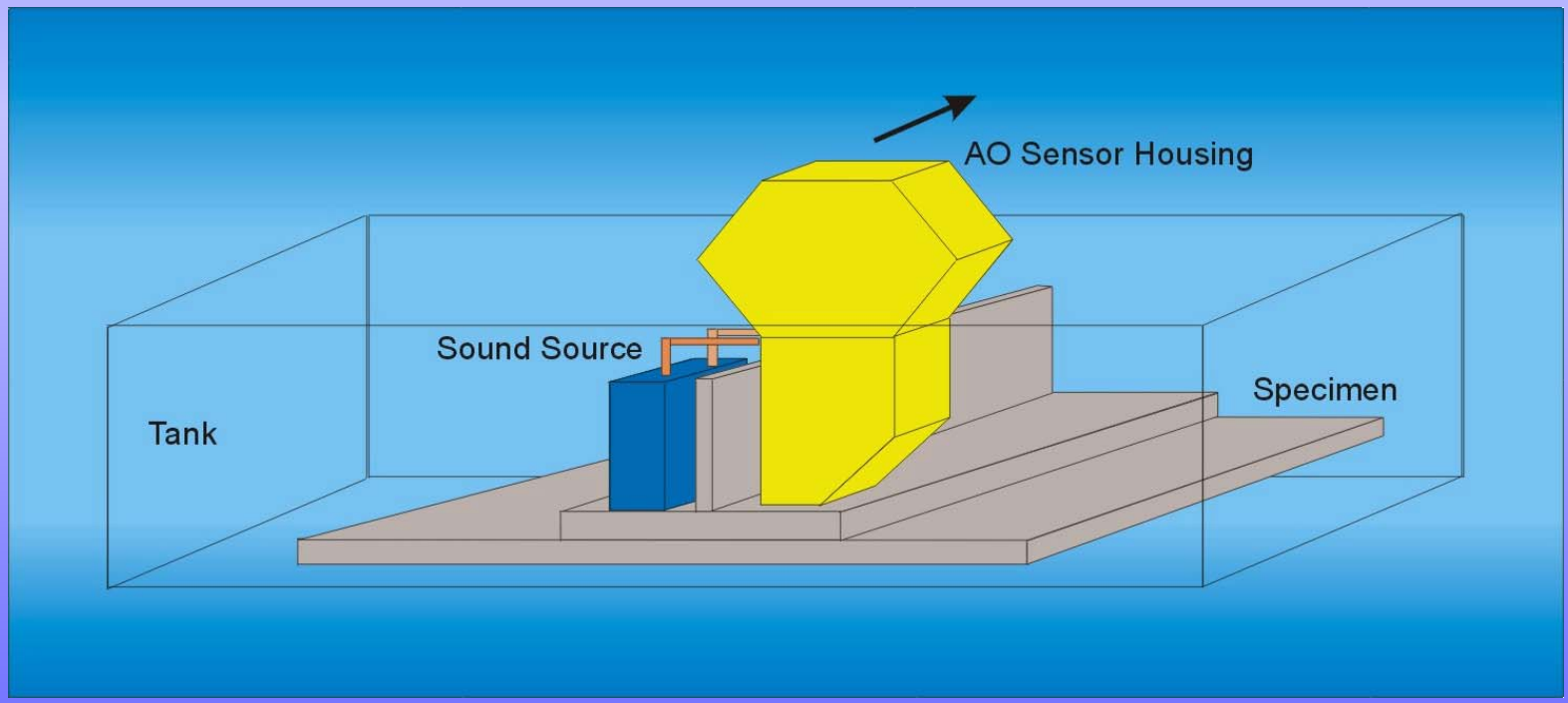

SANTEC SYSTEMS INC.

NDT Applications
Through Transmission Mode UT
Inspection of Attachments

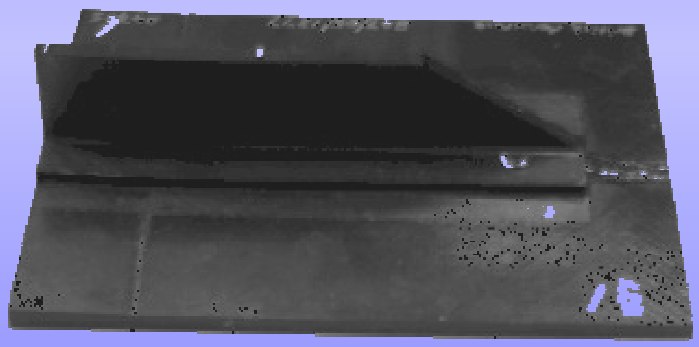

Composite Plate with
Vertical Attachment

SANTEC SYSTEMS INC.

Single Sided (Reflection Mode) UT

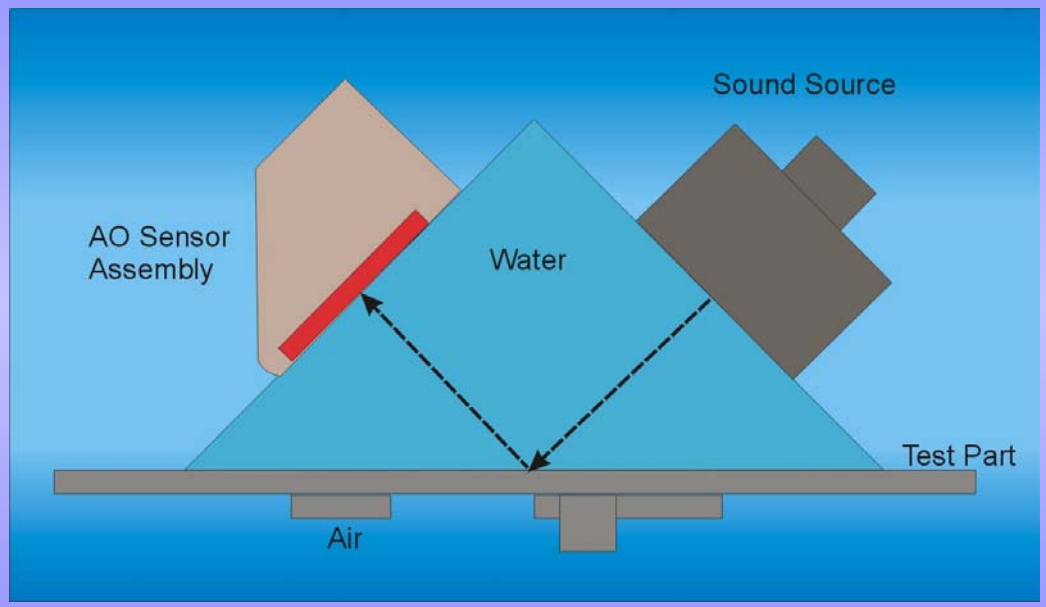

Basic Concept

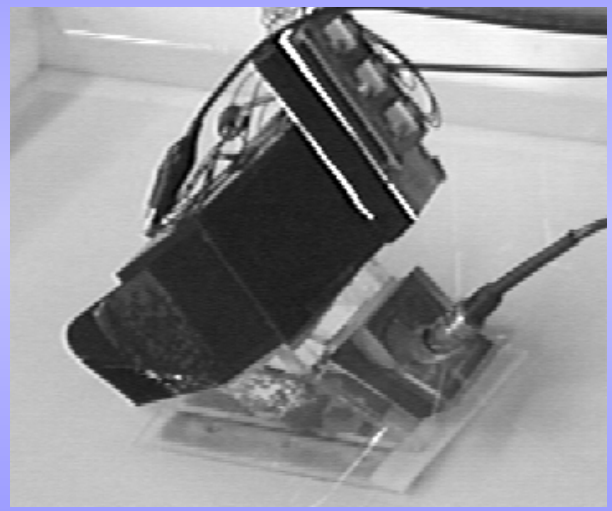

System Prototype

SANTEC SYSTEMS INC.

NDT Applications
Single Sided (Reflection Mode) UT

Plastic Test Panel Inspection

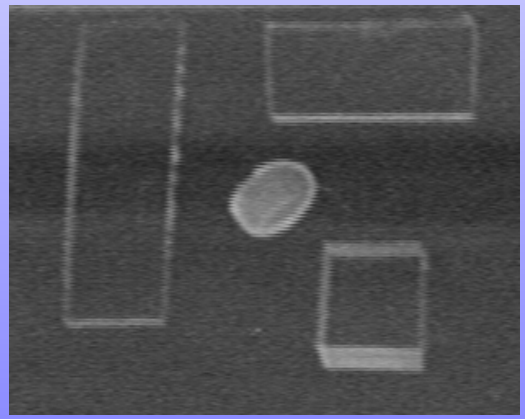

Test Panel

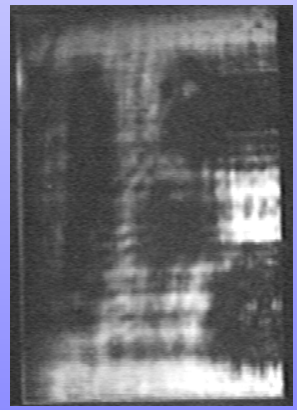

Preliminary
Acoustography Results

SANTEC SYSTEMS INC.

NDT Applications
Single Sided (Reflection Mode) UT

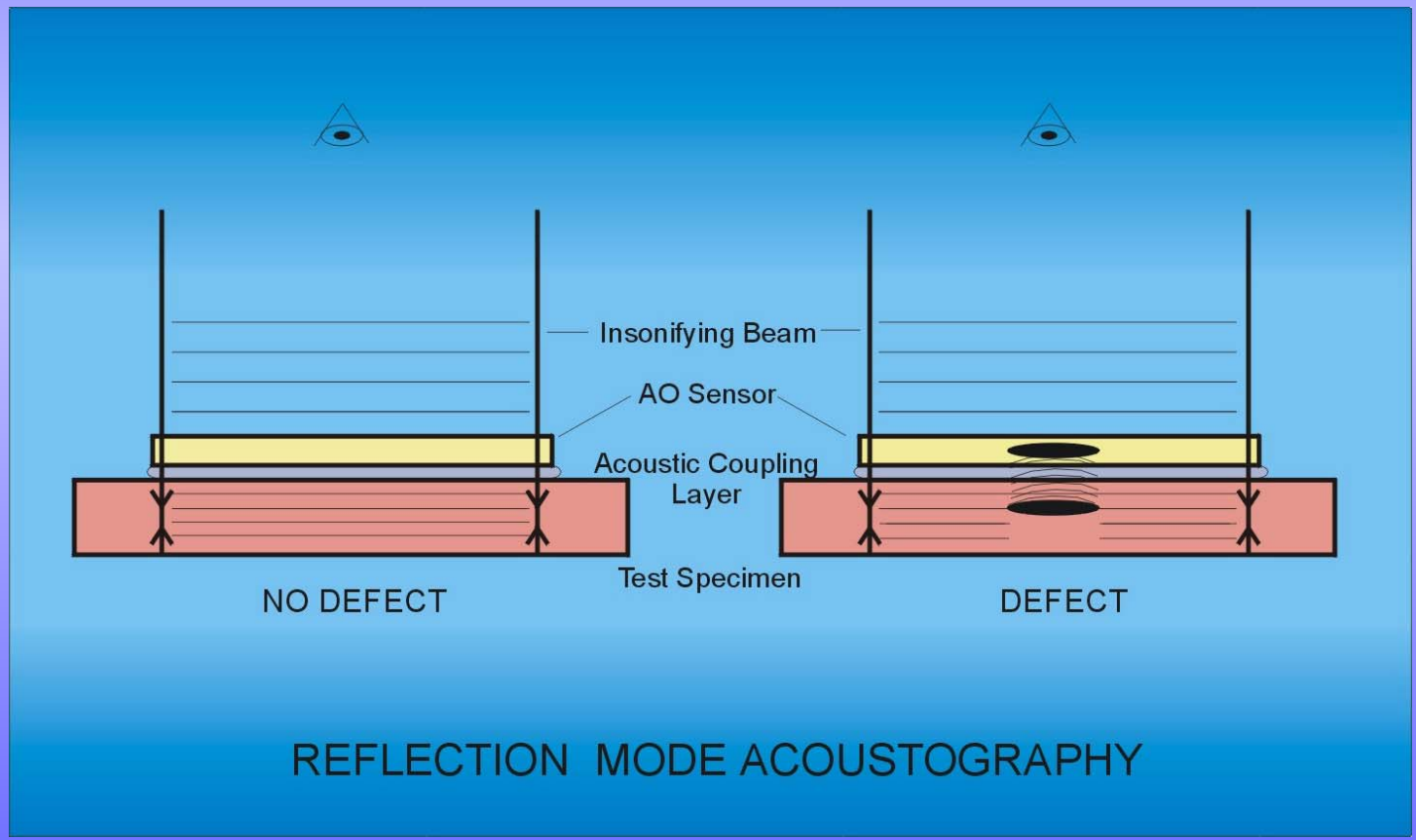

SANTEC SYSTEMS INC.

NDT Applications
Single Sided (Reflection Mode) UT

Plastic Test Panel Inspection

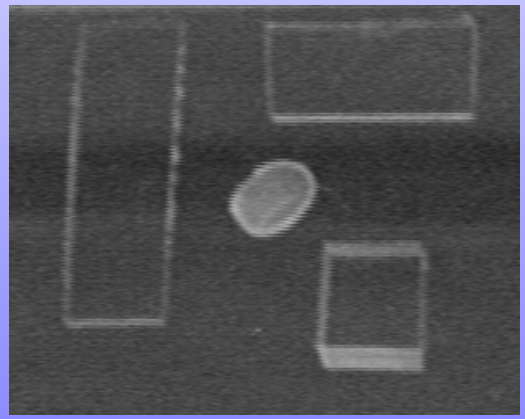

Test Panel

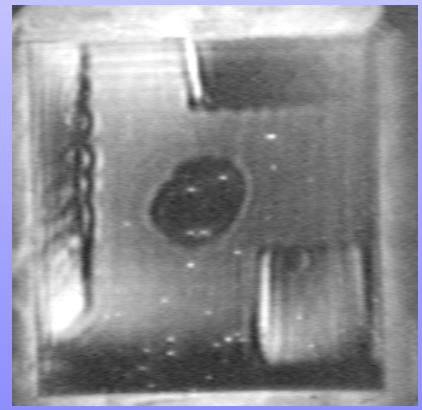

Preliminary
Acoustography Results

SANTEC SYSTEMS INC.

NDT Applications
Single Sided (Reflection Mode) UT

Composite Test Panel

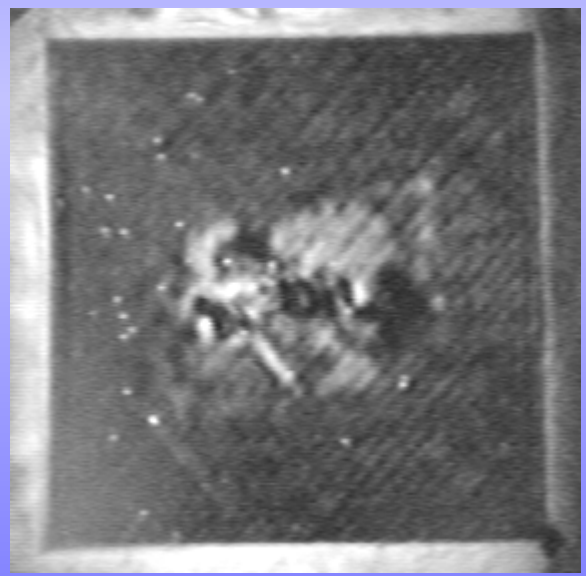

Impact Damage

Summary

- Acoustography could be a simple alternative to conventional point-by-point UT
- It can be used for Thru-Transmission UT
- It can be used for Single Sided (Reflection Mode) UT

Future Developments

- Increase field of view (e.g. 12”x 12”)
- Refine Single Sided (Reflection Mode) UT
- Develop acoustic coupling for non-immersion UT
- Develop Flexible AO Sensors

SANTEC SYSTEMS INC.

Further Information

Contact:

Santec Systems, Inc.

716 South Milwaukee Avenue
Wheeling, IL 60090

Tel. 847-215-8884
Fax. 847-215-8847

website: www.santecsystems.com

NDE of Friction Stir Welds in Aerospace Applications

Author
David G. Kinchen, Lockheed Martin Michoud Space Systems
Department 4630 M/S 4310, P.O. Box 29304, New Orleans, LA USA 70189
Phone: (504) 257-1454; Fax: (504) 257-4445; email: david.kinchen@maf.nasa.gov

Co-Author
Esma Aldahir, Lockheed Martin Michoud Space Systems
Department 3700 P/A 3741, P.O. Box 29304, New Orleans, LA USA 70189
Phone: (504) 257-0879; Fax: (504) 257-4403; email: esma.aldahir@maf.nasa.gov

Abstract

Friction Stir Welding (FSW) is a solid state joining process, which utilizes a cylindrical, shouldered pin tool with a radiused tip that is rotated and plunged into the weld joint. Frictional heating beneath the shoulder, and surrounding the pin tip causes the material to plasticize, intermix and consolidate into a weldment without melting the parent material. FSW in aluminum alloys has many advantages such as low distortion and shrinkage, excellent mechanical properties, and no porosity.

However, the propensity of the FSW process to create detrimental defects does exist, and is dependent on FSW parameter limits and controls. Inspection processes for FSW must also be selected and implemented concurrent with the new weld process. This paper describes the efforts by Lockheed Martin and NASA to find proper NDE techniques for detecting and characterizing the anomalies that may be caused by operating outside the envelope of optimized FSW parameters. Potential defects are identified and the results of the exploration of numerous NDE techniques including visual, liquid penetrant, multiple ultrasonic methods, eddy current and conductivity are discussed.

Friction Stir Welding

Developing and implementing new processes to enhance the performance, reliability and safety of aerospace hardware is a primary ongoing objective for both government and industry programs. TWI in Cambridge, UK, invented friction Stir Welding [1] in the early 90's and Lockheed Martin began its development activities in 1995. FSW development continued at Marshall Space Flight Center (MSFC) through 2001 for various NASA applications including man-rated flight hardware.

Friction Stir Welding is accomplished with both monolithic and multiple piece pin tools rotating at several hundred RPM and traversing a square butt weld joint of the same design configuration used for fusion welding. A plunge load is imparted through a spindle, driven by a FSW machine and reacted against a backside anvil. Frictional heating under the pin tool and around the pin tip generate sufficient heat to locally plasticize the aluminum alloys to be welded. Tool rotation during the FSW process imparts a material flow in three dimensions to the plasticized weldment, causing complete mixing of the alloys. Consolidation of the weldment occurs via an extruding/forging action under the pin tool shoulder as the pin tool is traversed down the length of the weld. See Figure 1 for a schematic representation of the FSW process.

FSW enjoys a number of advantages over fusion welding processes including the elimination of welding consumables such as gas, filler wire and electrodes. As a joining process based on frictional heating due to mechanical work, FSW has only three primary weld variables to control. These are plunge force, rotation speed and weld travel speed.

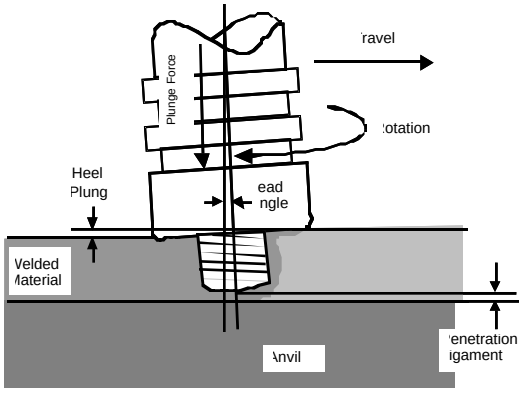

Schematic Of FSW

Figure 1. Friction Stir Welding Process

The 2XXX series aluminum alloys have long been the workhorse of aerospace programs for high strength, lightweight applications. New materials such as Al2195 Aluminum-Lithium alloy provided significant base material improvements over its predecessor Al2219. Improved strength at both room and cryogenic temperatures were significant benefits of the new alloy, however weldability was sometimes a challenge, which prompted efforts to improve the process and ultimately led to the development and implementation of FSW. Al2195 alloy has

proven to be highly receptive to the FSW process, overcoming some of the production difficulties experienced in early development and implementation of Al2195 with conventional fusion weld processes. [2]

Inspection of Friction Stir Welds

Attendant with the new Friction Stir Weld process, are new inspection requirements for both visual and NDE techniques. FSW enjoys freedom from most fusion weld process defects, however the demands of many aerospace applications require proof testing as well as full NDE of man rated hardware.

Existing processes such as radiographic and penetrant inspections will remain for FSW inspection, however they will be supplemented by new automated NDE. Long term, the automated NDE will replace part of the conventional NDE and ultimately achieve a productivity enhancement for inspection.

Understanding the potential flaws for the FSW process requires an understanding of the metallurgy. Figure 2 provides a cross-section view of a completed FSW allowing one to observe the metallurgical structure associated with a FSW of AL2195.

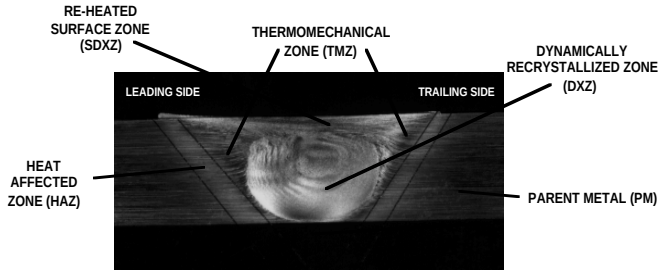

Figure 2. FSW Microstructure

The FSW nugget is formed as frictionally heated metal flows around the pin tool and consolidated under the shoulder. Flaws observed during FSW development present a challenge requiring a blend of several complementary NDE methods to provide adequate inspection. The flaws observed during FSW development range from surface defects such as excess flash, to lack of fill under the FSW tool shoulder, to internal porosity and Lack Of Penetration. (LOP).

In every case the FSW flaw was linked to one or more FSW process conditions or parameters that were related directly as causative factors for the defect.

To assess and select appropriate NDE techniques a logic diagram was generated to integrate candidate NDE techniques, testing and development for NDE, procedures and documentation, process validation and the requirements of fracture control. Factors assessed in evaluating NDE techniques included the Critical Initial Flaw Size (CIFS), potential flaws detected by a given method, the capability of candidate NDE techniques, and their maturity for production use. This assessment has explored a wide variety of NDE methods encompassing visual, several liquid penetrant techniques, ultrasonic inspections of differing types, radiography, and eddy current. One of the newest NDE technologies assessed was MWM® conductivity, a technique that maps surface conductivity in the area of the weldment.

Visual Inspection

Perhaps the most straight forward and simplest inspection technique, visual inspection is an excellent means of inspecting for surface features including excess flash, galling, shoulder voids, and even weld misalignment. Figure 3 shows an example of a shoulder void.

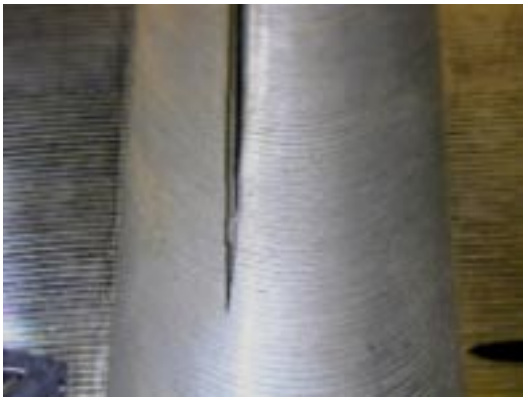

Figure 3. Shoulder Void in FSW.

Workmanship standards were constructed to illustrate acceptable and unacceptable crown and root side surface conditions such as these. These defects are visible to the naked eye, are attributed to out of family welding parameters; such as excessive travel speed (IPM), excessive rotational speed (RPM), inadequate plunge force loads, and improper seam tracking.

The principle unacceptable root side condition is LOP. Of all of defects, LOP was considered, early on in the friction stir welding program, to be the most critical type of defect. As a result, most NDE testing was conducted with this flaw type.

Visual examination of the root side of the weld demonstrated that LOP flaws were detectable, when inspected in the post etched condition. Etching is a post weld chemical treatment performed most often to prepare mechanically worked surfaces prior to penetrant inspection. In this case, the etching process clearly delineates the weld nugget Dynamically Recrystallized Zone (DXZ), and its surrounding Heat Affected Zone (HAZ) making the lack of FSW nugget a distinct feature visible to the trained eye. The cause for the successful detection rate is due to the fact that it is easy to discern the DXZ from the surrounding parent material and HAZ in the post etch condition. Therefore, visual inspection is a reliable technique to confirm suspected LOP conditions. Figure 4 is a 3X magnification view of an LOP defect on the root side of a FSW panel after etching.

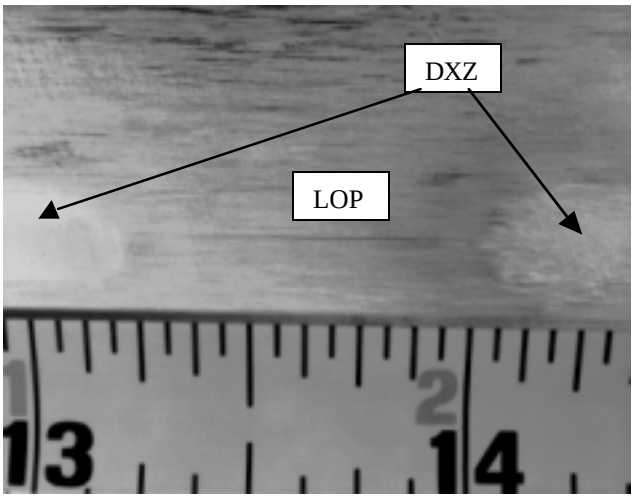

Figure 4. LOP in FSW after post weld etch.

The metallurgical characteristics of the LOP flaw are the determining aspects of the flaw and relate directly to the ability of ultrasonics and penetrant inspection techniques to detect LOP. These characteristics are likewise, directly linked to the weld process itself. Primary factors affecting the LOP during welding include heat input or material flow, and most importantly, the depth of the FSW pin tool.

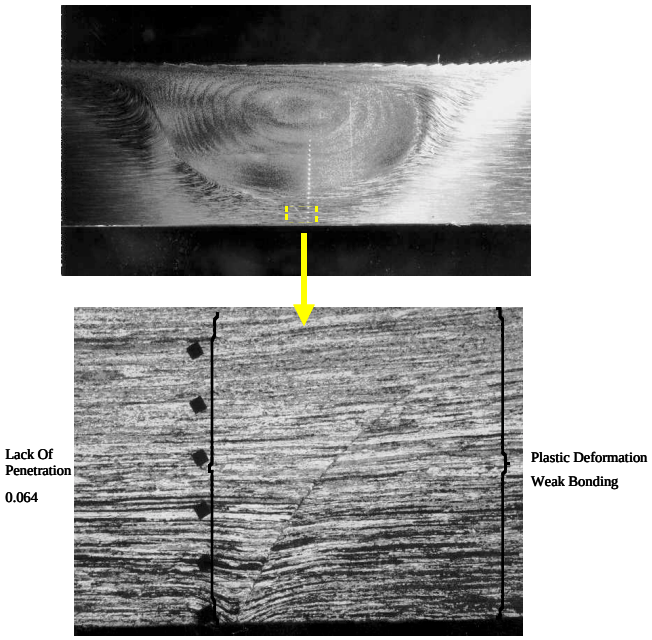

Figure 5. Metallurgical cross section of LOP flaw.

Figure 5 illustrates the metallurgical features which include the total depth of LOP, the depth of plastically deformed material and the tight bond at the LOP interface. The most significant of these with regard to NDE, is the degree of "tightness" of the "kissing bond" created at the LOP interface. Conventional NDE techniques rely heavily on a physical separation, void or air gap, as the means to provide a response from such a defect. The less significant this separation, the more problematic is its detection.

Penetrant Inspection

Penetrant inspection via P135E and P6F4 was performed on FSW test panels in the as welded, single etch, and double etched condition. In addition, penetrant inspections were performed with and without developer, and with varying penetrant dwell times. Penetrant inspection of the FSW test panels in the as welded condition was determined to be an unacceptable method, due to poor detection and the excessive background noise produced by the surface, which interferes with the inspection.

Inspection of FSW in the etched condition via P135E and P6F4 consistently and successfully detected root side LOP flaws. However, because the sensitivity level of detection for each penetrant solution is different, the results were dissimilar. P135E successfully detected LOP flaws that were greater than or equal to 0.064" deep, and P6F4 successfully detected LOP flaws that were greater than or equal to 0.050" deep. Double etching, via caustic etchant solution, prior to the application of penetrant enhanced the detection of LOP in comparison to single etching.

The difference between single etching and double etching is that single etching removed 0.0002" to 0.0004" of metal and double etching removed 0.0004" to 0.0006" of metal. Test results demonstrated that etching to remove a minimum of 0.0004"of metal prior to the application of penetrant improved the detectability of LOP.

Due to the outcome of the test results it was decided that penetrant inspection include the removal of 0.0004" to 0.0006" of metal via caustic etch solution prior to the application of penetrant solution. In addition, extended penetrant dwell times and the use of developer were evaluated and the results yielded no improvement in the detection of LOP flaws.

Ultrasonic Inspection

AIS (Automated Inspection Systems), RD/Tech, Lockheed Martin, and MSFC NDE engineers and technicians performed ultrasonic inspection on FSW test panels. Conventional UT as well as multi-element probes were evaluated, as were L wave and shear wave techniques and multiple angle transducers. The results initially demonstrated that the technique(s) could detect LOP flaws at 15% to 20% of the material thickness or greater.

However changes in FSW tooling directly affected the LOP flaw metallurgical characteristics, making the flaw more tightly closed and thus more difficult to detect. This affect of improving the weld process without sufficient regard for its effects on other parts of the manufacturing process, including inspection became a recurring theme in pursuing automated NDE. Ultimately, improvements to RD/Tech Phased Array UT inspection technique resulted in detection at 25% to 30% of thickness and greater.

The response for Phased Array provides multiple views of the FSW at one time, allowing position location information, as well as through thickness data to be portrayed for detected

flaws. This is accomplished through the use of a 32-element probe, electronically rastering the UT beam across the weld as the probe is automatically scanned down the length of the weld. The result for an LOP flaw is depicted in Figure 6.

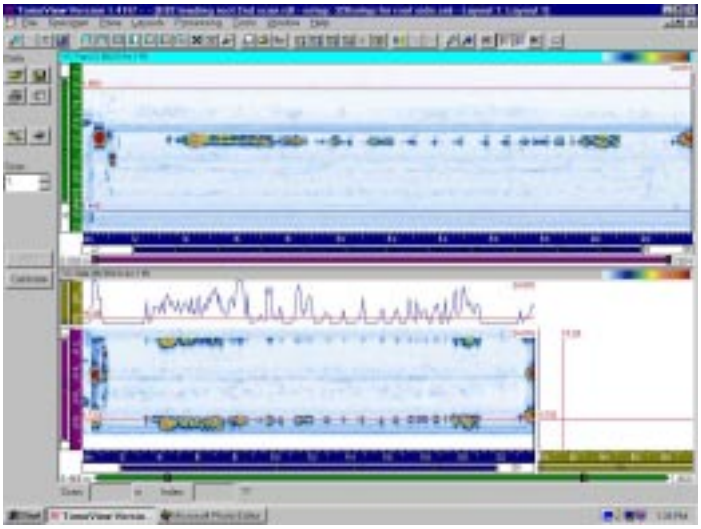

Figure 6. Phased Array scan of LOP flaw.

The top portion of Figure 6 provides a C-scan image of the weld with the weld and the flaw running from left to right. The lower portion of the figure is a longitudinal side view showing the material thickness and the location of the flaw at the bottom of the image, which is the root side of the weld. Note detection is discontinuous at some points, which again relates to the metallurgical nature of the LOP flaw.

Radiographic Inspection

Radiographic inspection was performed via film and digital methods on FSW test panels. Test results demonstrated that we could reliably (90% probability / 95% confidence) detect LOP flaws that are greater than or equal to 30% of the material thickness. However, dissimilar alloy welds posed a challenge in film radiography, in that it is difficult to discern an LOP flaw.

The reason for this is two-fold. First the joining of dissimilar alloys aluminum yields a weldment that is a commingling of the two alloys, which vary in chemical composition by several percentage points of copper and lithium. The difference in copper, greatly affects transmission of the X-ray, requiring an interpreter to “train” his eyes to accurately interpret the film radiograph. Figure 7 provides a view of the metallurgical difference evident in a dissimilar alloy weld of Al2219 to Al2195. The lighter etched portion is Al2219, and the wavy boundary where the two alloys intermix is reflected in radiographs of these welds.

Figure 7. Al2219 to Al2195 Dissimilar Alloy FSW.

The second reason for harder detectability in dissimilar alloys FSW is the tendency for the LOP flaw to be more tightly bonded in this alloy combination (Al 2219 to Al2195). Several in-depth studies of the metallurgy of the FSW has proven the relationship, mentioned earlier with the characteristics of the LOP and its NDE detectability.

Eddy Current and Conductivity Inspection

Conventional Eddy Current inspection was performed on FSW test panels by the use of a 1 MHz pencil probe, and a 300 kHz differential rotating probe. Initial Eddy current (EC) results demonstrated reliable detection by both MSFC and Lockheed Martin techniques for Al2195/Al2195 friction stir welds containing at least 0.065” or deeper LOP. The extreme difference in EC across dissimilar alloy welds yielded an EC response from virtually all panels making discrimination of LOP versus No LOP panels unreliable. These promising results changed as changes were made to improve the FSW process by changing the FSW tooling.

Reliable detection during automated NDE is critical to the integrity of aerospace applications. To assess the latest technology other than conventional EC, Lockheed Martin approached Jentek Sensors, Inc. to develop their technology for FSW inspection.

This new approach to EC type inspection is based on conductivity, first explored under LMCO IRAD activity [3]. Jentek Sensors, Inc. was asked to perform various tasks from 1998 through 2001 relative to process monitoring and post weld inspection with their inspection systems.

The promising results of their MWM® conductivity methods resulted in a contract to complete technique development and a custom sensor design specific for FSW applications. This work has been completed and provides a risk mitigation complimenting the current plans for radiographic, penetrant and ultrasonic inspection techniques for production NDE of FSW.

The multi-element MWM® sensor, Figure 8, has demonstrated detection of 0.050-in. and deeper LOP in Al2195-to-Al2195, as well as in dissimilar alloy Al2219-to-Al2195 FSWs [4].

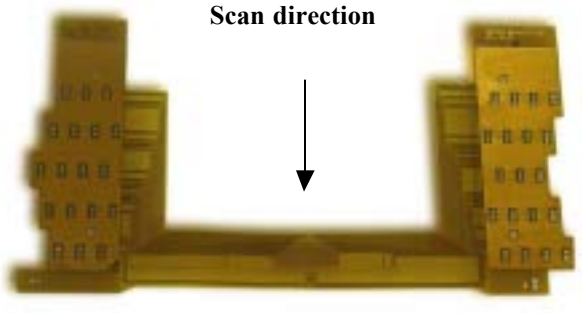

Figure 8. Jentek MWM Multi-element Sensor.

The Jentek MWM® system consists of a PC or Laptop computer, Gridstation Software, Instrumentation Module and MWM® probe and sensors.

The conductivity probe provides automated scanning, however it is easily used in manual mode as well. Like the multi-element UT probes, the Jentek sensor is comprised of some 37 elements. The MWM-Array employs approximately 30 elements in the primary area of the weldment, with the remaining elements spaced approximately 3 inches apart to track the edges of the weld land. Individual element spacing and arrangement was customized to achieve optimum sensitivity for flaw detection.

Absolute electrical conductivity is a physical property of these aluminum alloys measured by the MWM-Array. Conductivity has long been used to inspect for heat treat condition in aluminum alloy knowing its relationship to changes in alloy composition and metallurgy. Its application for FSW inspection actually maps conductivity on the root side of the weld with a precision more than an order of magnitude better than other conductivity applications. Data is then processed and displayed as a conductivity map at the weld root surface. A C-scan image and profile image for a good weld is shown in Figure 9.

The C-scan view presents the inspection data as a top down view of the Friction Stir Weld. The weld in Figure 9 extends from left to right. The circular region on the right edge of the image is the terminus of the weld, and the yellow region indicates the FSW weld nugget (DXZ) exhibiting full weld penetration through the joint thickness.

The lower portion of the image in Figure 9 is a cross-section view of the inspection data. FSW DXZ is indicated in the middle of this profile view, while higher conductivity values, on either side of the DXZ, indicate changing conductivity in the Heat Affected Zone (HAZ). Blue to aqua colored zones map the HAZ on either side of the DXZ.

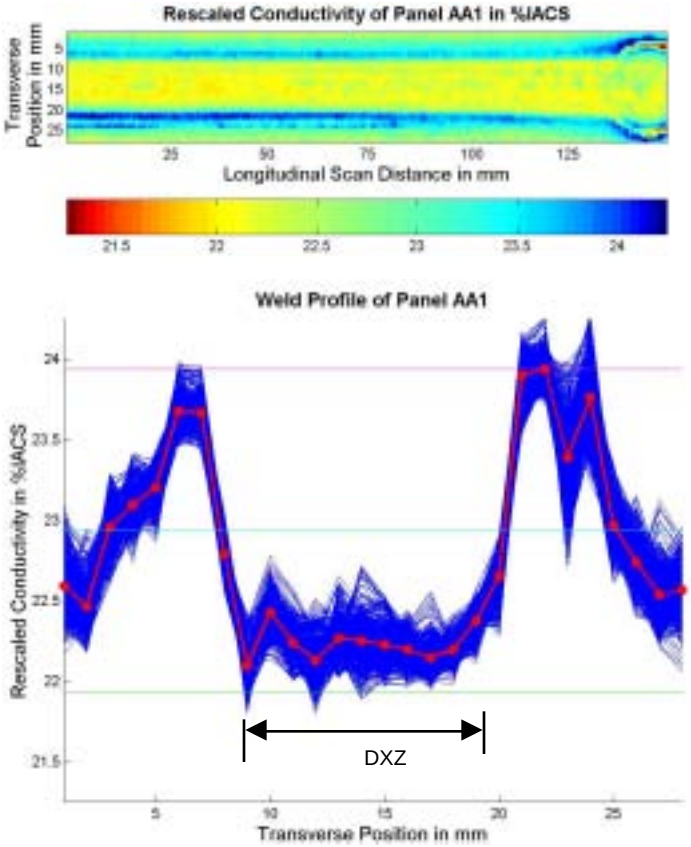

Figure 9. Full Penetration FSW Conductivity Map.

LOP, the failure of the FSW to fully penetrate the joint thickness, presents itself as significantly different conductivity patterns as illustrated in Figure 10. This FSW specimen contained 0.045" deep LOP and exhibits minimal DXZ, as well as several planar flaw indications.

Comparison of the profile in Figure 9 to that of Figure 10 reveals differences in conductivity values and their position are observed as changes to the shape of the profile. The presence of planar flaws is also noted as severe reductions (drop out) in the conductivity profile noted in Figure 10.

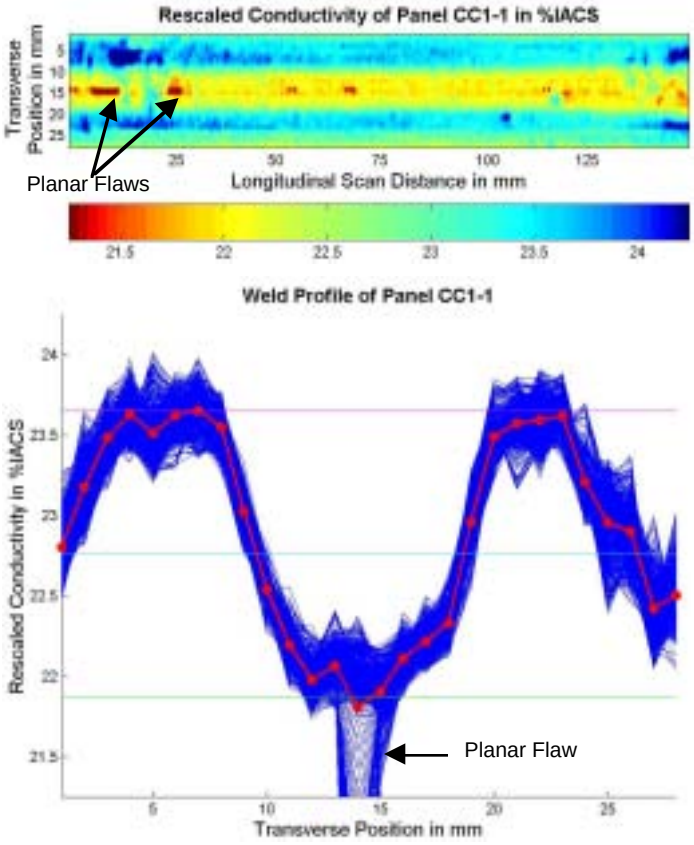

Figure 10. FSW with LOP Conductivity map.

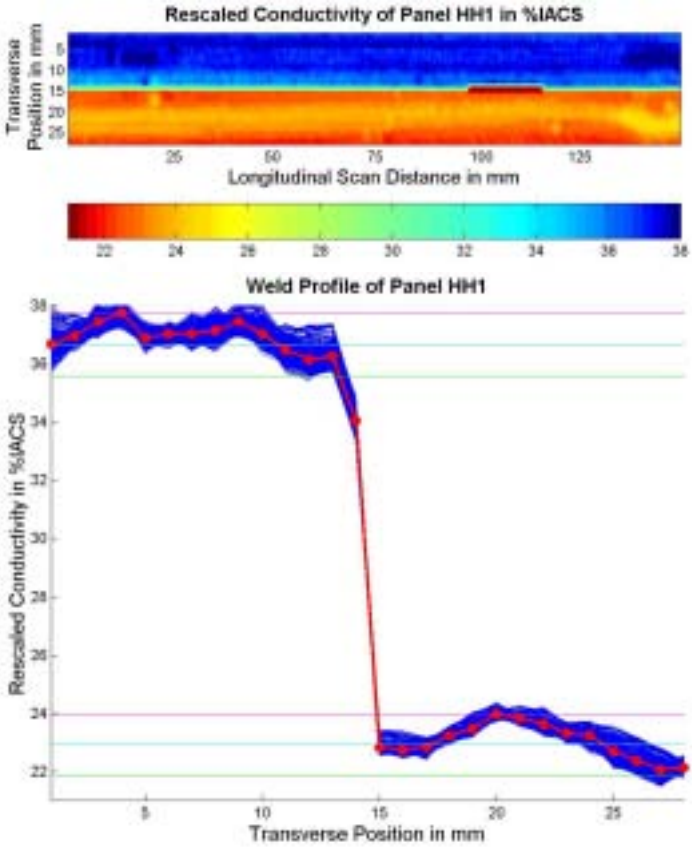

Figure 11. FSW LOP Conductivity map dissimilar alloy.

Dissimilar alloy FSW yield quite different patterns of conductivity via the Jentek MWM-Array technique due to the large differences in parent material conductivity. Al2219-T8 exhibits a typical conductivity of 34% IACS, while Al2195-T8 is 20. The profile in Figure 11 shows the high conductivity Al2219, to the left of the profile, decreasing rapidly as the conductivity drops into the DXZ area. The DXZ is bounded on either side by slight peaks in conductivity indicating the HAZ.

The specimen for this example contained LOP 0.057" deep. The key to developing criteria for detection of LOP via this technique lies in differences affecting the shape of the conductivity map include a sharp changes in the slope (rate of decrease) in conductivity from the Al2219 side of the FSW and a reduction to the extent of the weld DXZ.

Summary

NASA and Lockheed Martin are pursuing implementation of Friction Stir Welding (FSW) and automated NDE as part of a larger program to improve performance, safety and producibility for welded aerospace hardware. FSW is being implemented to take advantage of its high strengths and toughness, and its near defect-free welds in 2XXX aluminum and aluminum lithium alloys used for numerous aerospace applications.

Significant productivity gains are anticipated due to transitioning from conventional manual NDE inspection techniques to automated production NDE. Existing NDE methods including liquid penetrant and radiography will continue as automated Phased Array ultrasonics is implemented, and subsequently used to replace manual NDE.

To assure risk mitigation for conventional NDE inspection techniques a new technology utilizing MWM® conductivity mapping technique with a custom 37-element array sensor specific has been accomplished.

Acknowledgments

Acknowledgement and thanks is given to both NASA and Lockheed Martin personnel at the NASA Marshall Space Flight Center (MSFC) and to the staff at Automated Inspection Systems (AIS), Matec Instruments and Jentek Sensors, Inc. for their effort in this endeavor.

References

1. W.M. Thomas. et al.:"Friction Stir Butt Welding", International Patent Appl. No. PCT/GB92/02203 and GB Patent Appl. No. 9125978.8, Dec. 1991, U.S. Patent No. 5,460,317
2. William Arbegast, Paula Hartley: “Friction Stir Weld Technology Development at Lockheed Martin Michoud Space Systems – An Overview”, June 1998, AEROMAT.
3. Neil Goldfine, William Arbegast, et al.: “Friction Stir Weld LOP Defect Detection Using New High Resolution MWM-Array and Eddy-Current Sensors”, June 2001, AEROMAT.
4. David G. Kinchen, Neil Goldfine, et al.: “Friction Stir Weld Inspection Through Conductivity Imaging using Shaped Field MWM® Arrays”, April 2002, Trends In Welding Research.

NON ODC AIRCRAFT OXYGEN LINE CLEANING SYSTEM

Mr. John Herrington
Senior Logistician
Versar Inc.
39 W. Hunter Dr.
Enon, OH 45323
937-864-7812
Herrington@erinet.com

Mr. Terence A. Caldwell
Project Engineer
Versar Inc.
5717 E. I-240 Service Rd.
Oklahoma City, OK 73135
405-739-0062
tacaldwe@ou.edu

Mr. Jerry L. Gore
Air Force Project Engineer
OC-ALC/LIIRC
Staff Drive, STE 1AD2-90B
Tinker Air Force Base, OK 73145-3029
405-736-5080
Jerry.Gore@tinker.af.mil

ABSTRACT

Tinker Air Force Base, OK, in conjunction with the Environmental Security Technology Certification Program (ESTCP) and the Joint Group on Pollution Prevention (JG-PP) coordinated efforts with Versar Inc., in regard to pollution prevention issues identified during a defense system's acquisition process. The primary objectives of this task were to reduce or eliminate the use of CFC-113, a Hazardous Material (HazMat), and to avoid duplication of efforts in action required to reduce or eliminate HazMats through joint service cooperation and technology sharing. The Scope of work was to design, develop and construct a prototype oxygen line cleaning system (POLCS), and cleaning process, to precision-clean the critical life support oxygen distribution system for the Air Force B-1B weapon system (and other aerospace vehicles) while all equipment and tubing remains installed onboard the aircraft. The POLCS design will provide the Air Force with a suitable and applicable fluid system that will meet or exceed special operation and cleanliness requirements in accordance with Government and non-Government documents for maintaining on-board aerospace vehicle oxygen tubing. This effort also included testing, troubleshooting and the validation of a selected solvent solution on various aerospace vehicles using the POLCS. Laboratory testing began in October 1999; field-testing was conducted during fall 2001.

INTRODUCTION

The specific problem motivating replacement of many chlorofluorocarbon (CFC) solvents is their effect on ozone. Depletion of ozone layer in the upper atmosphere increases the intensity and range of harmful radiation transmitted to the earth surface. For this reason, the use of chemicals with known ozone depleting potential (ODP) is being phased out of industrial and commercial use. Although CFC's are still in limited commercial use, the Montreal Protocol phased out their production by year 2000, and Executive Decision Number 12856 has tasked the United States Air Force, as well as other government agencies, to identify a cleaning solvent to replace CFC-113, which is currently used for cleaning oxygen system of all military aircrafts.

Of the many manufacturing and processing activities affected by this decision, one has been the cleaning of oxygen distribution lines and storage systems in several military aerospace vehicles. Tinker Air Force Base (AFB), Oklahoma, in conjunction with Environmental Security Technology Certification Program (ESTCP) and the Joint Group for Pollution Prevention (JG-PP), coordinated efforts with Versar, Inc. to identify a suitable solvent system that can eliminate the use of CFC-113 for this application. Furthermore, by sharing technology through joint service cooperation, duplication of effort in actions required to reduce or eliminate the CFC-113 is avoided.

BACKGROUND

OXYGEN LINES

The oxygen lines on-board military aircraft consist of a series of tubing that are connected between a Liquid Oxygen (LOX) converter, low or high pressure cylinders, or Molecular Sieve Oxygen Generating (MSOG) system and an oxygen regulator. The regulator is connected to the oxygen mask of the crewmember. Many oxygen system components (i.e., pressure transducers, pressure relief valves, check valves, toggle switches…etc.) are placed strategically between the LOX converter, cylinder, or MSOG unit and the masks. The first objective of the project was to identify materials used within these components (metals, elastomers and plastics) and to find a solvent that causes minimal changes to these materials. The second objective was to design, develop and construct a Prototype Oxygen Line Cleaning System (POLCS) flexible enough to meet the cleaning requirements of all oxygen line systems (smallest to the largest).

The initial focus was to create a system that would successfully clean B1-B oxygen lines without costly removal of the lines. Potential risks involved with cleaning an actual
B1-B aircraft initiated an effort to design and construct a full-scale replica of the B1-B oxygen system. This allowed experimental testing which was used to verify and validate that the POLCS can successfully clean all areas within the oxygen lines.

The replica of B1-B system was also used to determine whether the previous test data for flow velocity and fluid composition was accurate and reproducible and to establish whether the system was capable of effectively removing particulates that have the strongest adhesion to the surface of the lines. Test cells were designed and constructed to visually qualify the cleaning ability of the solvent. A picture of a test cell is shown in Figure 1. After it was established that the POLCS could successfully clean the replica unit, the POLCS was used to clean the oxygen lines on an actual B1-B aircraft.

Figure 1: Test Cell Assembly

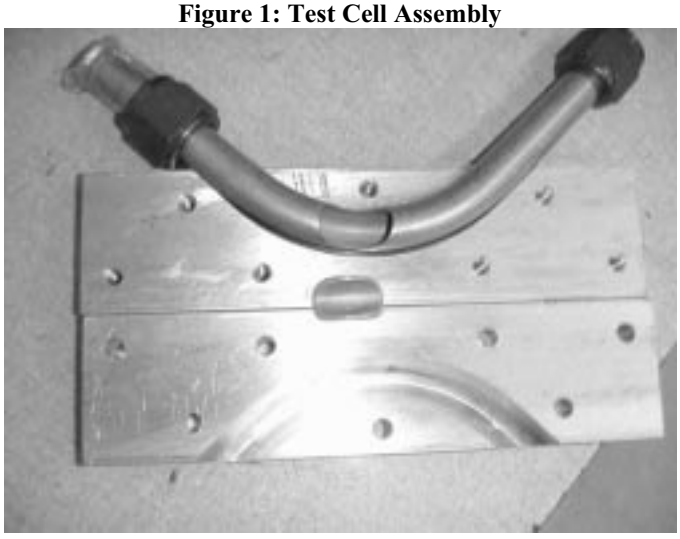

CONTAMINATION (Problems)

It is known that particulates and non-volatile residues (NVR) in oxygen systems can cause significant hazards to aircraft and harm to personnel. Particulates may include, but are not limited to, metal shavings, Teflon tape, and dust. NVR can range from Krytox greases to hydraulic oils. Particulates impinging on surfaces of concentrated oxygen streams can be a source of ignition and fire on military aircraft. Contaminates can plug pressure relief valves or foul regulators and result in system malfunctions, or even worse, catastrophic failure. Particulates can also pose a significant threat to the health of personnel in oxygen systems, as emphasized in EPA's revised guidelines for particulate matter. Personnel with health problems and/or aircraft malfunctions can lead to mission degradation, loss of combat readiness and, in some instances, loss of aircraft and/or personnel. In today's environment of pollution minimization, regular maintenance on these aircraft life support systems must incorporate environmentally acceptable solvents and processes that are efficient, yet safe to humans and the environment.

MATERIALS (Previous Studies)

The initial concept of this project was to combine the cleaning properties of a solvent and surfactant. However, laboratory testing had shown that using an adequate solvent and sufficient flow velocity would result in adequate cleaning without the introduction of additional chemicals into an aircraft system. The results of our early studies involving a solvent/surfactant solution are described in this section.

Surfactant Associates Inc. conducted primary studies for the solvent/surfactant selection for the POLCS. They identified three fluorosurfactants and five fluorosolvents (three perfluorocarbon solvents and two hydrofluorocarbon solvents) based on their ability to enhance particle removal. In their studies, they evaluated and compared the baseline fluid, CFC-113, to the above fluorosolvent and fluorosurfactants. Their studies showed that any of the solvent surfactant solutions far exceeded the cleaning ability of CFC-113. The three surfactants identified as test candidates were Krytox Alcohol (a nonionic fluorosurfactant), Zonyl UR (an anion fluorosurfactant) and Krytox 157 FSM (a nonionic fluorosurfactant). The perfluorocarbons tested in their study were FC-72, FC-77, and FC-43. The hydrofluorocarbon solvents tested were HFE 7100 and HFC-236 FA. All of the solvents and surfactants were made available by 3M or Dupont.

The contaminated sample surfaces were characterized using scanning electron microscopy (SEMs). These surfaces were initially marked to allow re-examination of the same area for direct comparison both before and after cleaning. Their results indicated that HFE 7100 was the appropriate solvent. The solvent is essentially non-toxic, non-flammable, non-ozone depleting, non-aqueous, and resistant to thermal breakdown which are all characteristics needed in oxygen service equipment. HFE-7100 has been tested and is LOX compatible.

The solvent/surfactant solution recommended for replacing CFC-113 was a mixture of the **solvent**, hydrofluoroether (HFE-7100) made by 3M, and the **surfactant**, Krytox alcohol (Hexaflouropropylene Oxide Homopolymer Alcohol) made by Dupont. The solvent and the surfactant are both fluorocarbons. A fluorocarbon compound has all its hydrogens on its carbon backbone replaced by fluoride. Fluorocarbons are unique in having the lowest surface tensions of any fluid. This allows the fluorocarbon molecules to quickly wet surfaces and penetrate pores and cracks that exist between particles and their supporting substrate. By lowering the surface tension, less energy is required to remove particles that have adhered to the surface. The force to remove the particles is supplied by passing a high velocity solvent/surfactant mixture across the contaminated surface. Prior testing has shown that the required velocity (energy) to overcome particulate adhesion forces is reduced with addition of a fluorosurfactant.

ADDITIONAL TESTING

Versar Inc. used the test data from earlier work by Surfactant Associates Inc. as a starting point to identify an optimum solvent/surfactant combination and flow velocity to target the worst realistic oxygen line contaminate and focus on its removal. The reason being that if the worst contaminate can be detached with acceptable results, the other contaminates will easily be removed. To identify the worst-case contaminant, hundreds of fluid velocity tests were conducted using various contaminates and solvent/surfactant mixtures.

These tests were conducted implementing a Waukesha model 60 positive displacement pump with a variable frequency drive to adjust the flow rate. A Hedland Flow meter with a range of 0 to 50 gallons-per-minute was implemented to observe the flow rate. A Test Cell was constructed to qualify the cleaning efficiencies of the solvent/surfactant solutions. In order to document results of solvent/surfactant cleaning using the Test Cell technology, a Sony Digital Camera was used to store images. Figures 2 & 3 show before and after cleaning using HFE-7100.

Figure 2: Before Cleaning

Figure 3: After Cleaning with HFE 7100

The results of the evaluations performed to identify the worst-case contaminant are provided in table 1.

Table 1: Average Flow rate required remove contaminates using HFE 7100

Contaminates	Solvent & 0.05 wt% Krytox	Flow Rate liter/min	Flow Time (Minutes)	Cleaning Efficiency (Range)
Hydraulic Oil & A.C. Fine Test Dust	HFE 7100	10	15	85 to 100 Percent
Hydraulic Oil & Powdered Zeolite	HFE 7100	10	15	85 to 100 Percent
Hydraulic Oil & A.C. Fine Test Dust	HFE 7100	10	15	85 to 100 Percent
Krytox Grease & Powdered Zeolite	HFE 7100	10	15	85 to 100 Percent
Krytox Grease & A.C. Fine Test Dust	HFE 7100	10	15	85 to 100 Percent
Acetone & Powdered Zeolite	HFE 7100	14	15	85 to 100 Percent
Acetone & A.C Fine Test Dust	HFE 7100	18.5	15	85 to 100 Percent
HFE-7100 & Powdered Zeolite	HFE 7100	14	15	85 to 100 Percent
HFE-7100 & A.C Fine Test Dust	HFE 7100	18.5	15	85 to 100 Percent
Tap Water & Powdered Zeolite	HFE 7100	16	15	85 to 100 Percent
Tap Water & A.C Fine Test Dust	HFE 7100	56	15	85 to 100 Percent
Distilled Water & Powdered Zeolite	HFE 7100	16	15	85 to 100 Percent
Distilled Water & A.C Fine Test Dust	HFE 7100	56	15	85 to 100 Percent

Results of these tests identified that the greases and hydraulic oils required the least amount of energy (flow rate) for removal. The most adhesive compound is a mixture of distilled water and A.C. Fine Test Dust from the Duke Scientific Company. Since this compound was the most difficult to remove, it became the target contaminate of the cleaning process. Flow rates were varied through a 5/8" test cell ranging from 2 to 20 gallons per minute for

10 to 20 minutes. Surfactant concentration varied from 0.05 to 0.15 wt. Percent. Data results indicated that the optimum concentration to-date was a ratio of 0.05 wt. percent surfactant in the solvent mixture and a flow rate of 56 liter per min in 5/8" line for 15 minutes.

In order to reduce the risk of inserting additional chemicals into an aircraft oxygen system, then having to remove it, further testing was accomplished using the HFE-7100 solvent alone for cleaning. Testing proved that similar and adequate cleaning could be achieved using the solvent alone with a flow velocity of 18-20 feet per second. A solvent/surfactant solution works well for some applications, but the addition of a surfactant only complicates the removal verification process and increases the risks involved in cleaning a human breathing system such as onboard an aircraft. From this stand point it was determined to operate the system with solvent only for the purpose of cleaning aircraft oxygen systems, while maintaining surfactant capability for other potential applications.

PROTOTYPE OXYGEN LINE CLEANING SYSTEM (POLCS)

DESIGN AND CONSTRUCTION PARAMETERS

The POLCS was constructed for testing and evaluation. The system is designed to meet or exceed the cleaning ability of CFC-113. To verify cleanliness levels, an in-line particle counter is implemented, and laboratory proof of concept test procedures have validated the removal of non-volatile residues. Safety and efficiency of the cleaning process is improved by fully automating the system and by distilling the solvent so that it can be reused for future cleanings. By recycling the solvent, a substantial amount of cost saving is realized. The process can also be modified to recycle a surfactant, if used, by implementing an in-line filtration unit. The filtration unit would separate the particulates from the surfactant molecules and organic materials (non-volatile residues). The surfactant must be periodically checked to assure that the accumulation of non-volatile residues does not exceed a specified level.

Another design parameter for the POLCS was to be fully transportable and operable in climatic conditions ranging from 40 to 120 ^{o}F (target). The system was designed with dimensions to fit in a trailer measuring 12' (long) x 7'(width, fender to fender) x 7'(high), with all sides having fold up or open panels for ease of maintenance and operation.

At this time, the POLCS prototype construction is complete and testing has been conducted on the B-1B, F-15, F-16 and C-130 aircraft. The design drawings are complete and the POLCS is a fully functional unit ready for implementation on an aircraft production line. Software programming was accomplished using National Instrument LabView graphical software language. The libraries and functions of this software are specifically designed for data acquisition and instrument control.

PROCESS DESCRIPTION

The cleaning process begins by connecting the lines on the POLCS to oxygen lines on board the aircraft. The aircraft oxygen supply unit is disconnected to provide a plumbing entry point. Oxygen regulators or devices at the end of the branch lines are disconnected as plumbing exit points. To check for leaks, the lines are first pressurized with dry air. This ensures that there will be no solvent loss during the cleaning process. Then a vacuum is applied to ensure a uniform vacuum is applied throughout the system to allow complete removal of solvent after the cleaning process. If the leakage rate is within acceptable guidelines, the cleaning process begins. If not, the location of the leakage must be identified and eliminated prior to starting the cleaning process. The next step is to pump solvent (without the surfactant) into the oxygen lines. The solvent is then circulated through each individual flow path for several minutes. A filter is used in the circulation loop to capture any particulates removed from the system. After the wash cycle is complete, a rinse cycle commences with fresh, pure solvent to insure no contaminant residue is left behind. A sample from the rinse cycle effluent is analyzed with an in-line particle counter. If the appropriate cleanliness level has not been achieved, the computer will initiate a series of steps to re-clean the lines. If the lines meet the cleaning criteria, the process continues with the evaporation cycle. The evaporation cycle consists of applying vacuum to vaporize the remaining solvent from the oxygen lines. Laboratory tests have shown that no detectable quantities of solvent remain in the system at pressures below 0.50 psia. The evacuation cycle continues until the system pressure has remained below 0.30 psia for five minutes. Upon completion of the evaporation cycle, the dry air purge begins. Dry air flows through the lines for at least 10

minutes. The dry air is then sampled by a halogen detector to measure the quantity of solvent vapor in the dry air stream. If the solvent concentration is above 40 parts per million, the dry air continues to flow through the system until a reading of less than 40 parts per million is achieved. If the solvent level is below 40 parts per million, the cleaning process is complete.

The LabView software program allows the operator to view (on the touch screen monitor) the cleaning cycles, the cycle time, and the cleanliness levels. It also alerts the operator of any problems that may occur and guides the operator (on screen) as to how to correct the problem. When the oxygen lines have been cleaned to an acceptable level, the program starts the distillation cycle to purify the solvent for future use.

This entire cleaning process can be carried out by one operator in less than four hours for an aircraft the size of the B1-B. It is our estimate that the oxygen lines on a B-1 aircraft can be cleaned for less than $2500. Larger aircraft with more outlets will require a longer time to clean. A manifold must be constructed specifically for the number of outlets on the aircraft being cleaned to regulate the velocity and flow paths of the cleaning fluid. A CD containing software-programming information will be provided for a specific aircraft type to control flow velocities and the operational sequence.

CONCLUSION

Once the Oxygen Line Cleaning system is validated and fielded, we are expecting to realize several benefits in the oxygen-cleaning arena. First and foremost, we will drastically reduce the amount of CFC-113 currently used in cleaning aircraft oxygen equipment and lessen the Air Force's dependence on the ODS. Secondly, laboratory testing has shown that the solvent cleans better than CFC-113. A third benefit is dramatic cost savings realized by not requiring the dismantling of contaminated aircraft in order to accomplish a complete system cleaning. The POLCS is estimated to save approximately $1,000,000 in labor and materials for each contaminated B-1 aircraft cleaned. We believe additional savings will be realized by increased reliability and by reducing system component failures due to particulate impacts once significant numbers of aircraft oxygen systems have been properly cleaned. This should reduce component failure rates for all weapon systems that employ this cleaning method.

REFERENCES

1. ASTM G 93 - 88 Standard Practice for Cleaning Methods for Material and Equipment Used in Oxygen Enriched Environments

2. Bardina J.; *Methods for Surface Particle Removal: A comparative Study,* "Particles on Surfaces 1 " 1988, pp. 329-338

3. Harwell J.H.; J. Scamehorn; S. Christian; "Short Course in Applied Surfactant Science and Technology", November, 1997

4. MIL-STD-1330D, Section 4.3.1.6

5. Musselman R.P. and T. W. Yarbrough, Shear stress removal of submicron particles from surfaces, J. Environmental Sci., 51 (January/February), 1987.

6. Newman Dr., “Particulate Removal From Oxygen Systems Using Surfactant Enhanced Fluorinated Solvents” Oklahoma University, Norman Oklahoma, 1999

7. Stowers I.F and H. G. Patton, in "Surface Contamination: Genesis, Detection and Control", Vol. l, pp. 341-349, 1984

8. Scientific and Technical Report prepared by BATTELLE; Analysis of Carrier Gas and Additives CDRL A002, DI-MISC-8-711 for R&M Assessment of Oxygen Line Cleaning, Contract No, F09603-95-D-0180-SD03

9. 3M Company, Hydrofluoroether Product Information, 3M Company, St. Paul Minnesota, October 1998.

Hydrogen Torch Braze for SSME Nozzle Tube Repair

JACK WEEKS
Boeing, Rocketdyne Power and Propulsion
555 Discovery Dr.
Huntsville, AL 35806
Phone: 256-544-2741
Fax: 256-544-2778
E-mail: Jack.L.Weeks@boeing.com

Arizona HydroGen distributes the Henes Browns Gas Generator, which makes its own hydrogen and oxygen from distilled water and burns them in a torch, producing a 6000 ºF flame. By using the booster unit, the flame temperature can be reduced to 4000 ºF to 4500 ºF. This temperature range is ideal for braze repair of SSME nozzle cooling tube repair. The process reduces heat input and thermal loads on adjacent tubes and eliminates several of the potential problems inherent to the arc processes currently used. This presentation will focus on the hot fire test results and the implementation process.

Evaluation Of New Repair Methods For Seal Surface Defects On Reusable Solid Rocket Motor (RSRM) Hardware

Dr. Stephanie Stanley, ATK Thiokol,
Building 4712, Room D113, Apollo Road
MSFC, AL 35812
(256) 544-0396
Stephanie.Stanley@ATK.com

Shawn Selvidge, NASA,
Building 4712, Apollo Road
MSFC, AL 35812
(256) 544-0481
Shawn.Selvidge@MSFC.NASA.gov
AMPET Conference,
September 16-18, 2002

The focus of the evaluation was to develop a back-up method to cell plating for the improvement or repair of seal surface defects within D6-AC steel and 7075-T73 aluminum used in the RSRM program. Several techniques were investigated including thermal and non-thermal based techniques. Ideally the repair would maintain the inherent properties of the substrate without losing integrity at the repair site. The repaired sites were tested for adhesion, corrosion, hardness, microhardness, surface toughness, thermal stability, ability to withstand bending of the repair site, and the ability to endure a high-pressure water blast without compromising the repaired site. The repaired material could not change the inherent properties of the substrate throughout each of the test in order to remain a possible technique to repair the RSRM substrate materials. One repair method, Electro-Spark Alloying, passed all the testing and is considered a candidate for further evaluation.

I. INTRODUCTION

The purpose of the testing was to test several possible methods for improving/repairing seal surface defects within D6-AC steel and 7075-T73 aluminum. The techniques tested were WIRE ARC Spraying, High Velocity Oxygen Fuel (HVOF) Thermal Spraying, Microplasma Transfer Arc (MPTA), Laser Induced Surface Improvement (LISI), Electro-Spark Alloying (ESA), and the application of an Epoxy-Metal Composite (DEVCON). These techniques were analyzed to be possible backups for cell plating being worked on in Utah. The problem with cell plating for the D6-AC is the issue of hydrogen embrittlement. This issue could cause problems in qualifying the cell plating method for RSRM flight requirements due to delayed failure caused by hydrogen embrittlement of the repaired area. The aluminum parts have successfully been repaired by cell plating therefore, this paper has only partial data on aluminum since a backup method was no longer needed.

The design criteria for the repair of RSRM hardware requires that all defects found in the defined seal zone be repaired by blending during the refurbishment cycle prior to flight. Blending creates a smooth transition between the bottom of the defect and the substrate. Damage of sealing surfaces is caused mainly by corrosion, along with assembly and disassembly handling. Damage or defects to the sealing surfaces can compromise the defined seal zone.

The coupons repaired by the various methods were tested by a series of pre-qualification tests including adhesion, surface roughness, thermal cycling, corrosion, and hardness.

II. SUMMARY

There were six different techniques tested during this plan to repair seal surface defects in materials used for RSRM hardware. All methods were tested on D6-AC steel whereas, only three of the methods were used on aluminum due to the success of cell plating on aluminum. The testing done with D6-AC steel will be discussed in the most detail since it is the substrate that a repair method is currently required. Five of the six methods failed at least one of the tests for the repaired coupon. The test all five failed was hardness. The repair methods made the repaired areas different from the substrate material mainly by having a heat-affected area. The only repair method to pass all tests subjected to the repaired material was ESA. ESA appears to be the most promising repair method to do possible further evaluation.

III. REPAIR METHODS

A. WIRE ARC Spraying

In the Arc Spray Process a pair of electrically conductive wires is melted by means of an electric arc. The molten material is atomized by compressed air and propelled towards the substrate surface. The impacting molten particles on the substrate rapidly solidify to form a coating. This process carried out correctly is called a "cold process" (relative to the substrate material being coated), as the substrate temperature can be kept low during processing avoiding damage, metallurgical changes and distortion to the substrate material. Arc spray coatings are normally denser and stronger than their equivalent combustion spray coatings. Low running costs, high spray rates and efficiency make it a good tool for spraying large areas and high production rates. Disadvantages of the process are that only electrically conductive wires can be sprayed and if substrate preheating is required, a separate heating source is needed.

B. High Velocity Oxygen Fuel (HVOF) Thermal Spray Process

The HVOF (High Velocity Oxygen Fuel) Thermal Spray Process is basically the same as the combustion powder spray process (LVOF) except that this process has been developed to produce extremely high spray velocity. There are a number of HVOF guns, which use different methods to achieve high velocity spraying. One method is basically a high-pressure water-cooled combustion chamber and long nozzle. Fuel (kerosene, acetylene, propylene and hydrogen) and oxygen are fed into the chamber; combustion produces a hot high-pressure flame, which is forced down a nozzle increasing its velocity. Powder may be fed axially into the combustion chamber under high pressure or fed through the side of a laval type nozzle where the pressure is lower. Another method uses a simpler system of a high-pressure combustion nozzle and air cap. Fuel gas (propane, propylene or hydrogen) and oxygen are supplied at high pressure, combustion occurs outside the nozzle but within an air cap supplied with compressed air. The compressed air pinches and accelerates the flame and acts as a coolant for the gun. Powder is fed at high pressure axially from the center of the nozzle. The coatings produced by HVOF are similar to those produced by the detonation process. Coatings are very dense, strong and show low residual tensile stress or in some cases compressive stress, which enable thicker coatings to be applied than previously possible with the other processes. The very high kinetic energy of particles striking the substrate surface does not require the particles to be fully molten to form high quality coatings. This is certainly an advantage for the carbide cermet type coatings and is where this process really excels.

C. Microplasma Transfer Arc (MPTA)

The process of MPTA is implemented by the use of plasma, a gas that is heated to an extremely high temperature and ionized so that it becomes electrically conductive. Similar to GTAW (TIG), the plasma arc welding process uses this plasma to transfer an electric arc to a work piece. The metal to be welded is melted by the intense heat of the arc and fuses together. In the plasma welding torch a tungsten electrode is located within a copper nozzle having a small opening at the tip. A pilot arc is initiated between the torch electrode and nozzle tip. This arc is then transferred to the metal to be welded. By forcing the plasma gas and arc through a constricted orifice, the torch delivers a high concentration of heat to a small area. With high performance welding equipment, the plasma process produces exceptionally high quality welds.

D. Laser Induced Surface Improvement (LISI)

The LISI process uses high-powered lasers to repair metal surfaces. The first step is to form the appropriate master alloy powder for the substrate that is being repaired and apply it to the surface of the substrate as a paint or thin film. The laser is then used to melt the master alloy layer into the substrate. The laser allows for uniform heating, precise control of location, and the laser dwells for short time periods allowing rapid cooling. The advantages of this process is the ability to select precisely the area to be modified, only small amounts of modifier alloy required, and the process is environmentally friendly and permanent.

E. Epoxy-Metal Composite (DEVCON)

High-performance, metal-filled epoxies permanently repair or rebuild critical equipment and quickly return it to service, minimizing expensive downtime and reducing costs. Metal-filled epoxies offer excellent resistance to a broad range of chemicals, good temperature resistance, and a room temperature cure. Plant personnel without special training can effectively apply it.

F. Electro-Spark Alloying (ESA)

The ESA process produces an electric arc through a moving electrode energized by a series of capacitors as it is short-circuited momentarily with the substrate. During the generation of the arc, small particles of the electrode material are melted, accelerated through the arc, impacted against the substrate, solidified rapidly, and built-up incrementally. The advantages to this process are the true metallurgical bond with substrate, substrate remains at/near room temperature, can form a wide range of surface alloys, unique geometry electrodes can be formed to process hard to reach crevices, and the surface buildup can occur with low to no heat affected zone.

IV. TESTING

A. High-Pressure Water Blast (HPWB)

Four 3" x 3" coupons with 20 mil defect repairs for each coating material by each technique were used to evaluate the adhesion and erosion of the repair material through use of the HPWB system. Two coupons were high-pressure water blasted without masking using the grease removal parameters. Two coupons were high-pressure water blasted using the paint removal parameters.

B. Salt Spray (Fog)

Three 3" x 3" coupons with 20-mil defect repairs for each coating material by each technique were used to evaluate corrosion of the repair and the perimeter of the repaired area. One coupon was exposed to a 5% salt spray environment per ASTM B 117 for 96 hours. The coating and substrate of each coupon were examined for corrosion. One coupon was exposed to simulated ocean water per ASTM D 1141 (without heavy metals) for 96 hours. The coating and substrate for each coupon were evaluated for corrosion each day according to the scale in ASTM D 610. One coupon was supposed to be exposed to inhibited soft water from the Component Refurbishment Center for two weeks with the exception of the coupons repaired by ESA due to the limited number of repaired coupons. This particular corrosion test was not done due to limits on repaired materials and time constraints.

C. Adhesion

Two coupons with 20-mil defect repairs for each coating material by each technique and all coupons from other test sections, which can be used once the other testing is complete, were tested with the P.A.T.T.I. tester according to LTP-2435-0988. The tensile strengths and failure modes were recorded.

D. Surface Roughness

Two coupons with 20-mil defect repairs for each coating by each technique were used to evaluate surface roughness. Surface roughness, rms, were determined by use of a Surtronic 10 stylus profilometer, or Hummel T500 stylus profilometer.

E. Thermal Cycling

Two coupons with 20-mil defect repairs for each coating by each technique were tested to determine the effects of thermal cycling on coating adhesion. The coupons were tape tested in accordance with MIL-STD-865C, heated to approximately 250^{o}F, allowed to cool to room temperature and tape tested again. The coupons were then heated to approximately 350^{o}F, and allowed to cool to room temperature and tape tested. The coupons were then heated to approximately 350^{o}F, and cooled to room temperature an additional 19 times, then inspected for cracking or any other thermal expansion mismatch that could cause coating failure. The samples were tape tested a final time.

F. Hardness Test

For D-6AC steel substrate, two coupons with 20-mil defect repairs for each coating by each technique and one control (unblended, unrepaired) D6-AC coupon were evaluated using a Rockwell C hardness test with a Brale indentor and a 150 kg major load, for high strength steel. For 7075 aluminum specimens, two coupons with 10-mil defect repairs for each coating by each technique and one control (unblended, unrepaired) aluminum coupon were evaluated using a Rockwell B hardness test with a 1/16 in. ball under a 100 kg. major load. The repaired area and surrounding substrate were evaluated for hardness using the appropriate techniques.

G. Microhardness Test

This test was a deviation from the original planning and the reason for the need for this test is explained in this section. Some of the techniques required heat being applied to the substrate to repair the defect. This increase in temperature of the substrate and repair material led to a heat-affected zone (HAZ) for some of the materials. A HAZ is considered unacceptable because it can change the inherent properties of the substrate. In order to evaluate the effect of the HAZ on appropriate materials repaired by techniques using an increase in temperature, a microhardness test was done on the coupons to determine the size and effect on the substrate by the HAZ. Microhardness is similar to hardness testing with the exception that the sample is cross-sectioned and the microhardness is measured through the repair all the way down to the substrate. The sample is magnified and photographed which enables a view of the HAZ.

V RESULTS

The results of the testing done on the six repair methods will be presented in tabular form with results explained as pass/fail for each test done on the repaired coupons. The results are shown in Tables 1-6. The repair method that appears to be viable as a repair method for RSRM hardware is ESA. Surface Treatment Technologies, a private company based out of Maryland, accomplished the repair method ESA for this testing. The company can make the method for repair of specific parts, for example a curved cathode to fit into joints. The coupons were repaired with two different materials, D6-ac steel and Inconel 625. The coupons were machined after being repaired but were not polished; therefore, the surface roughness data is higher than for previously reported repair methods. The other tests performed on the repaired coupons were; P.A.T.T.I., high-pressure water blast, thermal cycling, salt fog, ocean water, hardness, and microhardness. As previously stated, the ESA repaired coupons successfully passed all the tests. More in-depth testing is planned, specifically on the HAZ concern.

VI CONCLUSIONS

Of all the processes studied ESA seems the most viable as an alternate for the repair of RSRM hardware. Even though this method seems to work that does not mean other methods cannot be looked at in order to keep from putting all the effort in one method that might not pass more extensive testing. The

search for an alternate method should be an ongoing search since technology is constantly changing and improving. One method found late in this project that could be feasible if it is decided to explore it is Low Temperature Arc Vapor Deposition.

Table 1: **High-Pressure Water Blast Test Results**

Method	Material	Results
Trowel Application	Devcon Epoxy-Composite Titanium base	Devcon material eroded from the D6-AC substrate with each pass of the HPWB nozzle.
Trowel Application	Devcon Epoxy-Composite Steel base	Devcon material eroded from the D6-AC substrate with each pass of the HPWB nozzle.
Wire Arc spray	95% Nickel	Material was not removed but had a grit-blasted appearance. Pores or voids become visible on surface.
Wire Arc spray	80/20 Nickel - Chrome	Material was not removed but had a grit-blasted appearance. Pores or voids become visible on surface.
Wire Arc spray	High carbon steel	Material was not removed but had a grit-blasted appearance. Pores or voids become visible on surface.
High Velocity Oxygen fuel thermal spray	Microblaze LM	No test; repair material did not maintain the necessary integrity during initial polishing to be considered for testing.
High Velocity Oxygen fuel thermal spray	Inconel 718	No test; repair material did not maintain the necessary integrity during initial polishing to be considered for testing.
High Velocity Oxygen fuel thermal spray	Inconel 903	No test; repair material did not maintain the necessary integrity during initial polishing to be considered for testing.
Microplasma Transfer Arc Weld (MPTA)	Inconel 625	No failures in HPWB using adhesive removal parameters (most aggressive), includes coupons which have cycled through other tests.
(MPTA)	Microblaze LM	Not used in lieu of other material
(MPTA)	Miles steel 1020	Not used in lieu of Stainless steel 316
(MPTA)	Ni 61	No failures in HPWB using adhesive removal parameters (most aggressive), includes coupons which have cycled through other tests. Small problem seen in one coupon along an incomplete weld bead.
(MPTA)	Inconel 718	Some small defects created from the HPWB, generally very small edge failures at substrate-repair transition.
(MPTA)	Stainless Steel 316	No failures in HPWB using adhesive removal parameters (most aggressive), includes coupons which have cycled through other tests.
Laser Induced Surface Improvement (LISI)	Fe/ Ni	Small anomalies seen from HPWB due to the initial material application, Surface Treatment Technologies engineer assures that any application can be improved significantly.
Electro-Spark Alloying (ESA)	D6-AC Steel	No failures in HPWB using adhesive removal parameters (most aggressive), includes coupons which have cycled through other tests.
Electro-Spark Alloying (ESA)	Inconel 625	No failures in HPWB using adhesive removal parameters (most aggressive), includes coupons which have cycled through other tests.

Table 2: **Corrosion Test Results**

Method	Material	Results
Trowel Application	Devcon Epoxy-Composite Titanium base	No effects of corrosion from either 5% salt fog or simulated seawater in the composite material, the D6-AC steel has oxidized normally in the area surrounding the repair area
Trowel Application	Devcon Epoxy-Composite Steel base	No effects of corrosion from either 5% salt fog or simulated seawater in the composite material, the D6-AC steel has oxidized normally in the area surrounding the repair area
Wire Arc spray	95% Nickel	Heavy oxidation across entire surface of coupon. Signs of corrosion under repair area and a bubbling on repair area.
Wire Arc spray	80/20 Nickel - Chrome	No test; repair material did not maintain the necessary integrity during initial polishing to be considered for testing.
Wire Arc spray	High carbon steel	No test; repair material did not maintain the necessary integrity during initial polishing to be considered for testing.
High Velocity Oxygen fuel thermal spray	Microblaze LM	No test; repair material did not maintain the necessary integrity during initial polishing to be considered for testing.
High Velocity Oxygen fuel thermal spray	Inconel 718	No test; repair material did not maintain the necessary integrity during initial polishing to be considered for testing.
High Velocity Oxygen fuel thermal spray	Inconel 903	No test; repair material did not maintain the necessary integrity during initial polishing to be considered for testing.
Microplasma Transfer Arc Weld (MPTA)	Inconel 625	Repair has shown no effects of corrosion with either 5%salt fog or simulated seawater. The D6-AC substrate was heavily oxidized in salt fog and has begun to flake away.
(MPTA)	Microblaze LM	No test; material not used in lieu of other material which may perform better
(MPTA)	Miles steel 1020	Not used in lieu of Stainless steel 316
(MPTA)	Ni 61	Repair area has shown no effects of corrosion in either 5%salt fog or simulated seawater; surrounding D6-AC surface shows normal oxidation.
(MPTA)	Inconel 718	Repair area has shown no effects of corrosion in either 5% salt fog or simulated sea ater: un-repaired D6-AC shows normal oxidation.
(MPTA)	Stainless Steel 316	Repair area has shown no effects of corrosion in either 5% salt fog or simulated seawater: un-repaired D6-AC shows normal oxidation.
Laser Induced Surface Improvement (LISI)	Fe/ Ni	Simulated seawater had very minimal corrosion in both repair area and substrate. 5% salt fog had homogenous corrosion across entire surface of coupon , no failure of repaired area due to oxidized surface.
Electro-Spark Alloying (ESA)	D6-AC Steel	Repair area has shown normal oxidation for D6-AC in both 5% salt fog and simulated seawater: un-repaired D6-AC shows normal oxidation.
Electro-Spark Alloying (ESA)	Inconel 625	Repair area has shown no effects of corrosion in either 5% salt fog or simulated seawater: un-repaired D6-AC shows normal oxidation.

Table 3: **Adhesion Test Results**

Method	Material	Results
Trowel Application	Devcon Epoxy-Composite Titanium base	Pull test adhesive had a partial failure.
Trowel Application	Devcon Epoxy-Composite Steel base	Pull test adhesive had a partial failure
Wire Arc spray	95% Nickel	Adhesive failure between the adhesive and the substrate and the repaired area remained unaffected
Wire Arc spray	80/20 Nickel - Chrome	No test; repair material did not maintain the necessary integrity during initial polishing to be considered for testing.
Wire Arc spray	High carbon steel	No test; repair material did not maintain the necessary integrity during initial polishing to be considered for testing.
High Velocity Oxygen fuel thermal spray	Microblaze LM	No test; repair material did not maintain the necessary integrity during initial polishing to be considered for testing.
High Velocity Oxygen fuel thermal spray	Inconel 718	No test; repair material did not maintain the necessary integrity during initial polishing to be considered for testing.
High Velocity Oxygen fuel thermal spray	Inconel 903	No test; repair material did not maintain the necessary integrity during initial polishing to be considered for testing.
Microplasma Transfer Arc Weld (MPTA)	Inconel 625	No pull was obtained.
(MPTA)	Microblaze LM	Not used in lieu of other material
(MPTA)	Miles steel 1020	Not used in lieu of Stainless steel 316
(MPTA)	Ni 61	Adhesive failure between the adhesive and the substrate while the repaired area remained unaffected
(MPTA)	Inconel 718	Adhesive failure between the adhesive and the substrate while the repaired area remained unaffected
(MPTA)	Stainless Steel 316	Adhesive failure between the adhesive and the substrate while the repaired area remained unaffected
Laser Induced Surface Improvement (LISI)	Fe/ Ni	Adhesive failure between the adhesive and the substrate while the repaired area remained unaffected
Electro-Spark Alloying (ESA)	D6-AC Steel	Adhesive failure between the adhesive and the substrate while the repaired area remained unaffected
Electro-Spark Alloying (ESA)	Inconel 625	Adhesive failure between the adhesive and the substrate while the repaired area remained unaffected

Table 4: Hardness Test Results

Method	MATERIAL	Results
Trowel Application	Devcon Epoxy-Composite Titanium base	Test results were inconclusive due to partial hardness reading of the material substrate
Trowel Application	Devcon Epoxy-Composite Steel base	Test results were inconclusive due to partial hardness reading of the material substrate
Wire Arc spray	95% Nickel	Hardness values were obtained to an average of RHb of 65.9
Wire Arc spray	80/20 Nickel - Chrome	No test; repair material did not maintain the necessary integrity during initial polishing to be considered for testing.
Wire Arc spray	High carbon steel	No test; repair material did not maintain the necessary integrity during initial polishing to be considered for testing.
High Velocity Oxygen fuel thermal spray	Microblaze LM	No test; repair material did not maintain the necessary integrity during initial polishing to be considered for testing.
High Velocity Oxygen fuel thermal spray	Inconel 718	No test; repair material did not maintain the necessary integrity during initial polishing to be considered for testing.
High Velocity Oxygen fuel thermal spray	Inconel 903	No test; repair material did not maintain the necessary integrity during initial polishing to be considered for testing.
Microplasma Transfer Arc Weld (MPTA)	Inconel 625	Hardness values were obtained to an average of RHb of 66.1
(MPTA)	Microblaze LM	Not used in lieu of other material
(MPTA)	Miles steel 1020	Not used in lieu of Stainless steel 316
(MPTA)	Ni 61	Hardness values were obtained to an average of RHc of 24.4
(MPTA)	Inconel 718	Hardness values were obtained to an average of RHc of 20.2
(MPTA)	Stainless Steel 316	Hardness values were obtained to an average of RHc of 28
Laser Induced Surface Improvement (LISI)	Fe/ Ni	Hardness values were obtained to an average of RHc of 29.4
Electro-Spark Alloying (ESA)	D6-AC Steel	Hardness values were obtained to an average of RHc of 41.9
Electro-Spark Alloying (ESA)	Inconel 625	Hardness values were obtained to an average of RHc of 39.4

Table 5: **Thermal Cycling**

Method	Material	Results
Trowel Application	Devcon Epoxy-Composite Titanium base	No anomalies were noted. Repair area appeared normal following thermal cycling.
Trowel Application	Devcon Epoxy-Composite Steel base	No anomalies were noted. Repair area appeared normal following thermal cycling.
Wire Arc spray	95% Nickel	No anomalies were noted. Repair area appeared normal following thermal cycling.
Wire Arc spray	80/20 Nickel - Chrome	No test; repair material did not maintain the necessary integrity during initial polishing to be considered for testing.
Wire Arc spray	High carbon steel	No test; repair material did not maintain the necessary integrity during initial polishing to be considered for testing.
High Velocity Oxygen fuel thermal spray	Microblaze LM	No test; repair material did not maintain the necessary integrity during initial polishing to be considered for testing.
High Velocity Oxygen fuel thermal spray	Inconel 718	No test; repair material did not maintain the necessary integrity during initial polishing to be considered for testing.
High Velocity Oxygen fuel thermal spray	Inconel 903	No test; repair material did not maintain the necessary integrity during initial polishing to be considered for testing.
Microplasma Transfer Arc Weld (MPTA)	Inconel 625	No anomalies were noted. Repair area appeared normal following thermal cycling.
(MPTA)	Microblaze LM	Not used in lieu of other material
(MPTA)	Miles steel 1020	Not used in lieu of Stainless steel 316
(MPTA)	Ni 61	No anomalies were noted. Repair area appeared normal following thermal cycling.
(MPTA)	Inconel 718	No anomalies were noted. Repair area appeared normal following thermal cycling.
(MPTA)	Stainless Steel 316	No anomalies were noted. Repair area appeared normal following thermal cycling.
Laser Induced Surface Improvement (LISI)	Fe/ Ni	No anomalies were noted. Repair area appeared normal following thermal cycling.
Electro-Spark Alloying (ESA)	D6-AC Steel	No anomalies were noted. Repair area appeared normal following thermal cycling.
Electro-Spark Alloying (ESA)	Inconel 625	No anomalies were noted. Repair area appeared normal following thermal cycling.

Table 6: Surface Roughness

Method	Material	Results
Trowel Application	Devcon Epoxy-Composite Titanium base	Average readings from the Taylor-Hobson Surtronic Profilometer were 48.3 in
Trowel Application	Devcon Epoxy-Composite Steel base	Average readings from the Taylor-Hobson Surtronic Profilometer were 64 in
Wire Arc spray	95% Nickel	Average readings from the Taylor-Hobson Surtronic Profilometer were 25.3 in
Wire Arc spray	80/20 Nickel - Chrome	No test; repair material did not maintain the necessary integrity during initial polishing to be considered for testing.
Wire Arc spray	High carbon steel	No test; repair material did not maintain the necessary integrity during initial polishing to be considered for testing.
High Velocity Oxygen fuel thermal spray	Microblaze LM	No test; repair material did not maintain the necessary integrity during initial polishing to be considered for testing.
High Velocity Oxygen fuel thermal spray	Inconel 718	No test; repair material did not maintain the necessary integrity during initial polishing to be considered for testing.
High Velocity Oxygen fuel thermal spray	Inconel 903	No test; repair material did not maintain the necessary integrity during initial polishing to be considered for testing.
Microplasma Transfer Arc Weld (MPTA)	Inconel 625	Average readings from the Taylor-Hobson Surtronic Profilometer were 26.3 in
(MPTA)	Microblaze LM	Not used in lieu of other material
(MPTA)	Miles steel 1020	Not used in lieu of Stainless steel 316
(MPTA)	Ni 61	Average readings from the Taylor-Hobson Surtronic Profilometer were 7.3 in
(MPTA)	Inconel 718	Average readings from the Taylor-Hobson Surtronic Profilometer were 12 in
(MPTA)	Stainless Steel 316	Average readings from the Taylor-Hobson Surtronic Profilometer were 24.6 in
Laser Induced Surface Improvement (LISI)	Fe/ Ni	Average readings from the Taylor-Hobson Surtronic Profilometer were 5.3 in
Electro-Spark Alloying (ESA)	D6-AC Steel	Average readings from the Taylor-Hobson Surtronic Profilometer were 89.77 in
Electro-Spark Alloying (ESA)	Inconel 625	Average readings from the Taylor-Hobson Surtronic Profilometer were 77.72 in

ACKNOWLEDGEMENTS

The authors would like to thank everyone involved in the success of this project. Specifically, the authors would like to thank Dan Holt (NASA), Preston McGill (NASA), Robert McBride (Thiokol), Dennis Moore (NASA), Jason Parker (Thiokol), Pablo Torres (NASA), Mike Riley (STT), and Tim Langan (STT).

Microgravity Manufacturing: Extending Rapid Prototyping Past the Horizon

Ken Cooper, NASA Marshall Space Flight Center

Abstract

Over the last decade, rapid prototyping (RP) technologies have continued to advance in all aspects of operation and application. From continuously advanced materials and processes development to more hard-core manufacturing uses, the RP realm has stretched considerably past its original expectations as a prototyping capability. This paper discusses the unique applications for which NASA has chosen these manufacturing techniques to be utilized in outer space.

Background

Manufacturing capability in outer space remains one of the critical milestones to surpass to allow for humans to conduct long duration manned space exploration. The high cost-to-orbit for leaving the Earth s gravitational field continues to be the limiting factor in carrying sufficient hardware to maintain extended life support in microgravity or on other planets. Additive manufacturing techniques, or chipless fabrication, like RP are being considered as the most promising technologies for achieving in-situ or remote processing of hardware components, as well as for the repair of existing hardware. At least three RP technologies are currently being explored for use in microgravity and extraterrestrial fabrication.

Fused Deposition Modeling

Fused Deposition Modeling (FDM) is a rapid proto-typing process developed by Stratasys, Inc., which deposits a fine line of semi-molten polymer onto a substrate while moving via computer control to form the cross sectional shape of the part it is building. The build platen is then lowered and the process is repeated, building a component directly layer by layer. This method enables direct net-shape production of polymer components directly from a computer file. The layered manufacturing process allows for the manufacture of complex shapes and internal cavities otherwise impossible to machine.

The application of FDM to microgravity manufacturing has sustained the highest degree of preliminary testing thus far. A commercial FDM unit was first tested by rotating the system onto its side and successfully building parts, free hanging, against the pull of gravity. The ABS plastic components fabricated in this manner were comparable to parts fabricated in the upright position, which warranted further testing in the microgravity range. (*See Figure 1).*

Figure 1. The Fused Deposition Modeling process applied against gravity, on its side.

In light of those results, the FDM system was tested jointly by NASA s Marshall Space Flight Center (MSFC), Johnson Space Center (JSC) and the Milwaukee School of Engineering (MSOE) on board the NASA KC135 Reduced Gravity plane, and again yielded positive results. Seven geometries were successfully fabricated over a series of four flights, resulting in a total of approximately 1-hour of zero-g flight time on the system. In fact, it was found during the flight testing that part configurations that required supporting fixtures during normal operation could be constructed freeform, or without supports, which eliminated the need for scrap support materials.

The next step underway is to develop an FDM system to install on the Space Shuttle, in order to examine long-term microgravity operation characteristics and functionality. The current smallest commercial FDM system is still much too large and heavy for installation on a standard shuttle middeck locker rack. The largest attachment capability, the double adapter plate, will have to be used even with a smaller modified FDM system. Some necessary steps to acquire a flight-ready FDM system are as follows:

- Acquire candidate polymer hardware geometry currently stocked as spare parts on the space shuttle or station, and fabricate these designs using ground-based FDM systems with ABS plastic.
- Determine build time requirements for each component, in order to properly schedule parts to be built in space during a short duration mission.
- Determine maximum allowable factors for a space-based demonstration FDM unit, including weight and physical dimensions, environmental effects, i.e. toxicity, heat output and power consumption limits.
- Determine, from parts inventory and feasibility study, the maximum build envelope capacity of the reduced FDM system.

- Design and build part storage containers for safe return of test articles to Earth.
- Place the FDM demonstration flight unit in the queue for Space Shuttle flight experiments. The shuttle flight would accomplish or establish the following: demonstration of long duration flight operation of the FDM system, optimization of controls for astronaut friendly operation, allow for studying the effects of surface tension on build capability, build shuttle spare part geometries as fabricated on the ground for comparison and build microgravity-dependent part configurations to demonstrate advanced manufacturing.

Once a flight system is completed and is used to build parts during a mission, NASA must test components fabricated on the space shuttle for changes in mechanical properties, surface cohesion, layer-to-layer bonding and physical properties (porosity, density, dimensional stability, etc.)

NASA will benefit in a variety of ways from the successful completion of this project. First, fabrication of flight hardware spares in microgravity will lower flight weight, and particularly volume, due to excessive spares inventory. Second, the creation of new hardware, i.e. modified designs for other in-flight projects, will allow for innovation and optimization of flight experiments during a mission.

Selective Laser Sintering

Figure 2. A Selective Laser Sintering part just after fabrication.

Selective Laser Sintering (SLS) is a powder-based rapid prototyping process, which employs scanning laser technology to fuse the build material in the shape of the part cross-sections, one on top of the other. (*See Figure 2).* The current materials used with SLS include wax, polycarbonate, polyamide, nylon, polymer matrix metals and polymer matrix sand. NASA is exploring the possibility of using SLS based technology to form glass and structural materials from lunar and Martian soil, with the ultimate application being the fabrication of spacecraft glass, large lenses or mirrors, and even glass bio-domes directly on the

surface of the moon and Mars using the existing soil. This would have a tremendous positive impact on colonization, as the build materials required would not have to be transported from the Earth.

The SLS technology is probably the most versatile rapid prototyping process on the market as far as polymer materials capability. SLS is largely researched for advanced materials capability in academia, including direct metal sintering, direct ceramic powder sintering, and composite material RP development. Some preliminary studies have been conducted at various universities on the formation of glass using laser sintering technologies, using sand or lunar simulant. MSFC currently houses world-class experience in the formation of glass from lunar soil, and the intent of this study is to draw on that capability along with the in-house rapid prototyping expertise.

The next step will be to determine the feasibility of rapidly prototyping structural components using SLS and lunar soil simulants as a build material. Studies must be conducted to determine laser power requirements for small-spot glass formation, layer-to-layer bonding characteristics, and the effects of scaling up the process for large-scale component fabrication.

Successful determination of sintering parameters will lead to materials properties testing and International Space Station flight experiment development and demonstration. Power sources to be considered are laser and focused solar energy. A KC135 Reduced Gravity demonstration will proceed the space station flight to determine the feasibility of using this process in a low-gravity environment.

Laser Engineered Net Shaping

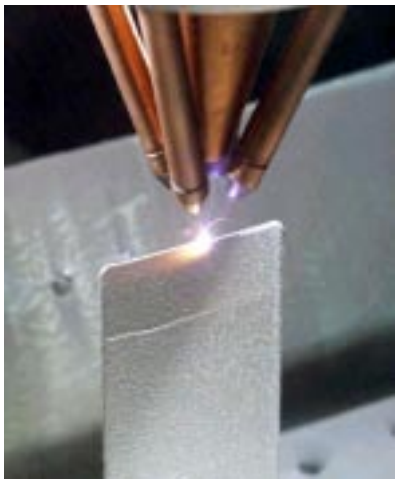

Figure 3. The Laser Engineered Net Shaping process during operation.

Laser Engineered Net Shaping (LENS) is a new rapid prototyping process developed by Sandia National Laboratories and marketed by Optomec Design Company, which sprays a fine line of metal powder into a moving, focused laser, building a component directly layer by layer. *(See Figure 3).* This method enables direct near-net-shape production of metallic components directly from a computer file. The layered manufacturing process allows for the manufacture of complex shapes and internal cavities otherwise impossible to machine. NASA will exploit the benefits of the LENS technique to quickly and inexpensively produce replacement components or repair broken hardware in a space shuttle or space station environment.

The LENS technology has been in operation for a very short time, although it has been tested against the pull of gravity by one of the current users of the system. In this application, the LENS head was placed on a multi-axis robotic arm, which allowed for the fabrication of part components even in upside-down situations. Additions were made to the system to keep powder overspray from accumulating on the laser lens, which would also be necessary in a microgravity environment. The next step will be to build a smaller, simpler LENS system in order to proof the feasibility of operation in a microgravity environment. As in the FDM process, there a various steps to accomplish a flight-ready LENS-type system, including:

- NASA must acquire candidate hardware component geometry currently stocked as spare parts on the space shuttle or station, and fabricate these designs using a ground-based LENS system with a suitable metal, i.e. stainless steel or aluminum.
- Determine maximum allowable factors for a space-based demonstration LENS unit, including weight, size and power consumption limits.
- Determine, from parts inventory and feasibility study, the maximum build envelope capacity of the reduced LENS system, in addition to most suitable build materials for microgravity, powder reclamation capability, and part removal from platen options.
- Fabricate a LENS demonstration flight unit.

After a flight unit is prepared, NASA must conduct flight feasibility studies using the NASA KC135 Reduced Gravity Flight Test and analyze the parts fabricated in Reduced Gravity Flight Test for consistency with ground-based fabricated components to determine if any modifications will be required prior to shuttle flight. NASA will then place the LENS demonstration flight unit in the queue for Space

Shuttle flight experiments, finally to test the components fabricated on the space shuttle for changes in mechanical properties.

NASA will benefit in a variety of ways from the successful completion of the LENS project. First, fabrication of flight hardware spares in microgravity will become a reality. Second, the repair of damaged or broken components may also be accomplished without affecting the materials properties of the repaired component. In addition, preliminary NASA studies of LENS-fabricated components have confirmed that the mechanical properties are actually stronger than wrought-annealed properties. This will lead to the use of more economical materials for higher performance applications.

NASA s advanced LENS system for use on space station will utilize an incorporated vision system for component inspection and selective repair, multiple build materials capabilities to meet various processing needs, low power (i.e. diode laser) consumption with maximum output, 100% powder reclamation capability and an integrated platen/part separation system. NASA is also currently pursuing development of hand-held LENS repair units for the regeneration of damaged spacecraft hulls during space flight. These systems will smart scan spacecraft hull surfaces for micro-meteorite damage detection and repair, using advanced digital imaging and void recognition software, and will selectively repair defects with parent material either manually or remotely by computer. Finally, large orbiting LENS systems are foreseen for major repair and overhaul requirements, in addition to in-situ fabrication of metal hardware from lunar, asteroid, or Martian soil. *(See Figure 4).*

Figure 4. A concept of a Martian rover duplicating itself from the Martian soil.

Ultrasonic Object Consolidation

Ultrasonic Object Consolidation (UOC) is an exciting new metal rapid prototyping process developed by Solidica, Inc. in Ann Arbor, MI. The UOC process is a low-heat, low-energy material

joining technique that shows the highest promise for fabricating aluminum or titanium hardware in microgravity. The process works on the same principal as solid state welding currently used in electronics manufacturing. Two thin layers of material are brought into contact under pressure, and are then submitted to ultrasonic vibration between them (on the order of a few microns). The rubbing action causes the oxide layers of each material to break away, exposing two atomic-clean metal surfaces to each other, causing a solid-state weld. Figure 5 demonstrates the UOC process.

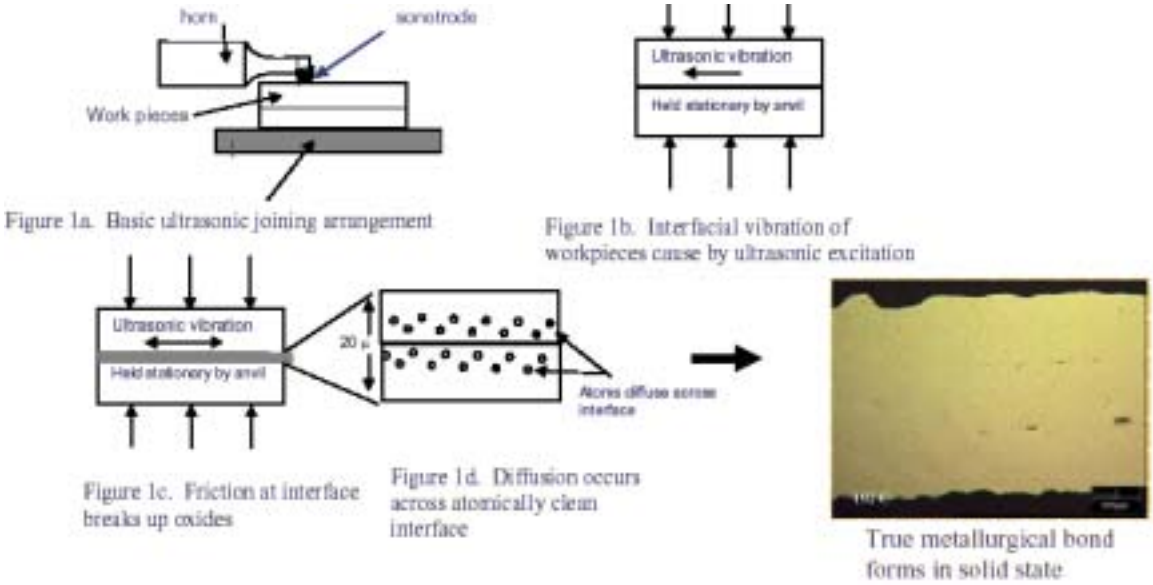

Figure 5. A Description of the Ultrasonic Object Consolidation (UOC) process from Solidica.

The amount of heat generated is negligible, and the energy and forces required to make a bond on thin material are very low as well. NASA/MSFC is currently working with Solidica to develop a machine based on this principal that will potentially be adaptable to use in microgravity. The main issues to be addressed for adaptation will then be system size (volume), and the noise/vibration effects.

Laser Engineering Net Shaping

- Task- Present some of RP Lab's findings and experiences with this technology.
- Standards- The audience; Experiment the variables of this machine s operation.
- Conditions- 45 minutes, lecture and Power Point presentation in classroom environment.

What It Is

- YAG Laser
- Controlled Environment (Argon)
- X,Y,Z= +/- .0005
- Two feed hoppers (bi-metal capable)
- Gas pressure feed with wheel pick up.

What It Isn t

- Perfected
- 100% Efficient
- Maintenance Free
- Cheap
- Real Smart

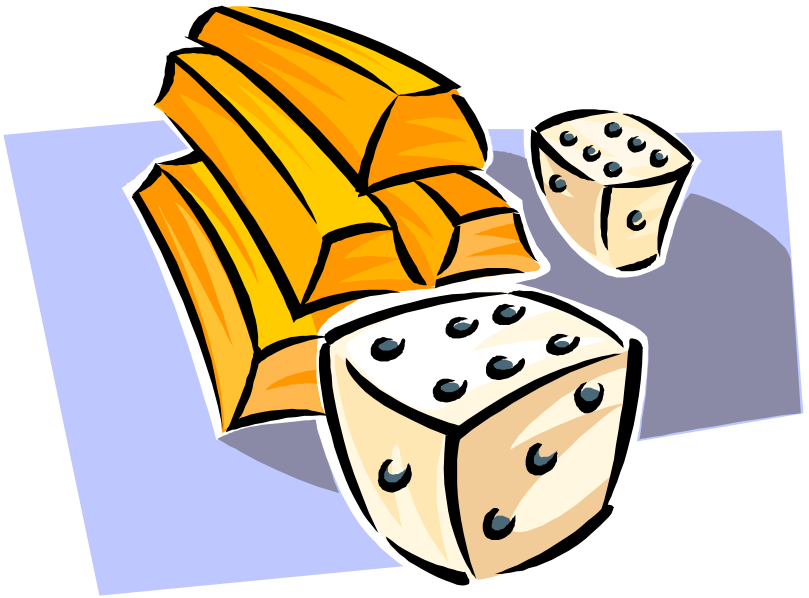

Our Machine

- LENS 750 by OPTOMEC
- 1999 Model
- Originally modified with powder recovery system & weld pool monitor (since removed)

At Work

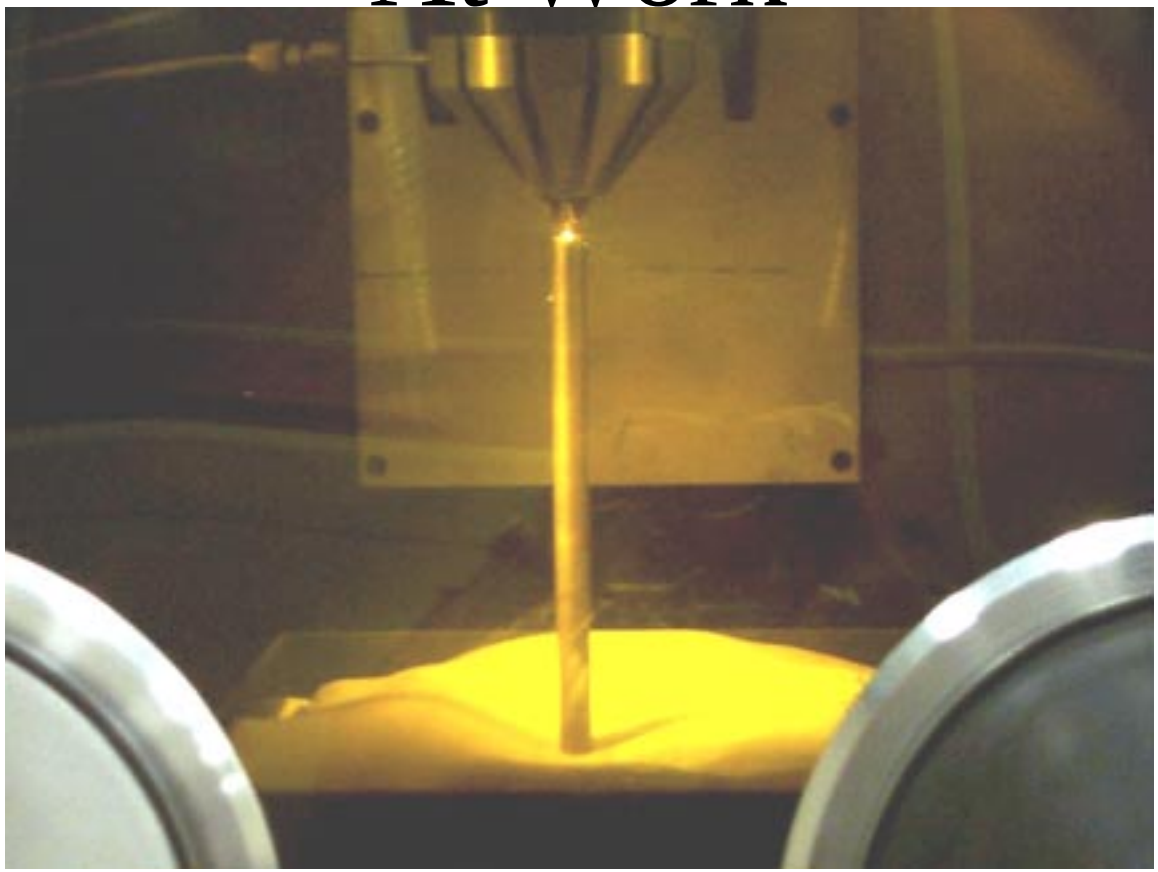

Screen 1- Variables

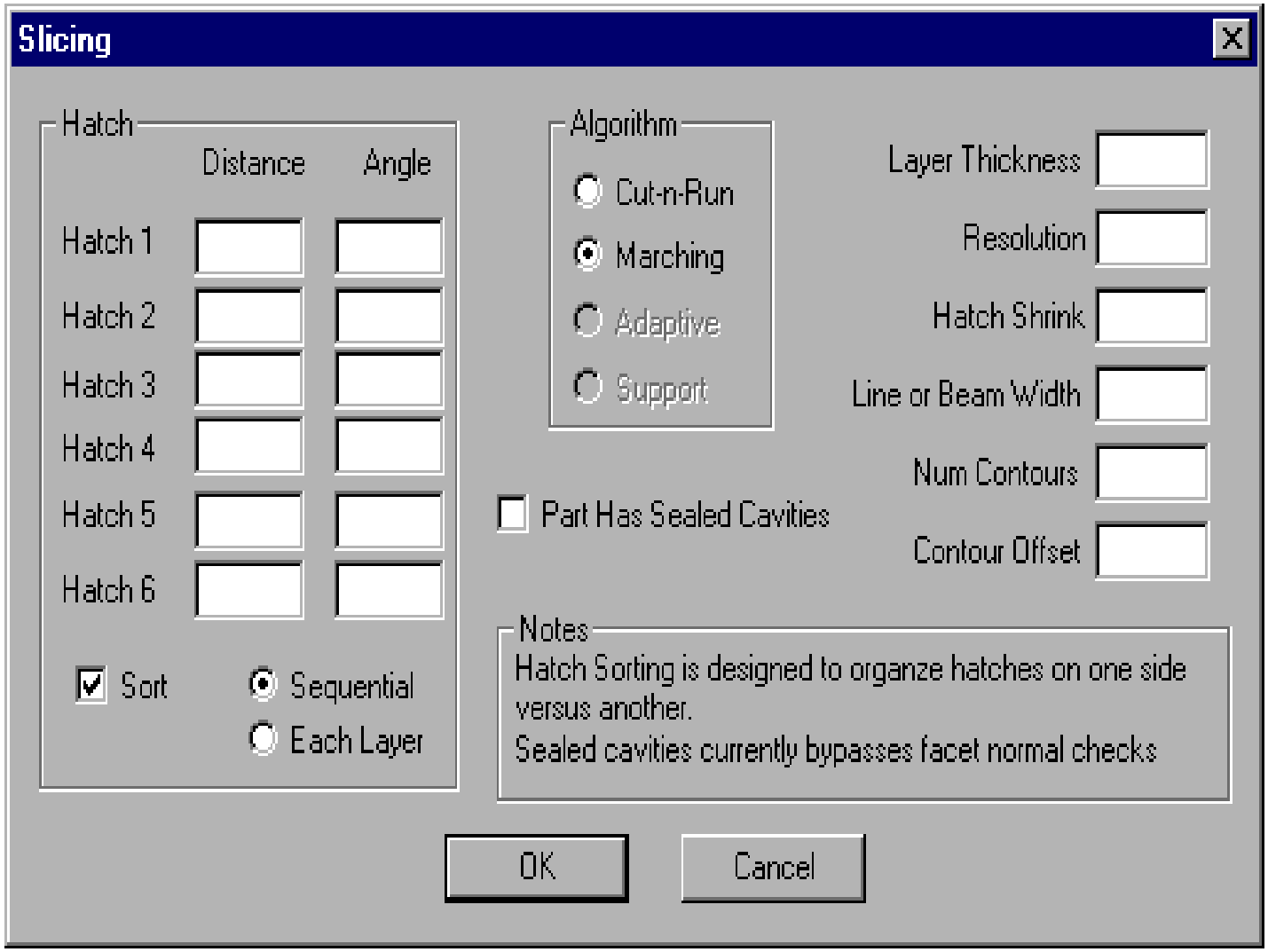

Screen 2- Variables

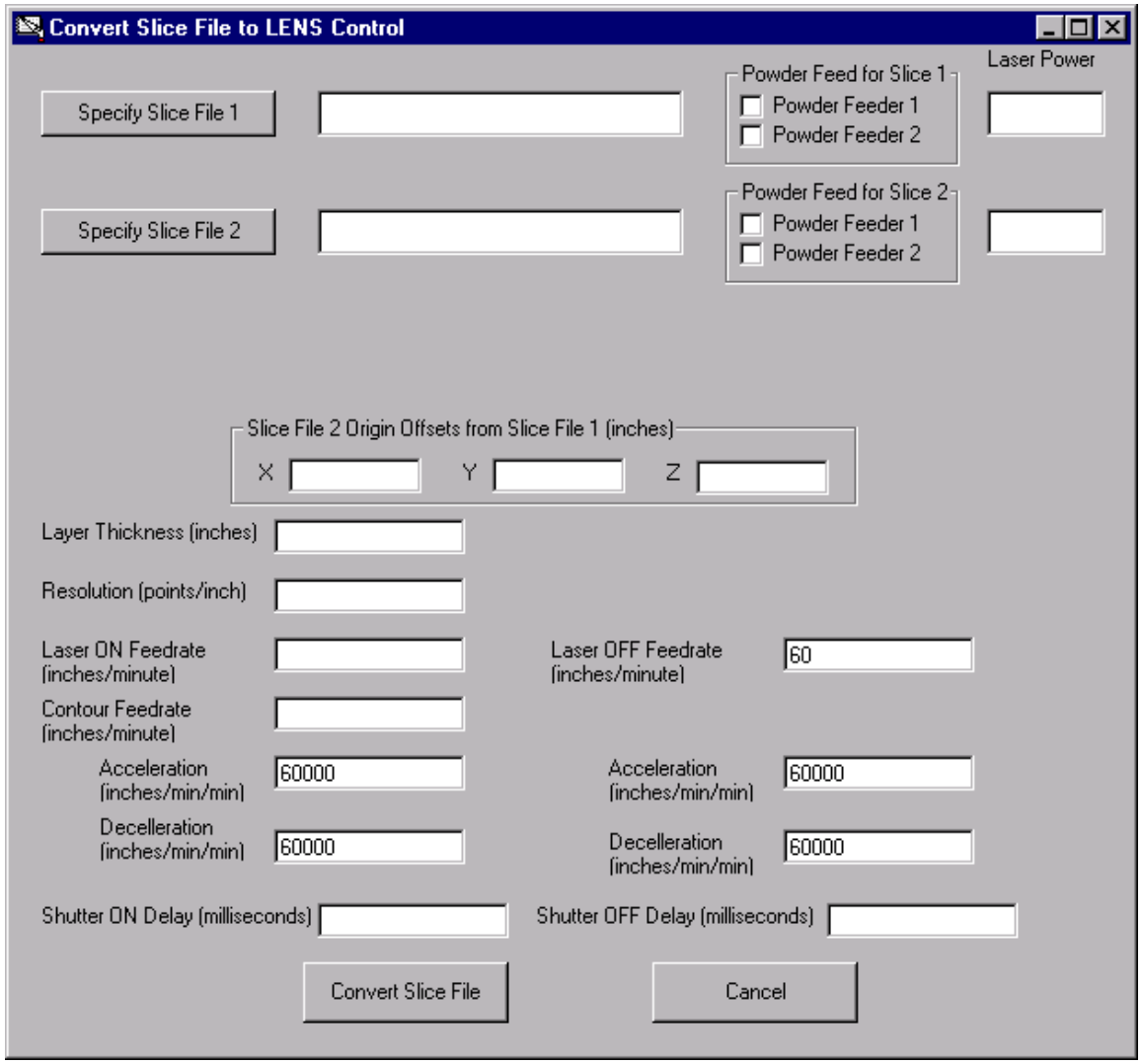

Considerations for Experiment Planning

Melting Temperatures of Constituents?

Oxidation & Effects?

Toxicity & Off-Gassing?

Spherical Diameter and Gradient?

Hydro & Feed Compatibility?

Materials We Have Tried-1

SS316 stainless steel	success
Inco718 (nickel based alloy)	success
Narloy Z (copper-silver alloy)+ Alumina Al2O3	didn’t deposit
Copper Chrome Niobium	didn’t deposit
Aluminum 2026	didn’t deposit
Inco718 + Alumina Al2O3 (mechanical mix)	deposit, but not homogeneous

Materials-2

SS316 + Alumina Al2O3 (new tricks)	success
Molybdenum-Rhenium	limited success
Nickel Aluminide	didn’t deposit
Copper Chrome Niobium (new tricks)	limited success
SS316 stainless steel	success
Inco718 (nickel based alloy)	success

Materials-3

Narloy Z (copper-silver alloy)	
+ Alumina Al2O3	didn’t deposit
Copper Chrome Niobium	didn’t deposit
Aluminum 2026	didn’t deposit
Inco718	
+ Alumina Al2O3 (mechanical mix)	deposit, but not homogeneous

Materials-4

SS316 + Alumina Al2O3 (new tricks)	success
Molybdenum-Rhenium	limited success
Nickel Aluminide	didn’t deposit
Copper Chrome Niobium (new tricks)	limited success

Laser Engineered Net Shaping Materials Status

- The initial mechanical properties tests are back
- Both Inco718 and SS316 LENS processed samples had, as advertised, better than wrought properties
- An extensive study will now be kicked in, to include 4 materials and 4 parameters, with a larger sampling of parts in each category.
- Will include strength, ductility, toughness and fatigue, with Ti and Al.

Material	Yield (ksi)	Ultimate (ksi)
LENS SS316	**58**	**120**
Wrought SS316	*40*	*85*
LENS Inco718	**190**	**215**
Wrought Inco718	*158*	*194*

Wrought vs. Deposited

MSFC Laser Engineered Net Shaping Materials Properties

	Yield (ksi)	Ultimate (ksi)
Stainless Steel 316	**58**	**120**
Wrought SS316	*40*	*85*
Inconel 718	**190**	**215**
Wrought Inco718	*158*	*194*

316-A AS FAB. LONG 25X

718-A AS FAB LONG 25X

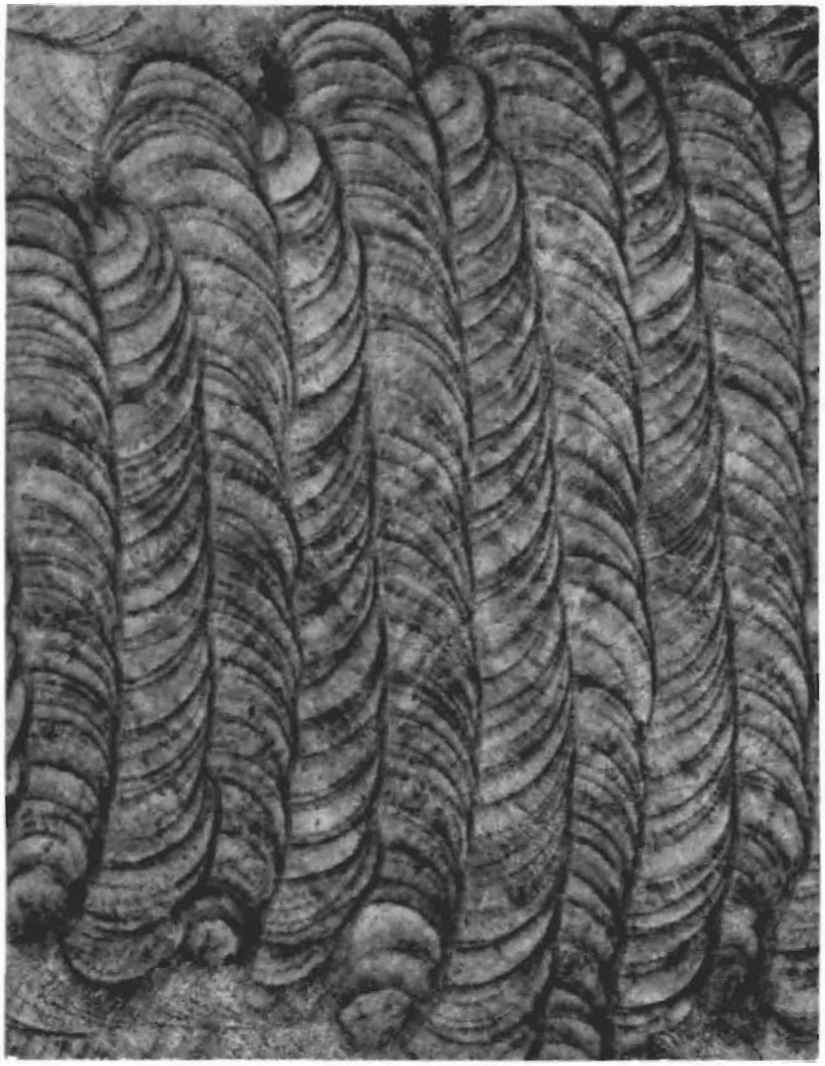

316-A AS FAB TRAN 25X

718-A AS FAB TRAN 25X

Nickel Based Powder

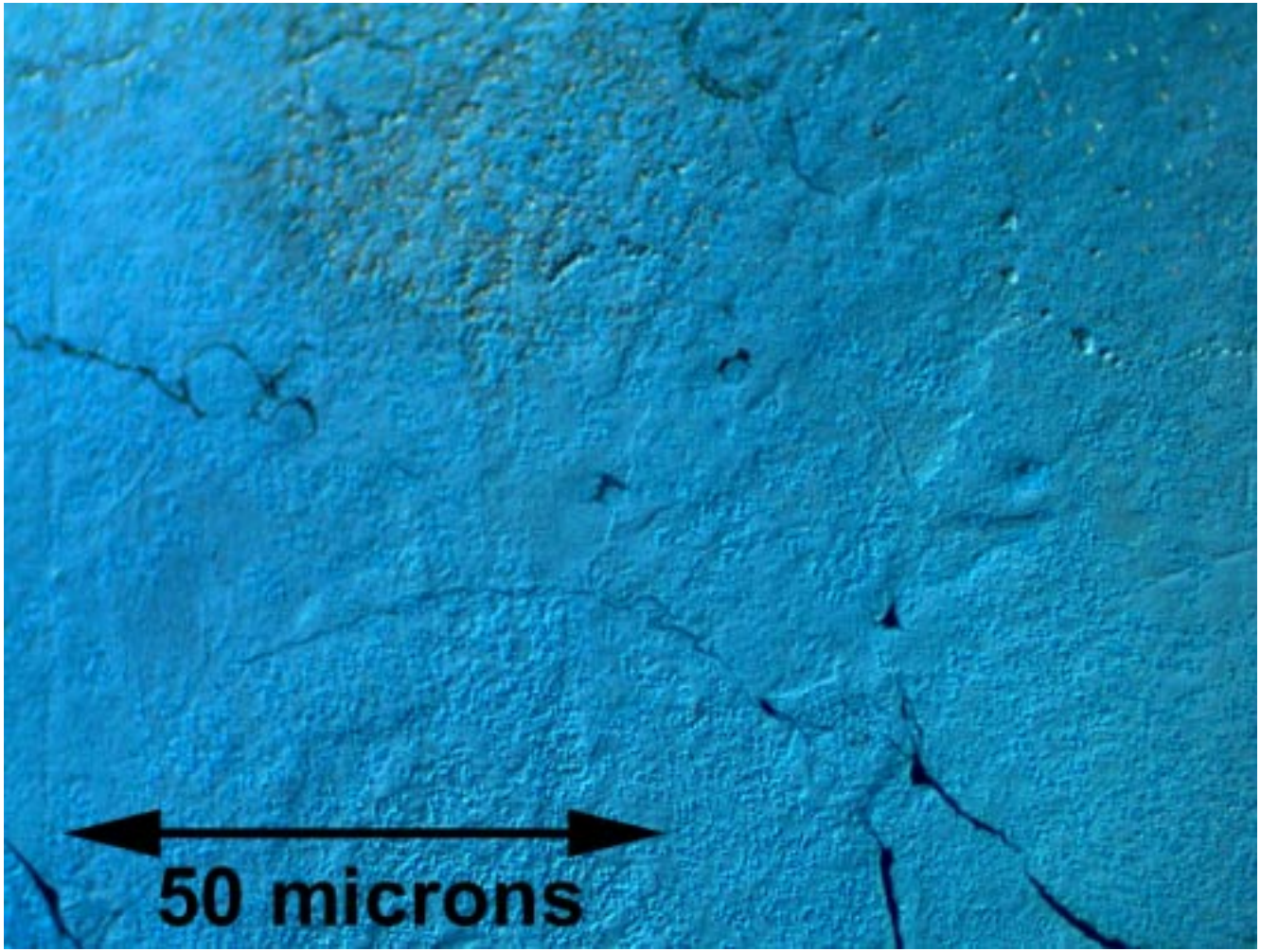

Copper Based Powder

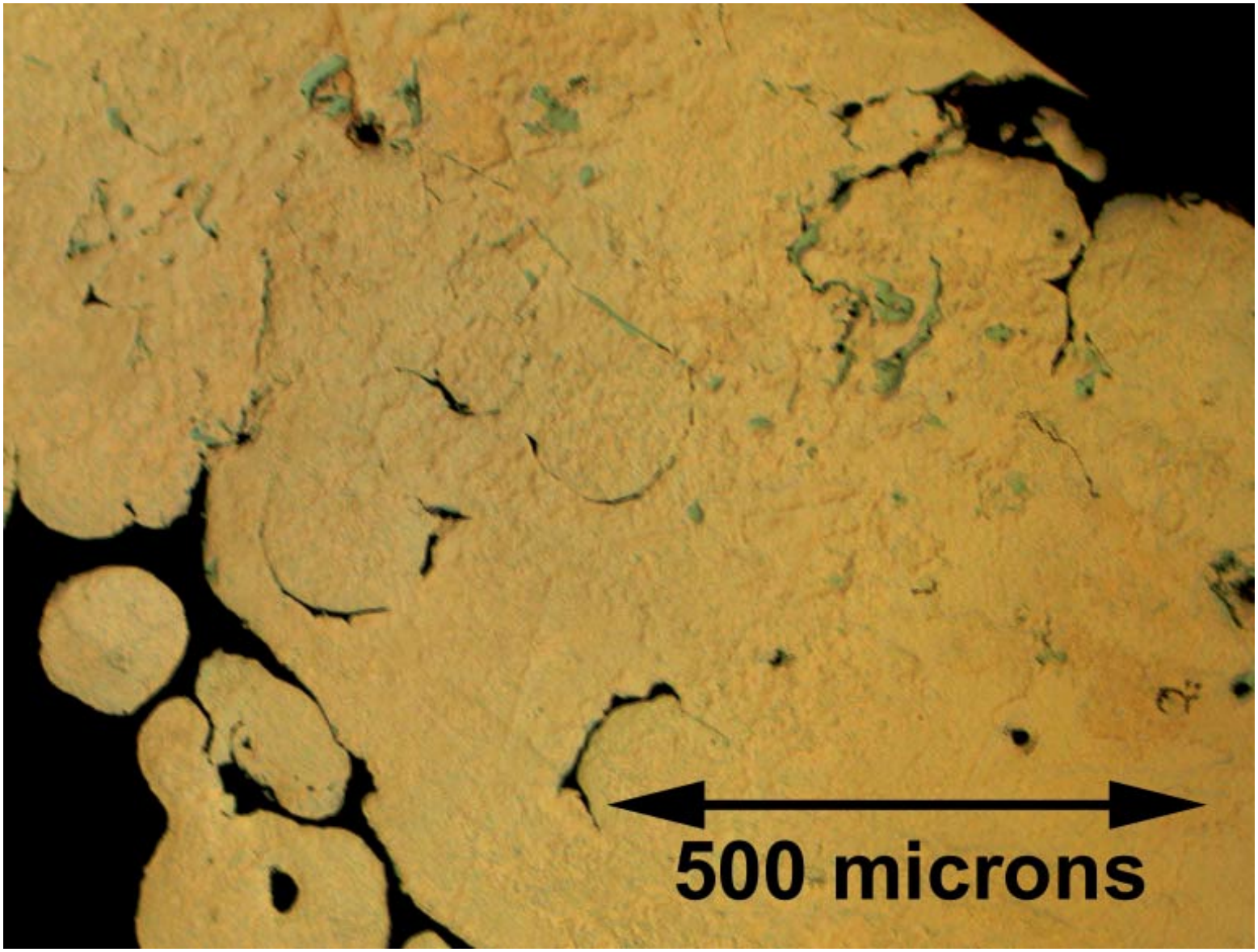

For More Information

Glenn.Williams@msfc.nasa.gov

(256) 544-1041

Ken.Cooper@msfc.nasa.gov

(256) 544-8591

http://ncam.msfc.nasa.gov

http://www.optomec.com

Shuttle Primary Reaction Control Subsystem Thruster Fuel Valve Pilot Seal Extrusion - A Failure Correlation

Jess Waller
Honeywell Technology Solutions Inc.
NASA Johnson Space Center
White Sands Test Facility
Las Cruces, New Mexico
(505) 524-5249
jwaller@wstf.nasa.gov

Regor L. Saulsberry
NASA Johnson Space Center
White Sands Test Facility
Las Cruces, New Mexico
(505) 524-5518
rsaulsbe@wstf.nasa.gov

Introduction

Pilot operated valves (POVs) are used to control the flow of hypergolic propellants monomethylhydrazine (fuel) and nitrogen tetroxide (oxidizer) to the Shuttle orbiter Primary Reaction Control Subsystem (PRCS) thrusters. The POV incorporates a two-stage design: a solenoid-actuated pilot stage, which in turn controls a pressure-actuated main stage. Isolation of propellant supply from the thruster chamber is accomplished in part by a captive polytetrafluoroethylene (PTFE) pilot seal retained inside a Custom 455®[1] stainless steel cavity.[2]

Extrusion of the pilot seal restricts the flow of fuel around the pilot poppet, thus impeding or preventing the main valve stage from opening. It can also prevent the main stage from staying open with adequate force margin, particularly if there is gas in the main stage actuation cavity. During thruster operation on-orbit, fuel valve pilot seal extrusion is commonly indicated by low or erratic chamber pressure or failure of the thruster to fire upon command (Fail-Off). During ground turnaround, pilot seal extrusion is commonly indicated by slow gaseous nitrogen (GN_2) main valve opening times (> 38 ms) or slow water main valve opening response times (> 33 ms). Poppet lift tests and visual inspection can also detect pilot seal extrusion during ground servicing; however, direct metrology on the pilot seat assembly provides the most quantitative and accurate means of identifying extrusion. Minimizing PRCS fuel valve pilot seal extrusion has become an important issue in the effort to improve PRCS reliability and reduce associated life cycle costs.

Background

Although PRCS thruster fuel valve pilot seal extrusion was first documented in 1994, inspection of valve maintenance records going back to 1981 revealed a significant number of earlier fuel valve failures. This necessitated a review of extrusion cases within the broader historical context of PRCS fuel valve failures, and a comparison of the service histories of failed versus active fuel valves.

---

[1] Custom 455® is a registered trademark of Carpenter Technology Corporation, Reading, Pennsylvania.
[2] Propellant isolation is also accomplished by the main poppet/seat.

Extrusion Mechanisms

Two primary mechanisms have been proposed for fuel valve pilot seal extrusion; one or both may be occurring. The first mechanism is referred to as *thermal extrusion,* which is thought to be caused by excessive or prolonged heating after thruster firing (soakback). Other heat inputs that may contribute to this type of extrusion are vacuum bakeouts during ground acceptance test procedures (ATP); or ascent, descent, and solar heating during mission.

The second mechanism is referred to as *oxidizer-induced extrusion*, which is thought to be caused by oxidizer leakage on-ground from the adjacent oxidizer valve on the same thruster and subsequent exothermic fuel-oxidizer reaction. The 1991 installation of the universal throat plug accessory (UTPA), which effectively traps leaking oxidizer vapor inside the thruster chamber, is thought to be one of the factors responsible for oxidizer-induced extrusion. To mitigate possible problems associated with the UTPA, a GN_2 trickle purge of all thrusters was implemented at Kennedy Space Center (KSC) between 1998 and 2000.

The common feature in thermal and oxidizer-induced extrusion is thermal-expansion mismatch of adjacent PTFE and Custom 455 thruster parts. Therefore, minimizing PRCS fuel valve pilot seal extrusion requires control of heat inputs during the seal's service lifetime. Cold flow and internal stress relief of PTFE seals in the absence of heating are other overlooked factors that may contribute to extrusion [1,2].

Extrusion Types

Two types of fuel valve pilot seal extrusion have been observed: extrusion of the whole seal across the sealing and nonsealing surfaces of the pilot seal (*Type I extrusion*); or extrusion of the non-sealing surface along the outer diameter of the seal (*Type II extrusion*). Micrographs of Type I and Type II extrusion appear elsewhere [1]. It is possible although not proven that oxidizer-induced extrusion results in Type I cases (more catastrophic), while thermal extrusion results in Type II cases (more incremental). Alternatively, both extrusion types could arise from differences in the cumulative loading at temperature during service, independent of oxidizer effects.

Failure Distribution

Understanding the distribution of fuel valve failures in general, and extrusion failures in particular, within the historical context of major PRCS milestones is informative (Figure 1). Extrusion was first documented after thruster Serial Number (S/N) 325 Failed-Off during Space Transportation System Flight (STS)-68 in December 1994 [3,4]. Through 2000, there have been ten other (eleven total) in-flight anomalies (IFAs) involving thrusters that were later shown to have extruded pilot seals. The breakdown of the IFAs in which extrusion was involved or detected during follow-up testing is as follows:

- 7 Fail-Off IFAs (caused by fuel valve pilot seal extrusion)
- 3 Fail-Leak IFAs (caused by oxidizer valve leakage)
- 1 Heater Fail-Off IFA (not caused by fuel or oxidizer valve failure)

Another 38 fuel valves with extruded pilot seals were detected between 1994 and 2000 during routine and nonroutine thruster repair and replacement (R&R) at NASA Johnson Space Center (JSC) White Sands Test Facility (WSTF) Depot, giving a total of 49 extrusion cases (Table 1).

Prior to STS-68, another 39 fuel valves were repaired for various reasons. Most of those valve repairs were made by Marquardt (Van Nuys, California; now General Dynamics, Redmond, Washington). Gypsum intrusion after the 1982 STS-3 landing, and the Shuttle Orbiter Forward Reaction Control Pod Number 2 (FRC2) Power-On anomaly during the 1986 STS-61C flow, account for 10 of the 39 pre-STS-68 failures. Extrusion has been implicated in 92 percent (49 of 53) of the fuel valve failures since and including STS-68; however, if or to what extent extrusion played a role in earlier thruster failures is unknown. Nonsystematic visual examination of pilot seals taken from valves that failed before STS-68 did not reveal severe extrusion.[1] Information about the specific causes of pre-STS-68 fuel valve failures (e.g., information contained in Marquardt-issued Failure Mode Reports) could offer added insight into the reasons behind past and present fuel valve failures.

---

[1] Wichmann, H. Private communication. Consultant, L&M Technologies, White Sands Test Facility, Las Cruces, New Mexico. December 2001.

Objective

The objective of this investigation was to correlate the incidence of PRCS fuel valve pilot seal extrusion with:

- Thruster R&R frequency at WSTF Depot
- Pilot seat assembly retainer weld type
- Service history (years in service and firing history)
- Attitude (solar), ascent, and descent heating
- Oxidizer valve R&Rs, especially those caused by leakage
- Other miscellaneous ground heating events, such as the May 1995 RP01 fire at KSC
- Vacuum bakeout histories

Approach

The approach consisted of examining the dependence of extrusion on service history parameters such as number of years in service,[1] number of burns, ontime, and time per burn. The correlation between extrusion and thruster duty cycle (firing priority, duration, and sequence during mission) was not investigated. The dependence of extrusion on oxidizer leakage was then examined, thus testing the validity of the oxidizer-induced extrusion mechanism. Finally, the dependence of extrusion on other heat sources such as attitude heating and vacuum bakeouts was examined.

Investigative Results

Firing history and flight data were obtained from JSC Orbital Maneuvering Subsystem (OMS)/RCS Operations. Fuel and oxidizer valve R&R and flush history data were obtained from KSC Reusable Space Systems and WSTF Depot. Desiccant tube changeout data from recent Orbiter Maintenance Down Period (OMDP) Shuttle flows were obtained from KSC. Vacuum bakeout histories were obtained from the WSTF Chamber Lab. Compilation and reduction of the above service history data was the basis for the current investigation.

Correlation with Thruster Repair and Replacement Frequency

Table 2 summarizes the failure distribution of PRCS thruster fuel valves from 1981 through 2000. Inspection of the fuel valve failure distribution since STS-68 in December 1994 shows that a majority of extrusion cases (28 of 49 cases, or 57 percent) were detected during routine OMDP water flushes (Table 2, column 3). To put this into historical context, OMDP water flushes were not begun until 1992 [5]. The first three OMDPs between 1992 and 1994 during the STS-53, -66, and -73 flows did not involve flushing of ship sets, while the most recent OMDPs between 1995 and 1999 during the STS-82, -89, -101, and -107 flows did.[2] Even more compelling than the high number of extrusion cases observed during OMDPs is the good correlation between the number of fuel valve failures and the number of thrusters submitted to WSTF Depot between 1991 and 2000. Most of the fuel valve failures between 1991 and 2000 (49 of 59 cases, or 83 percent) were due to extrusion. A plot of failures versus thrusters submitted revealed a correlation coefficient (goodness of fit parameter R^2) of 0.84 (Figure 2).

Between 1998 and 2000, 14 extrusion cases were observed, compared to 34 during the previous three-year interval between 1995 and 1997 (Table 2 and Figure 3). It would be tempting to attribute the lower extrusion incidence between 1998 and 2000 to the beneficial impact of the GN_2 purge at KSC, since this purge would reduce or eliminate the occurrence of oxidizer-induced extrusion. Full implementation of the GN_2 purge, however, was not completed until August 2000. Conclusions about the benefit of the purge are, therefore, premature. Also, the GN_2 purge would have had no effect on the incidence of thermal extrusion. Other factors could have contributed to a lower extrusion incidence:

- Fewer OMDPs – one between 1998 and 2000 compared to three between 1995 and 1997
- Fewer shuttle missions – 13 between 1998 and 2000 compared to 22 between 1995 and 1997
- Passing the maximum in the fuel valve failure distribution:
  - average service for active fuel valves = 10.1 years, 1373 burns, 410 s ontime

[1] The number of years in service for each valve was based on thruster installation and removal dates, instead of thruster shipping dates from the manufacturer or repair facility, or pod-on and pod-off dates at KSC.

[2] A ship set consists of 38 primary thrusters.

- average service for fuel valves exhibiting extrusion = 10.0 years, 2240 burns, 592 s ontime

- Beneficial effect of cycling firing priorities
  Water flushing and molecular sieve implementation (improved oxidizer valve reliability)

Correlation with Retainer Weld Type

Only one of 13 Type II extrusion cases had an intermittently welded pilot seat assembly, while about half (12 of 23) of Type I extrusion cases had intermittently welded assemblies. Intermittently welded assemblies are thought to be more prone to fuel migration through the pilot seal cavity, leading to an increased likelihood that fuel could react with oxidizer vapor downstream of the pilot seal, thus generating heat and causing extrusion. Therefore, it is tempting to categorize Type I cases as oxidizer-induced extrusion (more fuel migration), and Type II cases as thermal extrusion (less fuel migration). It must be noted, however, that weld type probably has less influence on fuel migration or leakage than pilot seal flaws, or poor fit between the pilot seal and pilot seal poppet. Also, comparison of years in service for all extrusion cases shows that Type II cases are slightly older (Figure 4), consistent with the presence of a deeper poppet footprint. Although the age difference is small (12.5 ± 3.0 years service on average for valves exhibiting Type II extrusion versus 8.9 ± 4.1 years service on average for valves exhibiting Type I extrusion), this difference suggests that extrusion type is influenced more by pilot seal age than retainer weld type.

Correlation with Firing History

Firing history data through STS-105 (flown August 2001) were obtained from JSC OMS/RCS Operations. Although most data are complete and in raw (unverified) or final (verified) form, gaps do exist (Table 3).

Available firing history data were combined with fuel valve R&R histories obtained from WSTF Depot (*PRCS Major Configuration Table*).[1] This allowed the years in service, number of burns, cumulative ontime, and average time per burn to be determined at the valve level. As a control, the firing histories of valves that failed due to extrusion were compared to the firing histories of active valves that have yet to fail for any reason.

Firing history distributions of Type I and II extrusion cases were compared and were found to overlap (Figure 5). Many Type I failures with a low number of burns were noted along the 'Years in Service' axis (from origin: P331, P601, P223, P227, P101, and P451), consistent with fewer valve actuations and a less prominent poppet footprint. Type II cases were characterized by slightly more burns (2373 versus 2256), higher ontimes (738 versus 531 s), and a slightly higher time per burn (0.31 versus 0.24 s) compared to Type I cases. The scatter in the data, however, would undercut assertions that such differences are significant.

Valves subjected to longer burns tended to fail with fewer accumulated burns than valves with shorter burns (Figure 5 inset). The correlations between time per burn and accumulated burns were weak ($R^2 = 0.17$ for Type I extrusion (23 cases); $R^2 = 0.36$ for Type II extrusion (13 cases); $R^2 = 0.45$ for extrusion cases of unknown type
(13 cases)), suggesting that other factors might be contributing to extrusion, such as oxidizer leakage, attitude heating, or vacuum bakeouts. Long burns were less of a factor in fuel valve failures attributed to reasons other than extrusion either before STS-68 ($R^2 = 0.03$ (39 cases)), or after STS-68 ($R^2 = 0.15$ (4 cases)). As a control, long burns were found to have virtually no effect on the number of burns accumulated by fuel valves still in use ($R^2 = 0.07$ (191 cases)).

The majority (36 of 49 cases, or 73 percent) of all extrusion cases have involved OEM-installed valves. This preponderance suggests that extrusion occurs preferentially in valves near the end of their service lifetime. If true, OEM valves with extruded pilot seals would be expected to have more accumulated service than OEM valves still in use. Available data do in fact show more accumulated burns despite having fewer years in service for OEM valves with extruded pilot seals (Table 4); however, the large data scatter lowers confidence in any conclusion.

Attitude, Ascent, and Descent Heating

---

[1] In-house document. *PRCS Major Configuration Table.* WSTF intranet at S4\:wstfgrp\prop\depot\p-config\ ps-config.mdb, NASA Johnson Space Center White Sands Test Facility, Las Cruces, New Mexico, most recent update.

Thruster P574 failed prematurely with the lowest number of burns (26) and highest time-per-burn ratio (2.65 s/burn) of all extrusion cases investigated to date. Initial indications were that long burns contributed to the failure. However, when corresponding mission data were analyzed, the most prominent thermal feature was not long burns (although temperatures in excess of 66 °C (150 °F) were noted), but attitude heating during STS-53, five missions before the failure during STS-72 (Figure 6, top). The attitude heating experienced by P574 in the left aft L1A position, however, was identical to the heating experienced by P417 in the right aft R1A position (Figure 6, bottom). Also, P417 was still active at the time of this report (no extrusion). Therefore, other factors may have contributed to the failure of P574.

Although the attitude heating experienced by P574 during STS-53 may not be unique, overall concerns about attitude, ascent, and descent heating cannot be dismissed completely. For example, flight rules are currently in place to protect orbiter hardware from overheating. Rules include but are not limited to restriction of the orbital β–angle, and consequently, the angle between incident solar radiation and affected components such as thrusters during mission.[1] Another study conducted by Marquardt during the early phases of the Shuttle program investigates worst-case thruster heating scenarios caused by excessive atmospheric friction during ascent and descent [6].

Correlation with Oxidizer Leakage

Between 1981 and 2000, 201 oxidizer valves were replaced, compared to 92 fuel valves.[2] The predominant mode of oxidizer valve failure was leakage, while that of fuel valve failure, at least since 1994, was pilot seal extrusion. Previous studies have implicated oxidizer leakage as a factor in fuel valve pilot seal extrusion [3]. One might, therefore, expect a higher incidence of concurrent oxidizer valve failure or oxidizer leakage in extrusion cases.

Comparison of R&R histories showed a lower incidence of concurrent oxidizer valve failure in extrusion (29 of 49 cases, or 59 percent) versus nonextrusion-related fuel valve failures (31 of 43 cases, or 72 percent) (Table 5, next-to-last row). The lowest incidence of concurrent oxidizer valve replacement was noted for Type I extrusion failures (11 of 23 cases, or 48 percent), contrary to the expectation that oxidizer valve problems would be prevalent in this type of extrusion. Last, the oxidizer : fuel valve replacement ratio in extrusion cases (46 oxidizer valves: 49 fuel valves = 0.94) was comparable to the oxidizer/fuel valve replacement ratio in nonextrusion-related fuel valve failures (35 oxidizer valves: 43 fuel valves = 0.81) (Table 5, last row).[3] For these reasons, extrusion does not appear to be linked to concurrent oxidizer valve failure.

To examine the possibility that extrusion was linked specifically to oxidizer leakage, R&R records [7] going back to July 1988 were examined (Table 6). These records contain a comment field for thruster cause for return. Typical entries include “IFA – Fail Off,” “Ox leakage – Grnd,” “OMDP,” etc. These records show:

- A higher incidence of current or previous oxidizer leakage in extrusion cases (26 of 49 cases or 52 percent) than in active fuel valves (39 of 130 or 38 percent) (Table 6, next-to-last row)
- A higher incidence of current oxidizer leakage in Type I extrusion cases (9 of 23 cases or 39 percent), than in Type II (2 of 13 cases or 15 percent) or unknown type extrusion cases (1 of 13 cases or 8 percent) (Table 6, second row)

Because of the abbreviated nature of the comment field in the KSC R&R records and the lack of complementary information about the severity and duration of oxidizer leakage events, it is unknown if the incidence of oxidizer leakage reported in extrusion cases (52 percent) is significantly higher than the incidence of oxidizer leakage reported for active fuel valves (38 percent). Also, although there was a higher incidence of current oxidizer leakage in Type I extrusion cases, those valves did not fail with less accumulated firing service on average than the other Type I extrusion cases with previously noted incidences or no incidence of oxidizer leakage.

After the 1991 UTPA implementation, desiccant tubes were installed on thrusters with leaky oxidizer valves to prevent moisture intrusion and nitric acid generation. Thrusters with severe oxidizer leakage required more desiccant tube change-outs. Data were collected for the number of desiccant tube change-outs for all thrusters with fuel valves exhibiting extrusion detected through mid-1998. This encompassed 22 of the 23 Type I cases, all 12 of

---

[1] Arrieta, S. Private communication. The Boeing Company, OMS/RSC Operations, Houston, Texas. April 2001.
[2] Valve replacement totals include only those valves that have known mission usage.
[3] Fuel valve R&Rs stemming from the STS-3 gypsum intrusion and STS-61C flow power-On anomalies not included.

the 13 Type II cases, and 4 of the 13 extrusion cases of unknown type. An oxidizer leakage—burns—onetime distribution (Figure 7) shows that oxidizer leakage was very pronounced for thrusters (left to right) P601, P223, P603, P332, P237, P317, and P571. Interestingly, only P223 was documented in R&R records as having been returned for repair due to oxidizer leakage [7]. The incidence of oxidizer valve leakage given in Table 6, therefore, could be underestimated.

Inspection of desiccant tube change-out data showed that as severity of leakage increased, there was numerical decrease in the number of years in service, number of burns, and cumulative ontime realized by affected thrusters (Table 7). However, even the best correlation, obtained by plotting the change-outs per day against the number of burns accumulated before fuel valve failure, was poor ($R^2 = 0.19$). This poor correlation, coupled with the large scatter in the data in Table 7, undercuts attempts to link extrusion with oxidizer leakage as measured by desiccant tube change-outs. There are other inconsistencies as well. First, no leakage (0 desiccant tube changeouts) was reported prior to the P325 failure during STS-68, which has been touted as a leading candidate for oxidizer-induced extrusion. Second, more leakage could entail a higher rate of thruster return and subsequent fuel valve R&R (Figure 3), thereby artificially lowering the number of years in service, number of burns, and cumulative ontime realized by a given thruster. Third, severe oxidizer leakage was observed for many thrusters that have yet to fail due to extrusion.

RP01 Ground Fire

On May 4, 1995, a fire erupted during the replacement of thruster P318[1] in position R1A on pod RP01 during the STS-69 flow at KSC. Four thrusters in close proximity to R1A later failed due to extrusion: 1) P219 in position R2U during STS-88 in December 1998 (Fail-Leak IFA); 2) P337 in position R2R after STS-80 in November 1996 (OMDP GN_2 response); 3) P476 in position R3R after STS-69 (oxidizer leakage); and 4) P628 in position R1U during STS-81 in January 1997 (Fail-Off IFA). The initial concern was that fire was a factor in these extrusion cases; however, the fuel valve on thruster P415 in position R3A (closest to R1A) passed response ATP shortly after the fire and is still active. Also, injector temperatures did not exceed 34 ºC (93 ºF) on any other thruster on RP01 at the time of or immediately after the fire.[2] In addition, inspection of the soot and burned areas after the fire showed that the fire burned upward and outward away from R1A. Together these observations indicate that the fire was localized to R1A and not a factor in later extrusion cases on the same pod.

Correlation with Vacuum Bakeout Histories

Potentially more problematic than heat soakback after thruster firing are vacuum bakeouts conducted during routine water-flushing and nonroutine valve R&R. During routine water flushing, thrusters are subjected to sequential 8-h and 1.5-h vacuum bakeouts.[3] During nonroutine valve R&R, an additional 8-h preburn bakeout is performed, followed by 8-h and 1.5-h postburn bakeouts.[4] Temperatures during bakeouts can range from 54 to 77 ºC (130 to 170 ºF) depending on the process. Thrusters also occasionally receive an epoxy coating, which is cured at 90 ± 5 ºC (194 ± 9 ºF) for 1 h. Bakeout and curing temperatures are of the same magnitude or greater than the maximum PRCS thruster operational temperature limit of 69 ºC (157 ºF) stipulated by flight rules.

By comparison, the older bakeout procedure performed by Marquardt entailed shorter times (3 h during initial decontamination and subsequent acceptance tests), and opening of the valve using a mechanical fixture to facilitate water removal [8]. There may be an added advantage to opening the valve during vacuum bakeouts. During vacuum bakeouts, the compressive force of the pilot poppet on the pilot seal is equal to the poppet spring force of 1.8 lb_f (2.6 MPa).[5] Valve opening during bakeout lessens the possibility that the compressive yield strength of the PTFE pilot seal could be exceeded (Figure 8).

To address concerns that vacuum bakeouts could be contributing to extrusion, WSTF vacuum bakeout histories were compiled (Table 8) using WSTF Chamber Lab Work Orders logged between January 1995 and

---

[1] P318 was shipped from WSTF on 1/12/00 after being on site for 1685 days, and was undergoing metrology to ascertain degree of pilot seal extrusion at the time of this report.

[2] Kelly, T. Private communication. The Boeing Company, HSF&E Florida Operations, Kennedy Space Center, Florida. January 2002.

[3] In-house document. *PRCS Thruster Flush Procedure.,* WJI-PROP-CTF-0010.D, Issued Sept. 17, 1999, NASA Johnson Space Center White Sands Test Facility, Las Cruces, New Mexico.

[4] In-house document. *WSTF PRCS Thruster Valve Overhaul and Repair – Valve Acceptance Test Procedure.,* WJI-PROP-CTF-0018.D, Issued Sept. 26, 1999, NASA Johnson Space Center White Sands Test Facility, Las Cruces, New Mexico.

[5] During mission, the compressive force of the pilot poppet on the pilot seal is the sum of the poppet spring force plus the force due to nominal propellant pressure of 3.8 lb_f (5.6 MPa), giving a total force of 5.6 lb_f (8.3 MPa).

May 1997. For thrusters processed at WSTF before or after the 1995-1997 interval, bakeout times were assumed (8 + 1.5 = 9.5 h at 130 +20 –10 °F for thruster flushes; 8 + 1.5 +8 + 8 + 1.5 = 27 h at 130 +20 –10 °F for valve R&Rs).

Results show that the total bakeout time at temperature was actually greater for fuel valves exhibiting no extrusion (columns 2 and 3: 23.4-24.4 h) compared to valves exhibiting extrusion (columns 4 and 5: 18.5 –21.6 h). Also, when OEM valves alone were compared (columns 2 and 4), it was determined that thrusters had been returned to Marquardt at the same rate (2.0 returns per thruster), regardless of whether or not they later failed due to extrusion. Consequently, earlier bakeouts performed at Marquardt do not appear to be predominantly linked to later observations of extrusion. The possible linkage between extrusion and exposure to epoxy curing temperatures was still being evaluated at the time of this report.

Conclusions

The conclusions of this investigation are summarized as follows:

- The incidence of extrusion follows R&R frequency. For example, the recent drop-off in the number of extrusion cases could be due to fewer OMDPs and missions since 1998 compared to the period from 1995 to 1997.
- Extrusion may have contributed to at least some of the fuel valve failures before STS-68, especially in view of the fact that 92 percent (49 of 53) of all fuel valve failures since STS-68 are thought to be due to extrusion.
- Valve age and cumulative poppet loading at temperature may explain the occurrence of Type II extrusion (deeper poppet footprint), not lack of oxidizer leakage.
- Although correlations are weak, long burns appear to be a factor in fuel valve pilot seal extrusion.
- The preponderance of extrusion cases (73 percent) involving OEM valves suggests that extrusion occurs preferentially in valves near the end of their service lifetime.
- Extrusion does not appear to be linked with oxidizer valve failure.
- Oxidizer leakage has been documented in a significant number of fuel valve failures in which there is no known extrusion.
- Available desiccant tube changeout data provide the most compelling evidence that oxidizer leakage contributes to extrusion; however, correlations are still low.
- The poor correlations and large data scatter noted throughout this investigation suggest multiple factors contribute to extrusion.
- Vacuum bakeouts do not appear to contribute to a higher incidence of extrusion.

Recommendations

Several recommendations stem from this investigation:

- Determine if thruster valves exposed to epoxy-curing temperatures had an increased incidence of failure due to extrusion.
- Pay special attention to any 2001-2002 OV-103 OMDP response failures.
- Determine annualized failure rates of OEM versus non-OEM replacement parts. A better understanding of failure rates could lend insight into the possible detrimental and beneficial roles of UTPA and GN_2-purge implementation, respectively.
- Investigate fuel valves on an individual basis that failed prematurely with low accumulated ontime or number of burns.
- Review Marquardt or other archival documentation, especially Marquardt Failure Mode Reports (FMRs) issued during the 1980s and early 1990s, for evidence of earlier occurrences of extrusion.

References

1. Waller, J. *Factors Contributing to the Extrusion of Monomethylhydrazine Pilot Operated Valve Seals*. WSTF-TR-0960-001. NASA Johnson Space Center White Sands Test Facility, Las Cruces, New Mexico, June 1, 2000.

2. Wichmann, H. *TFE Seat Evolution Report.* ICS Report 90201. PO T-92270, NASA Johnson Space Center White Sands Test Facility, Las Cruces, New Mexico, February 1999.

3. Ross, B., R. Lynch, and G. Pfeifer. *RA24(R) Failure Analysis Report, Primary Thruster S/N 325 Failed Off During STS-68.* WSTF-PT-FAR-003. NASA Johnson Space Center White Sands Test Facility, Las Cruces, New Mexico, September 29, 1995.

4. Litwinski, J., D. Sueme, and C. Wittman. *Failure Investigation of RCS Fuel Valve Extruded Teflon Seals.* M&P Engineering Report 5965-2007, Rockwell International Materials & Process Engineering Laboratories, Downey, California, April 1996.

5. Ross, B., L. Lueders. *White Sands Test Facility Depot.* AIAA/JANNAF Joint Conference, Cleveland, Ohio, July 1998.

6. Stechman, C. *Thermal Analysis Certification Report for the Space Shuttle Primary Reaction Control Thrusters.* Marquardt Report S-1444, August 15, 1978. Transmitted to Rockwell International Materials and Process Engineering Laboratories, Downey, California.

7. Kennedy Space Center. *RCS Primary Engine R&R History, July 1988 through December 2000.* Kennedy Space Center, Florida, 2000. URL: http://p51.ksc.nasa.gov/dept/oms/primary.htm.

8. Marquardt Test Specification 1323, *Acceptance Test Performance Reaction Control Subsystem Thruster.* Marquardt, Van Nuys, California, February 1978.

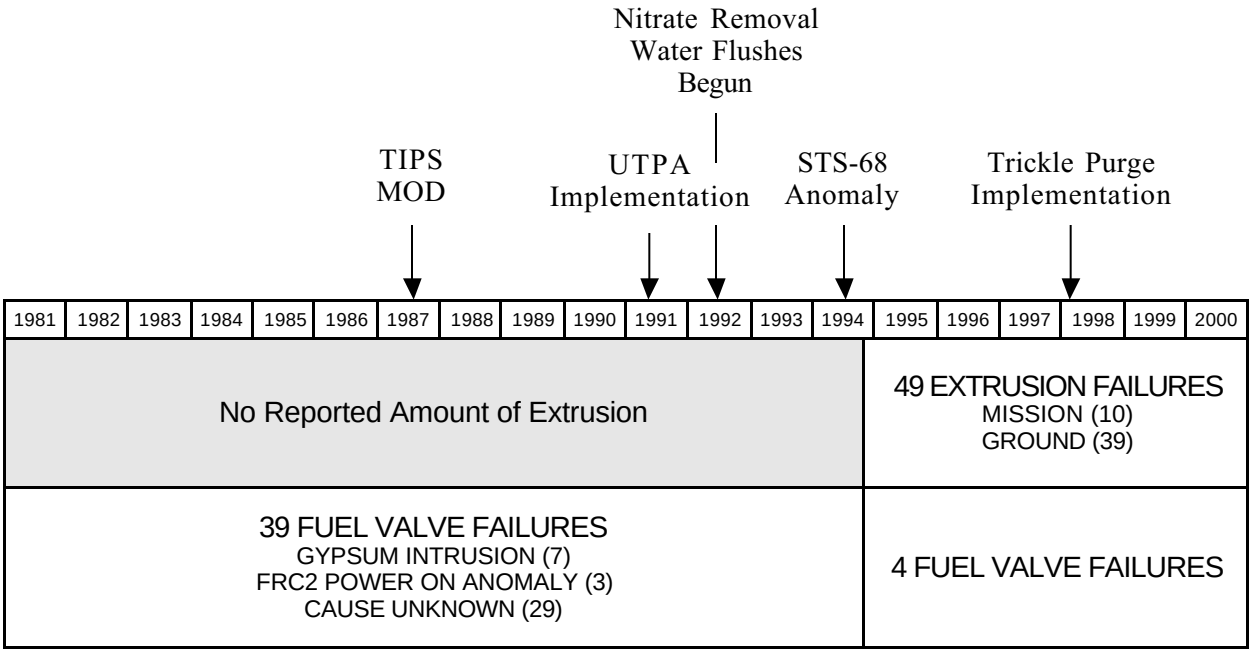

Figure 1
Chronological Distribution of PRCS Fuel Valve Failures, Including Extrusion
(numbers based on last mission service prior to failure)
(NOTE: TIPS = Thruster Instability Protection System)

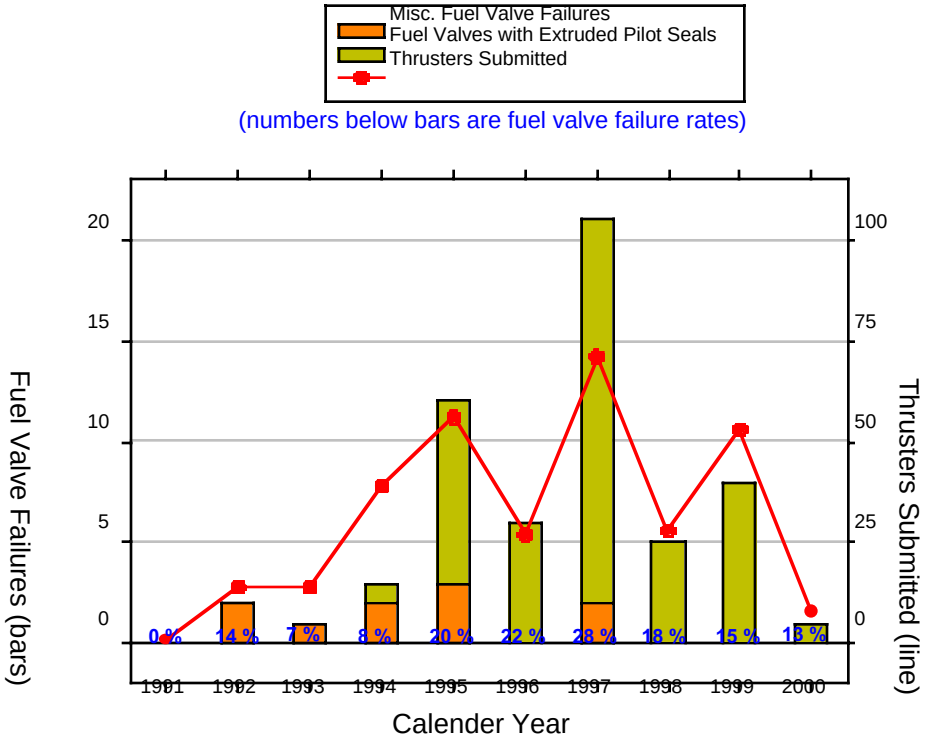

Figure 2
Incidence of PRCS Fuel Valve Pilot Seal Extrusion
(numbers based on dates corresponding thrusters were submitted to WSTF Depot)
(NOTE: OMDP flushes of ship sets occurred in 1995, 1996, 1997, and 1999)

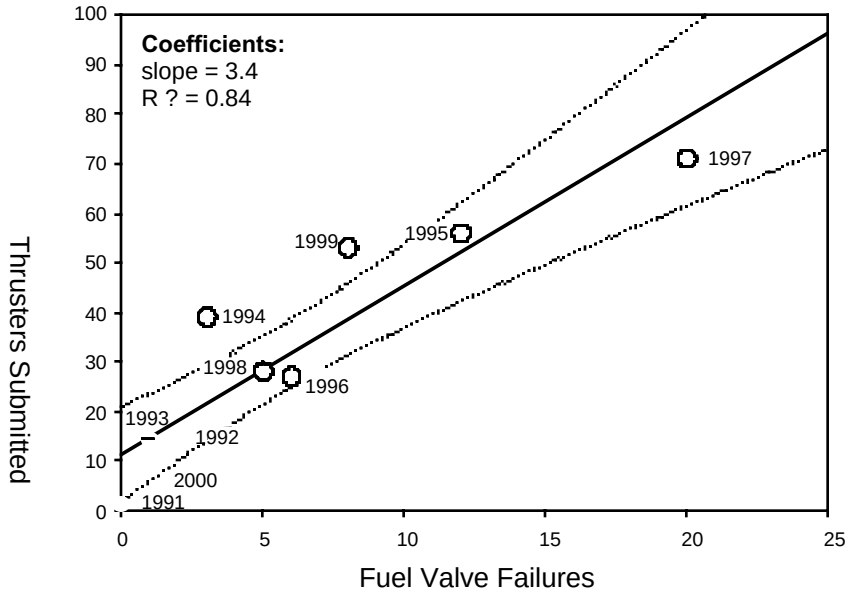

Figure 3
Correlation Between the Number of PRCS Fuel Valve Failures
and the Number of Thrusters Submitted to WSTF Depot
(49 of 58, or 84 percent of failures, were due to pilot seal extrusion)
(95 percent confidence interval given by dotted lines)

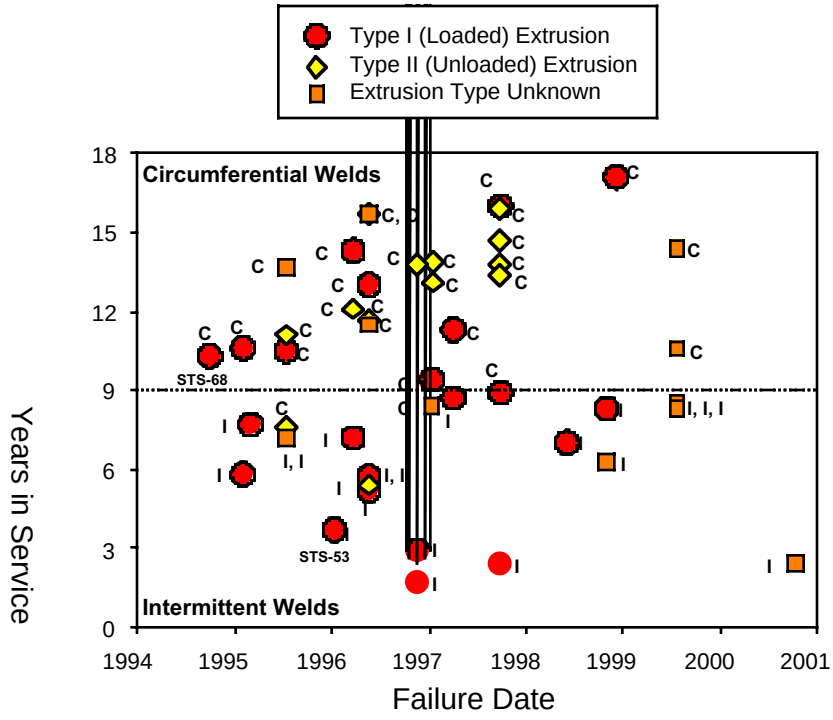

Figure 4
Distribution of Extrusion Type and Retainer Geometry
(NOTES: C = circumferentially welded (old design); I = intermittently welded (new design);
failure date based on last mission service)

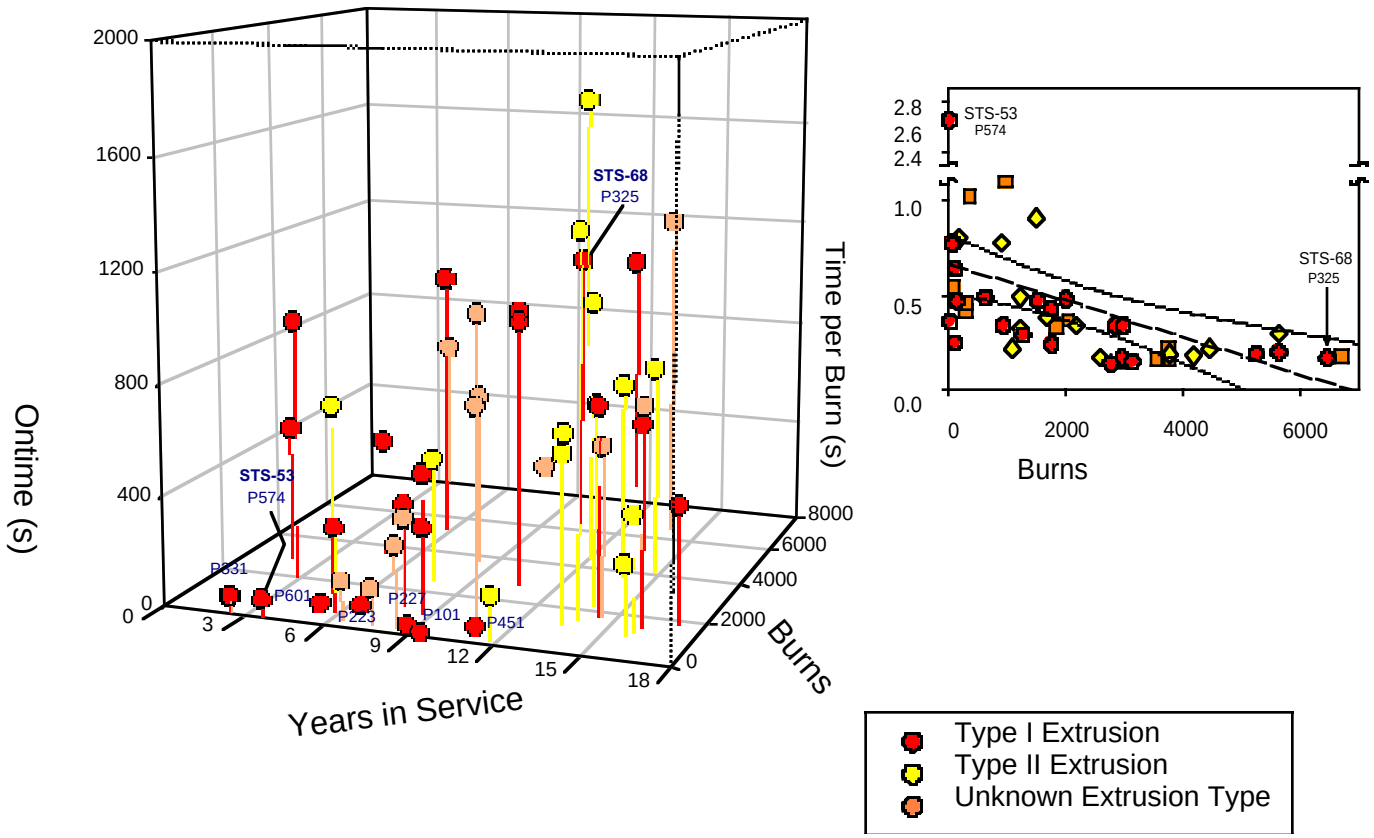

Figure 5
Distribution of Extrusion Type with Selected Service History Parameters (left), and Drop in Burn Time with Number of Burns for PRCS Fuel Valves with Extruded Pilot Seals (inset)
(95 percent confidence interval given by dotted lines in inset)

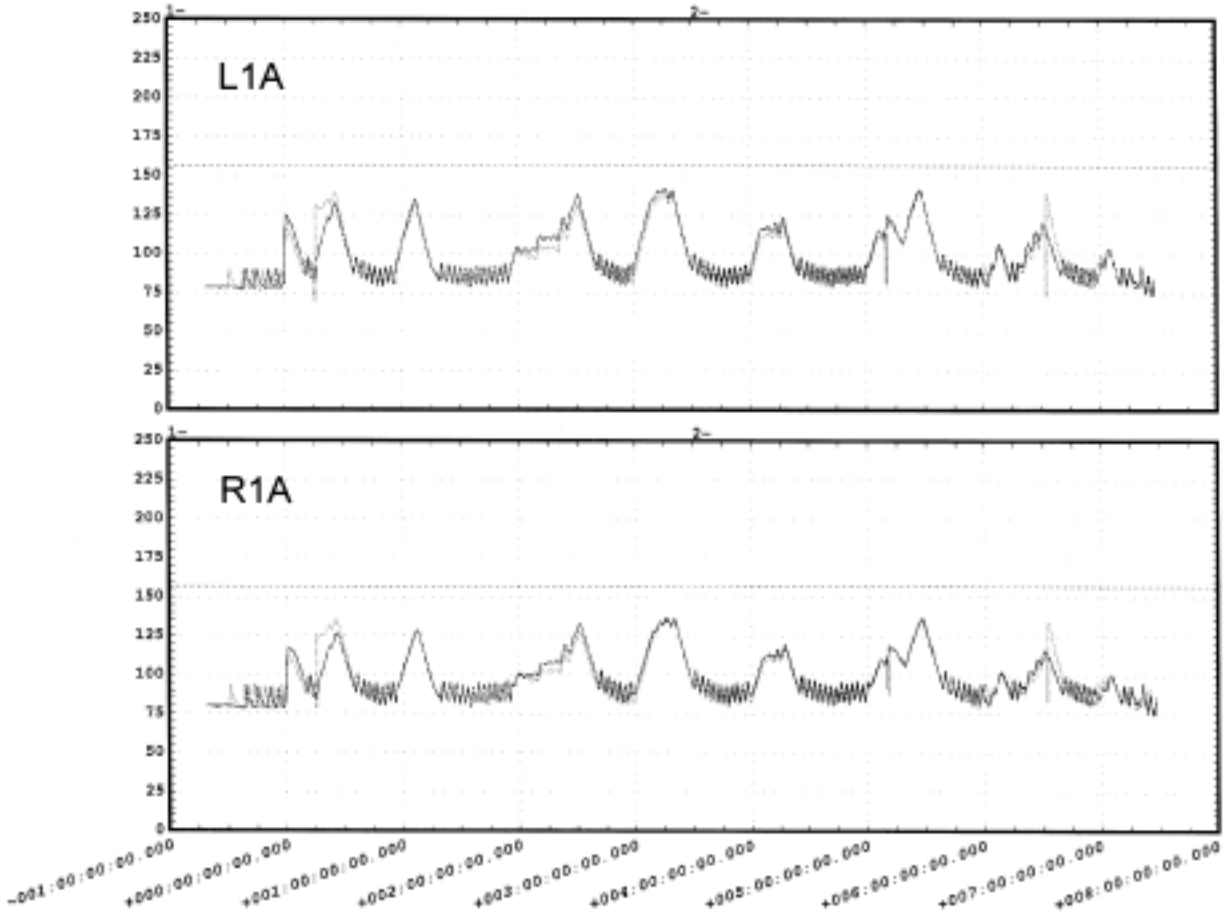

Figure 6
Left aft L1A (top) attitude heating during STS-53 for primary thruster S/N 574
five missions before STS-72 thruster failure due to fuel valve pilot seal extrusion.
Right aft R1A (bottom) heatings during STS-53 are shown for comparison.
(NOTE: Temperatures (ordinate) are in Fahrenheit, and were measured by thermocouples located at fuel and oxidizer stand-offs. Ox temp typically lower. Time stamps along abscissa are in day increments.)

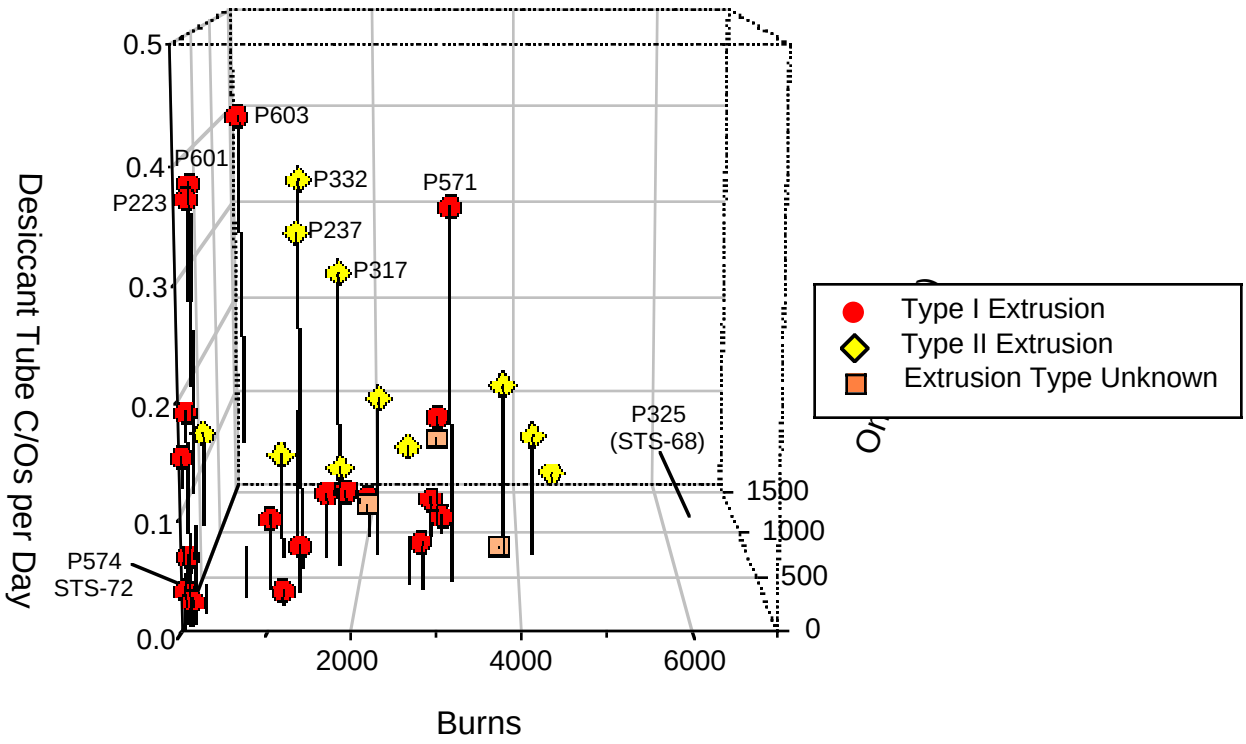

Figure 7

Oxidizer Leakage–Burns–Onetime Distribution Oxidizer leakage was measured by the number of desiccant tube changeouts during the Shuttle flow prior to failure.

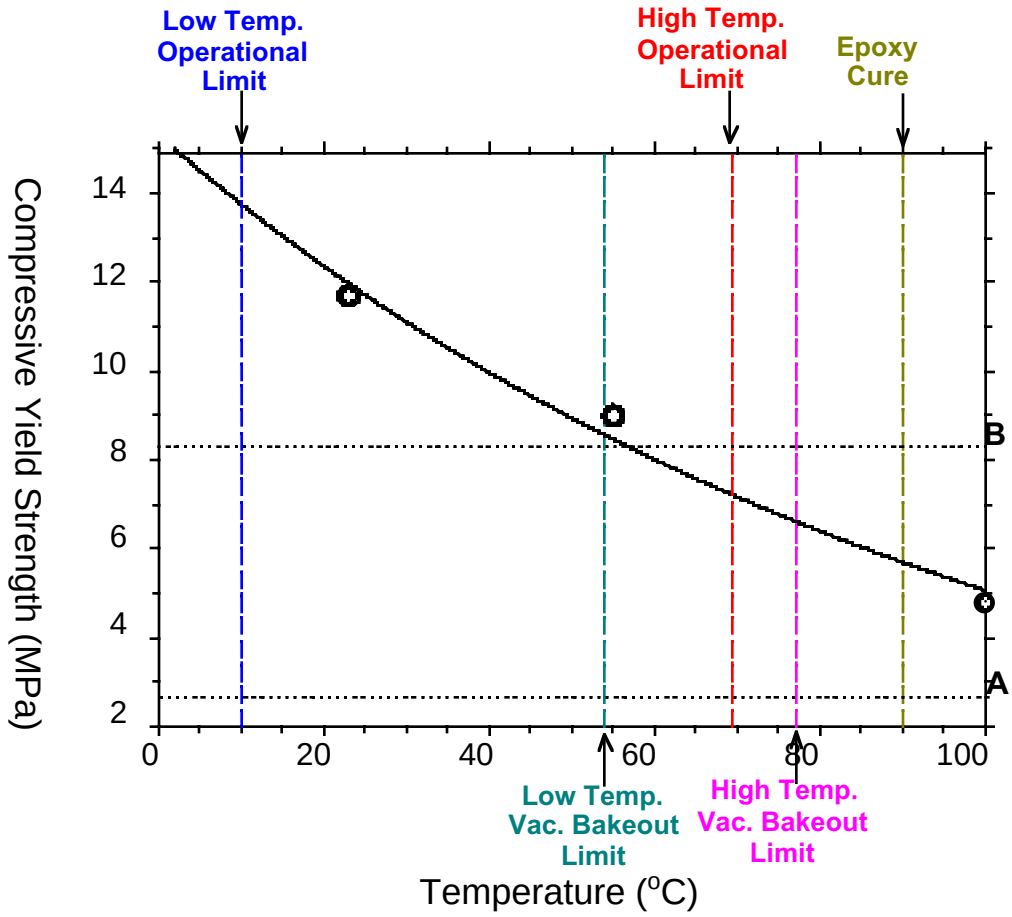

Figure 8
Drop in Compressive Yield Strength[1] of PTFE with
Respect to Operational and Ground Temperature Limits
(NOTE: Line A denotes compressive load of the pilot poppet distributed over pilot poppet/pilot seal contact area during vacuum bakeouts and epoxy cures (propellant absent). Line B denotes compressive load of the pilot poppet distributed over pilot poppet/pilot seal contact area during mission operation (propellant present).)

[1] Black solid line, adopted from McCane, D. I., *Encyclopedia of Polymer Science and Technology,* Wiley, New York, Vol. 13, 623 (1970).

Table 1

Known and Suspected Extrusion Cases through 2000

Case No.	Thruster S/N	Fuel Valve S/N	Last STS	Mission Date	Years in Service.	No. of Burns	Ontime (s)	Time per Burn (s)	Last Firing Position	Proud Height (in.)	Extrusion Type	Basis for Extrusion	Weld Type	Why Pulled
1	101	254	81	Jan-97	9.4	36	13	0.36	F3F	0.0093	Type I	water Mo, Met	C	IFA-Fail Off
2	217	508	86	Sep-97	16.0	1,532	720	0.47	R1A	0.0081	Type I	Water Mo, Met	C	OV 104 OMDP
3	219	525	88	Dec-98	17.1	1,772	432	0.24	R2D	0.0035	Type I	GN2 Mo & Mc, Met	C	IFA-Fail Leak
4	223	548	76	Mar-96	7.2	128	82	0.64	R4D	0.0047	Type I	GN2 & water Mo, PLT, Met	I	PM
5	227	681	86	Sep-97	8.9	114	29	0.25	L4U	0.0084	Type I	GN2 Mo, PLT, Met	C	OV 104 OMDP
6	228	724	95	Oct-98	8.3	9,221	1432	0.16	R4D	0.0078	Type I	GN2 Mo, Met	I	PM
7	234	528	76	Mar-96	14.3	1,772	754	0.43	R4R	0.0060[a]	Type I	Water Mo, PLT	C	IFA-Fail Off
8	305	710	83	Apr-97	8.7	938	320	0.34	F3D	0.0045[a]	Type I	GN2 Mo, PLT	I	PM – Ox Leak
9	325	530	68	Sep-94	10.3	6,471	1,068	0.17	L3D	0.0100	Type I	GN2 Mo, Met	C	IFA-Fail Off
10	325	553	80	Nov-96	1.7	2,976	500	0.17	R1U	0.0041	Type I	GN2 Mo, Met	I	OV 105 OMDP
11	327	580	77	May-96	13.0	5,648	1,107	0.20	R3D	0.0076	Type I	Water Mo, Met	C	PM-Ground Leak (Ox)
12	331	544	63	Feb-95	10.6	2,856	979	0.34	L2L	0.0065	Type I	GN2 Mo, PLT, Met	C	PM-Ground Leak (Ox)
13	331	718	86	Sep-97	2.4	78	61	0.78	R2R	0.0035[a]	Type I	GN2 Mo, PLT	I	OV 104 OMDP
14	337	594	80	Nov-96	12.9	2,014	962	0.48	R2R	0.0057	Type I	GN2 & water Mo, PLT	C	OV 105 OMDP
15	432	622	70	Jul-95	10.5	2,994	1,011	0.34	L2L	0.0070	Type I	Water Mo, Met	C	OV 103 OMDP
16	451	672	83	Apr-97	11.3	70	54	0.77	F3F	0.0033	Type I	PLT, Met	C	IFA-Fail Off
17	476	703	67	Feb-95	7.7	1,278	375	0.29	R3R	0.0075	Type I	GN2 Mo, PLT, Met	I	IFA-Fail Leak
18	497	744	63	Feb-95	5.8	5,252	1,008	0.19	R1U	0.0055	Type I	Met	I	IFA – Fail Leak
19	571	893	77	May-96	5.2	3,147	477	0.15	F3U	0.0065	Type I	GN2 Mo, Met	I	OV 105 OMDP
20	574	895	72	Jan-96	3.7	26	69	2.65	L1A	0.0034	Type I	GN2, Mo, PLT, Met	I	IFA-Fail Off
21	601	806	77	May-96	5.7	145	68	0.47	F3F	0.0073	Type I	GN2 Mo, Met	I	OV 105 OMDP
22	603	803	77	May-96	5.7	637	310	0.49	F2F	0.0045[a]	Type I	GN2 Mo, PLT	I	OV 105 OMDP
23	628	832	91	Jun-98	7.0	2,780	387	0.14	R2U	0.0075	Type I	PLT, Met	I	IFA-Fail Off
24	108	679	70	Jul-95	7.6	2,614	456	0.17	F3U	0.0020	Type II	GN2 &water Mo, Met	C	OV 103 OMDP
25	125	604	76	Mar-96	12.1	4,476	993	0.22	L2D	0.0011	Type II	GN2 Mo, PLT, Met	C	PM
26	126	263	77	May-96	15.7	1,109	249	0.22	L2D	0.0017	Type II	GN2 & water Mo, Met	C	OV 105 OMDP
27	229	552	86	Sep-97	14.7	4,193	770	0.18	L1U	0.0000[a]	Type II	GN2 Mo, PLT	C	OV 104 OMDP
28	237	543	86	Sep-97	15.9	1,249	418	0.33	L4L	0.0000[a]	Type II	GN2 Mo, PLT	C	OV 104 OMDP
29	317	584	86	Sep-97	13.8	1,515	1,373	0.91	R3A	0.0025[a]	Type II	GN2 Mo, PLT	C	OV 104 OMDP
30	332	569	86	Sep-97	13.4	1,230	608	0.49	R1R	0.0000[a]	Type II	GN2 Mc, PLT	C	OV 104 OMDP
31	335	575	70	Jul-95	11.1	5,659	1,719	0.30	R3R	0.0000[a]	Type II	GN2 Mo, PLT	C	OV 103 OMDP
32	411	637	81	Jan-97	13.9	2,181	736	0.34	F3L	0.0017	Type II	GN2 & water Mo, Met	C	PM
33	421	582	80	Nov-96	13.8	3,791	725	0.19	R4D	0.0012	Type II	GN2 Mo, Met	C	OV 105 OMDP
34	422	586	77	May-96	11.7	205	163	0.80	L4D	0.0000[a]	Type II	PLT	C	OV 105 OMDP
35	437	600	81	Jan-97	13.1	1,702	655	0.38	R4R	0.0000[a]	Type II	GN2 Mo, PLT	C	PM
36	616	823	77	May-96	5.4	929	728	0.78	R3A	0.0015[a]	Type II	PLT	I	IFA-Heater Fail Off
37	133	255	77	May-96	15.7	2,044	754	0.37	L3L	ND	Unknown	GN2 Mo	I	OV 105 OMDP
38	220	516	70	Jul-95	13.7	6,720	1,229	0.18	R3D	ND	Unknown	GN2 Mo	C	OV 103 OMDP
39	330	714	70	Jul-95	7.2	3,752	818	0.22	R1U	ND	Unknown	GN2 Mo	I	OV 103 OMDP
40	332	714	92	Oct-00	2.4	105	58	0.55	R2R	ND	Unknown	GN2 Mo, PLT	I	PM
41	427	630	93	Jul-99	14.4	1,839	610	0.33	L4U	ND	Unknown	GN2 Mo	C	OV 102 OMDP
42	428	711	70	Jul-95	7.4	311	130	0.42	R2D	ND	Unknown	Water Mo	I	OV 103 OMDP
43	430	588	77	May-96	11.5	2,979	443	0.15	L3D	ND	Unknown	GN2 & water Mo	C	OV 105 OMDP
44	463	646	93	Jul-99	10.6	989	1,089	1.10	F4R	ND	Unknown	GN2 Mo	C	OV 102 OMDP
45	488	208	81	Jan-97	8.4	3,557	617	0.17	F3U	ND	Unknown	Water Mo	C	PM
46	498	762	95	Oct-98	6.3	309	141	0.46	L3L	ND	Unknown	GN2 Mo	I	IFA-Fail Off
47	615	814	93	Jul-99	8.5	378	385	1.02	R1A	ND	Unknown	GN2 & water Mo	I	OV 102 OMDP
48	617	836	93	Jul-99	8.3	257	291	1.13	L1A	ND	Unknown	GN2 & water Mo	I	OV 102 OMDP
49	627	831	93	Jul-99	8.3	3,785	636	0.17	L2D	ND	Unknown	GN2 & water Mo	I	OV 102 OMDP

[a] Proud height (height of PTFE seal inner diameter above downstream metal) inferred from pilot poppet versus armature travel

Abbreviations used: S/N=serial number, STS=Space Transportation System Flight, ND=not determined, GN2=gaseous nitrogen, Met.=Metrology, Mo=main valve opening time, Mc=main valve closing time, PLT=poppet lift test, C=circumferential, I=intermittent, IFA=in-flight anomaly, OV=Orbiter Vehicle, OMDP=Orbiter Maintenance Down Period, PM=preventative maintenance flush, KSC=Kennedy Space Center, Ox=oxidizer (N_2O_4)

Table 2
PRCS Thruster Fuel Valve Failure Distribution from 1981 through 2000[a]

Year	Number Of Flights	Flight/Ground/OMDP Extrusion Failures	Total Extrusion Failures	Total Fuel Valve Failures	Number of Thrusters Submitted	Ship Set OMDP
1981-1990	38	–	–	34[b]	–	–
1991	6	–	--	0	1	0
1992	8	–	--	2	14	0
1993	7	–	--	1	14	0
1994	7	1 / 0 / 0	1	3[c]	39	0
1995	7	2 / 1 / 6	9	12	56	1
1996	7	2 / 3 / 1	6	6	27	1
1997	8	3 / 4 / 12	19	20	71	1
1998	5	1 / 0 / 4	5	5	28	0
1999	3	2 / 1 / 5	8	8	53	1
2000	5	0 / 1 / 0	1	1	8	0
10-yr Totals	63	11 / 10 / 28	49	58	311	4

[a] Numbers based on date thruster submitted to WSTF Depot
[b] Includes gypsum intrusion (STS-3) and FRC2 Power-On anomaly (STS-61C flow) failures
[c] Consists of STS-68 extrusion failure plus two other fuel valve failures that occurred before STS-68
NOTE: -- = no data available or data not applicable

Table 3
Firing History Data Status through June 2001 STS-105

Data Status	STS Flights (chronological order)	Number of Flights
Final data	26, 34, 36, 39, 53, 55, 51, 60	8
Raw data	6, 7, 8, 41A, 41C, 41D, 41G, 51A, 51C, 51D, 51B, 51G, 51F, 51I, 51J, 61A, 61B, 61C, 29, 30, 33, 32, 31, 41, 38, 35, 37, 40, 43, 48, 44, 42, 45, 49, 50, 46, 47, 52, 54, 56, 57, 61, 62, 59, 65, 64, 68, 66, 63, 67, 71, 74, 76, 77, 78, 79, 80, 81, 82, 83, 84, 94, 85, 86, 87, 89, 89, 90, 91, 95, 88, 96, 93, 103, 101, 106, 92, 98, 102, 105	80
Gaps in data	1, 2, 3, 4, 5, 41B, 27, 28, 58, 70, 69, 73, 72, 75	14
No data (being processed)	99, 97, 100	3

Table 4
Service Histories of OEM Fuel Valves[a]

Service History Parameter	OEM Fuel Valves Still in Use	OEM Fuel Valves w/ Extruded Seal	Other Fuel Valves w/ Extruded Seal	All Fuel Valves w/ Extruded Seal
Number of cases	120	36	13	49
Years in service	12.2 (5.1)	11.0 (3.8)	7.2 (3.2)	10.0 (4.0)
Number of burns	1668 (1994)	2334 (1873)	1980 (2675)	2240 (2091)
Cumulative ontime (s)	497 (414)	640 (387)	460 (477)	592 (415)

[a] The number in each parenthesis is the standard deviation

Table 5
Relative Incidence of Fuel and Oxidizer Valve R&Rs through 2000

Type of R&R	Type I Extrusion	Type II Extrusion	Extrusion Type Unknown	All Extrusion Cases	Other Fuel Valve Failures Pre-STS-68	Other Fuel Valve Failures Post-STS-68	All Other Fuel Valve Failures
Simultaneous Fu & Ox valve R&R	11	8	10	29	27	4	31
Fu valve R&R	12	5	3	20	12	0	12
Total Fu valve R&Rs	23	13	13	49	39	4	43
Other Ox valve R&Rs[a]	7	7	3	17	2	2	4
Total Ox valve R&Rs	18	15	13	46	19	6	25
Percentage of Fu valve R&Rs requiring simultaneous Ox valve R&R	48 (11 of 23)	62 (8 of 13)	77 (10 of 13)	59 (29 of 49)	69 (27 of 39)	100 (4 of 4)	72 (31 of 43)
Ox valve/Fu valve R&R ratio	0.78 (18/23)	1.15 (15/13)	1.00 (13/13)	0.94 (46/49)	0.74 (29/39)	1.50 (6/4)	0.81 (35/43)

NOTES: R&R = Repair and replacement; Fu = fuel; Ox = oxidizer
[a] Other oxidizer valves replaced on same thruster prior to fuel valve failure

Table 6
Incidence of Oxidizer Leakage during Fuel Valve R&R and Maintenance since STS-68[a]

Type of Valve R&R	Type I Extrusion	Type II Extrusion	Recent or Unknown Extrusion Type	All Extrusion Cases	Other Fu Valve Failures	Active Fu Valves
Total number of cases	23	13	13	49	4	130
Ox leakage during Fu valve R&R	9 (39)	2 (15)	1 (8)	12 (24)	2 (50)	….
Ox leakage during previous service	3 (13)	7 (54)	4 (31)	14 (28)	0 (0)	49 (38)
Total number of Ox valve leakage cases	12 (52)	9 (69)	5 (39)	26 (52)	2 (50)	49 (38)
No indication of Ox leakage	11 (48)	4 (31)	8 (61)	23 (48)	2 (50)	81 (62)

NOTES: R&R = Repair and replacement; Fu = fuel; Ox = oxidizer
Numbers in parentheses are percentages out of the total number of cases.

[a] Data valid for valves submitted for R&R after STS-68, but with a history of Ox leakage as early as July 1988.
[b] …. denotes no fuel valve R&R (not applicable)

Table 7
Effect of Oxidizer Leakage during Last Shuttle Flow on Valve Longevity[a]

Service History Parameter	Valves with Most Leakage	Valves with Moderate Leakage	Valves with No or Negligible Leakage
Number of cases	7	23	8
Avg. Desiccant Tube Changeouts per Flow	28 (5)	7 (4)	< 1 (<1)
Years in service	9.6 (4.6)	10.2 (4.1)	11.3 (2.8)
Number of burns	1150 (1037)	1808 (1383)	4788 (1973)
Cumulative ontime (s)	477 (442)	506 (326)	1036 (411)

NOTE: The numbers in parentheses are standard deviations
[a] Data good for the 38 extrusion cases known as of June 1998.

Table 8
WSTF Vacuum Bakeout Histories of OEM Fuel Valves[a]

Service History Parameter	No Extrusion (Still in Use)		With Extrusion (Failed)	
	OEM Fuel Valves	Active Fuel Valves	OEM Fuel Valves	Other Fuel Valves
Number of cases	120	83	36	13
WSTF vacuum bakeout hours at 130 +20 –10 °F per thruster[b]	24.4 (15.4)	23.4 (11.2)	18.5 (11.1)	21.6 (10.3)
Total number of returns to Marquardt[c]	240	55	73	15
Average number of returns to Marquardt per thruster	2.0	0.7	2.0	1.2

NOTES: OEM = Original Equipment Manufacturer
[a] The number in each parenthesis is the standard deviation.
[b] Estimated total bakeout time per thruster at WSTF between 1991 and 2000.
[c] Total number of thruster returns to Marquardt between 1981 and 1993.

The Puget Sound Clean Air Agency Aerospace NESHAP Inspection Program: Lessons Learned

Authors:

John Schantz, Inspector
206.689.4027
johns@pscleanair.org

Rick Hess, Supervising Inspector
206.689.4029
rickh@pscleanair.org

Organization and mailing address:
Puget Sound Clean Air Agency
110 Union Street, Suite 500
Seattle, WA 98101

The Federal Clean Air Act, under section 112, requires EPA to evaluate and control the emissions of Hazardous Air Pollutants (HAP) by source category. Aerospace manufacturing and rework facilities having the potential to emit at major source HAP thresholds are subject to Maximum Achievable Control Technology (MACT)- based standards regulated under the National Emission Standard for Hazardous Air Pollutants (NESHAP), 40 CFR Part 63 subpart GG, effective September 1, 1998.

For the aerospace industry, the MACT standards require affected facilities to reduce HAP emissions from solvents and other materials used in four types of aerospace operations: cleaning, primer and topcoat application, paint removal and the application of chemical milling maskants. This rule also has standards for work practices and requires extensive monitoring, recordkeeping, and self-reporting for certifying compliance. Furthermore, some processes and control requirements are exempt from the rule.

There are nine facilities subject to the Aerospace NESHAP (ANESHAP) spread across the central Puget Sound region. They are, by definition, also subject to the Title V air operating permit regulation. As the September 1, 1998 implementation date for the Aerospace NESHAP approached, the Agency organized what was dubbed the Aerospace Team.

Currently the Team consists of three inspectors, two engineers, a public educator, two senior staff members, and an administrative support person. The team was formed with the goals of establishing a consistent approach to conducting inspections and interpreting and applying the regulations. The team was tasked with focusing on becoming familiar with the ANESHAP and working together to reach consensus on interpreting and enforcing its provisions. It was also expected that this process would involve the team collaborating with the regulated facilities and serving as a resource for them. This, in retrospect, has been one of the most successful outcomes of the aerospace team.

Each inspector on the team is responsible for specific ANESHAP facilities. Responsible means they are the Agency contact person for that facility and they organize and prepare the team for inspections of that facility. We are required by the EPA to do an unannounced inspection of each ANESHAP facility at least once each

federal fiscal year. Inspections are unannounced to enable the Agency to observe each facility under normal operating conditions.

Inspection preparation begins with reviewing the facility s file and pinpointing areas of interest such as follow-up from the last inspection, information contained in reports each facility is required to submit under self-reporting requirements of the ANESHAP and air operating permits. These facilities are required to monitor their operations and submit periodic compliance status reports and deviation reports if they determine that they have violated regulations or permit conditions. Sometimes, we may just pick an area of the facility or a particular part of the regulations we haven t looked at in a while. The inspector prepares the inspection agenda and information packet for each team member and facility representatives. Each member of the inspection team takes responsibility for one or more items on the agenda; familiarizing themselves with background details, taking the lead during that part of the inspection and writing that section of the report.

A typical inspection lasts all day and begins with an agenda review at the opening inspection conference. We then aim to get out into the facility for a first-hand look at targeted operations and equipment. At times the team splits into two groups in order to cover more ground. These inspections usually include determining compliance with regulations other than the ANESHAP, such as asbestos, gasoline storage and dispensing, boilers, wastewater treatment, etc. The inspections also include a records review component. The ANESHAP and air operating permits require lots of record keeping. These records enable the facility to determine their compliance status and are the basis of their self-reporting and certifying compliance. We may also obtain copies of records and make them part of our report or retain them in support of an enforcement action. During the closing conference, we review the preliminary results of the inspection. If we have documented an apparent violation during the inspection we discuss the issue with the facility representatives at the time, but determining our enforcement response is generally not done at that time. An enforcement issue will be discussed off-site at a post-inspection debrief and the team will agree on the appropriate response.

The team s approach to enforcement is grounded in reaching consensus regarding which enforcement tool to use: Compliance Status Report, verbal warning, Written Warning, or Notice of Violation. A civil penalty can be assessed as a result of a Notice of Violation. Violations that are recurring or systemic or violators who are recalcitrant are the triggers for penalties. Equity is always a factor: how have we responded to similar situations at other facilities in the past? Enforcement actions are also based on information submitted by the facility, not just our observations during a compliance inspection.

We ve also worked on developing the kind of relationship with our sources that allows discussion of issues of mutual concern outside the context of a compliance inspection. We strive to clearly communicate standards to our sources and work with them to achieve success. We have a strong compliance assistance orientation. We advocate the development and implementation of environmental management systems. We want these affected facilities to find and fix problems before we find them. We understand the challenges they face in communicating with their employees about the requirements:

getting them to monitor and maintain their equipment and operations, create required records, and in some cases having them change work practices.

Our combined efforts seem to be paying off. The aerospace facilities in our jurisdiction subject to the NESHAP are reducing their emissions and reporting fewer violations and we are finding fewer violations during our compliance inspections.

Affirmative Procurement

Rhonda Mann

USA SQ&MA

United Space Alliance

Agenda

- What is Affirmative Procurement
- Definitions
- Regulatory Drivers
- Comprehensive Procurement Guidelines
- Benefits
- Misconceptions

What is Affirmative Procurement?

- Sometimes referred to as green purchasing or green procurement
- The process of purchasing environmentally preferable products, goods and services to the maximum extent practicable
  - Products containing recycled content
  - Environmentally preferable products
  - Bio-based products
  - Energy efficient products

Definitions

- Bio-based Products
  - A commercial or industrial product (other than food or feed) that utilizes biological products or renewable domestic agricultural (plant, animal, and marine) or forestry materials
  - Examples: Absorbents, adhesives, alternative fuels and additives, construction material, lubricants, vegetable starch products, solvents/cleaners/surfactants, paints and coatings, landscaping products
- Energy Efficient Products — Products that require less energy or alternative energy sources to operate
  - Computer monitors, florescent lighting, solar power, battery operated automobiles
- Environmentally Preferable Purchasing (EPP)
  - Buying products or services that have a lesser or reduced effect on human health and the environment, when compared with competing products or services that serve the same purpose.
  - Examples: recycled products, bio-based products, energy efficient products
- Post-consumer Material
  - A material or finished product that has served its intended use and has been discarded for disposal or recovery, having completed its life as a consumer item
  - Examples: Used cardboard boxes, old newspapers and magazines, salvaged metals, used grocery bags

Definitions

- **Pre-consumer Material**
  - —Materials generated in manufacturing and converting processes, such as manufacturing scrap and trimmings/cuttings
  - —Examples: Carpeting materials
- **Recovered Materials**
  - —Materials taken out of, or diverted from, solid waste streams
  - —Does not include those materials and byproducts generated from, and commonly reused within, an original manufacturing process
  - —For paper products — also includes manufacturing and forest residues and other items (40 CFR 247.3)
  - —Examples; Empty containers that are separated from trash and recycled

What are the Regulatory Drivers?

- Resource Conservation and Recovery Act (RCRA) section 6002 (42 USC 6962), enacted in 1976, as amended

- Executive Order (EO) 13101, Greening the Government through Waste Prevention, Recycling and Federal Acquisition —September 14, 1998
  - —Supersedes EO 12873 and 12995

- Federal Acquisition Regulation (FAR), Subchapter D, Part 23, Environment, Conservation, Occupational Safety and Drug-Free Workplace

RCRA 6002

- Based on Congressional findings that noted millions of tons of recoverable material which could be used were needlessly buried each year
- Established several objectives
  - —Protecting health and the environment
  - —Conserving valuable resources through improved solid waste management and resource recovery practices
- Applies to all Federal agencies, and their agencies contractors who use Federally appropriated funds
- Federal agencies must
  - —Give preference in their purchasing programs to products and practices that conserve and protect natural resources and the environment
  - —Establish Affirmative Procurement programs for recycled content products designated by the EPA

RCRA 6002, Continued

- The preference to purchase products containing recovered material must be used in all cases unless the item:
  - Is not available within a reasonable time period, or
  - Fails to meet the reasonable performance standards and specifications, or
  - Is not available at a reasonable price, or
  - Is not available from a sufficient number of sources to maintain a satisfactory level of competition

EO 13101

- Implements RCRA Section 6002
- Directs Federal agencies to acquire and use environmentally preferable products and services and implement cost-effective procurement preference programs favoring the purchase of these products and services
- Mandates RCRA s Affirmative Procurement Program by requiring consideration of the following factors during acquisition planning
  - Elimination of virgin material requirements
  - Use of bio-based products
  - Use of recovered materials
  - Product reuse and life cycle cost
  - Recyclable
  - Use of environmentally preferable products
  - Waste prevention including toxicity reduction/elimination
  - Ultimate disposal
- Is now part of EPA or State hazardous waste inspections
- Installations can get a notice of violation for failure to comply

EO 13101, Continued

- Recycled-content products do not need to be used if the products
  - Do not meet technical performance requirements
  - Cost more than comparable non-recycled-content products
  - Are sole-source items
  - Are not available in a timely manner

FAR

- Environmental considerations were officially incorporated in August 1997
- FAR was amended in August 2000 to implement EO 13101
- 7.103 Agency head responsibilities
- 7.105 Written acquisition plans
- 11.002 Policy/Agency needs
- 11.3 –Acceptable material
- 11.304 –Contract clause 52.211-5 Material requirements
- 13.201 RCRA and EO 13101 now applies to purchases at or below the micro-purchase threshold
- 52.223-4 Recovered materials
- 52.223-9 Estimate of percentage of recovered material content for EPA-designated products
- 52.223-10 Waste reduction program

FAR, Continued

- Acquisition planning
  - Indicates that agencies should ensure the procurement of recycled-content and environmentally preferable products and services become a fundamental building block for future planning efforts
  - One of the easiest ways to incorporate recycled-content products and EPP products and services into Federal purchasing decisions is to begin considering environmental performance during the acquisition planning phase
    - Design for Environment

Comprehensive Procurement Guidelines (CPG)

- The EPA designated list of items that can be used as a guide to buying recycled products
- Categories include the following items
  - Construction Products (insulation, carpet, latex paint, floor tiles)
  - Landscaping Products (hoses, hydraulic mulch, yard trimmings)
  - Non-paper Office Supplies (binders, plastic desk top accessories, toner cartridges, printer ribbons, plastic envelopes, plastic clipboards)
  - Paper and Paper Products (newsprint, tissue, writing/printing paper)
  - Park and Recreation (plastic fencing, playground surfaces, running track)
  - Transportation Products (delineators, parking stops, traffic cones)
  - Vehicular (coolants, re-refined lubricants, retread tires)
  - Miscellaneous (pallets, sorbents, awards and plaques, signage)
- Complete list can be found at the following URL
  - http://www.epa.gov/cpg/products.htm

What are the Benefits?

- Aids in the development of quality products and services that are energy and resource efficient, and that minimize harmful environmental effects
- Creates a market for recycles materials and agricultural or forestry wastes
- Creates a healthier living and working environment
- Strengthens environmental stewardship
- Fosters new technologies
- Can be cost-effective

The impact to the environment will be significant. For every ton of recycled paper purchased instead of virgin paper we save: 17 trees (which are capable of filtering half a ton of pollutants from the air each year), 7,000 gallons of water, 380 gallons of oil (4100 KWH of energy),, and 3 cubic yards of landfill space. Recycled paper making also produces 74% less air pollution and 35% less water pollution than virgin papermaking.

Misconceptions

- Recycled-content products are interior
- Recycled-content products always cost more
- These products have limited availability
- Manufacturing recycled content products uses more energy

Backup Charts

Save

Example of a Waiver Form

Request for Green Procurement Waiver

Tracking Number:

Item Description:

Item Part Number:

Requestor's Name:

Requestor's E-mail:

Requestor's Phone: *(include area code)*

Inadequate Competition

Unreasonable Price (> 10% over virgin materials based on life cycle costs)

Inability to Meet Performance or Quality Specifications

Not Available Within a Reasonable Time

This request for waiver is being submitted for the above listed item based on the following determinations:

JUSTIFICATION

Provide written justification below citing the applicable determinations and describe the reason why this requisition item MUST be purchased rather than an approved EPA designated item. Include any supporting detail, equipment specifications, item requirements, etc., that will support the procurement of this item.

Evaluating Costs

- COST ANALYSIS: More than just purchase price must be considered when determining the cost of an Affirmative Procurement item. The life-cycle cost should be used, which considers other factors such as maintenance cost and the total life of the product. To calculate the life cycle costing assessment for a product that deviates from the Affirmative Procurement Program, NASA recommends that each center evaluate the following cost criteria:
- Associated training and management
- Replacement
- Handling and transportation
- Treatment or disposal
- Potential liabilities
- Using the products
- Record keeping
- Waste minimization efforts

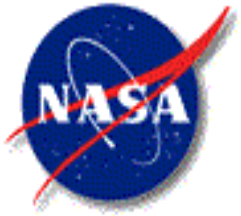

MARSHALL SPACE FLIGHT CENTER
HUNTSVILLE, AL

NASA Principal Center

for

Review of Clean Air Act Regulations

NASA/MSFC
ED36/ Marceia Clark-Ingram
September 17, 2002

Regulatory Background

- Clean Air Act (CAA) regulations have greatly impacted materials/ processes utilized in manufacture of aerospace hardware
  - Title I : Volatile Organic Compounds (coating applications)
  - Title III : Hazardous Air Pollutants (depainting operations)
  - Title VI : Ozone Depleting Chemicals (solvents, blowing agents)
- ***Code JE/ NASA's Environmental Management Office at Headquarters*** recognized the need for a formal, Agency-wide, review process of CAA regulations.

CAA Principal Center Concept

- Code JE developed the concept of a NASA Principal Center for the Review of Clean Air Act Regulations .
- The CAA Principal Center is tasked to
  - Provide centralized support to NASA/HDQ Code JE for the management and leadership of NASA s CAA regulation review process.
  - Identify potential impact from proposed CAA regulations to NASA program hardware and supporting facilities
    - The EPA is required by CAA to promulgate emission standards for approximately 188 HAPs.
    - Several National Emission Standards for Hazardous Air Pollutants (NESHAPs) potentially impact NASA facilities, programs and hardware.

MSFC - CAA Principal Center

- MSFC was selected as the Principal Center for Review of Clean Air Act Regulations
  - **Memorandum of Agreement (April 2000)**
- ED30/ Materials, Processes and Manufacturing Department at MSFC executes the Principal Center duties.
- MSFC has significant historical expertise in assessment and rule development of CAA regulations
  - Collaborative teaming with MSFC Space Shuttle Projects, MSFC s Environmental Management Office and ED30 on environmental regulatory issues
  - **Aerospace NESHAP,Critical Use Exemption for TCA, HCFC-141b waiver development**

Principal Points of Contact

- Code JE/ Environmental Management Office at NASA Headquarters
  - Ms. Olga Dominguez
  - Ms. Maria Bayon
- ED30/Materials, Processes & Manufacturing Department at MSFC
  - Dr. Paul M. Munafo
  - Mr. Dennis E. Griffin
  - Ms. Marceia Clark-Ingram
  - Ms. Rhonda Lash
- Earth Tech Corporation
  - Mr. Bill Swofford & Ms. Carole Frye

NASA Centers

NASA Center	Location	NASA Center	Location
Ames (ARC)	Moffett, CA	Michoud (MAF)	New Orleans, LA
Dryden (DFRC)	Edwards AFB, CA	Marshall (MSFC)	Huntsville, AL
Glenn (GRC)	Cleveland, OH	Stennis (SSC)	Stennis, MS
Jet Propulsion (JPL)	Pasadena, CA	Wallops (WFF)	Wallops Facility,VA
Johnson (JSC)	Houston, TX	White Sands (WSTF)	Las Cruces, NM
Kennedy (KSC)	KSC, FL	Goddard (GSFC)	Greenbelt, MD
Langley(LaRC)	Hampton, VA		

NASA s CAA Working Group

- NASA s CAA WG is comprised of membership from all NASA Centers and Facilities
- Principal Center is dependant on CAA WG for identification of facility-oriented impacts from CAA regulations
- Routinely convenes via bi-monthly teleconferences
- NASA s CAA WG members had a Face-to- Face meeting during November 2001

CAA WG Membership

NASA Center	Representative	NASA Center	Representative
ARC	**Dana Bolles**	GRC	**Christie Meyer**
DRFC	**Dan Morgan**	MAF	**Francis Celinos**
GSFC	**Kathleen Moxley**	MAF	**Melanie Jennings**
JPL	**James Pham**	MSFC	**Sharon Scroggins**
JSC	**Kirk Hummel**	MSFC	Nathan Coffee
KSC	**Denise De La Pasqua**	SSC	**Jeanette Gordon**
KSC	**Dan Rembert**	WFF	**Joel Mitchell**
LaRC	**Michelle Fraser**	WSTF	**Mike Zigmond**

Shuttle Environmental Assurance Initiative

- The Shuttle Environmental Assurance (SEA) initiative was formalized on August 28, 2000.
  - —Develop/implement a Space Shuttle Program (SSP) environmental plan
  - —Provide environmental insight into SSP operations
  - —Assess emerging environmental regulations to identify areas of potential programmatic impact
  - —Identify/assess materials issues potentially affecting SSP elements
  - —Categorize identified issues according to risk levels & consolidate resource needs for SSP

SEA Initiative

- The Principal Center is very dependant upon the SEA for assessment of potential impacts to NASA s programmatic hardware & operations from CAA regulations
- The SEA is comprised of approximately 100 Steering Group & Working Group members
  - SSP elements
  - SSP support contractors
  - Safety Mission Assu.
  - Materials Orgs.
  - -Procurement
  - -Legal
  - -Resources
  - -Environmental Management Offices

Shuttle Contractors

ELEMENT	SHUTTLE CONTRACTOR	LOCATION
External Tank	Lockheed Martin	New Orleans, LA
Redesigned Solid Rocket Motors	ATK Thiokol	Brigham City, Utah
Solid Rocket Boosters	United Space Alliance	KSC, Fl
Space Shuttle Main Engine	Rocketdyne	Canoga Park, CA
Space Shuttle Vehicle	Boeing	Huntington Beach, CA
Space Suits	Hamilton Sunstrand	Connecticut

SEA Points of Contact

SEA Role	Point of Contact
Shuttle Integration Office (SIO), Manager	Ms. Jolene Martin
SIO Technical Team Lead	Mr. Alan Murphy
SEA Technical Lead	Mr. Steve Glover
SEA Regulatory Lead	Ms. Gail Grafton
SEA Interfaces Lead	Ms. Anne Meinhold

Principal Center: Review Process

1. EPA disseminates CAA regulatory action.
2. PC identifies regulatory action from Federal Register or NFESC subscription
3. PC performs cursory analysis of emerging, proposed or final regulation for potential impacts to NASA s programs and facilities.
   - Attend stakeholder meetings
   - Participate in teleconferences with DoD, Industry
4. PC develops/disseminates a Call for Comments on regulatory action to CAA WG and SEA.

   -PC develops a summary of the regulatory action

   - Timelines & potential areas of concern are communicated.

Review Process (Cont d)

6. PC consolidates all comments/concerns into a NASA-wide response
   - Draft copy of comments forwarded to all submitters for final review
7. Draft of comments provided to NASA HQ/ Environmental Management Office
   - Concurrence from Office of General Counsel
   - Concurrence from Director of Environment Management Division
8. Finalized comments are provided to EPA s docket .
   - Copies of comments provided to appropriate points of contact at NASA s facilities and for NASA s programs.

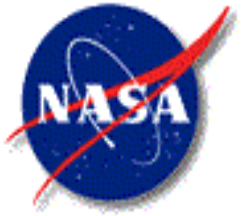

MARSHALL SPACE FLIGHT CENTER
HUNTSVILLE, AL

SUMMARY OF PRINCIPAL CENTERS CAA REGULATORY EFFORTS

CAA REGULATORY EFFORT

- NASA is tracking several Clean Air Act (CAA) regulations
  - Final
  - Proposed
  - Emerging
- 5 NASA Centers/Facilities are major sources of Hazardous Air Pollutants (HAPs)
  - KSC, MAF, MSFC, GRC, GSFC
  - Potential to emit 10 tons per year of 1 HAP or
  - Potential to emit 25 tons per year of any combination of HAPs

REGULATORY TRACKING

- FINAL
  - MACT Permit Hammer/ Application Part 1
- PROPOSED
  - Miscellaneous Coating Manufacturing
  - Semiconductor Manufacturing
  - Engine Test Cell/Stands
  - Fabric, Printing, Coating & Dyeing of Textiles
  - Site Remediation
  - Miscellaneous Metal Parts & Products
  - Proposed Settlement Accelerating the CAA Permit Hammer/Part 2
  - Protection of Stratospheric Ozone; Allowance System for Controlling HCFC Production, Import & Export

REGULATORY TRACKING (Cont d)

- Proposed (continued)
  - —Friction Products
  - —Reinforced Plastic Composites
- Emerging(not yet proposed)
  - —Combustion Turbine
  - —Industrial Commercial Boilers & Process Heaters
  - —Plastic Parts & Products Surface Coating
  - —Reciprocating Internal Combustion Engines
  - —Paint Stripping

NASA PROGRAMS & FACILITIES

- The NASA CAA regulatory effort has illustrated several trends
  - The NASA Programs such as the Space Shuttle Projects (SSP) are impacted by emission standards regulating materials, processes and manufacturing operations
    - Miscellaneous Coating Manufacturing
    - Fabric, Printing, Coating and Dyeing of Textiles
  - The NASA Centers/Facilities primarily are impacted by the facility-oriented NESHAPs
    - Industrial Boilers
    - Combustion Turbines
    - Site Remediation
  - Some of the NASA Centers/Facilities engaged in Research & Development activities are seeking de minimus exemptions.

Cross — Cutting Facilities

- MAF's comments incorporate concerns with both facility and programmatic environmental impacts
  - — MAF is a NASA facility
  - — Location for manufacture of External Tank
- KSC's comments incorporate concerns with both facility and programmatic impacts
  - -Shuttle processing
  - -Integration of elements
  - -Launch site

CONCLUSION

- The Principal Center concept has resulted in many benefits to NASA
  - —Supports the Administrator s vision for **one** NASA
  - —Provides unified NASA voice to the EPA
  - —Teaming within NASA programs and facilities
  - —Effective utilization of resources; decreased redundancy of efforts
  - —Focused effort results in a more environmentally-friendly NASA

Protecting the Global Environment - The Role of Industrial Process Engineers

CAROLE LEBLANC
Surface Solutions Laboratory
Toxics Use Reduction Institute
University of Massachusetts Lowell
One University Avenue
Lowell, MA 01854-2866
Phone: 978-934-3249
Fax: 978-934-3050
E-mail: Carole_LeBlanc@uml.edu

What is an industrial process engineer? Some definitions from the internet suggest that responsibilities include:

- Selecting materials and processes used to manufacture products
- Developing technology to enhance the production process
- Safety engineering
- Developing, installing and maintaining cost-effective methods of manufacturing as well as fair and equitable manufacturing operating standards in a safe environment

The industrial process engineer is a key player in creating demand for the materials consumed by industry and ultimately for their use, disposal, and release to the environment. Some of these materials create local or regional pollution problems, while others create little if any local notice but collectively result in significant global impact. The environmental impact of the collective weight of globally common industrial processes have resulted in global responses in the form of three treaties negotiated under the United Nations. They are Montreal Protocol on Substances that Deplete the Ozone Layer, the Kyoto Protocol on Global Climate Change, and the Basel Convention on Transboundary Shipment of Hazardous Waste.

This presentation will provide an overview of these three treaties, describe how they affect industrial process engineers, and how they can impact companies and industries that are not aware of them.

Metal Matrix Composite LOX Turbopump Housing Via Novel Tool-Less Net-Shape Pressure Infiltration Casting Technology

AMPET 2002

Huntsville, AL 35812

Authors:

Sandeep Shah, Jonathan Lee, Biliyar Bhat, Doug Wells, Wayne Gregg – NASA, Engineering Directorate

Matthew Marsh, Gary Genge, John Forbes – NASA, Transportation Dir.

Alex Salvi, James A. Cornie, Michael Sung, Shiyu Zhang – MMCC, Inc.

MMCC

Metal Matrix Cast Composites, Inc.

NASA

MSFC ENGINEERING DIRECTORATE

RESEARCH • TECHNOLOGY • DEVELOPMENT

WHY METAL MATRIX COMPOSITE FOR PROPULSION COMPONENTS

- **PERFORMANCE**
  - High Specific Strength & Specific Stiffness = Weight Savings
  - Compatibility With H_2 and O_2 -- Better Than PMC/CMC
  - Low Thermal Coefficient of Expansion
  - Higher Electrical & Thermal Conductivity than PMC
  - Ductility & Toughness From Metal Matrix
  - Particulate MMC's behavior More Like Metallic Alloys
- **AFFORDABILITY**
  - Complex Parts Can be Produced by Low Cost Casting
  - MMC Cost per Pound Comparatively Less Than PMC/CMC
  - Many Commercial & DoD Applications Now in Service

METAL MATRIX COMPOSITE TURBOPUMP HOUSING JOINT REDESIGN EFFORT

- **Metal Matrix Cast Composites, Inc.,**
  - **Phase II SBIR Award**
  - **Develop Materials And Manufacturing Process.**
  - **Cast 3 Full Scale "Redesigned" "Hybrid" Al MMC LOX Compatible Turbopump Housings**

- **NASA MSFC Space Transportation Team**
  - **Internal NRA Award**
  - **Re-analyze and Re-design Al MMC Pump Housing**

- **NASA To Provide New Pump Housing Design To MMCC. Inc.**

Redesign Objectives – 40% weight Savings

BASELINE PUMP DESIGN AND ANALYSIS

BASELINE PUMP HOUSING DESIGN AND STRESS ANALYSIS

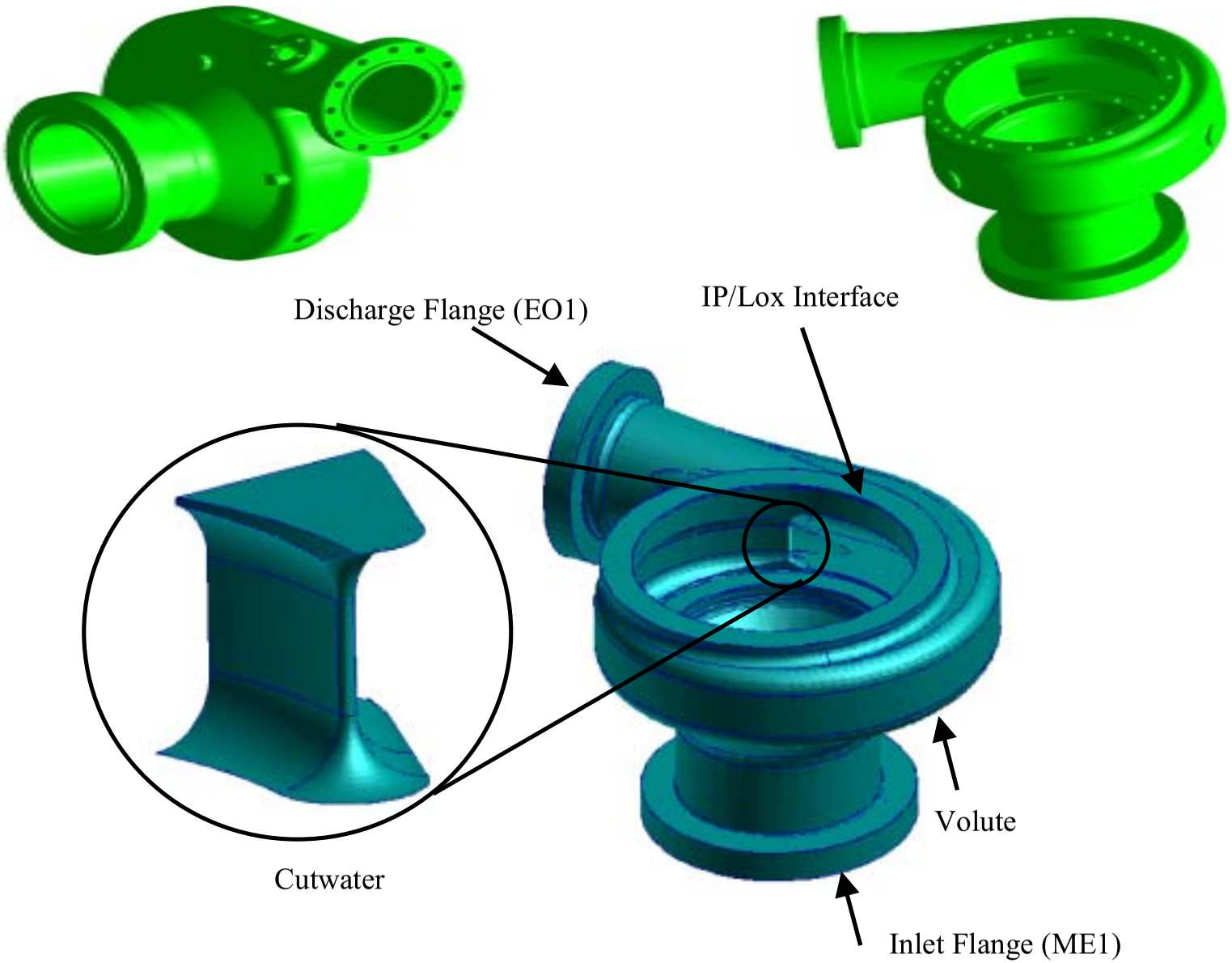

BASELINE PUMP HOUSING DESIGN AND STRESS ANALYSIS - Continued

Material : Microcast Inconel 718

E = 29.6 Msi, v = 0.29, d = 0.297 pci UTS = 140 Ksi, YS = 110 Ksi

Safety Factor: 1.4 on UTS LEFM

PEAK STRESSES IN CUTWATER LOCATION

Baseline Deformation Plot

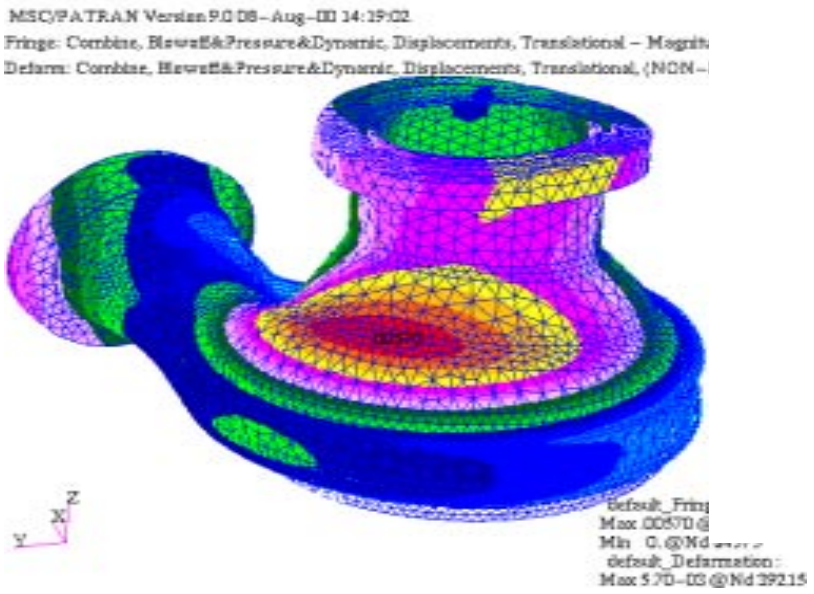

Baseline Stress Plot

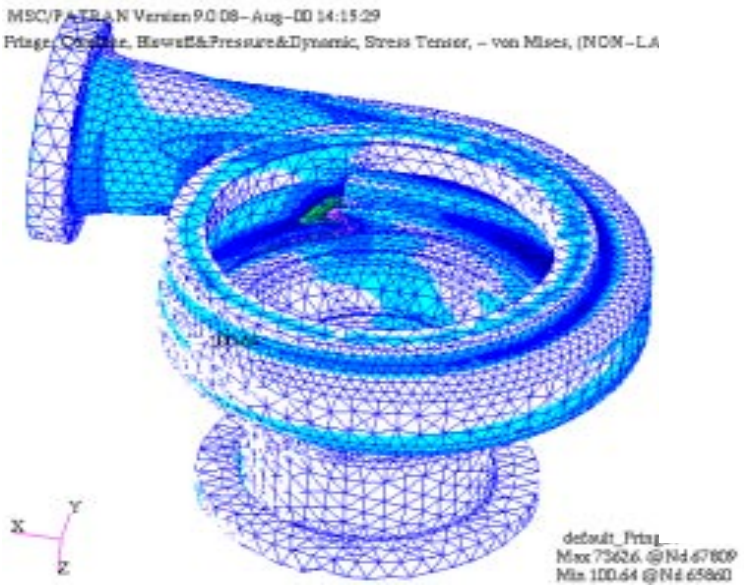

TOOL-LESS ADVANCED PRESSURE INFILTRATION CASTING PROCESS

TOOL-LESS ADVANCED PRESSURE INFILTRATION CASTING PROCESS

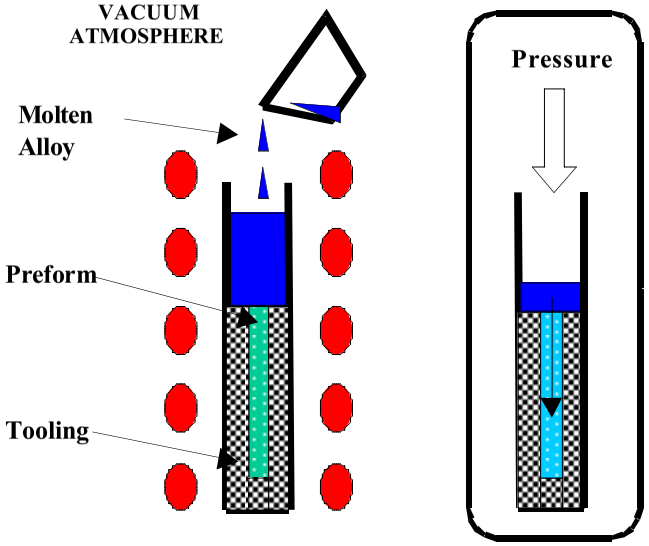

MMC

Header containing reservoir of molten alloy

Pre heated-pre evacuated mold vessel containing preforms

Autoclave for pressure infiltration

Two cubic foot casting being transferred to autoclave for pressure infiltration and directional solidification

TOOL-LESS ADVANCED PRESSURE INFILTRATION CASTING PROCESS: 3 Dimensional Printing (3DP) of Ceramic Preform

Novel 3D-Printing Technology

Advantages: From CAD file to preform with no tools; uniform defect-free preform

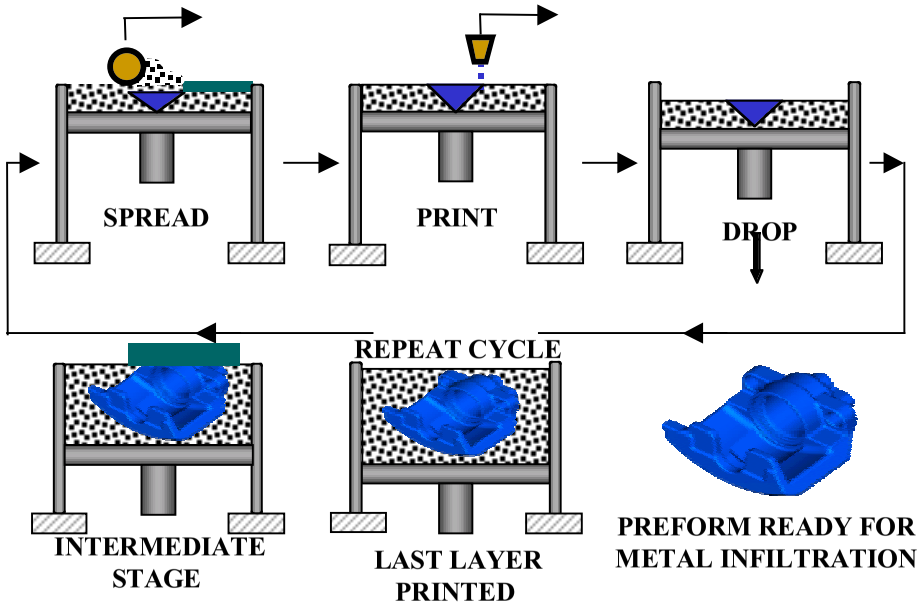

TOOL-LESS ADVANCED PRESSURE INFILTRATION CASTING PROCESS: Tool-Less Mold Process

3DP + ToolLess™ Mold = Breakthrough

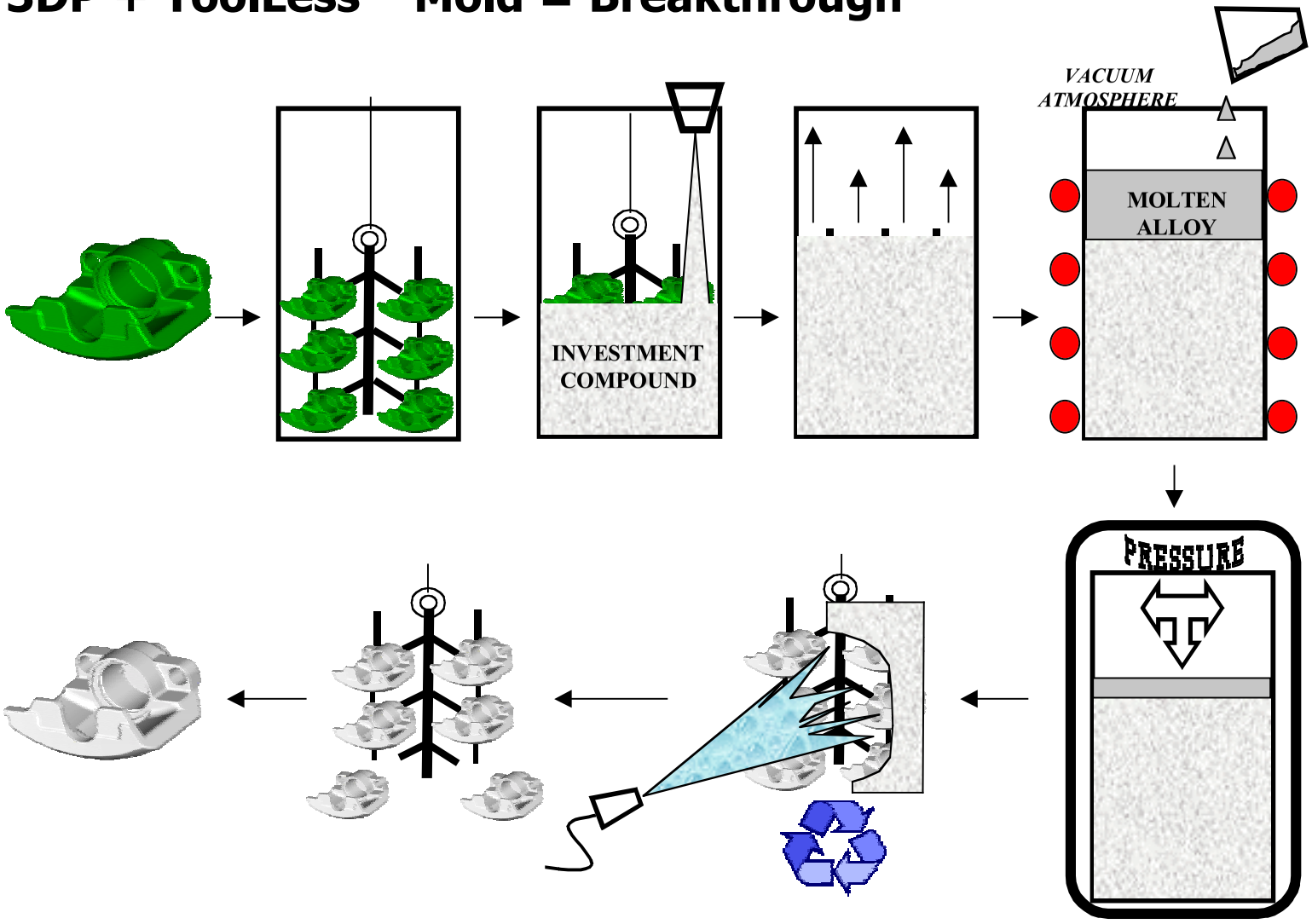

TOOL-LESS ADVANCED PRESSURE INFILTRATION CASTING PROCESS: Mechanical Properties and Microstructure Optimization

- **3DP Ceramic Reinforcement particle Size and Volume used**

Reinforcement Type	Particulate Size	Particulte Vf in final MMC Composite
Al2O3	(17 + 20% of 2.7) micron	35 - 38 %
Al2O3	17 micron	37 - 41 %
SiC	(17 + 20% of 2.7) micron	31 - 35 %

- **Typical microstructure of 3DP composite:**
  - isotropic in X-Y plane, anisotropic in X-Z plane

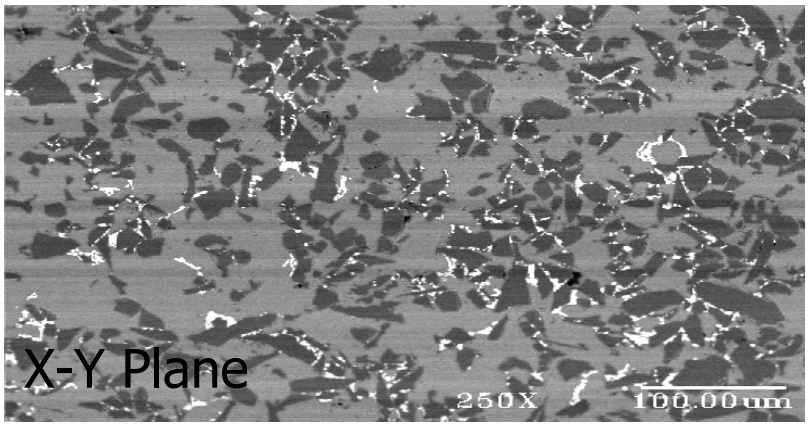

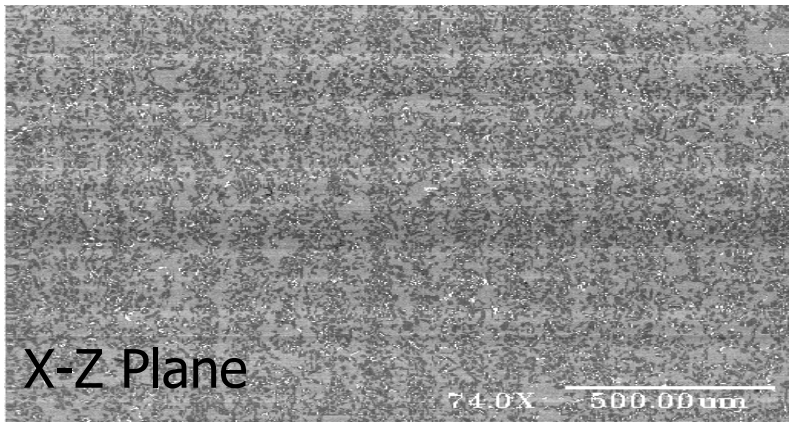

TOOL-LESS ADVANCED PRESSURE INFILTRATION CASTING PROCESS: Typical Mechanical Properties

- **3DP sintered alumina Al alloy composites: Strength, toughness vs alloy composition and particle size**

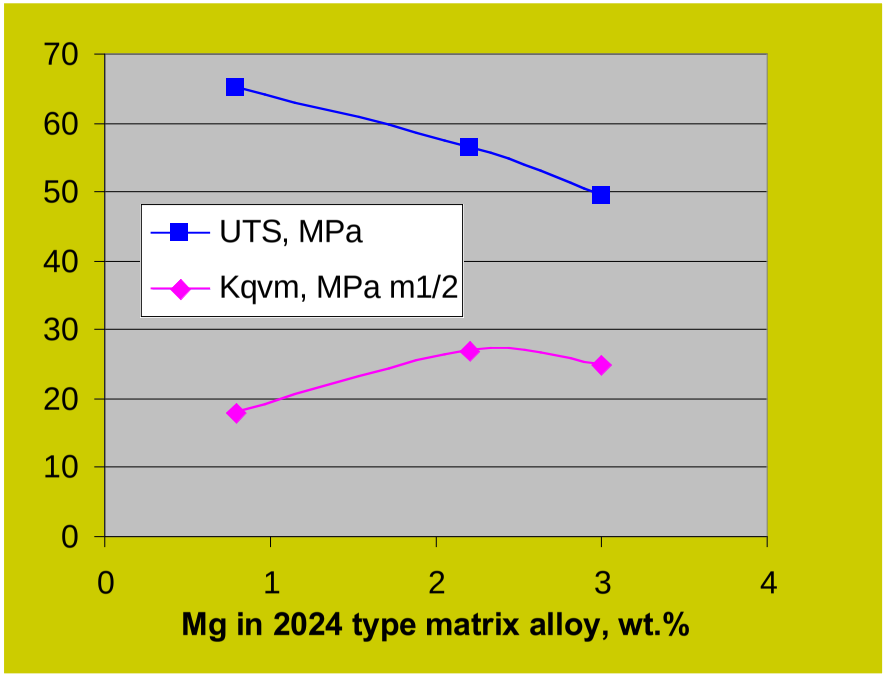

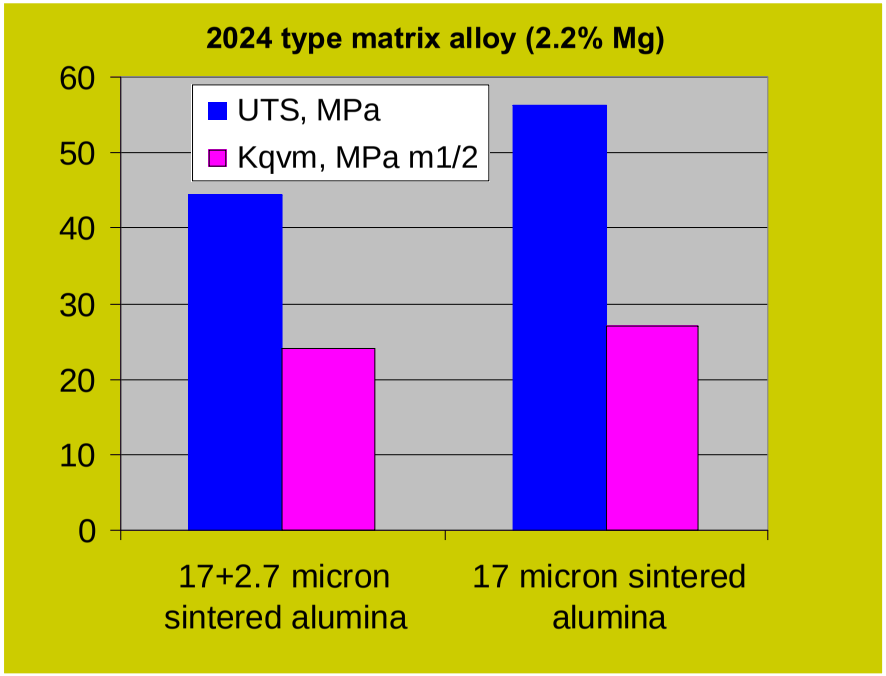

SUBSCALE PUMP HOUSING: Pressure Infiltration Casting Demonstration

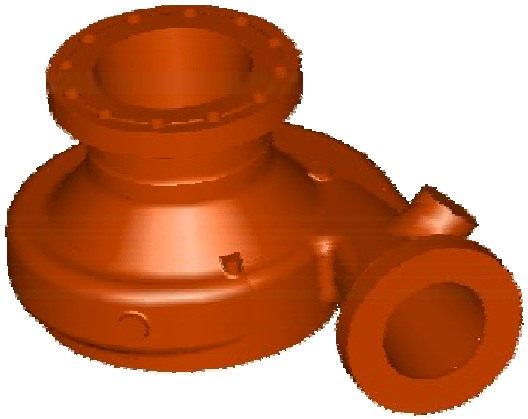

PREFORM SPLICING AND JOINING FOR LARGE COMPONENTS SUCH AS PUMP HOUSING

PREFORM SPLICING AND JOINING STUDY

3D PRINTING IS LIMITED IN SIZE REQUIRING SPLICING AND JOINING OF LARGE PART PREFORMS

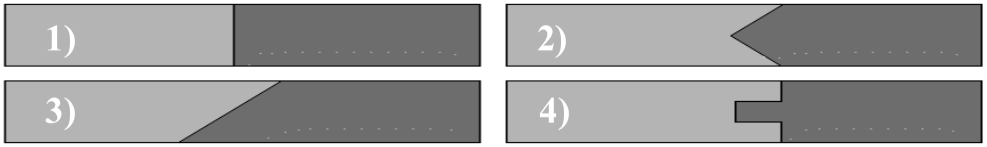

Joint type	Sintered	UTS		Std. Dev.	Sintering
	Connection	ksi	mPa	mPa	Lot #
# 1) Butt	yes	53.4	368	27.1	2
"	no	59.0	406.8	27.1	2
# 2) V-Joint	yes	62.1	428.1	9.5	1
"	no	56.6	390.5	15.1	1
"	no	51.1	352	28.8	2
# 3) 45 Degree	yes	67.9	468.4	26.2	1
"	yes	57.0	392.8	31.7	2
"	no	62.6	431.6	28.3	1
"	no	62.1	428.1	13.7	2
#4) Tongue & Grove	yes	55.6	383.0	36.4	1
	no	64.5	444.8	39.6	1
	no	59.4	409.4	37.9	2

1) 3DP Print Preforms
   - Join Preforms
   - Sinter Together
   - Infiltrate
   - Heat Treat
   - Tensile Test Coupon
2) 3DP Print Preforms
   - Sinter Separate
   - Join Preforms
   - Infiltrate
   - Heat Treat
   - Tensile Test Coupon

3DP- Al_2O_3 Particulate Preform Joining Study- Conclusions:

1. Tensile properties relatively insensitive to joint design
2. Components can be printed as parts and joined after sintering
3. These results lead to processing flexibility

FULLSCALE PUMP HOUSING REDESIGN

FULLSCALE PUMP HOUSING REDESIGN

Objective: Redesign the pump housing to reduce the maximum stress yet keeping the 40% weight savings.

Full Scale Manufacturing

Positive Margin in Design

FULLSCALE PUMP HOUSING REDESIGN-
Manufacturing Design Options Considered

Hybrid: Wrap fibers around volute in cutwater area

Alloy not suitable for hybrid reinforcement manufacturing complexity

Inconel718 insert in cutwater area

Manufacturing complexity

Cost and Schedule

Al particulate MMC with gussets in volute

Selected for Manufacturing Demonstration

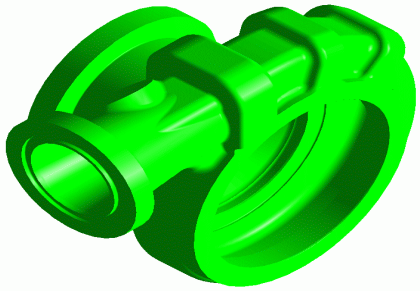

Hybrid: Sic Fiber stiffened gussets in volute

Cracking in Fiber/particulate interface in subscale specimen. Need to match CTE.

FULLSCALE PUMP HOUSING REDESIGN - FEM Analysis

FEM Analysis Particulate Al MMC Properties Used: **Linear Isotropic Material**

E = 22 Msi, UTS = 58Ksi, YS = 50Ksi, ν = 0.3, δ = 0.111 pci,

Factor of Safety = 2.0 on UTS Allowable Max Stress = 29 Ksi

Margin of Safety = ((actual safety factor/required safety factor) –1)

Al Particulate MMC Design Options Analyzed	Weight Lbs	Margin of Safety ***
Baseline - Inconel 718	25.95	0.0
Baseline - MMC	9.70	-0.606
Baseline + Thicker Volute	10.71	-0.518
Baseline + Thicker Volute+ Larger Cutwater Radius	10.70	-0.471
Baseline + 3 Radial Gussets Added to Volute	10.56	-0.455
Baseline + Deeper Radial Gussets, Larger Cutwater Radius	10.84	-0.372
Baseline + 4-ply SiC Fiber Reinforced Gussets	10.84	-0.371

*** MOS using a Factor of Safety = 2.0 and not 1.4

FULLSCALE PUMP HOUSING PREFORM - Spliced, Joined and Sintered Preform

Housing after sintering but prior to application of Soft-Shell^{tm} Tool-Less Mold compound-

(Note stainless steel threaded inserts in bolt circle)

FULLSCALE PUMP HOUSING - Casting

Inserts for threaded mechanical joint

Holes for Bolted Joints

FULLSCALE PUMP HOUSING – Lessons Learned

- Alloy composition needs further development for a hybrid design.
- Cracking at SiC fiber/particulate interface.
- 3 Dimensional printing of large preform sections resulted in sagging and loss of dimensional control of the preform.
- Obtaining surface finish with tool-less mold process needs more development. Surface finish is determined by perform technology, not by tool-less mold technology

SUGGESTED FUTURE DEVELOPMENTS

- For 100% particulate housing, the alloy can be optimized to produce higher strength MMC.
- Sagging can be avoided by printing thinner sections of 3DP preforms. Subsequently, preform joining technique can be used to obtain a complete part.
- Preform volume fraction limited to ~35-40%. Slurry/slip casting, an alternative to 3DP preforms can raise the volume fraction to 55%.
- Surface finish of MMC component is totally dependent upon surface of preform. Improve the surface of the preform prior to casting.
- CTE differences between SiC fibers and particulate composite that leads to cracking at fiber interface could be avoided or reduced by using Nextel fibers.

2002

AMPET CONFERENCE

Organic Binder Developments For Solid Freeform Fabrication

Prepared By:

Amir A. Mobasher
Alabama A&M University

Mr. Ken Cooper
NASA/MSFC Engineering Directorate

Introduction

What is rapid prototyping? Why is it important in the design process? Before we address these two crucial questions and have appreciation for rapid prototyping, we shall address and understand the design process. That is what are the steps required to be taken by the designer to bring his/her idea to reality and consequently to profitability? Although the process from design-to-manufacture varies from business to business, a general pass involves (1) The concept, (2) Preliminary Design, (3) Preliminary Prototype Fabrication, (4) Short-run Production and (5) Final Production. Any new product or an improvement to an existing product starts with a concept. The motivation for the concept is generally based on a need or a gap that may exist in our current life style, technology, etc. Once it is established that the need for a particular product exists, the idea might be carried into the next phase of preliminary design. In this step, the designer may prepare a two dimensional drawings or even a Computer Aided Design (CAD) solid model of the part to be built. In this phase the design may go through several iterations as the designer determines the feasibility of the product through discussions with colleagues and co-workers and presenting it to management. Once the design has been given the "go", a prototype must be fabricated to check out the design. Traditionally (Before Rapid Prototyping), this phase of the design was carried out either by hand working or machining the part. Both of these techniques require tremendous amount of man power and labor hours. The next stage of the process involves Short-run Production. This phase may be necessary to further proof a part before entering into final production. In this phase, from tens to hundred parts maybe produced and distributed for testing before entering the final production. Final step in the design involves the Final production. In this step, the parts are typically machined, injection molded or cast in large numbers depending on the design criteria and costs.

Traditionally the process of design-to-manufacture took several months or even years to fully mature. That is due to the overhead associated with iterations in steps (2) and (3). In that, the designer gave the preliminary design to the machine shop. Depending on the complexity of the part, this may take several days or even weeks to build the part. Then the part may go back to the designer for approval and verification. Then there may be additional modifications to the design which much be corrected in the prototyping phase. Rapid prototyping therefore is the process of replacing this time consuming process with a much more efficient and faster process. Rapid Prototyping (RP), referes to the layer-by-layer fabrication of three-dimensional physical models directly from a computer aided design (CAD). This additive manufacturing process provides designers and engineers to literally print out their ideas in three dimensions. The RP processes provide a fast and inexpensive alternative for producing prototypes and functional models as compared to the traditional routs for part production. The advantage of building parts in layers is that it allows you to build complex shapes that would be virtually impossible to machine, in addition to the more simple designs. RP can build intricate internal structures, parts inside parts, and very thin-wall features just as easily as building a simple cube. All of the RP processes construct objects by producing very thin cross sections of the part, one on top of the other, until the solid physical part is completed. This simplifies the three dimensional construction process in that the essentially two dimensional slices are being created and stacked together. For example, instead of of trying to cut out a sphere with a detailed machining process, stacks of various sized "circles" are build consecutively in the RP machine to create a sphere with ease.

History of Rapid Prototyping

RP stems from the ever-growing CAD industry, more specifically, the solid modeling side of the CAD. Solid modeling is the branch of CAD that produces true three dimensional objects in electronic format. A solid model has volume and is fully enclosed. Before solid modeling was introduced in the late 80's, three dimensional models were created with wire frames and surfaces. A wire frame is an approximate presentation of a three dimensional object. Not until the development of true solid modeling could innovative processes such as RP be developed. the first RP system was developed by Charles Hall in 1986, who also helped found 3D systems. This process, called sterolithography, builds objects by curing thin consecutive slices of certain ultraviolet light sensitive liquid resins with a low power laser. There are now many national and international companies manufacturing and selling RP processes. Among these machines are:

(1) JP-Sytem 5 (JP5), By Schroff Development- This process builds models from CAD Data using label paper and a knife plotter. JP5 is a simple and inexpensive modler for creating rough 3D models.
(2) Balistic Particle Manufacturing (BPM)- This process involves firing droplets of molten vax from a moving jet onto a stationary platform.
(3) The Model Maker (MM), and Rapid Tool Maker (RTM) by Sanders Prototype: This process produces highly accurate wax patterns using ink-jet printing technology with molten wax.
(4) Multi-Jet Modeling (MJM) used by 3D Systems, Inc.: This process uses inkjet printing technology with many jets enclosed into a single print head to produce concept modles.
(5) Direct Shell Production by Soligen Inc.: Uses Binder printing technology developed by MIT. The binder is printed by layers of ceramic powder to produce investment shells directly from CAD.
(6) The Z402 System by Z-Corp: Also uses MIT 3D printing technology to build very fast concept models from a starch like material
(7) Fused Deposition Modeling (FDM), by Strasys, Inc. Produces models from wax or ABS Plastic using motion control and extrusion technology similar to a hot glue gun.
(8) Laminated Object Manufacturing by Helisys, Inc. Builds physical models by stalking sheets of paper or plastic material and cutting away excess material with laser.
(9) Stereolithography, by 3D Systems, Corp. Is the oldest RP system and builds models by curing epoxy resins with a low power laser.
(10) Selective Laser Sintering, by DTM can build with a variety of materials and works by selective melting together powder with laser into a desired shape.
(11) Laser Engineered Net Shaping, by Optomec Design Co., builds parts directly by metal powders by fusing the powder together with a laser beam.

In the course of past few years some of these machines have gained considerable speed and accuracy such as Selective Laser Sintering (SLS). The NASA Marshall's National Center for Advanced Manufacturing RP center has variety of these machines available. A considerable amount of research is directed towards this area at this center. Among the goals of this center is to produce actual functional parts from metallic materials using current technologies such SLS machines. Potentially there exists a strong market for this technology. Among many applications of this technology is to build actual parts on demand on space for space vehicles rather than transporting the spare parts with the space vehicle.

Commercial Binder Developments

Fused Deposition Modeling (Stratasys)

The Titan system by Stratasys, Inc. has an internal oven to process high temperature polymers. Polycarbonate and Poly-Phenyl Sulfone (PPSF) are currently the two materials offered in addition to the previously offered ABS (acrylene butadiene styrene). The associated properties of each material, as published by Stratasys, Inc. are demonstrated in the following figures.

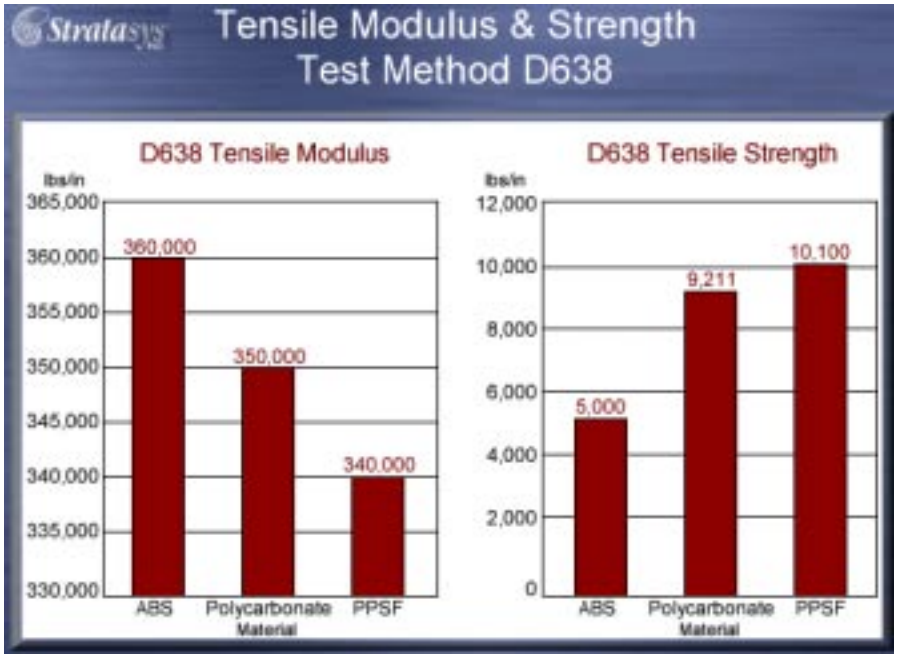

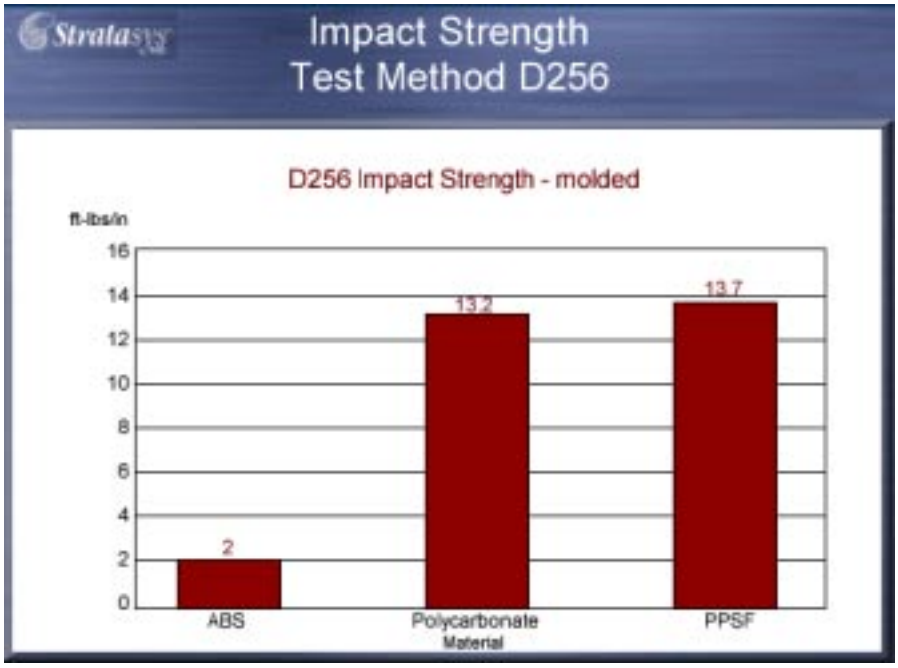

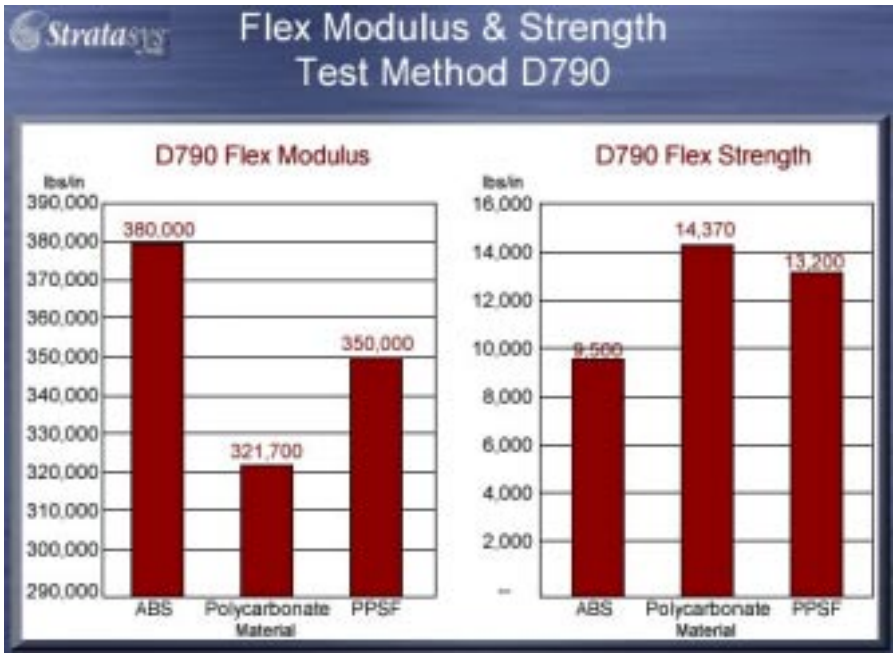

Three Dimensional Printing (Z Corp)

Zcorp's latest powder/binder combination for the 3D Printer provides a part that is easier to handle right out of the machine. Microstone (ZP100) is a plaster based material with about 10MPa strength, and can also be infiltrated with urethane or cyanoacrylate to be very tough and strong. A new material soon to be release is the Zcast system, which provides sand-like core and cavities for investment casting.

Selective Laser Sintering (3D Systems)

The Latest Tooling Material from 3D Systems for the Selective Laser Sintering Process is SLS LaserForm ST100. LaserForm is a polymer coated steel which is fused together by the SLS laser by melting only the polymer element of the powder. The material must then go through a burnout and infiltration process (24 hours), which includes removing the polymer binder and wicking with a secondary bronze material. Resulting parts are showing strengths and utilization comparable to stainless steel. The following figure shows the properties of SLS Laserform.

Mechanical Properties	Units	Test Method	SLS Laserform
Tensile - Yield strength (0.2%)	MPa	ASTM E8	305
Strength	MPa	ASTM E8	510
Elongation	%	ASTM E8	10
Young Modulus	GPa	ASTM E8	137
Compression - Yield Strength (0.2%)	MPa	ASTM E9	317
Hardness - Rockwell "B"			
as infiltrated	-	ASTM E18	87
as machined	-	ASTM E18	79

Research Binder Developments

The process of Selective Laser Sintering involves the acquisition of a layer of a part from a CAD drawing and fusing a powder with laser beam only in the regions where solid is present. This is a highly accurate process and the parts generated in this manner are extremely durable. The objective of this research effort is to establish parameters for the SLS Machine for producing functional parts from Titanium Alloys.

Methodology Adopted for the Laser Sintering Technique

There are primarily three parameters that dictate the quality of the part generated via SLS processing. These parameters are: (1) Laser Power, (2) Part Bed Temperature at which the part is built, and the (3) Layer Thickness for the part to be formed. At the first step of this process we formulated a test matrix which spanned the laser power from 5 to 40 watts, layer thickness from 0.003 to 0.012 and the part bed temperature from 40 to 100 C. This was necessary to zero in on the three parameters.

Results

As a result of this research effort, the following parameters were selected:

(1) part Bed temperature was to be maintained around 100
(2) Laser power was to be set around 30 Watts
(3) Powder layer thickness was to be set to minimum of 0.003 However since no satisfactory results were obtained here it was decided -to allow two passes of the roller on the powder before adding the powder to the part bed. At first the samples were tested -using the binder alone. Once the parameters for the binder was selected it was applied to the actual titanium alloy. A summary of the results is given in the following table (1).

Table 1. Summary of Results for the binder material

No.	Observations made	Photo
1	The sample was built to the height of 0.125 inches. Sample was run once with the thickness of 0.006. Shifting was present in the part. This is perhaps de to the shear force of roller on the powder. Part appeared to be very brittle and unstable.	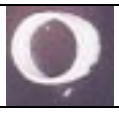

2	The sample was built to the height of 0.125 inches. The bed temperature was increased to 100 C. Sample was run twice with the thickness of 0.003. Shifting was still present in the part. Part appeared to be very brittle and unstable; however, the integrity of the part appeared to be a slightly better than the previous runs.	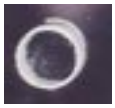
3	It is observed that the quality of the parts appears to be highly dependent on the part bed temperature. The par appeared to be more stable by increasing the temperature to 100 C. The parts still appear to be sheared off, so in the next run the powder will be added on top of the part instead of front of it. The temperature will be raised to 110 C.	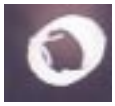
4	The sample was built to the height of 0.25 inches. The bed temperature was set to 100C. Sample was run once with the thickness of 0.003. In this run we sprayed a layer of powder on top of the part area so that shear force was minimized. Shifting was still present in the part but was corrected after several layers. Part appeared to be more stable than the previous runs. This might be attributed to the increase in surface contact area or binding area due to elimination of shifting.	
5	The sample was built to the height of 0.20 inches. The bed temperature was set to 100 C. Sample was run once with the thickness of 0.003. In this run we sprayed a layer of powder on top of the part area so that shear force was minimized. Shifting was eliminated entirely. Part appeared to be more brittle than the case where laser power was set to 40 Watts.	

Resources

The machine used for this project was the Selective Laser Sintering Machine (SLS2000) located in the RP laboratory of the NCAM at NASA Marshall. Material used in the research is the Titanium alloy. There are two software that drive the SLS process: Build Software and Sinter. The build prepares the stl files and gives a visual representation of the location of each part in the Part bed. The Sinter software is the driver software for the SLS machine, in which all the operations and control such as piston movement, loading and unloading the powder, movement of the roller, and latching and unlatching the doors for the machine are performed via this software.

Conclusion

1. The parameters established for this process are Part Bed Temperature of 100 C, Laser power of 25 to 30 and layer thickness of 0.003 or lower if possible.

2. Due to rarity of sample all cases were conducted in the presence of Oxygen. This might contribute to "vaporizing" The binder material before it is sintered.

3. It is essential to eliminate or at least minimize shifting. Shifting of layers causes decrease in the binding surface area and hence adds to instability of the part.

References

1. *Rapid Prototyping Technology, Selection and Application. Kenneth G. Cooper, Marcel Dekker, 2001*
2. *Producing Metal Parts with Selective Laser Sintering/Hot Isostatic Pressing, Suman Das, Martin Wohlert, Joseph J. Beaman and David L. Bourell, JOM, pp17-20, 1998*
3. *http://www.stratasys.com*
4. *http://www.zcorp.com*
5. *http://www.3dsystems.com*
6. *Development of Processing Parameters for Organic Binders Using Selective Laser Sintering, A. Mobasher, NASA/MSFC Summer Faculty Fellowship Report 2002.*

Environmentally Compatible Vapor-Phase Corrosion Inhibitor for Space Shuttle Hardware

Howard L. Novak
United Space Alliance (USA), LLC
8550 Astronaut Blvd.
Mail Stop: USK-864
Cape Canaveral, FL 32920
novakh@usasrb.ksc.nasa.gov
321-867-7054

Phillip B. Hall
NASA Marshall Space Flight Center
Mail Stop: ED 32
Marshall Space Flight Center, AL 35812
phillip.b.hall@msfc.nasa.gov
256-544-2525

ABSTRACT

USA-SRB Element is responsible for the assembly and refurbishment of the non-motor components of the SRB as part of Space Shuttle. Thrust Vector Control (TVC) frames structurally support components of the TVC system located in the aft skirt of the SRB. TVC frames are exposed to the seacoast environment after refurbishment and, also, to seawater immersion after splashdown, and during tow-back to CCAFS-Hangar AF refurbishment facilities. During refurbishment operations it was found that numerous TVC frames were experiencing internal corrosion and coating failures, both from salt air and seawater intrusions. Inspectors using borescopes would visually examine the internal cavities of the complicated aluminum alloy welded tubular structure. It was very difficult for inspectors to examine cavity corners and tubing intersections and particularly, to determine the extent of the corrosion and coating anomalies. Physical access to TVC frame internal cavities for corrosion removal and coating repair was virtually impossible, and an improved method using a Liquid (water based) Vapor-phase Corrosion Inhibitor (LVCI) for preventing initiation of new corrosion, and mitigating and/or stopping existing corrosion growth was recommended in lieu of hazardous paint solvents and high VOC / solvent based corrosion inhibitors. In addition, the borescopic inspection method used to detect corrosion, and/or coating anomalies had severe limitations because of part geometry, and an improved non-destructive inspection (NDI) method using Neutron Radiography (N-Ray) was also recommended.

INTRODUCTION

USA LLC is responsible for the assembly and refurbishment of the non-motor components of the SRB as part of the Space Shuttle system shown in Figures 1 and 2, and which is developed and managed by Marshall Space Flight Center (MSFC) in Huntsville, Alabama. Programs are underway to develop and evaluate environmentally acceptable LVCIs for use on aerospace flight hardware in order to eliminate and/or mitigate corrosion, and ultimately extend the useful service life of these unique and expensive hardware items. Figures 3 shows the location of both upper and lower TVC frames in the Aft Skirt of the SRB. SRB TVC frame material is made from 2219 Aluminum Alloy weldments that are final machined and painted internally and externally. Figures 4 and 5 show the internal cavities, Boss Port Plugs and general construction of Upper and Lower TVC Frames. Borescopic inspection has revealed corrosion in cavity surfaces of both Upper and Lower TVC Frames. Engineering requirements state that any visible corrosion is cause for rejection, and disallows the use of those discrepant frames, and there are significant numbers of TVC Frames that have been set aside because of internal corrosion. The initial objectives of this project were to verify the effectiveness of CORTEC LVCI 377 through the uses of the NASA Kennedy Space Center (KSC) Beach Exposure Corrosion Site, and the U. C. Davis / McClellan Nuclear Radiation Center (MNRC) located in Sacramento, CA. CORTEC also provided verification procedures for use of the LVCI in production at USA Florida Operations, with Refractometry, Titration and pH analysis. See USA LLC Copyright Agreement in References (2).

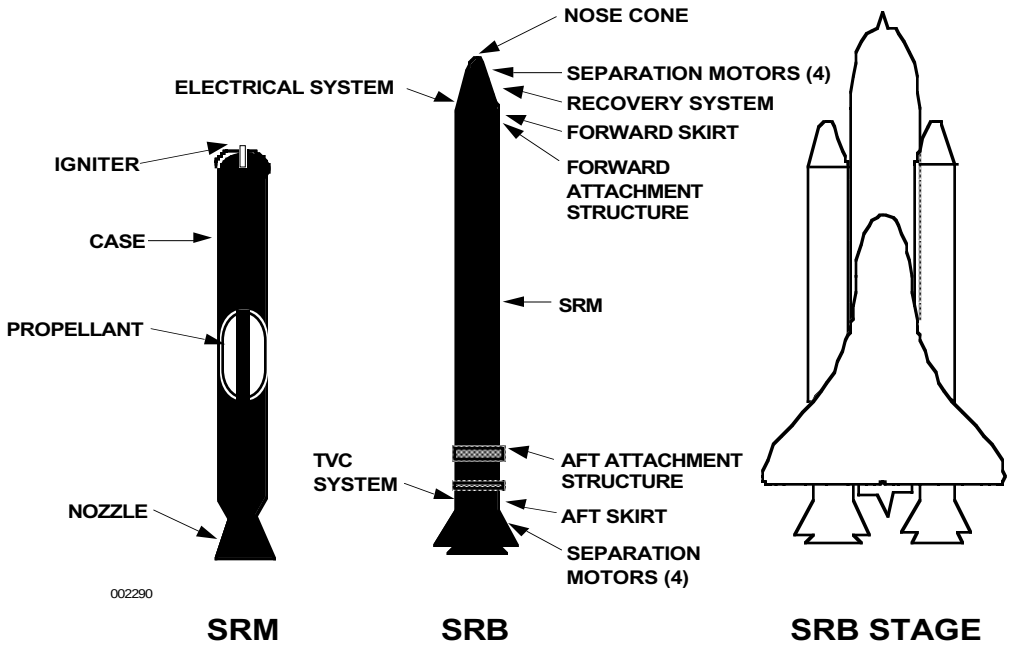

Figure 1. Space Shuttle's SRB

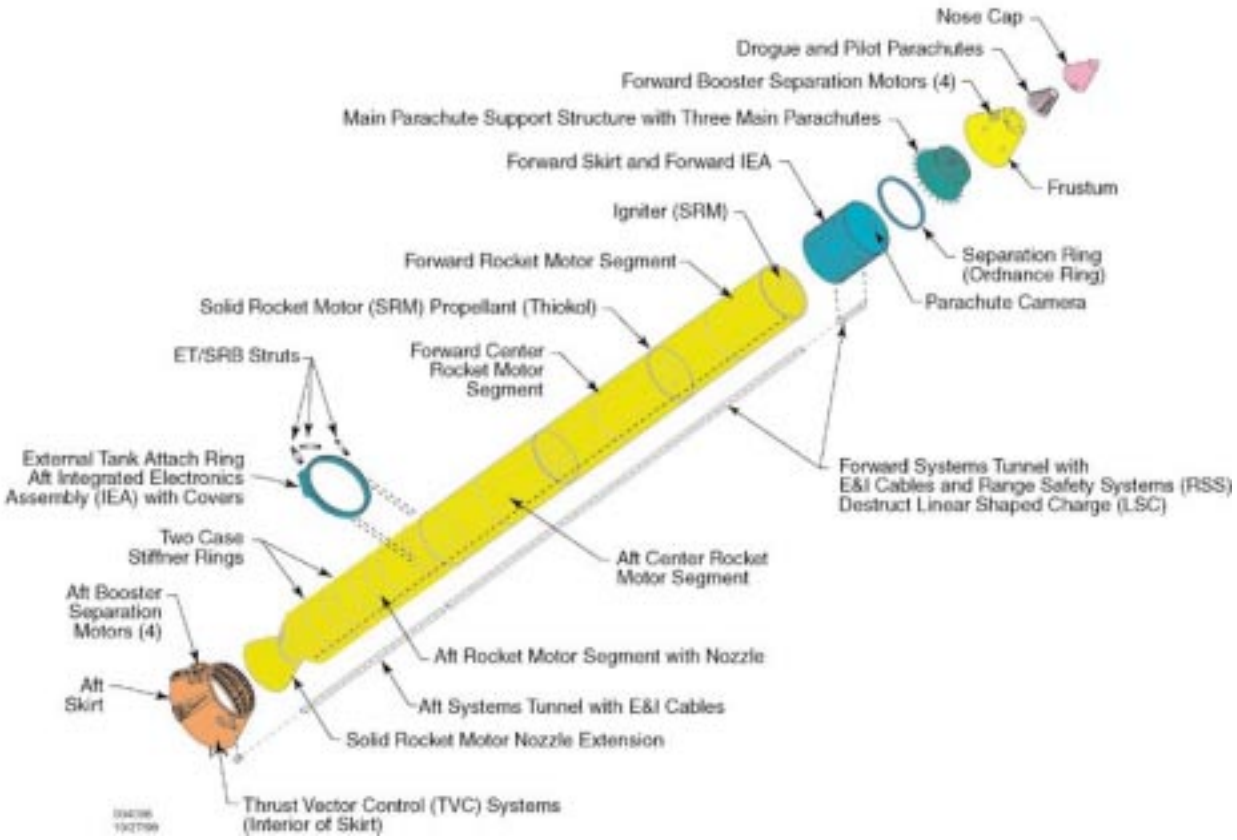

Figure 2. Solid Rocket Booster

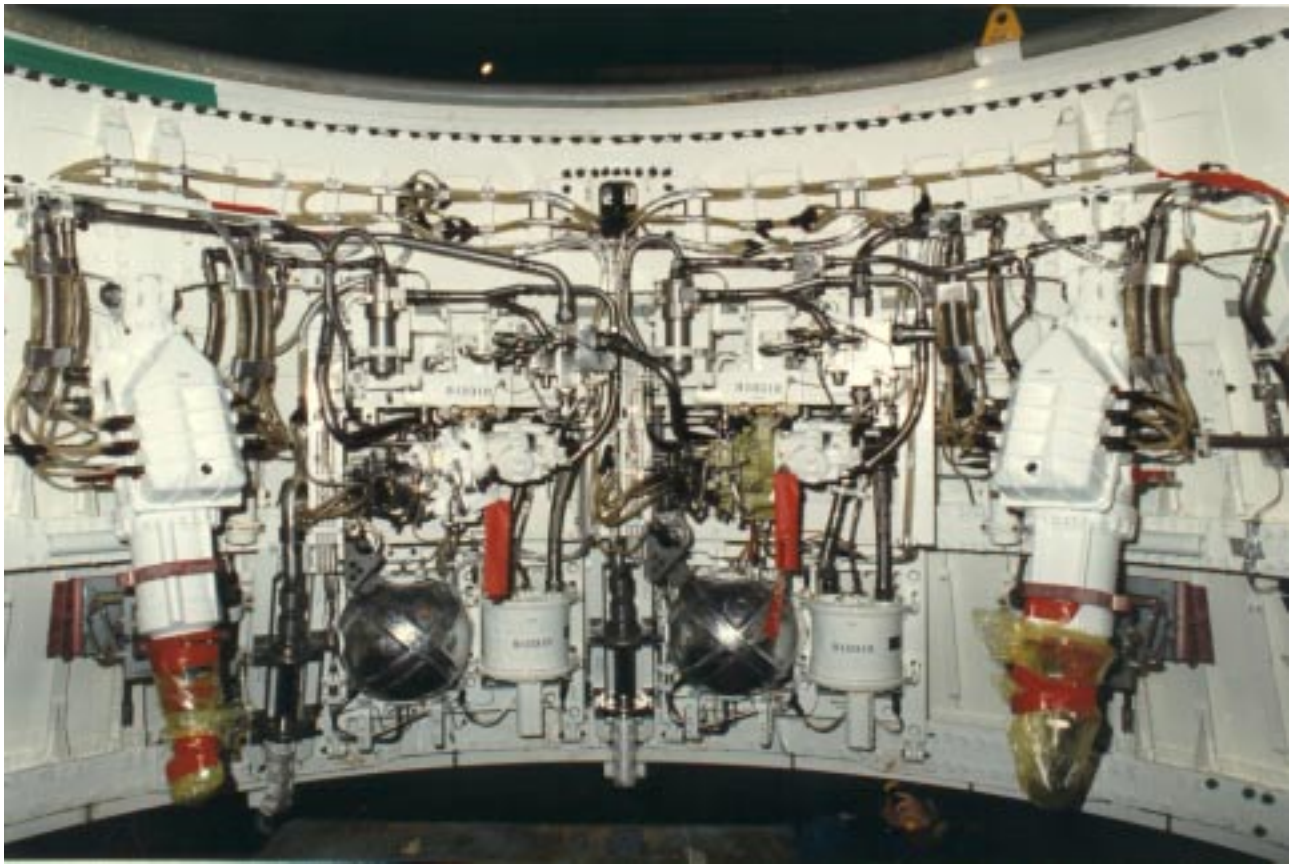

Figure 3. SRB Aft Skirt Location of TVC System

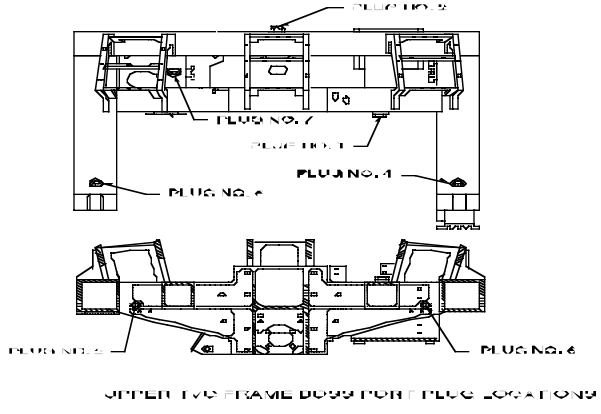

Figure 4. Sectional View of Upper TVC Frame

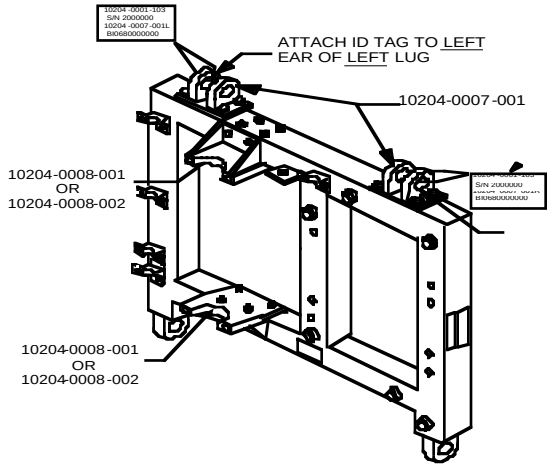

Figure 5. Construction of Lower TVC Frame

DISCUSSION

LVCI Evaluation

The first phase of this program involved the selection and screening of environmentally compatible, non-flammable LVCIs. CORTEC Corporation produces an excellent selection of LVCIs, and two were initially selected for evaluation. Of these two, one product (LVCI 377) evaluated for environmental compatibility, stability, flammability and
corrosion protection of 2219 Aluminum Alloy was selected. A non-flight TVC Frame was sectioned and used as an environmental chamber for placing 2219 -T87 Aluminum Alloy LVCI treated test coupons at the NASA KSC Beach Exposure Corrosion Site. Figure 6 shows the diluted (1 Part LVCI to 1 Part Water) LVCI used to treat the bare aluminum test coupons. Figure 7 shows the sectioned TVC Frame with coupons installed.

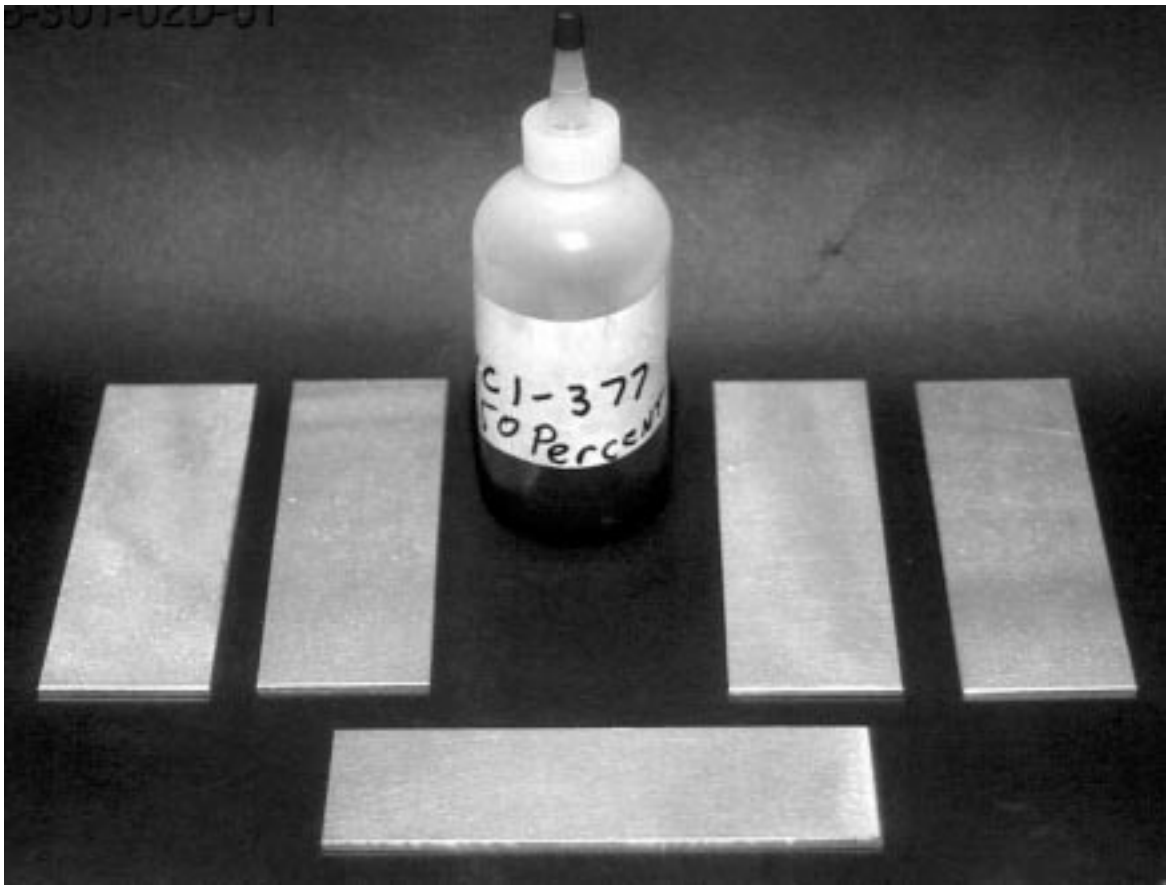

Figure 6. LVCI With Aluminum Test Coupons

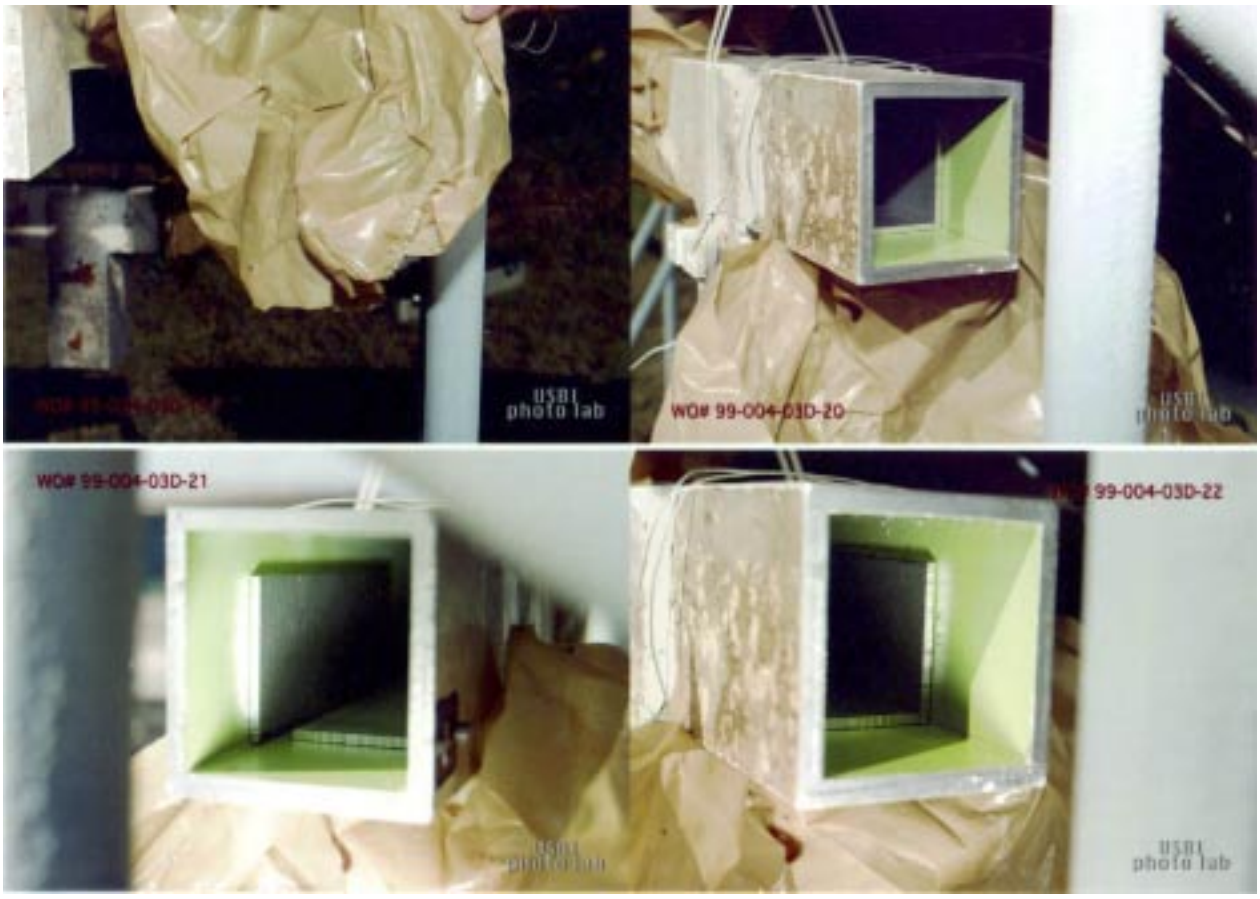

Figure 7. TVC Frames With Test Coupons at KSC Beach Exposure Corrosion Site

Sectioned TVC Frames and inserted test coupons were set on racks, approximately 100 meters from high tide line , and facing the Atlantic ocean. The salt fog and corrosive acidic condensates from the SRB plumes make the exposure site one of the most corrosive environments in the world. Periodic inspection and digital photos were made as part of the LVCI evaluation.

The MNRC has a TRIGA Reactor that produces sufficient thermal neutrons and complementary robotic work cells that allows for corrosion evaluation and accurate positioning of critical fighter and cargo aircraft parts. USA LLC was able to contract with MNRC to evaluate internal corrosion of Non-Flight SRB TVC Frames, and hopefully establish capability for potential future evaluation of SRB flight hardware. Two (2) Upper, and two (2) Lower TVC non-flight frames were used for Neutron Radiography (N-Ray) corrosion evaluation. Initial N-Ray Baselining was performed on untreated frames. The TVC frame cavities were then flushed with Grade A (Deionized) water, emptied, and then filled with LVCI. The LVCI was allowed to penetrate for one hour, with rotation of the frame to guarantee LVCI coverage. The LVCI was then pumped/vacuumed from the cavities, and Boss Port Plugs installed. Another series of N-Radiographs were made after the initial LVCI application. Subsequent N-Ray evaluations were made after 3 months, and then after 8 months exposure to the LVCI. MNRC was able to produce N-Radiographs using Film and also real-time with recordings on Video Tape. Figure 8 shows some typical work being done at the MNRC.

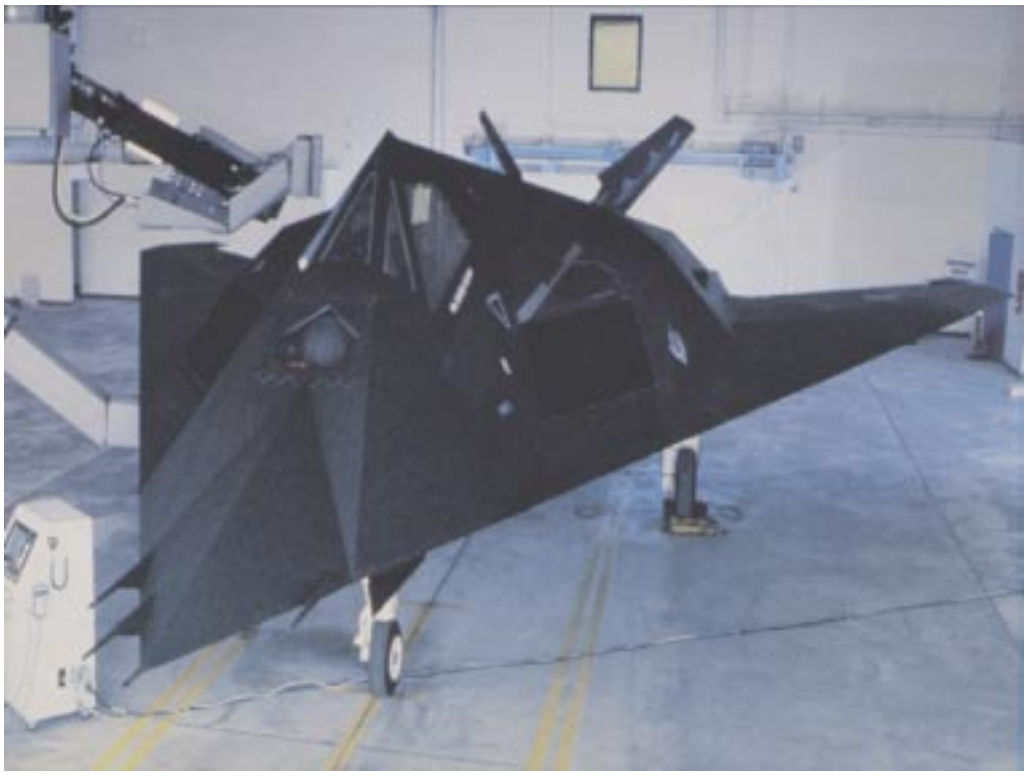

Figure 8. Radiographic Facility at McClellan Nuclear Radiation Facility

Test Results

NASA KSC Beach Exposure Corrosion Site evaluations and documentation were made on a regular basis. TVC frames were loosely covered with a secured plastic wrap, and allowed to remain exposed for almost a year. There was virtually no corrosion on the test coupons treated with the LVCI, One TVC frame exposed to hurricane force winds after 10 months exposure lost its plastic cover, and with internal test coupons sand blasted; experienced premature corrosion immediately after. Figure 9 shows typical surface conditions of aluminum test coupons after 7 months beach exposure. It should be noted that the slight brown color intermittently seen on the test coupon's surfaces, are trace amounts of LVCI that dried to a somewhat greater film thickness. Essentially, the test coupons were corrosion free. In many cases during evaluation of the LVCI effectiveness, residual water was found inside the TVC frame cavities, with no effect on corrosion of the test coupons. It would be very difficult to duplicate the environmental exposure given to the test coupons at the NASA KSC Beach Exposure Corrosion Site. Testing was also performed using ASTM B 117 (1) Neutral Salt Fog testing procedure as well as Temperature-Humidity cycling in an environmental test chamber. None of these tests revealed the true capability of the CORTEC LVCI 377, as did the NASA KSC Beach Exposure Corrosion Site evaluations.

MNRC personnel were able to produce an excellent series of Neutron Radiographs with Type SR Film, Screen, Gd and also with Real-Time imaging captured on Video Tape. Although Real-time Radiography was less sensitive than the Film Type, it was found to be adequate for locating internal TVC Frame corrosion sites. A combination of Real-Time and Film Radiography techniques would prove to be an economical combination. Initial Baseline N-Rays of the 4 frames allowed for comparison before and after LVCI application, and then after 3 month and 8 month exposures. It was interesting to note that the LVCI acted as an amplifier of corrosion in crevices that were not visible before application of the LVCI, and during N-Ray interrogation. Figures 10 and 11 show N-Rays of Upper and Lower TVC Frames.

Figure 9. Aluminum Test Coupons after 7 Months Beach Exposure

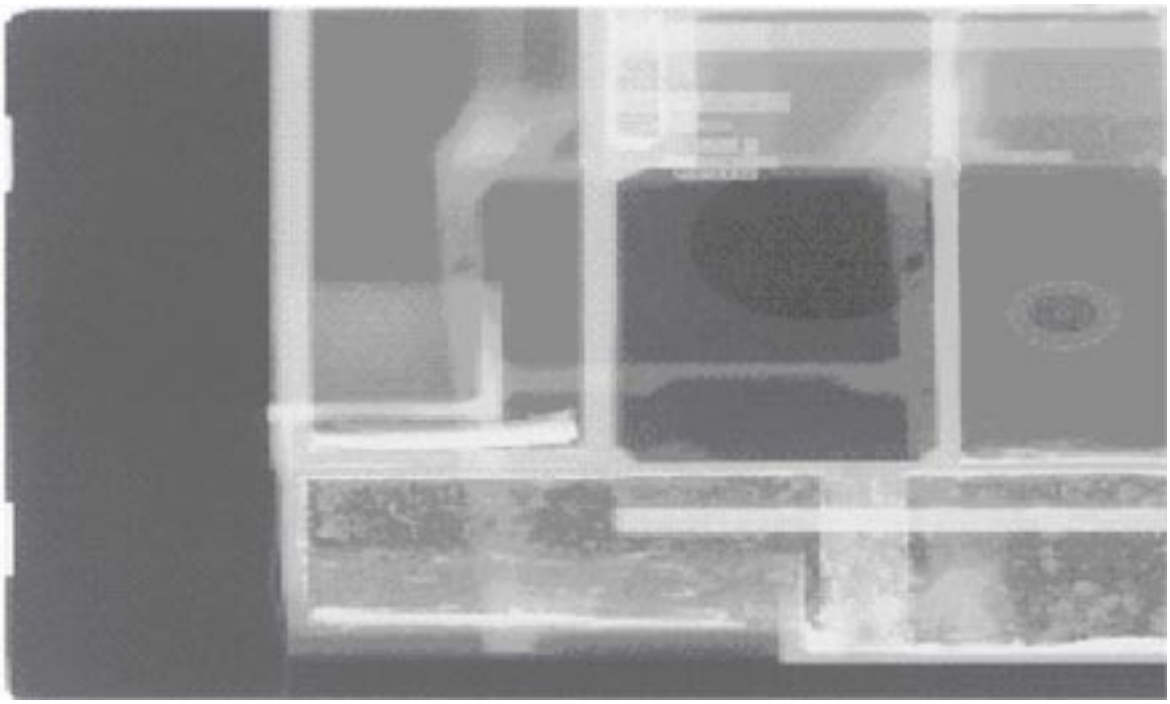

Figure 10. Neutron Radiograph (Film) of Upper TVC Frame

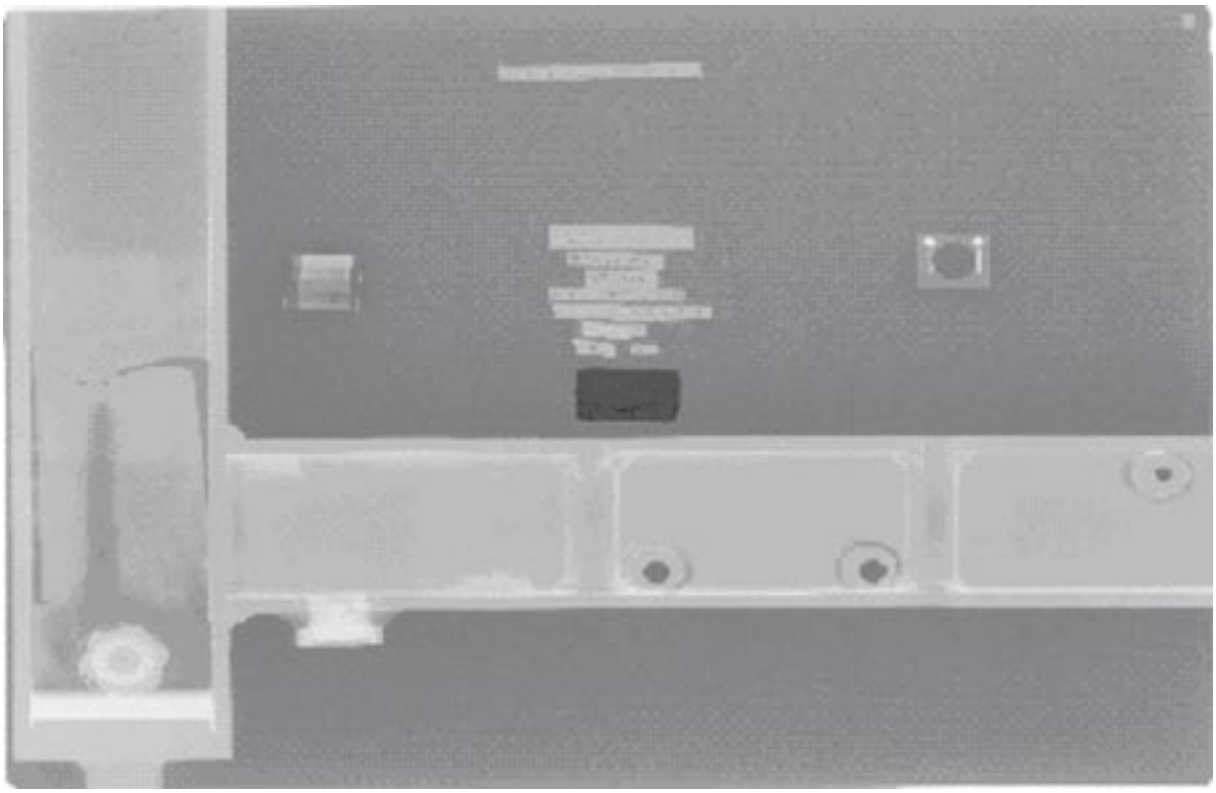

Figure 11. Neutron Radiograph (Film) of Lower TVC Frame

CONCLUSION

Testing and evaluation of an environmentally compatible LVCI was successfully accomplished as a team representing MSFC Non-destructive Evaluation and Tribology Branch, KSC Corrosion Engineering Branch, U.C. Davis/MNRC Nuclear Radiation Division, CORTEC Corporation, and USA Materials & Processes Engineering, Refurbishment Engineering, and Refurbishment Operations departments. It was found that cooperation from all of the team members was exceptional throughout the project. Testing at the KSC Beach Exposure Corrosion Site, revealed the excellent stability of LVCI-377 in one of the worlds most corrosive seacoast environments. Corrosion protection of the bare 2219 aluminum alloy test coupons remained excellent throughout the 1 year exposure period. Neutron radiography performed at the MNRC facility, showed excellent compatibility of the
LVCI with internal TVC Frame cavity materials, consisting of an epoxy polyamide primer and 2219 aluminum alloy welded structures. The use of N-Ray with real-time and film processes, showed internal corroded areas of TVC Frames not found with borescopic inspection, and was performed in a very efficient manner. USA Florida Operations are presently developing the documents necessary for implementing the environmentally compatible and effective LVCI on SRB TVC Frames.

ACKNOWLEDGMENTS

The authors would like to thank the various USA Departments both in Huntsville, Alabama and Kennedy Space Center, Florida for supporting and assisting in program management, production operations, logistics and testing. Many thanks to NASA Marshall Space Flight Center Materials and Processes Laboratory Departments, NASA Kennedy Space Center Corrosion Engineering Laboratory, U. C. Davis/McClellan Nuclear Radiation Center –Nuclear Radiation Division personnel who were all supportive of this program. Additional thanks are given to the CORTEC Corporation management, scientists, engineers, and marketing groups that helped make this program a success.

REFERENCES

(1). Annual Book of ASTM Standards, Vol. 03.02, “Wear and Erosion; Metal Corrosion”, ASTM, Philadelphia, PA 1997. (ASTM B 117)

Evaluation of EL-Form Rhenium for Zero Erosion Materials

RICHARD FOEDINGER
DE Technologies
3620 Horizon Drive
King of Prussia, PA 19406
Phone: 610-270-9700, ext. 125
Fax: 610-270-9733
E-mail: rfoedinger@detk.com

Jeffrey Price and Richard Lanam
DE Technologies
3620 Horizon Drive
King of Prussia, PA 19406
Phone: 610-270-9700
Fax: 610-270-9733

High-performance solid rocket motors (SRMs) for hypervelocity missile systems utilize reduced smoke propellants that have very high burning rates to deliver very short burn times (< 1 sec) at high pressures (3000 to 5000 psia). In addition, they must be energetic and deliver high specific impulse and thrust; thus, flame temperatures exceed 5000 °F. These high flame temperatures in conjunction with high operating pressures with relatively small nozzle throat diameters (1 to 2 in.) and high mass flow rates lead to unacceptable nozzle throat erosion rates, which, in turn, adversely affect motor-delivered performance and, therefore, missile system performance. Current SRM nozzle materials can experience significant throat erosion under these environments, resulting in lower delivered thrust and impulse levels.

Initial testing performed under a Phase II Small Business Innovation Research Program has demonstrated the performance of an electroformed (EL-Form) rhenium nozzle liner that offers zero erosion in a high burn rate, high-pressure and -temperature environment. Further development and follow-on tests are underway to evaluate El-Form rhenium-coated graphite throat inserts. The results of the nozzle insert design development, analysis, and testing will be discussed.

5th Aerospace Materials, Processes and Environmental Technology Conference
September 16–18, 2002, Von Braun Center, Huntsville, Alabama

Syntactic Metals: A Survey of Current Technology

Ray Erikson*
Flight Materials Group, 2 Collins Road, Wakefield MA 01880
Tel: 781-246-8239 Email: ray.erikson@flightmaterials.com

Syntactic metals are a relatively new development in materials science. Several approaches to synthesizing these materials have been tried, and the handful of researchers in this field are beginning to make progress in defining useful compositions and processes. Syntactic metals can provide materials with dramatically improved specific strength and stiffness over their parent alloys, while retaining the isotropy that makes ordinary metals preferable to fiber-reinforced laminated composites in many applications. This paper reviews syntactic material concepts in general, the current state of the art (including the author's own work in syntactic aluminum), and the direction of future developments.

Introduction

Syntactic metals are relative newcomers to the world of aerospace materials, and a lot remains to be learned about them. The huge variety of component materials available, the complexities and subtleties of processing, and the tremendous performance potential, have intrigued many investigators. The performance potential stems from the following figures of merit for specific strength and stiffness:

$$\frac{S}{\rho} \text{ and } \frac{E}{\rho} \text{ for strong, stiff tensile members}$$

$$\frac{S^{2/3}}{\rho} \text{ and } \frac{E^{1/2}}{\rho} \text{ for beams, shafts, columns}$$

$$\frac{S^{1/2}}{\rho} \text{ and } \frac{E^{1/3}}{\rho} \text{ for plates and shells}$$

where S is strength, E is modulus, and ρ is mass density. The specific strength and stiffness of a structure goes up much more quickly with decreasing density than with increasing strength or modulus — that is why we build more flight vehicles from aluminum than steel.

The earliest work in this area was presented in 1984 by Keshavaram et al at a conference in India. He and his colleagues investigated the behavior of some flyash- and glass-microsphere reinforced aluminum composites [13].

In 1989, Rickles, working under Cochran at the Georgia Institute of Technology, used hollow aluminum oxide spheres in his Master's Thesis on their experiments with what they called "Metal/Ceramic Syntactic Foam" [27]. Cochran has since focused on producing metallic spheres of nickel, titanium and stainless steel sintered together to form ultralight ($\rho < 1.0\,\mathrm{g/cm^3}$) all-metal syntactic foams with no matrix material [5, 6].

A team led by Rawal at Lockheed Martin Astronautics in Denver, Colorado, investigated what they also called "syntactic metal foams." From the late 1980's to the mid 1990's they produced several experimental material systems using hollow aluminum oxide spheres in A201 and A356 aluminum, and in Ti6Al4V titanium matrices [22, 23, 24, 25].

Using a pressure casting system very similar to the one developed by Blucher at Northeastern [4], Rawal made sandwich panels

*Principal Engineer.

with titanium facesheets and Hollow Ceramic Microsphere/Aluminum (HCM/Al) composite cores, where the titanium provided the preform in the pressure casting process. They also made some stand-alone plates of HCM/Ti composite, and investigated the reactions at the interface between the aluminum oxide spheres and the titanium matrix.

Rawal and his colleagues noted that as the mean microsphere diameter was decreased from 2300 microns to 60 microns the compressive strength of their A201 matrix composite increased from 30 to 65 ksi. Because the smaller spheres had proportionately thicker shells, the density also increased from 1.96 to 2.90 g/cc, but this still resulted in a net increase in specific strength over the parent alloy.

In 1993, Rohatgi patented a slurry method of forming metal matrix composites using flyash (mixed silica, alumina, iron and titanium oxides), glass or ceramic microspheres [26].

In 1996, Kampe of Virginia Tech conducted investigations of flyash-reinforced aluminum and titanium in association with University Partners, Inc. and Oak Ridge National Laboratory [12]. Additional studies of flyash composites have been made by investigators in Australia and India [18, 30, 13, 28, 29].

Since 1995, researchers at the University of California at Santa Barbara have used aluminum oxide spheres with A201 and A360 aluminum matrices in a series of detailed studies correlating measured properties with those predicted by a finite element model [14, 15]. This work has used relatively large spheres with mean diameters of 1.0, 1.5 and 2.5 mm, with corresponding relative wall thickness aspect ratios (t/R) of 0.5, 0.3 and 0.1, respectively.

The finite element models used by the UCSB researchers predicted significant increases in both strength and modulus compared to the unmodified matrix materials. Experimental results have been mixed; while some syntactic samples have displayed higher moduli and yield strengths up to three times as high as the corresponding neat alloy, other samples have failed at lower relative values. This has been attributed to residual thermal stresses developed in the spheres themselves during cooling, resulting in sphere cracking, especially in the larger, thinner spheres.

In 1998 and 1999 at Northeastern, Blucher and the author, using experience gained with polymer-matrix syntactics on a military aircraft program, began a study of aluminum matrix syntactics [7, 8]. Hollow alumina, mullite, glass and flyash microspheres ranging in size from 10 to 3000 microns were used in 413 (eutectic Al-Si), 1100, 2024 and pure aluminum.

The same phenomena as that described by the UCSB researchers were observed with larger ($>$ 1000 micron) alumina spheres, but significantly different behavior was seen in smaller spheres of different compositions. The smaller spheres ($<$ 200 micron) were much more stable against local failure, even with aspect ratios comparable to the larger spheres.

This work confirmed what had been observed by earlier workers in flyash; i.e., that reactions between the microspheres and the matrix, regarded as a nuisance by some researchers, appear to induce very useful bonding mechanisms for maintaining the integrity of the composite under loading.

In 1999, Cochran, Sanders, Nadler and others [20] began working with nickel and steel spheres in aluminum matrices — an approach that can obviously be extended to all sorts of useful alloy combinations.

Around that same time, PowderMet in Sun Valley, California, began developing metallic syntactics for aerospace applications by coating ceramic spheres with metals and sintering them together to produce materials with a wide variety of compositions and densities.

Composition

Alloys used so far in syntactic metals include pure aluminum, nickel and titanium; 201, 356, 360, 413, 1100, 2024 and 6061 aluminum; 405

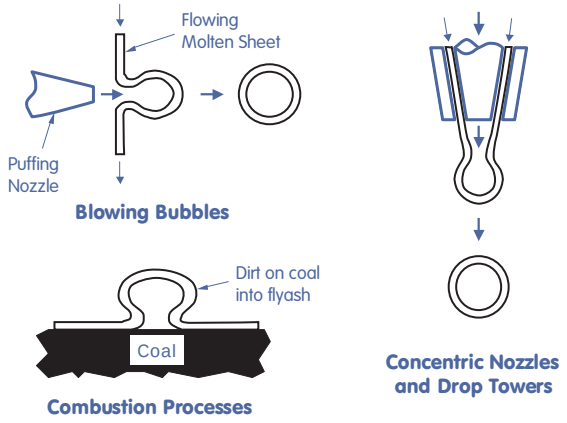

Figure 1: Methods of producing microspheres.

stainless steel and 6-4 titanium. PowderMet is also experimenting with molybdenum and rhenium alloys.

Microspheres can have many different compositions and are produced by several different methods, which include (1) using a puffing nozzle to blow bubbles from a flowing molten sheet of material; (2) using a concentric nozzle and a drop tower; (3) using the flyash produced by contaminants on coal; and (4) sol-gel methods. The first three are shown in Figure 1.

The microspheres investigated by the author in his own work encompass most of the spheres used by others. These include mullite spheres from Keith Ceramics in England; 14/40 and 36/F "Duralum AB" alumina spheres from Washington Mills in North Grafton, Massachusetts; "Aerospheres" (alumina) from Georgia Institute of Technology in Atlanta, Georgia; LV01, TV09 and AP05 "Recyclospheres" (flyash) from Sphere Services in Oak Ridge, Tennessee; SLG and SL-150 "Extendospheres" (flyash) from PQ Corporation and 110P8 "Sphericels" (borosilicate glass) from Potters Industries, both in Valley Forge, PA.

Sphere Price and Availability

Over fifty manufacturers of microspheres and ceramic products were contacted to define the price and availability of hollow ceramic microspheres. Price ranged from \$1.50/lb for flyash-derived spheres to \$4.00/lb for glass spheres to "very expensive" for the pure aluminum oxide spheres from Georgia Tech. Flyash and glass spheres are readily available; other types have lead times of weeks to months. Key findings:

- The smallest hollow ceramic microspheres currently available are 3M G-200 "Zeeospheres" with a mean diameter of 4.4 microns; however, with a density of 2.5 g/cc, they are not the best candidates for composites of aluminum and titanium. The smallest hollow microspheres with a true density under 1.0 g/cc are the Potters Industries 110P8 Sphericels with a mean diameter of 10 microns.

- There are currently only two sources of pure aluminum oxide hollow microspheres: Washington Mills and Georgia Tech. The Washington Mills spheres are small ($\sim$100 μm), cheap (\$1.00/lb) and readily available, but very rough and very porous, requiring a good deal of preprocessing, such as buoyant separation, before use. The Georgia Tech spheres are of excellent quality for composite use.

Sphere Density

Density measurement is a critical part of the production of lightweight materials. Measuring the density of microspheres is not as simple as it might seem, since in bulk the material behaves like neither solid nor liquid, but somewhere in between.

Bulk and tap density are readily determined with a graduated cylinder and a scale, although special standardized density testers (that apply standard tapping to the cylinder) have, of course, been developed. The true particle density of the spheres is more challenging. Devices called *pycnometers* have been developed to automate the process using liquids or gases to provide displacement information. Table 1 compares experimental values obtained by the author with vendor data sheet values.

Table 1: Experimental densities (g/cc) versus supplier specifications.

Supplier	Grade		Spec.	Meas.
PQ Corp.	SLG	Bulk	0.40	0.41
		True	0.72	0.60
Washington Mills	4/10	Bulk	0.60	0.48
		True	—	0.89
	10/20	Bulk	0.65	0.59
		True	—	1.19
Sphere Services	AP05	Bulk	0.37	0.32
		True	0.64	0.51
	TV09	Bulk	0.36	0.33
		True	0.54	0.52

True density can be used to complete morphological studies. While much information can be gathered by studying the exterior of the spheres with a microscope, direct determination of shell thickness depends upon observation of fractured spheres. With true density information, the mean shell thickness may be estimated from a relation developed by the author in previous work [7] as follows:

$$t = \frac{d}{2}\left\{1 - \left[1 - \left(\frac{\rho_t}{\rho_s}\right)\left(\frac{6a^3}{\pi N_u}\right)\right]^{1/3}\right\} \quad (1)$$

where d is the mean diameter, ρ_t is the true density, ρ_s is the shell material density, a is an empirical constant related to sphere packing efficiency with a typical value around 1.07, and N_u is another empirical constant with a typical value around 1.45. The shell thickness may then be used to calculate the sphere strength, though the details of that process are far beyond the scope of this paper.

Table 2: Composition of typical flyash-derived ceramic microballoons (%).

Component	PQ-SLG	SS-AP05	SS-TV09
SiO_2	59.0	60.0	54.5
Al_2O_3	38.0	31.8	36.1
Fe_2O_3	0.5	4.3	5.6
TiO_2	1.7	1.3	1.3
Other	0.8	2.6	2.5

Chemistry

Chemical analysis can be performed using acids to dissolve the spheres so that they may be treated with reagents in solution using "wet" chemistry methods. Alternatively, the spheres may be ground into fine powders and atomized into plasma streams for atomic emission (AE) spectroscopy. For microspheres that contain silicon, these techniques can be unreliable, because of secondary reactions that occur during processing.

The most reliable chemical analysis methods for powdered substances are x-ray diffraction, x-ray spectroscopy, auger electron spectroscopy, x-ray photoelectron spectroscopy, and ion-scattering spectroscopy [16]. Vendor specifications for PQ and Sphere Services products are listed in Table 2.

Processes

Processing Microspheres

Given a source of stock microspheres, it may still be necessary to separate spheres from a given batch by size, weight, and/or porosity. Several methods of separating desired spheres from undesired spheres were investigated during the course of this research.

Screening is a familiar process: increasingly fine wire meshes sort small particles from big

ones. Standard sieve sizes were first established in 1910. In 1970 the American Society for Testing Materials (ASTM) joined with the International Standards Organization (ISO) to define international sieve standards ASTM E11 and ISO 565. Although straightforward, conventional screening is limited to about the 400 mesh level (37 microns). At that size, the bulk powder has the consistency of baking flour. Finer particle resolution requires use of fluid filtering techniques, but even these become ineffective for particle sizes below about one micron.

Some commercial separators use a combination of mechanically-induced vibration screening and airflow. These are known as gravity separators, which are widely used in the agriculture and food processing industries for separating seeds and grains.

The author has used buoyant separation to obtain useful microspheres from raw stock. In any given batch of commercial microspheres, many will be broken or have wall thicknesses that make them nearly solid. Buoyant separation can be effective at eliminating both broken and excessively thick microspheres from a batch. The biggest obstacle to its use is microsphere density, since even relatively light spheres can have a true density approaching that of water. A variety of liquids were subjected to experiment.

Since the sphere shell material will be heavier than any common liquid, broken spheres and loose shards should, in theory, sink to the bottom. In practice, surface tension can skew the results. Spheres with small holes or cracks may float because the liquid surface tension prevents flow into the sphere. The smaller the sphere size, the greater the impact of surface tension. This problem can be ameliorated to some extent by the addition of surfactants.

Making Composites

The combination of spheres and matrix materials has been one of the main impediments to progress in this field. Blucher, Rawal and the author have used pressure infiltration. This method is tried and true in the laboratory fabrication of metal matrix composites, but it is not a method that lends itself to widespread commercial application.

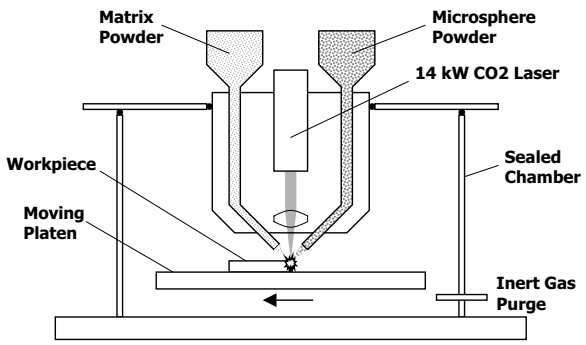

Figure 2: Direct laser sintering approach to syntactic metal development.

Slurry mixing makes use of the fact that the viscosity of a fluid increases with the addition of small particles. Some researchers have found that simply mixing the microspheres into a melt increases the viscosity of the melt enough to get a reasonably uniform sphere distribution.

Conventional powder metallurgy methods involving compaction for sintering have also been tried, but the fragility of individual hollow ceramic spheres does not lend itself to these processes readily. PowderMet has sidestepped the problem by coating the spheres with metal first, then sintering the *coatings* together.

Some new methods of fabrication may be derived from rapid prototyping techniques, such as Selective Laser Sintering (SLS) by DTM/3D Systems; RapidSteel from DTM Corporation; or LasForm by AeroMet. A notional diagram of this approach is shown in Figure 2.

Structure

Microsphere Structure

General particle structure can be determined with a low magnification light microscope or a scanning electron microscope (SEM). Several microsphere types have been examined by

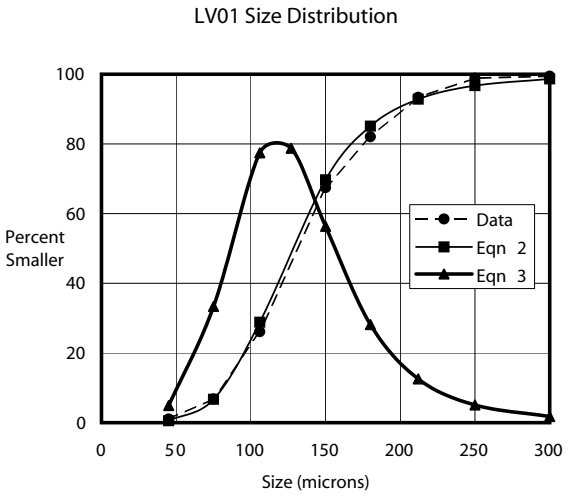

Figure 3: Size distribution curves for Sphere Services TV09 microballoons.

the author under both optical and electron microscopes. In shape, all microspheres examined are reasonably spheroidal. Surface texture ranges from relatively rough and irregular on the Washington Mills spheres to glassy on the PQ Sphere Services products. The Washington Mills aluminum oxide spheres and the mullite spheres from Keith Ceramics were also much more porous than the others.

Size and size distribution may be determined from vendor data, image analysis or screening. Distributions for one of the Sphere Services products, based on particles retained in a standard sieve series, are shown in Figure 3, where a cumulative distribution function has been fitted using the sigmoidal relation

$$F(x) = 100 - \frac{100}{1 + \left(\frac{x}{x_{\overline{F}}}\right)^{H}} \qquad (2)$$

where x is a particle size, $x_{\overline{F}}$ is the estimated mean particle size, and H is a curve shape factor. Given the cumulative distribution, the frequency distribution may be found from

$$f(x) = \frac{dF}{dx} = \frac{8000\left(\frac{H}{x_{\overline{F}}}\right)\left(\frac{x}{x_{\overline{F}}}\right)^{H-1}}{1 + 2\left(\frac{x}{x_{\overline{F}}}\right)^{H} + \left(\frac{x}{x_{\overline{F}}}\right)^{2H}} \qquad (3)$$

Size distribution may also be determined by screening, sedimentation, light scattering methods, electrozone size analysis, optical sensing zone analysis, and Fisher sub-sieve size analysis. All of these techniques have been commercialized into off-the-shelf lab equipment for batch analysis.

Composite Structure

A syntactic metal may be two-phase or three-phase. Two-phase syntactics can consist of metal or ceramic microspheres and the matrix metal (see Figure 4); or they can be comprised of metal microspheres sintered together, and the space between them. Three-phase syntactics consist of ceramic microspheres, metal coatings and the menisci they form, and the space between them.

A single sphere size can produce a density reduction of about 50 percent in a fully-infiltrated two-phase syntactic. By using multimodal size distributions to fill the interstices, density can theoretically be reduced to any desired level, though 20 percent that of the parent alloy is probably the near-term practical limit.

For producing a smooth skin on finished parts to improve strength and endurance, facesheets may be applied to form a conventional sandwich. On more complex geometries, various deposition techniques such as electroforming, flame spraying, etc. may be employed to form a "3-D sandwich."

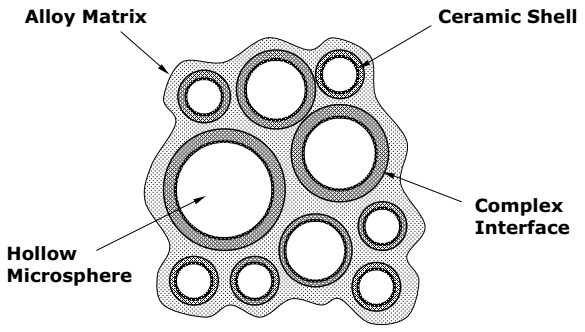

Figure 4: Cross-section of fully-infiltrated two-phase syntactic.

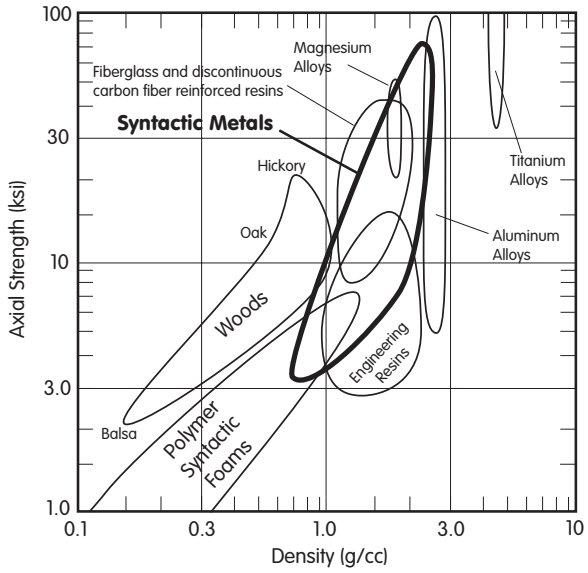

Figure 5: Ashby diagram showing ranges of strength and density achieved to-date in syntactic metals.

Properties

As with any composite, each property of a syntactic metal follows some form of mixture rule, though these rules tend to be somewhat more complicated than the usual partition by volume fraction. This is due to the tremendous range of interaction possible between the spheres and the matrix in denser systems, and the micromechanical behavior of the spheres themselves in lighter systems. The ranges of strength and density achieved by various workers so far are outlined in the Ashby diagram of Figure 5.

Modulus tends to decrease with decreasing density, but not necessarily linearly. The author has measured a modulus of 7.0 Msi in syntactic aluminum with a density of 1.69 g/cc, and it should be possible to tune composite modulus to some extent by appropriate selection of microsphere characteristics and volume fraction.

Other properties, such as thermal strain rate and thermal conductivity have yet to be investigated fully, but the combination of ceramic and metals suggests they may have excellent stability for cryogenic optics. Refractory alloys such as molybdenum and rhenium become more appealing for propulsion and electronics applications at lower densities. Syntactic metals may also provide a path to improved radiation shielding.

Although specific strength improves simply by reducing density, more may be possible by using the microspheres for dispersion hardening. Second phase hardening is derived from the line-tension model as

$$\frac{F}{L} = \frac{T}{R} = \frac{\alpha G b^2}{R} \tag{4}$$

where F is the force on an individual obstacle (particle), L is the distance between particles, T is the line tension in the dislocation encountering the obstacles, R is the radius of the bow produced in the dislocation, α is a constant (≈ 1), G is the shear modulus, and b is the Burgers vector. Orowan and Ashby have described this effect in terms of shear stress as

$$\tau_{sp} = \frac{0.8Gb}{2\pi L\sqrt{1-\nu}} \ln\left(\frac{2r}{r_o}\right) \tag{5}$$

where r is the size of the particle and r_o is the inner cutoff radius ($\approx b = a/2$, where a is the lattice constant). The Orowan-Ashby relation suggests that with small enough hollow microspheres (on the order of Buckyballs), syntactic metals could be up to three times as strong, as well as half as heavy, as current alloys.

Even with only modest reductions in microsphere size, other strengthening effects can make themselves apparent. For instance, Unsworth and Bandyopadhyay [34] explored the effect of 10–100 μm solid microspheres on dislocation and precipitate formation in the parent alloy. A mean strength gain of 31% was obtained in these composites relative to conventional 6061-T6 aluminum. They theorized that the observed strength increase was due to the following set of phenomena:

- Since ceramic microspheres have much smaller thermal strain rates than the aluminum, significant residual stresses develop in the matrix during cooling.
- These residual stresses increase the dislocation density in the matrix.

- The increased dislocation density facilitates the formation of larger numbers of Guinier-Preston zones and precipitates during subsequent heat treatment.

- The additional G-P zones and precipitates provide additional obstacles to dislocation motion during deformation.

Rawal and his colleagues also noted that as the mean microsphere diameter was decreased from 2300 microns to 60 microns the compressive strength of their A201 matrix composite increased from 30 to 65 ksi; i.e., more than doubled. Because the smaller spheres had proportionately thicker shells, the material density also increased from 1.96 to 2.90 g/cc, but a net increase in specific strength over the virgin A201 was still achieved.

Conclusions

Syntactic metals are a new class of metal matrix composites. They can achieve better specific strength and stiffness in particular applications than current alloys simply by lowering material densities. They have the same potential for increased absolute strength as dispersion-strengthened alloys. With sufficient development of component materials and synthesis processes, syntactic approaches should be able to make light alloys significantly lighter, and heavier alloys more palatable, in flight structural, propulsion, optical, thermal control and shielding applications.

References

[1] Ashby, M.F. (1999). *Materials Selection in Mechanical Design, 2nd Edition.* Boston: Butterworth-Heinemann.

[2] Ashby, M.F. et al. (2000). *Metal Foams: A Design Guide.* Boston: Butterworth-Heinemann.

[3] Bardella, L. & G. Francesco. (2001). On the elastic behavior of syntactic foams. *International Journal of Solids and Structures*, Vol.38, 7235–7260.

[4] Blucher, J.T. (1992). Liquid metal pressure infiltration to produce metal matrix composites. *Journal of Materials Processing Technology*, 30, 381–390.

[5] Clancy, R.B., Cochran, J.K. & Sanders, T.H. (1995). Fabrication and Properties of Hollow Sphere Nickel Foams. In D.L.Wilcox et al (Eds.), *Hollow and Solid Spheres and Microspheres: Science and Technology Associated With Their Fabrication and Application, MRS Symposium Proceedings, Volume 372.* Pittsburgh: Materials Research Society, 155–163.

[6] Clancy, R.B., Sanders, T.H. & Cochran, J.K. (1991). Fabrication of Thin-Wall Hollow Nickel Spheres and Low Density Syntactic Foams. In E.W.Lee & N.J.Kim (Eds.), *Light-Weight Alloys for Aerospace Applications II.* Pittsburgh: The Minerals, Metals & Materials Society, 477–485.

[7] Erikson, R.J. (1996). Mechanical evaluation of ARC syntactic foams. Nashua NH: Lockheed Martin report P950101-9.

[8] Erikson, R.J. (1999). Syntactic aluminum: Hollow ceramic microsphere reinforced metal matrix composites (Master's Thesis). Boston: Northeastern University.

[9] German, R.M. (1994). *Powder Metallurgy Science, 2nd Edition.* Princeton NJ: Metal Powder Industries Federation.

[10] Gibson, L.J. & Ashby, M.F. (1997). *Cellular Solids, Structure and Properties, 2nd Edition.* New York: Cambridge Univ. Press.

[11] Charles Hendricks. (1986). Method for Producing Solid or Hollow Spherical Particles of Chosen Chemical Composition and Uniform Size. U.S. Patent 4,774,037.

[12] Kampe, S.L. (1996). Composites of metal reinforced by flyash. Virginia Tech VTIP 96.041.

[13] Keshavaram, B. N.; Satyanarayana, K. G.; Majumdar, B.; Rohatgi, P. K.; Dattaguru, B. (1984). Studies on fracture and strength behaviour of Al-glass and Al-flyash particulate composites. *Fracture 84: Proceedings of the 6th International Conference on Fracture (ICF6)*, New Delhi, India. Vol. 4, pp2979–2987. Published by Pergamon Press, New York.

[14] Kiser, M.T., He, M., Wu, B. & Zok, F.W. (1995). Compressive Deformation of Hollow Microsphere Reinforced Metal Matrix Composites. In D.L.Wilcox et al (Eds.), *Hollow and Solid Spheres and Microspheres: Science and Technology Associated With Their Fabrication and Application, MRS Symposium Proceedings, Volume 372*. Pittsburgh PA: Materials Research Society, 173–178.

[15] Kiser, M.T., M. He, & F.W. Zok. (1999). Mechanical response of ceramic microballoon reinforced aluminum matrix composites under compressive loading. *Acta Metallurgica* Vol.47, No.9, 2685–2694.

[16] Klar, E. (Ed.). (1984). *Metals Handbook Volume 7: Powder Metallurgy*. Metals Park OH: American Society for Metals.

[17] Libenson, G. A. ; Lopatin, V. Y. (2001). Investigation of syntactic foam-type porous powder materials. *Conference: PM2TEC 2001: 2001 International Conference on Powder Metallurgy & Particulate Materials, New Orleans, 13–17 May 2001.*

[18] Liu, X.; Nilmani, M. (1996). The effect of particle volume fraction on the mechanical properties of aluminum flyash MMC. *Proceedings of Processing, Properties, and Applications of Cast Metal Matrix Composites, Cincinnati, 7-9 Oct. 1996*. Publisher: Minerals, Metals and Materials Society; Warrendale PA.

[19] Murray, J.L. & McAlister, A.J. (1984). The Al-Si (Aluminum-Silicon) System. *Bulletin of Alloy Phase Diagrams*, 5(1), 74–84.

[20] Nadler, J. H. ; Hurysz, K. M. ; Clark, J. L. ; Cochran, J. K. ; Lee, K. J. ; Sanders, T. H. (1999). Fabrication and microstructure of metal-metal syntactic foams. *Conference: MetFoam 99: International Conference on Metal Foams and Porous Metal Structures, Bremen, Germany, 14–16 June 1999*. pp179–182.

[21] Petzow, G. & Effenberg, G. (1990). *Ternary Alloys, Volume 3: Al-Ar-O to Al-Ca-Zn*. Weinheim, Germany: VCH.

[22] Rawal, S.P. & Misra, M.S. (1989). Development of a Ceramic Microballoon Reinforced Metal Matrix Composite. In 34th SAMPE Symposium on *Tomorrow's Materials: Today*, 122–125.

[23] Lanning, B.R., Rawal, S.P. & Misra, M.S. (1989). Interface Structure of a Cast Alumina Microballoon Reinforced Titanium Composite. In Gungor, Lavernia & Fishman (Eds.), *Proceedings of the Advanced Metal Matrix Composites for Elevated Temperature Conference*, 79–84.

[24] Rawal, S.P., Lanning, B.R. & Misra, M.S. (1992). Effect of Reinforcement Size and Distribution on Mechanical Properties of Microballoon Reinforced Metal Matrix Composites. Presented at *Aeromat '92*, Anaheim CA.

[25] Rawal, S.P., Lanning, B.R. & Misra, M.S. (1995). Processing and Mechanical Properties of Ti//(Alumina)mb/Al Core//Ti Sandwich Panels. In D.L.Wilcox et al (Eds.), *Hollow and Solid Spheres and Microspheres: Science and Technology Associated With Their Fabrication and Application, MRS Symposium Proceedings, Volume 372*. Pittsburgh PA: Materials Research Society, 269–275.

[26] Rohatgi, P. K. (1993). *Synthesis of Metal Matrix Composites Containing Flyash, Graphite, Glass, Ceramics or Other Metals*. U.S. Patent 5,228,494.

[27] Rickles, S.A. (1989). Microstructural and Compressive Properties of a Metal/ Ceramic Syntactic Foam. (M.S. Thesis). Atlanta: Georgia Institute of Technology.

[28] Satapathy, L.N. (2000). A study on the mechanical, abrasion and microstructural properties of zirconia-flyash material. *Ceramics International*, Vol. 26 (1), 39–45.

[29] Satapathy, L.N. (1998). The physical, thermal and phase identification studies of zirconia-flyash material. *Ceramics International*, Vol. 24 (3), 199–203.

[30] Sharma, S.C. et al. (1989). Fabrication and testing of flyash dispersed Al–Zn–Mg–Cu high strength particulate composites. *Proc. Seminar on Science and Technology of Composites, Adhesives and Sealants , Bangalore, India, 28–30 Sep 1989.*

[31] Sinha, S.H. & Rao, G.N. (1976). Cellular Metal. *NML Technical Journal*, 18, 21–24.

[32] Torobin, L.B. (1981). Method and Apparatus for Producing Hollow Metal Microspheres. U.S.Patent 4,415,512.

[33] Torobin, L.B. (1990). Method for Producing Hollow Microspheres Made From Particle Compositions. U.S. Patent 5,225,123.

[34] Unsworth, J.P. & Bandyopadhyay, S. (1994). Effect of Thermal Aging on Hardness, Tensile and Impact Properties of an Alumina Microsphere-Reinforced Aluminum Metal Matrix Composite. *Journal of Materials Science*, 29, 4645–4650.

[35] Wilcox, D., Liu J. & Look. (1994). Hollow Ceramic Microspheres by Sol-Gel Dehydration With Improved Control Over Size and Morphology. U.S. Patent 5,492,870.

[36] Liu, J. & David Wilcox. (1995). Factors Influencing the Formation of Hollow Ceramic Microspheres. *Journal of Materials Research*, 10, 84–94.

NASA AP2 Integrated Technology Database

DAVID CRAWFORD
International Trade Bridge, Inc.
1308 Research Park Drive
Beavercreek, OH 45432
Phone: 937-431-1990
E-mail: crawfordd@itb-inc.com

The NASA Acquisition Pollution Prevention (AP2) Office has developed a management tool used to identify common pollution prevention (P2) technology needs / opportunities and potential solutions. This database, called the NASA AP2 Integrated Technology Database will be used to integrate P2 needs with known technologies and / or solutions.

One of the key features of this tool is the ability to use the combination of process and hazardous material to search and compare other P2 technology needs identified by the Army, Air Force, and Navy, as well as the Strategic Environmental Research and Development Program (SERDP), the Environmental Security Technology Certification Program (ESTCP), and the National Laboratories. This unique capability provides a means to check for duplication of effort, enhances technology transfer, and provides for potential leveraging of resources through joint efforts in funding solutions or RDT&E. The database also acts as a repository for information such as success stories and potential solutions and a ranking algorithm that will score the need / opportunity based on potential cost impact, ESOH risks, pervasiveness, and compliance burden.

This management tool is becoming recognized for its potential to integrate all NASA P2 Technology needs and opportunities into one central data warehouse. The management tool will aid in identification, documentation, and then justification for expending resources to either solve or mitigate the need / opportunity.

Improving Profits with Materials Optimization in Manufacturing

CHRIS E. NUNEZ
Centor Software Corporation
20 Fairbanks
Irvine, CA 92618
Phone: 949-639-3504
Fax: 949-639-3511
E-mail: cnunez@centor.com

A materials optimization system in a large manufacturing firm can save millions of dollars annually by reducing raw material costs. The system puts a “best practice” process in place that encourages design engineers to optimize product attributes such as part weight, thickness, and material selections. This leads to a higher engineering confidence level with improved product quality and a reduction in overall product weight.

NASA Materials Related Lessons Learned

Danny Garcia
NASA Technical Standards Program Office
ED41/Building 4487
Marshall Space Flight Center, AL 35812
danny.garcia@msfc.nasa.gov

Paul S. Gill
NASA Technical Standards Program Office
ED41/Building 4487
Marshall Space Flight Center, AL 35812
paul.gill@msfc.nasa.gov

William W. Vaughan
University of Huntsville in Alabama
ED41/Building 4487
william.w.vaughan@msfc.nasa.gov

Background

Lessons Learned have been the basis for our accomplishments throughout the ages. They have been passed down from father to son, mother to daughter, teacher to pupil, and older to younger worker. Lessons Learned have also been the basis for the nation's accomplishments for more than 200 years. Both government and industry have long recognized the need to systematically document and utilize the knowledge gained from past experiences in order to avoid the repetition of failures and mishaps.

Through the knowledge captured and recorded in Lessons Learned from more than 80 years of flight in the Earth's atmosphere, NASA's materials researchers are constantly working to develop stronger, lighter, and more durable materials that can withstand the challenges of space. The Agency's talented materials engineers and scientists continue to build on that rich tradition by using the knowledge and wisdom gained from past experiences to create futuristic materials and technologies that will be used in the next generation of advanced spacecraft and satellites that may one day enable mankind to land men on another planet or explore our nearest star. These same materials may also have application here on Earth to make commercial aircraft more economical to build and fly.

With the explosion in technical accomplishments over the last decade, the ability to capture knowledge and have the capability to rapidly communicate this knowledge at lightning speed throughout an organization like NASA has become critical. Use of Lessons Learned is a principal component of an organizational culture committed to continuous improvement.

What are Lessons Learned?

Lessons Learned are the result of experiences with people, nature, and the products of our labors. The experiences may be positive, as in successful tests or missions, or negative, as in a mishap or failure. A Lesson Learned must be significant in that it has a real or assumed impact on operations, valid in that it is technically correct, and applicable in that it addresses a specific design process or decision that mitigates or eliminates the potential for failures, or reinforces a positive result.

The documentation of materials related Lessons Learned is important in order to convey information on usage experiences, test results, safety, and performance. Thus, they are an important and critical resource that can be used by materials engineers, scientists, and technicians to support the design of flight and ground support hardware, facilities, and procedures.

Lessons Learned should communicate only lessons, and should not be used as a replacement for other management information functions like self-assessment, failure investigation and corrective actions systems.

How are Technical Standards and Lessons Learned Related?

As life becomes more complex, more guidance is needed. Technical Standards are the documents that infuse this guidance throughout the social structure. The scope of Technical Standards includes standards, specifications, guidelines, recommended practices, and handbooks. Technical standards are: (1) Systematic collections of proven guidance/methods/requirements (frequently gleaned from Lessons Learned) integrated into recommended practices, (2) Generally based on inputs from many activities combining the expertise of national or even international experts, and (3) The basic tools commonly used as the foundation for the normal design/development process. Technical Standards educate users, simplify information, and conserve experiences. They are the essential tools in the interaction of people with their environment. They enable us to intelligently pass on knowledge and associated Lessons Learned for others to build upon. Technical Standards are a very logical way to communicate Lessons Learned.

The Problem.

The Agency's materials engineers and specialists are constantly trying to improve the formulas of materials and with the "explosion" in technical accomplishments during the last few decades, the ability to rapidly communicate Lessons Learned, and the knowledge gained from them has become critical. This is especially true for activities associated with NASA's advanced Programs and Projects such as the Space Launch Initiative (SLI). The Agency's quest for affordable and routine access to space will require new generations of materials and material technologies, which will in turn enable the development of new reusable launch vehicles and associated spacecraft systems. Expecting the Agency's materials engineers to search through the ever-increasing number and contents of materials lessons learned databases have proven to be less than productive.

A Solution.

The "marriage" of Lessons Learned with current Technical Standards offers the opportunity for significant improvement in our goal to achieve advanced products and the use of current products. The NASA Technical Standards Program through the development and use of its Preferred Technical Standards database available to the Agency's users via the NASA Technical Standards Website (http://standards.nasa.gov) offers the foundation to accomplish this goal. Figure 1 shows the homepage of the NASA Technical Standards Program's Website.

Figure 1. NASA Technical Standards Program Website

The Approach.

All NASA Programs/Projects are based on the application of Technical Standards, whether produced by NASA, other government organizations including DOD, or by non-Government standards developing organizations such as SAE, ASTM, ASME, and so on. These and other Technical Standards have gone through an extensive Agencywide review process pending their adoption/endorsement as NASA Preferred Technical Standards. Given this select database of Preferred Technical Standards, along with the existence of screened materials related lessons learned databases, a productive "marriage" is now readily possible. Figure 2 shows an example of the Document Summary Page with "linked" Lessons Learned.

Figure 2. Document Summary Page with Linked Lessons Learned.

On the surface this "marriage" or linkage appears to be an easily achieved action. However, such is not the case. While the task is readily achievable, it requires the talents of dedicated and experienced engineers who must

also possess the gifts of persistence and meticulous attention to detail. The material involved must be read and interpreted and then correlated. The lessons learned databases that contain specific materials related lessons learned must be related to the NASA's Preferred Technical Standards database which currently has over 1500 entries. The result will be an invaluable database whereby any NASA Preferred Technical Standard related to materials and required for an Agency Program or Project design, development, or operations process will also have identified with it any relevant materials related lesson(s) learned.

Value.

NASA conscientiously investigates, documents, and tracks all of its successes and failures. Yet, all of this effort is meaningless if the Agency fails to incorporate these experiences into our ongoing and future Programs/Projects and their operations. They need a viable mechanism to identify and incorporate Lessons Learned into their design, development, and operations efforts, thus reducing mission risk. The cost of achieving the "marriage" of Lessons Learned and Technical Standards will be modest compared to the significant results that will be achieved. Only one Mission saved, or whose performance is enhanced, will repay the cost of developing this Integrated Technical Standards System many fold.

Gill, Paul S., William W. Vaughan, and Danny Garcia, "Lessons Learned and Technical Standards: A Logical Marriage". ASTM Standardization News, Vol. 29, No.11. November 2001.

END

Colossal Tooling Design:
3D Simulation for Ergonomic Analysis

Steve L. Hunter, Ph.D.
Associate Professor
Forest & Wildlife Research Center
Mississippi State University
NASA MSFC ED42
Human Factors Specialist
shunter@CFR.MsState.edu

Robert E. Thomas, Ph.D.
Associate Professor
Industrial & Systems Engrg. Dept.
Auburn University

Charles Dischinger
NASA
Marshall Space Flight Ctr.
ED42 Lead

Majid Babai
NASA
Marshall Space Flight Ctr.
ED34 Lead

INTRODUCTION

In manufacturing, ergonomics and human factors issues must be considered during the design and utilization phases. These applied human factors concerns include but are not limited to, reach ability, visibility, lift factors, kilocalorie usage, repetitive motion, ventilation, lighting, and many more. When the tool size becomes colossal, say 35 feet or more in diameter and 90 feet or more in length; and the tool weights an estimated 200 tons, these normal human engineering factors become critical to the safety and health of the workers (see Figure 1). Schaub, et al, (1997) stated that preventive health care is one of the basic challenges facing ergonomics.

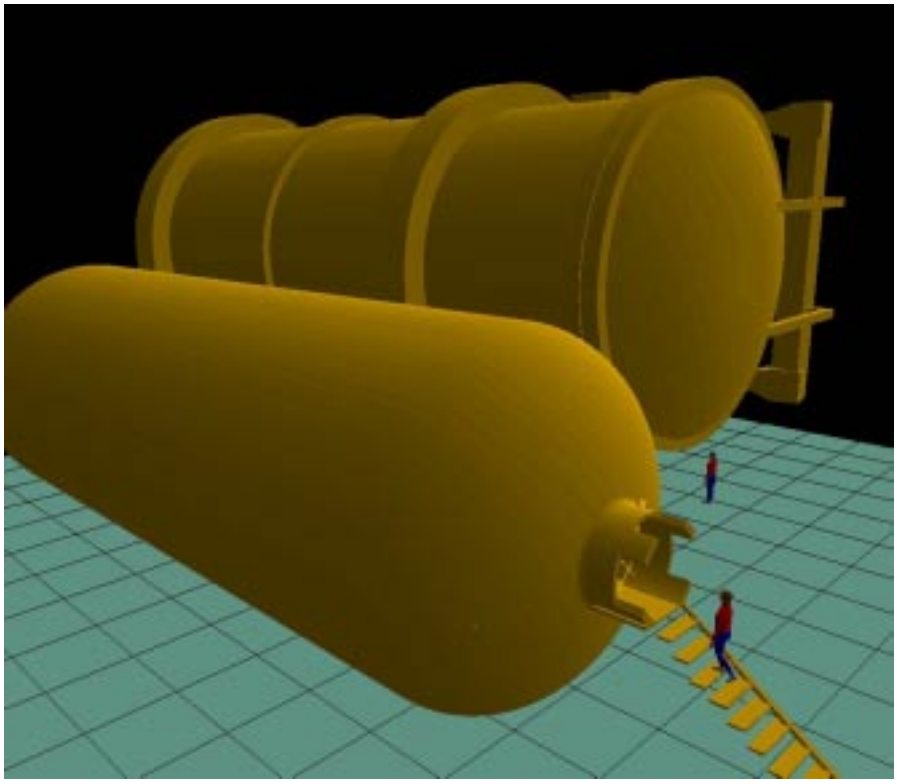

Figure 1: Colossal tooling and autoclave for composite tank lay up and cure.

These colossal mandrel tools will be used for composite lay up for the fabrication of aerospace related fuel tanks. It is no small task to manually disassemble the fully assembled tool that is surrounded by the finished composite shell; especially, when the mandrel tooling is composed of individual segments that may weight up to 2,400 pounds. In addition, the tool segments removal must be completed not only extremely carefully to protect workers carrying out the tool disassembly tanks but also to protect the thin, relatively fragile finished composite shell surrounding the tooling. Diehl et al (1997) relates how 3D simulation was originally developed partly due to the large expense and dangers of designing and testing complex systems. Compounding the problem, this disassembly effort is to be completed in a confined space that may contain material out gassing, poor ventilation, poor lighting, while carried out with the aid of large, bulky material handling equipment. The disassembled tooling segments must be removed from the composite shell through an opening less than six feet in diameter. The shear enormity of the tooling assembly and, especially, the disassembly operation takes human engineering in manufacturing system design to new vistas.

As early as 1995, Nayar warned the manufacturing world that we should not ignore the use of high level computer generated graphical ergonomics and human factors engineering during the product and tool design stages. This is especially true when designing very large tooling. Three-dimensional simulation to assist decision-making during the tooling design phase is extremely important and cost effective. The design and human factors engineers have opportunities to visualize and carry out various mechanical and ergonomic analyses along with what if scenarios. The list of ergonomic and human engineering tools in the Delmia ENVISION ERGO software package, used for this simulation, can be used to accomplish analyses that can provide detailed information on load and stress situations, which may effect the executability and tolerability of work situations (Schaub et al, 1997). The analysis and information gathering is completed while the design is still in the digital state. Therefore the design can be examined and tested without exposing workers to potentially dangerous situations while saving the organization the time and expense of physical mockups.

LITERATURE REVIEW

Research regarding utilization of 3D or virtual Reality (VR) simulation for the design and ergonomic analysis of extremely large tooling for composite lay up appears minimal. Several papers illustrate the use of computer simulation for testing of composite laminates. Krueger and O Brien (2001) described a shell/3D modeling technique development using a 3D solid finite element model for testing composite de-lamination. Aono et al (1994) reported that 3D simulation has been used as a modeling and optimization tool to fit composite woven fiber to curved surfaces. Aono did not mention the use of 3D simulation for tool design or human engineering analysis. Sundin (2001) describes participatory ergonomics using 3D computerized simulation as a means for improvements in both workplace design and product development. This approach utilizes people, especially workers directly involved in the process or area being studied, to work with manufacturing or design engineers during the design stage to improve the ultimate product. Diehl et al (1997) relates how 3D simulation was developed partly because of the expense and hazards of testing and evaluation of complex engineering projects. Diehl did not report any utilization of computerized 3D or VR simulation for modeling or human factors evaluation nor analysis of large tooling in manufacturing. As early as 1992, engineers and human factors specialists began using computers during the design of complex systems to investigate how the human/machine interface in these systems could be improved. Scanlon (1992) reported using computer-aided design (CAD) and human factors engineering to improve the maintainability of aircraft engines by aircraft maintenance personnel.

3D SIMULATION SOFTWARE TOOLS

According to ergonomics professionals, integrating knowledge gathered from human engineering research as early as possible in the design of a product or system, thus reaping the most benefit for the least outlay of funds, is an ultimate objective (Feyen et al, 1999). Several software programs are

commercially available that are capable of carrying out reliable ergonomic analysis. The software used for the ergonomic analysis of the colossal tooling design was ENVISION ERGO developed by Delmia Corporation in Auburn Hills, Michigan. The high-level graphics software has an array of analytical tools designed to be utilized with anthropometrically correct computer-generated digital humans. This sophisticated tool was central to the ergonomic analysis reported in this research.

COMPOSITE SHELL MANUFACTURING

The manufacturing sequence for a cylindrical tank is accomplished by wrapping composite material, in thin alternating layers, around a spinning mandrel of proper geometry. The mandrel may be manufactured from various materials; however it must have strength to withstand the composite laminate wrap crush forces while withstanding the curing temperatures of the autoclave. After wrapping, the composite covered mandrel must be autoclaved for composite curing. However, the mandrel designs must provide for ease of removal of the forming mandrel after the composite/resin application and curing cycle has been completed. Further, in the case of huge fuel tanks, the mandrel tool may have additional composite layers added. Thus, after each wrapping cycle the composites must be autoclaved for curing. After final curing, the mandrel tool and the composite shell must be carefully separated.

Core removal can be accomplished by several methods. Typically, the mandrel is collapsed, washed out if disposable material is used, melted out if eutectic material is utilized, or disassembled in a number of other methods and subsequently removed from the composite shell. At this point in the manufacturing sequence, the composite shell is completed or at least ready for secondary operations. In the case of colossal mandrel tooling, the mandrel may be composed of several hundred to several thousand longitudinal interlocking tooling segments. The total assembled segments represent the complete internal tooling mandrel for the composite shell.

For longitudinal interlocking tooling segments, tooling segment removal is a complicated and potentially dangerous process. With an internal diameter in the range of 35 to 40 feet and with mandrel tooling in a horizontal orientation, manufacturing engineers are faced with designing a disassembly operation that puts workers at heights up to four stories. Couple this working height with tool segments weighting up to 2,400 pounds, thus the disassembly requires specially designed material handling equipment. One must keep in mind that the tooling segments are removed beginning at the 12 o clock position with the keystone-tooling segment being removed first. The upper most segments can be lowered almost vertically to the tank horizontal centerline. However, 3D simulation immediately pointed out that as subsequent segments are removed they are displaced further away from the vertical position. The removal path becomes more horizontal as the disassembly process proceeds toward the nine o clock and three o clock positions. This situation forces the removal equipment to increasingly cope with segment removal from a horizontal position rather than from a vertical position. The opposite situation occurs as the workers pass the nine o clock and three o clock positions. Ultimately, the processes progresses to segments located at the six o clock position. The removal process then changes to a vertical lift in order to position tool segments on the tank s horizontal axis for removal to the outside via the narrow opening.

3D simulation, when used to analyze the above situation, clearly pointed out the need for special tooling segment removal equipment and material-handling devices. It became readily apparent that these devices would be critical to the success of this manufacturing process. The removal equipment should be divided into two categories. The first category would be equipment and material-handling devices to disassemble and transport tooling segments to the tank centerline. The second category of equipment would include machinery and material handling equipment for transporting tooling segments from the composite tank centerline and outside to a storage or assembly area adjacent to the tank. This is no small undertaking considering the large tooling segments that must be moved at least half the length or more of the roughly 100 foot long tank. In addition, some tooling segments and support ribs will have to be moved carefully through the very narrow openings.

The tank openings will be less than six feet in diameter (see Figure 2) considering that tooling segments will still be in place at that point of the disassembly process. Thus, ability to carry out specific delicate maneuvers to facilitate the removal of complex geometry segment and ribs from the interior finished shell is paramount. The most distance segments would be removed from the tank opening starting first with the uppermost keystone segments.

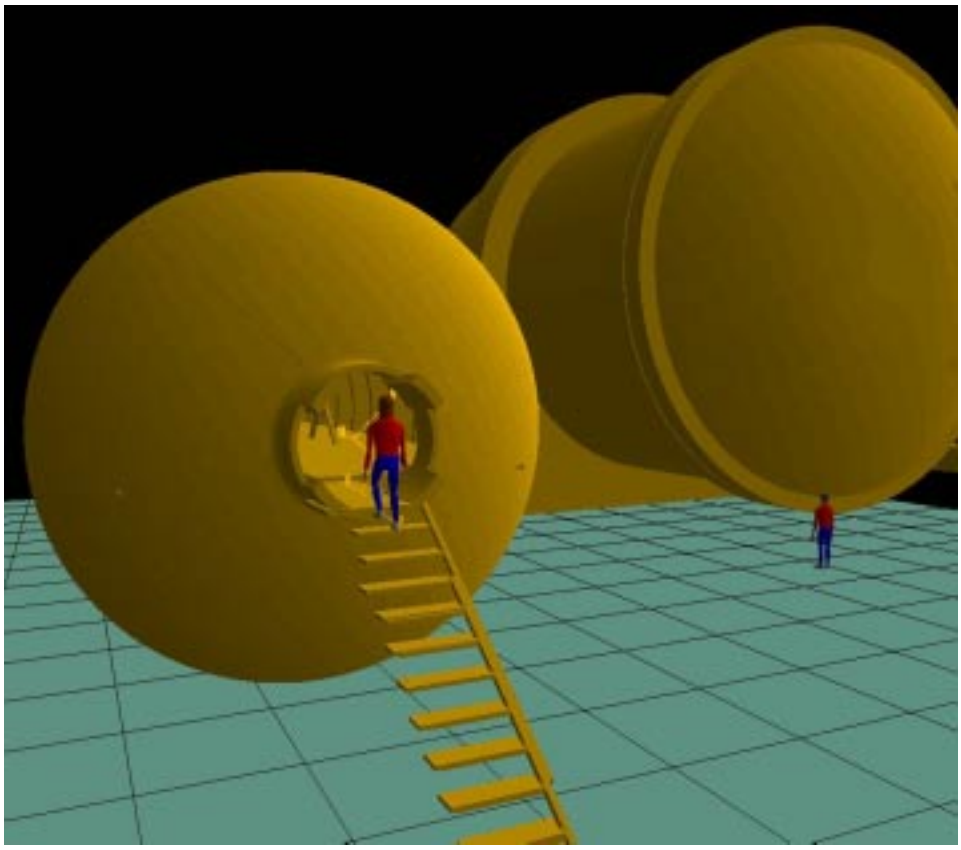

Figure 2: Simulated female worker entering tooling opening.

The high level 3D simulation also pinpointed the necessity of internal support for the composite shell as the tooling segments are removed. This support would also need to be designed modularly for rapid installation and removal. The modular function would allow supports to be added and removed with minimal worker effort while still providing proper internal support to prevent the composite structure from collapsing from its own weight. Also, it was envisioned that external support will be required to provide support of the tank shell during mandrel disassembly and storage.

SIMULATION RESULTS

The 3D simulation of the colossal tooling was found able to solve, digitally and without expensive mock-ups, man/machine interface issues. The initial concern was the disassembly simulation of the colossal tooling from the internal cavity of the finished composite shell. This process is potentially dangerous to the workers disassembling the tooling and to the composite shell, which was the designed purpose for the tank shell tooling. It was estimated that this would involve approximately 200 tooling segments weighting an average of 2,000 pounds each. First, the engineers and human engineering specialists were able to visualize the tasks to be done and the problems that needed to be addressed and solved to make the design workable. A CAD model of the mandrel tool then was generated. The model was composed of movable segments representing the actual mandrel tool segments. In addition to the mandrel tool, the need for various ancillary items became readily apparent from the graphic simulation. These pieces of equipment and material handling devices included portable stairs or a hydraulic man lift to allow workers access to the tooling opening. Figure three illustrates the enormity of the composite tank mandrel tooling and the autoclave model that will be used to cure the composite tank.

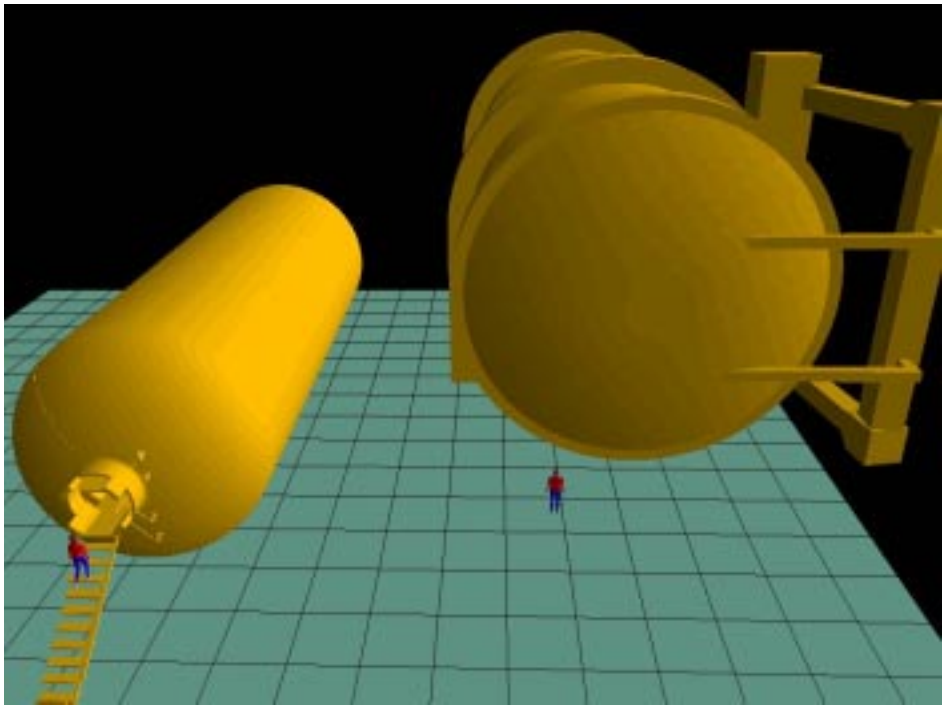

Figure 3: Colossal tool and autoclave used for composite tank fabrication.

The first challenge that was readily apparent was the magnitude of the effort needed to safely disassembling 2,000 pound tooling segments. The segments then had to be moved to the center line of the cylinder-shaped tank in order to transport them transversely through the tooling tank shell and through a narrow diameter exit. The workers would also need support equipment and tooling to access and remove the tooling segments. Adjustable modular platforms that safely support the removal equipment and workers would need to be built and systematically removed as the disassembly process advances toward the shell opening (see Figure 4). Support scaffolding, designed for rapid assembly/disassembly was identified, during the simulation and analysis, as necessary to provide the tank shell with internal support. Reach and visibility envelopes for the initial CAD models confirmed that the workers, with the assistance of adjustable scaffolding and material handling equipment, would be able to carry out the disassembly tasks. Operating forces and lifting issues were of foremost concern considering the size and weight of the tooling segments. Since it is impossible for a worker to physically move any of the tooling segments without mechanical assistance, the primary concerned was safety issues of the man/machine interfaces.

Figure 4: Assembly and disassembly tooling

Other important issues that arose during the human worker and mandrel tooling disassembly simulation included ventilation, lighting, and noise. Ventilation was of primary concern because of the large but still confined space and the fact of composite material out gassing. Lighting was a process and safety issue. Noise abatement was not critical since most of the equipment and material handling devices were not noise generators. However, if the design of tooling segment assembly utilized threaded fasteners then the use of pneumatic nutrunners are possible excessive noise producers.

The simulated work environment was built and populated with a 50 percentile female worker. The simulated environment and workers were to scale. The simulation had the worker climb stairs to the tank opening and then walks across a temporary platform to the center of the segmented tooling. With the platform slightly below the approximate centerline the worker would still be at least 15 feet above the bottom of the shell and roughly 20 feet below the upper most tooling segments and support ribs (see Figure 5). It is envisioned that various scissor lift type platforms will be raised to support workers during the unfastening tasks and then utilized to lower the removed segments to the removal equipment used to transport the segments from the tank shell.

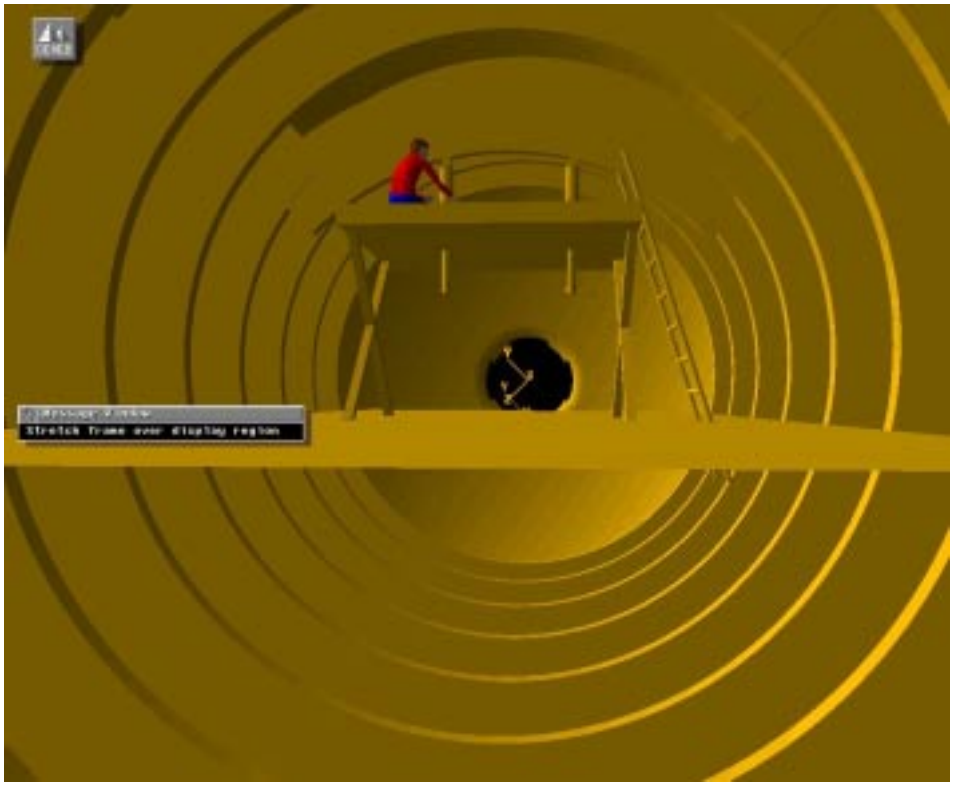

Figure 5: Equipment platform

SUMMARY

The application of high-level 3D simulation software to the design phase of colossal mandrel tooling for composite aerospace fuel tanks was accomplished to discover and resolve safety and human engineering problems. The analyses were conducted to determine safety, ergonomic and human engineering aspects of the disassembly process of the fuel tank composite shell mandrel. Three-dimensional graphics high-level software, incorporating various ergonomic analysis algorithms, was utilized to determine if the process was within safety and health boundaries for the workers carrying out these tasks. In addition, the graphical software was extremely helpful in the identification of material handling equipment and devices for the mandrel tooling assembly/disassembly process.

REFERENCES

[1] Aono, M., D.E. Breen, and M.J. Wozny. Fitting a Woven-cloth Model to a Curved Surface: Mapping Algorithms, Computer Aided Design, Vol. 26, n 4, April, 1994.

[2] Deitz, Dan. Human-integrated Design, Mechanical Engineering, Vol. 117, n 8, Aug. 1995.

[3] Diehl, Alan, V. Gawron, L. Canham. Modeling and Simulation Issues in Design, Test, and Evaluation, Proceedings of the Human Factors and Ergonomics Society, Vol. 2, 1997.

[4] Feyen, Robert, Y. Liu, D. Chaffin, G. Jimmerson, and B. Joseph. New Software Tools Improve Workplace Design, Ergonomics in Design, Vol. 7, n 2, 1999.

[5] Krueger, R. and T.K. O Brien. Shell/3D Modeling Technique for the Analysis of Delaminated Composite Laminates, Applied Science and Manufacturing, Vol. 32, n 1, Jan. 2001.

[6] Nayar, Narinder. Workplace Ergonomics and Simulation, Assembly Automation, Vol. 16, N 1, 1996.

[7] Scanlon, T.J. Application of Human Factors Engineering at General Electric Aircraft, SAE Technical Paper Series, 1992 SAE Aerospace Atlantic, April 7-10, 1992.

[8] Schaub, K., K. Landau, R. Menges, and K. Grobmann. A Computer-aided Tool for Ergonomic Workplace Design and Preventive Health Care, Human Factors and Ergonomics in Manufacturing, Vol. 7, n 4, 1997.

[9] Sundin, A. Participatory Ergonomics in Product Development and Workplace Design. Supported by Computerised Visualisation and Human Modelling, Doktorsavhandliingar vid Chalmer tekniska Hogskola, Sweden, n 1730, 2001.

Selection of a Non-ODC Solvent for Rubber Processing Equipment Cleaning

R. E. Morgan and T. N. Thornton
ATK Thiokol Propulsion
And
L. Semmel and S. A. Selvidge
NASA Marshall Space Flight Center

Abstract

NASA/MSFC has recently acquired new equipment for the manufacture and processing of rubber and rubber containing items that are used in the RSRM system. Work with a previous generation of rubber equipment at MSFC in the 1970's had involved the use of ODC's such as 1,1,1-Trichloroethane or VOC's such as Toluene as the solvents of choice in cleaning the equipment. Neither of these options is practical today. This paper addresses the selection and screening of candidate cleaning solvents that are not only effective, but also meet the new environmental standards.

Background

Rubber and elastomeric compounds play a vital role in the Reusable Solid Rocket Motor. Three kinds of rubber are used for insulation, two for internal insulation of the motor case and one kind for the exterior weather seals and system tunnels. This is in addition to the rubber used in o-rings and other joint thermal protection systems. Because of the number of ingredients and the changing nature of the specialty chemical business, some of the ingredients become obsolete and must be replaced. These changes require new chemicals to be thoroughly screened for their effects on the physical, chemical, and thermal properties of the resulting rubber compounds. Small scale batches of rubber have to be made to screen the new ingredients.

Figure 1 shows the small-scale rubber mixer that has recently been installed at MSFC for the purpose of making and testing small batches of rubber. The mixer is a 6 lb capacity Banbury style mixer that is similar to the full size production capacity mixers. These mixers use tremendous power to literally chew, or masticate, rubber and solid fillers into an acceptable mixture. The mixture is pulled from the mixer and then flattened, or calendered, into a thin sheet with a calender roll mill. Figure 2 shows the calender mill that was recently installed.

Natural rubber is used to clean the mixer and mill by removing gross contamination from the mixer or mill surfaces as shown in Figures 3 and 4. There still remains a film of rubber and traces of raw materials that need to be removed from the mixer or mill. This has usually required the use of solvents.

Figure 1 NASA MSFC Rubber Mixer

Figure 2 NASA MSFC Rubber Calender Mill

Figure 3 Rubber Mixer Cleaning with Natural Rubber

Figure 4 Rubber Mill Cleaning with Natural Rubber

Traditional Cleaning Solvents for Rubber

Traditionally solvents have been divided into 2 classes for cleaning rubber. These are flammable and non-flammable solvents.

Flammable Solvents

The first effective solvents for rubber were the flammable solvents benzene, toluene, xylene, methyl ethyl ketone and hexane. All of these, except hexane, are on the EPA's list of 17 chemicals targeted for elimination in the workplace due to serious health or environmental risks. Hexane is classified as a volatile organic chemical (VOC) which is a risk for producing low-level photo-chemical smog or ozone. This, in addition to its flammability, makes hexane a poor choice.

Non-Flammable Solvents

The non-flammable solvents were developed and touted as safe replacements for the aforementioned solvents. For years carbon tetrachloride, methyl chloroform, perchloroethylene, and methylene chloride were used with great success. Now these solvents are also targeted for elimination due to uncovered health and environmental risks. Even some of the newer replacements for these chemicals, such as n-propyl bromide, are under a cloud of doubt due to health concerns.

Clearly, in order to comply with newer regulations such as Presidential Executive Orders 12856 and Aerospace NESHAP, all of these older solvents must be considered unsuitable for routine use.

New Cleaning Solvents for Rubber

ATK-Thiokol Propulsion has investigated many replacement solvents and reported the results at previous conferences[1]. As a result of this testing three candidate solvents were selected based on their past test performance in attacking rubber. These solvents were each tested for compatibility and effective cleaning ability using both natural rubber and EPDM. An FTIR analysis was also performed for each contaminant cleaned with each solvent.

Compatibility Testing

Compatibility testing was performed on both the natural rubber and EPDM. The purpose of this testing was to determine the solvents ability to dissolve rubber. Samples were first weighed then immersed in the test solvents. After a two-hour immersion time, samples were removed and reweighed to see the effect each solvent had on the mass of each material. Visual observations were also recorded.

Compatibility Test Results

Results of the natural rubber compatibility test showed that Plus-4 had the greatest effect on mass with a change of + 56%. PF Degreaser had a change of + 38% while Spirit 126 had the least effect with a change of + 27%. Complete results for the natural rubber compatibility test can be found in Table I.

Table I: Compatibility Test Results for Cured Natural Rubber

Solvent	Mass / 0	Mass / +2	Change	Comments
PF Degreaser	6.2018	8.5311	+ 38%	Swelled / Soft
Plus-4	6.7630	10.5285	+ 56%	Swelled / Soft / Sticky
Spirit 126	6.4396	8.2021	+ 27%	Swelled / Soft

Plus-4 also had the greatest effect on the EPDM with a change of + 36% in mass. PF Degreaser had a change of + 25% while Spirit 126 had the least effect with a change of + 18%. Complete results for the EPDM compatibility test can be found in Table II.

Table II: Compatibility Test Results for Cured EPDM

Solvent	Mass / 0	Mass / +2	Change	Comments
PF Degreaser	4.284	5.341	+ 25%	Light swelling / Sticky
Plus-4	4.256	5.808	+ 36%	Light swelling / Sticky / Flaking
Spirit 126	4.288	5.039	+ 18%	Light swelling / Sticky

Cleaning Ability Testing

Cleaning ability testing was performed on each contaminant cleaned with each solvent. Stainless steel panels were contaminated with natural rubber or EPDM then cleaned with the appropriate test solvent. To apply the rubber, toluene was used to liquefy the natural rubber and EPDM and the resultant mixture was then brushed onto the stainless steel panels. The panels were allowed to sit at ambient laboratory conditions for 24 hours to allow sufficient time for the solvent to flash-off and for the rubber to be deposited on the panels. The panels were then cleaned with the solvents and rated according to their ability to remove the contaminant from the surface of the stainless steel panels. An explanation of the rating system follows:

0 – Does not completely remove the contaminant with any level of effort.
1 – Removes the contaminant with significant effort.
2 – Removes the contaminant with moderate effort.
3 – Removes the contaminant easily with minimal effort.

Cleaning Ability Test Results

Results of the cleaning ability test showed that Plus-4 removed the natural rubber easily with minimal effort. Both PF Degreaser and Spirit 126 removed the bulk of the natural rubber with moderate effort in less than 1 minute, but both solvents left a stain on the panels. The stain may not be rubber, but some form of oxidation. Complete results can be found in Table III.

Table III: Cleanability Test Results for Natural Rubber

Solvent	Score	Comments
PF Degreaser	0	Removed bulk but left stain
Plus-4	3	Cleaned best
Spirit 126	0	Removed bulk but left stain

Results of the EPDM clean-ability test showed that all three solvents removed the EPDM easily with minimal effort. Complete results can be found in Table IV.

Table IV: Cleanability Test Results for EPDM

Solvent	Score	Comments
PF Degreaser	3	Removed easily
Plus-4	3	Removed easily
Spirit 126	3	Removed easily

FTIR Analysis

An FTIR analysis was performed for each contaminant cleaned with each solvent. Toluene was used to liquefy the natural rubber and EPDM. The resultant mixture was then brushed onto stainless steel panels. The panels were allowed to sit at ambient laboratory conditions for 24 hours to allow sufficient solvent flash-off. The contaminated panels were then cleaned with the appropriate solvent and delivered to the FTIR lab for analysis to determine if any residue was left on the panel surface.

FTIR Analysis Results

Results of the FTIR analysis showed no detectable amount of the contaminants or the solvents remaining on the surface of any of the panels.

Conclusions

All three solvents demonstrated similar effects in each of the natural rubber and EPDM compatibility tests. Plus-4 had the greatest gain in mass with PF Degreaser second and Spirit 126 third.

Although all three solvents were shown to remove the bulk of the natural rubber, only Plus-4 removed all visual traces of the natural rubber from the stainless steel panels. All three solvents removed the EPDM easily with minimal effort. All three solvents removed both the natural rubber and EPDM to levels undetectable by FTIR.

As a result of this testing a preferred cleaner and an alternative were identified. These have been approved and used in the NASA MSFC rubber Lab for over one year now with good results.

Acknowledgements

The authors would like to thank Dink Harris, Jack Simms, Ken Peacock and Troy Daugette in the ODC Lab for their efforts on this project. We also acknowledge the work of Craig Meeks, the Lead Rubber Technician, in his continuing efforts to maintain the rubber equipment in peak condition.

References

1. Danieu, D***., Phase II ODC Elimination: Hand Wipe Cleaning*** Third Aerospace Environmental Technology Conference, June 1-3, 1998, pg 665.

Hazardous Chemical Replacement

Solvent Paint Strippers Replaced by Dry Media Blasting - Case Study

Presented by: Richard E. Buckholz
Materials and Process Engineer - Lead

Scope of Presentation

- Finding an Alternate to Solvent Strippers
- Dry Media Blasting a Viable Alternative
- The Down Side of Wheat Starch Media
- Wheat Starch Media use at Vought Aircraft
- Wheat Starch Attributes and Limitations
- Corn Hybrid Polymer as a Drop-in for Wheat Starch
- The Corn Hybrid Polymer Advantage
- Gaining Industry Wide Approval for Corn Hybrid Media
- References

Vought
Aircraft Industries, Inc.

Finding an Alternate to Solvent Strippers

- The Vought - Stuart Site mandate was to identify an alternative depainting system that does not rely on solvent strippers (methylene chloride) or slow acting non-chlorinated strippers, Turco 6776 L.O. (Formic acid) or Turco 6840S (alkaline based)
  - Both of the Turco products are environmentally safe products and meet NESHAP requirements.
  - The down-side of these products is that they work very slowly and require repeated applications to attain success in the stripping of aircraft primer and topcoats.

Vought
Aircraft Industries, Inc.

Dry Media Blasting a Viable Alternative

- Dry Media Blasting using Wheat Starch is a Cost Effective proven alternative for Solvent Stripping.
- The Joint EPA/NASA/USAF Interagency Depainting Study Final Report, dated 12/1999 found the wheat starch process effectively removed the topcoat and primer coating as the study requested. Coating removal was accomplished without substrate damage. Wheat Starch is an effective depainting method and and easily adaptable to existing equipment.

Vought
Aircraft Industries, Inc.

Dry Media Blasting a Viable Alternative - Continued

- Chemical Strippers; Dwell times for paint removal were longer than expected at Vought Stuart: 6 to 24 hours for acid strippers and even longer for alkaline strippers. Both strippers required multiple applications and as a result caused an excessive Hazardous Waste Stream. As much as 4 times as methylene Chloride strippers generated.
- Starch Dry Media; This process is well accepted throughout the aircraft and aerospace industry since the early 1990s. The media can be recycled up to 20 times and used in any blast unit designed for plastic media. Wheat Starch blasting is used for a variety of purposes, including depainting and deflash of bond-line adhesives. Wheat Starch can be used to selectively strip topcoat and primer coatings with the proper nozzle. Coating removal is accomplished without substrate damage.

Vought
Aircraft Industries, Inc.

The Down Side of Wheat Starch Media

- The use of Wheat Starch Dry Media requires certain investments to assure the process works effectively. The booth, cabinet or hangar must be designed or modified to assure the media stays dry. If not, the Wheat Starch will take on the appearance of semi-dry Cream of Wheat and stick to everything including booth, cabinet or hangar floors, walls and ceiling.
- When specifying a Wheat Starch Media enclosure the supplier should furnish equipment meeting NEC Code - Explosion Proof Class II and NEMA requirements.
  - —The Bottom Line: If the facility isn t set-up properly due to improper ventilation, excessive humidity, lack of media retrieval or filtration system the Wheat Starch Dry Media will not strip paint or deflash sealant effectively.

Vought
Aircraft Industries, Inc.

Wheat Starch Media Use at Vought Aircraft

- Vought Aircraft Industries Inc. - Dallas, installed a New Dry Media Blast Cabinet in 2000. The blast cabinet was purchased to evaluate Wheat Starch media in the Depainting of detail parts. The blast cabinet installation and testing received direct support from the blast cabinet manufacturer and ADM / Ogilvie the media manufacturer. Possible plans are to use the same booth for the de-flash of cured adhesive bond-line squeeze-out.
- At Vought Stuart a decision has been made to purchase a Portable Closed Cycle Blast Head Machine which is convertible to a Cabinet Blast Machine. This provides the versatility of placing detail parts in the machine for depainting or bringing the blast machine to the airframe for depainting.
- Recent repairs which required stripping of large areas of primer and topcoat coatings and a increase in FAA Repair Station activity has justified procurement of a Portable Closed Cycle Blast Head Machine made by Pauli Systems.

Vought
Aircraft Industries, Inc.

Wheat Starch Attributes and Limitations

- **Wheat Starch Media is very effective replacement for Chemical Solvent Stripping.**
  - **Dry organic 100% Wheat Starch Media (12/30 mesh) is specifically engineered to remove tenacious coatings from sensitive substrates.**
  - **The media is, all natural, nontoxic, biodegradable and can possibly be recycled by ADM/Ogilvie. Result: Little or No Waste Stream !!**
  - **The media is manufactured to strict tolerances to insure consistent performance.**
  - **Strip rate of 1 to 1 1/3 square foot per minute.**
  - **Vought Stuart investigated an Alternate Dry Media which works as well as Wheat Starch, but is less susceptible to moisture absorption. Florida is subject to High Heat and Humidity, The nemesis of Wheat Starch .**
  - **Corn Hybrid Polymer (CHP) may be the best answer !!!**

Vought
Aircraft Industries, Inc.

EnviroStrip Plus12/30 Mesh

EnviroStrip Plus®
New Condition

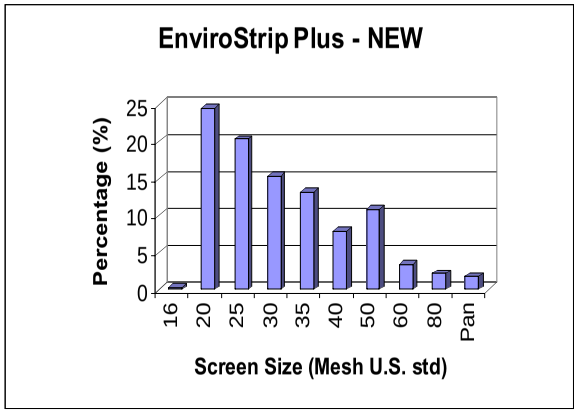

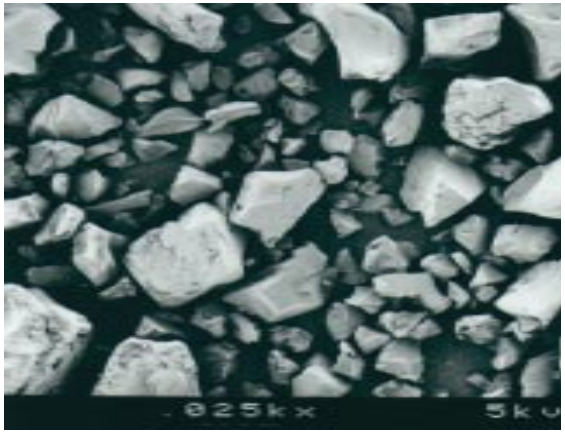

EnviroStrip Plus®
Inprocess Condition
Mixture of New and
Conditioned Media

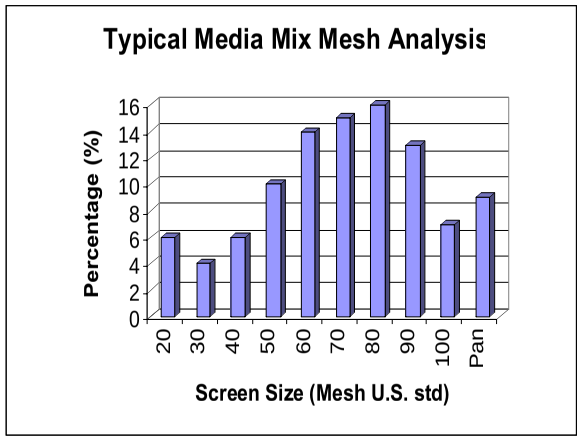

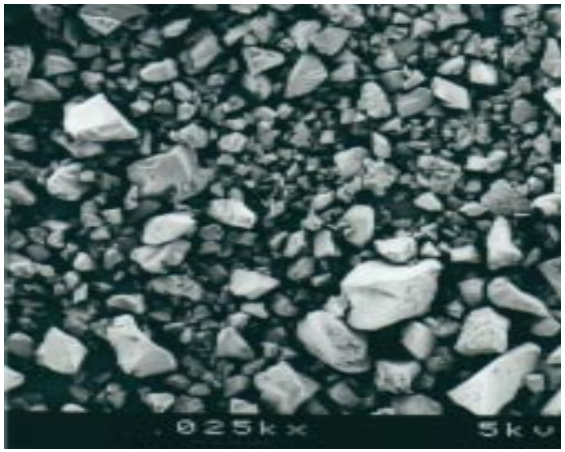

Vought
Aircraft Industries, Inc.

Corn Hybrid Polymer as a Drop-in for Wheat Starch

- EnviroStrip® XL Corn Hybrid Polymer (CHP) as developed by ADM/Ogilvie, is a molecularly engineered polymer that s 100% naturally organic.
  - Non-toxic and biodegradable.
  - Provides same advantages as Wheat Starch.
  - Crystalline shaped (sharp edges) remove coatings with cutting action causing minimal damage to substrate beneath the coatings.
- EnviroStrip® XL Corn Hybrid Polymer (16/60 mesh) is very similar to EnviroStrip Plus¤ Wheat Starch Media in effective coating removal and Type V plastic in respect to durability. CHP is primary candidate as a drop-in replacement for Wheat Starch Media.

Vought Aircraft Industries, Inc.

The Hybrid Corn Polymer Advantage

- **EnviroStrip® XL Hybrid Corn Polymer provides more distinctive advantages not available with EnviroStrip Plus® Wheat Starch.**
  - **CHP is similar to Type V plastic media in respect to flow characteristics and durability (low breakdown rate).**
  - **CHP is much less sensitive to moisture than Wheat Starch.**
  - **As a bonus CHP is fluorescent under black light, which provides Quality Assurance the ability to detect residual media during post stripping inspections.**

Vought Aircraft Industries, Inc.

Fluorescent Qualities of CHP - XL Media

Ultraviolet light response of CHP - XL (left) to Type V Plastic (right)

Vought
Aircraft Industries, Inc.

Gaining Industry Wide Approval for Corn Hybrid Media

- This Conference provides an ideal forum to develop a dialog in the Effort to Gain Industry Wide Acceptance for Corn Hybrid Media.
- ADM/Ogilvie completed a blast media evaluation of the following types of media:
  - EnviroStrip® Plus Wheat Starch Media
  - Envirostrip® XL Corn Hybrid Polymer (CHP)
  - Solidstrip L® Type V Plastic Media
  - The study was conducted to determine the effectiveness of coating removal from aluminum and composite skin structure using the above media. The results are as follows:

Vought
Aircraft Industries, Inc.

Gaining Industry Wide Approval for Corn Hybrid Media - Continued:

- CHP provides slightly faster coating removal than Wheat Starch.
- Analysis has proven that both dry medias successfully remove standard topcoat systems. There is no damage to aluminum (clad and bare) and composite including graphite epoxy substrates.
- Wheat Starch and CHP are compatible using the same blast equipment and nozzles. Wheat Starch has been proven in aircraft manufacture (both military and commercial).
- Corn Hybrid Polymer is definitely the dry media that will be used at Vought Stuart, upon procurement of Pauli Systems Portable Dry Media blast equipment.

Vought
Aircraft Industries, Inc.

References

- Cameron Drake - ADM/Ogilvie, Melbourne Beach, FL
- Robert Pauli - Pauli Systems, Fairfield, California
- Joint EPA/NASA/USAF Interagency Depainting Study, Final Report - December 1999 National Aeronautics and Space Administration - George C. Marshall Space Flight Center.

Vought Aircraft Industries, Inc.


Vought
Aircraft Industries, Inc.

Ozone Friendly Solvent Alternatives for Aerospace Applications

ABID N. MERCHANT
DuPont Fluoroproducts, CRP-711
Wilmington, DE 19804
Phone: 302-999-4269
Fax: 302-999-2093
E-mail: abid.n.merchant@usa.dupont.com

Several new hydrofluorocarbon (HFC) formulations have been developed for cleaning, verification of cleanliness, drying, deposition, and aerosol applications. These formulations are non-ozone depleting and have low global warming impact. This paper will present physical, chemical, and thermodynamic properties and environmental and safety profiles of these solvents, along with field test data on applications.

TESTING & QUALIFICATION OF A NON-CFC CLEANLINESS VERIFICATION AGENT

ERIC EICHINGER & STEVE ADAM
BOEING HUMAN SPACE FLIGHT & EXPLORATION
AMPET/MSFC
SEPTEMBER 17, 2002

Overview:

Orbiter Must Clean Approx. 1000 Critical Components

- **The Space Shuttle Orbiter Must Precision Clean & Verify All Fluid Systems Hardware**
  - **Detail Parts, Assemblies, & Components**
- **In the Past These Parts Were Cleaned/Verified With Freon 113**
- **The Orbiter Cleaning Facilities (KSC, Palmdale, White Sands, & Vendors) Are Now Transitioning To Freon Replacements**
- **This Presentation Summarizes the Ongoing Effort to Find the Best Cleaning Solvent for Orbiter Hardware**

Orbiter Cleaning Needs Make Solvent Selection Hard

- **The Program Expects (But Does Not Require) That The Final Fluid Used (To Verify LOX, GOX, & Oxidizer Hardware) Be LOX Compatible** **(NSTS 07700 Volume X - Book 1 para 3.6.12.1)**
- **Many Components Must Be Cleaned to Level 100A**
  - **NVR = Non Volatile Residue**

Cleanliness Level	Particle Size (microns)	Maximum Number of Particles per Sample	Maximum NVR per 100 ml
100A	< 25	No silting	1 mg
	25-50	68	
	>50-100	11	
	>100, Nonmetallic	1	
	>100, Metallic	0	

- **Most of the Replacement Solvents Will Not Dissolve the Variety of Orbiter Contaminants As Well As Freon 113**

BOEING

Many Potential Contaminants Affect Orbiter Cleaning

- **Contaminants Utilized For Precision Clean Evaluations**
  - **Braycote 601(B-601) - Fluorinated Grease**
  - **Dow Corning DC-33 - Silicone Grease**
  - **Mil-H-83282 Hydraulic Fluid - Medium Hydrocarbon**
  - **Mil-H-5606 Hydraulic Fluid - Medium Hydrocarbon**
    - **Data not Included Since 70% Volatile**
  - **Houghto Draw 3105 Bending Oil (LUBE 1) - Heavy Hydrocarbon**
  - **Houghto Draw 7007 Bending Oil - Heavy Hydrocarbon**
    - **Data not Included**
      - **Results Same As Houghto Draw 3105**
  - **Titan Lube Bending Oil (LUBE 2)- Heavy Hydrocarbon**
  - **Amberlube Water-based Bending Oil**
    - **Data not Included**
      - **Only Tested With Some of the Candidates**
      - **Results Same As Titan Lube Except (Freon 113 Control)**
        - **Freon 113 Did Not Remove Amberlube**

Orbiter Must Clean Assembled Hardware

- **Example of a "Worst Case" Orbiter Component**

Performance Screening Measured Solubility Of NVR

What We Did	What We Didn't Do	Why
6061-T6 Aluminum	Stainless, All Alloys	Established Procedure
1.5" by 3" Panel	Foil, Actual Hardware	Repeatability, Weight
6 Contaminants tested individually	Blend of Contaminants, All Possible Contaminants	Limited Scope, Single Contaminant Can Occur
10-150 mg. Soil/Panel	Less, More	Worst Case
Solvent Poured	Spray, Flush	Worst Case

7 “Non-Flammable”* Solvents Tested For Performance

Candidate Fluids
Freon TF (CFC 113)
DuPont **Vertrel XF** (HFC 43-10 *mee*)
DuPont **Vertrel MCA** (HFC 43-10 *mee* & trans 1,2-dichloroethylene azeotropic mixture, both with and without nitromethane)
Asahi Glass Asahiklin **(AK) 225G** (HCFC)
Albemarle **Abzol** VG &EnviroTech Int'l **Ensolv** (n-propyl bromide)
3M **HFE 7100** (methoxynonafluorobutane)
3M **HFE 7200** (ethoxynonafluorobutane)

* n propyl bromides fail LOX testing, 7200 appears to have a flashpoint
  Vertrel MCA & HFE 7100DE marginally failed LOX testing

Lab Data:

Vertrel MCA, & AK 225G Are Effective On Orbiter Contaminants

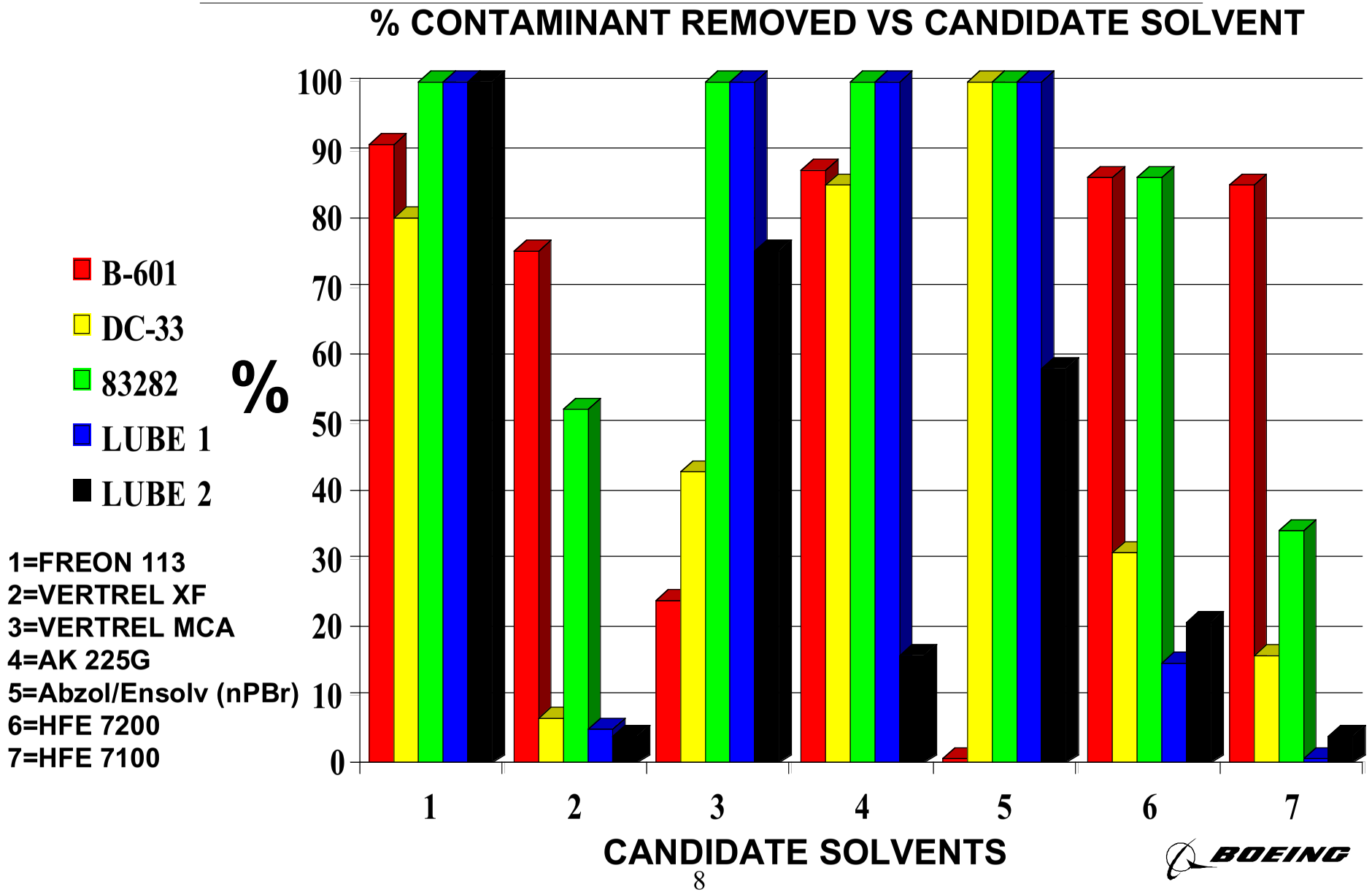

BOEING

5 New Solvents Have Recently Been Characterized

Material	Ingredients	% Comp.
HFE 301 (HFE 7000, L13791)	1-Methoxyheptafluoropentane	100%
Vertrel CF	1,1,1,2,2,3,4,5,5,5-Decafluoropentane (HFC 43-10mee) 1,1,1,3,3-Pentafluorobutane (HFE 365mfc)	59-61% 39-41%
Vertrel CCA (KCD-9583)	1,1,1,2,2,3,4,5,5,5-Decafluoropentane (HFC 43-10mee) 1,1,1,3,3-Pentafluorobutane (HFE 365mfc) Trans 1,2-Dichloroethylene (t-DCE)	32-34% 27-29% 38-40%
Vertrel C-HD* (KCD-9571)	1,1,1,2,2,3,4,5,5,5-Decafluoropentane (HFC 43-10mee) Trans 1,2-Dichloroethylene (t-DCE) Ethanol (EtOH)	20-30% 63-73% 1-11%
Vertrel KCD (KCD-9576)	1,1,1,2,2,3,4,5,5,5-Decafluoropentane (HFC 43-10mee) Trans 1,2-Dichloroethylene (t-DCE)	20-30% 73-83%

Exposure Limits:
HFE 301 = 75 ppm
Vertrel CF = 200 ppm
Vertrel CCA = 200 ppm
Vertrel C-HD = 200 ppm

Lab Data:

None Of The Newer Replacements Remove All Of The Orbiter Contaminants

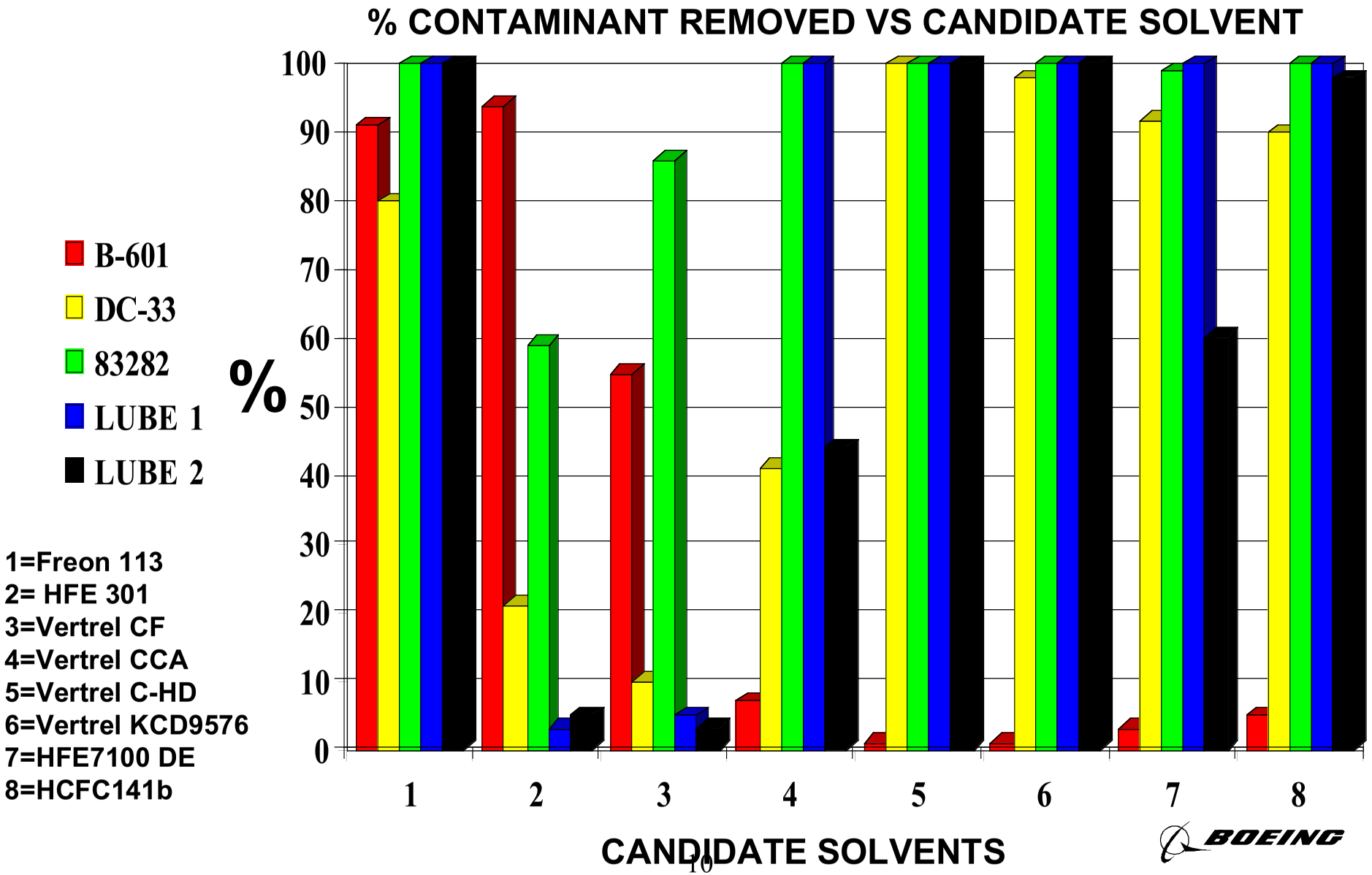

BOEING

Conclusions

- **The Solvent Best Able To Meet Orbiter Requirements Was AK-225G**
- **The Vertrel MCA & HFE 7100DE Were Runners Up**
  - **Marginal Fail In LOX Testing**
- **The Vertrel C-HD & KCD-9576 Removed Everything But The Fluorinated Grease (Braycote 601)**
  - **Both Failed LOX Impact Testing At WSTF**
- **HFE 7100 Picked For Hand Wipe Use Due To 750ppm Exposure Limit**
- **Newer Solvents Do Not Offer Advantages Over Older Solvents for LOX cleaning**

Summary

- **Orbiter Will Continue To Use AK-225G, Vertrel MCA, and HFE-7100 Until Superior Replacements Are Identified**

- **Other Applications May Be Found For Newer Alternatives That Offer Superior Performance But Do Not Meet LOX Requirements**

Optical Properties of Thin Film Molecular Mixtures

Donald A. Jaworske
NASA Glenn Research Center
21000 Brookpark Road
Cleveland, OH 44135
e-mail: Donald.A.Jaworske@grc.nasa.gov

Dean A. Shumway
Brigham Young University-Idaho
Rexburg, ID 83460

Introduction

Thin films composed of molecular mixtures of metal and dielectric are being considered for use as solar selective coatings for a variety of space power applications. By controlling the degree of molecular mixing, the solar selective coatings can be tailored to have the combined properties of high solar absorptance, α, and low infrared emittance, ε. On orbit, these combined properties would simultaneously maximize the amount of solar energy captured by the coating and minimize the amount of thermal energy radiated. Minisatellites equipped with solar collectors coated with these cermet coatings may utilize the captured heat energy to power a heat engine to generate electricity, or to power a thermal bus that directs heat to remote regions of the spacecraft.

Early work in this area identified the theoretical boundary conditions needed to operate a Carnot cycle in space, including the need for a solar concentrator, a solar selective coating at the heat inlet of the engine, and a radiator.[1] A solar concentrator that can concentrate sunlight by a factor of 100 is ideal. At lower values, the temperature of the solar absorbing surface becomes too low for efficient heat engine operation, and at higher values, cavity type heat receivers become attractive. In designing the solar selective coating, the wavelength region yielding high solar absorptance must be separated from the wavelength region yielding low infrared emittance by establishing a sharp transition in optical properties. In particular, a sharp transition in reflectance is desired in the infrared to achieve the desired optical performance. For a heat engine operating at 450°C, a sharp transition at 1.8 micrometers is desired.[2] The radiator completes the heat flow through the Carnot cycle.

Additional work has been done supporting the use of molecular mixtures for terrestrial applications.[3-4] Sputter deposition provides a means to apply coatings to the tubes that carry a working fluid at the focus of trough-style collectors. Sputtering offers considerable flexibility in coating conditions, including a wide variety of metal and dielectric targets. Coating designs range from simple two or three layer coatings to complex coatings that are purposely graded to be metal-rich at their base and oxide-rich at their surface in order to yield the desired solar selective properties. In these cermet coatings, molecular islands of metal are thought to be embedded in a three dimensional matrix of dielectric.

Recent work has identified the use of custom made ion beam sputter deposition targets to produce coatings containing molecular mixtures of metal and dielectric.[5] The targets are cylindrical and the surface consists of a gradually changing composition of metal and dielectric. Rotating the cylinder under the beam during ion beam sputter deposition yields a coating that is a molecular mixture of metal and dielectric, with the composition changing through the thickness of the coating. The optical properties of these coatings are not only dependent on their thickness and chemical composition, but are also dependent on the extent of the through thickness gradient established during deposition.

This paper presents a summary of the optical properties of several thin film molecular mixtures designed as solar selective coatings. Optical performance is first identified as a function of wavelength,

from the ultraviolet to the visible and infrared. Coating composition, thickness, and gradient from metal to dielectric also play an important role. Additional work for future activities is also identified.

Materials and Methods

The production of the thin film solar selective coatings has been summarized in detail elsewhere.[2] Briefly, ion beam sputter deposition is used to generate thin film molecular mixtures of metal and dielectric using a cylindrical target having a varying amount of metal and dielectric exposed around its perimeter. Figure 1 shows one of the targets installed in the ion beam sputter deposition facility. At the beginning of

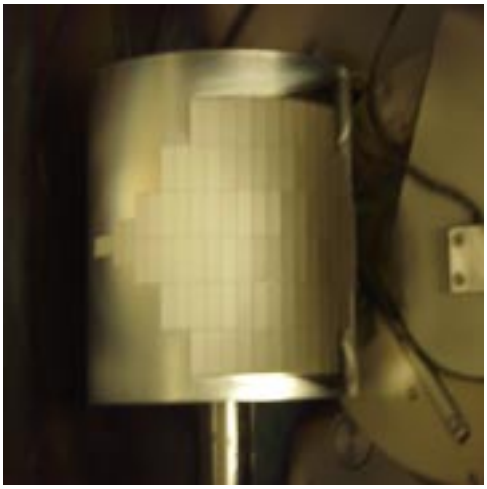

Figure 1. Aluminum/aluminum oxide target installed in the ion beam sputter deposition facility.

deposition, the ion beam is allowed to impinge on the metal-only portion of the target. As the deposition progresses, the cylindrical target is rotated under the beam thereby increasing the fraction of dielectric. At the end of deposition, the ion beam is impinging on the dielectric-only portion of the target. In practice, the deposition typically progresses in discrete steps. Given the geometry of the ion beam sputter deposition facility utilized in this work, eleven steps were used. In most cases, equal deposition time was spent at each step. In some cases, additional deposition time was spent on early steps to prepare metal-rich coatings or additional deposition time was spent on later steps to prepare oxide-rich coatings.

Samples were created from targets composed of aluminum/aluminum oxide, nickel/aluminum oxide, titanium/aluminum oxide, and platinum/aluminum oxide. All coatings were deposited on 2.54 cm diameter aluminum substrates, diamond turned to a mirror finish. The mirror finish was selected to help minimize emittance.

The optical performance of the solar selective coating was evaluated by measuring its reflectance in the wavelength range of 250 to 2500 nanometers utilizing a Perkin-Elmer Lambda-19 spectrophotometer equipped with a 15 cm diameter integrating sphere, and by measuring its reflectance in the wavelength range of 2 to 25 micrometers utilizing a Surface Optics Corporation SOC-400t portable infrared reflectometer. Solar absorptance was calculated by subtracting the reflectance at each wavelength in the wavelength range of 250 to 2500 nanometers from unity, and the resulting curve was weighted with respect to the air mass zero solar spectrum. Infrared emittance was calculated by subtracting the reflectance at each wavelength in the wavelength range of 2 to 25 micrometers from unity, and the resulting curve was weighted with respect to the black body curve for a given temperature , i.e. 25°C. Black body curves representing other temperatures could also be used in the calculation. In this approach, solar absorptance is independent of temperature and infrared emittance is dependent on temperature. The reflectance curves were combined and plotted on a logarithmic wavelength scale, for comparison.

Fused silica witness coupons present during sputter deposition were used to identify the thickness of each film using profilometry.

Results and Discussion

The ideal solar selective coating has the reflectance characteristics shown in Figure 2: a low reflectance in the visible spectral range, a high reflectance in the infrared spectral range, and a sharp transition in between. These reflectance characteristics yield in one surface the combined properties of high solar abosrptance and low infrared emittance. For applications that will operate in the vicinity of 450°C, the sharp transition between the two extremes should occur near a wavelength of 2 micrometers. At lower operating temperatures, the sharp transition may occur at longer wavelengths. However, at higher operating temperatures, the sharp transition must occur at shorter wavelengths and with the drawback of reduced solar absorptance.

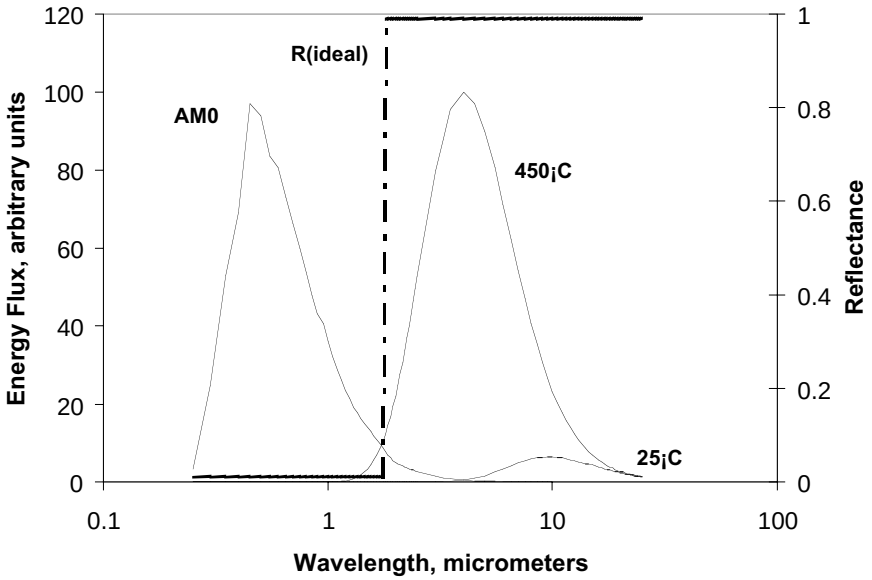

Figure 2. The air mass zero solar spectrum and blackbody curves for 25°C and 450°C.

In molecular mixtures of metal and dielectric, both the shape of the reflectance curve and the resulting α and ε values can vary with the chemical composition and the thickness of the coating.

Chemical Composition

The reflectance of four cermet coatings having four different chemical compositions is summarized in Figure 3. All four coatings were deposited by ion beam sputter deposition, and the change in their through thickness composition was created by the rotation and dwell time of their respective cylindrical target. Similar rotation and dwell time conditions were used for all four targets. Owing to differences in the sputtering of the target materials, thickness values varied: 3400 angstroms for the aluminum/aluminum oxide combination, 1800 angstroms for the nickel/aluminum oxide combination, 2400 angstroms for the titanium/aluminum oxide combination, and 5000 angstroms for the platinum/aluminum oxide combination. The titanium/aluminum oxide combination yielded the sharpest transition, with the transition occurring near the desired value of 2 micrometers. The nickel/aluminum oxide combination exhibited a less abrupt transition, at a value less than 2 micrometers.

Thickness

Deposition from each cylindrical target was controlled by rotation and dwell time. Given the great flexibility in selecting these parameters for ion beam sputter deposition from a cylindrical target, along with other parameters such as ionizing gas and beam current, many different deposition scenarios were tried and many different thin film mixtures were produced. The α and ε values for each metal/dielectric combination are presented here, in graphical form, as a function of coating thickness. By presenting the optical

properties data in this way, trade offs between α and ε as a function of coating thickness may be seen. A discussion of future work, including the need for high temperature durability testing, will follow.

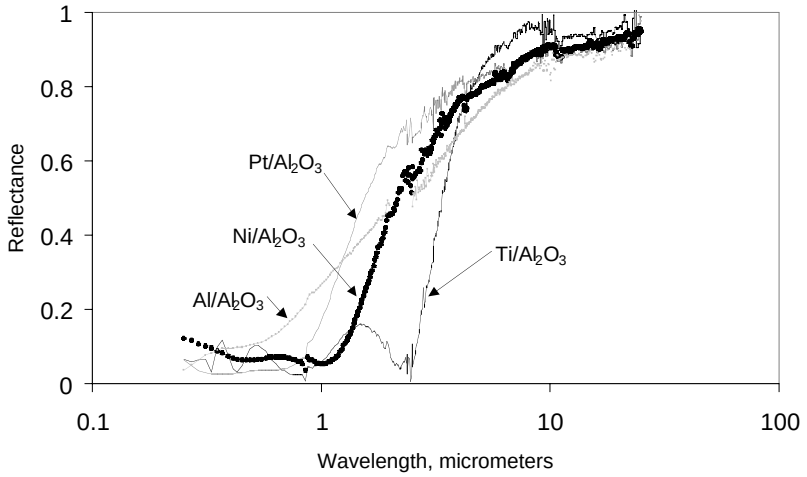

Figure 3. Reflectance as a function of wavelength for four molecular mixtures of metal and dielectric.

Figure 4 shows the α and $\varepsilon_{25^{\circ}C}$ values for the aluminum/aluminum oxide combination of cermet coatings. As the coating thickness increases, α increases to its maximum at approximately 2500 angstroms and declines gradually thereafter. As the coating thickness increases, ε remains essentially constant until reaching 2000 angstroms and increases gradually thereafter. To utilize aluminum/aluminum oxide cermet coatings for applications where it is important to absorb solar energy, optimum performance would be

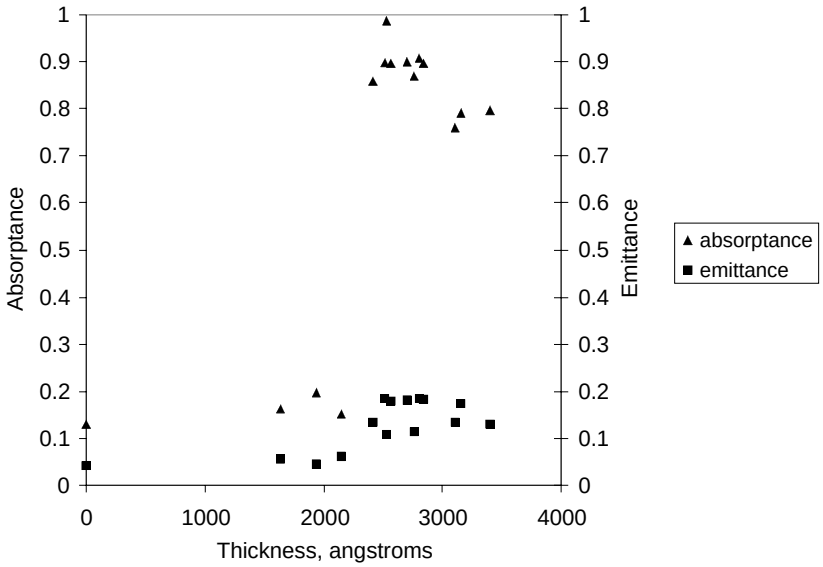

Figure 4. The α and $\varepsilon_{25^{\circ}C}$ values of aluminum/aluminum oxide thin film mixtures.

achieved where α is high, in the vicinity of 2500 angstroms. However, there is a small penalty to pay in performance because ε has already started to increase at that thickness.

Figure 5 shows the α and ε values for the nickel/aluminum oxide combination of cermet coatings. As the coating thickness increases, α increases to its maximum at approximately 2200 angstroms. As the coating thickness increases, ε remains essentially constant over the limited range that was tested. To utilize

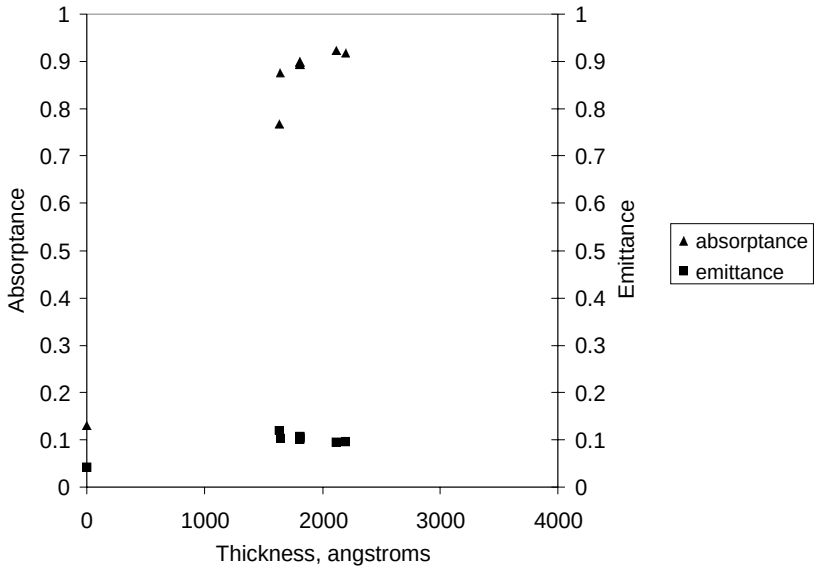

Figure 5. The α and $\varepsilon_{25°C}$ values of nickel/aluminum oxide thin film mixtures.

nickel/aluminum oxide cermet coatings for applications where it is important to absorb solar energy, optimum performance would be achieved where α is high and ε is low, in the vicinity of 2200 angstroms.

Figure 6 shows the α and ε values for the titanium/aluminum oxide combination of cermet coatings. In this case, as the coating thickness increases, α increases at thickness values of 1300 to 1900

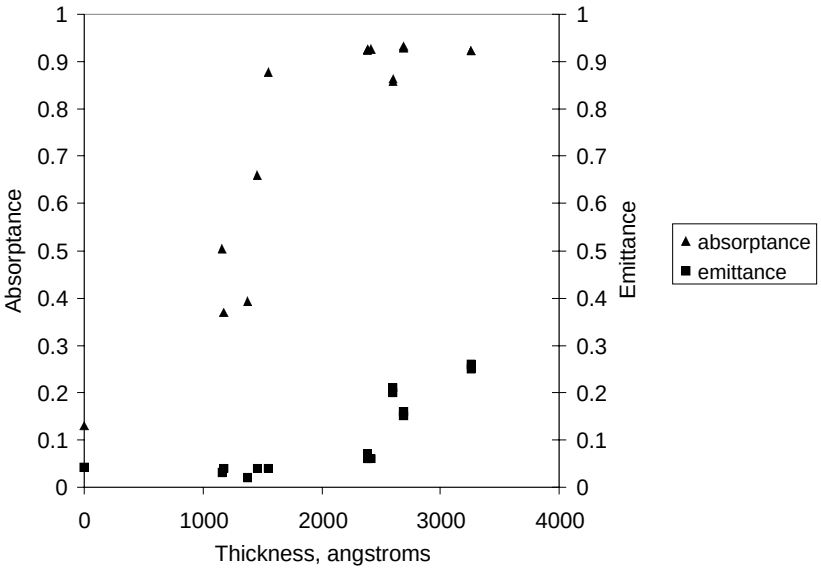

Figure 6. The α and $\varepsilon_{25°C}$ values of titanium/aluminum oxide cermet coatings.

angstroms, reaching its maximum at approximately 2500 angstroms. However, as the coating thickness increases, ε remains constant out to approximately 2200 angstroms and increases thereafter. Hence, optimum thermal performance of this cermet coating would occur in the vicinity of 2000 angstroms, with little to no penalty to pay in performance because ε remains low in this vicinity.

Additional work is underway utilizing the platinum/aluminum oxide cermet. The amount of platinum metal in the target is at a minimum and sputtering conditions are being chosen judiciously.

Future Work

Although this work has concentrated on utilizing several metals combined with one dielectric, additional work is needed to identify the optical performance of thin film molecular mixtures of combinations that utilize other dielectrics, such as silicon dioxide and aluminum nitride. Although high temperature performance of thin film molecular mixtures can be inferred from the high temperature characteristics of their constituents, additional work is needed to evaluate optical performance after heating. Future thermal modeling of potential hardware will need to consider the temperature dependence of the emittance. Additional work is also needed at the molecular level, to identify the mechanisms responsible for the observed optical properties. Auger profiling and x-ray photoelectron spectroscopy could be used to identify exact chemical composition as a function of thickness and shed some light on the types of chemical bonding that occur through the thickness of the coating. Finally, optical modeling is needed to help optimize current thin film molecular mixtures and to identify new candidate combinations for future cermet coatings.

Conclusions

Thin film molecular mixtures of metal and dielectric are being explored as candidates for solar selective coatings. The thin film molecular mixtures may be utilized to absorb solar energy at the heat inlet surface of a heat engine, or may be applied to the surface of a solar collector utilized to collect heat for a thermal bus application. The optical properties of four candidate thin film molecular mixtures were evaluated as a function of wavelength and as a function of film thickness. The four candidate coatings were sputter deposited molecular mixtures of aluminum and aluminum oxide, nickel and aluminum oxide, titanium and aluminum oxide, and platinum and aluminum oxide. Reflectance measurements indicated all four coatings exhibited the combined properties of high solar absorptance and low infrared emittance, to varying degrees, with the titanium and aluminum oxide combination having the best combined properties. Solar absorptance and infrared emittance summarized as a function of coating thickness revealed that the thin film mixtures must be at least 1800 to 2100 angstroms thick in order to provide adequate solar absorptance properties. However, care must be taken to avoid coatings that are too thick, yielding decreased optical performance at the expense of increased emittance.

References

1. Hahn, R. E., and Seraphin, B. O., "Spectrally Selective Surfaces for Photothermal Solar Energy Conversion," in G. Hass and M. H. Francombe, eds, *Physics of Thin Films*, *Volume 10*, Academic Press, New York, pp. 1-69, 1978.
2. Jaworske, D. A., and Hornacek, J., "Coatings for Solar Absorber Applications in Low Earth Orbit," 33rd International SAMPE Technical Conference, Seattle, WA, pp. 1573-1580, November, 2001.
3. Zhang, Q., et al., "High Performance Al-N Cermet Solar Coatings Deposited by a Cylindrical Direct Current Magnetron Sputter Coater," *J. Vac. Sci. Tech. A*, *17*(5), pp. 2885-2890, Sept./Oct. 1999.
4. Zhang, Q., "Recent Progress in High-Temperature Solar Selective Coatings," *Solar Energy Materials and Solar Cells, 62*, pp. 63-74, 2000.
5. D. A. Jaworske and J. Hornacek, "Thermal Performance of an Annealed Pyrolytic Graphite Solar Collector," Space Technology & Applications International Forum (STAIF-2002), Albuquerque, NM, pp. 88-93, February 2002.

Development of lightweight material using high strength fibers against space debris impacts

Makoto Tanaka* **and Yasuhiro Akahoshi****

*Tokai University, 1117 Kitakaname, Hiratsuka, Kanagawa 259-1292, Japan;
Phone +81-463-58-1211, makoto@cc.u-tokai.ac.jp

**Kyushu Institute of Technology, 1-1 Sensui-cho, Tobata-ku, Kitakyushu 804-8550, Japan;
Phone +81-93-884-3177, akaho@mech.kyutech.ac.jp

Introduction

Space debris larger than 10 cm in diameter have been tracked by ground-based radio frequency radars and optical observations. These orbital data obtained by radar measurement are available to avoid hypervelocity impacts of space debris. However, there are no data on debris of diameter between 1 cm and 10 cm. These medium size debris could give catastrophic damages to large-scale space structures such as the International Space Station (ISS). As a spacecraft becomes larger, the potential hazard of debris impacts becomes an ever more serious concern.

In order to protect spacecraft against hypervelocity impacts of debris and meteoroids, several researchers have studied shielding systems. Many space researchers have been pointing out that the protection capability of multi-shock bumper shields is not enough against hypervelocity impacts of medium size debris with 1 to 10 cm in diameter. In the future, it will be important to establish key technologies of protection and mitigation against medium size debris, because year-by-year scale and lifetime of spacecraft increase. The purpose of this study is to develop a new lightweight material and shield against hypervelocity impacts of medium size debris.

Vectran

To develop the lightweight shield for spacecraft, it is indispensable that the main material of the bumper is lightweight. In this respect, a fiber is one of potential materials, and available to transport to Low Earth Orbit. Especially, Vectran is new and one of the fiber materials. Vectran is expected to be used as the bumper materials of the debris shield. This high strength fiber has been used as airbags with the Mars Path Finder.

The Vectran is a liquid crystal polymer fiber developed by Hoechst-Celanese in USA. Only Kuraray Company in Japan has the technique for manufacturing the fabric. With yarn tenacity comparable to Kevlar, degree of moisture absorption is substantially zero percent. Table 1 shows the characteristics of various high strength fibers.

Table 1 Typical physical properties on high strength fibers [1,2]

	Vectran	*Kevlar*	*Nextel 610*
Density (g/cm^3)	**1.41**	1.45	3.88
Tensile Strength (GPa)	**3.61**	3.20	2.93
Tensile Modulus (GPa)	**83**	123	373
Decomposition Temp. (˚C)	**>400**	>400	1204 (Use Temp.)
Moisture Absorption Ratio (%)	**0**	4.3	---
Chemical Composition	**Thermotropic Liquid Crystal Fiber**	Liotropic Liquid Crystal Fiber	alpha Al_2O_3 Fiber

Development of lightweight materials and shields

We developed new bumper materials using Vectran, and impact experiments have been conducted. Table 2 shows the characteristics of various Vectran cloths of different fabric manufactured by Kuraray Company. The unit de (denier) indicates a weight per unit length. One de is equivalent to 1 gram/ 9000 m. The product HT4533 is wove using 3 fibers with 1500 de.

Fig. 1 shows the enlarge photos of new lightweigt materials developed by our laboratories. We developed a lump of Vectran threads, a knitted Vectran cloth with crochet stitch, and a sewn aluminum mesh using Vectran threads. The new debris shields are composed of these materials. As shown in Table 3, three kinds of shields were prepared for hypervelocity impact tests.

Table 2 Characteristics of Vectran cloths

Product No.	*HT4533*	*HT1536*	*HT1030*	*HT0544*
Stitch	3/3 mat	2/2 mat	1/1 plane	1/1 plane
Warp	1500de/1x3	1500de/1x2	1000de/1	500de/1
Woof	1500de/1x3	1500de/1x2	1000de/1	500de/1
Thickness (mm)	2.50	0.72	0.46	0.32
Areal Density (kg/m^2)	1.30	0.50	0.29	0.18

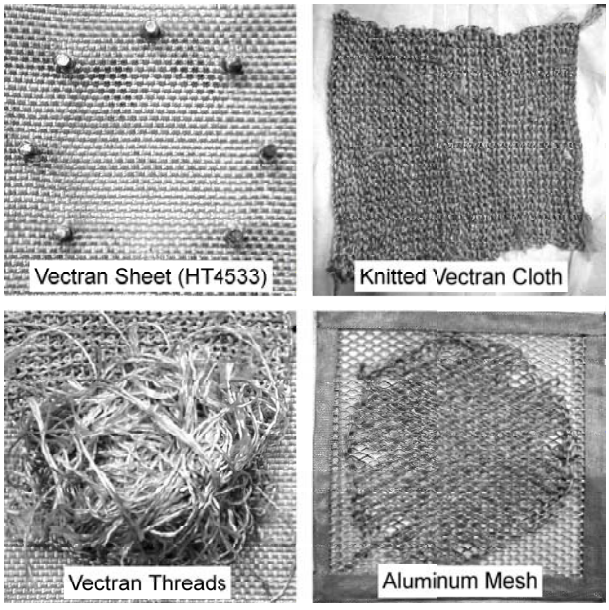

Fig. 1 Main materials of the developed bumper shield

Table 3 Characteristics of shielding materials [1,3]

Shield Type				*Material of Bumper*	*Areal Density (kg/m^2)*	*Total Areal Density (kg/m^2)*
I	Vectran Sheet			Vectran (HT4533)	1.30	**1.3**
II	Single Bumper			Vectran (HT1536)	0.50	**4.5**
				Al Mesh (AL2017)	0.54	
				Vectran Threads	1.99	
				Al Mesh (AL2017)	0.54	
				Vectran (HT1536)	0.50	
				Vectran (HT1030)	0.29	
				Vectran (HT0544)	0.18	
III	Double Bumper	1st	(1)	Stainless Mesh	1.96	**9.6**
			(2)	Vectran (HT4533)	1.30	
			(3)	Vectran (HT4533)	1.30	
		2nd	(4)	Vectran (HT4534)	1.30	
			(5)	Knitted Vectran	0.41	
			(6)	Vectran Threads	1.00	
			(7)	Knitted Vectran	0.41	
			(8)	Al Mesh (AL2017) with Vectran Threads	0.60	
			(9)	Vectran (HT4534)	1.30	
Mesh Stuffed Whipple Bumper Shield including Pressure Wall (JEM)				---	---	17.0 – 26.8

In this study, four kinds of Vectran cloths are used as bumper materials. To investigate the basic protection capability of one Vectran sheet, the type I shield was tested. The type I shield is composed of only one sheet of Vectran cloth (Product No. HT4533) with 3/3 mat stitch. The type II shield is a single multi-layers bumper. This bumper consists of three kinds of Vectran sheets with different stitches (HT1536, HT1030, and HT0544), aluminum meshes (AL2017), and a lump of Vectran threads. The type III shield were developed from consideration of a double-bumper multi-layers system. The first bumper is composed of a stainless mesh and two Vectran sheets, and has a role for breaking up space debris into a debris cloud at the beginning of impact. Two Vectran sheets of the first bumper cling with crossing stitch directions. The second bumper is composed of two Vectran sheets, a knitted Vectran cloth, a lump of Vectran threads, and an aluminum mesh.

Hypervelocity impact experiments

The hypervelocity impact tests were carried out by using the railgun accelerator of the Institute of Space and Astronautical Science in Japan. Fig. 2 and Fig. 3 show the system configuration and the principle of the railgun, respectively. This hypervelocity impact facility consists of a railgun, a vacuum chamber, and a velocity measurement system. The railgun is connected to the vacuum chamber as shown in Fig. 2. The inside of the chamber and the railgun bore is evacuated to the order of 130 Pa by a roughing pump. Before a test, an aluminum fuse is placed behind a projectile in the railgun bore. At the beginning of discharge an arc is initiated by the vaporization of the aluminum fuse at the starting position. The Lorentz force generated by the interaction between the magnetic field and an armature current accelerates the projectile as shown in Fig. 3. The accelerated projectile reaches a velocity of 7 km/sec. The projectile is made of cylindrical polycarbonate blocks with aluminum thin disks as shown in Fig. 4. For velocity measurement, two sensors are placed along the trajectory of the projectile. The main sensor is a pair of X-ray detectors, and the other sensor is an array of magnetic field probes. A velocity is calculated using the time interval between the two signals obtained by the X-ray detectors.

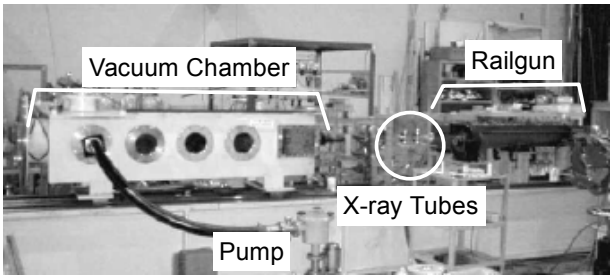

Fig. 2 The railgun facility

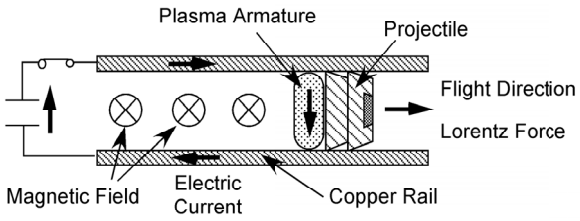

Fig. 3 Principle of a railgun

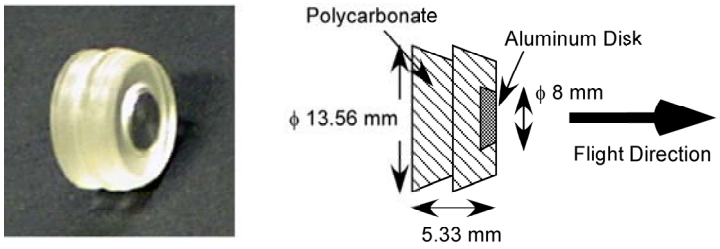

Fig. 4 Cross section of the projectile

In hypervelocity impact tests, bumper materials are fixed by two steel plates with holes (80 mm in diameter) and 8 bolts as shown in Fig. 5. In addition, the steel plates are installed on a steel frame by 4 bolts. Fig. 6 shows a schematic diagram of the test using the type III shield. A first metal plate with a hole at the center is used to stop the plasma cloud ejected from the railgun. Two bumpers with 80 - 90 mm spacing are installed on the steel frame as shown in Fig. 5. An aluminum block with 30 mm in thickness is located behind the target.

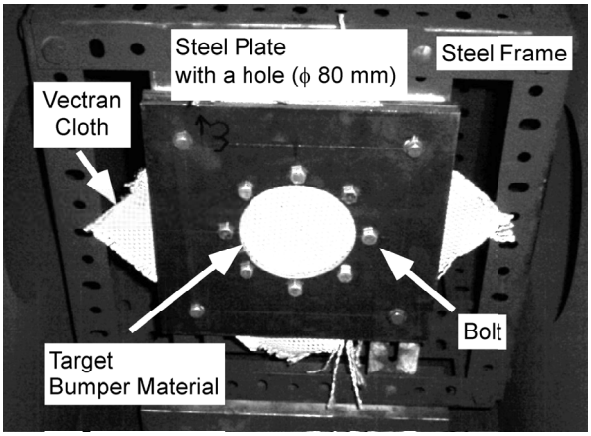

Fig. 5 Target installed on the steel frame

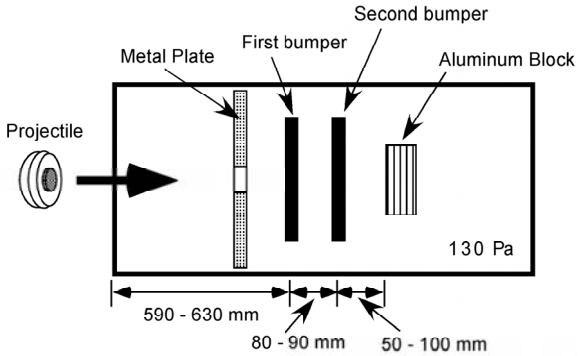

Fig. 6 Test configuration

Results

As shown in Table 4, three tests were conducted. In the impact experiments with the type I shield (Test No.1), a projectile penetrated the Vectran sheet and produced holes of 13 mm in diameter. At the surface of the aluminum

block behind the target, a crater with 28 mm in diameter was generated and then 7 smaller craters were found inside the crater (Fig. 7). This result indicated that the projectile was destroyed into more than 8 pieces after the impact. And furthermore, Vectran had the capability of breaking up the projectile made of polycarbonate.

In the impact experiments with the type II shield (Test No.2), no crater was generated at the surface of the aluminum block although a projectile penetrated the shield and produced a hole (rear side) of 29 mm in diameter (Fig. 8). The intermediate material, the lump of Vectran threads, was expanded behind the shield. A piece of the projectile was not found in the chamber.

Table 4 Conditions of hypervelocity impact tests, and results

Test No.	*Projectile*					*Shield Type*	*Result*
	Material	*Diameter (mm)*	*Thickness (mm)*	*Mass (g)*	*Velocity (km/s)*		
1	Polycarbonate	13.86	6.5	1.09	**4.74**	**I**	Perforation
2	Polycarbonate Aluminum	14.26 8.0	6.1 1.5	1.18	**3.65**	**II**	No perforation
3	Polycarbonate Aluminum	14.26 8.0	6.5 1.5	1.25	**3.14**	**III**	No perforation

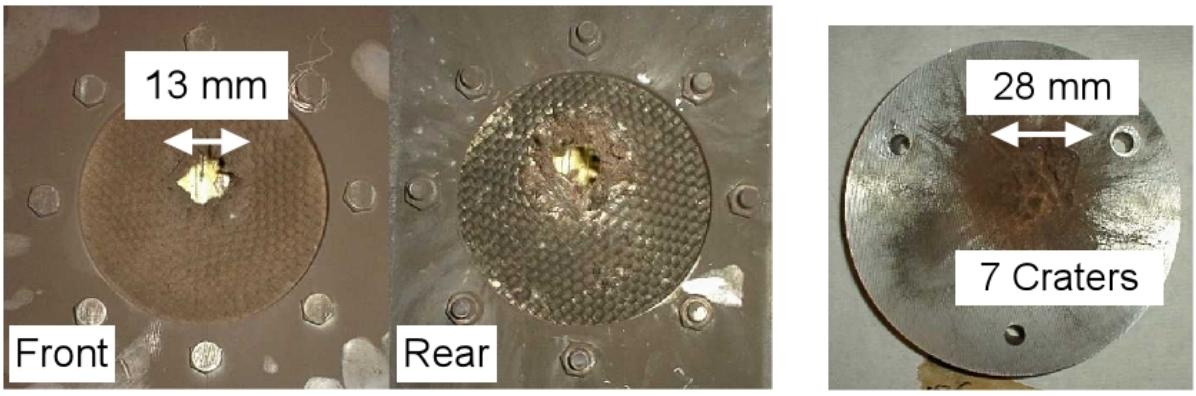

Fig. 7 Impact results on Test No.1, Type I (V=4.74 km/sec)

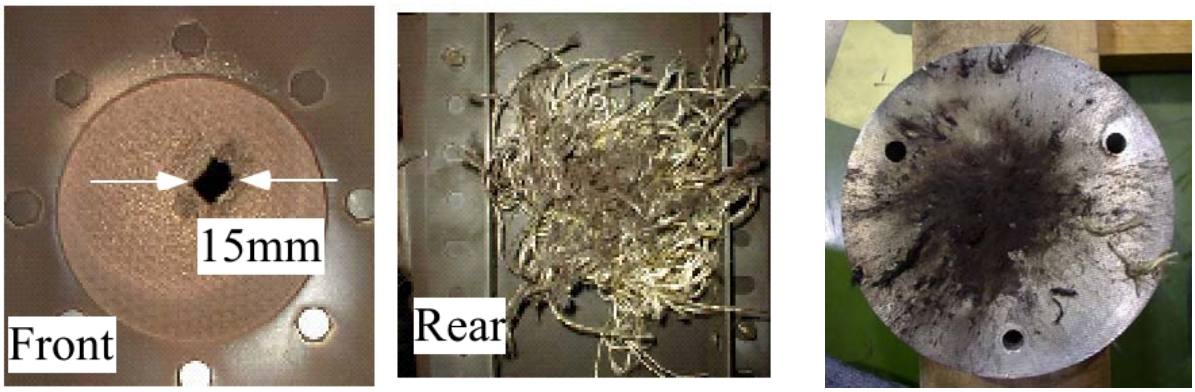

Fig. 8 Impact results on Test No.2, Type II (V=3.65 km/sec)

In the impact experiments with the type III shield (Test No.3), these developed shields stopped projectiles at the point of the intermediate layer composed of the lump of Vectran threads in the second bumper. Fig. 9 shows the damage of the first bumper on the Test No.3, and the impact velocity was 3.14 km/sec. A hole of 20 mm in diameter was produced on the stainless mesh, which was located at the front of the first bumper. On the other hand, a hole with the diameter of 50 mm was generated on the Vectran sheet, which was located at the rear of the first bumper. On the second bumper, a hole with expanded the Vectran threads were found on the first Vectran sheet as shown in Fig. 9. In addition, as the result of the observation of the intermediate layers, a projectile was stopped at the point of the lump of Vectran threads layer shown in Fig. 10-(6). The recovered projectile was a bit of polycarbonate with approximately 7 mm in length.

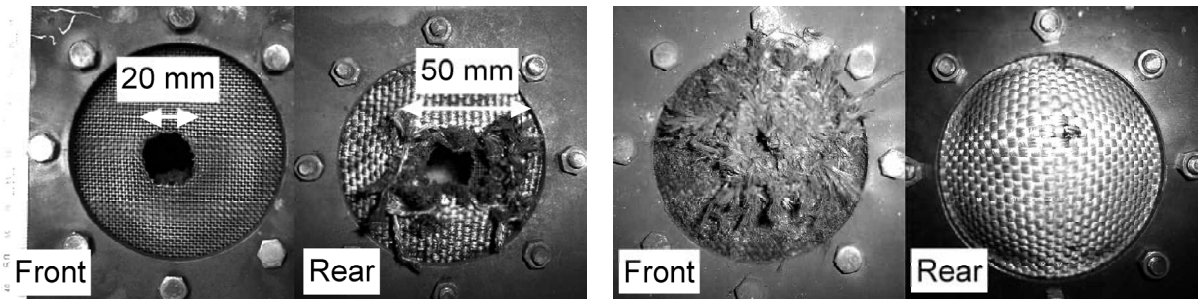

Fig. 9 Impact results of the first bumper(left) and the second bumper(right) on Test No.3, Type III (V=3.14 km/sec)

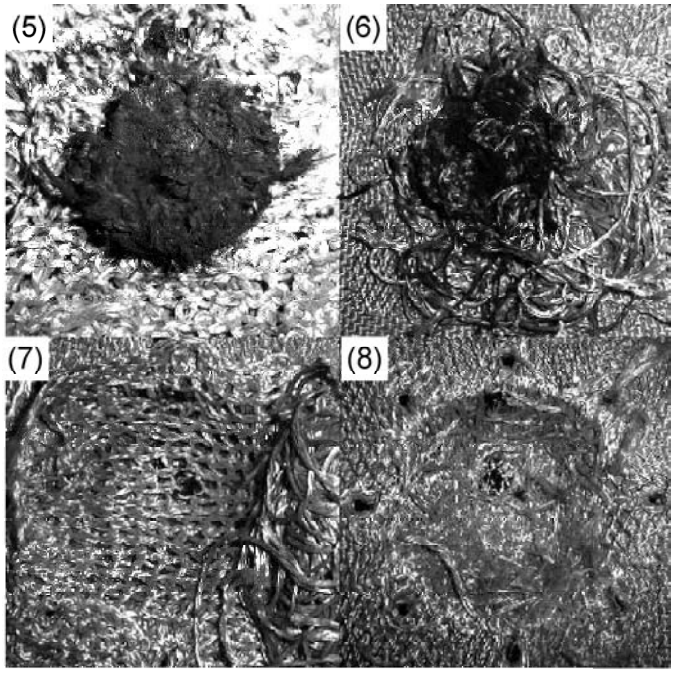

Fig. 10 Impact results of the multi-layer material in the second bumper on Test No.3, Type III (V=3.14 km/sec), Number in Figures corresponds to the number in Table 3

Application for debris mitigation

Using the developed lightweight bumper materials, several applications for debris mitigation are under consideration. There are two concepts in LEO and GEO. The purpose of the debris mitigation in LEO is to remove debris clouds that are potential candidates of generating second debris. Fig. 11 illustrates the concept for mitigation of debris clouds in LEO. The capsule with 10 m in diameter like a balloon captures debris cloud as the result of impacting. The capsule is composed of the developed lightweight bumper materials, and consists of two hemispheric deployable space structures. On the mitigation in GEO, the same concept of the capsule is available. Fig. 11 shows the concept of debris mitigation in GEO. After deploying a pair of the hemispheric structure in GEO, the capsule with 8 m in diameter takes into a satellite as debris. The capsule has the role of protecting debris impacts and preventing accidental explosion of debris in the capsule. Some of capsules decay into the atmosphere, others are removed from GEO to other obits.

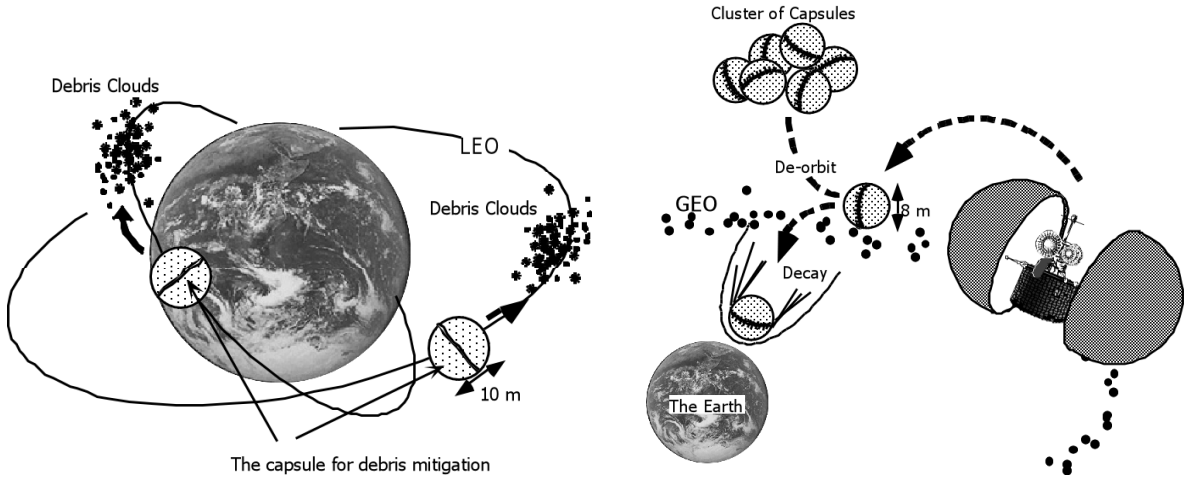

Fig. 11 Mitigation plans using the two hemispheric deployable space structures

Conclusions

We developed new bumper materials composed of a knitted cloth with crochet stitch, a lump of Vectran threads, and a sewn aluminum mesh using high strength fiber, Vectran. Three hypervelocity impact tests were conducted to examine the protection capability of the shield. The results showed the new bumper materials have high protection capability. The shields stopped the polycarbonate projectile with 13 mm in diameter, 1 gram in weight, and 3.14 km/sec in velocity, perfectly. The main reason for the high protection capability of our developed materials may be that the mixed bumper materials consisted of the knitted cloth and the lump of Vectran threads expands energy of shock waves caused by hypervelocity impacts. And also the method of sewing with high strength fiber may contribute to improve the protection capability of the aluminum mesh.

Acknowledgments

The authors acknowledge the contributions of Hiroshi Sugishima at Kuraray who provided us Vectran products, Akira Yamori and Susumu Sasaki on the railgun facility of the Institute of Space and Astronautical Science.

References

[1] Kuraray Co. Ltd. Technical Report of Vectran, 1998.
[2] 3M. Nextel Ceramic Fiber Technical Notebook, URL: http://www.mmm.com/ceramics/.
[3] Kuniaki Shiraki, Fumio Terada, Narihiro Noda, Masahide Katayama, Hydrocode simulation of JEM pressurized module structural performance for space debris hypervelocity impact, Journal of the Japan Society for Aeronautical and Space Sciences, Vol.47, No.544, 1999, pp.189-196.

Thermal Management Coating

Thermal Management Coating As Thermal Protection System for Space Transportation System

Raj Kaul M&P, NASA
C. Irvin Stuckey S&A, USA

AMPET September 2002

Thermal Management Coating

Background

- Thermal Protection System (TPS) loss from ET or SRB during Shuttle flight and related Orbiter tile damage necessitates development of a non-ablative thermal management coating
- Coating design requirements
  - Moisture resistance
  - CTE compatibility with aluminum
  - High temperature performance (Aerothermal test)
  - Maintain low temperature of the aluminum substrate during Shuttle flight
  - Minimum or no structural weight increase

Thermal Management Coating

Coating Study

- Coating formulation
  - High strain to failure binder
    - Flexible liquid epoxy resin
      - Low viscosity
      - Low moisture absorption
      - High temperature stability
  - Heat absorbing microcapsules as additive
      - Micro-encapsulated phase-change materials (15-100 micro)
      - Absorb or release tremendous amounts of heat without corresponding change in temperature

Thermal Management Coating

Coating Study (Cont.)

- Aerothermal Testing (MSFC Hot Gas Facility)
- Thermal Testing
  - TGA, DSC
  - Thermal Conductivity
  - Specific Heat
- Mechanical Testing
  - Strain Compatibility
  - Flatwise Tensile
  - Flatwise Tensile After Aerothermal Testing

Thermal Management Coating

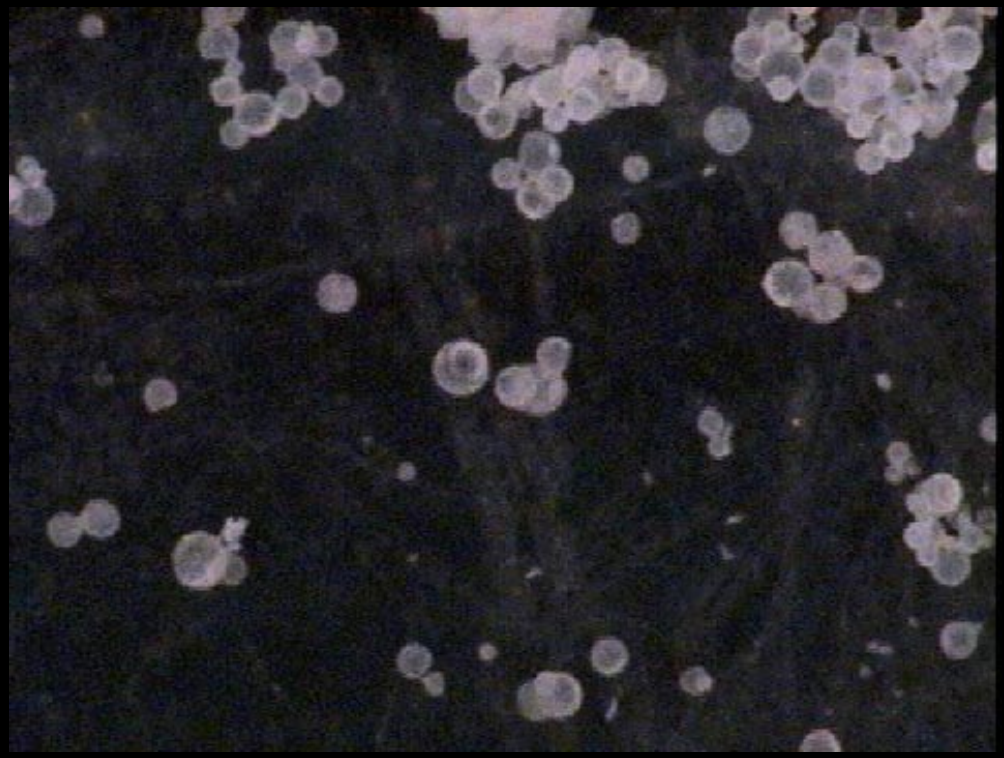

Microcapsules 20X

Thermal Management Coating

Aerothermal Testing

- Test Environment
  - SRB Nose Cap Design Environment (BP 1003)
    - Recovery Enthalpy 600 BTU/lb_m
    - Peak Heating Rate 9.4 BTU/ft^2-sec
- Evaluation Parameters
  - Substrate Temperature
  - Thickness Change
  - Variables
    - Coating thickness
    - Loading percentage of phase change material
    - Different latent heat microcapsules
    - Preconditioning of test specimens
      - Humidity chamber
      - Salt Fog
      - Lightning strike
      - Impact simulation
    - Reusability

Thermal Management Coating

Aerothermal Testing (Cont.)

- Evaluation Parameters
  - Substrate Temperature
  - Thickness Change
- Variables
  - Coating Thickness
    - Minimum Thickness – 25 mils
    - Maximum Thickness –105 mils
  - Loading Percentage
    - Minimum Loading – 33%
    - Maximum Loading – 70%
  - Latent Heat Microcapsules
    - PCM111
    - TH122
    - TH175

Thermal Management Coating

Preconditioning Environments

- Humidity Chamber
  - 95% Relative Humidity
  - 100°F
  - 10 Days
- Salt Fog
  - 5% Saline Solution
  - 100°F
  - 2 Days
- Lightning Strike
- Impact
  - Loads Simulating Ice Impact (14 to 48 ft/lbs)
- Reusability
  - Panel Exposed to SRB Design Environment BP 1003 5 Times

Thermal Management Coating

Test Observations

- Moisture Absorption
  - Slight weight gain (<4 gms after 10 days in humidity chamber)
- Lightning Strike
  - Good electrical insulator
- Impact Testing
  - Partial compaction recovery
- Substrate Temperature
  - Mainly dependent on coating thickness
  - Loading percentage of secondary importance
  - Not affected by preconditioning
  - Reuse causes little decrease in performance
- Thickness Change
  - Minimal recession when surface temperature <600°F
  - Very low recession rate at heating rates <10 BTU/ft^2-sec

Thermal Management Coating

Lightning Strike Test Panel

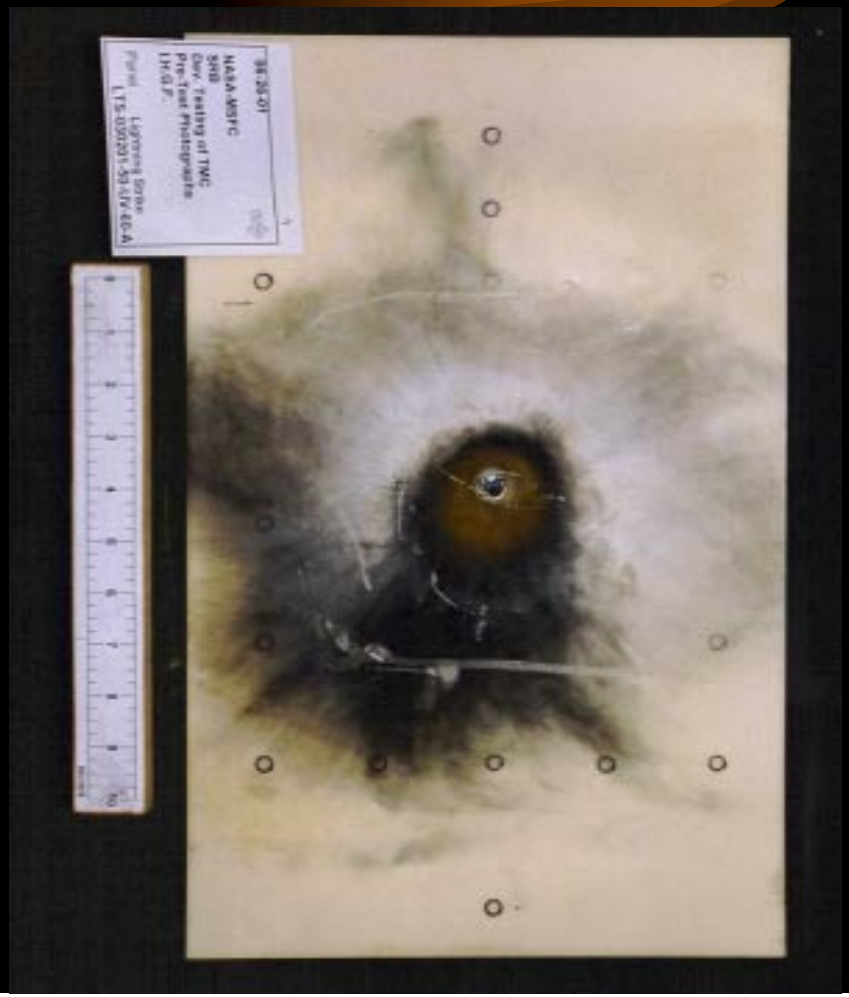

Thermal Management Coating

Test Panel After Impact Testing

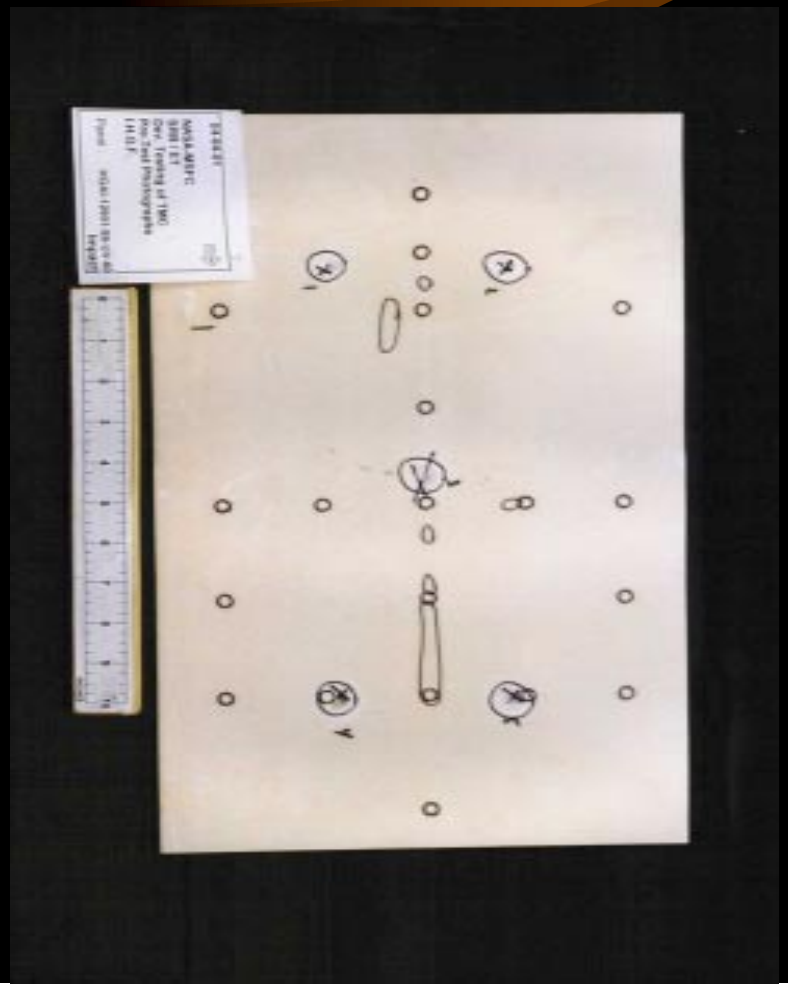

Thermal Management Coating

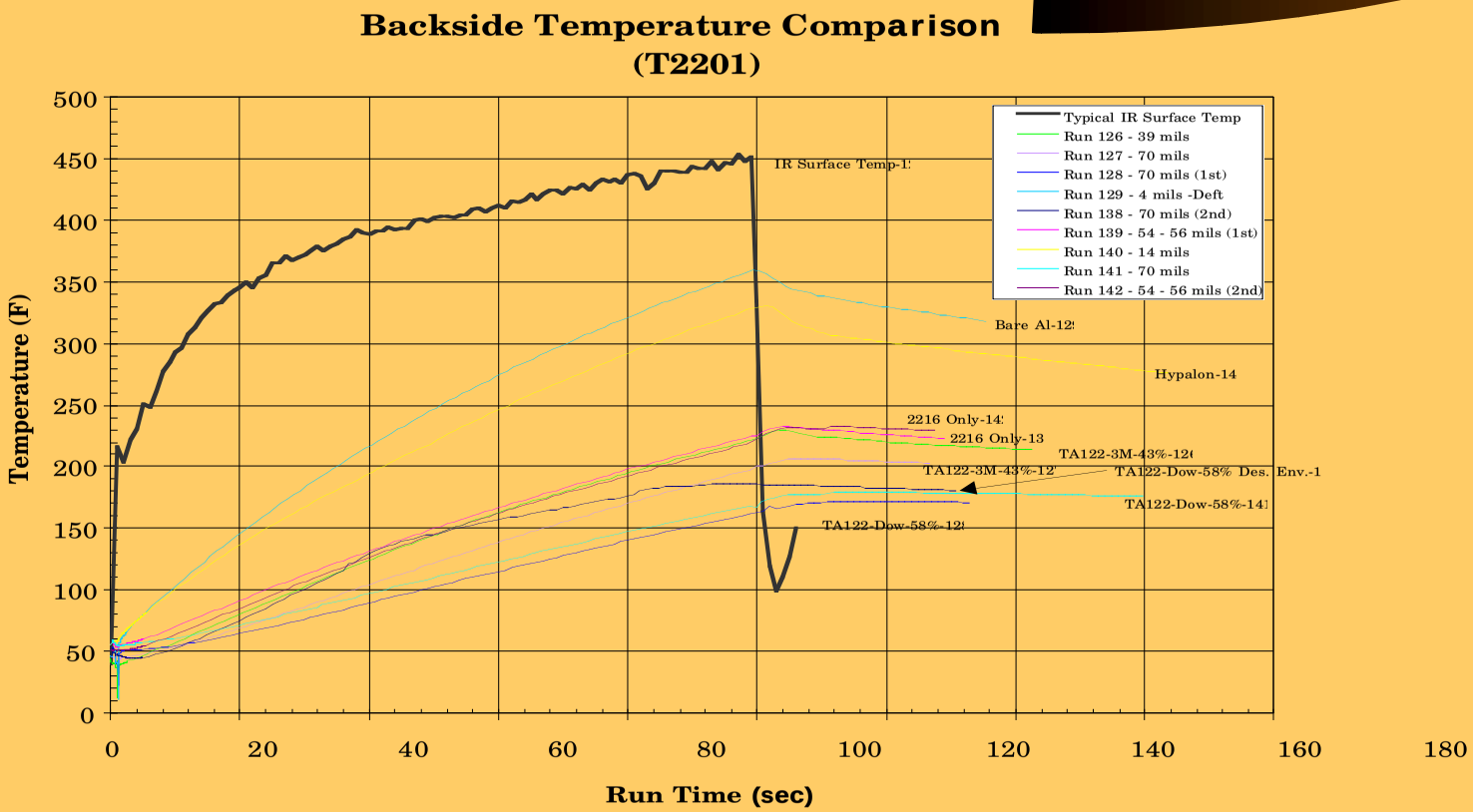

Thermal Management Coating

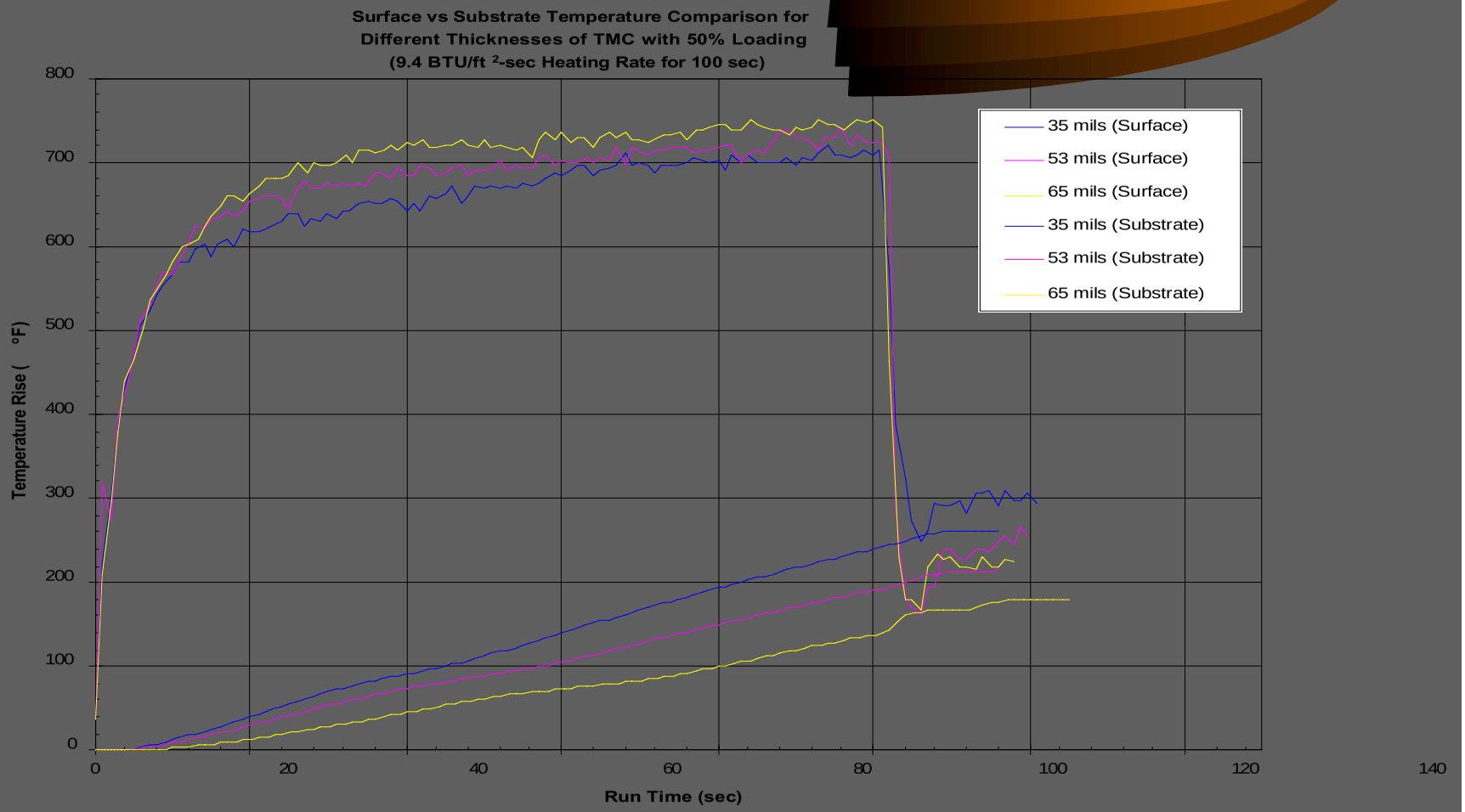

Thermal Management Coating

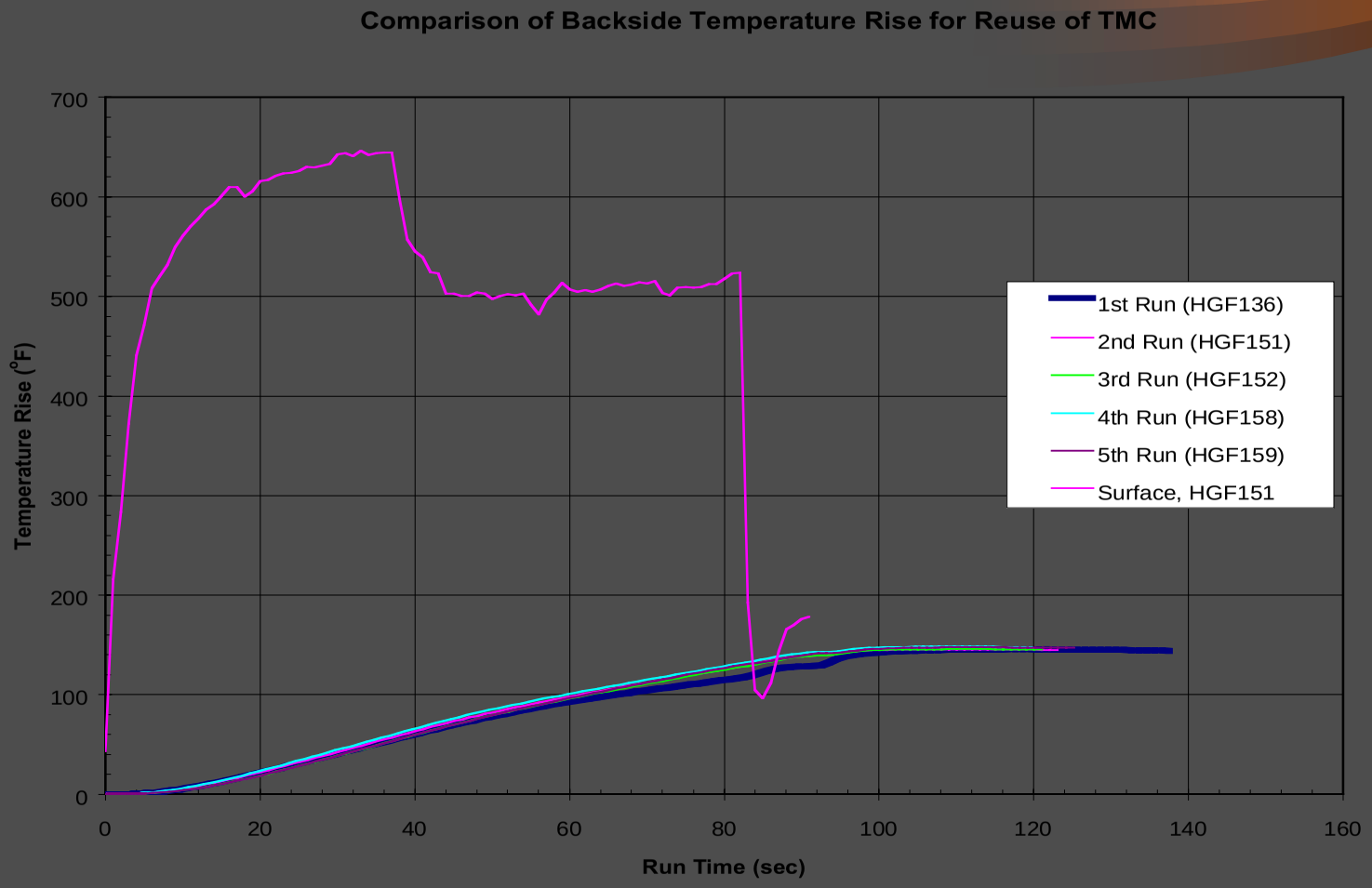

Thermal Management Coating

Thermal Testing

- Charring Temperature of Resin (TGA)
  - 612 °F in air
  - 615 °F in argon
- DSC Data Generated with Different % Loading
- Thermal Conductivity
  - Epoxy 1.52 (BTU-in/hr-ft_-°F) at 170°F
  - TMC 58% Loading 1.67 (BTU-in/hr-ft_-°F) at 170°F
  - TMC 70% Loading 1.65 (BTU-in/hr-ft_-°F) at 170°F
- Specific Heat
  - Epoxy 0.47 (BTU/lb-°F) at 170°F
  - TMC 58% Loading 1.23 (BTU/lb-°F) at 170°F
  - TMC 70% Loading 1.43 (BTU/lb-°F) at 170°F

Thermal Management Coating

Mechanical Testing

- Strain compatibility tensile testing
  - Coating applied to 6061T6Al
  - 50% and 58% loading in epoxy binder
  - The coating failure strain is same as of 6061T6Al

Thermal Management Coating

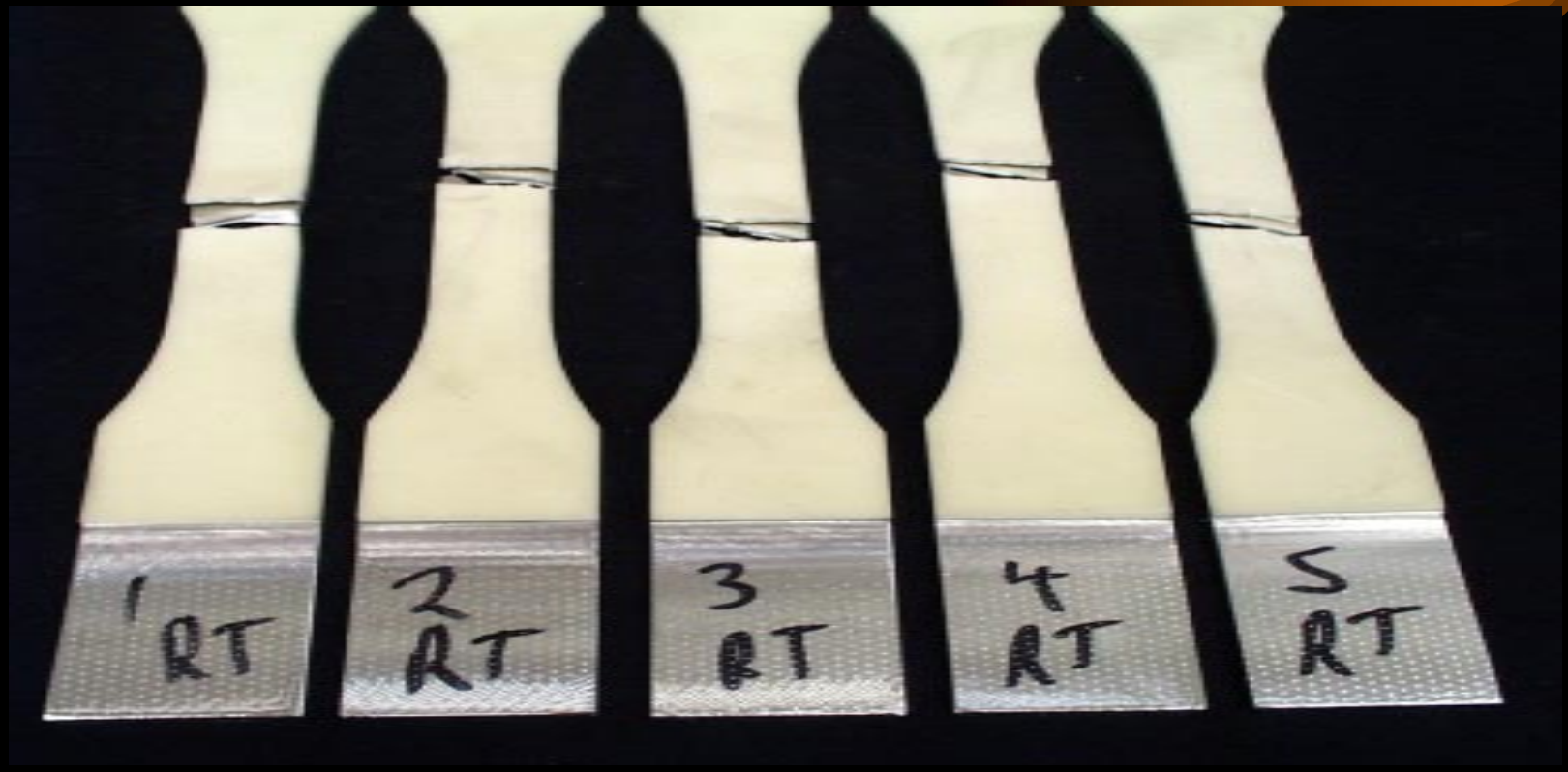

TMCSC-91458UV (58% Loading) Tested at RT

Thermal Management Coating

- Flat-wise Tensile Test Results

50%	Epoxy	60 mils	RT	205.20	Adh
58%	Epoxy	62 mils	RT	244.90	Adh
50%	Epoxy	60 mils	20°F	429.80	Adh
58%	Epoxy	62 mils	20°F	414.40	Adh
50%	Epoxy	60 mils	300°F	9.56	Paint
58%	Epoxy	62 mils	300°F	21.34	Paint
58%	Polyurethane	60 mils	RT	246.00	Adh/Coh
58%	Polyurethane	60 mils	300°F	37.96	Adh

Tensile Coating Film

Filler Loading	Binder	Tensile Strength psi	Tensile Strain (%)	Modulud psi	
50%	Epoxy	198.7	26.3	1262.13	

Thermal Management Coating

Binder	% Loading	Test Environment	Flatwise Tensile (As-Sprayed/Post-HG (psi)		
			20 °F	Ambient	300 °F
Epoxy	58	9.4 BFS for 100 sec	414.4/490.3	244.9/285.9	21.3/22.1
Epoxy	50	9.4 BFS for 36 sec 4.8 BFS for 44 sec	429.8/511.5	205.2/244.7	9.6/15.1
Epoxy	58	9.4 BFS for 36 sec 4.8 BFS for 44 sec	414.4/548.7	244.9/289.4	21.3/23.4

Thermal Management Coating

Conclusions

- Potential Replacement for Current SRB TPS Material and Other Launch Vehicles
- Exhibits Potential for Reusability
- Absorbs Little Moisture
- Good Electrical Insulator
- Further Investigation in Progress

Using Isothermal Microcalorimetry to Determine Compatibility of Structural Materials with High-Test Hydrogen Peroxide (HTP) Propellant

RUDY GOSTOWSKI
Marshall Space Flight Center, TD40
Huntsville, AL 35812
Phone: 256-544-0458
Fax: 256-544-1869
E-mail: Rudy.C.Gostowski@msfc.nasa.gov

Yvonne Villegas, NASA-USRP Intern
Our Lady of the Lake University
San Antonio, TX 79915
Phone: 915-592-6077
E-mail: uvilly@lake.ollusa.edu

Genne Nwosisi, NASA-EOO Intern
Florida A&M University
Tallahassee, FL 32307
Phone: 334-341-5560
E-mail: sweetnene@hotmail.com

High-Test Hydrogen Peroxide (HTP) propellant (≥70%) offers many advantages in space launch applications; however, materials used in construction of propulsion systems must be shown to be compatible with HTP. Isothermal Microcalorimetry (IMC) was used to determine the compatibility of several metallic and non-metallic materials with 90% HTP. The results of these experiments agreed with those from immersion bath tests when the values were converted to % Active Oxygen Loss per week (%AOL / wk).

NASA TECHNICAL STANDARDS PROGRAM

Paul S. Gill
NASA Technical Standards Program Office, NASA Marshall Space Flight Center,
Huntsville, AL 35812, 256-544-2557, paul.gill@msfc.nasa.gov

William W. Vaughan
University of Alabama in Huntsville, Huntsville, AL 35899

ABSTRACT

The NASA Technical Standards Program was officially established in 1997 as result of a directive issued by the Administrator. It is responsible for Agency wide technical standards development, adoption (endorsement), and conversion of Center-unique standards for Agency wide use. One major element of the Program is the review of NSA technical standards products and replacement with non-Government Voluntary Consensus Standards in accordance with directions issued by the Office of Management and Budget. As part of the Program's function, it developed a NASA Integrated Technical Standards Initiative that consists of and Agency wide full-text system, standards update notification system, and lessons learned—standards integration system. The Program maintains a "one stop-shop" Website for technical standards ad related information on aerospace materials, etc. This paper provides information on the development, current status, and plans for the NAS Technical Standards Program along with metrics on the utility of the products provided to both users within the nasa.gov Domain and the Public Domain.

NASA TECHNICAL STANDARDS PROGRAM

The NASA Technical Standards Program (http://standards.nasa.gov) was formally established in 1997 as an Agencywide effort by direction of the Administrator. It has the following principal elements:

***Increase NASA Use of Voluntary Consensus (non-Government) Technical Standards.
***Selective Development of NASA-Unique Technical Standards.
***Develop and Promote the Use of an Integrated Technical Standards Initiative (Full-Text Standards Access, Standards Update Notifications, and Lessons Learned—Standards Integration).
***Exploit the Potential of Web-based Standardization Information.

Technical Standards are an integral part of all engineering development efforts, especially those in the aerospace industry. Designers and engineers should be among the most aggressive supporters of a strong Technical Standards program. Standardization activities establish engineering and technical applications for processes and practices and, in doing

so, enhance engineering capabilities. Thus, they enable designers to not dissipate their energies on the costly exercise of "reinventing the wheel."

Like their colleagues in the private sector, NASA has also depended upon the active application of Technical Standards developed by the Agency through its various Centers, as well as Department of Defense (DoD) Technical Standards (i.e., Military Standards, Specifications, Handbooks, etc.) and those produced by non-Government Standards Developing Organizations (SDOs). Since the late 1990s, NASA has been engaged in a major Agencywide effort to review the Technical Standards produced by its Centers and, to the degree practical, utilizes a systematic consensus driven approach resulting in the adoption (endorsement) of relevant non-Government Technical Standards to replace its Center-developed Technical Standards. The adopted Technical Standards are known as "NASA Preferred Technical Standards." In areas where adoption is not practical, efforts have been made to consolidate similar Center-developed Technical Standards and produce replacement Technical Standards endorsed for Agencywide use. This substantial endeavor was undertaken and subsequently increased in response to the Office of Management and Budget (OMB) Circular A-119 "Federal Participation in the Development and Use of Voluntary Consensus Standards and in Conformity Assessment Activities", February 1998.

In the process of responding to the directives contained in OMB Circular A-119, it was discovered that the Agency's Programs/Projects and engineering staff were in need of a consolidated Web-based Technical Standards database accessible from a single source with engineering oversight. The information requested included full-text Technical Standards products issued by the Agency and its Centers, Department of Defense, and non-Government SDOs. In addition, requirements for timely information on changes in Technical Standards products were also noted.

The need for improving the process to address customer needs for efficiency in the acquisition of Technical Standards products is one of the Strategic Initiatives identified in the American National Standards Institute's (ANSI) National Standards Strategy For The United States (http://web.ansi.org/public/nss.html). In particular the document identified the need for cost-effective mechanisms such as update notification and electronic accessibility of Technical Standards products from SDOs. The NASA Integrated Technical Standards Initiative, while not developed to solve this problem for the United States, is a step toward solving the problem of Technical Standards distribution and, thus, enhancement of engineering capabilities within one Government Agency that has potential for use by others.

After several reviews and pilot exercises, additional dialog with several Program/Project Managers and engineering groups, the concept of a "One Stop Shop" web-based NASA Integrated Technical Standards Initiative began to materialize. The two main advantages that became immediately apparent were: (1) The Agency's engineering capabilities will be considerably enhanced by providing NASA's technical and engineering communities with immediate on-line access to Technical Standards products and (2) Significant cost savings could be realized by having one unified Agencywide Full-Text Technical

Standards System versus having fourteen or more individual groups within the Agency acquiring Technical Standard products independent of each other. Standards updates and lessons learned were also indicated as important information to enhance the engineering usage of Technical Standards. Thus, the unique "NASA Integrated Technical Standards Initiative" was born. The Initiative consists of the following three Systems:

(1) Agencywide Full-Text Technical Standards System

(2) Standards Update Notification System

(3) Lessons Learned/Best Practices/Application Notes—Standards Integration System.

The primary goal of the NASA Technical Standards Initiative is to develop a suite of collaborative tools to: (1) Augment NASA's use and support the adoption of non-Government Voluntary Consensus Standards by making them available from a single source, (2) Provide notifications on changes, updates, and revisions to existing Technical Standards, (3) Provide information on engineering lessons learned, best practices, and experiences related to specific Technical Standards products, and (4) Enhance the engineering capabilities of the Agency. Technical Standards provide a major opportunity to achieve the goal of enhancing engineering capabilities, especially when a process such as the NASA Integrated Technical Standards Initiative is implemented. This Initiative consists of the following Systems.

Agencywide Full-Text Technical Standards System

This System provides access to full-text on-line Technical Standards products and distribution for NASA use. Technical Standards products are currently available from 108 Standards Developing Organizations, including those of NASA, DoD, and other Agencies. For those Technical Standards not available electronically, a hardcopy is made available to the requester within 24-36 hours. A pilot version of the System was implemented in 2000 with favorable feedback leading to the Agencywide implementation of the System in June 2001. Currently their are over 5,500 registered NASA and supporting contractor users within the <nasa.gov> Domain.

Standards Update Notification System

This System provides NASA and its supporting contractors with notice of updates (revisions, cancellations, superseded documents, etc.) to Technical Standards products that they have identified for use on their Programs/Projects or research activities. This information is provided so that update notices of technical changes on a Technical Standards product can be evaluated by the Program/Project Manager for impact on the Program/Project requirements. This System is linked with the Agencywide Full-Text Technical Standards System to provide the latest full-text versions of the Technical Standards on demand. Documents identified by the user and accepted for update notification are screened relative to adoption as NASA Preferred Technical Standards.

The System was made available Agencywide in October 2001. There are now over 4,000 standards documents registered by users for update notifications.

Lessons Learned/Best Practices/Application Notes—Standards Integration System

This System provides links to Lessons Learned/Best Practices/Application Notes that have applicability to use of individual Technical Standards products. As of this date, 225 Lessons Learned from NASA's Lessons Learned Information System have been linked to 125 NASA Preferred Technical Standards listed on the NASA Technical Standards Program Website. Also, 140 Application Notes have been related to 95 NASA Preferred Technical Standards. Identifying other Application Notes and Lessons Learned to link with specific NASA Preferred Technical Standards is a continuing effort. These Lessons Learned, Best Practices, and Application Notes will also be of great benefit in identifying non-Government Voluntary Consensus Standards to adopt/endorse for NASA use. Over 150 links to engineering Lessons Learned/Best Practices Websites and documents have been identified and provided on the Program's Website. These additional sites are not only from NASA Facilities, but other Government and non-Government bodies. They provide users with technical information on a variety of aerospace engineering related lessons learned topics. The NASA Technical Standards Program Office prepared a paper entitled "Lessons Learned and Technical Standards—A Logical Marriage" that was published in the November 2001 issue of ASTM Standardization News and subsequently reprinted in DOD Standardization Journal and The Standards Forum of DOE. It focuses on the importance of the relationship between Lessons Learned and Technical Standards, and, thus, the enhancement of engineering capabilities.

An example is provided of what a NASA staff member or supporting contractor user of the NASA Technical Standards Program Website has available. It is shown on the figure of the document Summary Page. When the user calls up a NASA Preferred Technical Standard under the Agencywide Full-Text Technical Standards System, a document Summary Page will appear that provides summary information on the Technical Standard. When available, information on applicable Application Notes, Lessons Learned and Best Practices is provided along with link to the Standards Update Notification System to receive notice of any revisions, updates, cancellations, etc. on a given Technical Standard.

Conclusion

Figure one provides a view of the NASA Technical Standards Program Website Homepage. On it the NASA ACCESS and PUBLIC ACCESS menu items are noted along with some allied menu topics. To date, the usage of the three Systems in the NASA Technical Standard Initiative has been outstanding in terms of user interests and value to their work on NASA Programs/Projects and research activities. The metrics associated with each of these Systems continue to show increased usage. This is due to the ready availability of the NASA Technical Standards Program products and related information on-line, and reinforces the validity of the "One Stop-Shop" concept.

The integration of Technical Standards, update notifications, and lessons learned information is one step toward the goal of significantly enhancing engineering capabilities necessary to meet the future demands of the Agency for timely, productive, and reliable space systems and contributing to improved cost.

Figures two and three provide an overview on the current focus and future thrusts of the NASA Technical Standards Program. The conversion of Center-developed standards to NASA Preferred Technical Standards and adoption of non-Government standards remains a key focus of the Program. Improving the awareness of the Program and its products among the Agency's staff and supporting contractors continues to be a challenge. Promoting the development of new standards that will serve the Agency is a current initiative, capitalizing on new technology and experiences. Future thrusts will include additional efforts on the integration of lessons learned with technical standards. New venues will be explored relative to how the Program's products can better contribute to the Agency's engineering capabilities and the Administrator's "One NASA" initiative.

Bibliography

Gill, P. S., Barcia, D., and Vaughan, W. W. "Lessons Learned and Technical Standards: A Logical Marriage for Future Space Systems Design." 53rd International Astronautical Congress, The World Space Congress—2002, Paper # IAC-02-U.3.04, Houston, TX, October 10-19, 2002.

Gill, P. S., Vaughan, W. W., and Garcia, D., "Lessons Learned and Technical Standards: A Logical Marriage." *ASTM Standardization News*, Vol. 29. No. 11, November 2001. pp 2-27.

.

Prepared For Presentation at:
5th Aerospace Materials, Processes, and Environment Technology Conference
Von Braun Center
Huntsville, Alabama

September 16-17, 2002

Figure 1. NASA Technical Standards Program Homepage

NASA TECHNICAL STANDARDS PROGRAM

PROGRAM STRATEGY OVERVIEW

- **CURRENT FOCUS**
  - —Conversion of Center-developed Standards Into NASA Preferred Technical Standards
  - —Adoption/endorsement of Non-government VCS Products
  - —Maintaining And Enhancing Program Website Contents
  - —Trying To Make All Agency Employees And Support Contractors Aware of The Program s Website And Contents
  - —Explore New Or Candidate Program Thrusts That Support The Enhancement Of Agency Engineering Capabilities, I.E., Alert/suns Utility, Lessons Learned Integration, Collaboration With Knowledge Management, Information Technology, Etc.
  - —Promote New Standards Development, Both NASA And VCS, That Serve Agency Needs

Figure 2

NASA TECHNICAL STANDARDS PROGRAM

PROGRAM STRATEGY OVERVIEW (Cont'd)

- **Future Thrusts:**
  - —Assessment Of Program Products Impact On Agency Engineering And Program/project Management Activities
  - —Increase Effort On Lessons Learned —Standards Integration Initiative. Currently Resource Constrained
  - —Increase Activities Within Agency For Both NASA Developed Standards Proposals And VCS Development Participation.
  - —Explore New Venues The Technical Standards Program Products And Operational Format Can Contribute Relative To Better Contributing To Agency s Engineering Capabilities And NASA Administrator s One NASA Initiative.

Figure 3

STANDARDIZATION EFFORTS FOR MECHANICAL TESTING AND DESIGN OF ADVANCED CERAMIC MATERIALS AND COMPONENTS

Jonathan A. Salem
Life Prediction Branch
NASA Glenn Research Center
Cleveland, Ohio
(216) 433-3313
jsalem@grc.nasa.gov

Michael G. Jenkins
Department of Mechanical Engineering
University of Washington
Seattle, Washington
(206) 685-7061
jenkinsm@u.washington.edu

ABSTRACT

Advanced aerospace systems occasionally require the use of very brittle materials such as sapphire and ultra-high temperature ceramics. Although great progress has been made in the development of methods and standards for machining, testing and design of component from these materials, additional development and dissemination of standard practices is needed. ASTM Committee C28 on Advanced Ceramics and ISO TC 206 have taken a lead role in the standardization of testing for ceramics, and recent efforts and needs in standards development by Committee C28 on Advanced Ceramics will be summarized. In some cases, the engineers, etc. involved are unaware of the latest developments, and traditional approaches applicable to other material systems are applied. Two examples of flight hardware failures that might have been prevented via education and standardization will be presented.

INTRODUCTION

Environmental and energy concerns (often bolstered by governmental regulations) have placed increasingly greater demands on materials used in advanced engineering designs such as aerospace systems. For example, as greater efficiencies are sought and achieved in the design of gas turbine engines, so too have the temperature, strength and weight requirements of their components changed to "push the limit" of the mechanical properties of the various materials (generally metallic alloys). Large amounts of time and effort have been devoted to the search for structural materials that will keep pace with these engineering demands. Often these searches identify underutilized materials that can be classified as “brittle.” In some cases, such as sapphire for windows, processing successes (both primary and secondary) have led to the successful use of an advanced ceramic in demanding applications [1]. In other cases, in spite of tremendous strides in understanding and processing materials, only recently have structural ceramic materials, such as silicon nitrides or silicon carbide fiber-reinforced silicon carbide matrix composites, reached the developmental stage required to receive focused attention as plausible successors to the more traditional metallic alloys [2]. The applications contemplated require optimum material behavior with physical and mechanical property reproducibility, component reliability, and well-defined methods of data treatment and materials analysis. As advanced ceramics are contemplated for introduction into advanced heat engine, these issues are best dealt with via standard methods [2].

A variety of organizations, such as ASTM, ISO, and the NASA TSP, are involved with the development of standards, and the standards developed by one organization often feed into the development of standards in another organization. The American Society for Testing and Materials (ASTM) [a.k.a., ASTM International] is the primary standards writing establishment in the United States. As a private, nonprofit corporation, ASTM relies upon the voluntary cooperation of industry, government, and academe to develop standards by full consensus. ASTM Committee C28 "Advanced Ceramics" was formed in 1986 when it became apparent that ceramics were being considered for "high-tech" applications. More background on ASTM and its committees can be found at the organization’s website.[1]

Advanced ceramics are defined [3] as "highly-engineered, high-performance, predominantly non-metallic, inorganic ceramic material having specific functional attributes." A standard is defined by ASTM [4] as "a rule for an orderly approach to a specific activity, formulated and applied for the benefit and cooperation of all." The implication of the term "standards" is manifold. "Standards" may mean fundamental test methodologies and units of

[1] www.astm.org

measure to the researcher and the technical community. However, to the manufacturer or end-product user, "standards" are materials specifications and tests to meet requirements. Amongst designers, manufacturers and product users, commercial "standards" equate to the rules and terms of information transfer [5]. Because the term “standard” can be connoted differently depending on the user, it is the role of standards development organizations to assist in bringing together seemingly divergent interests of industry, government and academe by developing voluntary consensus "standards".

However, it is important to note that ASTM's organizational role is as a facilitator to the "real" standards writers, the task group members. The flow of the standardization process is from the task groups to the ASTM Committee on Standards (COS). An ASTM standard may take the form of a guide (a series of options or instructions that do not recommend a specific course of action), a practice (a definitive procedure for performing one or more specific operations or functions that does not produce a test result), a terminology standard (a document comprising definitions of terms; descriptions of terms; explanations of symbols, abbreviations, or acronyms), a test method (a definitive procedure for the identification, measurement, and evaluation of one or more qualities, characteristics, or properties of a material, product, system, or service that produces a test result). In addition, a standard may also be in the form of a classification (a systematic arrangement or division of materials, products, systems, or services into groups based on similar characteristics such as origin, composition, properties, or use) or a specification (a precise statement that indicates the procedures for determining whether each of the requirements of a material, product, system, or service is satisfied).

ASTM Committee C28 is organized into various non-administrative subcommittees including C28.01 Properties and Performance, C28.02 Design and Evaluation, C28.05 Characterization and Processing, C28.07 Ceramic Matrix Composites, C28.91 Nomenclature and Education, and C28.94 ISO TAG, with task groups addressing specific technical topics under each subcommittee. Leadership and membership of the committee and various subcommittees are distributed over approximately 100 representatives from industry, government, and academe. Currently (August 2002) there are 40 standards for advanced ceramics under the jurisdiction of Committee C28 as shown in Table 1, and 3 new standards in the balloting process as also shown in Table 1.

Outside the United States, the International Organization for Standardization (ISO) is recognized as the international forum for normalization that crosscuts regions and nations. ISO standards are often not intended to be new standards but instead are intended to harmonize existing standards to provide consensus documents that promote compliance by agreement and “buy-in.” Because of this, ISO standards developed by three guiding principles (consensus, industry-wide, and voluntary) are widely recognized, giving clear benefits to industry and consumers. Some examples of successful ISO standards include ISO film speed codes, ISO standardized telephone and banking card formats, standardized freight containers, standardized symbols for the SI systems of units, and standardized paper sizes. More background on ISO and its committees can be found at the organization’s website.[2]

ISO defines standards as documented agreements containing technical specifications or other precise criteria to be used consistently as rules, guidelines, or definitions of characteristics to ensure that materials, products, processes and services are fit for their purposes. Thus, the term “ISO standard” includes all types of standards from test method to specification. Over 140 member nations participate in ISO activities. A single standards writing organization from each member nation (e.g., ANSI for the USA) provides the technical and administrative expertise for ISO efforts. In the USA, because ANSI is an association of many different standards writing organizations (SDOs) within the USA, actual technical work for an ISO committee is often carried out by a technical advisory group (TAG) within one of these SDOs (e.g., ASTM). Just as in ASTM, the actual development of standards within ISO is decentralized, and carried out in 2850 committees, subcommittees and working groups within ISO. Although the “real work” of ISO is carried out by the technical experts, the Central Secretariat in Geneva acts to ensure the flow of documents, clarifies administrative details, coordinates balloting on draft international standards, and convenes meetings of committees. The scope of ISO not limited to any particular topic (except electrical and electronic engineering standards). Over 224 different technical committees address topics ranging from information technology to threaded fasteners, to paper to glass containers to nuclear energy to earth moving equipment to environmental management to civil defense.

[2] www.iso.ch

ISO Technical Committee (TC) 206 was established in 1993 to address issues of harmonizing and advancing standards in the area of fine (advanced, technical) ceramics. Japan is the committee secretariat. Currently, TC206 is comprised of 14 participating (P) members and 19 observer (O) members, each representing a different nation that provides technical experts for its 28 working groups. While the primary focus of the committee to date has been structural applications of ceramics (e.g., mechanical properties), non-structural applications such as coatings, insulators, etc are well within its scope. The standards process within TC206 is initiated by a P member who submits a new work item proposal. This proposal can be accepted after first meeting several criteria: at least two national/regional standards must currently exist in the topical area, a market need exists for the proposed standard (minimum rating score of 15 out of a possible 25 points), a working draft of the proposed standard must be prepared and at least 5 P members must be willing to serve on the working group. Once a new work item is accepted, a working group is established and the technical experts refine the working draft (WD) to a committee draft (CD). When the document has reached sufficient maturity it is submitted for a TC vote to elevate it to a draft international standard (DIS). If no technical objections are raised, the document finally advances to international standard (IS). Table 2 is a list of IS and DIS documents generated by TC206 to date. Numerous other WD and CD documents developed by the 28 working groups are not shown.

At NASA, the NASA Technical Standards Program (TSP) is charged with not only developing an integrated NASA Preferred Technical Standards System that improves the availability of technical standards for design, development and operation of NASA's Programs and Projects, but also to increase use and development of voluntary, non-government standards by enhancing the awareness of standardization in NASA. Just as with ASTM and ISO, the NASA TSP recognizes certain types of standards products. These include technical standards (uniform engineering and technical requirements for processes, procedures, practices and methods); specifications (in support of acquisition by clearly and accurately describing technical requirements); handbooks (authoritative engineering technical, or design information and data relating to processes, procedures, recommended practices and methods); guidelines (technical information in support of standards, specifications and handbooks); regulations (standards accepted and enforced by the Government); and codes (a group of standards dealing with one subject). More background on NASA TSP can be found at the organization's website.[3]

A very visible aspect of NASA TSP is its publicly accessible website and its link to "Lessons learned" database [6]. This comprehensive database has the potential of being a boon to technical personnel because it links relevant technical standards to lessons learned in both developing and using standards. Such lessons in the past have often been anecdotal and as such were not documented. The NASA TSP provides an archival resource to not only document past experience but also a mechanism for extrapolated future efforts as part of long range planning for future standards development based on past needs.

This introduction has provided a brief background on the status of some of the higher profile standardization efforts for advanced ceramics (ASTM and ISO) as well as a forum in which standards and lesson learned have been combined (NASA TSP) to provide an archival data base for current usage and future development of standards. In the next section, some examples of advanced ceramics applications are discussed as a background for potential standardization. These examples are followed by discussion and conclusions sections in which some future directions for standards on advanced ceramics are posed.

EXAMPLES OF NEEDS FOR STANDARDS

Example 1 - Failure of a Leading Edge

Background: In order to improve the maneuverability and aerodynamics of future generations of re-entry vehicles and airframes, sharper leading edges are required. Sharper leading edges result in higher edge temperatures and the need for more oxidation and temperature resistant leading edge materials. One class of materials for such applications is commonly referred to as UHTC's (ultra-high temperature ceramics) that are refractory metal diborides containing additives such as SiC and possibly carbon. Recent testing of three candidate UHTC materials resulted in catastrophic failure of a number of the segments, as shown in Figure 1.

[3] http://standards.nasa.gov

Table 1 Summary of Completed and In-ballot Standards of ASTM Committee C28 "Advanced Ceramics"

Responsible Subcommittee	**Designation** (Year adopted)	**Title**
C28.01 Properties and Performance	C1161-01 (1990)	Test Method for Flexural Strength of Advanced Ceramics at Ambient Temperatures
	C1198-01 (1991)	Test Method for Dynamic Young's Modulus, Shear Modulus, and Poisson's Ratio for Advanced Ceramics by Sonic Resonance
	C1211-02 (1992)	Test Method for Flexural Strength of Advanced Ceramics at Elevated Temperatures
	C1259-01 (1994)	Test Method for Dynamic Young's Modulus, Shear Modulus, and Poisson's Ratio for Advanced Ceramics by Impulse Excitation of Vibration
	C1273-95 (1994)	Test Method for Tensile Strength of Monolithic Advanced Ceramics at Ambient Temperatures
	C1291-95 (1995)	Test Method for Elevated Temperature Tensile Creep Strain, Creep Strain Rate, and Creep Time to Failure for Advanced Monolithic Ceramics
	C1323-96 (1996)	Test Method for Ultimate Strength of Advanced Ceramics with Diametrally Compressed C-Ring Specimens at Ambient Temperatures
	C1326-99 (1996)	Test Method for Knoop Indentation Hardness of Advanced Ceramics
	C1327-97 (1996)	Test Method for Vickers Indentation Hardness of Advanced Ceramics
	C1361-01 (1996)	Practice for Constant-Amplitude, Axial, Tension-Tension Cyclic Fatigue of Advanced Ceramics at Ambient Temperatures
C28.02 Design and Evaluation	C1366-97 (1997)	Test Method for Tensile Strength of Monolithic Advanced Ceramics at Elevated Temperatures
	C1368-01 (1997)	Test Method for Determination of Slow Crack Growth Parameters of Advanced Ceramics by Constant Stress-Rate Flexural Testing at Ambient Temperature
	C1421-01 (1999(	Test Methods for the Determination of Fracture Toughness of Advanced Ceramics
	C1424-99 (1999)	Test Method for Compressive Strength of Monolithic Advanced Ceramics at Ambient Temperatures
	C1465-00 (2000)	Test Method for Determination of Slow Crack Growth Parameters of Advanced Ceramics by Constant Stress-Rate Flexural Testing at Elevated Temperature
	C1470-00 (2000)	Guide for Testing the Thermal Properties of Advanced Ceramics
	C1499-01 (2002)	Test Method for Monotonic Equibiaxial Flexural Strength Testing Of Advanced Ceramics At Ambient Temperature
	In ballot (2002)	Test Method for Ultimate Strength of Advanced Ceramics with Diametrally Compressed O-Ring Specimens at Ambient Temperatures
	In ballot (2002)	Determination of Slow Crack Growth Parameters of Advanced Ceramics by Constant Stress Flexural Testing (Stress Rupture) at Ambient Temperature
	C1175-99 (1991)	Guide to Test Methods for Nondestructive Testing of Advanced Ceramics
	C1212-98 (1992)	Practice of Fabricating Ceramic Reference Specimens Containing Seeded Voids
	C1239-95 (1993)	Practice for Reporting Uniaxial Strength Data and Estimating Weibull Distribution Parameters for Advanced Ceramics
	C1331-96 (1996)	Practice for Measuring Ultrasonic Velocity in Advanced Ceramics with the Broadband Pulse-Echo Cross-Correlation Method
	C1332-96 (1996)	Test Method for Measurement of Ultrasonic Attenuation Coefficients of Advanced Ceramics by the Pulse-Echo Contact Technique
	C1336-96 (1996)	Practice for Fabricating Non-Oxide Ceramic Reference Specimens Containing Seeded Inclusions
C28.05 Characterization and Processing	C1251-95 (1993)	Guide for Determination of Specific Area (of Advanced Ceramics) by Gas Adsorption
	C1274-95 (1994)	Test Method for Advanced Ceramic Specific Area by Physical Adsorption
	C1282-96 (1995)	Test Method for Determining Particle Size Distribution of Advanced Ceramics by Centrifugal Photo Sedimentation
	C1322-96 (1996)	Practice for Fractography and Characterization of Fracture Origins in Advanced Ceramics
	C1494-01 (2001)	Test Method for Determination of Mass Fraction of Carbon, Nitrogen, and Oxygen in Silicon Nitride Powder
	C1495-01 (2001)	Test Method for Effect of Surface Grinding on Flexure Strength of Advanced Ceramics
	In-ballot (2001)	Test Method for Particle Size Distribution of Silicon Nitride or Silicon Carbide by X-ray Monitoring of Gravity Sedimentation

Table 1 Summary of Completed and In-ballot Standards of ASTM Committee C28 "Advanced Ceramics" (cont'd)

C28.07 Ceramic Matrix Composites	C1275-00 (1994)	Test Method for Monotonic Tensile Strength Testing of Continuous Fiber-Reinforced Advanced Ceramics with Solid Rectangular Cross Sections at Ambient Temperatures
	C1292-95 (1995)	Test Method for Shear Strength of Continuous Fiber-Reinforced Advanced Ceramics at Ambient Temperatures
	1337-96 (1996)	Test Method for Creep and Creep Rupture of Continuous Fiber-Reinforced Advanced Ceramics under Tensile Loading at Elevated Temperatures
	C1341-00 (1996)	Test Method for Flexural Properties of Continuous Fiber-Reinforced Advanced Ceramics
	C1358-96 (1996)	Test Method for Monotonic Compressive Strength Testing of Continuous Fiber-Reinforced Advanced Ceramics with Solid Rectangular Cross Sections at Ambient Temperatures
	C1359-96 (1996)	Test Method for Monotonic Tensile Strength Testing of Continuous Fiber-Reinforced Advanced Ceramics with Solid Rectangular Cross Sections at Elevated Temperatures
	C1360-01 (1996)	Practice for Constant-Amplitude, Axial, Tension-Tension Cyclic Fatigue of Continuous Fiber-Reinforced Advanced Ceramics at Ambient Temperatures
	C1425-99 (1999)	Test Method for Test Method for Interlaminar Shear Strength of 1-D and 2-D CFCCs at Elevated Temperatures
	C1458-00 (2000)	Test Method for Transthickness Tensile Strength of Continuous Fiber- Reinforced Advanced Ceramics with at Ambient Temperatures
	In-ballot (2002)	Test Method for Tensile Strength and Young's Modulus for High-Modulus Single Filament Advanced Ceramics
C28.91 Nomenclature	C1145-94 (1989)	Definition of Terms Relating to Advanced Ceramics
	C1286-95 (1995)	System for Classification of Advanced Ceramics

* As of August 2002 **Note:** CXXXX is the permanent designation, -XX is the year of the most recent modification

Table 2 Summary of Completed and Draft Standards of ISO Technical Committee TC206 "Fine (Advanced, Technical) Ceramics"

Designation (Year adopted)	**Title**
ISO 14703 (2000)	Fine ceramics (advanced technical ceramics) – Sample preparation for the determination of particle size distribution of ceramic powders
ISO 14704 (2000)	Fine ceramics (advanced, technical ceramics) – Test method for flexural strength of monolithic ceramics at room temperature
ISO 14705 (2000)	Fine ceramics (advanced technical ceramics) – Test method for hardness of monolithic ceramics at room temperature
ISO 15165 (2001)	Fine ceramics (advanced technical ceramics) – Classification system
ISO 15490 (2010)	Fine ceramics (advanced technical ceramics) – Test method for tensile strength monolithic ceramics at room temperature
ISO 15733 (2001)	Fine ceramics (advanced technical ceramics) – Test method for tensile stress-strain behavior of continuous fiber reinforced composites room temperature
ISO 15761 (2002)	Fine ceramics (advanced technical ceramics) – Test method for elastic moduli of monolithic ceramics at room temperature by sonic resonance
ISO 15762 (2001)	Fine ceramics (advanced technical ceramics) – Test method for linear thermal expansion of monolithic ceramics by push rod technique
ISO/DIS 15732	Fine ceramics (advanced technical ceramics) – Test method for fracture toughness of monolithic ceramics at room temperature by SEPB method
ISO/DIS 17565	Fine ceramics (advanced technical ceramics) – Test method for flexural strength of monolithic ceramics at elevated temperature
ISO/DIS 18754	Fine ceramics (advanced technical ceramics) – Determination of density and apparent porosity
ISO/DIS 18756	Fine ceramics (advanced technical ceramics) – Determination of fracture toughness of monolithic ceramics at room temperature by SCF method
ISO/DIS 18757	Fine ceramics (advanced technical ceramics) – Determination of specific surface area of ceramic powders by the gas adsorption using the BET method
ISO/DIS 20501	Fine ceramics (advanced technical ceramics) – Weibull statistics for strength data
ISO/DIS 20507	Fine ceramics (advanced technical ceramics) – Terminology
ISO/DIS 20508	Fine ceramics (advanced technical ceramics) – Determination of light transmittance of ceramic thin films with transparent substrates.

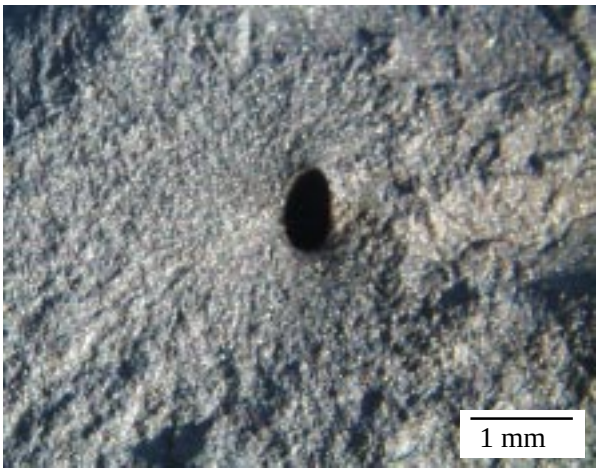

Figure 1. Failed test specimen showing thermocouple hole.

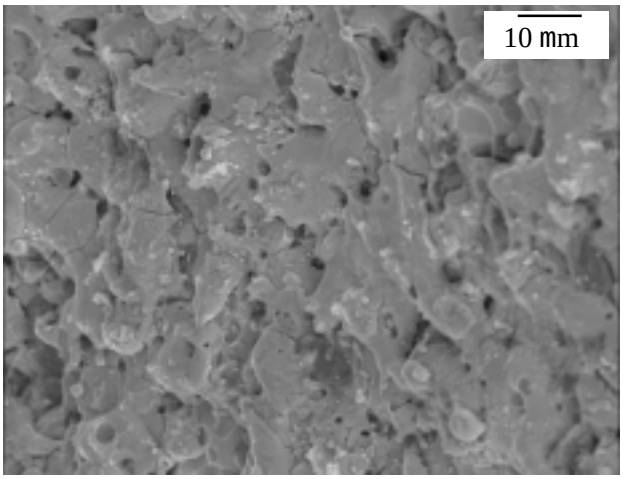

Figure 2. Crack network inside of the thermocouple hole.

Observations: Investigations [7, 8] indicated that the edge segments frequently failed from machining damage associated with the thermocouple holes in the edge segments. The holes were generated via EDM (electro-discharge machining), which lead to the severe cracking showing in Figure 2.

Potential for Standards: The use of better EDM machining procedures or the choice of a different technique that minimizes damage might have prevented the failures. Should standards have played a role? Currently no machining standard exists for ceramics, however, several standards do give guidance on how to machine specimens for a specific standard method, and some general literature exists. The current standards for test specimens generally prevent failure from machining damage. Unfortunately, the generalization of standards-specific techniques can lead to problems for the multiaxial stress states that are encountered in real-word components. Thus a guideline on how to machine a variety of test specimens and components is needed and likely could minimize failures do to machining damage.

In addition, during the failure investigation, it was noted that fracture mirror constants were lacking for estimating the failure stress of components made from advanced materials such as such as whisker, particulate, or *in-situ* reinforced ceramics. Also, a concise methodology to measure ill-defined mirror boundaries and thereby minimize subjectivity was noted. In addition, a function to place confidence levels on the estimated fracture stress was not available. A standardized procedure for measuring mirror boundaries and estimating the fracture stress and associated standard deviation might also benefit the ceramics community. Such a procedure could be added to existing fractography standards such as ASTM Practice C1322 [9].

Example 2 - Test Specimens for a Combustion Facility Window

Background: Design and life prediction of sapphire windows for use in the International Space Station Fluids and Combustion Facility (ISSFCF) required generation of strength and slow crack growth data under the conditions of interest. At the time, the only standardized test specimen that was practical was the uniaxial flexure test specimen. As a result, two sets of test specimens were machined according to typical scratch-dig [10] specifications.

Observations: During testing, one data set exhibited substantially greater scatter than the other data set [11]. Investigations using x-ray topography indicated that although both sets met scratch-dig specifications and appeared optically adequate, the sets contained substantially different amounts of subsurface machining damage, as shown in Figure 3. In follow-up discussions with the vendor [12], it was indicated that polishing of beams, rather than flat plates, is more difficult, and that they have less experience in estimating the appropriate forces and rates to use. A second procurement of circular plates of sapphire indicated this to be the case, as shown in Figure 4.

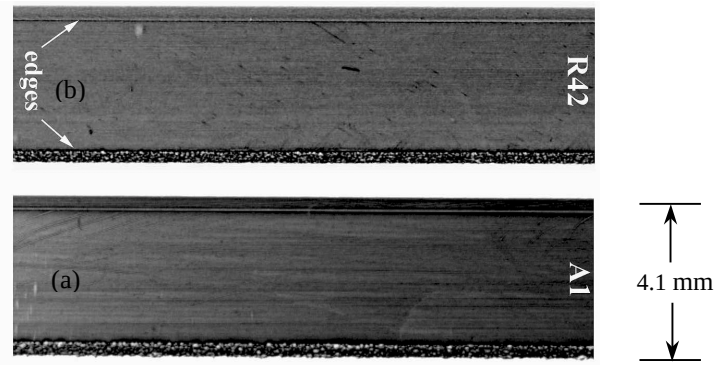

Figure 3. X-ray topographs of the tensile face of (a) an *a*-plane flexure test specimen and (b) an *r*-plane flexure test specimen. Note the asymmetric bevel finish on both test specimens and the remnant, longitudinal grinding marks on the *a*-plane test specimen (a).

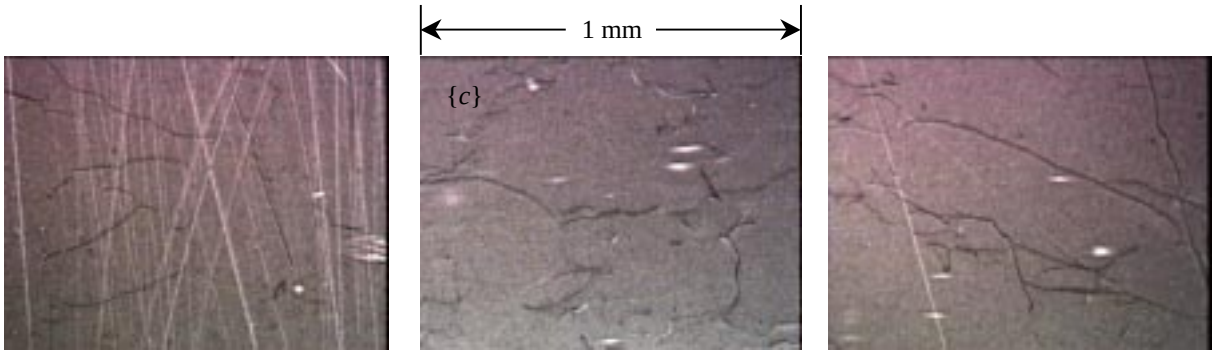

Figure 4. X-ray topographs of the faces of three, 50.4 mm disk test specimens showing a near dislocation level finish. The face of the disks is the *c*-plane.

Potential for Standardization: How could standards have improved the data quality? As in the previous example, a machining guideline may have eliminated the subsurface damage. In addition, had a specification for biaxial testing of plate-like specimens, rather than beams, been available, then multiple improvements in the test results and design could have been made: (1) plates likely would have had less subsurface damage, even without a machining guideline; (2) plates would have been a better representation of the component (a plates-like window), thereby minimizing the degree of extrapolation required in the design; (3) plates are less sensitive to edge chips than beams, and plates thus would have better represented the flaw distribution actually encountered in the windows.

Example 3 - Measurement of Inert Strength

Background: Ceramics and glasses exhibit stress corrosion or "slow crack growth" when subjected to stress in a corrosive environment such as water. Estimation of slow crack growth design parameters for glasses and ceramics via "dynamic" and "static" loading requires measurement of the materials strength both in the environment of interest and in the absence of the corrosive environment. The strength measured in the absence of the corrosive species is known as "inert strength."

Observations: A variety of methods, such as vacuum, low temperature, dry nitrogen, mineral oil, and silicone oil have been used, and several ASTM and ISO standards [13, 14] allude to these techniques.

Unfortunately, no systematic verification of the techniques has been performed, and the techniques do not produce statistically equivalent results to the ideal case of a vacuum, as shown in Figure 5. This occurs because the different techniques eliminate the environment to differing degrees. The use of "silicone oil" as an environmental barrier ignores the availability of several grades of silicone oil for use in diffusion pumps and transformers. The diffusion pump oils have differing degrees of permeability, and thus may allow differing rates of diffusion of the corrosive media. The use of dry nitrogen is also not without complication. A sufficient time for the nitrogen to dry the test specimen is required, especially if the material is porous. For the Dry N_2 Rate A tests, a flow rate of 2400 ml/min for 2 minutes was used, whereas for Dry N_2 Rate B tests, a flow rate of 3200 ml/min for 3 minutes was used. The flow rates and times corresponded to replacing the chamber volume 3 times and 6 times, respectively.

Potential for Standardization: Further investigation and the publication of a standard or guide for the measurement of inert strength is needed to insure consistent, accurate results.

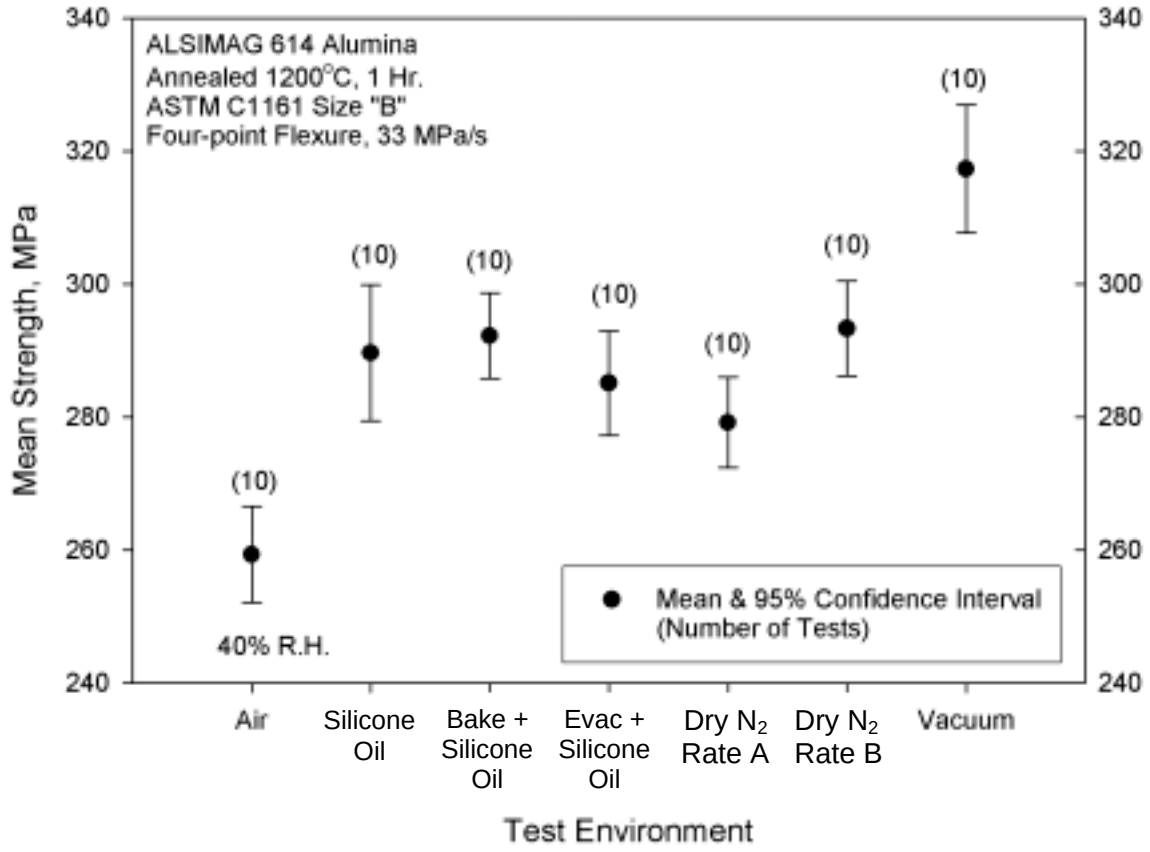

Figure 5. Inert strength of an alumina as a function of test environment.

Example 4 - Failure of a Sapphire Solar Collector

Background: Solar concentrator systems harness the sun's energy and concentrate it so that useful work can be extracted. The use of a system with both primary and refractive secondary concentrators (RSC's) provides higher solar concentrations ratios, efficiency, and heat receiver cavity flux tailoring as compare to conventional hollow refractive parabolic concentrator systems [15, 16]. The materials considered for RSC's are generally single crystal oxides such as sapphire (Al_2O_3), yttria-stabilized zirconia (Y_2O_3-ZrO_2), yttrium-alumina-garnet ($Y_3Al_5O_{12}$ or YAG), and magnesium oxide (MgO). These materials are relatively brittle, and the reliability of such RSC's under

the thermal shock conditions encountered during space mission sun-shade transitions is of great concern. Not only will the concentrator material experience thermal shock, but also large temperature gradients may be sustained at elevated temperature.

Observations: Recent testing of a sapphire RSC [17] resulted in severe cracking of the lens and transition sections, as shown in Figure 6. Failure analysis of the RSC indicated a large "bruise" on the face of the lens, as shown in Figure 7. Coarse machining marks within the bruise implied that it was made during machining and polishing, rather than during rig setup and testing. Failure likely occurred from either the bruise or a sharp transition that contain a steep temperature gradient. Elimination of the bruise and better design of the transition to minimize temperature gradients and thermal stresses would have improved the survivability of the RSC.

Potential for Standardization: As with the leading edge previously discussed, a standard for machining, polishing and handling might be beneficial. In addition, mirror constants for single crystal materials such as sapphire, were lacking. Once again, a standardized procedure for measuring mirror boundaries and estimating fracture stresses might benefit the ceramics community.

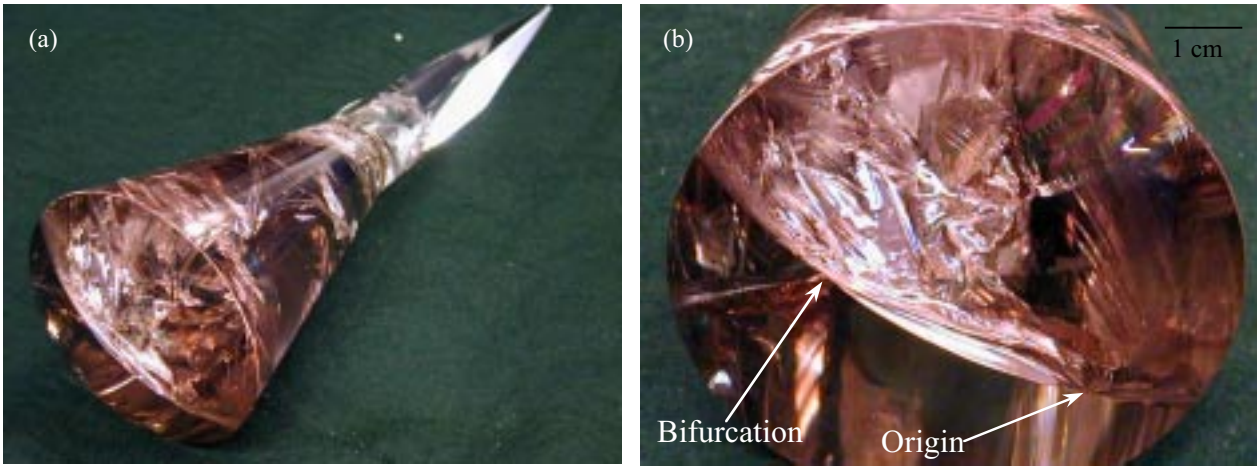

Figure 6. Solar refractive secondary concentrator after testing: (a) Overall view, and (b) Lens face.

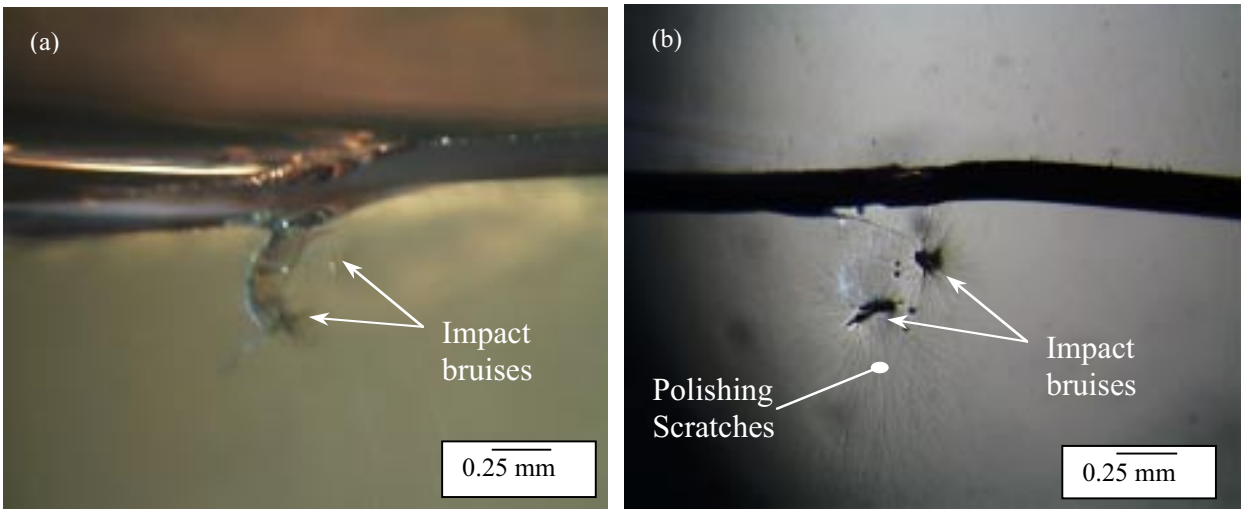

Figure 7. Lens face of a solar RSC observed under (a) transmitted and (b) reflective lighting conditions. Note the scratch marks and cracks within and emanating from the bruises, respectively.

Example 5 - Design Guides for Failure Critical Optical Components

Background: One other aspect of designing components such as the solar concentrator and leading edge segments is the choice of design methodology. Currently two approaches are generally considered: a deterministic (safe-life), fracture mechanics approach via the FLAGRO[1] computer code, and a probabilistic, Weibull strength based approach via the CARES[2] computer code. The FLAGRO analysis is required for all NASA fracture critical hardware.

Observations: The FLAGRO approach has the advantage of defining a flaw of inspectable size that can be insured via proof testing and inspection of the actual component, thereby lending confidence to the predictions. Unfortunately, proof testing is not easy for components such as the RSC. The probabilistic approach is convenient because it requires only strength data as an input to the code. However, it has the disadvantage that complete similitude is required: the flaw distribution causing failure in the test specimens must be identical in behavior to those in the component for the analysis to be accurate. Another disadvantage of the Weibull approach is that test specimen strength data, which typically has large statistical variability, is extrapolated in both scale and time, thereby resulting in low confidence in component predictions. Although the probabilistic approach incorporates fracture mechanic failure criteria, the analysis is based on strength statistics and does not use the fracture toughness of the material or relate it to a flaw size.

Potential for Standardization: For critical situations, a window must be sufficiently thick so that a critical flaw can readily be detected. Thus the fracture toughness of the material is the necessary basis of the design. The use of strength based design, probabilistic or otherwise, may be somewhat misleading for such situations because the "strength" of very well polished test samples and components can be quickly degraded in the service by small scratches, etc. Thus, designs base purely on strength statistics should only be used with caution. Some guideline for choosing the appropriate design method might be beneficial.

DISCUSSION AND CONCLUSIONS

The preceding examples provide evidence of lessons that could be learned for developing standards for advanced ceramics. Each example gives a real world scenario with attended problems of using ceramics in structural applications. In each case, observations were made that lead to conclusions that either existing standards had not fully addressed the problem encountered or no standard existed to address the problem. The two SDOs (ASTM and ISO) of the authors direct involvement, have developed about 50 highly useful standards for advanced ceramics. However, as useful as these standards may be, they only address the measurement of fundamental properties of advanced ceramics, and even then only within the limited experience of the technical experts who write the standards (e.g., silicon nitrides for heat engine applications). Additional development of standards is needed to promote the continued safe use and future introduction of advanced ceramics in demanding applications.

Lessons learned from the examples outside the experience base of the technical experts who populate the current SDOs for ceramics could be used to either extend existing standards or develop new standards. The growing web-based database of lessons learning and technical standards supported by NASA TSP provides a worldwide and publicly accessible means of documenting and archiving such examples and resulting standards.

ACKNOWLEDGEMENTS

The authors acknowledge Paul Gill of the NASA Standards Program for funding work on several standards currently being developed.

[1] NASA/FLAGRO 3.0.11," JSC 22267A, NASA Johnson Space Flight Center, May 1994.

[2] CARES Users and Programmers Manual, NASA Technical Paper TP2916, 1990

References

[1] Harris, D.C. Materials for Infrared Windows and Domes, SPIE Optical Engineering Press, Bellingham, WA, pp 173-177 (1999)

[2] VanRoode, M and Ferber, M. K, Progress in Advanced Ceramics for Gas Turbine Applications, ASME International, New York, NY 2002.

[3] American Society for Testing and Materials, C1145-95 "Standard Terminology of Advanced Ceramics," 1995 Annual Book of ASTM Standards, Vol. 15.01, ASTM International, West Conshohocken, PA (2001)

[4] American Society for Testing and Materials, Standards Make the Pieces Fit, ASTM International, West Conshohocken, PA (1994).

[5] Schneider, S.J. and Bradley, D.R., "The Standardization of Advanced Ceramics," Advanced Ceramic Materials, Vol. 3, No. 5, pp. 442-448 (1988)

[6] Gill, P., Vaughan, W.W., Garcia, D, "Lessons Learned and Technical Standards: A Logical Marriage," ASTM Standardization News, pp. 24-27, November (2001)

[7] Salem, J.A., "Failure Analysis and Failure Stress Estimation of a UHTC HfB_2-SiC Segment used in the SHARP B2 Flight Experiment" NASA Technical Memorandum 2002-211480, NASA Glenn Research Center, Cleveland, Ohio, March (2002).

[8] Mecholsky, J.J., "Reliability of UHTC Materials for Next Generation Space Vehicles," Sandia Report SAND2001-2896, Sandia National Laboratories, October 2001.

[9] ASTM C 1322-96a "Standard Practice for Fractography and Characterization of Fracture Origins in Advanced Ceramics, "ASTM *Annual Book of Standards*, Vol. **15.01**, ASTM International, West Conshohocken, PA (2001)

[10] MIL-PRF-13830B, "Optical Components for Fire Control Instruments, General Specifications Governing the Manufacturing, Assembly and Inspection of," Defense Quality and Standardization Office, Falls Church, VA, (1997)

[11] Salem, J.A., Powers, L., Allen, R., and Calomino, A., "Slow Crack Growth and Fracture Toughness of Sapphire For a Window Application," pp. 41-52 in Window and Dome Technologies and Materials VII, Vol. 4375, R.W. Tustison, ed., Proceedings of the SPIE, SPIE, Bellingham, WA, 2001.

[12] Private Communication, Klaus Burckhardt, ISACO, Quakertown, PA, August (2000).

[13] ASTM C 1368-01 "Determination of Slow Crack Growth Parameters of Advanced Ceramics by Constant Stress Rate Testing," Annual Book of ASTM Standards, V. 15.01, American Society for Testing and Materials, West Conshohocken, Pennsylvania, (2001).

[14] ISO 14704, "Fine ceramics (advanced, technical ceramics) – Test method for flexural strength of monolithic ceramics at room temperature," Geneva, Switzerland (2000)

[15] Soules, J.A., Buchele, D.R., Castle, C.H., and Macosko, R.P., "Design and Fabrication of a Dielectric Total Internal Reflecting Solar Concentrator and Associated Flux Extractor for Extreme High Temperature (2500K) Applications," NASA CR 204145, NASA Glen Research Center, November 1997.

[16] Ning, X., Winston, R., and O'Gallagher, J., "Dielectric Totally Internally Reflecting Concentrators," Applied Optics, 26 [2], 300-305, 1987.

[17] Wong, W.A., Castle, C.H., "High Temperature Solar Vacuum Testing of a Sapphire Refractive Secondary Concentrator," in proceedings of the Space Technology and Applications International Forum--STAIF 2002, Mohamed S. El-Genk, ed., Albuquerque, New Mexico, 3-6 February 2002.

STANDARDS DEVELOPMENT AT NASA WHITE SANDS TEST FACILITY*

D. L. Baker
H. D. Beeson
R. L. Saulsberry
NASA Johnson Space Center White Sands Test Facility
Las Cruces, NM

H. L. Julien
S. S. Woods
Honeywell Technology Solutions Inc.
Las Cruces, NM

ABSTRACT

The development of standards and standard activities at the JSC White Sands Test Facility (WSTF) has been expanded to include the transfer of technology and standards to voluntary consensus organizations in five technical areas of importance to NASA. This effort is in direct response to the National Technology Transfer Act designed to accelerate transfer of technology to industry and promote government-industry partnerships. Technology transfer is especially important for WSTF, whose long-term mission has been to develop and provide vital propellant safety and hazards information to aerospace designers, operations personnel, and safety personnel. Meeting this mission is being accomplished through the preparation of consensus guidelines and standards, propellant hazards analysis protocols, and safety courses for the propellant use of hydrogen, oxygen, and hypergols, as well as the design and inspection of spacecraft pressure vessels and the use of pyrovalves in spacecraft propulsion systems. The overall WSTF technology transfer program is described and the current status of technology transfer activities are summarized.

INTRODUCTION

Following passage of the Technology Transfer and Advancement Act of 1995 (NTTAA)[1], government, academia, and industry have focussed on expanding technical interchange through voluntary consensus organizations. This action comes at a time of significant changes in the aerospace environment. Changes include reorganization in the aerospace industry, reduction in force within government, greater standards coordination at an international level, replacement of military (MIL) specifications with performance specifications, and conversion of government guidelines and standards with voluntary consensus standards. To keep pace with these changes, NASA White Sands Test Facility (WSTF) has evolved a model of technical interchange that recognizes the synergy and interrelationship between the fundamental aerospace activities of research, hazard analysis, and training with the development of standards for aerospace fuel, operations, and systems. This model is being developed for safety standards contributions involving propellants (hydrogen, hypergol, and oxygen), composite pressure vessels, and pyrovalves. Concurrent with these WSTF aerospace activities are related technology transfer efforts to develop non-aerospace standards, publish propellant hazards analysis protocols, and provide safety courses for industry and other sectors of the economy.

This paper reports on these efforts and describes WSTF's overall voluntary consensus standards program to coordinate the interchange of NASA's propellant hazards and safety information with industry and the public.

---

* Approved for public release; distribution is unlimited.

A NEW AND CHANGING ENVIRONMENT

The rapid pace of transfer of government activities to the aerospace industry, along with the increasing incidence of aerospace corporate mergers, have the potential for disrupting coordination and flow of vital propellant safety and hazards information among personnel involved in design, operations, and safety of propellant systems. Within this setting exist the risks associated with employees' potential exposure to hazardous chemicals in governmental and industrial work environments. The latter has led to detailed governmental regulations that specify a highly trained work force, the use of hazards review methodologies, hazards communications with employees and the surrounding community, and adequate emergency preparedness. How can the effects of these potentially opposing forces be countered?

Consensus as a Means of Communication

One response is for government and industry to cooperate within the framework provided by a Voluntary Consensus Organization (VCO), which acts as a clearinghouse for critical information, helps identify top expertise, and offers training. The democratic structure of VCOs enables them to develop voluntary consensus standards that meet the needs of both government and industry. Easily leveled criticisms of standards efforts conducted within government agencies are that the results are inadequate, one-sided, and inaccessible. The NTTAA has forced government to reevaluate its standards efforts. But for NASA, an agency that has been always been proactive with regard to public outreach and technology transfer, NTTAA provides the basis for even greater interaction with industry and the public.

Aside from the primary goal of managing standards through a VCO, other positive attributes should arise from pursuit of the law. These attributes include improved communication within government agencies and between industrial entities, as well as interagency/interindustry connections. This has the potential to bring different interests together and lead to the establishment of a common ground in which research and development can take root. It is likely that VCOs will continue to be a focal point for general information related to voluntary consensus standards, such as identifying where particular expertise can be found.

NASA's interest in participation with VCOs in the safety arena includes the transfer of hazards manuals and the development of voluntary consensus standards. In theory, hazards information is better distributed by VCOs, with the cost being covered by the program interests that need the information rather than subsidized by the government. One goal is to promote the creation of general safety standards for propellant use that can be applied in government-industry contract negotiations.

For agencies that are not proactive in response to NTTAA, it will be interesting to see how the law will work in the future. The Office of Management and Budget (OMB) requires federal agencies to report on the status of their efforts to meet the law. Already the mobile home construction industry has brought a legal challenge[2] against legislation pending in Congress, the American Homeownership and Opportunity Act, H.R. 1776, citing conflicts with NTTAA. The industry is claiming that preexisting law directs them through VCOs to keep standards for manufactured homes up-to-date and the new law is not needed.

New Developments

Changes have continued in recent years that more than ever point to the need for voluntary consensus standards. Government continues to reduce the civil service resources and this has led to several effects. NASA often relies on project teams staffed by both government and contractor team members operating at a greater level of integration than practiced in the past. In addition, downsizing has made single-project orientation of an organization no longer feasible. Not only must NASA program managers run multiple projects, they must also share work with contractor team members and serve clients in other branches of government or private industry. Further, organizations must consider a wide variety of work supported by multiple-fund sources from both government and industry to keep the best talent available. Different kinds of changes are affecting the aerospace industry, including a recent turnover in the suppliers of hypergolic fuels.

By design, NTTAA has prompted a new, more cooperative environment between government and industry that accelerates technology transfer to industry and promotes government-industry partnerships. But technology transfer from government to industry involves more than simply relaying scientific data and technology development. It also involves sharing hazards review and training expertise and making the information and techniques used by government laboratories more accessible to industry and the public. Technology transfer activities also drive government efforts to be more attuned to industry needs. In all of these areas, the improved connectivity, communications, and consensus on issues provided by VCOs will help smooth the transition inherent with the changing environment.

WSTF TECHNOLOGY DEVELOPMENT IN SUPPORT OF STANDARDS

WSTF has been involved with testing of hazardous fluids, components, and materials in direct support of NASA safety standards since 1966. The emphasis has been on the safe use of aerospace fuels and oxidizers. This work has included material compatibility testing, fuel ignition testing, and explosion testing. More recently, work on composite pressure vessels (COPV) and pyrovalves has been conducted in support of standards. With the new direction prompted by NTTAA, a relationship among research and development, hazards analysis protocols, safety course development, voluntary consensus standards activities, and industry communications has become apparent.

Interrelationship of Standards Development, Hazard Analysis, Research, and Training

The process of technology transfer at WSTF (Figure 1) shows standards development proceeding with information input from “Research and Development”, “Hazards Analysis”, and “Safety Courses.” The hazards analysis process is depicted at the center of the overall technology transfer process as the information gained by hazards analyses can serve as input to VCOs, research, and training. Conversely, VCO committees, research groups, and trainers can have influence on hazards analysis protocols. For this scheme to function effectively, some group in industry or government must have a vested interest in tracking, documenting, and communicating key information obtained from the use of hazards analysis protocols. At present, WSTF is funded to do this work. A logical extension of who performs this sort of work would include the VCOs themselves.

One of WSTF’s primary goals is to support NASA’s propellant safety efforts, which involve testing, research and development, and hazards analysis of cryogenic and hypergolic propellants. These activities are organized to support queries from industry and the public, provide training to those who need it, and collaborate with VCOs to develop voluntary consensus standards. Important insights into the role hazards analyses can play in the overall direction and planning of safety research have become apparent. WSTF is recognized throughout NASA and the aerospace community for its formalized approach to oxygen hazards analysis, and has designed other protocols for application to hydrogen, hydrazine fuels, and nitrogen tetroxide.

WSTF Hazards Analysis Support Services

In their traditional roles, project- and program-oriented groups use hazard analysis as a means of identifying and remediating potential component and system inadequacies. But sometimes during the course of an analysis, a need arises for data that do not exist. For example, the assessment of propellant hazards may involve the need for combustion or materials data that are not currently available but can be gained through testing. But if the team determines that testing is too difficult or expensive, the analysis might prompt a system redesign, the acceptance of greater risk, or a new method for assessing the hazards. Therefore, hazard analysis can be considered a tool that provides knowledge about what we need to know.

Several specialized hazard analysis protocols have been developed at WSTF to analyze detailed system data and efficiently document hazards information. These protocols work by identifying operating conditions, examining in detail all components and materials exposed to a particular propellant, analyzing likely failure modes involving flammability and ignition, determining the consequence(s) of a particular

failure to the system, and qualitatively assessing the risk for the system owners. The benefits derived from this analysis go beyond identifying hazards. Design teams have a better understanding of their systems. The system "owners" and the design teams are much better prepared for higher-level reviews. Higher-level review teams have shown great respect for the protocols because of their rigor.

Protocols for oxygen, hydrogen, and hypergols have been established, and a protocol for pyrotechnics is under discussion. The protocols address primarily combustion hazards. The protocols are backed by safety databases established and maintained by WSTF. Hazards analysis services have been provided by WSTF to government and industry over the past 15 years. Within NASA, use of the protocols has met with an overwhelmingly positive response. Protocol descriptions available from WSTF upon request are:

- ASTM G63, "Guide for Evaluating Nonmetallic Materials for Oxygen Service"[3]
- ASTM G88, "Guide for Designing Systems for Oxygen Service"[4]
- ASTM G94, "Guide for Evaluating Metals for Oxygen Service"[5]
- TP-WSTF-937, "Guide for Hydrogen Hazards Analysis on Components and Systems" [6]
- TP-WSTF-953, "Guide for Hydrazine Hazards Analysis on Components and Systems" [7]
- TP-WSTF-959, "Guide for Nitrogen Tetroxide Hazards Analysis on Components and Systems" [8]

Training Support Services

WSTF has provided safety training courses in specialized areas for over 15 years. The course materials have been developed to meet the requirements of the NASA Safety Training Center (NSTC). The courses include:

• Oxygen Safety Classes* (4):	ASTM Technical and Professional Training Course, "Fire Hazards in Oxygen Systems" [9] (several versions exist that are tailored to particular audiences, such as design engineers, technicians, and the scuba community) Oxygen Systems Operation and Maintenance Oxygen Systems Management, Design, Operation and Maintenance ISS Oxygen Systems Assembly, Operations, and Maintenance
• Hypergol Safety Class (1):	NSTC 055, Hypergol Systems: Design, Buildup, & Operation
• Hydrogen Safety Classes (2):	NSTC 054, Hydrogen Safety Operations NSTC 037, Hydrogen Safety
• COPV Inspection Class (1):	Inspection for Damage to Carbon/Epoxy Composite Overwrapped Pressure Vessels

The courses have been taught at various government and industrial locations. Within NASA, they are available through the NSTC. For non-NASA government groups and private industry, the safety classes are available directly through WSTF. The oxygen classes are taught through the American Society for Testing and Materials (ASTM).

JSC WSTF STANDARDS DEVELOPMENT AND TECHNOLOGY TRANSFER PROGRAM

Special responsibilities for COPV, hydrogen, hypergol, oxygen, and pyrovalve standards development reside at WSTF. The overall responsibility for standards transfer at NASA rests with the NASA Engineering Standards Steering Council (NESSC). WSTF participates directly with the NESSC but also receives specific tasks from the NASA Office of Safety and Mission Assurance (HQ/OSMA) (Code Q).

* Courses are offered by ASTM as a part of their program of ASTM Technical and Professional Training. The NSTC coordinates NASA courses through ASTM. Instructors are from WSTF.

The process of standards development as it applies to technology transfer of in-house NASA standards can be considered as occurring in three phases as shown in Figure 1. Phase I begins with direction from Code Q and a survey of VCOs. The VCOs identified as candidates to host the standards are contacted. One is selected based on a match of the VCO's goals with NASA's goals and their ability to meet publication requirements. In Phase II, the committee and its business are developed. The VCOs host committee meetings, coordinate committee activities, and help publish special reports, technical guides, and consensus standards. Standards maintenance and participation become a routine element of WSTF participation in Phase III.

At present, oxygen standards activities are performed through the ASTM, the National Fire Protection Association (NFPA), and the International Standards Organization (ISO). Hydrogen standards development is performed through the American Institute for Aeronautics and Astronautics (AIAA), the National Hydrogen Association (NHA), and ISO. Hypergolic standards are developed through AIAA. Pressure vessel and pyrovalve standards are also being developed through AIAA.

Accomplishments to Date

WSTF's parallel efforts to promote safety research and develop safety standards have become a vital part of its mission. This section outlines specific achievements in the standards areas.

Propellant Oxygen

Research into propellant oxygen hazards has been ongoing at WSTF since the mid-1970s and is its most mature expression of the interrelationship among research, hazards analysis, and VCO participation. Technical communications and technology transfer with industry are achieved through long-standing participation with ASTM Committee G4 on Compatibility and Sensitivity of Materials in Oxygen Enriched Atmospheres and the NFPA committees on Health Standards and Hyperbaric Standards. The oxygen hazards analysis protocol has been in use for over a decade. WSTF researchers have developed an oxygen safety training course, "Fire Hazards in Oxygen Systems,"[9] that is offered through ASTM. At the request of the NASA HQ/OSMA, WSTF developed a safety standard for oxygen and subsequently collaborated with ASTM to publish it as Manual 36, "Safe Use of Oxygen and Oxygen Systems."[10] WSTF's progress in the oxygen arena serves as a model for its development of hydrogen and hypergol propellant programs. The following documents are available for oxygen safety assessment:

- ASTM MNL36, "Safe Use of Oxygen and Oxygen Systems" [10]
- NASA Safety Standard 1740.15, "Safety Standard for Oxygen and Oxygen Systems" [11]
- NASA Technical Memorandum 104823, Guide for Oxygen Hazards Analyses on Components and Systems" [12]
- NFPA 53, "Recommended Practice in Oxygen-Enriched Atmospheres"[13]

Propellant Hydrogen

WSTF participates in the development of both aerospace and general hydrogen safety standards. This work is performed in cooperation with AIAA, NHA, and ISO Technical Committee 197 Hydrogen Technologies (ISO/TC 197).

To develop aerospace hydrogen standards, WSTF has worked to form the AIAA Hydrogen Committee on Standards (HCOS). This committee seeks to identify aerospace hydrogen safety concerns, develop safety documents where needed, and promote the dissemination of hydrogen safety information. Committee membership includes representatives from academia, the aerospace industry, DOE, DOD, FAA, hydrogen suppliers, and NASA. The HCOS is currently working to assess the need for hydrogen safety standards in the aerospace community. NASA has an interest in the development of a general hydrogen safety standard that could be cited to establish acceptable practice in contracts. Toward that end, the HCOS is working to publish a consensus guide based on the NASA hydrogen safety standard. Because of the intense interest in hydrogen safety beyond aerospace applications, the HCOS maintains

liaisons with the NHA and ISO. Ultimately, the HCOS will seek to promote AIAA documents as national aerospace standards.

In a parallel effort, WSTF works with the NHA on national hydrogen safety issues and with ISO/TC 197 to promote the development of international hydrogen safety standards. These activities began in 1998 when NASA was invited by the DOE and the NHA to help represent U.S. trade interests by contributing hydrogen safety expertise to work with the international community to develop hydrogen standards for commerce. Recent accomplishments include WSTF's contribution to Working Group 7 for the development of the final draft of ISO/PDTR 15916, "Basic considerations for the safety of hydrogen systems." This document will serve as the cornerstone safety document for ISO hydrogen standards for commerce. Reinforcing this involvement with general hydrogen standards is the request by both the AIAA Standards Executive Council and the NASA Engineering Standards Steering Council (NESSC) for the AIAA HCOS to consider the relationship and synergy between general hydrogen and aerospace hydrogen standards. WSTF regularly contributes presentations at NHA/DOE forums and expertise to support work on national hydrogen standards development. This participation has evolved to include issues involving hydrogen storage within composite pressure vessels. The following documents are or soon will be available for use:

- NASA Safety Standard 1740.16, "Safety Standard for Hydrogen and Hydrogen Systems"[14]
- RD-WSTF-0001, "Ignition and Thermal Hazards of Selected Aerospace Fluids" [15]
- AIAA Hydrogen Safety Guide (publication planned for 2003)
- ISO/PDTR 15916, Basic Considerations for the Safety of Hydrogen Systems (subject to international approval, Fall 2002)

Hypergolic Fuels and Oxidizers

Progress in the hypergol safety arena parallels WSTF's oxygen and hydrogen efforts in that several manuals covering the hazards of hypergolic propellants have been developed at WSTF. This is just the kind of information that could better serve the aerospace community if it was managed by a VCO. In collaboration with AIAA, WSTF promoted the formation of the recently initiated AIAA Liquid Propellant Committee on Standards (LPCOS) to serve as a forum for discussion of hypergolic and related propellant safety issues. This committee has an agenda to oversee the development of voluntary consensus standards covering hydrazine, monomethylhydrazine, dinitrogen tetroxide, and other aerospace fluids of interest. WSTF hypergolic hazards manuals have been transferred to AIAA for distribution as AIAA Special Projects. The agreement stipulates that needed updates of hypergolic hazards information will be published through AIAA Special Projects or Guides. In addition to the AIAA committee work, JSC has funded development of a hazards analysis protocol for hypergolic propellants. Also, NASA HQ/OSMA has funded WSTF for development of a hypergol safety training course. The following documents are available for hypergolic safety assessment:

- RD-WSTF-0001, "Ignition and Thermal Hazards of Selected Aerospace Fluids"[15]
- RD-WSTF-0002, "Fire, Explosion, Compatibility, and Safety Hazards of Hydrazine" [16]
- RD-WSTF-0003, "Fire, Explosion, Compatibility, and Safety Hazards of Monomethylhydrazine" [17]
- RD-WSTF-0017, "Fire, Explosion, Compatibility, and Safety Hazards of Nitrogen Tetroxide" [18]
- AIAA SP-084-1999, "Fire, Explosion, Compatibility, and Safety Hazards of Hypergols – Hydrazine" [19]
- AIAA SP-085-1999, "Fire, Explosion, Compatibility, and Safety Hazards of Hypergols – Monomethylhydrazine" [20]
- AIAA SP-086-2001, "Fire, Explosion, Compatibility, and Safety Hazards of Nitrogen Tetroxide" [21]

There is also a current effort to develop a technical manual for hydrogen peroxide.

Pressure Vessel Standards

WSTF conducted an extensive testing program that involved developing a database to evaluate impact damage to composite overwrapped pressure vessels (COPVs) used in space vehicle applications. This database provides the basis of a WSTF training course entitled “Inspection for Damage to Carbon/Epoxy Composite Overwrapped Pressure Vessels.” These data were used to establish a standard for COPVs sponsored by an AIAA Pressure Vessel Standards Working Group. WSTF technical personnel participate in this working group in the maintenance of the following AIAA pressure vessel standards:

- Metal pressure vessels
- Composite overwrapped pressure vessels
- Composite structures
- Solid rocket motor case
- Composite pressure vessels
- Composite overwrapped pressure vessels with nonmetallic liners.

Pyrovalve Standard

A WSTF research and development program directed towards establishing a technical database to assure the safe use of pyrovalves in space vehicles is relatively new. Our initial concern was to understand observed deflagration of fuel resulting from introduction of a pyrotechnic charge from the valve into the fuel with the objective to avoid this catastrophic event in space vehicle propulsion systems on future missions. However, the introduction of a new interference fit type ram to minimize pyrotechnic blowby into the fuel line results in new reliability concerns. As a result, the test program was expanded to look at various types of interference fit rams and NDE inspection techniques that can be used to evaluate flight valve integrity.

Test data obtained since 1996 provide the technical basis of a NASA Pyrovalve Handbook that is being drafted and will ultimately be converted to an AIAA Pyrovalve Handbook to be sponsored by the AIAA Energetic Components and Systems Technical Committee. A parallel effort to develop NASA and AIAA Pyrotechnics Training Courses is also underway.

Planned Future Activities

The importance of WSTF’s continued active participation in the activities of the Voluntary Consensus Organizations cannot be overestimated. The technologies that provide the basis for standards development have been and will continue to be developed at WSTF. It is also in the best interest of NASA that WSTF participation assures that those requirements of importance to NASA operations and facilities remain intact. This is especially important in the beginning phases of the standards committee where the membership development goal of achieving equal participation from government, industry, and academia to assure consensus is critical.

The transition of WSTF technical manuals, available in the form of VCO Special Project Reports to Technical Guides requires the participation of WSTF technical personnel, especially those individuals that developed the information through test and analysis of test data. The subsequent conversions to Recommended Practices and Standards shall require some but significantly less involvement.

Finally, safety research and development must continue at WSTF in order to answer the many inquires we receive from industry and to gain a better understanding of very complex technical issues associated with the safe use of aerospace fuels and oxidizers. This effort and our expanding efforts in providing hazards analysis and training will maintain WSTF as a key element in the aerospace community in the future.

SUMMARY AND CONCLUSIONS

The goal of this paper has been to inform aerospace researchers and engineers of improved opportunities for communicating safety concerns and to raise awareness of WSTF's continuing involvement in aerospace safety standards development. The nexus of propellant activities for oxygen, hydrogen, and hypergol safety underway at WSTF can aid researchers with locating critical information, expertise, testing services, and training. The authors encourage those who have a stake in making this kind of information available to their own organizations to participate in VCO activities, such as the ASTM Committee G4 and the AIAA Liquid Propellant Committee on Standards. For hydrogen, readers are encouraged to contact AIAA and/or the WSTF Propellant Hazards Program for further information.

The NTTAA has pointed the way for reconsideration in the way government and industry interact. For the maximum benefit to accrue in the propellant safety arena, industry and government representatives must participate through the technical committees of the VCOs chartered to manage this information.

REFERENCES

1. Public Law 104-113 (104th Congress). *National Technology Transfer and Advancement Act of 1995*. 15 USC 3701. Washington, D.C. Signed by the President, March 7, 1996.

2. ASME. *ASME Letter to the Honorable Constance A. Morella Regarding the Proposed Manufactured Housing Improvement Act*. American Society of Mechanical Engineers, New York, NY, Feb. 11, 2000. http://www.asme.org/gric/00-02.html.

3. ASTM G 63. *Standard Guide for Evaluating Nonmetallic Materials for Oxygen Service*. Annual Book of ASTM Standards, American Society for Testing Materials, Philadelphia, PA (1992, or latest revision).

4. ASTM G 88. *Standard Guide for Designing Systems for Oxygen Service*. Annual Book of ASTM Standards, American Society for Testing Materials, Philadelphia, PA (1990, or latest revision).

5. ASTM G 94. *Standard Guide for Evaluating Metals for Oxygen Service*. Annual Book of ASTM Standards, American Society for Testing Materials, Philadelphia, PA (1992, or latest revision).

6. Woods, S. S., G. Packard, and H. D. Beeson. *Guide for Hydrogen Hazards Analysis on Components and Systems.* TP-WSTF-937, NASA Johnson Space Center White Sands Test Facility, Las Cruces, NM, August 19, 1998.

7. Rathgeber, K. A., L. J. Bamford, and D. L. Baker. *Guide for Hydrazine Hazards Analysis on Components and Systems.* TP-WSTF-953, NASA Johnson Space Center White Sands Test Facility, Las Cruces, NM, publication in process.

8. Rathgeber, K. A., L. J. Bamford, and D. L. Baker. *Guide for Nitrogen Tetroxide Hazards Analysis on Components and Systems.* TP-WSTF-959, NASA Johnson Space Center White Sands Test Facility, Las Cruces, NM, publication in process.

9. "Fire Hazards in Oxygen Systems," Technical & Professional Training Course, American Society for Testing and Materials, West Conshohocken, PA, latest version.

10. Beeson, H. D., W. F. Stewart, and S. S. Woods, Eds., "Safe Use of Oxygen and Oxygen Systems: Guidelines for Oxygen System Design, Materials Selection, Operations, Storage, and Transportation," ASTM MNL36, American Society for Testing and Materials, West Conshohocken, PA, January 2000.

11. NASA Office of Safety and Mission Assurance. *Safety Standard for Oxygen and Oxygen Systems (Guidelines for Oxygen System Design, Materials Selection, Operation, Storage, and Transportation).* NSS 1740.15, Office of Safety and Mission Assurance, Washington, D.C., January 1996.

12. Stoltzfus, J. M., J. Dees, and R. F. Poe. *Guide for Oxygen Hazards Analyses on Components and Systems*. NASA Technical Memorandum 104823, Johnson Space Center, Houston, TX, October 1996.

13. NFPA 53. *Recommended Practice on Materials, Equipment, and Systems Used in Oxygen-Enriched Atmospheres*. National Fire Protection Association, Quincy, MA (1999, or latest revision).

14. NASA Office of Safety and Mission Assurance. *Safety Standard for Hydrogen and Hydrogen Systems (Guidelines for Hydrogen System Design, Materials Selection, Operations, Storage, and Transportation).* NSS 1740.16, Office of Safety and Mission Assurance, Washington, D.C., February 1997.

15. Benz, F. J., C. V. Bishop, and M. D. Pedley. *Ignition and Thermal Hazards of Selected Aerospace Fluids*. RD-WSTF-0001, NASA Johnson Space Center White Sands Test Facility, Las Cruces, NM, October 14, 1988.

16. Pedley, M. D., D. L. Baker, H. D. Beeson, R. C. Wedlich, F. J. Benz, R. L. Bunker, and N. B. Martin. *Fire, Explosion, Compatibility, and Safety Hazards of Hydrazine*. RD-WSTF-0002, NASA Johnson Space Center White Sands Test Facility, Las Cruces, NM, February 20, 1990.

17. Woods, S. S., D. B. Wilson, R. L. Bunker, D. L. Baker, and N. B. Martin. *Fire, Explosion, Compatibility, and Safety Hazards of Monomethylhydrazine*. RD-WSTF-0003, NASA Johnson Space Center White Sands Test Facility, Las Cruces, NM, May 5, 1993.

18. Davis, D. D., D. L. Baker, L. A. Dee, B. Greene, C. H. Hart, and S. S. Woods. *Fire, Explosion, Compatibility, and Safety Hazards of Nitrogen Tetroxide*. RD-WSTF-0017, NASA Johnson Space Center White Sands Test Facility, Las Cruces, NM, November 15, 1999.

19. AIAA SP-084-1999. *Fire, Explosion, Compatibility, and Safety Hazards of Hypergols – Hydrazine*. American Institute of Aeronautics and Astronautics, Reston, VA, 1999.

20. AIAA SP-085-1999. *Fire, Explosion, Compatibility, and Safety Hazards of Hypergols – Monomethylhydrazine*. American Institute of Aeronautics and Astronautics, Reston, VA, 1999.

21. AIAA SP-086-2001. *Fire, Explosion, Compatibility, and Safety Hazards of Nitrogen Tetroxide*. American Institute of Aeronautics and Astronautics, Reston, VA, 2001.

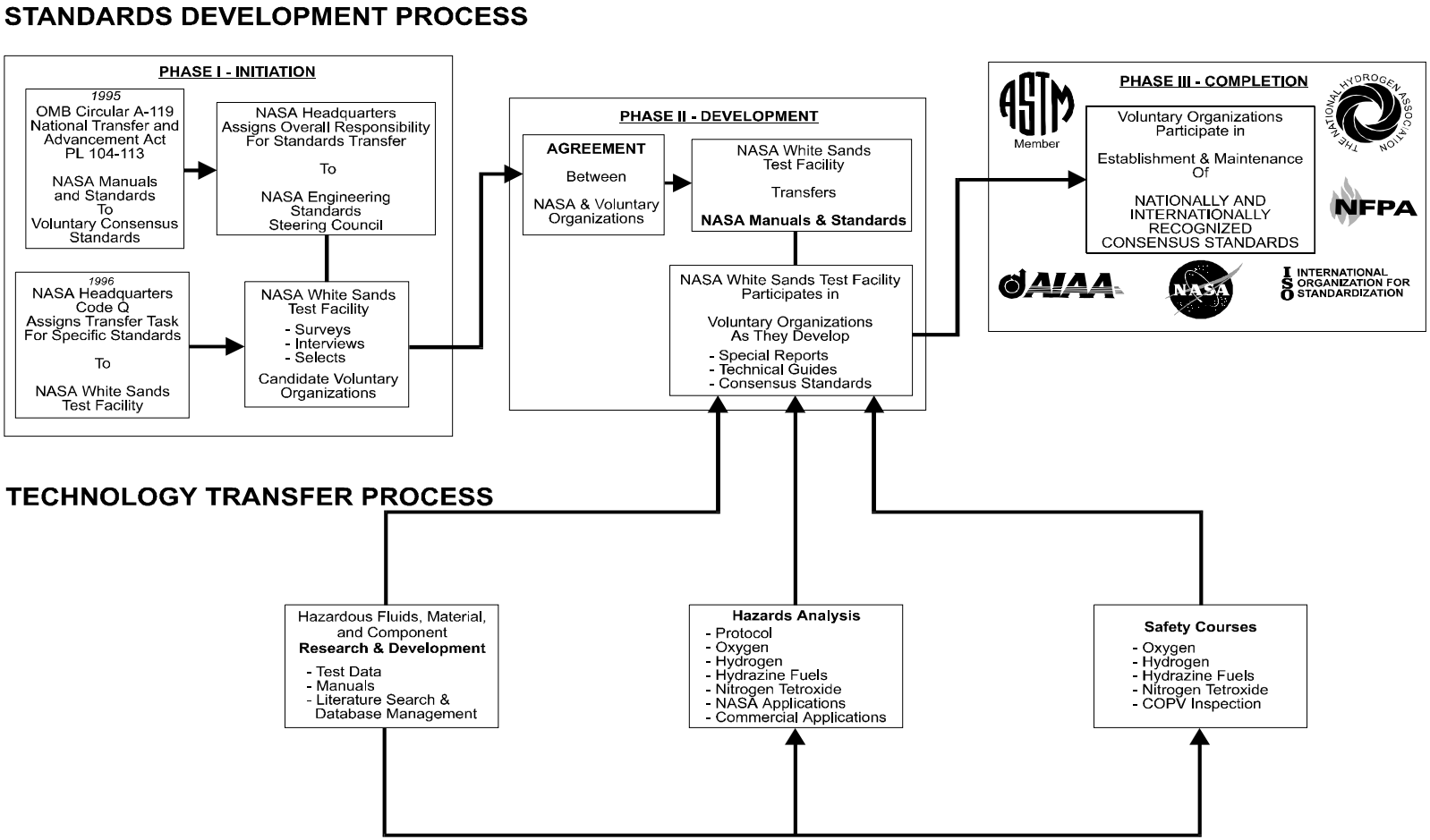

Figure 1. JSC WSTF Standards Development and Technology Transfer

Corrosion of Highly Specular Vapor Deposited Aluminum (VDA) on Earthshade Door Sandwich Structure

DANIEL PLASKON
Jet Propulsion Laboratory, MS 158-224
4800 Oak Grove Drive
Pasadena, CA 91109
Phone: 818-354-5924
Fax: 818-393-4860
E-mail: daniel.plaskon@jpl.nasa.gov

Cheng Hsieh
Jet Propulsion Laboratory, MS 158-224
4800 Oak Grove Drive
Pasadena, CA 91109
Phone: 818-354-8105
Fax: 818-393-4860
E-mail: cheng-hsien.hsieh-103502@jpl.nasa.gov

High-resolution infrared (IR) imaging requires spacecraft instrument design that is tightly coupled with overall thermal control design. The JPL Tropospheric Emission Spectrometer (TES) instrument measures the 3-dimensional distribution of ozone and its precursors in the lower atmosphere on a global scale. The TES earthshade must protect the 180-K radiator and the 230-K radiator from the Earth IR and albedo. Requirements for specularity, emissivity, and solar absorptance of inner surfaces could only be met with vapor deposited aluminum (VDA).

Circumstances leading to corrosion of the VDA are described. Innovative materials and processing to meet the optical and thermal cycle requirements were developed. Examples of scanning electronmicroscope (SEM), atomic force microscope (AFM), and other surface analysis techniques used in failure analysis, problem solving, and process development are given. Materials and process selection criteria and development test results are presented in a decision matrix. Examples of conditions promoting and preventing galvanic corrosion between VDA and graphite fiber-reinforced laminates are provided.

Fluorescent Cleaning Process

JIM DEARDORFF
Superior Coatings, Inc.
1713 Bryan Street, P. O. Box 317
Chilicothe, MO 64601
Phone: 660-646-6355
E-mail: jdeardorffsupct@yahoo.com

In recent years, the tremendous growth in available technology and the resulting trend toward component miniaturization and increased product reliability has challenged many companies to upgrade their current cleaning operations to satisfy the higher quality standards required by new product designs.

A new, integrated process that combines cleaning methods with fluorescence-based monitoring promises to increase operational efficiency significantly and to provide low-cost quality assurance to a greater range of cleaning operations. Fluorescent (FP) cleaning makes use of modified cleaning agents containing an internal fluorescent / phosphorescent dye that produces a highly visible response when exposed to ultraviolet or visible illumination.

FP cleaning offers many performance advantages over traditional cleaning operations. Uniform coverage of all surface areas and complete saturation of available contaminants can be easily monitored by suitable light inspection. Small parts or parts with complicated surfaces are also uniformly covered and complete saturated by FP cleaning. Cleanliness quality is verified, after the removal of the FP cleaner and suspended contaminants, by the total absence of visible fluorescence. Fluorescent inspections can be performed at virtually any point during the assembly phase or at future intervals to support on-going contamination control maintenance.

Analysis of Non-Volatile Residues with a Standard FTIR Accessory, The VSphere™

M. MARTIN SZCZESNIAK
Surface Optics Corporation
11555 Rancho Bernardo Rd.
San Diego, CA 92127
Phone: 858-675-7404
Fax: 858-675-2028
E-mail: martinsz@surfaceoptics.com

Michael Beecroft
Surface Optics Corporation
11555 Rancho Bernardo Rd.
San Diego, CA 92127

Paul Shelley
The Boeing Company
P. O. Box 3707, M/C 9U-EA
Seattle, WA 98124-2207
Phone: 425-234-4171
Fax: 425-234-8501
E-mail: paul.h.shelley@boeing.com

The VSphere™ was developed for analysis of non-volatile residues (NVRs) in solvents in the process of cleanliness evaluation. The solvent to be analyzed is placed in a small gold-plated cup and evaporated. A thin film of NVR is formed on the cup's wall. The cup is attached to the illumination / detection optics. An infrared spectrum is recorded and analyzed. The VSphere™ provides a superior way of NVR analysis over traditional horizontal ATR accessories or KBR pellets.

The original VSphere™ accessory was built for the SOC 400 Hand Held FTIR. It was immediately implemented at Boeing Rockedyne for evaluation of cleanliness of rocket engines. A number of practical applications were developed at Boeing Commercial Airplane. Recently, the availability of the VSphere accessory has been broadened to Nicolet FTIR spectrometers. This version allows for parallel infrared and gravimetric analysis of the same specimen. The presentation will provide a detailed technical description of the accessory and its applications.

Use of FT-IR Analysis to Support Contamination Studies for Bonding Surfaces

RICHARD BOOTHE
Marshall Space Flight Center, ED31
Huntsville, AL 35812
Phone: 256-544-3028
Fax: 256-544-0212
E-mail: richard.boothe@msfc.nasa.gov

The FT-IR analysis technique has become increasingly important for measuring and verifying coating levels on calibration standards and bonding specimens used to evaluate the effects of contamination on rocket motor bondlines. Use of this technique for evaluating solvent effectiveness for contamination removal is also increasing. Typical testing scenarios, analysis techniques, and instrumentation used at MSFC will be described.

YDZ-2363
VISUALS

A STUDY OF STAINS ON METALS USING INFRARED HYPERSPECTRAL IMAGING

G. L. Powell

Y-12 National Security Complex*
BWXT Y-12, L. L. C.
Oak Ridge, Tennessee

R. L. Cox
Oak Ridge National Laboratory
Oak Ridge, Tennessee

and

M. Beecroft
M. Dombrowski
P. Mattison
M. M. Szczesniak

Surface Optics Corporation,
11555 Rancho Bernardo Road.
San Diego, CA, 92127.

Date of Issue: August 28, 2002

These visuals were prepared for presentation at

5th AMPET Conference
Huntsville, Alabama
September 16-18, 2002

Prepared by the
Y-12 National Security Complex
managed by
BWXT Y-12, LLC.
for the
U. S. DEPARTMENT OF ENERGY
under contract DE-AC05-00OR22800

IMAGING FTIR SPECTROSCOPY WITH CONTINUOUS SCAN INTERFEROMETER

G.L. Powell,
Y-12 National Security Complex*, Oak Ridge, Tennessee
R.L. Cox,
Oak Ridge National Laboratory, Oak Ridge, Tennessee
and
M. Beecroft, M. Dombrowski, P. Matison, M. Szczesniak,
Surface Optics Corporation, San Diego, California

5th AMPET Conference
Huntsville, Alabama
September 16-18, 2002

*Managed by BWXT Y-12, LLC.
for the U. S. DEPARTMENT OF ENERGY under contract DE-AC05-00OR22800

CONTRIBUTORS

M. Milosevic, J. Lucania, N. J. Harrick
Harrick Scientific
Ossining, New York

J. D. Lemay
Lawrence Livermore National Laboratory
Livermore, California

G. Auth
MIDAC Corporation
Irvine, CA

B. H. Nerren
Marshall Space Flight Center
Huntsville, Alabama

E. R. Engberg
U. S. Army Environmental Center
Aberdeen Proving Grounds, Maryland

J. T. Neu, R. Dummer
Surface Optics Corporation
San Diego, California

T. E. Barber, J. E. Parks, II
Oak Ridge National Laboratory
Oak Ridge, Tennessee

R. L. Hallman, Jr.
Y-12 National Security Complex
Oak Ridge, Tennessee

J. P. Baiardo
Los Alamos National Laboratory
Los Alamos, New Mexico

J. Bajaj, K. Vural
Rockwell Science Center, L.L.C.
Thousand Oaks, California

DRIFT
Diffuse Reflectance Infrared Fourier Transform

- Remote-sensing diffuse-reflectance optics has been used to obtain Fourier transform mid-infrared spectra from surfaces for the nondestructive inspection of these surfaces for characteristics, films, and contamination.

- The practical success of this technique has led to the development of a small portable surface inspection spectrometer,

  - translation stages for spectral surface mapping ,
  - software to synchronize spectrum collection with sample position,
  - the ability to observe the specimen through the infrared optics,

    and
  - to reduce the spectral data to images.

Barrel Ellipse Surface Analysis System

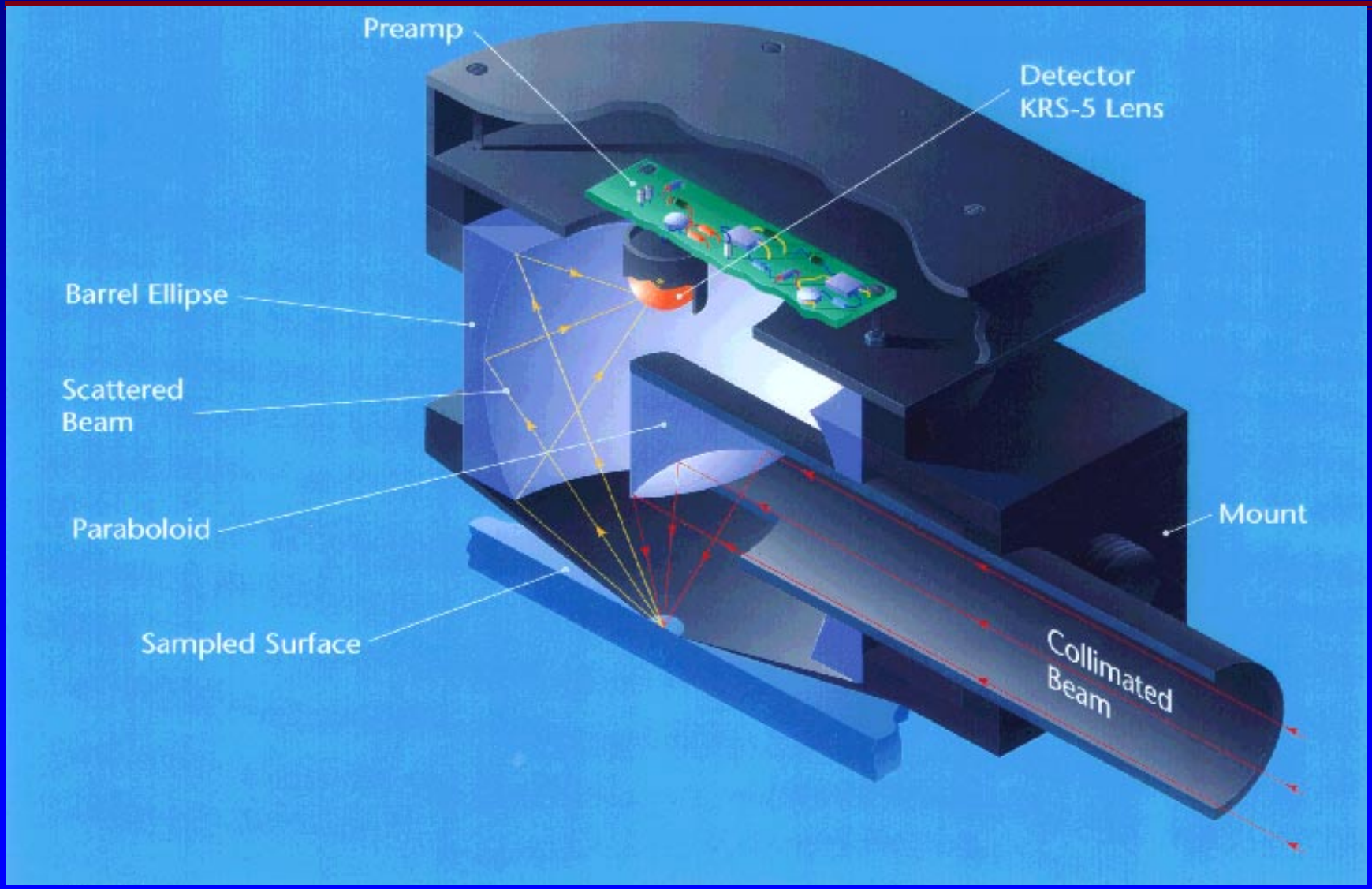

DRIFT

- Given the capability to obtain an image consisting of pixels each containing a high quality mid-infrared spectrum;
- Practical large surfaces can now be examined and analyzed using the host of techniques such as
  - peak height and area,
  - color discrimination,
  - chemometrics,
  - and chemical intuition.
- Surface features may be compared and contrasted in a manner similar to that used by a good chemist to choose a reference spectrum.
- DRIFT is slow, but not labor intensive.
- DRIFT represents the limit of what may be done with other infrared imaging techniques
  - that must compromise spectral quality in the name of speed and convenience.

UTILIZATION OF FTIR SPECTROSCOPY IN SURFACE INSPECTIONS

ONE CAN APPLY ALL OF THE ADVANTAGES OF INFRARED SPECTROSCOPY TO SURFACE INSPECTIONS, BY EMPLOYING THE PORTABLE INFRARED REFLECTOMETER, THE SOC 400.

Line of Accessories

- Diffuse Reflectance.

- Specular Reflectance.

- Grazing Angle Specular Reflectance.

- ATR (diamond, germanium)

- VSphere™

THE SOC-400D LONGNECK

The barrel ellipse optics sampling point is located at the end of an optical transfer tube that allows the inspection to be done at distances on the order of a meter from the spectrometer for industrial applications.

THE SOC-400D LONGNECK

The barrel ellipse optics sampling point is located at the end of an optical transfer tube that

- allows the inspection to be done at distances from 10 cm to ~1 m from the spectrometer for industrial applications,
- allows for interchangability of instruments with 30 μm precision,
- allows for an optical sensor that looks sideways,
- allows for specular reflectance head,
- allows for spectral mapping by manipulating the inspected object,
- allows for adaptation to a glove box window,
- and allows for a visualization option that lets the region to be inspected to be observed through the infrared optics.

GLOVE-BOX VISUALIZATION MAPPER

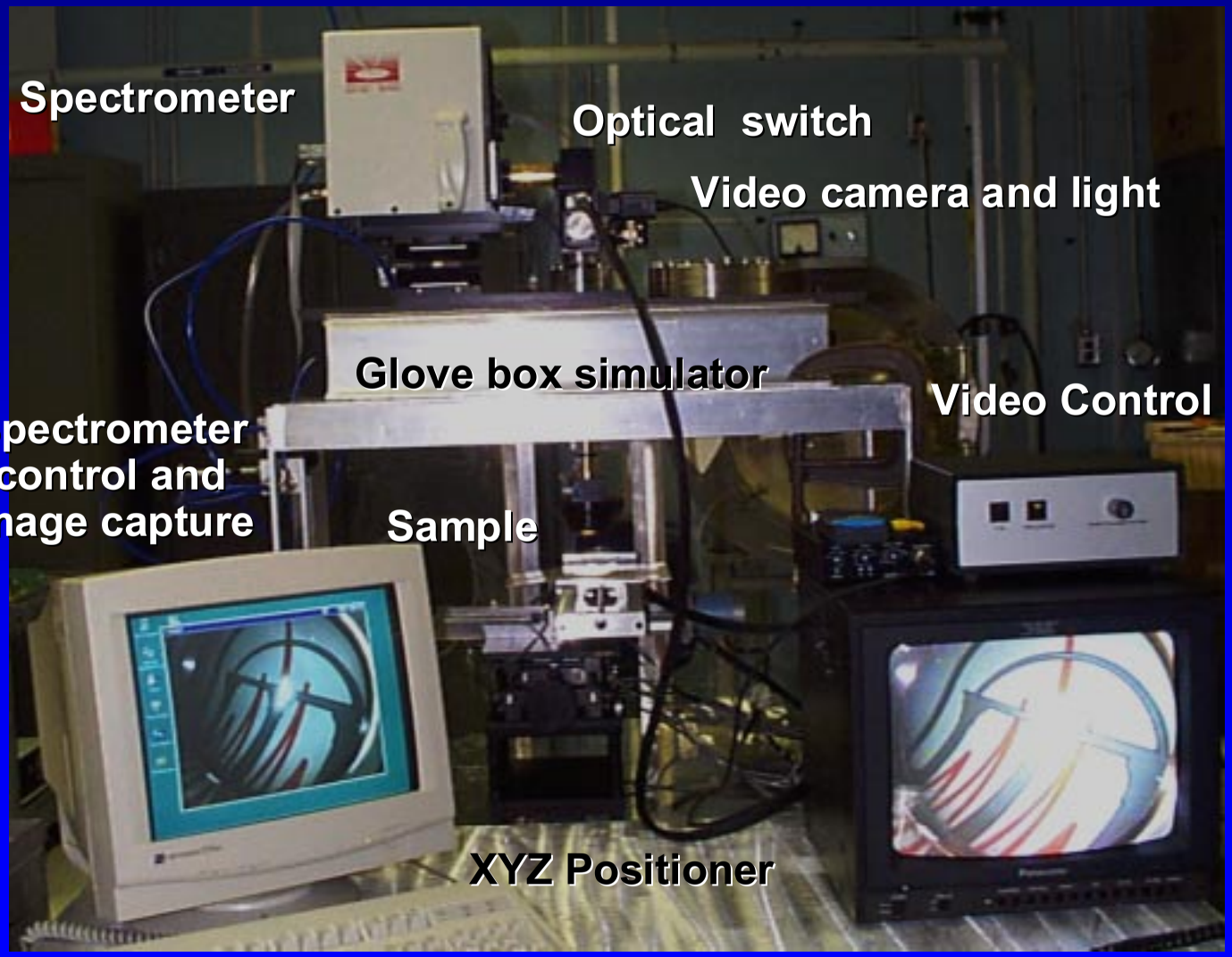

THE VISUALIZATION OPTION

- Recent developments in the SOC-400 design, led by Los Alamos National Laboratory, allows the SOC 400D to analyze specimens inside glove boxes.

- Along with the glove box extension was developed a *Visualization Option* that allows a video observation of the spot to be analyzed through the *SOC 400* optics.

- Magnification is controlled by moving the specimen up or down relative to the sampling point using a motorized lab jack.

- Spectral imaging is easily done using the Visualization Option to locate the center of the image about which an XY grid is mapped.

MAPPING OPERATIONS

- The SOC 400D looks down onto paper specimen while *MIDAC/GRAMS/32* collects individual spectra, and gives a serial instruction to a Velmex slide to reposition the specimen according to a prescribed grid.

- Upon completion of the data collection routine, the spectra are "packaged" as a GRAMS multifile that is ordered in a manner such that a spectral reduction program can produce another multifile of peak heights (or other results) representing chemical moeities on the the XY grid.

- The *MIDAC/GRAMS/32* operating system can display the reduced spectral data in the 3-D mode or

- GRAMS-3D can display the data along with coordinates of a selected point.

VISUALIZATION OPTION VIEW

50 mm

10 mm

The visualization option field of view is equal to the distance that the sample is removed from the diffuse reflectance sampling point. The specimen was then moved left and down to a point from which a rectangular grid would be centered on the spectral map.

OIL STAIN SPREAD EXPERIMENT

- The spread of oil drops (<1 μL) have been used to arrive at a calibration factor for DRIFT spectra of oil stains on sandblasted metals.
  - A not-too-viscous, non-volatile oil is applied to a sandblasted metal surface using either a microliter syringe or while weighing the metal substrate on an analytical balance with 0.01 mg resolution.
  - The oil drop then spreads over the surface of the metal achieving a mound like shape having a maximum thickness of ~1 mm.
  - A spectral map is measured over the entire stain (71 x 71 array, 1 mm steps).
  - A reduced spectral map is determined based on peak heights or areas.
  - This map is numerically integrated yielding a number having units of $a.u./m^2$.
  - The number divided into the weight of the oil drop yields the calibration factor ($g\ (m^2\ a.u.)^{-1}$).
- In the following experiment, a very light silicone oil (0.5 mg, DC 200-5 cps) is allowed to collide with a 0.9 mg olive oil stain as they spread on a freshly cleaned (Formula 409) sandblasted gold surface.

STAINS ANALYSIS ON SANDBLASTED GOLD

Four co-added scans at 16 cm^{-1} resolution

Olive oil

Silicone

Sand

Organic Acid?

Fingerprint

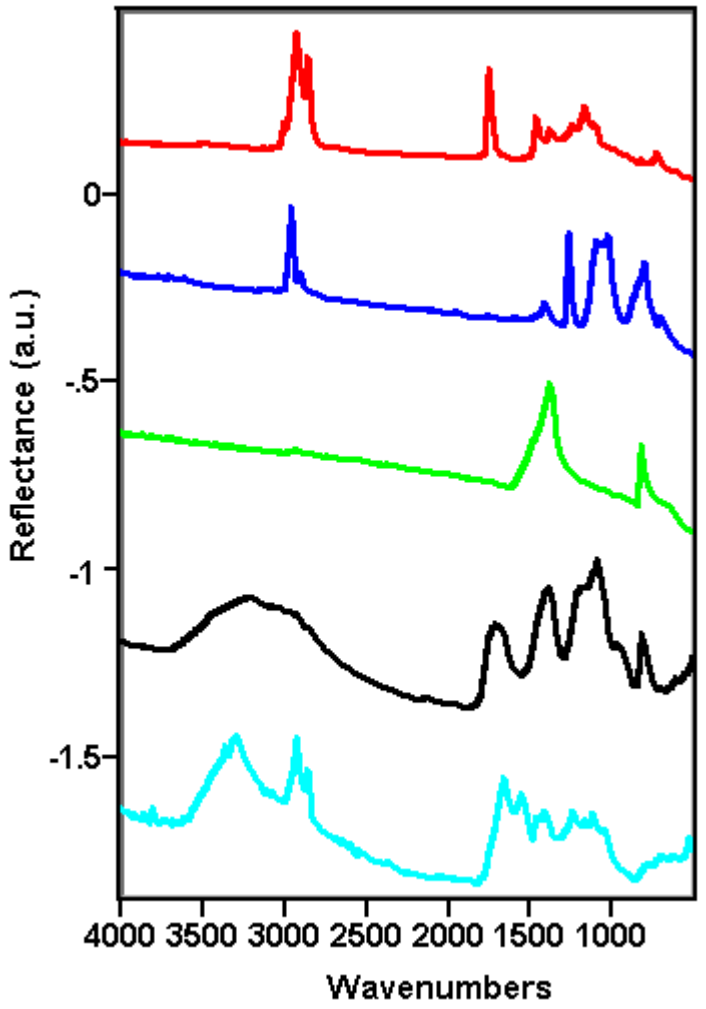

OIL STAIN ANALYSIS ON SANDBLASTED GOLD

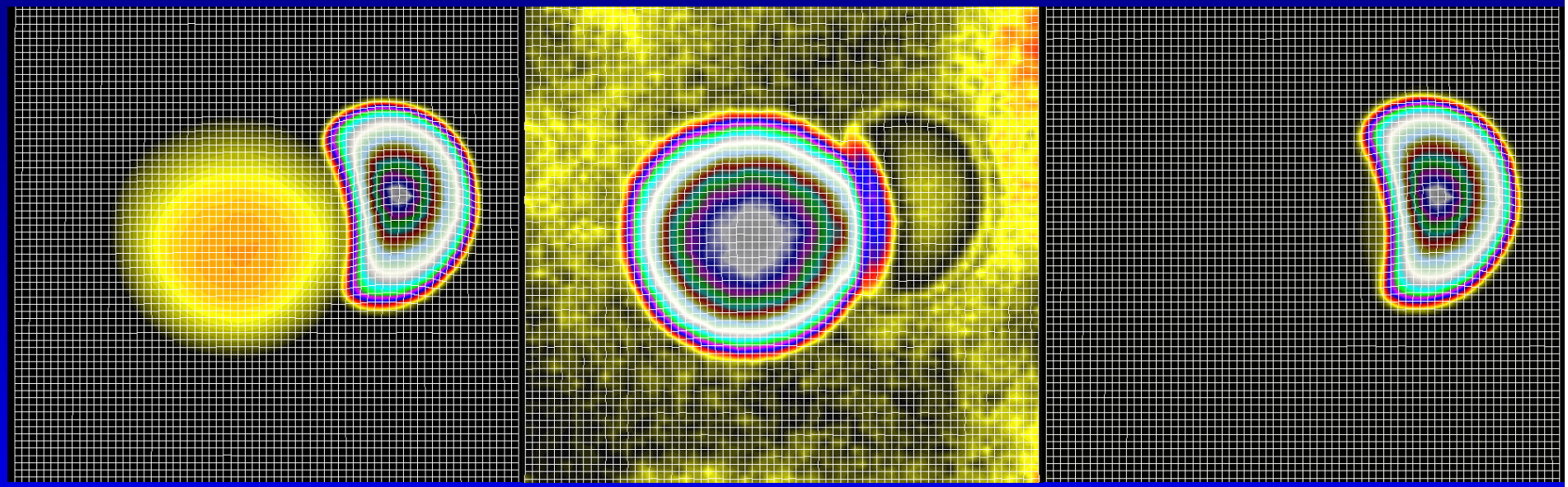

C-H Stretch
2900-3000 cm^{-1}

Silicone
800 cm^{-1}
0.5 days

Olive Oil C=O
1752 cm^{-1}

A 0.5 mg light silicone oil spot and a 0.9 mg olive oil spot spreads toward each other, collide after an hour, and the above maps were obtained with 1 mm resolution over a 10 hour period.

OIL STAIN ANALYSIS ON SANDBLASTED GOLD
The 800 cm^{-1} Silicone band

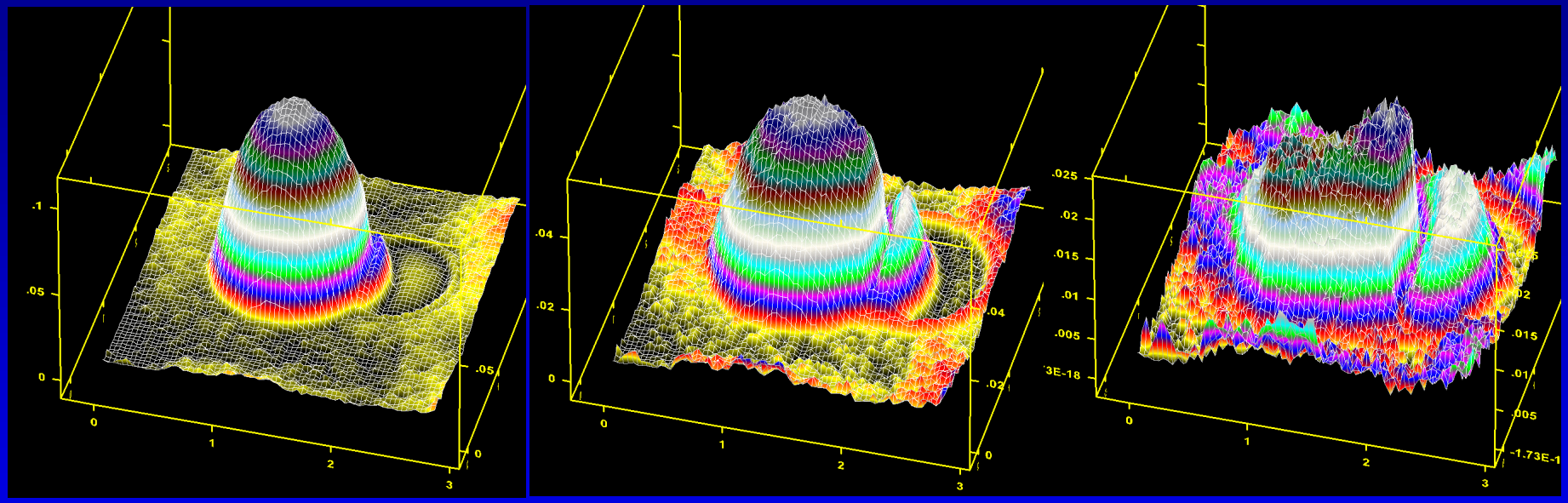

0.5 days | 1.3 days | 4.5 days

The silicone oil migration hit a barrier at the olive oil interface, but was able to undermine it as indicated by these spectral maps of the 800 cm^{-1} band.

OIL STAIN ANALYSIS ON SANDBLASTED GOLD
The 800 cm^{-1} Silicone band

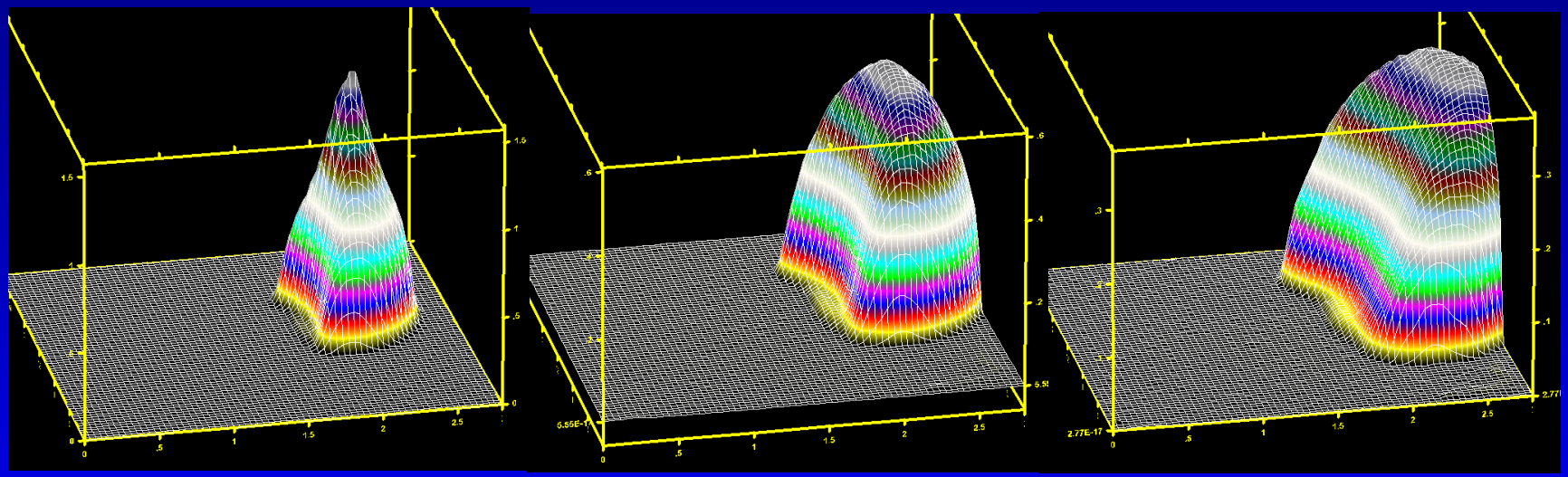

0.5 days 1.3 days 4.5 days

The olive oil migration hit a barrier at the silicone interface, but there was little mixing with the silicone oil as indicated by these spectral maps of the 1731 cm^{-1} C=O band.

Aliphatic hydrocarbon

Maximum value
2800-3000 cm^{-1}

1.60 a.u.

Silicone oil 0.5 mg

Olive oil 0.9 mg

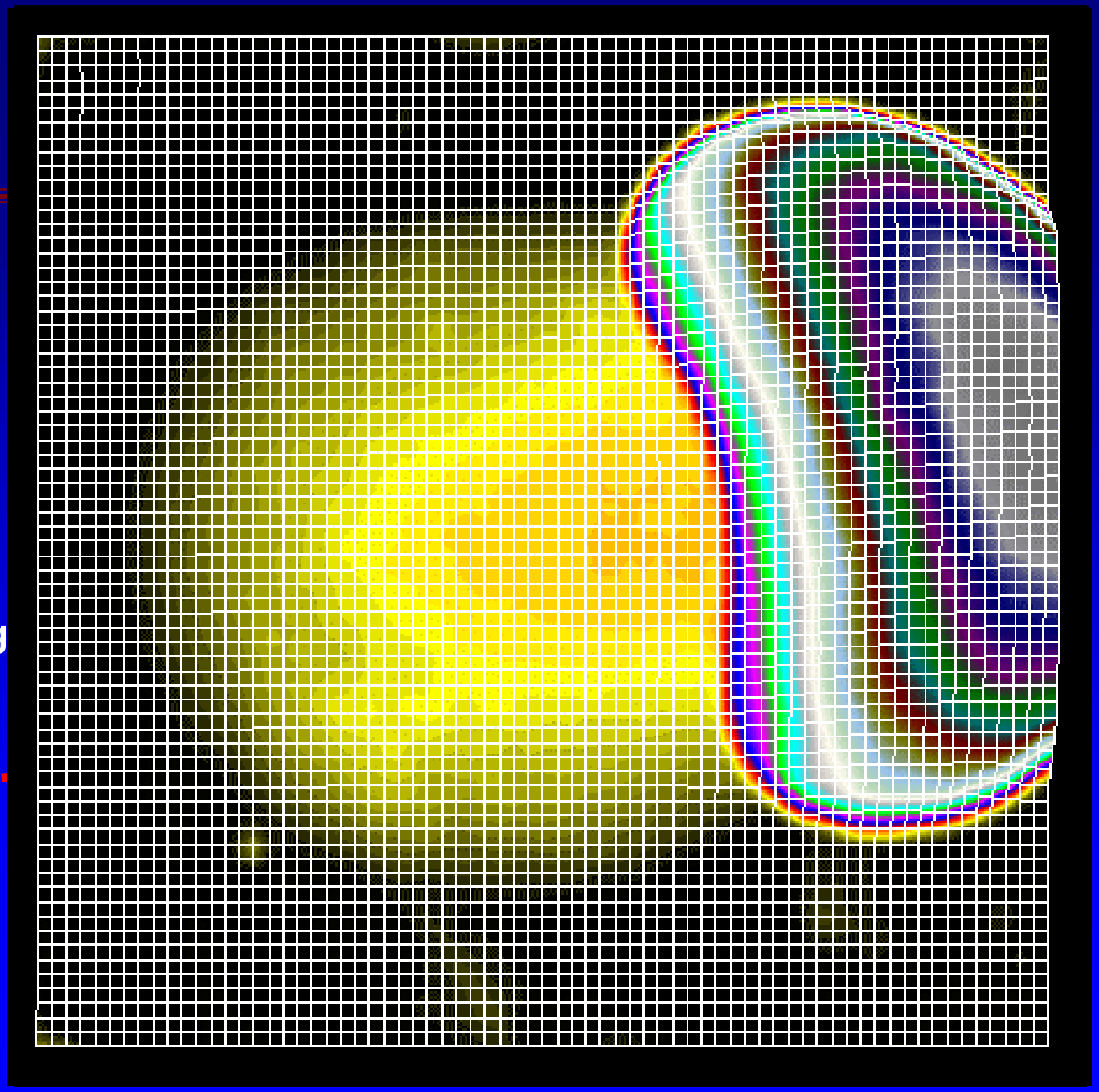

Ester carbonyl

Maximum value
1700-1750 cm^{-1}

1.42 a.u.

Silicone oil 0.5 mg

Olive oil 0.9 mg

Time=0.5 days

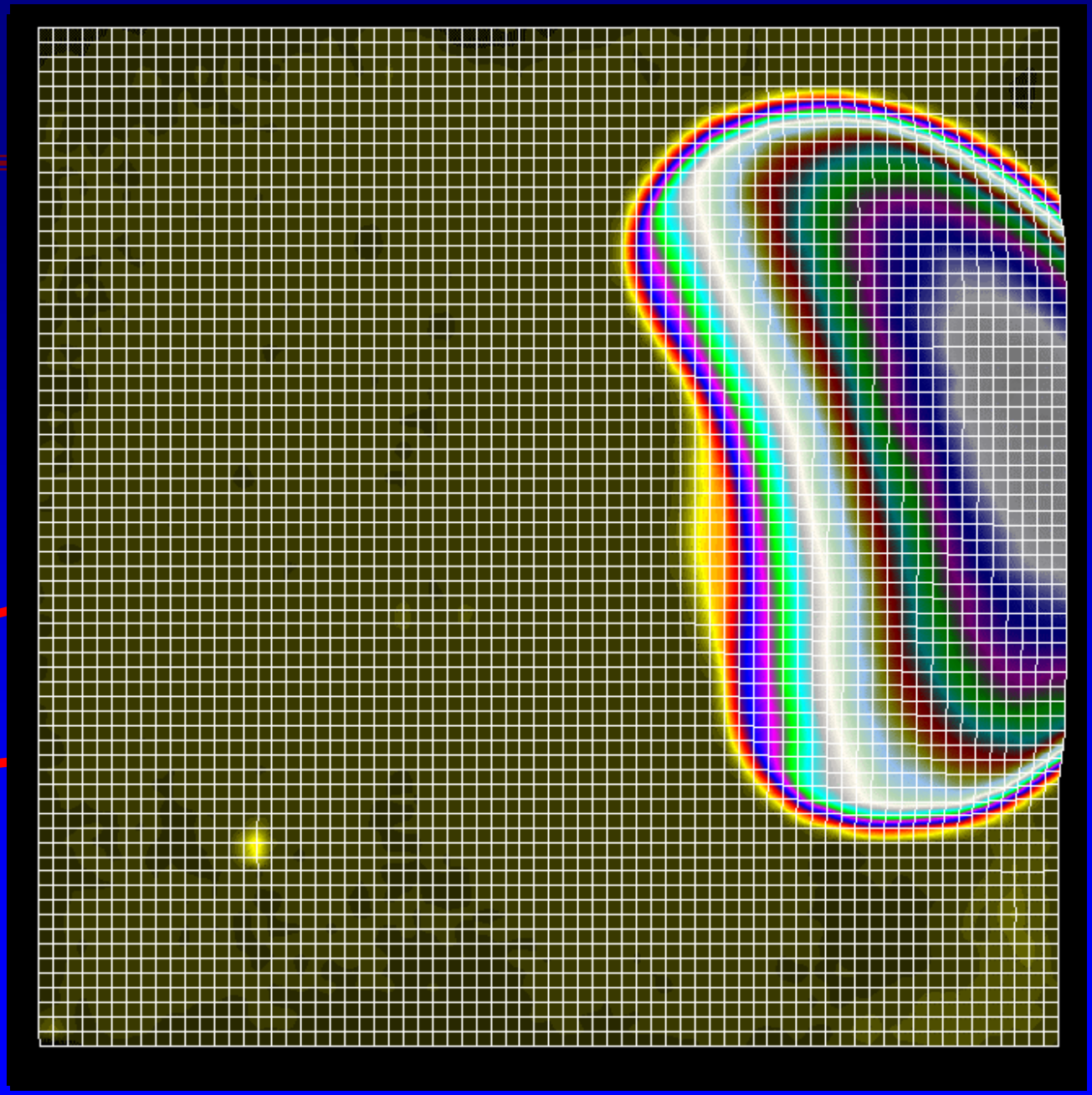

Polysiloxane

Maximum value
1700-1750 cm^{-1}

0.110 a.u.

Silicone oil 0.5 mg

Olive oil 0.9 mg

Time=0.5 days

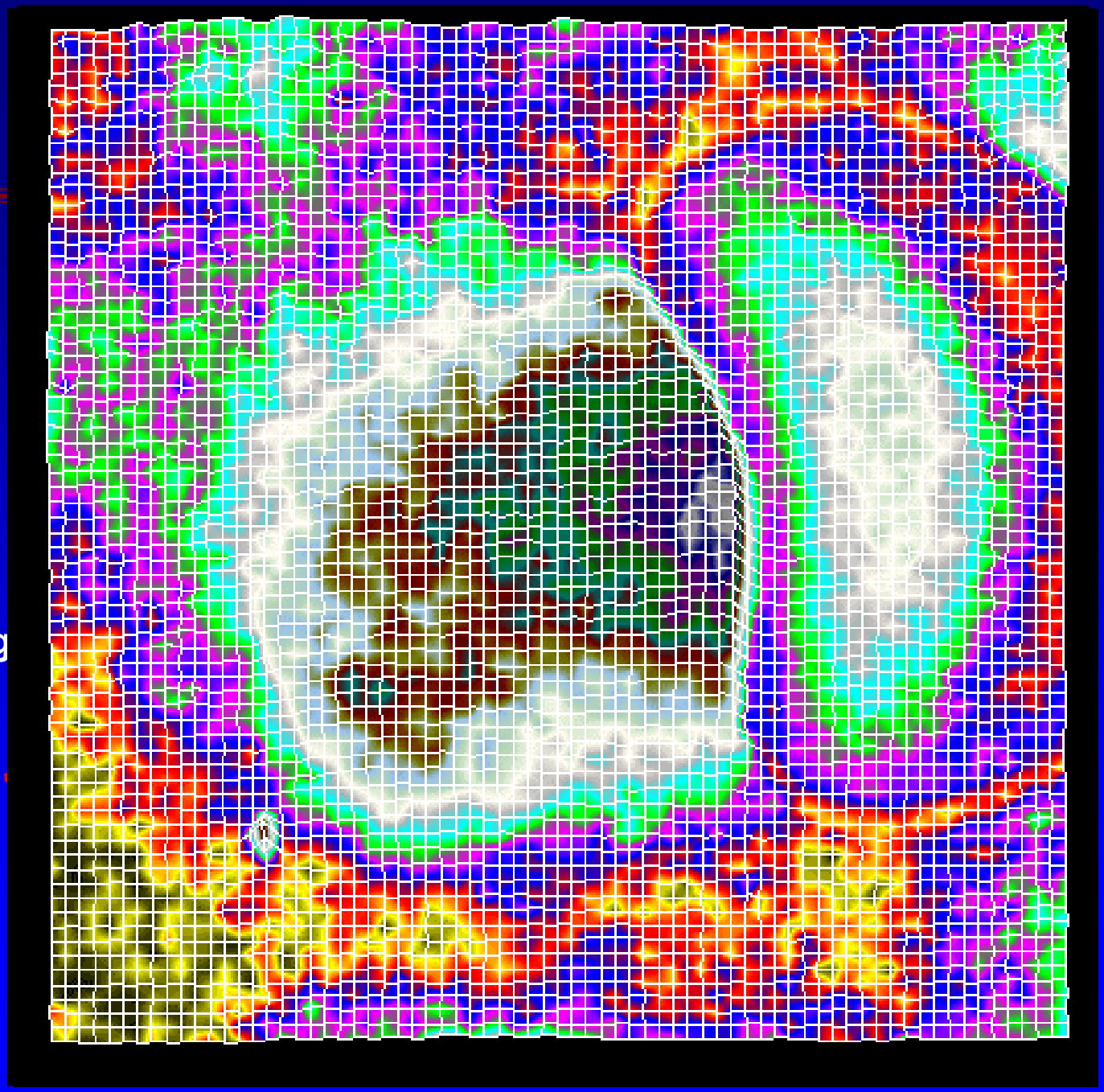

OIL STAIN ANALYSIS ON SANDBLASTED GOLD

The VSO allows the focal point to be placed in the mm-sized opening in the corner of the plate.

The early stages of the oil drop spread can be observed below. (0.5 mg olive oil, 0.5 mg silicone oil)

OIL STAIN ANALYSIS ON SANDBLASTED GOLD

Olive oil (0.5 mg) was deposited and spread for 40 days. HYDROCARBON 2800 -3000 cm^{-1}

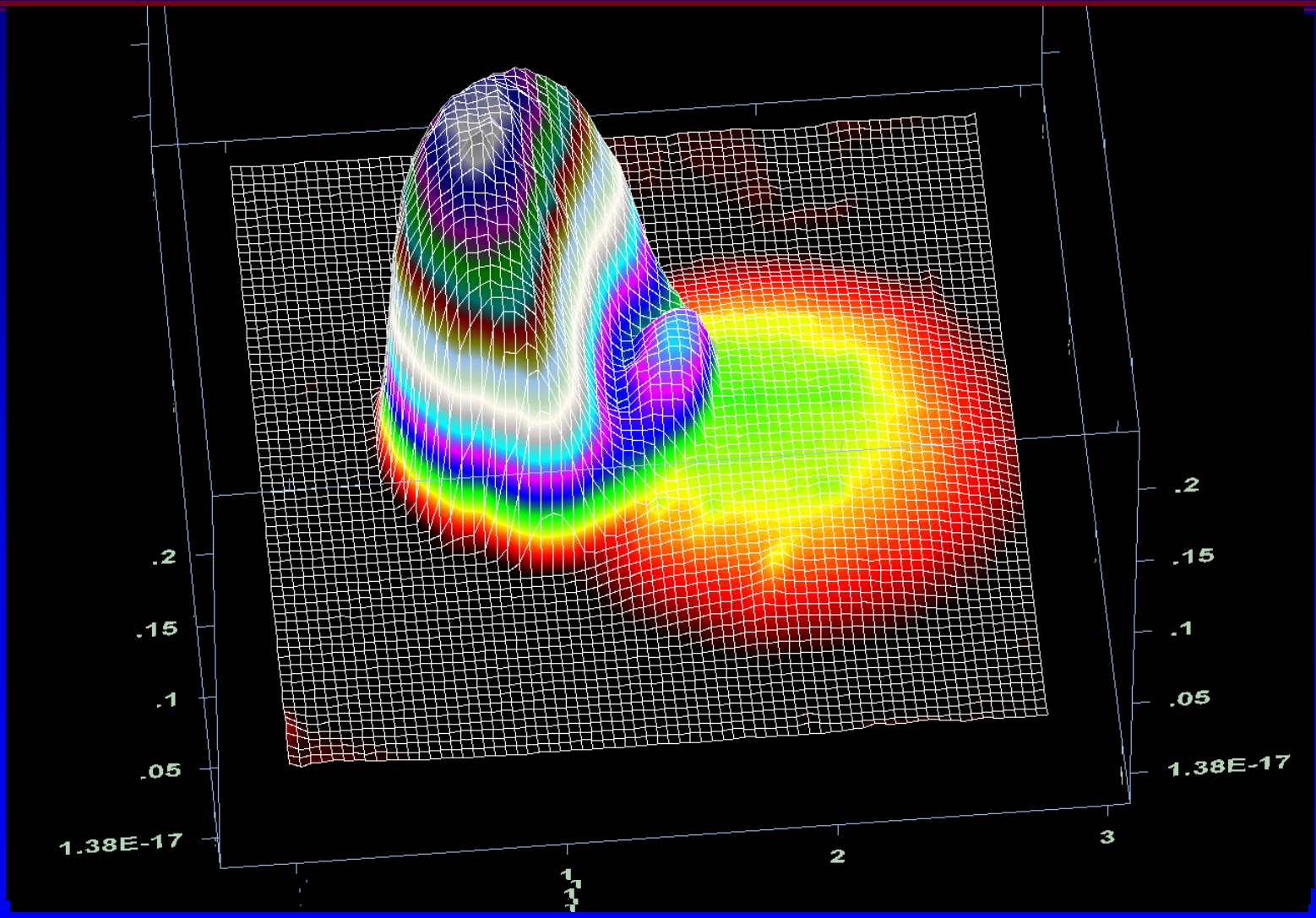

OIL STAIN ANALYSIS ON SANDBLASTED GOLD

Olive oil (0.5 mg) and, next day, silicone oil was deposited and spread for 16 days.

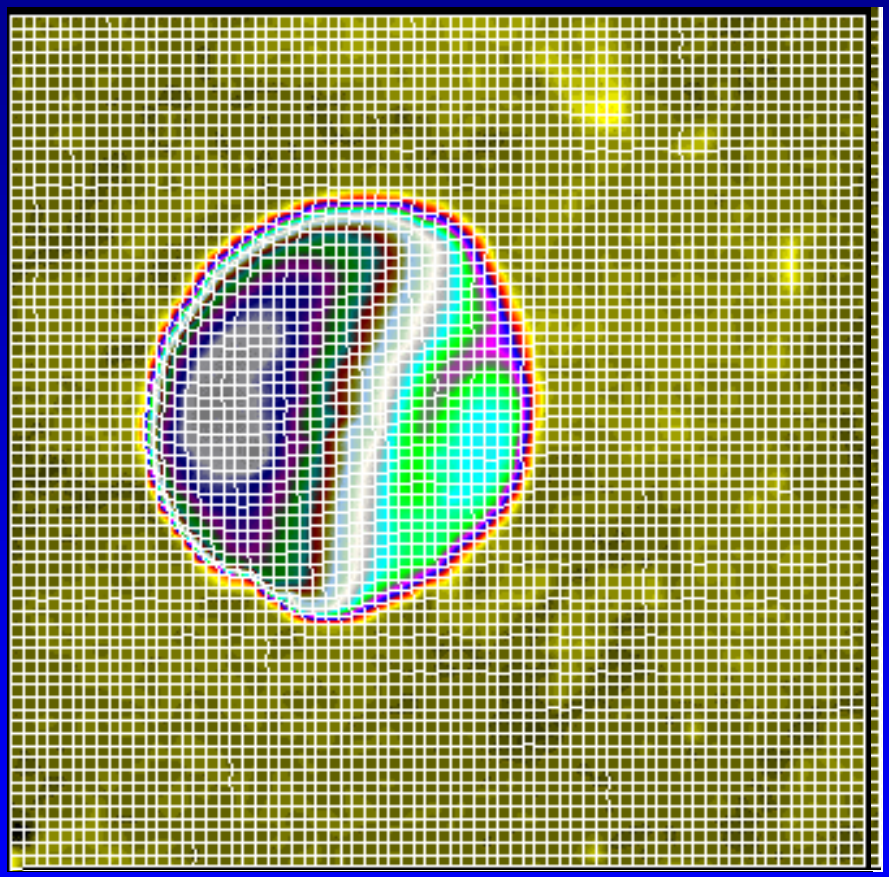

0.5 mg olive oil

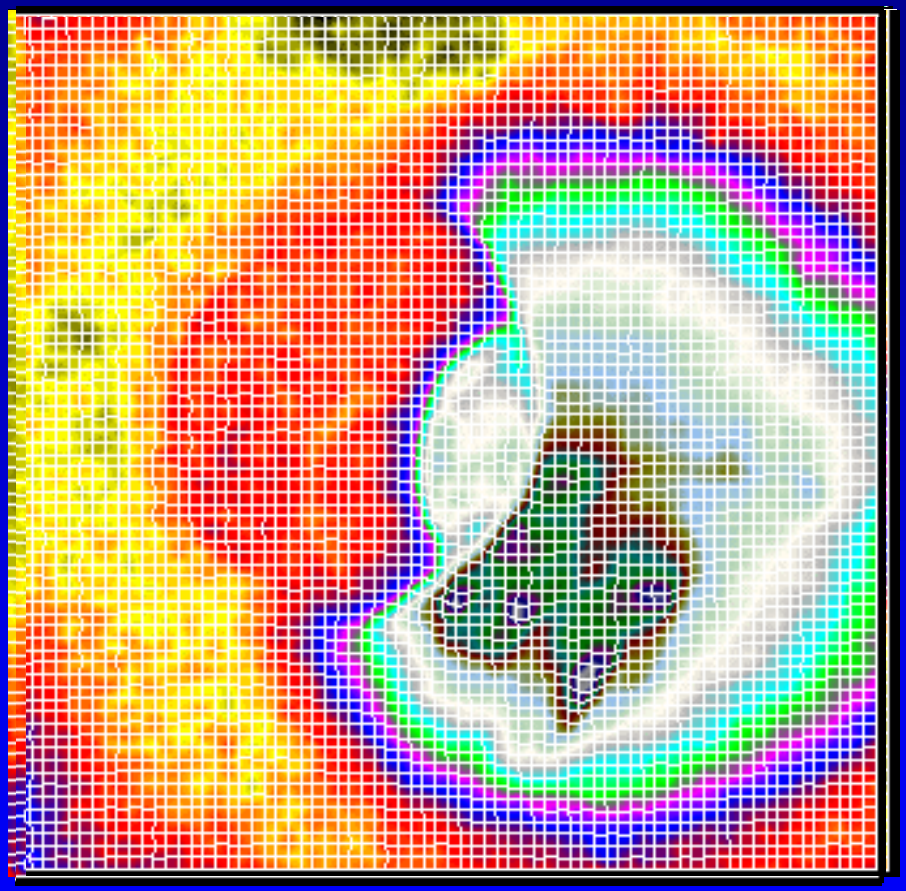

0.5 mg silicone oil

Spectral line maps define the interfaces between stains at early times!

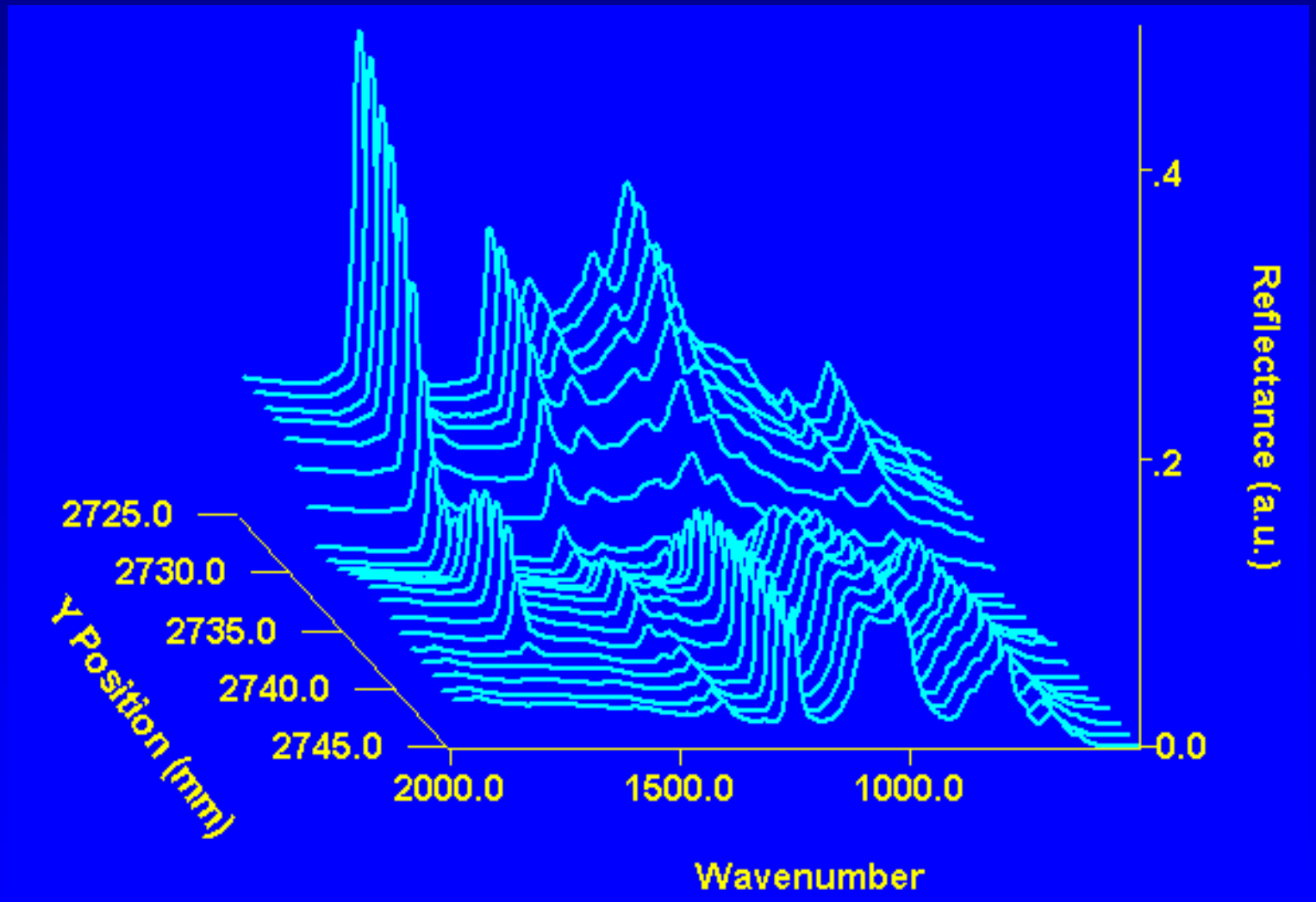

Spectral line maps define the interfaces between stains at early times!

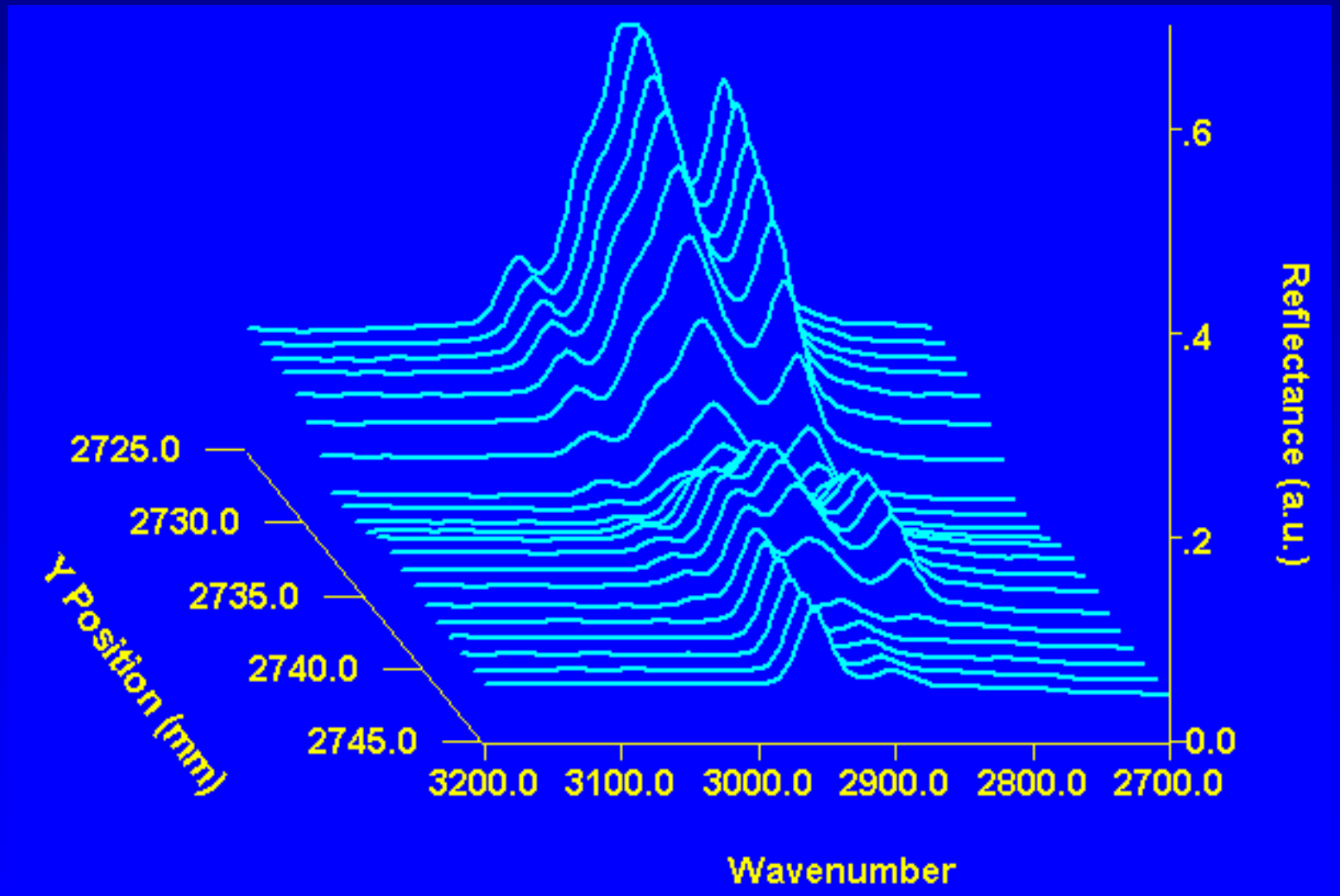

Spectral line maps define the interfaces between stains after a week!

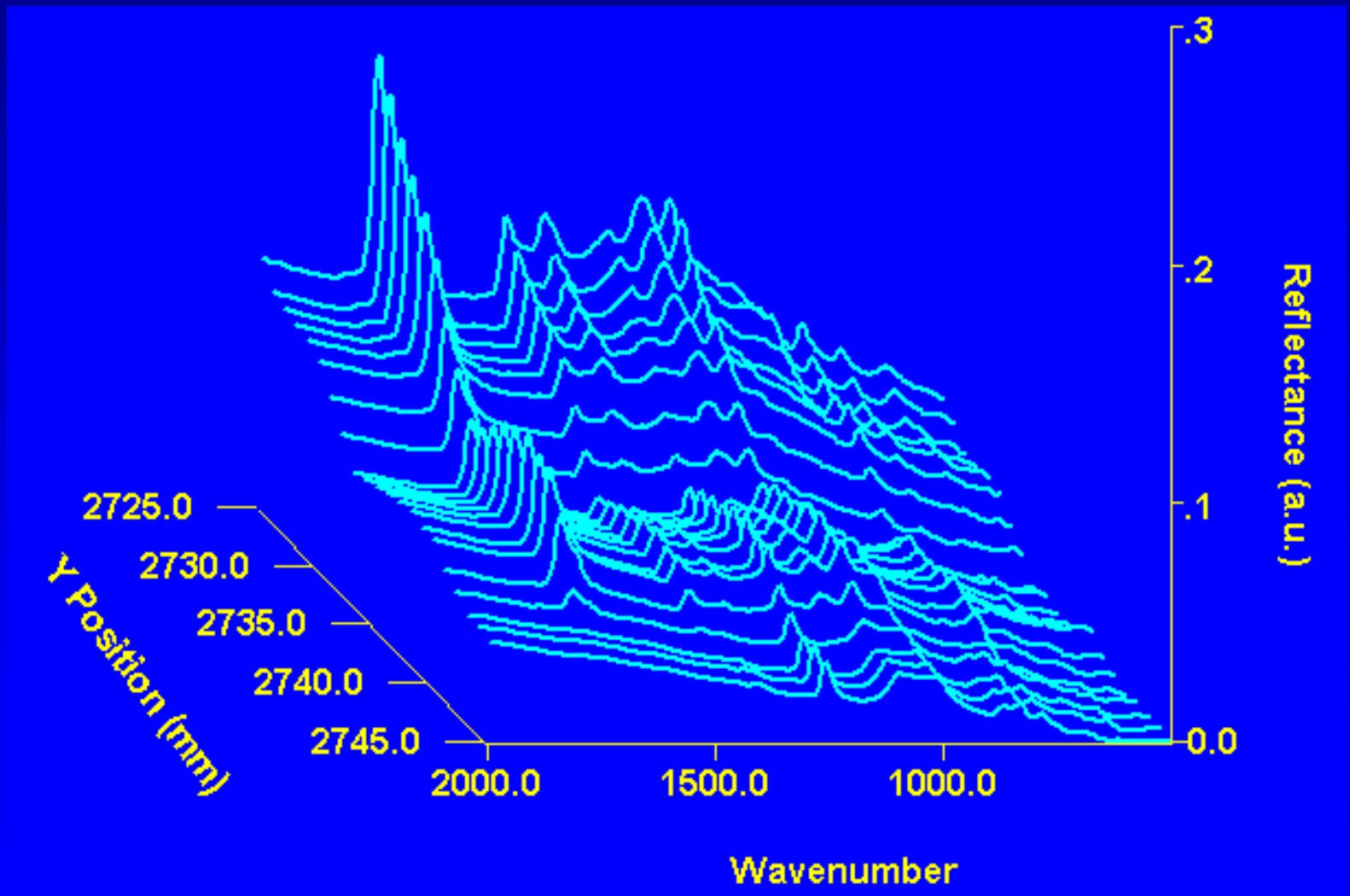

Spectral line maps define the interfaces between stains after a week!

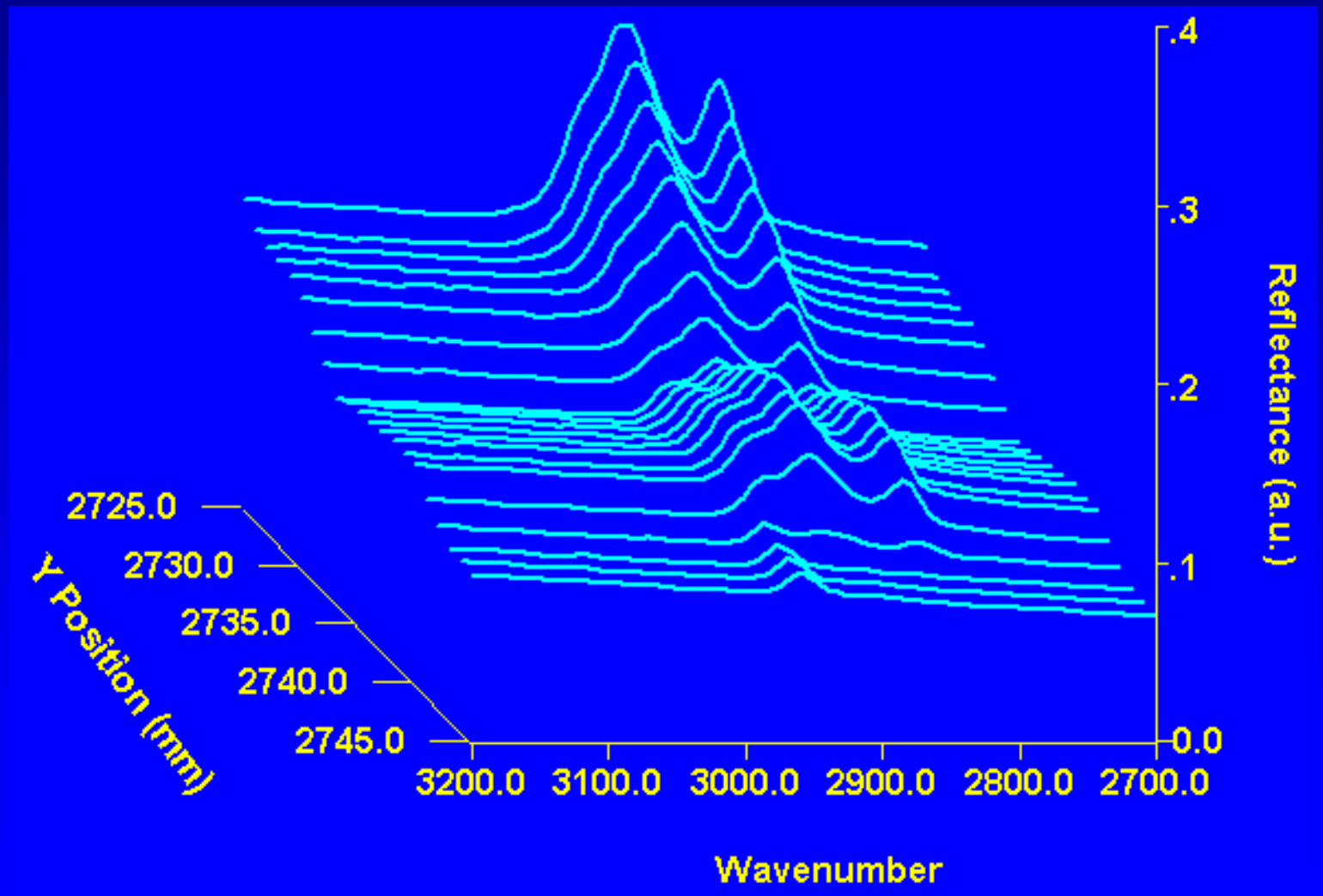

OIL STAIN ANALYSIS ON SANDBLASTED GOLD

Maps were obtained twice daily for 5 days.

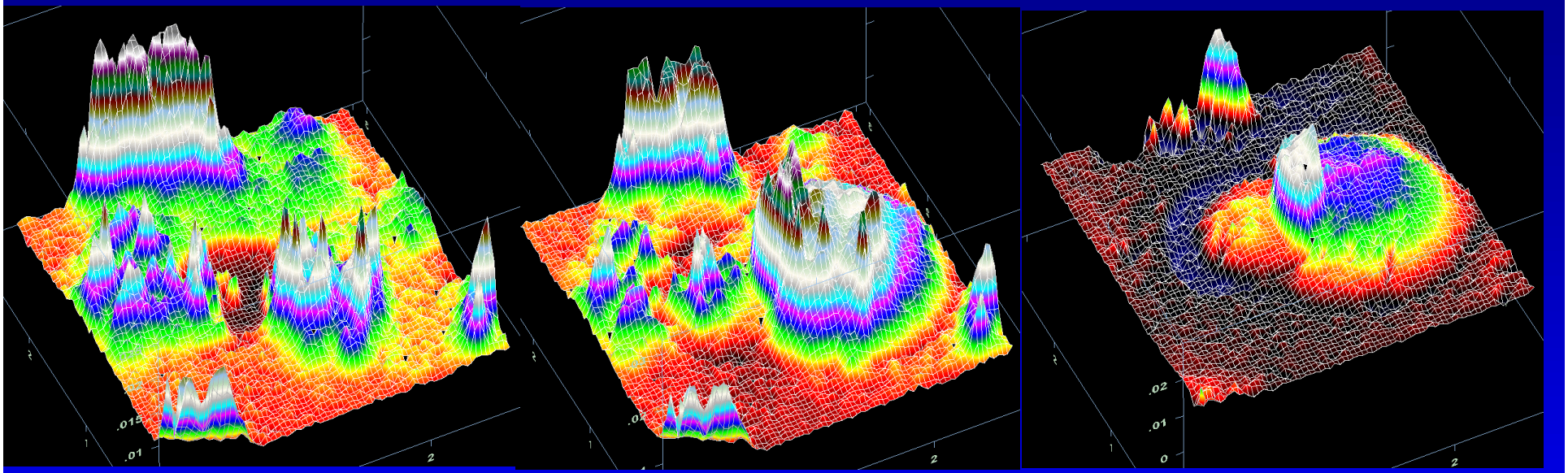

First Day **First Week** **Difference**

Olive Oil Only

Sand embedded in the gold resulted in a peak at 813 cm^{-1} that interfered with the silicone band at 797 cm^{-1}.

In GRAMS, the images can be mathematically processed.

OIL STAIN ANALYSIS ON SANDBLASTED GOLD

The original silicone overrun of the olive oil stain trapped olive oil between the stain perimeters.

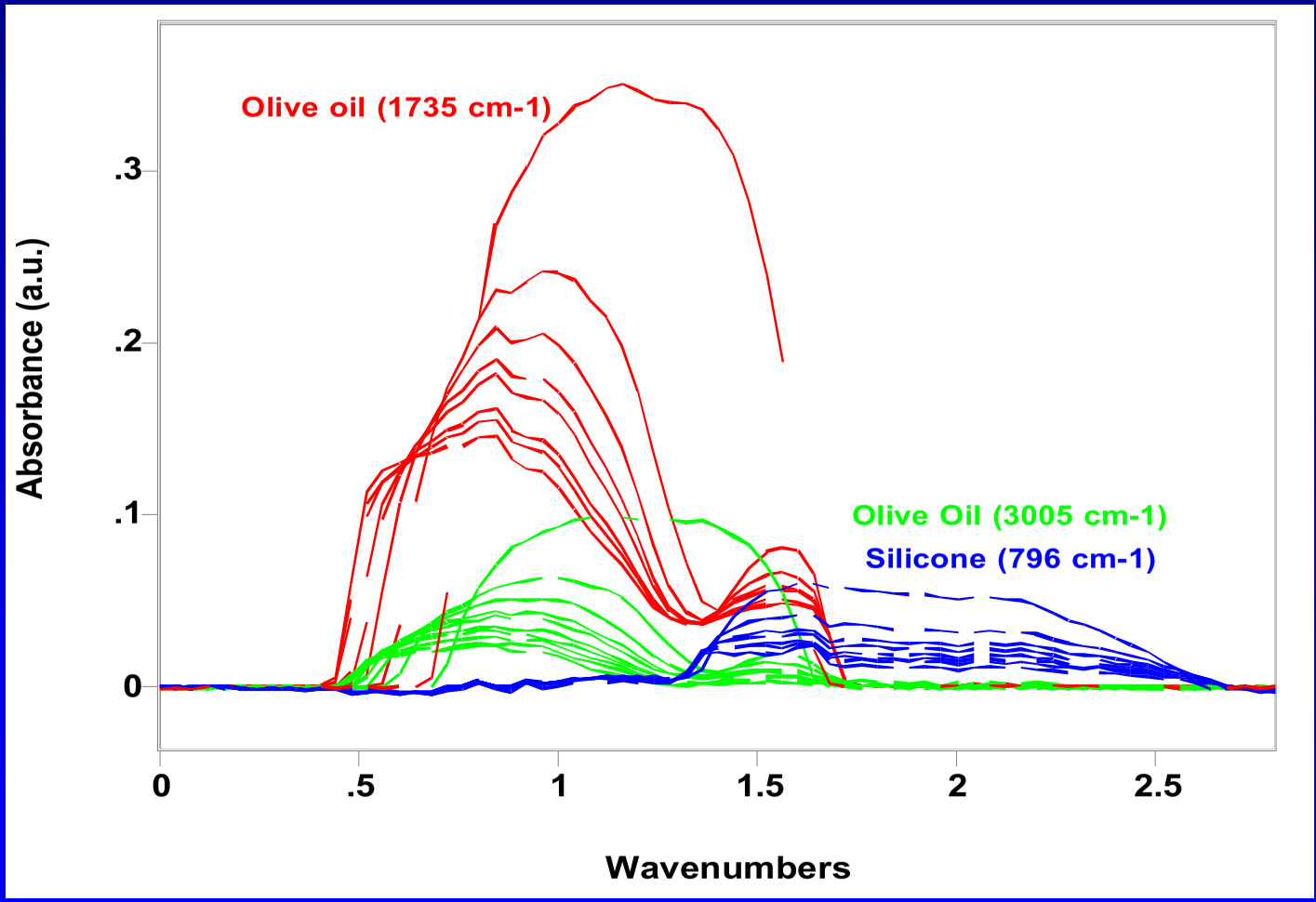

OIL STAIN ANALYSIS ON SANDBLASTED GOLD

The unsaturated =C-H stretch (3005 cm^{-1}) decayed more rapidly probably by oxidation.

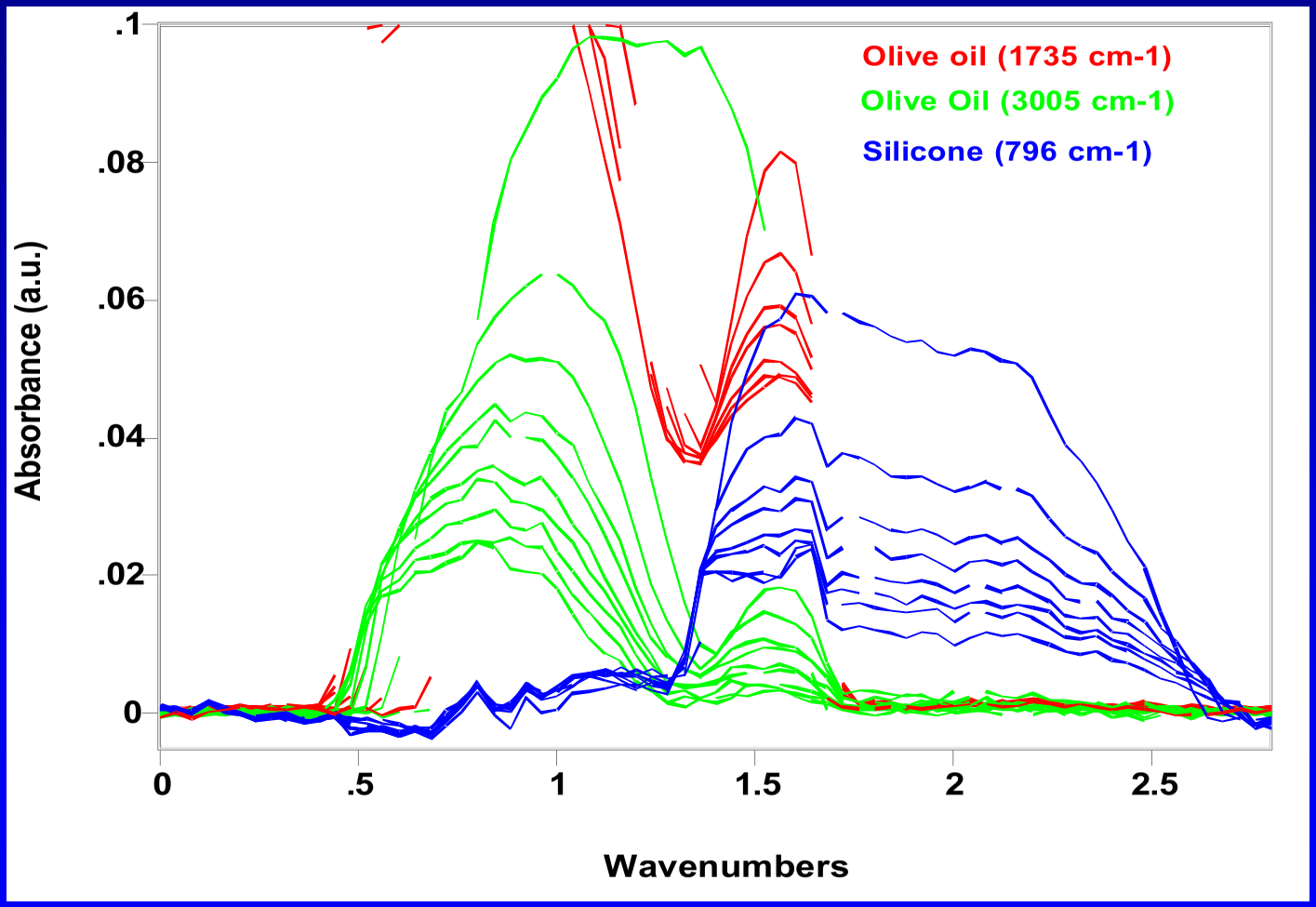

Map Integration yields calibration factors. Sensitivity diminishes with time.

Time	Second Experiment Calibration Factor (g m^{-2} $a.u.^{-1}$)				
Days	1743	1257	2922/2690	794	3003
0.35	4.99		4.04	17.67	
1. 28	5.78	10.30	3.21	23.92	16.86
1.91	6.19	12.37	3.53	27.18	21.50
2.48	6.51	13.43	3.76	30.95	26.06
3.06	6.66	14.12	3.88	32.28	29.20
3.43	6.90	14.85	4.07	37.93	32.92
3.94	7.05	15.43	4.18	41.14	36.47
4.36	7.26	17.09	4.38	48.08	41.24
4.92	7.38	17.02	4.50	55.63	44.22
5.51	7.51	17.48	4.62	62.74	48.41
6.49	7.43	18.38	4.78	71.33	58.86
16.05	8.36	22.00	5.67	157.16	136.45
402.94	11.52	86.62	12.15	23115.21	156.02

Map Integration yields calibration factors. Sensitivity diminishes with thickness.

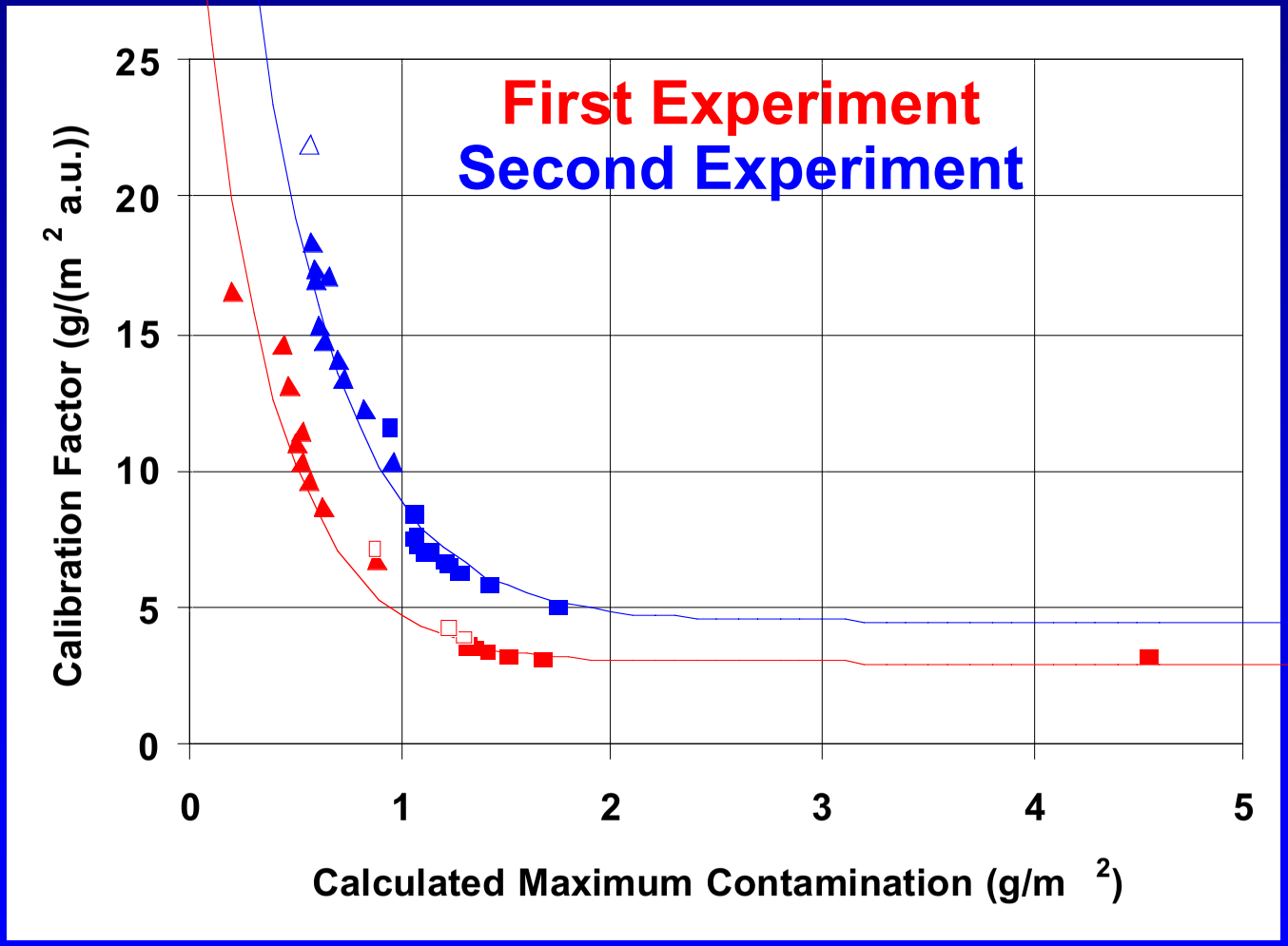

Spectral Map Integration yields higher sensitivity as shown by this average of 100 spectra in a clean area (10 mm x 10 mm).

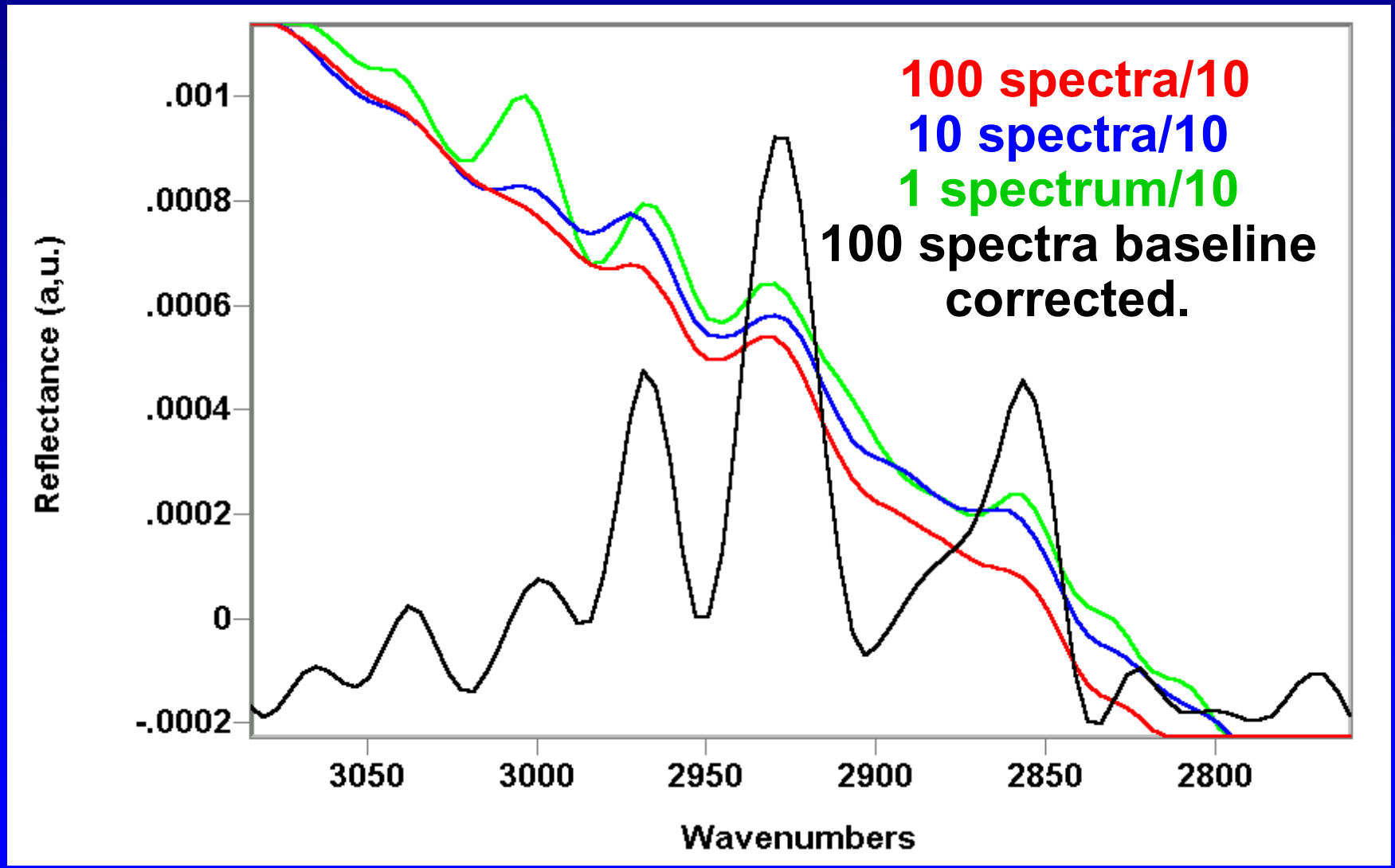

Map Integration yields calibration factors. Sensitivity diminishes with time.

- The calibration units of g m^{-2} a.u.$^{-1}$ are approximately equivalent to μm a.u.$^{-1}$ for oils with specific gravity ~ 1.0.
- The first standard error of the reduced spectral mass peak heights is typically <0.001 a.u. on a clean gold surface,
- indicating a detection limit of <10 mg m^{-2} (<10 nm).
- By averaging the spectra over a 10 mm by 10 mm area (100 spectra) this detection limit can be improved
  - ➢by an order of magnitude
  - ➢yielding a better areal representation of the cleanliness .
- The increase in the calibration factor may be due to
  - ➢real physical or topographical changes in the oil on the surface,
  - ➢band shape changes related to structural changes, or
  - ➢loss of oil by ev aporation .

HIGH SPEED FTIR IMAGER

- With the growth in FTIR imaging technology, the chemist is beginning to see FTIR data packaged as hyperspectral image cubes consisting of two dimensions in space and a third as spectra.
- The chemist exploits this cube by interpreting the spectrum chemometrically, representing the spectral dimension as the value of one component of this reduced spectrum.
- A hyperspectral image cube may be converted into as many images as the chemist s creativity will allow, and displays chemical moeities as spatial images, yielding interesting results.
- To that end, Surface Optics Corporation and the Y-12 National Security Complex has collaborated on developing a

HIGH SPEED FTIR IMAGER.

Dewar Mounted MCT FPA

- The project started with the acquisition of dewar mounted, Mercury-Cadmium-Telluride

  128 X 128 pixel

  Focal Plane Array Detectors

  (MCT FPA, Model TCM 1150)

- From:

  Rockwell Science Center, L.L.C.

  Thousand Oaks, California

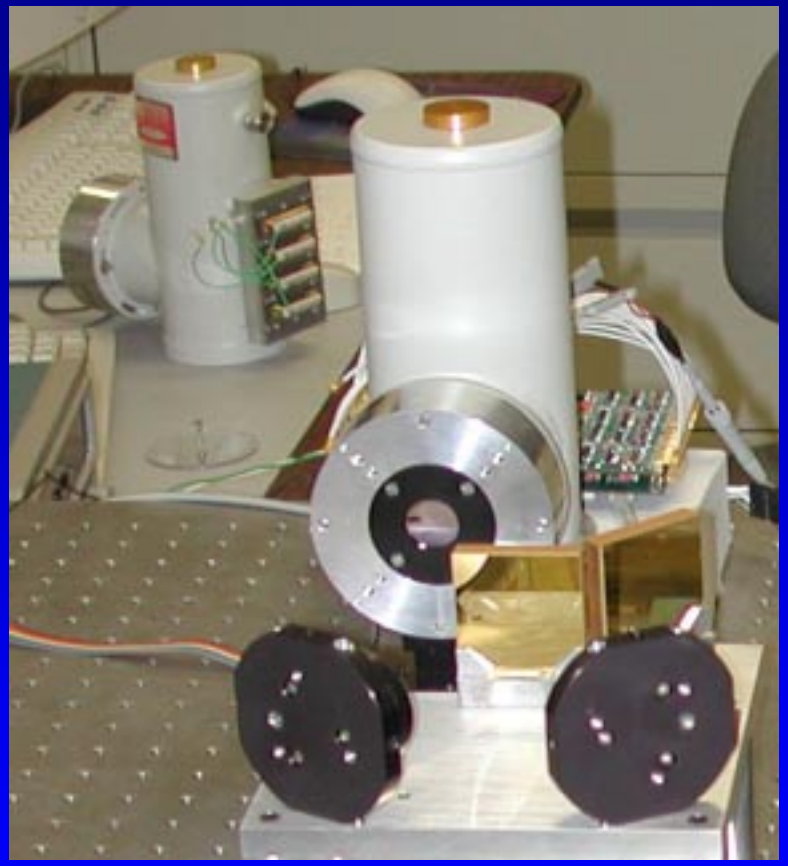

The optics consists of a specular reflectance system where a 10 mm X 10 mm area of a specimen was illuminated by an SOC 400 FTIR source.

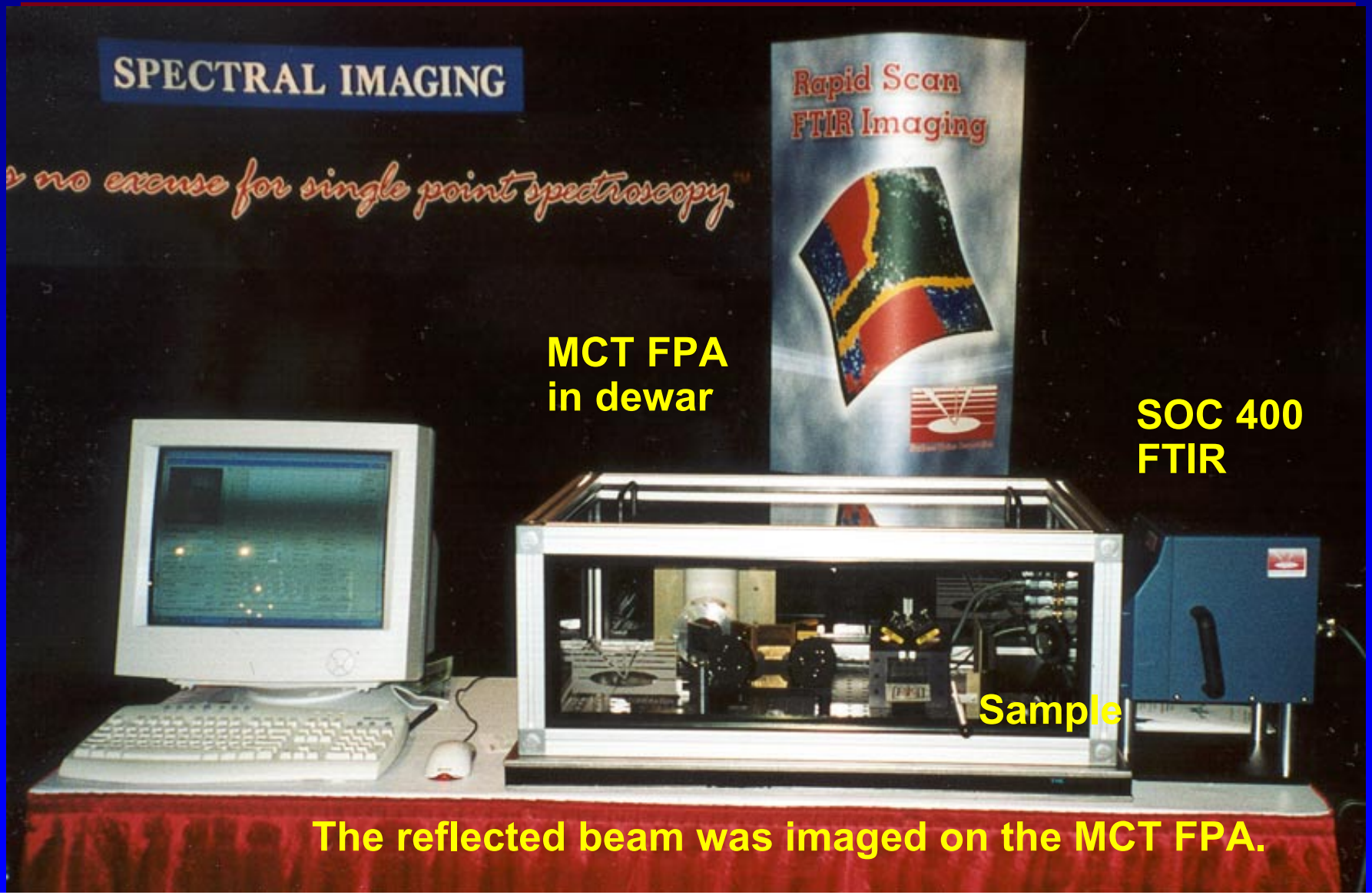

The reflected beam was imaged on the MCT FPA.

Data Acquisition Controls

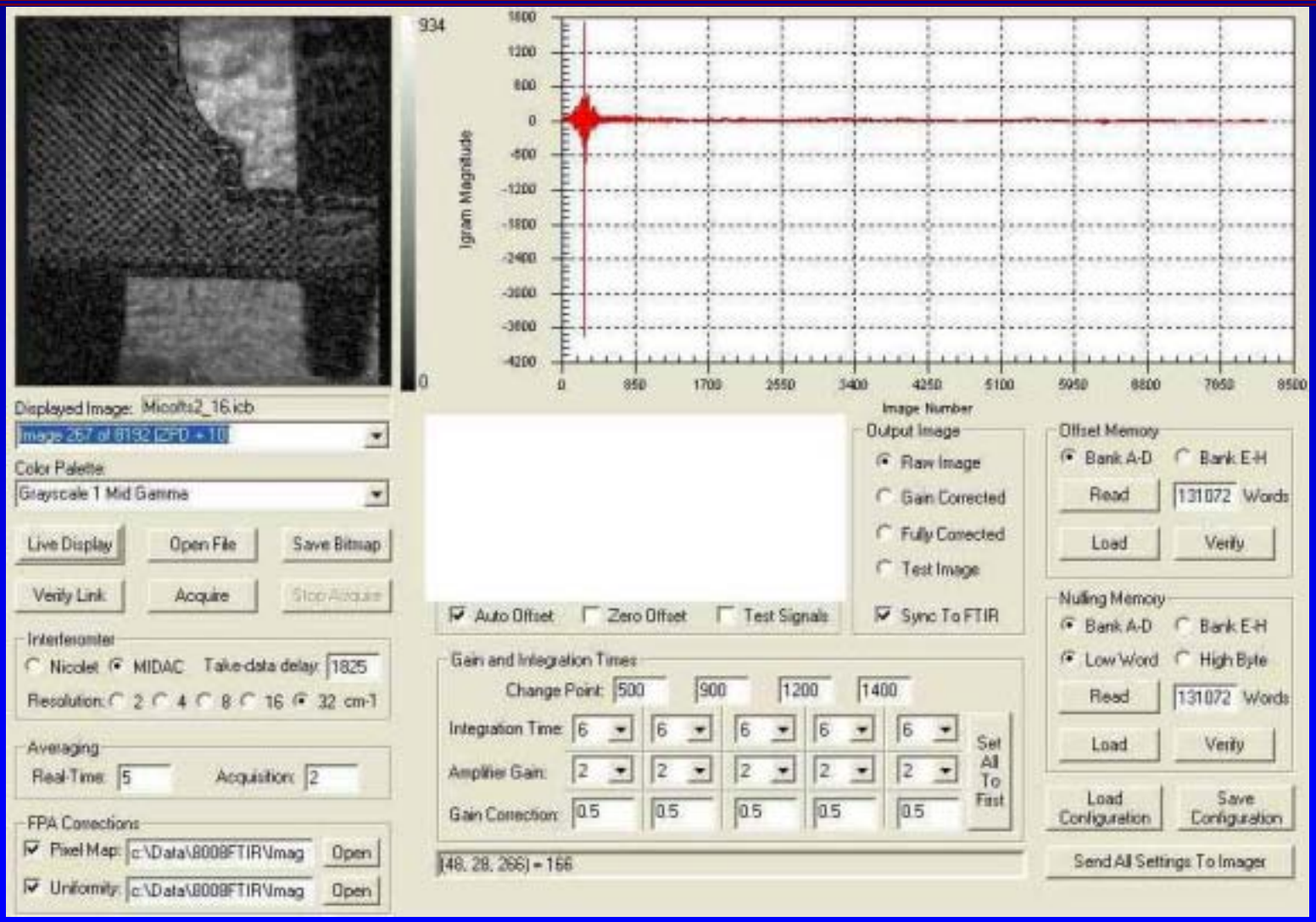

Data Acquisition

- The illumination beam is modulated at 2.5 kHz for the full laser cycle of the SOC 400.
- With each cycle, the analog output for each MCT FPA pixel is integrated for 17 μs, then locked using sample-and-hold devices.
- The analog voltages of the pixels are read four columns at a time through 32 outputs and four, 14-bit analog-to-digital converters
  - ➢ for storage in on-board memory and
  - ➢ subsequent transfer to a computer for averaging scans.
- Operating System Software allows for gain control and instrument settings, and
- allows the image to be observed as it is collected (or after collection), along with the data in time for a selected pixel.

Spectral Quality Is Good.

Collection time = 100 m, S/N = 2000:1
Iinterferogram image is a function of ZPD

ZPD

ZPD+24

ZPD+63

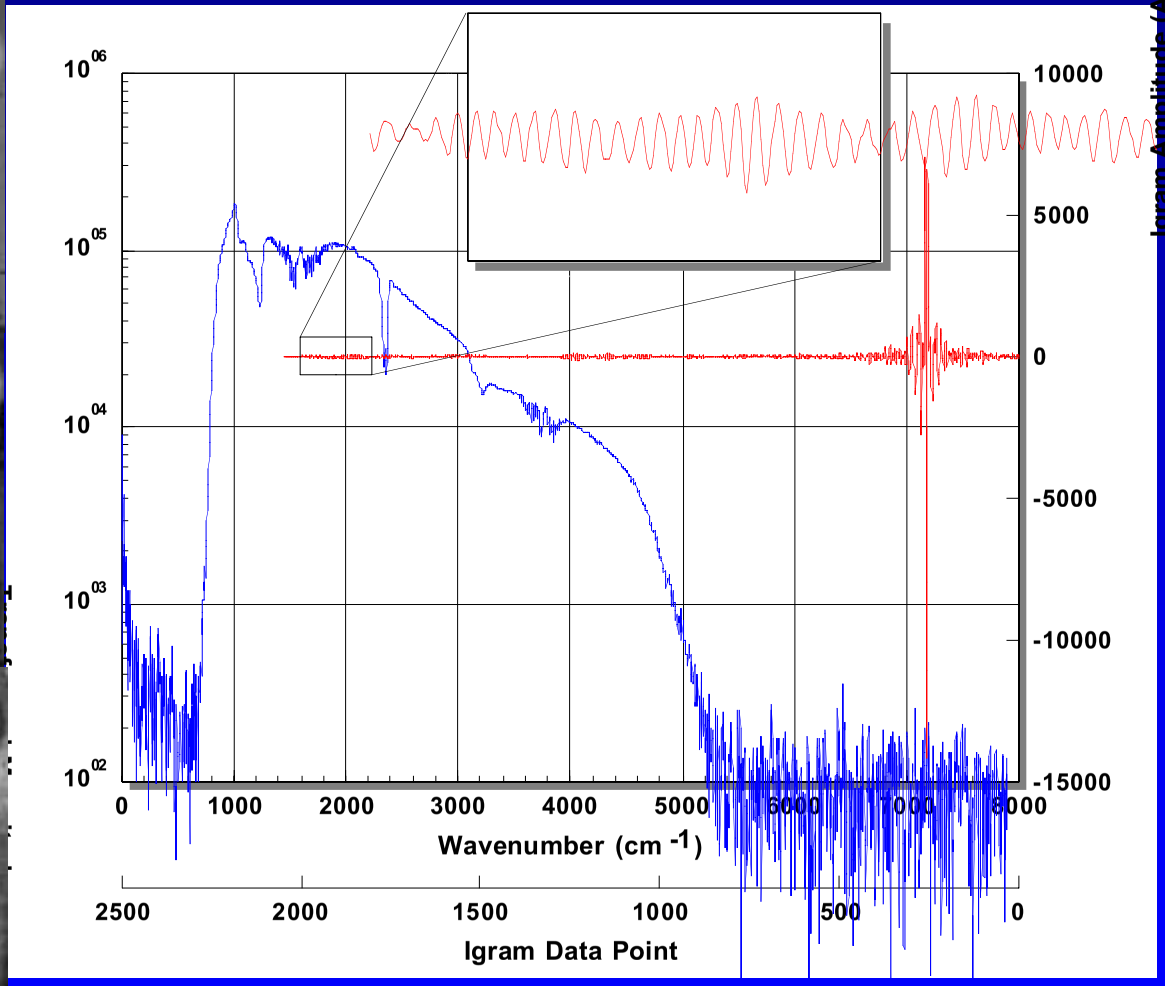

Contamination Migration Kinetics

Vegetable Oil (lower spot)/Silicone Oil (upper spot)
Interferogram ZPD Image

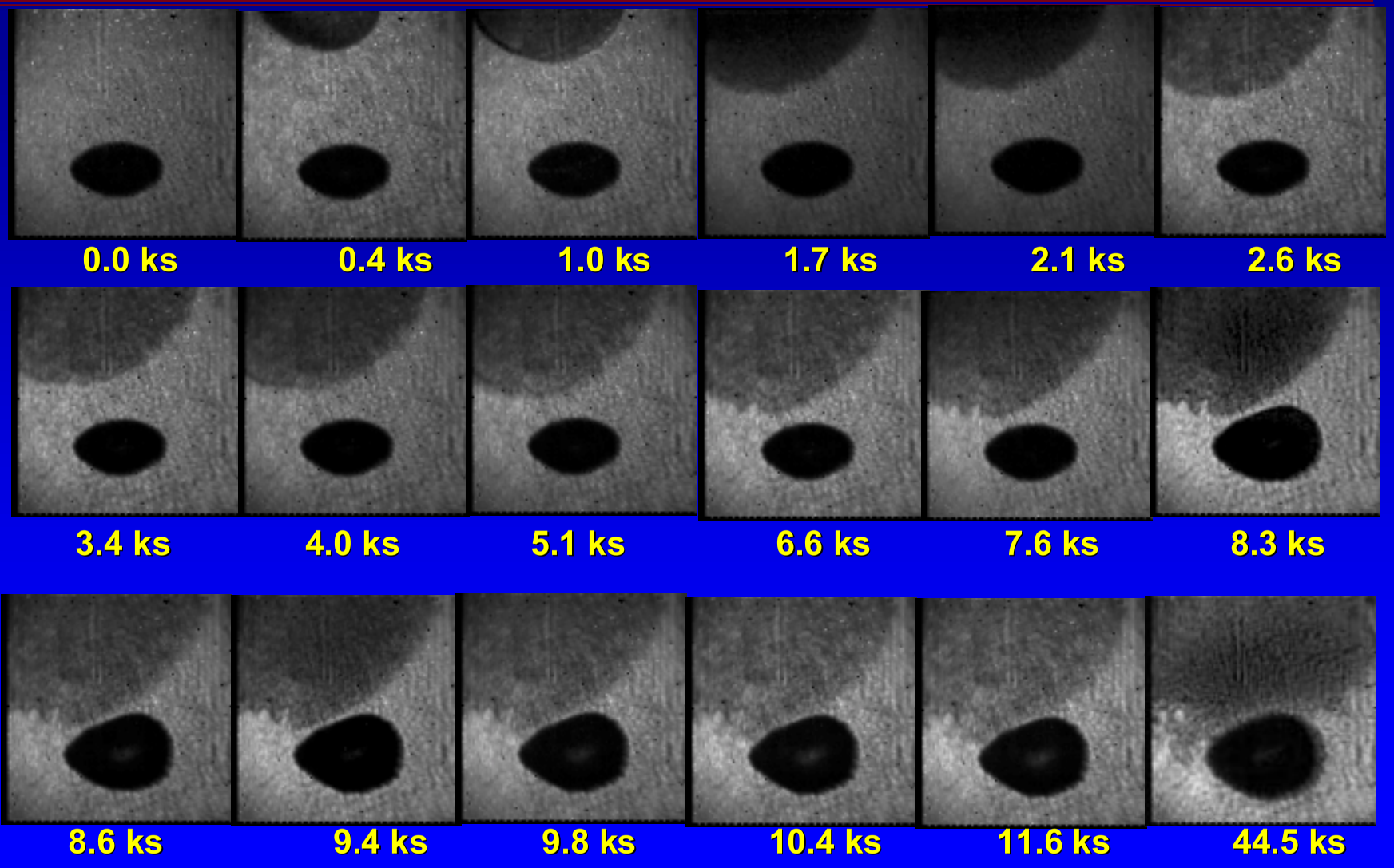

Contamination Migration Kinetics (GRAMS 3D)

Vegetable Oil (lower spot)
Silicone Oil (upper spot)
Interferogram ZPD Image
Using GRAMS Multifile to
Multifile data reduction of
Interferogram center-burst
amplitude.

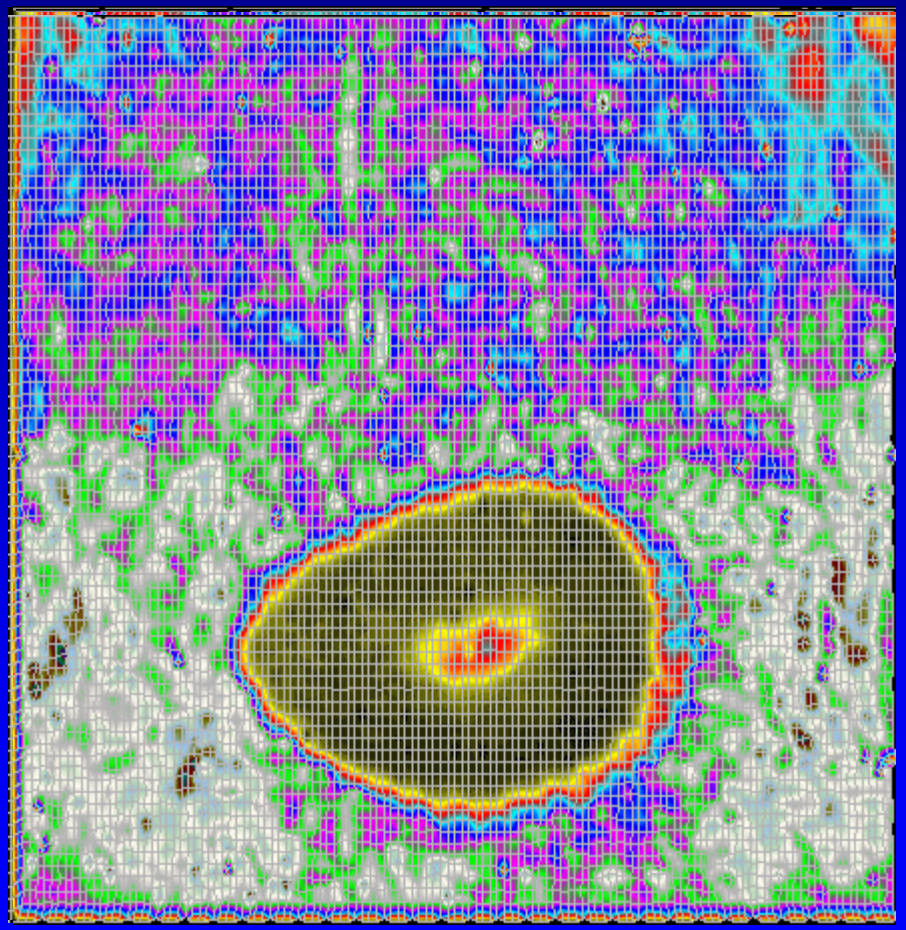

CONCLUSIONS

- The spectral mapping of macroscopic objects to obtain DRIFT spectra is applicable to manufacturing environments.
- Hardware and software are available to obtain laboratory quality spectra in a user friendly fashion.
- The visualization capability simplifies setup of the mapping array.
- The contrast in the reduced spectral maps give the analysis a distinct confirmation that what is observed is real.
- Only the simplest spectral algorithms have been used so far. Just think what can be done with *real chemometrics*!
- FTIR imaging is now available at single spectrum collection rates and perhaps soon an FTIR portrait camera.

Distribution:

Oak Ridge National Laboratory

R. L. Cox

Surface Optics Corporation

M. Beecroft
M. Dombrowski
P. Mattison
M. Szczesniak,

Y-12 National Security Complex

R. B. Bonner
G. L. Powell
P. E. McKenzie/M. L. Baker
K. F. Simon/P. E. McKenzie
R. S. Steele, Jr.
Y-12 Central Files - (RC)

The SOC 400

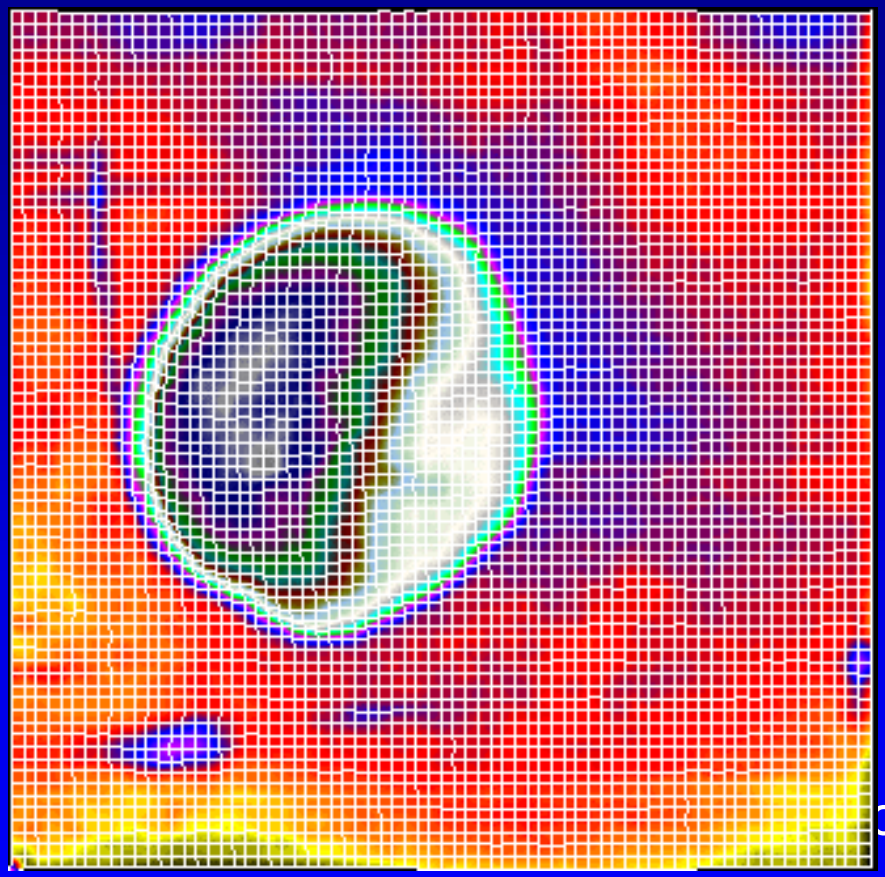

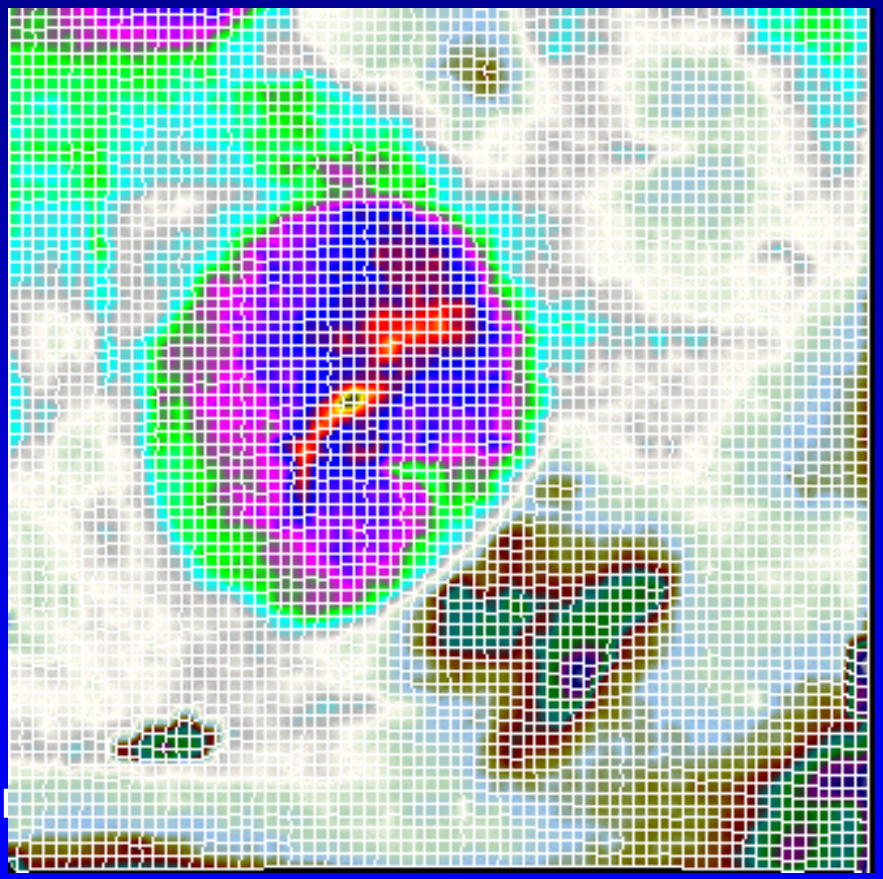

Corrosion Prevention Compound Evaluation Method

Sarah J.H. Kuhlman
Garry H. Abfalter
Jim Dante
University of Dayton Research Institute
Dayton, OH 45469-0135 USA
Phone: (937) 229-4704
Fax: (937) 229-3433
E-mail: Sarah.Kuhlman@udri.udayton.edu
abfalter@udri.udayton.edu
james.dante@wpafb.af.mil

Introduction

Many high-strength aluminum alloys employed in aircraft structures are subject to stress corrosion cracking and corrosion fatigue cracking. If a crack is initiated by stress corrosion, the crack may propagate under fatigue loading. Significant fatigue data exists on the effects of environment on the fatigue life of these materials. Corrosion prevention compounds (CPCs) are used as a fast, inexpensive method to reduce corrosion related damage. Environmental exposure studies have demonstrated that CPCs improve the corrosion resistance of high strength aluminum alloys. In a study by F. Gui and R. Kelly (2) of the University of Virginia, it was stated that all the CPCs tested improved the corrosion resistance, but that the CPCs were application sensitive. Such studies demonstrate the need for tests that simulate the both the chemistry and geometry in which the CPC will be applied.

New CPCs are continually being developed in response to environmental concerns and advances in technology. These CPCs need to be screened for their effectiveness and to confirm that the CPCs do not have an adverse effect on fatigue crack growth. The University of Dayton Research Institute (UDRI) developed a simple, cost-effective test method to screen and evaluate the performance of CPCs during fatigue crack growth. Due to the complexity and number of variables involved, this effort was limited to developing a test method and verifying its effectiveness to screen a few CPCs. This paper describes the test method, procedures used, and the results.

Experimental Details

Fatigue crack growth was performed on a C(T) specimen in L-T orientation in accordance with ASTM E 647 (1.) A width of 5.0 inches was chosen to allow the collection of multiple data sets from one specimen, and a thickness of 0.5 inches was chosen to prevent buckling (see Figure 1). Thirty specimens were cut from a single plate of unclad aluminum 7075-T6, purchased from Copper & Brass Sales in Cleveland, Ohio.

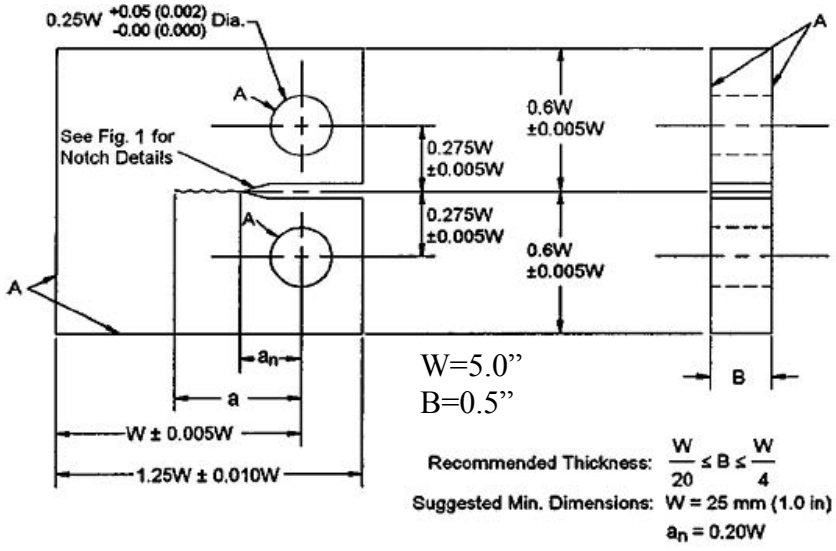

Figure 1: C(T) Specimen

Specimens were tested on a closed-loop servo-controlled hydraulic test machine. Test control and data collection was accomplished by software developed by UDRI. Crack length was measured using the compliance method, and was periodically confirmed optically using a traveling microscope. All testing was performed in tension-tension with a force ratio of 0.1 The specimens were pre-cracked in the NaCl and high humidity environment and tested at 2 hertz. This frequency was chosen to balance the need to allow the environment to affect the crack growth with the need to complete the project in a timely fashion.

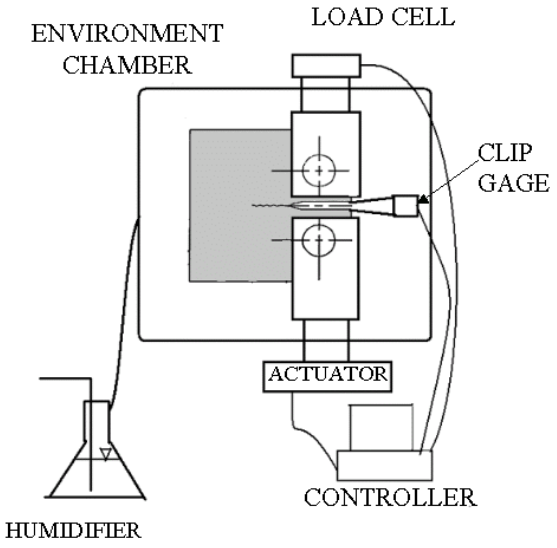

Figure 2 Test Apparatus

Total immersion tests do not accurately model the environment experienced by the CPCs, so an environment chamber was built to attain relative humidity to levels approaching 100%. The high humidity was produced by bubbling air through warm, de-ionized water and piping it to the environment chamber. Figure 2 is a diagram of the test apparatus. To simulate the effects of NaCl in the aircraft environment, one side of the C(T) panel was coated with a film of NaCl.

Specimens were prepared by polishing both sides of the panel to facilitate optical measurements. Specimens were then cleaned using acetone and denatured alcohol. Specimens were sprayed on one side with 3.5 wt. % NaCl solution so that the samples were evenly coated with 1-2 mm diameter droplets. The droplets were dried onto the panel.

Test Procedure

This test was designed to measure the ability of a candidate CPC to affect the chemistry at a crack tip in a manner that reduces the crack growth rate. At the high relative humidity of the environment chamber, the NaCl coat dissolves and wets the side of the specimen. A continuous chloride electrolyte is supplied to the crack tip. Since an aggressive environment is constantly available, this test does not measure the barrier properties of a candidate CPC.

Crack growth rate curves were generated for four baseline environmental conditions: lab air, which was maintained at 50% relative humidity; lab air with uncontrolled humidity that was typically lower than 20% R.H.; 100% R.H. air in an environment chamber; and 100% R.H. air in an atmosphere chamber with the NaCl coating on one side of the C(T) panel.

CPCs can be classified into three general groups: thin, water-displacing; waxy coating; and hard coating. One compound from each group was chosen: LPS-2 for the thin, water-displacing group; VCI-368 for the waxy coating group; and Cor-Ban 35 for the hard coating group. These CPCs were chosen with the expectation that the test results would vary significantly, permitting the development of a metric for effectiveness. The test matrix can be seen in Table 1.

Table 1 Test Matrix

CPC Classification	Thin & Water Displacing	Waxy Coating	Hard Coating
CPC Name	LPS-2	VCI 368	Cor-Ban 35
Number of Specimens	3	3	3

All the specimens used to test CPCs were pre-cracked and tested in the high humidity environment with the NaCl coating on one side of the specimen. Early tests consisted of growing the crack at a constant stress intensity factor range (ΔK) then applying the candidate CPC. All of the CPCs were sprayed onto the specimen. VCI-368 was first diluted half and half with mineral spirits. The Cor-Ban 35 was given one hour to dry and the VCI-368 was given two hours to dry. The crack was grown at a constant ΔK through and past the CPC as seen in Figure 3.

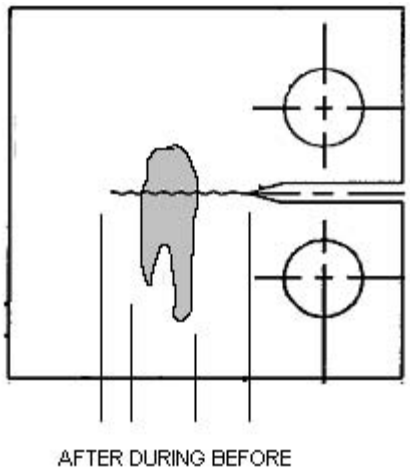

Figure 3 Initial CPC Application

Following the constant ΔK tests, the CPC was reapplied and dried between alternating ΔK decreasing and ΔK increasing test segments. Later tests involved only one application of the CPC followed by a 24 hour drying time.

Results

Testing and data analysis were hampered by scatter in the data. Some of the scatter could be attributed to the uncertainty in the measurement and control of the stress intensity range during constant ΔK tests. Scatter was greatly reduced by adjusting the range of the clip gage and increasing the crack length interval between measurements. Before the clip gage range was adjusted, it was discovered that there was less scatter during ΔK increasing and ΔK decreasing tests. Constant ΔK tests were performed to provide before and after CPC information. The variability in the crack growth rate for a given constant ΔK approached half a decade, which made it difficult to compare crack growth rate behavior. It was more useful to analyze crack length versus cycle data and fit a straight line to the information. The slopes of the lines were used to estimate overall the changes in crack growth rates for the portion of the record fitted.

The crack growth rate with CPC consistently converged with the baseline curve for NaCl coated aluminum at higher ΔK values (this shift can be seen clearly in Figures 9, 11, and 15). Speculation that the CPC had not finished drying before the fatigue cycling began led researchers to increase the drying time before testing. The shift remained despite the extra drying time. The shift may be explained as a shift in the primary crack mechanism from environmental to mechanical. It may be evidence that the chloride environment was wicking to the crack tip faster than the CPC. The shift may also be the result of the NaCl having greater time on the non-CPC side to corrode the aluminum.

Baseline Results

Two specimens each tested in the 100% R.H. condition and the 100% R.H. with NaCl condition demonstrated good repeatability in the crack growth rate data. The baseline tests demonstrated that the crack growth rate was about the same for 50% and 100% R.H., but was measurably accelerated in the presence of NaCl as seen in Figure 4. During baseline testing it was observed that water from the humid air in the atmosphere chamber condensed and wetted the NaCl side of the specimen. The water then came through the crack and formed droplets along the crack on the unsalted side, ensuring crack tip wetting.

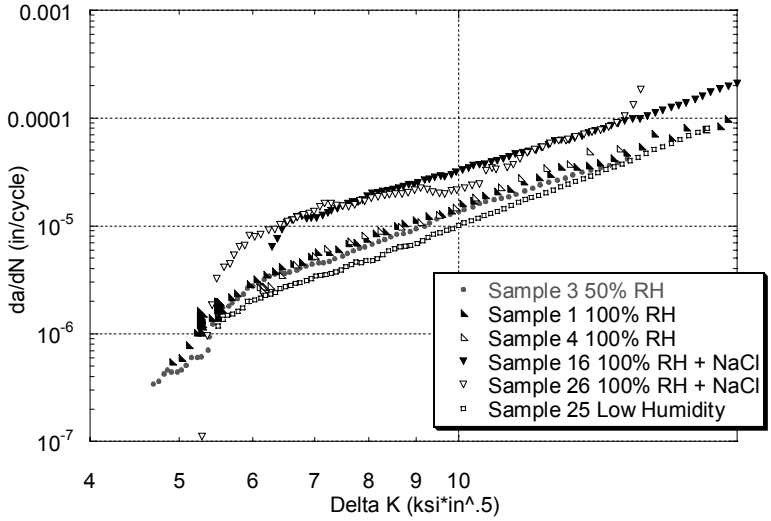

Figure 4 Baseline Fatigue Crack Growth Rate (FCGR) Test Results

LPS-2

One ΔK increasing test was made with the LPS-2 with a short drying time. The crack growth rate information presented in Figure 5 indicates that the LPS-2 counteracted some of the effects of the NaCl on the crack growth rate. Specimen 18 had a 24 hour drying time. The constant ΔK data for the LPS-2 (Figure 6) indicate the CPC had a minor effect on the crack growth rate. ΔK increasing and ΔK decreasing tests performed on specimen 18 demonstrate that the LPS-2 counteracts some of the NaCl effects at lower crack growth rates. (Figure 7)

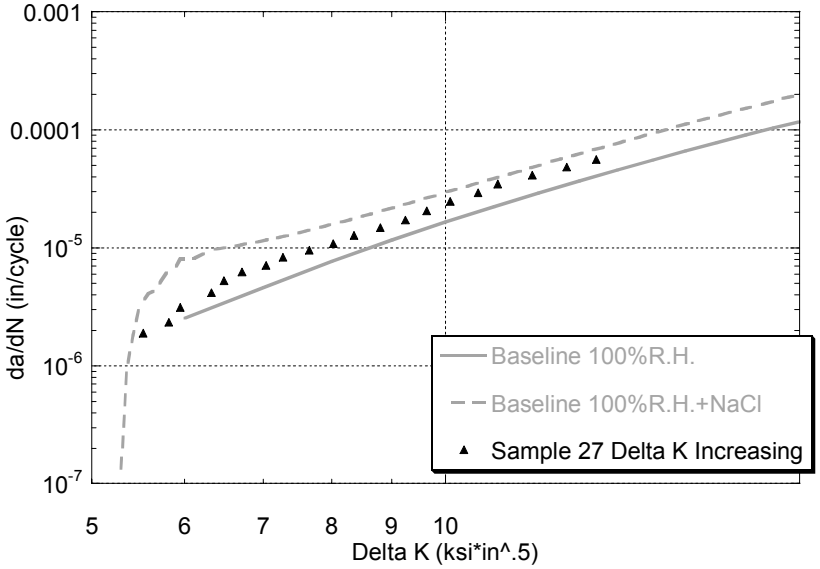

Figure 5 FCGR Data for Specimen 27 with LPS-2 Compared to Baseline

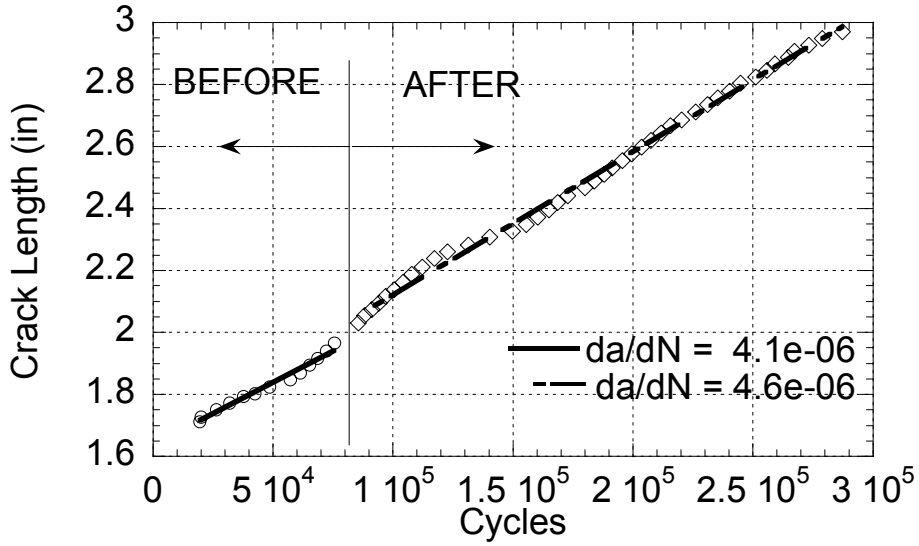

Figure 6 Specimen 18 with LPS-2 at ΔK = 6.1

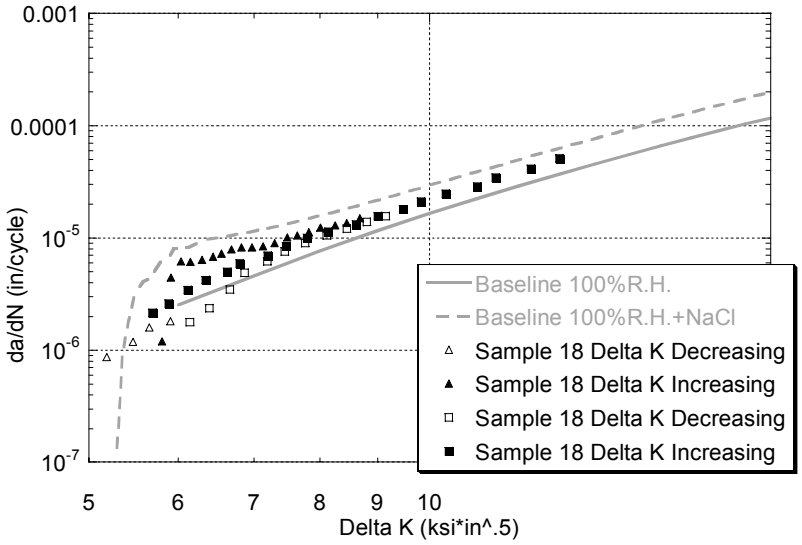

Figure 7 FCGR Data for Specimen 18 with LPS-2 Compared to Baseline

VCI-368

Of the CPCs tested, VCI-368 provided the most consistent decrease in crack growth rate. Figures 8 and 9 show data generated with the two hour drying time for the CPC. Figures 10 and 11 show data generated after a 24 drying time. Figures 8 and 10 demonstrate a very small reduction in the crack growth rate with the application of the VCI-368. In Figures 9 and 11, the increasing ΔK and decreasing ΔK crack growth rate with CPC is seen to be lower than the NaCl environment. The lower crack growth rate curves in Figure 11 indicate that the VCI-368 performed better after a longer drying time.

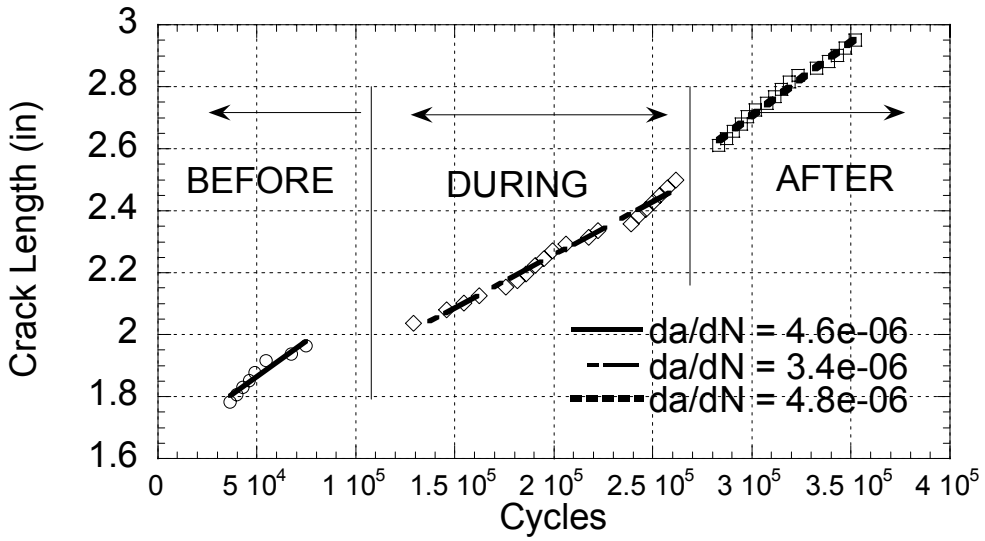

Figure 8 Specimen 20 with VCI-368 at ΔK = 6.1

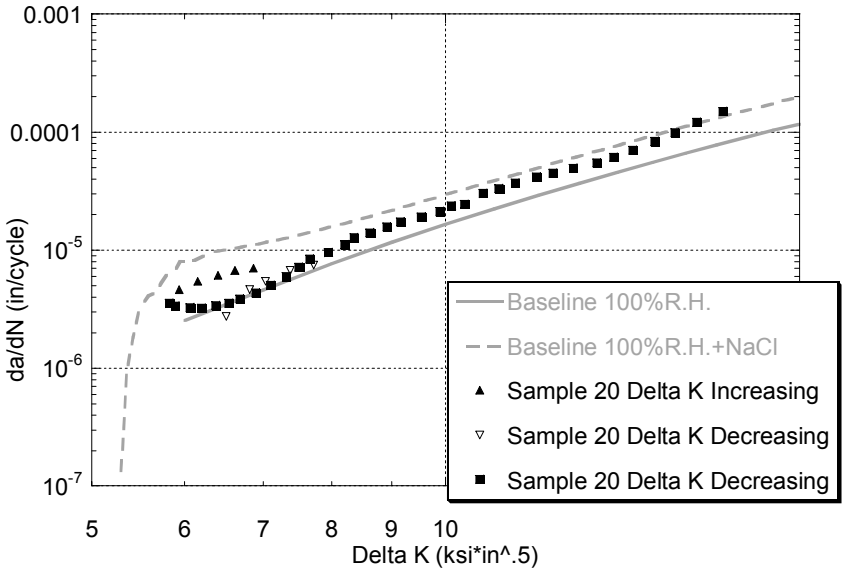

Figure 9 FCGR Data for Specimen 20 with VCI-368 Compared to Baseline

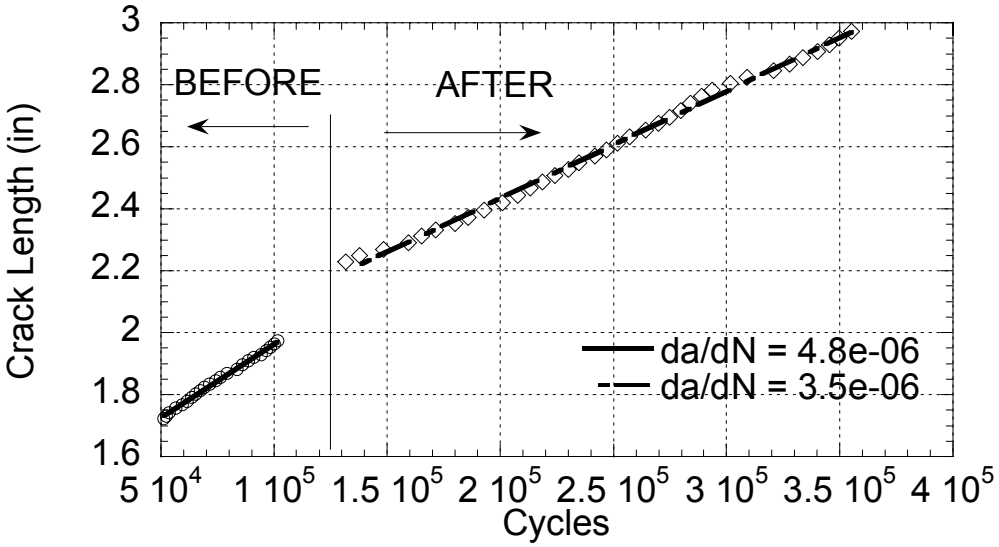

Figure 10 Specimen 22 with VCI-368 at ΔK = 6.1

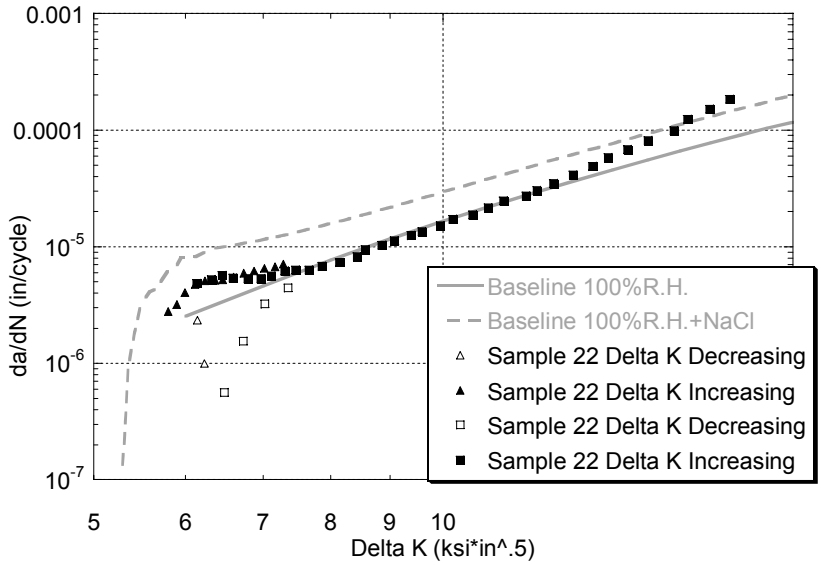

Figure 11 FCGR Data for Specimen 22 with VCI-368 Compared to Baseline

COR-BAN 35

Of the CPCs tested, Cor-Ban was the least consistent. In some tests it appeared to increase the crack growth rate (Figure 12). Figure 13 demonstrates that the crack growth rate was somewhat slower with the CPC than the NaCl baseline, but higher than the humidity only baseline. Specimen 28 was tested using the 24 hour drying time. In contrast to the specimens run with a shorter drying times, data from this specimen showed a consistently lower crack growth rate using the Cor-Ban 35. (Figures 14 and 15)

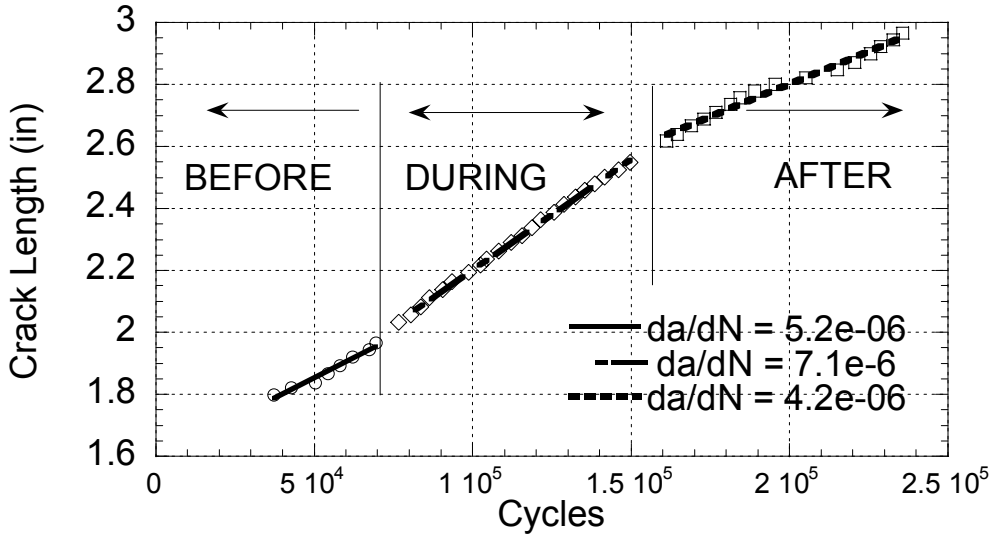

Figure 12 Specimen 19 with Cor-Ban 35 at ΔK = 6.1

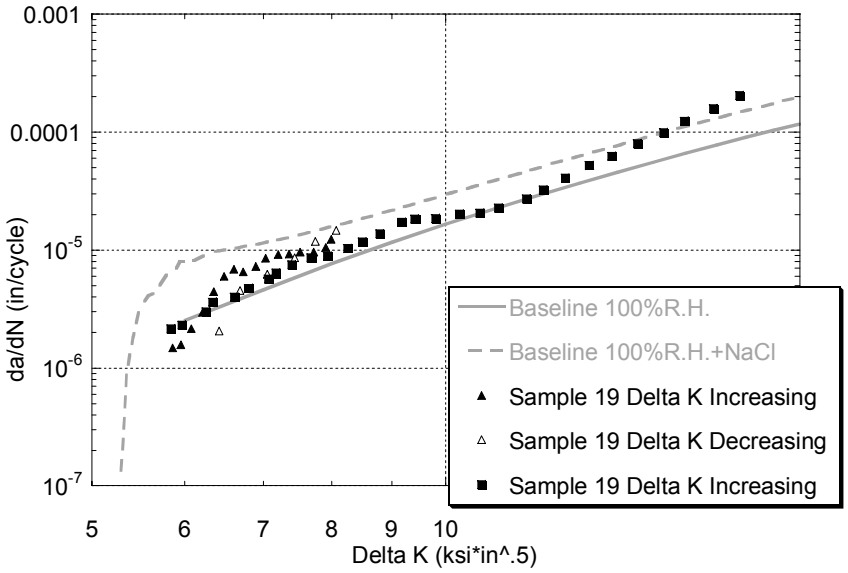

Figure 13 FCGR Data for Specimen 19 with Cor-Ban 35 Compared with Baseline

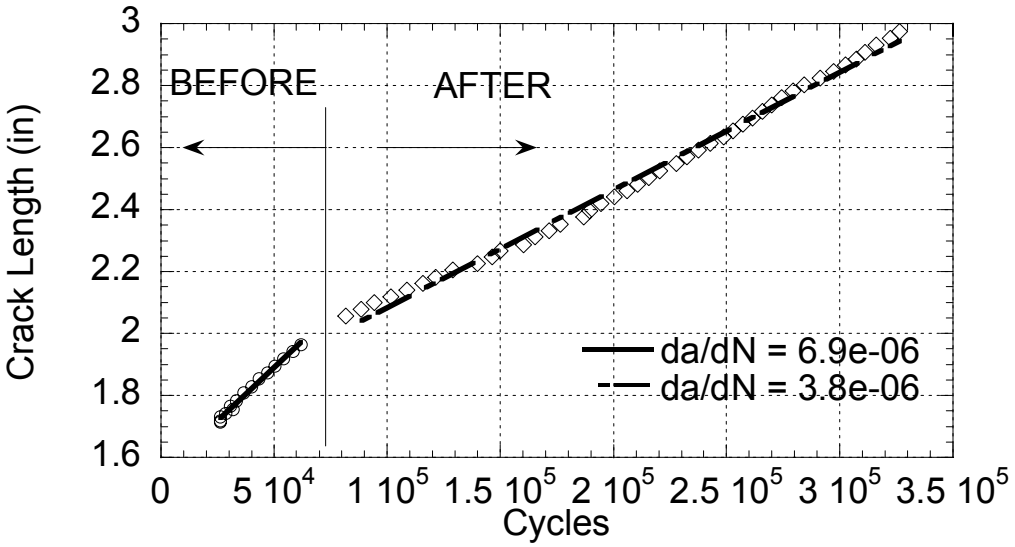

Figure 14 Specimen 28 with Cor-Ban 35 at $\Delta K = 6.1$

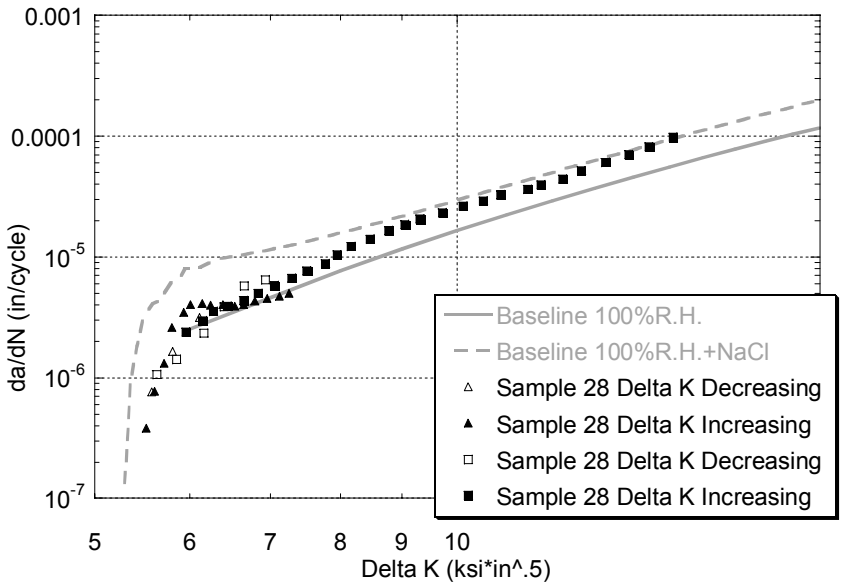

Figure 15 FCGR Data for Specimen 28 with Cor-Ban 35 Compared with Baseline

Conclusions

A test method for determining the influence of different corrosion prevention compounds on crack growth rate was developed. Conditions were generated to simulate the environment of a crack tip in an aircraft structure. The structure of the data collection and analysis permitted researchers to tolerate moderate scatter in the data.

Acknowledgements

This work was performed under USAF Contract Number F42620-00-D-0039-RZ0101. We gratefully acknowledge Technical POC Dr. Deborah T. Peeler for making this study possible. Special thanks belong to John Ruschau and Ryan Leard for their advice and assistance with fatigue crack growth testing and CPC selection. Thanks also to Dr. Peter Sjöblom for general guidance throughout the project.

References

1. American Society for Testing Materials. Standard Test Method for Measurement of Fatigue Crack Growth Rates, ASTM E 647-00. West Conshohocken, PA. 2001.

2. Gui and Kelly. Laboratory Evaluations of CPC Characteristics and Performance: Preliminary Report. In 2001 USAF Aircraft Structural Integrity Program Conference, Proceedings. 2001.

INFRARED SPECTROSCOPY AS A CHEMICAL FINGERPRINTING TOOL

Timothy L. Huff
NASA Marshall Space Flight Center
Mail Stop ED36
Huntsville, AL 35812

Telephone: 256-544-4259
Email:tim.huff@msfc.nasa.gov

Introduction

Infrared (IR) spectroscopy is a powerful analytical tool in the chemical fingerprinting of materials. Any sample material that will interact with infrared light produces a spectrum and, although normally associated with organic materials, inorganic compounds may also be infrared active. The technique is rapid, reproducible and usually non-invasive to the sample. That it is non-invasive allows for additional characterization of the original material using other analytical techniques including thermal analysis and RAMAN spectroscopic techniques. With the appropriate accessories, the technique can be used to examine samples in liquid, solid or gas phase. Both aqueous and non-aqueous free-flowing solutions can be analyzed, as can viscous liquids such as heavy oils and greases. Solid samples of varying sizes and shapes may also be examined and with the addition of microscopic IR (microspectroscopy) capabilities, minute materials such as single fibers and threads may be analyzed. With the addition of appropriate software, microspectroscopy can be used for automated discrete point or compositional surface area mapping, with the latter providing a means to record changes in the chemical composition of a material surface over a defined area. Due to the ability to characterize gaseous samples, IR spectroscopy can also be coupled with thermal processes such as thermogravimetric (TG) analyses to provide both thermal and chemical data in a single run. In this configuration, solids (or liquids) heated in a TG analyzer undergo decomposition, with the evolving gases directed into the IR spectrometer. Thus, information is provided on the thermal properties of a material and the order in which its chemical constituents are broken down during incremental heating. Specific examples of these varied applications will be cited, with data interpretation and method limitations further discussed.

Liquid Phase Analysis

Samples in this physical state can be further categorized as free-flowing aqueous or non-aqueous solutions and viscous liquids. This distinction is important in the selection of a proper technique as certain techniques may be incompatible with the sample or not produce optimal spectra. In Figure 1 below, transmission by liquid cell was chosen because the samples were free flowing, relatively transparent in nature and produced strong infrared spectra. This example was part of a study to determine the feasibility of separating a solvating agent from a solvating agent/fuel mixture with the intention of recovering the solvent for reuse. The first two spectra are the infrared fingerprints of the virgin solvent and hydrocarbon fuel, respectively. The third spectrum was produced following processed separation of the solvent/fuel mixture. Spectral subtraction of the processed mixture from the virgin fuel produced the spectrum shown

at the bottom, which contained peaks consistent with that of the solvent. This was an indication of incomplete separation of the two components under the processing conditions employed.

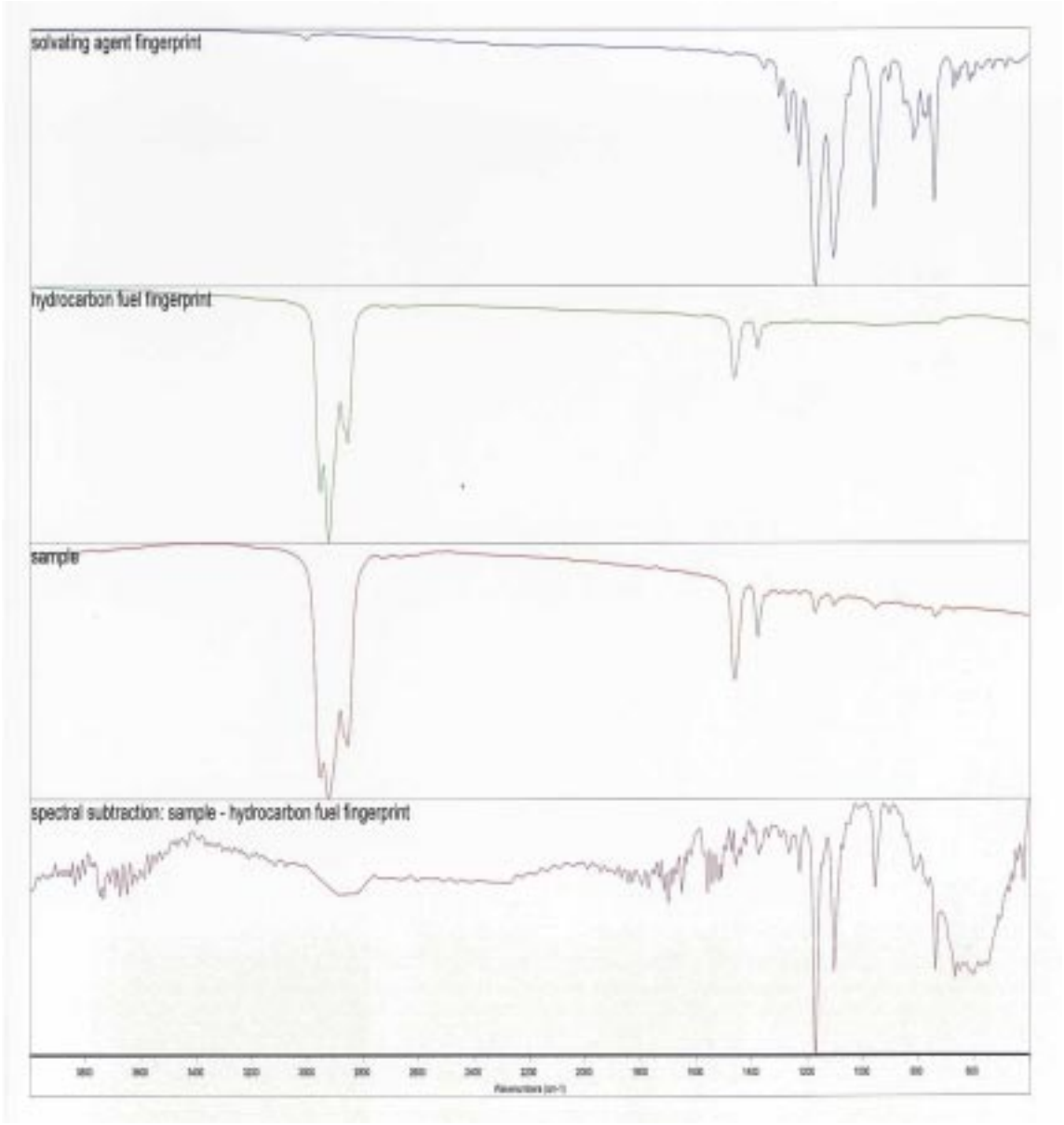

Figure 1

Solid Phase Analysis

The categories within this material state vary greatly, as do the techniques for their analysis. The material may be present as a powder, a thin or thick film and vary in shape from a pellet to a fiber. Other factors to consider include if only surface characteristics is required or depth profiling is necessary. The example in Figure 2 is a surface scan of a reflective material using an automated microscopic technique. In operation, infrared radiation travels through the microscope objective, striking the surface and reentering the lens where the signal is directed to the infrared detector. A spectral fingerprint of the virgin material was previously collected and served as the background for the run. At each pre-programmed point, the collected spectrum is subtracted from the background and the difference presented. This particular scan

encompassed a linear range of approximately 5000 micrometers with a surface contaminant detected from approximately 2000 to 3500 micrometers.

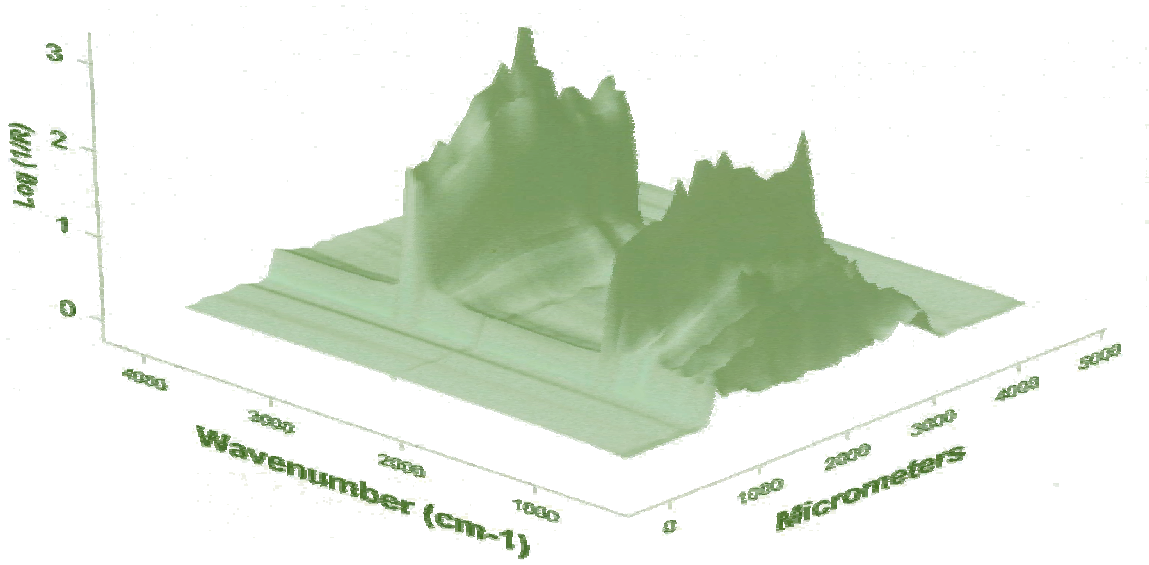

Figure 2

Figure 3 is a second example of a spectroscopic scan of a material using the automated microscope system. In this case, the base material was non-reflective in nature and required analysis by an infrared technique known as Attenuated Total Reflectance (ATR). Unlike reflectance, this method requires surface contact using a suitable crystal for transferring the infrared radiation to and from the material. As with reflectance, the method is non-destructive. The data is presented in what is sometimes referred to as a waterfall representation, again showing surface contamination as the sample moves across the microscope stage.

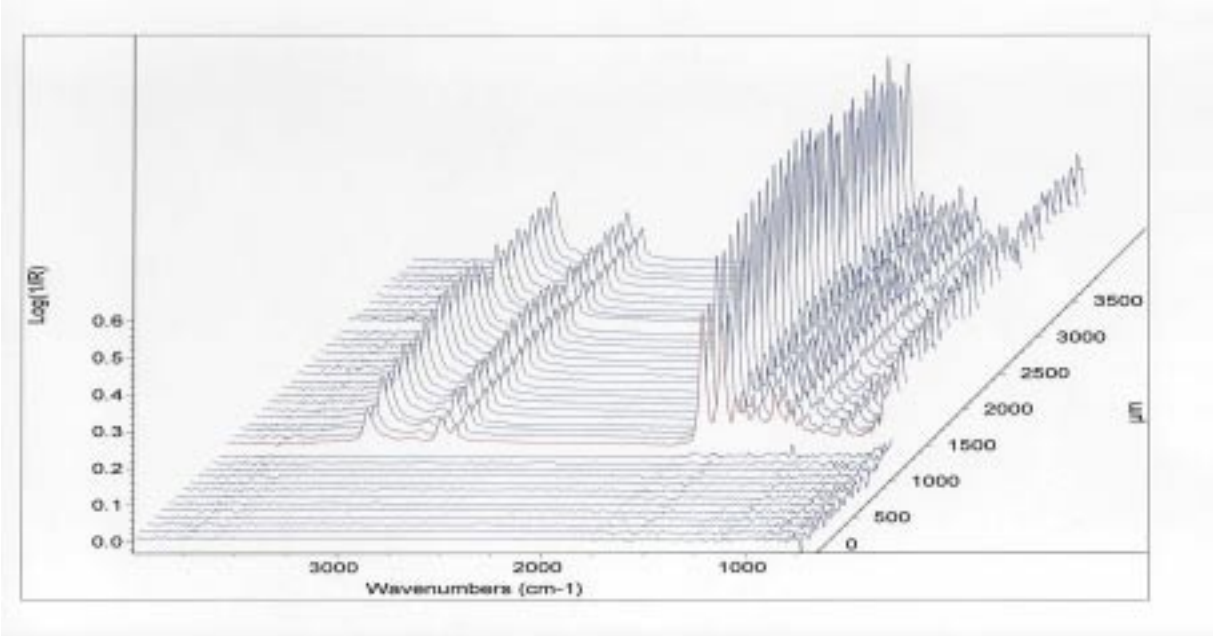

Figure 3

As mentioned previously, minute materials may also be examined by infrared techniques. The photographs in Figure 4 were taken of a fiber measuring approximately 15 micrometers in diameter. The rectangular light is the infrared beam area, which can be varied along the X and Y axes such that discrete sample areas can be analyzed. This is shown in the second of the two photographs, with the beam positioned only over the single-stranded fiber.

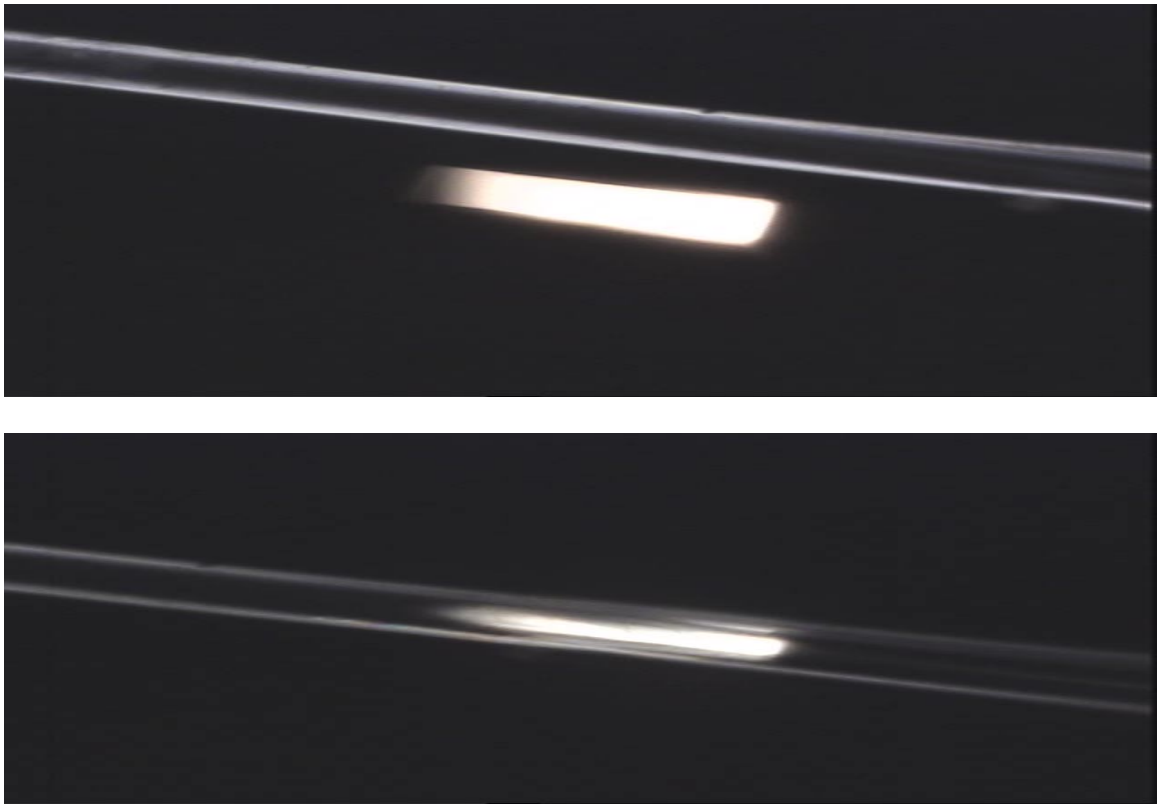

Figure 4

Figure 5 is the collected spectrum, which allowed identification of the fiber as a polypropylene material.

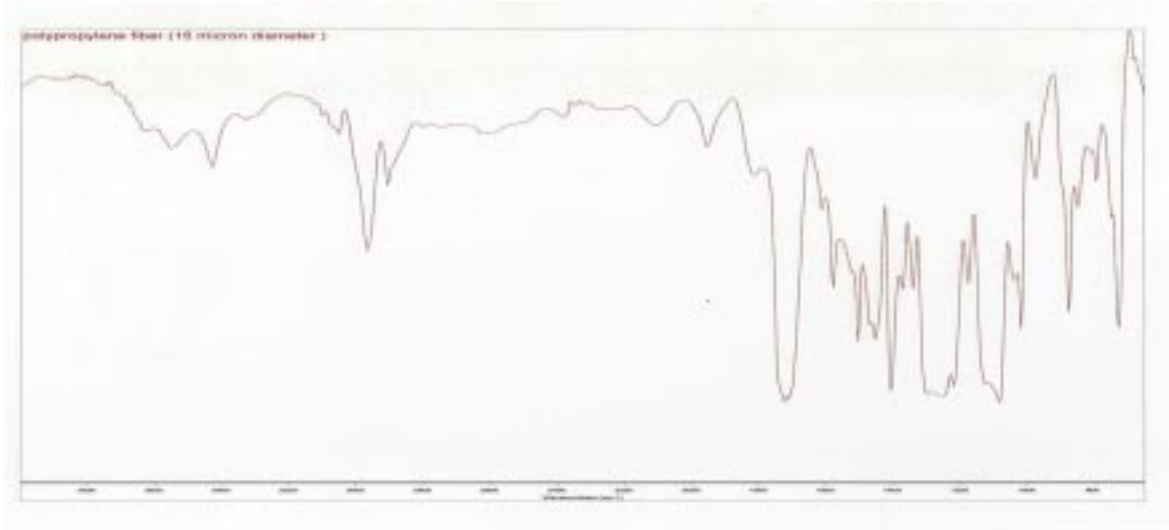

Figure 5

Gas Phase Analysis

In general, any sample that is a gas at room temperature may produce an infrared spectrum using appropriate techniques. These techniques may also be expanded to include both solid and liquid samples through coupling of infrared techniques with other analytical methodologies such as thermogravimetric (TG) analysis. In TG analysis, the solid or liquid sample is heated at a controlled rate and the sample weight monitored. As sample heating proceeds, a weight change occurs due to sample decomposition, with the gaseous decomposition products being released. Normally, these constituents are exhausted from the system without further characterization. However, by redirecting these evolving gases into an infrared analyzer, chemical speciation of these products is possible. Thus a more complete material characterization may be achieved by providing both a chemical and thermal fingerprint of the sample. In practice, the evolving gas is purged through a transfer line into a gas cell within the FTIR. Temperatures in both the transfer line and gas cell are held at approximately 250 degrees Celsius (^{o}C) to prevent condensation of the gases during the sample run. The purge gas may be either high purity air or an inert gas such as nitrogen to allow oxidative and pyrolytic processes to be examined, respectively. Spectra collected during an oxidative run are usually characterized by a predominant carbon dioxide peak due to oxidation of some evolving carbon constituents with the air or sample charring. An inert atmosphere generally provides more functional group information, as the evolving species are less reactive with the atmosphere. During the decomposition process, the evolving gases directed to the FTIR are analyzed real-time for chemical groups. At the end of a run, the data can be presented as a "stacked plot" that presents the spectral data plotted against time (or temperature) throughout the heating cycle for the sample. This allows for the observation of increases and decreases in individual chemical groups (based on peak height and location) as the run progresses. An example of such a plot is presented in the upper region of Figure 6 below.

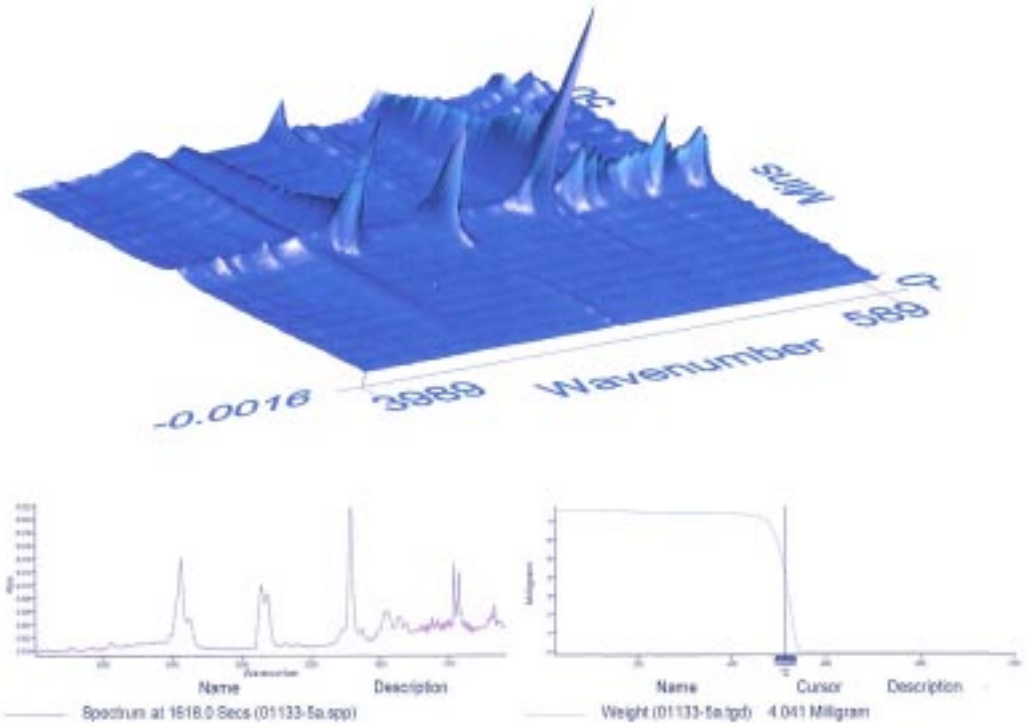

Figure 6

Additionally, weight loss data can be incorporated into the spectral data, with specific "slices" in the plot generated that correlate individual point-in-time spectra with observed weight changes. In the example above, a spectrum collected during a weight loss event occurring at approximately 500^{o}C in seen in the lower left of the figure with the corresponding weight loss profile to the right. By observing the peak

locations on the X-axis, information on the types of chemical groups evolving at that time are obtained. In this example, the observed peaks indicate the presence of carbon dioxide, carbon monoxide, carbonyl (C=O) and non-aromatic hydrocarbon functional groups.

Practical Considerations

Although useful in the chemical fingerprinting of materials, considerations must be made in the use of these infrared techniques. Notable is the importance of reproduction of the infrared data, a function of both the technique and specific instrument parameters. Different techniques may produce differing spectra for the same material, both in terms of observable spectral peaks and, for quantitative applications, varying peak areas. In Figure 7 below, a halogenated film was run using both transmission and ATR techniques. As can be seen, the spectral profiles of the same material differ depending on the technique chosen.

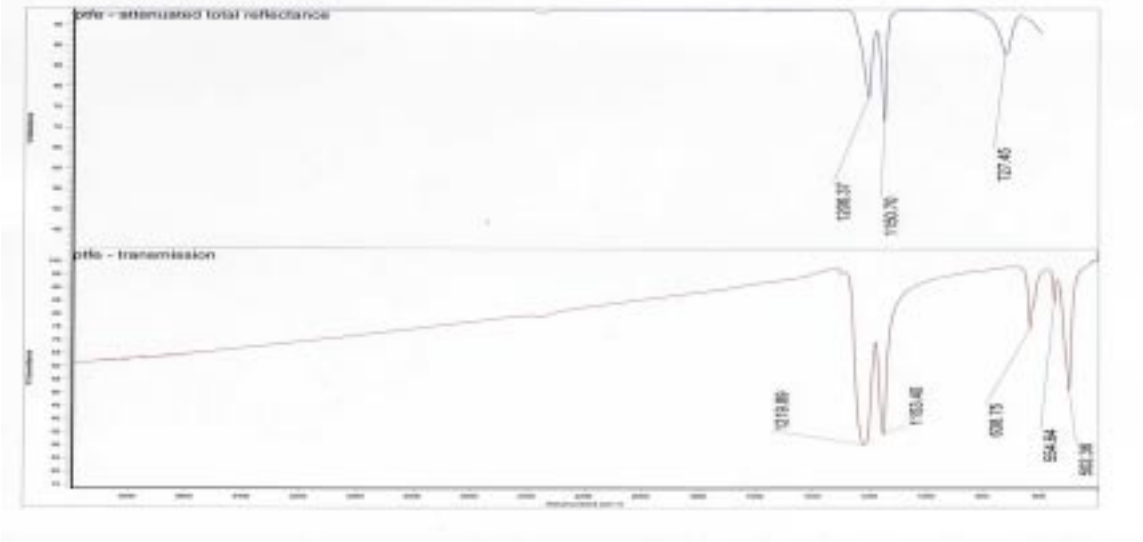

Figure 7

When these same techniques were used to analyze a polyethylene film, significant differences were observed in the measurable peak areas of the sample (Figure 8).

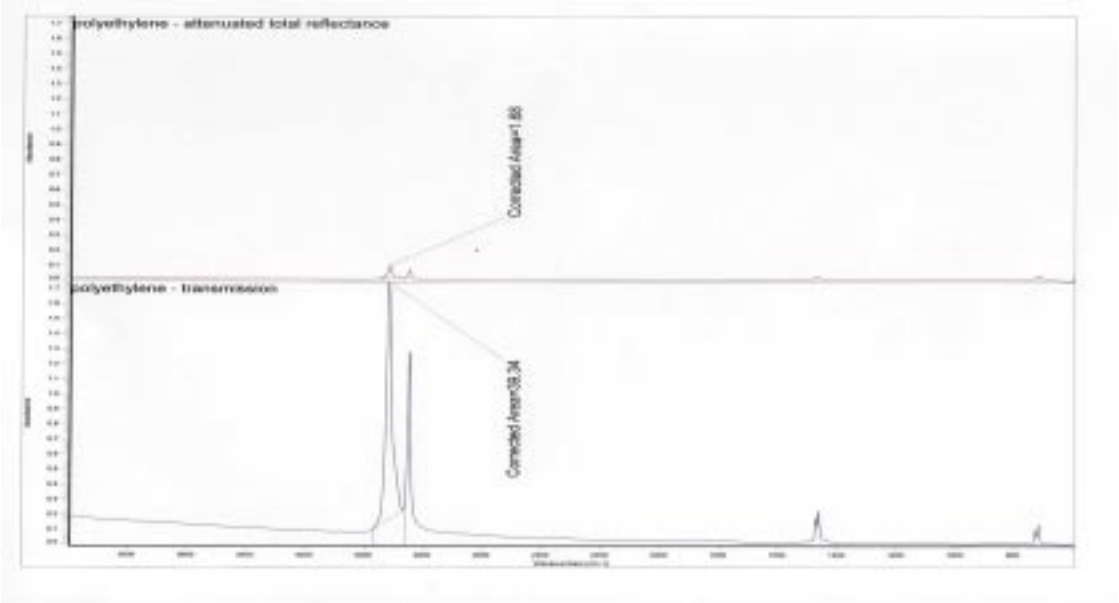

Figure 8

Spectral differences can occur even within a common technique if the parameters employed in the collection of the data are not consistent. In Figure 9, a polyethylene film was analyzed at different resolutions, a parameter used to determine how close two peaks can be and still be identified as separate peaks. At a resolution of eight (8) the peaks are indistinct whereas a resolution of four (4) produces well-defined spectral peaks. This can be an important distinction in chemical fingerprinting when comparing "standard" spectrum peaks with subsequent samples. In this instance, the doublet observed at 730 and 719 cm-1 is actually an important indicator of whether the sample is a low density or high density polyethylene materials.

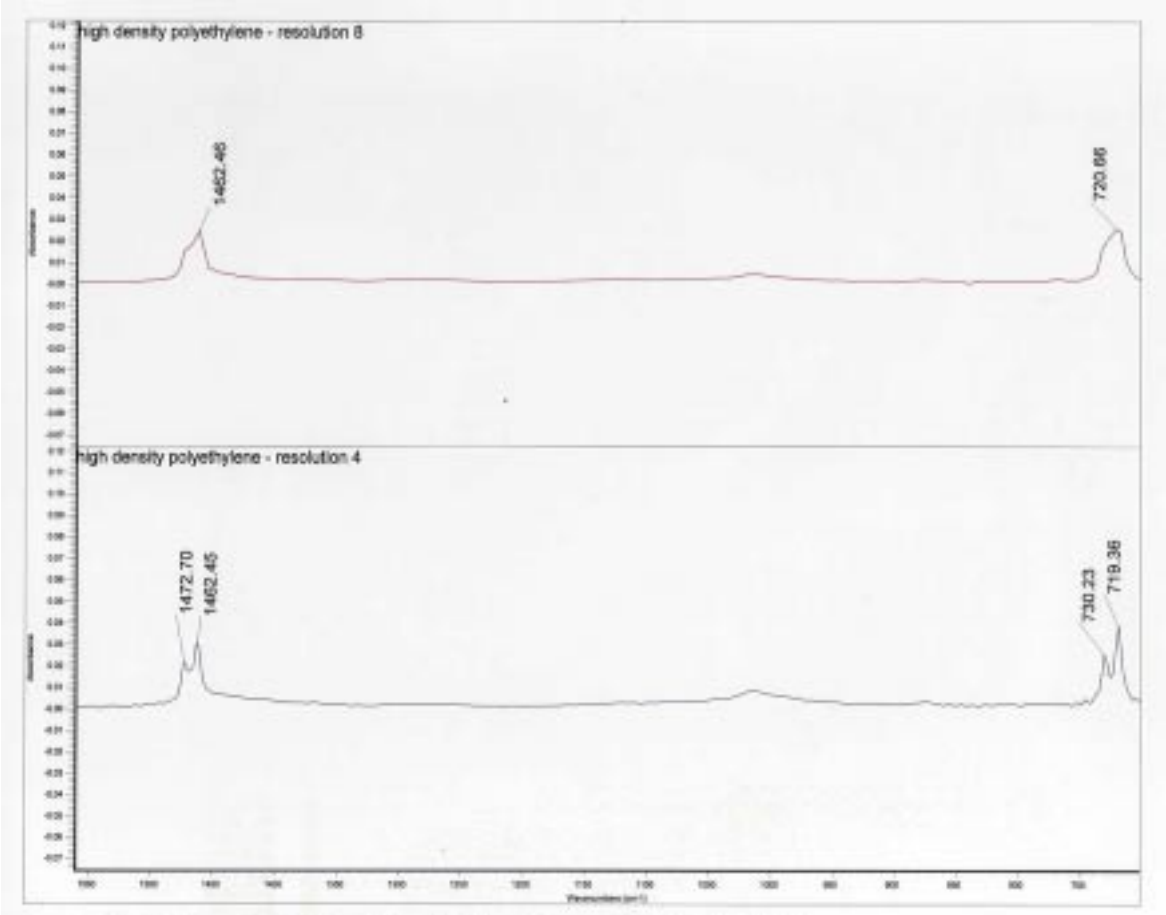

Figure 9

Limitations

Infrared spectroscopy depends upon interaction of infrared light with specific chemical functional groups. However, not all chemical groups are readily detectable due to the nature of the infrared-chemical bond interaction. Diatomic groups such as disulfides (S-S) and symmetrically substituted carbon-carbon double bonds are only weakly infrared active, if at all. Instrument limitations also must be considered when these techniques are employed. For example, infrared interactions with metal atoms are below the wavenumber range of most detectors employed in infrared spectrometers. In some instances these differences may be overcome by converting infrared inactive groups to a more active form. In Figure 10 below, a metal disulfide constituent in a mixture was being investigated for thermal breakdown characteristics. Since the mixture was complex in nature, it was difficult to determine by thermal analysis alone when this particular constituent was decomposing. Also, the nature of the metal disulfide complex prohibited TG-IR analysis due to the limitations mentioned above. However, by performing the thermal portion of the TG-IR run in an oxidative atmosphere, the complex was oxidized upon decomposition to form infrared active

sulfur/oxygen groups at approximately 1375 and 1339 cm-1. Thus, the temperature of decomposition of the metal disulfide constituent was inferred from appearance of these bonds. As shown, an inert atmosphere did not produce spectral peaks in this region.

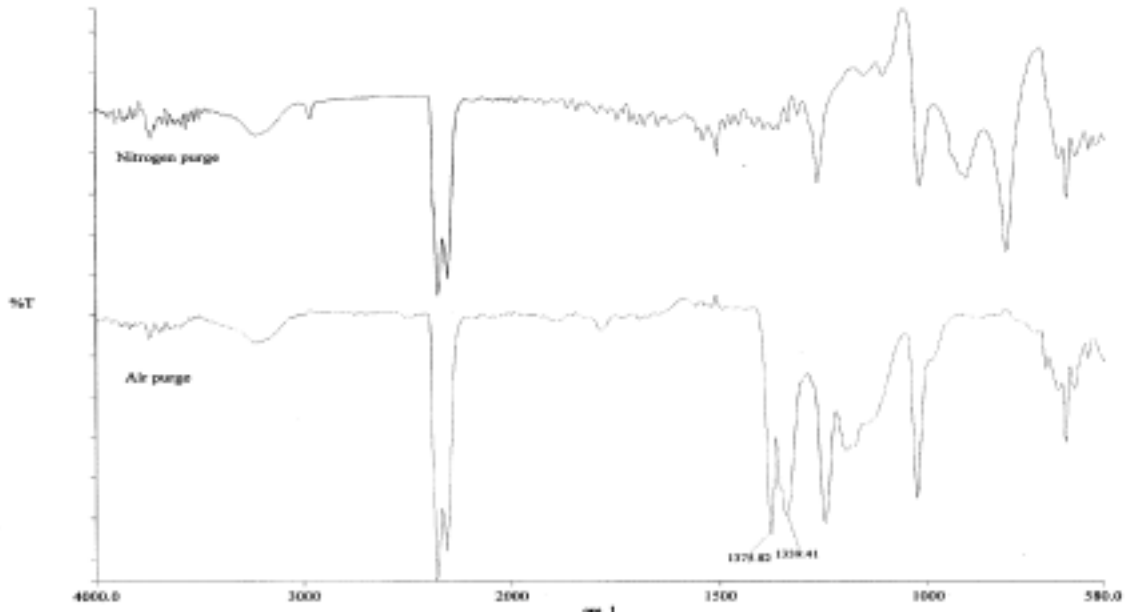

Figure 10

In other cases, alternate methodologies such as RAMAN spectroscopy are required. This technique is actually complementary to infrared techniques in that both are vibrational spectroscopic techniques and operate in the same relative wavenumber range. However, RAMAN spectra are not dependent on the dissimilarity of molecules i.e. the presence of a strong dipole moment. Thus, diatomic groups and symmetrical double bonded groups are readily observable. Also, the instrument operating range extends into lower wavenumber regions where metal complexes are better detectable. In Figure 11 below, the carbon-carbon double bond present in styrene butadiene is readily apparent in the 1680-1630 cm-1 region using a RAMAN spectrometer but absent in the infrared technique.

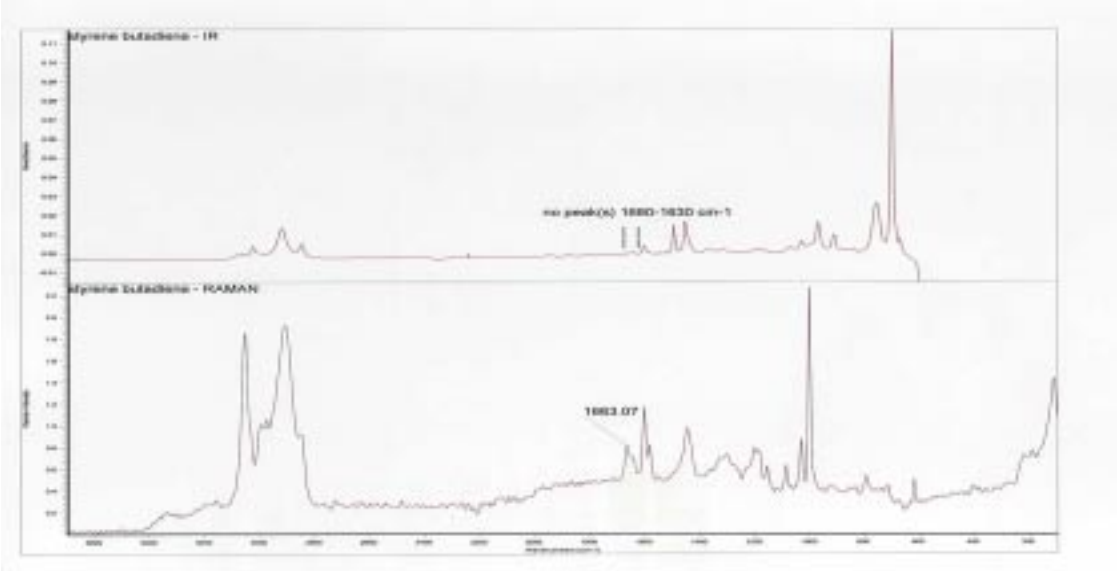

Figure 11

Unlike infrared techniques, RAMAN can be destructive to the sample due to heat generated from the intense beam of radiation. In addition, fluorescing and highly absorbing materials can interfere with spectral analysis. Another important consideration is cost, which may be considerably greater than that of an infrared spectrometer.

Conclusion

Infrared spectroscopy provides a rapid, reproducible means for chemical fingerprinting of materials in any physical state. That the method is non-destructive allows additional characterization of the material by other analytical techniques such as thermal analysis, coupled thermogravimetric–infrared analysis and RAMAN spectroscopy. In conjunction, these techniques can provide important information on the properties of a given material.

Reference Material Kydex® 100 Test Data Message for Flammability Testing

Carl D. Engel, Ph.D.
Qualis Corporation
Marshall Space Flight Center, ED36
Huntsville, AL 35812
Phone: 256-544-6032
E-mail: Carl.D.Engel@msfc.nasa.gov

Erin Richardson
Marshall Space Flight Center, ED36
Huntsville, Al 35812
Phone: 256-544-2873
E-mail: erin.richardson@msfc.nasa.gov

Eddie Davis
Marshall Space Flight Center, ED36
Huntsville, Al 35812
Phone: 256-544-2490
E-mail: eddie.davis@msfc.nasa.gov

Introduction

The Marshall Space Flight Center (MSFC) Materials and Processes Technical Information System (MAPTIS) database contains, as an engineering resource, a large amount of material test data carefully obtained and recorded over a number of years. Flammability test data obtained using Test 1 of NASA-STD-6001 (Ref. 1) is a significant component of this database. NASA-STD-6001 recommends that Kydex® 100 be used as a reference material for testing certification and for comparison between test facilities in the round-robin certification testing that occurs every 2 years. As a result of these regular activities, a large volume of test data is recorded within the MAPTIS database (Ref. 2). The activity described in this technical report was undertaken to "mine" the database, recover flammability (Test 1) Kydex® 100 data, and review the lessons learned from analysis of these data.

Kydex® 100 Characteristics

Kydex® 100 is a thermoplastic that, according to the Material Safety Data Sheet, consists of 92-94% polyvinylchloride/polyacrylic mix, 0.1-3.0% organotin compound (trade secret); 4–6 solid lubricants, stabilizers, pigments. The material is provided in sheet form. Sheets of several thicknesses have been tested. This analysis was limited to data for nominal thickness sheets (0.06 in.) to eliminate thickness as a variable.

Non-repeatable flammability behavior of Kydex® 100 has been noted previously (Ref. 3). This work identified ignition source variability, contamination of the test environment, and batch sensitivity as potential causes. The work of Reference 3 explored batch sensitivity issues and contributed significant data to the database.

The large potential variation in the organotin compound has been identified as a potential variable and is the subject of a complementary parallel investigation. In planning this work, discussions with the manufacturer revealed that, about 1990, the organotin compound was substituted as the stabilizer for the previously used compound (barium with cadmium organic compounds). Data in MAPTIS, which could have been affected by this previously unidentified change, were examined, records verified, and appropriate database changes made. All of the test data presented herein are from post-1990 samples.

The burning characteristics of Kydex® 100 are described in NASA-STD-6001's Good Laboratory Practices section describing Test 1. These data are reproduced in Table 1.

Table 1. Test 1 Data from NASA-STD-6001(1)

Material Identification	Atmosphere (% O_2)	Average Burn Length		Standard Deviation	
		(in.)	(cm)	(in.)	(cm)
Kydex® 100, 0.06-in. (0.15 cm) thickness	25.9(2)	2.7	6.9	0.3	0.8
	20.9(3)	1.7	4.3	0.1	0.25

Notes:
(1) Data are from 10 replicate tests.
(2) Pressure for 25.9-% oxygen was 14.3 psi (98.7 kPa).
(3) Pressure for 20.9-% oxygen was 14.7 psi (101.3 kPa).

Approach

Test 1 (Upward Flammability) test data found in MAPTIS for 0.6-in. thick Kydex® 100 were downloaded and entered into an EXCEL™ workbook for analysis. Some of the paper files for the tests were reviewed for details not currently recorded in the MAPTIS system. Videotapes were secured from the Materials Combustion Research Facility (MCRF) files, and most were reviewed at least twice. Event timing data and observations were made from the film and recorded in EXCEL™ workbook format for analysis.

Data Review and Analysis

The Kydex® 100 burn length data recorded for standard Test 1 conditions were plotted as a function of oxygen concentration (Figure 1). Data from individual runs were used, rather that the average of data sets or groups. The data produce a pattern that indicates the burn length data forms two groups of data, which become increasingly separated as the oxygen concentration increases. This separation into two groups is the primary focus of the remainder of this study and shows that the data in the lower set agrees with the data expectation from NASA-STD-6001 (Table 1) for the higher oxygen concentration (25.9%). The expected data range from NASA-STD-6001 for 20.9-% oxygen is somewhat lower than the data.

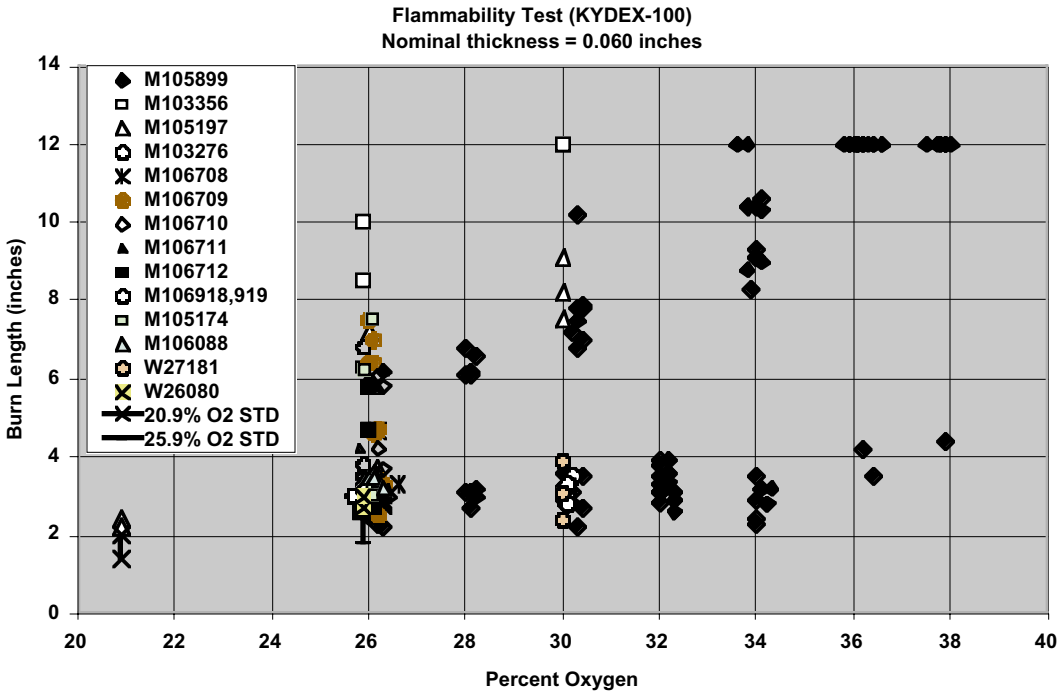

Figure 1. Kydex® 100 Burn Length Data

The Kydex® 100 data are for a variety of total pressures. The burn length data clearly shows the two groupings and that data from the same test are in both groupings. Since the burn length is used as a pass or fail criterion, the data were divided into burn length above and below 6.0 in. The resulting data are shown in Figure 2.

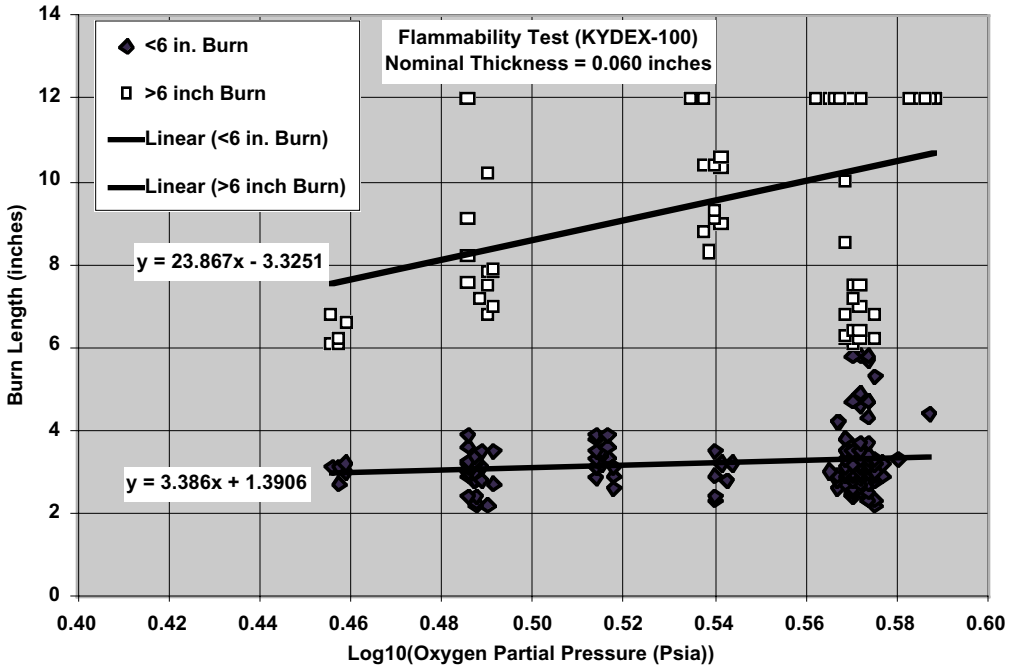

Figure 2. Burn Length Segregated Kydex®100 Data

By segregating the burn length data into two groups, fit-comparisons of the data were produced. The linear data fit-comparisons show a dramatic difference in the two data sets. Note that data comparable to the standard exist in the lower burn length set and the upper set across the whole range of oxygen concentrations.

In Test 1, the burn rate and burn length for each sample are recorded. The burn rates corresponding to the two groups of burn lengths are plotted in Figure 3. Note that some of the burn rate data for burn lengths greater than 6 in. groups with the burn rate data for burn lengths less than 6 in.

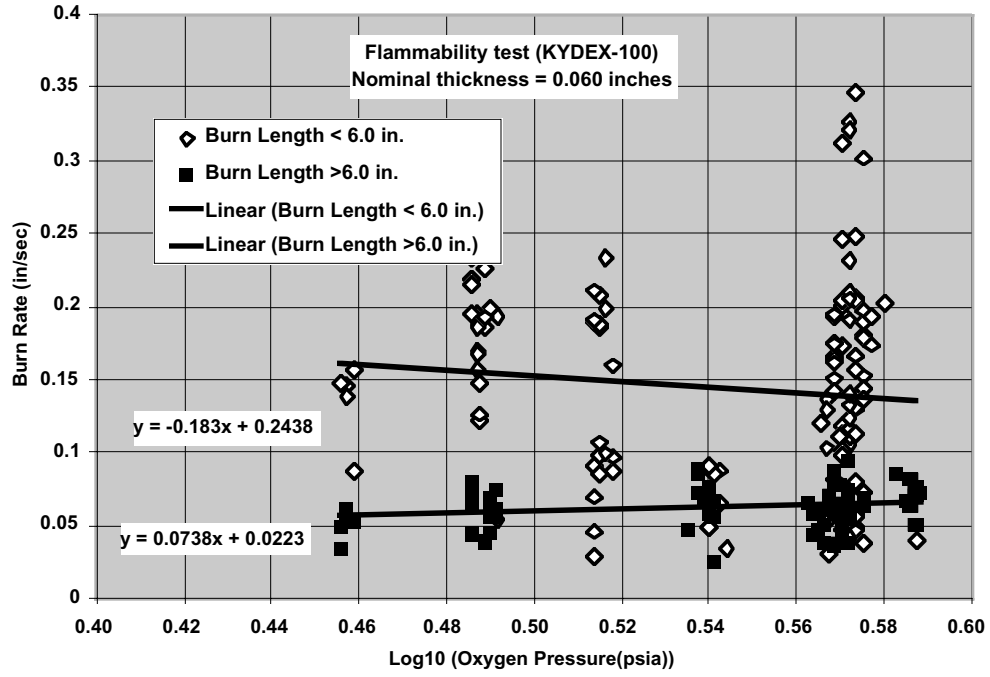

Figure 3. Kydex® 100 Burn Rate Data as a Function of Oxygen Partial Pressure

This effect can be more clearly seen in Figure 4, in which burn length is plotted against burn rate. The test number identifies the data, and no segregation was made by burn length. Data for burn rates above 0.1 in./sec all agree with the 25.9-% oxygen criterion from NASA-STD-6001. When the burning rate is lower, the burning length tends to increase. Many of the tests plotted are from Reference 3, in which each test number corresponded to a different batch of 10 tested samples of Kydex® 100. Note that data from several of the test numbers exist in both the constant-burn-length range and the burn-rate-independent region. This tends to indicate that batch properties did not change the burning characteristics.

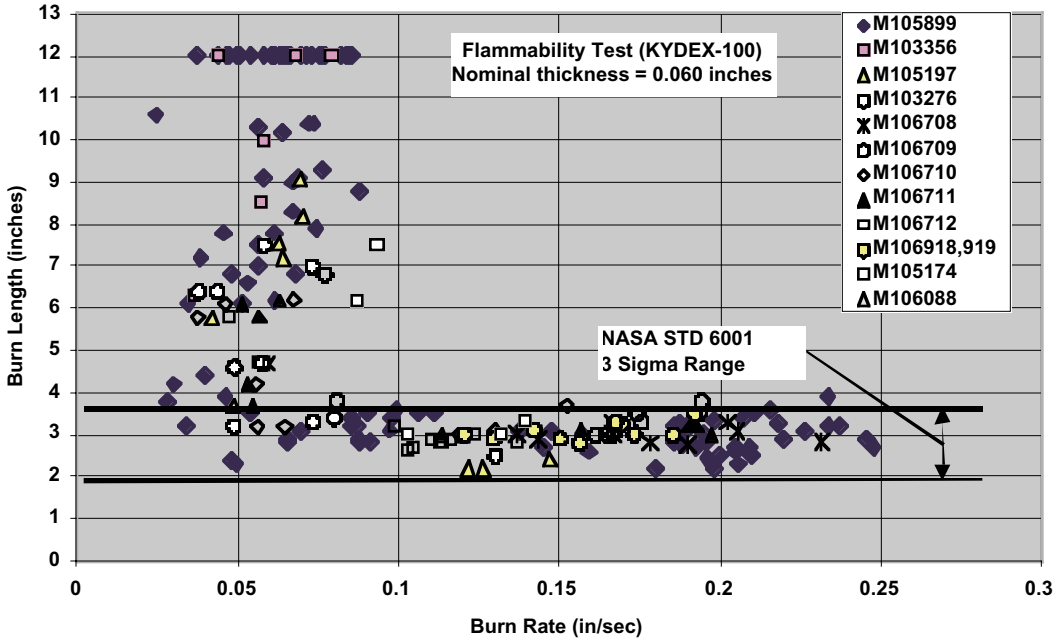

Figure 4. Burn Length versus Burn Rate Data

The batch-sensitivity study data are further examined in Figure 5, in which burn length is plotted against sample number. Sample number usually corresponds to run sequence number. Note the appearance of the two groups of low and high burn rates. The occurrence of a low or high burn length appears to be random, and all batches exhibit this characteristic.

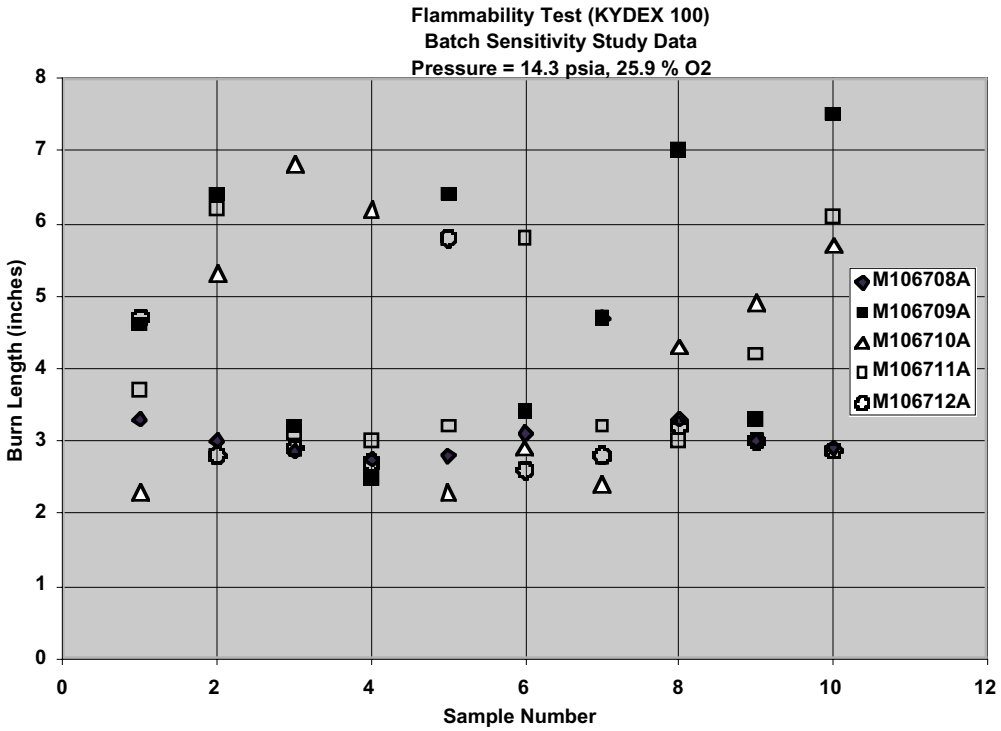

Figure 5. Burn Length versus Sample Number

Sufficient data are available at the seven oxygen concentrations (from 26 to 38% in 2-% increments) to determine the sample frequency for a given burning length. The sample frequency provides a measure of the percent of time a given burn length will be obtained. Data from 93 specimens tested in 25.9- to 26-% oxygen were grouped to determine the burn length sample frequency for one test condition. These data are shown in Figure 6. A sparse data sample of 10 samples is available for 28-% oxygen (Figure 7).

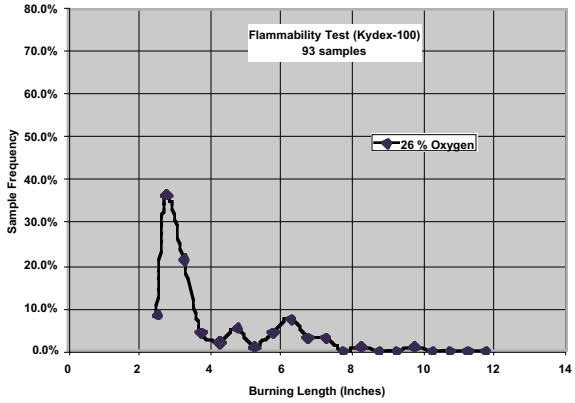

Figure 6. Sample Frequency versus Burn Length at 26% Oxygen

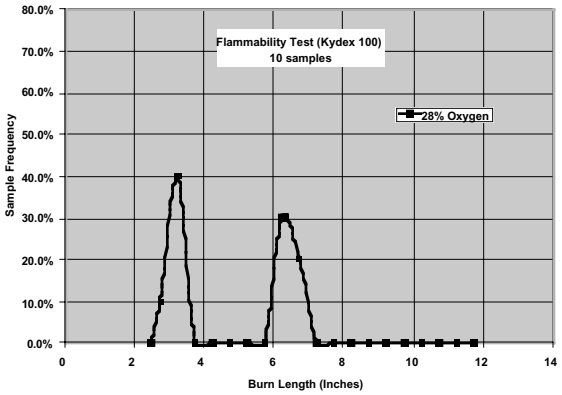

Figure 7. Sample Frequency versus Burn Length at 28% Oxygen

Data from 34 specimens tested in 30-% oxygen were grouped to determine the burn length sample frequency at another test condition. These data are shown in Figure 8. Note that three peaks appear. A substantial number of the samples exhibit burning lengths below 6.0 in. Another group partially sustains burning and burns in the 6- to 8-in. range. A group of 8.8% exhibits total burns.

Similar plots are provided for 32-, 34-, 36-, and 38-% oxygen (Figures 9 to 12, respectively). These plots show the two groups discussed throughout this section. The first group clusters about a burn length of approximately 2.7 in. This is interpreted as the burn length realized from the application of the energy from the igniter. Without the igniter energy application, a certain percent of the samples will not have enough energy to sustain burning and will extinguish shortly after the igniter stops burning. Another percentage will have sufficient energy to continue burning and then self extinguish or continue burning until the fuel is consumed. The higher oxygen concentration environment produces a more rapid production of combustion energy; thus, the higher burning lengths are observed, and propagation from extinguishment to sustained burning occurs more frequently.

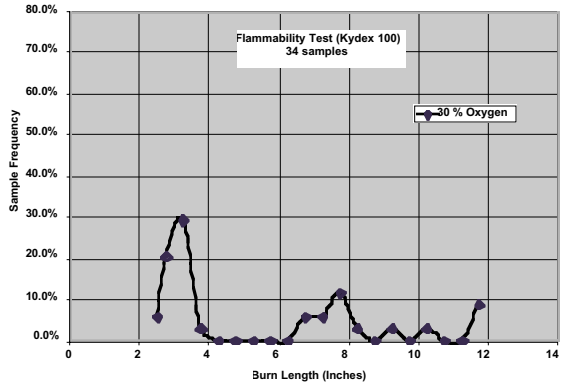

Figure 8. Sample Frequency versus Burn Length at 30% Oxygen

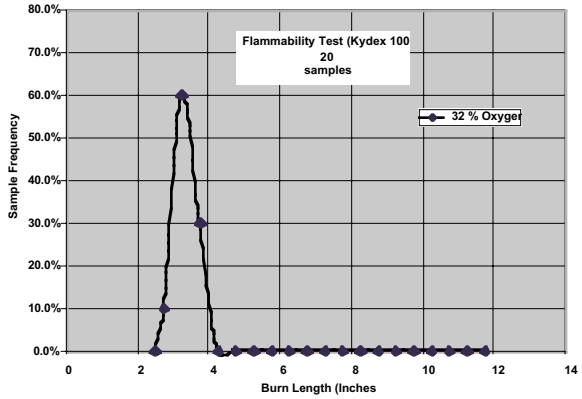

Figure 9. Sample Frequency versus Burn Length at 32% Oxygen

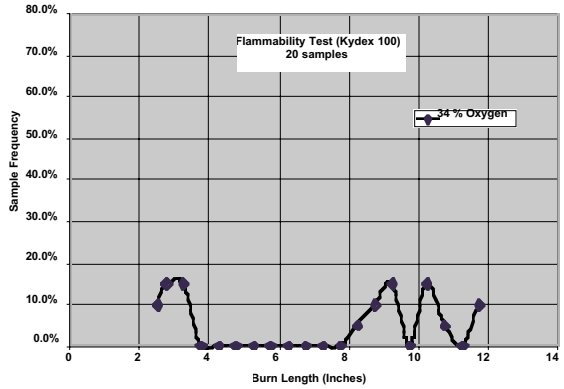

Figure 10. Sample Frequency versus Burn Length at 34% Oxygen

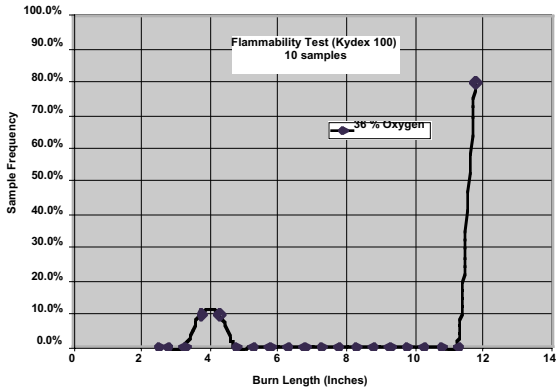

Figure 11. Sample Frequency versus Burn Length at 36% Oxygen

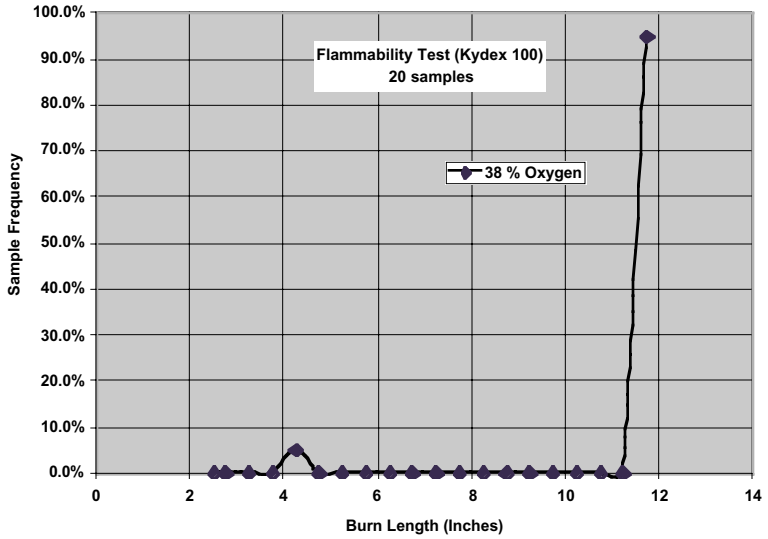

Figure 12. Sample Frequency versus Burn Length at 38% Oxygen

The integral of the sample frequency (the cumulative distribution) is provided in Figure 13. The distribution shows that at 25.9-% oxygen, 84% of the samples tested will not burn more than 6.0 in.; but 14% of the samples will burn more than 6.0 in. Also, note that none of the samples produced sustained burning by consuming all 12 in. of the sample. At the higher oxygen concentration of 30%, 42% of the samples will not burn 6.0 in.; accordingly, 58% will burn more than 6.0 in.

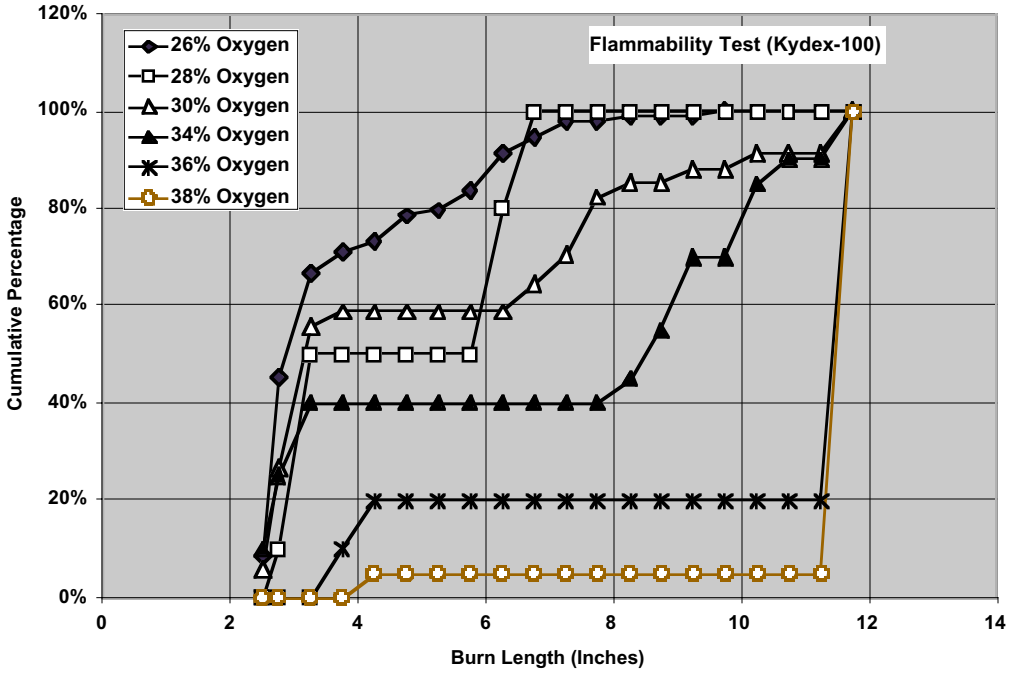

Figure 13. Kydex® 100 Burning Length Cumulative Percentage Distributions

A clearer understanding of the burning length probability can be seen by plotting the burning length frequency for burning lengths above 6.0 in., using the data in Figure 13. These data are shown in Figure 14, in which the burning frequency shows a near linear increase with oxygen concentration. An exception is at 32-% oxygen, where 20 samples were tested and none burned 6.0 in. or more.

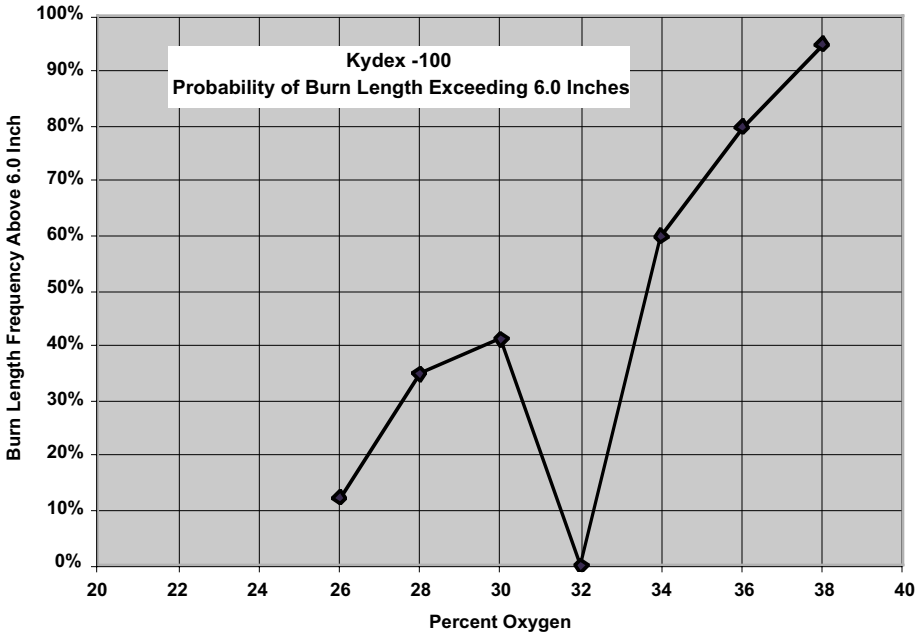

Figure 14. Probability of Kydex® 100 Burn Lengths above 6.0 in.

The data in Figures 13 and 14 challenge the prevailing concept of oxygen level thresholding. If sufficient samples are tested, some burn lengths above 6.0 in. will occur for all oxygen concentrations above 26-% oxygen, and the frequency of burn length above 6.0 in. increases with oxygen level. Of those samples that burn more than 6.0 in., only a few have the independent energy production to sustain burning up to 12.0 in. This implies that the material will extinguish itself.

Figure 15 shows the percent of samples tested that had a total burn versus oxygen concentration level. In these cases, sufficient energy was released to sustain continuous burning well after the igniter was out. The character of these data versus oxygen concentration appears to fit the oxygen thresholding concept.

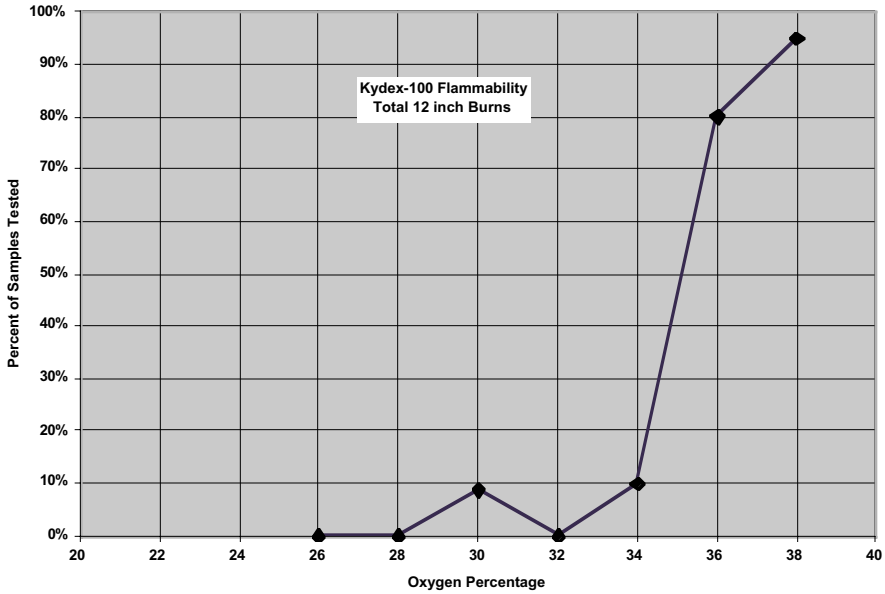

Figure 15. Probability of Kydex® 100 Burn Lengths of at least 12 in.

Probability and Sample Number Discussion

The concern for providing an accurate characterization of material flammability has persisted over the years of testing and data sampling. Reference 4 highlights the key role of the number of samples tested in establishing the error associated with the samples tested for promoted combustion testing (Test 17). Reference 4 provides the formula (from Reference 5) for the maximum error of estimate for a given confidence level.

$E = Z_{\alpha/2} / (2n^{1/4})$ percent error
n = number of test specimens
$Z_{\alpha/2}$ = normal distribution factor

where $Z_{\alpha/2} = 1.96$ for $\alpha = 0.050$
$Z_{\alpha/2} = 2.576$ for $\alpha = 0.010$

This formula yields the following values:

Test Error Estimate

Zalp/2 =	1.96	2.576
no of test	95% conifidence	99% conifidence
3	57%	74%
5	44%	58%
10	31%	41%
16	25%	32%
40	15%	20%
100	10%	13%

The practice of using a small sample size leads to a very large uncertainty in the data obtained; moreover, the foregoing analysis assumes the data are at least near a normal distribution. As shown in the preceding section, the material Kydex® 100 may form threes subset distributions within the total distribution of flammability burn lengths. This confounds the ability to determine accurately the number of samples needed to minimize the error in each of the three subsets of distributions to a quantifiable level.

Conclusions

Based on the substantial test data obtained over the years, several conclusions can be drawn for the flammability characteristics of Kydex® 100.

1. Kydex® 100 flammability characteristics do not agree with the NASA-STD-6001 stated burning length range.
2. The burning length range stated in NASA-STD-6001 appears to be produced by igniter-on conditions and does not represent the material's burning characteristic once ignited but without the ignition source energy input.
3. No batch burning characteristics were identified, but batch effects on the probability of different burn length classes were not specifically eliminated.
4. The concept that there is a single oxygen level that defines whether a sample will burn less or greater than 6.0 in. is seen to be quite inadequate.
5. Sufficient testing can establish material characteristics probability curves to provide the engineer with the probability that the material will sustain a burn length of at least 6.0 in. or will sustain burning until all material is consumed. A simple pass/fail criterion may not be possible or practical. Future application of flammability data for some material classes may require the design engineer to assess the risk based on the probability of an occurrence and the probable outcome with different materials as characterized with cumulative burn length distribution for specific use conditions.
6. Flammability data for other materials and other classes of materials should be examined to determine if similar probabilistic burning characteristics are found. The similarity between the upward flammability and promoted combustion tests, along with the apparent uncertainty in determining a unique threshold pressure for metals, suggests that the data should be reexamined to determine if a probability distribution curve versus pressure level is established by the data.

7. Based on the current work, the minimum number of samples recommended for standard Test 1 testing is 10 for each test condition. Evaluation of Test 1 data for other materials may suggest this number be increased.

Acknowledgements

Flammability test data were obtained through access to the MAPTIS database. The review and discussions of the analysis approach and data results by Bob Jacobs materially contributed to the understanding of flammability testing. His assistance is greatly appreciated.

References

1. NASA-STD-6001, "Flammability, Odor, Offgassing, and Compatibility Procedures for Materials in Environments that Support Combustion," Test 1, "Upward Flame Propagation," NASA Headquarters, February, 1998.
2. MAPTIS, Materials and Processes Technical Information System, NASA Marshall Space Flight Center, ED XX, MSFC, Al 35812, Contact: D. E Griffin.
3. Richardson, Erin H., "Batch/Lot Ignition and Combustion Sensitivity of Nonmetallic Materials," Project No. 00-10. (Paper in review for publication.)
4. Key, C. Frank, F. S. Lowery, S. P. Darby, and R. S. Libb "Factors Affecting the Reproducibility of Upward Propagation Thresholds of Metals in Gaseous Oxygen," *Flammability and Sensitivity of Materials in Oxygen Rich Atmospheres,* Eighth Volume, ASTM STP 1319, William T. Royals, Ting C. Chow and Theodore A. Steinberg, Editors, October 1997.
5. Miller and Freund's Probability and Statistics for Engineers, R. A. Johnson, Prentice-Hall, Englewood Cliffs, NJ, 1994.

The Effect of Gravity on the Combustion Synthesis of Porous Biomaterials

M. Castillo[1,2], X. Zhang[1,3], J. J. Moore[1,3], F. D. Schowengerdt[1,5], R. A. Ayers[1,6]

[1] Center for the Commercial Applications of Combustion in Space (CCACS), Colorado School of Mines, 1500 Illinois St, Golden, CO 80401, United States
[2](303) 273-3091, macastil@mines.edu
[3](303) 273-3091, xzhang@mines.edu
[4](303) 273-3770, jjmoore@mines.edu
[5](303) 384-2091, fschowen@mines.edu
[6](303) 384-2337, ruayers@mines.edu

Abstract

Production of highly porous composite materials by traditional materials processing is limited by difficult processing techniques. This work investigates the use of self propagating high temperature (combustion) synthesis (SHS) to create porous tricalcium phosphate ($Ca_3(PO_4)_2$), TiB-Ti, and NiTi in low and microgravity. Combustion synthesis provides the ability to use set processing parameters to engineer the required porous structure suitable for bone repair or replacement. The processing parameters include green density, particle size, gasifying agents, composition, and gravity. Tricalcium phosphate produced through the reaction:

$$3CaO + P_2O_5 = Ca_3(PO_4)_2 \qquad (1)$$

has the ability of being resorbed in-vivo. Currently titanium is used in a number of biomedical applications. The reactions incorporating Ti investigated here are:

$$(x+y)Ti + xB = yTi + xTiB \qquad (2)$$

$$Ni + Ti = NiTi \qquad (3)$$

The advantage of the TiB-Ti system is the high level of porosity achieved together with a modulus that can be controlled by both composition (TiB-Ti) and porosity. At the same time, NiTi exhibits shape memory properties. SHS of biomaterials allows the engineering of required porosity coupled with resorbtion properties and specific mechanical properties into the composite materials to allow for a better biomaterial.

Introduction

Currently a wide range of porous materials are being investigated for bone reconstruction purposes. In conjunction with this research, new processing methods of these materials (i.e. use of gravity) are also being studied. The advantage of porous over solid materials is their ability to provide a biologic interlock with the surrounding tissues by providing a scaffold for vascularization, soft and bone tissue infiltration, and allowing for the capacity to match the mechanical properties of the device to the surrounding tissue[1]. Bioresorbable materials have the added caveat that the material must be removed at the same rate as new tissue is generated[1, 2].

Materials & Methods

SHS reactions take advantage of the process exothermicity of various chemicals[3]. When certain chemical reactants are combined and excited to a high enough temperature, they will combust and produce enough heat to ignite the next layer of reactants. This process will continue or self propagate until the reactants have been exhausted. Temperature-enthalpy relations, as shown below in Figure 1, determine theoretically if SHS reactions are possible. An SHS reaction will take place when 1) the enthalpy of the products has a greater negative value than the reactant, 2) the adiabatic temperature (Tad) is ~1800°C, and 3) there is enough enthalpy to ignite the next layer considering heat loss through conduction and radiation. Figure 1 shows the theoretical temperature enthalpy diagram for the $3CaO + P_2O_5 = Ca_3(PO_4)_2$ reaction system in a 1 g environment. The adiabatic temperature (T_{ad}) is the theoretical temperature that corresponds to the maximum temperature achieved during reaction with no heat loss. If there is significant heat loss, then the reaction will not sustain itself. Considering this heat loss, the measured maximum temperature achieved during reaction is the combustion temperature (T_c). The diagram shows the start of the reaction at the initial temperature (T_o). For this system it is very difficult to measure the ignition temperature since the reaction occurs in propagating mode.

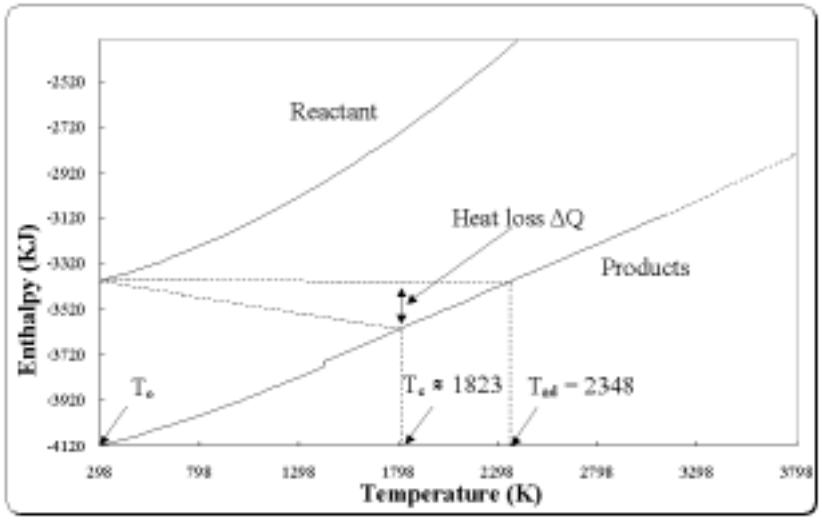

Figure 1. Theoretical temperature enthalpy diagram for the $3CaO + P_2O_5 = Ca_3(PO_4)_2$ system.

A typical SHS process includes 1) mixing of reactant powders, 2) forming of pellet by uniaxial or preferably isostatic pressing, 3) loading into the combustion chamber, and 4) ignition of the combustion reaction.

All samples were pressed into cylinders (dia =1.27cm., h=1.27-2.1cm) and ignited via a tungsten coil in an argon atmosphere. Reaction systems including the combination of CaO and P_2O_5, require that all mixing, pressing, and test reactions occur in a high purity inert atmosphere (i.e. glovebox). This is due to the hygroscopic nature of the P_2O_5. Physical data for the reactants are listed below in Table 1.

Table 1. Physical data for the reactant powders.

	CaO	P_2O_5	Ti	B	Ni
Particle Size (μm)	<45	<94	<45	<45	<45
Purity (%)	99.99	99.9	99.5	99	99.9
Melting Point (°C)	2888		1660	2300	1453
Molecular Mass (g/mol)	56.07	141.92	47.87	10.81	58.69

SHS experiments were conducted in low gravity through the NASA KC-135A Reduced Gravity Research Program. Parabolic flight patterns are used to obtain ~20 seconds of low gravity and 40 parabolas per day are generally flown. A special rack is used to perform the SHS experiments aboard the plane. Temperature, video, and pressure data are obtained together with the production of samples.

Process parameters include green density, particle size, gasifying agents, composition, and gravity. All of the processing parameters affect the porosity, amount of interconnected pores, and pore shape. These properties allow the engineering of SHS produced materials with specific porosities as well as the construction of functionally graded porosities.

Scanning Electron Microscope (SEM) images were produced using a JEOL JXA-840 SEM. The SEM analysis was coupled with a Thermo NORAN Lithium drifted 10mm2 Electron Dispersive X-ray (EDX). Samples were coated with Gold for SEM analysis. Xray Diffraction (XRD) analysis was performed with a Philips X'Pert MPD Pro Theta/Theta X-ray diffraction system. The microstructure of the TiB-Ti samples was studied with an Olympus SZX12 stereoscope.

Results

SEM micrographs shown below in Figure 2, show the difference in microstructure. Figure 2 (A) is a micrograph of a sample reacted in low gravity and partially cooled in a low gravity and ~2 g environment, due to the parabolic flight pattern of the KC-135. The grain exhibits the characteristics of particle ripening and six sided grain

growth features. Figure 2 (B), shows grains that have cooled in a 1g environment. The microstructure exhibits longitudinal grains with characteristic spots.

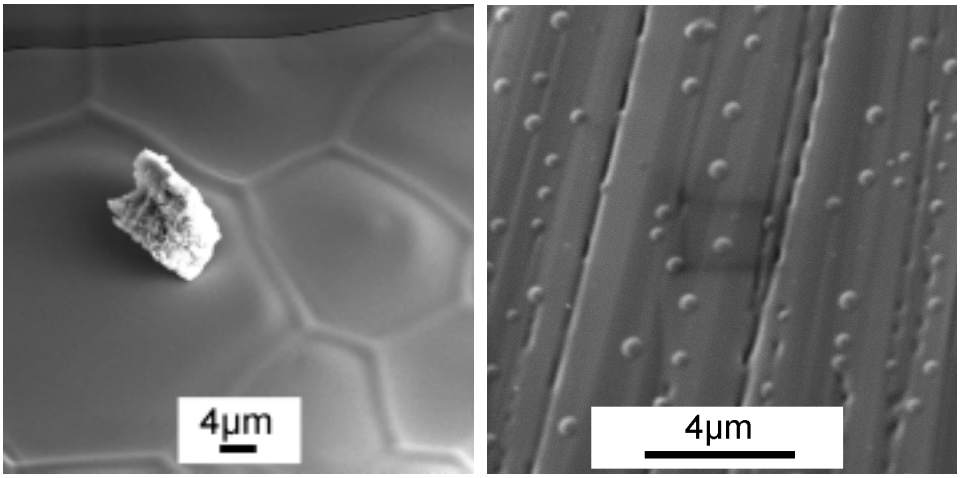

(A) (B)

Figure 2. SEM images of $Ca_3(PO_4)_2$ produced in low gravity (A) and at 1 g (B).

EDX analysis (Figure 3) show spectra taken from the center of both grains from Figure 2. The low gravity sample shows almost the same calcium to phosphorus ratios while the 1 g sample exhibits a lower calcium to phosphorus ratio. The EDX/SEM samples were coated in gold, therefore deconvolution of the phosphorus and gold peak was performed.

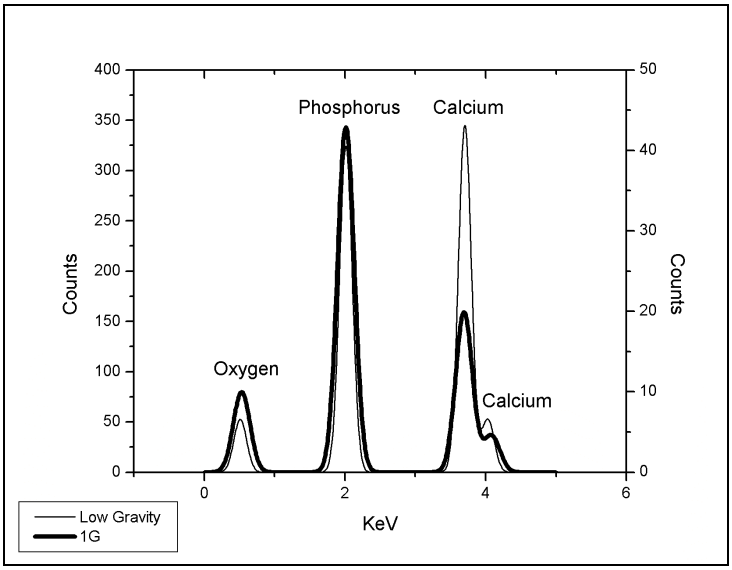

Figure 3. EDX spectra for $Ca_3(PO_4)_2$ produced in low gravity and at 1 g conditions.

XRD analysis of both the low-gravity and 1 g samples are shown below in Figure 4. Both spectra match the alpha phase for tricalcium phosphate (PDF 70-0364). Note that this is a bulk analysis and the above EDX analysis is a microanalysis.

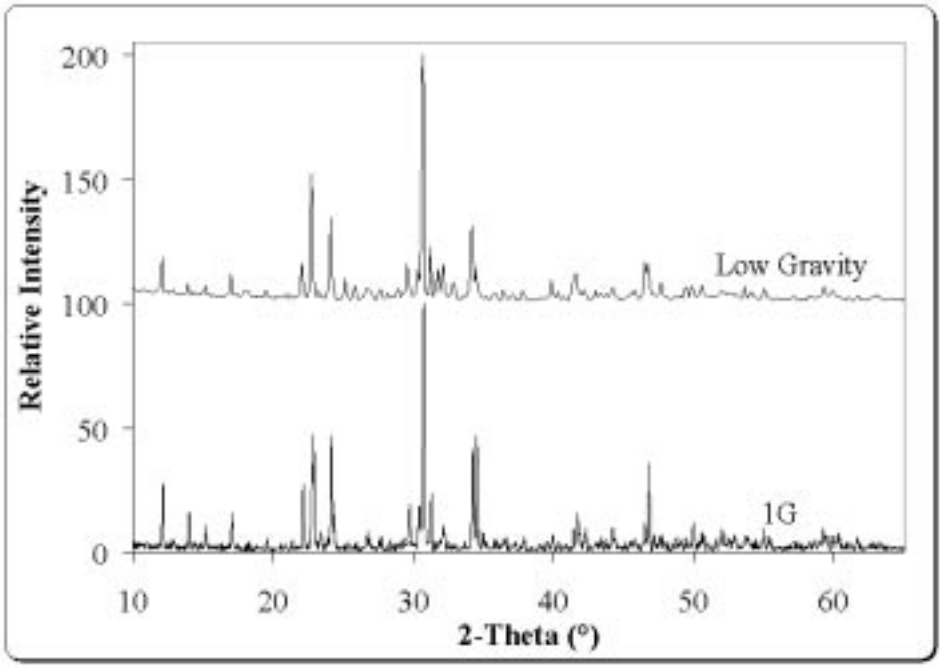

Figure 4. XRD spectra for $Ca_3(PO_4)_2$ produced in low gravity and 1 g conditions. Both spectra match PDF file 70-0364 alpha tricalcium phosphate (monoclinic).

The effect of gravity on the (x+y)Ti + xB = yTi + xTiB is shown below in Figure 5. The longitudinal or propagating direction is shown below with ignition from the lower side (bottom of sample). Sphere-like pores were produced in low gravity environments and radial pores were produced under terrestrial conditions.

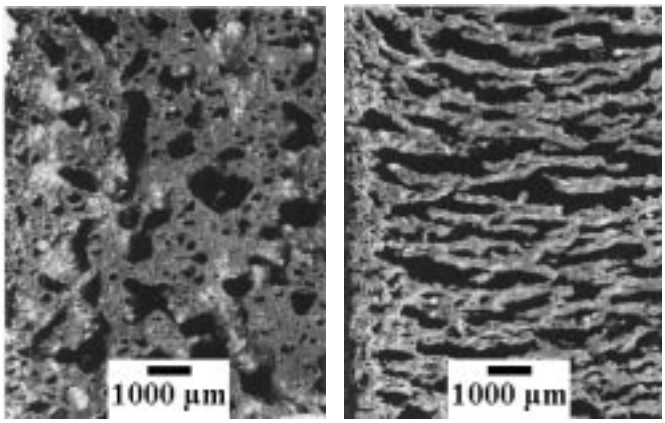

(A) (B)

Figure 5. Effect of gravity on reaction system (x+y)Ti + xB = yTi + xTiB. The as-produced materials are 92% TiB and 8%Ti. A was produced in low gravity and B was produced in terrestrial conditions aboard the KC-135.

SHS reactions were also investigated for the NiTi system. XRD analysis of NiTi produced via SHS is given in Figure 6. Ni3Ti and NiTi2 were formed with the NiTi in the combustion process (nonequlibrium).

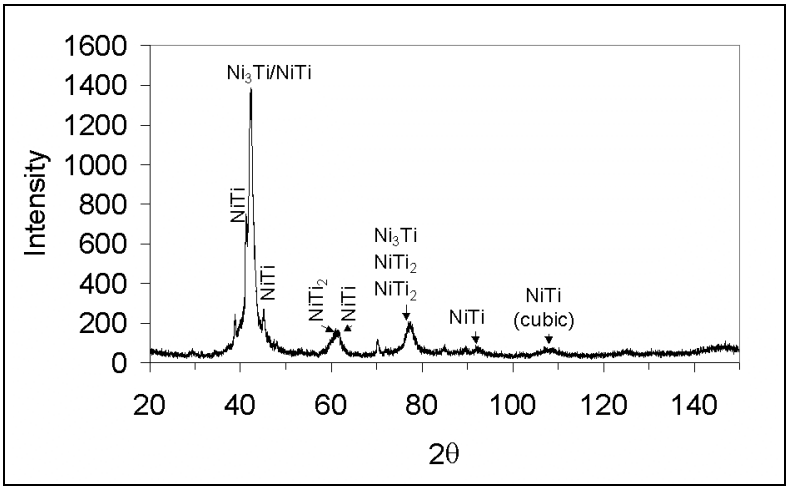

Figure 6. XRD of SHS produced NiTi under terrestrial conditions.

Discussion

Different gravity environments have a great effect on the $Ca_3(PO_4)_2$ microstructure produced by SHS. It is shown on the micrometer scale that the grain structure is significantly different according to Figure 2. Low gravity produces the classic Al_2O_3 type grain growth while the terrestrial environment yields long radial grains with characteristic spots. In Figure 3, EDX analysis shows that the calcium to phosphorus ratio is unity for grains manufactured on the KC-135 while the calcium to phosphorus ratio is lower for the sample produced under terrestrial conditions. The samples produced on the KC-135 were partially cooled in low gravity (~0 g) and high gravity (~2 g) conditions due to the parabolic flight path of the KC-135. Bulk analysis performed with XRD (Figure 4), showed that both $Ca_3(PO_4)_2$ samples produced in microgravity formed the alpha phase of tricalcium phosphate. The microstructure studied at the surface via EDX is in need of further investigation to explain the overall balance in the calcium to phosphorus atomic ratio. EDX will have to be carried out at the grain boundaries and throughout other features not shown in Figure 2. Longer low-gravity conditions (available on the International Space Station) may also prove to produce a more homogeneous sample. The processing conditions greatly affect the surface chemistry, which is directly related to the bioactivity of the sample in-vivo.

The TiB-Ti system produced in variable gravity is shown to have a great influence on the formation of pores. Spherical-like pores are produced in low gravity while longitudinal-radial pores are produced in terrestrial conditions. The pore structure is directly related to the strength of the material, in-vivo vascularization, and tissue ingrowth properties.

Ni_3Ti and $NiTi_2$ were formed together with the equiatomic NiTi during SHS according to the XRD results obtained in Figure 6. This is due to the non equilibrium conditions that are involved with SHS reactions. The formation of equiatomic NiTi only happens in a narrow almost equiatomic region (50-55 atomic %) in the phase diagram. The NiTi phase exhibits shape memory and superelasticity properties that are desirable for specific implant applications. The NiTi system is continually being investigated to produce a greater amounts of the equiatomic NiTi phase and ways to produce this material in variable gravity situations.

Acknowledgements

This work was supported by the NASA Space Product Development Program through the Center for Commercial Applications of Combustion in Space at the Colorado School of Mines under Cooperative Agreement Numbers NCCW-0096 and NCC8-238, and by the NASA Microgravity Research Division under Cooperative

Agreement Numbers NCC3-659. Additional funding was provided by the Colorado Commission on Higher Education, the Colorado School of Mines and the CCACS Industrial Partners.

References

1. Ayers R.A., Bateman T.A., S.J. Simpske, Porous Materials for Bone Engineering, Porous Materials for Tissue Engineering, Dean-Mo, Vivek Dixit, Trans Tech Publications, Switzerland 1997
2. Ethridge E.C., Hench L.L., Biomaterials: An Interfacial Approach, Academic Press, New York, 1982.
3. Feng H.J., Moore J.J., Combustion Syynthesis of Advanced Materials: Part II. Classification, Applications and Modeling, Progress in Material Science, 39, 1995, 275-316

Effect of Molding and Machining on Neoflon CTFE M400H Polychlorotrifluoroethylene Rod Stock and Valve Seat Properties

Jess M. Waller
Project Leader, Honeywell Technology Solutions Inc., NASA Johnson Space Center White Sands Test Facility,
P. O. Box 20, Las Cruces, NM 88004
505-524-5249
jwaller@wstf.nasa.gov

Barry E. Newton
Engineer, Wendell Hull & Associates, Inc., 1020 South Main, Las Cruces, NM 88005
505-532-5623
bnewton@cs.com

Harold D. Beeson
Special Projects Manager, NASA Laboratories Office, NASA Johnson Space Center White Sands Test Facility,
P. O. Box 20, Las Cruces, NM 88004
505-524-5543
hbeeson@wstf.nasa.gov

Introduction

Since 1997 numerous fires have been reported to the Food and Drug Administration involving cylinder valves installed on medical use oxygen cylinders sold and operated within the United States. All of the cylinder valves in question had polychlorotrifluoroethylene (PCTFE) valve seats. Subsequent failure analysis showed that the main seat was the primary source of ignition. A review of the incidents involving cylinder valve fires indicated three possible ignition mechanisms: contaminant promotion, flow friction, and resonance. However, gas purity analysis showed that uncombusted, residual oxygen was within specification. Infrared and energy dispersive spectroscopy further showed that no contaminants or organic compounds were present in the remaining, uncombusted valve seat material or on seat plug surfaces [*1*]. Therefore, contaminant-promoted ignition did not appear to be responsible for the failures.

Observations of extruded material along the outer edge of the coined or loaded seat area [*1*] produced by cylinder overuse or poppet overload led to concerns that accelerated gas flow across a deformed seat surface could generate enough localized heating to ignite the polymeric seat. Low molecular weight or highly amorphous quick-quenched PCTFE grades might be expected to be especially prone to this type of deformation. Such a failure mechanism has been described as "flow friction;" however, the corresponding mechanistic parameters are poorly understood.

Subsequent revelation of low-temperature dimensional instability by thermomechanical analysis (TMA) in a variety of PCTFE sheet and rod stock samples [*1*] led to new concerns that PCTFE valve seats could undergo excessive expansion or contraction during service. During expansion, additional extrusion and accompanying "flow friction" could occur. During contraction, a gap between the seal and adjacent metal surfaces could form. Gas flowing past the gap could, in turn, lead to resonance heating and subsequent ignition as described in ASTM Guide for Evaluation Nonmetallic Materials for Oxygen Service (G 63).

Attempts to uncover the origins of the observed dimensional instability were hindered by uncertainties about resin grade, process history, and post-process heat history introduced by machining, annealing, and sample preparation. An approach was therefore taken to monitor property changes before and after processing and machining using a single, well-characterized lot of Neoflon CTFE®[1] M400H resin. A task group consisting of the current PCTFE resin supplier, two molders, and four valve seat manufacturers was formed, and phased testing on raw resin, intermediate rod stock, and finished valve seats initiated. The effect of processing and machining on the properties of PCTFE rod stock and oxygen gas cylinder valve seats was then determined. Testing focused on two types of extruded rod stock and one type of compression-molded rod stock. To accommodate valve seat manufacturer preferences for certain rod stock diameters, two representative diameters were used (4.8 mm (0.1875 in.) and 19.1 mm (0.75 in.)). To encompass a variety of possible sealing configurations, seven different valve seat types with unique geometries or machining histories were tested. The properties investigated were dimensional stability as determined by TMA, specific gravity, differential scanning calorimetry (DSC), compressive

[1] Neoflon® is a registered trademark of Daikin America, Inc., Orangeburg, New York.

strength, zero strength time, and intrinsic viscosity. Findings are discussed in the context of polymer structure-process-property relationships whenever possible.

Experimental

Materials

Two commercial varieties of PCTFE were tested: Kel-F 81[2] formulation 6060 in the form of pellets and 6.4 mm (0.25 in.) diameter rod stock; and Neoflon CTFE M400H in the form of coarse granular powder, 4.9 mm (0.1875 in.) and 19.1 mm (0.75 in.) diameter rod stock, and valve seats. The Kel-F 81 resin (lot # 610) was obtained from NASA stock (Kennedy Space Center, FL) and had a reported starting zero strength time (ZST) of 401 sec. Kel-F 81 rod stock (Polyflon Corp., molded ca. 1979, lot unknown) was obtained from internal WSTF stock (ZST unknown). Neoflon CTFE M400H coarse granular powder (lot # DFH4R99006) was obtained from Daikin America, Inc. (Orangeburg, NJ) and had a reported starting ZST of 411 sec. The Neoflon M400H resin was used to prepare all rod stock and valve seat specimens (Figure 1). All valve seats were received in free-standing condition, i.e., were not pressed into metal retainers.

Extruded rod stock was obtained from two molders (Molders 1 and 2) and compression-molded rod stock was obtained one molder (Molder 2). To accommodate valve seat manufacturer preferences for certain rod stock diameters, two representative diameters were supplied to valve seat manufacturers: 4.8 mm (0.1875 in.) and 19.1 mm (0.75 in). Of the 3.7 m (12 ft.) of each of the six types of rod stock manufactured for this study, 0.30 m (1.0 ft.) was provided to White Sands Test Facility for thermal and mechanical property characterization, and 0.60 m (2.0 ft.) was provided to each of the participant valve seat manufacturers, the remainder was kept as reserve or allocated for other purposes.

To encompass a variety of oxygen regulator sealing configurations, testing was conducted on seven different valve seat types supplied by four valve seat manufacturers (Manufacturers 1, 2, 3, and 4). Valve seats with different machining processes were tested (Manufacturer 2, Processes 1 and 2), and different designs from the same manufacturer were tested (Manufacturer 3, Designs 1, 2, and 3). All valve seats were machined from 4.8 mm or 19.1 mm diameter rod stock except for valve seats from Manufacturer 2, which were machined from 6.4 mm (0.25 in.) diameter rod stock obtained by turning down 19.1 mm diameter rod stock (Figure 2).

Molding Conditions

Extruded rod (Molders 1 and 2) was molded in slightly oversized diameters and centerless ground to the desired finish tolerances. A metal jacket was used to support the larger diameter extruded rod, while the smaller diameter rod was extruded directly into air. All extruded rod tested was air cooled (versus water quenching). Compression-molded rod (Molder 2) was obtained by bandsaw cutting an 8.0 mm (0.31 in.) and 24.1 mm (0.95 in.) thick sheet into rectangular bars, which were turned down on a lathe to 7.6 mm (0.30 in.) and 20.3 mm (0.80 in.) diameter, annealed, and centerless ground to the final 4.9 mm and 19.1 mm diameters and finish tolerances. The same molding and follow-up pressures were used for both diameters of compression-molded rod.

Thermal Analysis

A Haake-Fisons (formerly Seiko) Model 120C Thermomechanical Analyzer equipped with a liquid nitrogen cooling accessory was used to measure dimensional stability. Specimens with diameters larger than could be accommodated by the TMA cell diameter> 10-mm (0.39 in.)) were sectioned. Other details about specimen preparation appear elsewhere [*1*]. Dimensional stability was evaluated by cycling each specimen three times between -20 and 150 °C, followed by measuring the permanent height change at 0 °C. Melting (T_m) and crystallization temperatures (T_c), supercooling ($\Delta T = T_m - T_c$), and heat of fusion (ΔH_f) and crystallization (ΔH_c) were determined using a TA Instruments Model 2920 DSC in accordance with procedures given in ASTM Test Method for Transition Temperatures and Heats of Transitions of Fluoropolymers by Differential Scanning Calorimetry (D 4591). Care was taken to sample rod stock and valve seat material from consistent locations with respect to the transverse (radial) direction. To minimize annealing, specimens (10 mg) were ramped from ambient temperature to

[2] Kel-F® (obsolete) is a registered trademark of 3M, St. Paul, MN.

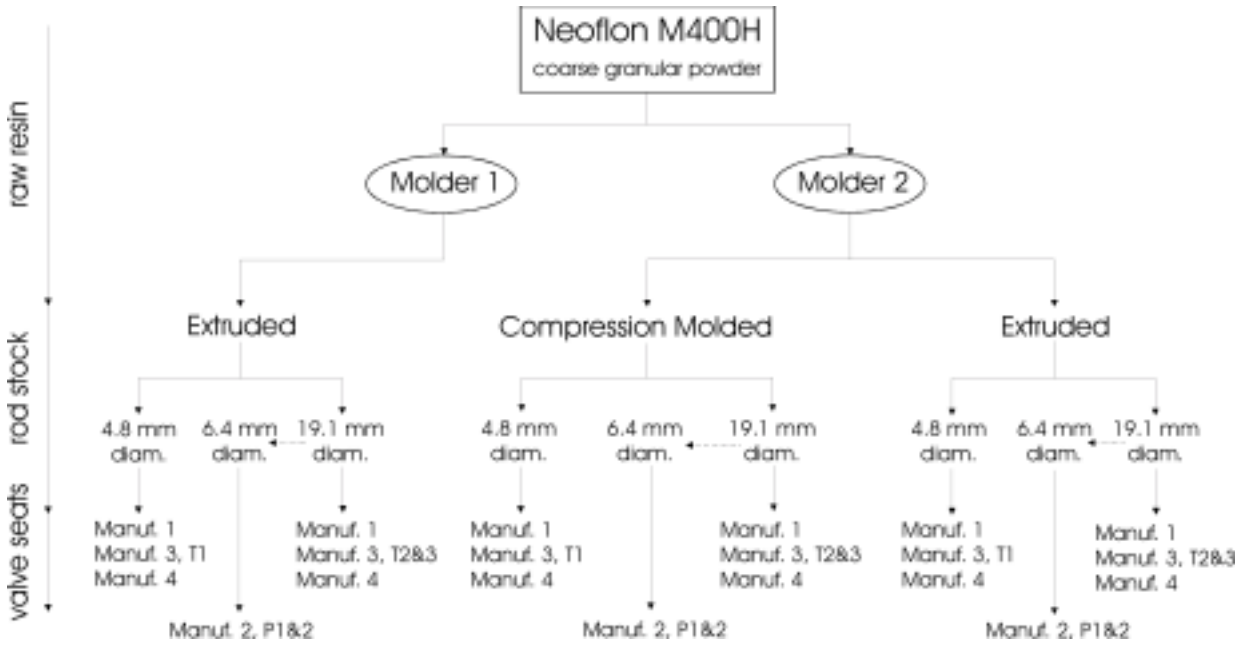

Figure 1 – *Tracking chart showing allocation of Neoflon M400H PCTFE resin to molders, and molded rod stock to valve seat manufacturers (dashed lines indicate a latheing operation performed on rod stock)*

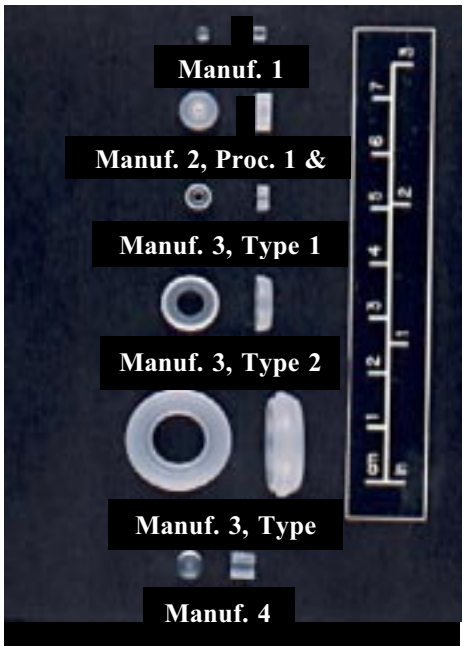

Figure 2 – *PCTFE valve seat varieties used in oxygen cylinder applications*

175 °C at the maximum possible instrument heating rate (~125° min^{-1}), then heated at a controlled rate of 10° min^{-1} to 250 °C. All DSC determinations were conducted under nitrogen.

Physical and Mechanical Property Evaluations

Specific gravity was determined by ASTM Test Method for Specific Gravity of Plastics by Displacement (D 792) and weight percent crystallinity, W^c, calculated based on assumed values for the densities of pure amorphous and pure crystalline phases [*2*] according to the relationship:

$$W^c = \frac{\rho_c}{\rho}\left(\frac{\rho - \rho_a}{\rho_c - \rho_a}\right)\times 100\% \quad (1)$$

Compressive strength at 25-percent strain was determined using an Instron® Model TTC Universal Tester and specimens with a 2:1 height:width ratio according to ASTM Test Method for Compressive Properties of Rigid Plastics (D 695).

ZSTs were determined per ASTM Standard Specification for Polychlorotrifluoroethylene (PCTFE) Plastics (D 1430-95) using 4.8 mm (0.1875 in.) wide by 1.6 mm (0.0625 in.) thick V-notched test strips machined directly from as-molded bar stock.

Intrinsic viscosity, [η], was determined per ASTM Standard Practice for Diluted Solution Viscosity of Polymers (D 2857) at 130 ± 0.2 °C in a DC550 silicone bath and using 98 % 2,5-dichlorobenzotrifluoride (DCBTF, t_o > 150 sec) as the solvent. Dissolutions were carried out at 150 °C in a micro-Ubbelohde viscometer for a minimum of 20 hr under constant stirring to give an initial concentration of 0.5 g dL^{-1}. Extrapolation to infinite dilution allowed the number average molecular weight, $\overline{M}_n$, to be calculated using the Mark-Houwink equation and assumed values of 6.15×10^{-5} and 0.74 for parameters *K* and *a*, respectively [*3*]:

$$[\eta] = K\overline{M}_n^a \quad (2)$$

Results and Discussion

PCTFE Grade Differences

Initial efforts focused on evaluating the differences between the two principle grades of PCTFE resin historically used to manufacture oxygen gas cylinder valve seats, namely, Kel-F 81 and Neoflon CTFE. Since Kel-F 81 was emulsion-polymerized and Neoflon CTFE is suspension-polymerized, possible differences attributable to polymerization route were considered.

Emulsion polymerizations generally proceed more rapidly at a given temperature, and higher molecular weights are obtained than in suspension polymerizations conducted at the same rate [*4*]. This difference arises from isolation of the initiation step, which occurs in the aqueous phase, from the propagation and termination steps, which occur in the oil phase (dispersed micelles). In a suspension polymerization, the initiation, propagation, and termination steps all occur in the oil phase (dispersed monomer droplets). The suspension polymerization rate thus depends on initiator concentration, while the emulsion polymerization rate does not. Increasing the polymerization rate in a suspension polymerization by increasing initiator concentration produces more active chains competing for a finite amount of monomer, which can result in lower molecular weight. Both high polymerization rates and molecular weights can be achieved in emulsion polymerizations by increasing the micelle concentration [*5*]. Because the initiation rate, polymerization rate, monomer concentration, and micelle concentration remain relatively constant during much of an emulsion polymerization, resulting molecular weight is less affected by percent conversion. This usually results in a narrower molecular weight distribution (MWD) as defined by the polydispersity index (= $\overline{M}_w \div \overline{M}_n$) than obtained in a suspension polymerization [*5*]. Since many end-use properties have optimum values over a discrete molecular weight range, a broader MWD is generally undesirable from a practical applications standpoint.

A small batch emulsion process was used to produce Kel-F, requiring a combination of many batches to give a single lot, while a large single batch/single lot suspension processes is used to produce Neoflon CTFE [*6*]. Therefore, it is unclear if the polydispersity advantages inherent to the emulsion process are undermined by a combination of multiple batches to give a multimodal distribution. Last, the use dispersants and oil-soluble initiators in the suspension polymerization and fluorosurfactants [*7*] in the emulsion polymerization of PCTFE presents unique challenges during polymer isolation and purification. Although purity considerations are of paramount importance in oxygen applications, resin purity was not investigated in this study.

DSC showed that the Neoflon M400H coarse granular powder underwent more supercooling (ΔT) and had a lower heat of crystallization (ΔT = 38.8 ± 1.2 °C; ΔH_c = 12.8 ± 0.9 J g^{-1}) than the Kel-F 81 pellets tested (ΔT = 26.2 ± 1.9 °C; ΔH_c = 14.4 ± 0.4 J g^{-1}) (Figure 3). Broad MWD, low molecular weight, nucleating agents, or impurities can lower ΔT; while low molecular weight is generally associated with high heats of crystallization [*8*]. The Kel-F 81 and Neoflon M400H resins tested, however, did not contain nucleating agents [*6*]. Also, Kel-F 81 pellets had a higher heat of crystallization despite having a higher molecular weight ($\overline{M}_n$ = 712,000 ± 25,000 g mol^{-1}) than the Neoflon M400H coarse granular powder ($\overline{M}_n$ = 659,000 ± 33,000 g mol^{-1}) (Figure 4). These observations suggest that crystallization of Neoflon M400H was suppressed by a broader MWD. Additional evidence of MWD broadening in the Neoflon M400H resin is provided by the larger melting and crystallization peak widths at half height (w $_{,m}$ = 6.3 °C, w $_{,c}$ = 6.8 °C) compared to the Kel-F 81 resin (w $_{,m}$ = 3.8 °C, w $_{,c}$ = 5.0° C) (Figure 3).

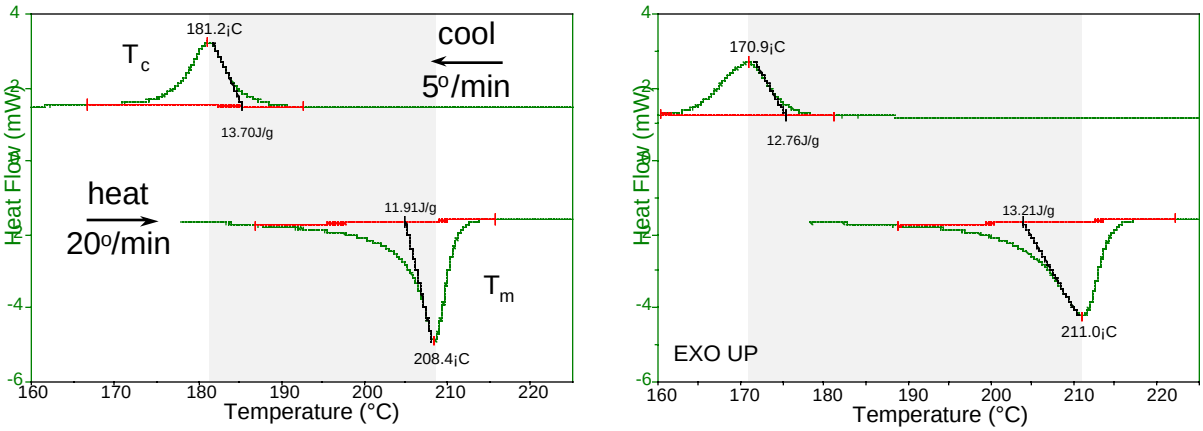

Figure 3 – *Representative DSC thermograms showing lower supercooling and higher heat of crystallization for Kel-F 81 (left) versus Neoflon M400H (right)*

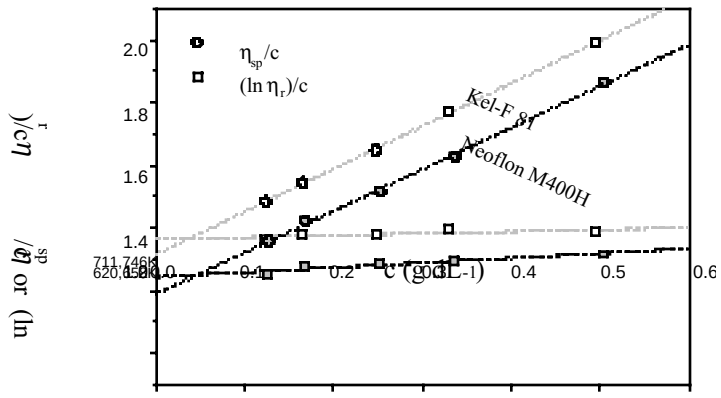

Figure 4 – *Representative dilute solution viscosity data for as-polymerized Kel-F 81 and Neoflon M400H PCTFE*

Figure 5 – *Representative cross-sections of extruded (left) and compression-molded (right) Neoflon M400H rod stock (19.1 mm (0.75 in.) diameter)*

Visual Appearance of Molded PCTFE Rod Stock

All rod stock samples were identical in appearance except for visible differences in exterior and cross-sectional translucency. For example, extruded 4.8 mm-diameter extruded rod stock from Molder 1 was noticeably more translucent than the extruded or compression-molded 4.8 mm-diameter rod stock from Molder 2 (not shown). Inspection of 19.1 mm-diameter rod stock cross-sections also revealed concentric, translucent swirls in the two extruded stocks, while no swirls were visible in the compression-molded stock (Figure 5). Also, there appeared to be several dark inclusions (located at six and seven o'clock in Figure 4, left, for example) in the extruded rod stock from Molder 2; however, no attempt was made to characterize the inclusions. Inspection of water (quick)-quenched and air (slow)-quenched compression-molded Neoflon M400H sheet has shown that translucent PCTFEs tend to be more amorphous, while more opaque PCTFEs tend to be more crystalline [*9*]. Crystallite (spherulite) size differences could also account for the observed variation in translucency.

Effect of Process History on Rod Stock Properties

Because of 1) the use of higher process temperatures during extrusion molding, 2) the well-known sensitivity of PCTFE to high process temperatures, and 3) the greater likelihood of molecular orientation (property anisotropy) and shear degradation (molecular weight reduction) during extrusion, it was suspected that extruded rod stock might exhibit a poorer balance of properties than compression-molded rod stock. Also, since heat is retained longer in the interior of larger molded articles, often leading to 'skin-core' morphology, the effect of rod stock diameter on property heterogeneity was investigated.

DSC, ZST, and intrinsic viscosity data on processed rod stock samples revealed significant increases in the heat of fusion and crystallization, accompanied by parallel drops in the ZST and number average molecular weight (Table 1, Figure 6). Unfortunately, the ZST does not appear to be very sensitive to molecular weight variation above a $\overline{M}_n$ -threshold of approximately 600,000 g mol^{-1}. The largest molecular weight decreases (-29 to –33 percent) were observed for extruded rod stock from Molder 1. The large decreases in ZST and molecular weight may be due to higher melt temperatures, excessively long residence times, or shear degradation during extrusion. The large increases in the heat of fusion (+21 to +26 percent) observed for compression-molded rod stocks from Molder 2 may be due to the higher percent crystallinities developed during slow cooling under load (2.0 to 2.5 hr). The increases in the heat of fusion (+14 to +16 percent) observed for extruded rod stock from Molder 1 may instead be due to the molecular weight decreases leading to increased chain flexibility in the melt. Little or no change was observed in the post-process values for T_m, T_c, and ΔT compared to the starting Neoflon M400H resin. The anomalous observation of a higher molecular weight for the 4.9 mm diameter compression-molded rod stock (697,000 g mol^{-1}) compared to the starting resin (659,000 g mol^{-1}) was attributed to data scatter and molecular weight variation within the lot of Neoflon M400H CTFE coarse granular powder used in this study.

Table 1 — *Properties of Molded PCTFE Rod Stock*[a]

Property	Starting Resin	4.9 mm extruded, Molder 1	19.1 mm extruded Molder 1	4.9 mm extruded Molder 2	19.1 mm extruded Molder 2	4.9 mm compr.-mold Molder 2	19.1 mm compr.-mold Molder 2
ΔH_f (J g^{-1})	13.9 (1.1)	16.3 (0.7)	15.8 (0.3)	14.8 (0.8)	15.4 (0.9)	16.8 (0.1)	17.5 (0.3)
% change		+17	+14	+6	+11	+21	+26
ΔH_c(J g^{-1})	12.8 (0.9)	16.0 (0.6)	14.9 (0.9)	15.7 (1.0)	14.7 (1.4)	14.4 (0.2)	14.0 (0.3)
% change		+25	+16	+23	+15	+13	+9
W^c (%)	…	61 (9)	62 (1)	42 (9)	58 (1)	61 (9)	66 (3)
ZST (s)	411[b]	205 (1)	276 (6)	410 (5)	392 (1)	414 (4)	407 (7)
$\overline{M}_n$ ($\cdot 10^{-6}$ g mol^{-1})[c]	6.59 (0.33)	4.41	4.70	6.01	6.37	6.97	6.56
% change		-33	-29	-9	-3	+6	NC
$\overline{M}_n$ ($\cdot 10^{-6}$ g mol^{-1})[d]	…	…	TBD	…	TBD	…	TBD
% change			-/+		-/+		-/+
$\sigma_{c,\,25\%}$ (MPa)	…	68 (<1)	95 (<1)	72 (<1)	83 (1)	79 (2)	92 (6)

[a] Abbreviations used: heat of fusion (ΔH_f), heat of crystallization (ΔH_c), weight percent crystallinity (W^c), zero strength time (ZST), number average molecular weight ($\overline{M}_n$), no change (NC); measurement not performed or not applicable (…), compressive strength at 25% strain ($\sigma_{c,\,25\%}$); numbers in parentheses are standard deviations.

[b] Starting resin ZST was determined on molded bars and therefore does not correspond to the molecular weight of the unprocessed coarse granular powder.

[c] Specimens taken across cross-section of 4.9 mm diameter rod, and middle of 19.1 mm diameter rod.

[d] Specimens taken from outer edge of 19.1 mm diameter rod.

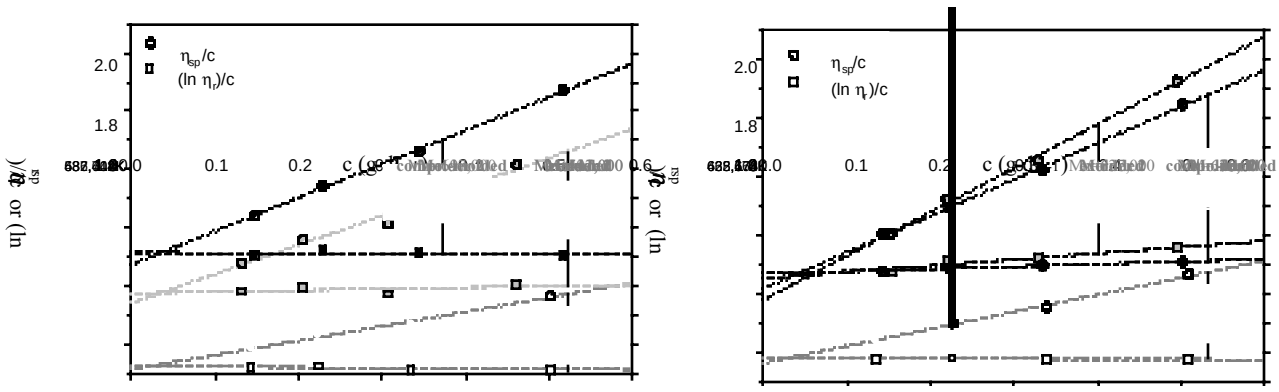

Figure 6 – *Dilute solution viscosity data for 4.9 mm (0.1875 in.) (left) and 19.1 mm (0.75 in.)(right) diameter Neoflon M400H PCTFE rod stock*

Representative 3/16 in. diameter rod

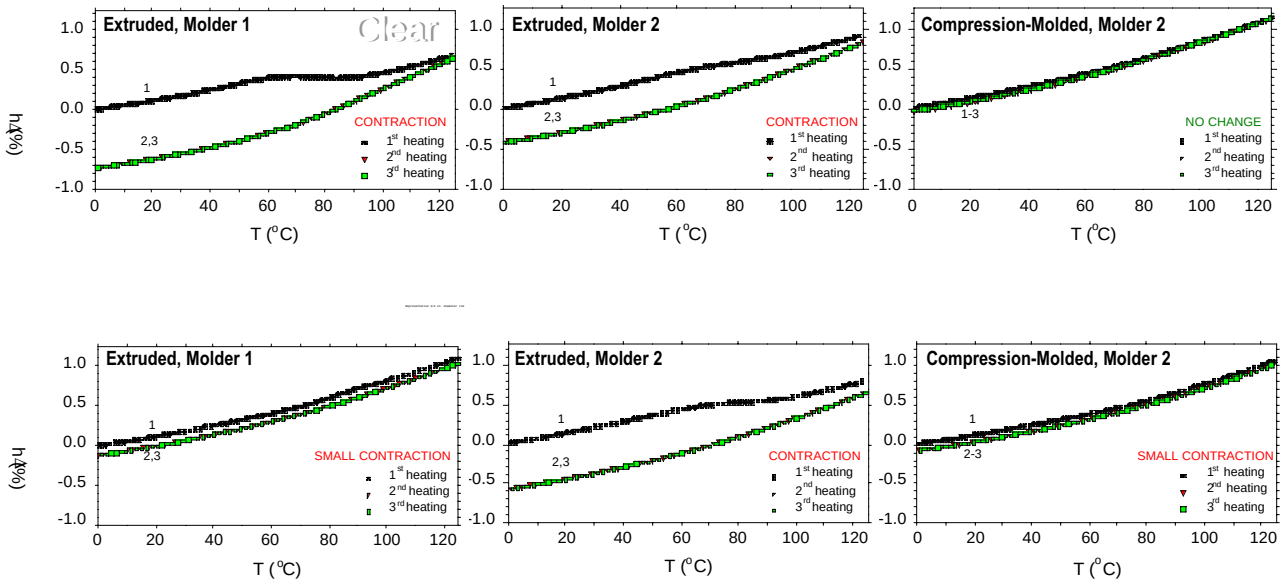

Figure 7 – *TMA thermograms showing the effect of thermal cycling on the permanent height change of 4.9 mm (0.1875 in.) (top) and 19.1 mm (0.75 in.)(bottom) diameter Neoflon M400H PCTFE rod stock*

The effect of skin-core molecular weight variation in the thicker 19.1 mm diameter rod stock was examined by comparing the intrinsic viscosity of specimens taken from the outside edge of the rod (next-to-last row, Table 1). Results showed significant molecular weight segregation in the extruded rod stock, but virtually no segregation in the compression-molded rod stock.

Dimensional Stability of Rod Stock

The compressive strength (at 25-percent strain) of the 4.9 mm diameter rod stock was found to follow ZST, molecular weight, and dimensional stability (Table 1, last row), while the compressive strength of the 19.1 mm diameter rod stock was found to follow dimensional stability. This lack of correlation between the compressive strength and other properties appears to derive from the use of an annealing step by Molder 1 to give a strong, dimensionally stable material despite having a low ZST (276 s) (Figure 7, lower left-hand corner). By comparison, the extruded 19.1 mm diameter rod stock from Molder 2 was unannealed, but had a lower compressive strength despite having a higher ZST (392 s) (Figure 7, lower center). At temperature below 150 °C (300 °F), annealing can be used to relieve localized stresses within the amorphous phase as well as enhance crystal perfection (secondary crystallization). If conducted at temperatures near 175 °C (375 °F), at which the maximum crystallization rate occurs, annealing can result in increased percent crystallinity (primary crystallization). These observations suggest annealing can be used to improve dimensional stability and mechanical strength under load. Such property enhancements may be particularly important in valve applications requiring close tolerances to be maintained over nominal temperature excursions. Annealing may even compensate for the adverse effects of molecular weight degradation caused by non-optimized processing.

Previously published data [*1*] shows considerable variation in the permanent height change as measured by TMA caused by thermal cycling of several varieties of PCTFE, including valve seats taken from oxygen and corrosive gas service, as well as molded bar stock and sheet. These materials exhibited permanent expansions as high as +3.9 percent and permanent contractions as low as –8.5 percent following repetitive thermal cycling between -20 °C (-4 °F) and 150 °C (300 °F). Furthermore, dimensional relaxation was observed as evidenced by the appearance of inflections or maxima as low as 37 °C (99 °F) in the height versus temperature curve during the first

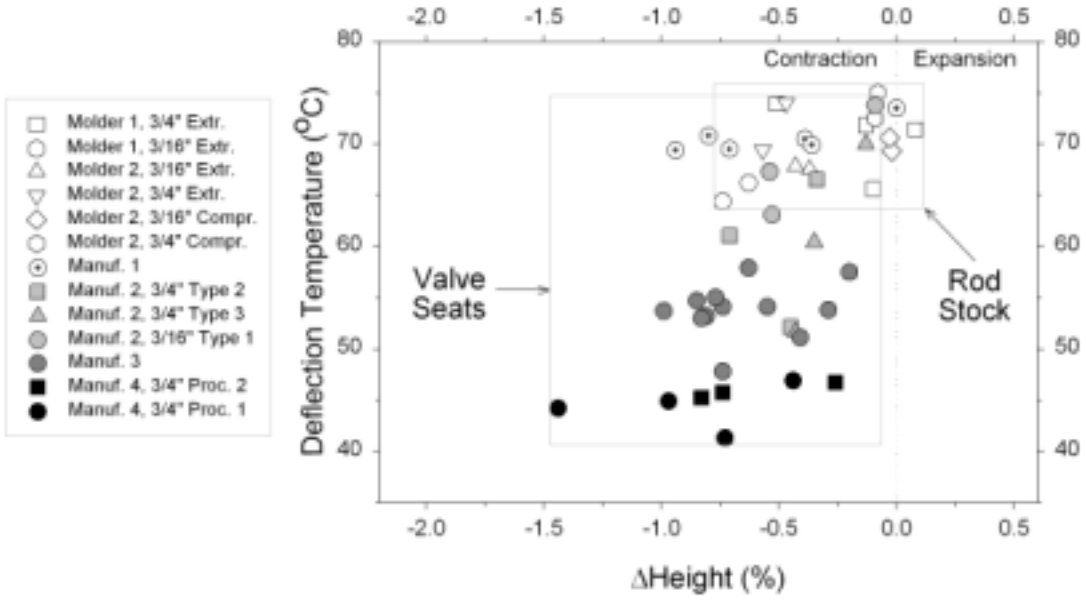

Figure 8 – *Scatter plot showing the distribution of deflection temperature and net height change for molded rod stock (open symbols) and machined valve seats (filled symbols)*

heating. The close correspondence of the low temperature TMA deflections with the glass transition, which has a published value of ca. 52 °C (126 °F) per DIN 53736 [*10*], suggests the deflections originate from molecular relaxation within the amorphous phase.

By comparison, the TMA deflection data distribution for the molded rod stock used in this study was narrower; permanent expansions as high as +0.08 percent and permanent contractions as low as –0.74 percent were observed (Figure 8). Also, the inflections or maxima indicative of dimensional relaxation occurred at higher temperatures; between 64.4 (148 °F) and 75.0 °C (167 °F).

Effect of Machining on Valve Seat Properties

Final efforts focused on determining the effect of machining on valve seat properties. The final properties of semicrystalline thermoplastics such as PCTFE are governed by the cumulative heat history. Most heat history is introduced during processing (melting). However, significant heat history can also be introduced during post-process operations, such as latheing and machining, or pressing of seats into metal retainers at temperature. Attempts were therefore made to determining the effect of post-process heat histories on valve seat properties.

Inspection of Figure 8 also shows that TMA valve seat data tended to be grouped according to seat manufacturer, especially for Manufacturers 1 and 3. The TMA deflection data distribution for the machined valve seats was also shifted to larger percent contractions (contractions as large as –1.44 percent were observed) (Figures 8 and 9), and the deflections observed during first heatings occurred at lower temperatures; for example, inflections or maxima as low as 41.3 °C (106 °F) were observed. The reasons behind these shifts are unclear; however, the largest shift was observed for the valve seats supplied by Manufacturer 4 (Figure 8, black symbols). These valve seats happened to have been subjected to the greatest amount of machining, involving turning down of the 19.1 mm to 6.4 mm diameter rod stock (Figure 1). Efforts are underway to determine the effect of lathe speed, heat treatments, cutting tool materials, and cutting fluids, on finished valve seat properties.

Another reason for the shift of the TMA data towards larger percent contraction and lower deflection temperature could be the 'skin-core' morphological heterogeneity and choice of TMA sampling location. For example, the valve seats from Manufacturer 2 were obtained from the middle of the 19.1 mm diameter rod stock (Figure 9, also see Figure 5) were noticeably clearer in appearance, similar to the 4.9 mm diameter extruded rod from Molder 1 which exhibited the poorest dimensional stability of all the rod stock materials examined in this study (Figure 7, top left). Lower crystallinity does not appear to be a reason for the increased translucency, since the middle of the 19.1 mm diameter rod stock would be expected to be more crystalline due to retention of heat for longer periods during solidification from the melt. However, DSC measurements on the finished valve seats had not

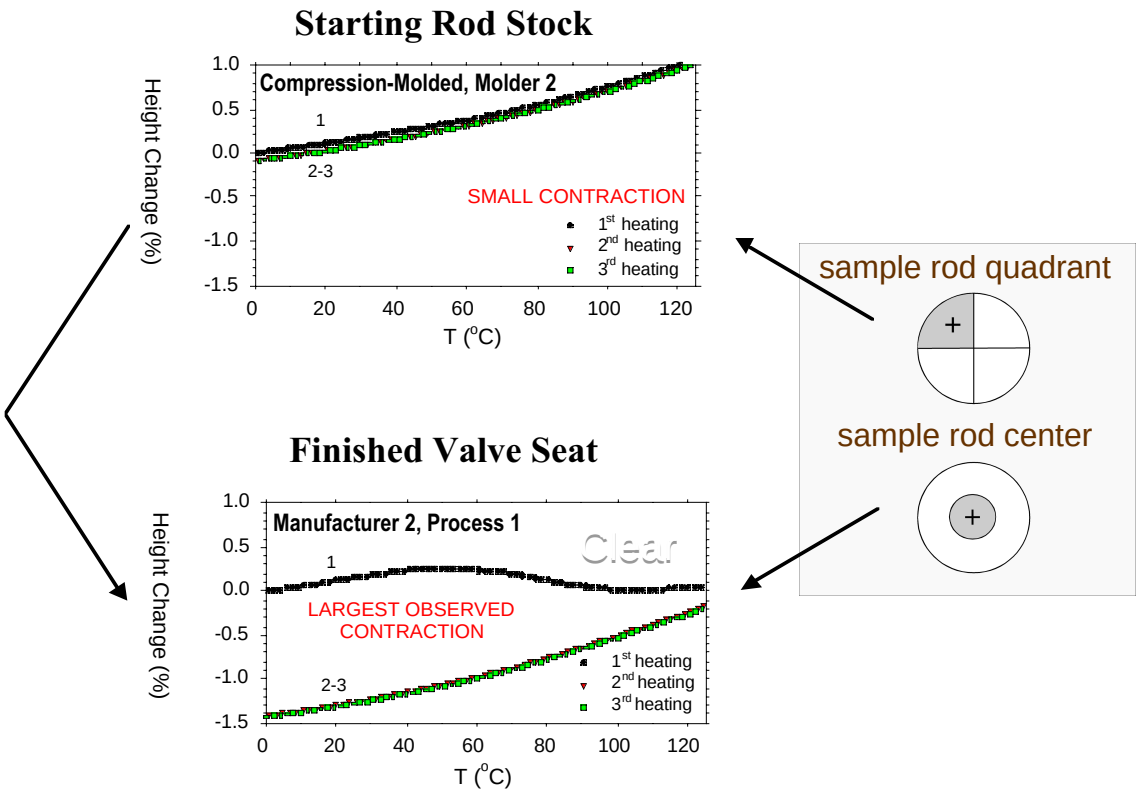

Figure 9 – *TMA thermograms showing different dimensional stability of the molded rod stock (top) versus machined valve seats (bottom) fabricated from it*

been conducted at the time of this report, nor had crystallite size been evaluated by polarized light microscopy. The possible effect of molecular weight on translucent appearance and low dimensional stability was investigated, but did not appear to be much of a contributing factor either. For example, the $\overline{M}_n$ of the valve seat in question that gave the large deflection (Figure 9) was 614,000 g mol^{-1}, which is only slightly less than the 656,000 g mol^{-1} value measured for the starting bar stock (Table 1).

Conclusions

The effect of processing and machining on the properties of polychlorotrifluoroethylene (PCTFE) rod stock and oxygen gas cylinder valve seats was determined. Testing focused on two types of extruded rod stock and one type of compression-molded rod stock. Conclusions may be summarized as follows:

- DSC gave evidence of possible MWD differences between emulsion-polymerized Kel-F 81 and suspension-polymerized Neoflon M400H, which may in turn have important property ramifications.
- Processing led to significant increases in the heat of fusion and crystallization, accompanied by parallel drops in the ZST and number average molecular weight.
- The properties of PCTFE rod stock varied significantly depending on the molding process (extrusion vs. compression-molding) and molding conditions used (Molder 1 versus 2).
- Annealing may compensate for the adverse effects of molecular weight degradation caused by non-optimized processing.
- Although good correlation was obtained between ZST and intrinsic viscosity data, ZST does not appear to be very sensitive to molecular weights above a $\overline{M}_n$ -threshold of approximately 600,000 g mol^{-1}.
- TMA data for valve seat and valve seats diverged. The reasons for this divergence could be property variation within a given rod, machining differences, or 'skin-core' morphology and choice of sampling location.

- TMA valve seat data tended to be grouped by seat manufacturer, suggesting dimensional stability was affected by machining process differences.
- Sample translucency appears to be related dimensional stability.

Acknowledgments

The authors are indebted to P. Spencer (WSTF) and B. Wolle (WSTF) for mechanical properties evaluations, B. Greene (WSTF) and D. Mast (WSTF) for DSC work, Anna De Armond (WSTF) for help with intrinsic viscosity measurements, and R. Frentz (Afton Plastics) for providing the ZST data.

References

[1] Waller, J. M., Newton, B. E., Haas, J. P., Beeson, H. D., "Comparison of the Dimensional Stability of Kel-F 81 and Neoflon CTFE M400H Polychlorotrifluoroethylenes used in Valve Seat Applications," *Flammability and Sensitivity of Materials in Oxygen-Enriched Atmospheres: Eighth Volume, ASTM STP 1395*, T. A. Steinberg, H. Barthelemy, Beeson, H. D., Newton, B. E., Eds., American Society for Testing and Materials, West Conshohocken, PA, 2000.

[2] Hoffman, J. D., Weeks, J. J., "The Specific Volume and Degree of Crystallinity of Polychlorotrifluoroethylene," *J. Polymer Sci.,* 1958, 28(117), 472-475.

[3] Walsh, E. K., Kaufman, H. S., "Intrinsic Viscosity-Molecular Weight Relationship for Polychlorotrifluoroethylene," *J. Polymer Sci.,* 1957, 26, 1-7.

[4] Flory, P. J., "Copolymerization, Emulsion Polymerization, and Ionic Polymerization," *Principles of Polymer Chemistry*, Cornell University Press, Ithaca, NY, Chapter V, 1986.

[5] Odian, G., "Emulsion Polymerization," *Principles of Polymerization,* 2nd Edition, John Wiley and Sons, New York, NY, Chapter 4, 1981.

[6] Lin, G. private communication, Daikin America, Inc., April 2002.

[7] Chandrasekaran, S., "Chlorotrifluoroethylene Polymers," *Encyclopedia of Polymer Science and Engineering,* 2nd Edition, Kroschwitz, J. I., Editor-in-Chief, John Wiley and Sons, New York, NY, Vol. 3, 473, 1990.

[8] Shalaby, S. W., "Thermoplastic Polymers," *Thermal Characterization of Polymeric Materials*, Chapter 3, Turi, E. A., Ed., Academic Press, Inc., 1981.

[9] Waller, J. M., Haas, J. P., Beeson, H. D., "Polymer-Oxygen Compatibility Testing: Effect of Oxygen Aging on Ignition and Combustion Properties," *Flammability and Sensitivity of Materials in Oxygen-Enriched Atmospheres: Ninth Volume, ASTM STP 1395*, T. A. Steinberg, H. D. Beeson, B. E. Newton, Eds., American Society for Testing and Materials, West Conshohocken, PA, 2000.

[10] *Tecaflon PCTFE, Technical Data Sheet*, Ensinger GbbH & Co., Rudolf-Diessel Str. 8, Nufringen, Germany, 2000.

CRYOGENIC TEMPERATURE EFFECTS ON PERFORMANCE OF POLYMER COMPOSITES

David Hui* and P.K. Dutta**

October 2002

* Dept of Mechanical Engineering, University of New Orleans, New Orleans, LA 70148
** U S Army Engineer Research and Development Center, CRREL, Hanover NH 03755

1. INTRODUCTION

The objective of this study is to evaluate the low temperature behavior of polymer composites down to the cryogenic temperature range. This would be accomplished by study of its behavior in several ways. First we would study the microfracture growth by observing the acoustic emission as the temperature is lowered. We would also note any damage growth by ultrasonic velocity testing applying the pulse echo method. Effects of such low temperature would then be studied by examining the shear properties by the short beam shear test, and also the fracture toughness properties over a wide range of strain rate and temperature. At present these studies are continuing. The limited data obtained from these studies are reported in this report.

2. BACKGROUND

In near future the lightweight composites will be used in the NASA re-entry vehicles. The structural systems of such re-entry vehicles must withstand rapid loading, vibration, high acceleration at take off from launching platforms in most severe environments, while internally containing liquid oxygen and hydrogen at cryogenic temperatures. Polymer composites, a multiphase material will be subjected to extremely high differential stresses within the phase components itself. In the past, careful manufacturing condition under controlled pressure and temperature in the autoclave systems provided reasonably satisfactory control of development of micro cracks during curing and subsequent applications in severe temperatures. In the new low cost, high volume manufacturing process, called the VARTM (Vacuum Assisted Resin Transfer Molding) process, control of the development of residual stress induced micro fracture will be extremely difficult. Research is needed to characterize such microstructures, monitor development and progression of the micro cracks under cryogenic temperature and service conditions, and finally assess the influence of such fracture growths on the performance of such structures by fracture mechanics studies. The current research program address some of these issues.

2.1 Failure modes

The primary concern for composites being used in the new generation of the re-entry vehicles is not only premature failure, but that they must not leak excessively even after multiple launches. Composites in space applications, whether used as rocket shell, satellite structures, or sensor platforms involve extremely high temperature and load variation at extremely high rates not only on its surface, but also through the thickness. Thick-section composites typically fail at stresses and strains that are well below the expected failure limits. Delamination is a common mode of failure. When cold, they fail with very small amount of strain, with more violence and high-energy release. This early failure is often attributed to the existence of critically sized processing and/or material defects and interfacial problems in the interphase region between the matrix and the reinforcing phase (Drzal 1983, 1986; Sottos 1990; Palmese 1992; Skourlis

1995; Hrivnak 1996; Harik 1997; VanLandingham 1997; Fink and McCullough 1999). Evaluation of interphasial mechanical properties has been carried out experimentally (Sottos 1990; VanLandingham 1997) and theoretically (Palmese 1992; Chu and Rokhlin 1996). The extent of the interphase region in composites is significant (Hughes 1991). For instance, a 1 cm^3 of a composite when filled with a fiber volume content of 60% contains as many as 3 million single filaments. The total area of the fiber surface is 3,400 cm^2. As a result, the matrix and its ability to adhere to a fiber are paramount to the effective transfer of the mechanical load in the composite (Erikson and Plueddemann 1974; Drza11983, 1986; Fishman 1991; Piggott 1991). The large surface area plays a direct role in the load transfer from the matrix to the reinforcing constituent. The way the interphase interacts with the matrix and with the fibers is quite important in determining damage initiation in composite materials and its ability to maintain sufficient impermeability to liquids and gases.

2.2 Strain-rate Effect and Microsturctural Failure

Micro structural study by Dutta et al (2000) of Gr/Ep composite fragments at CRREL, Hanover, NH and at the Air Force Wright Laboratory, Dayton, Ohio, has clearly shown that both temperature and the rate of loading significantly influence the interphase stress transfer mechanisms and final fracture that can influence the permeability as well as reliability in the performance of multiple launch. Reinforcing fibers and particles themselves may serve as stress raisers and lead to interfacial cracking (Eshelby 1957). Fiber-matrix debonding and cracks may significantly reduce the load transfer between matrix and the fibers and cause cracking in composites (Sottos, Li, and Agrawal 1994; Budiansky, Hutchinson, and Slutsky 1995). Interfacial damage (Keer, Dundurs, and Kiattikomol 1973; Hashin 1991; Pan, Green, and Hellman 1996) or material inhomogeneity of interphases also affects the elastic properties of composites (Jasiuk and Kouider 1993; Lagache et al. 1994; Low et al. 1995; Theocaris and Demakos 1995; Lutz and Zirnmennan 1996), the residual stresses (Jayaraman and Reifsnider 1993), and their macroscopic behavior (Tsai, Arocho, and Gause 1990; Kharik 1997; Kim and Mai 1991, 1998).

2.3 Residual Stress of Low-Temperature

Manufacturing of composites involves the use of a thermosetting polymeric material as the matrix phase. The polymeric matrix in the presence of a catalyst, heat, and pressure solidify through an irreversible exothermic chemical reaction (cure). Before curing, the polymer phase is a viscous fluid. It flows under pressure. As a result of curing, the polymer forms a covalently bonded three-dimensional molecular network with increasing viscosity and gel formation. The flow ceases at this stage but reactions continue to form a tightly cross-linked structure with characteristics of glassy solid (Rosen, 1993). The problem in composite cure is the problem of controlling the reaction exotherm and heat transfer so that uniform cure and minimum residual stresses are achieved (Bogetti et al. 1992). During the curing stage as the chemical reactions proceed residual stresses are developed with progressive changes in modulus and thermal expansion coefficients, and volume shrinkage of the resin. At the microstructural level

influence of low temperature on the induced stresses at the matrix/fiber interfaces, within the matrix, and in the interlaminar layers has been analyzed and experimentally investigated by many authors (Jones 1975, Lord and Dutta 1988, Dutta1988, Dutta and Lampo 1993). These results have shown that a difference between the curing temperature and the operating temperature may be as large as 200°C (392°F) in ususal cold environment, and the residual stresses may be sufficiently large to cause microcracking within the matrix and matrix/fiber interfaces. The computation of residual stresses using the Tsai and Hahn method (19) for unidirectional composites in longitudinal direction as:

$$\sigma_{mL} = (V_f E_f E_m)(\alpha_f - \alpha_m)(T - T_0)/(V_f E_f + V_m E_m) \qquad (1)$$

shows that at the cryogenic temperature of -180°C the matrix stresses could be as high as 12000 psi. Thus, the large residual stresses induced at lower temperatures become potentially damaging for polymer matrix composites with curing temperature environment. The damage may begin with the formation of microscopic cracks in the matrix or at the fiber/matrix interface. When these cracks develop to a certain density and size, they will tend to coalesce to form macroscopic matrix cracks (Wang, 1986). Transverse matrix cracking in composites affect stiffness, strength, dimensional stability, and fatigue resistance.

2.4 Fracture Toughness of Fiber/Matrix Interphase

An understanding of the failure process at the interphase at the cryogenic temperatures is essential to develop optimal performance capability at those temperatures. For this, one must closely examine the polymer matrix and its interaction with the interfacial surfaces (Wool 1995; Hrivnak 1996),). Many studies, as reviewed by Cantwell and Morton (1991), have concluded that composites are particularly susceptible to damage by delamination, which is particularly dangerous because it is often not visible from surface. The composites property measured in the fracture mechanics study of the resistance to delamination is the critical energy release rate, or fracture toughness, which is a measure of the energy consumed during the creation of unit area of fracture surface during delamination. Three modes of crack loading can occur, namely mode I (tensile opening), modeII (in-plane shear) and mode III (out-of-plane shear). In practice, modes I and II and combinations of mode I and II are the most important.

Test methods for measuring the interlaminar fracture toughness (K_C) at slow rate in mode I, II and mixed I/II are well established and several standards exist for mode I (ASTM D5528, ASTM E399, ISO CD 15024 version 97-02-24, and JIS K 7086 of 1993). Various test methods are currently being pursued for the other modes. However, currently no appropriate high rate-loading test, especially under cryogenic conditions exists, and all previous attempts to extend the slow speed test methods to high rates have met with significant obstacles (Blackman and Williams 1998). The first obstacle is in experimental test equipment to be capable of rapidly accelerating the test specimen

and then accurately recording the forces applied and the deformation occurred. Second, the dynamic effects are invariably induced at the high rate tests and it is critical that these effects are carefully considered, and accurately accounted for, if accurate and valid K_C values are to be measured. Indeed, this probably accounts for the conflicting nature of some of the test results reported in the literature. For example, Smiley and Pipes (1987) pointed to very large reductions in the values of K_{IC} of K_{IIC} for brittle epoxy as well as for thermoplastic polyether etherketone (PEEK) composites, as the test rate was increased from a few mm/min to about 1m/s. On the other hand, Beguelin et al (1991) reported mode I results of a PEEK matrix carbon composites only a small reduction in the value of K_{IC} as the test rate was similarly increased. In a third study by Aliyu and Daniel (1985) on similar materials, increasing followed by decreasing values of K_{IC} was reported as the test rate was increased. The differences in experimental results reported were further highlighted in a recent review by Cantwell and Blyton (1998). Their review indicated that the rate sensitivity of the composites was dominated by the toughness of the matrix, with brittle matrix composites exhibiting much less of a rate effect than tough matrix composites.

3. EXPERIMENTAL STUDY

We have undertaken the experimental study to determine how the composites behavior change as we approach the cryogenic temperature range by performing five series of tests: (1) Shear response at cryogenic temperatures, (2) Microfracture growth monitoring by acoustic emission as the temperatures are reduced, (3) Modulus degradation evaluation by ultrasonic wave transmission (pulse-echo) method, (4) Shear property degradation by short beam shear property evaluation, and by (5) fracture properties over a wide strain rate and temperatures.

3.1 Shear Response at Cryogenic Temperatures

These tests were performed to study the effects of temperature on the interlaminar shear resistance. The range of temperature was varied from -100^0C to 80^0C. The results showed a drastic reduction of interlaminar shear strength with the temperature rise from 50^0C to 80^0C.However the increase in the shear strength with decreasing temperature is more gradual. The test specimens were prepared from a pultruded glass fiber reinforced composite square bar of 0.5 in. × 0.5 in. section. From this stock the specimens were machined with the fibers oriented in longitudinal direction. The rectangular specimens had a dimension of 1.5 in × 0.5 in × 0.25 in. Figure 1 shows a typical specimen. These specimens were then tested for interlaminar shear strength using the ASTM D2344-84 (The ASTM standard D2344-84 specifies the span to thickness ratio of 5. In our case the ratio is 3.26.

3.1.1 Testing

The tests were performed in an environment chamber which could be cooled with liquid nitrogen, or heated by a heating coil. The cooling system involves a supply of liquid nitrogen from the commercially available liquid nitrogen tank through a control valve which releases the evaporated liquid nitrogen into the environment chamber. A feedback loop of temperature sensed by a thermocouple controls the release of liquid nitrogen so that the temperature inside the chamber is maintained steady within +/- 1 ^{0}C.

The chamber could also be heated to a higher temperature by the heating coil mounted inside the test chamber. Figure 2 shows the test chamber with the heating coil. Again a feed back loop control using the thermocouple controls the temperature of the chamber.

For testing at temperatures other than the room temperature the specimens were soaked at that temperature for a minimum of 45 minutes. The short beam shear test was performed in a MTS machine using the Wyoming test fixture for three point bending.

3.1.2 Test Results

Table-1 shows the results of the test. Figure 3 shows the variation of the shear strength with temperature. Figure 4 shows the force displacement curves at different temperatures. Figure 5 shows the displacement at peak load at different temperatures.

3.1.3 Discussion

From Figure 3 we see that there is a drastic decrease of shear strength with increasing temperature from 23^{0}C to 80^{0}C.Possibly the higher temperature softened the matrix of the composite. From 23^{0}C to -100^{0}C we observe that the shear strength increases linearly. However this increase is more gradual. The increase in strength with temperature reduction can be modeled by the following equation:

$$S_H = -15.7494\,T + 8935.36 \qquad (2)$$

Where S_H = Shear Strength (psi), T = Temperature (°C)

Figure 4 gives the force-displacement curves. Figure 5 shows that the displacements at peak load decreases with decreasing temperature. Also the peaks are not sharp at higher temperatures (Figure 4). The sharp peaks at lower temperature denote brittleness of the material. We conclude that (1) Shear Strength decreases drastically with increasing temperature. (2) At low temperatures shear strength increases almost linearly. (3) The material becomes more brittle at lower temperatures as seen by reduced deflection and sharp peaks.

Table 1. Temperature effect on Shear Strength in Quasi Isotropic test

Temp. (°C)	No. of Samples	Shear Strength S_H (psi)	Displ. at peak load (in)	Standard Deviation

- 100	6	10510.8	0.020	349.7
- 5	6	9014.6	0.021	365.9
23	6	8309.8	0.022	288.0
50	6	4926.2	0.031	195.0
80	6	2721.8	0.051	96.2

Figure 1 The view of interlaminar shear test specimen

Figure 2 The test chamber with the heating coil

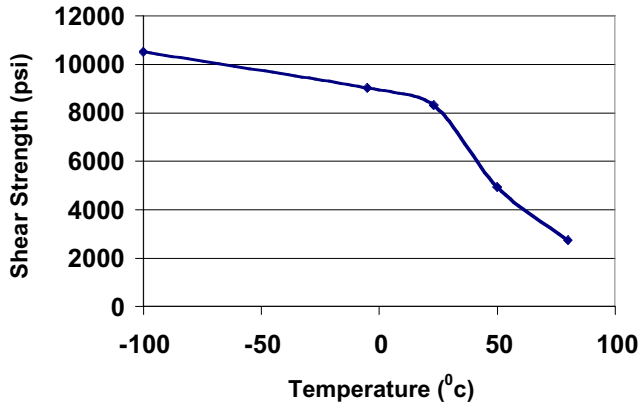

Figure 3. Variation of the shear strength with temperature

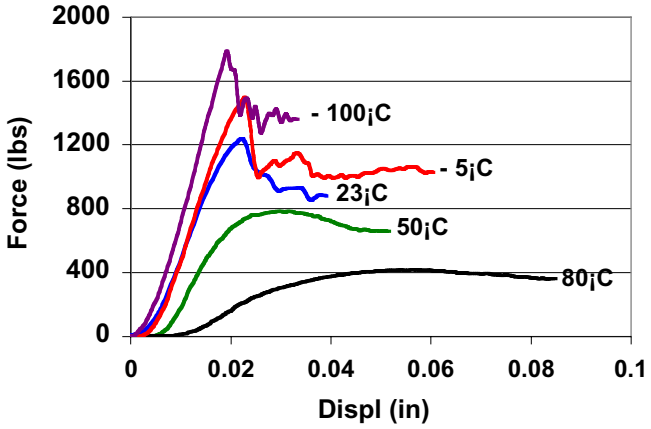

Figure 4 Force vs displacement at different temperatures

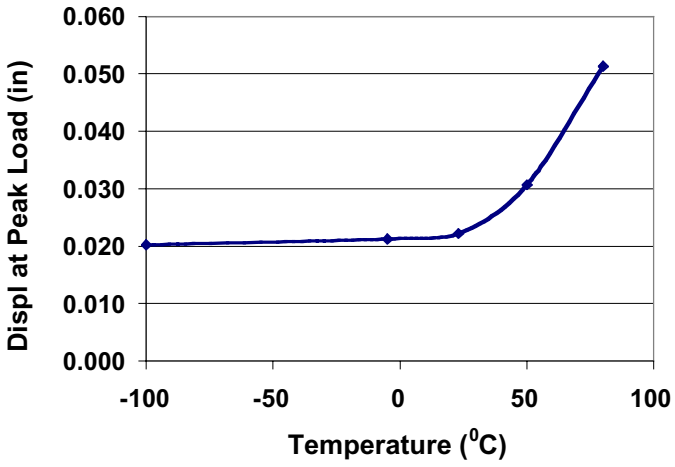

Figure 5 Variation of displacement at peak load with temperature

4. CRYOGENIC FRACTURE TOUGHNESS

The plain strain fracture toughness is the stress concentration at the crack tip under conditions of plane strain, and is regarded as the basic material property. The fracture toughness was determined by applying bending load to the notched specimens as shown in Figure 6.

4.1 Specimen Dimensions

The material of test specimen is a commercial pultruded composite product, which uses E-glass fiber and isophthalic polyester resin. The details of the test material are given in Table 2 and Figure 7.

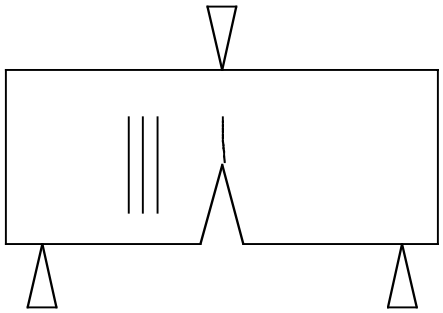

Figure 6 Test configurations for the Fracture Toughness Test

Table 2 The specification of test material

E-glass FRP composite
Used Process: Pultrusion method
Reinforcing Fiber: E-glass
Matrix: Polyester
Density: 0.071 lb/in^3 (0.971 g/cm^3)
Volume Fraction of Fiber: 0.593
Notch angle: 90 degree
Dimensions: -
Length: 1.511in (38.38mm)
Width: 0.494in (12.55mm)
Thickness: 0.521in (13.23mm)

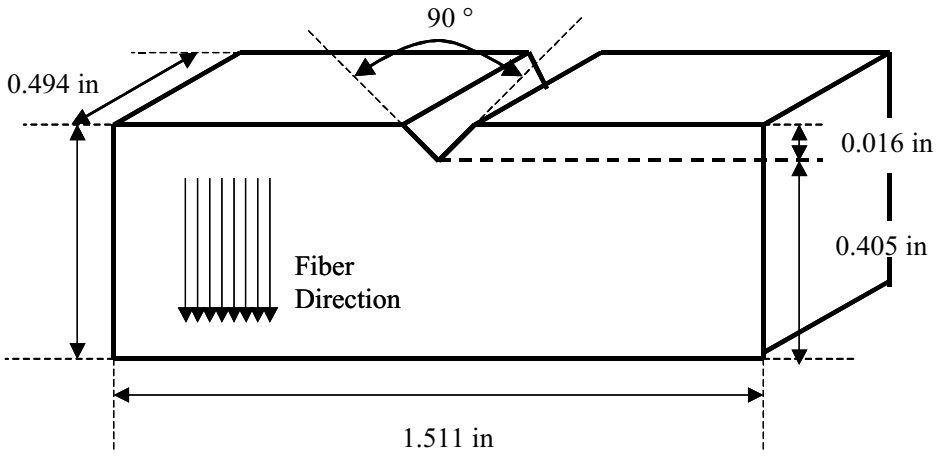

Figure 7 Schematic of the composite test specimen

4.2 TESTING

The speciemens were tested both quasi statically and dynamically using the ASTM D70 three point-bending test.

4.2.1 Quasi-static Tests

Quasi-static tests were performed on the glass fiber specimen of 90-degree fiber orientation at room temperature (23 C) and at low temperature (-30C) with a servo controlled hydraulic testing machine driving the loading platen at a speed of 0.01 inch/min. An environmental chamber was used for all low temperature tests. The chamber was cooled with chilled nitrogen gas slowly vented through a regulating valve controlled by a temperature sensor near the test specimen. Tests were performed only when a stable temperature was established for about 15 minutes within the chamber. Load and displacement were recorded using the load cell and the LVDT transducer attached to the testing systems and the data were automatically transferred to the same digital data acquisition system.

4.2.2 Dynamic Test

4.2.2.1 Experimental Approach

We performed a study of the interlaminar Mode I fracture toughness, K_{IC}, of unidirectional composites at room and cryogenic temperatures using a modification of Split Hopkinson Compression Bar Apparatus (SHBA). By using SHBA we had overcome the difficulties encountered by the researchers in measuring loads and deformation while using the traditional servo hydraulic machines at rate above 1m/s. SHBA would allow a rate up to 100m/s. The past researchers did not take into account the problems of low temperatures associated with high rate loading.

Our approach to measure the cryogenic high-strain-rate fracture toughness for composites is new and unique. The details of the proposed system, a preliminary model of which has already been developed, is shown in Figure 8(a) and 8(b). The typical stress waves used for computation of the force-displacement curves are shown in Figure 8(c). As shown in this Figure, we modified the SHBA interface to represent a three-point loading system of a single notch prismatic composite sample, which is mounted in between the two interfaces of the SHBA. The intact and the fracture samples are shown in Figure 9. Figure 10 shows the sample in the SHBA set up, and Figure 11, the cryogenic cooling with liquid nitrogen. The entire fracturing process would be performed in a cryogenic chamber built around the SHBA interfacial impact zone. We plan to measure the crack opening force and the corresponding displacements exactly the same way as we do in a standard Hopkinson Bar by integrating the incident, reflected and transmitted strain waves in each bar (Dutta 1987). The system will allow K_{IC}. to be measured with samples in which fiber orientation is parallel to the notch axis.

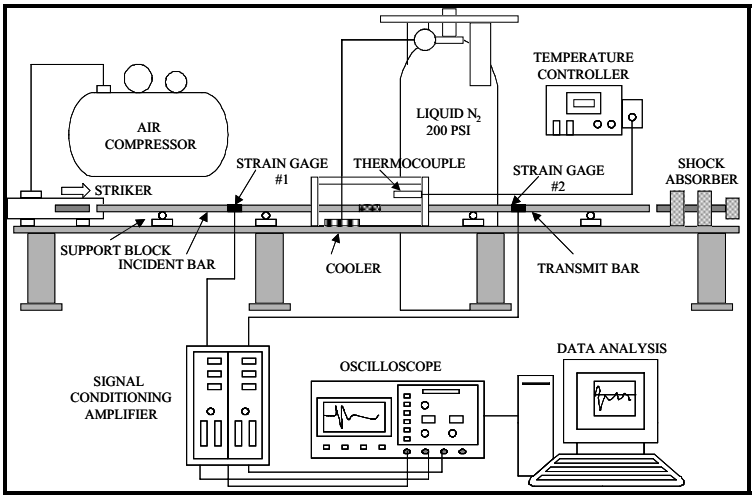

(a) Split Hopkinson pressure bar system schematic

(b) CRREL Split Hopkinson Bar apparatus

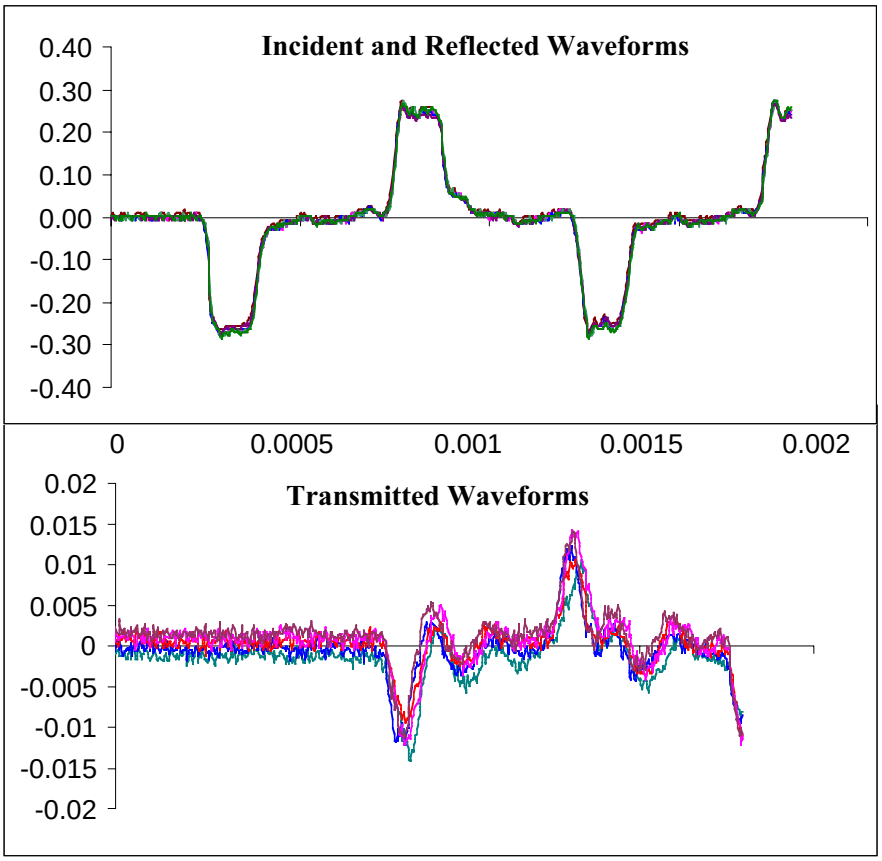

(c) Incident and Reflected Waveforms for five tests

Figure 8. The Cryogenic SHBA experiment

4.2.2.2 Analytical approach

For a specimen in three point loading (Figure 3), K_{IC} is calculated using the expression of Brown and Strawley (1966),

$$K_{IC} = \frac{6M}{Bd}\sqrt{a}F(a/d)\cdots\cdots$$

$$M = Pl/2$$

where $F(a/d)$ is the finite width correction factor given by $F(a/d) = 1.99 - 2.47(a/d) + 12.97(a/d)^2 - 23.17\,(a/d)^3 + 24.80(a/d)^4$

where a = crack length, d = specimen depth, M = ultimate bending moment, P = applied load, l = shear span, and B = specimen width.

4.2.3 RESULTS AND DISCUSSION

Quasi static test at room temperature gave the K_{IC} value of 6.9 ksi√in. The batches for dynamic test of the notched samples (Figure 9(a)) were tested at different temperatures. A representative specimens which failed under the dynamic tests is as shown in Figure 9(b).

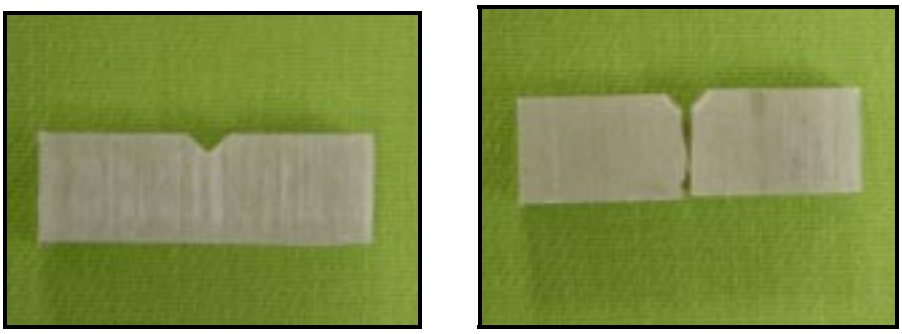

(a) Sample before test *(b) Sample after test*

Figure 9 GFRP samples before and after dynamic test

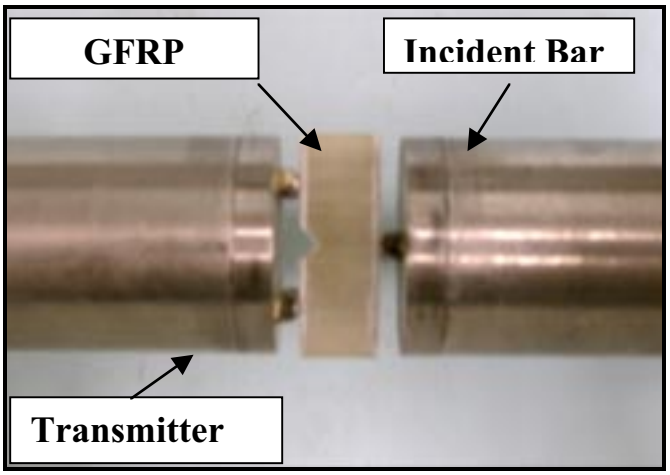

Figure 10 Loading position of the specimen

Figure 11. The chamber used to keep the test specimen cold

It is clear that there are multiple cracks along the fracture path in the test specimens. No significant differences in the crack patterns were observed between high temperature and low temperature fracturing. The force-displacement characteristics and then the energy absorbed to develop the crack were determined. The absorbed energy versus time plot at different temperatures are shown in figure 12.

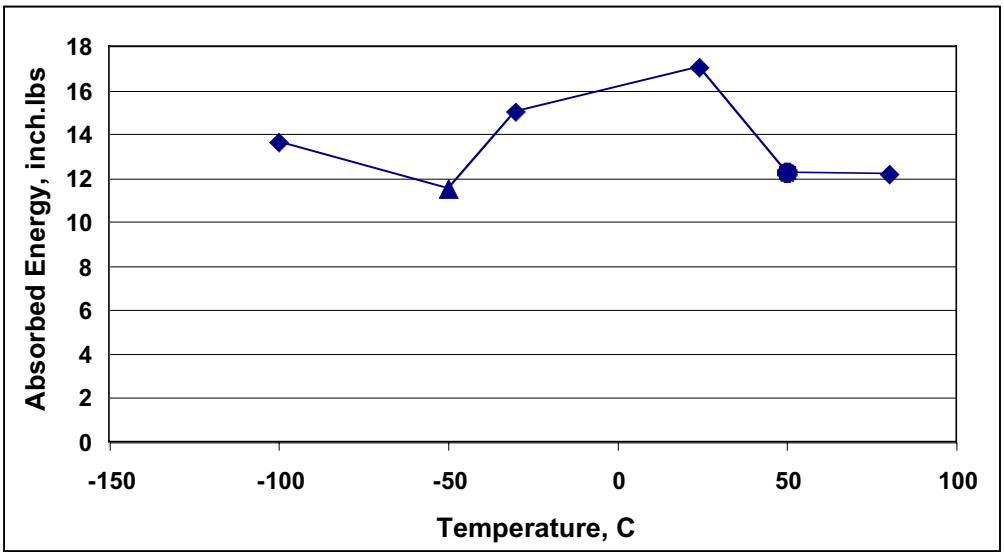

Figure 12. Average energy absorbed at different temperatures

From Figure 12 we observe that the energy absorbed within the system is higher at –30 C and room temperature as compared to –50 C and 80 C.

The force-displacement curve showed a dramatic increase in stiffness and brittleness of both specimens in dynamic fracturing**.** The displacement at the peak force was assumed as the fracture initiation point. Because of the visco-elastic nature of the composite matrix, we do not always find any sharp failure point. At this point, there is considerable amount of scatter for the peak force. This is expected in Extren, which is a pultruded composite in which fiber volume percentage is low and many resin-rich areas occur. The peak force was used to calculate the fracture toughness, K_{IC}. The calculated values of K_{IC} are summarized in Table 3 and plotted in Figure 13.

Table 3: Summary of result of fracture toughness

Temperature (˚C)	Avg. Maximum Energy (inch. lbs)	Avg. Maximum Displacement (in.)	Avg. Maximum Force (lbs)	Avg. Fracture Toughness (Ksi.√in)
80	20.29	0.01259	1321.0	6.114
50	12.38	0.01217	1398.7	6.000
24	19.82	0.00630	1359.7	6.900
-30	14.03	0.01349	1126.6	5.307
-50	11.82	0.00821	893.4	5.146
-100	13.61	0.00515	1476.4	4.381
-150		0.00561	1262.5	3.746

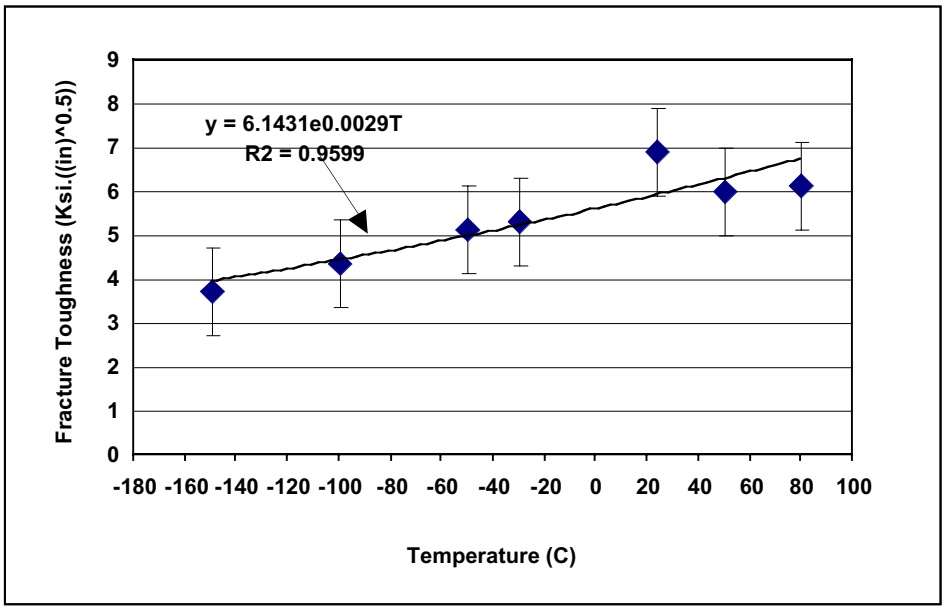

Figure 13 Fracture Toughness at different Temperatures

The K_{IC} values were plotted against the test temperatures. It is seen from the graph that fracture toughness varies with temperature. K_{IC} increase with increase in temperatures. As

stated before, many factors contribute into the value of K_{IC} for a given material. The strain rate data is summarized in the Table 4.

Table 4 Strain rate at different temperatures.

Temperature (˚C)	Avg. Maximum Force (lbs)	Strain	Strain Rate (Strain/sec)
80	1320.9	3591.75	49.885
50	1398.6	3803.03	52.819
24	1359.6	3696.94	51.346
-30	1126.6	3063.24	42.545
-50	893.4	2429.15	33.738
-100	1476.3	4014.31	55.754
-150	**1262.5**	**3432.73**	**47.676**

It is concluded that the low temperature reduces the fracture toughness of the compsites. However fracture toughness increase with increase in temperature with the average strain rate of 40 ~ 50strain/sec. The strain rate was calculated by assuming that the maximum force reached the value at approximately 72 microseconds. The maximum value of force was considered applied to load a bending. Low temperature influence the energy absorption characteristics of the GFRP, i.e. it absorbs less energy at low temperatures as compared to high temperatures. After the fracture of the specimen, multiple cracks were observed along the fracture path but it was found that there is no significant difference in crack pattern between low and high temperatures.

5. Acoustic Emission Study

We hypothesized that the growth of microcracks in composite are likely to happen when the temperature is lowered to the cryogenic range.

5.1 Procedure for Acoustic Emission test

The procedure for the acoustic emission test is described below.

A 50-ply carbon test sample of size 4”length, 0.75”width and 0.25” thickness is taken and a transducer is placed on the sample. Vacuum grease is used as a fluid between the sample and the transducer to ensure the proper transformation of signals from sample to transducer. The transducer is then clamped tightly (Figure 14) with sample so that it does not move during the test. A thermocouple is clamped with specimen to note the

temperature of sample. The thermocouple is connected to a datalogger, which reads the temperature of specimen for every 2 or 4 sec and sends the data to a computer. The software used for this is called CAMPBELL SCIENTIFIC software.

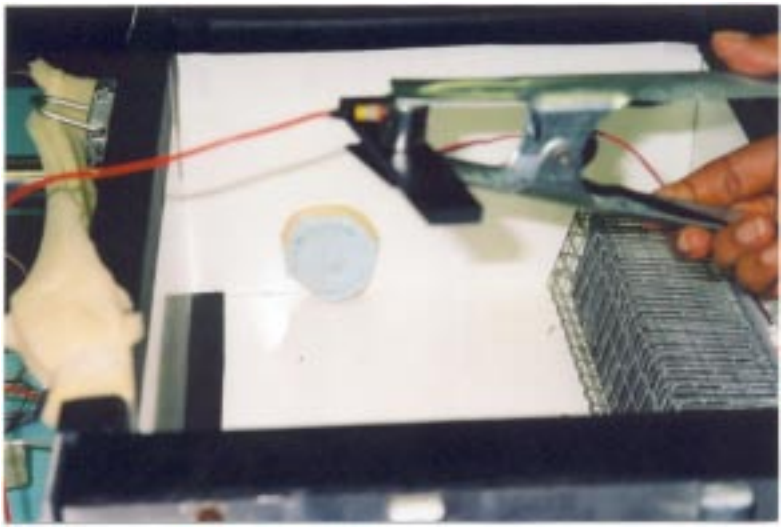

Figure 14 Clamping of the transducer for acoustic emission test

The specimen is kept in a test chamber which was cooled by liquid nitrogen The transducer collects the data of the time and accumulated events whenever an event occurs on the specimen.(i.e. when ever the specimen has micro cracks).

The software used to record the events data is MISTRAS software of PHYSICAL ACOUSTIC EMISSIONS CORP. The sample is subjected from room temperature to low temperatures (23,-5,-50,-100, and -150C) and kept at each of these temperatures for approximately 10 minutes, then the temperature was raised from –150C to room temperature. The data of time,events and temperature is recorded throughout.

Graphs were plotted between the time vs temperature and time vs accumulated events (Figure 15). We observe that the rate of events increases from room to low temperatures but from -150C to room temperature, the rate of increase of events is very low. This indicates that the cracks produced were high during the first half of the test and less during the second half of the test.

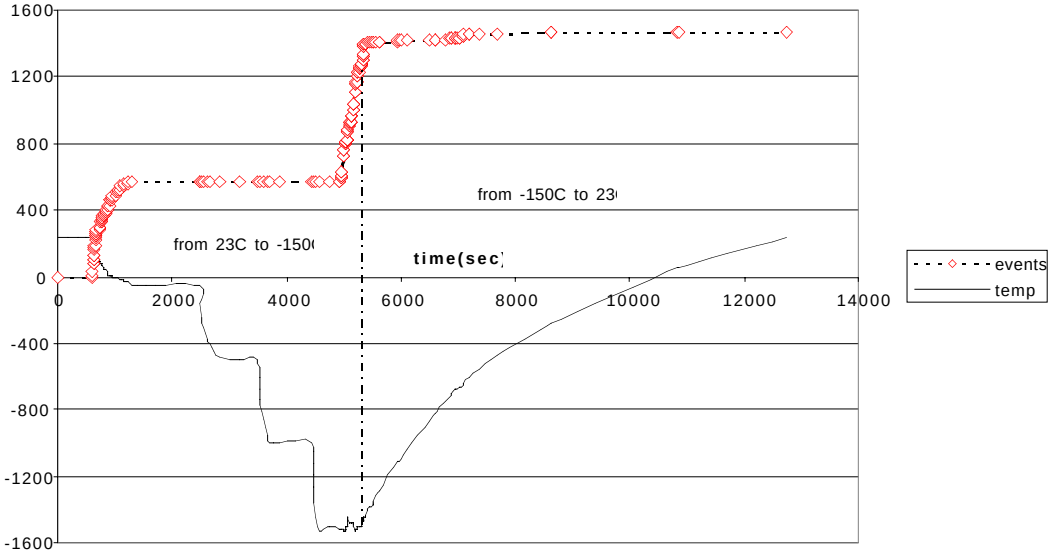

Figure 15 Increase in acoustic events with temperature

5.2 Results

Maximum no. of events counted for each sample is given in Table 5.

Table 5 Maximum no. of acoustic emission events

Samples	Temp (°C)	Max no. of events on lowering of temperature	Max no. of events on warming to room temp
1	-161	1492	---
2	-154	1930	33
3	-150	1280	186
4	-150	3789	82
5	-150	3495	249

6. Ultrasonic test evaluation at cryogenic temperature

6.1 Liquid nitrogen immersion test

In the first series of tests composites samples were immersed in liquid nitrogen (Temperature, – 196 C) for different durations. The samples, immediately (within 5 to 10 seconds) after removal from the liq Nitrogen bath were tested for determining the ultrasonic velocities (Figure 16(a)). Figure 16(b) shows the velocity measurement by the ultrasonic technique. The same samples were again tested for velocities when they achieved the room temperature after a day. Table 6 shows the immersion times vs velocity and Young's modulus. The results are also shown graphically in Figure 17. Figure 18 and 19 shows the Young's modulus of each speciemen.

Table 6 Immersion and rapid test data

Temperature (°C)	Immersed Time (min)	Velocity at cryogenic temp immediately after removing from Liq Nitrogen (m/s)	Velocity at room temperature long after removing from Liq Nitrogen (m/s
	60	2559	2248
	45	2559	2255
	30	2559	2294
Cryogenic (-190)	15	2511	2306
	5	2464	2368
Room (24C)	None	2376	2376

(a) Ultrasonic testing machine

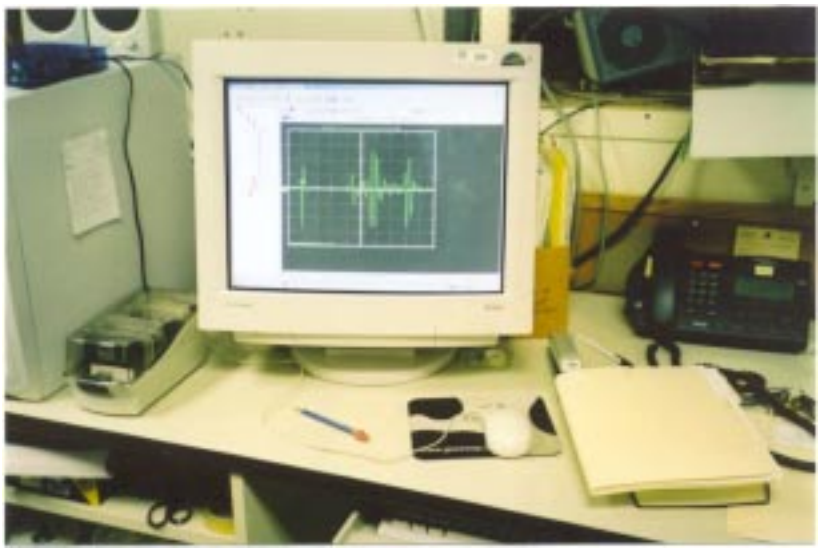

(b) pulse-eco signals in the ultrasonic testing

Figure 16 Ultrasonic testing technique

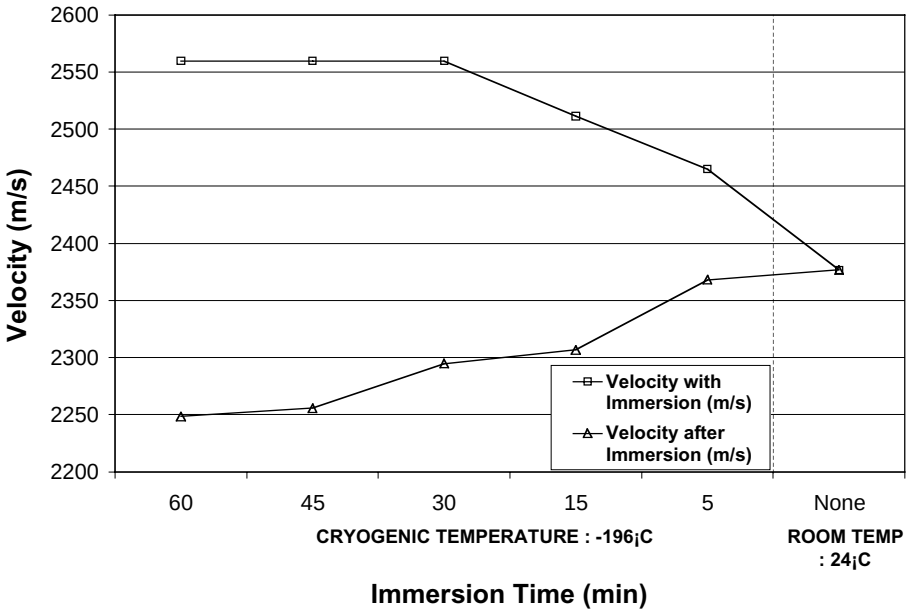

Figure 17 Change of velocities with different immersion times in Liq Nitrogen. The point at right shows the room temperature velocity data.

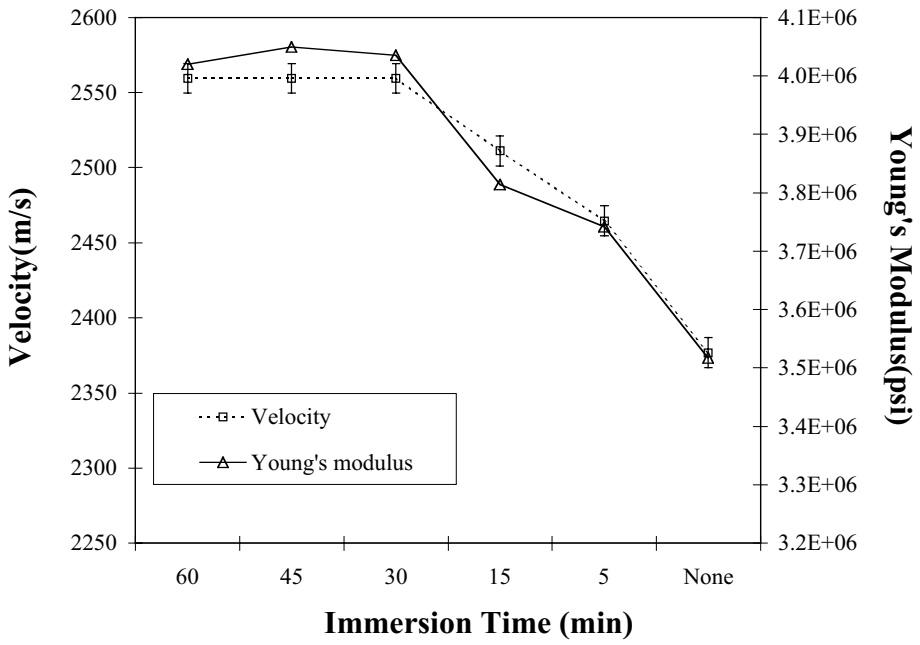

Figure 18 The Young's modulus of CFRP specimens just after the immersion test

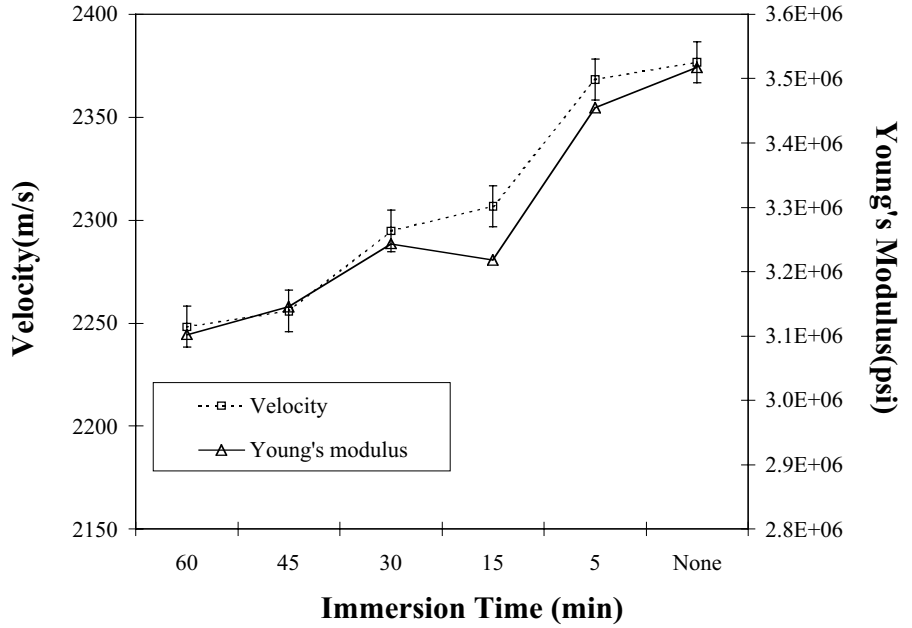

Figure 19 The Young's modulus of CFRP specimens that kept it at room temperature for 2 days after the immersion test

6.2 Room and Liquid Nitrogen Comparison Test

In the second series of tests one composite sample was first tested for the velocities at room temperature. And then the sample was immersed in liquid nitrogen, and kept immersed for one hour. Then the sample was taken out and tested for acoustic emission till the specimen achieved room temperature. The specimen was again tested for velocity. Figure 20 shows the acoustic emission results. Figure 21 shows the results of the velocity and Young's modulus of CFRP sample after immersion test.

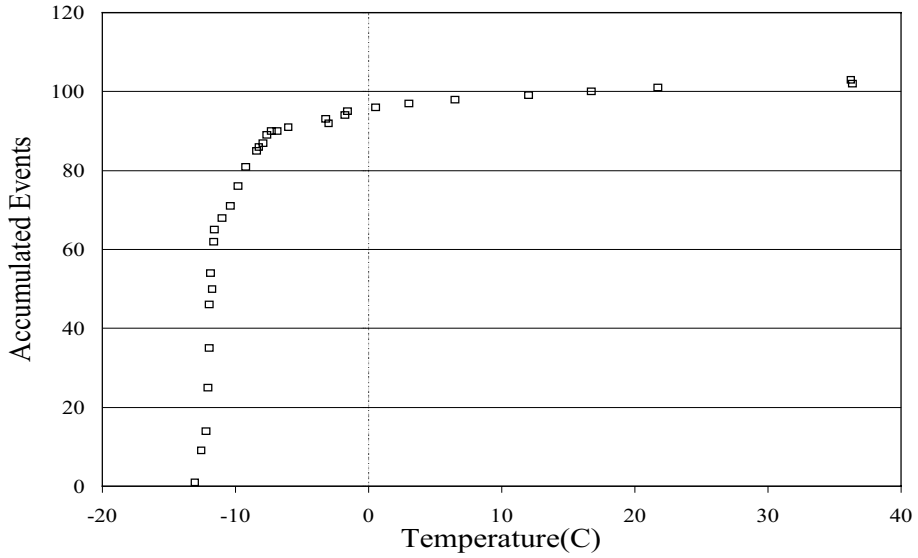

Figure 20 The acoustic emission results

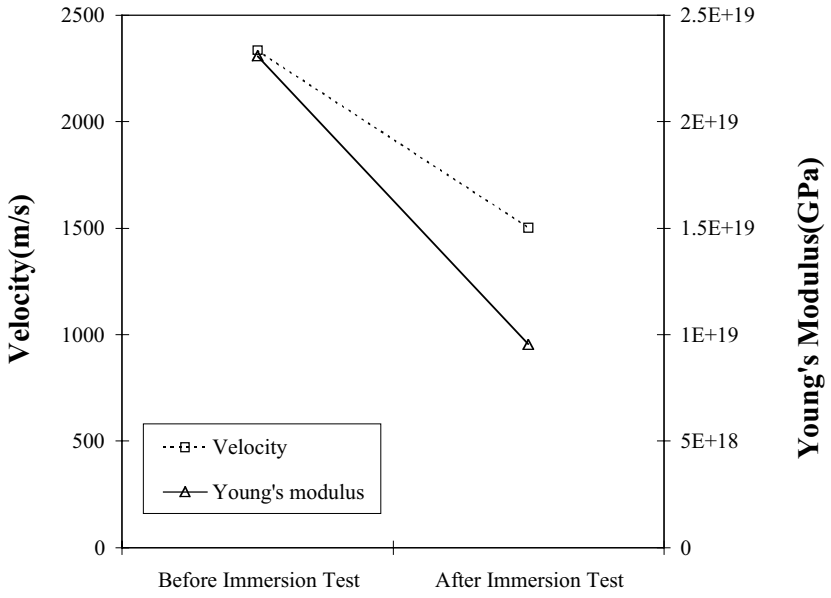

Figure 21 The results of velocity and Young's modulus after immersion test

6.3 Ultrasonic evaluation of cryogenically exposed samples

In this series of tests ultrasonic velocities were determined for all samples, which were subjected to the acoustic emission tests. The results are given in Table 7. Note that there is asmall change in the velocities after exposure to the liquid nitrogen, which can account for the microcrack generated emissions from the composites when cooled.

Table 7 Velocities after the exposure to cryogenic temperatures

Sample #	Velocity (m/sec)
1	2713
2	2721
3	2721
4	2713
5	2713
Average	2716

Note that before immersion, the room temp velocity was 2737 m/sec (average of 3 samples). The average velocity after the exposure was 2716, a reduction of 21 m/sec for the damage growth.

7. CONCLUSIONS

Cryogenic exposure of graphite epoxy and other composites show that residual stresses at the fiber matrix boundary and at the interlaminar zone increase significantly. The increase may be sufficient to develop microcracks, which can be monitored by acoustic emission. Degradation of interlaminar shear strength is not sufficient, rather the low temperature increased the strengths. However, the fracture toughness decreased with lowering of temperatures. The degradation was also noticed by decrease in ultrasonic velocities.

The results presented here are mostly preliminary. As the testing are going on, more data are expected and characterization at the cryogenic temperatures will be more certain.

7. ACKNOWLEDGMENT

This research was supported by the National Aeronautics and Space Administration George C. Marshall Space Flight Center through Grant/Cooperative Agreement Number NCC8-223 for the National Center for Advanced Manufacturing - Louisiana Partnership.

Any opinions, findings, and conclusions or recommendations expressed in this material are those of the author(s) and do not necessarily reflect the views of the National Aeronautics and Space Administration.

8. REFERENCES

1. Brown, W. F. (1970) "Review of Developments in Plane Strain Fracture Toughness testing," ASTM STP 463.
2. Dorn, John E. (1961) "Mechanical Behavior of Materials at Elevated Temperatures," McGraw-Hill Book Company, Inc.
3. Dutta, Piyush K. (1988) "Hopkinson Pressure Bar Data Acquisition and Analysis Methods," CRREL Technical Report
4. Dutta, Piyush K. and David Hui (1996) "Low-Temperature and Freeze-Thaw Durability of Thick Composites," COMPOSITES: PART B, Vol.27B, No.3/4, pp.371-379
5. Dutta, Piyush K., Dennis Farrell and John Kalafut (1988) "Hopkinson Pressure Apparatus- A Tool for Rapid Assessment of Material Properties at High-Strain Rates," Proceedings of TEST TECHNOLOGY SYMPOSIUM I, Volume II, J-20
6. Dutta, Piyush K. David Hui and Magna R. Altamirano (1991) "Energy Absorption of Graphite/Epoxy Plates Using Hopkinson Bar Impact," CRREL Report 91-20
7. Dutta, P. K. D. Hui and Akshay Patil (2001) "High-Strain-Fracture Energy of Unidirectional Composites," ICCE-8
8. Dutta, P.K., Mamidi Kumar, David Hui. (1994) "Dynamic Tensile Strength of Glass Fiber Reinforced Pultruded Composites," Page 357-363, ASME PD Vol. 62, Materials and Design Technology.
9. Dutta, P. K. (1994) "Low-Temperature Compressive Strength of Glass-Fiber Reinforced Polymer Composites," Journal of offshore Mechanics and Arctic Engineering, Vol. 116 , pp.167-172.
10. Dutta P. K., David Hui and Rathi Bhattacharya (1995) "On the Effects of Moisture and Low Temperature on Polymeric Composites," SES'95, 32nd Annual Technical Meeting, New Orleans, LA.
11. Dutta, Piyush K. and David Hui, (1995) "Low-Temperature High-Strain-Rate Behavior of GR/EP Laminate Under Transverse Impact," Advanced Structural Fiber Composites, pp. 455-468.
12. Dutta, Piyush K., (1993) "Compressive Failure of Polycrystalline Ice Under Impact," Proceeding of 3rd International Offshore and Polar Engineering Conference, Singapore, pp. 573-580.
13. Flaggs, D. L., (1985) "Prediction of Tensile Matrix Failure in Composite Laminates," Journal of Composites Materials, Vol. 19, pp.29-50.
14. Hann, H. Thomas, (1976) "Residual Stresses in Polymer Matrix Composites Laminates," J. Composite Materials, Vol. 10, pp. 226-278.
15. Hertzberg, Richard W., (1989) "Deformation and Fracture Mechanics of Engineering Materials," 3rd Edition, John Wiley & Sons.

16. Hui, David and Piyush Dutta, (1992) "Stress Wave Propagation through the Thickness of Graphite/Epoxy Laminated Plate Using PVDF Sensors," 6th Japan-US conference on Composites Materials, Orlando, FL, pp 845-854.
17. Hui, D., A. Patil. and P. Dutta, (2002) "Effects of Temperature on Fracture Toughness of Glass Fiber Reinforced Polymer (GFRP)," ICCE/9, July 2002
18. Jones, Robert M., (1975) "Mechanical of Composites Materials," Hemisphere Publishing Corporation.
19. Liebowitz., (1969) "FRACTURE: An Advanced Treatise," Volume IV Engineering Fracture Design 1969, Academic Press
20. Lord, Harold W., (1988) "On the Design of Polymeric Composite Structures for Cold Regions Applications, " Journal of Reinforced Plastics and Composites, Vol. 7, pp. 435-458.
21. McClintock, Frank A. and Ali S. Argon, ( ) "Mechanical Behavior of Materials," Addison-Wesley Publishing Company, Inc., Addison-Wesley (Canada) Ltd.
22. Nairn, J. A., (1997) "Fracture Mechanics of Composites with Residual Thermal Stresses," Journal of Applied Mechanics, In Press/1-11
23. Nwosu, Sylvanus N., Piyush K. Dutta, and David Hui, (1994) "Stress Wave Propagation in Rocks and Unsolidated Soil Samples by Vertical Dynamics Hopkinson Bar," ICCE/1, pp. 373-374.
24. Nwosu, Sylvanus N., Piyush K. Dutta, and David Hui, (1994) "Characterization of Composites Materials by Vertical Dynamics Hopkinson Bar," American Society of Mechanical Engineers, pp. 141-151.
25. Nwosu, S. N., S. K. Sivapuram, P. K. Dutta and D. Hui, (1995) "Hopkinson Bar Performance of Laminated Composites" ICCE/2, New Orleans, LA, pp.559-560.
26. Rolfe, Stanley T. and John M. Borsom, (1977) "Fracture and Control Fatigue in Structures: Applications of Fracture Mechanics," Prentice Hall, Inc., Englewood Cliffs, New Jersey
27. Springer, George S. (1988) "Environmental Effects on Composite Materials," Vol. 3, Technomic Publishing Co. Inc.
28. Standard Test Method for Plane-Strain Fracture Toughness of Metallic Materials, Designation: E399- 90
29. Sun-Pui Ng, Piyush K. Dutta and David Hui, (1999) "Energy Balance in Hopkinson Bar Under Oblique Impact," ICCE/6, Orlando, Florida, pp.675-676.
30. Soutis, C. and D. Turkmen "High Temperature on the Compressive Strength of Glass Fiber Reinforced Composites", ICCM-9 COMPOSITES: Properties and Applications Vol. VI, pp. 581-587.
31. Smiley, A. J. and R. B. Pipes (1986) "Rate Sensitivity of Inter-Laminar Fracture Toughness in Composites Materials," Proceeding of American Society of Composites, 1st Technical Conference, pp. 434-449.
32. Taya, Minoru and Tsu-Wei Chou, "Prediction of the Stress-Strain Curve of a Short-Fiber Reinforced Thermoplastic," Journal of Materials Science 17, pp. 2801-2808.
33. Takao, Y., T. W. Chou, M. Taya, (1982) "Effective Longitudinal Young's Modulus of Misoriented Short Fiber Composites," Transactions of the ASME, Vol.49, pp.536-540.

34. Vaidya U.K., M. Kulkarni, M.V. Hosur, Arnold Mayer and Piyush Dutta, (2001) "High Strain Rate Impact Response of S2-Glass/Epoxy Composites with Polycarbonate Facing," Polymers and Polymers Composites, Vol. 9 No. 2, pp. 67-79.
35. VanDerSluys, W. A., B.A. Young, D. Doyle, and P. Neubrand, (2000) "Dynamic Fracture Toughness Results of High Strength Pressure Vessel Weldments in the Brittle-to-Ductile Transition Region," ASME Pressure vessel and Piping Conference, Seattle, Washington, MTI 00-02 pp.1-6.
36. Warren, P.D., (1995) "Determining the Fracture Toughness of Brittle Materials by Hertzian Indentation," J. Euro. Ceram. Soc, 15, pp. 385-394.
37. Aliyu A.A., and Daniel, I.M.,Effects of Strain Rate on Delamination Fracture Toughness of Graphite Epoxy, Delamination and Debonding of of Materials, ASTM STP 876, Philadelphia, 336-348, (1985).
38. Ashby, M.F.FRS, Easterling, K.E., Harryson, R., and Maiti, S.K., The Fracture and Toughness of Woods, Proc. Royal Soc. London, A398, pp 261-280 (1985).
39. Beguelin, Ph, Barbezat, M., Kausch, H.H., Mechanical characterization of Polymer Composites with Servo hydraulic high speed tensile tester, J. Physics, III France !, 1867-1880, (1991)
40. Blackman B.R.K., Dear J.P., Kinloch, A.J., McGillivary, H., Wang, Y., Williams J.G., Yala, P., The Failure of Fiber Composites and Adhesively Bonded Fiber Composites under High Rates of Test, J. Mater. Science, Vol 31, 4467-4477, (1996).
41. Brown, W.F., and Strwley, J.E., in Plane Strain Crack Toughness Testing of High Strength Metallic Materials, ASTM STP410, ASTM, Philadelphia p.11, 1966.
42. Cantwell, W.J. and Morton J. The Impact Resistance of Composite Materials – A Review, "Composites", Vol 22, No. 5 (1991)
43. Cantwell, W.J. and Blyton P., A Study of Skin –Core Adhesion in Glass Fiber Reinforced Sandwich Materials, Applied Composite Materials, Vol 3, pp 407-420, (1998).
44. Drzal, L. T. "Composite Interphase Characterization. SAMPE Journal, pp. 7-13, September/October,1983
45. Dutta, P.K., Hui, D., Kadiyala, S.V., A Microstructural Study of Gr/Ep Composite Material Subjected to Impact, Computers and Structures, Elsvier Science Ltd pergamon, Vol 76, pp 173-181, 2000.
46. Dutta, P.K., Farrell, D, Kalafut J., (1987) The CRREL Hopkinson Bar Apparatus, CRREL Special Report.
47. Smiley, A.J., and Pipes, R.B., Rate Effects on Mode I Interlaminar Fracture Toughness in Composite Materials, J. Composite Materials, Vol 21 (7), pp 670-687, (1987)
48. Sih, G.C., Paris, P.C. & Irwin,G.R., Int. National Journal of Fracture Mechanics, , Vol 1, p 189, 1965.,
49. Wool, R. P. polymer Interphases. Munich: Hanser, 1995.

Toward Healing of Composite Cryogenic Tanks

RICHARD PATTON
Mechanical Engineering Department, PO Box ME
Mississippi State University
Mississippi State, MS 39762
Phone: 662-325-7311
Fax: 662-325-7223
E-mail: patton@me.msstate.edu

Judy Schneider
Mechanical Engineering Department, PO Box ME
Mississippi State University
Mississippi State, MS 39762
Phone: 662-325-9154
Fax: 662-325-7223
E-mail: schneider@me.msstate.edu

Charles Pittman, Jr.
Chemistry Department, PO Box 9573
Mississippi State University
Mississippi State, MS 39762
Phone: 662-325-7617
Fax: 662-325-7611
E-mail: cpittman@msstate.edu

The final report on the X-33 composite hydrogen fuel tank investigation showed that microcracking and the associated leaks of hydrogen played an important role in the failure of the X-33 composite hydrogen fuel tank. Development of future composite tanks would benefit from the incorporation of self-healing technology. Initial experiments concerning crack-healing methods used manual intervention schemes to heal cracks. Recently, a major conceptual breakthrough was reported on the development of a self-healing resin. An epoxy resin was prepared containing microencapsulated spheres of the liquid resin precursor, dicyclopentadiene (DCPD). A catalyst to polymerize and crosslink DCPD was also incorporated into the epoxy resin before curing. The resulting cured epoxy resin contained molecularly dispersed catalyst and encapsulated spheres of DCPD. The capsule shells prevented the catalyst from contacting the DCPD until the stress-induced presence of the growing crack tips ruptured the capsules. This released liquid DCPD into the crack where it encountered the catalyst in the walls of the epoxy resin. Upon this encounter, the liquid DCPD cured to polyDCPD, which is a tough resin that plugged, sealed, and healed the crack.

Other healing schemes are also possible for optimization of the process to apply toward fuel tank fabrication. Rather than embed capsules of the healing agent in the matrix, alternative methods of transporting the healing agent to the crack(s) are being considered in this study. For example, the tank can be brought to cure temperature, put under pressure, and DCPD monomer added to the tank as a vapor, which infuses the crack and begins the healing process. Use of the self-healing concept in composite tank manufacturing can also consider incorporation of pre-cycling to heal cracks before putting the tank into service. This pre-cycling or 'tank healing' process would subject the tank to repeated cycles of cryocooling, cracking, warming and healing. This technique would be beneficial if a progressive reduction is demonstrated in the tendency of the tank to crack when cryocooled is demonstrated, along with retention of toughness.

Numerical Modeling, Thermomechanical Testing, and NDE Procedures for Prediction of Microcracking Induced Permeability of Cryogenic Composites

Jae Noh, John Whitcomb*
Bongtaek Oh, Dimitris Lagoudas
Konstantin Maslov, Atul Ganpatye, Vikram Kinra

Center for Mechanics of Composites
Aerospace Engineering Department
Texas A&M University
College Station, TX 77843-3141

INTRODUCTION

Reusable Space Vehicles will include light cryogenic composite fuel tanks that must not leak excessively even after multiple launches. Damage in cryogenic composite fuel tanks induced during manufacturing and advanced by thermomechanical cycling can accelerate leakage of the propellant. Whether the leakage exceeds tolerable levels depends on many factors, including pressure gradients, microcrack density, other damage such as delamination, connectivity of the cracks, residual stresses from manufacture, service-induced stresses from thermal and mechanical loads, and composite lay-up. Although it is critical to experimentally characterize permeability during various thermal and mechanical load histories, optimal design depends on having analytical models that can predict the effect of various parameters on performance. Our broad goal is to develop such models that are experimentally validated by destructive and non-destructive evaluation means.

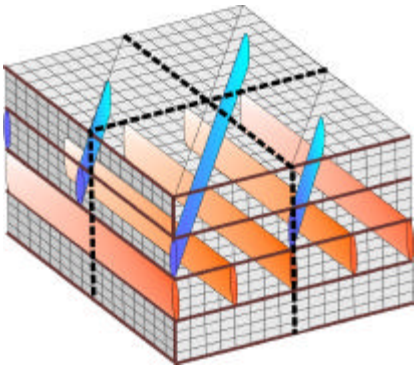

Figure 1. Angle ply laminate with transverse matrix cracks

The literature provides limited studies on the mechanical performance of and damage development in polymer matrix composites operating at cryogenic temperature. Adams, *et al.* [1] investigated thermally induced matrix cracking for graphite/epoxy cross-ply laminates exposed to thermal cycles (-250°F to 250°F). They found the crack density increases with thermal cycles for all laminate configurations tested. Kessler et al. [2] have cycled carbon/polymer composites with a combined cycle to simulate the operating environment of the X-33's composites fuel tanks. A single cycle consisted of a cool-down from 300K to 20K, a heat-up 400K, and then back to 300K. There were no microcracks present or apparent loss in stiffness or strength properties after 10 cycles in quasi-isotropic laminates which are identical to the material used on the X-33. Different types of the cross-ply and quasi-isotropic laminates were thermo-mechanically cycled to examine the initiation and development of damage [3-5]. The literature survey suggests that the detailed study on the damage characterization for cross- and angle- ply laminates must be performed for various loading histories. The current study will include a comparison of damage development in accordance with loading history.

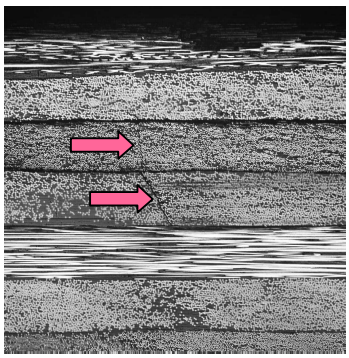

Figure 2. Micrograph showing cracks in a laminate

There are a few recent studies that investigated the possibility of predicting leakage of cryogenic fuel from composite tanks. Some experiments with measurement of the leak rate through polymer composite are found in the literature [2,6-10]. McManus, *et al.* presented analytical and experimental results for crack induced permeability under cryogenic conditions [7,8]. Kumazawa conducted numerical analysis to predict the leak rates at cryogenic temperature [9]. They took into account the influences of both thermal contraction and reduced molecular dynamics. They developed an analytical method to quantitatively predict the leakage based on the simple assumption that there is a relationship between

* E-mail: whit@aero.tamu.edu Phone: 979-845-4006

leakage and opening displacement of matrix cracks. The study on the leakage at cryogenic condition is at a preliminary stage. Many factors (damage state, opening displacement, permeability, etc) affecting the leakage must be carefully examined to develop an analytical model and compare with experimental results.

Since the amount of leakage will increase with crack opening volume (COV), it is essential that we understand crack opening and factors that affect the crack opening. One of objectives in the current work is to show that the crack opening volume can be directly related to the degradation behavior of the effective moduli of a cracked ply. The effect of damage on effective moduli has been studied extensively [11-15]. A simple expression for the COV will be derived based on the modulus reduction and the volume averaged strain or stress of a cracked ply for a given crack density. The study on the opening will extend to consider the delamination and matrix cracking together. For example, the amount of opening is directly influenced by the delamination length. As far as the opening due to delamination and matrix crack is involved, there is no work reported in the literature.

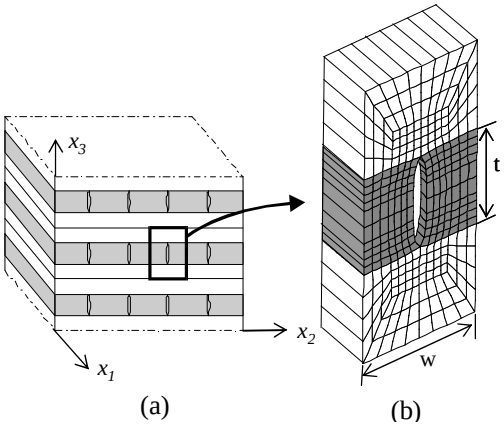

Figure 3. Modeling a laminate with transverse matrix cracks (TMC).

In order to understand delamination growth from crossing matrix cracks, a computational model for strain energy release rate calculation will be developed. Some researchers [16-18] have studied delamination near the crossing cracks. However, they considered only cross-ply laminates and did not perform a parametric study to determine the effects of various parameters on the strain energy release rates.

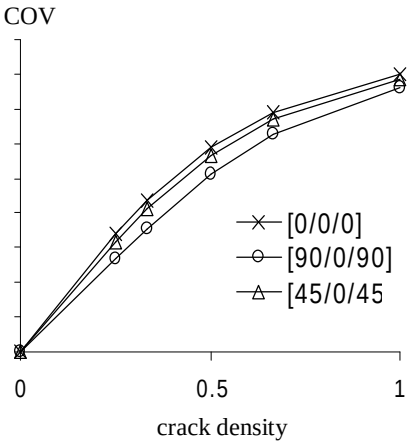

Figure 4. Effect of adjacent ply orientation and crack density on effective modulus E_{22} and crack opening volume (COV).

In this paper, our progress in developing a predictive model will be summarized. Our efforts will focus on three areas. The first is determining the effect of laminate design on opening of transverse matrix cracks and delaminations. Quasi-3D and fully three-dimensional finite element models were used to determine the effect of parameters such as loading, stacking sequence, and material properties on opening of the leakage path. As an example, Figure 1 shows a typical configuration of an angle ply laminate with transverse matrix cracks in each ply. The cracks are shaded in two of the plies. Two of the other variations studied include configurations with only one cracked ply or delamination at the intersection of transverse matrix cracks. The second area is experimental characterization and development of predictive models for initiation and evolution of damage during thermomechanical cycling. The loading currently consists of various sequences of uniaxial mechanical load combined with change in temperature from room temperature down to that for liquid nitrogen. Figure 2 shows a typical micrograph of a laminate with cracks which are microscopic and sparse. The third area is three-dimensional description of the damage state for laminates with known permeability. This last area has required the evaluation and development of destructive and non-destructive techniques for detecting the damage. Optical microscopy, x-radiography with various dye penetrants, and several ultrasonic NDE techniques are being explored.

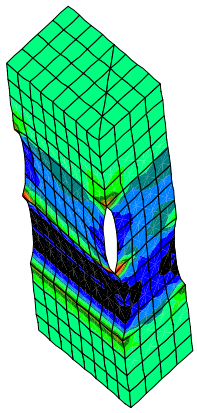

Figure 5. FEM Modeling of $[90/0_c/45_c/\ 90]_?$ laminate with transverse matrix cracks in multiple plies.

The studies in these areas will be integrated to build analytical models that predict the effect of various parameters on permeability. The following sections describe progress in analytical and experimental studies including destructive and non-destructive techniques.

ANALYSIS OF DAMAGE

In this section, we will describe progress in developing models to predict the initiation, evolution, and opening of damage. Most of the analytical work for formation of damage was on transverse matrix cracks. However, initial studies were conducted and are continuing to determine the interaction of transverse matrix cracks and delaminations. There were also some experimental studies of damage formation. The discussion of the development of the experimental equipment and the results are discussed later.

In order to simulate cracks occurring in laminates a finite element model for a representative volume element (RVE) was built. The RVE (or unit cell) is defined herein as the smallest region that represents the behavior of the entire region without any mirroring or rotation transformations. Figure 3(a) shows a laminate with matrix cracks, which are idealized based on the assumptions that the cracks are parallel to the x_1x_3-plane and extend through the entire length and thickness of the ply. The cracks are also assumed to be periodically distributed. Due to the assumptions, periodic boundary conditions are applied to the RVE. The RVE with one crack is extracted from the laminate. A finite element mesh was built for this RVE as shown in Figure 3(b). It has been shown in the previous work that the degree of degradation of a cracked laminate is directly related to the crack opening displacements [19]. Hence, the understanding developed in the extensive parametric studies performed earlier by numerous researchers to determine the effective properties can be re-interpreted using formulas developed in Reference 11 to obtain insights about opening displacements, which are of great interest to this work. One major question addressed was whether the laminate stacking sequence can be designed such that when a crack does form, the opening is minimized. This is discussed next.

It is assumed that the x_2 direction is oriented perpendicular to the crack faces. The crack opening volume (COV) can be obtained from the u_2 displacements of the crack faces. In particular, the COV is defined to be

$$COV = \int_{CS} u_2 n_2 \, dS \tag{1}$$

where CS denotes the crack surface. Reference 19 derived the following formula to calculate the crack opening volume (COV) for a laminate based on the degradation of the E_{22} of a cracked lamina.

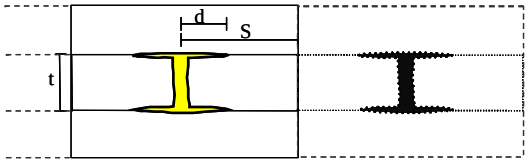

Figure 6. Modeling of delamination at crack tips

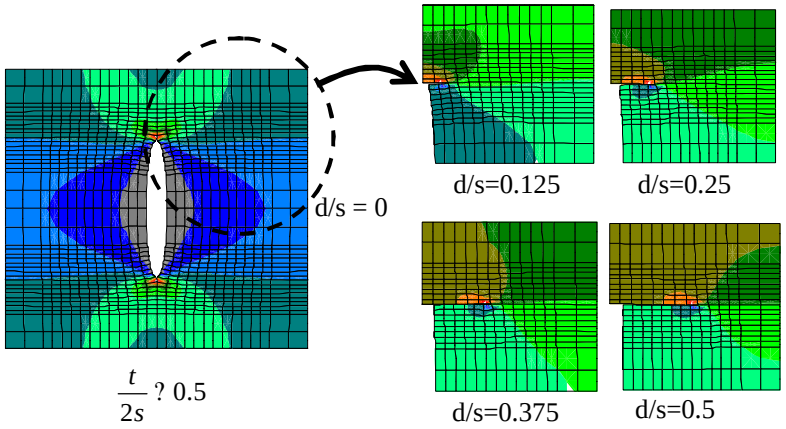

Figure 7. Effect of delamination length on deformation.

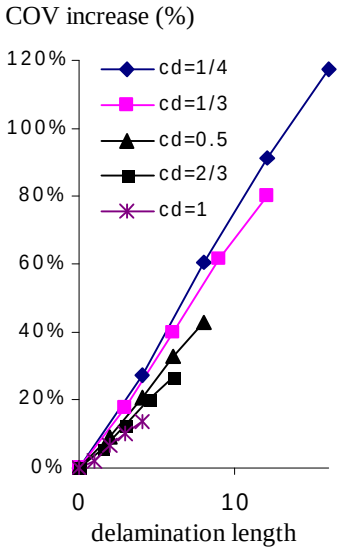

Figure 8. COV increase vs. delimitation length

$$COV = V \left[\left(\bar{S}_{22} - S_{22} \right) \langle \sigma_2 \rangle + \left(\bar{S}_{24} - S_{24} \right) \langle \sigma_4 \rangle \right] \quad (2)$$

where $V, \bar{S}_{22}$, and $\langle \sigma_2 \rangle$ are the volume, the effective compliance, and the volume averaged stress σ_2 of a cracked lamina, respectively. This formula can be approximated by

$$COV = V \left[\frac{1}{\bar{E}_{22}} - \frac{1}{E_{22}} \right] \langle \sigma_2 \rangle \quad (3)$$

where the $\bar{E}_{22}$ is the degraded E_{22} of a cracked ply. Figure 4 shows crack opening volume for three laminates with various crack densities in the middle lamina. The results suggest that the crack opening volume is not very sensitive to the laminate design. The COV was also calculated for [0/90$_c$/0$_c$/90$_c$/0] and [90/0$_c$ /45$_c$ /90] laminates with transverse matrix cracks in multiple plies. The deformed FEM mesh for [90/0$_c$ /45$_c$ /90] is shown in Figure 5. The contour shows the variation of σ_{22}. The COV calculation based on Eqs. 2 and 3 were in very good agreement with FEA results. A more detailed description of this work can be found in Reference 19.

Microcracking can lead to other forms of damage such as delamination. Whether delaminations form and their size will greatly affect how easily fuel can pass through the maze of cracks. Laminate design may have a significant affect on the delamination initiation. A study is also being performed for delaminations that can form near the matrix crack tip (Figure 6). In Figure 6, t, s, and d are the thickness of the cracked ply, the transverse matrix crack spacing, and one-half of the delamination length, respectively. In this model, by changing the s and d, one can obtain different transverse matrix crack densities and delamination lengths. The opening displacement for this model has been studied. Figure 7 shows FEM meshes for the delamination near transverse matrix crack tips. In this FEA, the t and s were held constant as the delamination length d increases. Displacement boundary conditions were imposed to obtain <σ_{22}>=1%. As shown in Figure 7, the opening increases with the delamination length. The effect of delamination length on the effective properties of the entire laminate with the middle cracked ply was examined. The study showed that degradation of E_{22}, G_{23}, G_{13}, and E_{33} of the laminate is very sensitive to the delamination. By assuming that the transverse matrix cracking and delamination affect only the properties of the middle ply, the reduced properties of the middle ply can be obtained. The additional E_{22} reduction of the middle ply due to delamination at the matrix crack was calculated. The laminates [0/0/0], [45/0/45], and [90/0/90] with the different crack densities (.25-1.0) were analyzed to examine the effect of adjacent ply orientation and the crack density. It was found in the study that the E_{22} reduces almost linearly with the delamination length. The E_{22} reduction due to the delamination can be determined using FEA or a localization formula which is based on the homogenization formula presented in Reference 20. Also, a simple formula based on strength of materials was developed to calculate the E_{22} reduction. The results based on the localization and simple formulas were compared with the results by FEA and a good agreement was obtained. The FEM calculation for the increase of crack opening due to delamination is shown in Figure 8.

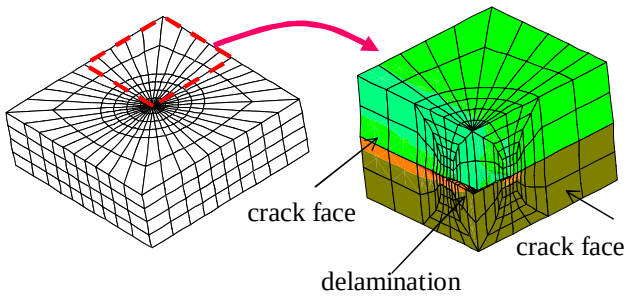

Figure 9. Modeling of delamination at the intersection of cracks.

A simple relationship for average strain energy release rate associated with pop-in of transverse matrix cracks was developed and verified. The strain energy release rate for matrix cracking can be obtained easily for a displacement controlled case since the strain energy release rate is calculated using only the strain energy W (i.e. the work of the surface tractions is zero). The strain energy is $W = 1/2 \langle \sigma_i \rangle \langle \sigma_i \rangle V$ where <> indicates the volume averaged

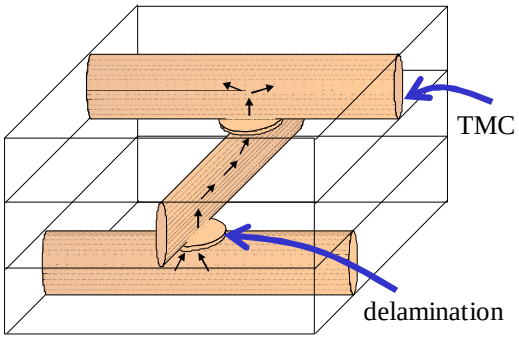

Figure 10. Network of matrix cracks and delaminations

value over a volume V. The strain energy can be rewritten as $W = 1/2\ \bar{S}_{ij} \langle \sigma_j \rangle \langle \sigma_i \rangle V = 1/2\ \bar{C}_{ij} \langle \varepsilon_j \rangle \langle \varepsilon_i \rangle V$. The effective stiffness matrix $\bar{C}$ and compliance matrix $\bar{S}$ of the laminate can be determined as a function of crack density using the modulus degradation for a middle cracked ply and homogenization techniques. Therefore, for given volume averaged strain or stress information, the strain energy and the strain energy release rate can be determined. The understanding developed in the parametric studies performed earlier to determine the effective properties can be re-interpreted using the formulas developed herein to obtain insights about strain energy release rate. This analysis helps understand whether the laminate stacking sequence can be designed such that cracks are prevented from occurring. It was found in the study that the strain energy release rate is sensitive to the type of loading but not very sensitive to adjacent ply orientation. This is expected since the strain energy depends on only the modulus degradation behavior and the volume averaged stresses and strains. Therefore, the strain energy release rate and the modulus degradation rate must show the same pattern. The results imply that the laminate stacking sequence does not much affect the resistance of the material to transverse matrix crack initiation and growth during service. Of course, stacking sequence can affect the stress state within a lamina, which is very important in determining the damage state. It has been known for a long time that delaminations often initiate at intersections of transverse matrix cracks [21].

The strain energy release rate for a delamination at the intersection of matrix cracks (Figure 9) was also calculated. Figure 9 shows a finite element model with a circular delamination at the crossing matrix cracks. The strain energy release rate has been calculated for various stacking sequences for circular delaminations. Future efforts will explore other delamination shapes which are more realistic. The opening due to matrix cracks and the delamination at the crossing matrix cracks is currently being investigated. Finite element models were developed and analyzed under axial and biaxial loadings. Further work is needed to examine the effect of various parameters such as delamination shapes (circle or ellipse…) and stacking sequence.

Parametric studies of the effective permeability are in progress based on models that consist of matrix cracks and delaminations (Figure 10).

EXPERIMENTAL CHARACTERIZATION

Experimental results are needed to verify the FEA models described in the above section. In this section, the experimental work on characterization of damage developed during thermomechanical cycling of cryogenic composite laminates will be discussed. Some researchers [2-5] have studied the damage evolution of cryogenic composites by applying different types of thermomechanical loading. Thermal loading usually consists of cycling between room or a higher temperature and a cryogenic temperature (most often liquid nitrogen, i.e. -196?C). Mechanical loading typically takes place at cryogenic temperatures, with an applied maximum stress level being a portion of the ultimate strength. In this section, combined thermal cyclic loading (room temperature to -196?C) and mechanical loading at -196?C and room temperature are performed on IM7/977-2 composite laminates. More specifically, thermal cycling (room temperature to -196?C) in the absence of mechanical load, thermal cycling followed by mechanical cycling at room temperature, and mechanical cycling at cryogenic temperatures are the three loading paths that have been investigated.

A high density polyethylene cryogenic dewar was used for the thermal cycles and an MTS 880 Materials Test System was used for the mechanical loading of the composite laminates tested at both room and cryogenic temperatures. Figure 11 shows the custom designed cryogenic chamber, which was mounted on the MTS 880 frame. The chamber was built of stainless steel, since steel has a relatively low thermal conductivity at cryogenic temperatures. An aluminum foil insulator was added around the chamber in order to improve insulation. A sealant was used to avoid leakage from the bottom of the chamber. After the sealant was cured at room temperature for 36 hours, the chamber was filled with liquid nitrogen. The composite specimens were held for 30 minutes in liquid nitrogen to guarantee that they had reached the same temperature as liquid nitrogen. Subsequently, the specimens were mechanically loaded while still being held in the liquid nitrogen. During the mechanical loading, the stress and strain values were obtained. The strain values were calculated by using the cross-head displacement, while the stress values were determined from a load cell attached on the cross-head.

After two thermal or mechanical cycles, the specimens were examined using an optical microscope to collect damage state information, such as crack density for each ply and delamination length occurring at interfaces between plies.

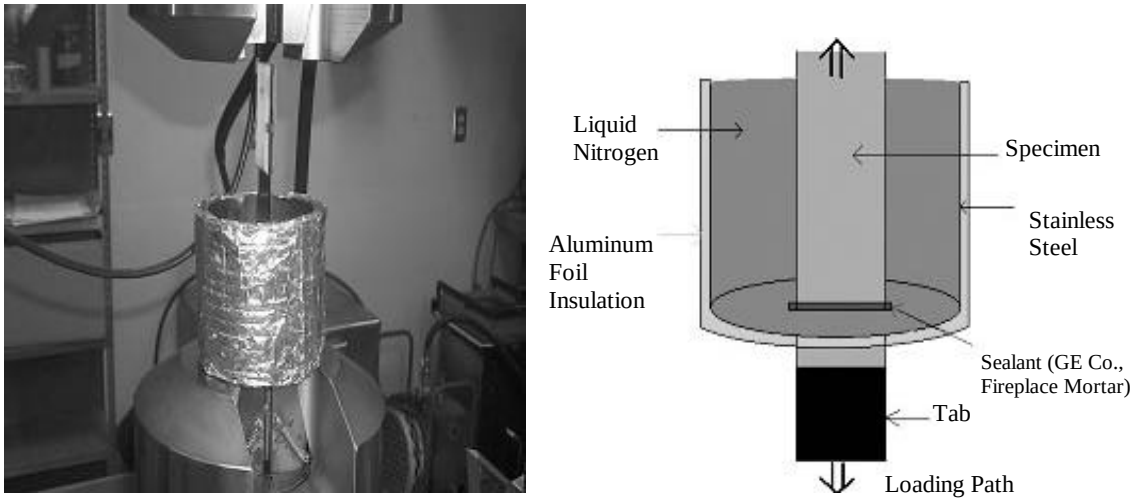

Figure 11. Cryostat system mounted on an MTS 880 frame

The specimens tested were provided by Lockheed Martin, and they were 18-ply graphite epoxy IM7/977-2 laminates with $[0/-45/90/45/0/45/90/-45/0]_S$ stacking sequence, and with dimension of 11.75" X 3.5". The specimens had undergone prior thermomechanical testing, including thermal cycles from room temperature to liquid Nitrogen (-196?C) and mechanical cycles at cryogenic temperatures (-196?C). From the specimens received, several were tested under additional thermomechanical loading, and others were tested nondestructively for the evaluation of their damage state. For the thermomechanical loading tests, the original specimens were cut into three pieces, as indicated in Figure 12.

First, a laminate specimen was mechanically tested at room temperature in uniaxial tension to failure in order to determine the Young's modulus and ultimate tensile strength. The Young's modulus and ultimate tensile strength were determined to be 61.2 GPa and 787.02 MPa, respectively. Then, a second laminate that had undergone four mechanical and thermal cycles, was cut into three pieces from the original specimen shown in Figure 12, and machined with a dimension of 10" x 1" according to ASTM standards, D3039/3039M-00 recommendation.

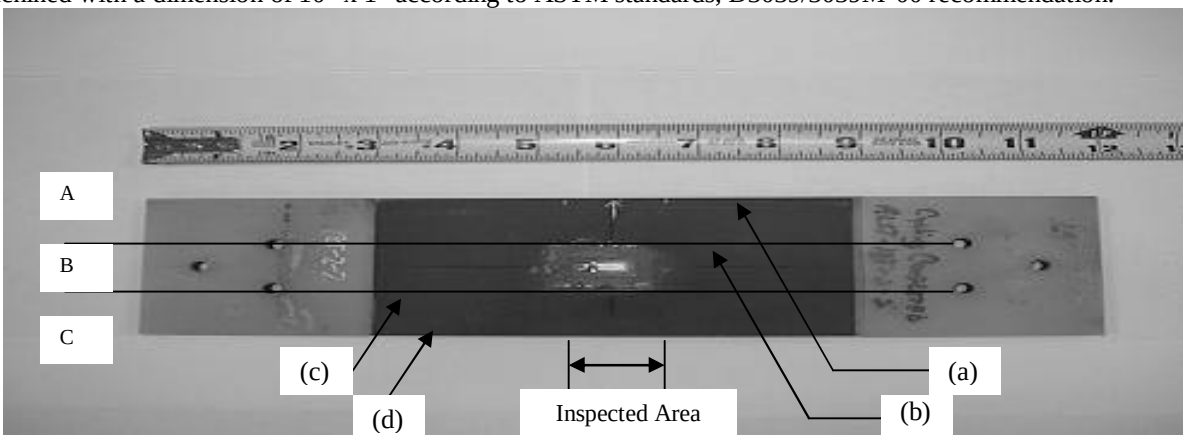

Figure 12. Cryogenic composite laminate - IM7/977-2

The three resulting specimens, indicated as A, B, and C in Figure 12, were characterized for damage before any loading cycle was applied. Cracks were counted in each non-zero degree ply along a 1.26" (32 mm) span centered lengthwise on each specimen. Specimen A underwent a total of 20 thermal cycles. Specimen B was subjected to 2 thermal cycles followed by 2 mechanical cycles at 60% of the ultimate tensile strength at room temperature. The 4 cycles were repeated three times, and the specimen was inspected after each mechanical and thermal loading cycle. Mechanical loading at cryogenic temperatures was applied to specimen C, but the test was terminated early due to delamination reaching the grips.

Figure 13 shows the crack densities of the second ply from the outer surface [-45], and their increase with the number of loading cycles for specimens A, B, and C, respectively. Similar trend in the rate of crack density growth has been observed in the third ply [90] of the specimens tested. The zero in the horizontal axis defines the initial

state of each specimen, while each cycle on the graph corresponds to two physical cycles, either mechanical or thermal. When thermal cycles (specimen A) alone were applied, there were no additional cracks in the material up to 20 cycles. However, thermal cycling, followed by mechanical cycling at room temperature (specimen B), resulted in a rapid increase of microcracking induced damage, which saturated after it reached a level of about eight times the initial damage. Even higher rate of increase of damage densities were observed in specimen C, which was mechanically cycled at cryogenic temperatures, but delamination at the grips resulted in termination of the experiment.

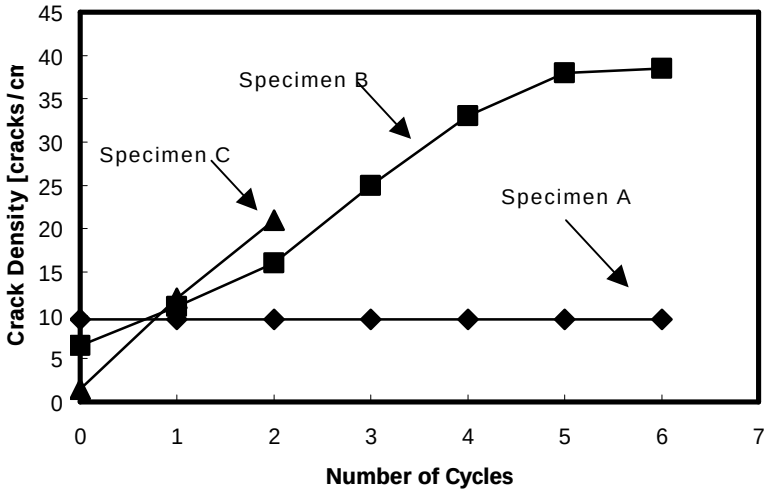

Figure 13. Micro-crack density versus number of cycles for the [–45] ply (second from outer surface)

Figure 14 shows typical optical micrographs taken in the middle of the specimen edge at the end of the loading cycles. The initial damage state, which is the damage of specimen A is shown in Figure 14(a). The damage state after twelve loading cycles for specimen B and four mechanical cycles for specimen C are shown in Figure 14(b) and 14(c), respectively. Cracks were found only in plies 2, 3, and 4 in the $[0/-45/90/45/0/45/90/-45/0]_S$ laminate. This is an unusual case, and a possible cause can be due to the presence of residual stresses resulting from manufacturing process or stress concentrations at micro cracks in the above plies.

Delaminations were observed between plies 2,3, and 3,4. The majority of the interface cracks were observed between plies 2,3, as shown in Figure 14(c). From the above results, one can conclude that for simultaneous mechanical loading in a cryogenic environment, the chances of delamination and hence leakage is higher than thermal testing followed by mechanical loading at room temperature. Delaminations at transverse crack tips were also observed, which could be more critical for the permeability and leakage problem.

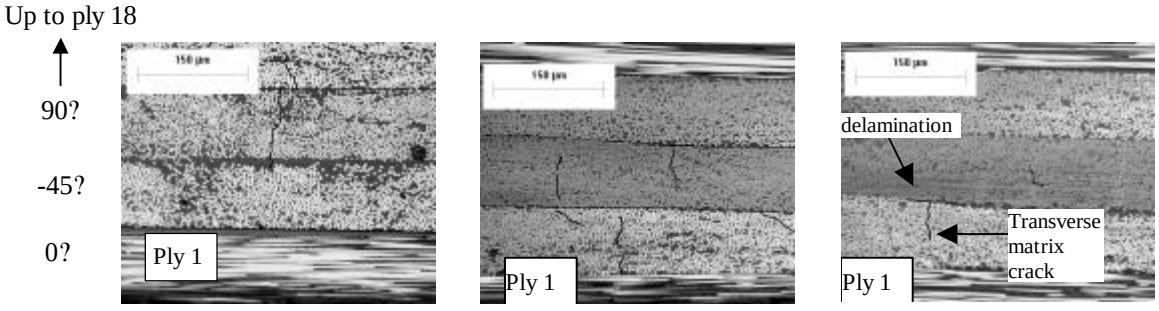

(a) Specimen A (b) Specimen B (c) Specimen C

Figure 14. Micrographs showing damage after testing

Additional loading conditions such as thermal cycling at constant load and also variable mechanical load are being planned for cryogenic composite laminates with an undamaged initial state. This would facilitate the verification of loading condition importance in damage development. Also, the influence of thermal gradients on damage development will be investigated, as specimens are brought to cryogenic conditions. Such large temperature

variations through the thickness may result in thermal stresses and possible delaminations at the interfaces. The influence of thermal gradients on damage development will be investigated both experimentally and numerically, using a FEA model. In future work, thermomechanical loading tests will be accompanied by a concurrent nondestructive evaluation of damage; these NDE techniques are described next.

PLY-TO-PLY DETERMINATION OF DAMAGE

In the following, we briefly discuss salient features of these NDE techniques (optical edge examination, X-ray radiography and ultrasonics) for a ply-by-ply determination of damage.

Optical Examination of Edges

Edges of each specimen were polished progressively using 600 and 1200 grit sandpapers and then using high purity 0.3 ?m alumina powder to get a near optical-quality finish. Edge cracks were mapped using an optical microscope (200X magnification) equipped with a motorized positioning stage controlled by a computer. The recorded data files were later used to generate crack map (schematics), which were subsequently compared with images obtained from X-ray and ultrasonic examinations. Though optical examination of edge cracks provides one of the simplest forms of damage evaluation and is fairly reliable (doubtful places can be reexamined at higher magnification), it fails to provide any information regarding the extent to which cracks have propagated through the width of a laminate. In other words, optical examination cannot provide any information about the extent of partial cracks (cracks that appear only at one of the two edges) or the presence of internal cracks (cracks that do not appear on any of the edges); such cracks were found very frequently in the laminates tested. As an example, one of the 18-ply graphite epoxy IM7/977-2 specimens mentioned in the previous section was cut into three pieces (as shown in Figure 12) and the edge cracks in the 3rd [90] ply were examined. The resulting damage densities are presented in Figure 15 for the edges indicated in Figure 12. This specimen underwent thermomechanical testing at cryogenic temperatures, similar to the specimens tested in the previous section, and in addition a Helium leak testing was also performed. A careful examination of this data revealed that a vast majority of the cracks do not traverse the entire width of the specimen.

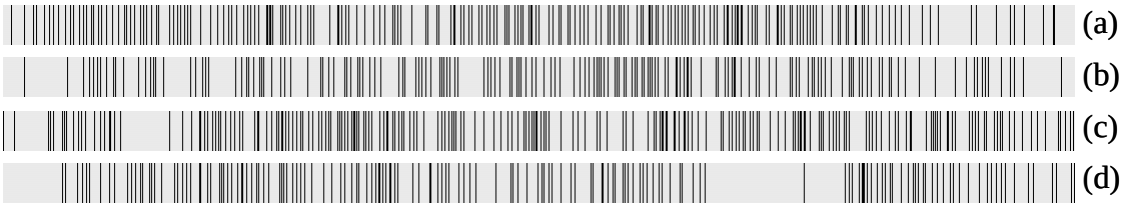

Figure 15. Relative crack position in 3rd [90^0] ply of 3.6'' wide 18-ply [0/-45/90/45/0/-45/90/45/0]$_s$ laminate at specimen edges (a),(d) and at cuts at 1.2'' (b) and 2.4'' (c) distance from edge (a).

X-Ray Radiography

Penetrant enhanced X-ray radiography is one of the most widely used techniques for damage characterization, and frequently considered the best NDE technique available for imaging the crack distribution in composite. With the use of a proper contrasting agent (in the present case, diiodomethane [22]), a clear picture of matrix cracks is seen as dark lines in the X-ray images (see Figure 16). This has been further confirmed by a comparison of X-ray images with optical and ultrasonic techniques. A part of the X-ray image of matrix cracks in highly damaged 8-ply laminate, is presented in Figure

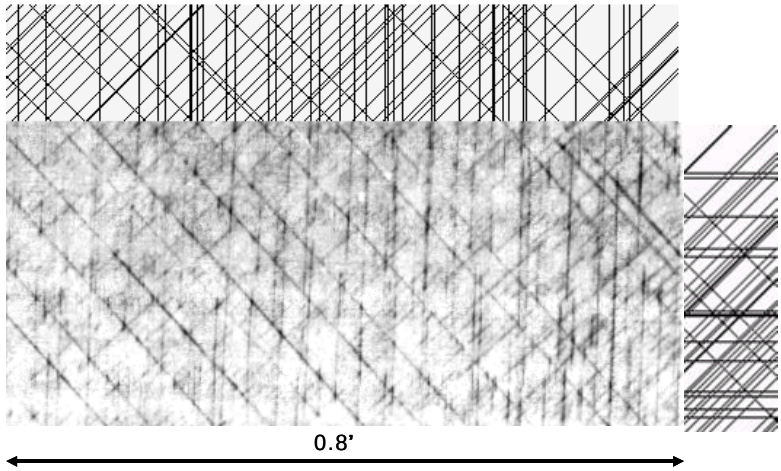

Figure 16. A comparison of a part of the X-ray image of the 8-ply, [90/45/0/-45]$_s$, laminate with a schematic of optically detected matrix cracks (top and right side of the picture).

16. At the top and the side of the figure, a schematic of the optically detected edge cracks is plotted. Cracks found in 90^o plies are plotted as vertical lines, cracks found in 45^o plies are plotted as lines at 45^o, and so forth. Fairly good correlation of the position of dark lines in the figure with the schematic of the optically detected matrix cracks confirms that the dark lines which look like cracks in the figure are indeed matrix cracks. However, as is well known, an X-ray image is a 2-D projection of the damage, which makes ply-by-ply damage evaluation difficult. In a real life situation where one does not have assess to the composite edges the techniques becomes inapplicable. Moreover, it is not a "true" nondestructive technique because of possible specimen degradation by the penetrant.

Ultrasonics

The laminates were tested extensively using different ultrasonic techniques and transducer combinations. These include through-transmission, scattering in transmission (pitch-catch), and polar backscattering for detection of matrix cracks. The standard pulse-echo C-scan technique was used to detect delaminations. By appropriately time-gating the output signals, it was found possible to carry out a ply–by–ply examination.

Polar backscattering technique, i.e. scattering of ultrasound by crack and ply boundary back toward inclined transducer, using a spherically-focused, 25-MHz transducer was found to be the best technique for imaging matrix cracks including internal cracks [23,24]. In this technique a single transducer is used as a transmitter and receiver. The signal-to-noise ratio was found to be rather high (in some cases more then 30 dB) indicating a high level of confidence of detection.

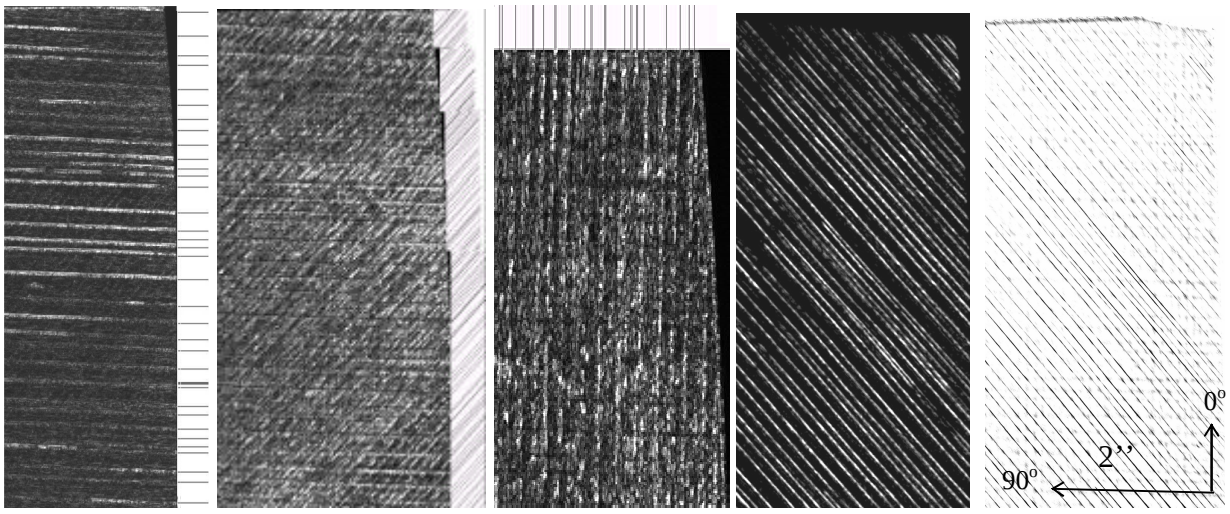

Figure 17. From left to right: Ultrasonic images of 1st, 2nd, 3rd, and 4th plies, and filtered X-ray images of cracks in the 4th ply of the 8-ply, $[90/45/0/-45]_s$, specimen.

A comparison of the ultrasonic (polar backscattering) and X-ray (filtered to remove lines in all other directions) images of the second ply of the 8-ply specimen is presented in Figure 17. An excellent correlation can be seen between them. Moreover, both the images correlate well with optical edge crack detection results. The information obtained from the aforementioned NDE techniques is complementary to each other and a high degree of reliability can be achieved in damage characterization with a judicious combination of all three techniques.

CONCLUDING REMARKS

Optimal design of composite cryogenic tanks requires an analysis that can predict microcracking induced permeability. The current work is focused on laying the foundation for such an analysis. This requires a combination of parametric analytical and experimental studies and development of techniques to determine the 3D distribution and connectivity of damage. This paper briefly described progress in these areas.

ACKNOWLEDGEMENT

This work was supported by NASA through the National Center for Advanced Manufacturing Louisiana

Partnership, Grant # NCC8-223. Any opinions, findings, and conclusions or recommendations expressed in this material are those of the authors and do not necessarily reflect the views of the National Aeronautics and Space Administration.

REFERENCES

1. D.S. Adams, D.E. Bowles and C.T. Herakovich. "Thermally Induced Transverse Cracking in Graphite/Epoxy Cross-Ply Laminates," *Journal of Reinforced Plastics and Composites*, Vol. 5, July, pp. 152-169. 1986.
2. S.S. Kessler, T. Matuszeski and H. McManus. "Cryocycling and Mechanical Testing of CFRP for the X-33 Liquid H_2 Fuel Tank Structure," *Proceedings of the American Society for Composites (ASC)*, Sept. 9-12, 2001, Virginia Tech, Blacksburg.
3. R.Y. Kim, S.L. Donaldson, "Experimental Observation of Microcracking of Composite Laminates under Cryogenic Temperature", AIAA, Aug., 28-30, 2001.
4. V.T. Bechel, M.B. Fredin, and S.L. Donaldson. "Combined Cryogenic and Elevated Temperature Cycling of Carbon/Polymer Composites", Society for the Advancement of Materials and Process Engineering, Long Beach, CA, May 2002.
5. S.L. Donaldson, R.Y. Kim, "Fatigue of Composites at Cryogenic Temperature", Society for the Advancement of Materials and Process Engineering, Long Beach, CA, May 2002
6. H.K. Rivers, J.G. Sikora, and S.N. Sankaran, "Detection o Micro-Leaks Through Complex Geometries under Mechanical Load and at Cryogenic Temperature," AIAA 2001-1218.
7. H.L. McManus and J.R. Maddocks, "On Microcracking in Composite Laminates under Thermal and Mechanical Loading," *Polymers and Polymer Composites*, Vol. 4, No. 5, 1996, pp. 304-314.
8. H.L. McManus, A. Faust, and S. Uebelhart. "Gas Permeability of Thermally Cycled Graphite-Epoxy Composites," *Proceedings of the American Society for Composites (ASC), Sept. 9-12, 2001*, Virginia Tech.
9. H. Kumazawa, T. Aoki, T. Ishikawa, and I. Susuki. "Modeling of Propellant Leakage Through Matrix Cracks in Composite Laminates," AIAA-2001-1217.
10. T. Yokozeki, T. Aoki, and T. Ishikawa. "Transverse Crack Propagation Process across the Specimen Width in Toughened CFRP Laminates,", AIAA-2001-1639.
11. J. Noh and J. Whitcomb. "Effect of Various Parameters on the Effective Properties of a Cracked Ply," Journal of Composite Materials, Vol. 34, 2001.
12. Z. Hashin. "Analysis of Cracked Laminates: A Variational Approach," *Mechanics of Materials*, 4:121-136, 1985.
13. J.A. Nairn. "Some New Variational Mechanics Results on Composite Micro Microcracking," *Proc. 10th Int. Conf. on Comp. Mat.*, Whistler, B.C., Canada. 110, 1995.
14. G.J. Dvorak, N. Laws, M. Hejazi. "Analysis of Progressive Matrix Cracking in Composite Laminates I. Thermoelastic Properties of a Ply with Cracks," *Journal of Composite Materials*, 19: 216-234, 1985.
15. P. Gudmendson. and W. Zang. "An Analytical Model for Thermoelastic Properties of Composites Laminates Containing Transverse Matrix Cracks," *International Journal of Solids and Structures*, 23: 1301-1318, 1993.
16. R.D. Jamison. "Advanced Fatigue Damage Development in Graphite/Epoxy Laminates," Ph.D. Dissertation, College of Engineering, Virginia Polytechnic Institute and State University, 1982.
17. A.S. Wnag, N.N. Kishore and C.A. Li. "Crack Development in Graphite-Epoxy Cross-ply Laminates under Uniaxial Tension," *Composites Science and Technology*, 24, 1-31, 1984.
18. J. Whitcomb. 1992. "Analysis of Delamination Growth near Intersecting Ply Cracks," *Composite Journal of Composite Materials*, Vol. 26, No. 12, pp. 1844-1858, 1992.
19. J. Noh and J. Whitcomb. "Effect of Laminate Design and Loads on Crack Opening Volume in Laminates Used in Cryogenic Tanks," *Proceedings of 43rd AIAA/ASME Structures, Structural Dynamics and Materials Conference*, Denver, April, 2002.
20. J. Whitcomb and J. Noh. "Concise Derivation of Formulas for 3D Sublaminate Homogenization," *Journal of Composite Materials*," 34(6):522-535, 2000.
21. A.L. Highsmith, and K.L. Reifsnider "On Delamination and the Damage Localization Process," *AMD, ASME, 74:71-87*.
22. E.A. Birt, "The application of X-radiography to the inspection of composites," *INSIGHT* Vol 42, No. 3, pp. 151-157, 2000.
23. K. Maslov, R. Kim, V. Kinra, N. Pagano. 'A new technique for the ultrasonic detection of internal transverse cracks in carbon-fibre/bismaleimide composite laminates," *Composite Science and Technology*, Vol. 60, pp. 2185-2190, 2000.
24. K. Steiner, R. Eduljee, X. Huang, J. Gillespie Jr. "Ultrasonic NDE techniques for the evaluation of matrix cracking in composite laminates", *Composite Science and Technology*, Vol. 53, pp. 193-198, 1995.

SOLID STATE FRICTION STIR WELDING

G.R. Buchanan, Department of Civil Engineering, (931) 372-3486, gbuchanan@tntech.edu

J. Peddieson, Department of Mechanical Engineering, (931) 372-3472, jpeddieson@tntech.edu

G.R. Ramirez, , Department of Civil Engineering, (931) 372-3261, gramirez@tntech.edu

S. A. Idem, Department of Mechanical Engineering, (931) 372-3607, sidem@tntech.edu

Tennessee Technological University, Cookeville, TN 38505, USA

INTRODUCTION

The purpose of this paper is to report progress on mathematical modeling of the friction stir welding process supported by NCAM. The friction stir welding mechanism is described in numerous publications [2,3,4,6,8] and will be briefly described here. Two pieces of aluminum sheet are to be edge-joined using a weld and are placed with edges fitted together. A tool, referred to as a 'pintool', actually creates the weld. A retractable pintool, developed at Marshall Space Flight Center, consists of a mechanism that can be compared to a plunge router. The shoulder of the tool houses the pin and is placed at the intersection of the edge-joined materials. The shoulder applies pressure and rotates to create frictional heat as it is pressed against the material joint. The frictional heat must reach a temperature that allows the aluminum to flow plastically. The pin is inserted into the material and as it rotates the material is actually stirred, meaning that the material from one plate actually replaces a corresponding amount of material in the second plate. The pintool moves with sufficient speed along the joint to continue to heat new material that can be stirred into the weld. Cooling occurs as the tool moves away from the welded material and the aluminum solidifies to become solidly welded. The retractable pintool enables a weld strip that can end without leaving a hole in the workpiece. The mechanism of the actual placement of the flowable material in front of the pintool to a position behind the pintool is the primary topic of research.

Friction stir welding offers advantages over more traditional welding methods, including higher joint strength, lower residual stress, improved microstructure, lower energy consumption, and lower joint weight. Such advantages make friction stir welding methods potentially very valuable in manufacture and repair of traditional structures as well as for the next generation of reusable launch vehicles. The technology has far outdistanced the theoretical understanding and mathematical modeling of the friction stir welding technique. The development of mathematical models would appear to be a very logical task. Such models have potential applications in manufacturing planning and simulation, and thus would aid in the development of advanced manufacturing techniques applicable to large scale composite structures for cryogenic and dry applications.

It is convenient to divide the NCAM supported work into four parts. The first is the development of a three dimensional transient heat conduction finite element based code capable of dealing with moving heat sources. The second is the identification and development of closed form solutions for heat transfer due to moving sources. The third is the creation of a simplified thermal network model of the heat transfer processes associated with friction stir welding. The fourth is the development of a semi-analytical model of the metal flow and heat transfer in the vicinity of the moving pintool. All four parts of the work have been completed. Only the finite element modeling will be discussed in detail in the present paper in order to conform to the page length limitations associated with this conference. However, some important conclusions that are pertinent to the other three parts will be listed.

METHODOLOGY

A finite element analysis of transient heat conduction was carried out with the intent of identifying the thermally active zone associated with current applications of friction stir welding. The model accommodates a moving heat source that simulates the applied heat flux that, in turn, simulates the frictional heating associated with

the rotating pintool. The analysis was accomplished using both two and three- dimensional finite element formulations.

The theory of transient heat conduction is recorded in numerous textbooks, such as Schneider [7], and need not be derived from first principles. The governing equation is second order in temperature T and in Cartesian coordinates is as follows,

$$\rho c \frac{\partial T}{\partial t} = \frac{\partial}{\partial x}\left(k_x \frac{\partial T}{\partial x} \right) + \frac{\partial}{\partial y}\left(k_y \frac{\partial T}{\partial y} \right) + \frac{\partial}{\partial z}\left(k_z \frac{\partial T}{\partial z} \right) + Q \qquad (1)$$

where k_i (i = x, y, z) are the thermal conductivities in the respective directions, _ is the density, c is the specific heat and Q is an external heat source. For an isotropic material, such as aluminum, it is customary to let $k_x=k_y=k_z=k$ and define a thermal diffusivity

$$\alpha = \frac{k}{\rho c} \qquad (2)$$

A finite element formulation lends itself toward maintaining the definition of Equation (1). Even though the material is isotropic, the thermal conductivities may be temperature dependent and could vary from element to element. The term _c is called the thermal capacity and can be assumed constant or variable.

Boundary conditions may have a significant effect upon modeling the friction stir process and three types of boundary conditions were deemed appropriate. The most elementary boundary condition involves specifying the temperature at specific locations and is referred to as a boundary condition of the first kind. A boundary of the second kind involves specifying a heat flux at a specific location. The heat flux is the heat-transfer rate per unit area in terms of the local temperature gradient in a direction normal to the surface. The outward heat flux is defined as q and is defined as follows

$$q_i = -k_i \delta_{ij} \frac{\partial T}{\partial x_j}, \qquad q = n_i q_i \qquad (3)$$

where δ_{ij} is the Kronecker delta and n_i is an outward unit vector normal to the surface. Classically, the boundary condition of the third kind is called a convective boundary condition and is defined as

$$q = h\left(T - T_\infty\right) \qquad (4)$$

where h is the convection coefficient and T_∞ is the temperature of the surrounding atmosphere.

Equation (1), subject to any of the aforementioned boundary conditions, was solved numerically using the finite element method of analysis. Any or all of the material properties that have been discussed can be temperature dependent and may vary within the coordinate space defining the problem. An isoparametric four node quadrilateral finite element was used for two-dimensional studies, while an eight node brick isoparametric element was used for three-dimensional studies.

Finite elements for heat conduction can be derived using the classical Rayleigh-Ritz method or as an application of the Galerkin method. Specific details can be found in Buchanan [1], or for an in- depth treatment, Reddy [5].

RESULTS AND DISCUSSION

Fundamental numerical studies were carried out in an attempt to identify the thermally active zone that would occur during solid-state friction stir welding. Initially it was assumed that heating occurred at the surface of the aluminum specimen and was distributed into the aluminum slab through the process of conduction. Therefore, a flux was applied at the surface of the specimen and the time dependent temperature distribution was computed. The aluminum specimen is shown in Figure 1 and was modeled after that reported by Chao and Qi [2]. The heat flux was applied on the surface, z=6.4mm, x=0 along the y axis, which is a line of symmetry along the direction of an assumed moving heat source. Numerous models were studied and the results reported here correspond to a specimen with actual dimensions, h=6.4mm, W=20mm (one-half of the width because of symmetry) and L=60mm. Representative values were assumed for material constants, k=220$Wm^{-1}C^{-1}$ and _c=2.5(10^6)$Jm^{-3}C^{-1}$.

Throughout the numerous studies additional results were computed for different values of the convection coefficient defined as h in Equation (4). Based upon [2] h was initially assumed as 30$Wm^{-2}C^{-1}$ for free surfaces exposed to air and 200 $Wm^{-2}C^{-1}$ for the bottom surface of the specimen that rested upon an anvil. The surface x=0 is a line of symmetry and was treated as insulated. Varying the convective heat transfer coefficient over a reasonable range of values did not have much effect upon the final results.

A heat flux was applied at the surface (x=0, y=6.4mm, z=0) beginning at x=0 and moved with velocity 2mm/sec in the y direction. Eventually, the heat source was assumed to have a width of 10mm based upon the diameter of the pintool being 19mm. The limiting temperature at the surface of the specimen or at any other location was initially assumed to be approximately 450 °C. The highest temperature consistently occurred at the surface of the specimen where the heat flux was applied. In order for the welding process to occur the temperature distribution would be required to reach a limiting temperature where the aluminum could approach a melting temperature and the stirring action could begin to occur. Numerous numerical experiments were performed and in every case it appeared that the temperature at the surface would be well above the limiting temperatures before the material inside the specimen was hot enough for welding (stirring action) to occur. The conclusion was that heating would need to occur inside the specimen and that the model should approximate such an action.

The applied heat flux was then modified and was applied across the specimen on the surface extending 10mm along the x direction as in the previous analysis and also approximately 5mm into the depth of the specimen along the z axis. The total distributed heat flux was again assumed to move with velocity of 2mm/sec along the y direction. Typical results are shown in Figures 2 and 3. Figure 2 corresponds to the temperature distribution at 10 seconds, when the flux has moved 20mm along the y axis. Figure 2c shows the computed temperature distribution along the x axis when the flux is applied in both the x and z directions. The temperature at the surface is about 400 degrees and about 310 degrees at the bottom of the specimen. Obviously, these temperatures are not sufficient to support the friction stir process. Attention is directed to Figure 3c that shows the results when the source reaches 40mm or 20 seconds into the process. The temperature is significantly higher at the surface and is well over 450°C at 13mm above the base of the specimen. In other words, the temperature distribution is believable in terms of supporting the friction stir welding process. Figures 2d and 3d show the corresponding temperature distribution along the y axis and x=0. At 10 seconds the temperature behind the source is about 280 degrees and is about 100 degrees in front of the source. At 40mm, 20 seconds, the temperature is close to 320 degrees at some distance in front of and behind the flux source, also at the same time the temperature at 20mm out the x axis is nearly the same, about 340 degrees.

Figures 2a and 2b correspond to Figures 2c and 2d in every respect except the flux is applied only on the surface. The results verify that a uniform distribution of temperature in the z direction does not seem to be possible when only the surface is heated. Again, Figures 3a and 3b correspond to surface heating when the source reaches 40mm, 20 seconds.

Additional results are shown in Figures 4 and 5 in the form of contour plots of temperature at 10 seconds and 20 seconds and correspond to the results of Figures 2c and d, and 3c and d. The flux has moved 20mm in Figure 4 and it can be observed that the heating behind the source is still uneven along the x axis. In other words, considerable heat is being lost through the surface y=0. Figure 5 demonstrates the somewhat symmetrical distribution of temperature when the source reaches 40mm. In fact, once the source is sufficiently beyond the free

surface y=0, a somewhat steady distribution of temperature moves uninterrupted along the x axis. The additional contour plots in Figures 4 and 5 are slices removed from the specimen at the various locations and give a visual representation of the temperature distribution.

Figure 6 is included as a contour plot of the results shown in Figures 3a and 3b. The contour slices show the insufficient heating into the depth of the specimen.

CONCLUSIONS

Two important conclusions were drawn from the work was concerned finite element modeling of the thermally active zone associated with solid state friction stir welding. These are that the applied heating must extend into the specimen in order to maintain a thermal distribution that would support friction stir welding and that modeling the heat conduction process requires a model of sufficient length to develop the heat flow in front of and behind the applied flux, but will not necessitate modeling the entire specimen.

The important conclusion that can be drawn from work on closed form solutions is that realistic models of friction stir welding must sometimes account for transient heating effects. Based on physically realistic input data, closed form solutions predict that the workpiece material temperatures in the immediate vicinity of the pin-tool are functions of time. However, based upon physically realistic input data, no more than two minutes are required to approach to within 90% of the steady solution, and the assumption of a quasi-steady state may often be justified.

The work on the thermal network model leads to the conclusion that such models have potential to predict the temperature distribution throughout workpiece, including the vicinity of the pin-tool. It is required that additional heat transfer mechanisms be incorporated into the model so as to more realistically represent the temperature profile as a function of pertinent input parameters.

Three important conclusions were drawn from the semi-analytical modeling of metal flow and heat transfer in the vicinity of the moving pintool. These are that viscoplastic material models (of which the rigid/perfectly plastic model is a special case) are capable of predicting the main features of metal flow associated with friction stir welding, that the metal flow and heat transfer predictions of the semi-analytical model demonstrate that the spatial scale of heat transfer phenomena is considerably greater than that of metal flow phenomena, and that a special case of the predictions of the semi-analytical model can be put in a form coincident with a thermal network analysis.

ACKNOWLEDGEMENTS

The work reported here was financially supported by the National Center for Advanced Manufacturing. The authors also appreciate the technical support offered by Dr. Art Nunes of the Marshall Space Flight Center.

REFERENCES

1. Buchanan, G.R. Theory and Problems of Finite Element Analysis. Schaum's Outline Series, New York: McGraw-Hill, 1995.
2. Chao, Y.J. and X. Qi., Thermal and Thermo-Mechanical Modeling of Friction Stir Welding of Aluminum Alloy 6061-T6. Journal of Materials Processing and Manufacturing Science. Vol. 7. 1998. 215-233.
3. Colligan, K. Material Flow Behavior during Friction Stir Welding of Aluminum, Welding Journal. Vol. 78. 1999. 229s-237s.
4. Li, Y., L.E. Murr, and J.C. McClure. Solid-State Flow Visualization in the Friction-Stir Welding of 2024 Al to 6061 A1, Scripta Mateialia. Vol. 40. 1999. 1041-1046.

5. Reddy, J.N. An Introduction to the Finite Element Method, 2nd edition. New York: McGraw-Hill, 1993.

6. Reynolds, A.P. Visualization of Material Flow in Autogenous Friction Stir Welds, Science and Technology of Welding and Joining. Vol. 5. 2000. 120-124.

7. Schneider, P.J., Conduction Heat Transfer. Cambridge: Addison-Wesley. 1955

8. Seidel, T.U. and A.P. Reynolds. Correlation of Weld Temperatures with Material Flow in Solid-State Friction Stir Welds, Developments in Theoretical and Applied Mechanics. Vol. 20. Paper MF90. 2000.

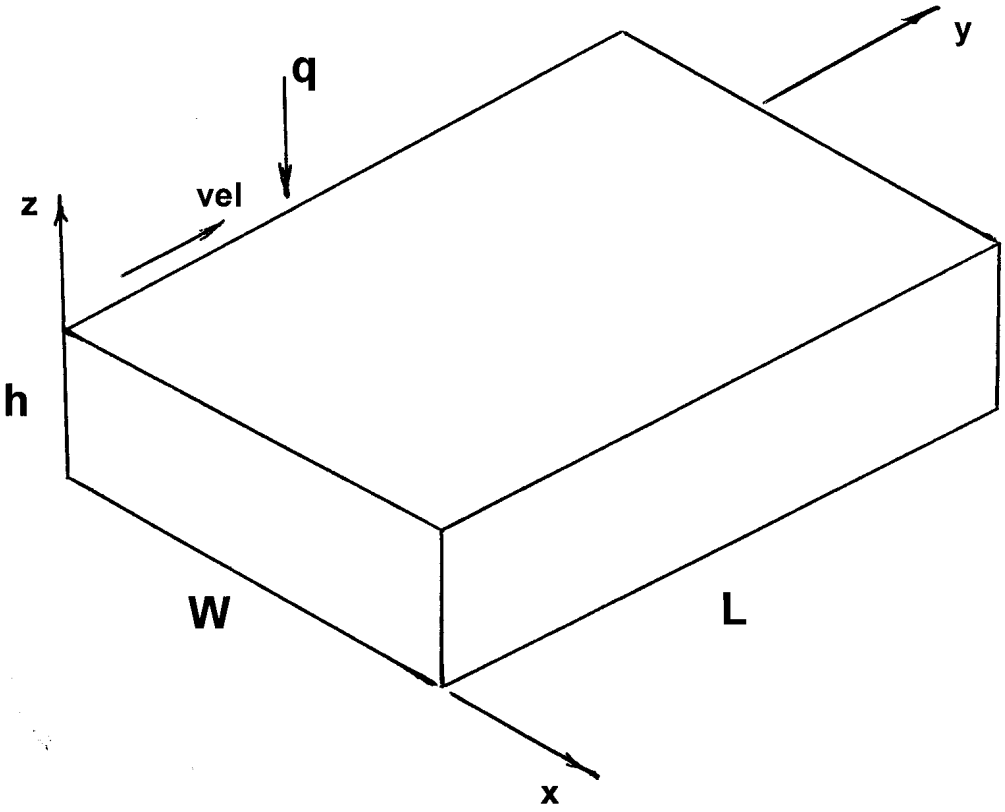

Figure 1. Specimen and Coordinate System

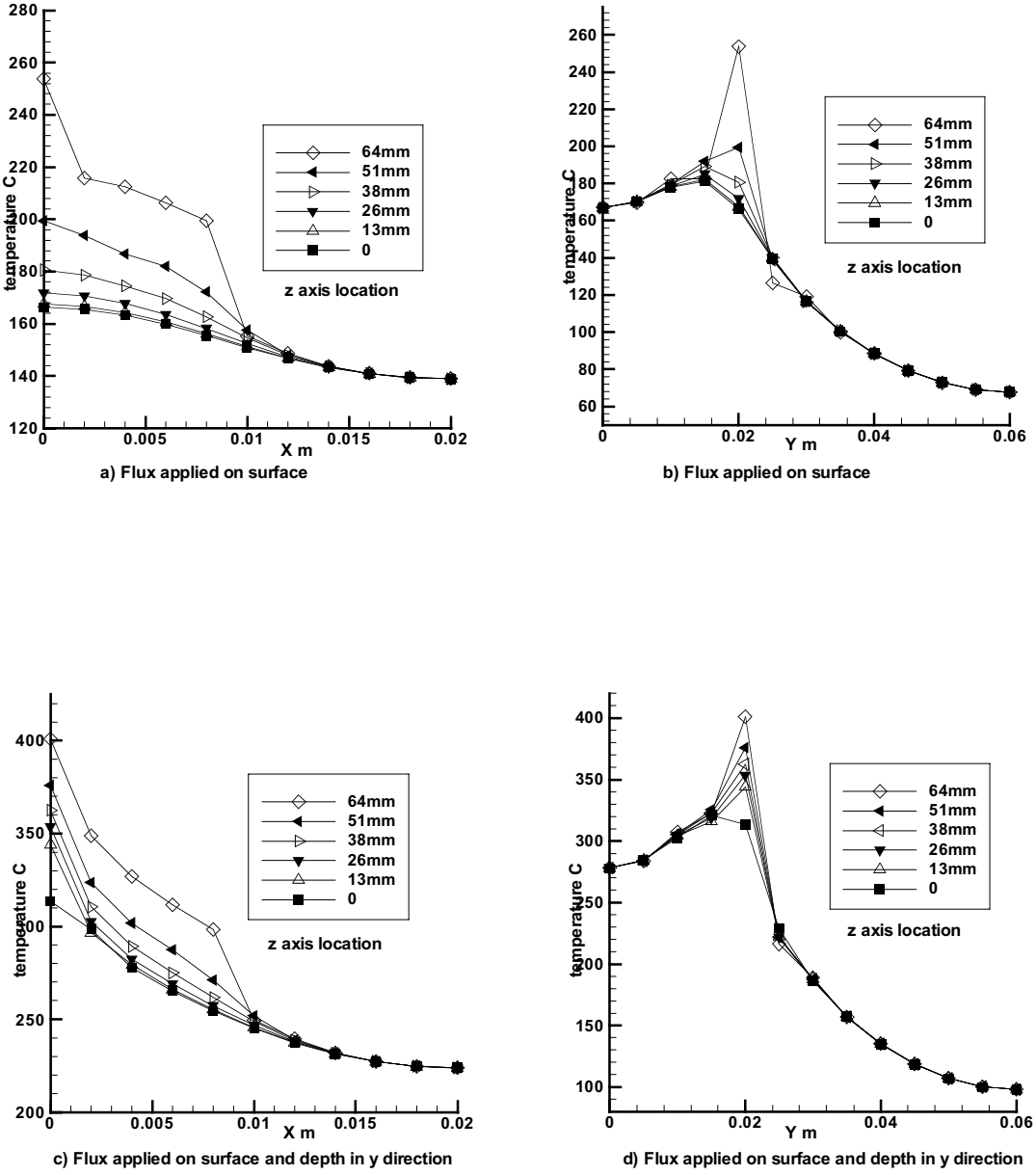

Figure 2. Temperature Distribution at 10 Seconds for Heat Flux Positioned at 20mm Along the y Axis

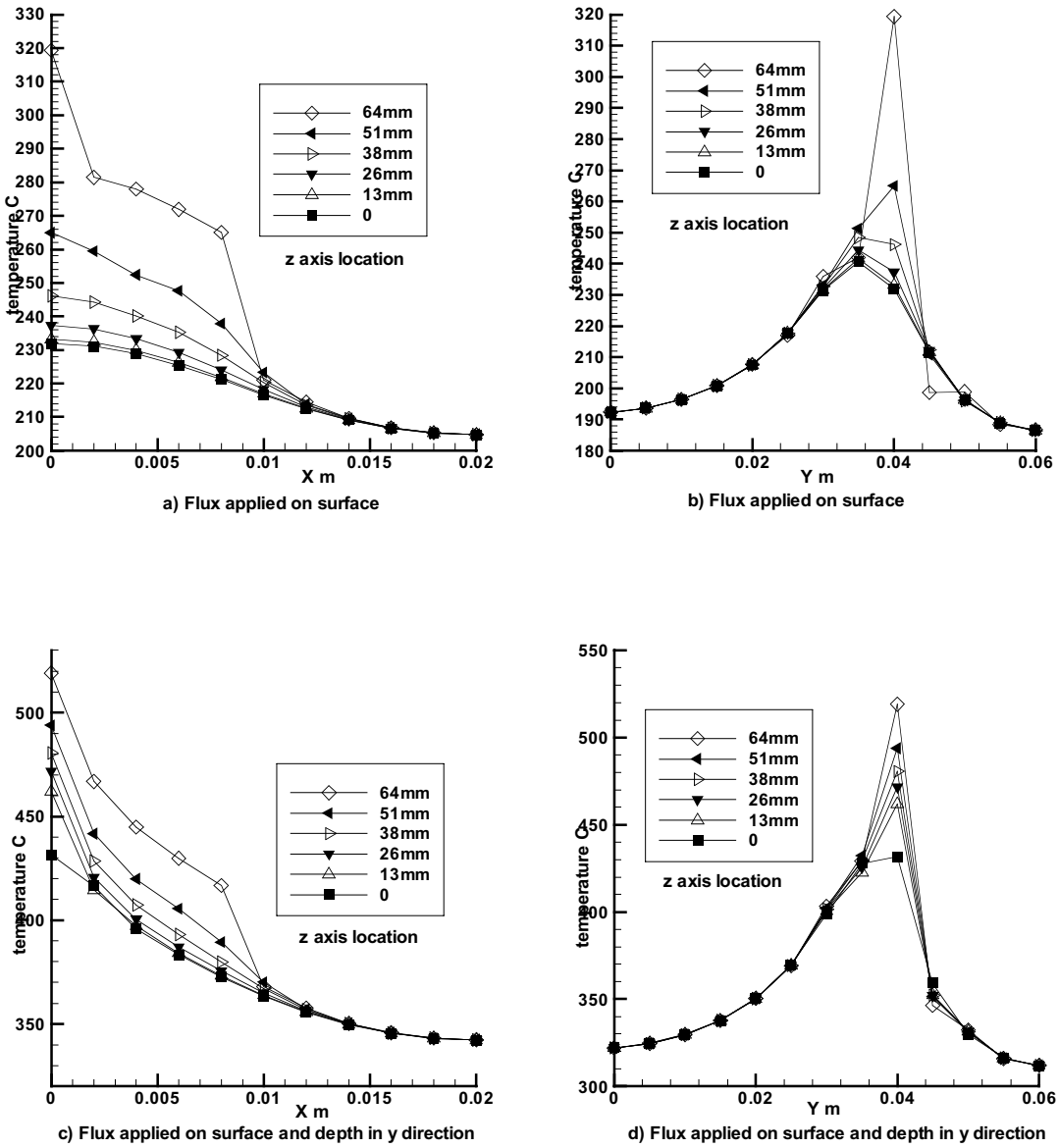

Figure 3. Temperature Distribution at 20 Seconds for Heat Flux Positioned at 40mm Along the y Axis

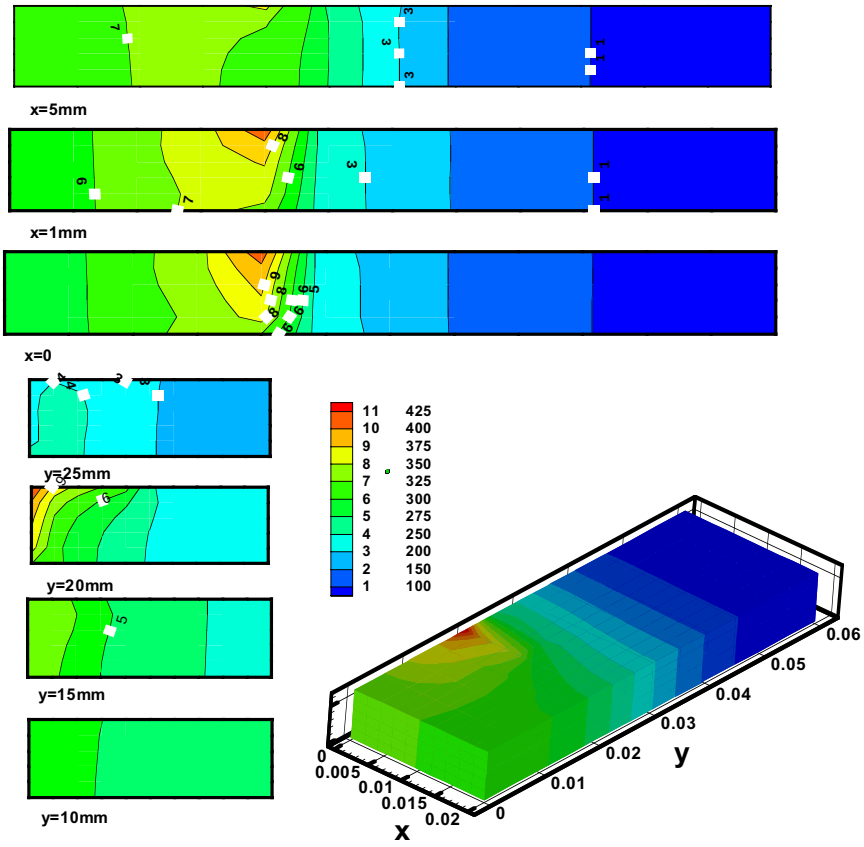

Figure 4. Contour Plot and Contour Slices Showing Temperature Distribution at 10 Seconds for Heat Flux Applied on Surface and Depth in the z Directions

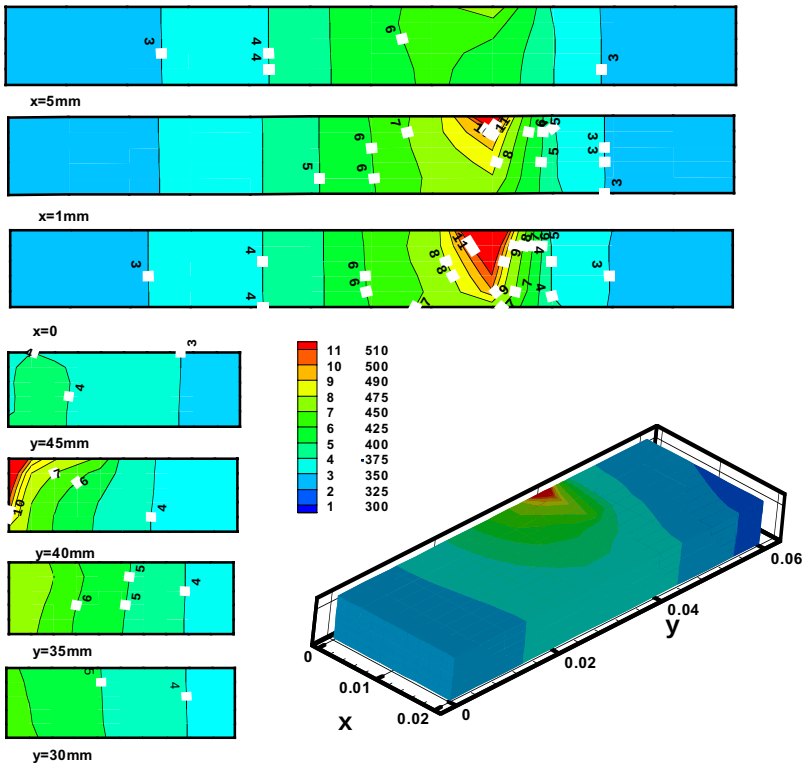

Figure 5. Contour Plot and Contour Slices Showing Temperature Distribution at 20 Seconds for Heat Flux Applied on Surfaces and Depth in the z Direction

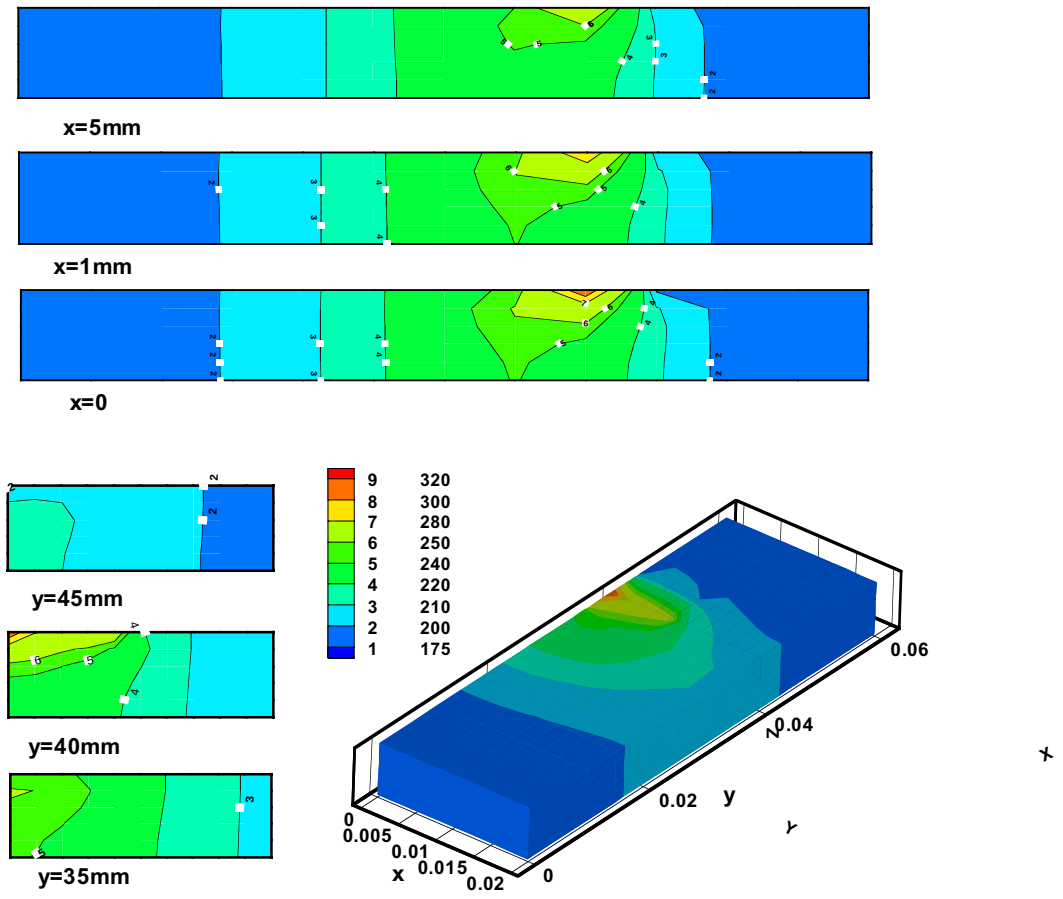

Figure 6. **Contour Plot and Contour Slices Showing Temperature Distribution at 20 Seconds for Heat Flux Applied only on the Surface**

Non-Autoclave Processing of Large Re-Usable Aerospace Structures

AL LOOS
National Center for Advanced Manufacturing
and
Department of Engineering Science and Mechanics
Mail Code 0219, 320 Norris Hall
Virginia Polytechnic Institute and State University
Blacksburg, VA 24061
Phone: 540-231-4713
E-mail: aloos@vt.edu

Romesh Batra, Robert H. Sturges, and Dwight D. Vieland
National Center for Advanced Manufacturing
and
Virginia Polytechnic Institute and State University
Blacksburg, VA 24061

High-specific strength and stiffness make composite materials ideal for aerospace applications; however, widespread use of composite materials for these applications has been limited by high manufacturing costs. Current autoclave methods for manufacturing reusable aerospace structures are time-consuming, expensive, and unreliable. Additionally, these methods are not conducive to the manufacturing of new "smart" composite materials with embedded sensors. Non-autoclave processes that reduce material and assembly labor costs must be developed for composites to compete effectively with traditional materials.

The overall objective is to investigate the use of cost effective, non-autoclave manufacturing techniques for fabricating large, reusable composite structures for aerospace applications. Over the course of this 3-year initiative, three parallel tasks will be integrated to achieve the project objective:

- First, develop non-autoclave processes for manufacturing composite materials.
- Second, realize an intelligent manufacturing system for composite materials and structures.
- Third, develop innovative manufacturing methods for nondestructive evaluation (NDE) and enhanced reliability.

Composite fabrication is a complex process with numerous physical phenomena occurring simultaneously, including heat transfer, resin flow, ply compaction, resin cure kinetics, and void growth and collapse. The Virginia Tech interdisciplinary research team will develop comprehensive models for composite manufacturing and develop new sensor materials for NDE of composite systems.

Precision Clean Hardware: Maintenance of Fluid System Cleanliness

Sheila Sharp
Materials & Processes
International Space Station Program
September 18, 2002

Acknowledgements

- All work conducted under NASA contract
  - NAS15-10000 International Space Station Integration and Operations
- Co-authors
  - NASA
    - Dr. Mike Pedley, Tim Bond
  - Boeing
    - Joseph Quaglino, Mary Jo Lorenz, Michael Bentz, Richard Banta, Nancy Tolliver, John Golden, Ray Levesque, and Sarah Densmore

S110E6027

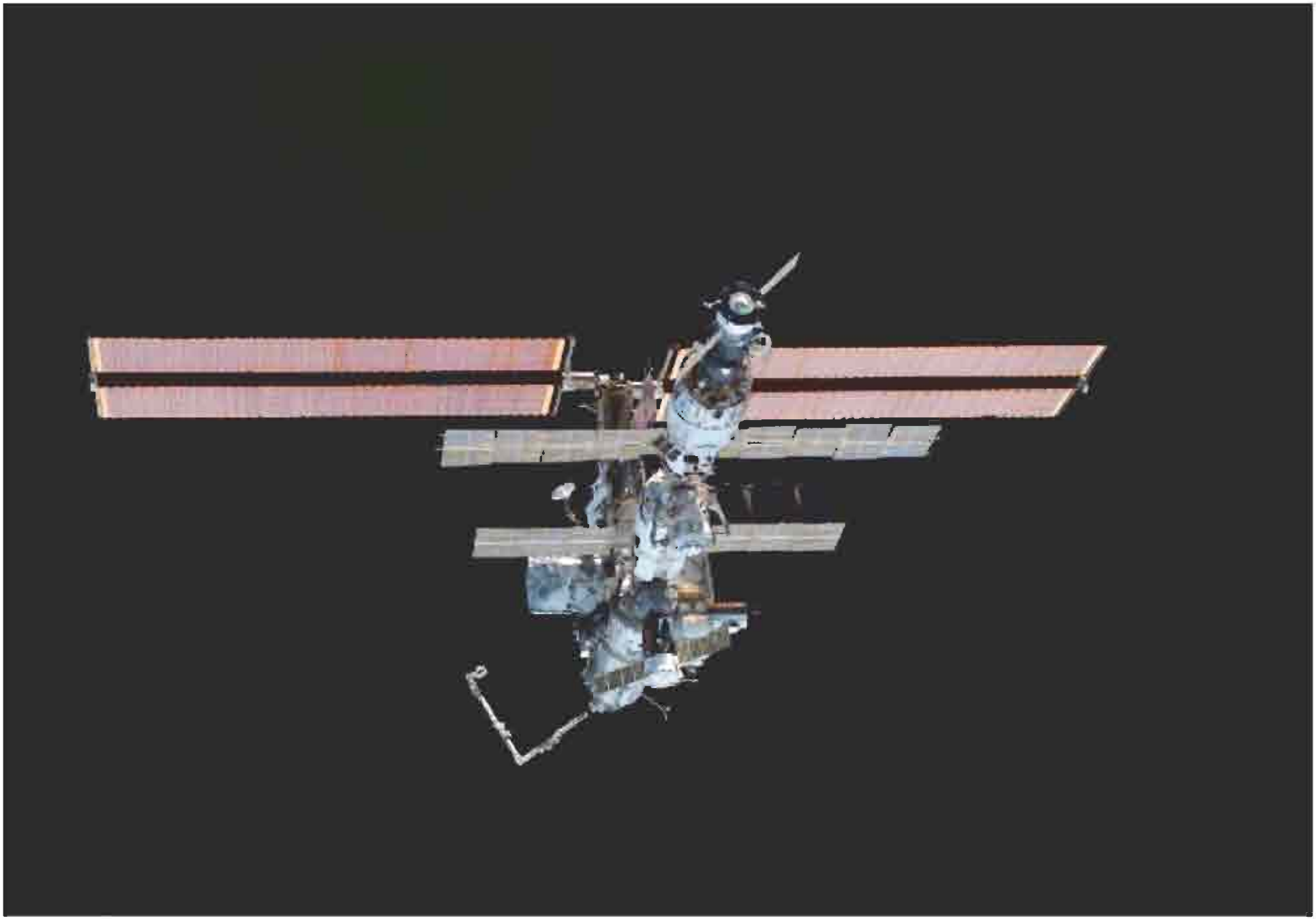

S11DE5905

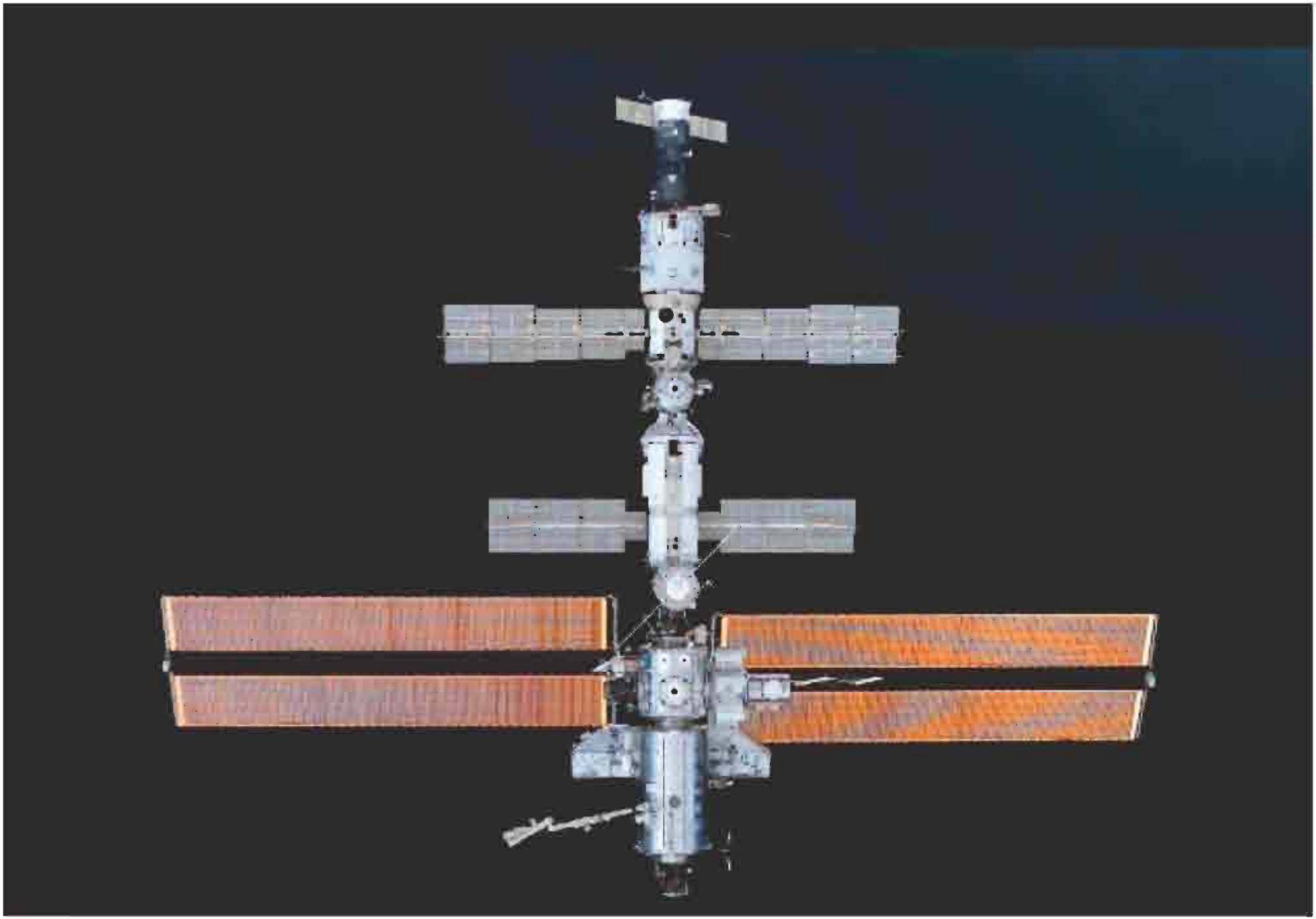

S11DE5932

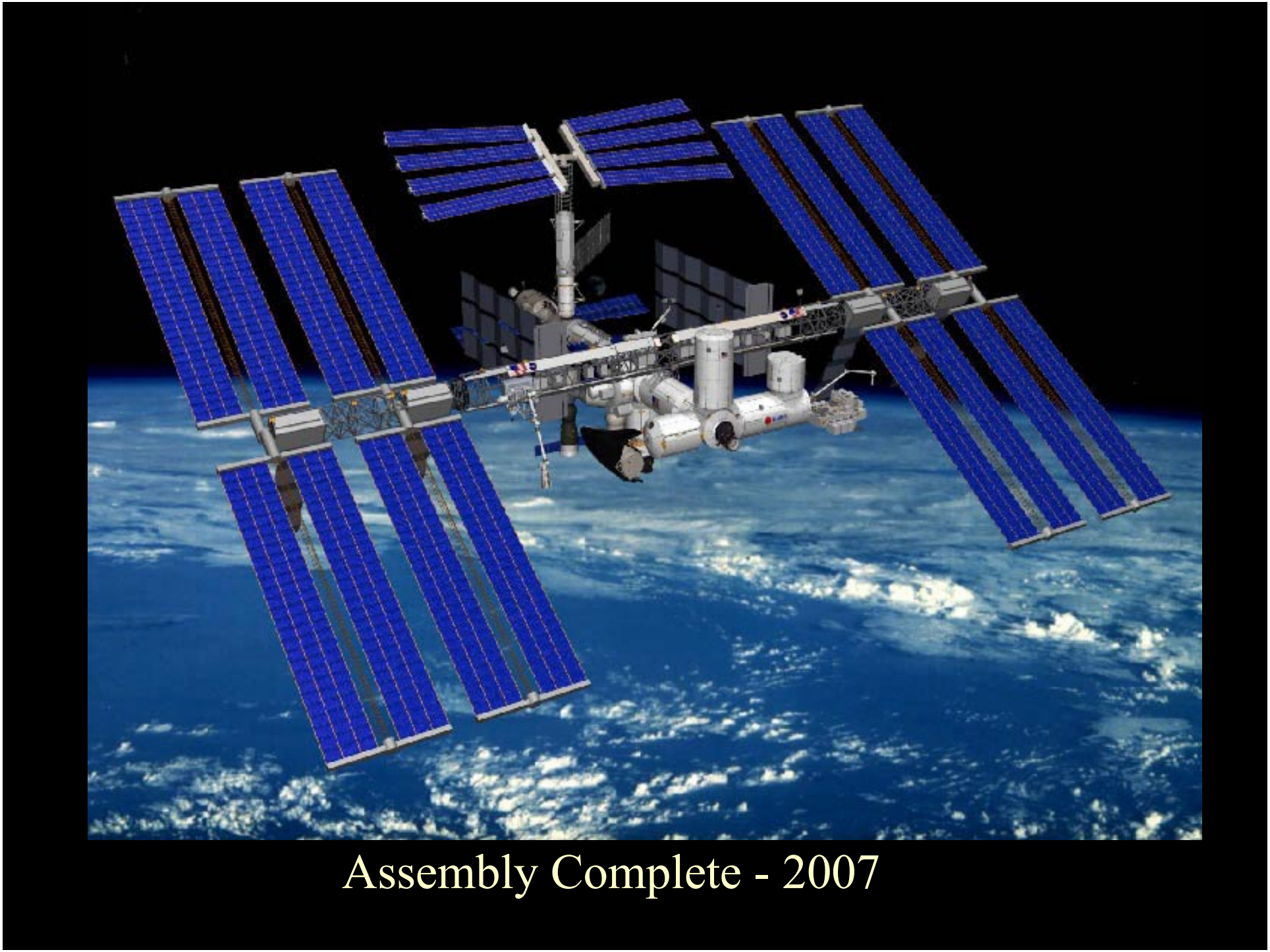

Assembly Complete - 2007

Philosophy

- The ISS fluid systems are so complex that fluid system cleanliness cannot be verified at the assembly level.
- A “build clean / maintain clean” approach was used by all major fluid systems.
  - Verify cleanliness at the detail and subassembly level.
  - Maintain cleanliness during assembly.

Background

- Leakage in ISS ammonia system Quick Disconnect (QD) hardware led to the establishment of a “Clean Team”.
- Analysis of contaminants indicated multiple contamination sources.
- “Clean Team” was to identify and eliminate as many contamination sources as possible.

Background cont'd

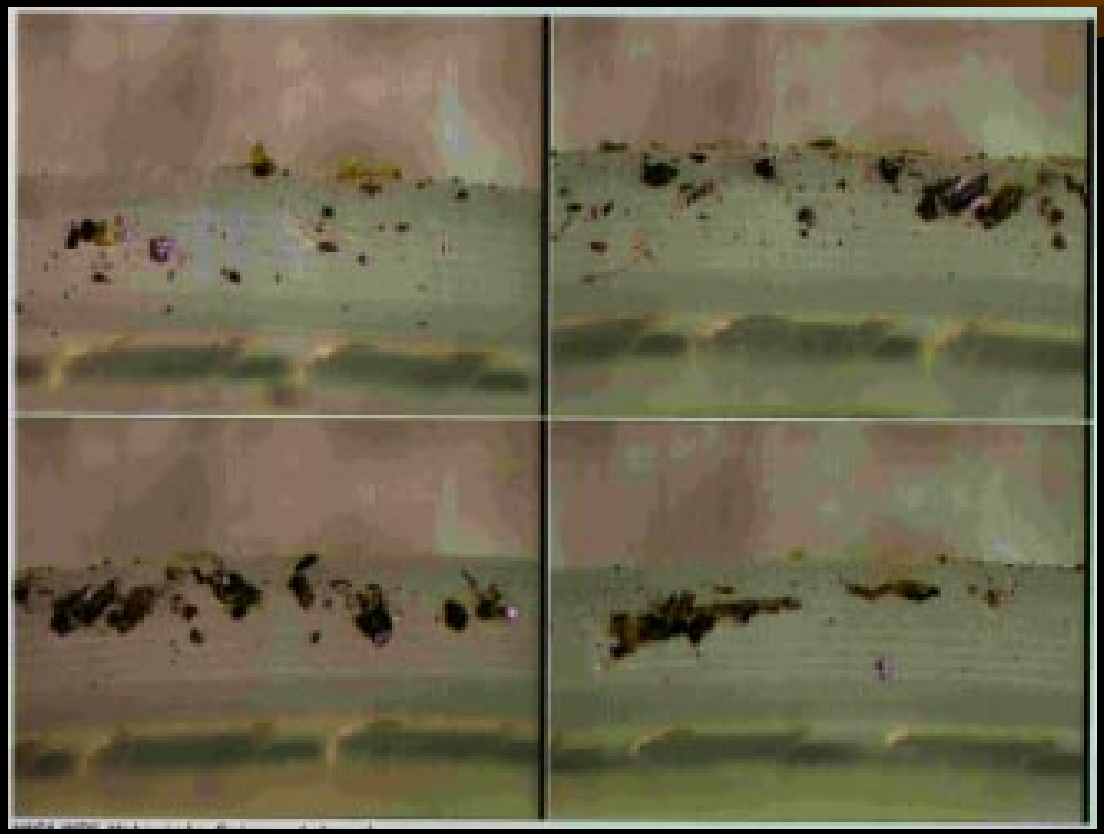

Figure 1. Contaminated QD Seal

Background cont'd

- Clean Team visited the ISS hardware manufacturing sites and reviewed all procedures used to produce and maintain precision cleaned hardware.
- Result was a set of recommendations or "best practices" to be used in the manufacture of precision cleaned hardware.

Documentation

- ISS-PI-044,
  Maintenance of Fluid Systems Cleanliness
- SSP 30573,
  Space Station Program Fluid Procurement and Use Control Specification

Training

- All personnel working around precision cleaned hardware in the ISS program are required to attend TR001484, ISS, Maintenance of Fluid Systems Cleanliness training course

Definition of Precision Cleanliness

- Clean rooms are enclosed, environmentally controlled areas for the performance of work on contamination sensitive hardware or assemblies. Consists of Class 100,000 or cleaner.
- Precision cleanliness shall be maintained to program requirements (e.g. SN-C-0005 Level 200)
  - SN-C-0005 Level 200 states that there should not be any particles of a size greater than 200 microns present in a 100 milliliter sample of fluid from the system

Welding Practices

- All welding of assemblies for precision cleaned hardware will be performed in a dedicated class 100,000 Clean Work Area (CWA)
- Temporary tents and local monitors may be required to maintain the 100k environment

Welding Practices cont'd

- Accurate monitoring of local contamination is required
- Portable particle counters shall be located as close to the work area as possible during tube preparation and welding

Welding Practices cont'd

- A proven method of contamination prevention such as tube plugs is required
- Installation and removal of such plugs shall be tracked and independently verified by Quality Assurance
- Prior to plug removal, the tube ID shall be cleaned with a swab and approved solvent
- Positive back pressure shall be maintained as the plug is removed

Welding Practices cont'd

Figure 2. Damage from not removing a plug

Welding Practices cont'd

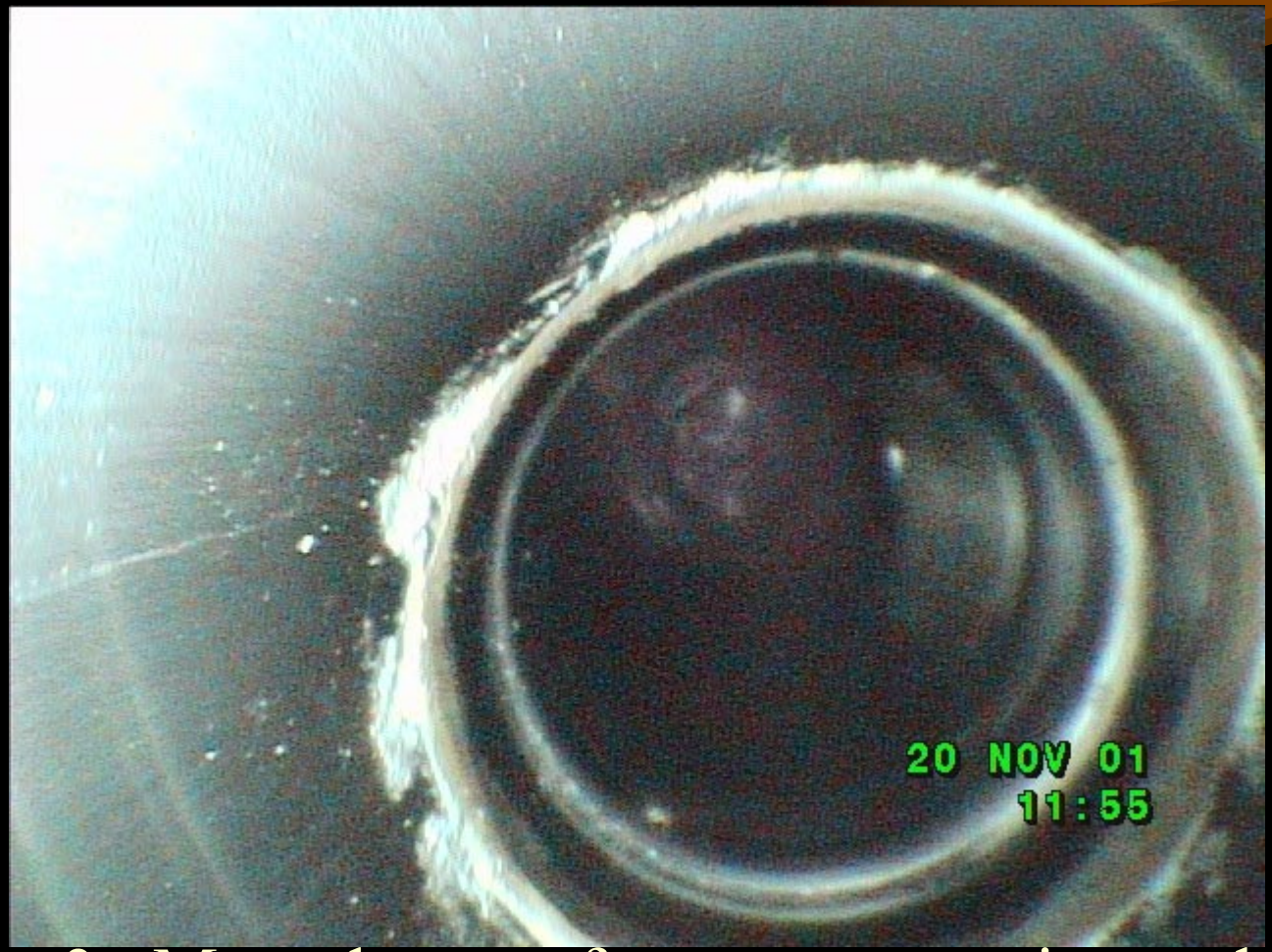

Figure 3. More damage from not removing a plug

Welding Practices cont'd

- After each tube preparation and prior to welding, a high-velocity gas blow down shall be performed
- Gas velocity target shall be the maximum attainable using a 90 psig purge gas source
- CAUTION, use only approved purge gases per SSP 30573

Welding Practices cont'd

- Tube cutters shall use a sharp blade, changed frequently
- Cutting shall be performed with minimal cutting pressure to prevent particle generation

Tube Facing Practices

- Vacuum shall be used during tube facing operations
- Whenever possible, facing operations shall be performed away from the weld assembly area
- Tube facing shall be accomplished without the use of cutting oils, lubricants or coolants
- Abrasives, such as sandpaper or abrasive pads shall not be used inside tubes or when unprotected internal surfaces are exposed

Tool Preparation

- Inspection tools (e.g., borescopes) that may be exposed to precision cleaned systems hardware shall be visibly cleaned and maintained clean
- Tools used in weld preparation and welding, such as cutters, weld heads and files, shall be visibly cleaned and maintained clean (e.g. bagged when not in use).

Tool Preparation cont'd

- Purge caps, mating QDs and vent tools shall be precision cleaned to at least the level of the associated system and bagged after use

Purge Gas Practices

- Purge gas used during facing and welding shall meet the hydrocarbon and particulate controls per SSP 30573
- Purge gas used during facing and welding shall be supplied through precision cleaned low NVR/particulate tubing such as polyethylene, nylon, Teflon, or ethyl vinyl acetate
- Standard grade Tygon is not suitable

Ground Support Equipment

- Ground Support Equipment (GSE) that interfaces with precision cleaned flight fluid systems shall incorporate interface filters per SSP 30573
- These filters shall be located as close to the interface as possible
- Outlet lines require filters if it is determined that reverse flow could occur during the servicing or deservicing operation

Ground Support Equipment cont'd

- GSE that interfaces with precision cleaned flight fluid systems shall be cleaned to at least the level of cleanliness of the flight hardware
- GSE fluid hardware, such as hoses and servicing units shall be handled with the same cleanliness procedures as flight hardware

Cleaning Convoluted Flex Hoses

- Cleaning Convoluted Flex hoses requires special attention
- Detail flex hoses shall be cleaned and verified precision clean in a vertical orientation:

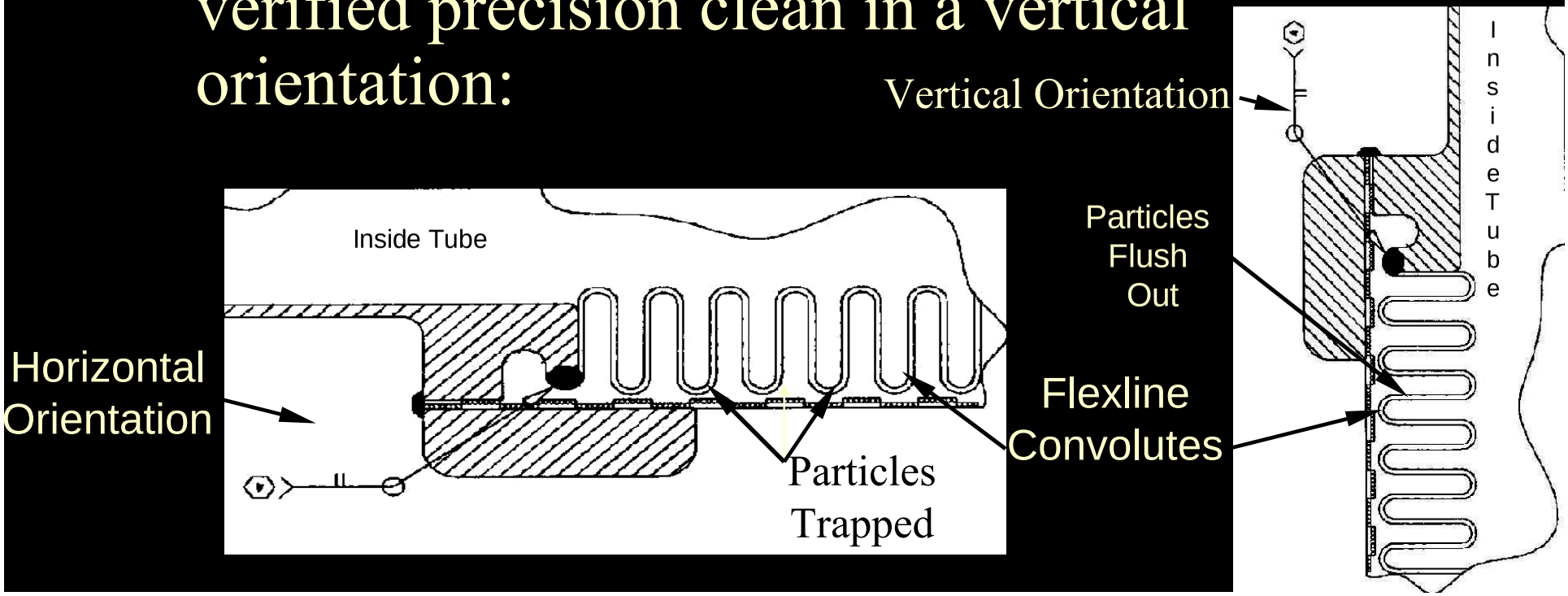

Cleaning Convoluted Flex Hoses cont'd

- Cleanliness is verified by sampling the rinse fluids. The sample must meet the flex hose engineering cleanliness requirement
- For flex hoses that are one inch or greater in diameter
  - Rinse fluid is applied to all internal surfaces with a high pressure nozzle

Cleaning Convoluted Flex Hoses cont'd

- For flex hoses that are less than one inch diameter
  - Use of high pressure nozzles is preferred, but cleaning by flushing the rinse fluid though the length of the hose with agitation is acceptable

Maintenance of System Cleanliness

- All precision cleaned open tubes and lines must be protected, i.e. wrapped or bagged with approved materials, as soon as possible after fabrication
- Tubes and lines must remain wrapped until final installation

Oxygen Systems

- Regulators used during purging operations shall have O_2 compatible grease
- Purge tubing must be O_2 compatible
- Bagging materials used to store O_2 components shall be cleaned to the same level of cleanliness as the O_2 hardware, and must be O_2 compatible

Sampling for Residual Solvent

- Liquid solvents become trapped in crevices or absorbed into soft goods.
- Some fluid systems are quite sensitive to these contaminants.
- ISS uses a 24-hour “lock up”, to ensure gas sampling accurately reflects residual solvent concentration.

General Practices

- Solvents such as IPA, reagent grade or better, shall be filtered to 10 microns or better prior to use
- Precision cleaned hardware that has been welded shall remain properly capped during the x-ray operations to avoid potential contamination

General Practices cont'd

- Hardware that has not been precision cleaned shall not be brought into the vicinity of unprotected precision cleaned flight hardware
- Flight hardware must be wrapped in approved packaging material
- All precision cleaning fluid systems configured for flight shall have integrity seals installed

General Practices cont'd

- Precision cleaned hardware can not be exposed to an uncontrolled environment.
  This includes flow benches providing 100,000 CWA or better during inspections
- Bag hardware that must be transported outside the clean room
- Clean room gloves are required when handling any precision cleaned flight hardware

Summary

- Many of the “best practices” are simple and straightforward.
- However, the different heritage ISS organizations had different priorities for meeting the same end product requirements.
- The “Clean Team” has provided a common focus, and significantly reduced the incidents of contamination induced failures.

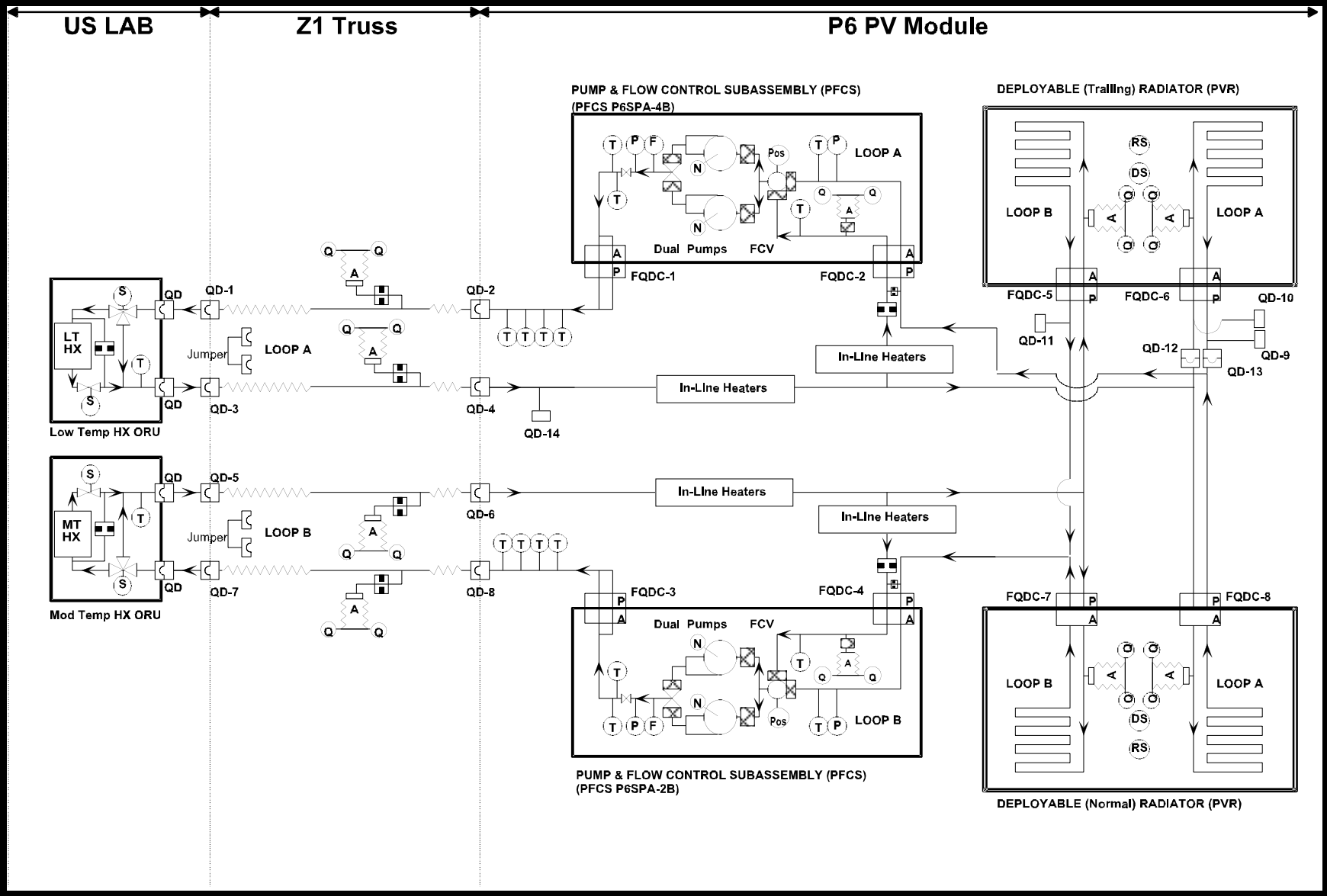

External Thermal Control System Schematic

Title: **Novec™ Engineered Fluids**

Author: David A. Hesselroth
3M Performance Materials Division
Bld. 236-2B-01, 3M center
St. Paul, MN 55144
651-736-6191
dahesselroth@mmm.com

Novec™ Engineered Fluids are useful as cleaning solvents, carrier solvents, heat transfer liquids, Halon replacements and machining lubricant fluids. Currently there are twelve commercial Novec™ products. Four pure segregated hydrofluoroether (HFE) products, five segregated hydrofluoroether azeotropic blended products, two segregated hydrofluoroether machining blends and one perfluoroketone. The physical and Environmental, Health, Safety and Regulatory (EHS&R) properties with discussion about the advantages of using blends of HFEs in cleaning applications will be the major focus of this paper.

The aerospace industry has taken advantage of the hydrofluoroether products to meet the changing environmental and health restrictions put on many solvents. Their ability to remove both hydrocarbon and halocarbon soils make them useful in many areas. The neat products are oxygen compatible making them excellent for particulate removal and verification solvents. Testing has shown that the Novec™ solvents will meet the qualification tests required in most aerospace specifications that are controlled by major airframe manufacturers, the U.S. Military and NASA. The electronics, semiconductor, medical industries as well as many other industrial applications take advantage of the excellent environmental properties, worker exposure guidelines as well as the range of solvents strengths and compatibilities. As the number of Novec™ products grows, through new HFE molecules, azeotropes and blends, the number of applications will expand.

The segregation of the hydrofluoroether molecule makes the Novec™ hydrofluoroether fluids unique. Testing has shown [1] that separating the carbon/fluorine bonds from the hydrogen/carbon bonds across the ether linkage leads shorter atmospheric lifetimes. The Fluorochemical side of the HFE molecule provides excellent stability in thermal and chemical applications while the hydrocarbon side enhances the hydrocarbon solubility, useful in cleaning applications. As with other halogenated materials they have high density, low viscosity and surface tension. The neat hydrofluoroethers do not contribute to smog formation and qualify for VOC exemption by the U.S. EPA. All of the Novec™ products are non-flammable, non-ozone depleting (ODP) and have Global Warming Potentials (GWP) below 400. The information listed in Table 1&2 contain environmental information for the HFE products.

Table 1, Environmental Properties Novec™ Engineered Fluid Neat Hydrofluoroethers

	HFE-7100	HFE-7200	HFE-7000	HFE-7500
Ozone Depletion Potential (ODP)	**0**	**0**	**0**	**0**
Volatile Organic Compound (VOC)	**Exempt**	**Exempt**	**Pending**	**Pending**
Atmospheric Lifetime	**4.1**	**0. 8**	**4.7**	**2.2**
Global Warming Potential (100 yr-ITH)	**320**	**55**	**400**	**100**

Table 2 Environmental Properties of Novec™ Engineered Fluids Azeotropes

	HFE-71DE	HFE-72DE	HFE-71DA	HFE-72DA	HFE-711PA
Ozone Depletion Potential (ODP)	0	0	0	0	0
% VOC exempt	50%	30%	54%	30%	95%
Atmospheric Lifetime (HFE Portion)	4.1	0.8	4.1	0.8	4.1
Global Warming Potential (100 yr-ITH)	160	43	172	43	304

The family of HFEs has grown to four main molecules with boiling points ranging from 34 to 130 C. Their high molecular weight, low viscosity, low heat of vaporization and low surface tensions have been found beneficial for solvent containment in vapor degreasing cleaning applications. The viscosity and surface tension have also been proven beneficial for particulate removal and applications where surface wetting is important. When blended with other solvents the solvency of HFEs can be enhanced without significantly compromising the EH&SR properties of the materials. Tables 3&4 contain physical property information for the Novec™ Engineered Fluids.

Table 3 Physical Properties

	HFE-7100	HFE-7200	HFE-7000	HFE-7500
Boiling Point, (°C)	61	76	34	130
Freezing Point, (°C)	-135	-117	-123	-100
Flash Point	None	None	None	None
Liquid Density, (g/ml)	1.52	1.43	1.40	1.61
Viscosity, (cst)	0.61	0.61	0.32	0.77
Heat of Vap. (cal/g)	29	30	34	21

Table 4 Physical Properties

	HFE-72DE	HFE-72DA	HFE-71IPA	HFE-71DE	HFE-71DA
Boiling Point (°C)	43	42	54	41	40
Flash Point (°C)	None	None	None	None	None
Liquid Density, (g/ml)	1.28	1.27	1.48	1.37	1.33
Viscosity	0.45	0.40	0.48	0.45	0.43
Heat of Vap. (cal/g)	52	60	40	48	50
Kauri-Butanol Value	54	58	11	27	33
Largest Soluble n-Hydrocarbon	22	22	12	16	16

Trans 1,2 dichloroethylene (DCE) has proven to be an excellent solvent in blends with hydrofluoroethers. It forms azeotropes with all of the Novec™ hydrofluoroethers at various percentages. In addition data has indicated that when blended with more than one HFE, the blend of azeotropes assume the properties of the binary mixtures enabling the content of DCE to be varied based on the applications needs for compatibility or solvent strength. Chart 1 shows the Largest Soluble Hydrocarbon values for blends of HFE-7000, HFE-7100 and HFE-7200 with DCE. Table 5 contains information related to the binary azeotropic formulations for the hydrofluoroethers. Boiling point suppression is one of the characteristics of an azeotropic composition. Boiling point suppression is also observed in the blends of azeotropes. The boiling temperature is lower than any single component in the mixture; but is typically between the boiling points of the two-separate azeotropes. As with other azeotropes the blends of azeotropes maintain a consistent composition during distillation. Novec™ Engineered Fluid HFE-72DE and HFE-72DA are examples of commercial solvents containing HFE-7200, HFE-7100 and DCE. This formulation was developed to enable a high percentage of DCE to be used safely in a vapor degreaser. HFE-7200 is a non-flammable hydrofluoroether; however, it has flame limits. Trans 1,2 dichloroethylene is flammable. Blending a flammable solvent with one that has flame limits can reduce the effectiveness of its ability to mitigate flammability. HFE-7100 has been shown to mitigate the flammability of DCE at levels as low as 1% in a vapor degreaser. Adding specific amounts of HFE-7100 to a mixture of DCE and other HFEs causes the boiling liquid to revert to the azeotropic compositions of each component. A blend of HFE-7000, HFE-7100 and DCE can also be formulated to reduce the amount of DCE. The blend possibilities can range from as low as 22% to as high as 70%. Application needs can be met by adjusting the solvent strength. Chart 2&3 contains data measured during evaporation of two solvent blends comparing the composition of the three-component blend to percent evaporated. This data shows that the DCE content will not increase during evaporation maintaining a safe non-flammable composition if solvent is lost.

Chart 1, Largest Soluble Hydrocarbon in DCE/ HFE mixtures
(The arrow indicates the binary azeotropic composition of the individual mixtures)

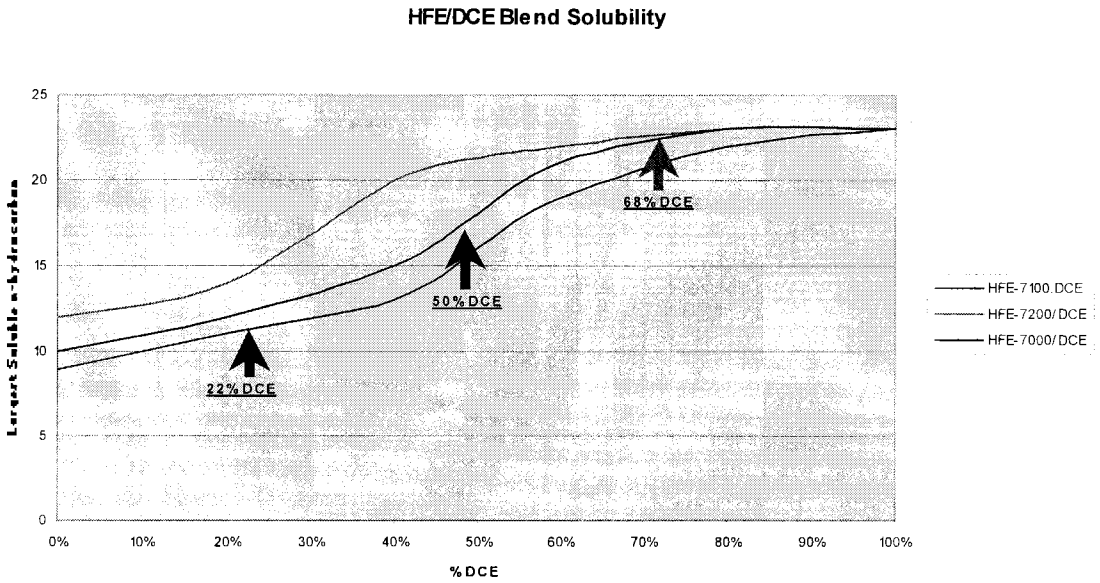

Table 5, Azeotropic percentage of DCE in Novec ™ HFEs

Novec™ Fluid	Azeotropic Composition trans 1,2 dichloroethylene	Largest Soluble n- Hydrocarbon
HFE-7000	22%	13
HFE-7100	50%	16
HFE-7200	68%	22

Chart 2&3 Composition –vs-Evaporation, HFE-72DE and HFE-7000/HFE-7100/DCE Bend

Note that the evaporation profile follows the same compositional shift as a binary azeotrope. The ternary blend will be rich in HFE at the end of evaporation.

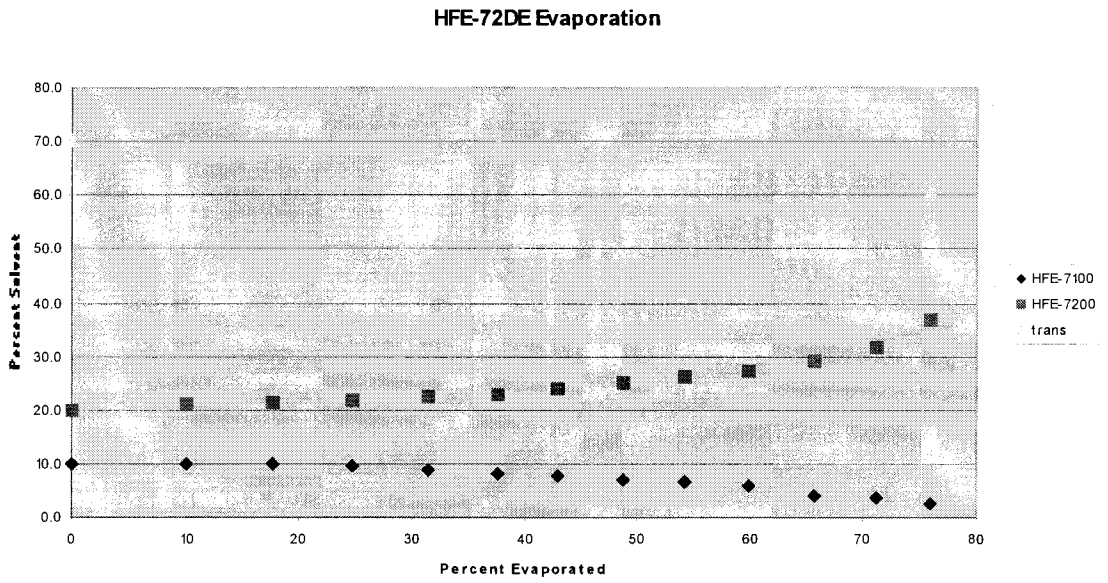

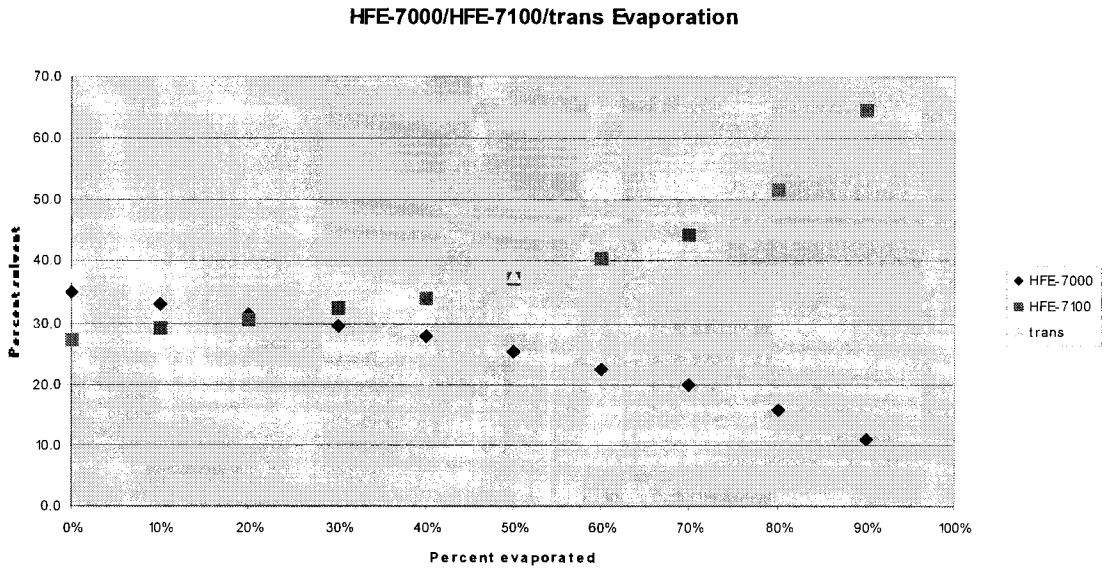

Trans 1,2 dichloroethylene also has favorable Toxicological Environmental and Regulatory properties. ACGHI has set the 8 hr PEL exposure guideline at 200 ppm. It is not considered a carcinogen and has very favorable short-term exposure limits when compared to other chlorinated solvents. Table 6&7 contains a comparison of exposure limits and regulatory status for DCE compared to other chlorinated solvents.

Table 6 Exposure data for trans 1,2 dichloroethylene

	TCA	TCE	MeCl	t-DCE
Acute Lethal 4hr LC50 Concentration (ppm)	16,000	8450	14,400	21,700
Exposure Guideline (8-hr Time Wt. Avg.)	350 ppm	50 ppm	25 ppm	200 ppm
STEL, 15 minute maximum exposure	450[1] ppm	100[1] ppm	125[1] ppm	None
Dermal Irritant	YES	YES	YES	YES
Ocular Irritant	YES	YES	YES	YES

Table 7 Regulatory Status of trans 1,2 dichloroethylene

Regulation	Trans-1,2-dichloroethylene	TCE	Perc	Methylene Chloride
VOC	Yes (Exemption petition filed)	Yes	Exempt	Exempt
Reportable Qty for Accidental Release	1,000 lbs for pure trans	100 lbs	100 lbs	100 lbs
HAP	No	Yes	Yes	Yes
Annual Reporting (EPCRA 313) (SARA)	No	Yes	Yes	Yes
OSHA list of toxins / carcinogens	No	Yes	Yes	Yes
NJ or CA hazardous list	No	Yes	Yes	Yes

Blends containing other solvents such as HFC-365mfc alcohols, trans 1,2 dichloroethylene, and other hydrocarbon solvents may be formulated as safe effective cleaners. Lower cost alternatives such as HFC-365mfc have been blended with hydrofluoroethers to reduce the overall cost of the material. HFC-365mfc has desirable Health, Safety and Regulatory properties. HFC-365mfc is VOC exempt, with a GWP below 1000 and is expected to have a favorable 8 hr PEL. HFC-365mfc is similar to the hydrofluoroethers as it is also a mild solvent. This makes the addition of stronger components necessary for many cleaning applications. HFC-365mfc has a flash point below –20°C. It does not form an azeotrope with HFEs making blends for use in vapor degreasing more difficult. Blends containing HCF-365mfc are typically targeted at aerosol or cold-cleaning applications where the evaporation profile can be adjusted to ensure the last residual solvent contains adequate amounts of HFEs to keep the remaining composition non-flammable. Blends containing HFEs, HFC-365mfc, trans 1,2 dichloroethylene, hydrocarbon solvents and alcohols have been found to be safe effective cleaners for cleaning fluxes, oils, greases and particulates. The multi component mixtures produce very effective cleaners at a cost that is favorable for aerosol applications.

Regulatory constraints continue to be an issue for solvent use. The National Emission Standards for Hazardous Air Pollutants (NESHAP) covering the National Emission Standards for Aerospace Manufacturing and Rework Facilities and the Significant New Alternatives Policy (SNAP), are standards that must be followed for compliance in aerospace applications. All Novec™ fluids and their components, intended for cleaning, are SNAP approved. The Novec™ products can be compliant as defined on page 7 Option 1 or 2, of the NESHAP document covering aerospace cleaning applications. [2] The neat Novec™ fluids are exempt as VOCs enabling them to meet the Option 1 criterion. The remaining Novec™ Fluids can be used under Option 2 which requires diligent containment of the new and used solvent, including disposal of wipers, flush solvent and other waste in a containment system which is sealed at all times other than adding waste. If Option 1 or 2 cannot be met for hand wipe applications, Option 3 found on page 10 of the aerospace NESHAP document [2] may be applicable. It states for Option 3:

" Demonstrate that the volume of hand-wipe cleaning solvent usage has been reduced by at least 60 percent from an approved baseline that is adjusted for production. Calculate the baseline by using 1996 or 1997 data, or as otherwise agreed upon by your permitting agency. The baseline must be approved by the EPA or the permitting agency and be included as part of your title V or Part 70 permit [63.744(b)(3)]"

The use of Novec™ Engineered Fluids azeotropes can reduce the percentage of non-compliant solvent, by the quantity of exempt solvent they contain. For example HFE-71DE contains 50% HFE-7100. Volumes may be shown to be a 60% or greater reduction by subtracting the amount of exempt solvent along with the lower volume of total solvent use. Option 3 may be proposed to your local permitting agency. For any option, compliance with the most current rulings must be followed. Consult your local permitting agency for current requirements. State and local restrictions may be more stringent than stated in the documents,. Check with your local agencies for restrictions that apply in your specific location.

Novec ™ Engineered Fluids have been tested and found compliant to the common tests required for aerospace compliance. Most of the testing on Novec™ fluids was performed by Scientific Materials International Inc [3] Table 8 contains the tests and ASTM test methods performed on HFE-7100, HFE-7200 and HFE-71DE. These tests were performed to gain approval or compliance for use in aerospace applications in the airframe and military aviation areas.

Table 8, Aerospace Compatibility and Compliance Test Methods

• Effect on Painted Surfaces	(ASTM F502)
• Residue Test	(ASTM F485)
• Sandwich Corrosion Test	(ASTM F1110)
• Acrylic Stress Crazing Test (HFE-71DE showed crazing)	(ASTM F484)
• Cadmium Removal Test	(ASTM F483)
• Low-Embrit. Cadmium Plate	(ASTM F1111)
• Hydrogen Embrittlement	(ASTM F519, 1C)
• Flash Point	(ASTM D56)
• Immersion Corrosion Test	(ASTM F483)
• Stress Corrosion (modified)	(ASTM D945

Novec™ Engineered Fluids provide sustainable solutions for applications that require excellent Environmental, Health, Safety and Regulatory properties. Their range of cleaning abilities and compatibility make them an excellent family of products to meet most cleaning needs. New Novec™ Engineered Fluids will be introduced to meet the changing needs of the cleaning applications. For further information please refer to the website www.3M.com/fluids.

[1] Owens, J.G., Segregated Hydrofluoroethers: Low GWP Alternatives to HFCs and PFCs, Proceedings of the Joint IPCC/TEAP Expert Meeting on Options for the Limitation of Emissions of HFCs and PFCs, Energieonderzoek Centrum Nederland, Petten, The Netherlands, 1999.

[2] National Emission Standards for Aerospace Manufacturing and Rework Facilities: Summary of Requirements for Implementing the NESHAP, document number EPA-456/R-97-006 dated January 2001.

[3] Scientific Materials International Inc. is located in Miami Florida.

Cleaning to 6 Sigma Standards

DONALD BOWDEN
Bowden Industries
1004 Oster Drive
Huntsville, AL 35816
Phone: 256-382-3700, ext. 225
Fax: 256-382-7917
E-mail: Helen.Sainker@bowdenindustries.com

Bowden Industries Inc., a manufacturer of high-volume, industrial parts washing equipment, detergents, and related services, performs cleaning to 6 Sigma standards. 6 Sigma production "is a quality improvement methodology" using the statistical measurement of no more than 3 defects per million opportunities. Organizations pursuing 6 Sigma goals focus on obtaining predictable performance in all processes, such as machining, painting, and gauging to increase operating and profit margins. If a company is to meet its 6 Sigma goals, it must demand predictable performance in all processes, including parts washing.

The benefits of 6 Sigma cleaning include:

- Reduction of downstream rejects because of dirty parts, gauging, leak checking, and welding
- Reduction of failures related to sand, chips, or other contaminants
- Reduction of labor costs by eliminating scheduled servicing
- Reduction of energy costs
- Elimination of stacks through the roof
- Reduction of water and chemical costs
- Reduction of required floor space.

A LUBRICANT FOR MACHINING CARBON FIBER COMPOSITES CLEANLY

Dean S. Milbrath, 3M Performance Materials Division, St. Paul, MN
Matthew E. Fox, University of Manchester Institute of Science and Technology, Manchester, UK

ABSTRACT

Composite materials have become valuable materials of construction in the aerospace industry because of their strength and light weight. Composite components routed to final dimensions and are joined by mechanical fasteners such as bolts and rivets in most assembly operations just as the metal parts they have replaced. To use these fasteners, accurate, precise high quality holes need to be drilled to ensure proper and durable assemblies. In addition some components are joined with high tech adhesives. Conventional machining fluids are somewhat effective for machining of composites such as carbon fiber/resins. Water based fluids cool the tool and oil based fluids provide lubrication, but both types of fluids leave substantial residues of oils, surfactants, and additives that can interact with the composite materials and may lead to cracking or delamination in extreme cases. Residues can also interfere with adhesion when parts are bonded and post assembly coating, sealing, and painting if not removed. As a result many routing and drilling operations are done without lubricant or dry to avoid these extra cleaning steps. A fully volatile drilling fluid has been developed for aluminum, which cools, lubricates and evaporates fully. This fluid kept drill bits cool and lubricated the drilling process on carbon fiber/epoxy composite materials such that good quality holes were produced. The volatile fluid also was shown to reduce residues to a small fraction of those produced with conventional cutting fluids. The new volatile fluid appears to deliver good performance and should increase assembly process productivity as a result.

KEY WORDS: composite materials, drilling, routing, lubricant

INTRODUCTION

Machining of composite materials has been a subject of much interest and discussion since good quality edges and holes and their surface finish are very important to any manufacturing operation utilizing these advanced materials. Specifically machining results are critical in structural components of airplanes, helicopters and launch vehicles. Work has been reported on changes in tooling that can dramatically change drilling and routing performance and tool

life. (1) This work has lead to a series of specialized tooling with rake angle, point angle, and multiple angle geometries as well as specialized bit coatings, which are not at all similar to conventional metal-cutting tooling. However, this improved tooling has not completely assured the efficient production.

Cutting fluids also are needed for consistent performance. Conventional fluids for metal working operations are either water-based emulsions of oils or straight oils which operate by removing heat (cooling) or preventing heat from being generated (lubricating). (2) Fluid formulations have been designed for specific tool and workpiece combinations in metalworking but there has been little work done to optimize cutting fluids for machining of composites. Depending upon the formulation of conventional fluids, varying amounts of oil, surfactant, and additives end up as a residue on the surfaces of the composite workpieces and holes. Some of these residuals are known to be incompatible with resins or with coatings, sealants, or paints that are used to finish the assembled structures. Residues have also been shown to significantly degrade adhesive bond strengths. As a result cleaning is required to remove the residues and this adds significant production time to a manufacturing process.

To eliminate solvent cleaning steps, machining is also done without lubricant so that no lubricant residues are produced.. Without a lubricant, however, tooling gets very hot and tool life is dramtically reduced. Frequent tool changes also take valuable production time and reduce overall productivity. Shortened tool life also necessitates the maintenance of a significantly larger tool inventory (higher capital expense) to keep production moving optimally.

Basic hole diameter and surface finish are used to measure hole quality while edge finish and fiber fraying are monitored for routing operations. However, common surface defects such as surface delamination, internal interply delamination, fiber/resins debonding, and fiber/resin pullout can lead to varying degrees of material failures. These defects are related to combinations of the heat produced in the maching process and the chemical interaction of the lubricant and its residues with the composite materials. Excessive heat can change resin physical properties and bonding to fibers quite dramatically once a threshold temperature is reached. This threshold depends upon the chemical composition, curing parameters, and thermal history of the resins used.

Regardless of the specific composite, the amount of heat produced in a drilling operation needs to be minimized. Drilling fluids generally do a good job of controlling the amount of heat developed in a tool and workpiece. However, residues from these fluids will act to reduce bond strengths by changing the surface interactions (surfactants), weakening the resins (oils) and encouraging rewetting (additives and surfactants) by water or solvents in microscopic defects in the composite surfaces if they are not removed.

Over forty years ago, The Boeing Company patented a fully volatile drilling fluid composed of CFC-113 and a volatile additive, butyl cellosolve, which became known as Freon TB1. (3) Other fluids known as vanishing oils, which combined a volatile solvent,

trichloroethane, with a small amount of mineral oil, were also in widely used. Both types of fluids were effective lubricants for machining operations and were particularly effective in drilling operations. However, both materials are unavailable now since their principle components were highly ozone depleting solvents. Water based materials, chlorinated oils and synthetic oils have taken their place. Unlike their predecessors, these substitutes leave significant residues.

A number of non-ozone depleting solvents have been introduced which retain many of the same properties of CFCs such as very low toxicity, non-flamability and good materials compatibility without ozone depleting drawbacks. These materials offer the possibility to reformulation the older volatile lubricants with modern materials. Many of the advantages of using fully volatile lubricants can be regained without the older materials environmental baggage.

A new fully volatile lubricant contains a hydrofluoroether solvent, HFE-7100, in place of the CFC-113 or trichloroethane. The lubricious additive of the earlier formulations was also upgraded from butyl cellosolve (which has now been found to have toxic properties) to safer, more effective and fully volatile esters of lower fatty acids. These formulations have been found to provide very good lubrication in drilling aluminum, magnesium, and other non-ferrous materials. (4) They minimize galling and appear to extend tool life when compared to a number of the straight oils used in the aerospace industry. Because of their performance and the lack of a residue, they are now finding acceptance in operations where cleaning is difficult and/or time consuming, such as in assembly operations.

One of these fluid formulations 3M™ Novec™ MW-2410 was used to evaluate its performance in drilling a carbon fiber/epoxy composite material using a laboratory test system and some simple evaluation techniques.

EXPERIMENTAL

Drilling Operations

The composite material used was a cured quasi-isotropic carbon fiber/epoxy prepreg. Test coupons were prepared that measured 10.16 x 15.24 x 0.46 cm thick. They were mounted into a fixture with 0.95 cm diameter holes drilled 1.27 cm on center in an array of 8 x 10 holes. This allowed 0.64 cm diameter through holes to be drilled without a backer at each hole, but with sufficient support for coupon stability. Holes were drilled with a Bridgeport Mill (Model 14447). A table (with linear X and Y encoders) was used to accurately position each hole during experimentation. The bits were either a Sterling Carbide Series 3000 "Dagger" solid carbide bit (0.630 x 7.62 cm), a Sterling Carbide Series 3200 8-facet solid carbide bit (0.630 x 7.62 cm) or a carbide tipped screw bit (Durapoint 0.635 x 7.62 cm). The bits were used as received and retired after the experimental series was completed. Generally, multiple bits were used for each condition so that any variation from individual bits was averaged.

Holes were drilled at a feed rate of 0.0038 cm per revolution at speeds of 1200 rpm (Dagger bit and 8-facet bits) and 3000 rpm (screw bits). The holes were drilled with no fluid application (dry) or with HFE-7100 (no lubricious additive) or MW-2410 as a spray from a modified Bijur FluidFlex applicator. [The air pressure used to spray the fluid was controlled to be approximately 1/3 of the fluid head pressure to assure application of the fluid as a liquid and not be fully evaporated in the air stream.] When drilling was completed fluid flow was stopped then the spindle was stopped and a type K thermocouple was used to determine the temperature of the bit by direct contact at the point of the bit. After the temperature was recorded, the machine table was moved to the next hole location the process was repeated. The time interval between holes was about 45 – 60 seconds. For each bit, a total of 20 holes were drilled to provide some measure of tool life and reproducibility. The Dagger bits were used for a second set of 20 holes after the first set were examined. Holes were examined for quality using visual methods, comparing the amount of surface splintering on the entrance and exit. They were also examined microscopically after sectioning to determine the quality of the hole surface.

Holes were also drilled in stacks of aluminum and composite to model common constructions used in aerospace. Two layer stacks of aluminum/composite or composite/aluminum were drilled with an 8-facet bit as above using MW-2410. Temperatures were recorded for a series of ten holes. Finally, a three layer stack of aluminum/composite/aluminum was drilled using MW-2410.

Lubricant Residue Measurements

The amount of lubricant residue from three types of lubricants (a water based lubricant formulation, a straight oil, and the volatile lubricant being tested) were determined using 2.5 x 5.4 x .46 cm coupons of the composite material used in the drilling experiments. Each coupon was thoroughly cleaned with 3M™ Novec™ HFE-71DE (an azeotropic cleaning solvent of 50% HFE-7100 and 50% trans-1,2-dichloroethylene) prior to obtaining a tare weight. Each coupon was then treated with 3 mls of Accululbe (using a dilution of 1:20 in water), Boelube, or MW-2410 being sure that all surfaces of the coupon were wetted. The coupons were allowed to dry for 30 minutes before they were weighed a second time to determine the residue left by the applied lubricant. The coupons were then cleaned with a 7 mls rinse of HFE-71DE and the coupons were weighed a final time to determine how easily any residue could be removed. All tests were run on triplicate coupons for each test fluid.

RESULTS AND DISCUSSION

Drill Bit Measurements

Bit temperatures for each bit are plotted against the hole number for the dry, HFE-7100 and MW-2410 tests of the carbide tipped screw bit (20 holes per bit), the Dagger bit (40 holes per bit) and the 8-facet bit (20 holes) in Figures 1 to 3. Drilling dry produces significant heat buildup in the bits and in the holes. All of the bits showed a gradual increase in temperature as more noles were drilled. A best fit line through the data

indicates that bit temperatures increased at the rate of 0.8 - 1°C per hole regardless of drill geometry. The specialized drill geometries, however, had a noticeable effect in reducing the bit temperatures. While the bit temperatures that were measured are below the temperature limits for the composite resins, the temperature at the cutting surface is likely to be well over that limit. In addition, the resin/carbon fiber "chips" will be significantly hotter and may produce localized thermal aging/damage of the composite material.

In all cases the use of HFE-7100 alone did reduce the observed temperatures. These values when plotted produce a much smaller increase in bit temperature, 0 – 0.2°C. By comparison the MW-2410 produced virtually no increase in bit temperature (0 – 0.1°C per hole) and is not likely to produce any thermal damage to the hole resin surface. It is also important to note that the addition of the lubricious additive to HFE-7100 produced a significant reduction in bit temperature over that observed when HFE-7100 alone was used. This indicates the additive in MW-2410 provides significant lubrication for cutting composites.

The carbide tipped screw bits were discolored due to the amount of heat that was produced in drilling 20 holes with no lubricant. The dagger bits also showed similar evidence of discoloration after drilling the second set of 20 holes without lubricant.

Figure 1
Temperature after Drilling with Carbide Tipped Screw Bits

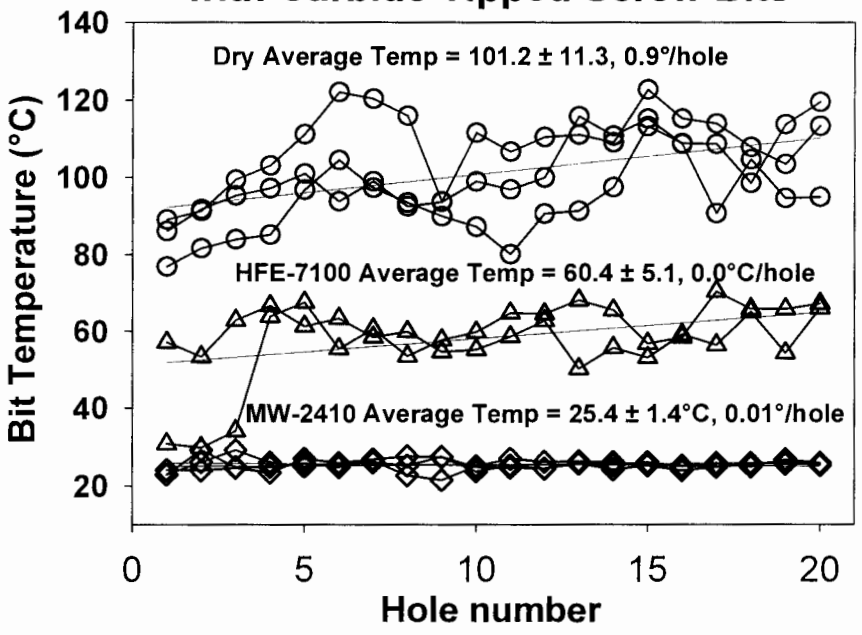

Figure 2
Bit Temperatures after Drilling with Dagger Bits

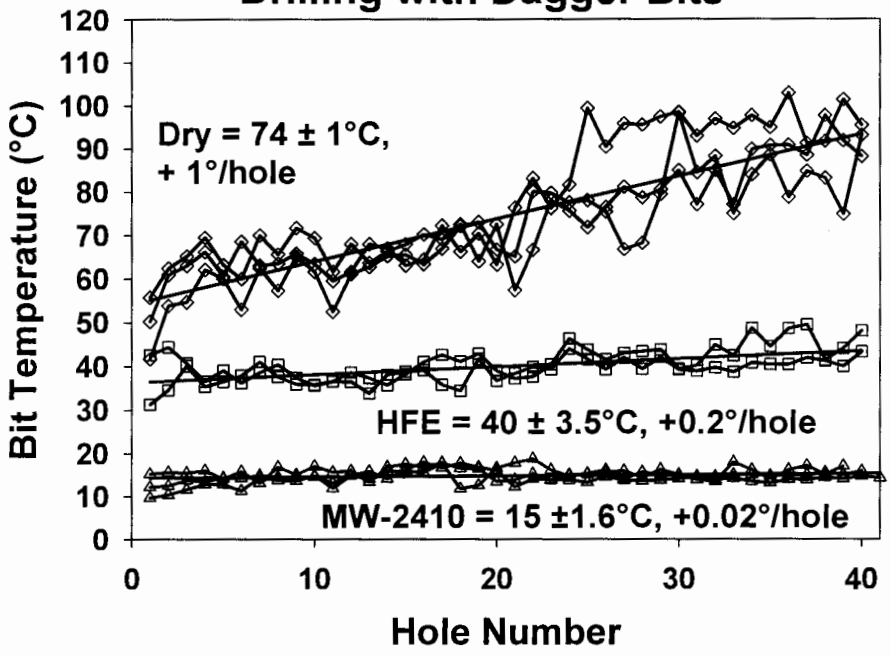

Figure 3
Bit Temperatures after Drilling with an Drill/Reamer Bit

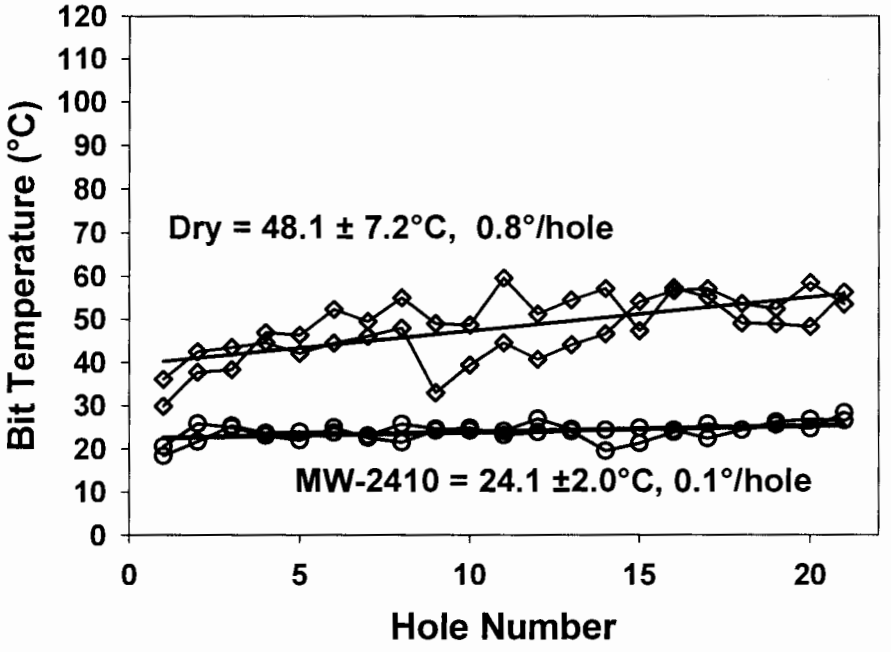

The discoloration after the second set of holes is consistent with the bit temperatures shown in the Figure 2 where the average dry temperature was 63.8°C for the first 20 holes and increased to 85.9°C over the next 20 holes. The discoloration and increasing temperatures also indicates that the life of the tooling had been reached. (5) Drill bits normally would have been changed before discoloration was observed.

Drilling aluminum/composite stacks with an 8-facet carbide bit produced nearly the same results a drilling just composites. The increased thickness or depth/diameter ratio can be seen to have increased bit temperatures slightly. With the two layer stacks with composite as the second layer the rate of termperature increase is accelerated. This is likely due to greater heat generation with composites and the reduced volume of fluid reaching the deeper holes. This depth effect is readily seen in the data for the first trial of three layer stacks. However, slowing the rpm and increasing feed rate (no net change in time needed to drill the hole) allowed more fluid to penetrate to the cutting zone and reduce bit temperatures to an acceptable level.

Table 1
Bit Temperatures with Multi-layer Stacks of Material

Composite Metal Stacks	Depth/Diam	Speed/Feed (rpm / ipr)	Average Temp (°C)	Temp Increase (°C/hole)
Al/Composite	1.7	3K / 0.0015	24 ± 2	0.5
Composite/Al	1.7	3K / 0.0015	23 ± 1	0.04
Al/Composite/Al	2.7	2K / 0.003	61 ± 8	3.5
Al/Composite/Al	2.7	1K / 0.006	28 ± 3	-1.6

Hole Evaluation
Visual inspection of the holes did not show a significant difference in the amount of surface defect produced at the hole entrance or exit when dry and lubricated results were compared for each type of bit. Hole diameters were also comparable when they were measured.

After cutting a line of holes in half to examine the holes, the surfaces were visually observed to be very different, particularly for holes drilled with Dagger bits. In the Figure 3 a photomicrograph of a part of these sections it is apparent that drilling dry with Dagger bits produces a shiny, glazed surface compared to the duller matt surface produced with lubricant. Closer examination indicates that "chips" of resin/carbon fiber have been re-welded to the hole surface obscuring the lines of the fiber layers in the

composite. This is evidence that the heat being produced by drilling dry is sufficient to melt the resin chips and form a glaze over the hole surface and perhaps to cause other types of thermal defect in the hole surface.

Figure 3
Photomicrograph of hole surfaces

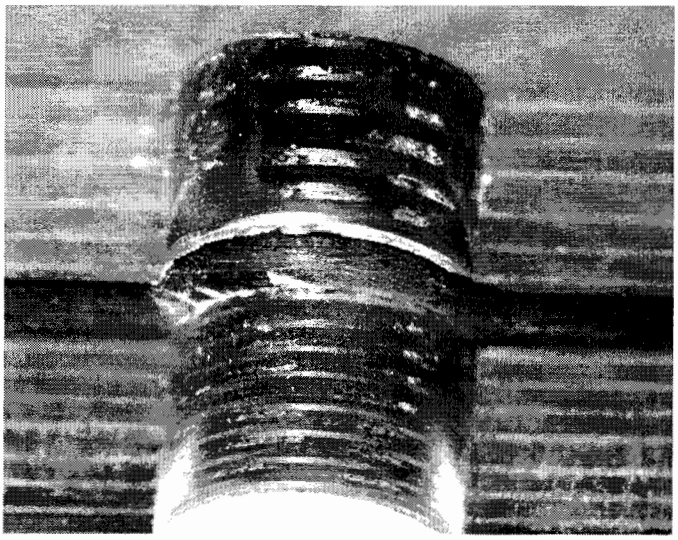

The upper composite hole sample produced with Dagger bit used dry produced appears to have a glossy surface while the lower composite hole sample produced by a similar Dagger bit with MW-2410 lubrication has a matt appearance. The fibers in the upper hole are partially obscured by the glaze produced by resin reweld, but all of the fibers are visible in the lower hole.

Lubricant Residue

The amount of residue found was minimal with MW-2410 when compared to the other lubricant types tested. Table 1 shows that there are 8.3 and 21.9 times the mass of lubricant residue left on the coupons by the water based Acculube and the straight oil Boelube, respectively, when compared to the volatile MW-2410. During the drying time substantially all of the MW-2410 evaporated while only the water of the Acculube preparation (5% lubricant preparation in water) dried. This can be seen from the percentage of the applied lubricant remaining on the surface. Since the Boelube tested was not diluted with a volatile solvent, the residue represents a fraction of the applied fluid that did not run off during the drying time.

The solvent rinse was used as a mild cleaning procedure with no physical wiping or agitation. Most of the residues were removed, but there was still significantly more Acculube and Boelube residue present after cleaning than the initial MW-2410 residue. More vigorous cleaning procedures certainly will reduce residues further from smooth surfaces such as the test coupons. However, residues will not be easily removed from surface cracks or defects and in the interfaces between joined surfaces by solvent wipes and even vigorous scrubbing.

Table 2
Measured Lubricant Residues on Carbon Fiber/Epoxy Composite

Lubricant Applied	Lubricant Residue (mg)	Residue % Of Applied	Residue/surface area (mg/cm2)	Residue after Solvent Rinse (mg)
Acculube (1:20 in water)	64.4	6.4	1.5	23.8
Boelube (straight oil)	170.7	21.3	5.0	17.8
MW-2410 (volatile lube)	7.8	0.2	0.2	2.0

SUMMARY

This study took a simple look at the performance of a newly formulated volatile lubricant in drilling carbon fiber/epoxy composites. Although the evaluation of the fluid is not as extensive as it could be, it is apparent that its use is significantly better than drilling without a lubricant. Both drilling with a volatile lubricant and without any lubricant avoids the issues of cleaning lubricant residues, but the volatile lubricant was shown to greatly reduce heat build-up on tooling and chip re-weld on the hole surface.

Excessive heat was produced on the dry tooling, which was observed as tool discoloration and was measured to be 60 to 75 °C higher than lubricated tooling. Heat buildup is related to faster tool wear. (5) Although tool wear was not measured in this study, the higher observed tool temperatures certainly should be viewed as a negative. The heat produced also was observed to produce a glaze on the surface of the finished holes. This glaze is likely to have been formed by remelting of resin chips onto the hole surface. Depending upon the resin's polymeric properties, this glaze can represent a material weakness that will alter the ultimate durability of the assembly.

The results with drilling appear to indicate that other machining operations such as routing of composites will also benefit from the use of a volatile lubricant. Additional studies are being undertaken to evaluate fluid application methods and flow rates as well as additional lubricious additives compatible with composite resins. Machining parameters such as feed and speed and additional tooling options are also being optimized for use with volatile lubricant formulations.

REFERENCES:

1. M. Mehta, A.H. Soni in T.S. Srivatsan, C.T. Lane, D.M. Bowden ed., Proceedings of the AMS 1993 Materials Conference, ASM International, Materials Park, Ohio, pp 139-152.
2. J.C. Childers, The Chemistry of Metalworking fluids in J.P. Byers, ed., Metalworking Lubricants, Marcel Dekker, Inc.New York, 1994, pp 165 – 189.
3. U.S. Pat. 3,129,182 "Cutting Fluid" (April 14, 1964) F.P McLean (to The Boeing Company)
4. U.S. Pat. 6,294,508 "Composition Comprising Lubricious Additive for Cutting or Abrasive Working" (September 25, 2001) D.S. Milbrath, M.W. Grenfell (to 3M Innovative Properties).
5. G. Spur, U. Lachmund in S. Jahanmir, M. Ramulu, P. Koshy ed., Machining of Ceramics and Composites, Marcel Dekker,Inc. New York, 1999 pp 231-234.

Durable surface contamination standards

Dr. Paul H. Shelley
Boeing Commercial Airplanes
PO Box 3707 M/C 6X-RR
Seattle, WA 98124-2207
paul.h.shelley@boeing.com

Introduction

Boeing uses portable and laboratory FT-IR systems to measure surface contamination on aircraft skin and parts. Contamination measurements are made with different spot sizes and different reflection angles, different reflection accessories and of course different spectrometers. Methods are also under development for measurement of surface contamination using methods other than infrared spectroscopy. It is important to understand the sensitivity of various measurement systems in order to be sure that the measurements being made have adequate sensitivity for the contamination being measured. It is also important to calibrate the measurement sensitivity of a particular measurement system over time and after repairs or adjustments to the system have been made. Standards with known amounts of contaminants on metal surfaces were needed to calibrate measurement systems and verify proper sensitivity of measurement systems over time. These standards are also useful for evaluation of new contamination measurement instruments or new accessories for existing measurement systems.

There are two general classes of contaminants that are generally of interest for aircraft skin and parts. One is hydrocarbon-based materials and the other is silicones. Oils and greases were tested as model contaminants for hydrocarbons, but these materials transferred to surfaces of measurement systems and changed with use and time. Silicone oils and greases had the same problem. Polystyrene was found to be a durable hydrocarbon standard and it has been an infrared spectroscopy standard for transmission measurements for a long time. Silicone rubber that cures with air and release of methanol was found for a silicone standard and proved to be very durable. This paper details the calibration and measurement of these materials as well as methods for applying the contaminants.

Calibration of durable standards at Boeing

Polystyrene and the uncured silicone rubber material used in this work are both very soluble in toluene. Solutions of 5% polystyrene and silicone rubber were made for spray applying the model contaminants on test coupons. Four inch by six inch 0.020 inch thick aluminum coupons were cleaned and tested for cleanliness against a sputtered gold standard using grazing angle reflectance in

a laboratory FT-IR system (Nicolet Magna 760 with a Harrick Refractor accessory). The coupons were then weighed sprayed with the contaminant solutions using an airbrush, allowed to dry for an hour and weighed again. The weight difference was used to calculate the contaminant concentration in milligrams per square foot. Each coupon was measured with grazing angle reflectance in the laboratory FT-IR system at 17 points according to the pattern shown in Figure 1. An appropriate analytical peak was chosen in the infrared spectrum of silicone rubber and polystyrene and the average peak area was calculated for the points measured.

Figure 1 Measurement spots on calibration coupons. Each spot is an oval approximately 1 inch by 0.5 inch. The center of the coupon is weighted with two extra spots.

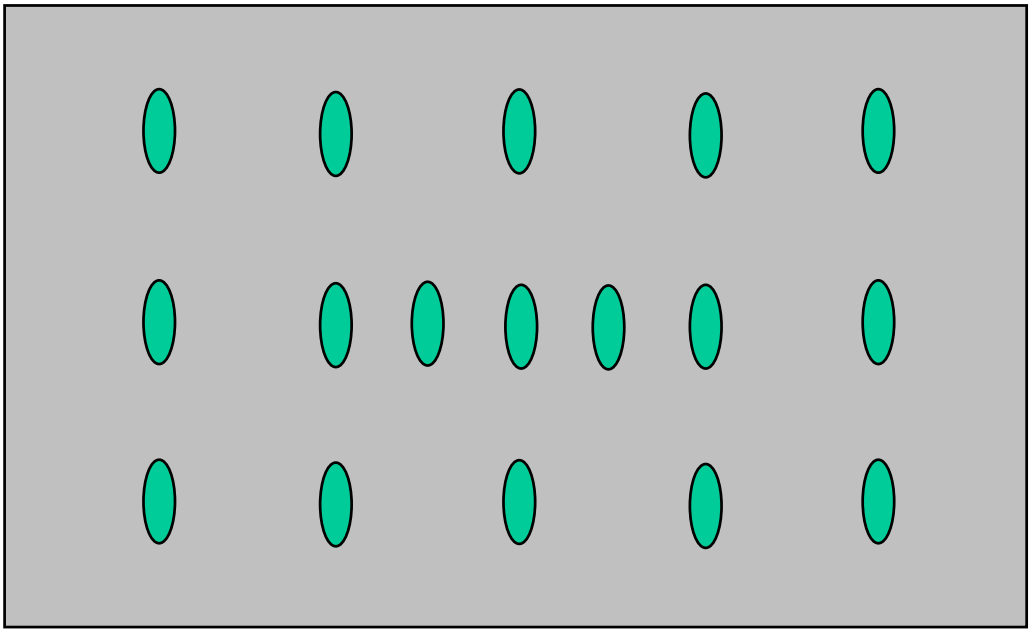

Seven coupons were used for the polystyrene calibration and the polystyrene weight in mg/ft^2 was plotted against the average infrared peak area for each coupon to get the polystyrene calibration. See Figure 2. Eight coupons were used for the silicone rubber calibration shown in Figure 3. In each case the plots included the zero point.

Figure 2 Polystyrene calibration plot

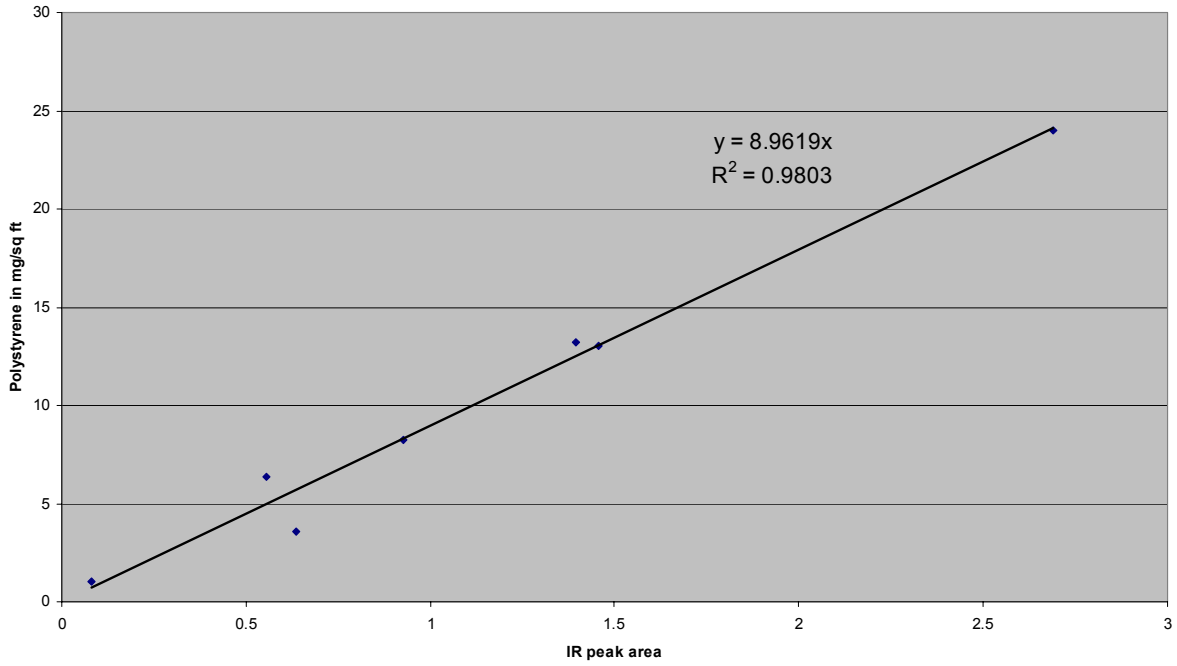

Figure 3 Silicone rubber calibration plot.

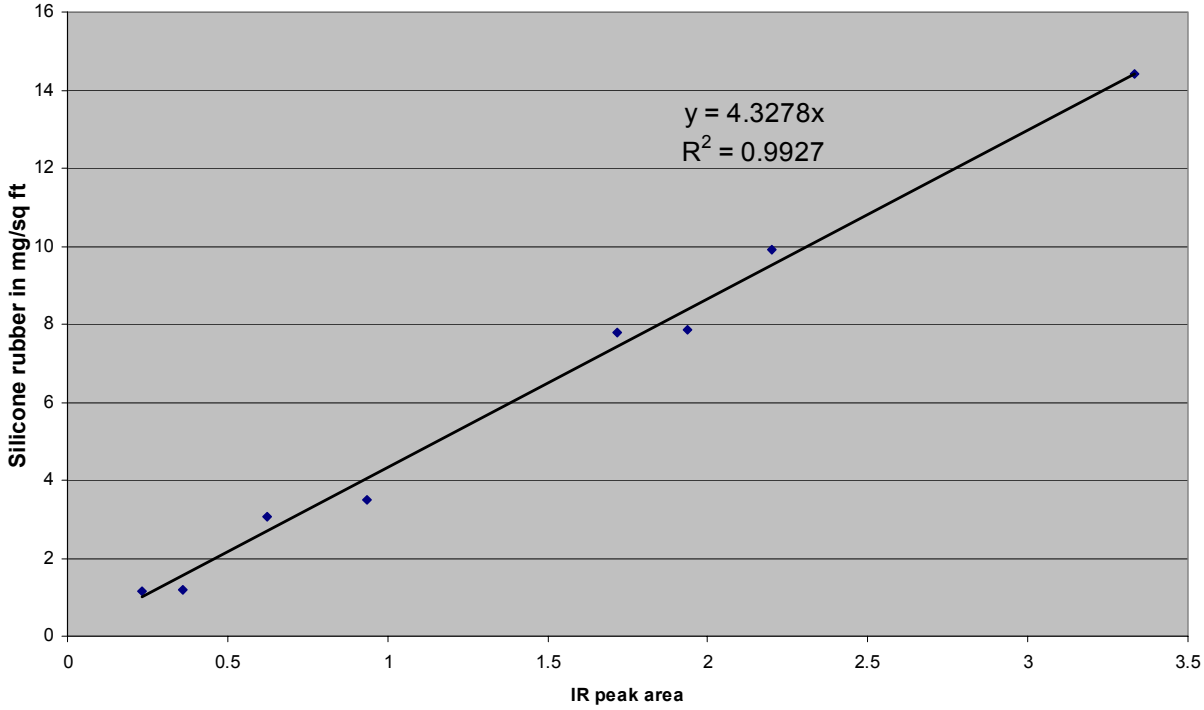

There were two problems with the standards made in this manner. One was a rather uneven distribution of the standard contaminants due to difficulty in using the airbrush and the other was lack of an independent reference method to verify the contaminant level on each coupon. The NASA surface contamination analysis team in Huntsville, Alabama was contracted by Boeing to make polystyrene and silicone rubber standards using their Sonotec machine. The Sonotec machine is made for the semiconductor industry to apply polymeric materials to silicone wafers in semiconductor manufacturing processes. Two inch by 3 inch polished and grit blasted stainless steel coupons were used for the NASA generated standards. Aluminum foil witness coupons were used to measure and set the steady state contaminant deposition rate of the Sonotec machine prior to making each level on contamination on the coupons.

The contaminant concentration range was targeted at 0.25 to 5.0 mg/ft^2. The coupons made at NASA were measured in 5 places with the Boeing laboratory FT-IR system and the calibration developed on that system for each of the contaminants. The polished coupons were used in this case because the grazing angle FT-IR accessory did not work well on the grit blasted coupons. A comparison of the NASA and Boeing results for the polished polystyrene coupons is shown in Table 1.

Table 1 Comparison of polystyrene concentration on NASA made polished coupons.

Target in mg/ft^2	NASA results mg/ft^2	Boeing results mg/ft^2
0.25	0.26	0.57
0.50	0.50	1.53
1.00	0.98	1.71
2.00	2.30	2.61
5.00	6.00	5.17

The NASA generated results and Boeing measured results are by very different measurement methods and give a reasonably good comparison. In the world of contamination measurement this is an excellent comparison and confirms the calibration method used at Boeing. The distribution of contamination on the NASA coupons is much more even than on the coupons made with the airbrush, which was confirmed with both macro and micro FT-IR measurements.

A micro image of a 5 mg/ft^2 polystyrene coupon made with the airbrush is shown in Figure 4 and a micro image of the 5 mg/ft^2 polystyrene coupon made at NASA is shown in Figure 5. The airbrush coupon is a series of unconnected islands and the Sonotec coupon shows a more even distribution of material that appears to be droplets that have flowed together.

Figure 4 Airbrush applied polystyrene at 5 mg/ft^2

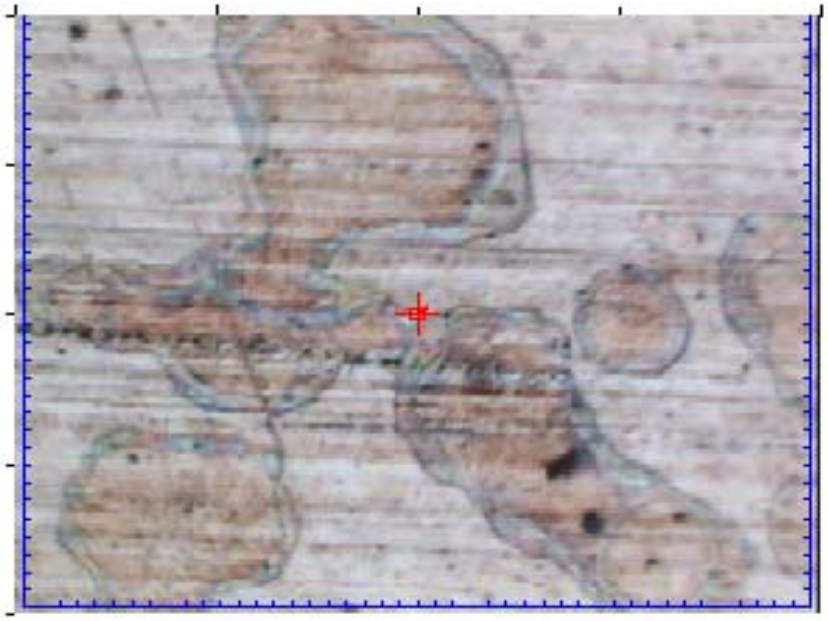

Figure 5 Sonotec applied polystyrene at 5 mg/ft^2

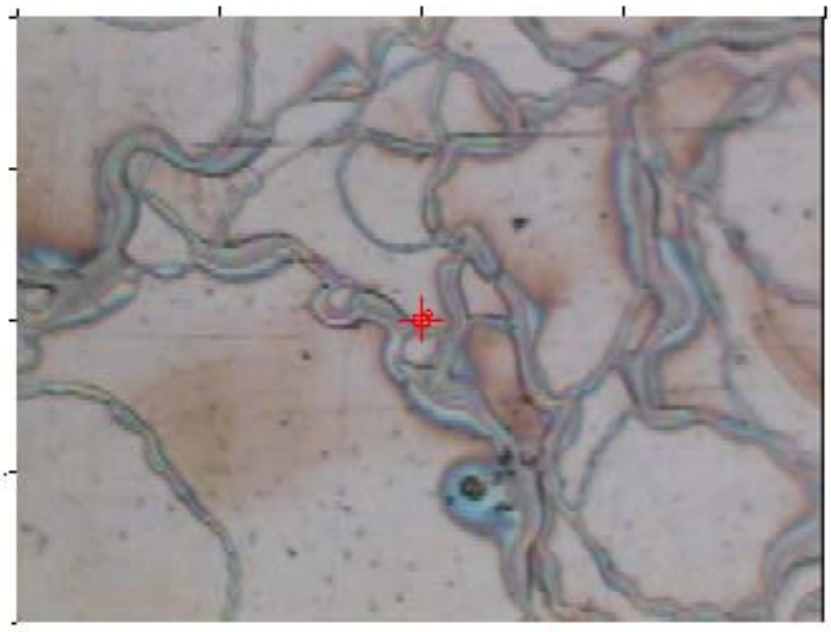

Larger area composite images were made that show the two different polystyrene distributions for the two different application methods. These are shown in Figures 6 and 7.

Figure 6 Composite image of polystyrene applied with an airbrush at 5 mg/ft^2

Figure 7 Composite image of polystyrene applied with Sonotec at 5 mg/ft^2

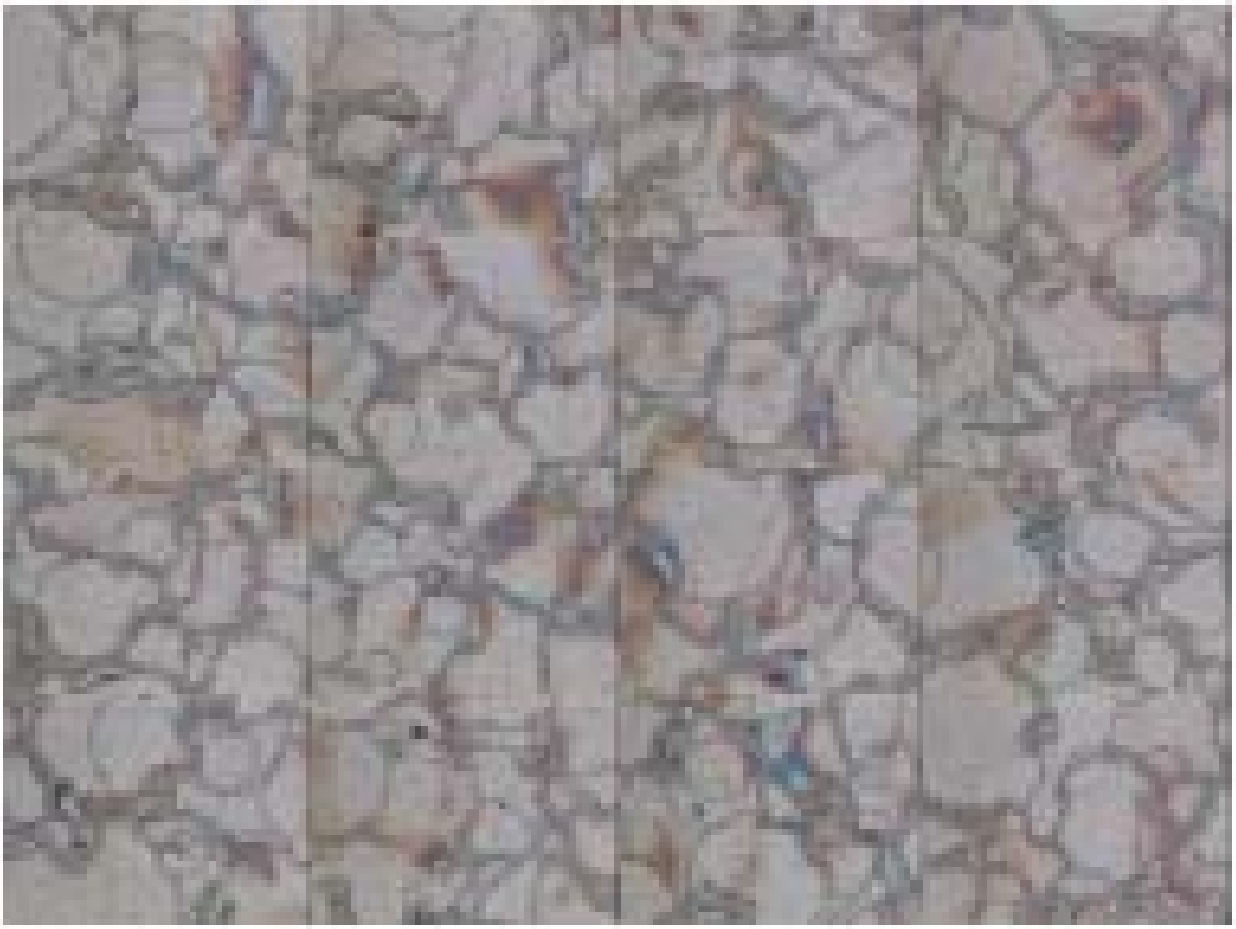

Findings and Conclusions

The Boeing airbrush made polystyrene standards have islands of contamination that must be relatively thick to generate the same macro concentration as the NASA made coupons with the Sonotec machine. The NASA coupons have micro-droplets that have run together in an irregular but continuous pattern. The macro and micro distribution of contaminants on the Sonotec made coupons is better than the airbrush made coupons.

The intention of the durable standards is for macro measurements with a variety of measurement devices and both sets of coupons have worked well for this purpose. Boeing has used the NASA generated coupons to evaluate the sensitivity of both portable and laboratory instruments with a variety of reflection

accessories. The durable standards have worked well in terms on not transferring to a measurement device that touches the surface of the standards which is often the case for FT-IR reflection measurements. Both sets of coupons are now being used to evaluate the sensitivity of infrared imaging systems for broad area contamination measurement.

Acknowledgments

DeWitt Burns NASA Marshall Space Flight Center
Sonotec calibration and contamination coupon design

Odell Huddleston Thiokol
Sonotec calibration and contamination coupon design

Boeing Phantom Works funding

Chris Moy Boeing Engineer
Boeing airbrush coupon generation

Effects of Thermal Exposure on Properties of Al-Li Alloys

by

S. Shah, D. Wells, W. Stanton, K. Lawless, C. Russell
NASA Marshall Space Flight Center

J. Wagner, M. Domack
NASA Langley Research Center

H. Babel, B. Farahmand, D. Schwab, M. Tarkanian, R. DeJesus
The Boeing Company

AMPET 2002

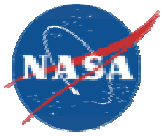

Outline

- Objective
- Al-Li Alloys Background
  - Compositions and Features
  - Key Characteristics of Al-Li Alloys
- Research Approach
  - Approach
  - Available Material
  - Thermal Exposure Matrix
- Results and Observations
- Summary

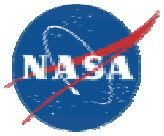

Objective

The objective of this investigation is to evaluate the effects of thermal exposure on the mechanical properties of both production mature and developmental Al-Li alloys

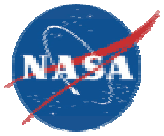

Al-Li Alloy Background

Aluminum-Lithium Alloys Composition and Features

Alloy	Heats to date	Rolled Gage Thickness	Density Lb/in^3	Cu	Li	Mg	Ag	Zr	Mn	Zn
2195	Many	2" max	0.098	4.00	1.00	0.40	0.40	0.12	-----	-----
2297	300 to 400	2" to 6"	0.096	2.90	1.25	-----	-----	0.11	0.35	-----
L277	~14	0.5" to 6"	0.098	3.50	0.90	0.40	0.40	0.10	0.35	-----
C458	~14	0.25" to 6"	0.095	2.60	1.80	0.30	-----	0.09	0.25	0.60

Key Characteristics of Al-Li Alloys

Alloy	Key Characteristics
2195	?? In production for Shuttle External Tank ?? Rolled and tested to thickness of 1.8 inch
2097 2297	?? In production for F-16 ?? Two AMS specs evolving for same application ?? Not designed for FSW or cryogenic use
L277	?? Developmental alloy with high toughness ?? Deriv ative of 2195 with 0.2% less Li
C458	?? Development alloy with high toughness ?? Developed under AF sponsorship

LT15

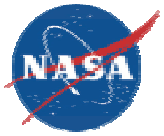

Research Approach

Approach

- Select 2195, C458, L277 and 2219 alloys and plate stock
- Select exposure temperature (200F to 350F) and time (0 to 1000 hrs)
- Thermally expose thin plate, thick plate and friction stir welds
- Test thin plate @ t/2, thick plate @ t/6 or 5t/6 and friction stir welds @ t/2 —through thickness
- Conduct room temperature tensile tests for all temperature/time exposure conditions
- Select temperature/time conditions for additional tests
- Additional tests include cryogenic tensile test, room and cryo fracture toughness (Kjic) test and microstructure evaluation

Available & Tested Material

Alloys	Thin Plate	Thick Plate	Friction Stir Welds
Baseline 2219	None	None	0.375 T8
2195	None	1.50 T8	0.75 T8
L277	0.85 T8	2.50 T8	0.85 T8
C458	0.50 T8	1.80 T8	0.75 T8

Thermal Exposure Matrix

	Hours of Exposure				
Temp.	0 hrs	50 hrs	100 hrs	500 hrs	1000 hrs
200 °F			RT	RT	RT, CT, F FSW-RT
250 °F			RT	RT	RT, CT, F FSW-RT
300 °F			RT	RT, CT FSW-RT, F	RT, CT, F FSW-RT
350 °F		RT	RT	RT	RT
unexposed	RT, CT, F, FSW-RT, F				

RT = Room Temp. tensile test

CT = Cryogenic (-320F) tensile test

F = Fracture Toughness (Kjic) tests conducted at room and cryogenic temperature

FSW = Friction Stir Welds, Plate to Plate.

Data presented from these blocks

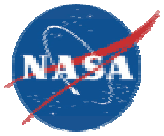

Results and Observations

Thin Plate Tensile Results – t/2, LT

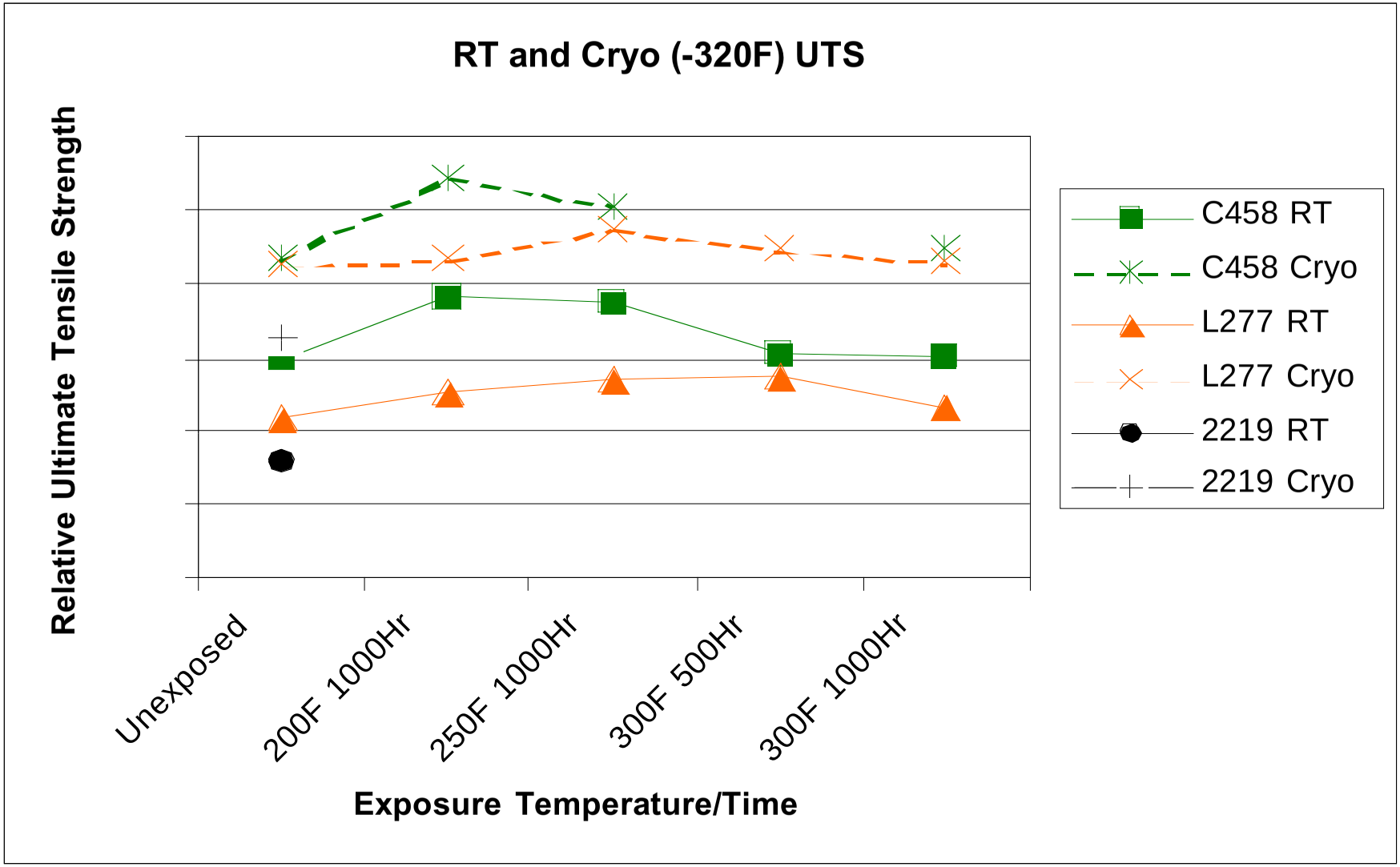

Thin Plate Tensile Results - t/2, LT

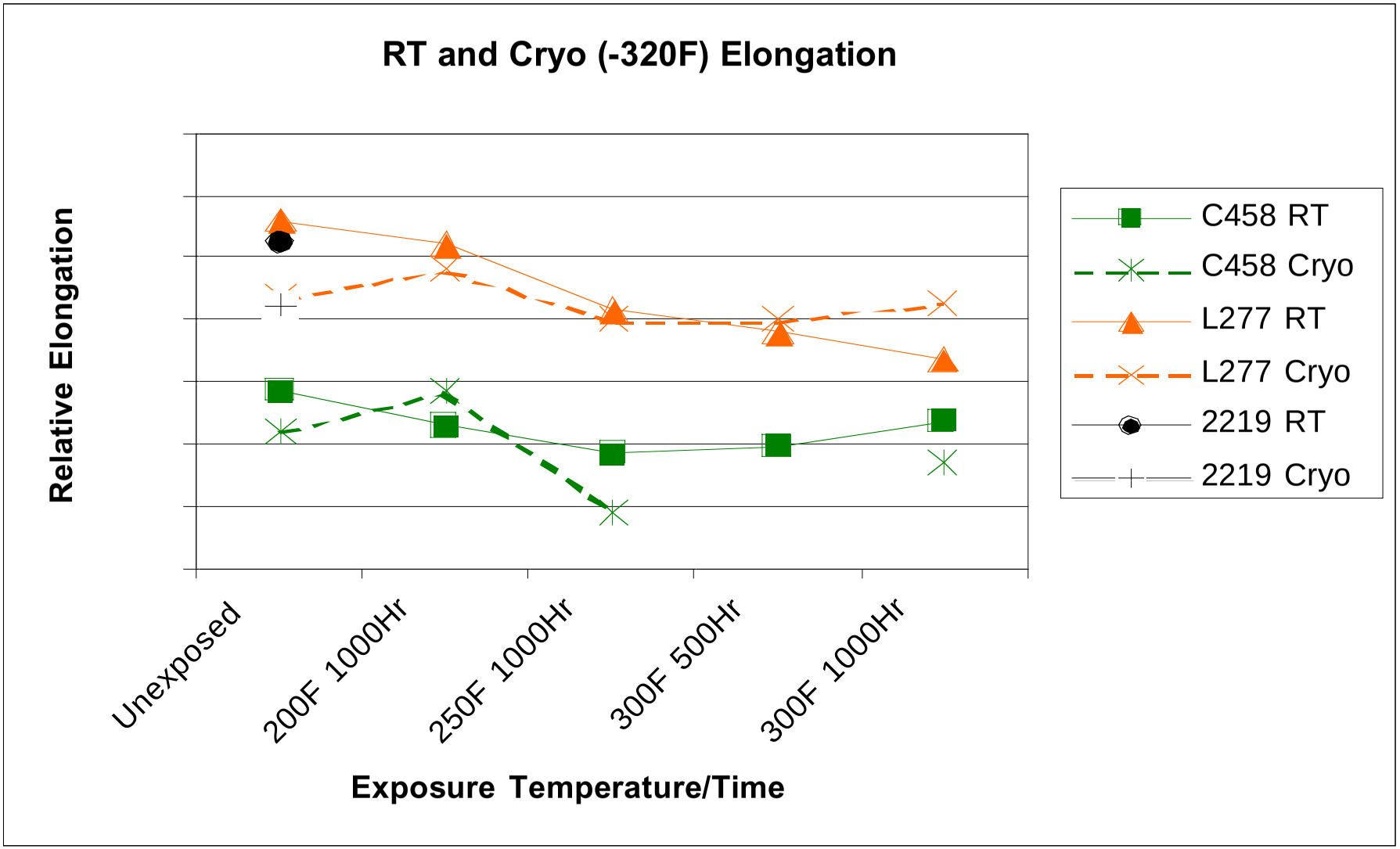

Thin Plate Tensile Observations

- For C458 and L277 Thin Plate RT and CT tests indicate that thermally exposed strengths are better than or equal to unexposed strength. Unexposed plate temper is below peak age condition. Elongation does not exhibit a consistent trend.

- All Thin Plate alloy exhibited and increase in cryo strengths over RT strengths for all exposure conditions. Elongation does not exhibit a consistent trend.

- In general alloy C458 has better strength than L277, and L277 has better ductility than C458.

Thick Plate Tensile Results - t/6, LT

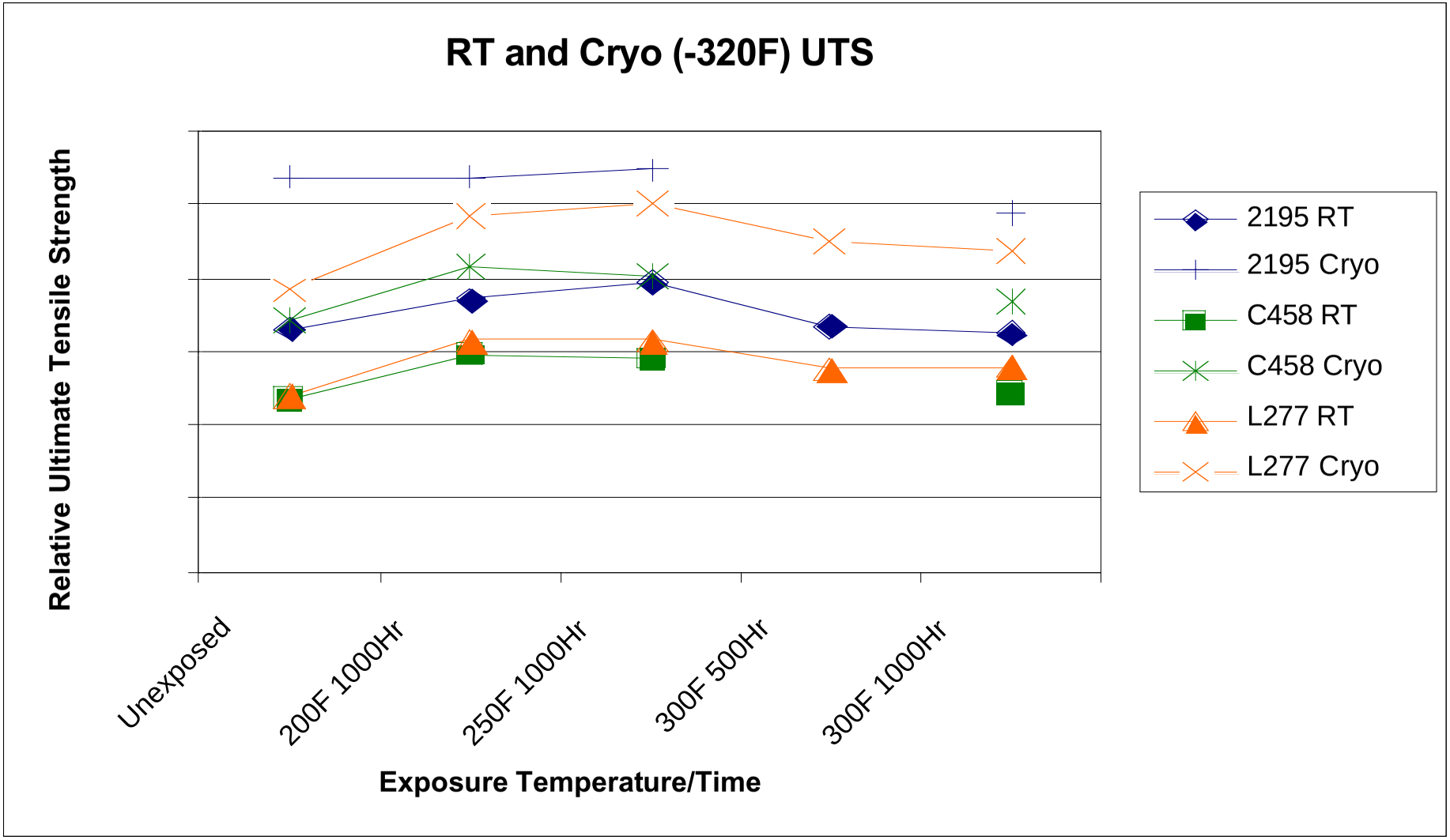

Thick Plate Tensile Results - t/6, LT

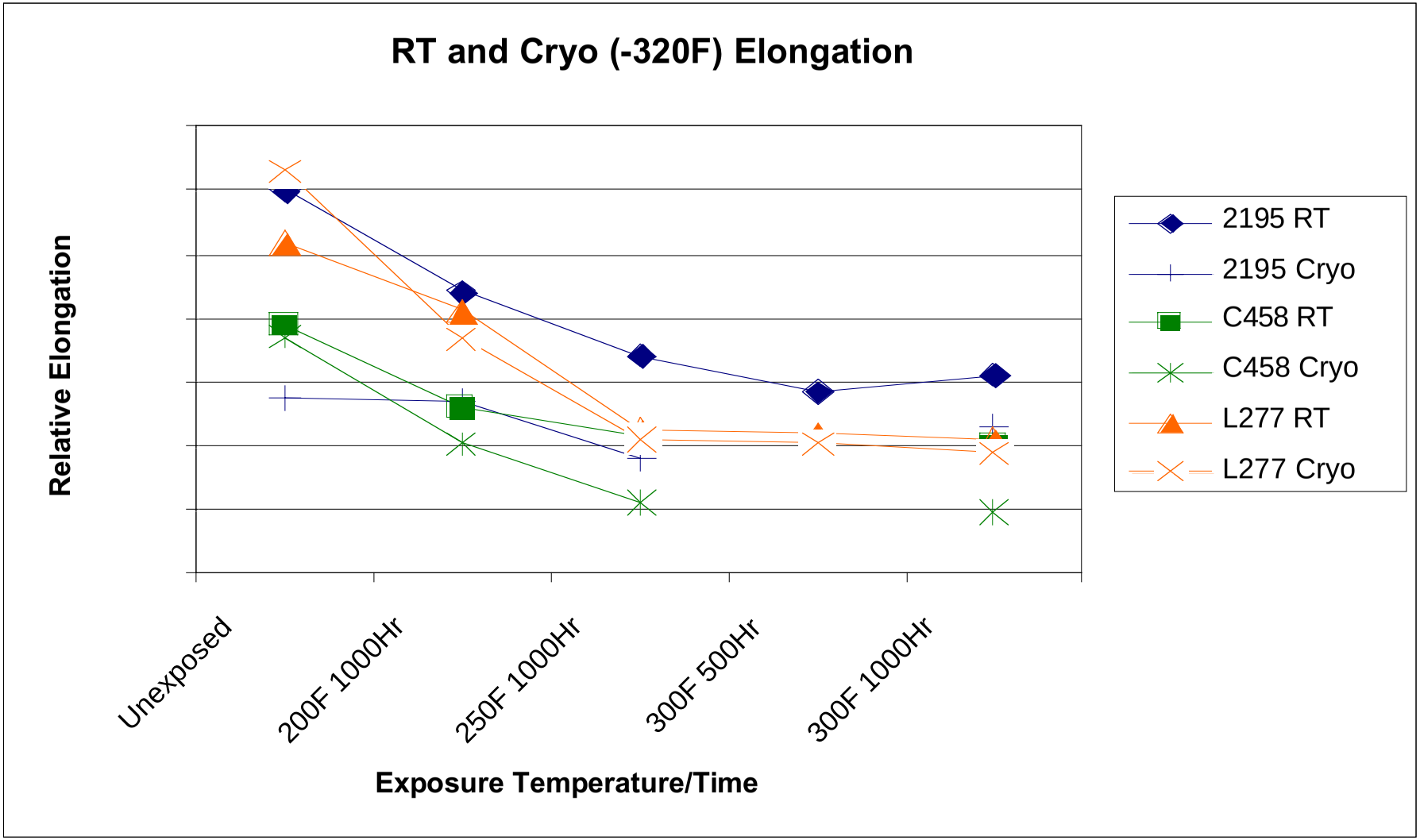

Thick Plate Tensile Observations

- In general, all Thick Plate alloy RT and CT tests indicate that thermally exposed strengths are better than or equal to unexposed strength (except 2195 at very high temperatures). Unexposed plate temper is below peak age condition.

- In general, all Thick Plate alloy elongation decrease with thermal exposure and seems to reach a plateau above 250 F.

- All Thick Plate alloys exhibit an increase in cryo strengths over RT strengths for all exposure conditions. Elongation, in general, is lower at cryo temperatures.

FSW Tensile Results - t/2

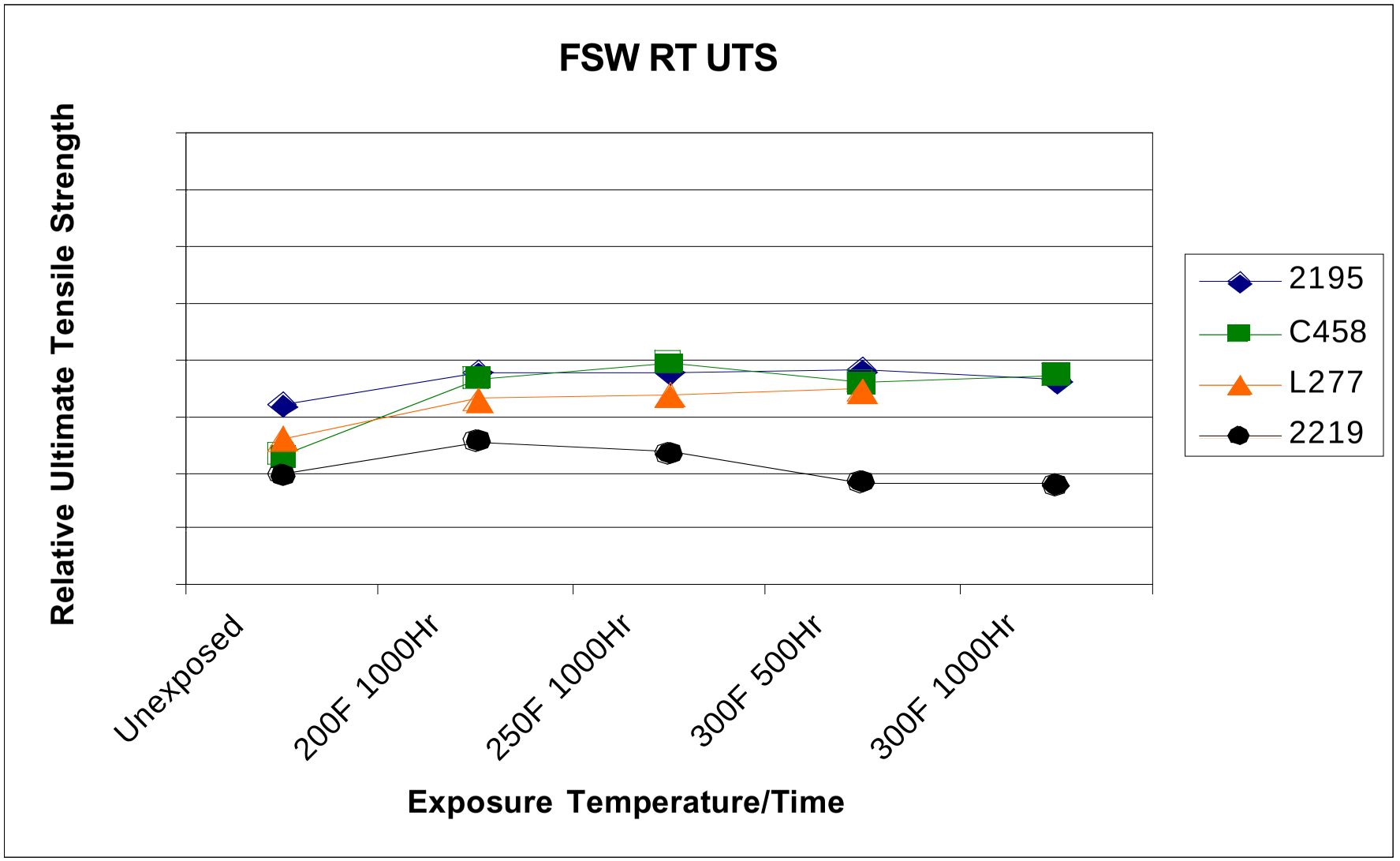

AMPET 2002

FSW Tensile Results – t/2

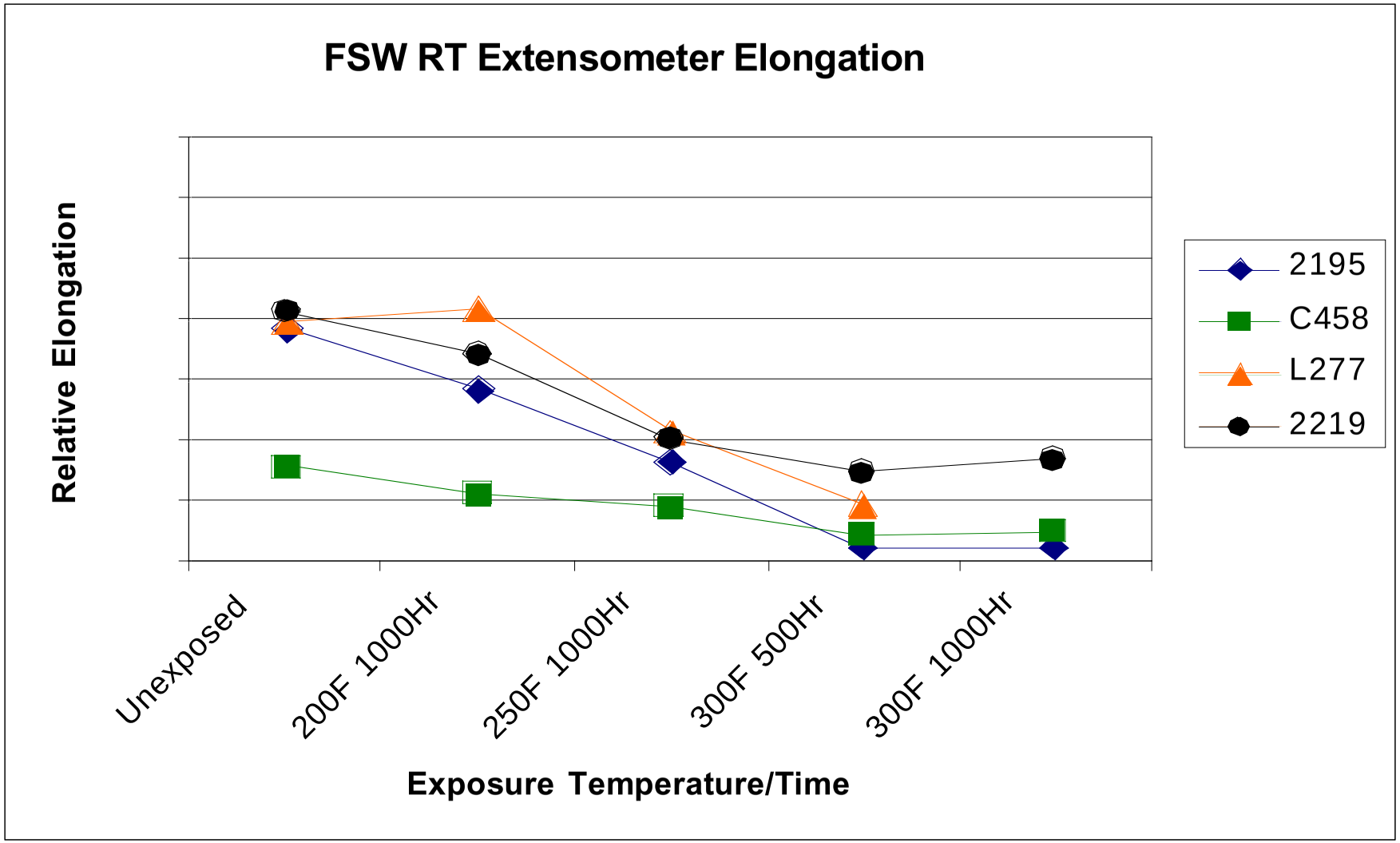

AMPET 2002

FSW Tensile Observations

- For all FSW alloys RT strengths generally increase with thermal exposure except for 2219.

- At high exposure temperatures, the elongation of the FSW welds decreases significantly, similar to the behavior of thick plates.

- Most of the tensile failures occur in heat affected zone rather than in the weld zone.

2195 K_{Jlc} (E1820) Results

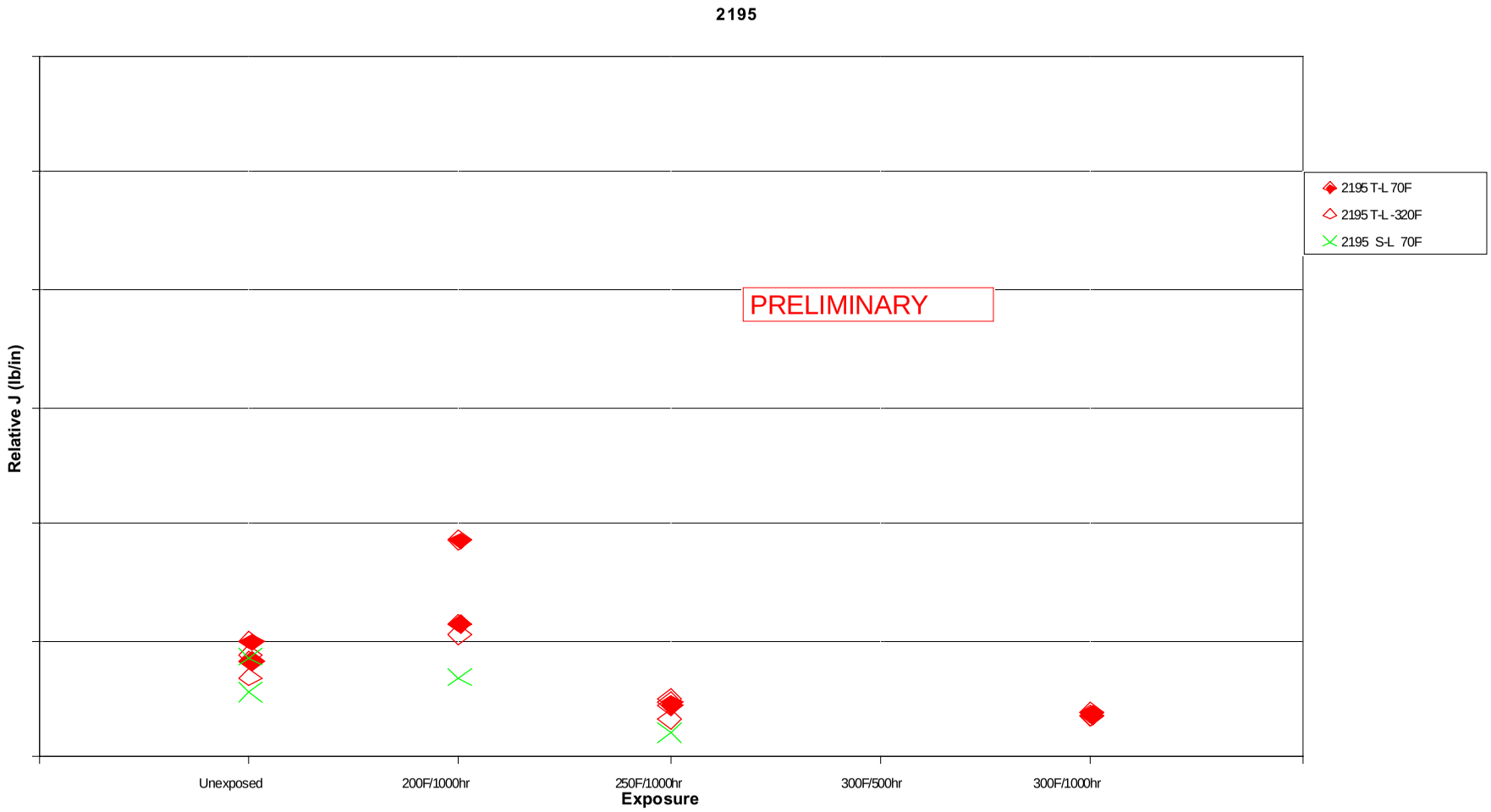

Includes results from Thick Plate, Orientation, Room & Cryo tests

L277 K_{Jlc} (E1820) Results

Includes results from Thin Plate, Thick Plate, Orientation, Room & Cryo tests

AMPET 2002

C458 K_{Jlc} (E1820) Results

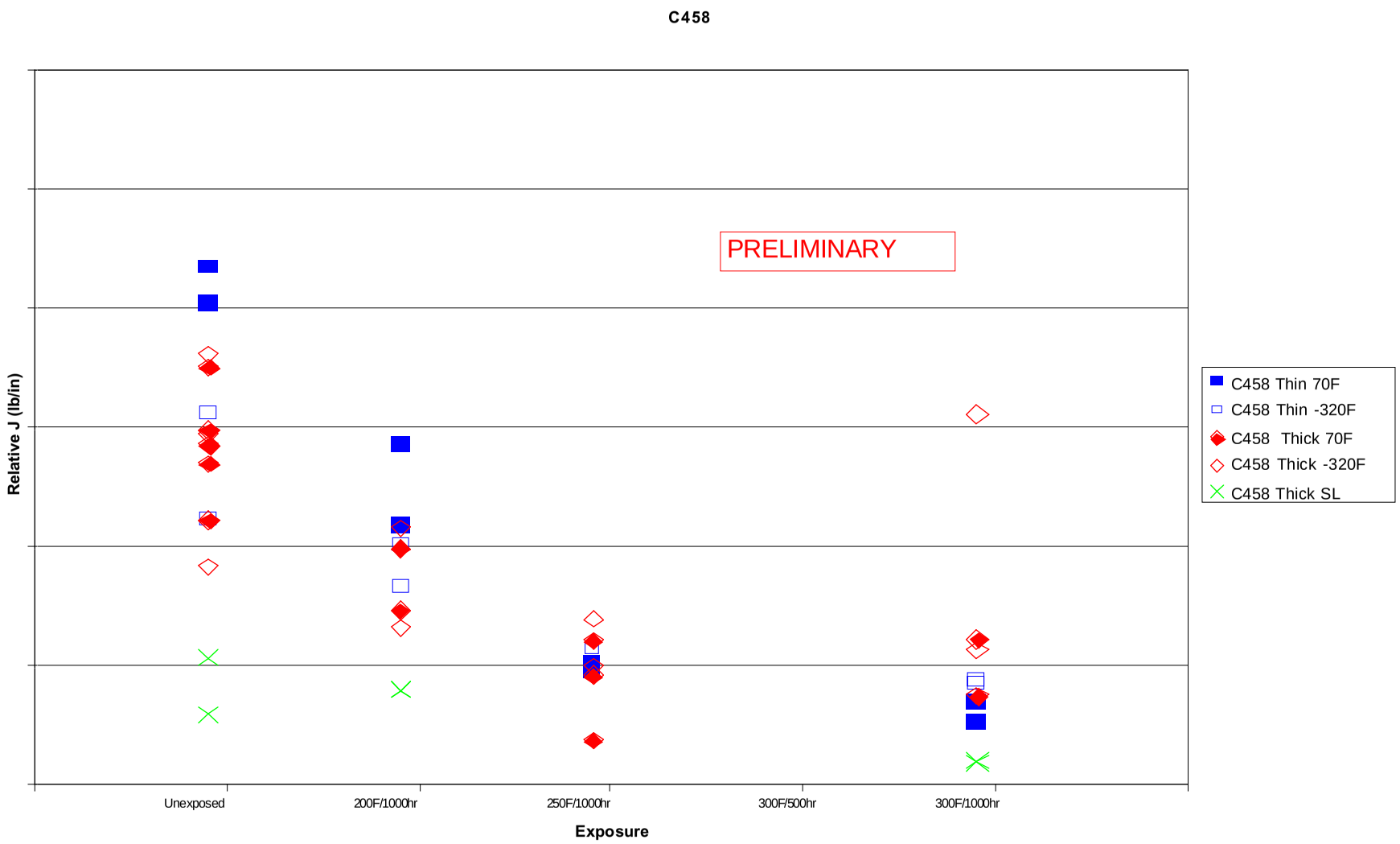

Includes results from Thin Plate, Thick Plate, Orientation, Room & Cryo tests

Alloy Plate Fracture Toughness Observations

- The data is preliminary and is still under investigation for validity in some tests.

- It appears that in 2195 thick plate and L277 thin plate the fracture toughness increases at lower temperature exposures but decreases at higher temperature exposures. For L277 thick plate, the toughness seems to decrease continuously with increasing exposure temperature.

- It appears that in C458 the fracture toughness, with few exceptions, decreases with higher temperature exposure.

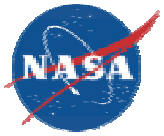

Summary

For the alloys, their tempers, gage thickness, and product form investigated, the data clearly shows that there is no deficit in mechanical properties at lower exposure temperatures in some cases, and a significant deficit in mechanical properties at higher exposure temperatures in all cases.

5th Conference on Aerospace Materials, Processes, and Environmental Technology (AMPET)
September 16-18, 2002
Von Braun Center
Huntsville, Alabama

Hydrogen Permeability of a Polymer Based Composite Tank Material Under Tetra-Axial Strain

Eric H Stokes
Southern Research Institute
Birmingham, AL

INTRODUCTION

In order to increase the performance of future expendable and reusable launch vehicles and reduce per-pound payload launch costs, weight reductions have been sought in vehicle components. Historically, the cryogenic propellant tanks for launch vehicles have been constructed from metal. These are some of the largest structural components in the vehicle and contribute significantly to the vehicles total dry weight. A successful replacement material will be conformable, have a high strength to weight ratio, and have a low gas-permeability to the cryogens being stored, i.e., oxygen and hydrogen. Polymer-based composites are likely candidates to fill this role. Polymer and polymer-based composites in general are known to have acceptable gas permeation properties in their as-cured state.[1] The use of polymer-based composites for this application has been proposed for some time.[2] Some successes have been reported with oxygen[3], but other than the DC-XA experience,[4,5] those with hydrogen have been limited. The primary reason for this has been the small molecular diameter of hydrogen, the lower temperatures of the liquid, and that the composite materials examined to date have all been susceptible to microcrack formation in response to the thermal-mechanical cycles experienced in the use-environment. There have been numerous accounts of composite materials with reported acceptable resistance to the formation of microcracks when exposed to various mechanical and/or thermal cycles. However, virtually all of these studies have employed uniaxial loads and there has been no discussion or empirical evidence pertaining to how these loads relate to the biaxial state of stress in the material in its use environment. Furthermore, many of these studies have suffered from a lack of instrument sensitivity in detecting hydrogen permeability, no standards, insufficient documentation of test conditions, testing of cycled materials in their unload state, and/or false assumptions about the nature of the microcracks in the material. This paper documents the results of hydrogen permeability testing on a Bis-maleimide (BMI) based graphite fiber composite material under a variety of tetra-axial strain states.

MATERIALS AND METHODS

Five flat 12 inch by 12 inch by roughly 0.055 inch polymer matrix graphite fiber composite panels were delivered for testing. All of the panels were constructed from ten plys of 5½ mil uniaxial graphite fiber tape. The polymer matrix for the panels was a BMI resin. Yarns were oriented [90/60/90/-60/0]s, i.e., [90/+60/90/-60/0/0/-60/90/+60/90], to simulate the architecture needed for a cylindrical tank requiring a 2:1 ratio of mechanical properties. Four of the five panels were delivered in there as-processed state. Panel 3 was delivered preconditioned through 2500 uniaxial 0 to 5000 micro-strain tensile cycles in the 0° direction followed by the same in the 90° direction. The cycling was done at liquid hydrogen temperatures. One nine-inch and up to four 2.1 inch diameter permeability specimens were machined from each test panel. Eight uniformly distributed slots were machined radially from various concentric diameters to the outer diameter of the nine inch specimen producing eight pull-tabs used to apply the areal tensile strain in the specimen. Care was taken to avoid contamination of the surface of the specimen during machining and subsequent handling. Eight uniaxial strain gages were adhesive attached every 45° on a 3.25 by 3.75 inch concentric annulus around the specimen. One strain gage was mounted on the centerline of each pull-tab. Two type E thermocouples were adhesively attached to the reverse side of the specimen 180° apart on a 4.5 inch concentric circle with the specimen.

The gas permeability facility utilized in this study was calibrated using NIST SRM 1470 as described in ASTM D 1434 - 82 (Reapproved 1997). Room temperature gas permeability was measured on the specimen in the thickness direction. A circular gage section with a diameter of 1.5 or 1.8 inches at the center of each specimen was the material employed to measure the material's permeability under strain. To run the test, the specimen was placed in the facility. A sealing gasket was placed on the downstream and upstream halves of the facility and the two halves were mated. A compressive force was applied to the two halves of the facility through stainless steel 1.0-inch diameter balls that insured the alignment and even distribution of force on the specimen seals. A dynamic vacuum was applied to the upstream, downstream, and edges of the specimen overnight or until the specimen ceased to outgas. The downstream valve between the vacuum pump and transducer was then closed. After a sufficient record was obtained at these settings, hydrogen gas at a fixed pressure was applied to the upstream surface from a high pressure, high purity (5.5) hydrogen gas source. The increase in pressure downstream as a function of time was converted to a mass flow rate using the ideal gas equation. The mass flow rate was corrected for background outgassing from the specimen. The permeability in mol*m/m^2*s*Pa was calculated from the mass flow rate, specimen dimensions, and differential gas pressure across the specimen.

For measurements under tetra-axial strain the strain gages on the specimen and load cells on the facility were calibrated and zeroed prior to specimen installation. The specimen was placed in the loading facility. Each pull-tab of the specimen was aligned with one of the eight grips on the loading facility. The tensile load on each pull-tab was increased until the predetermined strain in each of the eight directions was obtained. All permeability testing of specimens was done at uniform levels of strain in the eight in-plane directions within the material. A record of the final strain in each of the eight directions was obtained. In some cases at elevated strain levels strain gages were lost due to surface cracks that developed in the materials under the gages. In those cases, a plot of load versus strain was constructed for the strain gage that failed and strains were estimated by extrapolating the load vs. strain data to the higher level of strain of interest. Loads were then calculated and applied that provided the pre-selected strain level. The permeability facility was positioned in place over the center of the specimen for measurement of the specimen's permeability. Strain levels were monitored during the sealing process to insure that no bending stresses are introduced to the specimen. The permeability facility has the capability of adjusting specimen orientation in the facility to relieve any parasitic stress states that may develop during the sealing process. The specimen orientation in the facility was adjusted until the measured strain in each of the eight directions of the specimen were equal to the strain in the specimen prior to sealing. The permeability of the material was then measured as stated above.

RESULTS

The hydrogen permeability data for the unstrained material in its as-processed state at room temperature (RT) are shown for two 2.1" diameter specimens taken from Panel 1in Figure 1. The nine-inch specimen from this panel, S1, was taken to 2500 micro-strain (με) in 500 με increments at room temperature with no significant increase in permeability. Upon reaching 2500 με the specimen exhibited several audible micro-failures and the gage at 135° failed (infinite resistance across the gage). A couple of small cracks were observed in the visible part of the gage section upon inspection of the specimen while under strain. The cracks were not visible once the strain was removed. Subsequent permeability measurements indicated the failures were surface structures that did not extend contiguously through the thickness of the material.

The nine-inch specimen from Panel 2, S2, was taken to 2500 με in 500 με increments with a significant increase in lateral flow upon reaching 2500 με. The specimen did not exhibit any audible sounds upon reaching 2500 and all gages were functioning. Upon removing the strain the lateral flow returned to as-processed levels. When the specimen was taken down to LN2 temperature and strain applied, the 0 and 180° gages were lost (infinite resistance) between 1500 and 2000 με. Furthermore, background gas flow into the downstream chamber increased dramatically indicating that the surface layers of the specimen were developing a significant system of micro-cracks. Between 2000 and 2500 με, the four off-axis gages, i.e., 45, 135, 225, and 315°, were lost. Only the 90 and 270° gages continued to function out to 2500 με. Post-test inspection of the gages indicated the gages were broke in tension probably due to a crack crossing the gage element. The damaged gages were replaced and the specimen was then taken down to LHe temperature. The high background levels of flow were due to surface cracks, which did not form contiguous paths through the thickness of the material. Following the cryo testing at

2500 με, the strain in the specimen was removed, the specimen was returned to RT, and the permeability measured. The background levels of flow returned to as-processed levels. Figure 1 shows the permeability as a

Figure 1. Permeability of IM7/BMI (Panels 1 & 2)
as a Function of Axisymmetric Strain State

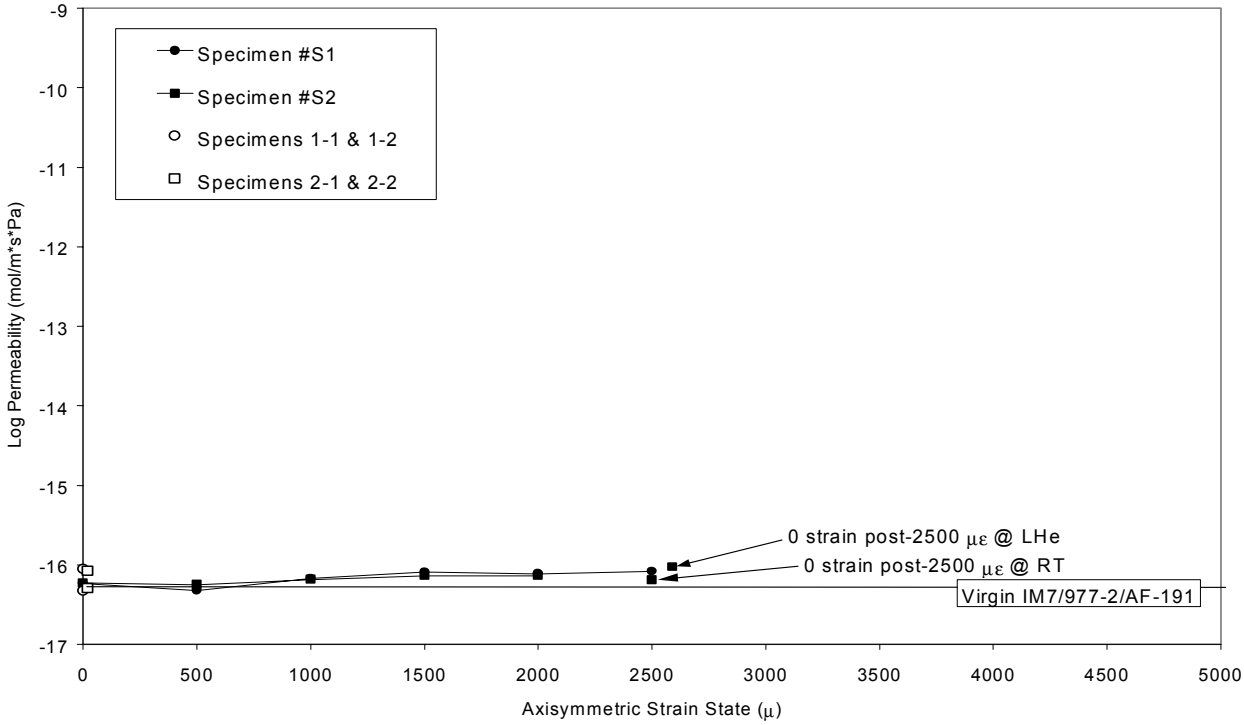

function of the applied tetra-axial strain for this specimen as well as two additional RT as-processed measurements from this panel.

The nine-inch diameter specimen from Panel 4, S4, was subjected to a number of modifications and load cycles. In addition, eight load cells were added to the permeability/strain facility prior to the testing of S4. Figure 2

Figure 2. Permeability of IM7/BMI (Panel 4)
as a Function of Axisymmetric Strain State

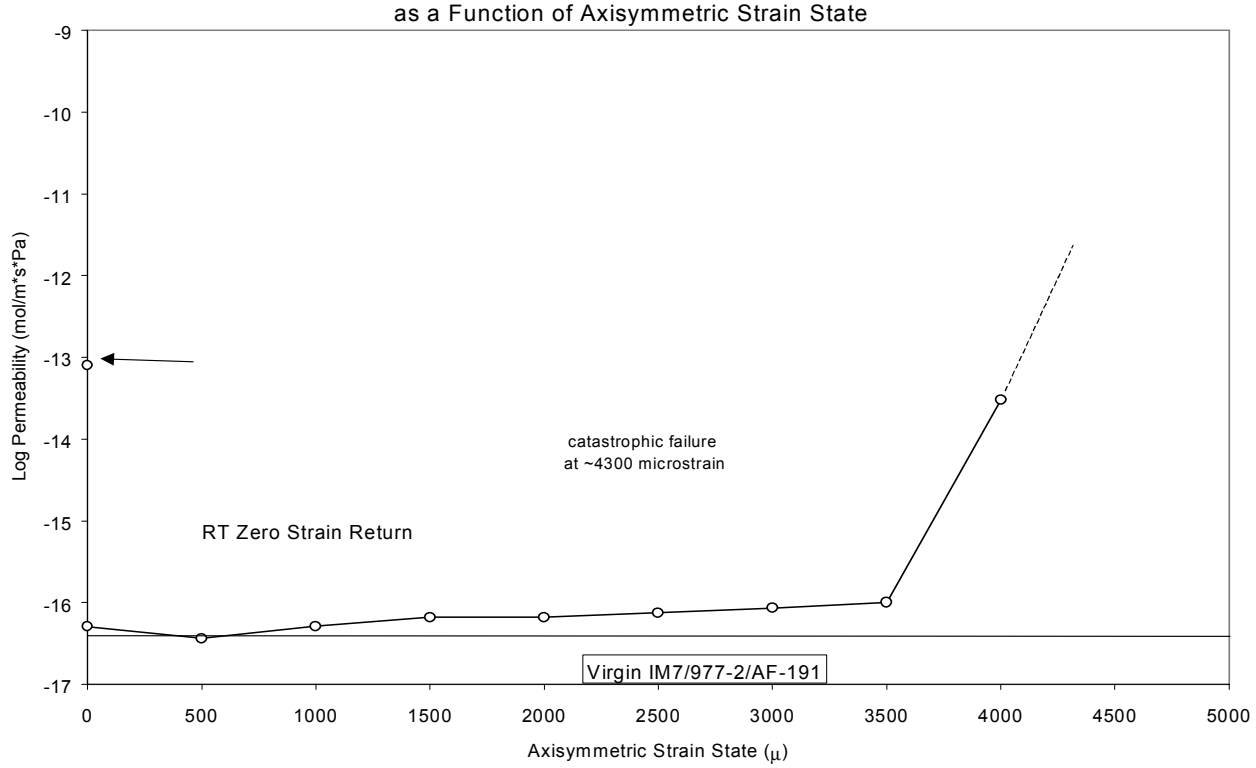

summarizes the permeability data for this specimen and compares it to the virgin unstrained quasi-isotropic IM7/977-2/AF-191.[6] The strain in specimen S4 was incrementally increased at room temperature. Small but steady increases in permeability (500 με excepted) were measured out to 3500 με. At 4000 με the specimen exhibited a large increase in hydrogen permeability. At approximately 4300 με the specimen catastrophically failed. Three of the eight pull-tabs (90, 135, and 180°) tore off at the inner most bolt circle. Hydrogen permeability of the specimen after it was removed from the loading facility was higher than the value obtained at 4000 με but lower than the anticipated permeability of the material at the point of failure (4300 με) by extrapolation of the log permeability vs. strain data (fig. 2).

Figure 3. Permeability of IM7/BMI (Panel 5) as a Function of Axisymmetric Strain State

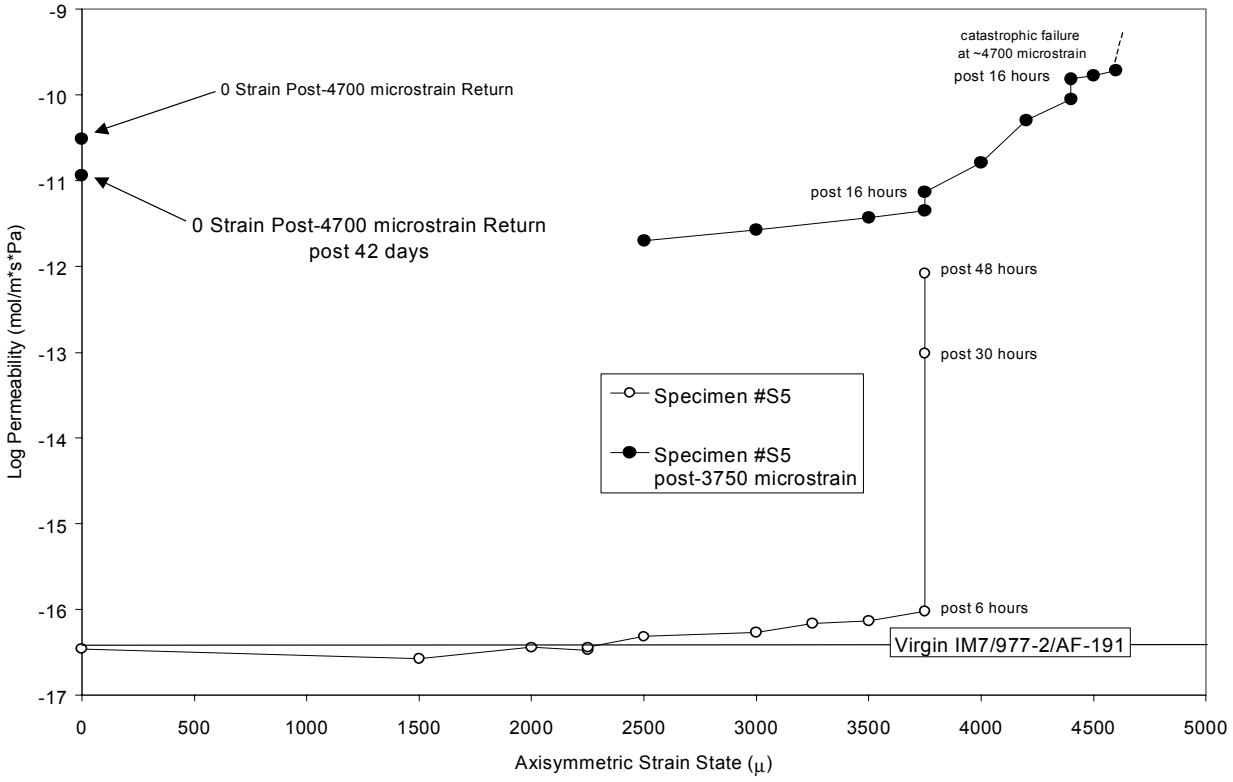

The tetra-axial strain in specimen S5 was likewise incrementally increased at room temperature. Small but steady increases in permeability were observed out to 3750 με. Smaller steps in strain were taken above 3000 με in order to more clearly observe the point where contiguous micro-crack development begins. At 3750 με the specimen exhibited a relatively small increase in hydrogen permeability consistent with the increases seen at lower strain levels. However, after 30 hours at 3750 με the specimen's permeability to hydrogen jumped by nearly three orders of magnitude over its permeability after 6 hours. After an additional 18 hours, the material's permeability to hydrogen increased by another order of magnitude. As might be anticipated, time at any elevated strain level is a significant factor in the development of a network of contiguous microcracks and rise in the material's permeability to hydrogen. A related behavior was also seen during off-loading when after dropping to some load level the strain, particularly in the 90 and 270° directions, was observed to creep to lower levels as a function of time. As with S4, significant surface cracks were detected upon reaching 2500 με. Figure 3 summarizes the permeability data for this specimen.

Figure 4 shows the load versus strain data for Run 2 Loading 1 (R2L1) of specimen S5. A curve is drawn through the 90° data showing the approximate shape of the curve describing this data. As can be seen in this figure the 90, 135, 180, and 315° directions exhibited strain offsets in the load versus strain data as low as 1500 με. Following the strain offset the slope of the load versus strain data generally became steeper indicating that a larger load

differential was required to cause a fixed incremental change in measured strain. This would be consistent with the formation of surface cracks that might partially de-couple the surface from the underlying material.

Figure 4. Mechanical Response of Specimen S5 to Tetra-Axial Tensile Loads
(Run 2 Loading 1)

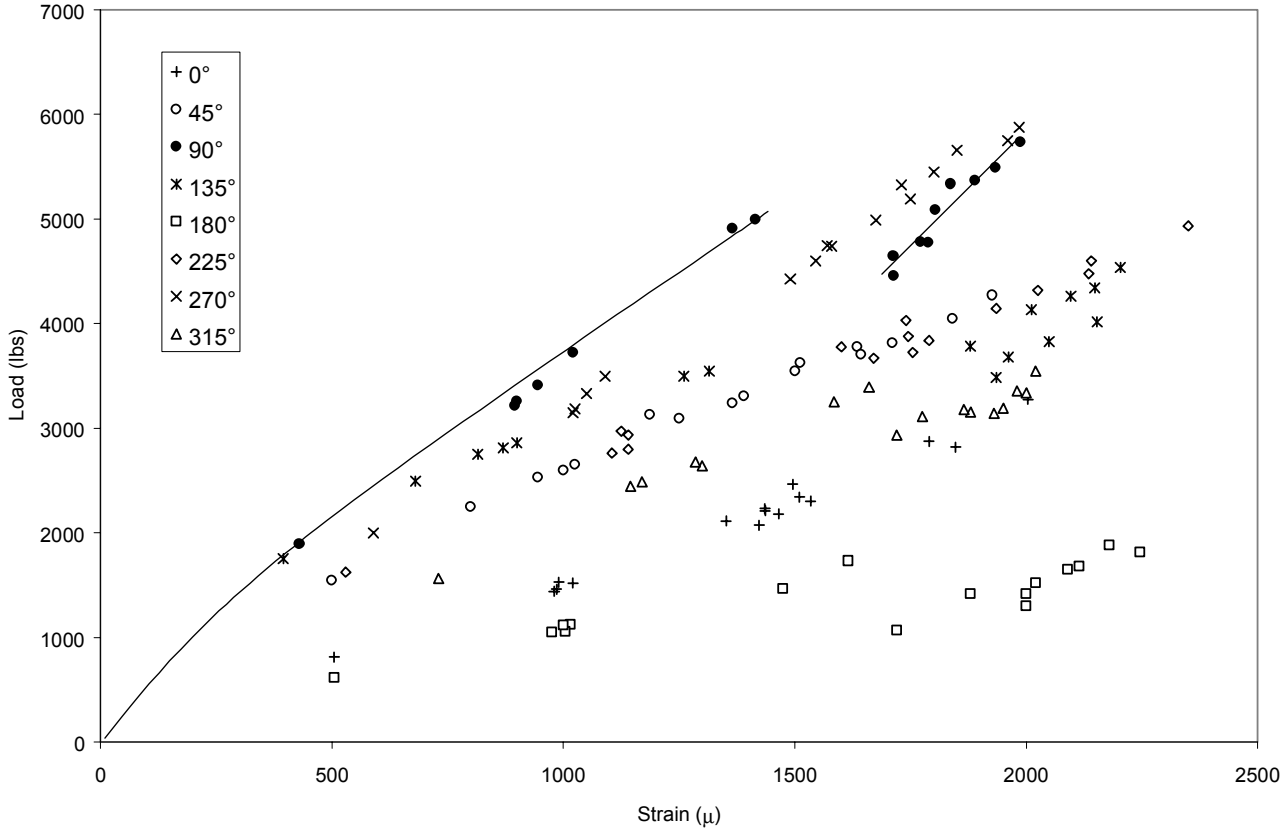

Permeability measurements were made following most runs after loads were removed. It was observed that these unstrained return values were generally higher than the values obtained prior to the application of load. Similar findings have been observed previously on other composite materials.[7,8] However, this response appears to be material specific.[9] Subsequent measurements of permeability on the unloaded specimens revealed that the permeability of the materials generally decreased with time and in some cases returned to pre-strained levels.[9] Figure 5 shows the loading and unloading data for Run 3 Loading 1 (R3L1) of specimen S5. There was a strong hysteresis exhibited by the material during offloading. This could explain the initial higher zero strain return permeability data that over time returns to the pre-strained levels. It is not clear at this point what is responsible for the time dependent strain recovery and changes in permeability during off-loading. However, movement of the softer cured resin into existing porosity under the influence of the residual stress in the graphite fibers during off-loading of the composite is suspected.

Figure 6 shows the load versus strain data for Run 3 Loading 2 (R3L2) of specimen S5. Above 3250 με the 90° data exhibited several large strain offsets. This was accompanied by the appearance of visible evenly spaced cracks spaced about 50 to 60 mils apart running in the 90-270° direction. The appearance of the cracks also coincided with the dramatic rise in hydrogen permeability measured at 3750 με (fig. 3). In addition, a strain offset was seen in the 45° direction above 3750 με.

Figure 7 shows a comparison of 90° data from a series of S5 loadings. The relatively small strain offset at 1500 με is visible with R2L1, as are the much larger strain offsets associated with R3L2. Contiguous through thickness micro-cracks had formed by the time S5 was offloaded from R3L2 as evidenced by the gas permeability data (fig.

Figure 5. Mechanical Response of Specimen S5 to Tetra-Axial Tensile Loads
(Run 3 Loading 1)

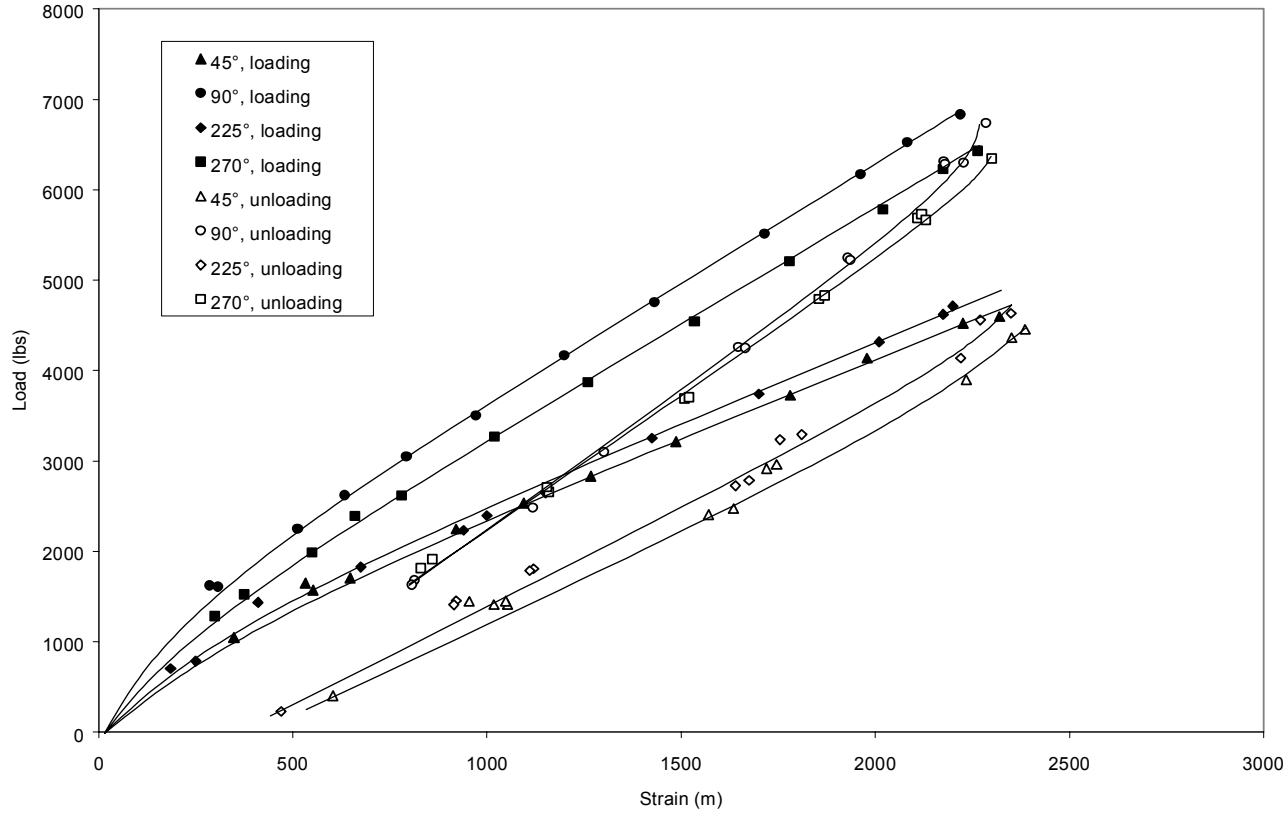

Figure 6. Mechanical Response of Specimen S5 to Tetra-Axial Tensile Loads
(Run 3 Loading 2)

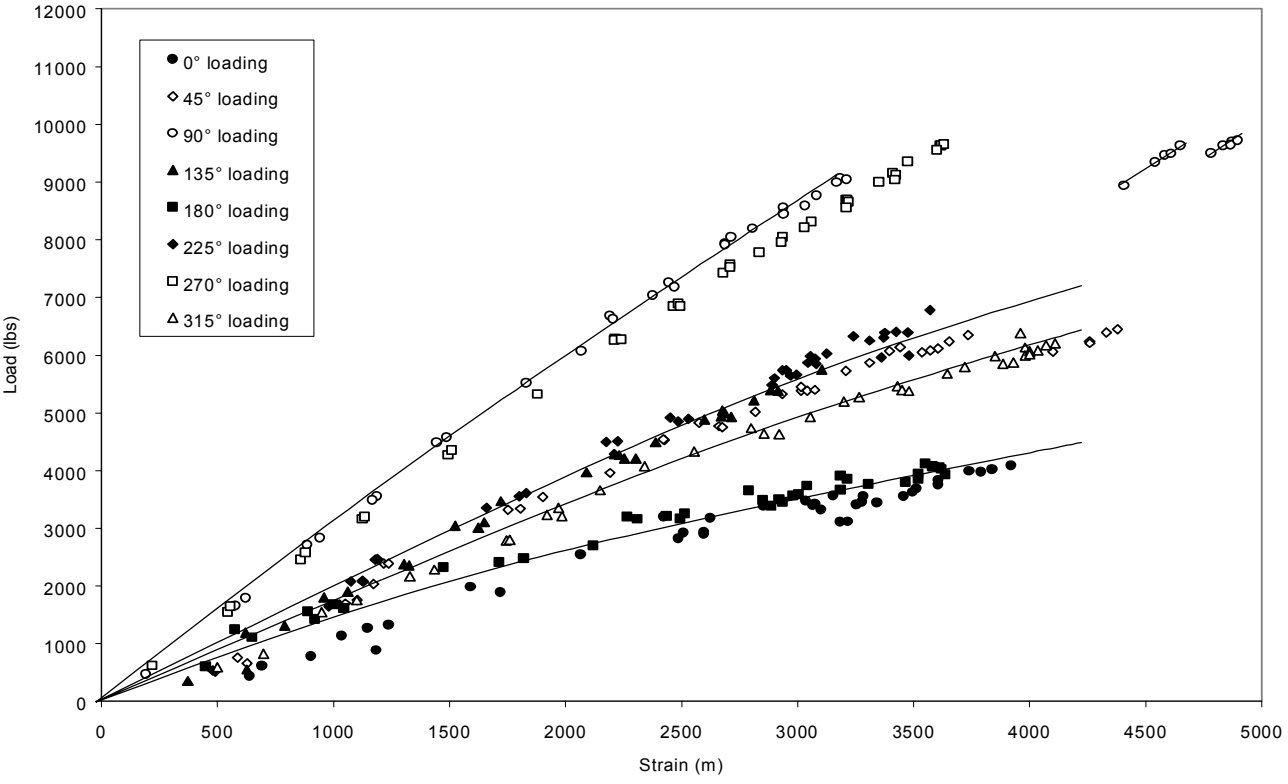

Figure 7. Mechanical Response of Specimen S5 to Tetra-Axial Tensile Loads
(Comparison of 90° Response)

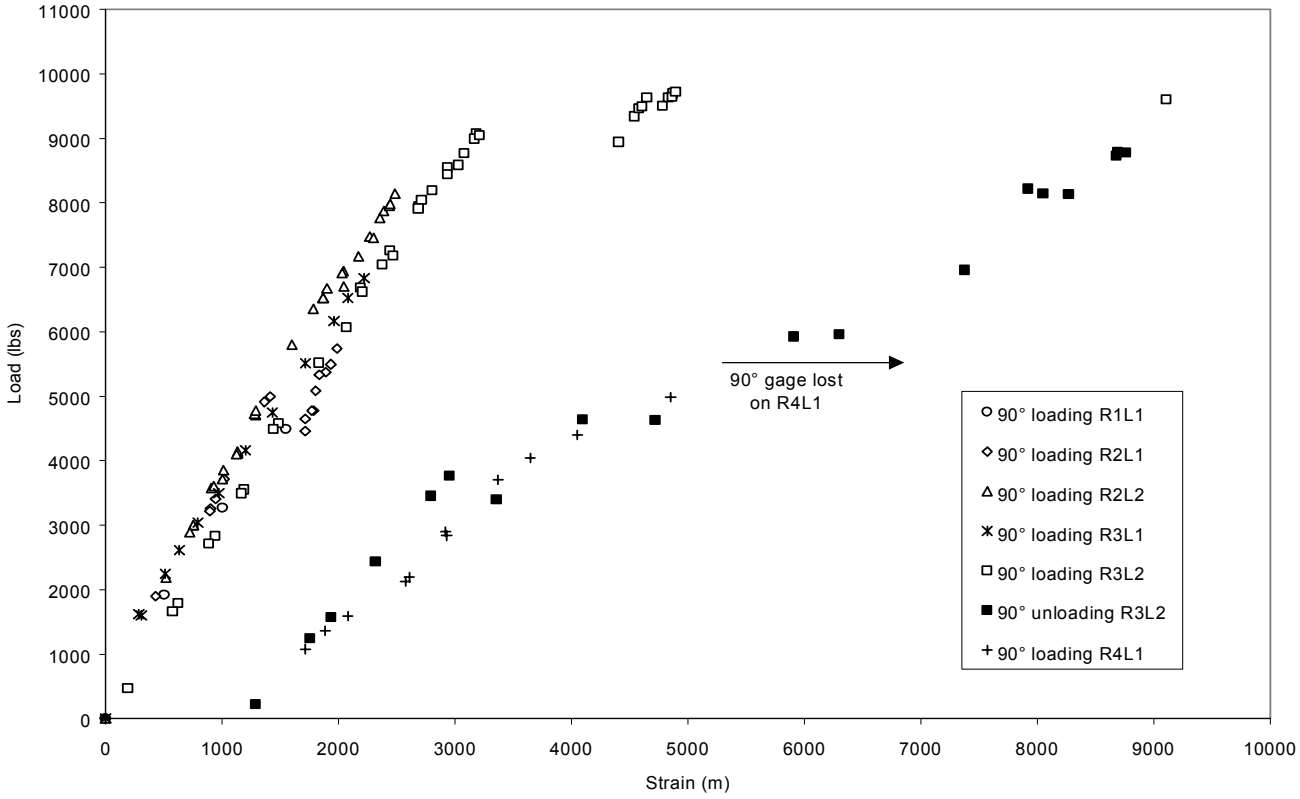

3). During loading in the subsequent run, R4L1, the specimen exhibited load versus strain behavior that followed the offloading curve of the previous run closely. This varied with the runs that followed the strain offsets prior to contiguous micro-crack formation indicating a significant change in tetra-axial tensile modulus with the development of through thickness cracks.

Figure 8 compares the hydrogen permeability data for the four specimens of virgin IM7/BMI (S1, S2, S4, & S5), one preconditioned IM7/BMI (S3), and virgin unstrained quasi-isotropic IM7/977-2/AF-191 (X-33).[6] Strain offsets in load versus strain data for the two specimens, S4 and S5, indicated that localized failures are occurring as low as 1500 με. These offsets are probably the result of the development of surface micro-cracks under the attached strain gages but indicate that the material is undergoing crack initiation as low as 1500 με under tetra-axial loading conditions. Widespread micro-cracking of the surface plies (90-270°) begins between 2500 and 3000 με at room temperature under uniform in-plane strain. Evidence for this can be seen in the high background flow rates seen with all four virgin specimens. These high backgrounds generally started at around 2500 με and progressively increased with applied strain. Strain measurements were made on the upstream surface of the specimen whereas flow measurements were made on the downstream surface so these two observations indicate that both surfaces are developing a system of micro-cracks at relatively low strain levels. In further support of these observations, an explosive gas detector was kept in close proximity to the test facility during all testing. It would routinely go off at around 2500 με when permeability testing was initiated and high-pressure hydrogen gas was being applied to the upstream surface of the specimen. This further supports the findings that surface cracks from both surfaces of the material were forming at comparatively low strain levels. However, through thickness flows were essentially constant out to much higher strain levels. The internal plies begin to micro-crack between 3500 and 4000 με at room temperature with uniform in-plane strain. These four observations would imply that crack initiation, with this material in the absence of any bending loads, begins at both surfaces and progressively extends toward the center of the panel.

Figure 8. Permeability of IM7/BMI as a Function of Axisymmetric Strain State

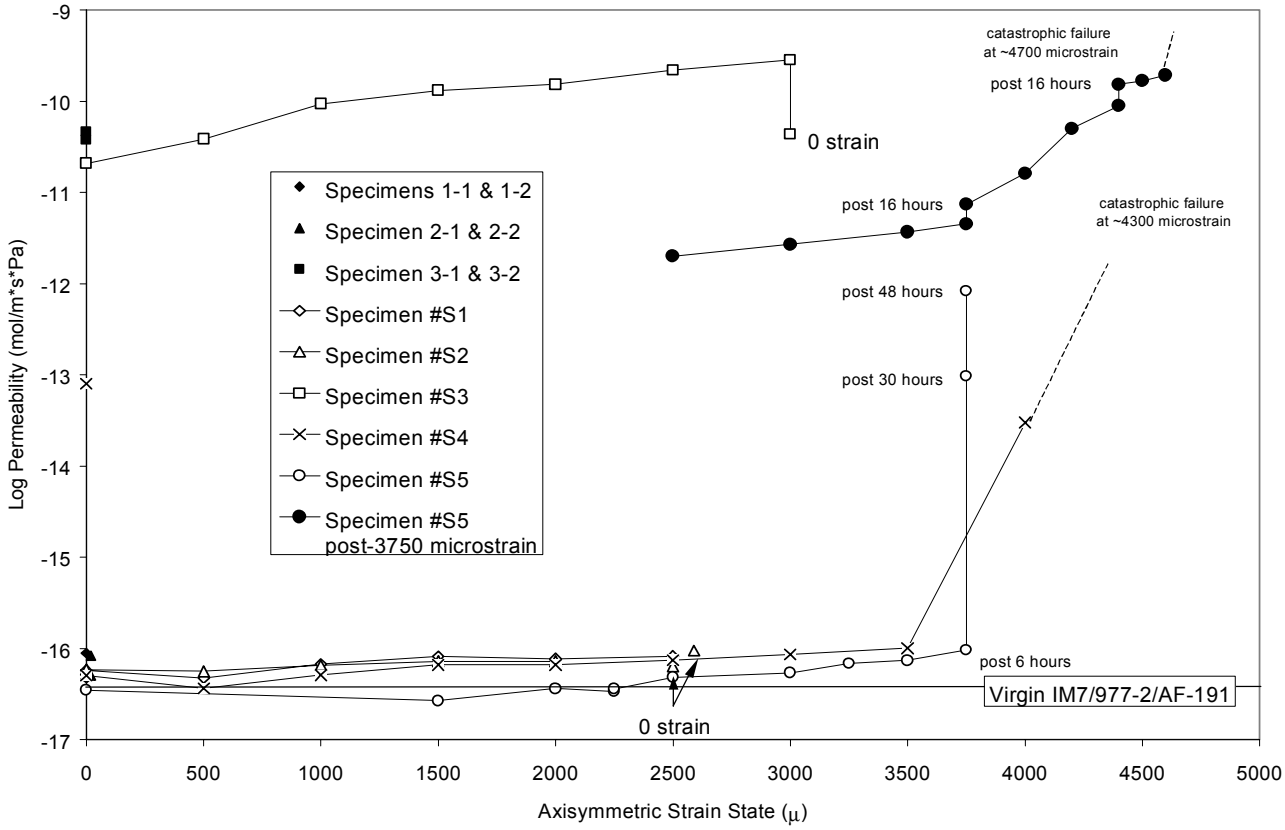

Figure 8 summarizes the effects of in-plane tetra-axial tensile strain on the hydrogen permeability of the Panel 3 material, S3. The unstrained preconditioned material had a permeability to hydrogen that was roughly 6 order of magnitude higher than the as-cured non-preconditioned material. The material exhibited consistent increases in hydrogen permeability with strain out to 3000 micro-strain, the maximum strain applied. There was greater than an order of magnitude increase in permeability between the initial unstrained and 3000 micro-strained states. Upon releasing the tetra-axial tensile load on the specimen following the application of 3000 micro-strain the material returned to the same permeability that it exhibited in its initial unstrained state.

Figure 9. Photomicrograph of 0/180° Slice (top) and 90/270° Slice (bottom) from Panel #3 (Preconditioned)

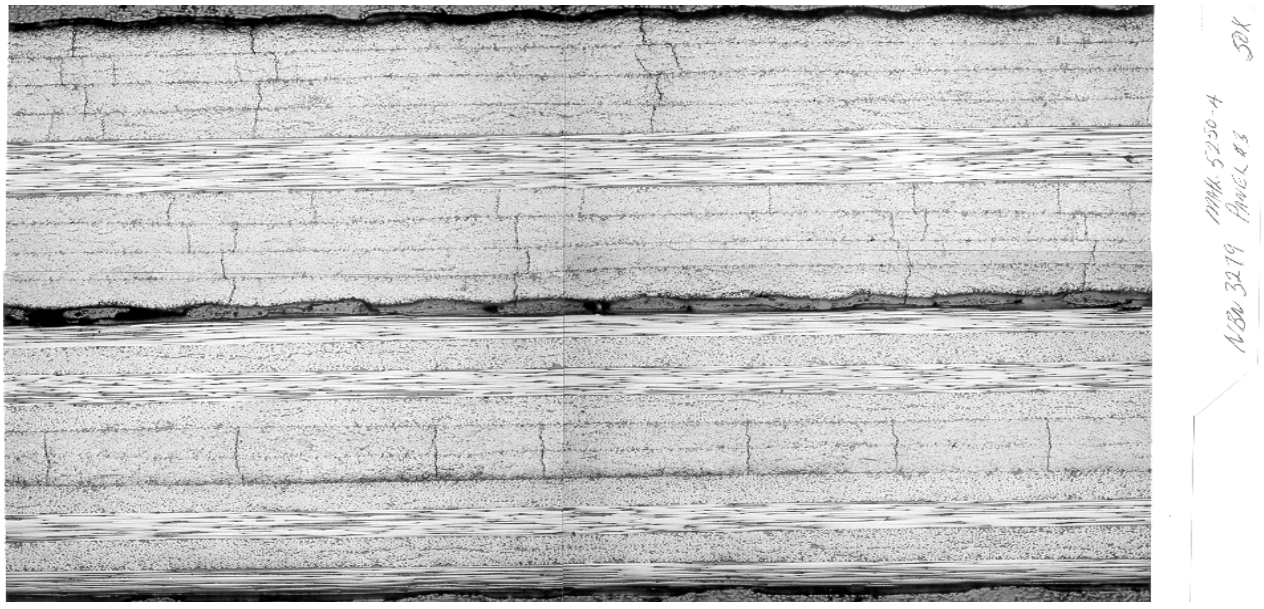

Figure 10. Crack Density by Ply for Five IM7 Based Preconditioned Composites

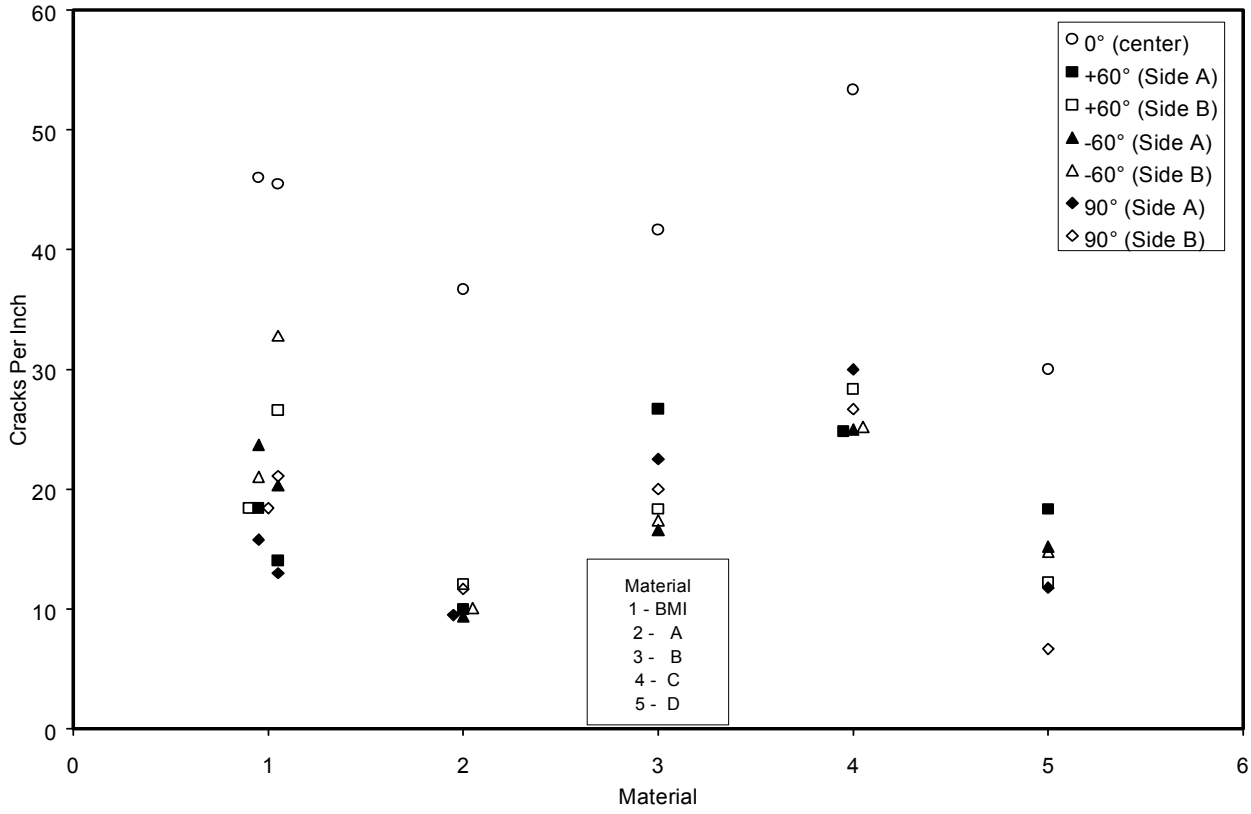

Figure 9 shows a photomicrograph of two stacked cross-sections through preconditioned Panel #3. The yarn architecture of the panel can be seen as well as a large number of cracks that run in the through thickness direction. The number of cracks per inch (crack density) varied from ply to ply. The plies lying in the center of the composite (0° plies) had the largest number of cracks per inch followed by the plies (-60°) that were adjacent to the center plies.

Figure 10 is a graph of the observed crack densities of five different preconditioned composite materials with the same yarn architecture by ply orientation. As can be seen in this graph the center 0° plies consistently had the highest crack densities. The adjacent –60° plies in all cases except the BMI material had crack densities that were similar to the other non-zero degree plies. In the case of the BMI material crack densities for the adjacent –60° plies was generally higher than the other non-zero degree plies.

CONCLUSIONS

1. Failure initiation for the BMI material under uniform in-plane strain is from the exposed surfaces and progresses toward the center of the material. In addition to the evidence of this from permeability testing, a post-test microscopic examination of the top and bottom four plies of the material indicate that wider cracks can be seen at the surface (90° plies) than in depth.
2. There is evidence that localized failures may be occurring in surface plies of the BMI material as low as 1500 micro-strain at room temperature with uniform tetra-axial in-plane strain.
3. Widespread micro-cracking of the surface plies of the BMI material begins between 2500 and 3000 micro-strain at room temperature under uniform tetra-axial in-plane strain.
4. A contiguous through-thickness crack system begins to form in the BMI material between 3500 and 4000 micro-strain at room temperature under uniform tetra-axial in-plane strain. It's unclear whether the 0 or –60° plies are the last to form microcracks. Intuitively, one might anticipate that the 0° plies would be the last to crack since they are mechanically the most supported and furthest from crack intiation. Microscopic evidence seems to

suggest the –60° (adjacent to the 0° plies) layers are the least open in the unstrained state. However, these plies are adjacent to the 0° plies, which would tend to close these cracks up on off-loading. Numerically, the –60° plies had the second highest crack density (cracks/inch) next to the 0° plies.

5. In addition to the material's strain level and temperature, permeability is a time dependent parameter for many of these the materials at RT and needs to be defined as such. Creep is an accepted phenomenon, particularly with polymers at elevated temperature or high loads. It's not clear how applicable it would be in a material that is generally mechanically loaded at cryogenic temperatures.

6. Catastrophic failure of the BMI material occurs somewhere above 4600 micro-strain at room temperature under uniform in-plane strain. Given the observed development of a significant crack system at 3750 micro-strain, the strain-to-failure of the material under axisymmetric loading can not be much greater than 5000 microstrain, which would be significantly less than that found when the material is unidirectional loaded.

7. For the BMI material that was not initially microcracked, strain was the first order variable with respect to the material's permeability.

8. For materials that already had a well-developed crack system, temperature was the first order variable with respect to the material's permeability. However, in most cases the applied strains were low relative to the anticipated strain-to-failure of these materials. Conversely, the general response of these materials to strain was highest at low strain levels suggesting that the changes observed out to 1500 με included the predominate response of the materials to changes in strain.[9,10]

9. The as-processed BMI material exhibited a time dependent sealing mechanism at room temperature after returning to an unstrained state from a series of microcrack inducing tetra-axial strain levels. A hysteresis effect between loading and unloading in load vs. strain curves generally accompanied this phenomenon. A similar mechanism was seen with some of the other preconditioned materials but more data is needed before definitive conclusions can be drawn with respect to these materials.

Acknowledgements

The author wishes to thank The Boeing Company, Huntington Beach, CA and in particular Jeff Eichinger, Mike Robinson and Scott Johnson for supporting this effort. This work was conducted with funds from NASA's SLI Program.

References

[1]Stokes, E. H., "Hydrogen Permeability of Polymers and Polymer-Based Composites," SRI-ENG-01-36-A392, July 2001, 72 p.

[2]Feldman, A., Giguere, A. J., Stang, D. A., "Design Application Of High-Modulus Filament-Wound Composites To Aerospace Propellant And Pressurization Tanks," In: MATERIALS AND PROCESSES FOR THE 70'S, SAMPE National Symposium And Exhibition, 15TH, Los Angeles, Calif, Apr. 29-May 1, 1969, Proceedings, pp. 151-161/A69-35501, 1969.

[3]Black, S., "X-34 Composite Liquid Oxygen Tank a First," High-Performance Composites, 2000(7-8):52-54, 2000.

[4]Nettles, A.T., "Permeability Testing of Composite Material and Adhesive Bonds for the DC-XA Composite Feedline Program," NASA TM 108483, March 1995.

[5] Cast, J., "Delta Clipper Rolls Out; Flight Tests to Begin in May," NASA Press Release #96-51, March 15, 1996. http://www.hq.nasa.gov/office/pao/History/x-33/nasa-96-51.htm

[6]Stokes, E. H., "Hydrogen Permeability Of Graphite Epoxy Composite Hydrogen Tank Materials As A Function Of Temperature And Bi-Axial Strain State," SRI-ENG-00-06-8657.22, February 2000, 253 p.

[7]Stokes, E. H., "Hydrogen Permeability at Room and Cryogenic Temperature of a Graphite Epoxy Composite Tank Panel Under Bi-Axial Strain," SRI-ENG-00-32-A194.01, December 2000, 33 p.

[8]Stokes, E. H., SRI-ENG-01-56-A435.0, November, 2001, 35 p.

[9]Stokes, E. H., "Hydrogen Permeability of Graphite Fiber Composite Hydrogen Tank Materials as a Function of Temperature and Tetra-Axial Strain State," SRI-ENG-02-17-A439, July 2002, 109 p.

[10]Eichinger, J. and Stokes, E.H., "Permeability Of Composite Hydrogen Tank Materials as a Function of Temperature and Strain State," In: Proceedings 44th AIAA/ASME/ASCE/AHS/ASC Structure, Structural Dynamics, and Material Conference, Special Session: Cryogenic Propellant Tanks and Integrated Structures for a Next Generation Reusable Launch Vehicle, April 7-10, 2003, Norfolk, VA, in press.

MICRO-RAMAN ANALYSIS OF IRRADIATED DIAMOND FILMS

Robert L. Newton
ED36A, Marshall Space Flight Center
Huntsville, AL 35812

Telephone: 256-544-7880, 256-544-5877 (fax)
robby.newton@msfc.nasa.gov

ABSTRACT

Owing to its unique and robust physical properties, diamond is a much sought after material for use in advanced technologies, even in Microelectromechanical Systems (MEMS). The volume and weight savings promised by MEMS-based devices are of particular interest to spaceflight applications. However, much basic materials science research remains to be completed in this field. Results of micro-Raman analysis of proton (10^{15} – 10^{17} H^+/cm^2 doses) irradiated chemical vapor deposited (CVD) films are presented and indicate that their microstructure is retained even after high radiation exposure.

INTRODUCTION

Diamond possesses many of the most sought after material properties desired in present day manufacturing. Its extreme hardness, high wear resistance, chemical inertness, optical transparency, and wide band-gap serve to illustrate this fact. As Figure 1 demonstrates, crystalline diamond has the highest elastic modulus and hardness values known (1).

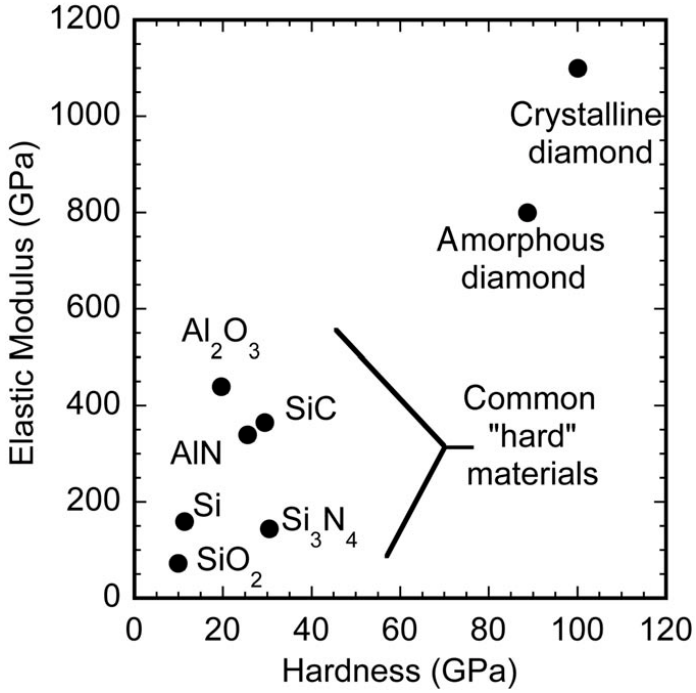

Figure 1. Comparison of hardness and elastic modulus values for a variety of "hard" engineering materials.

Synthetic 'Industrial diamond' has been commercially prepared for over thirty years yet it is polycrystalline diamond produced by techniques such as chemical vapor deposition (CVD) that show the greatest promise for insertion into advanced technologies such as electronics (2), MicroSystems (MST), and MicroElectroMechanical Systems (MEMS). In the rapidly growing areas of MST and MEMS technologies, recent work has demonstrated that diamond-based MEMS devices are feasible (3,4). Diamond offers significant advantages over silicon, the material currently used most often, especially in harsh environments such as high temperature or where high specific stiffness is required (5,6). Questions continue to be raised about silicon's durability in applications where high wear rates are involved.[7]

The understanding and control of film stress is a very important issue facing MEMS devices. MEMS materials should exhibit residual stresses of less than 10Mpa. This becomes even more significant for high modulus materials such as diamond. In diamond, the above stress level corresponds to an elastic strain of about 0.00001. This is equivalent to about 1Å of displacement for every 10 microns of beam length, assuming uniform loading. Of equal importance are strain gradients throughout the thickness of the film (8).

Diamond's resistance to radiation damage may prove to be one of its most valuable assets, especially for uses where exposure to potentially harmful radiation will be the norm, not the exception. Yet unlike silicon and most other materials, both single crystal and polycrystalline diamond have a tendency to convert to a physically very different, but compositionally identical, material upon sufficient irradiation…that being graphite. This is not surprising since graphite is the more thermodynamically stable form of carbon. Due to the large differences in the mechanical properties of these carbon polymorphs and the importance of understanding stress states in this material, it is important to characterize and understand this radiation-induced phenomenon, especially if the diamond film is to be used for structural purposes in MEMS/MST applications.

There are three major sources of ionizing radiation in the low-earth (LEO)/near earth environment: galactic cosmic rays, energetic electrons and protons trapped in the Earth's radiation belts, and solar particle events. However, protons and electrons dominate the radiation environment. The energy and Flux values for protons and electrons are given in Table 1(9).

Table 1. Particle type, energy and flux for LEO and near-Earth space environment.

Particle	**Energy (p/cm^2-day)**	**Flux (p/cm^2-day)**
Electron	100 keV-50MeV	10^2-10^{10}
Proton	100keV-10^3MeV	10^6-10^{10}

The goal of this investigation was to examine the relationship between proton dose and microstructure in chemical vapor deposited (CVD) diamond films using specimens mounted cross-sectionally. The use of protons allows one to not only study the charged particle that may cause the most microstructural damage in earth-orbit MEMS devices but also allows the study of relatively deeply buried damage inside the diamond material without resorting to MeV implant energies that may create extensive damage via the high energy needed for the implantation process itself. Since MEMS devices operating in space will not possess an opportunity to reverse radiation damage via annealing, only non-annealed specimens were investigated. Two high spatial resolution techniques – Scanning Electron Microscopy (SEM) and micro-Raman Spectroscopy (micro-Raman) were used to examine these relationships.

EXPERIMENTAL PROCEDURE

Polycrystalline diamond of approximately 20 microns in thickness was prepared at Vanderbilt University on a 2" single crystal silicon substrate by using microwave plasma assisted chemical vapor deposition (MPACVD) at a temperature of 800°C and a pressure of 110 Torr. The hydrogen flow rate was 479 sccm, methane flow rate was

18 sccm with a microwave power of 5 kilowatts. The total time of film deposition was twenty hours. Figure 2 illustrates a cross-sectional view of the as-deposited wafer.

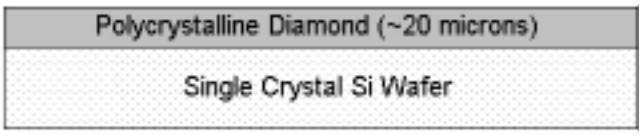

Figure 2. Schematic (cross-section) of polycrystalline diamond thin film prepared by microwave plasma-assisted chemical vapor deposition (MPACVD). The diamond is grown directly on the silicon substrate.

The samples were implanted with protons using a NEC Model 5SDH-2 Pelletron accelerator located at Alabama A&M University in Huntsville Alabama. 600KeV protons were implanted to dosages of $2x10^{15}H^{+}/cm^{2}$, $2x10^{16}H^{+}/cm^{2}$, and $2x10^{17}H^{+}/cm^{2}$, respectively, at room temperature. Based on theoretical calculations (TRIM software) this energy should deposit protons to a depth of ~4 microns into the films (10). The irradiation rate was kept below 10^{13} H^{+}/cm^{2}/sec so that non-linear effects could be avoided. After irradiation, the samples were cut and mounted on edge. They were then polished by personnel at both the Marshall Space Flight Center in Huntsville, AL and by personnel at the Oak Ridge National Laboratory in Oak Ridge, TN. SEM micrographs of the specimens were taken using an ElectroScan Environmental SEM located at the Marshall Space Flight Center in Huntsville, AL. Raman spectra were collected at Oak Ridge National Laboratories with a Dilor XY800 Raman microprobe (JY, Inc., Edison, NJ) configured as a single stage spectrograph using the microscope with a ~1 micron resolution. An Innova 308C Ar^{+} ion laser (Coherent, Inc., Santa Clara, CA) at 514.5 nm and 100 mW output power was used to excite the sample.

EXPERIMENTAL RESULTS

The diamond specimens were all taken from one 2" wafer. A composite photograph of all the specimens after each implantation regime is presented in Figure 3. The outline of the beam is visible in both the $2x10^{16}H^{+}/cm^{2}$ and $2x10^{17}H^{+}/cm^{2}$ implants.

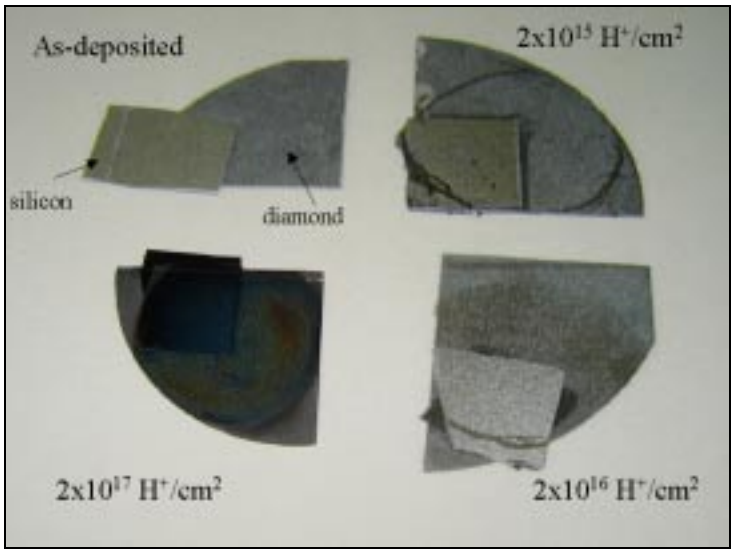

Figure 3. Photograph showing all specimens used in this investigation. The black lines on two of the samples were used to outline the beam diameter. Polycrystalline silicon specimens were also irradiated but results not presented in this paper.

No visible changes were observed in the $2x10^{15}$ H^+/cm^2 implant. For the $2x10^{16}$ H^+/cm^2 specimen, a mark was made on the surface of the specimen to delineate all of the irradiated area. Noticeable darkening was observed on the diamond specimen. The $2x10^{17}$ H^+/cm^2 implanted specimen was visibly much different than the as-deposited sample. Due to space limitations, the experimental data from the two mid-level implantations is not presented although some discussion of the experimental results for these are presented in the text.

Scanning Electron Microscopy (SEM) analysis was performed on all un-mounted specimens, examining both the top surfaces and the cleaved edges. Only the results from the as-deposited and most heavily irradiated specimens are presented herein. Prior to SEM analysis, all samples were rinsed with acetone, which was immediately blown off with compressed air. However, debris remained on the surface of all specimens. This debris was examined by x-ray fluorescence spectroscopy and was identified as being composed of elements such as Ca, K, and S although qualitative determination was not possible. Since the debris was present on all specimens, the material could not have been introduced via the implantation process. Also, this debris was absent on SEM analysis of the edge of the diamond specimens. As such, this debris was classified as surface contamination only. The top surface of the as-deposited diamond specimen indicated a <111> crystal growth with large facets. The grains are on the order of several microns in diameter with sharp, well defined edges. An SEM micrograph of the as-deposited specimen is shown in Figure 4. The top surface of the $2x10^{15}$ H^+/cm^2 implanted specimen appeared to be identical to the as-deposited material. No visible change in the surface of the diamond was detected. Careful inspection of the top surface of the $2x10^{16}$ H^+/cm^2 implanted specimen indicated that although the crystallites remained intact, dark regions randomly populate the micrograph. However, the edges of the crystals remained well defined.

The situation is significantly different for the $2x10^{17}$ H^+/cm^2 implanted material, that being the most heavily irradiated specimens. The wide-angle and close-up micrographs indicate severe degradation of the crystallite edges…so much so that the grains have a somewhat "melted" appearance. A close-up SEM micrograph is shown in Figure 5.

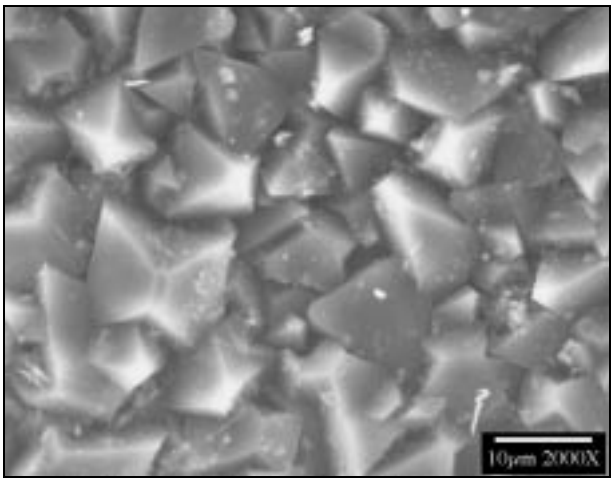

Figure 4. Scanning Electron Micrograph (SEM) of top surface of "as-deposited" polycrystalline diamond film.

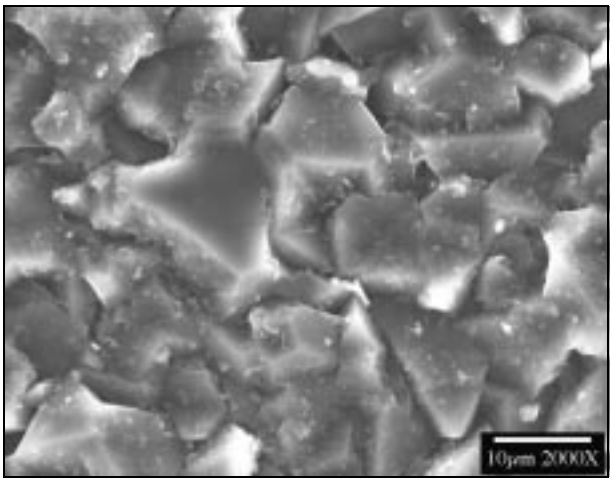

Figure 5. Scanning Electron Micrograph (SEM) of top surface of $2x10^{17}$ H^+/cm^2 proton implanted polycrystalline diamond film.

Raman spectra were collected in triplicate from the top surface of each specimen. While the penetration depth of the Raman laser signal will vary with opacity, surface roughness, laser energy, etc., the signal does penetrate several microns into the material (11). The spectra have been averaged, smoothed and normalized. A Lorentzian function was used for curve fitting and an example is shown in the inset for the "as-deposited" spectra (see Figure 6). Single crystal diamond exhibits a sharp Raman peak at ~1333 cm^{-1} with a Full Width at Half Maximum (FWHM) of less than 3.0 with no other spectral signatures present. The as-deposited material compared extremely well with high purity single crystal material, although the diamond used in this study was polycrystalline.

The diamond peak is sharp, well defined and symmetrical. The FWHM is close that that reported for high-purity single crystal material (~3 cm^{-1}). No graphitic or amorphous bands are observed. The Raman spectra for the diamond specimen irradiated with a proton dose of $2x10^{15}$ H^+/cm^2 compared favorably with the as-deposited material. The FHWM was slightly lower, but within experimental error for the as-deposited sample. No graphitic components were detected. The diamond peak is sharp, well defined, and symmetrical, indicating no measurable microstructural damage from the irradiation. The intensity of the peak matched very closely that of the as-deposited specimen. The Raman spectra from the top surface of the $2x10^{16}$ H^+/cm^2 implant began to show some effects from the implantation. Since a slight amount of darkening was present in this sample, the probe depth of the laser is reduced with respect to the as-deposited and $2x10^{15}$ H^+/cm^2 implanted samples. While the diamond peak is sharp, intense, and largely symmetrical, the peak is shifted slightly downward, indicating tension within the microstructure. The slight increase in the FWHM, taken with the 1630cm^{-1} peak present in the spectra, suggests that ion-induced defects are responsible.

The spectra taken from the top surface of the most heavily irradiated specimen indicates extensive ion-induced damage to the microstructure(see Figure 7). Due to the extreme darkening of the surface of this specimen, the probe depth of the Raman signal is attenuated in comparison to the as-deposited and $2x10^{15}$ H^+/cm^2 implanted samples. The first-order diamond peak is shifted downward by almost two wavenumbers. The intensity of the peak is greatly diminished. The FWHM broadening is due to the ion-induced defects which are observed from ~1490 to 1650 cm^{-1}. Peaks attributed to ion-implantation damage - i.e. the monovacancy (1490cm^{-1}), the split interstitial (1630cm^{-1}), and the broad graphitic band at ~1550cm^{-1}, are observed. Other damage related peaks are also observed. However, the sharp line located ~1430cm^{-1} is due to a detector malfunction within the Raman system.

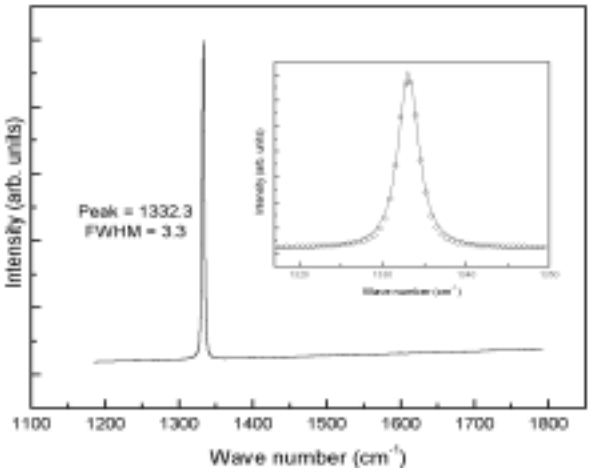

Figure 6. Micro-Raman spectra of top surface of "as-deposited" polycrystalline diamond wafer. Inset shows Lorentzian fit to experimental data.

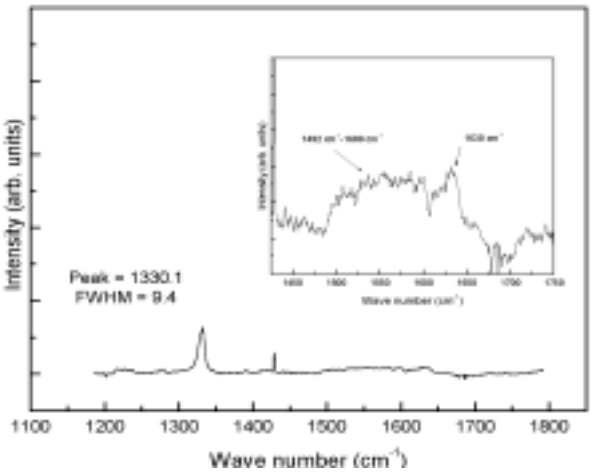

Figure 7. Micro-Raman spectra of top surface of $2x10^{17}$ H^+/cm^2 implanted polycrystalline diamond wafer. Implantation induced damage is shown in inset.

Figure 8 presents an overview of the top surface micro-Raman investigation. The first order Raman peak position and the first order peak FWHM are examined in relationship to proton dosage. With respect to the first order diamond peak position, within experimental error, the as-deposited and $2x10^{15}$ H^+/cm^2 implanted specimens are very similar to each other. The $2x10^{16}$ H^+/cm^2 and $2x10^{17}$ H^+/cm^2 implanted samples reveal increasing damage with increasing proton dosage. However, the first order diamond peak was still evident. This is not surprising since the greatest amount of microstructural damage is expected to occur near the end of range (EOR) of the implant,

which in this case is ~4 microns deep, and not near the surface of the material where the majority of the Raman signal originates from within the sample.

The FWHM follows a similar patter for these series of implantations. While the $2x10^{16}H^{+}/cm^{2}$ implant reveals a slight broadening, indicating microstructural damage, the $2x10^{17}H^{+}/cm^{2}$ implant indicates a much larger shift. Also, the as-deposited and $2x10^{15}H^{+}/cm^{2}$ implants were, within experimental error, unaffected by the irradiation.

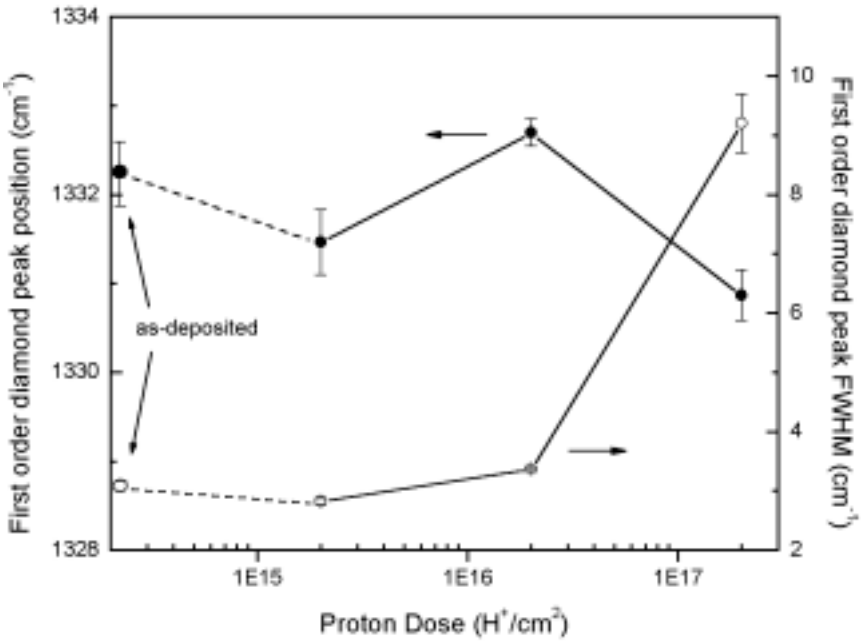

Figure 8. Graph showing first order diamond peak position and first order diamond peak Full Width at Half Maximum (FWHM) as a function of proton dosage for entire series.

After SEM analysis of the top surfaces of the diamond specimens, they were then examined along the fractured edges. This was done in order to visually examine any depth dependent effects the proton implantation might have created. The results of this investigation are shown in Figures 9 and 10 for the as-deposited and heavily irradiated specimens, respectively. SEM edge analysis of the as-deposited material revealed an extremely rough edge surface. The interface of the diamond film/silicon substrate is clearly evident. Columnar grain growth, typically seen in <111> diamond films, is difficult to detect in this specimen. The $2x10^{15}$ H^{+}/cm^{2} implanted film edge looks much like the as-deposited material. No radiation damage, either on the surface or down the edge, is observed in any of the specimens.

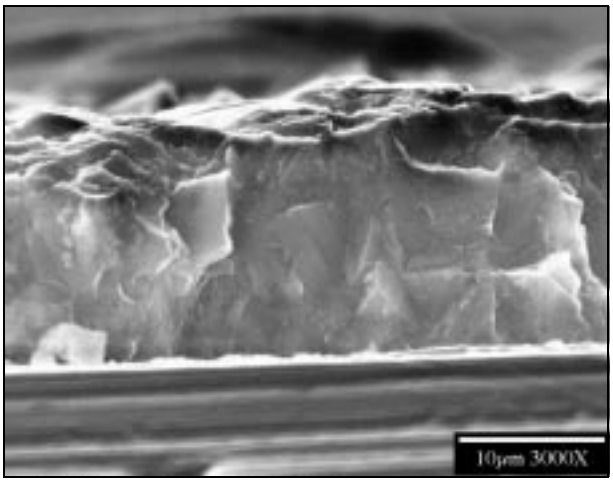

Figure 9. SEM micrograph showing the edge surface of the "as-deposited" polycrystalline diamond wafer. The diamond film/silicon substrate interface is indicated by the white horizontal line near the lower portion of the figure.

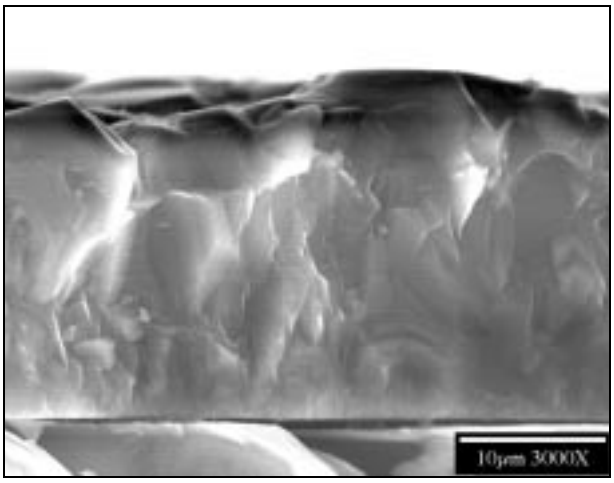

Figure 10. SEM micrograph showing the edge surface of $2x10^{17}$ H^+/cm^2 implanted polycrystalline diamond wafer.

Raman spectra were obtained on both unpolished and polished diamond specimens. No artifacts from the polishing were observed. However, since the polished specimens did provide a more uniform surface for investigation, they were used for the high resolution data collection.

The micro-Raman spectra were collected by performing a "line scan" across the specimen cross-section. Each "line scan" consisted of forty individual spectra that were collected at intervals of every micron. The scan would start on the silicon substrate and end past the edge of the sample. Since silicon and diamond have very different Raman signatures, locating the interfaces of the films was relatively simple. However, this was complicated due to the fact that near the films interfaces, the Raman spot size included contributions from both the silicon and diamond.

The spectra for the as-deposited material is shown in Figure 11. The 1um line scan contains a sharp first-order diamond peak at ~1332 cm^{-1}. However, the broad band from ~1450 to 1700 cm^{-1} is indicative of graphitic-like carbon. This is attributed to surface effects, were carbon exists in a variety of bonding configurations. The 2-6 micron scans are void of this broad peak signifying the high fidelity of the carbon film throughout the entire layer. This material appears to be free of depth-dependent stress and microstructural damage due to the fact that the first-order diamond peak shifted very little nor was there an increase in the FWHM.

The line scans for the $2x10^{15}$ H^+/cm^2 implanted specimen looked similar to the control specimen. The depth-dependent Raman line scans for the $2x10^{16}$ H^+/cm^2 implanted specimen revealed a defect-related peak at 1630 cm^{-1}. This defect is associated with the <100> split interstitial. This peak increased with depth and reached a maximum at 4 microns, beyond which it decreased rapidly and was absent at 6 microns. Also, there was a slight increase in the baseline between the regions of 1400 cm^{-1} and the 1630 cm^{-1} peak.

The proton implantation effect as a function of depth for the most heavily irradiated specimen, the $2x10^{17}$ H^+/cm^2 implant, is presented in Fig. 12. In this representative line scan series, extensive defect-related spectral signatures are evident even at 1um. The vacancy (1495 cm^{-1}), the broad amorphous region at ~1550 cm^{-1}, and the <100> split interstitial (1630 cm^{-1}) are all present. The first order Raman line is greatly diminished in intensity as compared to the control sample. The damage increases until reaching a maximum at 4 microns. At this depth, the diamond peak is diminished in intensity but still present. The 1495 cm^{-1} peak may be present but resolution is impossible due to the increase in baseline present throughout this entire region. The 1630 cm^{-1} peak grows in intensity as a function of depth until reaching a maximum at 4 microns as well. By 6 microns, the spectra returned

in appearance to looking very similar to the as-deposited specimen, although the baseline is still slightly elevated across the entire 1400 cm^{-1} to 1650 cm^{-1} region.

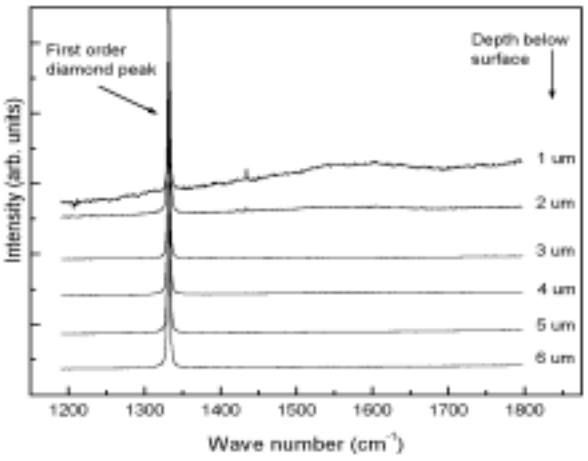

Figure 11. Micro-Raman spectra as a function of depth across the surface of the "as deposited" polycrystalline diamond film.

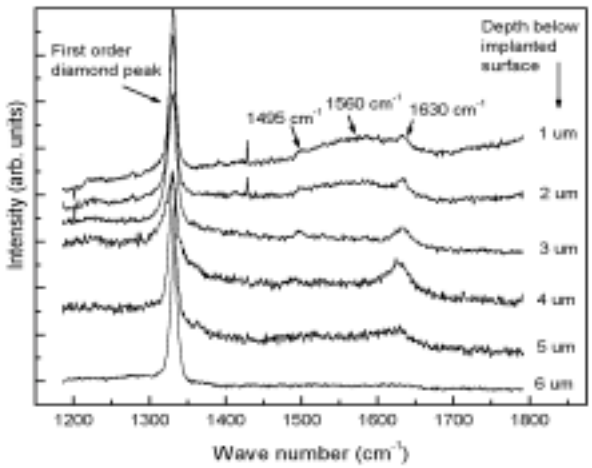

Figure 12. Micro-Raman spectra as a function of depth across the surface of the 2x101$^{7}H^{+}/cm^{2}$ polycrystalline diamond film.

Summary charts are presented in Figures 13 and 14 for the entire diamond series. First order diamond peak position is seen to shift for both the 2x10^{16} H^{+}/cm^{2} and the 2x10^{17} H^{+}/cm^{2} implant series. Likewise, the FWHM variation as a function of depth illustrates an increasing damage to the microstructure until reaching a maximum at the End of Range (EOR). This is to be expected due to the fact that the maximum carbon atom displacement occurs near the end of the proton travel where a maximum of nuclear energy is deposited. Past the EOR, a slow return to baseline is observed. In applications where extremely low stress/strain values in the film are critical, this effect could affect device performance.

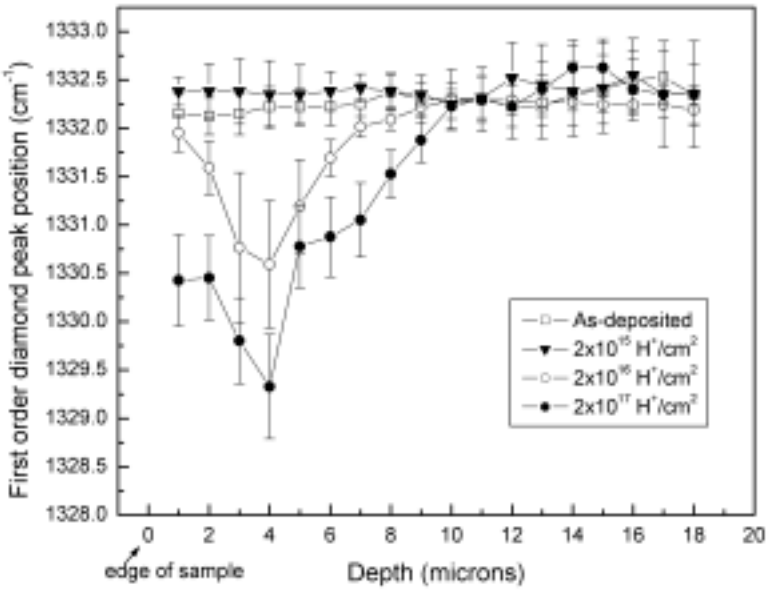

Figure 13. Variation in first order peak position as a function of depth for the entire series.

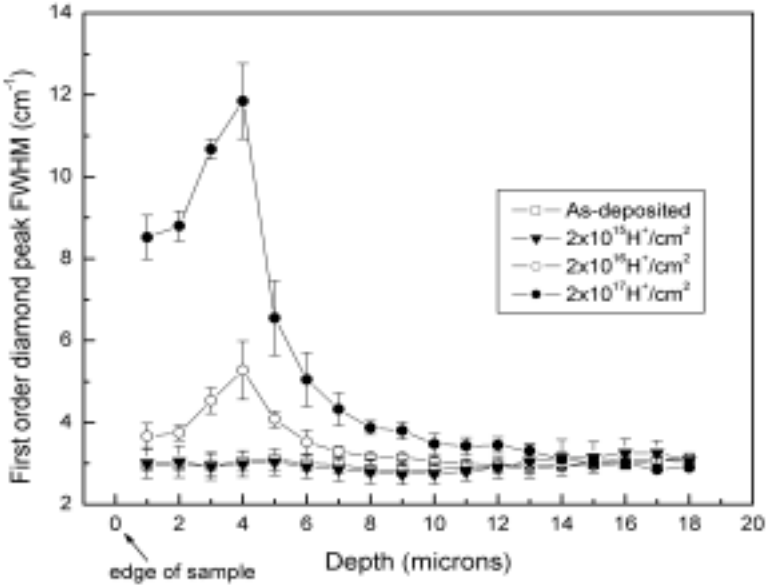

Figure 14. Variation in first order FWHM as a function of depth for the entire series.

CONCLUSIONS

The effects of proton irradiation on CVD diamond films have been examined using SEM and micro-Raman techniques. A proton dose of $2x10^{17}H^{+}/cm^{2}$ is sufficient to visibly darken and degrade the top surface of the films. Raman analysis indicated both a shift in first order diamond peak position and FWHM. These conditions indicate both stress and microstructural damage near the surface of the films.

In the cross-sectional analysis, TRIM software accurately predicted the implantation range of the protons. Across the series, the maximum peak shift and FWHM broadening occurred at ~4 microns from the surface. The damage increased with increasing dosage although the first order diamond peak was always present, implying that the diamond structure was not totally destroyed by the implantation.

ACKNOWLEDGEMENTS

The author gratefully acknowledges the support of Mr. Charles Griffith of MSFC and personnel from Oak Ridge National Laboratories for assistance with mounting and polishing the diamond films. Also, the assistance of the staff from the Ion Implantation facility at Alabama A&M as well as Dr. M. Lance (ORNL) is greatly appreciated. This work was funded by NASA-Marshall Space Flight Center's Engineering Directorate.

1. Sullivan, J.P., Friedman, T.A., and Hjort, K., MRS Bulletin, April 2001.

2. Railkar, T.A., et. al., Critical Reviews in Solid State and Materials Science, 25(3), 163, (2000).

3. Davidson, J.L., Kang, W.P., Gurbuz, Y., Holmes, K.C., Davis, L.G., Wisitsora-at, A., Kerns, D.V., Eidson, R.L., and Henderson, T., D., Diamond Relat. Mater. 8 , 1741 (1999).

4. Kohn, E., Gluche, P., and Adamschik, M., Diamond Relat. Mater. 8, 934 (1999).

5. Spearing, S.M., Acta. Mater. 48, 179 (2000).

6. Fahrner, W.R., Job, R., and Werner, M., Microsystem Technologies 7, 138, (2001).

7. Wang, et. al., Sensors & Actuators A, 97-98, 486, 2002.

8. Sullivan, J.P., Friedman, T.A., and Hjort, K., MRS Bulletin, April 2001.

9. NASA-MSFC Internal Technical Publication (1999).

10. Ziegler, J.F., Biersack, J.P., and Littmark, U., The Stopping and Range of Ions in Matter, Pergamon Press, New York, 1985.

11. Private communication with Dr. M. Lance, Oak Ridge National Labs.

High Strength and Wear Resistant Aluminum Alloy for High Temperature Applications

JONATHAN A. LEE
NASA-Marshall Space Flight Center (MSFC)
Mail Code ED33
Huntsville, AL 35812
Email: Jonathan.Lee@msfc.nasa.gov

Po Shou Chen
Morgan Research Corporation
4811 A Bradford Drive
Huntsville, AL 35805-1948
E-mail: Pchen@morganres.com

ABSTRACT

Originally developed by NASA as high performance piston alloys to meet U.S. automotive legislation requiring low exhaust emission, the novel NASA alloys now offer dramatic increase in tensile strength for many other applications at elevated temperatures from 450°F (232°C) to about 750°F (400°C). It is an ideal low cost material for cast automotive components such as pistons, cylinder heads, cylinder liners, connecting rods, turbo chargers, impellers, actuators, brake calipers and rotors. It can be very economically produced from conventional permanent mold, sand casting or investment casting, with silicon content ranging from 6% to 18%. At high silicon levels, the alloy exhibits excellent thermal growth stability, surface hardness and wear resistant properties.

INTRODUCTION

Aluminum-Silicon (Al-Si) alloys are most versatile materials, comprising 85% to 90% of the total aluminum cast parts produced for the automotive industry. Depending on the Si concentration in weight percent (wt.%), the Al-Si alloy systems fall into three major categories: hypoeutectic (<12% Si), eutectic (12-13% Si) and hypereutectic (14-25% Si). However, most Al-Si alloys are not suitable for high temperature applications because tensile and fatigue strengths are not as high as desired in the temperature range of 500 °F - 700 °F. In recent years, the development of diesel and direct fuel injection gasoline engines with high specific powers have resulted in a big performance impact on piston materials due to increased combustion pressures and piston temperatures.

To date, most of the Al-Si cast alloys are intended for applications at temperatures of no higher than about 450 °F. Above this temperature, the alloy's microstructure strengthening mechanisms will become unstable, rapidly coarsen and dissolve resulting in an alloy having an undesirable microstructure for high temperature applications. Such an alloy has little or no practical application at elevated temperatures because the alloy lacks the coherency between the aluminum solid solution lattice and the precipitated strengthening particles (1-2). In general, a large mismatch in lattice coherency contributes to an undesirable microstructure that cannot maintain excellent mechanical properties at elevated temperatures. FIG. 1(A) is a diagram illustrating a coherent particle that has similar lattice parameters and crystal structure relationship with the surrounding aluminum matrix atoms. FIG. 1(B) is a diagram illustrating a non-coherent particle having no crystal structural relationship with the aluminum atoms, which results in an alloy that has little or no practical application at elevated temperatures.

One approach taken by the prior art is to use particulate reinforcements to increase the strength of Al-Si alloys. This approach is known as the aluminum Metal Matrix Composites (MMC) technology (3-5). It is noted that the strength for most particulate reinforced MMC's manufactured from an Al-Si matrix alloy are still inferior for high temperature applications because the alloy major strengthening phases are unstable for long term exposure at high temperatures. An alternative is the use of ceramic fibers reinforced MMC, which is a relatively expensive process to produce for most automotive engine parts.

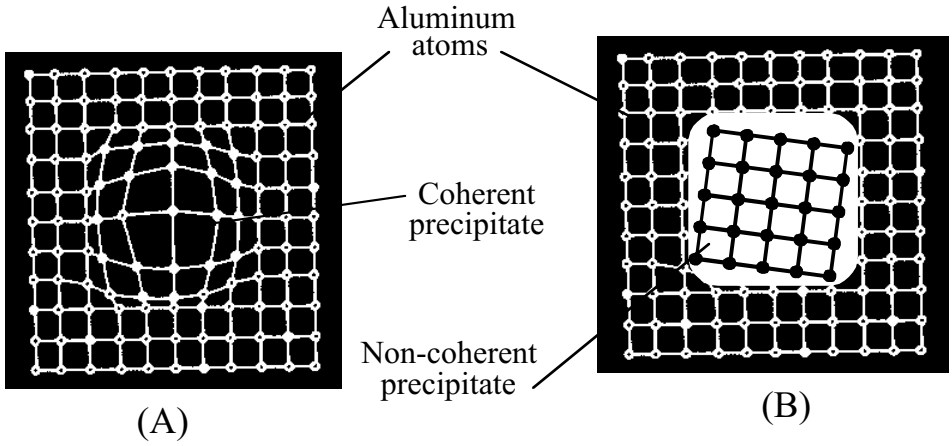

FIG. 1(A) illustrates a coherent precipitated particle that has similar crystal structure relationship with the surrounding aluminum matrix atoms. FIG. 1(B) illustrates a non-coherent precipitated particle.

The new NASA high strength alloy is an ideal low cost aluminum alloy for high temperature cast components such as pistons, cylinder heads, cylinder liners, connecting rods, turbo chargers, impellers, actuators, brake calipers and rotors. NASA 398 is an aluminum-silicon alloy that may be used in a bulk alloy form with silicon content ranging from 6% to 18%. At high silicon levels the alloy exhibits excellent surface hardness and wear resistance properties.

Due to increasingly stringent emission regulations for internal combustion engines, NASA 398 alloy is uniquely applicable for new piston design to reduce emission. Combustion analysis from engines has shown that the unburned fuel comes mostly from a ring-shaped crevice that is formed between the cylinder wall surface, the piston outside wall, and the top of the piston ring (6-8). If the flame in the combustion chamber cannot travel deep into the piston's wall and enter the inside of the crevice, the unburned fuel is exhausted out of the combustion chamber in the expansion stroke as the main source of hydro-carbon emissions (9-10). Current modification is to reduce the piston's crevice volume by moving the top piston ring closer to the top of the piston. Such piston modifications would require a stronger alloy to prevent the piston failure due to high mechanical and thermal loading of the top piston's ring groove and ring lands. NASA alloys can be used for high performance pistons requiring high fatigue strength in the pin boss area and high wear resistance of the flanks of the first ring groove.

ALLOY PROCESSING PARAMETERS

NASA 398 is a hypereutectic alloy (16% w. Si), which has similar specifications for usage to conventional A390.0, Mahle 126, Zolloy Z16 and AE 425. It is a heat treatable Al-Si alloy consisting of small polygonal primary silicon particles evenly distributed in an aluminum matrix for high strength and high wear resistance applications at elevated temperatures. NASA alloys can also be made in eutectic and hypoeutectic forms (<13% wt. Si), which is similar to A384.0, A413.0, AE 413, Mahle 124, 356, 359, 360. NASA alloys can be produced economically from conventional permanent mold or sand casting, and they are best used for applications from 500°F (260°C) to about 750°F (400°C). Figure 2A and 2B show the typical microstructure of NASA alloys in hypereutectic and eutectic form, respectively.

In both types of NASA alloys, the silicon gives the alloy a high elastic modulus and low thermal coefficient of expansion. The addition of silicon is essential in order to improve the fluidity of the molten aluminum to enhance the castability of the Al-Si alloy. At high silicon levels the alloy exhibits excellent surface hardness and wear resistance properties. Strontium is used to modify the Al-Si eutectic phase, and phosphorus is used to modify the silicon primary particle size when the silicon concentration is greater than about 14 wt%. Both strontium and phosphorous are used today as a conventional grain refinement practice for all Al-Si alloys. Effective modification is achieved at a very low additional level, but the range of recovered strontium and phosphorus of 0.001 to 0.1 wt.% is commonly used.

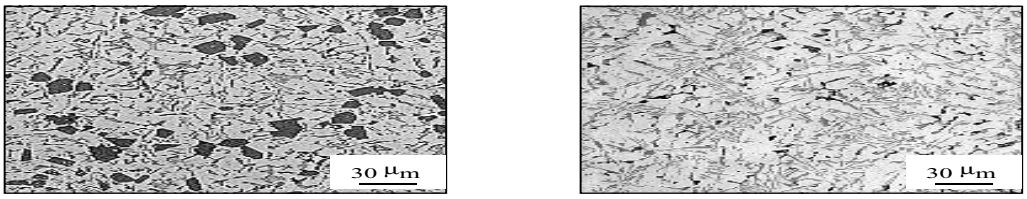

(A) (B)

Figure 2(A & B) show typical microstructure of NASA alloys in hypereutectic and eutectic, respectively.

To significantly enhance the tensile strength at high temperatures, small amounts of transition elements are added to the Al-Si alloy to modify the lattice parameter of the aluminum matrix by forming compounds of the type Al_3X having $L1_2$ crystal structures. In order to maintain high degrees of strength at temperatures very near to their alloy melting point, both the aluminum solid solution matrix and the particles of Al_3X compounds are designed to have similar face-centered-cubic (FCC) crystal structure. They are also coherent because their lattice parameters and dimensions are closely matched. When substantial coherency for the lattice is obtained, these dispersion particles are highly stable, which results in high mechanical properties for the alloy during long exposures at elevated temperatures. In order for these strengthening mechanisms to function properly within the alloy, the heat treatment is specifically designed to maximize the performance of the unique chemical composition.

The compounds of the type Al_3X particles also act as nuclei for grain size refinement upon the molten aluminum alloy being solidified from the casting process. They also function as dispersion strengthening agents, having the $L1_2$ lattice structure similar to the aluminum solid solution, in order to improve the high temperature mechanical properties.

MECHANICAL PROPERTIES

FIG 3 illustrates the dramatic improvement in the ultimate tensile strength (UTS) at elevated temperatures for a cast article produced from NASA alloys as compared with three well-known conventional alloy 332, 390 and 413 (11). The UTS data is tested at 500 °F, 600 °F and 700 °F, after exposure of all test specimens to a temperature of 500 °F, 600 °F and 700 °F for 100 hours, respectively. It is noted that the tensile strength of NASA alloys, is more than three times that of those prepared from the conventional eutectic 413.0 alloy, and more than four times that of those prepared from hypo-eutectic 332.0 alloy and the hyper-eutectic 390.0 alloy, when tested at 700 °F.

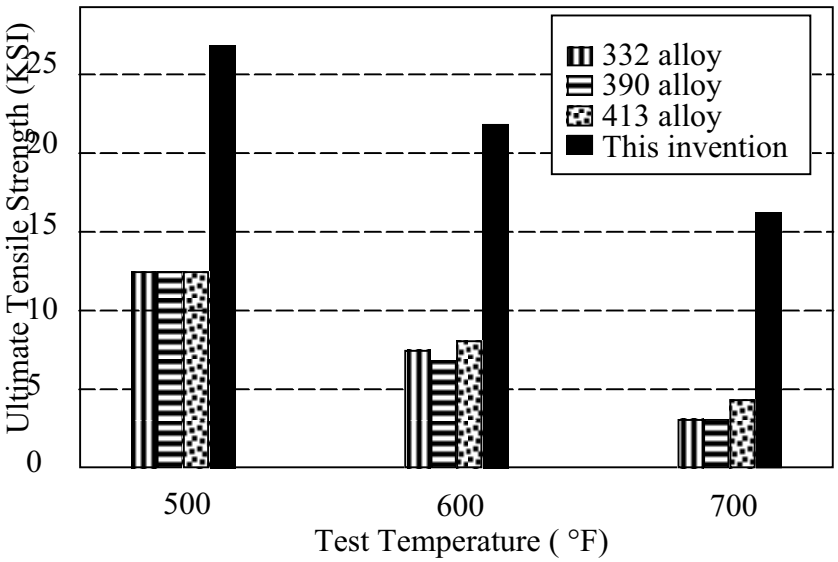

FIG 3 illustrates the dramatic improvement in tensile strength at elevated temperatures for NASA alloys.

THERMAL AND PHYSICAL PROPERTIES

At room temperature, the density for the eutectic and hypereutectic alloys is not much different from most conventional Al-Si alloys, about 2.76 g/cm^3 (0.099 lb/in^3) for NASA 398, and 2.73 g/cm^3 (0.098 lb/in^3) for NASA 388. The modulus of elasticity is about 12.8 Msi (88.6 Gpa), and a hardness value of 71 HRB (Rockwell B scale). Since NASA alloys are specifically designed for high temperature applications, the room temperature tensile and yield strengths are in the same range for most conventional 300-series cast aluminum alloys. The typical thermal properties as a function of temperature are given in Table 1. The liquidus temperature is 619°C (1156°F) for NASA 398, and 581°C (1078°F) for NASA 388. The solidus temperature is 486°C (907°F) for NASA 398, and 483°C (901°F) for NASA 388. The solidification temperature range is 619°C-486°C for NASA 398, and 581°C-483°C for NASA 388, respectively.

TABLE 1 Typical Thermal and Physical Properties for NASA 398 alloy.

Temperature		Thermal expansion (a)	Thermal diffusivity	Specific heat	Thermal conductivity	Density
°F	°C	(10^{-6}.K)	(cm^2/sec)	(J/kg.K)	(W/m.K)	(g/cm^3)
72	25	18.50	0.525	820	120.0	2.76
212	100	18.65	0.519	874	125.4	…
392	200	19.17	0.506	915	128.0	…
572	300	19.72	0.489	952	129.0	…
662	350	19.93	0.480	990	131.4	…

(a) Thermal expansion coefficients given for hypereutectic alloy (16% Si).

HEAT TREATMENT AND PROCESSING COST

A low cost heat treatment process, similar to the T5 treatment, is recommended by aging NASA alloys at 400 °F to 500 °F for four to twelve hours. This unique heat treatment schedule complements the unique alloy composition to form a maximum amount of precipitates with uniform distribution and optimum particle size. Thus, NASA alloys have high temperature strength properties that are superior to the prior art alloys because of a unique combination of chemical composition and heat treatment processing. Implementation of NASA 398 could actually be cheaper than some conventional alloys and cost saving can be realized if a specific component's heat treatment can be switched to T5 from previous specifications of either T6 or T7, when appropriate.

Initial production and casting trials have shown that NASA alloys can be cast and processed at a mass production value that is comparable with most conventional 300-series aluminum (<$0.90/lb). NASA alloys can be cast using conventional gravity casting in the temperature range of about 1325 °F to 1450 °F, without the aid of external pressure. However, further improvement of tensile strengths will be obtained when NASA alloys can be processed with external pressure such as squeeze casting. NASA alloys are best used for applications from 450°F (232°C) to about 750°F (400°C). For instance, strength improvement for NASA 398 can be as much as 3 to 4 times higher than conventional cast aluminum alloys when tested at 600°F (315°C), after soaking the alloy at 600°F for 100 hours.

POTENTIAL APPLICATIONS

Table 2 shows a guideline for material selection and potential applications of NASA alloys to meet substantially higher elevated temperature strength requirements than other conventional casting aluminum alloys. NASA alloys may be used in bulk alloy forms as hypoeutectic (6% –9% Si), eutectic (10% - 13% Si) or hypereutectic (16% - 18% Si). It is an ideal low cost material for cast automotive components such as pistons, cylinder heads, cylinder liners, connecting rods, turbo chargers, impellers, actuators and brake calipers. At high silicon levels, the alloy exhibits excellent thermal growth stability, surface hardness and wear resistant properties.

Table 2 Guideline for material selection and potential applications of NASA alloys.

NASA alloys	Potential Replacement	Applications
MSFC 398 (16% - 18% Si)	**390, Zollner 16 Mahle 126 AE 425**	• Pistons • Bearings • Cylinder liners • Brake calipers
MSFC 388 (10% - 13% Si)	**383, 384 413, Mahle 124 Thermodur**	• Cylinder blocks • Cylinder heads • Connecting rods • Pistons
MSFC 358 (6% - 9% Si)	**356, 357 359. 360 201, 206, 224, 242**	• Jet engine parts • Turbochargers • Metal composites • Impellers

NASA alloys may also be used as an alloy matrix for the making of aluminum metal matrix composites (MMC), which comprise a filler material in the form of particles, whiskers, chopped fibers and continuous fibers. The filler materials in the composite should not be confused with the strengthening particles Al_3X. The filler materials or reinforcement materials added into the aluminum MMC usually have minimum dimensions typically in the range of 1 to 20 microns. Suitable reinforcement materials for making aluminum MMC include common materials such as Silicon Carbide (SiC) and Aluminum Oxide (Al_2O_3). These reinforcements are present in volume fractions up to about 60% by volume. In stir-casting technique for composites, the approach involves mechanical mixing and stirring of the filler material into a molten metal bath. The temperature is usually maintained below the liquidus temperature to keep the aluminum alloy in a semi-solid condition in order to enhance the mixing uniformity of the filler material.

CONCLUSION

Originally developed as piston material to meet U.S. automotive legislation requiring low exhaust emission, the novel NASA alloys also offer dramatic increase in strength, enabling components to utilize less material, which can lead to reducing part weight and cost as well as improving gas mileage and performance for auto engines. In hypereutectic form, the alloys also have greater wear resistance, surface hardness and dimensional stability compared to conventional cast aluminum alloys. NASA high strength alloys can be produced economically from conventional permanent mold, sand casting or investment casting, and they are best used for high temperature applications from 450°F (232°C) to 750°F (400°C).

REFERENCE

1. D. Askeland, "The Science and Engineering of Materials," PWS-Kent Publishing Co., Boston, 1989.

2. L. E. Samuels, "Metals Engineering: A Technical Guide," ASM International, Metals Park, OH, 1988.

3. R. Bowles, "Metal Matrix Composites Aid Piston Manufacture," Manufacturing Engineering, 5/1987.

4. Shakesheff, "Elevated Temperature Performance of Particulate Reinforced Aluminum Alloys," Mater. Sci. Forum, Vol. 217-222, pp. 1133-1138 (1996).

5. P. Rohatgi, "Cast Al Matrix Composites for Automotive Applications," Journal of Metals, 4/1991.

6. J. T. Wentworth, "The Piston Crevice Volume effect on Exhaust Hydrocarbon Emission," Combust. Sci. & Tech., Vol. 4, pp. 97-100, 1971.

7. T. Saika, "Effects of a Ring Crevice on Hydrocarbon Emission from Spark Ignition Engines," Combust. Sci. & Tech., Vol. 108, pp.279-295, 1995.

8. J. Heywood, "Internal Combustion Engine Fundamental," McGraw-Hill, Inc., NY, 1987.

9. W. Haskell, "Exhaust Hydrocarbon Emissions from Gasoline Engines-Surface Phenonmenon," Soc. Auto. Eng., Paper #720255, 1972.

10. J. Wentworth, "Piston and Ring Variables Affect Exhaust Hydrocarbon Emissions," Soc. Auto. Eng., Paper #680109, 1968.

11. J. Kaufman, "Properties of Aluminum Alloys," ASM International, Materials Park, OH, 1999.

12. J. Lee, "High-Strength Aluminum Casting Alloy for High-Temperature Applications," MSFC-CDDF, Final Report 97-10, NASA/TM-1998-209004, December 1998.

ALUMINIUM LITHIUM ALLOYS USE FOR REUSABLE FUTURE LAUNCHER CRYOGENIC METALLIC TANKS

Jean Pierre BONNAFÉ, Daniel GABARD, Eric GROSJEAN*

EADS-LV : 66 route de Verneuil – BP 3002, 78133 Les Mureaux Cedex, France
(jean-pierre.bonnafe@launchers.eads.net)
(daniel.gabard@launchers.eads.net)
* GIE EADS CCR : 12 rue Pasteur – 92150 Suresnes, France
(eric.grosjean@eads.net)

ABSTRACT

In the context of future European TSTO (Two Stages To Orbit) reusable launch vehicles, development of reusability concepts implies the strong evolution of both technical and mechanical requirements on the launcher structure design, and more precisely on the cryogenics tanks.

It is clear that for reaching this reusability concept, it is now necessary to introduce new design criteria and mechanical requirements in order to achieve mass reduction of the different structures of the launcher with improved and increased stress conditions, together with a capability to be reused after reduced maintenance operations. This is particularly crucial on cryogenic tanks which will be for the first time reusable.

Aluminium-lithium alloy 2195 is a quite new weldable alloy with a low density and improved mechanical properties compared to 2219 aluminium alloy used on ARIANE 5 cryogenic tank. The introduction of this alloy on conventional cryogenic tanks allows drastic mass reduction but on reusable tanks, this introduction will be unavoidable in order to obtain the lowest flyable weight.

Furthermore, 2195 demonstrates a clear ability to answer the reusability requirements including fatigue behaviour, thermal cycling or extended defects propagation which have to fit the new enhanced functions of the reusable tank in both parent metal and welded joints.

Keywords : Reusable Launch Vehicle, Cryogenic Tank, 2195 aluminium-lithium alloy, mechanical behaviour

1 - INTRODUCTION

The new generation of launchers that are now studied in Preliminary Design Studies department for a potential use in 20 - 25 years, will be reusable launchers.

This choice is driven by the search for more and more competitive launch costs. In theory, this choice seems to be attractive, but in the meantime, it is clear that the technological step which leads from today expandable launchers to tomorrow reusable "Two Stages To Orbit" type launchers shown on figure 1 (TSTO) is a major one.

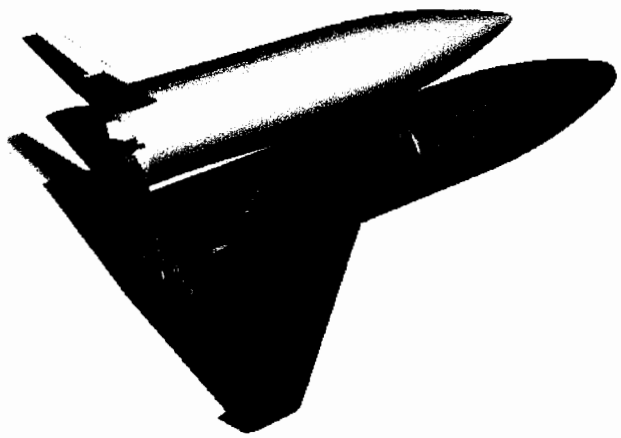

Figure 1 : TSTO Reusable Launcher

Besides the doubts concerning some technological choices for which the potential growth is not yet known, a lot of options may lead to major changes, or even to the renunciation to existing solutions used for a long time. These uncertainties, together with strong requirements for low development costs tending to maintain classical solutions, pilot today studies : this will be presented in the following part of this text, particularly for the application to propellant tanks.

2 - STUDY BACKGROUND

Within ARIANE family (figure 2), EADS LV has acquired a great experience in the building of propellant tanks for expandable launchers. For the first generations (ARIANE 1 to 4), the choice lead to 15 CDV 6 steel alloy for the first stage (liquid storable propellant), and to 7020 aluminium alloy for both second stage (liquid storable propellant) and cryogenic third stage.

With the next generation - ARIANE 5 - using a cryogenic first stage, an improved aluminium alloy was selected : 2219 alloy presents indeed good mechanical characteristics along with weldability, does not required post welding specific treatment, presents a good tolerance to repair after welding and moreover, whose properties are improved when used at cryogenic temperatures. Furthermore good formability allows large dimensions tanks to be obtained. [1]

For TSTO launchers, cryogenic tanks must be compatible with operation requirements leading first to a potential large propellant volume representing a tank diameter between 6 and 9 meters, and second to a capability to add several cold and hot thermal insulation layers in spite of a skin thickness between 3 and 5 mm.

When introducing full reusability concept for launch vehicles, applied for the first time on cryogenic propellant tanks, new design criteria and then new requirements are necessary in addition to conventional design criteria for current expandable tanks, to take into account all the new aspects induced by reusability concept.

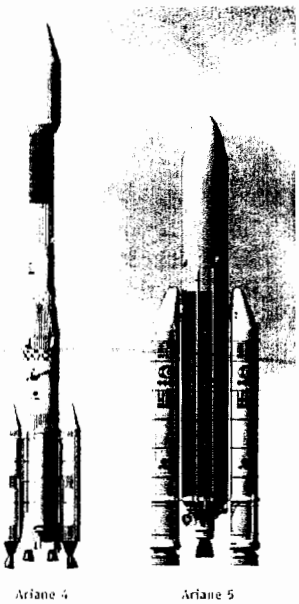

Figure 2 : General View of Ariane 4 & 5

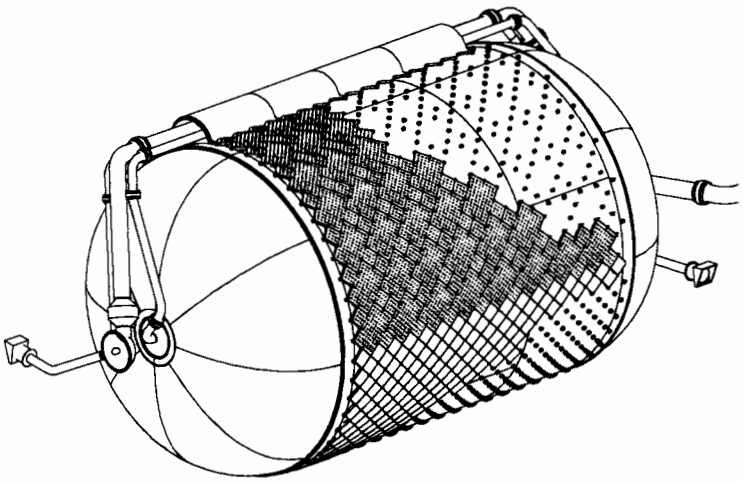

Figure 3 : Orbiter LH_2 cryogenic Tank

In such a TSTO design (as can be seen on figure 3), cryogenic tanks of both orbiter and booster are supposed to be reusable. This is, up to now, the first time that this reusability concept is applied on cryogenic tanks. The actual definition of a RLV (Reusable Launch Vehicle) and its missions constitutes already a major technological step.

The life duration of the vehicle should be of at least 30 years, years during whose the vehicle will fulfill a total amount of 120 missions for a maximum average rate of 8 flights per year with a maximal furbishment duration between two missions of one to three weeks.

In addition to conventional requirements such as static behavior at both room and cryogenic temperatures or weldability, new stress configurations induced by the reentry and the iterated use of the vehicle need to be taken into account such as fatigue behavior, thermal stability and aging.

The conditions of use, mission plans and life duration imply, besides, heat resistance, corrosion resistance and limited control operations and reduced maintenance or replacement work. To fulfil all these requirements for the new generation tanks, the simplest way is to use again all the materials and technologies used for previous generation ones.

Unfortunately, system studies performed on the overall vehicle architecture show rather quickly the limitations of this approach : performances of 2219 aluminium alloy are no more sufficient to fulfill tank structure requirements on reusable launchers. So, it became necessary to look for materials that would be simultaneously lighter and stronger, at cryogenic temperatures (tank environment during take-off phases) as well as at room or mild temperatures (tank environment during return phases). Then two alternative solutions can be used to face this difficulty : on one hand, another material can be identified, close enough of the previous one, but presenting the required complementary properties to allow to maintain the quite complete present technology and know-how. On the other hand, a more important technological step can be decided, leading to a change of the material nature and use. This second alternative solution is the one chosen when composite materials are expected to be used for propellant tanks

The first alternative solution that we propose to develop in this paper, tempts to extract from the last generations of aluminium alloys their best improvements : among the possible candidates to replace 2219 alloy, new weldable aluminium lithium alloys and more precisely 2195 alloy appear at the top of the list. This alloy has never been industrially used in Europe but some data are available from preliminary analysis, showing its high potential. From these data, this alloy seems to be light, strong, formable and weldable using technologies similar to the ones used for 2219 alloy. It also seems to show interesting mechanical characteristics when used under static or dynamic stresses, whatever the temperature in a range of 20K up to 400K. Nevertheless, before the beginning of the overall and detailed architecture studies, it was necessary to verify that this material was really as interesting as it promises to be.

Developments led by Lockheed Martin and NASA on the External Tank of the Shuttle, induced the elaboration of a new aluminium-lithium alloy family, the Weldalite® 049™ produced by Pechiney (former McCook Metals) [4]. Among the alloys of this family, 2195 was defined in order to achieve a low density, weldable and cryogenic alloy able to replace 2219 on cryogenic space tanks. By the way, 2195 knew its first main success with the first SLWT (SuperLightWeightTank) on the Shuttle in June 98 [2]. In comparison with the first generation of aluminium-lithium alloys, 2195 is said to exhibit a better mechanical behavior (tensile properties, fracture toughness, SCC ...) which is achieved through a higher copper content and a lower lithium content resulting in an increased density.

EADS has been working on the Weldalite family since the late eighties. Preliminary work on the potential of 2195 alloy was performed in order to validate the suitability of the alloy properties with EADS LV requirements for cryogenic tanks and secondly to offer design criteria for improved tanks in 2195. [3]

The definition of the tests program was based on three main criteria :

1) Validation of the properties required for 2219 T87 on cryogenic components (basic properties for cryogenic tanks : tensile tests, fracture toughness...),
2) Feasibility of industrial structures (Assessment of weldability, formability, compatibility with propellants...),
3) Assessment of newly required properties induced by reusability concept (Fatigue, Ageing, Long term corrosion ...).

The present work aims to acknowledge the suitability of 2195 T8R78 to the specific reusability requirements.

3 – MATERIAL EVALUATION

The material was supplied by Pechiney through 22 mm thick plates on T8R78 Temper, which is supposed to offer an optimised behaviour for cryogenic applications. T8R78 Temper consists in a 3.5% stretching after rolling, followed by an ageing treatment of 40 hours at 143°C.

Standardised chemical composition of 2195 is given in the table 1.

2195	Li	Cu	Mg	Ag	Mn	Si	Fe	Zn	Zr	Ti
standard	0.8/1.2	3.7/4.3	0.25/0.8	0.25/0.6	< 0.25	< 0.12	< 0.15	< 0.25	0.08/0.16	< 0.1

Table 1 : Chemical Composition of 2195 alloy

3.1. TENSILE TESTS

Tensile tests were performed at room temperature with 4 mm thick flat specimen taken at mid-thickness of the plate. The tests were conducted in 3 directions (longitudinal, transverse and 45° directions) in order to evaluate the anisotropy of the material.

In the longitudinal direction, 2195 T8R78 exhibits an ultimate tensile strength over 600 MPa. Whatever the direction, the ultimate tensile strength remains over 520 MPa with a really good ductility over 13%. In the same time, it appears that the plastic gap (UTS - YS) is limited around 6 to 9 % of the ultimate tensile strength (as shown in Table 2).

Alloy	Thickness	Location	Direction	E (GPa)	YS (MPa)	UTS (MPa)	A%
2195 T8R78	22 mm	t/2	L	74.0	566	603	13.4
2195 T8R78	22 mm	t/2	45°	77.0	481	525	13.7
2195 T8R78	22 mm	t/2	LT	77.5	536	579	13.1

Table 2 : Tensile properties of 2195 T8R78

Compared to 2219 T87, 2195 T8R78 exhibits at room temperature a considerably improved tensile resistance (from 20 to 45% depending on the selected parameter), as can be seen on figure 5.

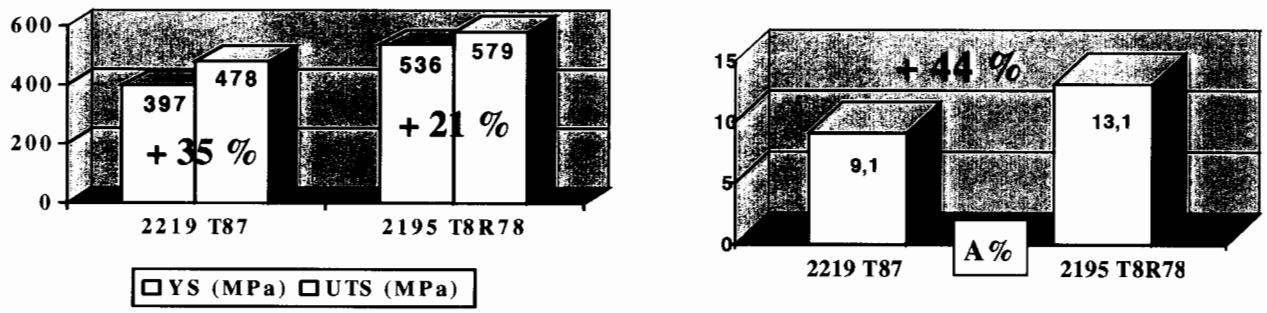

Figure 5 : Comparison between 2219 T87 and 2195 T8R78 in the transverse direction

Lithium influence on 2195, compared to 2219, can be highlighted through the improvement of the stiffness (from 72.5 GPa to 77.5 GPa) for a density reduction from 2.85 to 2.72.

3.2. WELDABILITY ASSESSMENT

The fusion welding of aluminium alloys requires the use of a filler wire in order to ensure the geometric aspect, the quality and the mechanical behaviour of the weld. The wire allows to limit hot cracking phenomena and shrinckages during solidification and strongly contributes to the mechanical behaviour by its alloying elements and the ability to provide a convex weld. Ideally, the best wire should present the same chemical composition as the parent metal. Practically, up to now, it is not possible to have aluminium-lithium filler wires due to the strong oxidation potential of lithium element [5], [6], [7].

On this basis, the selection of the filler wire was performed following practical welding tests and a rough evaluation of the welds obtained with different wires on an as-welded condition.

The assessment of weldability was tested by GTA (Gas Tungsten Arc) continuous techniques under helium protection (to prevent oxidation) on a vertical ascent configuration, process already used for the industrial production of RIE 2219 tanks on ARIANE 5 launchers.

The tests were conducted on rectangular plates (125 x 500 x 4 mm) taken at mid-thickness of the 22 mm plates. The optimisation of welding parameters was conducted on "welding line" configuration for each wire, the mechanical evaluation including both "welding line" and butt joint configurations. The welding line was along the transverse direction. No specific surface treatment was applied before welding, the surfaces to be welded were just chemically cleaned then manually scrapped off.

Figure 6 : An example of the obtained 2195 weld

Whatever the configuration and the wire, 2195 exhibits a really good weldability (see figure 6). The welding operation is regular, without any smoke, the solidification waves are small, the general aspect of the GTA welds is completely similar to 2219 welds. The weldability appears similar for each wire, welding parameters remain quite close for wire with an average dilution of 17%.

No defect (metallurgic or geometric) was detected both by RX examination and destructive observation after mechanical testing. Some small porosities were locally detected [$\varnothing < 0.1$ mm] and are fully acceptable by welding standards.

As shown on figure 7, the length of the HAZ and ZF is quite important around 30 mm but is comparable to 2219 welds on the same thickness. Hardness profiles are comparable for each wire. The hardness decrease in the fusion zone (from 180 Hv for parent metal to 95 Hv in the weld) is probably induced by the full dissolution of T_1 phases.

On this basis, the best results were obtained with 2319 (Al-Cu) filler wire already used for 2219 welds.

Figure 7: 2195 T8R78 GTA weld – 2319 wire (front side)

The full static evaluation was conducted at room temperature, on unshaved weld (butt joint configuration) following the length direction (weld perpendicular to specimen axis). The results are given in the table hereafter (table 3) and are compared to both parent material and 2219 GTA welds on figure 8.

Alloy	Wire	YS (MPa)	UTS (MPa)	A%
2195 T8R78	2319	180	369	5.5

Table 3 : Tensile behaviour of 2195 unshaved welds

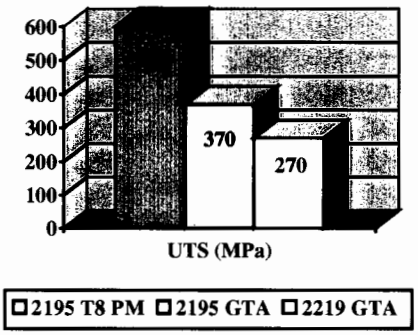

Figure 8 : Comparison with 2219 weld

The comparison with 2219 weld highlights again the superior behaviour of 2195 T8R78, up to 37% on as-welded ultimate strength.

3.3. CRYOGENIC EVALUATION

Tensile tests were performed at room temperature with 2 mm thick flat specimen taken at mid-thickness of the plate. The tests were conducted in the transverse direction on the specific cryogenic device.

Tests were conducted at 3 different temperatures :

- 20 K (-253°C) : Liquid Hydrogen Temperature,
- 77 K (-196°C) : Liquid Nitrogen Temperature,
- 173 K (-100°C) : intermediate temperature between cryogenic and room temperatures.

Under cryogenic conditions, 2195 T8R78 exhibits a major increase of both yield strength and ultimate tensile strength compared to the values at room temperature and a major superiority compared to 2219 T87 (Table 4).

Temperature	E (GPa)	YS (MPa)	UTS (MPa)	A%
-253°C	84.4	724	813	14.0
-196°C	83.1	672	732	13.6
-100°C	80.4	610	653	13.1

Table 4 : 2195 T8R78 Tensile Properties under cryogenic temperatures

Yield strengths are 28% higher at 20K and 21% at 77K than at room temperature and around 50% higher than 2219 T87. For ultimate tensile strengths, results are similar : +37% at 20K and +26% at 77K, and around 30% higher than 2219 T87. Elongation remains at the same level as the one at room temperature.

The same evaluation was conducted with GTA welds on as-welded conditions. The comparison of the results with the parent material is given in the following figure (Figure 9).

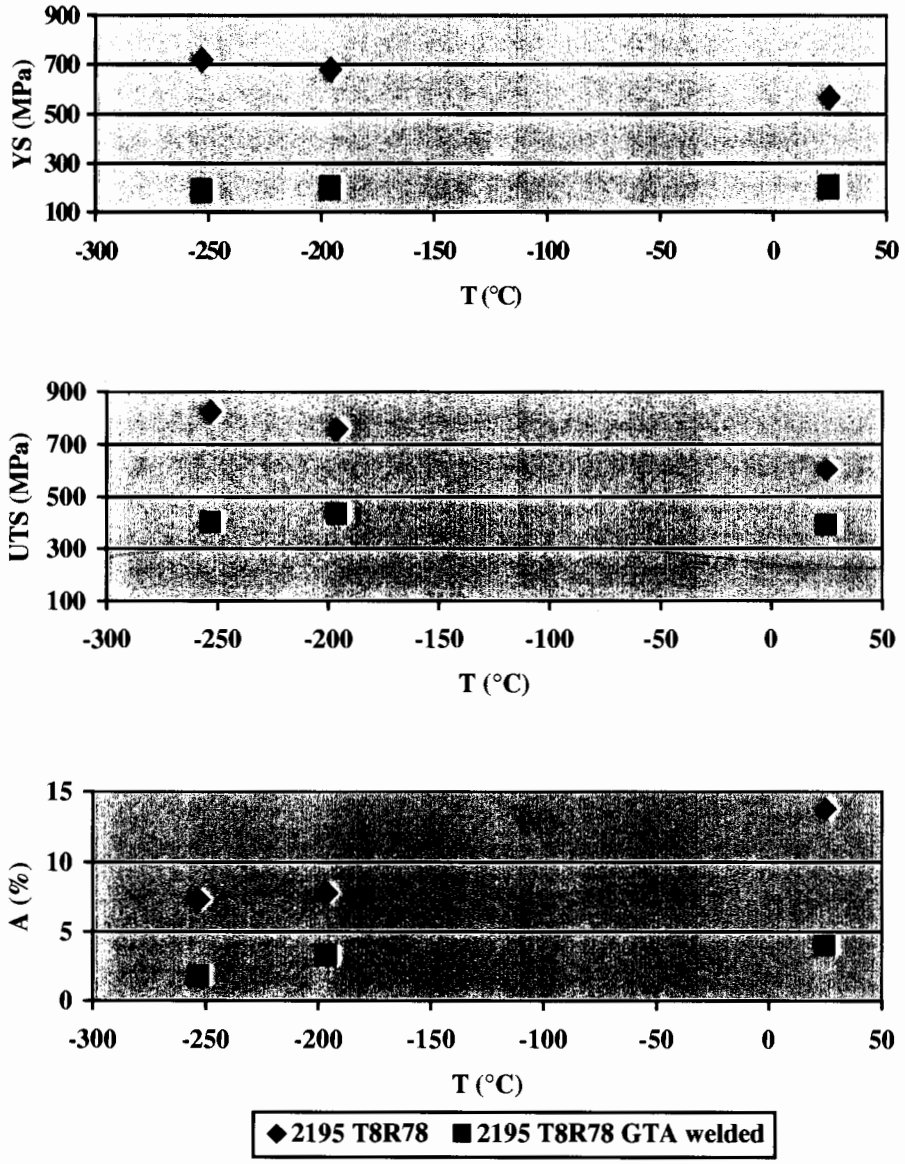

Figures 9 : Comparison of cryogenic Tensile Properties between GTA welds and 2195 T8R78 parent metal

On GTA welds, no positive influence of lower temperatures is observed. At 20K and 77 K, yield and ultimate strength remain quite close from the value at room temperature, but compared to 2195 T8R78, the gap between welded material and parent material significantly increases due to the very good behaviour of 2195 T8R78. On the contrary, on these first results, the elongation obtained on the welds at cryogenic temperatures is quite low and need to be slightly improved.

In order to achieve a preliminary evaluation of reusable requirements, additional tests were performed like fatigue behaviour, long term corrosion and ageing evaluation.

3.4. FATIGUE BEHAVIOUR

For example, the first evaluation of fatigue behaviour was defined with tension fatigue (R ratio = 0.1) on flat specimen (Kt = 1.03) taken at mid-thickness of the plate in the transverse direction. As a reference, the same tests were conducted on 2219 T87 (see figure 10).

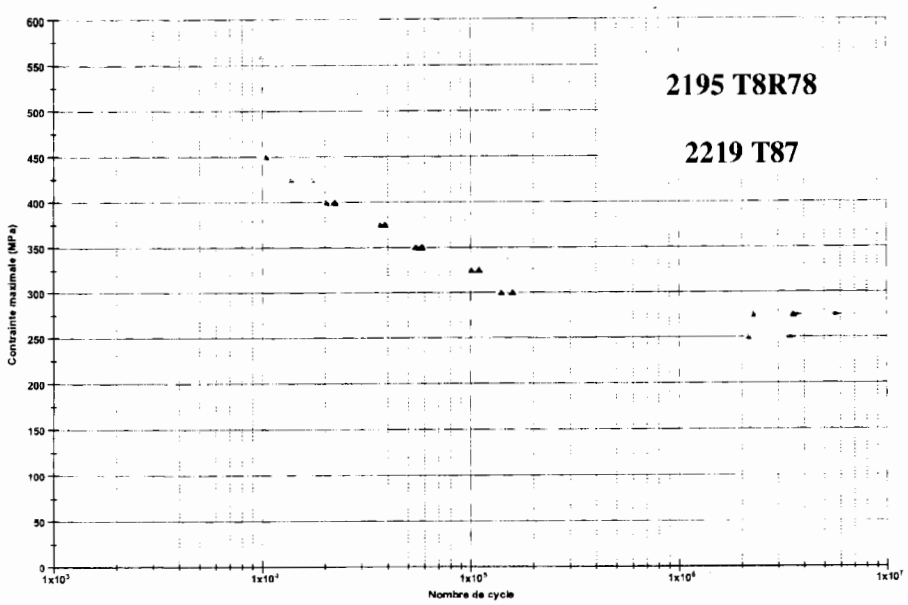

Figure 10 : Fatigue behaviour of 2195 T8 R78

Under these conditions, it is clear that 2195 T8R78 exhibits a very interesting behaviour with a maximal stress of 400 MPa at 100000 cycles that could represent the life duration target of reusable launchers. The difference between 2195 T8R78 and 2219 T87 is particularly important for high stresses.

These results allows to prove that 2195 T8R78 will ensure an excellent fatigue behaviour which could answer reusable vehicle requirements.

3.5. CORROSION BEHAVIOUR

The conventional tests for aeronautic materials are based on natural exposure in marine environment. Samples are exposed for 4, 12 and 24 months on "Le Pilier" Island in the Atlantic Ocean near the French coast, then observed through micrographic examination. The results presented hereafter (figure 11) are those after a 4 months exposure, the other samples are still under exposure. The samples are exposed after a superficial machining in order to evaluate the material in its use conditions.

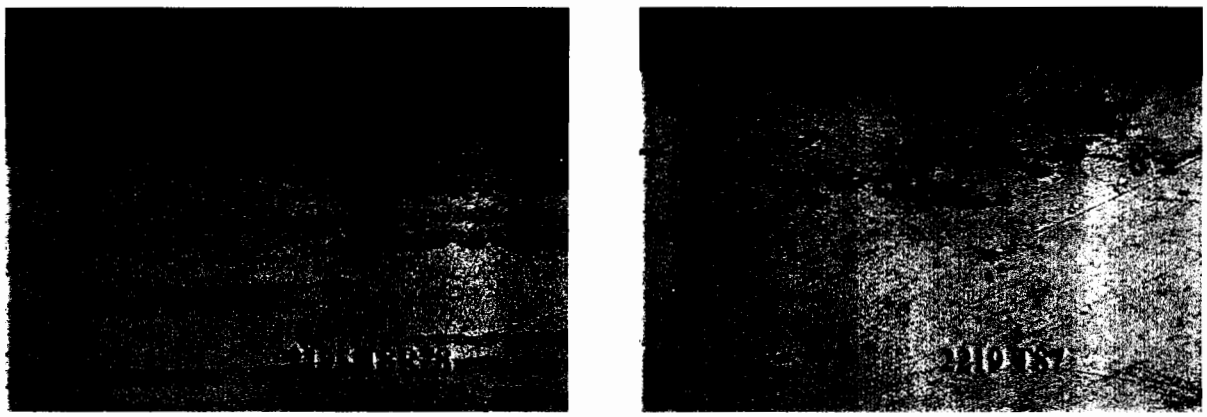

Figure 11 : Micrographic examination of 2195 T8R78 and 2219 T87 after a 4 months exposure

The micrographic examination of the samples of 2195 T8R78 points out a maximal depth of corrosion of 60 µm compared to the 100 µm obtained on 2219 T87. The superior behaviour of 2195 T8R78 could be explained

by the reduced amount of copper addition (4% in 2195 versus 6% in 2219). The nature of the corrosion appears to be pitting with a slight intergranular tendency oriented following the rolling direction.

These results seem to demonstrate that 2195 T8R78 has a better corrosion behaviour than 2219 T87 which conforts the abandon of 2219 to the profit of 2195 for reusable applications. However these results will have to be adjusted following the final mission profile and use conditions of the future reusable products.

3.6. THERMAL STABILITY

The first generation of aluminium-lithium was proven to be sensitive to thermal instability, that is to say that their properties, particularly mechanical properties, could evolve during product life. This phenomenon, if still effective on this alloy, would be without any influence for expandable products but could become damageable on reusable structures.

That is why thermal stability is included in this workprogramme. Regarding the limited data on the life duration of a reusable cryogenic tank, in a first approach, the selected test is based on EADS experience for aeronautic products, which will be more severe than the real conditions and lead to an artificial aging of 1000 hours at a temperature of 85°C.

Different tests were carried out to evaluate post-treatment including microstructural evaluation, Differential Scanning Calorimetry, tensile test and corrosion tests.

- microstructural analysis,
  After artificial aging, no significative modification was observed on the microstructure of the rolled product (no grain size or form modification, no hardness modification...).

- DSC (Differential Scanning Calorimetry),
  DSC tests are currently used in order to determine phasis nature in close link with microstructural evaluation or in our case to evaluate phasis modification induced by heat treatments. The DSC tests were conducted on the material before and after treatment. The results are given in the figure hereafter (figure 12).

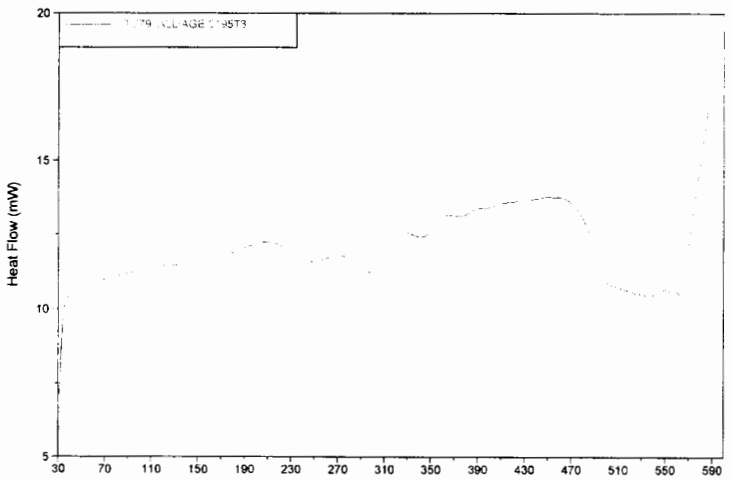

Figure 12 : DSC results on 2195 T8R78 (Green) and 2195 after artificial ageing (red)

This figures demonstrates that both curves present the same peaks at the same temperatures which proves that no significant phasis transformation occurred during the artificial aging. However it also appears that both curves do not present the same amplitude, this could indicate a potential growth of the main phases T1.

- Tensile test
  The tensile properties given in table 5 after aging are close from the original ones, less than 5% (in accordance with the standards) except for the elongation which is slightly reduced. This could confirm the growth of the main phases.

2195	YS (MPa)	UTS (MPa)	A%
T8R78	566	603	13.4
Artificial Aging	601	633	8.2

Table 5 : tensile properties after artificial aging

- Corrosion tests
  No difference was identified compared to the first trials.

In conclusion, 2195 T8R78 do not demonstrate a thermal instability in the targeted conditions.

CONCLUSION

This first technical evaluation of 2195 T8R78 alloy confirms the excellent potential of this alloy for the replacement of 2219 T87 for cryogenics tanks. In the development of Reusable Launch Vehicles, its introduction may lead to strong weight reduction in cryogenic components and so facilitate the design of new concepts unachievable without important improvement by conventional alloys and processes. First analysis lead to a potential weight reduction of 25% compared to a 2219 solution due to both reduced density and major properties increase. Further studies will demonstrate the complete required reusable properties and evaluate the potential of this alloy for non-cryogenic components.

BIBLIOGRAPHIC REFRENCES

[1] **2219 VALUES COMES FROM ALUMINIUM ALLOY 2219** - AEROSPACE STRUCTURAL METALS HANDBOOK - CODE 3205 - **1967**

[2] **NEW SUPER LIGHTWEIGHT TANK FUELS STS-91** - SHUTTLE VEHICLE INFORMATION - SPACE SHUTTLE PROJECTS OFFICE. - HTTP://SHUTTLE.MSFC.NASA.GOV - **1998**

[3] BONNAFÉ J.P., GABARD D., GROSJEAN E. - **ALUMINIUM LITHIUM ALLOYS APPLICATION FOR FUTURE LAUNCHER CRYOGENIC METALLIC TANKS** - EADS - 3RD EUROPEAN CONFERENCE ON LAUNCHER TECHNOLOGY- STRASBOURG **2001**

[4] CHO A., GREENE R., SKILLINGBERG M., CASSADA W., EDWARDS M., FIELDING P. - **STATUS OF HIGH STRENGTH AL-LI ALLOY DEVELOPMENT AT REYNOLDS METALS COMPANY** - REYNOLDS METALS COMPANY, CORPORATE RESARCH AND DEVELOPMENT - METALLIC MATERIALS FOR LIGHTWEIGHT APPLICATIONS - AUGUST **1993**

[5] KOSTRIVAS A., LIPPOLD J. - **WELDABILITY OF LI-BEARING ALUMINIUM ALLOYS** - OHIO UNIVERSITY - INTERNATIONAL MATERIALS REVIEW - **1999**

[6] LIPPOLD J., LIN W. - **WELDABILITY OF COMMERCIAL AL-CU-LI ALLOYS** - EWI - OHIO STATE UNIVERSITY - MATERIALS SCIENCE FORUM - **1996**

Vacuum Plasma Spray Forming of Copper Alloy Liners for Regeneratively Cooled Liquid Rocket Combustion Chambers

FRANK ZIMMERMAN
Marshall Space Flight Center, ED33
Huntsville, AL 35812
Phone: 256-544-4958
Fax: 256-544-0212
E-mail: frank.zimmerman@msfc.nasa.gov

Vacuum plasma spray (VPS) has been demonstrated as a method to form combustion chambers from copper alloys NARloy-Z and GRCop-84. Vacuum plasma spray forming is of particular interest in the forming of CuCrNb alloys such as GRCop-84, developed by NASA's Glenn Research Center, because the alloy cannot be formed using conventional casting and forging methods. This limitation is related to the levels of chromium and niobium in the alloy, which exceed the solubility limit in copper.

Until recently, the only forming process that maintained the required microstructure of CrNb intermetallics was powder metallurgy formation of a billet from powder stock, followed by extrusion. This severely limits its usefulness in structural applications, particularly the complex shapes required for combustion chamber liners.

This paper discusses the techniques used to form combustion chambers from CuCrNb and NARloy-Z, which will be used in regeneratively cooled liquid rocket combustion chambers.

Joint Group on Pollution Prevention

Joint Logistics Commanders and NASA

Lead-Free Solder Project

5th Conference on Aerospace Materials, Processes, and Environmental Technology Storefront
Sep. 16 - 18, 2002
Von Braun Center, Huntsville, AL,

Brian Greene, ITB, Inc.
NASA Acquisition Pollution Prevention Office
Kennedy Space Center, FL

Uses of Lead in Electronic Components

- Provides final surface finish to printed circuit boards
- Applied to component leads for compatibility with solderable surfaces
- Used to attach electronics components on printed circuit board
  - Manual soldering
  - Automated soldering (wave & reflow)

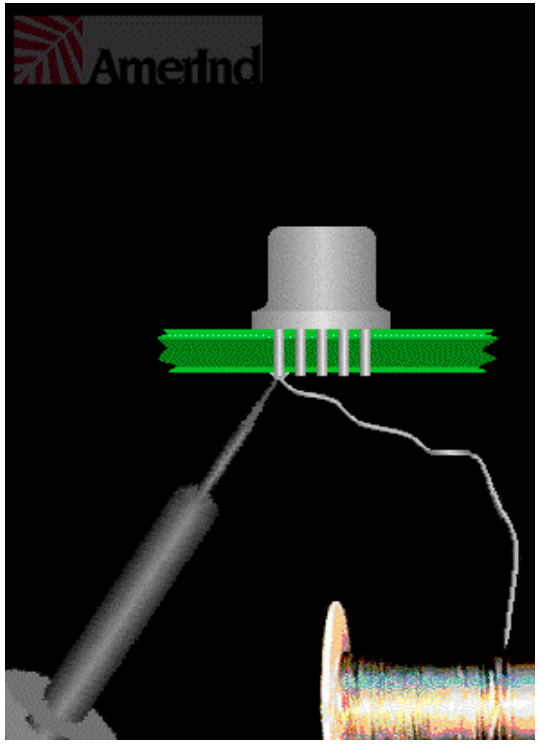

Issues/Drivers

- Use of conventional Sn-Pb solders for electronics is threatened by:
  1. Present and future U.S. and European regs.
  2. Market forces (domino effect)
     - i. Consumer electronic component and solder manufacturers to eventually discontinue tin-lead.
     - ii. Aerospace community may have little leverage once lead-free movement begins.
     - iii. Ability of the military and NASA to sustain current and future space systems would be impeded → parts obsolescence.
     - * Technical risk: Long-term reliability unknown
     - * Financial risk: SnPb cost will increase (remember Freon?)
- Also, improved lead-free solder test data now available

Initiatives in Lead-Free Soldering
- Lead-Free: A Potential Scenario -

Commercial Electronics Lead-Free Scenario

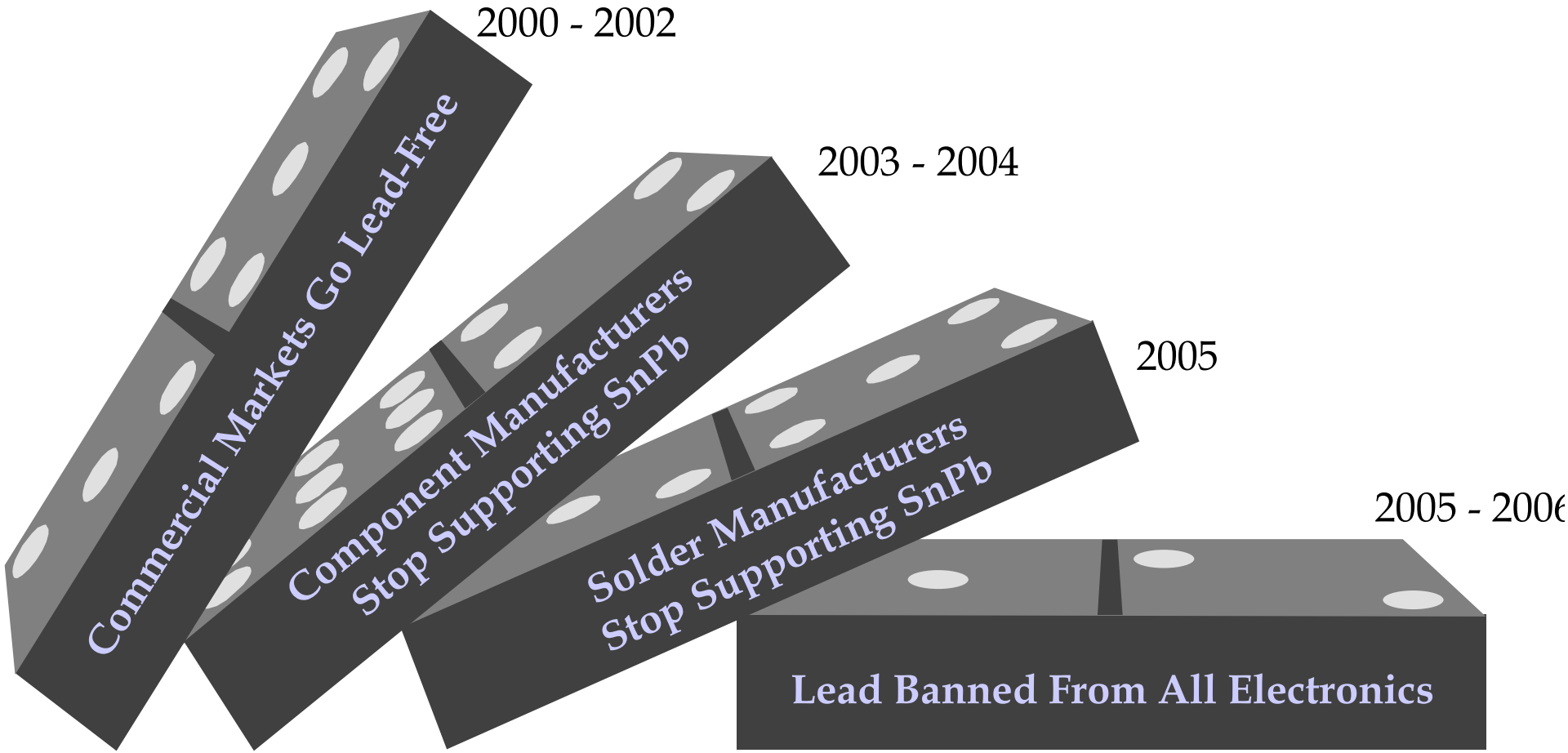

Consumer Electronics Driving Force in Electronics Market

High Reliability "Aerospace" Electronics < 1.0 % of Total Electronics Market (Source: IPC)

(This slide courtesy of Lee Whiteman, ACI, Mar 2002)

Difficulties to Implementation

General

- Higher operating temperatures
- Tin whiskering
- Environmental concerns of some alternatives
- Recycling

PWB Repair

- Lead contamination
- Different solders may be required
- Parts tracking

JG-PP Pb-Free Solder Project Overview

Objective:

Joint project to qualify and validate lead-free solder alloys for use in manufacture and repair of electronic equipment

Scope:

- The interconnection of components to substrates with a lead free solder alloy at operating conditions below 205 deg. C.
- Test for functional (electrical) reliability, not integrity
- Indirectly test effectiveness of repairing Pb-containing PWBs with Pb-free solder
- Test board to reflect 50+% of circuits now on defense/space systems
  - Surface Mount Technology and Plated Through Hole
  - Mixture of old and new components

Project Participants

DoD MAJCOMs, Depot Process Owners, NASA Centers

U.S. Original Equipment Mfrs. and Electronics Materials Suppliers

U.S.EPA DfE/ Univ. of Tennessee

JG-PP LFS Project

International OEMs and Industry Agencies

International Defense Agencies (pending)

Industry Association Experts (NCMS, ACI)

Project Participants

U.S. Government

Army

- AMCOM
- Research Development & Engineering Center-Redstone Army Arsenal
- U.S. Army Communications Electronic Command (CECOM)
- U.S. Army Tank-Automotive and Armaments Command (TACOM)

Navy/Marine Corps

- Naval Air Systems Command (NAVAIR)
- NAVSEA
- Potomac Hudson Engineering/U.S. Marine Corps
- TRW/Marine Corp.

Air Force

- F-15 Program/Robins Air Force Base
- Hanscom Air Force Base
- Hill Air Force Base
- ICBM
- Tinker Air Force Base
- Wright Patterson Air Force Base

NASA

- NASA-Goddard Space Flight Center
- NASA-Jet Propulsion Lab
- NASA-Kennedy Space Center
- NASA-Marshall Space Flight Center
- United Space Alliance/Solid Rocket Boosters

Dept. of Energy

- Sandia Labs

U.S. Manufacturers

- Alliant Tech Systems
- The Boeing Company
- Goodrich
- Harris
- Honeywell
- I TT
- Lockheed Martin
- Lucent Technologies
- Motorola
- Northrop Grumman
- Raytheon
- Rockwell-Collins
- Texas Instruments

U.S. Industry and Academic Associations

- American Competitiveness Institute
- IPC
- National Center for Manufacturing Sciences
- NIST
- University of Tennessee

Vendors

- Intersil
- Mitsui Comtek/Senju Metals Co.

Non U.S. Organizations

- Astrium (UK)
- British Aerospace Systems (UK)
- Institute of Welding and Quality (Portugal)
- MBDA (UK)

Joint Group on Pollution Prevention

- Chartered by DoD Joint Logistics Commanders (JLC)
- Members: Army, Navy, Marine Corps, Air Force & NASA
- Primary objectives:
  - Eliminate HazMats — joint cooperation
  - Avoid duplication of effort
- Defense/space system life cycle (acquisition → sustainment)

JG-PP Methodology

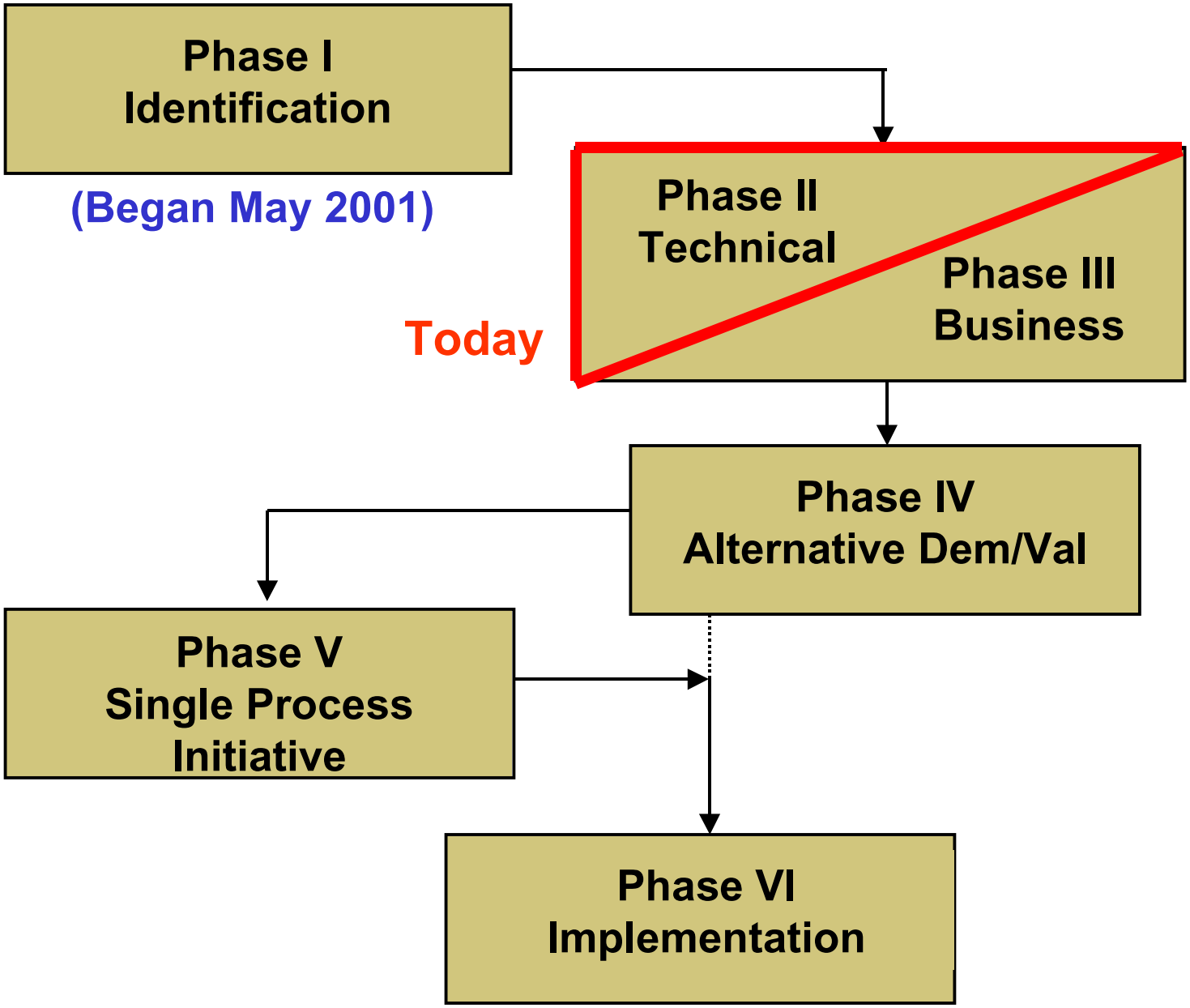

JG-PP Products

Joint Test Protocol (JTP)

- Defines tests required to qualify/validate alternatives

Potential Alternatives Report (PAR)

- Documents alternative selection process

Cost Benefit Analysis (CBA)

- Quantifies economic effects
- Supports business case
- Use as a decision tool
- Limited distribution

Joint Test Report (JTR)

- Documents test results

Project Funding Approach

- **Identification and Technical Phases (to date)**
  - —JG-PP (via contractors such as CTC & ITB) are preparing technical documents, hosting some teleconferences, and maintaining Web site
  - —OEMs and Services hosting meetings & some telecons, & providing labor for document preparation
- **Testing Phase (Forecast)** ***(> 90% of project cost)***
  - —May be able to get component and solder suppliers to donate materials for testing.
  - —OEMs plan to donate labor for vehicle design
  - —Several stakeholders have offered to do testing as their in-kind contribution
- **SPI and Implementation Phases (Forecast)**
  - —Similar approach as Technical Phase above

Solder Downselection Approach

- Excellent performance based on prior test data
  - —NCMS
  - —NEMI
  - —Other published studies
- Commercially available
- Popular; wide usage anticipated
- Formulation constituents not likely to be regulated in near future
- Mindful of life cycle considerations

JG-PP Proposed Solder Alloys [a]

- **Lead-Free Solder**
  - —SnAgCu = Sn3.9Ag0.6Cu
  - —SnAgCuBi = Sn3.4Ag1.0Cu3.3Bi
  - —SnCu = Sn0.7Cu
- **Baseline**
  - —Sn63 = Sn37Pb

[a] Numbers preceding chemical element are % of formulation

JTP Tests

Validation Test	JTP Section	Reference	Electrical Test	Acceptance Criteria [(a)]
Vibration	3.2.1	MIL-STD-810F, Method 514.5, Procedure 1	Electrical continuity failure	Better than or equal to tin/lead controls
Mechanical Shock	3.2.2	MIL-STD-810F, Method 516.5, Procedure 1	Electrical continuity failure	Better than or equal to tin/lead controls
Thermal Shock	3.2.3	MIL-STD-810F, Method 503.4, Procedure 1	Electrical continuity failu re	Better than or equal to tin/lead controls
Highly Accelerated Life Test	3.2.5	Not Applicable	Electrical continuity failure	Better than or equal to tin/lead controls
Thermal Cycling	3.2.6	IPC -SM- 785	Electrical continuity failure	Better than or equal to tin/lead controls

Project Milestones

- ☑ Early customer-interface mtg. May 2001
- ☑ Project added to website Jun 2001
- ☑ Complete CBA-A Jun 2002
  - Complete PAR Dec 2002
  - Complete JTP Dec 2002
  - Begin testing 2003

Project Schedule

(estimate as of Aug 2002)

|----- Funded -----||----------- Unfunded -----------|

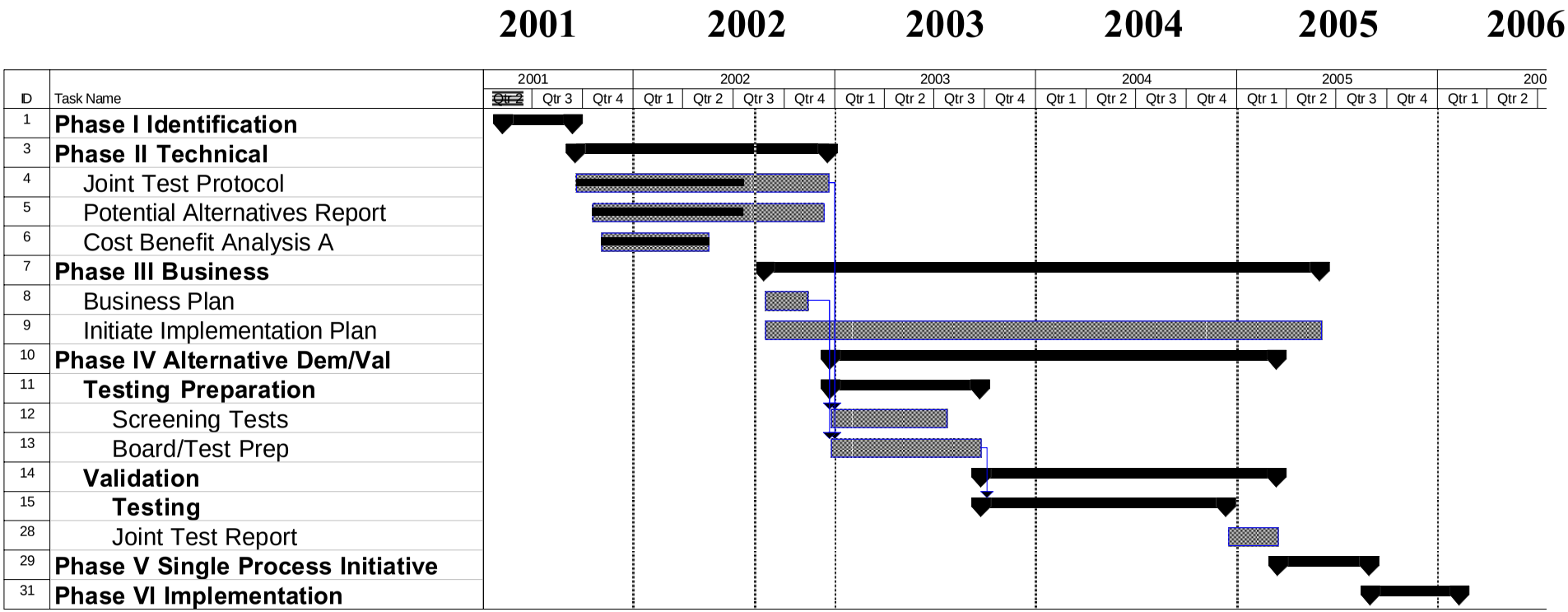

Next Steps (2nd half 2002)

Technical

- Resolve remaining technical issues so that JTPs and PAR can be completed
- Distribute JTPs to Program Managers for endorsement

Business

- Refine testing cost estimate
- Tap funding sources
- Agree to testing locations and appropriate contract vehicle

JG-PP Solder Project Leaders

JG-PP Web site: http://www.jgpp.com

Brian Greene
Project Integrator, JG-PP Lead-Free Solder
ITB, Inc.
NASA Acquisition Pollution Prevention Office
Kennedy Space Center, FL
Phone: 321-867-8481
E-Mail: GreenBE@kscems.ksc.nasa.gov

Warren Assink
Government Project Manager,
JG-PP Lead-Free Solder
Wright-Patterson Air Force Base, OH
Phone: 937-904-0151
E-Mail: Warren.Assink@wpafb.af.mil

Backup Slides

JG-PP Lead-Free Solder Project

JG-PP lead-free solders and their properties

LEAD-FREE SOLDER COMPOSITION	MELTING POINT RANGE	JG-PP MFR. JTP	JG-PP REPAIR JTP	COMMENTS
62Sn-37 Pb	183°C	Reflow & Wave	Reflow, Wave & Manual Repair of Reflow & Wave-Soldered 63Sn-37Pb Manual Repair of Reflow & Wave-Soldered SnCu, SnAgCu, & SnAgCuBi??	- Baseline. Necessary to compare performance against that of lead-free solders
99.3Sn-0.7Cu	227°C	Wave??	Manual Repair of Reflow & Wave-Soldered 63Sn-37Pb Manual Repair of Reflow & Wave-Soldered Sn-0.7Cu??	**Advantages** - High strength and high melting point - Jan 2008 JEMI recommended Sn0.7Cu for use by industry as a standardized lead free solder for wave soldering - Alloy has been investigated in a number of initial lead-free wave solder trials. (D. Hillman) - Available at Radio Shack and used by depots (Robins AFB). (A. Pattnaik) **Concerns** - Wetting problems - It is desirable to have Reflow/Manual Solder (for repair work) that would exist behave approximately to that of other Radio Shack binary alloy, namely, Sn/0.7 Cu (A. Pattnaik). However, at this time, the electronics industry views Sn/0.7Cu solder alloy as strictly a wave solder alloy, so there are probably no SMT parts (J. Bradford)
Sn-3.9 Ag-0.6 Cu	216°C	Wave & Reflow	Manual Repair of Reflow & Wave-Soldered 63Sn-37Pb Manual Repair of Reflow & Wave-Soldered Sn-3.9Ag-0.6Cu??	**Advantages** - Jan 2008 JEMI recommended Sn3.9Ag0.6Cu for use by industry as a standardized lead free solder for reflow applications - Malicious: Tin silver copper alloys perform better than Sn0.7Cu for wave soldering. (T. Woodrow) - Sn/Ag/Cu alloy system is the leading candidate from a cost and manufacturing standpoint. (D. Hillman) - From contamination point of view, this alloy should approximate the behavior of the Radio Shack alloy, Sn/3.6Ag, used in repair at Robins AFB. (A. Pattnaik) **Concerns** - Wave solder not economical. (J. Bradford)
92.4Sn-3.4Ag-1Cu-3.3Bi	206°-214°C	Reflow	Manual Repair of Reflow & Wave-Soldered 63Sn-37Pb Manual Repair of Reflow & Wave-Soldered Sn-3.4Ag-1Cu-3.3Bi??	**Advantages** - Far East Market. Sn/Ag/Cu/Bi alloy system is the leading candidate system for electronics. (D. Hillman) - 2001 NCMS Study. Sn/Ag/Cu/Bi performed very well for reflow soldering in high-temperature, fatigue resistant solder study **Concerns** - It might be expensive to fill a wave solder machine with it. (T. Woodrow) - It may exhibit fillet lifting problems due to the bismuth. (T. Woodrow)

General notes:

Copper
- Copper in formulation retards copper dissolution, lowers the melting temp., and improves wettability, creep & thermal fatigue characteristics.
- There is some general industry apprehension on a manufacturer's ability to monitor/regulate the copper content of wave solder systems in relation to solder alloy composition. (D. Hillman)

Bismuth
- The Bi content in the solder support both a solid solution strengthening and precipitation hardening mechanisms. Both mechanisms are very effective towards limiting dislocation motion in the material, particularly at elevated temperature. (These are the same mechanisms used to stabilize jet aircraft turbine blade alloys.) Since dislocation motion is responsible for sub-grain and grain development as part of thermal mechanical fatigue in solders, the inhibition of that dislocation motion by the Bi atoms (solid solution) and particles (precipitation hardening) is the likely reason(s) that the solder exhibits good thermal fatigue resistance. (P. Vianco)
- General industry apprehension on the potential formation of low melting point Bismuth intermetallic phases. (D. Hillman)
- Probably should avoid mixing with lead. Least contamination can form 51.5%Bi-15.5%Sn-33%Pb ternary eutectic which melts at 95 deg. C and could severely hurt the reliability of the solder joint. Bismuth-containing solders can also exhibit "fillet lifting" which may not affect reliability of wave soldered joints. (T. Woodrow)

Proposed Test Vehicle

- Surface finishes: One Pb-free (Immersion Ag) & baseline (Pb HASL)
- Component finishes: Two Pb-free (Sn & Au/Pd/Ni) & baseline (Sn/Pb)
- Component styles: CLCC, PLCC, Dpak, TSOP, TSSOP, TQFP, SOIC, BGA, CSP, PDIP, chip capacitors (0402, 0805, 1206), resistors (0402, 0805, 1206), and hybrids
- Component sizes (1): typical I/O size
- Five (5) test vehicles per test in the test matrix α 30 total of each component in the test

Mfg JTP Test Vehicle Matrix

Type	Laminate	Surface Finish	Reflow Solder	Wave Solder
Lead-Free	High tg	Immersion Silver	SnAgCu	SnAgCu
			SnAgCuBi	SnCu
Base-line (control)	High tg	HASL	Sn63	Sn63

3 x 5 = 15 test vehicles per test

Repair JTP Test Vehicle Matrix

Type	Laminate	Surface Finish	Reflow & Wave Solder Alloy	Repair Solder Alloy SMT	Repair Solder Alloy PT
Repair	FR4	HASL	Sn63	SnAgCuBi	SnCu
				SnAgCu	SnAgCu
Repair Control	FR4	HASL	Sn63	Sn63	Sn63

3 x 5 = 15 TEST VEHICLES per test

Proposed Test Flow Diagram

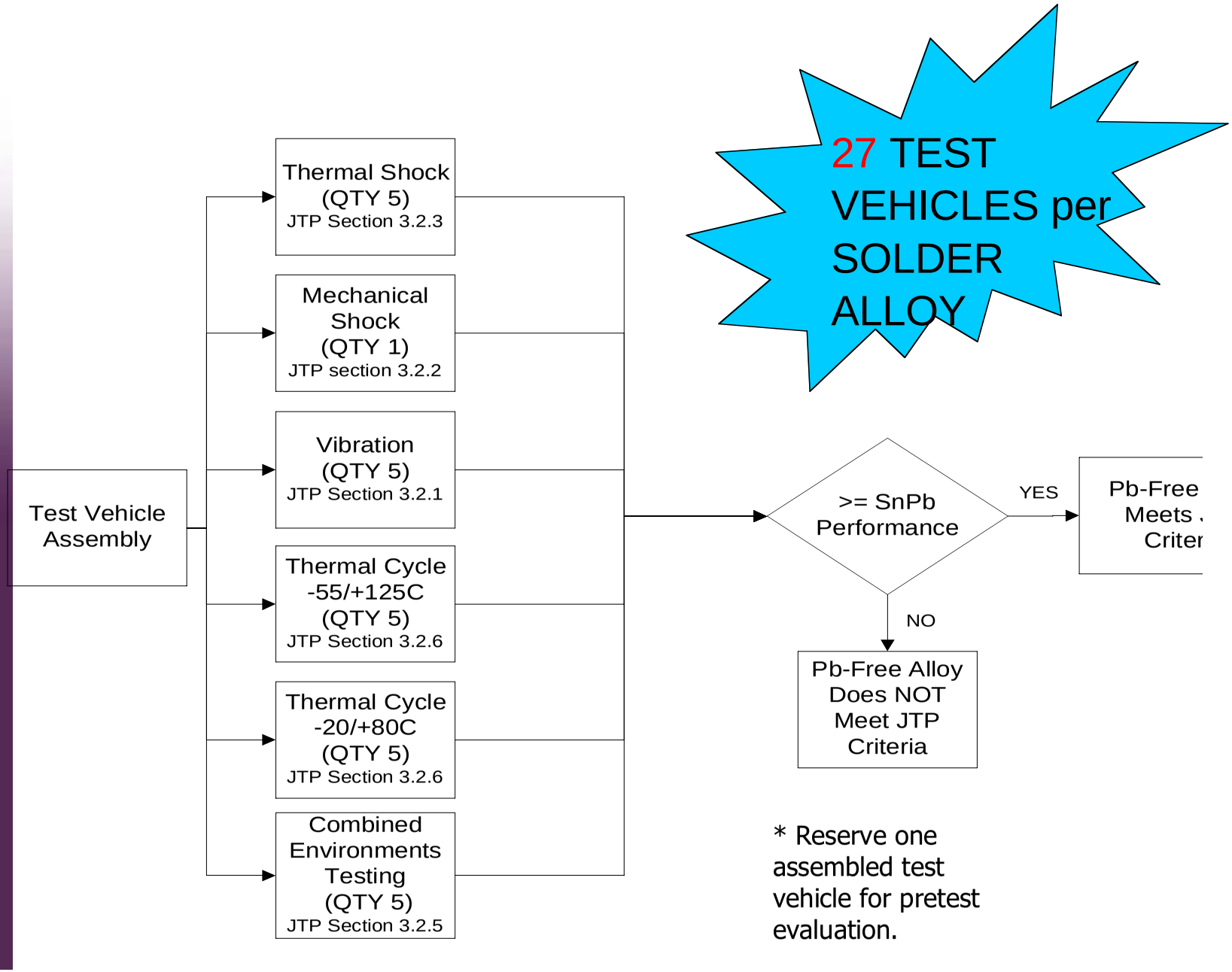

Acknowledgements

OEMs

- Boeing —Tom Woodrow
- Raytheon — Joe Felty & Jeff Bradford
- Rockwell Collins — Dave Hillman

NASA & DoD

- NASA —Mark Strickland, MSFC
- Army — Dave Locher& Martha Schuster, AMCOM
- Navy — Dave Nelson & Celeste Roper, China Lake
- Air Force —Mark Stibitz, F-15/WR-ALC

Other Organizations

- ACI —Lee Whiteman
- NCMS — Duane Napp

LOCKHEED MARTIN

Friction Stir Process Mapping Methodology

Gerry Bjorkman

Alex Kooney

Lockheed Martin Space Systems Company

Carolyn Russell

Marshall Space Flight Center

Process Overview

- Friction Stir Welding (FSW)
  - FSW is a solid-state process using a rotating tool with a shoulder and a projecting pin.
  - The pin tool is rotated and plunged into the joint until the shoulder contacts the top surface.
  - The frictional heating between the pin tool and the joint plasticizes the material in the local region near the pin.
  - The material at the weld centerline is joined through a combination of forging processes that occurs in the local region of the pin tool.
  - Three significant parameters: spindle speed, travel speed, plunge load or plunge position

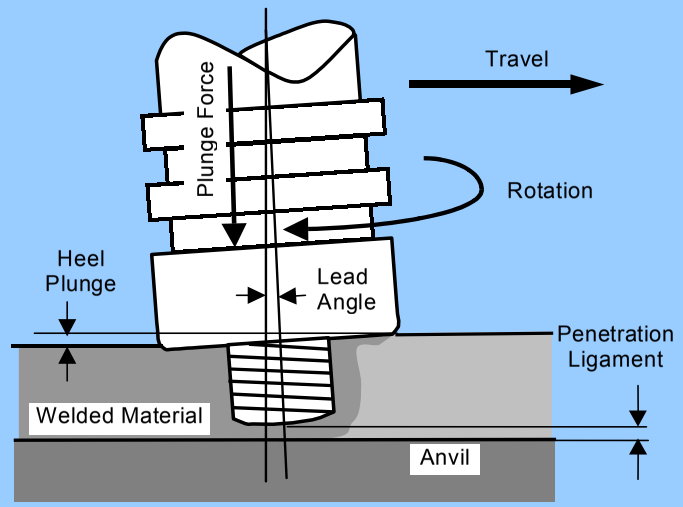

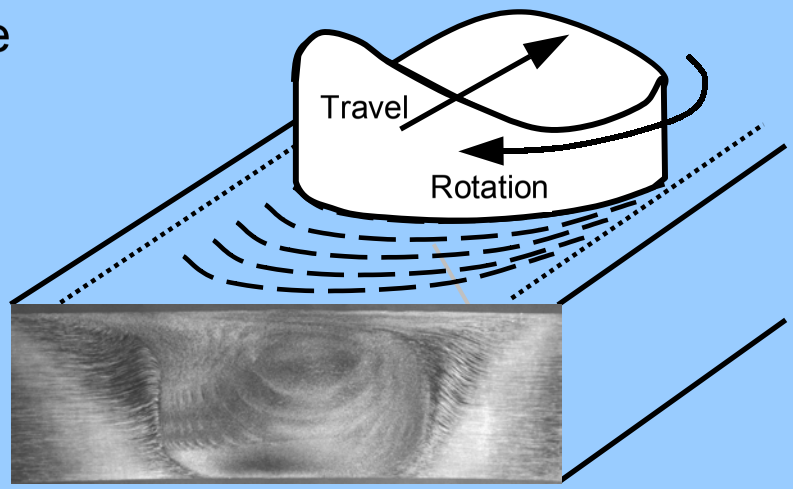

FSW Process Maps

LOCKHEED MARTIN

- A process map summarizes the weld process performance for a given pin tool geometry and joint configuration.
- Targeting a consistent penetration ligament, the process is simplified into two parameters: travel speed and rotation speed.
- Other parameters, such as plunge force, traverse force, weld nugget geometry, NDE response, and mechanical properties are assumed to be dependent variables.

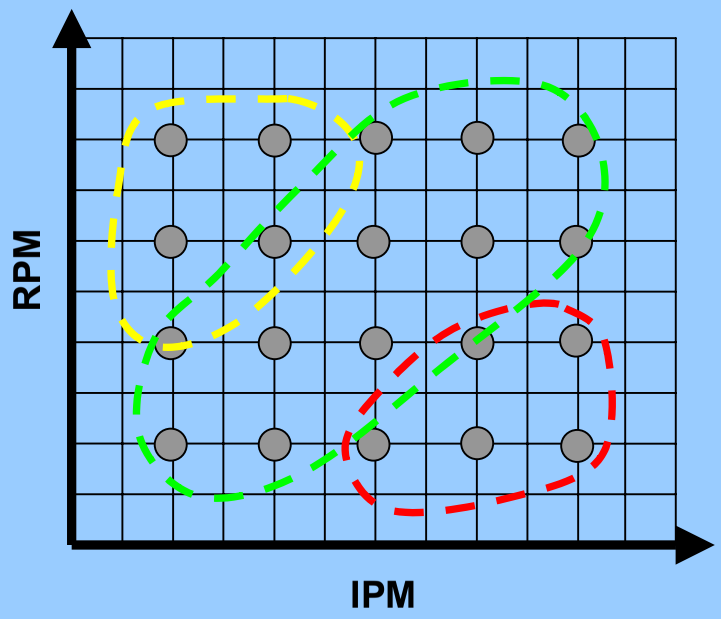

- **YELLOW:** Unusual flow patterns, unstable position and process loads, excessive flash, poor mechanical properties
- **GREEN:** Symmetric flow patterns, stable position and process loads, good strength
- **RED:** NDE rejections, volumetric defects, poor strength, excessive process loads

FSW Process Maps

- A selected rpm/ipm combination (weld schedule) provides a specific nugget geometry, heat input, and mechanical strength.
- The selected nominal weld schedule, or sweet spot, is the best compromise between process stability, mechanical strength, NDE response, and machine capability.
- Once the nominal schedule is selected, process loads and heel positions are explored to determine their acceptable operating windows.
- Statistical process control in conjunction with the process map data provides quality control and grounds for reduced NDE requirements.

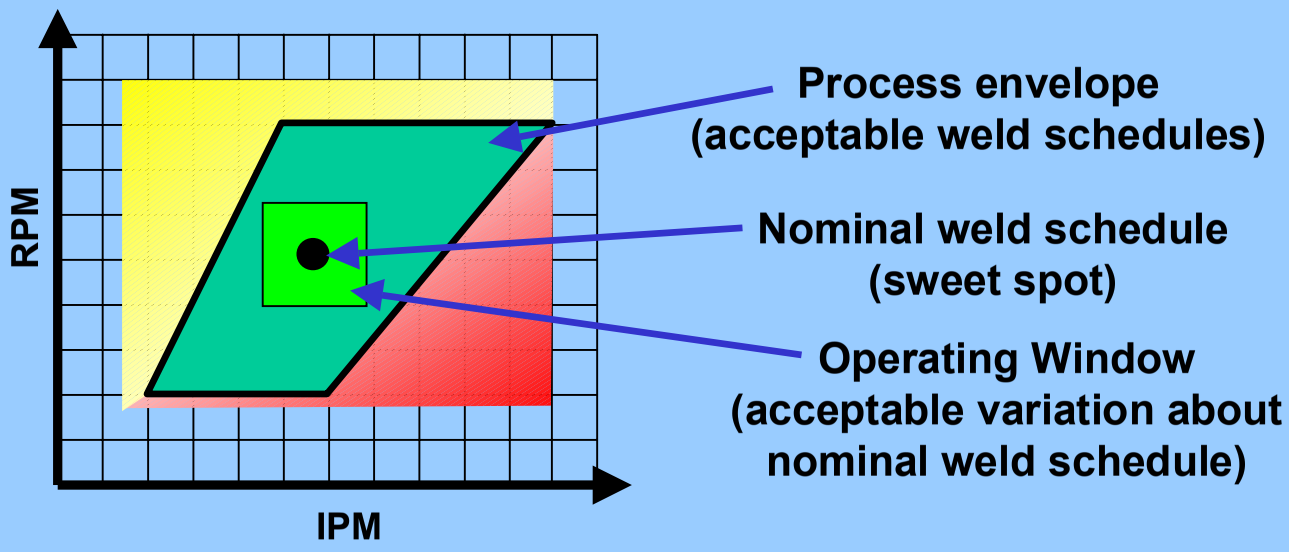

FSW Process Maps

LOCKHEED MARTIN

- Methodology Overview

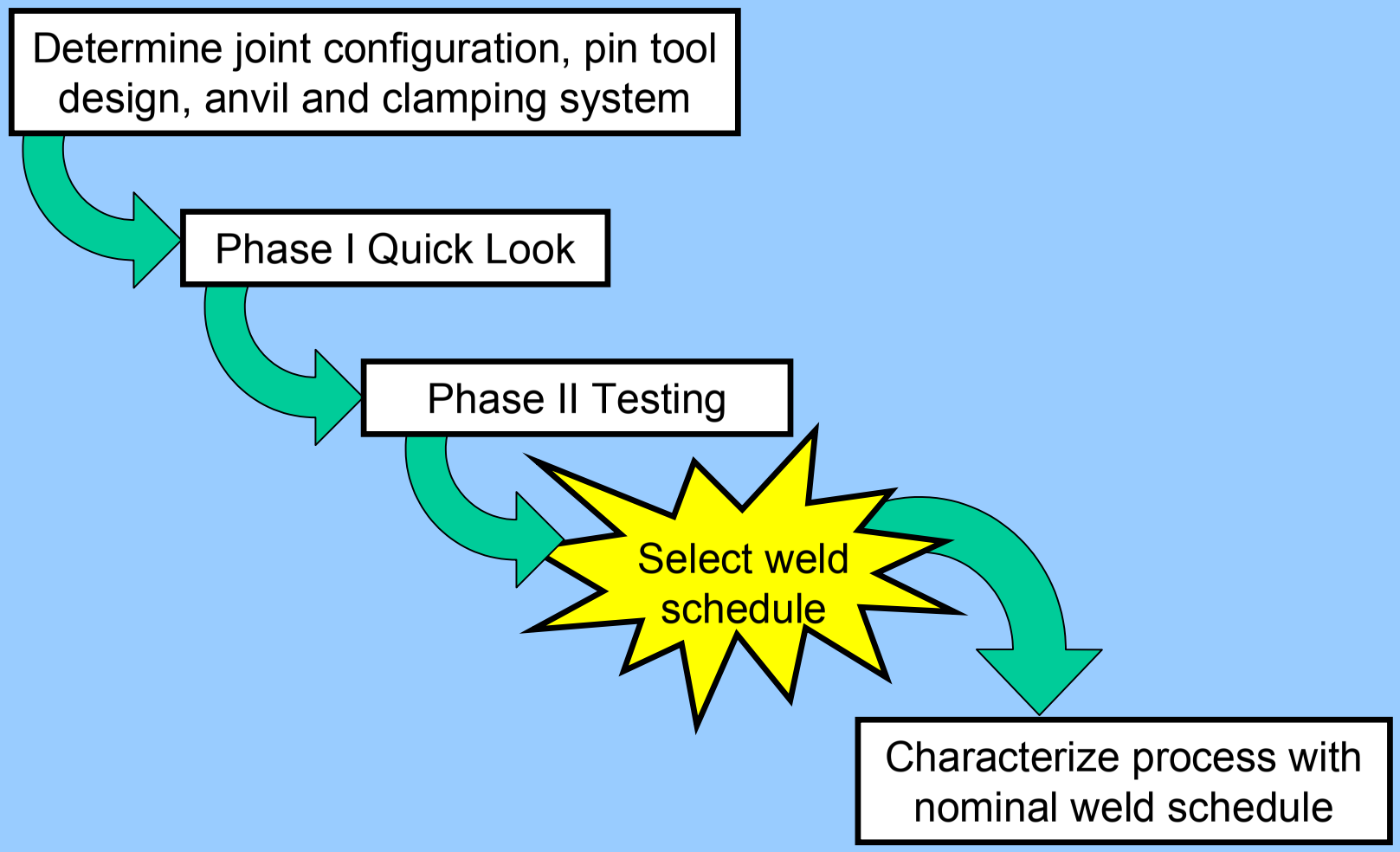

Phase I Quick Look

LOCKHEED MARTIN

- The “quick look” provides a general overview of the process map
  - Three weld schedules are performed on a 24 inch long test panel
  - Weld schedules are performed “hot” to “cold” by changing the travel speed (constant rotation speed)
  - Metallographic samples are excised near the end of each weld schedule

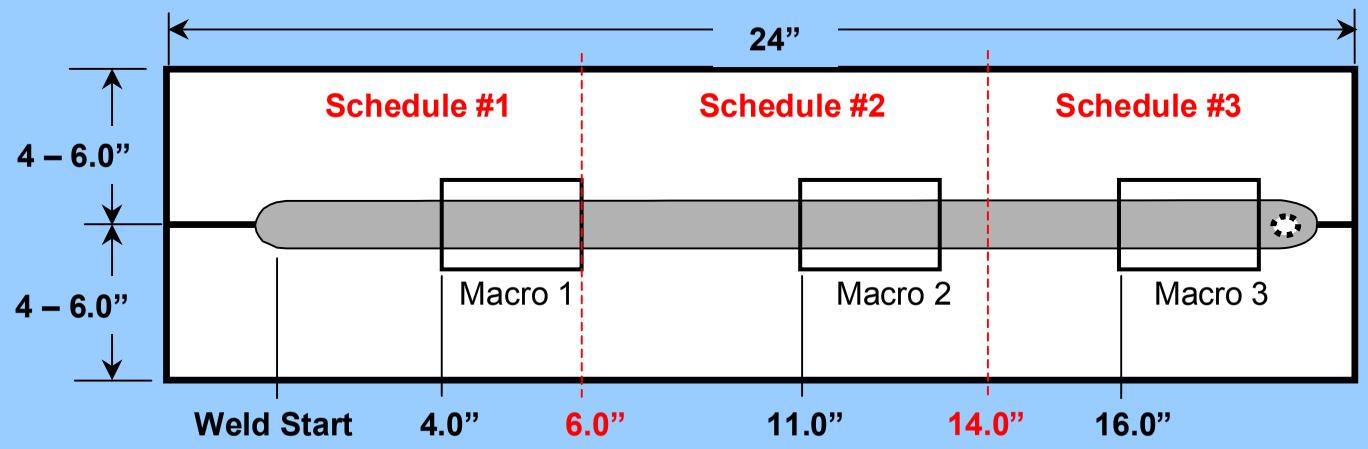

Phase I Quick Look

LOCKHEED MARTIN

- Yellow, Green, and Red regions are delineated based on the metallographic data from the Quick Look welds.

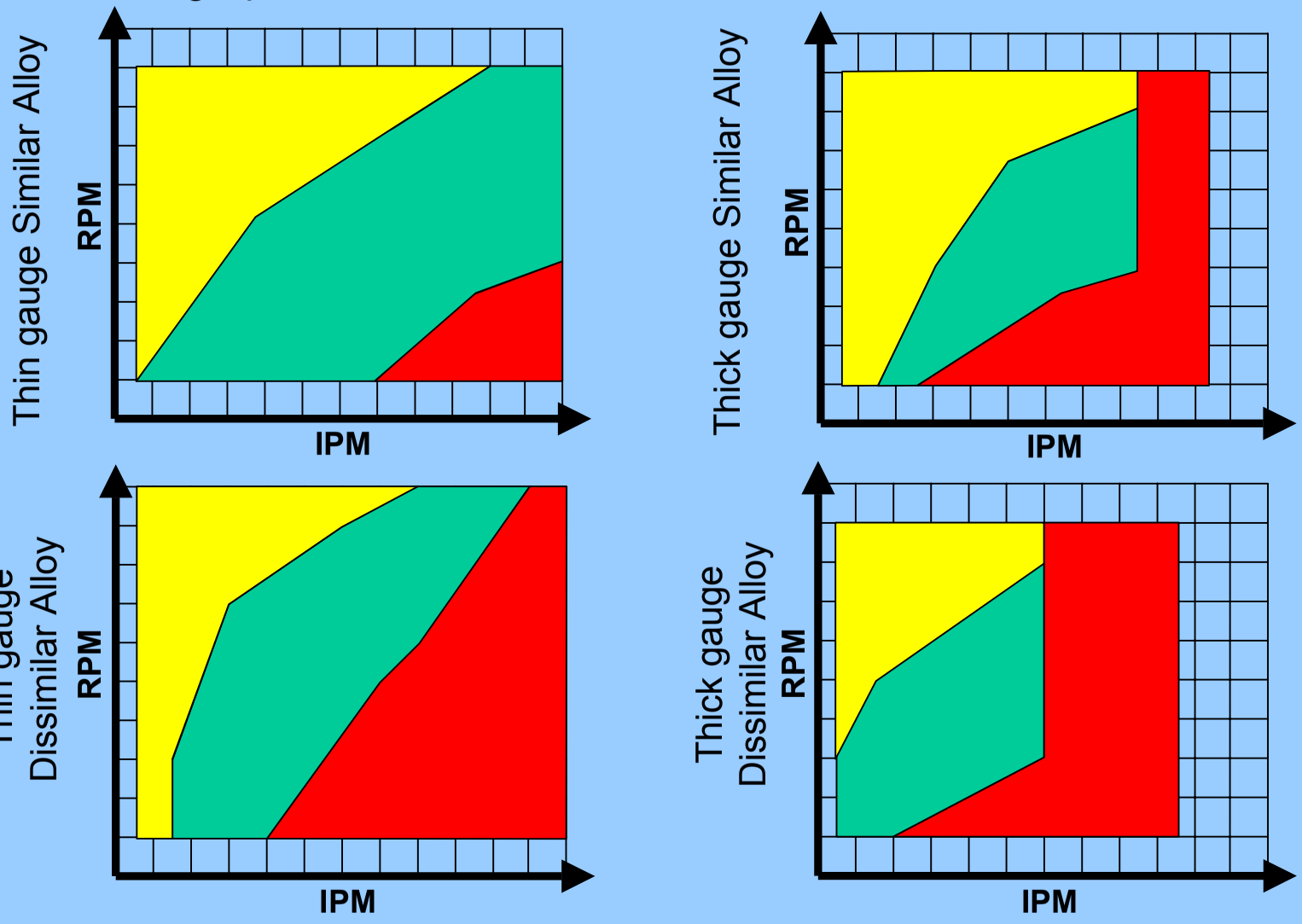

Phase I Quick Look

LOCKHEED MARTIN

- Thin gauge similar alloy configuration
  - **Low (A), medium (B), and high (C) heat input**

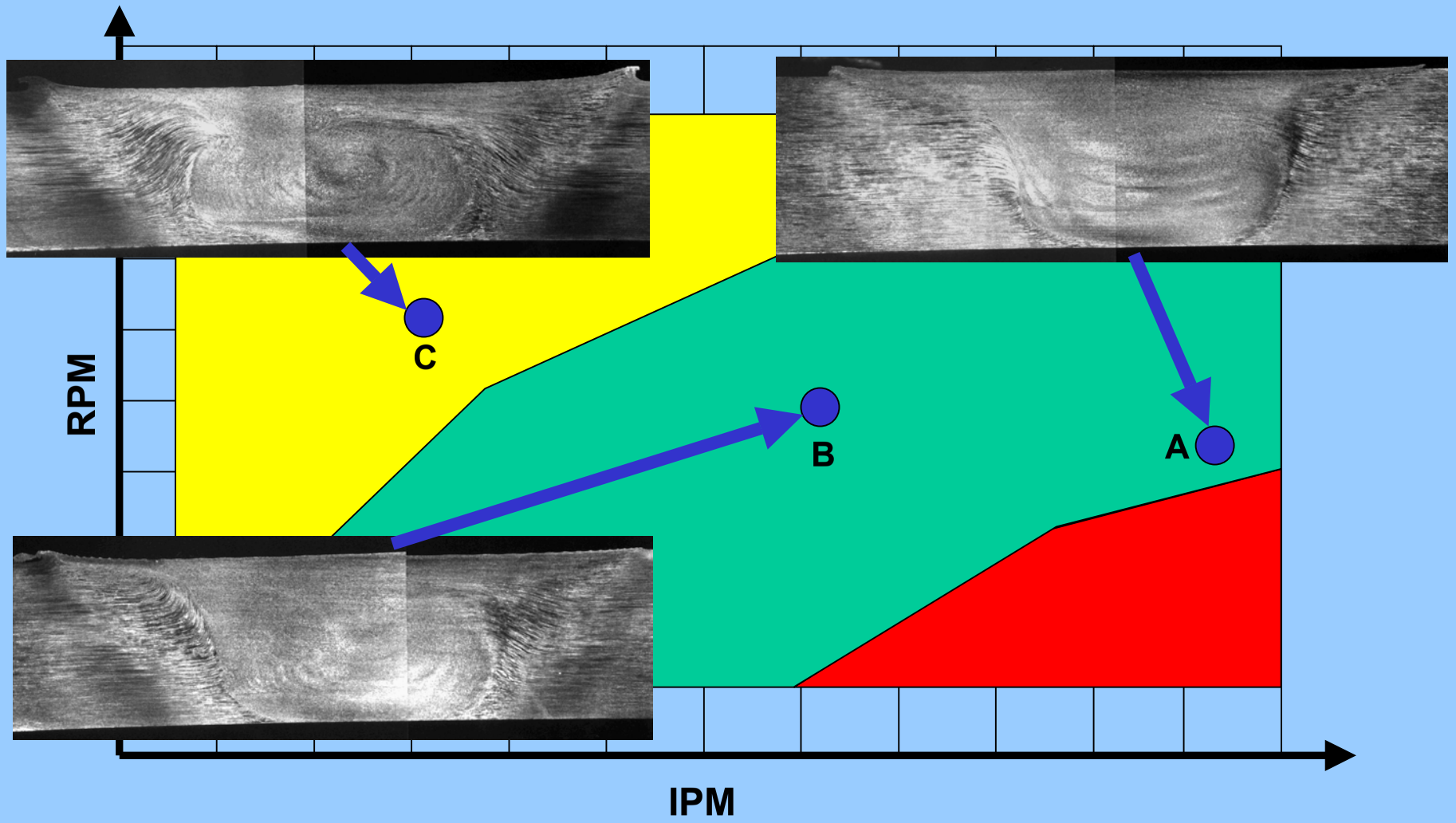

Phase I Quick Look

LOCKHEED MARTIN

- Thin gauge similar alloy configuration
  - Heel plunge vs. travel rate

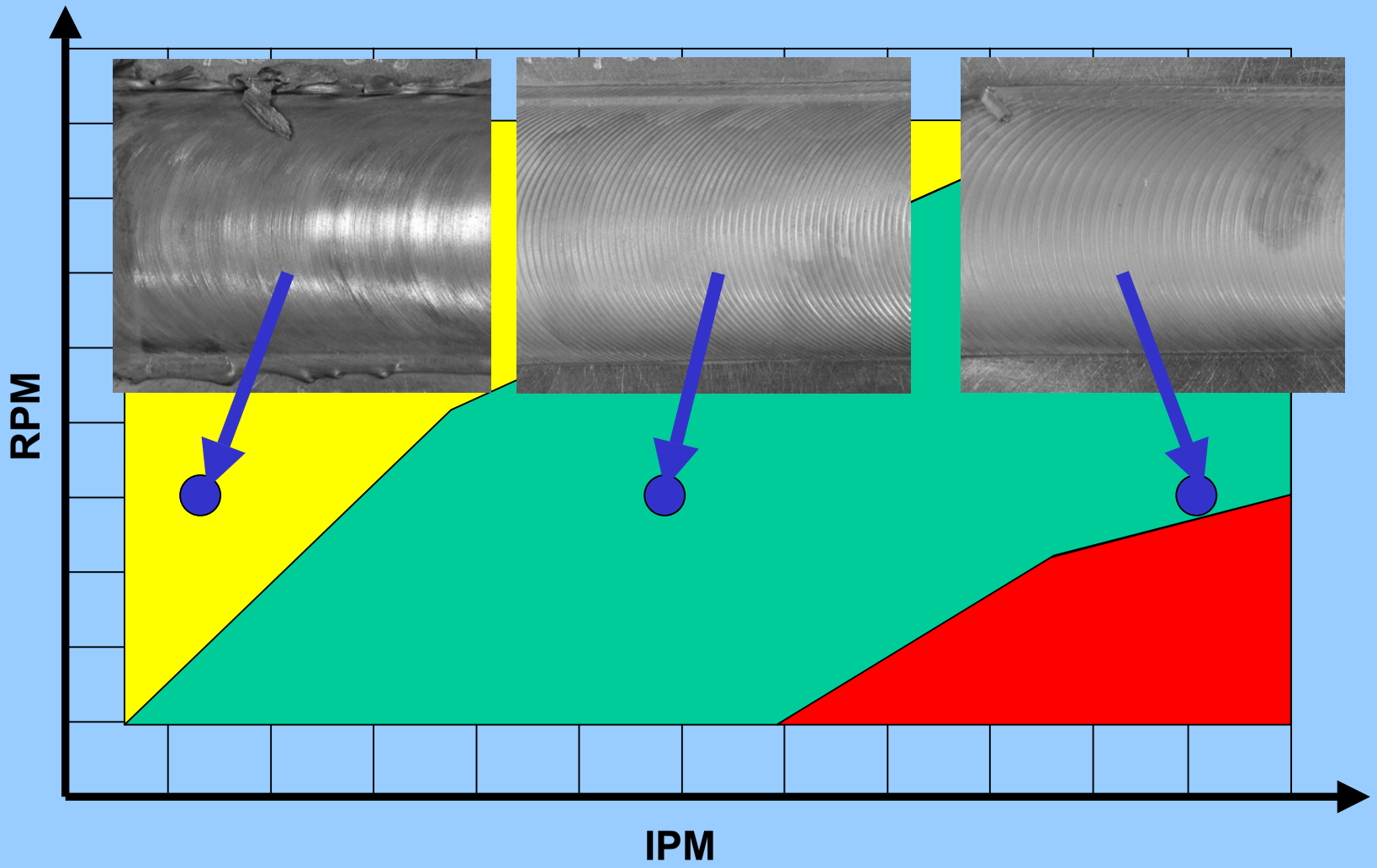

Phase I Quick Look

LOCKHEED MARTIN

- Thin gauge similar alloy configuration
  - Scaling/ Galling

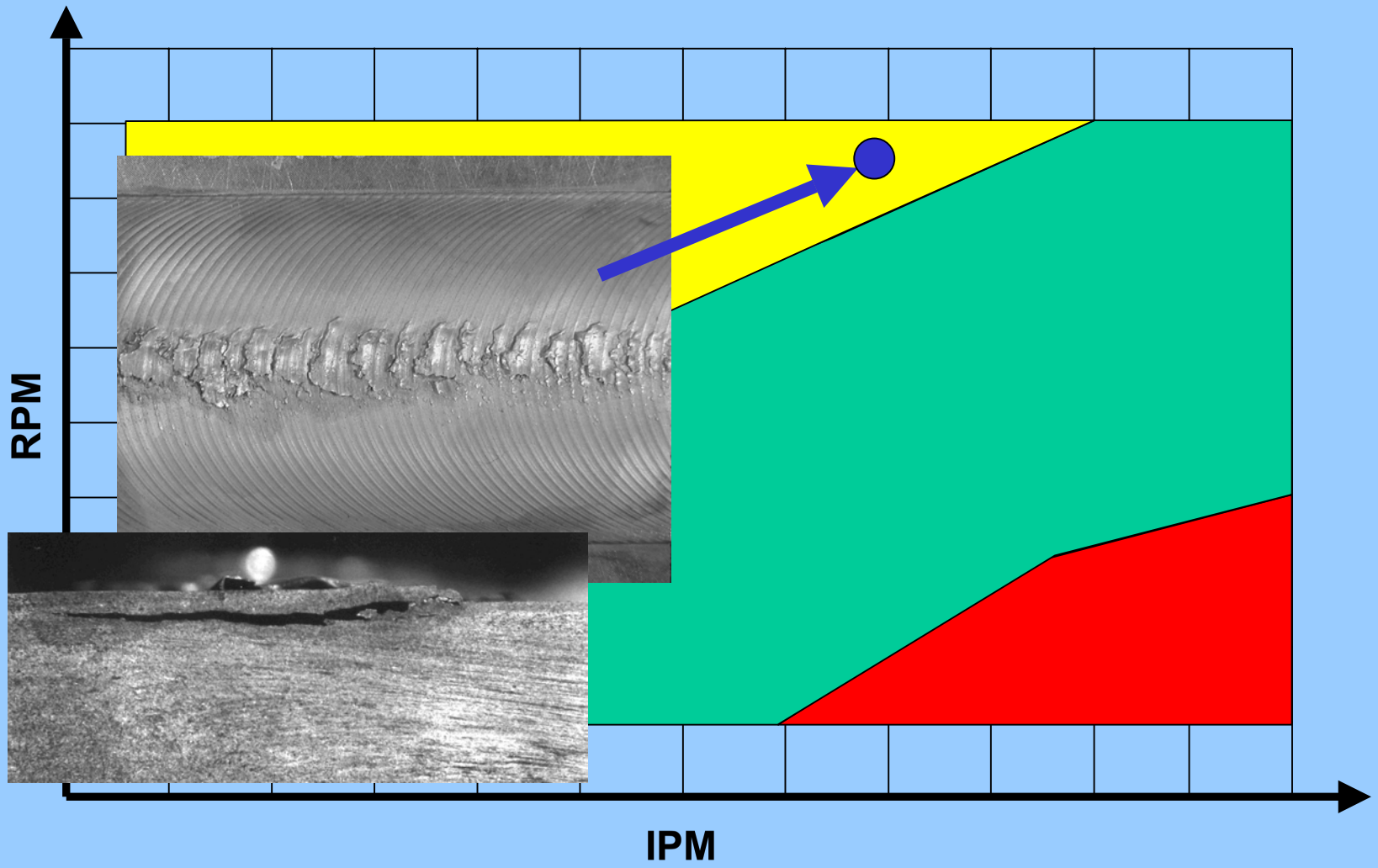

Phase I Quick Look

LOCKHEED MARTIN

- Thin gauge similar alloy configuration
  - Large Weld Nugget and Excessive Flash

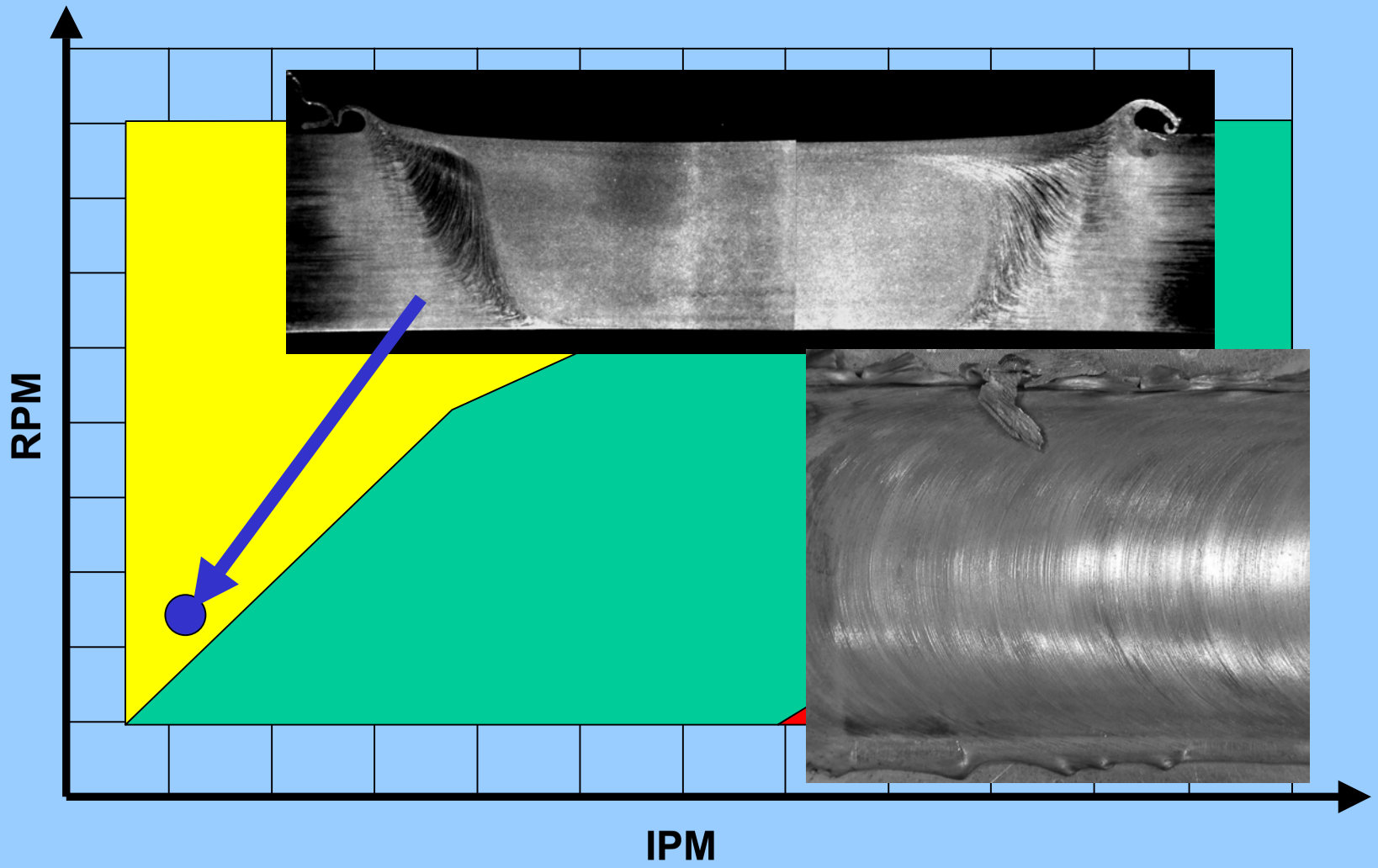

Phase I Quick Look

LOCKHEED MARTIN

- Thin gauge similar alloy configuration
  - Root voids and “worm holes”

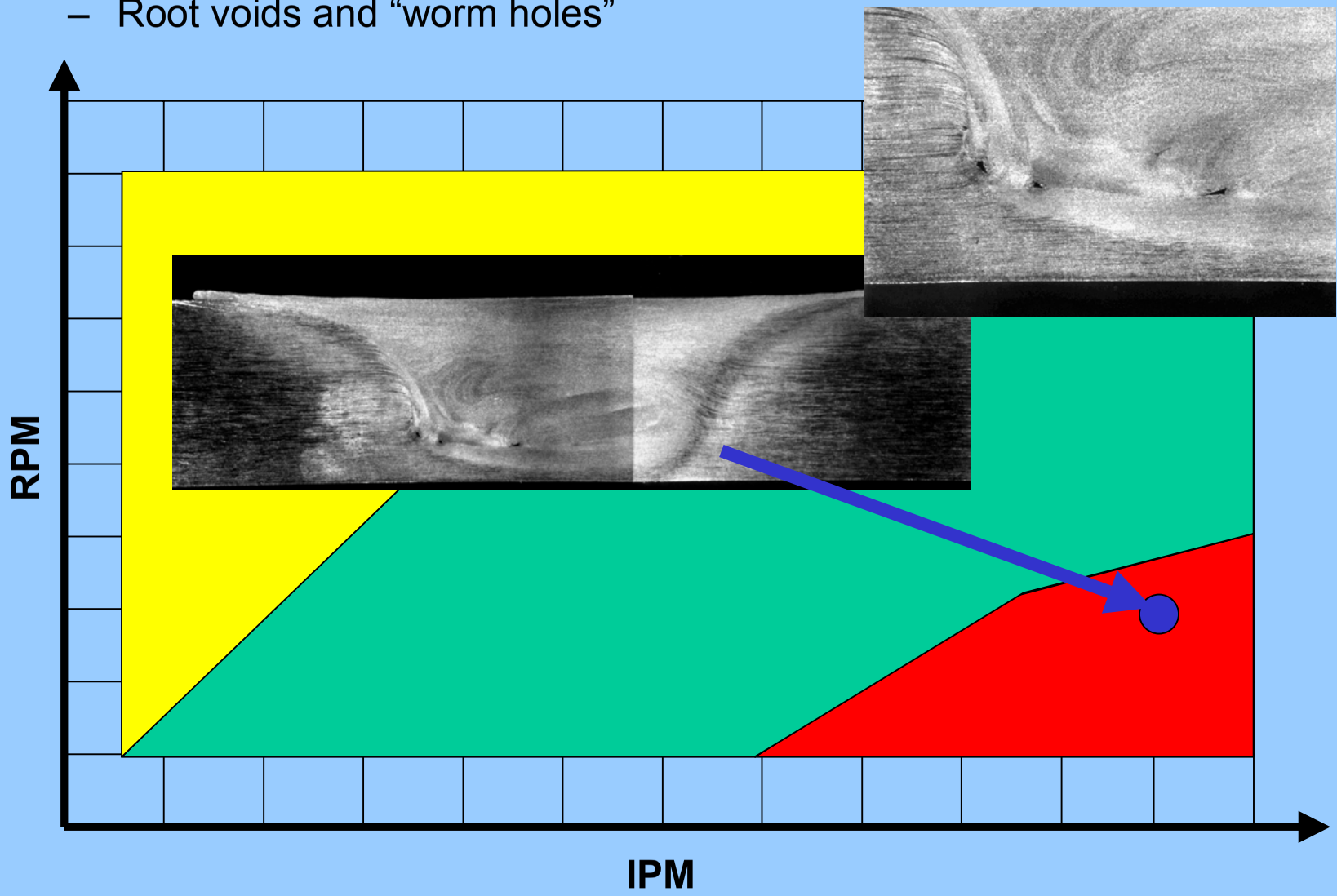

Phase I Quick Look

LOCKHEED MARTIN

- Thick gauge similar alloy configuration
  - Low (A), medium (B), and high (C) heat input

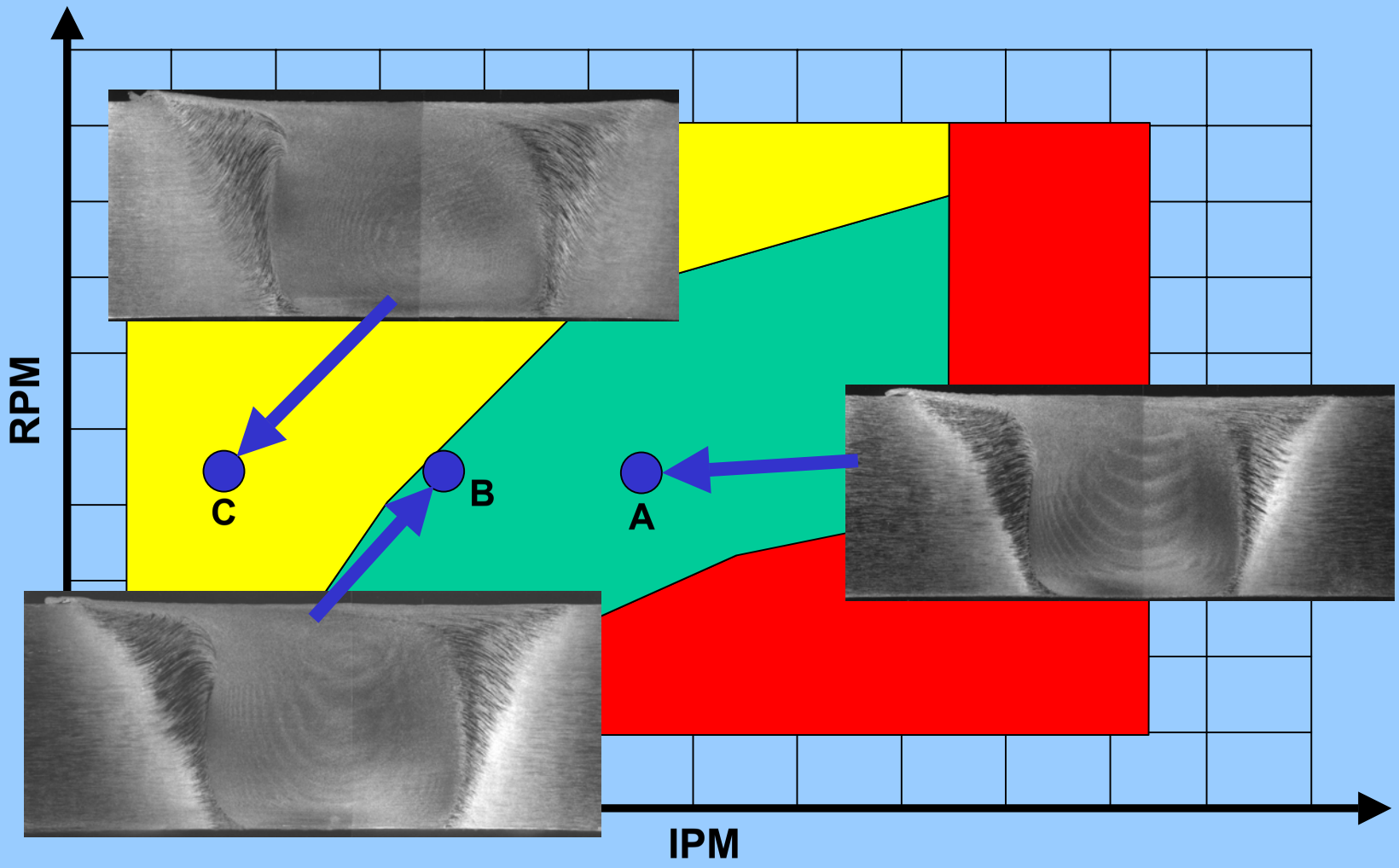

Phase I Quick Look

LOCKHEED MARTIN

- Thin gauge dissimilar alloy configuration
  - Low (A), medium (B), and high (C) heat input

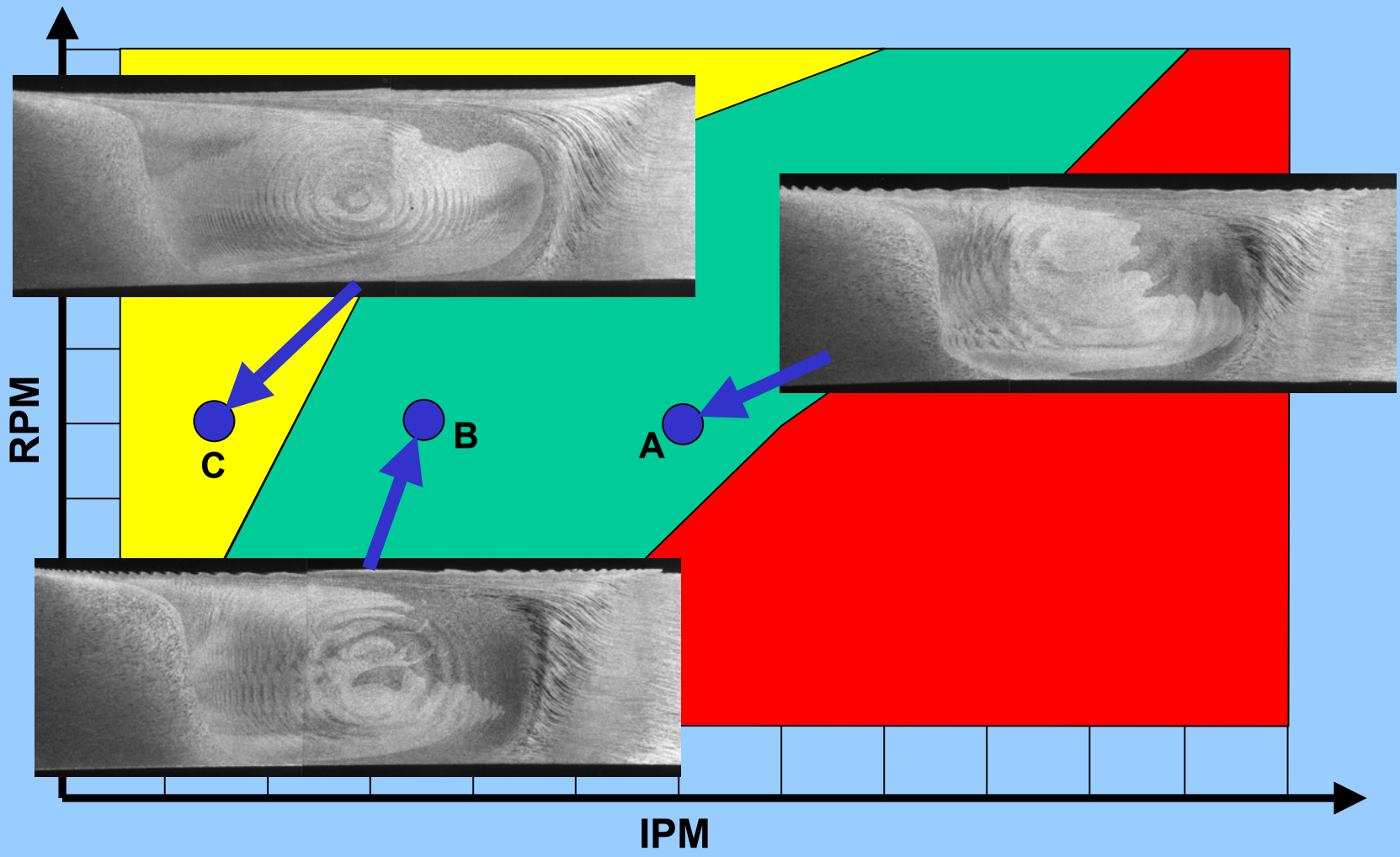

Phase I Quick Look

- Thin gauge dissimilar alloy configuration
  - Root void and “worm hole”

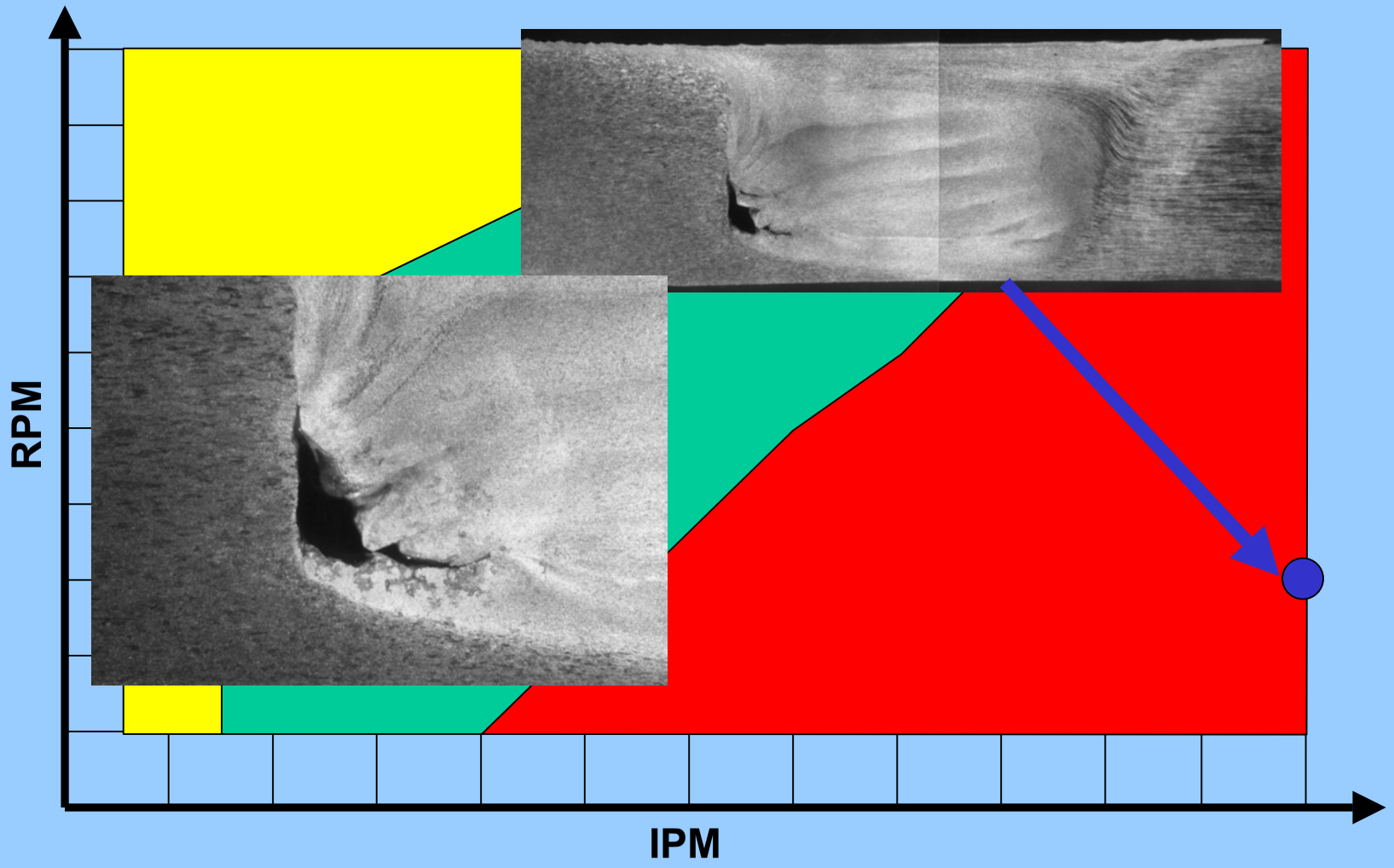

Phase I Quick Look

LOCKHEED MARTIN

- Thin gauge dissimilar alloy configuration
  - Irregular nugget flow
  - Location of particular alloy influences flow within the nugget

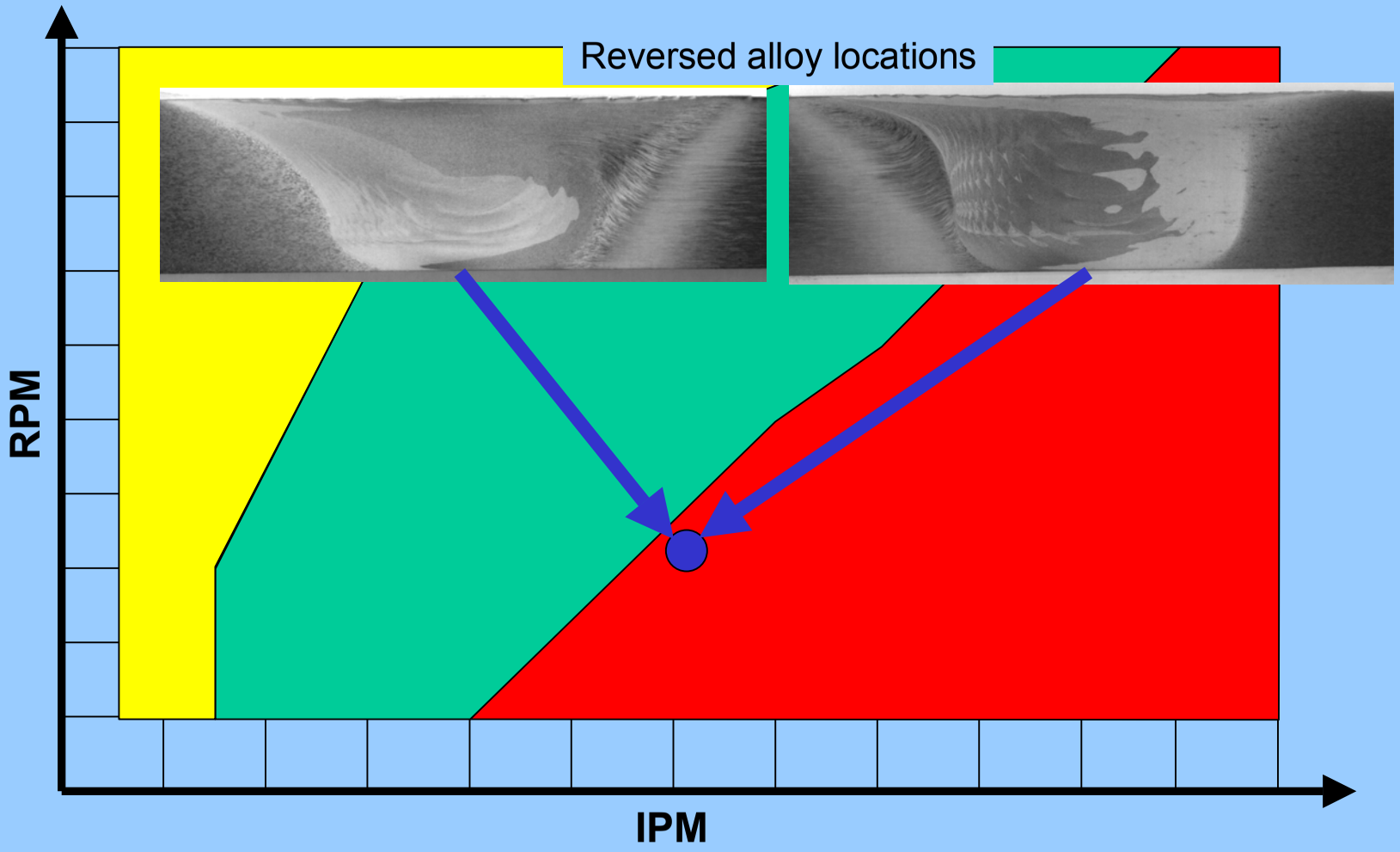

Phase I Quick Look

LOCKHEED MARTIN

- Thick gauge dissimilar alloy configuration
  - Low (A), medium (B), and high (C) heat input

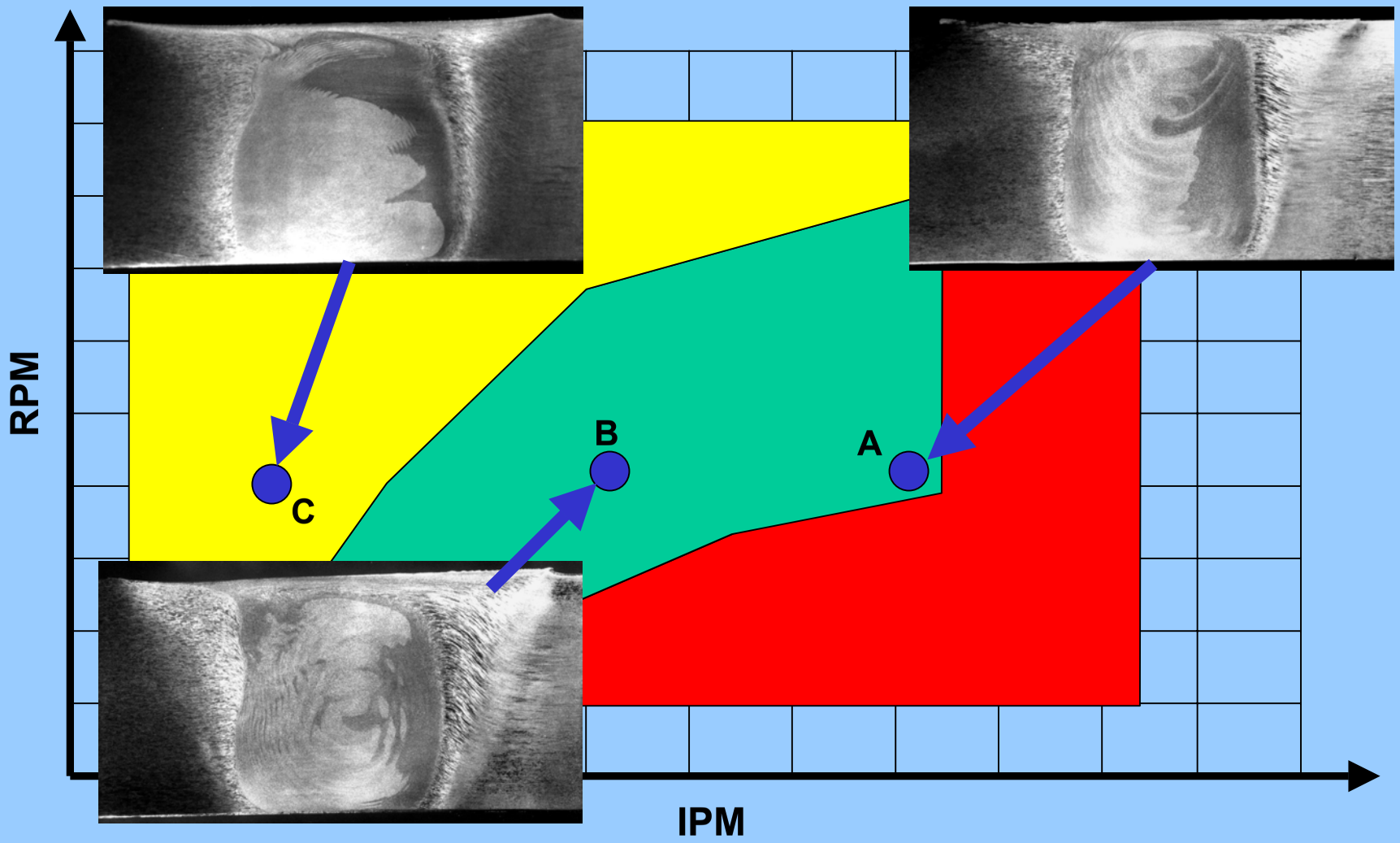

Phase I Quick Look

LOCKHEED MARTIN

- Thick gauge dissimilar alloy configuration
  - High heat input weld/ collapse weld nugget with “worm holes”

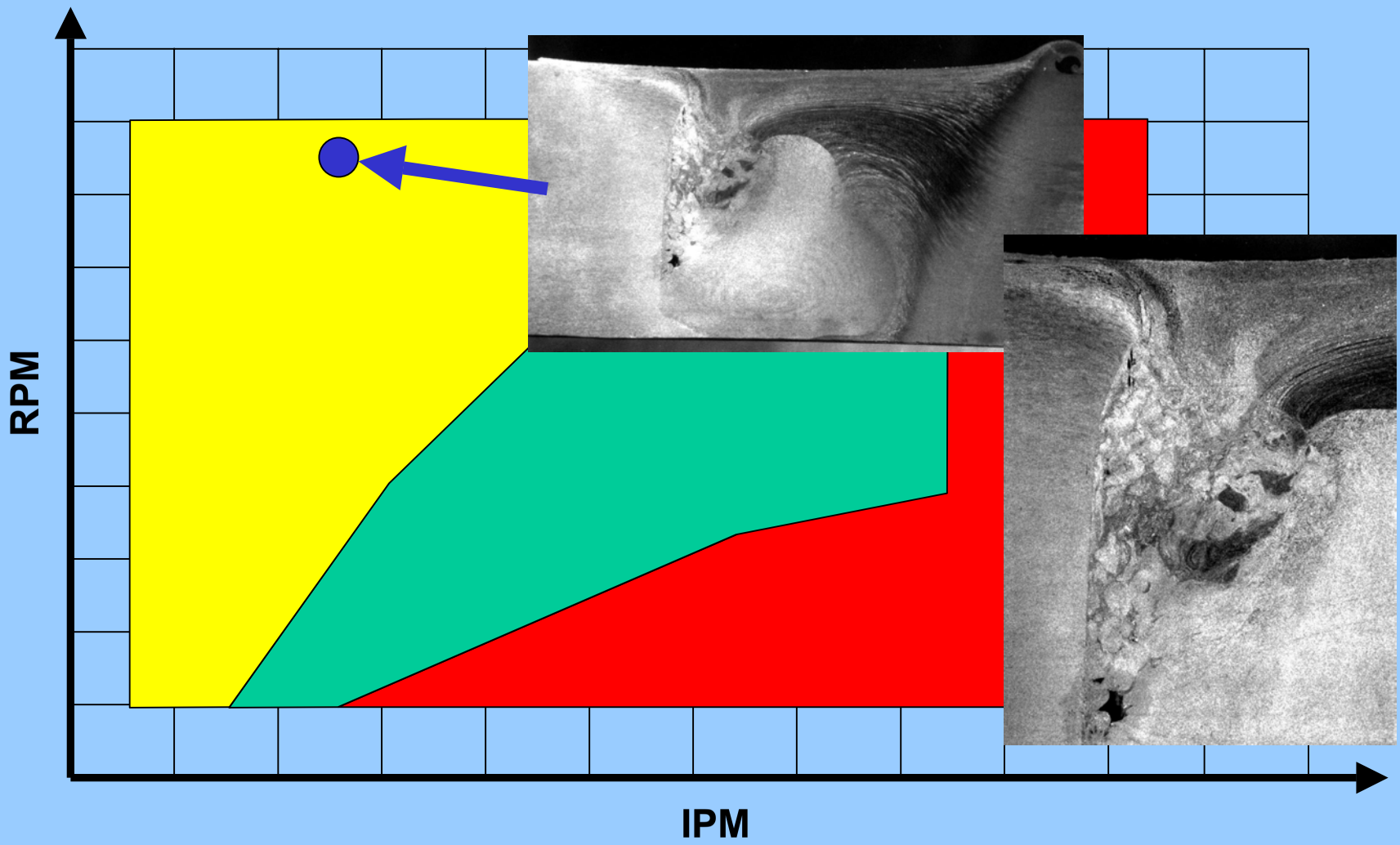

Phase I Quick Look

LOCKHEED MARTIN

- Thick gauge dissimilar alloy configuration
  - **Low Heat Input Weld with "Worm Holes"**

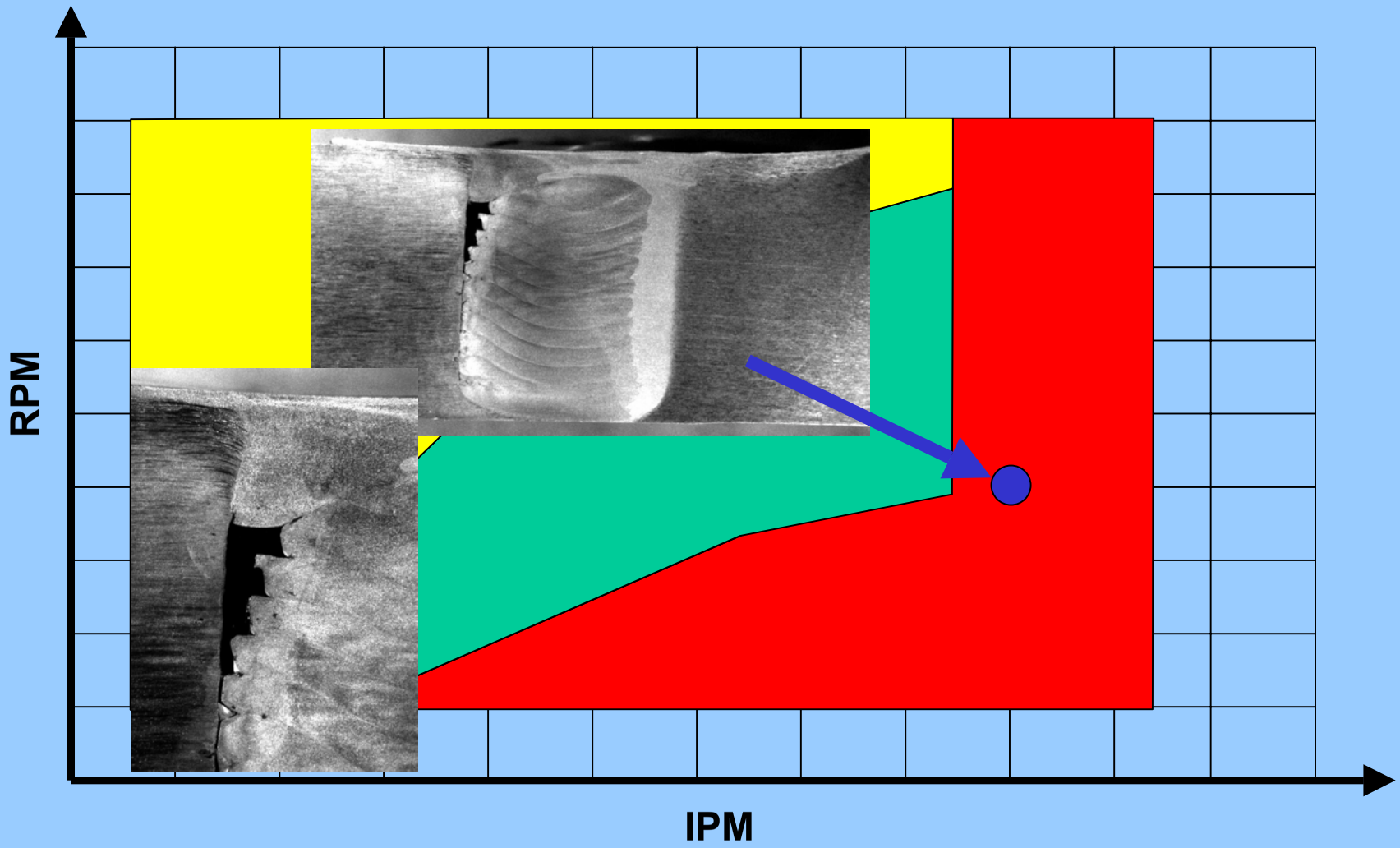

Phase II Testing

- Weld schedules that provide acceptable metallographic profiles from Phase I are performed on 24” long test panels.
  - The longer weld provides adequate time for weld to reach stability
    - More reliable NDE response and tensile tests
  - Process load data becomes more consistent
- Tensile tests are conducted at the expected service temperatures of the weld
- These tests define the process envelope and begin to focus in on the “sweet spot”

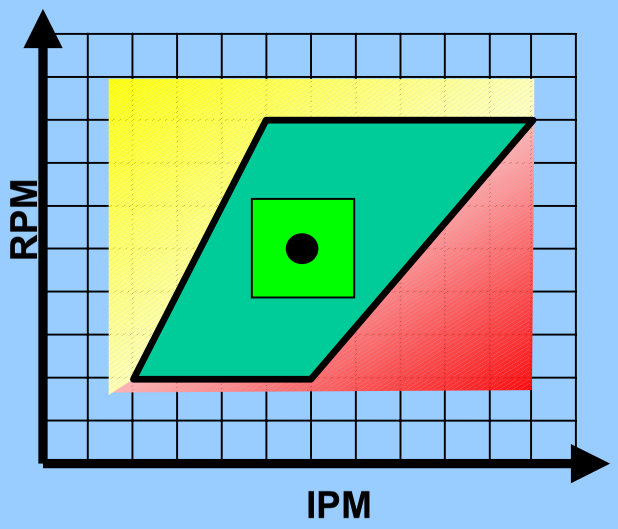

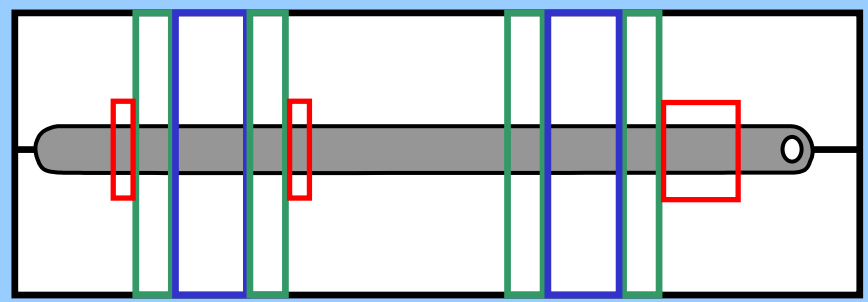

12”x24” Test Panel

Phase II Testing

LOCKHEED MARTIN

- The process envelope is delineated using the Phase II test data
  - **Mechanical strength, NDE, and tool performance are factors to consider**

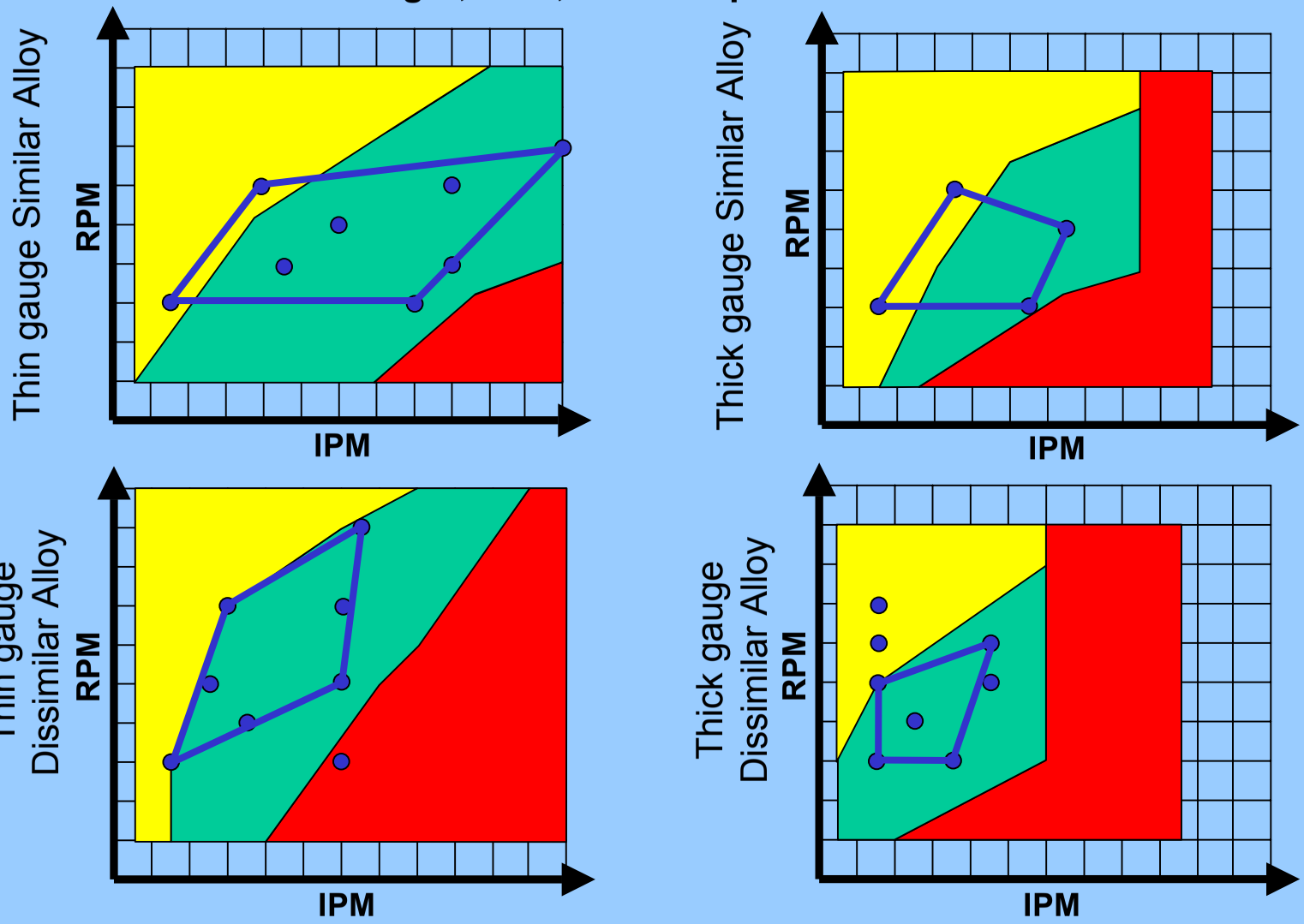

Phase II Testing

- Tensile strength increases with faster travel speeds
  - Cryogenic strength is more sensitive than room temperature strength to heat input
- Process loads, especially traverse loads, increase with travel speed
- The ability to perform cold welds depends on the machine's control system response

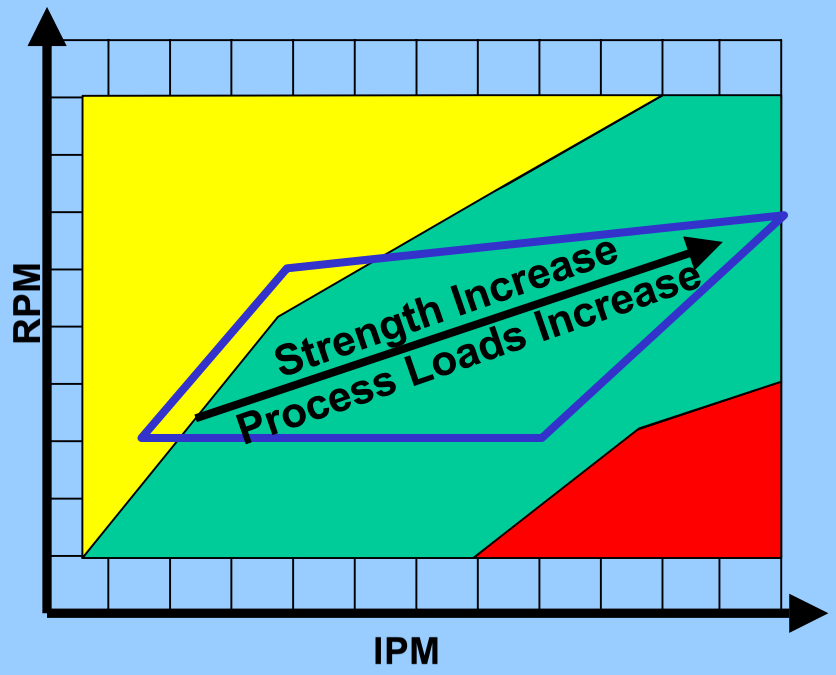

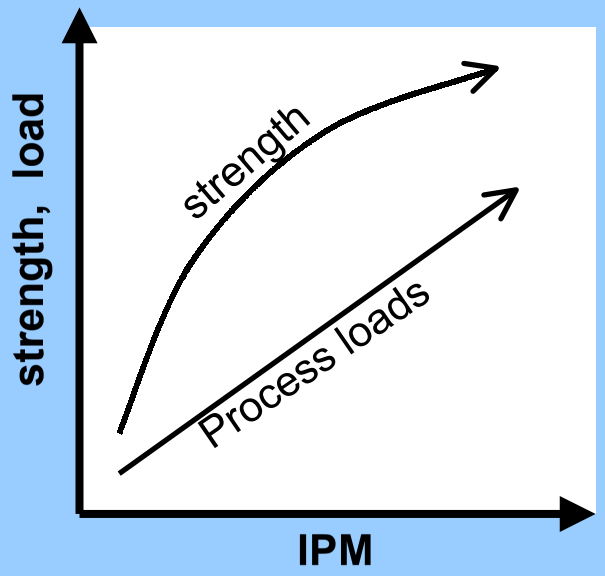

Weld Schedule Selection

LOCKHEED MARTIN

- Schedule selection is the best compromise between the following factors:
  - Process stability
  - Mechanical strength
  - NDE response
  - Machine capability
- The nominal schedule should be near the center of the process envelope to ensure robust performance to variations in the manufacturing environment

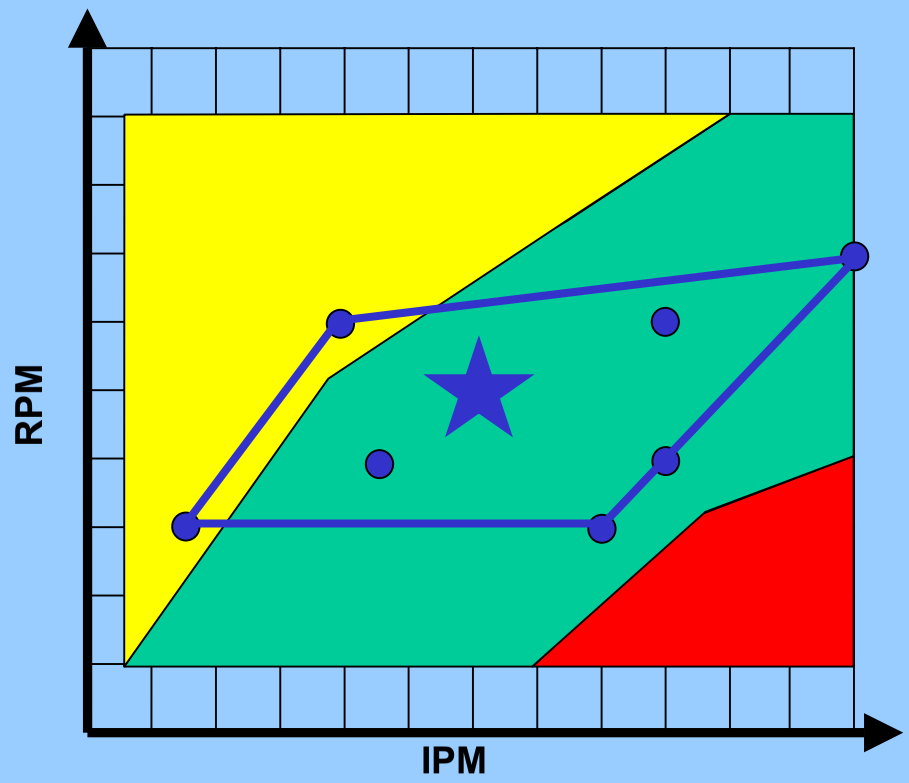

Process Characterization

LOCKHEED MARTIN

- Multiple welds are performed with varied setup conditions
- Process information, such as plunge load, is collected and acceptable bounds are established

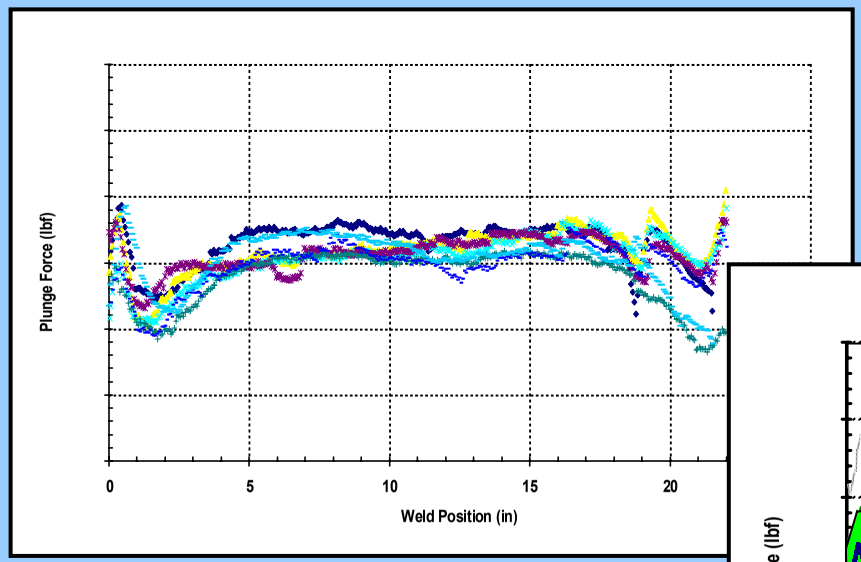

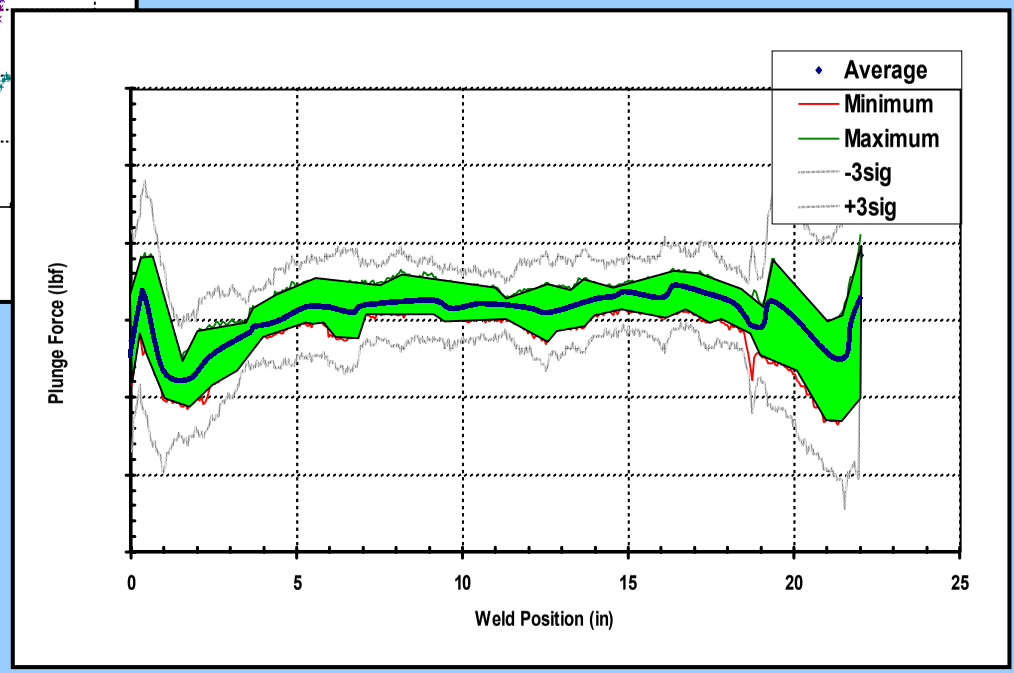

FSW Process Map Summary

LOCKHEED MARTIN

- The weld process performance for a given weld joint configuration and tool setup is summarized on a 2-D plot of RPM vs. IPM
- A process envelope is drawn within the map to identify the range of acceptable welds
- The sweet spot is selected as the nominal weld schedule
- The nominal weld schedule is characterized in the expected manufacturing environment
- The nominal weld schedule in conjunction with process control ensures a consistent and predictable weld performance

Synthesis and Characterization of Carbon Nanotubes for Reinforced and Functional Applications

SHEN ZHU
United Space Research Association
Marshall Space Flight Center, SD46
Huntsville, AL 35812
Phone: 256 544-2916
E-mail: shen.Zhu@msfc.nasa.gov

Many efforts have been engaged recently in synthesizing single-walled and multi-walled carbon nanotubes because of their superior mechanical, electrical, and thermal properties, which could be used for numerous applications to enhance the performance of electronics, sensors, and composites. This presentation will demonstrate the synthesizing process of carbon nanotubes by thermal chemical vapor deposition and the characterization results by using electron microscopy and optical spectroscopy.

Carbon nanotubes could be synthesized on various substances. The conditions of fabricating single-walled or multi-walled carbon nanotubes depend strongly on temperature and hydrocarbon concentration but weakly on pressure.

The sizes, orientations, and growth modes of carbon nanotubes will be illustrated. The advantages and limitations of several potential aerospace applications such as reinforced and functional composites using carbon nanotubes will be discussed.

Synthesis and Coating of Nanoparticles

ABRAHAM ULMAN
Polytechnic University
Six Metrotech Center
Brooklyn, NY 11201
Phone: 718-260-3119
Fax: 810-277-6217
E-mail: aulman@duke.poly.edu

Sonochemistry and microwave heating have been used for the preparation of magnetic and semiconductor nanoparticles. We show that

- Block copolymer surfactants provide relative control of size and size distribution of cobalt nanoparticles
- Sonochemistry provides mixing at the atomic level and can be used to prepare nanoparticles with designed properties
- Microwave heating is an excellent technique for the preparation of semiconductor nanoparticles with controlled size.

This ability to control composition, size, and size distribution in nanoparticles is promising when the design of advanced catalysts is concerned.

Deposition of Nanostructured Thin Film from Size-Classified Nanoparticles

Renato P. Camata, Nicholas C. Cunningham
Department of Physics, University of Alabama at Birmingham, Birmingham, Alabama 35294-1170

Kwang Soo Seol, Yoshiki Okada, and Kazuo Takeuchi
Nanomaterials Processing Laboratory, The Institute of Physical and Chemical Research (RIKEN)
Wako, Saitama 351-0198, JAPAN.

Abstract

Materials comprising nanometer-sized grains (~1_50 nm) exhibit properties dramatically different from those of their homogeneous and uniform counterparts. These properties vary with size, shape, and composition of nanoscale grains. Thus, nanoparticles may be used as building blocks to engineer tailor-made artificial materials with desired properties, such as non-linear optical absorption, tunable light emission, charge-storage behavior, selective catalytic activity, and countless other characteristics. This bottom-up engineering approach requires exquisite control over nanoparticle size, shape, and composition. We describe the design and characterization of an aerosol system conceived for the deposition of size-classified nanoparticles whose performance is consistent with these strict demands. A nanoparticle aerosol is generated by laser ablation and sorted according to size using a differential mobility analyzer. Nanoparticles within a chosen window of sizes (e.g., (8.0±0.6) nm) are deposited electrostatically on a surface forming a film of the desired material. The system allows the assembly and engineering of thin films using size-classified nanoparticles as building blocks.

Introduction

An important thrust in current nanotechnology research is the idea of using nanoparticles as building blocks for the creation of advanced artificial materials [1]. One of the main reasons for this concept is the size-dependent properties exhibited by nanoparticles and nanocrystals. This opens the way for engineering the properties of a material by tuning the size of its individual constituents. However, the controlled assembly of materials systems from nanoparticles is a challenging endeavor and is being attempted by a variety of physical and chemical routes. Chemical strategies currently being explored involve molecular cross-linking [2], template patterning [3], solvent evaporation [4], and surfactant-assisted reverse micelle synthesis [5]. Given the complexity of the task, and the variety of physical systems of interest, alternative techniques are sought that can be generalized and combined with chemical routes to deliver these nanostructured materials with desired functionality.

Aerosol processes provide an interesting platform for controlled generation, assembly and deposition of nanostructured thin films from gas-borne nanoparticles. A promising aerosol strategy for the controlled synthesis of nanostructured materials involves continuous nanoparticle generation followed by size classification and subsequent deposition of size-selected nanoparticles on a solid substrate [6]. In this approach, an aerosol of nanoparticles of the material of interest (e.g., elemental, compound, organic) can be generated by a variety of methods such as spark discharge [6], thermal evaporation [7], and laser ablation [8]. Active aerosol size classification is then used to select only the desired nanoparticle size and subsequent deposition can lead to an extended ensemble of nanoparticles on a solid substrate. In this manner extended nanostructured films may be generated and their properties engineered to meet current needs for advanced materials.

This approach is endowed of remarkable flexibility as it can be applied to virtually any material that can be condensed from a vapor. Although this principle of material assembly has been demonstrated in a variety of contexts, the process has so far encountered serious limitations in applications that require significant nanoparticle throughput. There is great need to optimize the processes of generation, size classification, and deposition from the point of view of materials synthesis.

In this paper, we describe the design, characterization and performance of an aerosol instrument that tailors the processes of size classification and nanoparticle deposition for the specific purpose of fabrication of nanostructured thin films. As it will become clear in the following sections, two of the key issues addressed in this new instrument are the space charge and diffusion effects. Space-charge effects and diffusion losses are minimized by the careful choice of the design parameters and their optimization for operation in the 1-10 nm size range. The aerosol system developed is capable of performing size classification and deposition of a wide variety of nanoparticles and the design parameters have been optimized to enable high-resolution and high-throughput size classification and deposition of nanoparticles as small as 1 nm.

Size classification of aerosol nanoparticles

The differential mobility analyzer (DMA) is the key instrument in the measurement of ultrafine aerosol particles [9,10]. The DMA is the aerodynamic analog of a dispersive mass spectrometer. Physically, this instrument is a capacitor in which charged aerosol particles migrate across a laminar flow of a particle-free sheath gas as a result of an electric field. Because the particle electrical mobility is a function of its projected area, particles with different mobilities have distinct trajectories inside the DMA. A sampling orifice suitably placed at the analyzer electrode opposite to the aerosol inlet extracts only particles in a narrow window of mobilities. By varying the voltage across the capacitor, the applied field is varied and the mobility of the classified particles can be continuously tuned.

The basic physical principles that govern particle transport in this instrument are relatively simple and may be understood purely in terms of classical particle motion in a fluid suspension. Neglecting Brownian diffusion and space charge effects for the time being, the equation of motion of a particle suspended in a gas of viscosity μ and flowing with velocity $\vec{u}$ may be written from Newton's law simply as

$$m\frac{d\vec{v}}{dt} = \frac{3\pi\mu D_p}{C_c}\left(\vec{u} - \vec{v}\right) + q\vec{E} \tag{1}$$

where D_p, m, and q are the diameter, the mass, and the electric charge of the particle, respectively, and $\vec{E}$ is the applied electric field. The first term on the right-hand side of this equation is the drag force on a particle moving with velocity $\vec{v}$ in a fluid with velocity $\vec{u}$, and the second term is the electrical force. The quantity C_c is the slip correction factor which accounts for deviations from the Stokes drag for particles that are small compared to the mean free path of the gas molecules and is given by

$$C_c = 1 + Kn\left[\alpha + \beta\exp\left(-\frac{\gamma}{Kn}\right)\right] \tag{2}$$

where Kn is the Knudsen number, defined as the ratio of the gas mean free path to the particle radius (i.e., $Kn = 2\lambda/D_p$. The parameters α, β, and γ have been determined in numerous experiments [11]. The difference in the values of C_c for different sets of α, β, and γ is always below about 2% for Kn ranging from 0.001 to 100. Commonly accepted values are

$$\alpha = 1.257,\ \beta = 0.40,\ \gamma = 1.10 \tag{3}$$

and these will be used throughout this paper.

The steady state solution for Eq. (1) gives a particle migration velocity $\vec{v}$ parallel to the applied electric field $\vec{E}$.

$$\vec{v} = Z_p\vec{E} \tag{4}$$

where the proportionality constant, Z_p, is the particle electrical mobility which is defined as

$$Z_p = \frac{qC_c}{3\pi\mu D_p} \tag{5}$$

Thus, the electrical mobility of a particle and its migration velocity increase with decreasing particle size. This establishes the basis for size classification based on differences in particle mobility, provided that particles can be suitably extracted from the capacitor region without disturbing the flow and electric fields. As can be seen from Eq. (5), control over the charge state of the aerosol is also necessary for a one-to-one relationship between particle diameter D_p and electrical mobility Z_p. Multiply charged particles in the DMA will lead to multiple peaks in the size distribution of the classified aerosol.

Differential mobility analyzers are commonly implemented in a cylindrical geometry as illustrated in Fig. 1 In this configuration a sheath gas flows in the annulus between two concentric cylindrical electrodes with radii r_1 and r_2 at a volumetric rate Q_{sh} while the electrodes are maintained at a constant voltage difference. The aerosol is introduced in the annulus at a volumetric flow rate Q_a through a circular slit in the outer electrode and charged particles migrate toward the inner electrode due to the electrostatic force. Particles with electrical mobility within a certain range are extracted through a slit at the inner electrode by a sampling flow Q_s. If all charged particles have one elementary charge, the extracted particles are size classified and have a diameter $D_p \pm \Delta D_p$ [9].

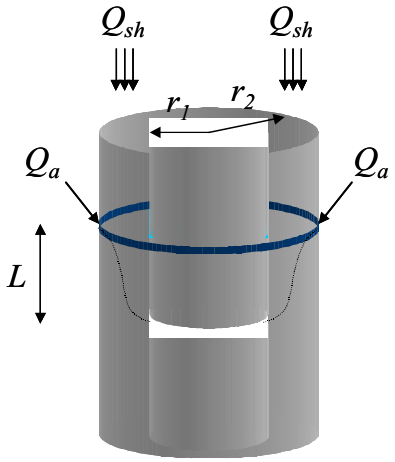

Fig. 1: Cylindrical geometry in which most differential mobility analyzers are implemented. The geometrical parameters are the radii of inner and outer electrodes (r_1 and r_2) and the length of the classification region (L).

Although this principle of size classification has now been applied in a variety of deposition experiments targeting the creation of new materials containing size-classified nanoparticles [6,12-16], the process has so far encountered serious limitations in applications that require significant nanoparticle throughput. This is because available DMAs have been developed to classify aerosols at relatively low concentrations ($<10^5$ cm^{-3}). Under these conditions, charged particle losses within the classification region of the DMA are small and space charge effects are expected to be minor. However, in applications of the DMA that involve high particle concentrations space charge effects cannot be ignored. Since DMAs are now being used to sort aerosol particles with respect to size to generate deposits for study of size dependent properties and fabrication of nanoparticle-based microelectronic and optical devices, the production of dense deposits in reasonable times, require that high concentration aerosols are processed through the DMA. When this is attempted, the performance of the size classification is seriously compromised due to the space charge field in the instrument [17].

We have devised a method to choose the values of the inner electrode radius r_1, the electrode separation r_2 - r_1, and the column length L of the DMA in order to maximize its throughput and resolution in a specific size range. Our method uses two factors to determine the best choice of r_1, r_2 - r_1, and L namely the space charge number Sc and the diffusion broadening parameter $\tilde{\sigma}$. A detailed explanation of the physical meaning of these quantities is provided in the sections that follow.

Minimizing space charge effects during size classification of nanoparticles

Materials synthesis from size-classified aerosol nanoparticles calls for the deposition of the gas-borne particles on a substrate. Assuming unity collection efficiency and neglecting particle pile-up, the time t required to generate a uniform one-monolayer deposit of singly charged nanoparticles over an area A is given by

$$t = \frac{4A}{NQ_s \pi D_p^2} \tag{6}$$

where D_p is the nanoparticle diameter, N is the particle number concentration and Q_s is the volumetric flow rate of the aerosol containing the classified particles. A plot of this equation as a function of number concentration is shown in Fig. 2 for the generation of a 1-mm diameter circular deposit using an aerosol flow rate of 1 SLM (standard liter per minute). This figure illustrates the need for high aerosol concentrations in the deposition of macroscopic amounts of size-classified nanoparticles. It is apparent that for low aerosol concentrations of 10^4 cm^{-3}, several days are necessary to deposit one monolayer of 10-nm particles. Deposits of smaller particles may demand weeks. Operation for such extended periods of time is usually impractical even for fully automated systems. High throughput and reasonable collection times can be achieved, however, if elevated number concentrations are processed in the DMA.

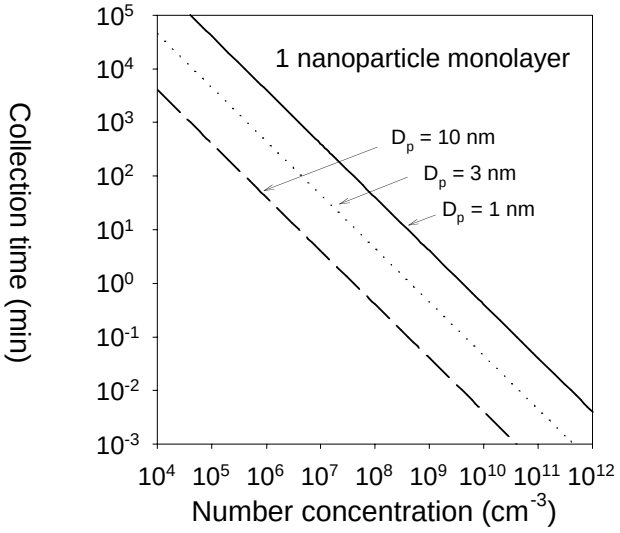

Fig. 2: Time required to deposit one nanoparticle monolayer as a function of number concentration for different particle diameters. Calculation for a nozzle-to-plane electrostatic precipitator with singly charged particles, aerosol flow rate of 1 SLM and deposit radius of 1 mm.

Ideally, one would like to perform size classification at concentrations in the 10^7 – 10^9 cm^{-3} range to generate deposits equivalent to several nanoparticle monolayers in a matter of hours or even minutes. Reliable operation in this regime would fully enable the size classification process as a materials processing technique.

Currently available DMAs cannot perform reliable size classification at these high number concentrations of charged particles. This is because under these conditions the electric field created by the particles undergoing classification becomes comparable to the applied electric field. Thus, space charge effects degrade the resolution and accuracy of the instrument.

However, changes of design parameters and operation conditions can help mitigate this problem. A useful guide in this area is the *space charge number*, Sc, a dimensionless group that roughly estimates the importance of the space charge field in a DMA [17]. Although this dimensionless group does not capture the details of the physical phenomenon involved, its scaling provides the essential features of the process and can be useful in the design of a DMA tailored for operation at high concentration of charged particles.

For a cylindrical DMA the space charge number may be written as [17]

$$\mathrm{Sc} = \frac{Ne}{\varepsilon V} G_F \tag{7}$$

where N is the concentration of charged particles in the DMA, e is the elementary charge, ε is the dielectric permittivity, V is the applied voltage, and G_F is a factor that depends on the flow rates and the geometry of the DMA [17]. This dimensionless group gives an idea of the importance of the space charge effect in a DMA under given operating conditions. Its value can be interpreted as an estimate, in percent, of the magnitude of the space charge field inside the DMA with respect to the applied electric field. Although helpful to elucidated the physical meaning of the space charge number, Eq. (7) is not in the appropriate form for our purposes. This is because in our analysis the voltage V also depends on r_1, r_2 - r_1, and L. Recollecting that

$$V = \frac{Q_{sh}}{2\pi L Z_p} \ln(r_2 / r_1) \tag{8}$$

and

$$Q_{sh} = \frac{\pi \nu \,\mathrm{Re}(r_2 + r_1)}{2(1+\beta)}, \tag{9}$$

where Re is the Reynolds number, ν is the fluid viscosity and β is given by

$$\beta \equiv \frac{Q_a + Q_s}{Q_e + Q_{sh}}, \tag{10}$$

the space charge number takes the form

$$\mathrm{Sc} = \frac{4Ne}{\varepsilon \nu \,\mathrm{Re}} \frac{(1+\beta)L}{(r_2 + r_1)\ln(r_2/r_1)} G_F(r_1, r_2, \beta) Z_p \tag{11}$$

The detailed expression for the factor G_F (r_1, r_2, β), which depends only on r_1, r_2, and β may be found in reference [17]. It is not included in Eq. (11) for the sake of simplicity.

A high-throughput DMA must be defined as an instrument that, for a given elevated concentration of charged particles N, presents Sc less than a few percent in order to avoid severe electric field distortions. Figure 3 presents a surface plot showing how the value of the space charge number Sc varies as a function of r_1 and r_2 - r_1. Not surprisingly, the figure shows that Sc is minimized when the electrode separation (i.e., r_2 - r_1) is minimized. This minimization of Sc leads to a maximized applied electric field and, consequently, to the minimization of space charge effects.

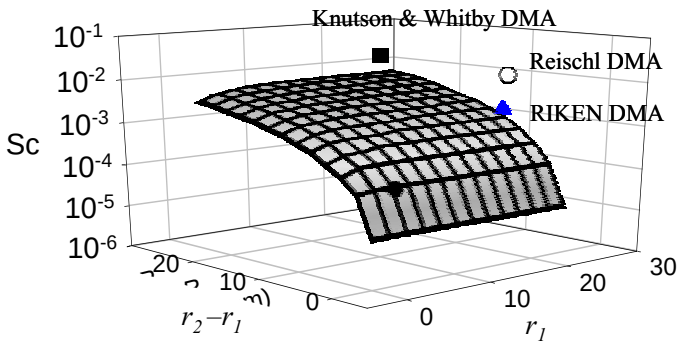

Fig. 3: Surface plot showing how the space charge number changes as a function of r_1 and r_2 - r_1 for $N = 10^9$ cm^{-3}, $\beta = 0.1$, $L = r_2 - r_1$, and $D_p = 1$ nm. The square (■), open circle (◦), and triangle (□) shown on the plot represent values of Sc for the same conditions for commercially available DMAs. The full circle (●) shows the value of Sc expected for the geometry we have chosen in our instrument.

Minimizing Brownian diffusion effects during size classification of nanoparticles

The physical mechanism that limits the resolution of aerosol size classification in a DMA is Brownian diffusion [18]. A simple model to predict the resolution of a DMA including Brownian diffusion effects was first introduced by Stolzenburg [19]. In a number of validation experiments this model has been found to describe the DMA performance satisfactorily in the nanometer size regime [19,20]. According to the model, the probability that a particle with a certain normalized mobility $\tilde{Z}_p \equiv Z_p / Z_p^*$ will be transmitted through the DMA is given by

$$\Omega(D_p) = \frac{\tilde{\sigma}}{\sqrt{2}\beta(1-\delta)}\left[\varepsilon\left(\frac{\tilde{Z}_p-(1+\beta)}{\sqrt{2}\tilde{\sigma}}\right)+\varepsilon\left(\frac{\tilde{Z}_p-(1-\beta)}{\sqrt{2}\tilde{\sigma}}\right)-\varepsilon\left(\frac{\tilde{Z}_p-(1+\beta\delta)}{\sqrt{2}\tilde{\sigma}}\right)-\varepsilon\left(\frac{\tilde{Z}_p-(1-\beta\delta)}{\sqrt{2}\tilde{\sigma}}\right)\right]$$

$$\beta \equiv \frac{Q_a + Q_s}{Q_e + Q_{sh}} \qquad (12)$$

$$\delta \equiv \frac{Q_a - Q_s}{Q_e + Q_{sh}}$$

where Q_a, Q_{sh}, Q_s, and Q_e are the aerosol, sheath, sample, and excess volumetric flow rates, respectively and $\varepsilon(x)$ is defined in terms of the error function erf(x) as

$$\varepsilon(x) \equiv \int_0^x erf(u)du = xerf(x) + \frac{1}{\sqrt{\pi}}\exp(-x^2) \qquad (13)$$

An inspection of Eqs. (12) reveals that the broadening parameter $\tilde{\sigma}$ is the quantity that determines the DMA resolution. For a cylindrical DMA and assuming plug flow, $\tilde{\sigma}$ may be found from [21]

$$\tilde{\sigma} = \frac{8D(D_p)}{\upsilon \mathrm{Re}}\left(\frac{1+\beta}{r_2-r_1}\right)\left[\frac{r_2^2+r_1^2}{r_2^2-r_1^2}(1+\beta)^2 L + \frac{r_2^2-r_1^2}{2}\frac{1}{L}\right] \qquad (14)$$

where $D(D_p)$ is the nanoparticle diffusivity, ν is the gas kinetic viscosity, and Re is the Reynolds number.

A large value of $\tilde{\sigma}$ corresponds to low resolution. Thus, the best DMA resolution is attained when $\tilde{\sigma}$ is minimized. According to Eq. (14), for a given particle size and flow rate regime, a choice of r_1 and $r_2 - r_1$ leads to a value of $L=L_{min}$ that minimizes $\tilde{\sigma}$. Figure 4 shows a surface plot of how $\tilde{\sigma}$ changes as a function of r_1 and $r_2 - r_1$. For every point on the surface, $L=L_{min}$ for particles with D_p = 1 nm. Due to the inherent nature of aerodynamic processes, there exists a limit in the practically achievable size resolution of an aerodynamic spectrometer like the DMA. This limit is believed to lie in the 3-5% range [22]. Thus, an instrument that can perform classification at a size resolution better than 5% is considered a high-resolution device.

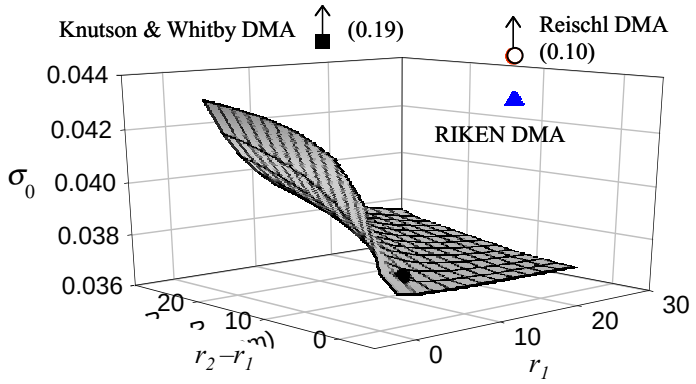

Fig. 4: Surface plot showing how the broadening parameter $\tilde{\sigma}$ changes as a function of r_1 and r_2 - r_1 for $L=L_{min}$, D_p = 1 nm, Re = 2200, β = 0.01, $L = r_2$ - r_1 (assuming plug flow). The square (■), open circle (◙), and triangle (□) shown on the plot represent values of $\tilde{\sigma}$ for the same conditions for commercially available DMAs. The full circle (●) shows the value of Sc expected for the geometry we have chosen in our instrument.

An instrument that simultaneously minimizes space charge and diffusion broadening

In this work we have designed an instrument for high-resolution size classification of particles in the 1-nm range that also meets the requirement for high throughput. This instrument achieves this high performance because its values of r_1, $r_2 - r_1$, and L have been chosen in order to minimize $\tilde{\sigma}$ and the space charge number Sc simultaneously. According to Eqs. (11) and (14) maximum throughput is enabled when Sc is minimized while maximum resolution is achieved when $\tilde{\sigma}$ is minimized. In order to perform size classification at high-throughput (up to 10^9 particles/cm^3 with less than 5% electric field distortion) and high-resolution (less than 5% size dispersion) the following conditions must be satisfied simultaneously

$$Sc < 0.05 \tag{15}$$

$$\tilde{\sigma} < 0.05 \tag{16}$$

Figure 5 shows the region in the $r_2 - r_1$ vs. r_1 space where the conditions of Eqs. (15) and (16) are satisfied simultaneously. The figure also shows the region of acceptable flow rates (less than 50 SLM).

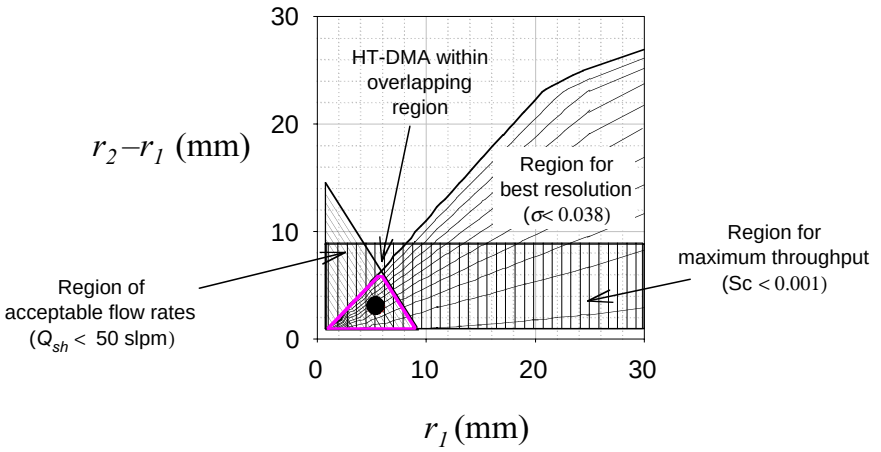

Fig. 5: Regions in the r_2 - r_1 vs. r_1 space where, according to Figs. 3 and 4 the space charge number Sc and the broadening parameter $\tilde{\sigma}$ are minimized for $L=L_{\min}$, D_p = 1 nm, Re = 2200, β = 0.01. Also shown is the region where flow rates are below 50 standard liters per minute. The geometrical parameters of our instrument were chosen within the overlapping region shown in the figure.

Incorporation of size classification into a materials deposition process

We have incorporated the size classification approach described above into a streamlined deposition process capable of creating homogeneous samples containing nanoparticles of uniform size. This process is depicted in Fig. 6. Gas-suspended nanoparticles generated by the ablation of a solid target go through an ionization zone where they acquire an equilibrium charge distribution. The charged nanoparticles are then sorted according to size based on their different migration velocities in an electric field across a particle-free laminar gas stream. Nanoparticles are extracted from the classification region within a desired window of sizes and deposited electrophoretically on a substrate placed perpendicularly to the gas flow.

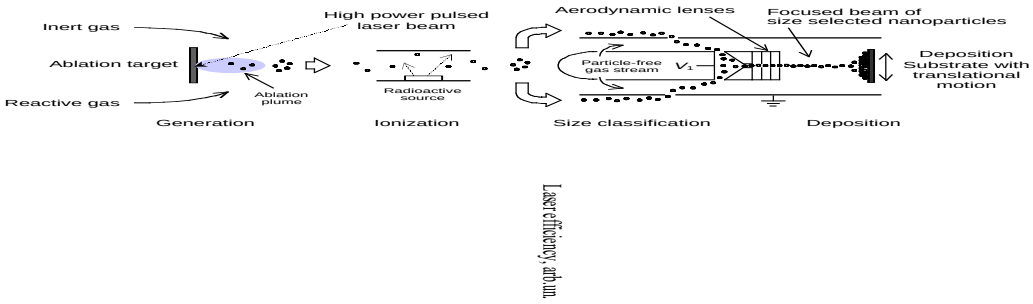

Fig. 6: Schematic showing the incorporation of the size classification approach into a laser ablation source of nanoparticles allowing the deposition of size-selected nanoparticles.

A schematic of the experimental setup implementing this deposition scheme may be seen in Fig. 7. In this case, an aerosol of silver (Ag) nanoparticles was obtained by the ablation of a Ag target in inert atmosphere by the focused beam of a pulsed Nd:YAG laser. The aerosol was then run through a small chamber containing a ^{241}Am radioactive source that created an equilibrium ion distribution in the carrier gas. This

allowed the charging of the nanoparticle aerosol. Charged nanoparticles where then introduced into the size classifier (DMA) and deposited on a silicon [110] surface. A sample obtained using this system is shown in Fig. 8, which displays Atomic Force Microscopy (AFM) scans. For this experiment nanoparticles were size selected at (8.0 ± 0.6) nm. Figure 8(a) illustrates the remarkable uniformity of the nanoparticle ensembles, which extends to regions several millimeters across while Fig. 8(b) shows a small area scan. The deposition of size-selected Ag nanoparticles establishes a benchmark performance for our system and we are currently employing this strategy for other materials with potential for aerospace applications.

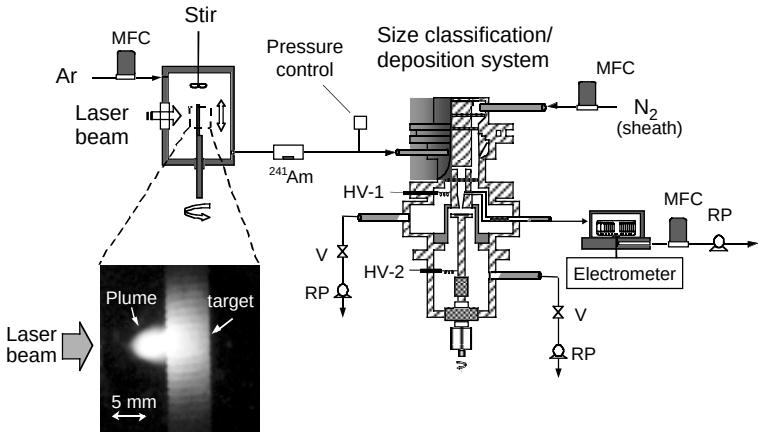

Fig. 7: Laser ablation setup used in combination with the size classifier to obtain nanostructured thin films.

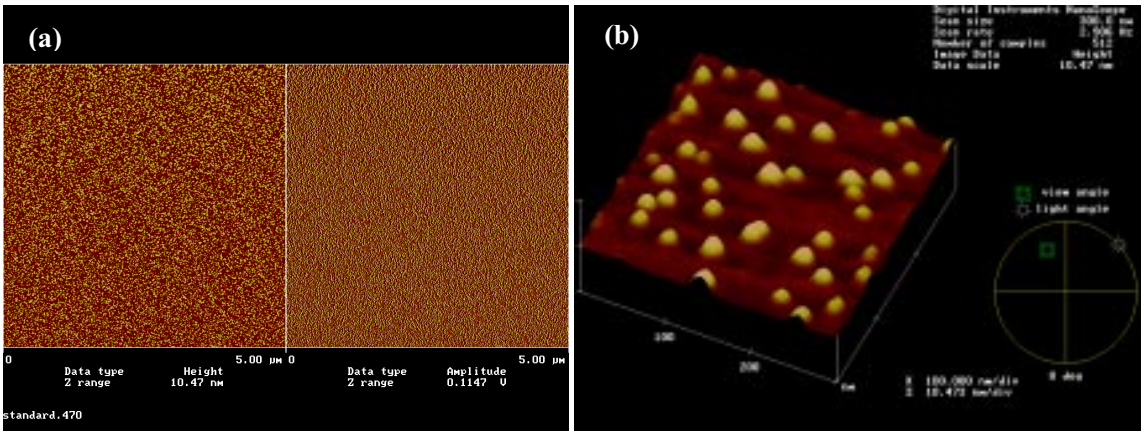

Fig. 8: Atomic Force Microscopy scans of size-selected Ag nanoparticles (8.0 ± 0.6 nm) deposited on a [110] silicon surface. (a) 5-micron scan (height and amplitude signals) and (b) 300-micron scan (3D view).

Acknowledgements

This research was supported in part by grants from the National Science Foundation (NSF) (MRI/DMR#0116098) and the National Aeronautics and Space Administration (Alabama NASA EPSCoR Core Infrastructure Development Program). Nicholas C. Cunningham acknowledges support from the NSF-funded Research Experiences for Undergraduates program at The University of Alabama at Birmingham (NSF-DMR# 0243640)

References

1. Alivisatos, A. P., *Science* **289**, 736 (2000).
2. Mirkin, C. A., Letsinger, R. L., Mucic, R. C., and Storhoff, J. J., *Nature* 382, 607 (1996).
3. Boeckl, M S; Baas, T; Fujita, A, *Biopolymers* **47**, 185 (1998).
4. Ueda, M.; Kreuter, J.**,** *Journal of microencapsulation* **14**, 593 (1997).
5. Li, M., Schnablengger, H., and Mann, S., *Nature* **402**, 393 (1999).
6. Camata, R. P., Atwater, H.A., Vahala, K. J., and Flagan, R. C., *Applied Physics Letters* **68**, 3162 (1996).
7. Dinh L. N., Chase, L. L., Balooch, M., Siekhaus, W. J., and Wooten, F. *Physical Review B* **54**, 5029 (1996).
8. Camata, R.P., Hirasawa, M., Okuyama, K., Takeuchi, K., *Journal of Aerosol Science* **31**, 391 (2000).
9. Knutson, E.O. and Whitby, K.T., *Journal of Aerosol Science* **6**, 453 (1975).
10. Flagan, R. C., Aerosol Science and Technology **28**, 301 (1998).
11. Allen, M. D. and Raabe, O. G., Journal of Aerosol Science 13, 537 (1982).
12. Deppert, K., Magnusson, M. H., Samuelson, L., Malm, J.-O., *Journal of Aerosol Science* **5**/**6**, 737 (1998)
13. Magnusson, M. H., Deppert, K., Malm, J.-O., Svensson, C. *, Journal of Aerosol Science* **28**, S471 (1997).
14. Kruis F.E., Fissan H., Peled A., *Journal of Aerosol Science* **29**, 511 (1998).
15. Seto T, Kawakami Y, Suzuki N., *J. Nanoparticle Research* **3**, 185 (2001).
16. Seto T, Kawakami Y, Suzuki N., *Nano Letters* **1**, 315 (2001).
17. R. P. Camata, H. A. Atwater, and R. C. Flagan, *Journal of Aerosol Science* **32**, 583 (2001).
18. Kousaka, Y., Okuyama, K., Adachi, M. and Mimura, T. *J. Chem. Eng. Japan* **19**, 401-407. (1986).
19. Stolzenburg, M.R., *An Ultrafine Aerosol Size Distribution Measuring System*, Ph.D. Thesis, University of Minnesota. (1988).
20. Zhang, S.-H and Flagan, R.C., *Journal of Aerosol Science* **27**, 1179 (1996).
21. Flagan, R.C., *Aerosol Science and Technology* **30**, 556 (1999).
22. De Juan, L., Fernandez de la Mora, J., *Journal of Aerosol Science.* **29**, 617 (1998).

The "Ship-in-a-bottle" Approach to Synthesis of Nano Materials Via Sonolysis.

Devinder Mahajan [a,b*], Hanaa Khalil [a], Miriam H. Rafailovich [b] and Henry J. White [b]

[a]Building 815, Advanced Fuels Group, Energy Sciences & Technology Department, Brookhaven National Laboratory, Upton, New York 11973 USA
(Tel.: (631) 344-4985; E-mail: dmahajan@bnl.gov)

[b]Department of Materials Science and Engineering, Stony Brook University, Stony Brook, New York 11794-2275 USA
(Tel.: (631) 632-8483; E-mail: mrafailovich@ms.cc.sunysb.edu)

Introduction

Coating surfaces with specific materials can alter the properties of the coated surface for specific applications that include biocompatibility, chemical or wear resistance, durability and thermal and mechanical properties [1]. Nanocoatings that are defined as those containing particle sizes of less than 100 nm [2] can further impart unique properties to the surfaces to enhance smoothness and ultraviolet (UV) resistance. One unique feature of nanocoatings is that these can also make the coated surface transparent because the particle size of the coating is smaller than the wavelength of the visible light (400-700 nm). This has led to a tremendous interest in devising methods to synthesize and application of nanocoatings. The most common method to form thin-film coatings is to employ the sol-gel technique that involves initially synthesizing the precursor solutions followed by spinning and dipping [3,4]. This multi-step coating process is cumbersome and the desired smoothness of the finished surface is not attained. Many processing techniques and synthetic routes such as physical vapor deposition (PVD) [5-7], chemical vapor deposition (CVD) [8,9], pulsed-laser deposition [10] and other unconventional methods that optimize the properties of the nanocoating or control the layers of the coating.

Polymer-based nanocoatings are indeed of interest because mechanical flexibility, ideal viscosity and smooth homogeneous coating properties make these easily adhere to different surfaces. Polymers such as polyvinylpyrrolidone, poly-dimethylphyneleneoxide have been evaluated as a dispersing medium for metal and metal oxides but the stability of the nanoparticles was not established since a mixture of both the zero-valent and higher oxidation states of the metal were reported in such systems [11]. Therefore, little work has been reported on a convenient method, i.e., one-step room temperature preparation of polymer-metal nanocomposites [12].

A recently established joint effort between Stony Brook University (SBU) and Brookhaven National Laboratory (BNL) is specifically aimed at developing polymer-nanosized metal-based nanocoatings. From our perspective, in addition to the properties mentioned above, polymer-based coatings can be utilized to protect the highly reactive and thermodynamically unstable zero-valent metal nanoparticles from oxidation for an extended period of time. This long-term stability may allow preparation and convenient transport of materials, hence we have coined the term "ship-in-a-bottle" approach to describe these materials. We view the challenge to synthesize these materials as a two-step problem. First, a method must be selected to synthesize the nano particles. Second, a polymer material must be selected and introduced to form a weakly bonded complex between the nanometal and the selected polymer. For nanometal synthesis, we selected sonolysis as the method. The use of acoustics for the synthesis of iron nanoparticles was initially reported by Suslick [13] is now extensively being used to synthesize nano metal oxides whose applications range from coatings to magnetic fluids. The sonolysis technique involves passing sound waves of fixed frequency through a slurry or solution of carefully selected metal complex precursors. In a solvent with vapor pressure of certain threshold, the alternating waves of expansion and compression cause cavities to form, grow and implode [14]. During this event, the attained temperature and pressure were calculated to be about 5200K and 30MPa, respectively with lifetime of 2µs to < 1ns [15]. Due to extremely high cavity collapse rates ($2x10^{9}$ $K.s^{-1}$ -10^{13} $K.s^{-1}$), the sound energy translates into sonoluminescence [16]. But if a suitable metal complex is present, the energy can be harnessed to break metal-ligand bonds [13]. The use of metal carbonyl precursors to synthesize a mixture of metal clusters and nanometer metal particles both in zero-valent state and as oxides has been reported [17-19].

In this paper, we describe our initial results in this effort wherein we have synthesized and characterized a nanocoating containing iron nanometal and polyethyleneglycol (PEG). Preliminary measurements of the coating characteristics of the Fe-PEG nanocoating are also presented.

Experimental

Materials. Pentacarbonyliron (99.5%), hexadecane (99+%, anhydrous), hexanes (98.5+%, ACS reagent grade) were purchased from Aldrich Chemical Co. and polyethyleneglycol -400 (PEG-400) was obtained as a gift from Dow Chemical Co. Ar and N_2 gases were obtained from Scott Specialty Gases. Since $Fe(CO)_5$ is a toxic and flammable liquid, all manipulations were carried-out in a fume hood with appropriate precautions that conformed to the Material Safety and Data Sheet (MSDS).

Sonolysis Unit. All experiments were carried out using an ultrasonic liquid processor Model XL2020, from MISONIX, Inc., with a variable power output of up to 550 watts at a fixed frequency of 20kHz. The unit was fitted with a 5-inch long half wave extender tip with a probe tip of diameter 0.5". The unit allowed precise control of power output, processing time and PULSAR cycle for cyclic intermittent operation to avoid heat build-up.

Synthesis of Fe and Fe-PEG-400 nano particles. For the work described herein, the following aspects need to be emphasized. 1) The reaction vessel, purchased from Ace Glass, Inc., was a borosilicate glass 4-neck flask with walls tapered inward toward bottom that allowed maximum solution in the middle of the flask for adequate immersion of the sonication probe, 2) a series of O-rings and standard greased ground-glass joints ensured tight seals to maintain rigorous exclusion of air or gas leakage from the flask during sonication, 3) any gas evolved during sonolysis was collected and analyzed and 4) the flask was immersed in a constant temperature (held within $\pm$ 1 ^{o}C) bath. Prior to sonication, the hexadecane solvent was thoroughly degassed with argon followed by the addition of metal carbonyl. In a typical run of the Fe system, a degassed yellow homogeneous solution of $Fe(CO)_5$ (8 - 16 mmol) in 100mL hexadecane was sonicated in the dark ($Fe(CO)_5$ is light sensitive) at 100% intensity and 80% pulsed cycle settings. Gas evolution with concomitant appearance of a black slurry in the reaction vessel was evident within minutes that was indicative of the $Fe(CO)_5$ decomposition reaction. Therefore, almost quantitative decomposition of $Fe(CO)_5$ was measured by monitoring the gas evolution as a function of time till the desired decomposition was achieved. The collected gas was analyzed and the flask containing the black slurry was moved to an argon-filled glove box. The product work-up was as follows. The black slurry was centrifuged and the upper hexadecane solvent layer was decanted to separate the product. The remaining black solid was washed three times with hexane (3 x10 mL) to remove residual hexadecane and any unreacted $Fe(CO)_5$. The resulting black solid was dried *in vacuo* and the dried solid was stored in a gas-tight vial in the glove box to avoid any sample oxidation. A small sample of this black solid was used for spectroscopic analysis.

For the synthesis of Fe-PEG-400 complex, a calculated quantity of degassed PEG-400 was added along with degassed hexadecane and $Fe(CO)_5$ and the resulting pale yellow homogeneous solution was sonicated as described above. The crucial measurement was the recording of CO evolution as a function of time that was an excellent measure of the extent of the $Fe(CO)_5$ decomposition from which the formation of the Fe complex was directly calculated using CO/Fe of 5/1 mole/mole ratio.

Analytical.

The collected gas (CO) was analyzed on a Gow-Mac Model 580 gas chromatograph. That was fitted with a molecular sieve column (9" x 1/8") under He.

For the infrared (IR) measurements, the sample was spread between two KBr discs and the spectra were recorded on an ATI Mattson FTIR spectrophotometer. For nanocoating studies, the Fe-PEG sample was coated on a gold surface and the change in the IR spectra were recorded as a function of temperature.

The transmission electron microscopy (TEM) images were recorded on a Philips CM12 STEM, 120 KV model to determine the particle size.

The X-ray powder diffraction (XRD) data were collected at the beam line X7B of the National Synchrotron Light Source [20] at BNL. A small portion of the sample was mounted in 0.5 mm diameter quartz capillary inside a glove

box to avoid air oxidation of the sample. Two-dimensional powder patterns were collected with a Mar345 image plate system. The diffraction rings were integrated with the FIT2D program [21]. The wavelength of 0.09200 nm was determined from a LaB_6 standard. For data analysis, the powder diffraction pattern was modeled with the REFLEX module in the Accelrys Materials Studio system [22]. This generated the peak lines and the best-fit curve of the data.

The XRD data were complemented by the X-ray Absorption Fine Structure (XAFS) spectroscopy measurements to determine the structure and the valence state of the Fe-PEG samples. The Fe K-edge XAFS measurements were carried out using a Si(111) double crystal monochromator on the beamline X-11A of the National Synchrotron Light Source, BNL. The storage ring was operated at 2.8 GeV and the typical ring current was 200 mA. The monochromator was detuned by 30% to achieve higher harmonic rejection. The beamline X-11A is equipped with three gas flaw ionization chambers to monitor the intensities of the incident and the transmitted X-ray beams. For XAFS measurements special air-tight sample holders with X-ray transparent Mylar windows were used. The samples were prepared inside a glove box and the XFAS measurements were carried out within an hour of preparation. Extra precautions were taken to avoid air exposure to the samples. The samples were prepared in a glove box and the XAFS experiments were carried out within an hour of preparation. XAFS measurements were also carried out on a number of model compounds including Fe foil, $Fe(CO)_5$, Fe_2O_3, $Fe(acetate)_2$ and Ferrocene.

Results and Discussion

Synthesis of nano Fe-PEG-400

The sono induced decomposition of $Fe(CO)_5$ in hydrocarbon solvents is known to yield Fe nano particles [15]. We introduced PEG-400 as the reactive polymer during the decomposition reaction with the strategy that it would react with the nano particles of zero-valent iron that are produced during sonolysis of $Fe(CO)_5$ that induces its decomposition (Equations 1 and 2):

$$M(CO)_x \xrightarrow{)))} \text{“M”} + x\,CO \quad (1)$$

$$\text{“M”} + H\text{-}O\text{-}(\text{-}CH_2\text{–}CH_2\text{–}O\text{-})_n\text{-}H \rightarrow M\text{–}O\text{-}(\text{-}CH_2\text{–}CH_2\text{–}O\text{-})_n\text{-}M \quad (2)$$

Potentially, one or both H atoms of the terminal –OH groups of PEG can be displaced by the Fe atoms. The selection of PEG-400 is appealing because it is liquid at room temperature and could serve as a ligand as well as a storage solvent after sonolysis without requiring any additional work up. During the sonolysis reaction, the temperature of the reaction medium was maintained at 40 ^oC. First, the decomposition kinetics of $Fe(CO)_5$ in hexadecane was studied at three different concentrations and the data are shown in Table 1. The extent of the $Fe(CO)_5$ decomposition can be calculated

Table1. Sonolysis induced iron pentacarbonyl decomposition data in hexadecane at 40 ^oC.

Initial $Fe(CO)_5$ mol	Total CO evolved mol	Slope	Total $Fe(CO)_5$ Decomposition
0.0254	0.127	0.068	97%
0.0182	0.083	0.076	91%
0.0195	0.095	0.074	98%

from the total CO evolution. As listed in Table 1, > 90% decomposition was achieved in all three runs. The CO versus time data over the entire length of the run for each run were also plotted. Such a plot of the data from the first run in Table 1are shown in Figure 1. The best fit shows that the reaction was zero order. The slope values listed in Table 1 were obtained from such zero-order plots for the runs. Within experimental error, the slope values of 0.068, 0.076 and 0.074 are considered essentially constant.

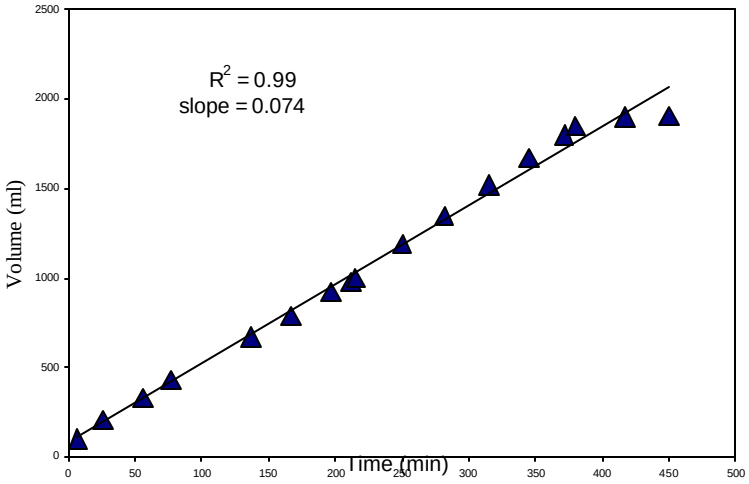

Figure 1. CO evolution versus time profile of sono dec omposition of $Fe(CO)_5$ in hexadecane

Next, the reaction was carried out in the presence of PEG-400 at three different ratios of Fe/PEG-400: 1/1.6, 1/1, 1/0.5. Since PEG-400 has two reactive protons (Equation 2), the Fe/PEG-400 ratio of 1/0.5 is considere d stoichiometric. As shown in Table 2, the $Fe(CO)_5$ decomposition that varied from 71% - 100% was successfully achieved in the presence of PEG-400 in all three cases. Interestingly, the slope values were obtained from zero order plots such as the one show n in Figure 2. All three values are in excellent agreement. The decomposition kinetic is faster than that reported for the thermolysis of $Fe(CO)_5$ in the presence of polystyrene -butadiene [23].

Table 2. Sonolysis induced iron pentacarbonyl decompositio n data in hexadecane in the presence of PEG -400 at 40°C.

Initial $Fe(CO)_5$ Mol	Initial PEG-400 Mol	Total CO evolved mol	Slope	Total $Fe(CO)_5$ Decomposition
0.0179	0.0285	0.064	0.057	71%
0.0259	0.0284	0.114	0.057	88%
0.0255	0.0128	0.127	0.058	100%

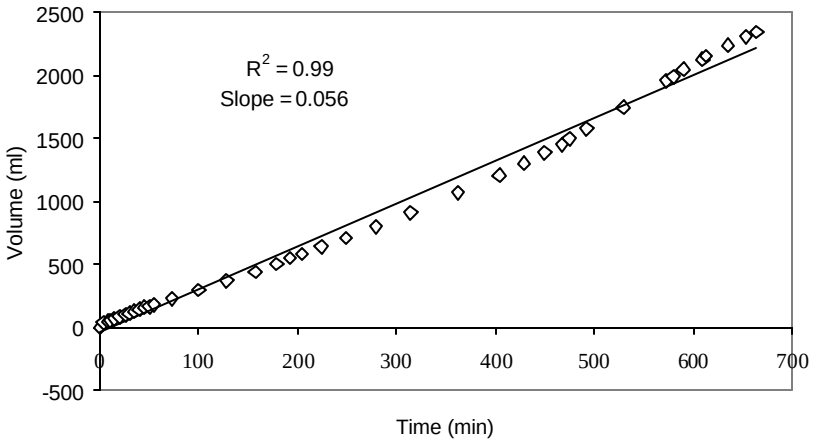

Figure 2. CO evolution versus time profile of sono decomposition of $Fe(CO)_5$ in hexadecane/PEG-400.

Material Characterization

Described below are various spectroscopic techniques that have been used to charact erize the nano Fe-PEG-400 materials. These studies concentrated on the Fe-PEG-400 complex formed in which Fe/PEG-400 ratio of 1/0.5 was used.

FTIR data. The FTIR spectra of the reference PEG-400 solvent and the Fe-PEG-400 complex are shown in Figure 3.

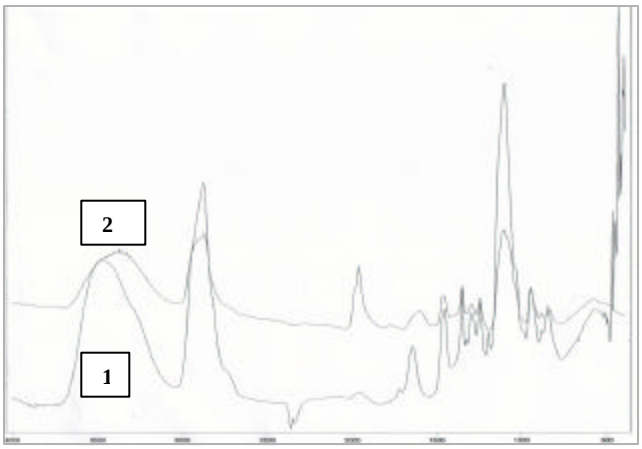

Figure 3. FTIR spectrum of 1) PEG-400 and 2) Fe nanoparticles coated with PEG-400.

The presence of typical PEG bands in the IR spectrum of the iron-PEG complex indicates successful coating of iron with PEG. Some noted differences in the Fe-PEG spectrum are observed. The broad absorption bands centered at 3460 cm^{-1} and 1640 cm^{-1}, due to stretching and bending modes respectively of the -OH group of the PEG, are shifted to 3374 cm^{-1} and 1600 cm^{-1}. These shifts of 86 cm^{-1} and 40 cm^{-1} indicate an interaction of the -OH group of the PEG with the Fe nanoparticles. A new absorption band at 1960 cm^{-1} in the Fe-PEG-400 spectrum cannot be assigned to the Fe-CO bond because these bands are typically extremely intense. We also rule out the presence of $Fe(CO)_5$ because the sample was thoroughly washed with hexanes to remove any unreacted liquid $Fe(CO)_5$ after sonolysis work up. This peak assignment is still under review.

TEM data. The TEM images of the Fe-PEG-400 materials were also recorded (Figure 4). The material appears highly amorphous and exhibits grape-like morphology with mean particle diameter (MPD) of less than 2 nm. The TEM image of a dilute solution of nano Fe in PEG-400 (first run in Table 2) was also measured. In this case, the Fe-PEG-400

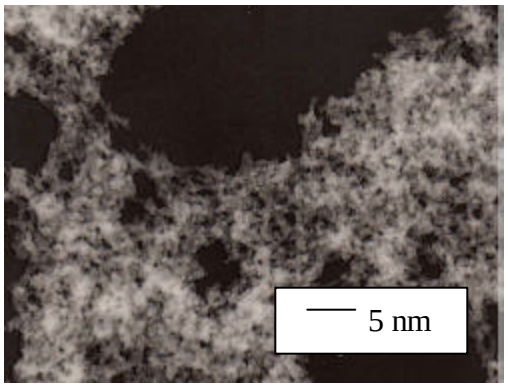

Figure 4. The TEM of Fe-PEG-400 (Fe/PEG-400 = 1/0.5).

complex was dissolved in toluene and a few drops were added to a carbon -coated copper TEM grid. The dilute material shows discrete particles of Fe embedded in the PEG matr ix that are different from the concentrated material. The particle size was estimated to be ~ 3 nm (Figure 5).

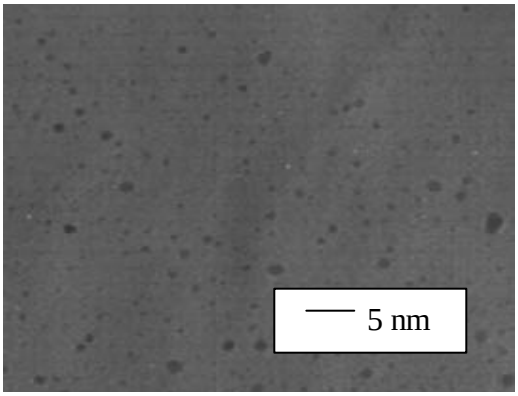

Figure 5. The TEM of a dilute solution of Fe nanoparticles in PEG.

XRD data. The recorded XRD spectrum of the Fe-PEG-400 material is shown in Figure 6. The pattern can be interpreted as a superposition of three very broad diffraction peaks from a material that closely matches an Fe_2O_3 like material [24]. The peak widths imply that the particles diameter is less than 1 nm and the material is highly amorphous. This interpretation is consistent with the data but there are not enough data to demonstrate that it is only correct solution. There is a very strong background peak emerging from behind the beam stop that coul d be attributed to the small angle scattering from very small particles.

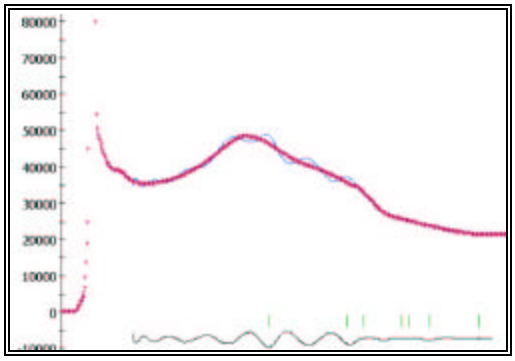

Figure 6. The XRD pattern of Fe-PEG-400 (fitted curve) and the calculated pattern. The predicted positions of Fe_2O_3 are shown as vertical lines at the base of the spectrum. Th e differential spectrum between the observed and the calculated patterns is shown at the base.

XAFS/XANES data. The normalized XANES spectra for an Fe foil, Fe particles obtained from the sonication of Fe(CO)5, and Fe/PEG samples are shown in Figure 7. The corresponding derivative spectra are shown in Figure 8. The shoulder around 7112 eV in the XANES spectra (Figure 7) is due to an excitation of 1s electron to the empty d band orbital below the vacuum level. The intensity of this peak is lower for t he Fe-PEG-400 sample as compared to the Fe(0) sample. For both the samples, the edge position and hence the oxidation state, obtained from the first inflection point is same as that for the Fe foil indicating that the Fe is in zero valence state. However, the main edge for both the samples is shifted by about 3 eV indicating that a fraction of Fe is in a higher oxidation state.

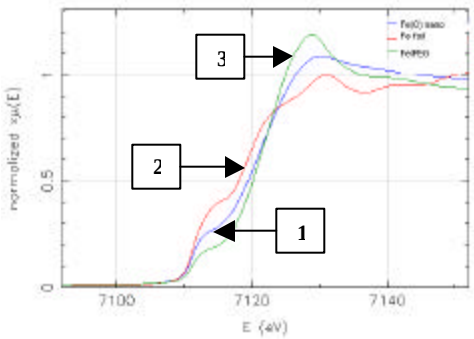

Figure 7. The normalized XANES spectra of: 1) Fe foil, 2) nano Fe and 3) Fe-PEG-400.

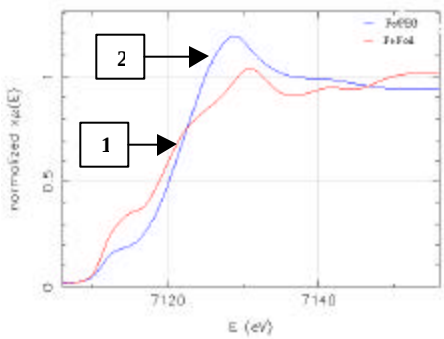

Figure 8. The derivative spectra from the data in Figure 7. 1) Fe foil and 2) Fe-PEG-400.

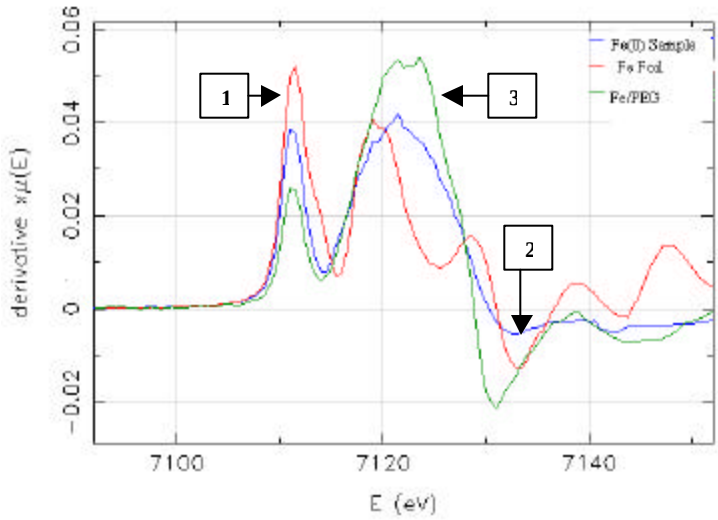

Figure 9. The EXAFS of: 1) Fe foil, 2) nano Fe and 3) Fe-PEG-400.

In order to determine the local structure of Fe, EXAFS analysis was carried out. Figure 9 shows the Radial Structure Functions (RSF) for Fe(0) and Fe/PEG samples. For both samples a wide peak around 2 Å is seen. The absence of any structure beyond this peak shows that the samples are highly amorphous and that there is no order beyond 3 Å. Detailed EXAFS analysis shows that this peak corresponds to two or possibly 3 shells and that the major contribution is from a low-Z scatterer such as C or O. This peak was further analyzed using Fe-C (Ferrocene reference compound) and Fe-Fe (Fe foil, FEFF calculations) interactions as the models. Preliminary EXAFS analysis shows that on an average Fe is surrounded by three Carbon/Oxygen atoms at 2.05(0.01) A and 1 Fe at 2.57 (0.03) Å. Further modeling as well as XANES analysis is under progress.

In Figure 9, it is seen that the Fe-PEG-400 sample shows a significant shoulder around 3 A. Such a feature is nearly absent for the Fe (0) sample. We believe that this peak is a result of the bonding between the Fe particles and the matrix.

Coating Characteristics of Fe-PEG Materials

One of the intended applications of the Fe-Peg-400 material is its utility as a nanocoating. To this effect, a preliminary study was carried out to evaluate its performance as a coating. A thin film of the Fe-PEG was spread over a

gold sample at room temperature and then heated at 80°C and 100°C and the changes in the complex characteristics were studied by FTIR (Figure 10). It is evident that at a low temperature of 100°C, >50% of the PEG matrix decomposed and a

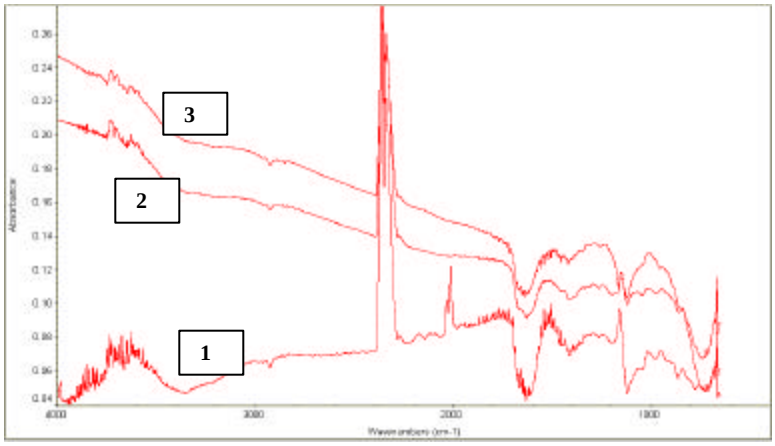

Figure 10. FTIR spectra of the Fe-PEG-400 material as a function of temperature. 1) at room temperature, 2) 80°C, 3) 100°C.

new intense signature CO_2 band at ~ 2320 cm^{-1} appeared that is typical of PEG decomposition. Such low temperature behavior of the Fe-PEG-400 has important implication. A systematic study is now underway to confirm these findings.

Summary

In this study, in situ coating of sono-synthesized iron nanoparticles with polyethylene(glycol)-400 is described. The Fe-PEG-400 formation follows zero-order kinetics. The interaction between Fe and PEG via the Fe-O formation is confirmed by FTIR, XRD and XAFS/XANES studies. Morphological studies via TEM show a grape-like morphology of PEG with Fe with particle size less than 2 nm. Preliminary FTIR study indicates that the Fe-PEG-400 is a low temperature nanocoating material because the material conveniently decomposed at 100°C in air. Furthermore, sonolysis is a convenient method to produce nanocoatings that can be stored and conveniently used when needed (the ship-in-a-bottle approach). Work is now in progress to measure the magnetic and other physical properties of these materials. Our study now includes PEG complexes of Mo, Ni and other metals for potential nanocoating application.

Acknowledgment

We thank Drs. Kaumudi Pandya for the XAFS and Jonathan C. Hanson for XRD measurements at the National Synchrotron Light Source (NSLS) at the Brookhaven National Laboratory (BNL). The work was conducted by utilizing facilities at both Stony Brook University (SBU) and BNL. The funding for the work was provided by the United States Department of Energy (US DOE) under Contract No. DE-AC02-98CH10886) to BNL and through the Provost's grant by SBU.

References

1. Malshe, A.P.; Jiang, A.; Dhamdhere, A.R., J. of Materials, 28, 2002.
2. Bertran, E., Thin Solid film, 377, 495, 2000.
3. Taylor, D.J.; Fleig, P.F.; Schwab, S.T.; Page, R.A., Surf. & Coat. Tech. 120/121, 465, 1999.
4. Caruso, R.A.; Antonietti, M., Chem. Mater. 13, 3272, 2001.
5. Chen, H.; Ding, C.X., Surf. & Coat. Tech., 150,31,2002.

6. Veovodin, A.A.; J. P. O' Neill, J.P.; Zabiniski, J.S., Surf. & Coat. Tech., 116, 36, 1999.
7. Jensen, H., Surf. & Coat. Tech., 116,1070, 1999.
8. Bertran, E.; Viera, G.; Martínez, E.; Esteve, J.; Maniette, Y.; Farjas, J.; Roura, P., Thin Solid Films, 377, 495, 2000.
9. Fu, Y.; Bibo, Y.; Lam, L.N.; Chang, S.; Peter, H., Mater. Sci. Eng. A, 282, 38, 2000.
10. Voevodin, A.A.; Donlney, M.S.; Zabinski, J.S., Surf. & Coat. Tech., 92, 42, 1997.
11. De Caro, D.; Ely, T.O.; Mari, A.; Chaudret, B., Chem. Mater., 8, 1987, 1996.
12. Nandi, A.; DuttaGupta, M.;banthia, A.K., Mater. Lett. 52, 203, 2002.
13. Suslick, K.S., Hyeon, T., Fang, M., Cichowlas, A.A., Chapter 8 in reference 1.
14. Suslick, K.S., MRS Bulletin, 29, April 1995.
15. Suslick, K.S., Choe, S-B., Cichowlas, A.A., Grinstaff, M.W., Nature, 353, 414, 1991.
16. Suslick, K.S., Flint, E.B., Grinstaff, M.W., Kemper, K.A., J. Phys. Chem. 97, 3098, 1993.
17. Suslick, K.S., Goodale, J.W., Schubert, P.F., Wang, H.H., J. Am. Chem. Soc. 105, 5781, 1983.
18. Kataby, G., Ulman, A., Prozorov, R., Gedanken, A., Langmiur, 14, 1512, 1998.
19. Shafi, K., Ulman, A., Yan, X., Yang, N., Estournes, C., White, H., Rafailovich, M., Langmiur, 17, 5093, 2001.
20. Hastings, J.B., Suorti, P., Thomlinson, W., Kvick, A.; Koetzle, T. *Nucl. Instrum.* Methods, 208, 55, 1983.
21. Hammersley, A.P. ESRF Internal Report, ESRF98HA01T, "FIT2D V9.129 Reference Manual V3.1", 1998.
22. Materials Studio Reflex module Accelrys Corp.
23. Smith, T.W.; Wychick, D., J. Phys. Chem., 84, 1621, 1980.
24. JCPDS Powder diffraction file No. 33-0664. International Center for diffraction data, Swarthmore, PA

Development of High Performance Nanocomposite Pyroelectric Detectors: a Possible Approach

A. K. BATRA
M. D. Aggarwal, R. B. Lal
Microgravity Science Laboratory, Department of Physics
Alabama A&M University
P.O. Box 1268
Normal, AL 35762
Phone:256-858-8109
E-mail: abatra@aamu.edu

Recently, there has been immense interest in the use of ferroelectric thin films in pyroelectric IR sensors and thermal imaging arrays and their integration with silicon IC technology. The materials used for fabricating pyroelectric IR devices are polyvinylidene fluoride, triglycine sulfate, lead titanate, lithium tantalate, lead zirconate titanate, and others.

Our approach is to fabricate pyro-ceramic/copolymers 0-3 nanocomposite thin films such as those consisting of nanosized pyro-ceramic particles embedded in poly vinylidene fluoride. The advantages of this approach are that dielectric and pyroelectric properties of diphasic composite materials can be tailored by varying the ceramic volume fraction and, hence, sensor performance can be optimized and that pyroelectric response can get reinforced while piezoelectric effect cancels, thereby minimizing microphony effect.

In this presentation, methodology and technology used for the preparation of nanoparticles such as lead titanate and others, along with fabrication of nanocomposite film/detectors, will be described and discussed.

Rotational Molding of Thermotropic Liquid Crystal Polymers

Martin Rogers
Luna Innovations, Inc., 2851 Commerce Street, Blacksburg, VA 24060
Phone: 540-953-4280; E-mail: rogersm@lunainnovations.com

Paige Stevenson
Luna Innovations, Inc., 2851 Commerce Street, Blacksburg, VA 24060
Phone: 540-961-4529; E-mail: rogersm@lunainnovations.com

Paul Clark
1290 Flint Drive, Christiansburg, VA 24073
Phone: 540-818-1549; E-mail: clarkp@megahits.com

Donald Baird
Department of Chemical Engineering, Virginia Tech, Blacksburg, VA 24061
Phone: 540-231-5998; E-mail: dbaird@vt.edu

Rotational molding is a unique process for producing hollow plastic parts. Rotational molding offers low cost tooling and can produce very large parts with complicated shapes. Products made by rotational molding include water tanks with capacities up to 20,000 gallons, truck bed liners, playground equipment, air ducts, Nylon fuel tanks, pipes, toys, stretchers, kayaks, pallets, corn harvester points, and many others.

Rotational molding forms hollow structural parts adopting the shape of the inside wall of the mold. Figure 1 illustrates the rotational molding process. There are four basic steps in the rotational molding process. (1) The first step involves adding a preweighed amount of granulated plastic in one half of a mold. The mold is mounted onto a machine and closed using clamps or bolts. In the second step, the mold is rotated biaxially about a perpendicular axis and put into an oven. The mold is heated to a temperature where the plastic granules can melt and fuse together. As the material melts and becomes tacky, it sticks to the mold wall in successive layers to form the part. After melting and consolidation of the material, the mold is cooled below the melting or solidification point of the plastic material. Rotation continues during cooling to prevent sagging of the material. The final step involves removing the part from the mold.

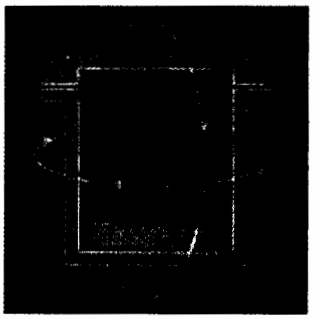

Figure 1. Diagram illustrating the rotational molding process (2)

Figure 2. Rotationally molded HDPE Tank with integrally molded flanged outlet

Rotationally molded tanks can be interfaced to other components with integrally molded flanges, inserts, or through standard fittings. Figure 2 shows an example of a rotationally molded 10,000-gallon liquid storage tank produced by PolyProcessing Company, with an integrally molded flanged outlet.

High performance, light-weight materials are needed in cryogenic storage devices planned for future transportation systems. Rotational molding is a process well suited to make hollow tubing and liners used in

cryogenic storage devices. However, materials commonly used in rotational molding such as high density polyethylene, nylon and polycarbonate do not have sufficient physical properties for use in cryogenic applications. Materials used in cryogenic applications should have low thermal expansion, low gas permeability, high tensile strength, modulus and fatigue resistance. (3) Low temperature properties of thermotropic liquid crystalline materials warrant their consideration in cryogenic applications. (4)

Thermotropic liquid crystalline polymers (TLCP) are an important class of engineering resins employed in a wide variety of applications. TLCP resins are composed of semirigid, nearly linear polymeric chains resulting in an ordered mesomorphic phase between the crystalline solid and the isotropic liquid. Ordering of the rigid rod-like polymers in the melt phase yields microfibrous, self-reinforcing polymer structures with outstanding mechanical and thermal properties.

TLCP parts have the following major advantages over other plastic materials used currently used in rotational molding: a) TLCP resins can be used in high heat environment as well as under cryogenic conditions. Thermotropic LCP have excellent thermal stability and maintain mechanical integrity at temperatures as high as 350°C. b) TLCP resins have low coefficients of thermal expansion that can be matched to glass, ceramics and metals through resin selection and parts. (5) TLCP materials undergo only minimal dimensional changes from high temperatures to cryogenic environments. c) TLCP resins have exceptional mechanical strength and stiffness allowing parts to bear significant loads without deformation or failure. d) TLCP resins have very low water absorption and high chemical resistance enabling there use in humid or corrosive environments. e) TLCP resins have an inherent resistance to burning and very low smoke generation. f) With densities similar to other thermoplastic materials, TLCP resins enable the production of lightweight materials.

Several TLCP are sold commercially into fiber, film and molded parts. A few examples are listed in Table 1 along with their respective manufacturers. These resins are principally aromatic polyesters and polyamides produced by condensation polymerization. Common monomers used in producing TLCP resins are depicted in Figure 2. Each of these resins is offered in a range of grades; including different compositions, melt temperatures, and fillers. For example, Vectra A and Vectra B TLCP resins include 2,6-hydroxynaphthoic acid in their formulations. Vectra A is prepared with a 73/27 molar ratio of p-hydroxybenzoic acid and 2,6-hydroxynaphthoic acid, while Vectra B contains a 60/20/20 molar ratio of 2,6-hydroxynapthoic acid, p-hydroxyacetaniline, and terephthalic acid. (6)

Table 1 - Commercial Thermotropic Liquid Crystalline Polymers

Tradename	**Supplier**
Titan™	Eastman Chemical Company
Vectra™	Ticona
Vectran™	Ticona
Xydar®	Solvay
Zenite™	Du Pont
Ekono™	Sumitomo
Ekonol™	Sumitomo

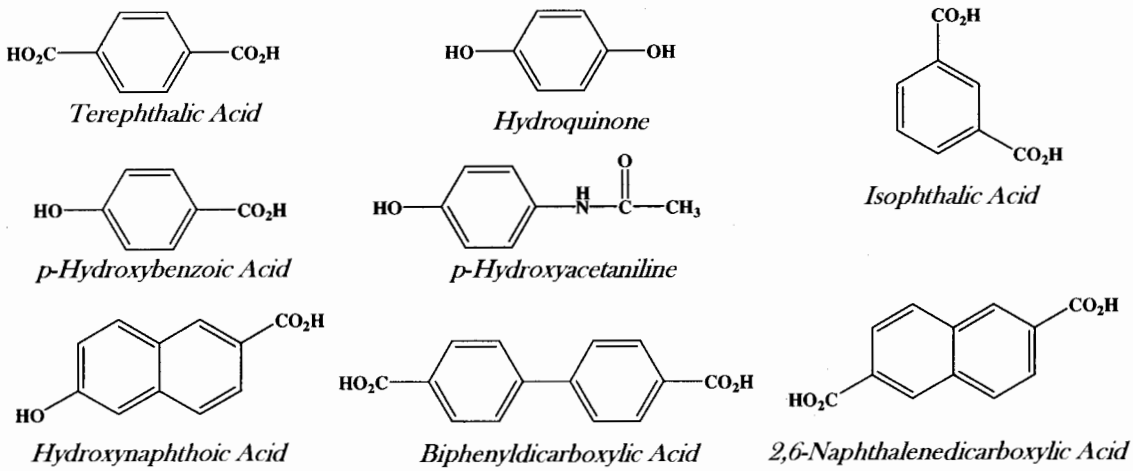

Figure 3. Typical monomers used in TLCP resins

Commercially, thermotropic liquid crystalline polyesters are produced by a melt acidolysis polycondensation reaction. (7) Melt acidolysis involves combining the acetyl derivatives of aromatic hydroxyl compounds and aromatic dicarboxylic acids at temperatures of 280 – 360°C.

Laboratory scale rotational molding trials were performed using two commercially available TLCP resins. One is granulated Vectra B 950 and pellets of Ticona's LKX-1107 resin. The laboratory scale molding was performed with a 1.5" diameter x 3" long mold. All trials used resins dried for at least 24 hrs at 100 °C. Cylinders were produced from 40 grams of Vectra B950 granules. The oven temperature was set at 330°C and was controlled to within ±1°. This was to ensure the mold cavity temperatures reached at least 320°C. The rotation was set at approximately 5 rpm. Cycle time was set to 30 minutes once the oven set point was reached. After 30 minutes at the set point the oven was shut off and opened to allow the still rotating mold to cool. The resulting cylinders were continuous with a fairly uniform wall thickness. Some bubbles were trapped against the mold surface during densification. Figure 4 depicts a cylinder produced from Vectra B950.

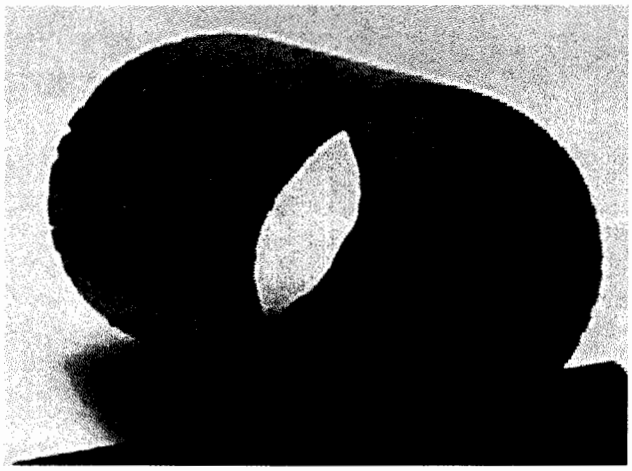

Figure 4 - Laboratory scale rotationally molded tubes 1.5" x 3"

Another TLCP from Ticona, LKX-1107, was evaluated for rotational molding as a pellet. The material is reported to have a melting point of 225°C. 40 grams was loaded in the 3" by 1.5" single axis rotational mold, after being dried in a vacuum oven for 48 hours at 105 °C, and rotated at 10rpm. The oven temperature was set at 260°C and was controlled to within ±1°. Cycle time was set at 40 minutes, this included heat up time (ambient to set point

in approximately 9 minutes). Cool down was performed by turning off the heating elements and air circulator, opening the oven door and allowing the unit to cool to ambient while continuing to rotate. The formed parts are shown in Figure 5.

Figure 5 - Cylinders of LKX-1107 Produced by rotational molding of pellets as received from Ticona

Rotational molding trials were performed at PolyProcessing Company using LKX-1107 pellets. The molding trials resulted in parts with consolidated material along the walls and only slight surface roughness. The inner surfaces were smooth. The wall thickness varied from 1.5 to 3.5 mm. These test samples are shown in Figure 6. Molding cycles for these tanks were 12 minutes at an oven temperature of 287 °C, followed by 22 minutes at an oven temperature of 343 °C. A rotation ratio of 4:1 was used, and the shot weight loaded to the mold was 0.9 lb in each case.

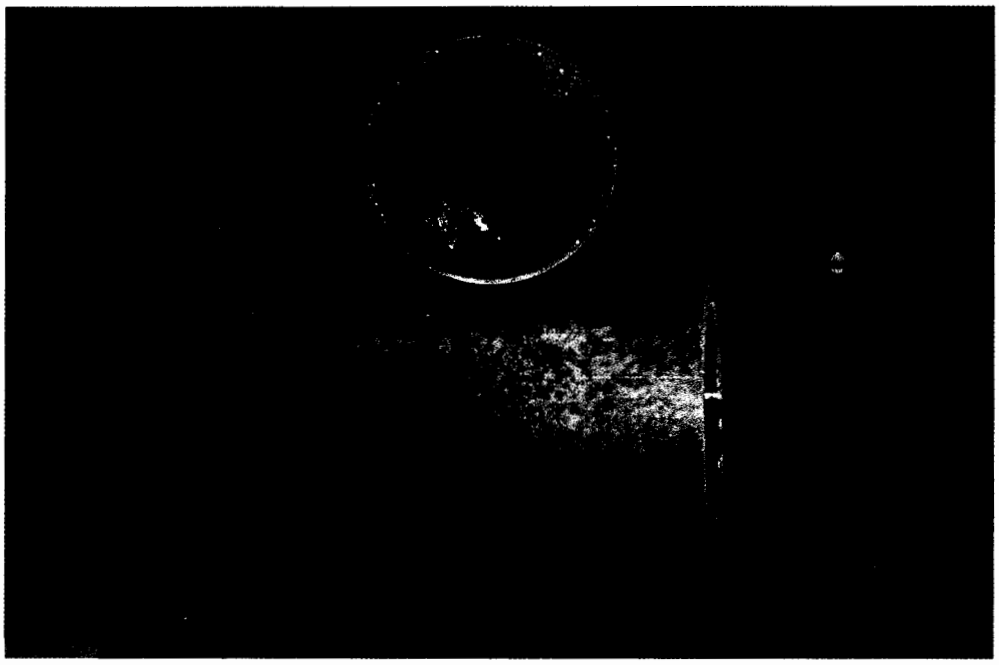

Figure 6 - Rotationally molded LKX-1107 tubes produced at PolyProcessing facilities

A burst test device was conceived and designed as shown in Figure 7. The device is designed to fit the 1.5 inch diameter tubes. The design consists of two aluminum plates, with recesses cut out for the test sample, holes

drilled at the corners for reinforcing bars, and a normal pipe thread (NPT) type fitting in the center of one plate for delivering pressurized fluid. The sample tube (brown) is shown enclosed in the fixture. The fluidic seals were made with rubber gasket material, and the ends were sealed with silicone grease.

One of the rotationally molded tubes from was attached to a burst test apparatus. The tube had an average thickness of 2.12 mm. The tube was pressurized to 68 psig in helium without signs of leakage (as determined by submerging the pressurized part under water) and was subsequently pressurized with silicone oil to 230 psig before bursting.

Figure 7 - LCP tube in pressure test device, before and after test

The ability to produce TLCP hollow structures by rotational molding has been demonstrated. Future efforts will focus on optimizing the various processes involved in producing TLCP rotationally molded parts and demonstrating their use in cryogenic applications.

REFERENCES

(1) Nugent, P., "Rotational Molding: A Practical Guide", page 46 (2001).
(2) http://www.ferryindustries.com
(3) Schutz, J. B., "Properties of composite materials for cryogenic applications", *Cryogenics*, **38**, 3-12 (1998).
(4) Evans D., Morgan, J. T., "Low-temperature mechanical and thermal-properties of liquid-crystal polymers", *Cryogenics*, **31(4)**, 220-222 (1991).
(5) McChesney, C. E., "Liquid Crystal Polymers (LCP)" in Engineered Materials Handbook, Vol. 2, Engineering Plastics, ASM International (1988).
(6) Jin, X., Pramoda, K. P., and Chung, T.-S., "The thermal stability and degradation behavior of thermotropic liquid crystal polymers (TLCPs)", *in* Thermotropic Liquid Crystal Polymers, Tai-Shung Chung Ed., Technomic, Lancaster, PA, (2001).
(7) Figuly, G. D., "Liquid crystalline polymers" in *Polymeric Materials Encyclopedia* edited by J. C. Salamone, Vol. 5, CRC Press, New York, New York (1996).

Manufacturing Process Simulation of Large-scale Cryotanks

Majid Babai
ED34/Bldg 4712
Marshall Space Flight Center, AL 35812
(256) 544-2795
Majid.Babai@msfc.nasa.gov

Steven Phillips
ED34/Bldg 4712
Marshall Space Flight Center, AL 35812
(256) 544-0626
Steven.Phillips@msfc.nasa.gov

Brian Griffin
Intergraph/Bldg 4487
Marshall Space Flight Center, AL 35812
(256) 544-6656
Brian.Griffin@msfc.nasa.gov

Introduction

NASA's Space Launch Initiative (SLI) is an effort to research and develop the technologies needed to build a second-generation reusable launch vehicle. It is required that this new launch vehicle be 100 times safer and 10 times cheaper to operate than current launch vehicles. Part of the SLI includes the development of reusable composite and metallic cryotanks. The size of these reusable tanks is far greater than anything ever developed and exceeds the design limits of current manufacturing tools. Several design and manufacturing approaches have been formulated, but many factors must be weighed during the selection process. Among these factors are tooling reachability, cycle times, feasibility, and facility impacts.

The manufacturing process simulation capabilities available at NASA's Marshall Space Flight Center have played a key role in down selecting between the various manufacturing approaches. By creating 3-D manufacturing process simulations, the varying approaches can be analyzed in a virtual world before any hardware or infrastructure is built. This analysis can detect and eliminate costly flaws in the various manufacturing approaches. The simulations check for collisions between devices, verify that design limits on joints are not exceeded, and provide cycle times which aide in the development of an optimized process flow. In addition, new ideas and concerns are often raised after seeing the visual representation of a manufacturing process flow.

The output of the manufacturing process simulations allows for cost and safety comparisons to be performed between the various manufacturing approaches. This output helps determine which manufacturing process options reach the safety and cost goals of the SLI.

As part of the SLI, The Boeing Company was awarded a basic period contract to research and propose options for both a metallic and a composite cryotank. Boeing then entered into a task agreement with the Marshall Space Flight Center to provide manufacturing simulation support. This paper highlights the accomplishments of this task agreement, while also introducing the capabilities of simulation software.

Factory Layout and Process Flow Simulations

The size of the cryogenic tanks needed to accomplish the goals of SLI is on a colossal scale. Preliminary designs for both the composite and metallic tanks had the tank dimensions in the neighborhood of 30 ft. in diameter by 100 ft. in length. Not only is it a challenge to build a tank of this size, but throw in the need for adequate tooling and you have a truly daunting task. Simulations proved very valuable at looking at the interfaces between tooling and parts. As these tanks are being built, the tooling has to be assembled and disassembled without colliding with or damaging the tank in any way.

Early in the design process, design details for individual parts and workcells do not exist. However, a well laid out manufacturing process plan for the composite tank did exist. This written process was translated into a simulation to help give a visual representation of the factory floor as well as preliminary tooling footprint information. The baseline manufacturing process included the use of an autoclave, fiberplacement machine, and a Nondestructive Test (NDT) cell.

Figure 1 (below) is a view into this simulation. It gives an overall perspective of the preliminary factory floor layout. In the forefront is the NDT cell. In the middle of the factory floor the internal tool, on which the tank will be built, is stationed at the fiberplacement machine. The autoclave can be seen in the background. Figure 2 (below) gives a better perspective as to the colossal size of the tank and required tooling. In this figure, the internal tool is entering the autoclave. The two human figures in the foreground are 5' 9" tall.

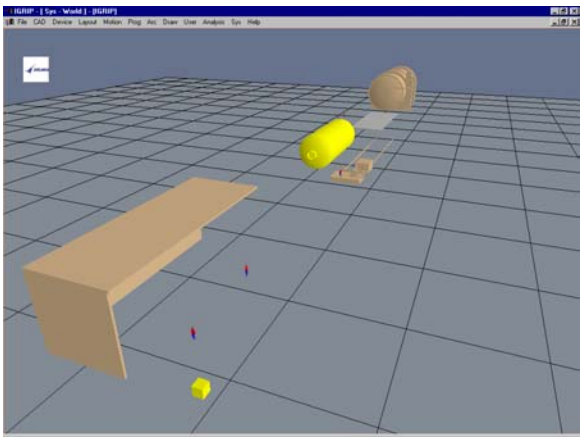

Figure 1 – The preliminary layout of the factory floor

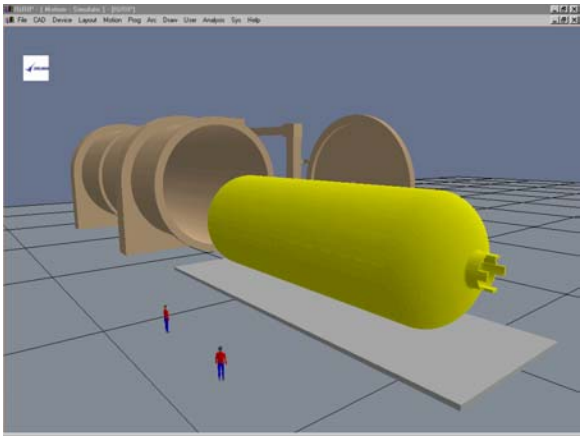

Figure 2 – Internal tool stationed at the autoclave

The Power of Simulations

Simulations are not mere pretty cartoons. While simulations do add life and action to the manufacturing processes, simulation software offers a wealth of output data. The software has the capability to check for collisions between parts, compare joint geometry values against design tolerances, calculate cycle times, and produce machine optimization charts among others. The MSFC simulation team utilized each of these capabilities to verify the design concepts proposed by the Boeing Composite Tank and Metallic Tank Teams.

Joint Tolerances

Figure 3 (right) shows the internal tool stationed in the Nondestructive Test cell. This simulation tested a preliminary inspection method. As the simulation runs, the software dynamically displays and compares the joint values of the inspection device against design tolerances. If a joint violation is detected, the errant joint will highlight in a different color. This is a powerful feature of simulation software. Without the use of simulation software, a post-production violation of design joint tolerances would be very costly to fix and retool. By testing the design upfront with simulation software, costly design flaws can be eliminated since the software verifies that the tooling design will work properly within the given production environment.

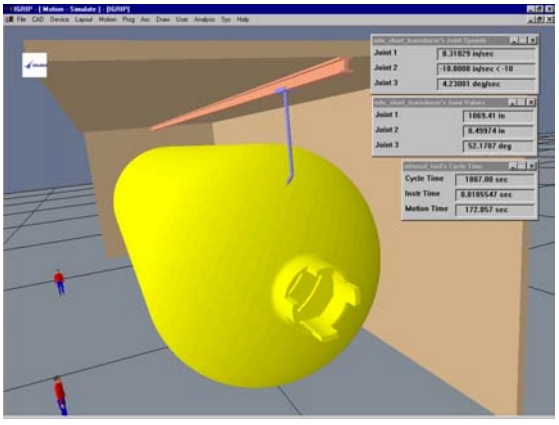

Figure 3 – Software output values for the NDE cell

Machine Optimization

Another powerful capability of simulation software is its ability to calculate machine usage. Busy and processing times for each machine in a factory simulation can be collected. Given this type of data, bottlenecks can be detected along with under usage of a machine. Figure 4 shows the actual output of the Element Utilization analyses for the preliminary process flow of the Composite Cryotank. As you can see, there is severe idle time for the autoclave and NDT cells. To better optimize machine usage, one possible scenario would be to build multiple tanks simultaneously (Figure 5).

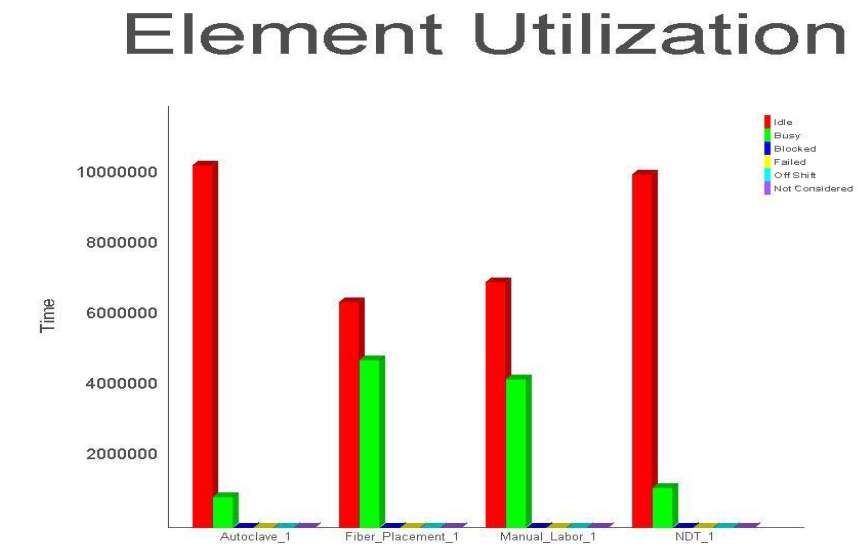

Custom_Report_1

	Autoclave_1	Fiber_Placement_1	Manual_Labor_1	NDT_1
Avg. Utilization (%)	7.741936	42.580646	37.677419	10.064516
Idle Time (hr)	2860.000069	1780.000043	1932.000047	2788.000068
Busy - Processing Time (hr)	144.000003	960.000023	1168.000028	216.000005
Busy - Setup Time (hr)	96.000002	360.000009	-	96.000002

Figure 4 – Machine utilization chart for the preliminary composite tank process flow

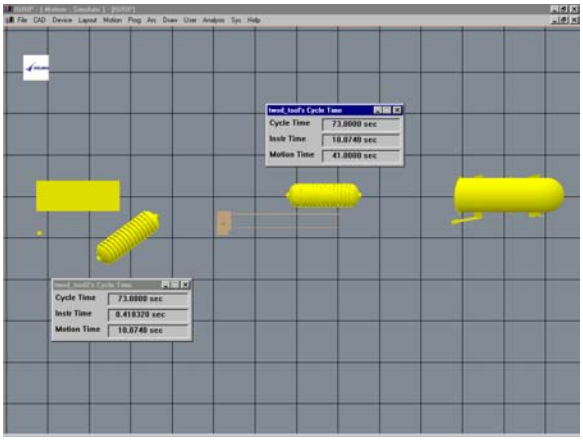

Figure 5 – Simulation showing multiple tanks being built simultaneously (Top view)

Assembly/Disassembly Simulations

One of the most useful features of simulation software is the ability to simulate assembly/disassembly sequences. These type simulations verify the following:

1) The feasibility of the assembly/disassembly sequence(s)
2) That parts do not collide with one another
3) That part clearances are not violated.

Assembly/disassembly simulations were utilized on both the metallic and composite cryotanks. To build the metallic tank, a sequence of welds must take place. The tank is built by first welding together barrel sections. Once welded together, these sections form the body of the tank. Additional formed pieces of metal are welded together to form the tank domes. Once the domes and body have been manufactured, they are then joined together to form the metallic tank. Using preliminary design sketches, a simulation was developed showing the assembly process in sequence.

Figure 6 is a view into the simulation showing the welding of the barrel panels. Notice the massive internal tooling and clamps used to hold the barrel sections in place while the welding is taking place. The human figure in the lower right-hand corner helps give perspective to the size of the tooling. Figure 7 shows the barrel section after the welding process has finished. The barrel section is now ready to have the domes attached. Figure 8 shows the welding of the dome panels.

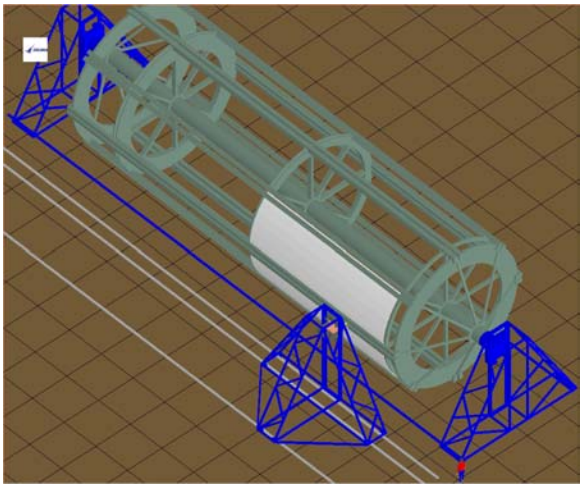

Figure 6 – Welding of the barrel panels

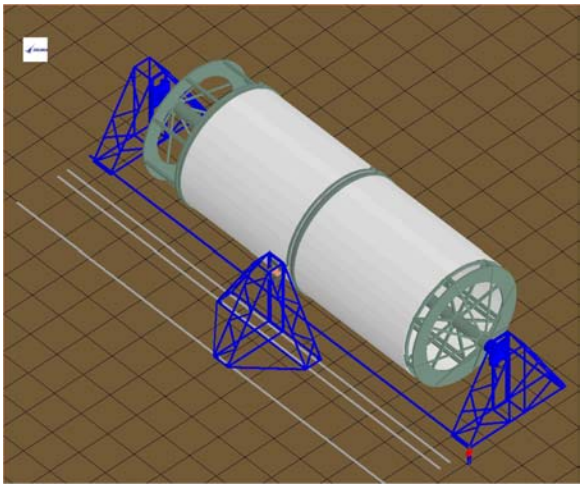

Figure 7 – A finished barrel section

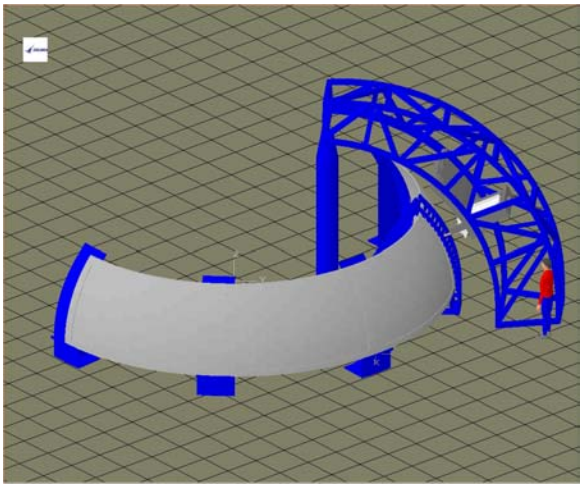

Figure 8 – Welding of the dome panels

The composite tank is built by using an internal tool. This internal tool allows for the manufacturing of a single piece tank. A great challenge for this manufacturing method is the removal of the internal tool once the tank has been cured. One leading candidate was a multi-piece, breakdown internal tool. Using this tooling approach, the internal tool must be broken down and removed via the port ends after the tank has been fabricated. Manufacturing simulations were used to verify this disassembly process. The internal tool was composed of 100s of different segments, along with both radial and longitudinal stiffeners. One important question was whether the individual segments could be removed without colliding with other segments, stiffeners, or port openings.

Figure 9 below shows the process of removing the internal tool's segments. A boom has entered through the porthole and has begun to lift the segment up and through the longitudinal stiffeners. Once this segment has cleared the stiffeners, it is brought to the centerline of the tank and removed via the porthole (Figure 10). The clearances on this design were very close, but the simulation did verify that the segments could be removed through the porthole without colliding with other segments or the porthole itself.

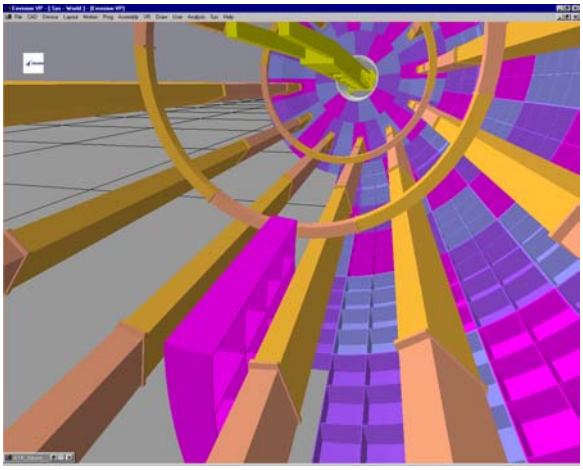

Figure 9 – Lifting the segment to the centerline

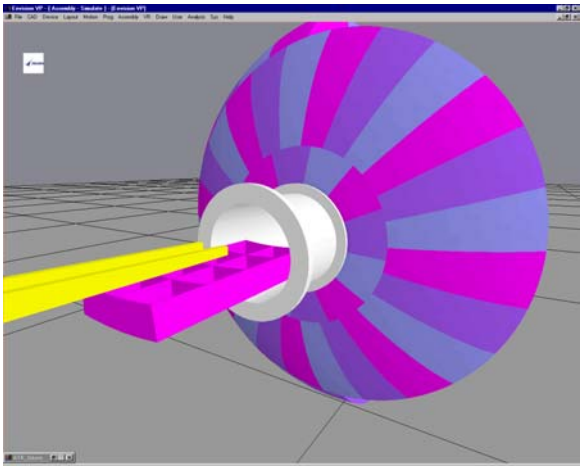

Figure 10 – Extraction of the segment via the boom

Conclusion

The goal of the basic period contract between The Boeing Company and NASA's Marshall Space Flight Center was to provide baseline simulations of the manufacturing process for both the metallic and composite cryotanks. High fidelity geometry did not exist at this early point in the design stage, however the groundwork has been laid. As more refined processes and higher fidelity models are provided, these baseline simulations can easily be updated to execute against the new geometry. Once the updated simulations are executed, the output values that were detailed in this paper can be fed back to design engineers. This feedback may or may not lead to further design and process modifications. The end product of this cyclic process will be highly defined simulations that thoroughly examine, analyze, and verify the manufacturing processes for the metallic and composite cryotanks. The cost and safety benefits gained by using simulation software cannot be ignored as NASA and industry strive toward the goal of developing this nation's next generation of space launch vehicles.

Toroidal tank development for upper-stages

- Tom DeLay ED34 MSFC
- Keith Roberts ATK Thiokol SEHO

Background

- Past interest in upper stages
  - Orbit transfer vehicle programs; toroidal tanks were under study
    - Compact LOX Feed System Study AFRL TR-86-045
- Current interest
  - SLI architecture studies
  - JPL satelllites
- Potential Benefits
  - Packing efficiency
  - Weight savings
- Challenges
  - Manufacturing methods
  - Fluid acquisition

Why are we building toroidal tanks?

- CDDF (Center Director's Discretionary Fund)
  - SLI 2nd and 3rd gen programmatic interest
  - Manufacturing hurdles challenged before architecture is defined
- Joint IR&D
  - New pressure vessel technologies developed by MSFC
  - Conformal CNG tank technology developed at THIOKOL
  - Combined effort to leverage results

MSFC IR&D Effort

- Development of tank and pressure vessel concepts for upper stages
  - Address permeation issues with pressurant gasses (Helium)
  - Develop processes adaptable to conformal tanks
  - Consider lined and unlined composite tank concepts
    - Liner development based on contained fluids
  - Produce ultra-light vessels that are suitable for satellites and scalable to upper stages
  - Develop technology that may be transferred to industry

MSFC IR&D Effort

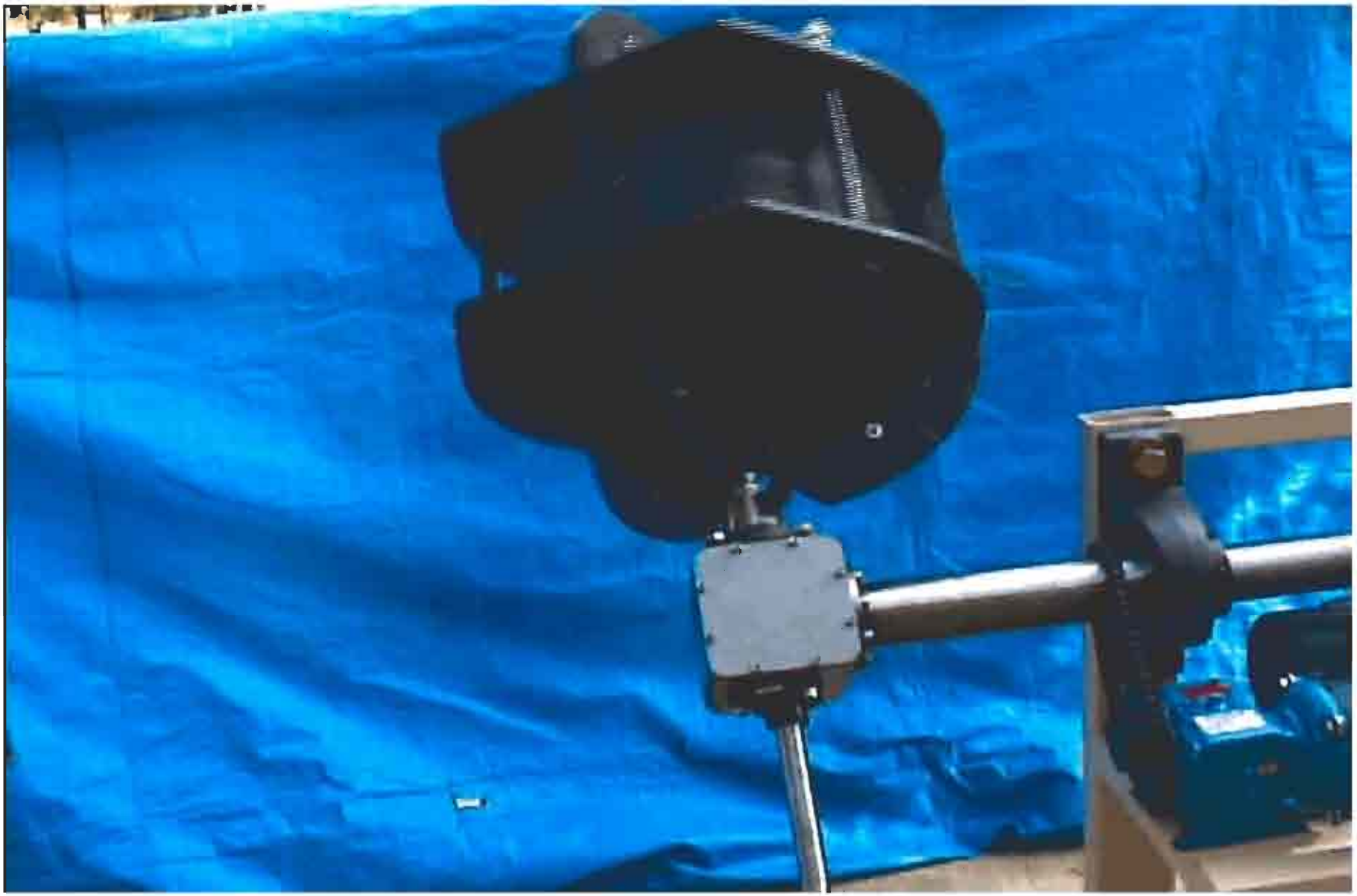

MSFC IR&D Effort

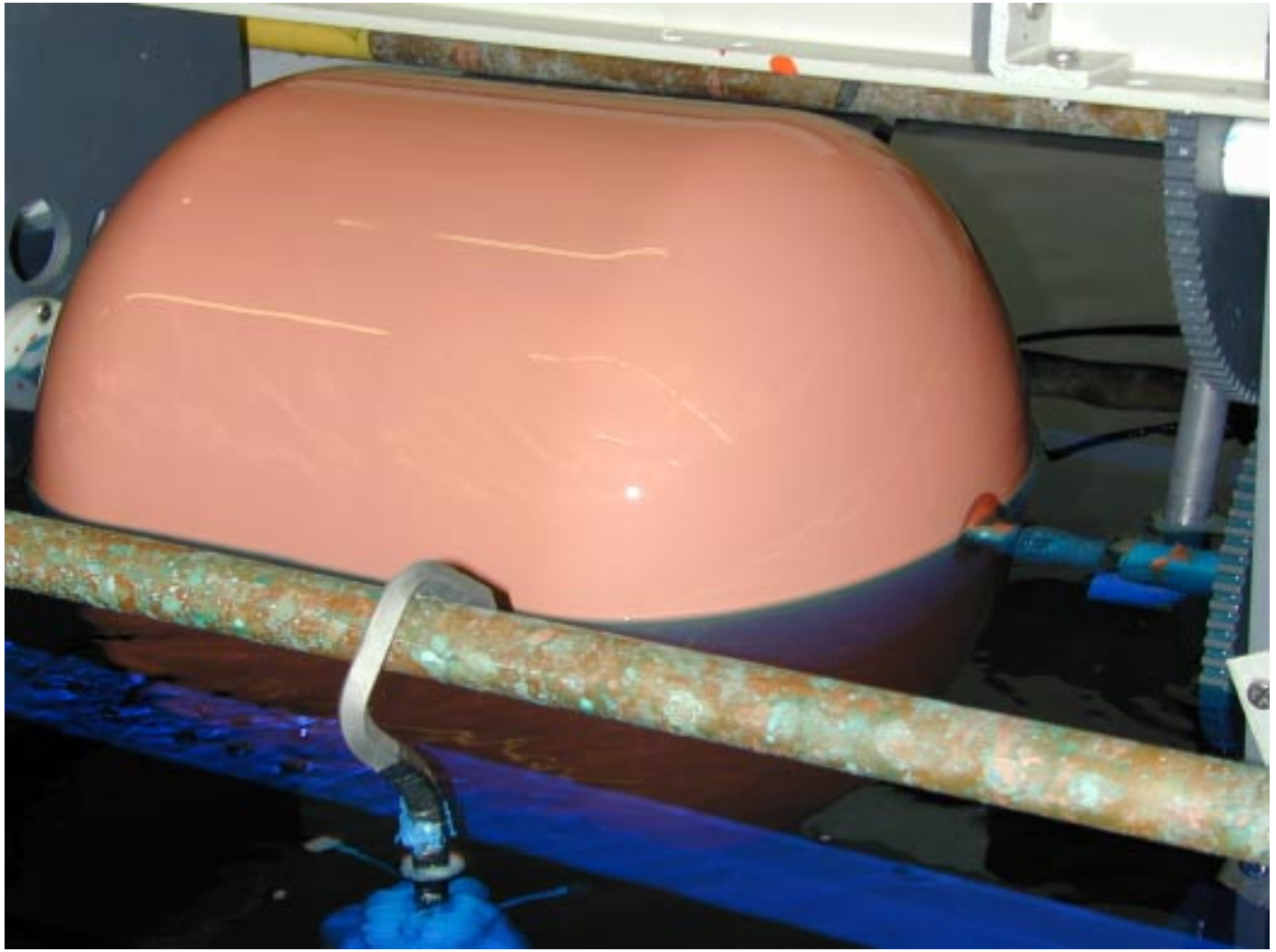

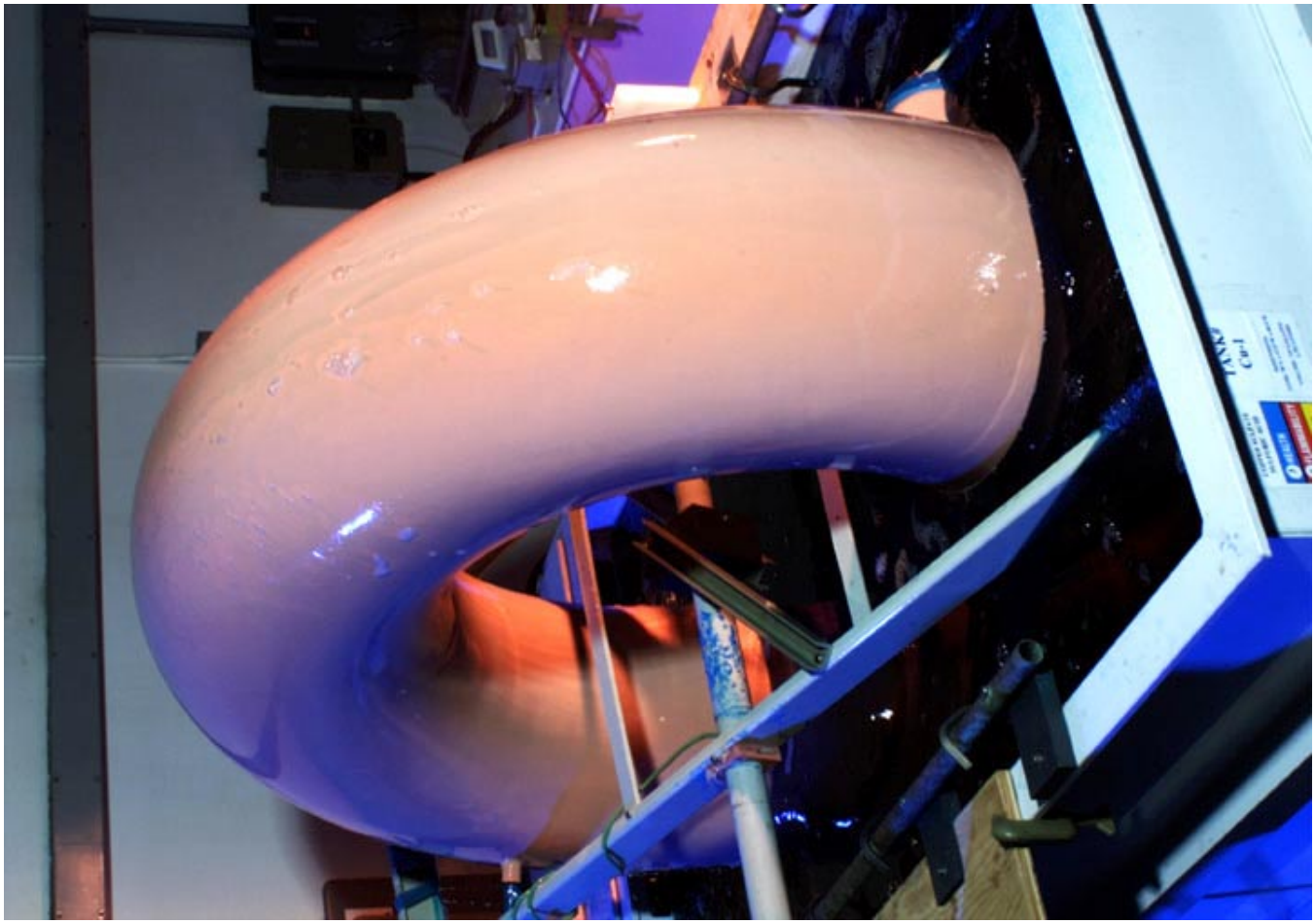

MSFC IR&D Effort

MSFC IR&D Effort

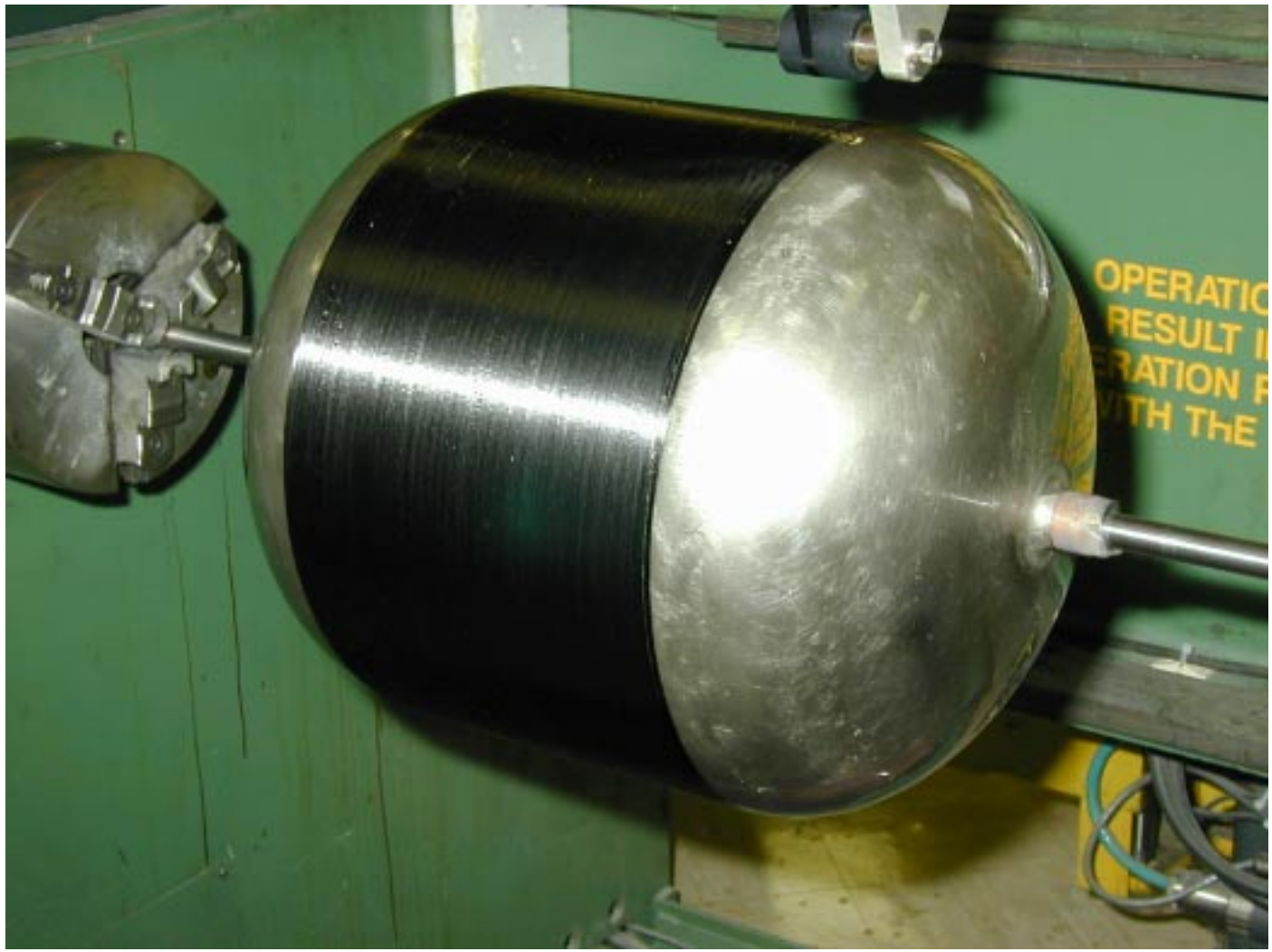

MSFC IR&D Effort

THIOKOL Conformal Tank Technology Development

Aluminum Propane Tank Product Overview

- **Cylindrical tanks provide near-optimum pressurized fuel storage**
- **Cylinders often do not fit well within the available vehicle space**
- **Conformable concepts adapt to the available vehicle space**
- **New technology propane fuel storage tanks**
  - Interlocking aluminum extrusions reduce the number and criticality of longitudinal welds in the assembly
- **Unit cost is more than cylindrical tank, but offers significant advantages**
    - Extends vehicle **range**: up to 50%
    - Reduces **weight**: aluminum construction
    - Reduces system **complexity**:
      - Eliminates "ganged cylinders"
      - Lowers overall system cost
- **Complete family of ASME certified tanks available as commercial products**

Composite Tank Product Overview

- Composite tank development has been completed using Department of Energy funding
  - Both tanks are for gaseous fuel storage
    - CNG at 3,600 psig
    - Hydrogen at 5,000 psig
  - Both tanks are made using aluminum polar bosses, plastic liners, and TCR composite over wrap
  - Both tanks have been designed to fill Ford P2000 envelope (13 in. x 22 in. x 28 in.)

- Tanks are in the process of certification to industry standards
  - CNG tank has completed commercial NGV2-1998 certification testing
  - Hydrogen tank will also complete all certification testing by June 01 to modified NGV2-1998 standard
  - Next step is to address specific OEM test criteria
- Significant interest in both CNG and hydrogen tanks from after market and OEM customer base


THIOKOL


THIOKOL

Approach To Producing Toroids

- Continuous circular toroid
  - Tooling
  - Materials
  - Design
  - Advantages and challenges
- Conformal/segmented toroid
  - Tooling
  - Materials
  - Design
  - Advantages and challenges

Continuous Composite Toroidal Tank fabrication

- Several methods approached to consider:
  - Scalability
    - What is the representative size that may be needed
    - Are the processes adaptable
  - Manufacturability
    - Tooling methods to be developed
    - Automation vs. hand-layup
  - Operational environment
    - Operational pressures
    - Fluid management, slosh
    - Chemical compatibility of fluid and permeability of gasses

Continuous Composite Toroidal Tank fabrication

- Tooling, materials, design
  - Rotationally molded thermoplastic liner/mandrels
  - Liner pressurized while over-wrapped and cured
  - Lower temperature cured graphite epoxy over-wrap
  - Nylon end fitting machined and bonded
  - 1/3 scale version of what could fit in delta 4 faring

Continuous Toroidal Tank fabrication

Continuous Toroidal Tank fabrication

Continuous Toroidal Tank fabrication

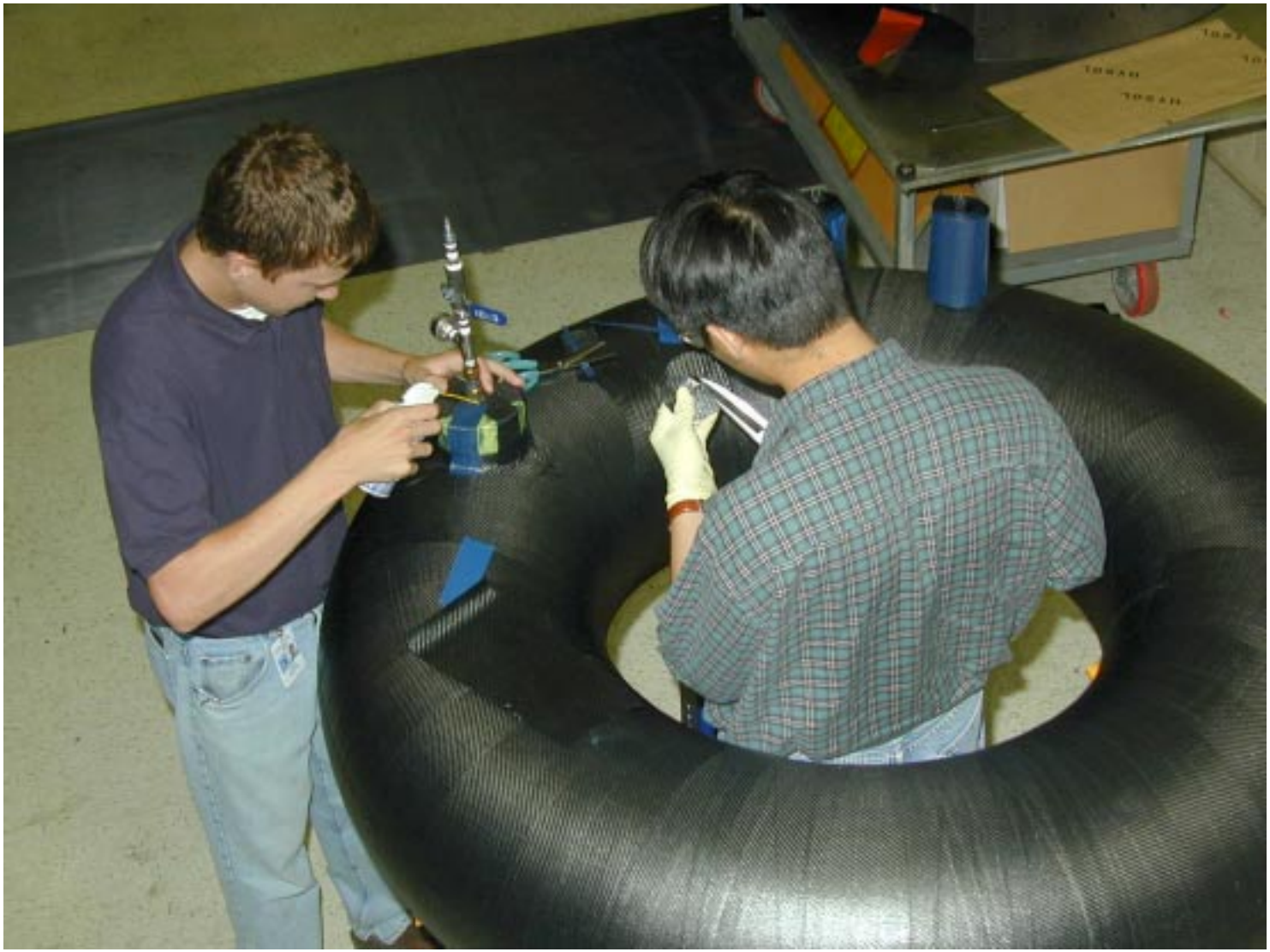

Continuous Toroidal Tank fabrication

Continuous Toroidal Tank fabrication

Continuous Toroid Traits

- 60 inch outside diameter, 16 inch cross section
- 5 inch diameter port 180 degrees on the opposite side of 1 inch port
- The composite toroid weighed less than 40 lbs.
- It contained 120 gallons of water, 27,793 cubic inches
- Total weight slightly more than 1,000 pounds,full
- Predicted burst pressure 375 psi
- Actual burst pressure 425 psi
- Area of highest strain, inner radius
- Packing efficiency(38% more volume than multiple spheres constrained by the same space)

Inspection and test of continuous toroid

- Vessel was inspected with thermography
  - No surface wrinkles, very minor de-bonds
- Triaxial strain gauges used to help predict burst

Inspection and test of continuous toroid

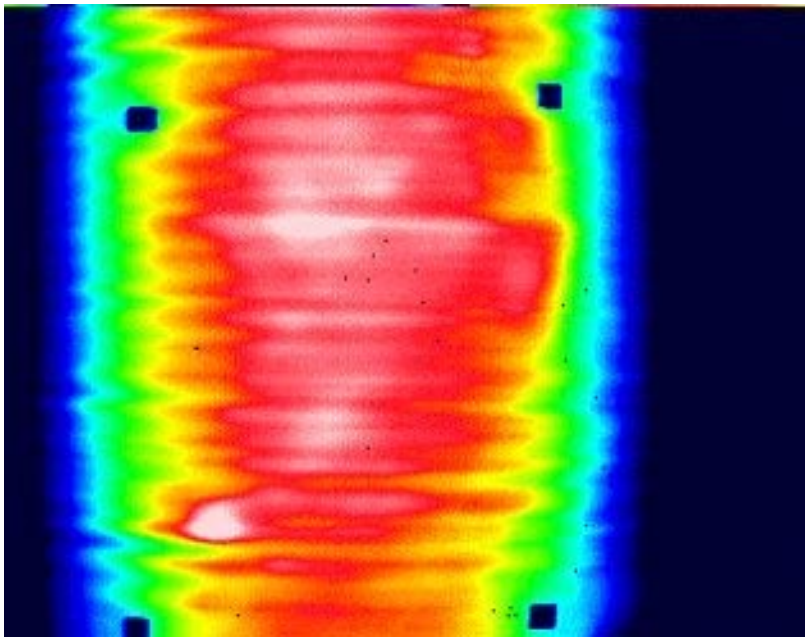

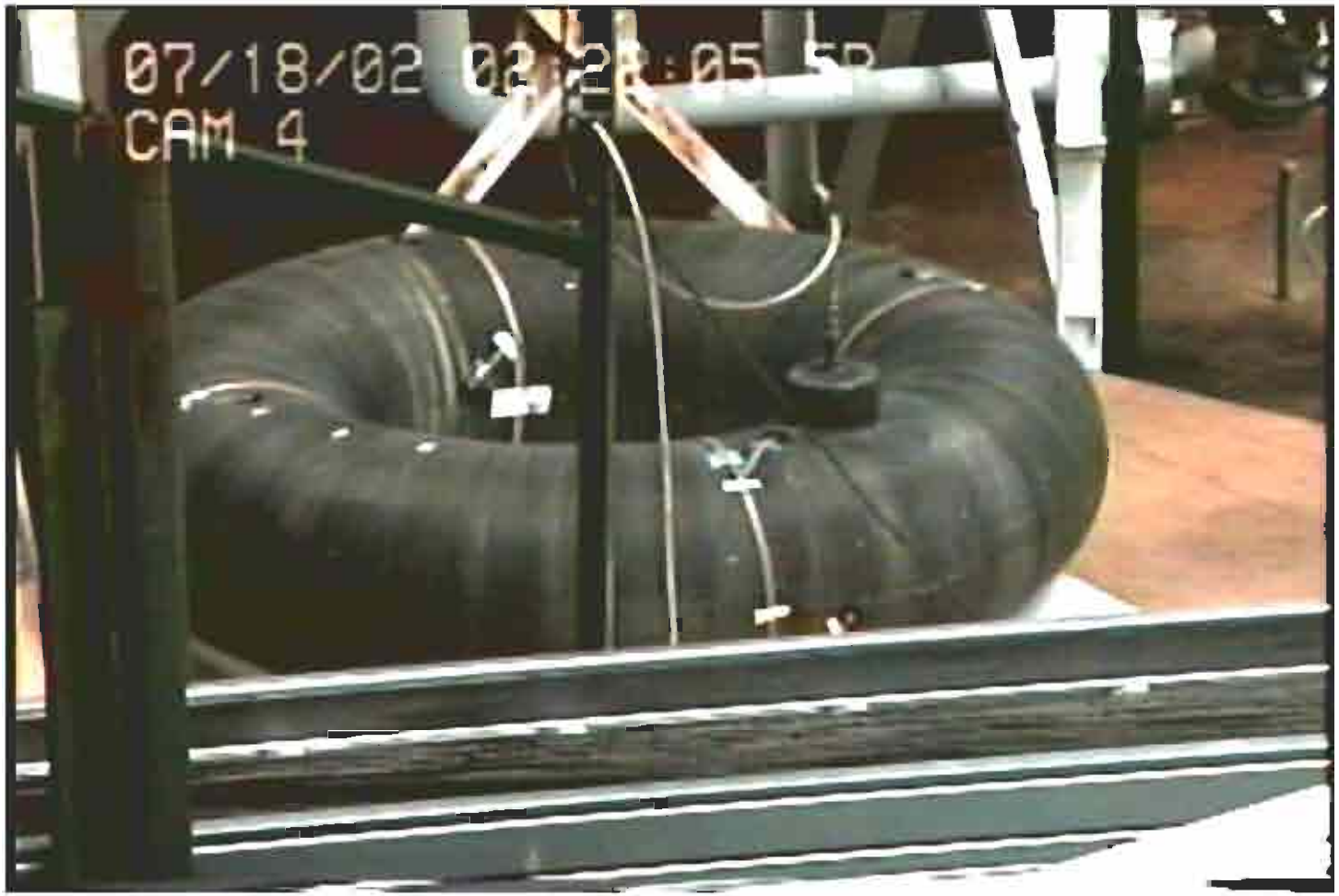
07/18/02
CAM 4

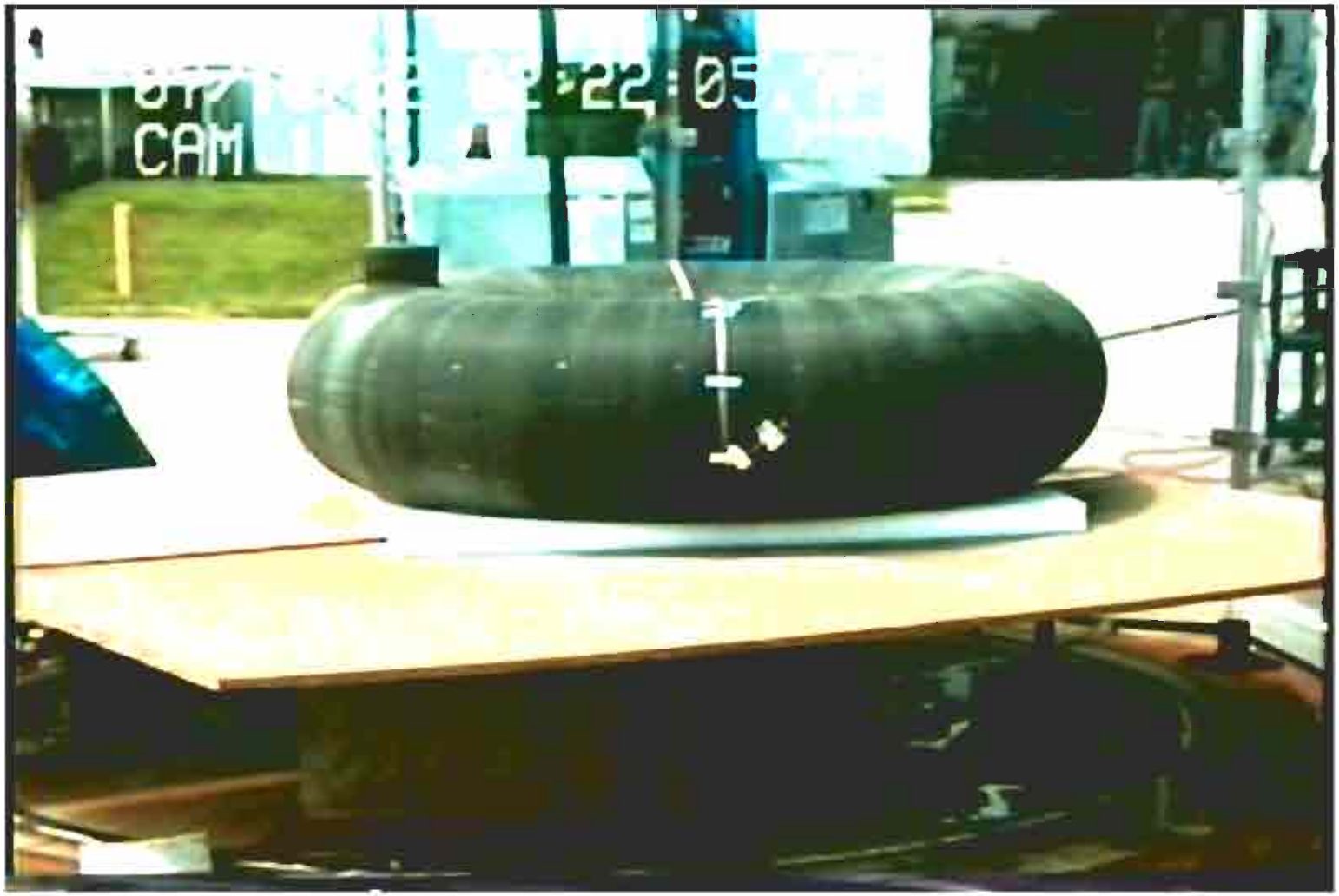
CAM
22:05

Segmented Composite Toroidal Tank fabrication

- Several methods approached to consider:
  - Scalability
    - What is the representative size that may be needed
    - Are the processes adaptable
  - Manufacturability
    - Tooling methods to be developed
    - Automation vs. hand-layup
  - Operational environment
    - Operational pressures
    - Fluid management, slosh
    - Chemical compatibility of fluid and permeability of gasses

Segmented Composite Toroidal Tank fabrication

- Tooling, materials , design
  - Machineable wax mandrel outfitted with end fittings and copper plated
  - Graphite epoxy over-wrap
    - Each segment filament wound with graphite/epoxy
  - Conformal tank geometry proprietary
  - Slightly less volume than continuous toroid ;however, higher pressure applications likely
  - Process being scaled and modified
  - Sub-scale assembly useful for demonstrating concept

Segmented toroid

Segmented toroid

Segmented toroid

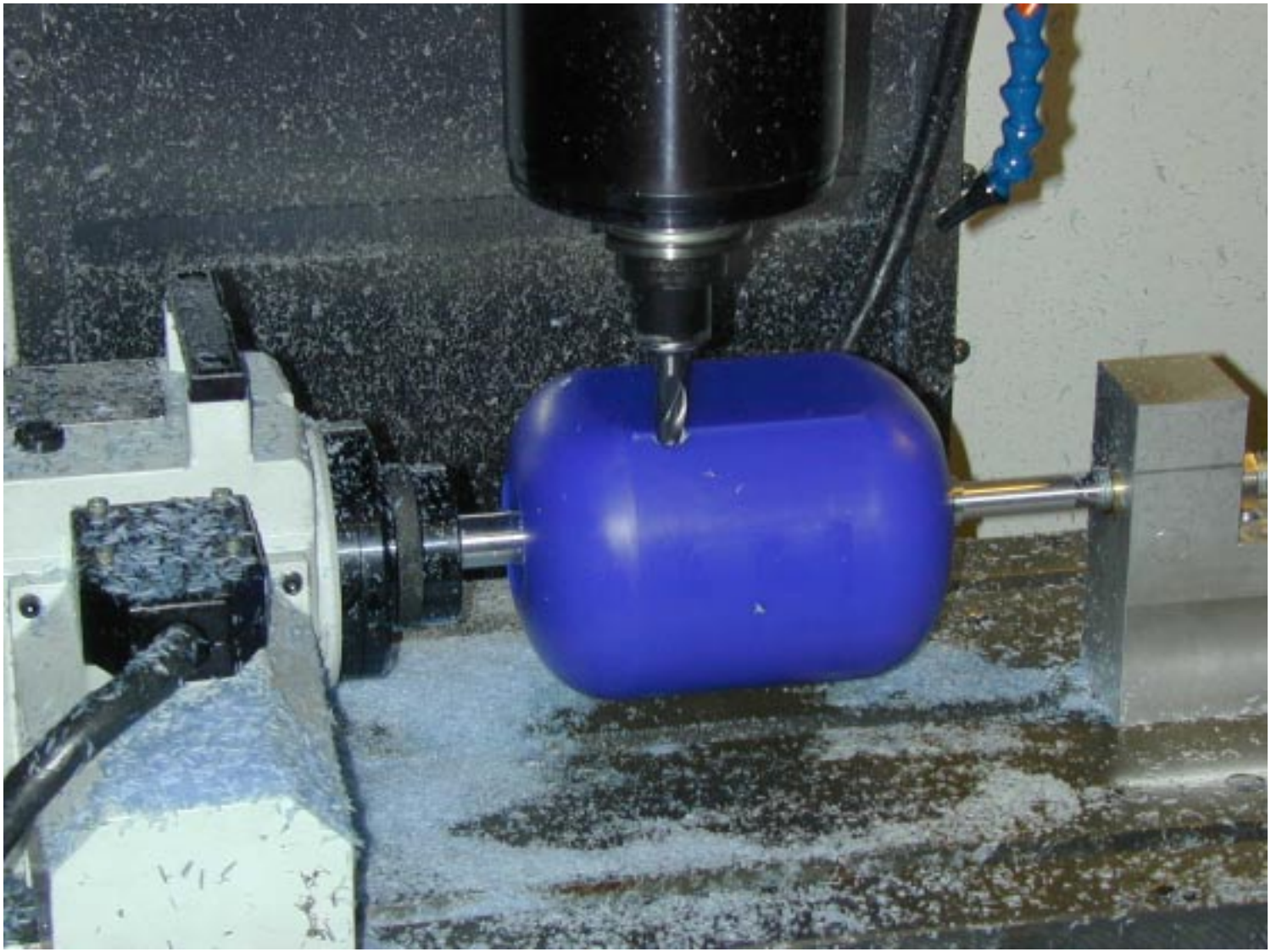

Segmented toroid

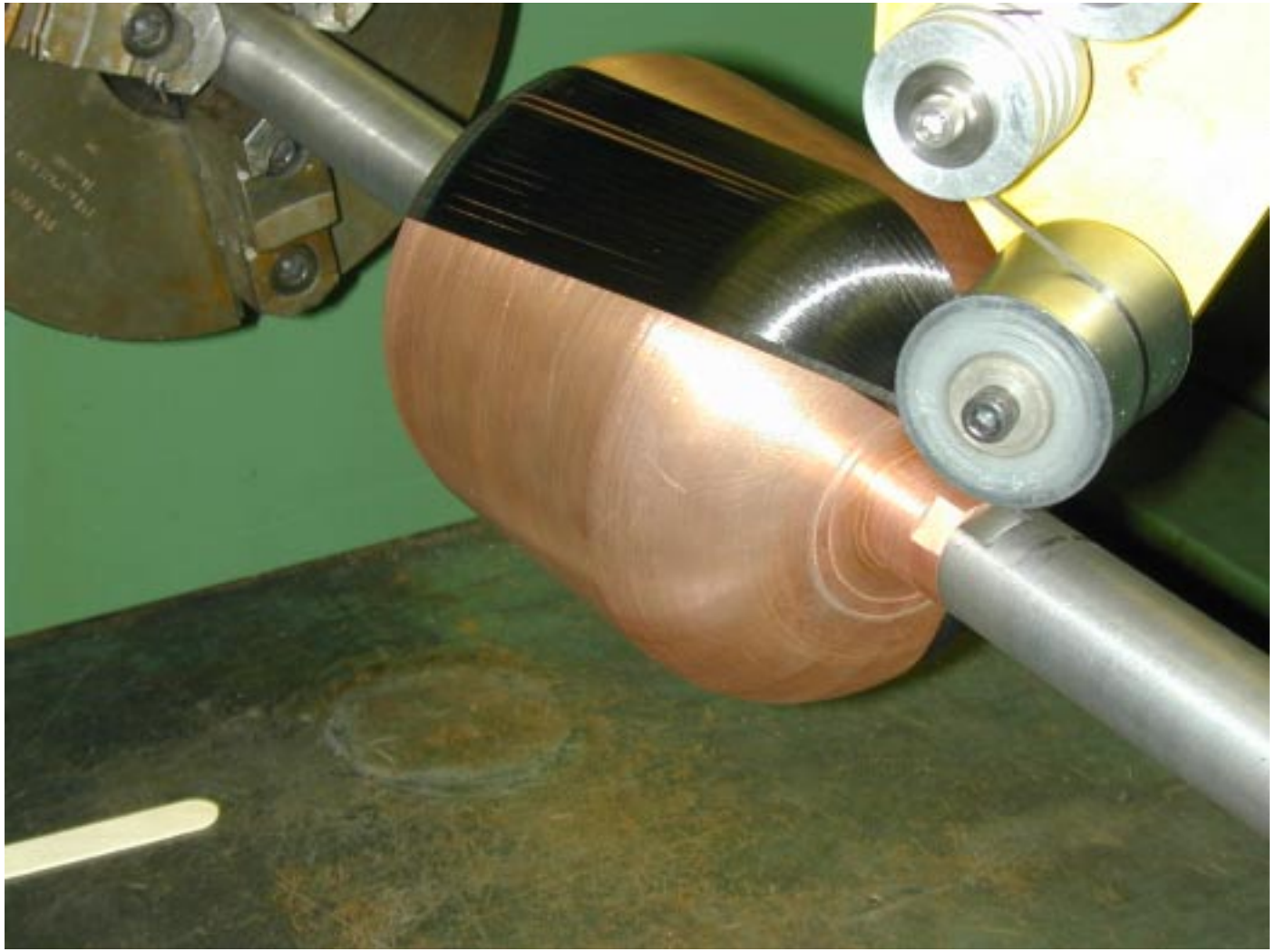

Segmented toroid

Potential advantages of segmented toroid

- Management of fluid acquisition
  - Slosh modes unique to toroids
- Packaging of oxidizers and fuels
  - Alternate tanks to control center of gravity
  - 10-20% more efficient than cluster of cylindrical tanks
- Replacement of damaged unit in the assembly
- Adaptable to very long toroid assemblies
- Customize to propulsion system requirements
  - Pressure fed system vs. pump fed

Where next?

- Continue development of segmented toroid
  - High cycle testing of assembly
  - Investigate application to SLI architecture or commercial applications
- Fabrication of additional circular toroids
  - Consider additional burst test or flow studies
  - Investigate slosh management
    - Positive expulsion bladder
- Consider partnerships if appropriate

LINER-LESS TANKS FOR SPACE APPLICATION – DESIGN AND MANUFACTURING CONSIDERATIONS

Brian H. Jones, Ph.D., bhjones@kaisercompositek.com
Min-Chung Li, Ph.D., mcli@kaisercompositek.com
Kaiser Compositek Inc., 1095 Columbia St., Brea, CA 92821
(714) 990-6300

ABSTRACT

Composite pressure vessels, used extensively for gas and fuel containment in space vehicles, are generally constructed with a metallic liner, while the fiber reinforcement carries the major portion of the pressure-induced load. The design is dominated by the liner's low strain at yield since the reinforcing fibers cannot operate at their potential load-bearing capability without resorting to pre-stressing (or autofrettaging). An ultra high-efficiency pressure vessel, which operates at the optimum strain capability of the fibers, can be potentially achieved with a "liner-less" construction. This paper discusses the design and manufacturing challenges to be overcome in the development of such a pressure vessel. These include: (1) gas/liquid containment and permeation, (2) design and structural analysis, and (3) manufacturing process development. The paper also presents the development and validation tests on a liner-less pressure vessel developed by Kaiser Compositek Inc. (KCI). It should be noted that KCI's liner-less tank exhibits a highly controlled leak-beofre-burst mode. This feature results in a structure having the highest level of safety.

1. INTRODUCTION

Many pressurized tanks utilized in space applications typically use a metal liner reinforced with a high-performance filamentary composite material such as carbon, graphite, aramid and glass. If tank structural efficiency is to be maximized, it is necessary to operate at strains that may be of the order of 1%, assuming, say, a safety factor of 1.5. This is particularly desirable if carbon filaments are used, as they typically exhibit endurance limits that may be 75% to 80% of ultimate. Table 1 describes typical carbon fibers widely used in the manufacturing of filament-wound pressure vessels. The design efficiency of filament-wound, metal-lined, pressure vessels is controlled by the behavior of the liner while the efficiency of a similar plastic lined vessel is influenced by the parasitic weight of the liner.(1) In contrast, an ultra high-efficiency pressure vessel can be potentially achieved if a "liner-less" construction is employed. For a design of this type, a number of advantages immediately accrue. First, removing the liner and replacing it with a material having generally higher specific strength and stiffness, results in a lower weight tank. Second, removing the need for strain compatibility between the liner and the composite over-wrap permits a design to be achieved that is controlled by the behavior of the reinforcing fiber, resulting in a structure having inherently superior fatigue performance. Third, the tank will generally be of lower cost, since the metal liner typically dominates the overall cost of the vessel. However, a linerless tank presents a number of design and manufacturing challenges, including gas (or liquid permeation) and the need to create a means to wind the pressure vessel in the absence of the liner. Micro-cracking that occurs in the composite matrix due to transverse straining compounds the challenge of containing gas or liquid.(1) These issues are discussed in what follows. Afterwards, development and validation tests of KCI's liner-less tanks will be presented.

2. GAS PERMEATION AND CONTAINMENT

In producing a liner-less tank, two immediate design issues relating to gas containment must be addressed. The first relates to the fact that the composite laminate is subjected to bi-directional stresses which will result in transverse micro-cracking at levels of strain significantly below the strain to failure along the fiber. The second is the fact that all polymers are gas permeable to varying degrees.

2.1 Transverse Micro-Cracks Since a pressure vessel may be considered as being in a state of in-plane biaxial strain, high strains in the direction of the filaments will be associated with comparable strains in the transverse direction. Because transverse failure strains caused by matrix cracks occur at about 0.5%, it is evident that in a design based upon "large" strains of the order of 1% along the filament direction will result in transverse "micro-

cracks". The obvious effect of these micro-cracks is to provide a leakage path for the contained gas (or liquid) from the interior. Therefore, it is necessary to prevent the gas from leaking through the over-wrapped composite of the pressure vessel. A further concern is to prevent moisture entering the micro-cracks produced on the exterior of the vessel. If freezing of the moisture occurs; it can result in progressive damage to the composite laminate. The solution to these problems is to apply appropriately compliant coatings on the interior and exterior surface of the vessel capable of containing the micro-cracks.

Table 1: Carbon fibers, which are widely used to produce filament-wound pressure vessels

Fiber	Modulus (MPa)	Ultimate Strain (%)	Endurance Limit (e.g. 80% of Ultimate)	Operating Stain with a Safety Factor of 1.5
Toray T-1000GB, 12K	296,010	2.1	1.68	1.12
Toray T-800, 12K	296,010	1.8	1.44	0.96
Toray T-700, 24K	231,840	2.1	1.68	1.12
Herculus, IM7, 12K	276,000	1.8	1.44	0.96
Mitsubishi, Grafil MR50, 12K	285,660	1.9	1.52	1.01

2.2 Polymeric Coating Material Selection An extensive literature survey was conducted into the use of various polymer and elastomer films and coatings to decrease the permeation of gases such as helium, hydrogen and oxygen through composite laminates. Figure 1 summarizes the helium permeability of some polymers and elastomers as the result of the literature search. Among them, ethylene vinyl alcohol (EVOH) and vinylidene chloride (PVDC) are superb barriers against the permeation of helium. On the other hand, fluoropolymers have very high permeability against helium. Among the elastomers found in the literature, polysulfide, polyurethane, nitrile and butyl have very low permeability. However, silicone and neoprene are very poor barrier materials.

ASTM 1434 test method was utilized to characterize the permeability of composite laminates containing EVOH films. Table 2 shows the laminate architecture of the test coupons. Figure 2 shows details of the permeation test setup. The test cell consists of a stainless steel chamber, closed by a three-inch diameter diaphragm made from the composite laminate under evaluation. The chamber is pressurized with either helium or oxygen. Pressure fluctuation was observed through a transducer that is accurate to ± 1 psi. or a digital pressure gauge that is sensitive to ± 0.25 psi. and accurate to ± 1.25 psi. Additionally, a dial gauge monitored the diaphragm deflection under pressure when required. A major challenge of the permeation test is sealing of the diaphragm to the gas filled chamber. It is achieved with a lead annular gasket, a butyl O-ring and a torque of 25 to 30 ft.-lbs. on the bolts used to clamp the upper and lower sections of the test chamber.

Table 2: Permeability test coupon laminate architecture, cure condition and gas with which the test is conducted

Reference	Lay-up	Thickness (in.)	Notes
1	$90/0_2/90/FM300/0_2/FM300/EVOH/FM300$	0.043	T700/epoxy laminate, vacuum bagged and oven cured, tested with helium
2	$90/0_2/90/FM300/0_2/FM300/EVOH/FM300$	0.043	T700/epoxy laminate, vacuum bagged and oven cured, tested with oxygen
3	FM300/EVOH/0/90/0/EVOH	0.052	T1000/epoxy filament-wound laminate, autoclave cured, tested with helium

Pressurization was accomplished using a container of pressurized gas regulated to the required level (100 psig. to 400 psig.). For tests carried out at elevated and cold temperatures, the test cell was placed into an environmental chamber that was maintained at the required temperatures.

Test results are shown in Figures 3 to 5 in the form of pressure and temperature histories. Figure 3 exhibits the temperature and helium pressure history of coupon 1 in Table 2 at ambient temperature, -100°F and 140°F. As noted, the pressure drops by about 20 psig. in 6 days. For the same laminate architecture tested with oxygen at the same pressure, no indication of pressure decrease was observed, as shown in Figure 4. Figure 5 shows helium pressure and temperature histories of coupon 3 in Table 2. There is no evidence of pressure drop for an autoclave-

cured laminate. Although leaking through gaskets, O-rings and fittings might be a concern and laminate architectures are not quite the same between the coupons tested, it is believed, predictably, that autoclave-cured laminate provide better structural integrity than those that were vacuumed-bagged and oven-cured. It is also shown that EVOH has very good permeability properties when the substrate laminate is autoclave-cured.

3. MANUFACTURING PROCESS DEVELOPMENT AND STRUCTURAL ANALYSIS

The design of a liner-less tank involves particular attention to features that are somewhat unique to this type of construction. They include end-fitting design, ratio of fitting size to the tank size and the impact of the tank aspect ratio on the tank efficiency factor (PV/W). These subjects were discussed in great detail in Reference 1. What follows discusses topics involving manufacturing process development and structural analysis.

3.1 Manufacturing Process Development To fabricate a liner-less pressure vessel, the reinforcing fibers must be wound onto a mandrel that is either water soluble, collapsible, or otherwise removable. The applicability of each concept will be dependent upon the physical size of the vessel and also the size of the opening. If the fitting size at the dome ends is small, water–soluble and collapsible tooling may not be feasible. The presence of permeation barrier films, coatings etc. on the interior surface will also limit the type of mandrel that is suitable. KCI's patented design of the liner-less pressure vessel evolves around a thin composite shell that is obtained by filament winding with a hard tooling. The hard tooling describes precisely the interior profile of the finished pressure vessel. After being cured in an autoclave, the structural composite shell is sectioned in half and taken off the tooling for preparation of joint, fitting installation and polymeric permeation coating application. Afterwards, the composite shell is joined together by bonding and the rest of composite, as required by design, will be wound on the composite shell to obtain the liner-less pressure vessel.

3.2 Structural Analysis Detailed 3-D finite element models were developed to design/analyze the composite laminate architectures of the liner-less pressure vessel. It should be noted that the geodesic filament-winding pattern results in a constant changing ply architecture (thickness and orientation) throughout the dome and particularly in the region of the fittings. As such, accurate modeling of the region is critical. A further challenge was created by the availability of data for composites and adhesives at the low operating temperatures required for the pressure vessels. Additionally, shear behavior of most epoxy adhesive is very non-linear.(2) For those adhesives which have their shear behavior characterized, data were usually available in a temperature range of -55ºC (-67ºF) and 82ºC (180ºF) from a single-lap shear test (ASTM D1002).(3) This is not a good indication of adhesive shear behavior due to the thin adherends (1.6 mm or 0.063 in.) used. During such a test, peel is inevitably induced across the adhesive bond line. Thus, indication of shear strength tends to be compromised. More accurate shear behavior could be obtained from a KGR-1 single-lap shear test with thick adherends. Therefore, the nonlinear behavior of the adhesive has to be accounted for in the design and analysis to obtain accurate analysis predictions.

4. DEVELOPMENT AND VALIDATION TESTS

Development and validation tests were conducted in sub-scale and full-size levels. Table 3 shows the specifications of the sub-scale and full-size H_2 and O_2 tanks. The sub-scale tank size is about one-third that of the full-size H_2 tank. Development and validation tests includes pressure proof and cycle tests at ambient and low temperatures, leak check at ambient temperature after the tanks went through each pressure test and hydraulic and pneumatic burst tests.

4.1 Sub-Scale Tank Development Test A sketch of the sub-scale tank test setup for proof and cycle tests is shown in Figure 6. To accommodate test temperatures down to –120°F, ethyl alcohol was used as the test media and an accumulator was installed between the pump and the tank outside of the test chamber to separate the ethanol and the hydraulic fluid. On one of the sub-scale tanks, strain gauges were installed to record the strains at various pressures. Data were compared with FEM predicted strain results. Leak checking was conducted after the tanks were subjected to the proof test or pressure cycle test to confirm that the permeation rate satisfied the requirements of Table 3.

Figures 7 to 8 are sample results of the sub-scale tank development tests. In Figure 7, reasonable agreement between strain gauge data and analytical prediction is observed. Figure 8 shows the temperature and pressure history of a helium leak check conducted after a sub-scale tank was subjected to a proof test of 1,015 psig. producing the same strain level in a full-size H_2 tank at its MEOP (400 psig.). Also shown in Figure 8 is the permeation or leak rate estimation of a full-size tank of the same laminate thickness from the leak check of the sub-scale tank. As seen in Figure 8, leak rate tested by helium easily satisfies the specification requirement.

Table 3: Sub-scale and full-size liner-less pressure vessel specifications

	Sub-scale Tank	H_2 Tank	O_2 Tank
OD (in.)	12.9	40.7	31.7
Length (in.)	22.5	55.1	41.7
Boss OD (in.)	2	2.375	2.375
Target Weight (lbs.)	9.1	31	16
Volume ($in.^3$)	1,791	56,494	25,156
Aspect Ratio	1.74	1.35	1.32
MEOP (psig.)	1,000	400	400
Proof Pressure (psig.)	up to 1,100	440	440
Min. Burst Pressure (psig.)	1,500	600	600
Min. T (F)	-120	-120	-120
Max. T (F)		140	140
Tank Life to MEOP (cycles)	2,000	5,000	5,000

To obtain the failure mode of KCI's liner-less tanks, one sub-scale tank was subjected to pneumatic burst test. The tank exhibited a failure mode of leak-before-burst. The test result proved that the liner-less tank KCI designed has the highest level of safety due to the fact that there is no sudden and potentially unstable transfer of load between the composite structure and the metal liner when either one fails. Figure 9 show the sub-scale tank after the pneumatic burst test. The tank was apparently not ruptured and leaking was observed throughout the tank surface.

4.2 Full-Size Ground-Test Tank Validation Test Full-size ground-test H_2 and O_2 tanks were designed to have a safety factor three times of that of the H_2 and O_2 tanks specified in Table 3. The size of the full-size tanks prohibited the use of the in-house hydraulic pump for the pressure tests. Therefore, a test setup combining pneumatic and hydraulic means of pressurization was designed and assembled in house. A schematic diagram of the setup is shown in Figure 10. Both H_2 and O_2 ground-test tanks were subjected to proof test to 600 psig. and 2,000 cycles of pressurization test to 400 psig. at ambient temperature. Permeation test with helium was conducted after the proof and cycle tests. Results of the permeation test were shown in Figure 11. It can be seen that, after the proof test, practically no leak was detected. After cycle testing, however, some leakage or permeation was detected within the limits specified by the specifications.

5. SUMMARY

Composite pressure vessels, which have a metallic or a plastic liner, cannot achieve maximum efficiency because the liner does not have the same high specific stiffness, specific strength or strain capability as the composite over-wrap. An ultra high-efficient pressure vessel, which operates at a strain level of the order of 1%, can be achieved using a liner-less construction as proved by the sub-scale development tests described. Among the polymeric film and coating materials investigated, ethylene vinyl alcohol (EVOH) is a useful permeation barrier material. Autoclave-cured laminates have better structural integrity than vacuum-bagged, oven cured laminates and are the choice of substrate for polymeric coating materials. Furthermore, KCI's patented liner-less pressure vessel exhibits the highest level of safety with a benign failure mode of leak-before-burst.

6. ACKNOWLEDGEMENT

The work was partially sponsored by AeroVironment, Inc. in Simi Valley, California under funding from the NASA ERAST program.

7. REFERENCES

1. Li, Min-Chung and Jones, Brian H., "The Design of Composite Pressurized Tanks with and without Liners for Use in Space Applications", 33rd International SAMPE Technical Conference, Seattle, WA, Nov. 5-8, 2001
2. Heslehurst, R. B., SAMPE International Symposium 2001, 380 (2001).
3. American Society for Testing and Materials, "ASTM D1002-99, Standard Test Method for Strength Properties of Adhesives in Shear by Tension Loading (Metal-to-Metal)", ASTM, West Conshohocken, Pennsylvania, 1999.

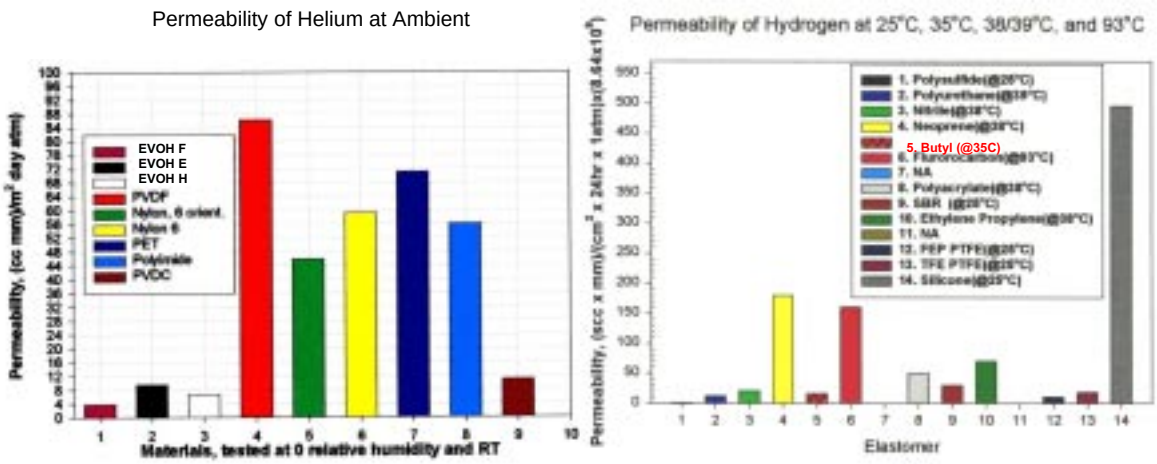

Figure 1: Helium and hydrogen permeability of various polymers and elastomers from literatures

Figure 2: Permeation test setup

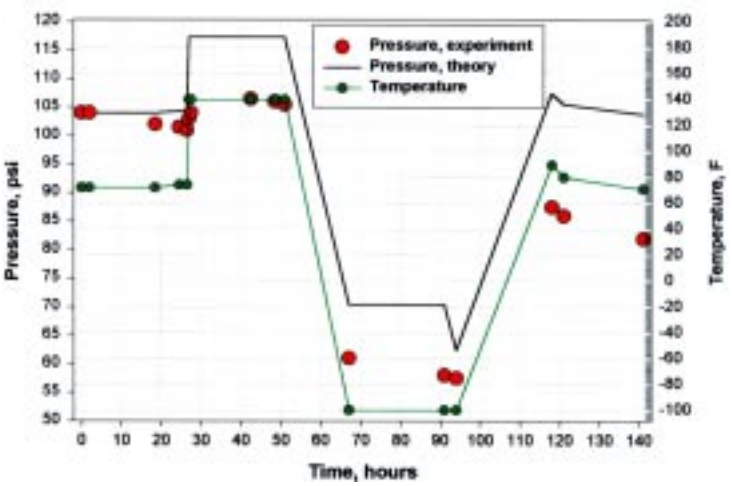

Figure 3: Pressure and temperature histories of coupon 1 of Table 2 from the permeation test

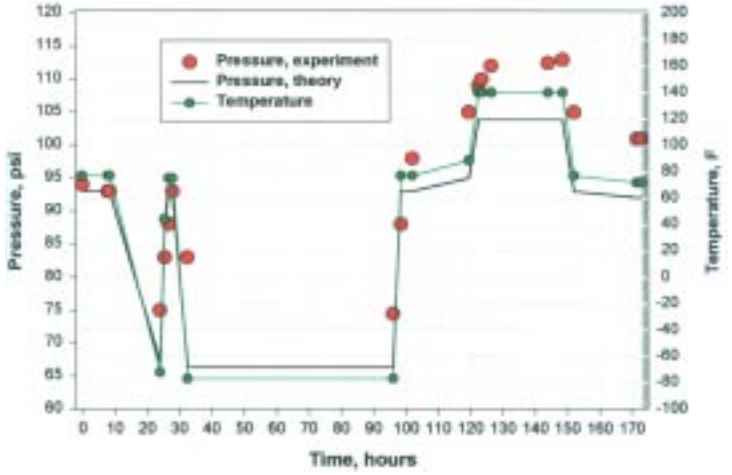

Figure 4: Pressure and temperature histories of coupon 2 of Table 2 from the permeation test

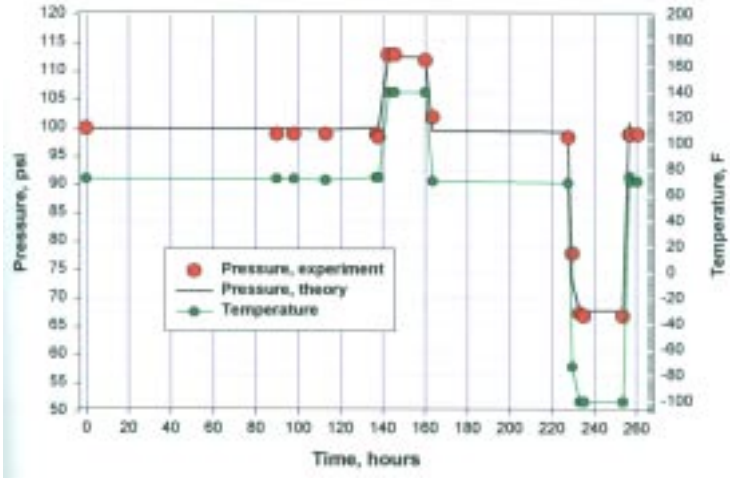

Figure 5: Pressure and temperature histories of coupon 3 of Table 2 from the permeation test

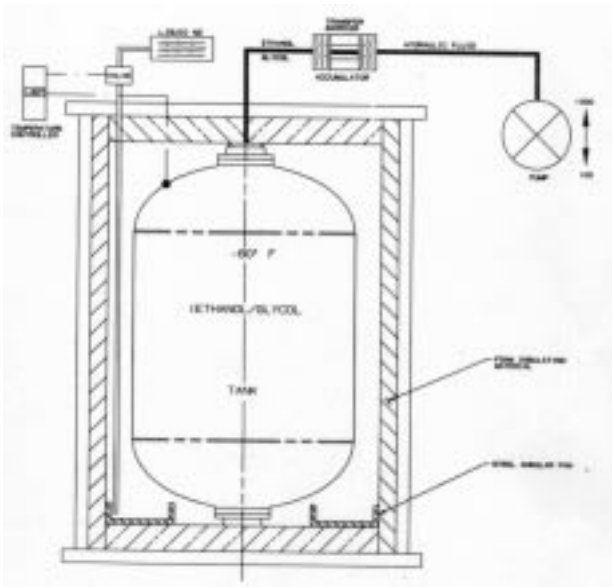

Figure 6: Pressure proof and cycle test setup for a sub-scale liner-less pressure vessel

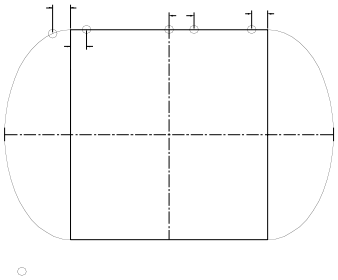

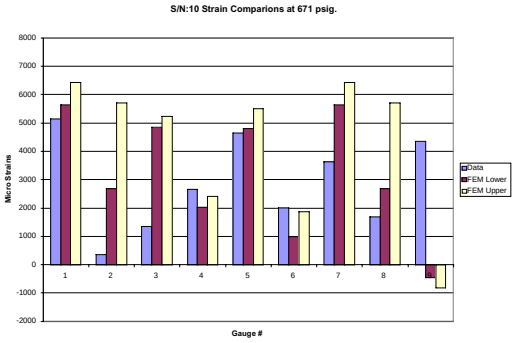

Figure 7: Strain gauge locations and strain data versus FEA results

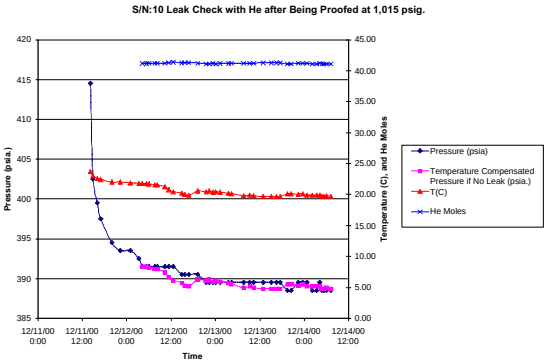

S/N:10 Leak Check Summary and Full-Size H2 Tank Fuel Leak Rate Estimation			
Subscale Tank Test Summary		**Full-size H2 Tank Leak Rate Estimation**	
Volume (in^3)	2276	Volume	51,925
Surface Area (in.^2)	848.6	Surface Area (in.^2)	6,929.7
Initial Pressure (psia)	391.5	Allowable Leak Volume at -40F at 400 psig for 180 days (in.^3)	2,596.3
Initial Temperature (F)	71.2	Allowable Leak Volume at RT at 1 atm (in.^3) for 180 days	**96,207**
Initial Moles of He	41.137	Estimated leak Volume at RT at 1atm for 180 days (in.^3)	**23,058**
Final Pressure (psia)	388.5		
Final Temperature (F)	67.4		
Final Moles of He	41.117		
Moles of He Leaked	0.021		
Elapsed Time (day)	2.124		
Volume of He Leaked at 1atm (in.^3) at RT	31.350		

Figure 8: Helium leak check data and permeation/leak estimation of a sub-scale liner-less pressure vessel

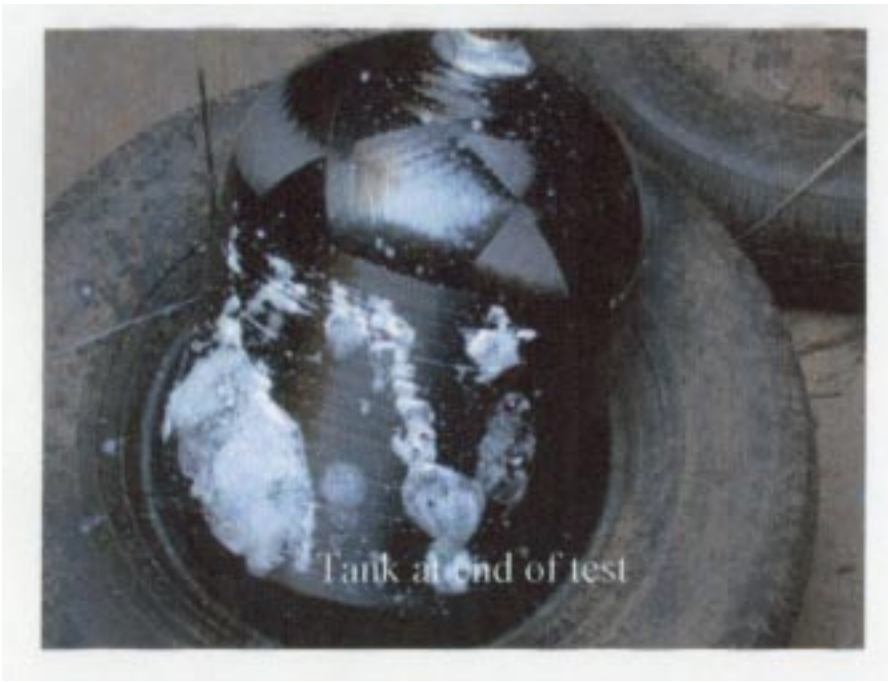

Figure 9: Leak-check on a liner-less tank after a pneumatic burst test shows an inert failure mode

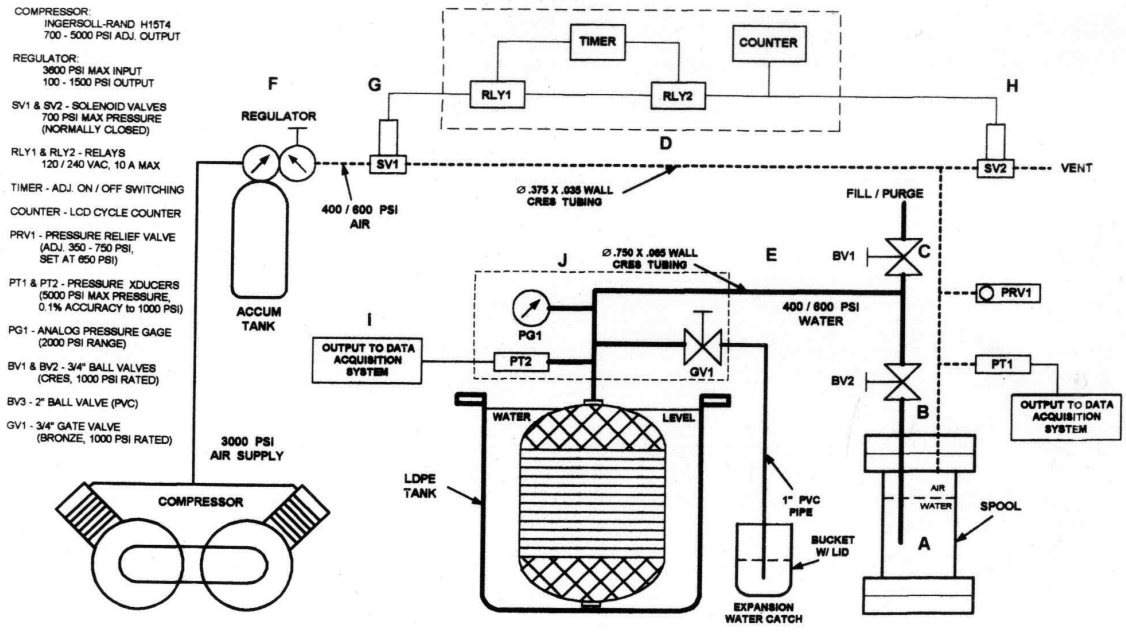

Figure 10: Full-size ground-test tank pressure proof and cycle test setup

H2 Ground Test S/N:1 He Leak Check after Proof to 600 psig. at RT

Test Summary		Leak Rate Estimation	
Volume	56,494	Allowable Leak Volume at -40F at 400 psig for 180 days (in.^3)	2,824.7
Surface Area (in.^2)	7,371.2	Allowable Leak Volume at RT at 1 atm (in.^3) for 180 days	**103,274**
Initial Pressure (psia)	320.69	Estimated leak Volume at RT at 1atm for 180 days (in.^3)	**-336,846**
Initial Temperature (F)	81.01		
Initial Moles of He	821.22		
Final Pressure (psia)	325.82		
Final Temperature (F)	88.42		
Final Moles of He	823.10		
Moles of He Leaked	-1.877		
Elapsed Time (day)	1.94		
Volume of He Leaked at 1atm (in.^3) at RT	-2834.375		

O2 Ground Test S/N:1 1st He Leak Check after Proof to 600 psig. at RT

Test Summary		Leak Rate Estimation	
Volume	25,156	Allowable Leak Volume at -40F at 400 psig for 180 days (in.^3)	1,257.8
Surface Area (in.^2)	4,274.5	Allowable Leak Volume at RT at 1 atm (in.^3) for 180 days	**45,986**
Initial Pressure (psia)	317.22	Estimated leak Volume at RT at 1atm for 180 days (in.^3)	**-367,619**
Initial Temperature (F)	80.19		
Initial Moles of He	362.27		
Final Pressure (psia)	322.89		
Final Temperature (F)	86.78		
Final Moles of He	364.30		
Moles of He Leaked	-2.028		
Elapsed Time (day)	1.94		
Volume of He Leaked at 1atm (in.^3) at RT	-3062.678		

H2 Ground Test S/N:1 He Leak Check after 2,000 Cycles to 400 psig. at RT

Test Summary		Leak Rate Estimation	
Volume	56,494	Allowable Leak Volume at -40F at 400 psig for 180 days (in.^3)	2,824.7
Surface Area (in.^2)	7,371.2	Allowable Leak Volume at RT at 1 atm (in.^3) for 180 days	**103,274**
Initial Pressure (psia)	399.07	Estimated leak Volume at RT at 1atm for 180 days (in.^3)	**20,437**
Initial Temperature (F)	71.87		
Initial Moles of He	1039.52		
Final Pressure (psia)	401.61		
Final Temperature (F)	75.33		
Final Moles of He	1039.38		
Moles of He Leaked	0.143		
Elapsed Time (day)	1.96		
Volume of He Leaked at 1atm (in.^3) at RT	215.259		

O2 Ground Test S/N:1 He Leak Check after 2,000 Cycles to 400 psig. at RT

Test Summary		Leak Rate Estimation	
Volume	25,156	Allowable Leak Volume at -40F at 400 psig for 180 days (in.^3)	1,257.8
Surface Area (in.^2)	4,274.5	Allowable Leak Volume at RT at 1 atm (in.^3) for 180 days	**45,986**
Initial Pressure (psia)	410.99	Estimated leak Volume at RT at 1atm for 180 days (in.^3)	**2,050**
Initial Temperature (F)	68.10		
Initial Moles of He	480.12		
Final Pressure (psia)	417.37		
Final Temperature (F)	76.31		
Final Moles of He	480.11		
Moles of He Leaked	0.015		
Elapsed Time (day)	2.01		
Volume of He Leaked at 1atm (in.^3) at RT	22.915		

Figure 11: Helium permeation/leak check result of full-size ground-test tanks before and after a pressure cycle test

Friction Stir Welding of Tapered Thickness Welds using an Adjustable Pin Tool

GLYNN ADAMS
Lockheed Martin Space Systems Company, Michoud Operations
Department 4630 Bldg. 101/1/EC25
P.O. Box 29304
New Orleans, LA 70189
Phone: 504-257-1510
Fax: 504-257-1210
E-mail: glynn.adams@maf.nasa.gov

Richard Venable
Lockheed Martin Space Systems Company
Marshall Space Flight Center
Huntsville, AL 35812
Phone: 256-544-2757
Fax: 256-544-3920
E-mail: richard.venable@msfc.nasa.gov

Kirby Lawless
Marshall Space Flight Center, ED33
Huntsville, AL 35812
Phone: 256-544-2821
Fax: 256-544-0212
E-mail: Kirby.lawless@msfc.nasa.gov

Friction stir welding (FSW) can be used for joining weld lands that vary in thickness along the length of the weld. An adjustable pin tool mechanism can be used to accomplish this in a single-pass, full-penetration weld by providing for precise changes in the pin length relative to the shoulder face during the weld process. The difficulty with this approach is in accurately adjusting the pin length to provide a consistent penetration ligament throughout the weld. The weld technique, control system, and instrumentation must account for mechanical and thermal compliances of the tooling system to conduct tapered welds successfully.

In this study, a combination of static and *in-situ* measurements, as well as active control, is used to locate the pin accurately and maintain the desired penetration ligament. Frictional forces at the pin/shoulder interface were a source of error that affected accurate pin position. A traditional FSW pin tool design that requires a lead angle was used to join butt weld configurations that included both constant thickness and tapered sections. The pitch axis of the tooling was fixed throughout the weld; therefore, the effective lead angle in the tapered sections was restricted to within the tolerances allowed by the pin tool design. The sensitivity of the FSW process to factors such as thickness offset, joint gap, centerline offset, and taper transition offset were also studied. The joint gap and the thickness offset demonstrated the most adverse affects on the weld quality. Two separate tooling configurations were used to conduct tapered thickness welds successfully. The weld configurations included sections in which the thickness decreased along the weld, as well as sections in which the thickness increased along the weld. The data presented here include weld metallography, strength data, and process load data.

Automatic Ply Verification

SCOTT BLAKE
Assembly Guidance
315 Littleton Rd.
Chelmsford, MA 01824
Phone: 978-244-1166
Fax: 978-244-9288
E-mail: sb@assemblyguide.com

For a composite part to perform as required, all manufacturing processes must be performed correctly. Many complex composite parts are fabricated manually, taking advantage of assembler flexibility and tactile and visual senses. Manual manufacturing is also characterized by weaknesses in the areas of meticulousness, speed, and precision.

The Automatic Ply Verification (APV) Poster shows a new system that supplements the hand-laid composite manufacturing process, utilizing existing CAD data, laser projection, optics, and networking. The APV System provides the assembler / manufacturer with an economical, automatic, in-process quality monitoring capability. The assembler wears a small, wireless camera-illumination-referencing system that is manually placed at locations on the part as pointed out by the laser projector. Images are captured and analyzed under the guidance of CAD data. Fully traceable data are available for each ply in the laminate. Ply presence, location, fiber orientation, and material type are verified as required by the process planner.

The poster displays system components in operation, input data, captured and processed images, and output data from a Sikorsky Aircraft rotor blade component. Sikorsky Aircraft and Assembly Guidance are in the process of implementing APV for production of the RAH-66 Comanche at Sikorsky's new manufacturing facility in Bridgeport, Connecticut.

Standard Chemical Ignition Source Characteristics for Flammability Testing

Carl D. Engel, Qualis Corporation

Problem: Validation data were needed for igniter performance

Chemical Igniter

Composition of Chemical Ignitors Used in Material Flammability Testing

- 70.3% Hexamethylenetetramine ($(CH_2)_6N_4$)
- 26.3% Anhydrous Sodium Metasilicate (Na_2SiO_3)
- 3.5% Arabic Gum – Acacia Gum (Carbonydrate Polymer); Water Soluble

Performance Specifications

- Flame Temperature: 1100 ± 30 °C (2000 ± 160 °F)
- Igniter Burn Time: 25 ± 5 s
- Flame Height: 6.4 ± 0.64 cm (2.5 ± 0.25 in)

Test Results:

Figure 1. Equilibrium Chemical Igniter Weight Ratios as a Function of Humidity Level

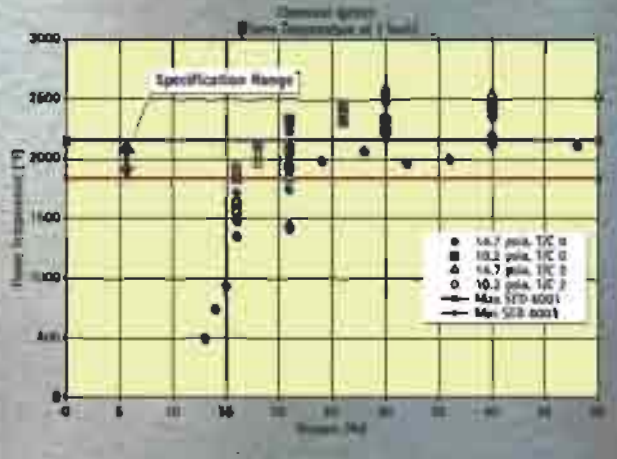

Figure 2. Igniter Flame Temperature at 1 inch

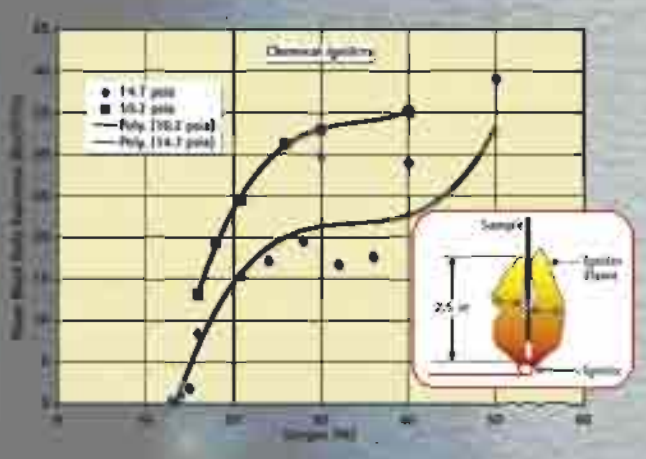

Figure 3. Flame Black Body Radiation

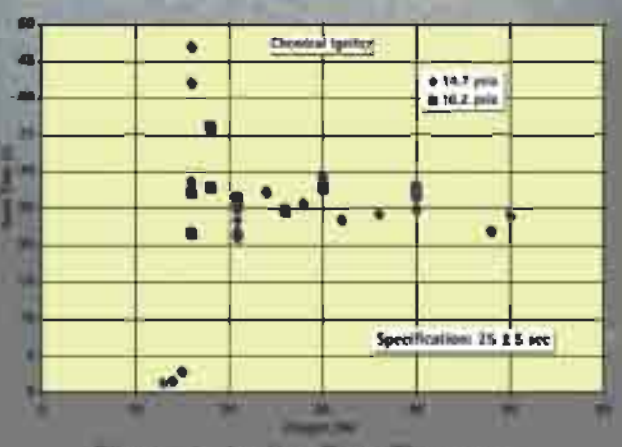

Figure 4. Igniter Burn Time as a Function of Oxygen Level

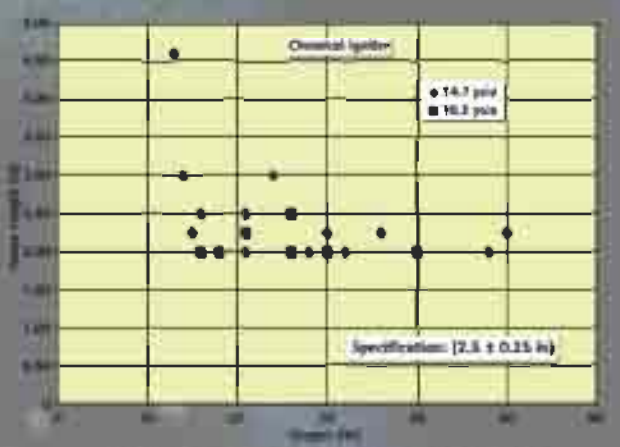

Figure 5. Maximum Flame Height

Conclusions:

- Chemical igniter weights: determined to be within the STD 6001 range; form normal distribution across range; average weight = 0.2168 g
- Humidity effects: minimal when humidity <40%; potentially very significant effects when >40%
- Igniter flame temperatures: drop <1840 °F at <18% O_2 conditions; measured >2160 °F for 10.2 psia and >20% O_2
- Potential radiation heating from igniter flame to sample changed from 16 to 35 Btu/ft^2/s when changing from 20% to 50% O_2 at 14.7 psia. Temperature implied radiative heating was always higher for lower pressure (10.2 psia) than for higher pressure (14.7 psia) at the same O_2 level
- Flame height: outside specifications 60% of the time
- Burn time correlated by burn weight; within specifications for >20% O_2 concentrations
- Demonstrated capability of LabVIEW™ data acquisition system to capture transient data for new MAPTIS system

Qualis

MSFC Materials Combustion Research Facility

Research performed under contract NAS8-01050, *Materials Testing for Aerospace Environments at MSFC*

High Temperature Thermographic Phosphor Coatings Development

SHAWN GOEDEKE
Department of Mechanical Engineering
Tennessee Technological University
Cookeville, TN 38505
Phone: 865-376-7595
E-mail: SMG2886@tntech.edu

S.W. Allison, D.L. Beshears, T. Bencic, M.R. Cates
Oak Ridge National Laboratory
National Transportation Research Center
2360 Cherahala Blvd., MS-6472
Knoxville, TN 37932

W.A. Hollerman, R. Guidry
Department of Physics
University of Louisiana at Lafayette
Lafayette, LA 70504

For many years, phosphor thermometry has been used for non-contact temperature measurements. A large number of applications have been associated with high temperatures, especially for aerospace systems where blackbody radiation backgrounds are large and in challenging environments, such as vibration, rotation, flame, or noise. These environments restrict the use of more common thermocouples or infrared thermometric techniques. In particular, temperature measurements inside jet turbines, rocket engines, or similar devices are especially amenable to phosphor techniques.

Often the fluorescent materials are used as powders, either suspended in binders and applied like paint or applied as high-temperature sprays. Thin coatings that are less than 50 μm thick are used on the surfaces of interest. These coatings will quickly assume the same temperature as the surface to which they are applied. The temperature dependence of fluorescent materials is a function of the base matrix atoms and a small quantity of added activator or "dopant" ions.

Often for high temperature applications, the selected materials are refractory and include rare earth ions. Phosphors like $Y_3Al_5O_{12}$ (YAG) doped with Eu, Dy, or Tm, Y_2O_3 doped with Eu, or similar rare earth compounds, will survive high temperatures and can be configured to emit light that changes rapidly in lifetime and intensity. For example, researchers at Oak Ridge National Laboratory recently observed fluorescence from YAG:Dy and YAG:Tm at temperatures above 1400 ºC.

One of the biggest challenges is to locate a binder material that can withstand tremendous variations in temperature in an adverse aerospace environment. This poster will provide an overview into our attempt to utilize phosphors for thermometry purposes. Emphasis will be placed on the use of selected binder materials that can withstand high temperatures. This research was completed for the National Aeronautics and Space Administration's Glenn Research Center in Cleveland, Ohio.

SLI Complex Curvature Friction Stir Weld Risk Reduction Program

PAULA J. HARTLEY
Lockheed Martin Space Systems - Michoud Operations
13800 Old Gentilly Rd.
New Orlean, LA 70129 USA
Phone: 504-257-3161
Fax: 504-257-1210
E-mail: paula.j.hartley@lmco.com

Jules Schneider
Lockheed Martin Space Systems - Michoud Operations
13800 Old Gentilly Rd.
New Orlean, LA 70129 USA

Chip Jones, Kirby Lawless, Carolyn Russell
NASA Marshall Space Flight Center / ED33
Huntsville, AL 35812
Phone: 256-544-2701, 256-544-2821, 256, 544-2705
E-mail: Clyde.S.Jones@msfc.nasa.gov, Kirby.G.Lawless@msfc.nasa.gov,
Carolyn.K.Russell@msfc.nasa.gov

The Space Launch Initiative Program (SLI) in conjunction with the National Center for Advanced Manufacturing (NCAM) will demonstrate the ability to produce large-scale complex curvature hardware using the self-reacting friction stir welding process. This multi-phased risk reduction program includes friction stir welding process development and manufacture of a 22-ft diameter quarter dome using a conventional tooling approach; it culminates in a 27.5-ft diameter quarter dome demonstration performed on a 5-axis Universal Weld System. The design, fabrication, and installation of the Universal Weld System is made possible through a collaboration between the State of Louisiana, NASA, and the University of New Orleans. The Universal Weld System, manufactured by MTS Systems Corporation, will be installed at the Michoud Assembly Facility in New Orleans, Louisiana, and will be capable of manufacturing domes up to 30 ft in diameter.

All welding will be accomplished using the Adaptable Adjustable Pin Tool (AdAPT) weld head and controller manufactured by MTS. Weld parameters will be developed for an aluminum alloy in gauges ranging from 0.320 to 0.400 in. thick. Weld quality will be verified through radiography, mechanical property testing at ambient and LN_2 temperatures, and metallurgical analysis. The AdAPT weld head will then be mounted on a 22-ft diameter dome tool, which will be modified to include a welding track and drive system for moving the AdAPT weld head along the weld joint. This tool will then be used to manufacture a 22-ft diameter dome of an aluminum alloy, with 0.320-in. constant thickness joints, consisting of three individual gore panels. Finally, the 27.5-ft diameter quarter dome will be welded on the Universal Weld System. The quarter dome will consist of three individual gore panels with weld lands tapering from 0.320 to 0.360 in. in thickness. With the demonstration of these welds, the ability to manufacture large diameter domes using the friction stir weld process in conjunction with a universal weld system provides a low risk approach to the fabrication of aluminum tanks for future launch vehicle applications.

Introduction to Proton Microscopy

WILLIAM A. HOLLERMAN
University of Louisiana at Lafayette
P.O. Box 44210
Lafayette, Louisiana 70503
Phone: 337-482-6691
Fax: 337-482-6190
E-mail: hollerman@louisiana.edu

T. L. Stanaland
Department of Physics
University of Louisiana at Lafayette
P.O. Box 44210
Lafayette, LA 70503

The Department of Physics at the University of Louisiana at Lafayette brings unique materials modification and analysis capabilities to Louisiana. The heart of this capability is the Louisiana Accelerator Center (LAC), which houses a 1.7-MV, model 5SDH-2 tandem Pelletron accelerator from National Electrostatics Corporation. With dual plasma and sputter sources, this accelerator is capable of providing beams for ion beam analysis, ion implantation, and nuclear microprobe analysis and imaging. The high-energy scanning nuclear microprobe system became operational in June 2000 and is the only one of its kind in Louisiana. This instrument delivers ion beams as small as 1 x 1 μm (horizontal x vertical) to a stationary target with sufficient current to provide two-dimensional elemental maps and depth profiles in microscale areas. Three-dimensional microscale etching using maskless MeV ion beam irradiation has also been demonstrated. The U.S. Department of Energy (DOE) and the Louisiana Education Quality Support Fund (LEQSF) under contract numbers DOE/LEQSF (1993-95)-03 and DE-FC02-91ER75669 supported this research.

Thermo-Optical and Mechanical Property Testing of Candidate Solar Sail Materials

WILLIAM A. HOLLERMAN
University of Louisiana at Lafayette
P.O. Box 44210
Lafayette, Louisiana 70503
Phone: 337-482-6691
Fax: 337-482-6190
E-mail: hollerman@louisiana.edu

T. L. Stanaland and F. Womack
Department of Physics
University of Louisiana at Lafayette
P.O. Box 44210
Lafayette, LA 70503

David Edwards and Whitney Hubbs
Marshall Space Flight Center, ED31
Huntsville, AL 35812

Charles Semmel
Qualis Corporation
Marshall Space Flight Center, ED31
Huntsville, AL 35812

Solar sailing is a unique form of propulsion where a spacecraft gains momentum from incident photons. Since sails are not limited by reaction mass, they provide continual acceleration, reduced only by the lifetime of the lightweight film in the space environment and the distance to the Sun. Practical solar sails can expand the number of possible missions, enabling new concepts that are difficult by conventional means. The National Aeronautics and Space Administration's Marshall Space Flight Center (MSFC) is concentrating research into the utilization of ultra-lightweight materials for spacecraft propulsion. Solar sails are generally composed of a highly reflective metallic front layer, a thin polymeric substrate, and occasionally a highly emissive back surface. The Space Environmental Effects Team at MSFC is actively characterizing candidate sails to evaluate the thermo-optical and mechanical properties after exposure to electrons. This poster will discuss the preliminary results of this research.

Composite LOX Tank Development

Michael C. McBain
Lockheed Martin Space Systems Co., Michoud Operations
13800 Old Gentilly Rd
New Orleans, LA 70129

Abstract

The development of polymer composite cryogenic tanks is a critical step in creating the next generation of launch vehicles. Future launch vehicles need to minimize the gross liftoff weight (GLOW), which is possible due to the 28%-41% reduction in weight that composite materials can provide over current aluminum technology. The development of composite cryogenic tankage, feedlines, and un-pressurized structure are key enabling technologies for performance and cost enhancements for Reusable Launch Vehicles (RLVs). The technology development for composite tanks has provided direct and applicable data for feedlines, un-pressurized structure, material compatibility, and cryogenic fluid containment for highly loaded complex structures and interfaces. All three types of structure have similar material systems, processing parameters, scaling issues, analysis methodologies, NDE development, damage tolerance, and repair scenarios. Composite cryogenic tankage is the most complex of the 3 areas and provides the largest breakthrough in technology. A building block approach has been employed to bring this family of difficult technologies to maturity. This approach has matured composite materials, processes, design, analysis, and test methods technologies through a series of composite test programs beginning with the NASP program, to meet aggressive performance goals for reusable launch vehicles. In this paper, the development and application of advanced composites for RLV use is described with special emphasis on the X-34 composite LOX tank test article.

Correlating Flammability of Materials with FTIR Analysis Test Results

Robin Moore (Integrated Concepts & Research Corp) and Steve Whitfield (NASA)

PURPOSE: Correlate flammability data with FTIR test results.

MATERIAL: Kydex 100 is a blend of chlorinated polyvinyl chloride and polymethylmethacrylate, with some filler materials. Samples supplied were 0.125" thick.

METHOD: 10 samples were taken from a sheet of Kydex and analyzed for flammability and by FTIR spectroscopy.

ADDITIONAL INFORMATION: This material was utilized as a round robin sample for flammability testing per NASA–STD–6001 (formerly NHB 8060.1c, Test 1), performed at the Materials Combustion Research Facility at MSFC. The flammability test results were found to vary across the same sheet.

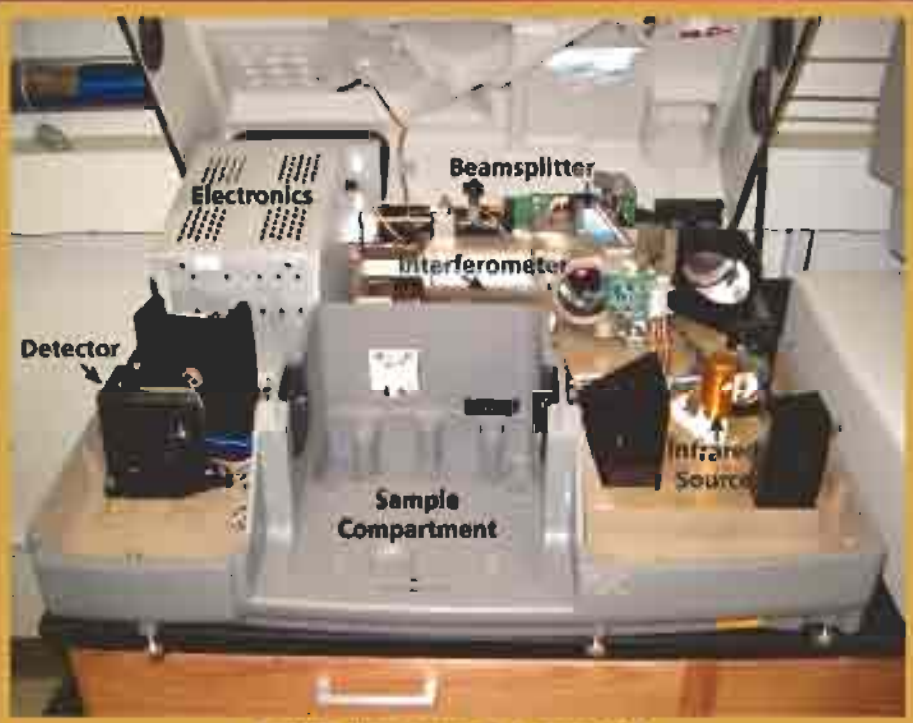

FTIR Internal Layout

FTIR Spectrometer

BASIC FTIR PRINCIPLE

- An infrared light source induces vibrations within the molecules of a sample.
- Different molecular functional groups generate characteristic peaks within the infrared spectra. These peaks assist in identification of the molecule.

The infrared source beam is split in two parts by the beamsplitter and then recombined. The difference in the signal generated in the fixed mirror and moving mirror produces a signal called an interferogram. The recombined beams shine back through the beamsplitter, then through the sample. The interferogram generated is Fourier Transformed (a mathematical operation). This generates a spectral signature unique to that sample. The laser is used to calibrate the wavelength. The detector converts the infrared signal into an electrical signal.

Overall Schematic of an FTIR

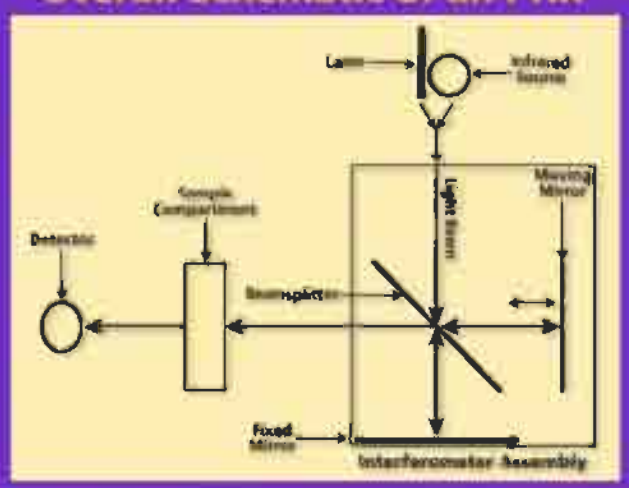

ICRC

Materials Combustion Research Facility

Each 24"x 48" sheet was cut into 2.5"x 12" pieces for flammability testing. The adjoining pieces were cut into pieces 2.5"x 1" for the FTIR analysis, so the FTIR samples could be directly compared with the flammability samples.

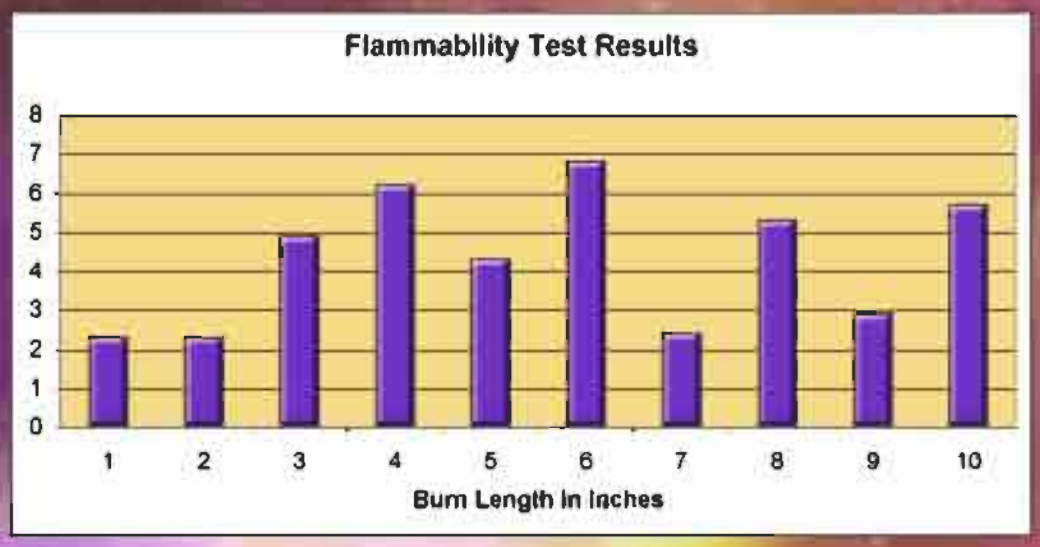

FTIR Sample Preparation Methods:

1. Cut out thin sections with diamond-tipped knife to plane off thin sections of the material, which were then pressed to the correct thickness.
2. Cut out small cubes with scissors and press a cross section of the sample several times until attaining the right thickness.

FTIR DATA RESULTS

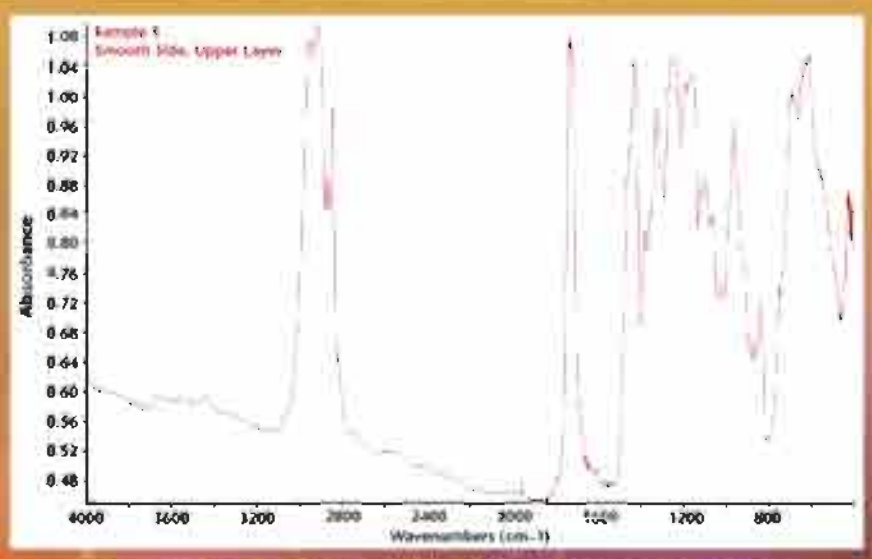

Sample 5, Smooth Side, Upper Layer

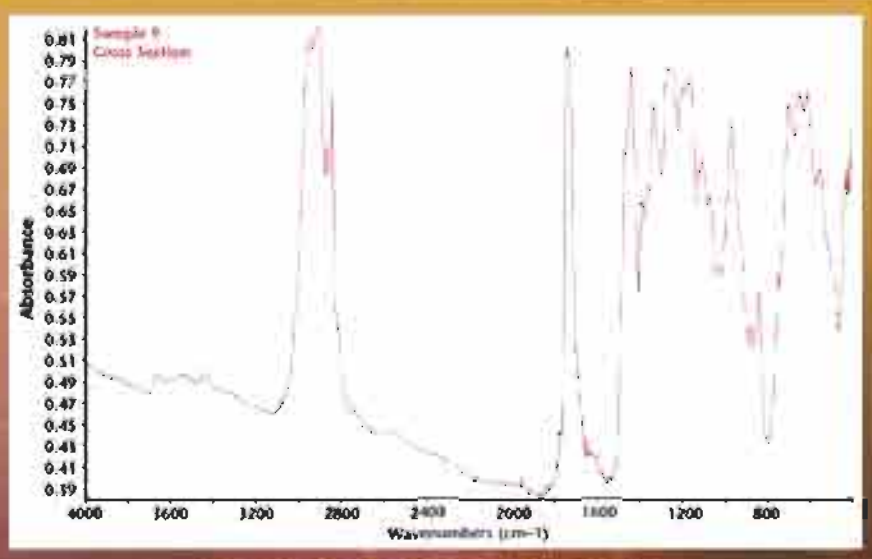

Sample 9, Cross Section

Communication with the manufacturer revealed no apparent reason for the variations in flammability. There was speculation that an unknown organotin (concentration 0.1%–3.0%) could cause the variations; however, there was no obvious spectroscopic clue that an organotin was present. After running different areas of each sample numerous times, the samples appeared to be homogenous with very few differences among different portions of the Kydex sheet.
It is possible that an instrument equipped with an infrared hyperspectral array detector could be more suited to this type of screening procedure. This type instrument, instead of a single detector, has hundreds of detector elements, which could provide a rapid scan of the entire exterior of a sample.

ICRC
Materials Combustion Research Facility

Abstract on MicroDeformation Technology

MicroDeformation Technology is the newest patented material-forming technology developed by Wolverine Tube. Originally developed to fin copper tubes, Wolverine has advanced the technology to process a variety of materials, including special alloys such as Titanium, Silver, Gold, Teflon, Rubber, Plastic, etc.

MD Technology can be applied to form OD material as large as a drive shaft for a ship, or as small as mesh with hole size of 5-8 micron. There are almost unlimited applications in materials forming needs for aerospace, shipbuilding, filtration, electronics and other industries.

The first major advantage of MD material forming technology is that existing shop equipment can be utilized. No special equipment is required to apply the technology. The second major advantage of the DC forming technology is clean operation. There is no yield loss, no scrap nor lubricant to create disposal issues. The forming technique does not generate enough heat to change the properties of the material to be formed, so no special treatment of the material is required after the forming process. Additional advantages include:

- Multifunctional process to create a variety of products
- Large material base from which to choose
- Can be applied to standard metal cutting equipment
- No machining chips / no removal of base metal

Potential applications for MD forming technology includes the following:

- Reconditioning dimensions and quality of worn surfaces.
- Filtration : mesh from precious material not currently available as wire or sintered powder (Ti, zirconium, palladium).
- Surface hardening.
- Heat transfer
- Capillary structures
- Miniature heat pipes / heat exchangers
- Cooling for electronics
- Surface treatment to increase strength to the base metal

Wolverine Tube is interested to further explore applications and expand the horizon of MD Technology. We are interested to discuss applications with potential users of this unique technology.

Contact Information

Wolverine Tube, Inc.	Rob Kukowski	C.M. Ng
Suite 1000, 200 Clinton Ave	Ph (256)580-3954	(256)580-3511
Huntsville, AL 35801	e-mail kukowskir@wlv.com	ngcm@wlv.com

An Evaluation of the Oxygen Compatibility of Composite Materials

Erin H. Richardson and Joylene Hall
Chemistry Group, Materials, Processes and Manufacturing Department
Marshall Space Flight Center

Objective: To evaluate the oxygen compatibility characteristics of multiple composite materials

Mechanical Impact Bruceton "Up and Down" Method

The Mechanical Impact Test evaluates a material's resistance to ignition when mechanically impacted. A specimen is immersed in liquid or gaseous oxygen and a 20-lb plummet is dropped from 43.3 in to deliver an energy of 72 ft-lb. A reaction is determined through a flash, audible report, or obvious charring of the sample. The material meets NASA's acceptance criteria if zero reactions are noted within 20 trials at 72 ft-lb.

Representative Pretest Photo of Mechanical Impact Test Specimen

Representative Posttest Photo of Reacted Specimens. Note the Charred and Burned Material.

The Bruceton "Up and Down" Method is used to determine the drop height at which 50% of samples tested react. The height is converted to the 50% reaction energy. The test method provides a ranking for the materials — no pass/fail criteria exist for the method.

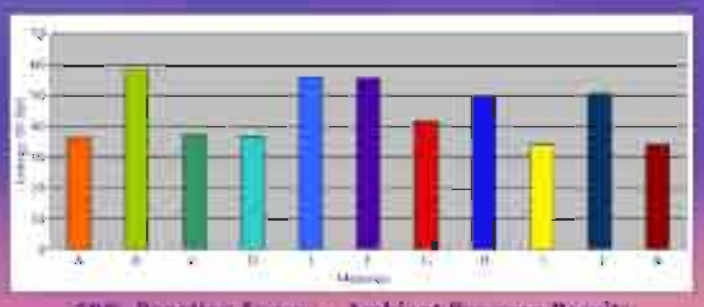

50% Reaction Energy – Ambient Pressure Results

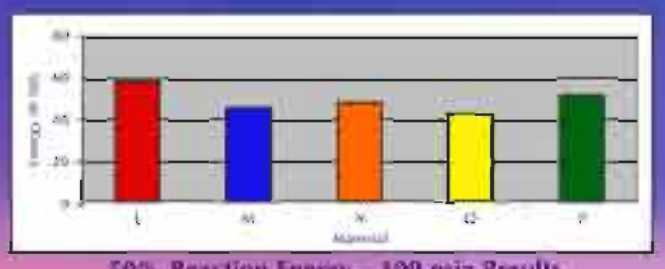

50% Reaction Energy – 100 psia Results

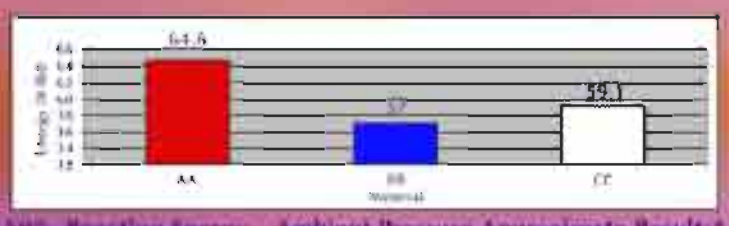

50% Reaction Energy – Ambient Pressure Approximate Results*

*Results are approximate as samples did not react consistently at the highest energy level tested.

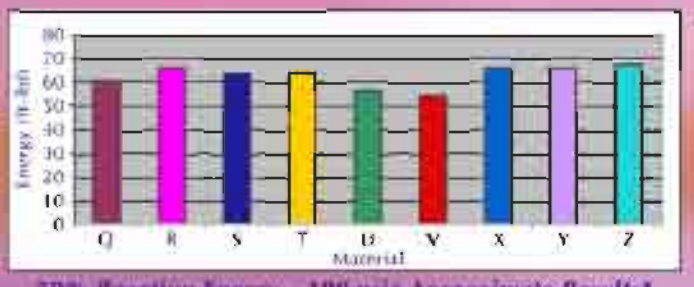

50% Reaction Energy – 100 psia Approximate Results*

*Results are approximate as samples did not consistently react at the highest energy level tested.

Materials Combustion Research Facility

NASA

Promoted Combustion

The Promoted Combustion Test evaluates the flammability characteristics of a material in 100% gaseous oxygen (GOX) when ignited at the bottom by an aluminum promoter. The specimens are 12 in long, and a minimum of five specimens must be tested. A material is considered flammable at the test conditions if one specimen burns more than 6 in.

Representative Pretest Photo of Promoted Combustion Specimen

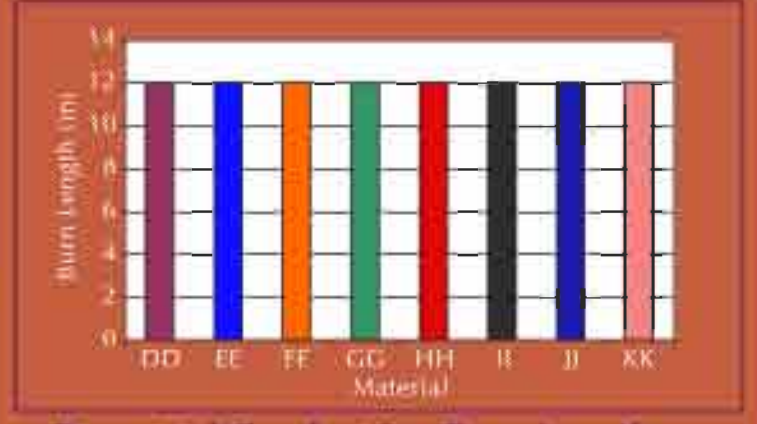

Promoted Combustion Burn Lengths – 50-psia GOX

Electrostatic Discharge

The Electrostatic Discharge (ESD) Test evaluates whether a spark is a credible ignition source for a material used in an oxygen environment. A specimen is placed in a box that is purged with gaseous oxygen for 20 to 30 s. The specimen is tested when a 5000-V, 112.5-J spark is discharged onto the surface of the specimen. A material is considered to be susceptible to ignition by ESD if it ignites and burns.

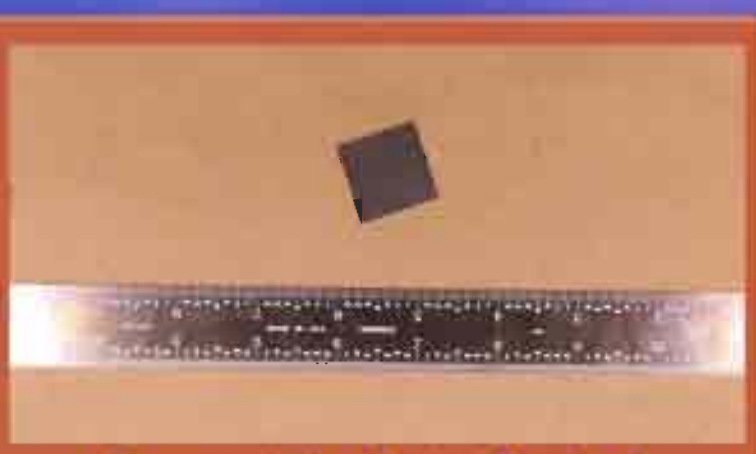

Representative Pretest Photo of Electrostatic Discharge Test Specimen

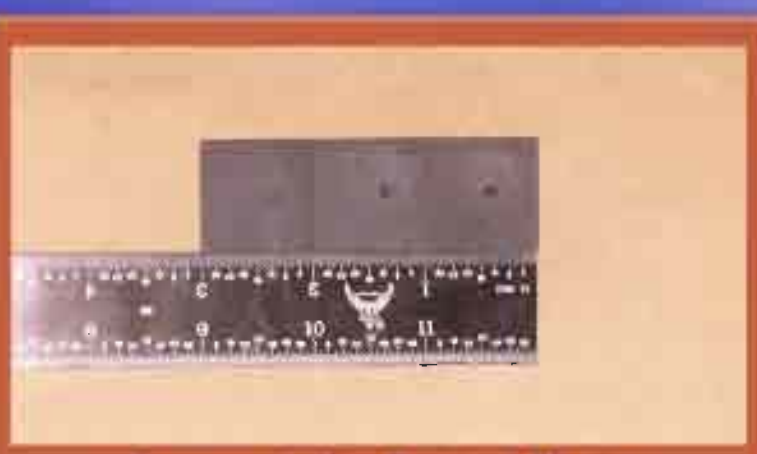

Representative Posttest Photo of Electrostatic Discharge Test Specimens

Note the surface imperfections caused by the discharge. No specimen ignited and burned.

For further information concerning this poster presentation or for other oxygen compatibility test services, contact Erin Richardson, ED36, Chemistry Group, Marshall Space Flight Center, Alabama.

Materials Combustion Research Facility

NASA

Ammonia Analysis by Gas Chromatography/Infrared Detector (GC/IRD)

Joseph P. Scott, *Integrated Concepts & Research Corporation (ICRC)*
Steve W. Whitfield, *NASA MSFC/ED36*

Methods are being developed at Marshall Space Flight Center's Toxicity Lab on a CG/IRD System that will be used to detect ammonia in low part per million (ppm) levels. These methods will allow analysis of gas samples by syringe injections. The GC is equipped with a unique cryogenic-cooled inlet system that will enable our lab to make large injections of a gas sample. Although the initial focus of the work will be analysis of ammonia, this instrument could identify other compounds on a molecular level. If proper methods can be developed, the IRD could work as a powerful addition to our offgassing capabilities.

Agilent 6890 Gas Chromatograph/Infrared System

Conditions for Analysis:
40 cc injection of 100 ppm Ammonia Gas Standard
Oven Temp: –20°C for 4 min, Ramp 50°C/min to 400°C
Carrier Gas: Helium 4.5 ml/min Constant Flow Rate
Column: Restek RT-Q-Plot, 30 m, 0.32 mm ID

Specifics of the Inlet Liner:
Joint Analytical Systems (JAS) UNIS 2000 Injection System
The inlet is cryogenically cooled using LN_2 to trap the gases on the packed liner.
Inlet Temp: –75°C for 2.5 min, Ramp 720°C/min to 250°C

Chromatogram of the Ammonia Standard

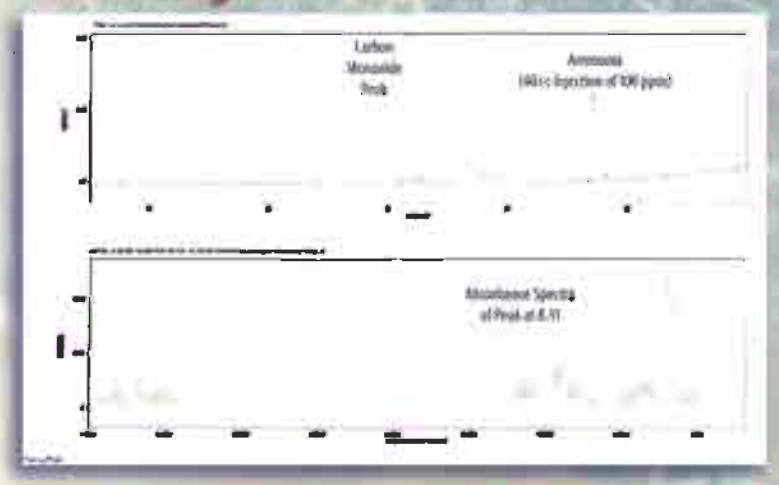

Spectral Library Identification of the Ammonia Standard

Initial development of the testing performed included:

1. Injecting known amounts of a certified gas standard (100 ppm ammonia) by gas tight syringe.
2. Determining the proper temperatures and run times for the ammonia analysis.
3. Determining the elution time and verifying the identification of the ammonia.

ICRC

Materials Combustion Research Facility

Ammonia Analysis by Gas Chromatography/Infrared Detector (GC/IRD)

Joseph P. Scott, *Integrated Concepts & Research Corporation (ICRC)*
Steve W. Whitfield, *NASA MSFC/ED36*

The research performed during this testing applies to standard NASA–STD–6001 Determination of Offgassed Products–Test 7.

Toxicity Lab: Marshall Space Flight Center performs all Materials and Flight Hardware Offgas testing in the Materials Combustion Research Facility's Toxic Offgassing Lab in Building 4623.

Toxicity Lab Oven Room: Materials and Flight Hardware Assemblies are loaded into these two ovens for testing. Chart recording devices and internal thermocouples continuously monitor the oven temperatures.

Experiment Hardware After Removal from Mounting Plate

Flight Hardware Positioned Over Test Chamber Using Lifting Bracket

Hardware Being Lowered Into Test Chamber

These pictures show the loading of the Optical Properties Monitoring experiment, slated for flight aboard the *International Space Station (ISS)*, into the Toxicity test chamber.

The Determination of Offgassed Products Test is utilized to determine the identity and quantity of volatile organic offgassed products from materials and assembled articles. Test articles are measured, weighed, and loaded into various size clean chambers. The chamber is purged with high purity air, then sealed and loaded into an oven where it will be thermally conditioned at 49 ±3 °C for 72 hours. Subsequently, the chamber is removed from the oven and allowed to cool to ambient temperature. Gas samples are collected from the chamber by syringe and analyzed using Gas Chromatography/Mass Spectrometry (GC/MS) techniques. The data obtained from this analysis determines the quantity of the material that may be flown safely in the habitable areas of the spacecraft. This test also determines if flight hardware assemblies may be flown safely in the habitable areas of the spacecraft. This test is performed to ensure the safety of the crew aboard the Space Shuttle and the *International Space Station*.

Lid of Test Chamber Being Secured

ICRC

Materials Combustion Research Facility

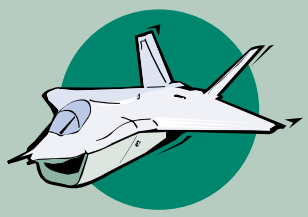

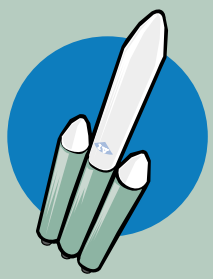

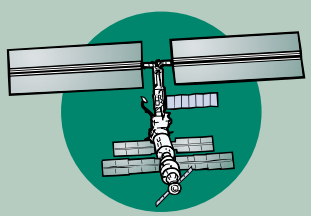

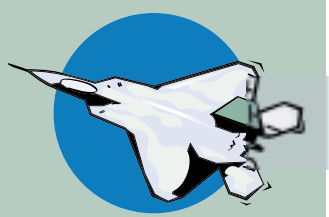

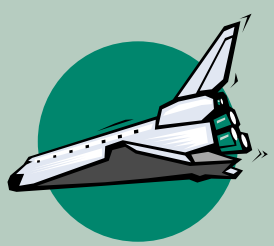

PROGRAM

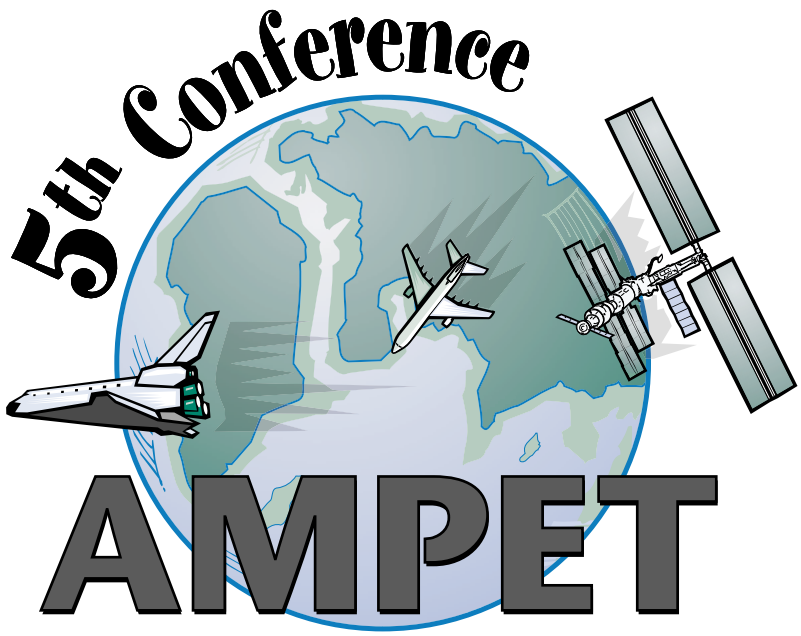

Aerospace Materials, Processes, and Environmental Technology

September 16, 17, 18, 2002
Von Braun Center • Huntsville, Alabama

Website: http://ampet.msfc.nasa.gov

NP-2002-09-131-MSFC

Fifth Conference
on
Aerospace Materials, Processes, and Environmental Technology

AMPET Conference Venues

1. Von Braun Center (Conference)
2. Huntsville Museum of Art (Welcoming Reception)
3. Hilton Huntsville (Lodging and Tour Start)

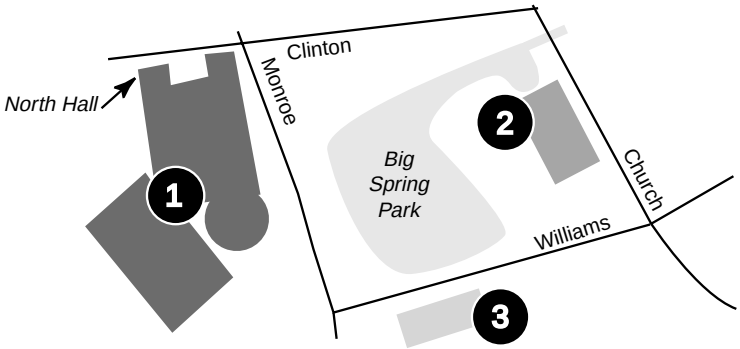

September 16, 2002

8:00 am - 12 noon	***TUTORIALS***		
	All tutorials will be conducted in the Von Braun Center North Hall Salons and Orchestra Room. See back cover for North Hall floor plan.		
7:30 am	Registration	AMPET Staff	VBC North Hall Gallery
8:00 am - 12 noon	Oxygen Compatibility	Dr. Harold Beeson, Ms. Erin Richardson	Orchestra
8:30 am - 10:00 am	Space Environmental Effects	Dr. David Edwards	Salon 1
8:30 am - 10:00 am	Section 112: MACT Program Basics	Mr. Rick Colyer	Salon 2
10:00 am - 11:30 am	Hot Cities Phenomena	Dr. Dale Quattrochi	Salon 2
10:00 am - 12 noon	Chemical Fingerprinting	Dr. William McClennan, Dr. Doris Drouant	Salon 1
12 noon - 4:30 pm	***REGISTRATION - Hilton Huntsville***		
1:00 - 4:30 pm	***PRE-CONFERENCE TOURS***		
1:00 pm	Buses depart from the Hilton Huntsville *Huntsville's Waste to Steam Facility* *The National Space Science and Technology Center*		
4:30 pm	Buses return to the Hilton Huntsville		
6:00 - 7:30 pm	***WELCOMING RECEPTION - HUNTSVILLE MUSEUM OF ART***		

Enjoy an evening of art and southern hospitality at the AMPET Welcoming Reception in the elegant Great Hall of the Huntsville Museum of Art, overlooking Big Spring Park. This nationally accredited museum is the premier visual arts center in North Alabama and Southern Tennessee. In its seven spacious galleries, visitors enjoy a wide array of exhibitions, prestigious traveling exhibitions, works by nationally and regionally acclaimed contemporary artists, and shows featuring some of the 2,300 works in the Museum's permanent collection. On exhibit throughout the AMPET Conference are "Silver Menagerie: The Betty and Charles Grisham Collection of Buccellati Animals," "Art At Play," "Views of the Collection: Our Alabama Heritage," and "The Red Clay Survey: Eighth Biennial Exhibition of Contemporary Southern Art." For additional information about the museum and these collections, visit http://www.hsvmuseum.org/.

Harpist Kathryn Hoppe will grace the reception with musical selections from her award-winning repertoire. Ms. Hoppe, a senior at Randolph School, is harpist with the Huntsville Youth Orchestra and the Alabama All State Orchestra; she also performs with the Shoals Symphony Orchestra and the Huntsville Opera Theater Orchestra. This spring, she won both the Huntsville Youth Orchestra's Concerto Competition and the Huntsville Symphony Young Artist Competition. Ms. Hoppe's elegant music is sure to entertain all at our Welcoming Reception.

SEPTEMBER 17, 2002

7:00 am	***Registration Opens - Von Braun Center North Hall Gallery***
8:00 am	***OPENING SESSION***

Conference Welcome & Introduction — Paul M. Munafo, Manager, Materials, Processes, and Manufacturing Department, Marshall Space Flight Center

Conference Welcome — Art Stephenson, Director, Marshall Space Flight Center

Keynote Addresses — Teresa Harten, Director, Environmental Technology Verification Program Environmental Protection Agency

Robert Sackheim, Assistant Director and Chief Engineer for Space Propulsion, Marshall Space Flight Center

9:15 - 10:00 am — ***Break -- Exhibit Area***

10:00 am - 12 noon — ***SESSION A***

A1 - Pollution Prevention Efforts (Salon 2)

Session Chair: Farley Davis, Marshall Space Flight Center

- Urban Plant Potentiality for VOC Detoxification
  Irene I. Patalakh, Dnipropetrovsk National University
- JSC Metal Finishing Waste Minimization Methods
  Erica N. Sullivan, Johnson Space Center
- Design for the Environment
  Gene Harm, United Space Alliance
- Waste Water Recycling at Space Launch Complex 6
  Rhonda Cardinal, Boeing
- Oxygen and Breathing Air Hardware Cleaning and Verification Technique at NASA's Johnson Space Center's Neutral Buoyancy Facility
  Pat Hudnall, SAIC

A2 - Innovative Inspection Techniques (Salon 1)

Session Chair: Rick Hess, Puget Sound Clean Air Agency

- Fatigue Crack and Porosity Measurement in Composite Materials by Thermographic and Ultrasonic Methods
  James L. Walker, Marshall Space Flight Center
- Quantitative Remaining Life Assessments for Aerospace Components using Photon Induced Positron Annihilation (PIPA)
  Douglas W. Akers, Positron Systems, Inc.
- Acoustography-Based Inspection of Composites
  Jas Sandhu, Santec Systems, Inc.
- NDE of Friction Stir Welds on the Space Shuttle External Tank
  David Kinchen, Lockheed Martin Space Systems
- Non-ODC Aircraft Oxygen Line Cleaning System
  John Herrington, Versar, Inc.

A3 - Advancements in Manufacturing and Repair (Orchestra)

Session Chair: Mel Bryant, Marshall Space Flight Center

- Hydrogen Torch Braze for SSME Nozzle Tube Repair
  Jack Weeks, Boeing-Rocketdyne
- Evaluation of New Repair Methods for Seal Surface Defects on RSRM Hardware
  Stephanie Stanley, ATK Thiokol
- Microgravity Manufacturing
  Ken Cooper, Marshall Space Flight Center
- Advanced Material Developments with Laser Engineered Net Shaping
  Glenn Williams, Marshall Space Flight Center
- Shuttle PRCS Thruster Fuel Valve Pilot Seal Extrusion -- A Cradle-to-Grave Service History Correlation
  Jess Waller, Honeywell Technology Solutions, Inc.

12 noon - 1:30 pm — ***Lunch -- Exhibits***

12:30 pm — *Demonstration: FIRST Robot Expo (Exhibit Area)*

***Fowl Play**, Lincoln County High School, Fayetteville, Tennessee*

***Midnight,** Lee High School, Huntsville, Alabama*

1:30 - 3:30 pm — SESSION B

B1 - Environmental Regulatory Issues (Salon 1)

Session Chair: Gail Murphree-Grafton, United Space Alliance

- The Puget Sound Clean Air Agency Aerospace NESHAP
  John Schantz, Puget Sound Clean Air Agency
- Green Purchasing Overview
  Rhonda Mann, United Space Alliance
- NASA's Principal Center for Review of Clean Air Act Regulations
  Marceia Clark-Ingram, Marshall Space Flight Center
- Protecting the Global Environment – The Role of Industrial Process Engineers
  Carole LeBlanc, University of Massachusetts

B2 - Advanced Materials I (Orchestra)

Session Chair: Ron Daniel, Boeing-Rocketdyne

- Metal Matrix Composite LOX Turbopump Housing via Novel Tool-less Net-Shape Pressure Infiltration Casting Technology
  Sandeep Shah, Marshall Space Flight Center
- Advancements in Binder Systems for Solid Freeform Fabrication
  Ken Cooper, Marshall Space Flight Center
- Environmentally Compatible Vapor-Phase Corrosion Inhibitor for Space Shuttle Hardware
  Howard Novak, United Space Alliance
- Evaluation of EL-Form Rhenium for Zero Erosion Materials
  Richard Foedinger, DE Technologies
- Syntactic Metals: A Survey of Current Technology
  Ray Erikson, ETA Flight Materials Group

B3 - Information Tools (Salon 2)

Session Chair: Bruce Askins, Marshall Space Flight Center

- NASA AP2 Integrated Technology Database
  David Crawford, International Trade Bridge, Inc.
- Improving Profits with Materials Optimization in Manufacturing
  Chris Nunez, Centor Software Corporation
- NASA Materials Related Lessons Learned
  Danny Garcia, Marshall Space Flight Center
- Colossal Tooling Design: 3D Simulation for Ergonomic Analysis
  Steve Hunter, Mississippi State University

3:30 - 4:00 pm — Break -- Exhibits

4:00 - 5:30 pm — SESSION C

C1 - Evaluation of Solvent Substitutes (Salon 1)

Session Chair: Howard Novak, United Space Alliance

- Selection of a Non-ODC Solvent for Rubber Processing Equipment Cleaning
  Richard Morgan, ATK Thiokol
- Case Study on Hazardous Chemical Replacement – Solvent Paint Strippers Replaced by Dry Media Blasting
  Richard Buckholz, Vought Aircraft Industries, Inc.
- Ozone Friendly Solvent Alternatives for Aerospace Applications
  Abid Merchant, DuPont Fluoroproducts

C2 - Advanced Materials II (Salon 2)

Session Chair: Jill Keen, ATK Thiokol

- Optical Properties of Thin Film Molecular Mixtures
  Donald A. Jaworske, Glenn Research Center
- Development of Lightweight Material using High Strength Fibers against Space Debris Impacts
  Makoto Tanaka, Tokai University
- Replacement of Ablators with Phase-Change Material for Thermal Protection of STS Elements
  Raj Kaul, Marshall Space Flight Center

C3 - Technical Standards and Aerospace Materials (Orchestra)

Session Chair: Paul Gill, Marshall Space Flight Center

- NASA Technical Standards Program
  William Vaughan, The University of Alabama in Huntsville
- Standardization Efforts for Mechanical Testing and Design of Advanced Ceramic Materials and Components
  Jonathan Salem, Glenn Research Center
- Standards Development Activities at WSTF
  Harold Beeson, White Sands Test Facility

4:00 - 5:30 pm — SESSION C (concluded)

C1 (concluded)

- Evaluation of Cleaning Solvents for Oxygen Systems
  Eric Eichinger, Boeing

C2 (concluded)

- Using Isothermal Microcalorimetry to Determine Compatibility of Structural Materials with High-Test Hydrogen Peroxide (HTP) Propellant
  Rudy Gostowski, Marshall Space Flight Center

C3 (concluded)

- Corrosion of Highly Specular Vapor Deposited Aluminum (VDA) on Earthshade Door Sandwich Structure
  Daniel Plaskon, Jet Propulsion Laboratory

5:30 - 6:30 pm — EXHIBITORS RECEPTION -- Exhibit Area

6:00 - 7:00 pm — POSTER SESSION -- North Hall Gallery

Instructions for Poster Presenters

- Complete poster assembly in the North Hall Gallery by 9:30 am on Tuesday, September 17. You may set up your poster as early as Monday afternoon.
- Remove posters between 2 pm and 6 pm Wednesday, September 18.
- Be available at your poster site during the Poster Session.
- The Break-Out Room is reserved from 7 am to 4 pm Wednesday for one-on-one or round-table discussions about your poster topic. Reserve space at the conference registration desk.

Friction Stir Welding of Tapered Thickness Welds using an Adjustable Pin Tool
Glynn Adams, Lockheed Martin Space Systems

Automatic Ply Verification
Scott Blake, Assembly Guidance

Flammability Testing Igniter Characteristics
Carl D. Engel, Qualis Corporation

High Temperature Thermographic Phosphor Coatings Development
Shawn Goedeke, Tennessee Technological University

SLI Complex Curvature Friction Sti Weld Risk Reduction Program
Paula J. Hartley, Lockheed Martin Space Systems

Introduction to Proton Microscopy
William A. Hollerman, University of Louisiana at Lafayette

Thermo-Optical and Mechanical Property Testing of Candidate Solar Sail Materials
William A. Hollerman, University of Louisiana at Lafayette

Composite LOX Tank Development
Michael C. McBain, Lockheed Martin Space Systems

Correlating Flammability of Materials with FTIR Analysis Test Results
Robin E. Moore, ICRC

MicroDeformation Technology
Chun Man Ng, Wolverine Tube, Inc.

An Evaluation of the Oxygen Compatibility of Composite Materials
Erin Richardson, Marshall Space Flight Center

Ammonia Analysis by Gas Chromatograph/Infrared Detector (GC/IRD)
Joseph P. Scott, ICRC

Poster Session Format

- Presentations will be 5 minutes, followed by 5-minute question-and-answer periods.
- Presentations will be repeated throughout the Poster Session length.
- Detailed discussions can be scheduled with the presenter in the Break-Out Room from 7 am to 4 pm Wednesday.

People's Choice Award

Poster Session visitors will choose a presentation to receive the People's Choice Award.

- Posters will be judged on relevance, creativity, and speaker's presentation.
- If you attend at least 4 presentations, you may vote for 3 presentations.
- The presentation receiving the most votes will win the People's Choice Award. Presentations that receive the second and third most votes will win runner-up prizes.
- The People's Choice Award and other poster recognitions will be presented at the Wednesday luncheon.

SEPTEMBER 18, 2002

8:00 - 10:00 am — SESSION D

D1 – Surface Cleanliness Inspections (Salon 2)

Session Chair: Dewitt Burns, Marshall Space Flight Center

- Fluorescent Cleaning Process
  Jim Deardorff, Superior Coatings, Inc.
- Analysis Of Non-Volatile Residues with a Standard FTIR Accessory, The VSphere™
  Martin Szczesniak, Surface Optics Corporation
- Use of FT-IR Analysis to Support Contamination Studies for Bonding Surfaces
  Richard Boothe, Marshall Space Flight Center
- A Study of Stains on Metals using Infrared Hyperspectral Imaging
  G. L. Powell, Y-12 National Security Complex

D2 – Materials Test Methods and Evaluation I (Salon 1)

Session Chair: Ben Coby, Boeing-Rocketdyne

- Corrosion Prevention Compound Evaluation Method
  Sarah J. H. Kuhlman, University of Dayton Research Institute
- Infrared Spectroscopy as a Chemical Fingerprinting Tool
  Tim Huff, Marshall Space Flight Center
- Reference Material Kydex-100 Test Data Message for Flammability Testing
  Carl Engel, Qualis Corporation
- The Effect of Gravity on the Combustion Synthesis of Porous Biomaterials
  Martin Castillo, Colorado School of Mines
- The Effect of Molding and Machining on the Dimensional Stability of Neoflon CTFE M400H Polychlorotrifluoroethylene Rod Stock and Valve Seats
  Jess Waller, Honeywell Technology Solutions, Inc.

D3 – Advanced Manufacturing Research (Orchestra)

Session Chair: Bruce Brailsford, University of New Orleans

- Cryogenic Temperature Effects on Performance and NDE of Polymer Composites
  David Hui, University of New Orleans
- Toward Healing of Composite Cryogenic Tanks
  Richard Patton, Mississippi State University
- Prediction of Microcracking Induced Permeability of Cryogenic Composite Tanks
  John Whitcomb, Texas A&M University
- Solid-State Friction Stir Welding
  George Buchanan, Tennessee Technological University
- Non-Autoclave Processing of Large Re-Usable Aerospace Structures
  Al Loos, Virginia Polytechnic Institute

10:00 - 10:30 am — Break -- Exhibits

10:15 am — *Demonstration: Thermographic Inspection (Exhibit Area)*

James L. Walker, Marshall Space Flight Center

10:30 am - 12:30 pm — SESSION E

E1 – Environment-Friendly Cleaning Products and Processes (Salon 2)

Session Chair: Rick Golde, ATK Thiokol

- Precision Clean Hardware: Maintenance of Fluid Systems Cleanliness
  Michael D. Pedley, Johnson Space Center
- Novec™ Engineered Fluids
  David Hesselroth, 3M Performance Materials Division

E2 – Materials Test Methods and Evaluation II (Salon 1)

Session Chair: Harold Beeson, White Sands Test Facility

- Durable Surface Contamination Standards
  Paul Shelley, Boeing
- Effects of Thermal Exposure on Properties of Al-Li Alloys
  Sandeep Shah, Marshall Space Flight Center

E3 – Developments in Metallic Processes (Orchestra)

Session Chair: Ralph LeBoeuf, Lockheed Martin Space Systems

- High Strength and Wear Resistant Aluminum Alloy for High Temperature Applications
  Jonathan A. Lee, Marshall Space Flight Center
- Aluminum Lithium Alloys Use for Reusable Future Launcher Cryogenic Metallic Tanks
  Eric Grosjean and Jean-Pierre Bonnafe, EADS Launch Vehicles

10:30 am - 12:30 pm — SESSION E (concluded)

E1 concluded

- Cleaning to 6 Sigma Standards
  Donald Bowden, Bowden Industries
- Clean Machining with New Volatile Lubricant Fluid
  David Hesselroth, 3M Performance Materials Division

E2 concluded

- Hydrogen Permeability of Composite Tank Materials under Biaxial Strain
  Erik Stokes, Southern Research Institute
- Micro-Raman Analysis of Irradiated Diamond Films
  R. L. Newton, Marshall Space Flight Center

E3 concluded

- Vacuum Plasma Spray Forming of Copper Alloy Liners for Regeneratively Cooled Liquid Rocket Combustion Chambers
  Frank Zimmerman, Marshall Space Flight Center
- JG-PP Lead-Free Solder Project
  Brian Greene, International Trade Bridge, Inc.
- Friction Stir Process Mapping Methodology
  Alex Kooney, Lockheed Martin Space Systems

12:30 pm - 2:00 pm — Lunch -- Exhibits

1:00 pm — Poster Session People's Choice Award Presentation (Exhibit Area)

1:15 pm

Demonstration: Adiabatic Compression (Exhibit Area)
Eddie Davis, Marshall Space Flight Center

2:00 pm - 4:00 pm — SESSION F

F1 – Synthesis of Nano Materials (Salon 1)

Session Chair: Michael Watson, Marshall Space Flight Center

- Synthesis and Characterization of Carbon Nanotubes for Reinforced and Functional Applications
  Shen Zhu, USRA
- Synthesis and Coating of Nanoparticles
  Abraham Ulman, Polytechnic University
- A New Process for the Deposition of Nanostructured Thin Films from Size-Classified Nanoparticles
  Renato P. Camata, The University of Alabama at Birmingham
- A "Ship-in-the-Bottle Approach" to Synthesis of Nano Materials via Sonolysis
  Devinder Mahajan, Brookhaven National Laboratory
- Development of High Performance Nanocomposite Pyroelectric Detectors: a Possible Approach
  A. K. Batra, Alabama A&M University

F2 – Composite Cryotank Processing (Orchestra)

Session Chair: James Walker, Marshall Space Flight Center

- Rotational Molding of Thermotropic Liquid Crystal Polymers
  Martin Rogers, Luna Innovations, Inc.
- Manufacturing Process Simulation of Large-Scale Cryotanks
  Steven Phillips, Marshall Space Flight Center
- Development of Segmented Composite Toroidal Tanks
  Thomas DeLay, Marshall Space Flight Center
- Linerless Tanks for Space Application: Design and Manufacturing Considerations
  Brian Jones, Kaiser Compositek, Inc.

4:00 pm — END OF CONFERENCE

VBC North Hall Floor Plan

N

First Floor

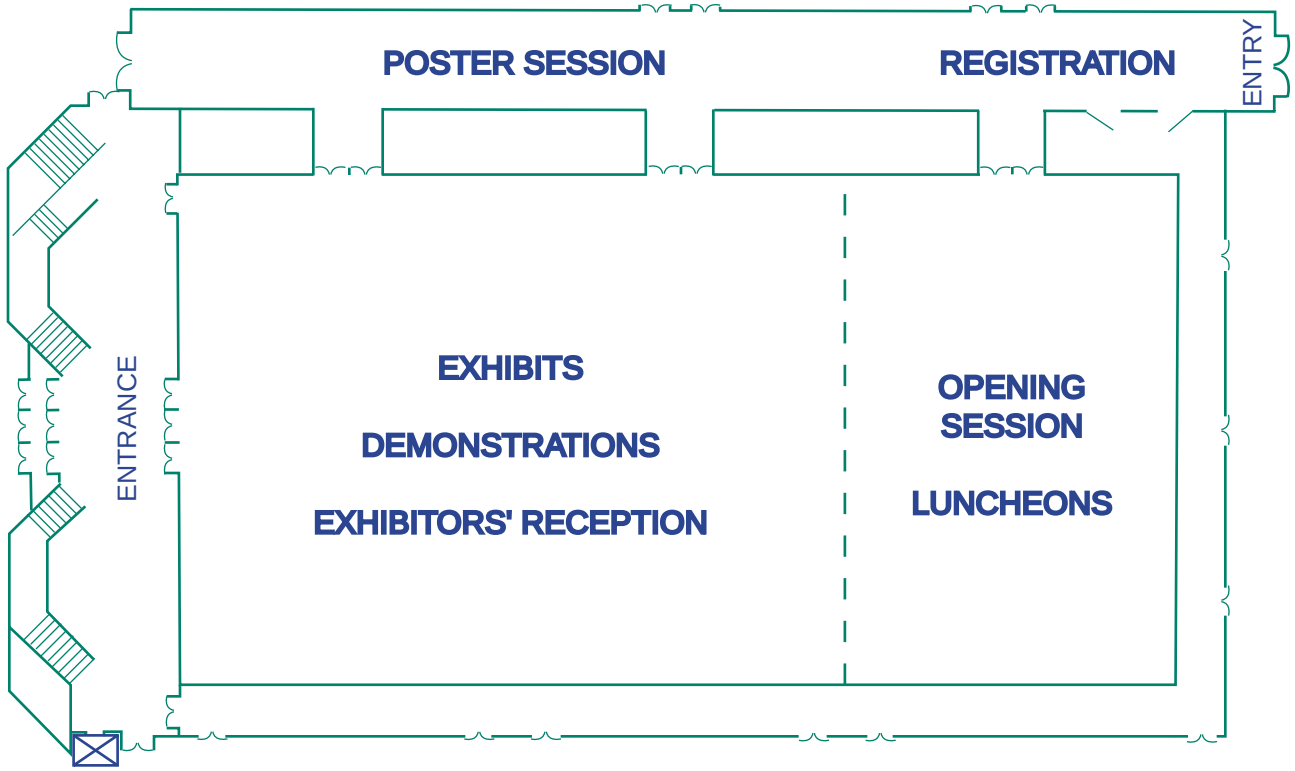

Elevators

Second Floor

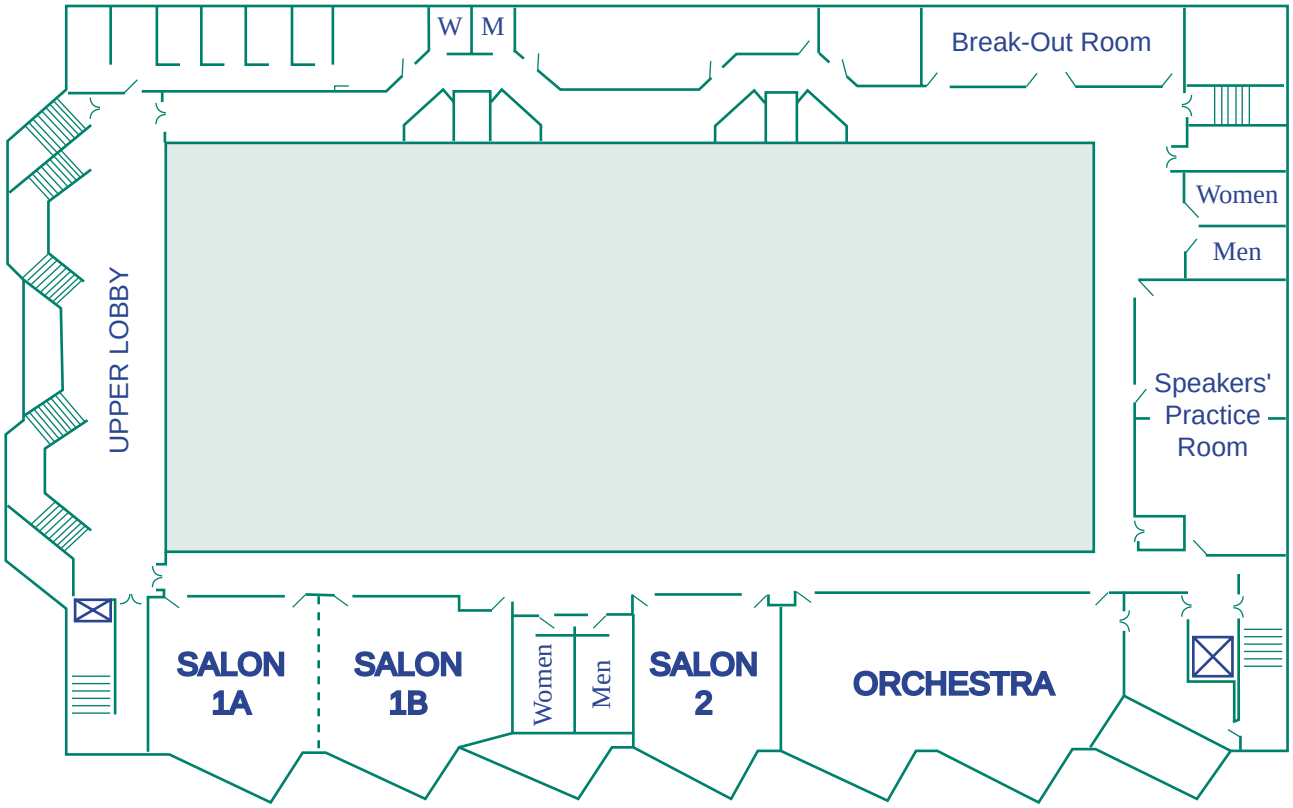

Name	Address 1	Address 2	City	State	Zip	Country	Association	Phone	E-mail	Role
Abfalter, Gary	300 College Park	KL545	Dayton	OH	45469	USA	University of Dayton Research Institute	937-229-4704	abfalter@udri..udayton.edu	Speaker
Adams, Glynn	Michoud Assembly Facility	PO Box 29304	New Orleans	LA	70189	USA	Lockheed Martin - Michoud Operations	504-257-1510	glynn.adams@maf.nasa.gov	Poster
Aggarwal, Pravin	Marshall Space Flight Center	ED22	Huntsville	AL	35812	USA	NASA/MSFC	256-544-5345	Pravin.K.Aggarwal@nasa.gov	Attendee
Akers, Doug	6151 N. Discovery Way		Boise	ID	83713	USA	Positron Systems	208-672-1923	curtr@positronsystems.com	Speaker
Albyn, Keith	Marshall Space Flight Center	ED31	Huntsville	AL	35812	USA	NASA/MSFC	256-544-8011	Keith.C.Albyn@nasa.gov	Attendee
Allen, John	Marshall Space Flight Center	ED38	Huntsville	AL	35812	USA	NASA/MSFC	256 544-1026	John.D.Allen@nasa.gov	Attendee
Allen, Trudy	Marshall Space Flight Center	SD46	Huntsville	AL	35812	USA	ICRC	256-544-6088	trudy.l.allen@msfc.nasa.gov	Attendee
Andrasik, John	300 Aerospace Parkway		Brookpark	OH	44142	USA	ZIN Technologies, Inc.	216-977-0327	john.andrasik@grc.nasa.gov	Attendee
Antolino, Ed	56 Hudson Street		Northborough	MA	1532	USA	Matec Instruments	508-393-0155		Exhibitor
Askins, Bruce	Marshall Space Flight Center	ED38	Huntsville	AL	35812	USA	NASA/MSFC	256-544-1096	Bruce.Askins@nasa.gov	Session Chair
Atwood, Clint	PO Box 5800, MS-1008		Albuquerque	NM	1008	USA	Sandia National Laboratories	505-844-0816	datwoo@sandia.gov	Attendee
Auchterlonie, Carla	2100 Market St. NE		Decatur	AL	35601	USA	Wolverine Tube, Inc.	256-580-3954		Exhibitor
Babai, Majid	Marshall Space Flight Center	ED34	Huntsville	AL	35812	USA	NASA/MSFC	256-544-2795	majid.k.babai@nasa.gov	Speaker
Baker, Kathy	Marshall Space Flight Center	ED36	Huntsville	AL	35812	USA	ICRC	256-961-0357	Kathy.Baker@msfc.nasa.gov	Attendee
Barre, Kevin	13800 Old Gentilly Rd		New Orleans	LA	70129	USA	Lockheed Martin Space Systems Company	504-257-4188	Kevin.J.Barre@maf.nasa.gov	Exhibitor
Barret, Chris	Marshall Space Flight Center	TD40	Huntsville	AL	35812	USA	NASA/MSFC	256-544-7118	Chris.Barret-1@nasa.gov	Attendee
Batra, A.K.	Micrgravity Science Laboratory	PO Box 1268	Normal	AL	35762	USA	Alabama A&M University	256-858-8109	abatra@aamu.edu	Speaker
Beeson, Harold	White Sands Test Facility	PO Box 20	Las Cruces	NM	88004-0020	USA	NASA/WSTF	505-524-5542	hbeeson@nasa.gov	Speaker (tutorial)/Session Chair
Bell, Leon	Marshall Space Flight Center	ED18	Huntsville	AL	35812	USA	NASA/MSFC			Attendee
Berryman, Richard	8152 Lindenwood Drive		Huntington Beach	CA	92646-1779	USA	Northrop Grumman Electronic Systems	626-812-1907	Richard.Berryman@NorthropGrur	Attendee
Bishop, Ken	56 Hudson Street		Northborough	MA	1532	USA	Matec Instruments	508-393-0155		Exhibitor
Blake, Scott	315 Littleton Road		Chelmsford	MA	01824	USA	Assembly Guidance	978-244-1166	sb@assemblyguide.com	Poster
Blalock, Carol	Marshall Space Flight Center	ED30	Huntsville	AL	35812	USA	NASA/MSFC	256-544-2335	Carol.A.Blalock@nasa.gov	Staff
Blevins, Elana	PO Box 9008	Marshall Space Flight Center	Huntsville	AL	35812	USA	Lockheed Martin	256-544-2772	elana.c.blevins@msfc.nasa.gov	Attendee
Boland, Edward F.	700 Blair Road		Carteret	NJ	07008	USA	Englehard-CLAL LP	732-205-5727	ed.boland@engelhard.com	Attendee
Bonnafe, Jean-Pierre	66 route de Verneuil-BP 3002	78133 Les Mureaux	Cedex			France	EADS-LV		jean-pierre.bonnafe@launchers.e	Speaker
Boothe, Richard	Marshall Space Flight Center	ED31	Huntsville	AL	35812	USA	NASA/MSFC	256-544-3028	richard.e.boothe@nasa.gov	Speaker
Bowden, Donald R.	1004 Oster Drive, NW		Huntsville	AL	35816	USA	Bowden Industries, Inc.	256-382-3700	Helen.Sainker@bowdenindustries	Speaker
Brailsford, Bruce	University of New Orleans	National Center for Advanced Manufacturing	New Orleans	LA		USA	University of New Orleans	504-257-0931	bbrailsf@uno.edu	Session Chair
Brobst, Keith E.	316 Henderson Ct.		Berryville	VA	22611	USA	3M Company	1-800-603-0377	kebrobst@mmm.com	Exhibitor
Brown, Christina	100 CTC Drive		Johnstown	PA	15904	USA	International Trade Bridge, Inc			Exhibitor
Brown, Greg	1103 Putman Drive		Huntsville	AL	35816	USA	Brown Precision, Inc.	256-830-1990		Exhibitor
Brown, Michael	The Millenium Center	RR1, Box 100B	Triadelphia	WV	26059-9707	USA	Touchstone Research Laboratory	304-547-5800	mrb@trl.com	Attendee
Bryant, Mel	Marshall Space Flight Center	MP21	Huntsville	AL	35812	USA	NASA/MSFC	256-544-0825	melvin.A.bryant@nasa.gov	Session Chair
Bryson, Craig	Marshall Space Flight Center	ED32	Huntsville		35812	USA	NASA/MSFC	256-544-2553	Charles.C.Bryson@nasa.gov	Attendee
Buchanan, George	Department of Civil and Environmental Engineering		Cookeville	TN	38505	USA	Tennessee Technological University	931-372-3486	gbuchanan@tntech.edu	Speaker
Buckholz, Richard E.	1801 E. Airport Road	M/S F16-077	Stuart	FL	3499-4012	USA	Vought Aircraft Industries, Inc.	772-220-5665	BUCKHRI@voughtaircraft.com	Speaker
Burdo, Anna	315 Littleon Road		Chelmsford	MA	08124	USA	Assembly Guidance	978-244-1166		Exhibitor
Burger, Nancy	PO Box 368		Jacksonville	AR	72078	USA	Modern Chemical, Inc.	501-988-1311		Exhibitor
Burlingame, Steve	Marshall Space Flight Center	ED34	Huntsville	AL	35812	USA	NASA/MSFC	256-544-8860	Steven.W.Burlingame@nasa.gov	Attendee
Burns, Dewitt	Marshall Space Flight Center	ED31	Huntsville	AL	35812	USA	NASA/MSFC	256-544-252	Dewitt.Burns@nasa.gov	Session Chair
Burnum, James	Marshall Space Flight Center	MP51	Huntsville	AL	35812	USA	NASA/MSFC	256-544-4008	James.R.Burnum@nasa.gov	Attendee
Camata, Renato	1300 University Blvd	CH 310	Birmingham	AL	35294-1170	USA	University of Alabama in Birmingham	205-934-8143	camata@uab.edu	Speaker
Campbell, David	1302 E. 3075 N.		No. Ogden	UT	84414	USA	ATK Thiokol	435-863-3463	David.Campbell@atk.com	Attendee
Campbell, Michael	1780 Rohrerstown Road		Lancaster	PA	17601-2334	USA	Hamilton Precision Metals	717-569-7061		Exhibitor
Carruth, Ralph	Marshall Space Flight Center	ED30	Huntsville	AL	35812	USA	NASA/MSFC	256-544-7647	Ralph.Carruth@nasa.gov	Attendee
Castaneda, Bill	7819 Riverside Dr.		Sumner	WA	98309	USA	American Autoclave Company	888-796-3373		Exhibitor
Castillo, Martin	1500 Illinois Street		Golden	CO	80401	USA	Colorado School of Mines	303-273-3091	macastil@mines.edu	Speaker
Cardinal, Rhonda	PO Box 5219		Vandenberg AFB	CA	93437	USA	The Boeing Company	805-606-6340	rhonda.e.cardinal@boeing.com	Speaker
Choate, Tab	Marshall Space Flight Center		Huntsville	AL	35812	USA	Boeing	256-544-6830	Tab.N.Choate@msfc.nasa.gov	Attendee
Clark, Johnnie	Marshall Space Flight Center	ED34	Huntsville	AL	35812	USA	NASA/MSFC	256-544-2799	Johnnie.J.Clark@nasa.gov	Attendee
Clark, Paul A.	1290 Flint Drive		Christiansburg	VA	24073	USA		540-818-1549	clarkp@megahits.com	Attendee
Clark-Ingram, Marcei	Marshall Space Flight Center	ED36	Huntsville	AL	35812	USA	NASA/MSFC	256-544-6229	Marceia.A.Clark-Ingram@nasa.go	Speaker/Committee
Coby, Ben	Marshall Space Flight Center	MP21	Huntsville	AL	35812	USA	Boeing	254-544-2781	Ben.Coby@msfc.nasa.gov	
Colberg, Wendell	Marshall Space Flight Center	ED30	Huntsville	AL	35812	USA	NASA/MSFC	256-544-2725	Wendell.R.Colberg@msfc.nasa.g	Committee
Cole, Ross	9605 Highway 80 West		Fort Worth	TX	76116	USA	DCM Clean Air Products, Inc.	817-654-2829		Exhibitor
Coleman, Sandra	Marshall Space Flight Center	SD03	Huntsville	AL	35812	USA	NASA/MSFC			Attendee
Collins, Brian	Marshall Space Flight Center	MP71	Huntsville	AL	35812	USA	NASA/MSFC	256-544-2943	Brian.W.Collins@nasa.gov	Attendee
Colyer, Rick	Office of Air Quality Planning and Standards	Mail Drop C504-03	Research Triangle Park	NC	27711	USA	Environmental Protection Agency		Colyer.Rick@epamail.epa.gov	Speaker (tutorial)
Cook, Beth	Marshall Space Flight Center	ED30	Huntsville	AL	35812	USA	NASA/MSFC	6-544-2545	Mary.B.Cook@nasa.gov	Committee
Cooper, Carol	Marshall Space Flight Center	ED36	Huntsville	AL	35812	USA	ICRC	256-544-4794	Carol.Cooper@msfc.nasa.gov	Staff
Cooper, John	56 Hudson Street		Northborough	MA	1532	USA	Matec Instruments	508-393-0155		Exhibitor
Cooper, Ken	Marshall Space Flight Center	ED34	Huntsville	AL	35812	USA	NASA/MSFC	256-544-8591	Kenneth.G.Cooper@nasa.gov	Speaker
Corl, Mary Lynn	1103 Putman Drive		Huntsville	AL	35816	USA	Brown Precision, Inc.	256-830-1990	mlcorl@brownpreci.com	Exhibitor
Crawford, David	1308 Research Park Drive		Beavercreek	OH	45432	USA	International Trade Bridge, Inc	937-431-1990	crawfordd@itb-inc.com	Speaker
Crawford, Robert	1780 Rohrerstown Road		Lancaster	PA	17601-2334	USA	Hamilton Precision Metals	717-569-7061		
Dahlgren, Jeff	5700 Skylab Road		Huntington Beach	CA	92647	USA	Airtech Advanced Materials	714-899-8100		Exhibitor
Dalton, David	Marshall Space Flight Center	ED36	Huntsville	AL	35812	USA	Qualis Corporation	256-544-4377	David.B.Dalton@msfc.nasa.gov	Staff
Daniel, Ron	Marshall Space Flight Center	Bldg. 4711, Room W155	Huntsville	Al	35812	USA	Boeing-Rocketdyne	256-544-3701		Session Chair
Davis, Eddie	Marshall Space Flight Center	ED36	Huntsville	AL	35812	USA	NASA/MSFC	256-544-2490	Samuel.E.Davis@nasa.gov	Committee/Demonstration
Davis, Farley	Marshall Space Flight Center	AD10	Huntsville	AL	35812	USA	NASA/MSFC	256-544-6935	Farley.Davis@nasa.gov	Session Chair
Davis, Joe	Marshall Space Flight Center	ED38	Huntsville	AL	35812	USA	NASA/MSFC	256-544-1090	Joe.D.Davis@nasa.gov	Attendee
Davis, John	Marshall Space Flight Center	ED35	Huntsville	AL	35812	USA	NASA/MSFC	256-544-2494	john.davis@nasa.gov	Attendee
Deardorff, Jim	1713 Bryan Street	PO Box 317	Chilicothe	MO	64601	USA	Superior Coatings, Inc	660-646-6355	jdeardorffsupct@yahoo.com	Speaker
Deem, Victoria J.	894 Pine Baugh		Rockledge	FL	32955	USA	United Space Alliance-Logistics	321-861-5879	victoria.j.deem@usaqo.ksc.nasa.	Attendee
Delay, Tom	Marshall Space Flight Center	ED34	Huntsville	AL	35812	USA	NASA/MSFC	256-544-1131	Thomas.K.Delay@nasa.gov	Speaker
DeMeza, Norman E.	PO Box 5800		Albuquerque	NM	87185-0960	USA	Sandia National Laboratories	504-257-2523	nedemez@sandia.gov	Exhibitor
Deramus, Gordon	Marshall Space Flight Center	ED33	Huntsville	AL	35812	USA	NASA/MSFC	256-544-2597	Gordon.E.Deramus@nasa.gov	Attendee
DeWeese, Darrell	Marshall Space Flight Center	ED34	Huntsville	AL	35812	USA	NASA/MSFC	256-544-5120	Charles.D.DeWeese@nasa.gov	Attendee
Dooley, Craig D.	13800 Old Gentilly Rd	Dept. 3614	New Orleans	LA	70129	USA	Lockheed Martin Space Systems Company	504-257-0204	craig.d.dooley@lmco.com	Attendee
Doty, Tom	5700 Skylab Road		Huntington Beach	CA	92647	USA	Airtech Advanced Materials	714-899-8100		Exhibitor
Drouant, Doris	Michoud Assembly Facility		New Orleans	LA	70129	USA	Lockheed Martin - Michoud Operations	504-257-0228	Doris.s.drouant@maf.nasa.gov	Speaker (tutorial)

Edwards, David	Marshall Space Flight Center	ED31	Huntsville	AL	35812	USA	NASA/MSFC	256-544-4081	David.L.Edwards@nasa.gov	Speaker (tutorial)
Eichinger, Eric	5001 Bolsa Avenue		Huntington Beach	CA	90247	USA	West Boeing	714-372-5197	eric.c.eichinger@Boeing.com	Speaker
Elliott, Louie	7001 Shallowford Road		Chattanooga	TN	37421	USA	Accurate Automation Corporation	423-894-4646	lelliott@accurate-automation.co	Attendee
Engel, Carl D.	Marshall Space Flight Center	ED36	Huntsville	AL	35812	USA	Qualis Corporation	256-544-6032	carl.engel@msfc.nasa.gov	Speaker
Engel, Mary	6767 Old Madison Pike	Suite 105	Huntsville	AL	35806	USA	Qualis Corporation	256-971-1707	mary.engel@qualis-corp.com	Attendee
Ennis, Doug						USA	SMDC			Attendee
Erikson, Ray	Two Collins Road		Wakefield	MA	01880-2513	USA	Flight Materials Group	781-246-8239	ray.erikson@flightmaterials.com	Speaker/Poster
Evelyn, Leslie	4900 Meridian Street		Normal	AL	35762	USA	Alabama A&M University	256-851-5866	leslie@aamuri.aamu.edu	Exhibitor
Finckenor, Miria	Marshall Space Flight Center	ED31	Huntsville	AL	35812	USA	NASA/MSFC	256-544-9244	Miria.Finckenor@nasa.gov	Attendee
Fisk, Mike	Sverdrup Technology	Marshall Space Flight Center	Huntsville	AL	35812	USA	Sverdrup Technology	256-544-6456		Exhibitor
Foedinger, Richard	3620 Horizon drive		King of Prussia	PA	19406	USA	DE Technologies	610-270-9700	rfoedinger@detk.com	Speaker
Fossett, Karen	Detroit Operations Unit	1115 East Whitcomb Avenue	Madison Heights	MI	48071	USA	ICRC	248-823-4272	kfossett@icrc-detroit.net	Staff
Frazier, Michael	Marshall Space Flight Center	ED34	Huntsville	AL	35812	USA	NASA/MSFC	256-544-4968	Michael.Frazier@nasa.gov	Attendee
Frye, Carole	Marshall Space Flight Center		Huntsville	AL	35812	USA	Earth Tech	256-885-7474		Attendee
Funk, Joan	Marshall Space Flight Center	UP50	Huntsville	AL	35812	USA	NASA/MSFC	256-544-3298	Joan.Funk@nasa.gov	Attendee
Garcia, Danny	Marshall Space Flight Center	ED41	Huntsville	AL	35812	USA	NASA/MSFC	256-544-4138	Danny.Garcia-1@nasa.gov	Speaker
Gardner, Terrie	Marshall Space Flight Center	ED35	Huntsville	AL	35812	USA	NASA/MSFC	256-544-4549	Terrie.M.Gardner@nasa.gov	Attendee
Gholston, Susan	Marshall Space Flight Center	ED36	Huntsville	AL	35812	USA	ICRC	256-961-0350	Susan.Gholston@msfc.nasa.gov	Staff
Giles, John	13350 US Hwy 19 N	MS 225-1	Clearwater	FL	33764	USA	Honeywell Space Systems	727-539-2270	john.giles@honeywell.com	Attendee
Gill, Paul	Marshall Space Flight Center	ED40	Huntsville	AL	35812	USA	NASA/MSFC	256-544-2557	paul.gill@nasa.gov	Session Chair
Glover, Steve	Marshall Space Flight Center	MP71	Huntsville	AL	35812	USA	NASA/MSFC	256-544-5016	Steve.E.Glover@nasa.gov	Committee
Goedeke, Shawn	Department of Mechanical Engineering		Cookeville	TN	35805	USA	Tennessee Technological University	865-376-7595	SMG2886@tntech.edu	Poster
Golde, Rick						USA	ATK Thiokol			Session Chair
Gordon, Brian	The Millenium Center	RR1, Box 100B	Triadelphia	WV	26059-9707	USA	Touchstone Research Laboratory	304-547-5800	blg@trl.com	Attendee
Gordon, Gail	Marshall Space Flight Center	ED34	Huntsville	AL	35812	USA	NASA/MSFC	256-544-2726	Gail.H.Gordon@nasa.gov	Attendee
Gordon, Jenette	Stennis Space Center	RA00	Stennis Space Center	MS	39529	USA	NASA/SSC	228-688-1416	Jenette.B.Gordon@nasa.gov	Attendee
Gostowski, Rudy	Marshall Space Flight Center	TD40	Huntsville	AL	35812	USA	NASA/MSFC	256-544-0458	rudy.gostowski@nasa.gov	Speaker
Greene, Brian	Mail Stop ITB	HQ Bldg, Room 3481	Kennedy Space Center	FL	32899	USA	International Trade Bridge, Inc	321-867-8481	Brian.Greene-2@ksc.nasa.gov	Speaker
Griffin, Dennis	Marshall Space Flight Center	ED36	Huntsville	AL	35812	USA	NASA/MSFC	256-544-2493	Dennis.E.Griffin@nasa.gov	Committee
Grooms, Jason	13350 US Hwy 19 N	MS 225-1	Clearwater	FL	33764	USA	Honeywell Space Systems	727-539-2577	jason.c.grooms@honeywell.com	Attendee
Grosjean, Eric	12 rue Pasteur		Suresnes		92150	France	EADS CCR	33-01-46-97-3086	eric.grosjean@eads.net	Speaker
Gross, Uwe	4300 B Street	Suite 407	Anchorage	AK	99503	USA	Koniag	907-561-2668	ulgross@aol.com	Attendee
Hall, Joylene	Marshall Space Flight Center	ED36	Huntsville	AL	35812	USA	NASA/MSFC	256-544-1402	joylene.hall@msfc.nasa.gov	Poster
Hall, Phillip	Marshall Space Flight Center	ED32	Huntsville	AL	35812	USA	NASA/MSFC	256-544-2525	Phillip.B.Hall@nasa.gov	Attendee
Hamilton, David	Marshall Space Flight Center	ED35	Huntsville	AL	35812	USA	NASA/MSFC	256-544-2578	David.Hamilton@nasa.gov	Attendee
Hamilton, George	Marshall Space Flight Center	ED42	Huntsville	AL	35812	USA	NASA/MSFC	256-544-4963	George.S.Hamilton@nasa.gov	Attendee
Hammonds, Earline	Marshall Space Flight Center	ED36	Huntsville	AL	35812	USA	NASA/MSFC	256-544-7023	Earline.J.Hammonds@nasa.gov	Attendee
Hampton, Tammy	Marshall Space Flight Center	ED36	Huntsville	AL	35812	USA	ICRC	256-544-0597	Tammy.Hampton@msfc.nasa.go	Attendee
Harbour, Daniel	8 Draco Drive		Edwards AFB	CA	93524	USA	US Air Force	661-275-5374	daniel.harbour@edwards.af.mil	Attendee
Harm, Gene	8550 Astronaut Blvd.	USK-890	Cape Canaveral	FL	32420	USA	United Space Alliance	321-867-9856	harmg@usasrb.ksc.nasa.gov	Speaker
Harris, Mary JO	Marshall Space Flight Center	MP41	Huntsville	AL	35812	USA	NASA/MSFC	256-544-2729	mary.j.harris@nasa.gov	Attendee
Harris, Yolanda	Marshall Space Flight Center	MP21	Huntsville	AL	35812	USA	NASA/MSFC	256-544-3001	Yolanda.B.Harris@nasa.gov	Committee
Harten, Teresa	Environmental Technology Verification Program	26 W ML King Dr. MS 235	Cincinnati	OH	45268	USA	Environmental Protection Agency	513-569-7565	Harten.Teresa@epamail.epa.gov	Keynote Speaker
Hartley, Paula	Michoud Assembly Facility	13800 Old Gentilly Road	New Orleans	LA	70129	USA	Lockheed Martin - Michoud Operations	504-257-3161	paula.j.hartley@lmco.com	Poster
Hasegawa, Keiichi	1-Koganezawa Kihigaya		Kakuda	Miyagi	981-1525	Japan	National Aerospace Laboratory	81-244-68-3947	khasegawa@kakuda-splab.go.jp	Attendee
Hedlund, Maurice	13620 110th Ave. Ct. E		Puyallup	WA	98374	USA	Boeing Commerical Airplanes	425-234-5639	maurice.c.hedlund@boeing.com	Attendee
Henderson, Charles	Marshall Space Flight Center	ED34	Huntsville	AL	35812	USA	NASA/MSFC	256-544-2727	Charles.E.Henderson@nasa.gov	Attendee
Herrington, John	39 W. Hunter Drive		Enon	OH	45523	USA	Versar, Inc.	937-864-7812	herrington@erinet.com	Speaker
Hess, Rick	110 Union Street	Suite 500	Seattle	WA	98101	USA	Puget Sound Clean Air Agency	206-689-4027	rickh@pscleanair.org	Session Chair
Hesselroth, David	3M Center		St. Paul	MN	55144	USA	3M	650-736-6191	dahesselroth@mmm.com	Speaker
Hessler, Susan	Marshall Space Flight Center	ED30	Huntsville	AL	35812	USA	Morgan Research Corporation	256-544-8153	susan.hessler@msfc.nasa.gov	Staff
Herald, Stephen	Marshall Space Flight Center	ED36	Huntsville	AL	35812	USA	ICRC	256-544-3885	stephen.herald@msfc.nasa.gov	Attendee
Hill, Dewayne	Marshall Space Flight Center	ED36	Huntsville	AL	35812	USA	Qualis Corporation	256-544-7047	dewayne.hill@msfc.nasa.gov	Attendee
Hissam, Andy	Marshall Space Flight Center	TD62	Huntsville	AL	35812	USA	NASA/MSFC	256-544-8388	Andy.Hissam@nasa.gov	Attendee
Hollerman, William	PO Box 44210		Lafayette	LA	70503	USA	University of Louisiana at Lafayette	331-82-6691	hollerman@louisiana.edu	Poster
Holmes, Steve	Marshall Space Flight Center	MP31	Huntsville	AL	35812	USA	NASA/MSFC	256-544-8713	Steven.G.Holmes@nasa.gov	Attendee
Hooper, Carlla	Marshall Space Flight Center	ED30	Huntsville	AL	35812	USA	NASA/MSFC	256 544-2614	Carlla.G.Hooper@nasa.gov	Staff
Horowitz, Dennis	2100 Market St. NE		Decatur	AL	35601	USA	Wolverine Tube, Inc.	256-580-3954		Exhibitor
Hudnall, Pat	13000 Space Center Blvd.		Houston	TX	77059-3556	USA	Johnson Engineering Corporation	281-792-5703	phudnall@ems.jsc.nasa.gov	Speaker
Hudson, Wanda	Bldg 4712, M/S E61A	Marshall Space Flight Center	Huntsville	AL	35812	USA	ATK Thiokol	256-544-5553	Wanda.Hudson@ATK.com	Attendee
Huff, Tim	Marshall Space Flight Center	ED36	Huntsville	AL	35812	USA	NASA/MSFC	256-544-4259	Timothy.L.Huff@nasa.gov	Speaker
Hui, David	Department of Mechanical Engineering		New Orleans	LA	70148		University of New Orleans	504-257-0969	dhui@uno.edu	Speaker
Hulcher, Bruce	Marshall Space Flight Center	ED34	Huntsville	AL	35812	USA	NASA/MSFC	256 544-5124	Anthony.B.Hulcher@nasa.gov	Attendee
Hunter, Steve L.	100 Blackjack Road		Starkville	MS	39759	USA	Mississippi State University	662-325-8344	shunter@cfr.msstate.edu	Speaker
Huntley, M.L.	PO Box 368		Jacksonville	AR	72078	USA	Modern Chemical, Inc.	501-988-1311		Exhibitor
Huntley, ___	PO Box 368		Jacksonville	AR	72078	USA	Modern Chemical, Inc.	501-988-1311		Exhibitor
Jaworske, Donald	21000 Brookpark Rd.		Cleveland	OH	44135	USA	NASA/GRC	216-433-2312	Donald.A.Jaworske@nasa.gov	Speaker
Jennings, Tommy	2109 W. Chalet		Anaheim	CA	92804	USA	Hydro-Aire	818-526-2642	jenningt@hydroaire.com	Attendee
Johnson, Scott	952 Sunset Blvd.		West Columbia	SC	29169	USA	Correlated Solutions	803-926-7221	Johnson@CorrelatedSolutions.co	Exhibitor
Johnston, James	Marshall Space Flight Center	ED35	Huntsville	AL	35812	USA	NASA/MSFC	256-544-2495	James.E.Johnston@nasa.gov	Attendee
Jones, Brian	Kaiser Compositek, Inc.	1095 Columbia Street	Brea	CA	92821	USA	Kaiser Compositek, Inc.	714-990-6300	bhjones@kaisercompositek.com	Speaker
Jones, Chip	Marshall Space Flight Center	ED33	Huntsville	AL	35812	USA	NASA/MSFC	256-544-2701	Clyde.S.Jones@nasa.gov	Attendee
Kaul, Raj	Marshall Space Flight Center	ED34	Huntsville	AL	35812	USA	NASA/MSFC	256-544-1084	Raj.K.Kaul@nasa.gov	Speaker
Keen, Jill	Marshall Space Flight Center	Bldg 4204, Room 505	Huntsville	AL	35812	USA	Thiokol	256-544-2748		Session Chair
Kennedy, Paul	Marshall Space Flight Center	ED18	Huntsville	AL	35812	USA	NASA/MSFC	256-544-4117	Paul.A.Kennedy@nasa.gov	Attendee
Kiessling, Ed	Marshall Space Flight Center	ED01	Huntsville	AL	35812	USA	NASA/MSFC	256-544-1002	Edward.H.Kiessling@nasa.gov	Attendee
Kilpatrick, Bill	Marshall Space Flight Center	ED01	Huntsville	AL	35812	USA	NASA/MSFC	256 544-1000	John.W.Kilpatrick@nasa.gov	Attendee
Kinchen, David	PO Box 29304	M/S 4610	New Orleans	LA	70189	USA	Lockheed Martin-Michoud Operations	504-257-1454	david.kinchen@maf.nasa.gov	Speaker
Kooney, Alex P.	13800 Old Gentilly Rd		New Orleans	LA	70129	USA	Lockheed Martin Space Systems Company	504-257-0949	alex.kooney@maf.nasa.gov	Speaker
Kuhlman, Sarah	300 College Park		Dayton	OH	45469	USA	University of Dayton Research Institute	937-229-4704	kuhlman@udri.udayton.edu	Speaker
Kukowski, Rob	2100 Market St. NE		Decatur	AL	35601	USA	Wolverine Tube, Inc.	256-580-3954		Exhibitor
Lambdin, Robert	Marshall Space Flight Center	ED35	Huntsville	AL	35812	USA	NASA/MSFC	256 544-4953	Robert.C.Lambdin@nasa.gov	Attendee
Lanam, Richard D.	700 Blair Road		Carteret	NJ	07008	USA	Englehard-CLAL LP	732-205-7404	richard.lanam@engelhard.com	Attendee

Landers, Tamara	Marshall Space Flight Center	ED35	Huntsville	AL	35812	USA	NASA/MSFC	256-544-6818	Tamara.S.Landers@nasa.gov	Attendee
Lash, Rhonda	Marshall Space Flight Center	ED36	Huntsville	AL	35812	USA	NASA/MSFC	256-544-9137	Rhonda.Lash@nasa.gov	Committee
Lawless, Kirby	Marshall Space Flight Center	ED33	Huntsville	AL	35812	USA	NASA/MSFC	256-544-2821	Kirby.G.Lawless@nasa.gov	Attendee
LeBlanc, Carole	One University Avenue		Lowell	MA	01854-2866		University of Massachussetts Lowell	978-934-3249	Carole_LeBlanc@uml.edu	Speaker
LeBoeuf, Ralph	Michoud Assembly Facility	Bldg. 4700	New Orleans	LA	70129	USA	Lockheed Martin Space Systems	504-257-1785	Ralph.J.Leboeuf@maf.nasa.gov	Session Chair
Ledbetter, Debbie	Marshall Space Flight Center	ED38	Huntsville	AL	35812	USA	NASA/MSFC	256-544-1088	debbie.ledbetter@nasa.gov	Attendee
Ledbetter, Frank	Marshall Space Flight Center	ED34	Huntsville	AL	35812	USA	NASA/MSFC	256-544-2673	Frank.Ledbetter@nasa.gov	Attendee
Lee, Jonathan	Marshall Space Flight Center	ED33	Huntsville	AL	35812	USA	NASA/MSFC	256-544-9290	Jonathan.A.Lee@nasa.gov	Speaker
Lester, Carl	Marshall Space Flight Center	ED34	Huntsville	AL	35812	USA	NASA/MSFC	256-544-4804	Carl.n.Lester@nasa.gov	Attendee
Lexo, Jim	1033 N. Fairfax St.	Suite 400	Alexandria	VA	22314	USA	ICRC	703-519-9901	jlexo@icrc-hq.com	Attendee
Lindberg, Robert M.	2510 Kennedy Circle	311HSW/XPRA	Brooks-City-Base	TX	78235	USA	Brooks AFB	210-536-4457	robert.lindberg@brooks.af.mil	Attendee
Loos, Alfred	204 Flippin Circle		Blacksburg	VA	24060-1326	USA	Virginia Tech	540-231-4574	aloos@vt.edu	Speaker
Lucke, Wes	3131 Luallen Drive		Carrollton	TX	75007	USA	Poco Graphite, Inc.	972-492-2556	wlucke@poco.com	Attendee
Mahajan, Devinder	Building 815		Upton	NY	11973-5000	USA	Brookhaven National Laboratory	631-344-4985	dmahajan@bnl.gov	Speaker
Mann, Rhonda	555 Discovery Drive		Huntsville	AL	35806	USA	United Space Alliance	256-971-3128	rhonda.e.mann@usahq.unitedspa	Speaker
Manning, Curtis	Marshall Space Flight Center	ED34	Huntsville	AL	35812	USA	NASA/MSFC	256-544-7348	Curtis.W.Manning@nasa.gov	Attendee
Martin, Ellen							RJ Lee Microsystems			Exhibitor
Martin, Jolene	Marshall Space Flight Center	MP71	Huntsville	AL	35812	USA	NASA/MSFC	256-544-8540	j-sandhu@santecsystems.com	Attendee
Mayo, Joseph	50 W. Stonebrook Drive		Orange Village	OH	44022	USA	Metalex Manufacturing, Inc.	440-349-2019	Jolene.J.Martin@nasa.gov	Attendee
McBain, Michael	Michoud Assembly Facility	13800 Old Gentilly Road	New Orleans	LA	70129	USA	Lockheed Martin - Michoud Operations	504-257-5210	Michael.C.McBain@maf.nasa.gov	Poster
McClennen, William				UT		USA	ATK Thiokol		William.McClennen@ATK.com	Speaker (tutorial)
McGill, Preston	Marshall Space Flight Center	ED33	Huntsville	AL	35812	USA	NASA/MSFC	256-544-2604	Preston.B.McGill@nasa.gov	Attendee
Medley, Jay	Marshall Space Flight Center	ED38	Huntsville	AL	35812	USA	NASA/MSFC	256-544-1085	Jay.Medley@nasa.gov	Attendee
Meinhold, Anne	Marshall Space Flight Center	MP71	Huntsville	AL	35812	USA	International Trade Bridge, Inc	356-544-6494	anne.f.meinhold@msfc.nasa.gov	Committee
Mellen, Dan	Marshall Space Flight Center	ED41	Huntsville	AL	35812	USA	NASA/MSFC	256 544-7193	Dan.Me..en@nasa.gov	Attendee
Merchant, Abid	DuPont Fluoroproducts	CRP-711	Wilmington	DE	19804	USA	DuPont Fluoroproducts	302-999-4269	abid.n.merchant@usa.dupont.cor	Speaker
Metrokin, Dennis	4300 B Street	Suite 407	Anchorage	AK	99503	USA	Koniag	907-561-2668	dmetrokin@koniag.com	Attendee
Meyers, Charles	Marshall Space Flight Center	ED22	Huntsville	AL	35812	USA	NASA/MSFC	256-544-7192	Charles.A.Meyers@nasa.gov	Attendee
Mims, Kathy	Marshall Space Flight Center	ED21	Huntsville	AL	35812	USA	NASA/MSFC	256 544-1506	Katherine.Mims@nasa.gov	Attendee
Monteiro, Hubert	2200 Colonial Lake Drive	Apt. 2224	Madison	AL	35758-4014	USA	Royce International	256-772-6493	hubertmontiero@att.net	Attendee
Moore, Regina	Marshall Space Flight Center	ED34	Huntsville	AL	35812	USA	NASA/MSFC	256-544-8456	Regina.Moore@nasa.gov	Committee
Moore, Robin	Marshall Space Flight Center	ED36	Huntsville	AL	35812	USA	ICRC	256-544-2948	robin.moore@msfc.nasa.gov	Poster
Morard, Elizabeth	6767 Old Madison Pike	Suite 105	Huntsville	AL	35806	USA	Qualis Corporation	256-971-1707	elizabeth@qualis-corp.com	Attendee
Morgan, Richard	Bldg 4712, Room D113	Marshall Space Flight Center	Huntsville	AL	35812	USA	ATK Thiokol	256-544-4790	Richard.Morgan@ATK.com	Speaker
Morrison, Carolyn						USA	Petroferm			Exhibitor
Munafo, Paul	Marshall Space Flight Center	ED30	Huntsville	AL	35812	USA	NASA/MSFC	256-544-2566	Paul.M.Munafo@nasa.gov	Committee
Murphree-Grafton, G	Marshall Space Flight Center	Bldg. 4202, Room 415	Huntsville	AL	35812	USA	United Space Alliance	256-544-2483	Gail.Murphree-Grafton@msfc.nas	Session Chair
Nehls, Mary	Marshall Space Flight Center	ED01	Huntsville	AL	35812	USA	NASA/MSFC	256-544-6578	Mary.K.Nehls@nasa.gov	Attendee
Neidert, Jamie B.	2227 Drake Avenue		Huntsville	AL	35805	USA	Atlantic Research Corporation	256-883-0270	jneidert@arc-ag.com	Attendee
Neshan, Massaud	2100 Market St. NE		Decatur	AL	35601	USA	Wolverine Tube, Inc.	256-580-3954		Exhibitor
Newton, Robby	Marshall Space Flight Center	ED36	Huntsville	AL	35812	USA	NASA/MSFC	256-544-7880	robby.newton@nasa.gov	Speaker
Ng, Chun Man	Suite 1000	200 Clinton Avenue	Huntsville	AL	35801	USA	Wolverine Tube, Inc	256-580-3511	cmng@wlv.com	Poster
Niedermeyer, Mindy	Marshall Space Flight Center	ED34	Huntsville	AL	35812	USA	NASA/MSFC	256-544-1569	mindy.niedermeyer@nasa.gov	Attendee
Novak, Howard	8550 Astronaut Blvd.	USK-864	Kennedy Space Center	FL	32899	USA	United Space Alliance	321-967-7054	novakh@usasrb.ksc.nasa.gov	Speaker/Session Chair
Nunez, Chris	20 Fairbanks		Irvine	CA	92618	USA	Centor Software Corporation	949-639-3504	cnunez@centor.com	Speaker
Oka, Masahiko	20 Olympic Drive		Orangeburg	NY	10962	USA	Daikin	845-365-9544	Moka@daikin-america.com	Attendee
Otsuka, Takahide	600 Countess Drive		Yardley	PA	19067-4618	USA	Taka Otsuka Associates, Inc.	215-321-7067	t.otsuka@usa.net	Attendee
Owens, Karen	555 Discovery Drive		Huntsville	AL	35806	USA	United Space Alliance	256-544-5218	karen.owens@msfc.nasa.gov	Exhibitor
Panamaroff, Tom	4300 B Street	Suite 407	Anchorage	AK	99503	USA	Koniag	907-561-2668	tompan@ptialaska.net	Attendee
Panda, Binayak	Marshall Space Flight Center	ED33	Huntsville	AL	35812	USA	NASA/MSFC	256-544-6349	Binayak.Panda-1@nasa.gov	Attendee
Parker, Alan	PO Box 5800, MS-0958		Albuquerque	NM	87185-0958	USA	Sandia National Laboratories	505-844-9472	arparke@sandia.gov	Attendee
Patton, Richard D.	PO Box ME		Mississippi State	MS	39762-5925	USA	Mississippi State University	662-325-7311	patton@me.msstate.edu	Speaker
Patton, Scott	5700 Skylab Road		Huntington Beach	CA	92647	USA	Airtech Advanced Materials	714-899-8100		Exhibitor
Peddieson, John	1020 Stadium Drive	Prescott Room 414	Cookeville	TN	38505	USA	Tennessee Technological University	931-372-3615	jpeddieson@tntech.edu	Attendee
Pedley, Michael	Johnson Space Center	ES4	Houston	TX	77058	USA	NASA/JSC	281-483-8913	michael.d.pedley@nasa.gov	Speaker
Pelham, Larry	Marshall Space Flight Center	ED34	Huntsville	AL	35812	USA	NASA/MSFC	256-544-9111	Larry.Pelham@nasa.gov	Attendee
Perkins, James	Marshall Space Flight Center	ED36	Huntsville	AL	35812	USA	NASA/MSFC	256-544-2634	James.H.Perkins@nasa.gov	Committee
Phillips, Steven	Marshall Space Flight Center	ED34	Huntsville	AL	35812	USA	NASA/MSFC	256-544-0626	Steven.T.Phillips@msfc.nasa.gov	Speaker
Plaskon, Daniel	40 N. Altadena Drive		Pasadena	CA	91107	USA	NASA/JPL	626-795-4928	Daniel.Plaskon-107047@ipl.nas	Speaker
Powell, George L.	298 East Drive		Oak Ridge, TN	TN	37830	USA	Y-12 National Security Complex	865-574-1717	powellgl@y12.doe.gov	Speaker
Quattrochi, Dale	Marshall Space Flight Center	SD60	Huntsville	AL	35812	USA	NASA/MSFC	256-961-7887	Dale.Quattrochi@nasa.gov	Speaker (tutorial)
Raleigh, Shannon	Marshall Space Flight Center	CD70	Huntsville	AL	35812	USA	NASA/MSFC	256-544-5621	Shannon.E.Raleigh@nasa.gov	Attendee
Rayburn, Jeff	Marshall Space Flight Center	ED22	Huntsville	AL	35812	USA	NASA/MSFC	256-544-1564	Jeff.Rayburn@nasa.gov	Attendee
Richardson, Erin	Marshall Space Flight Center	ED36	Huntsville	AL	35812	USA	NASA/MSFC	256-544-2873	Erin.H.Richardson@nasa.gov	Speaker (tutorial)/Poster
Richardson, Stepher	Marshall Space Flight Center	ED23	Huntsville	AL	35812	USA	NASA/MSFC	256-544-1768	Stephen.W.Richardson@nasa.gov	Attendee
Rideout, Curt	6151 N. Discovery Way		Boise	ID	83713	USA	Positron Systems	208-672-1923	curtr@positronsystems.com	Exhibitor
Robinson, Mark	1780 Rohrerstown Road		Lancaster	PA	17601-2334	USA	Hamilton Precision Metals	717-569-7061		Exhibitor
Rogers, Martin	Luna Innovations, Inc.	2851 Commerce Street	Blacksburg	Va	24060	USA	Luna Innovations, Inc.	540-953-4280	rogersm@lunainnovation.com	Speaker
Roth, Axel	Marshall Space Flight Center	DA01	Huntsville	AL	35812	USA	NASA/MSFC	256-544-0451	Axel.Roth-1@nasa.gov	Attendee
Ruff, Gary A.	21000 Brookpark Rd.		Cleveland	OH	44135	USA	NASA/GRC	216-433-5697	gary.a.ruff@nasa.gov	Attendee
Russell, Carolyn	Marshall Space Flight Center	ED33	Huntsville	AL	35812	USA	NASA/MSFC	256-544-2705	carolyn.k.russell@nasa.gov	Attendee
Sackheim, Robert	Marshall Space Flight Center	DA01	Huntsville	AL	35812	USA	NASA/MSFC	256-544-1938	bob.sackheim@nasa.gov	Keynote Speaker
Sadlowski, Dave	1033 N. Fairfax St.	Suite 400	Alexandria	VA	22314	USA	ICRC	703-519-9901	dsadlowski@icrc-hq.com	Attendee
Salem, Jonathan	21000 Brookpark Rd.		Cleveland	OH	44135	USA	NASA/GRC	216-433-3313	Jonathan.A.Salem@nasa.gov	Speaker
Sams-Smiley, Jenee	Marshall Space Flight Center	SD12	Huntsville	AL	35812	USA	NASA/MSFC	256-544-6816	Madelyn.J.Sams@nasa.gov	Committee
Sandhu, Jas	716 South Milwaukee Avenue		Wheeling	Illinois	60090-6202	USA	Santec Systems, Inc.	847-215-8884	j-sandhu@santecsystems.com	Speaker
Saulsberry, Regor	White Sands Test Facility	PO Box 20	Las Cruces	NM	88004	USA	NASA/WTSF	505-524-5518	regor.l.saulsberry@nasa.gov	Attendee
Schantz, John	110 Union Street	Suite 500	Seattle	WA	98101	USA	Puget Sound Clean Air Agency	206-689-4027	JohnS@pscleanair.org	Speaker
Schmieder, Stephen	Marshall Space Flight Center	MP51	Huntsville	AL	35812	USA	NASA/MSFC	256-544-0112	Stephen.P.Schmieder@nasa.gov	Attendee
Schreier, Hubert W.	952 Sunset Blvd.		West Columbia	SC	29169	USA	Correlated Solutions	803-926-7221		Exhibitor
Schrock, Ken	Marshall Space Flight Center	ED18	Huntsville	AL	35812	USA	NASA/MSFC	256-544-1460	ken.schrock@nasa.gov	Attendee
Schutzenhofer, Sco	Marshall Space Flight Center	MP71	Huntsville	AL	35812	USA	NASA/MSFC	256-544-8496	Scott.A.Schutzenhofer@nasa.go	Attendee
Scott, Joseph	Marshall Space Flight Center	ED36	Huntsville	AL	35812	USA	ICRC	256-544-2976	Joseph.Scott@msfc.nasa.gov	Poster

Scroggins, Sharon	Marshall Space Flight Center	AD10	Huntsville	AL	35812	USA	NASA/MSFC	256-544-7932	Sharon.T.Scroggins@nasa.gov	Committee
Selvidge, Shawn	Marshall Space Flight Center	ED34	Huntsville	AL	35812	USA	NASA/MSFC	256-544-0481	Shawn.Selvidge@nasa.gov	Speaker
Shah, Sandeep	Marshall Space Flight Center	ED33	Huntsville	AL	35812	USA	NASA/MSFC	256-544-0836	sandeep.shah@msfc.nasa.gov	Attendee
Sharp, Sheila										Speaker
Sharpe, Jon	PO Box 9008	Marshall Space Flight Center	Huntsville	AL	35812	USA	Lockheed Martin	256-544-0441	jon.sharpe@msfc.nasa.gov	Attendee
Shea, Charlotte	Marshall Space Flight Center	ED36	Huntsville	AL	35812	USA	Qualis Corporation	256-544-3029	Charlotte.Shea@msfc.nasa.gov	Committee
Shelley, Paul	PO Box 3707	M/C 9U-EA	Seattle	WA	98124-2207	USA	Boeing Commerical Airplanes	253-581-7170	paul.h.shelley@boeing.com	Speaker
Shull, Douglas D.	1201 Edward H. White II Street		Patrick AFB	FL	32925	USA	USAF	321-494-3236	douglas.shull@patrick.af.mil	Attendee
Silvera, Antonio	2510 Kennedy Circle	311HSW/XPRA	Brooks-City-Base	TX	78235	USA	USAF	210-536-3657	antonio.slvera@brooks.af.mil	Attendee
Smelser, Jerry	Marshall Space Flight Center	MP31	Huntsville	AL	35812	USA	NASA/MSFC	256-544-4082	Jerry.W.Smelser@nasa.gov	Attendee
Smith, Brett	Marshall Space Flight Center	ED34	Huntsville	AL	35812	USA	NASA/MSFC	256-544-7036	Brett.H.Smith@nasa.gov	Attendee
Smith, Drew	Marshall Space Flight Center	ED20	Huntsville	AL	35812	USA	NASA/MSFC	256-544-4932	Drew.Smith@nasa.gov	Attendee
Smithers, Gweneth	Marshall Space Flight Center	ED34	Huntsville	AL	35812	USA	NASA/MSFC	256-544-0282	Gweneth.A.Smithers@nasa.gov	Attendee
Solomon, Marcella	P.O. Box 21233	MC: 721Z-K085	Kennedy Space Center	FL	32815-0233	USA	The Boeing Company	321-861-0908	marcella.solomon@boeing.com	Attendee
Sparks, Scott	Marshall Space Flight Center	ED34	Huntsville	AL	35812	USA	NASA/MSFC	256-544-2670	Jeffery.S.Sparks@nasa.gov	Attendee
Speece, Robert	Kennedy Space Center	MailCode PH-H2	Kennedy Space Center	FL	32899	USA	NASA/KSC	321-861-3637	Robert.F.Speece@nasa.gov	Attendee
Staab, Michael	1780 Rohrerstown Road		Lancaster	PA	17601-2334	USA	Hamilton Precision Metals	717-569-7061		Exhibitor
Stagliano, Steve	2201 Water Ridge Parkway	Suite 400	Charlotte	NC	28217	USA	AGA Chemicals, Inc.	704-329-7614		Exhibitor
Stanley, Dawn	Marshall Space Flight Center	AD40	Huntsville	AL	35812	USA	NASA/MSFC	256-544-1835	Dawn.C.Stanley@nasa.gov	Committee
Stanley, Stephanie	Bldg 4712, Room D113	Marshall Space Flight Center	Huntsville	AL	35812	USA	ATK Thiokol	256-544-0396	Stephanie.Stanley@ATK.com	Speaker
Stanton, Robin	26 Hammond Street		Waltham	MA	02453-3497	USA	Panametrics, Inc.	781-899-2719	stantonr@panametrics.com	Exhibitor
Stokes, Erik	757 Tom Martin Drive		Birmingham	AL	35211-4468	USA	Southern Research Institute	205-581-2649	stokes@sri.org	Speaker
Stone, Nick H.	340 Windbrook Drive		Norman	OK	73072	USA	Tinker Air Force Base	405-329-4763	nick.stone@tinker.af.mil	Attendee
Sturges, Robert	ISE Department	250 Durham Hall	Blacksburg	VA	24061	USA	Virginia Tech	540-231-7420	sturges@vt.edu	Attendee
Sullivan, Erica N.	2101 NASA Road 1	Johnson Space Center	Houston	TX	77058	USA	NASA/JSC	281-483-6233	erica.sullivan-1@nasa.gov	Speaker
Suits, Mike	Marshall Space Flight Center	ED32	Huntsville	AL	35812	USA	NASA/MSFC	256-544-8336	michael.w.suits@nasa.gov	Attendee
Swofford, Bill	4955 Corporate Drive		Huntsville	AL	35807	USA	Earth Tech	256-885-7870	wswofford@csc.com	Attendee
Szcesniak, M. Martin	11555 Rancho Bernardo R.		San Diego	CA	92127	USA	Surface Optics Corporation	858-675-7404	martinsz@surfaceoptics.com	Speaker
Talbot, Arin	13350 US Hwy 19 N	MS 310-1	Clearwater	FL	33764	USA	Honeywell Space Systems	727-539-4710	arin.talbot@honeywell.com	Attendee
Tanaka, Makoto	1117 Kitakaname		Hiratsuka	Kanagawa	259-1292	Japan	Tokai University	81-463-58-1211	makoto@cc.u-tokai.ac.jp	Speaker
Taylor, Irene	Marshall Space Flight Center	ED10	Huntsville	AL	35812	USA	NASA/MSFC	256-544-2051	Irene.E.Taylor@nasa.gov	Attendee
Terek, Jody	Marshall Space Flight Center	ED02	Huntsville	AL	35812	USA	NASA/MSFC	256-544-6817	Joanne.M.Terek@nasa.gov	Attendee
Thom, Robert	Marshall Space Flight Center	Ed32	Huntsville	AL	35812	USA	NASA/MSFC	256-544-2517	Robert.L.Thom@nasa.gov	Attendee
Throckmorton, Dave	Marshall Space Flight Center	ED01	Huntsville	AL	35812	USA	NASA/MSFC	256-544-1001	David.A.Throckmorton@nasa.go	Attendee
Topalian, John H.	1100 W. Hollyvale St.		Azusa	CA	91702	USA	Northrop Grumman	626-812-1729	John.Topalian@NorthropGrumma	Attendee
Towne, H. Baker, Jr.	595 John Downey Drive		New Britain	CT	06051	USA	Micro Care Corporation	860-827-0626	harrist@microcare.com	Exhibitor
Townsend, Tammy	Marshall Space Flight Center	ED36	Huntsville	AL	35812	USA	NASA/MSFC	256-544-2623	Tammy.L.Townsend@nasa.gov	Attendee
Tupper, Michael	2600 Campus Drive	Suite D	Lafayette	CO	80026	USA	Composite Technology Dvelopment	303-664-0394	mike@ctd-materials.com	Attendee
Tygielski, Phillip	Marshall Space Flight Center	TD62	Huntsville	AL	35812	USA	NASA/MSFC	256-544-7169	Phillip.J.Tygielski@nasa.gov	Attendee
Ulman, Abraham	Six Metrotech Center		Brooklyn	NY	12201	USA	Polytechnic University	718-260-3119	aulman@duke.poly.edu	Speaker
Vaughan, William	5606 Alta Dena Street		Huntsville	AL	35802	USA	University of Alabama in Huntsville	256-961-7759	vaughan@nsstc.uash.edu	Speaker
Vickers, John	Marshall Space Flight Center	ED34	Huntsville	AL	35812	USA	NASA/MSFC	256-544-3581	John.H.Vickers@nasa.gov	Attendee
Wagner, Carole	Marshall Space Flight Center	ED35	Huntsville	AL	35812	USA	NASA/MSFC	256-544-2719	Carole.Y.Wagner@nasa.gov	Attendee
Walker, James	Marshall Space Flight Center	ED32	Huntsville	AL	35812	USA	NASA/MSFC	256-961-1784	james.l.walker@nasa.gov	Speaker/Session Chair/Demonstration
Waller, Jess	3244 Hillrise Drive		Las Cruces	NM	88011	USA	Honeywell Technology Solutions, Inc	505-524-5249	jwaller@wstf.nasa.gov	Speaker
Watson, Michael	Marshall Space Flight Center	ED12	Huntsville	AL	35812	USA	NASA/MSFC	256 544-3186	Michael.D.Watson@nasa.gov	Session Chair
Watson, Sherry	AMSAM-RD-PS-AM		Redstone Arsenal	AL	35898	USA	US Army	256-876-4976	sherry.watson@redstone.army.m	Attendee
Weeks, Jack	555 Discovery Drive		Huntsville	AL	35806	USA	Boeing, Rocketdyne Power and Propulsion	356-544-2741	jack.l.weeks@boeing.com	Speaker
Weiner, Jodi			Huntsville	AL		USA	Consultant	256-533-5923	jweiner@aol.com	Committee
Wertz, George	Marshall Space Flight Center	ED31	Huntsville	AL	35812	USA	NASA/MSFC	256-544-2663	George.E.Wertz@nasa.gov	Attendee
Wilson, Scott	Sverdrup Technology	Marshall Space Flight Center	Huntsville	AL	35812	USA	Sverdrup Technology	256-544-6456		Exhibitor
Whitaker, Ann	Marshall Space Flight Center	SD01	Huntsville	AL	35812	USA	NASA/MSFC	256-544-2481	Ann.Whitaker@nasa.gov	Attendee
Whitcomb, John	Center for Mechanics of Composites	3141 TAMU	College Station	TX	77843-3141	USA	Texas A&M University	979-845-4006	jdw@tamu.edu	Speaker
Whitfield, Steve	Marshall Space Flight Center	ED36	Huntsville	AL	35812	USA	NASA/MSFC	256-961-0358	Steven.W.Whitfield@nasa.gov	Attendee
Whitmire, Nancy	3002 Flag Circle	#2620	Madison	AL	35758	USA	US Army	256-876-1667	nancy.whitmire@redstone.army.r	Attendee
Williams, Carl	1033 N. Fairfax St.	Suite 400	Alexandria	VA	22314	USA	ICRC	703-519-9901	cwilliams@icrc-hq.com	Attendee
Williams, Glenn	Marshall Space Flight Center	ED34	Huntsville	AL	35812	USA	NASA/MSFC	256-5441041	glenn.williams@nasa.gov	Speaker
Wise, Harry	Marshall Space Flight Center	ED36	Huntsville	AL	35812	USA	ICRC	256-544-3006	harry.wise@msfc.nasa.gov	Committee
Wormmeester, Meir	26 Hammond Street		Waltham	MA	02453-3497	USA	Panametrics, Inc.	781-899-2719		Exhibitor
Wright, Jerry	Marshall Space Flight Center	ED37	Huntsville	AL	35812	USA	NASA/MSFC	256-544-4443	Jerry.L.Wright@nasa.gov	Attendee
Yost, Vaughn	Marshall Space Flight Center	MP21	Huntsville	AL	35812	USA	NASA/MSFC	256-544-1998	Vaughn.H.Yost@nasa.gov	Committee
Zhao, Yi	500 Shadow Lakes Blvd	#133	Ormond Beach	FL	32174	USA	Embry-Riddle Aeronautical University	386-226-6746	yi.zhao@erau.edu	Attendee
Zhu, Shen	Marshall Space Flight Center	SD46	Huntsville	AL	35812	USA	United States Research Association	256-544-2916	shen.zhu@msfc.nasa.gov	Speaker
Zimmerman, Frank	Marshall Space Flight Center	ED33	Huntsville	AL	35812	USA	NASA/MSFC	256-544-4958	frank.r.zimmerman@nasa.gov	Speaker
___, Peter	5700 Skylab Road		Huntington Beach	CA	92647	USA	Airtech Advanced Materials	714-899-8100		Exhibitor

List of Participants by Organization

Association	Name	Address 1	Address 2	City	State	Zip	Country	Phone	E-mail	Role
3M	Hesselroth, David	3M Center		St. Paul	MN	55144	USA	650-736-6191	dahesselroth@mmm.com	Speaker
3M Company	Brobst, Keith E.	316 Henderson Ct.		Berryville	VA	22611	USA	1-800-603-0377	kebrobst@mmm.com	Exhibitor
Accurate Automation Corporation	Elliott, Louie	7001 Shallowford Road		Chattanooga	TN	37421	USA	423-894-4646	lelliott@accurate-automation.co	Attendee
AGA Chemicals, Inc.	Stagliano, Steve	2201 Water Ridge Parkway	Suite 400	Charlotte	NC	28217	USA	704-329-7614		Exhibitor
Airtech Advanced Materials	Dahlgren, Jeff	5700 Skylab Road		Huntington Beach	CA	92647	USA	714-899-8100		Exhibitor
Airtech Advanced Materials	Doty, Tom	5700 Skylab Road		Huntington Beach	CA	92647	USA	714-899-8100		Exhibitor
Airtech Advanced Materials	Patton, Scott	5700 Skylab Road		Huntington Beach	CA	92647	USA	714-899-8100		Exhibitor
Airtech Advanced Materials	___, Peter	5700 Skylab Road		Huntington Beach	CA	92647	USA	714-899-8100		Exhibitor
Alabama A&M University	Batra, A.K.	Micrgravity Science Laboratory	PO Box 1268	Normal	AL	35762	USA	256-858-8109	abatra@aamu.edu	Speaker
Alabama A&M University	Evelyn, Leslie	4900 Meridian Street		Normal	AL	35762	USA	256-851-5866	leslie@aamuri.aamu.edu	Exhibitor
American Autoclave Company	Castaneda, Bill	7819 Riverside Dr.		Sumner	WA	98309	USA	888-796-3373		Exhibitor
Assembly Guidance	Blake, Scott	315 Littleton Road		Chelmsford	MA	01824	USA	978-244-1166	sb@assemblyguide.com	Poster
Assembly Guidance	Burdo, Anna	315 Littleon Road		Chelmsford	MA	08124	USA	978-244-1166		Exhibitor
ATK Thiokol	Campbell, David	1302 E. 3075 N.		No. Ogden	UT	84414	USA	435-863-3463	David.Campbell@atk.com	Attendee
ATK Thiokol	Golde, Rick						USA			Session Chair
ATK Thiokol	Hudson, Wanda	Bldg 4712, M/S E61A	Marshall Space Flight Center	Huntsville	AL	35812	USA	256-544-5553	Wanda.Hudson@ATK.com	Attendee
ATK Thiokol	McClennen, William				UT		USA		William.McClennen@ATK.com	Speaker (tutorial)
ATK Thiokol	Morgan, Richard	Bldg 4712, Room D113	Marshall Space Flight Center	Huntsville	AL	35812	USA	256-544-4790	Richard.Morgan@ATK.com	Speaker
ATK Thiokol	Stanley, Stephanie	Bldg 4712, Room D113	Marshall Space Flight Center	Huntsville	AL	35812	USA	256-544-0396	Stephanie.Stanley@ATK.com	Speaker
Atlantic Research Corporation	Neidert, Jamie B.	2227 Drake Avenue		Huntsville	AL	35805	USA	256-883-0270	ineidert@arc-ag.com	Attendee
Boeing	Choate, Tab	Marshall Space Flight Center		Huntsville	AL	35812	USA	256-544-6830	Tab.N.Choate@msfc.nasa.gov	Attendee
Boeing	Coby, Ben	Marshall Space Flight Center	MP21	Huntsville	AL	35812	USA	254-544-2781	Ben.Coby@msfc.nasa.gov	
Boeing Commerical Airplanes	Hedlund, Maurice	13620 110th Ave. Ct. E		Puyallup	WA	98374	USA	425-234-5639	maurice.c.hedlund@boeing.com	Attendee
Boeing Commerical Airplanes	Shelley, Paul	PO Box 3707	M/C 9U-EA	Seattle	WA	98124-2207	USA	253-581-7170	paul.h.shelley@boeing.com	Speaker
Boeing, Rocketdyne Power and Propulsion	Weeks, Jack	555 Discovery Drive		Huntsville	AL	35806	USA	356-544-2741	jack.l.weeks@boeing.com	Speaker
Boeing-Rocketdyne	Daniel, Ron	Marshall Space Flight Center	Bldg. 4711, Room W155	Huntsville	AI	35812	USA	256-544-3701		Session Chair
Bowden Industries, Inc.	Bowden, Donald R.	1004 Oster Drive, NW		Huntsville	AL	35816	USA	256-382-3700	Helen.Sainker@bowdenindustrie	Speaker
Brookhaven National Laboratory	Mahajan, Devinder	Building 815		Upton	NY	11973-5000	USA	631-344-4985	dmahajan@bnl.gov	Speaker
Brooks AFB	Lindberg, Robert M.	2510 Kennedy Circle	311HSW/XPRA	Brooks-City-Base	TX	78235	USA	210-536-4457	robert.lindberg@brooks.af.mil	Attendee
Brown Precision, Inc.	Brown, Greg	1103 Putman Drive		Huntsville	AL	35816	USA	256-830-1990		Exhibitor
Brown Precision, Inc.	Corl, Mary Lynn	1103 Putman Drive		Huntsville	AL	35816	USA	256-830-1990	mlcorl@brownpreci.com	Exhibitor
Centor Software Corporation	Nunez, Chris	20 Fairbanks		Irvine	CA	92618	USA	949-639-3504	cnunez@centor.com	Speaker
Colorado School of Mines	Castillo, Martin	1500 Illinois Street		Golden	CO	80401	USA	303-273-3091	macastil@mines.edu	Speaker
Composite Technology Dvelopment	Tupper, Michael	2600 Campus Drive	Suite D	Lafayette	CO	80026	USA	303-664-0394	mike@ctd-materials.com	Attendee
Consultant	Weiner, Jodi			Huntsville	AL		USA	256-533-5923	jweiner@aol.com	Committee
Correlated Solutions	Johnson, Scott	952 Sunset Blvd.		West Columbia	SC	29169	USA	803-926-7221	Johnson@CorrelatedSolutions.c	Exhibitor
Correlated Solutions	Schreier, Hubert W.	952 Sunset Blvd.		West Columbia	SC	29169	USA	803-926-7221		Exhibitor
Daikin	Oka, Masahiko	20 Olympic Drive		Orangeburg	NY	10962	USA	845-365-9544	Moka@daikin-america.com	Attendee
DCM Clean Air Products, Inc.	Cole, Ross	9605 Highway 80 West		Fort Worth	TX	76116	USA	817-654-2829		Exhibitor
DE Technologies	Foedinger, Richard	3620 Horizon drive		King of Prussia	PA	19406	USA	610-270-9700	rfoedinger@detk.com	Speaker
DuPont Fluoroproducts	Merchant, Abid	DuPont Fluoroproducts	CRP-711	Wilmington	DE	19804	USA	302-999-4269	abid.n.merchant@usa.dupont.co	Speaker
EADS CCR	Grosjean, Eric	12 rue Pasteur		Suresnes		92150	France	33-01-46-97-3086	eric.grosjean@eads.net	Speaker
EADS-LV	Bonnafe, Jean-Pierre	66 route de Verneuil-BP 3002	78133 Les Mureaux	Cedex			France		jean-pierre.bonnafe@launchers.	Speaker
Earth Tech	Frye, Carole	Marshall Space Flight Center		Huntsville	AL	35812	USA	256-885-7474		Attendee
Earth Tech	Swofford, Bill	4955 Corporate Drive		Huntsville	AL	35807	USA	256-885-7870	wswofford@csc.com	Attendee
Embry-Riddle Aeronautical University	Zhao, Yi	500 Shadow Lakes Blvd	#133	Ormond Beach	FL	32174	USA	386-226-6746	yi.zhao@erau.edu	Attendee
Englehard-CLAL LP	Boland, Edward F.	700 Blair Road		Carteret	NJ	07008	USA	732-205-5727	ed.boland@engelhard.com	Attendee
Englehard-CLAL LP	Lanam, Richard D.	700 Blair Road		Carteret	NJ	07008	USA	732-205-7404	richard.lanam@engelhard.com	Attendee
Environmental Protection Agency	Colyer, Rick	Office of Air Quality Planning and Standards	Mail Drop C504-03	Research Triangle Park	NC	27711	USA		Colyer.Rick@epamail.epa.gov	Speaker (tutorial)
Environmental Protection Agency	Harten, Teresa	Environmental Technology Verification Program	26 W ML King Dr. MS 235	Cincinnati	OH	45268	USA	513-569-7565	Harten.Teresa@epamail.epa.gov	Keynote Speaker
Flight Materials Group	Erikson, Ray	Two Collins Road		Wakefield	MA	01880-2513	USA	781-246-8239	ray.erikson@flightmaterials.co	Speaker/Poster
Hamilton Precision Metals	Campbell, Michael	1780 Rohrerstown Road		Lancaster	PA	17601-2334	USA	717-569-7061		Exhibitor
Hamilton Precision Metals	Crawford, Robert	1780 Rohrerstown Road		Lancaster	PA	17601-2334	USA	717-569-7061		
Hamilton Precision Metals	Robinson, Mark	1780 Rohrerstown Road		Lancaster	PA	17601-2334	USA	717-569-7061		Exhibitor
Hamilton Precision Metals	Staab, Michael	1780 Rohrerstown Road		Lancaster	PA	17601-2334	USA	717-569-7061		Exhibitor
Honeywell Space Systems	Giles, John	13350 US Hwy 19 N	MS 225-1	Clearwater	FL	33764	USA	727-539-2270	john.giles@honeywell.com	Attendee
Honeywell Space Systems	Grooms, Jason	13350 US Hwy 19 N	MS 225-1	Clearwater	FL	33764	USA	727-539-2577	jason.c.grooms@honeywell.com	Attendee
Honeywell Space Systems	Talbot, Arin	13350 US Hwy 19 N	MS 310-1	Clearwater	FL	33764	USA	727-539-4710	arin.talbot@honeywell.com	Attendee
Honeywell Technology Solutions, Inc	Waller, Jess	3244 Hillrise Drive		Las Cruces	NM	88011	USA	505-524-5249	jwaller@wstf.nasa.gov	Speaker
Hydro-Aire	Jennings, Tommy	2109 W. Chalet		Anaheim	CA	92804	USA	818-526-2642	jenningt@hydroaire.com	Attendee
ICRC	Allen, Trudy	Marshall Space Flight Center	SD46	Huntsville	AL	35812	USA	256-544-6088	trudy.l.allen@msfc.nasa.gov	Attendee
ICRC	Baker, Kathy	Marshall Space Flight Center	ED36	Huntsville	AL	35812	USA	256-961-0357	Kathy.Baker@msfc.nasa.gov	Attendee
ICRC	Cooper, Carol	Marshall Space Flight Center	ED36	Huntsville	AL	35812	USA	256-544-4794	Carol.Cooper@msfc.nasa.gov	Staff
ICRC	Fossett, Karen	Detroit Operations Unit	1115 East Whitcomb Avenue	Madison Heights	MI	48071	USA	248-823-4272	kfossett@icrc-detroit.net	Staff
ICRC	Gholston, Susan	Marshall Space Flight Center	ED36	Huntsville	AL	35812	USA	256-961-0350	Susan.Gholston@msfc.nasa.gov	Staff
ICRC	Hampton, Tammy	Marshall Space Flight Center	ED36	Huntsville	AL	35812	USA	256-544-0597	Tammy.Hampton@msfc.nasa.go	Attendee
ICRC	Herald, Stephen	Marshall Space Flight Center	ED36	Huntsville	AL	35812	USA	256-544-3885	stephen.herald@msfc.nasa.gov	Attendee
ICRC	Lexo, Jim	1033 N. Fairfax St.	Suite 400	Alexandria	VA	22314	USA	703-519-9901	jlexo@icrc-hq.com	Attendee
ICRC	Moore, Robin	Marshall Space Flight Center	ED36	Huntsville	AL	35812	USA	256-544-2948	robin.moore@msfc.nasa.gov	Poster
ICRC	Sadlowski, Dave	1033 N. Fairfax St.	Suite 400	Alexandria	VA	22314	USA	703-519-9901	dsadlowski@icrc-hq.com	Attendee
ICRC	Scott, Joseph	Marshall Space Flight Center	ED36	Huntsville	AL	35812	USA	256-544-2976	Joseph.Scott@msfc.nasa.gov	Poster
ICRC	Williams, Carl	1033 N. Fairfax St.	Suite 400	Alexandria	VA	22314	USA	703-519-9901	cwilliams@icrc-hq.com	Attendee
ICRC	Wise, Harry	Marshall Space Flight Center	ED36	Huntsville	AL	35812	USA	256-544-3006	harry.wise@msfc.nasa.gov	Committee
International Trade Bridge, Inc	Brown, Christina	100 CTC Drive		Johnstown	PA	15904	USA			Exhibitor
International Trade Bridge, Inc	Crawford, David	1308 Research Park Drive		Beavercreek	OH	45432	USA	937-431-1990	crawfordd@itb-inc.com	Speaker
International Trade Bridge, Inc	Greene, Brian	Mail Stop ITB	HQ Bldg, Room 3481	Kennedy Space Center	FL	32899	USA	321-867-8481	Brian.Greene-2@ksc.nasa.gov	Speaker
International Trade Bridge, Inc	Meinhold, Anne	Marshall Space Flight Center	MP71	Huntsville	AL	35812	USA	356-544-6494	anne.f.meinhold@msfc.nasa.gov	Committee
Johnson Engineering Corporation	Hudnall, Pat	13000 Space Center Blvd.		Houston	TX	77059-3556	USA	281-792-5703	phudnall@ems.jsc.nasa.gov	Speaker
Kaiser Compositek, Inc.	Jones, Brian	Kaiser Compositek, Inc.	1095 Columbia Street	Brea	CA	92821	USA	714-990-6300	bhjones@kaisercompositek.com	Speaker
Koniag	Gross, Uwe	4300 B Street	Suite 407	Anchorage	AK	99503	USA	907-561-2668	ulgross@aol.com	Attendee
Koniag	Metrokin, Dennis	4300 B Street	Suite 407	Anchorage	AK	99503	USA	907-561-2668	dmetrokin@koniag.com	Attendee
Koniag	Panamaroff, Tom	4300 B Street	Suite 407	Anchorage	AK	99503	USA	907-561-2668	tompan@ptialaska.net	Attendee
Lockheed Martin	Blevins, Elana	PO Box 9008	Marshall Space Flight Center	Huntsville	AL	35812	USA	256-544-2772	elana.c.blevins@msfc.nasa.gov	Attendee
Lockheed Martin	Sharpe, Jon	PO Box 9008	Marshall Space Flight Center	Huntsville	AL	35812	USA	256-544-0441	jon.sharpe@msfc.nasa.gov	Attendee

Lockheed Martin - Michoud Operations	Adams, Glynn	Michoud Assembly Facility	PO Box 29304	New Orleans	LA	70189	USA	504-257-1510	glynn.adams@maf.nasa.gov	Poster
Lockheed Martin - Michoud Operations	Drouant, Doris	Michoud Assembly Facility		New Orleans	LA	70129	USA	504-257-0228	Doris.s.drouant@maf.nasa.gov	Speaker (tutorial)
Lockheed Martin - Michoud Operations	Hartley, Paula	Michoud Assembly Facility	13800 Old Gentilly Road	New Orleans	LA	70129	USA	504-257-3161	paula.j.hartley@lmco.com	Poster
Lockheed Martin - Michoud Operations	McBain, Michael	Michoud Assembly Facility	13800 Old Gentilly Road	New Orleans	LA	70129	USA	504-257-5210	Michael.C.McBain@maf.nasa.gov	Poster
Lockheed Martin Space Systems	LeBoeuf, Ralph	Michoud Assembly Facility	Bldg. 4700	New Orleans	LA	70129	USA	504-257-1785	Ralph.J.Leboeuf@maf.nasa.gov	Session Chair
Lockheed Martin Space Systems Company	Barre, Kevin	13800 Old Gentilly Rd		New Orleans	LA	70129	USA	504-257-4188	Kevin.J.Barre@maf.nasa.gov	Exhibitor
Lockheed Martin Space Systems Company	Dooley, Craig D.	13800 Old Gentilly Rd	Dept. 3614	New Orleans	LA	70129	USA	504-257-0204	craig.d.dooley@lmco.com	Attendee
Lockheed Martin Space Systems Company	Kooney, Alex P.	13800 Old Gentilly Rd		New Orleans	LA	70129	USA	504-257-0949	alex.kooney@maf.nasa.gov	Speaker
Lockheed Martin-Michoud Operations	Kinchen, David	PO Box 29304	M/S 4610	New Orleans	LA	70189	USA	504-257-1454	david.kinchen@maf.nasa.gov	Speaker
Luna Innovations, Inc.	Rogers, Martin	Luna Innovations, Inc.	2851 Commerce Street	Blacksburg	Va	24060	USA	540-953-4280	rogersm@lunainnovation.com	Speaker
Matec Instruments	Antolino, Ed	56 Hudson Street		Northborough	MA	1532	USA	508-393-0155		Exhibitor
Matec Instruments	Bishop, Ken	56 Hudson Street		Northborough	MA	1532	USA	508-393-0155		Exhibitor
Matec Instruments	Cooper, John	56 Hudson Street		Northborough	MA	1532	USA	508-393-0155		Exhibitor
Metalex Manufacturing, Inc.	Mayo, Joseph	50 W. Stonebrook Drive		Orange Village	OH	44022	USA	440-349-2019	Jolene.J.Martin@nasa.gov	Attendee
Micro Care Corporation	Towne, H. Baker, Jr.	595 John Downey Drive		New Britain	CT	06051	USA	860-827-0626	harrist@microcare.com	Exhibitor
Mississippi State University	Hunter, Steve L.	100 Blackjack Road		Starkville	MS	39759	USA	662-325-8344	shunter@cfr.msstate.edu	Speaker
Mississippi State University	Patton, Richard D.	PO Box ME		Mississippi State	MS	39762-5925	USA	662-325-7311	patton@me.msstate.edu	Speaker
Modern Chemical, Inc.	Burger, Nancy	PO Box 368		Jacksonville	AR	72078	USA	501-988-1311		Exhibitor
Modern Chemical, Inc.	Huntley, M.L.	PO Box 368		Jacksonville	AR	72078	USA	501-988-1311		Exhibitor
Modern Chemical, Inc.	Huntley, ___	PO Box 368		Jacksonville	AR	72078	USA	501-988-1311		Exhibitor
Morgan Research Corporation	Hessler, Susan	Marshall Space Flight Center	ED30	Huntsville	AL	35812	USA	256-544-8153	susan.hessler@msfc.nasa.gov	Staff
NASA/GRC	Jaworske, Donald	21000 Brookpark Rd.		Cleveland	OH	44135	USA	216-433-2312	Donald.A.Jaworske@nasa.gov	Speaker
NASA/GRC	Ruff, Gary A.	21000 Brookpark Rd.		Cleveland	OH	44135	USA	216-433-5697	gary.a.ruff@nasa.gov	Attendee
NASA/GRC	Salem, Jonathan	21000 Brookpark Rd.		Cleveland	OH	44135	USA	216-433-3313	Jonathan.A.Salem@nasa.gov	Speaker
NASA/JPL	Plaskon, Daniel	40 N. Altadena Drive		Pasadena	CA	91107	USA	626-795-4928	Daniel.Plaskon-107047@jpl.nas	Speaker
NASA/JSC	Pedley, Michael	Johnson Space Center	ES4	Houston	TX	77058	USA	281-483-8913	michael.d.pedley@nasa.gov	Speaker
NASA/JSC	Sullivan, Erica N.	2101 NASA Road 1	Johnson Space Center	Houston	TX	77058	USA	281-483-6233	erica.sullivan-1@nasa.gov	Speaker
NASA/KSC	Speece, Robert	Kennedy Space Center	MailCode PH-H2	Kennedy Space Center	FL	32899	USA	321-861-3637	Robert.F.Speece@nasa.gov	Attendee
NASA/MSFC	Aggarwal, Pravin	Marshall Space Flight Center	ED22	Huntsville	AL	35812	USA	256-544-5345	Pravin.K.Aggarwal@nasa.gov	Attendee
NASA/MSFC	Albyn, Keith	Marshall Space Flight Center	ED31	Huntsville	AL	35812	USA	256-544-8011	Keith.C.Albyn@nasa.gov	Attendee
NASA/MSFC	Allen, John	Marshall Space Flight Center	ED38	Huntsville	AL	35812	USA	256 544-1026	John.D.Allen@nasa.gov	Attendee
NASA/MSFC	Askins, Bruce	Marshall Space Flight Center	ED38	Huntsville	AL	35812	USA	256-544-1096	Bruce.Askins@nasa.gov	Session Chair
NASA/MSFC	Babai, Majid	Marshall Space Flight Center	ED34	Huntsville	AL	35812	USA	256-544-2795	majid.k.babai@nasa.gov	Speaker
NASA/MSFC	Barret, Chris	Marshall Space Flight Center	TD40	Huntsville	AL	35812	USA	256-544-7118	Chris.Barret-1@nasa.gov	Attendee
NASA/MSFC	Bell, Leon	Marshall Space Flight Center	ED18	Huntsville	AL	35812	USA			Attendee
NASA/MSFC	Blalock, Carol	Marshall Space Flight Center	ED30	Huntsville	AL	35812	USA	256-544-2335	Carol.A.Blalock@nasa.gov	Staff
NASA/MSFC	Boothe, Richard	Marshall Space Flight Center	ED31	Huntsville	AL	35812	USA	256-544-3028	richard.e.boothe@nasa.gov	Speaker
NASA/MSFC	Bryant, Mel	Marshall Space Flight Center	MP21	Huntsville	AL	35812	USA	256-544-0825	melvin.A.bryant@nasa.gov	Session Chair
NASA/MSFC	Bryson, Craig	Marshall Space Flight Center	ED32	Huntsville		35812	USA	256-544-2553	Charles.C.Bryson@nasa.gov	Attendee
NASA/MSFC	Burlingame, Steve	Marshall Space Flight Center	ED34	Huntsville	AL	35812	USA	256-544-8860	Steven.W.Burlingame@nasa.gov	Attendee
NASA/MSFC	Burns, Dewitt	Marshall Space Flight Center	ED31	Huntsville	AL	35812	USA	256-544-252	Dewitt.Burns@nasa.gov	Session Chair
NASA/MSFC	Burnum, James	Marshall Space Flight Center	MP51	Huntsville	AL	35812	USA	256-544-4008	James.R.Burnum@nasa.gov	Attendee
NASA/MSFC	Carruth, Ralph	Marshall Space Flight Center	ED30	Huntsville	AL	35812	USA	256-544-7647	Ralph.Carruth@nasa.gov	Attendee
NASA/MSFC	Clark, Johnnie	Marshall Space Flight Center	ED34	Huntsville	AL	35812	USA	256-544-2799	Johnnie.J.Clark@nasa.gov	Attendee
NASA/MSFC	Clark-Ingram, Marceia	Marshall Space Flight Center	ED36	Huntsville	AL	35812	USA	256-544-6229	Marceia.A.Clark-Ingram@nasa.g	Speaker/Committee
NASA/MSFC	Colberg, Wendell	Marshall Space Flight Center	ED30	Huntsville	AL	35812	USA	256-544-2725	Wendell.R.Colberg@msfc.nasa.g	Committee
NASA/MSFC	Coleman, Sandra	Marshall Space Flight Center	SD03	Huntsville	AL	35812	USA			Attendee
NASA/MSFC	Collins, Brian	Marshall Space Flight Center	MP71	Huntsville	AL	35812	USA	256-544-2943	Brian.W.Collins@nasa.gov	Attendee
NASA/MSFC	Cook, Beth	Marshall Space Flight Center	ED30	Huntsville	AL	35812	USA	6-544-2545	Mary.B.Cook@nasa.gov	Committee
NASA/MSFC	Cooper, Ken	Marshall Space Flight Center	ED34	Huntsville	AL	35812	USA	256-544-8591	Kenneth.G.Cooper@nasa.gov	Speaker
NASA/MSFC	Davis, Eddie	Marshall Space Flight Center	ED36	Huntsville	AL	35812	USA	256-544-2490	Samuel.E.Davis@nasa.gov	Committee/Demonstration
NASA/MSFC	Davis, Farley	Marshall Space Flight Center	AD10	Huntsville	AL	35812	USA	256-544-6935	Farley.Davis@nasa.gov	Session Chair
NASA/MSFC	Davis, Joe	Marshall Space Flight Center	ED38	Huntsville	AL	35812	USA	256-544-1090	Joe.D.Davis@nasa.gov	Attendee
NASA/MSFC	Davis, John	Marshall Space Flight Center	ED35	Huntsville	AL	35812	USA	256-544-2494	john.davis@nasa.gov	Attendee
NASA/MSFC	Delay, Tom	Marshall Space Flight Center	ED34	Huntsville	AL	35812	USA	256-544-1131	Thomas.K.Delay@nasa.gov	Speaker
NASA/MSFC	Deramus, Gordon	Marshall Space Flight Center	ED33	Huntsville	AL	35812	USA	256-544-2597	Gordon.E.Deramus@nasa.gov	Attendee
NASA/MSFC	DeWeese, Darrell	Marshall Space Flight Center	ED34	Huntsville	AL	35812	USA	256-544-5120	Charles.D.DeWeese@nasa.gov	Attendee
NASA/MSFC	Edwards, David	Marshall Space Flight Center	ED31	Huntsville	AL	35812	USA	256-544-4081	David.L.Edwards@nasa.gov	Speaker (tutorial)
NASA/MSFC	Finckenor, Miria	Marshall Space Flight Center	ED31	Huntsville	AL	35812	USA	256-544-9244	Miria.Finckenor@nasa.gov	Attendee
NASA/MSFC	Frazier, Michael	Marshall Space Flight Center	ED34	Huntsville	AL	35812	USA	256-544-4968	Michael.Frazier@nasa.gov	Attendee
NASA/MSFC	Funk, Joan	Marshall Space Flight Center	UP50	Huntsville	AL	35812	USA	256-544-3298	Joan.Funk@nasa.gov	Attendee
NASA/MSFC	Garcia, Danny	Marshall Space Flight Center	ED41	Huntsville	AL	35812	USA	256-544-4138	Danny.Garcia-1@nasa.gov	Speaker
NASA/MSFC	Gardner, Terrie	Marshall Space Flight Center	ED35	Huntsville	AL	35812	USA	256-544-4549	Terrie.M.Gardner@nasa.gov	Attendee
NASA/MSFC	Gill, Paul	Marshall Space Flight Center	ED40	Huntsville	AL	35812	USA	256-544-2557	paul.gill@nasa.gov	Session Chair
NASA/MSFC	Glover, Steve	Marshall Space Flight Center	MP71	Huntsville	AL	35812	USA	256-544-5016	Steve.E.Glover@nasa.gov	Committee
NASA/MSFC	Gordon, Gail	Marshall Space Flight Center	ED34	Huntsville	AL	35812	USA	256-544-2726	Gail.H.Gordon@nasa.gov	Attendee
NASA/MSFC	Gostowski, Rudy	Marshall Space Flight Center	TD40	Huntsville	AL	35812	USA	256-544-0458	rudy.gostowski@nasa.gov	Speaker
NASA/MSFC	Griffin, Dennis	Marshall Space Flight Center	ED36	Huntsville	AL	35812	USA	256-544-2493	Dennis.E.Griffin@nasa.gov	Committee
NASA/MSFC	Hall, Joylene	Marshall Space Flight Center	ED36	Huntsville	AL	35812	USA	256-544-1402	joylene.hall@msfc.nasa.gov	Poster
NASA/MSFC	Hall, Phillip	Marshall Space Flight Center	ED32	Huntsville	AL	35812	USA	256-544-2525	Phillip.B.Hall@nasa.gov	Attendee
NASA/MSFC	Hamilton, David	Marshall Space Flight Center	ED35	Huntsville	AL	35812	USA	256-544-2578	David.Hamilton@nasa.gov	Attendee
NASA/MSFC	Hamilton, George	Marshall Space Flight Center	ED42	Huntsville	AL	35812	USA	256-544-4963	George.S.Hamilton@nasa.gov	Attendee
NASA/MSFC	Hammonds, Earline	Marshall Space Flight Center	ED36	Huntsville	AL	35812	USA	256-544-7023	Earline.J.Hammonds@nasa.gov	Attendee
NASA/MSFC	Harris, Mary JO	Marshall Space Flight Center	MP41	Huntsville	AL	35812	USA	256-544-2729	mary.j.harris@nasa.gov	Attendee
NASA/MSFC	Harris, Yolanda	Marshall Space Flight Center	MP21	Huntsville	AL	35812	USA	256-544-3001	Yolanda.B.Harris@nasa.gov	Committee
NASA/MSFC	Henderson, Charles	Marshall Space Flight Center	ED34	Huntsville	AL	35812	USA	256-544-2727	Charles.E.Henderson@nasa.gov	Attendee
NASA/MSFC	Hissam, Andy	Marshall Space Flight Center	TD62	Huntsville	AL	35812	USA	256-544-8388	Andy.Hissam@nasa.gov	Attendee
NASA/MSFC	Holmes, Steve	Marshall Space Flight Center	MP31	Huntsville	AL	35812	USA	256-544-8713	Steven.G.Holmes@nasa.gov	Attendee
NASA/MSFC	Hooper, Carlla	Marshall Space Flight Center	ED30	Huntsville	AL	35812	USA	256 544-2614	Carlla.G.Hooper@nasa.gov	Staff
NASA/MSFC	Huff, Tim	Marshall Space Flight Center	ED36	Huntsville	AL	35812	USA	256-544-4259	Timothy.L.Huff@nasa.gov	Speaker
NASA/MSFC	Hulcher, Bruce	Marshall Space Flight Center	ED34	Huntsville	AL	35812	USA	256 544-5124	Anthony.B.Hulcher@nasa.gov	Attendee
NASA/MSFC	Johnston, James	Marshall Space Flight Center	ED35	Huntsville	AL	35812	USA	256-544-2495	James.E.Johnston@nasa.gov	Attendee
NASA/MSFC	Jones, Chip	Marshall Space Flight Center	ED33	Huntsville	AL	35812	USA	256-544-2701	Clyde.S.Jones@nasa.gov	Attendee
NASA/MSFC	Kaul, Raj	Marshall Space Flight Center	ED34	Huntsville	AL	35812	USA	256-544-1084	Raj.K.Kaul@nasa.gov	Speaker
NASA/MSFC	Kennedy, Paul	Marshall Space Flight Center	ED18	Huntsville	AL	35812	USA	256-544-4117	Paul.A.Kennedy@nasa.gov	Attendee
NASA/MSFC	Kiessling, Ed	Marshall Space Flight Center	ED01	Huntsville	AL	35812	USA	256-544-1002	Edward.H.Kiessling@nasa.gov	Attendee

NASA/MSFC	Kilpatrick, Bill	Marshall Space Flight Center	ED01	Huntsville	AL	35812	USA	256 544-1000	John.W.Kilpatrick@nasa.gov	Attendee
NASA/MSFC	Lambdin, Robert	Marshall Space Flight Center	ED35	Huntsville	AL	35812	USA	256 544-4953	Robert.C.Lambdin@nasa.gov	Attendee
NASA/MSFC	Landers, Tamara	Marshall Space Flight Center	ED35	Huntsville	AL	35812	USA	256-544-6818	Tamara.S.Landers@nasa.gov	Attendee
NASA/MSFC	Lash, Rhonda	Marshall Space Flight Center	ED36	Huntsville	AL	35812	USA	256-544-9137	Rhonda.Lash@nasa.gov	Committee
NASA/MSFC	Lawless, Kirby	Marshall Space Flight Center	ED33	Huntsville	AL	35812	USA	256-544-2821	Kirby.G.Lawless@nasa.gov	Attendee
NASA/MSFC	Ledbetter, Debbie	Marshall Space Flight Center	ED38	Huntsville	AL	35812	USA	256-544-1088	debbie.ledbetter@nasa.gov	Attendee
NASA/MSFC	Ledbetter, Frank	Marshall Space Flight Center	ED34	Huntsville	AL	35812	USA	256-544-2673	Frank.Ledbetter@nasa.gov	Attendee
NASA/MSFC	Lee, Jonathan	Marshall Space Flight Center	ED33	Huntsville	AL	35812	USA	256-544-9290	Jonathan.A.Lee@nasa.gov	Speaker
NASA/MSFC	Lester, Carl	Marshall Space Flight Center	ED34	Huntsville	AL	35812	USA	256-544-4804	Carl.n.Lester@nasa.gov	Attendee
NASA/MSFC	Manning, Curtis	Marshall Space Flight Center	ED34	Huntsville	AL	35812	USA	256-544-7348	Curtis.W.Manning@nasa.gov	Attendee
NASA/MSFC	Martin, Jolene	Marshall Space Flight Center	MP71	Huntsville	AL	35812	USA	256-544-8540	j-sandhu@santecsystems.com	Attendee
NASA/MSFC	McGill, Preston	Marshall Space Flight Center	ED33	Huntsville	AL	35812	USA	256-544-2604	Preston.B.McGill@nasa.gov	Attendee
NASA/MSFC	Medley, Jay	Marshall Space Flight Center	ED38	Huntsville	AL	35812	USA	256-544-1085	Jay.Medley@nasa.gov	Attendee
NASA/MSFC	Mellen, Dan	Marshall Space Flight Center	ED41	Huntsville	AL	35812	USA	256 544-7193	Dan.Me..en@nasa.gov	Attendee
NASA/MSFC	Meyers, Charles	Marshall Space Flight Center	ED22	Huntsville	AL	35812	USA	256-544-7192	Charles.A.Meyers@nasa.gov	Attendee
NASA/MSFC	Mims, Kathy	Marshall Space Flight Center	ED21	Huntsville	AL	35812	USA	256 544-1506	Katherine.Mims@nasa.gov	Attendee
NASA/MSFC	Moore, Regina	Marshall Space Flight Center	ED34	Huntsville	AL	35812	USA	256-544-8456	Regina.Moore@nasa.gov	Committee
NASA/MSFC	Munafo, Paul	Marshall Space Flight Center	ED30	Huntsville	AL	35812	USA	256-544-2566	Paul.M.Munafo@nasa.gov	Committee
NASA/MSFC	Nehls, Mary	Marshall Space Flight Center	ED01	Huntsville	AL	35812	USA	256-544-6578	Mary.K.Nehls@nasa.gov	Attendee
NASA/MSFC	Newton, Robby	Marshall Space Flight Center	ED36	Huntsville	AL	35812	USA	256-544-7880	robby.newton@nasa.gov	Speaker
NASA/MSFC	Niedermeyer, Mindy	Marshall Space Flight Center	ED34	Huntsville	AL	35812	USA	256-544-1569	mindy.niedermeyer@nasa.gov	Attendee
NASA/MSFC	Panda, Binayak	Marshall Space Flight Center	ED33	Huntsville	AL	35812	USA	256-544-6349	Binayak.Panda-1@nasa.gov	Attendee
NASA/MSFC	Pelham, Larry	Marshall Space Flight Center	ED34	Huntsville	AL	35812	USA	256-544-9111	Larry.Pelham@nasa.gov	Attendee
NASA/MSFC	Perkins, James	Marshall Space Flight Center	ED36	Huntsville	AL	35812	USA	256-544-2634	James.H.Perkins@nasa.gov	Committee
NASA/MSFC	Phillips, Steven	Marshall Space Flight Center	ED34	Huntsville	AL	35812	USA	256-544-0626	Steven.T.Phillips@msfc.nasa.go	Speaker
NASA/MSFC	Quattrochi, Dale	Marshall Space Flight Center	SD60	Huntsville	AL	35812	USA	256-961-7887	Dale.Quattrochi@nasa.gov	Speaker (tutorial)
NASA/MSFC	Raleigh, Shannon	Marshall Space Flight Center	CD70	Huntsville	AL	35812	USA	256-544-5621	Shannon.E.Raleigh@nasa.gov	Attendee
NASA/MSFC	Rayburn, Jeff	Marshall Space Flight Center	ED22	Huntsville	AL	35812	USA	256-544-1564	Jeff.Rayburn@nasa.gov	Attendee
NASA/MSFC	Richardson, Erin	Marshall Space Flight Center	ED36	Huntsville	AL	35812	USA	256-544-2873	Erin.H.Richardson@nasa.gov	Speaker (tutorial)/Poster
NASA/MSFC	Richardson, Stephen	Marshall Space Flight Center	ED23	Huntsville	AL	35812	USA	256-544-1768	Stephen.W.Richardson@nasa.gov	Attendee
NASA/MSFC	Roth, Axel	Marshall Space Flight Center	DA01	Huntsville	AL	35812	USA	256-544-0451	Axel.Roth-1@nasa.gov	Attendee
NASA/MSFC	Russell, Carolyn	Marshall Space Flight Center	ED33	Huntsville	AL	35812	USA	256-544-2705	carolyn.k.russell@nasa.gov	Attendee
NASA/MSFC	Sackheim, Robert	Marshall Space Flight Center	DA01	Huntsville	AL	35812	USA	256-544-1938	bob.sackheim@nasa.gov	Keynote Speaker
NASA/MSFC	Sams-Smiley, Jeneene	Marshall Space Flight Center	SD12	Huntsville	AL	35812	USA	256-544-6816	Madelyn.J.Sams@nasa.gov	Committee
NASA/MSFC	Schmieder, Stephen	Marshall Space Flight Center	MP51	Huntsville	AL	35812	USA	256-544-0112	Stephen.P.Schmieder@nasa.gov	Attendee
NASA/MSFC	Schrock, Ken	Marshall Space Flight Center	ED18	Huntsville	AL	35812	USA	256-544-1460	ken.schrock@nasa.gov	Attendee
NASA/MSFC	Schutzenhofer, Scott	Marshall Space Flight Center	MP71	Huntsville	AL	35812	USA	256-544-8496	Scott.A.Schutzenhofer@nasa.go	Attendee
NASA/MSFC	Scroggins, Sharon	Marshall Space Flight Center	AD10	Huntsville	AL	35812	USA	256-544-7932	Sharon.T.Scroggins@nasa.gov	Committee
NASA/MSFC	Selvidge, Shawn	Marshall Space Flight Center	ED34	Huntsville	AL	35812	USA	256-544-0481	Shawn.Selvidge@nasa.gov	Speaker
NASA/MSFC	Shah, Sandeep	Marshall Space Flight Center	ED33	Huntsville	AL	35812	USA	256-544-0836	sandeep.shah@msfc.nasa.gov	Attendee
NASA/MSFC	Smelser, Jerry	Marshall Space Flight Center	MP31	Huntsville	AL	35812	USA	256-544-4082	Jerry.W.Smelser@nasa.gov	Attendee
NASA/MSFC	Smith, Brett	Marshall Space Flight Center	ED34	Huntsville	AL	35812	USA	256-544-7036	Brett.H.Smith@nasa.gov	Attendee
NASA/MSFC	Smith, Drew	Marshall Space Flight Center	ED20	Huntsville	AL	35812	USA	256-544-4932	Drew.Smith@nasa.gov	Attendee
NASA/MSFC	Smithers, Gweneth	Marshall Space Flight Center	ED34	Huntsville	AL	35812	USA	256-544-0282	Gweneth.A.Smithers@nasa.gov	Attendee
NASA/MSFC	Sparks, Scott	Marshall Space Flight Center	ED34	Huntsville	AL	35812	USA	256-544-2670	Jeffery.S.Sparks@nasa.gov	Attendee
NASA/MSFC	Stanley, Dawn	Marshall Space Flight Center	AD40	Huntsville	AL	35812	USA	256-544-1835	Dawn.C.Stanley@nasa.gov	Committee
NASA/MSFC	Suits, Mike	Marshall Space Flight Center	ED32	Huntsville	AL	35812	USA	256-544-8336	michael.w.suits@nasa.gov	Attendee
NASA/MSFC	Taylor, Irene	Marshall Space Flight Center	ED10	Huntsville	AL	35812	USA	256-544-2051	Irene.E.Taylor@nasa.gov	Attendee
NASA/MSFC	Terek, Jody	Marshall Space Flight Center	ED02	Huntsville	AL	35812	USA	256-544-6817	Joanne.M.Terek@nasa.gov	Attendee
NASA/MSFC	Thom, Robert	Marshall Space Flight Center	Ed32	Huntsville	AL	35812	USA	256-544-2517	Robert.L.Thom@nasa.gov	Attendee
NASA/MSFC	Throckmorton, Dave	Marshall Space Flight Center	ED01	Huntsville	AL	35812	USA	256-544-1001	David.A.Throckmorton@nasa.go	Attendee
NASA/MSFC	Townsend, Tammy	Marshall Space Flight Center	ED36	Huntsville	AL	35812	USA	256-544-2623	Tammy.L.Townsend@nasa.gov	Attendee
NASA/MSFC	Tygielski, Phillip	Marshall Space Flight Center	TD62	Huntsville	AL	35812	USA	256-544-7169	Phillip.J.Tygielski@nasa.gov	Attendee
NASA/MSFC	Vickers, John	Marshall Space Flight Center	ED34	Huntsville	AL	35812	USA	256-544-3581	John.H.Vickers@nasa.gov	Attendee
NASA/MSFC	Wagner, Carole	Marshall Space Flight Center	ED35	Huntsville	AL	35812	USA	256-544-2719	Carole.Y.Wagner@nasa.gov	Attendee
NASA/MSFC	Walker, James	Marshall Space Flight Center	ED32	Huntsville	AL	35812	USA	256-961-1784	james.l.walker@nasa.gov	Speaker/Session Chair/Demonstration
NASA/MSFC	Watson, Michael	Marshall Space Flight Center	ED12	Huntsville	AL	35812	USA	256 544-3186	Michael.D.Watson@nasa.gov	Session Chair
NASA/MSFC	Wertz, George	Marshall Space Flight Center	ED31	Huntsville	AL	35812	USA	256-544-2663	George.E.Wertz@nasa.gov	Attendee
NASA/MSFC	Whitaker, Ann	Marshall Space Flight Center	SD01	Huntsville	AL	35812	USA	256-544-2481	Ann.Whitaker@nasa.gov	Attendee
NASA/MSFC	Whitfield, Steve	Marshall Space Flight Center	ED36	Huntsville	AL	35812	USA	256-961-0358	Steven.W.Whitfield@nasa.gov	Attendee
NASA/MSFC	Williams, Glenn	Marshall Space Flight Center	ED34	Huntsville	AL	35812	USA	256-5441041	glenn.williams@nasa.gov	Speaker
NASA/MSFC	Wright, Jerry	Marshall Space Flight Center	ED37	Huntsville	AL	35812	USA	256-544-4443	Jerry.L.Wright@nasa.gov	Attendee
NASA/MSFC	Yost, Vaughn	Marshall Space Flight Center	MP21	Huntsville	AL	35812	USA	256-544-1998	Vaughn.H.Yost@nasa.gov	Committee
NASA/MSFC	Zimmerman, Frank	Marshall Space Flight Center	ED33	Huntsville	AL	35812	USA	256-544-4958	frank.r.zimmerman@nasa.gov	Speaker
NASA/SSC	Gordon, Jenette	Stennis Space Center	RA00	Stennis Space Center	MS	39529	USA	228-688-1416	Jenette.B.Gordon@nasa.gov	Attendee
NASA/WSTF	Beeson, Harold	White Sands Test Facility	PO Box 20	Las Cruces	NM	88004-0020	USA	505-524-5542	hbeeson@nasa.gov	Speaker (tutorial)/Session Chair
NASA/WTSF	Saulsberry, Regor	White Sands Test Facility	PO Box 20	Las Cruces	NM	88004	USA	505-524-5518	regor.l.saulsberry@nasa.gov	Attendee
National Aerospace Laboratory	Hasegawa, Keiichi	1-Koganezawa Kihigaya		Kakuda	Miyagi	981-1525	Japan	81-244-68-3947	khasegawa@kakuda-splab.go.jp	Attendee
Northrop Grumman	Topalian, John H.	1100 W. Hollyvale St.		Azusa	CA	91702	USA	626-812-1729	John.Topalian@NorthropGrumm	Attendee
Northrop Grumman Electronic Systems	Berryman, Richard	8152 Lindenwood Drive		Huntington Beach	CA	92646-1779	USA	626-812-1907	Richard.Berryman@NorthropGr	Attendee
Panametrics, Inc.	Stanton, Robin	26 Hammond Street		Waltham	MA	02453-3497	USA	781-899-2719	stantonr@panametrics.com	Exhibitor
Panametrics, Inc.	Wormmeester, Meindert	26 Hammond Street		Waltham	MA	02453-3497	USA	781-899-2719		Exhibitor
Petroferm	Morrison, Carolyn						USA			Exhibitor
Poco Graphite, Inc.	Lucke, Wes	3131 Luallen Drive		Carrollton	TX	75007	USA	972-492-2556	wlucke@poco.com	Attendee
Polytechnic University	Ulman, Abraham	Six Metrotech Center		Brooklyn	NY	12201	USA	718-260-3119	aulman@duke.poly.edu	Speaker
Positron Systems	Akers, Doug	6151 N. Discovery Way		Boise	ID	83713	USA	208-672-1923	curtr@positronsystems.com	Speaker
Positron Systems	Rideout, Curt	6151 N. Discovery Way		Boise	ID	83713	USA	208-672-1923	curtr@positronsystems.com	Exhibitor
Puget Sound Clean Air Agency	Hess, Rick	110 Union Street	Suite 500	Seattle	WA	98101	USA	206-689-4027	rickh@pscleanair.org	Session Chair
Puget Sound Clean Air Agency	Schantz, John	110 Union Street	Suite 500	Seattle	WA	98101	USA	206-689-4027	JohnS@pscleanair.org	Speaker
Qualis Corporation	Dalton, David	Marshall Space Flight Center	ED36	Huntsville	AL	35812	USA	256-544-4377	David.B.Dalton@msfc.nasa.gov	Staff
Qualis Corporation	Engel, Carl D.	Marshall Space Flight Center	ED36	Huntsville	AL	35812	USA	256-544-6032	carl.engel@msfc.nasa.gov	Speaker
Qualis Corporation	Engel, Mary	6767 Old Madison Pike	Suite 105	Huntsville	AL	35806	USA	256-971-1707	mary.engel@qualis-corp.com	Attendee
Qualis Corporation	Hill, Dewayne	Marshall Space Flight Center	ED36	Huntsville	AL	35812	USA	256-544-7047	dewayne.hill@msfc.nasa.gov	Attendee
Qualis Corporation	Morard, Elizabeth	6767 Old Madison Pike	Suite 105	Huntsville	AL	35806	USA	256-971-1707	elizabeth@qualis-corp.com	Attendee
Qualis Corporation	Shea, Charlotte	Marshall Space Flight Center	ED36	Huntsville	AL	35812	USA	256-544-3029	Charlotte.Shea@msfc.nasa.gov	Committee
RJ Lee Microsystems	Martin, Ellen									Exhibitor

Royce International	Monteiro, Hubert	2200 Colonial Lake Drive	Apt. 2224	Madison	AL	35758-4014	USA	256-772-6493	hubertmontiero@att.net	Attendee
Sandia National Laboratories	Atwood, Clint	PO Box 5800, MS-1008		Albuquerque	NM	1008	USA	505-844-0816	datwoo@sandia.gov	Attendee
Sandia National Laboratories	DeMeza, Norman E.	PO Box 5800		Albuquerque	NM	87185-0960	USA	504-257-2523	nedemez@sandia.gov	Exhibitor
Sandia National Laboratories	Parker, Alan	PO Box 5800, MS-0958		Albuquerque	NM	87185-0958	USA	505-844-9472	arparke@sandia.gov	Attendee
Santec Systems, Inc.	Sandhu, Jas	716 South Milwaukee Avenue		Wheeling	Illinois	60090-6202	USA	847-215-8884	j-sandhu@santecsystems.com	Speaker
SMDC	Ennis, Doug						USA			Attendee
Southern Research Institute	Stokes, Erik	757 Tom Martin Drive		Birmingham	AL	35211-4468	USA	205-581-2649	stokes@sri.org	Speaker
Superior Coatings, Inc	Deardorff, Jim	1713 Bryan Street	PO Box 317	Chilicothe	MO	64601	USA	660-646-6355	jdeardorffsupct@yahoo.com	Speaker
Surface Optics Corporation	Szcesniak, M. Martin	11555 Rancho Bernardo R.		San Diego	CA	92127	USA	858-675-7404	martinsz@surfaceoptics.com	Speaker
Sverdrup Technology	Fisk, Mike	Sverdrup Technology	Marshall Space Flight Center	Huntsville	AL	35812	USA	256-544-6456		Exhibitor
Sverdrup Technology	Wilson, Scott	Sverdrup Technology	Marshall Space Flight Center	Huntsville	AL	35812	USA	256-544-6456		Exhibitor
Taka Otsuka Associates, Inc.	Otsuka, Takahide	600 Countess Drive		Yardley	PA	19067-4618	USA	215-321-7067	t.otsuka@usa.net	Attendee
Tennessee Technological University	Buchanan, George	Department of Civil and Environmental Engineering		Cookeville	TN	38505	USA	931-372-3486	gbuchanan@tntech.edu	Speaker
Tennessee Technological University	Goedeke, Shawn	Department of Mechanical Engineering		Cookeville	TN	35805	USA	865-376-7595	SMG2886@tntech.edu	Poster
Tennessee Technological University	Peddieson, John	1020 Stadium Drive	Prescott Room 414	Cookeville	TN	38505	USA	931-372-3615	jpeddieson@tntech.edu	Attendee
Texas A&M University	Whitcomb, John	Center for Mechanics of Composites	3141 TAMU	College Station	TX	77843-3141	USA	979-845-4006	jdw@tamu.edu	Speaker
The Boeing Company	Cardinal, Rhonda	PO Box 5219		Vandenberg AFB	CA	93437	USA	805-606-6340	rhonda.e.cardinal@boeing.com	Speaker
The Boeing Company	Solomon, Marcella	P.O. Box 21233	MC: 721Z-K085	Kennedy Space Center	FL	32815-0233	USA	321-861-0908	marcella.solomon@boeing.com	Attendee
Thiokol	Keen, Jill	Marshall Space Flight Center	Bldg 4204, Room 505	Huntsville	AL	35812	USA	256-544-2748		Session Chair
Tinker Air Force Base	Stone, Nick H.	340 Windbrook Drive		Norman	OK	73072	USA	405-329-4763	nick.stone@tinker.af.mil	Attendee
Tokai University	Tanaka, Makoto	1117 Kitakaname		Hiratsuka	Kanagawa	259-1292	Japan	81-463-58-1211	makoto@cc.u-tokai.ac.jp	Speaker
Touchstone Research Laboratory	Brown, Michael	The Millenium Center	RR1, Box 100B	Triadelphia	WV	26059-9707	USA	304-547-5800	mrb@trl.com	Attendee
Touchstone Research Laboratory	Gordon, Brian	The Millenium Center	RR1, Box 100B	Triadelphia	WV	26059-9707	USA	304-547-5800	blg@trl.com	Attendee
United Space Alliance	Harm, Gene	8550 Astronaut Blvd.	USK-890	Cape Canaveral	FL	32420	USA	321-867-9856	harmg@usasrb.ksc.nasa.gov	Speaker
United Space Alliance	Mann, Rhonda	555 Discovery Drive		Huntsville	AL	35806	USA	256-971-3128	rhonda.e.mann@usahq.unitedspa	Speaker
United Space Alliance	Murphree-Grafton, Gail	Marshall Space Flight Center	Bldg. 4202, Room 415	Huntsville	AL	35812	USA	256-544-2483	Gail.Murphree-Grafton@msfc.na	Session Chair
United Space Alliance	Novak, Howard	8550 Astronaut Blvd.	USK-864	Kennedy Space Center	FL	32899	USA	321-967-7054	novakh@usasrb.ksc.nasa.gov	Speaker/Session Chair
United Space Alliance	Owens, Karen	555 Discovery Drive		Huntsville	AL	35806	USA	256-544-5218	karen.owens@msfc.nasa.gov	Exhibitor
United Space Alliance-Logistics	Deem, Victoria J.	894 Pine Baugh		Rockledge	FL	32955	USA	321-861-5879	victoria.j.deem@usago.ksc.nasa	Attendee
United States Research Association	Zhu, Shen	Marshall Space Flight Center	SD46	Huntsville	AL	35812	USA	256-544-2916	shen.zhu@msfc.nasa.gov	Speaker
The University of Alabama at Birmingham	Camata, Renato	1300 University Blvd	CH 310	Birmingham	AL	35294-1170	USA	205-934-8143	camata@uab.edu	Speaker
The University of Alabama in Huntsville	Vaughan, William	5606 Alta Dena Street		Huntsville	AL	35802	USA	256-961-7759	vaughan@nsstc.uash.edu	Speaker
University of Dayton Research Institute	Abfalter, Gary	300 College Park	KL545	Dayton	OH	45469	USA	937-229-4704	abfalter@udri..udayton.edu	Speaker
University of Dayton Research Institute	Kuhlman, Sarah	300 College Park		Dayton	OH	45469	USA	937-229-4704	kuhlman@udri.udayton.edu	Speaker
University of Louisiana at Lafayette	Hollerman, William	PO Box 44210		Lafayette	LA	70503	USA	331-82-6691	hollerman@louisiana.edu	Poster
University of Massachussetts Lowell	LeBlanc, Carole	One University Avenue		Lowell	MA	01854-2866		978-934-3249	Carole_LeBlanc@uml.edu	Speaker
University of New Orleans	Brailsford, Bruce	University of New Orleans	National Center for Advanced Manufacturing	New Orleans	LA		USA	504-257-0931	bbrailsf@uno.edu	Session Chair
University of New Orleans	Hui, David	Department of Mechanical Engineering		New Orleans	LA	70148		504-257-0969	dhui@uno.edu	Speaker
US Air Force	Harbour, Daniel	8 Draco Drive		Edwards AFB	CA	93524	USA	661-275-5374	daniel.harbour@edwards.af.mil	Attendee
US Army	Watson, Sherry	AMSAM-RD-PS-AM		Redstone Arsenal	AL	35898	USA	256-876-4976	sherry.watson@redstone.army	Attendee
US Army	Whitmire, Nancy	3002 Flag Circle	#2620	Madison	AL	35758	USA	256-876-1667	nancy.whitmire@redstone.arm	Attendee
USAF	Shull, Douglas D.	1201 Edward H. White II Street		Patrick AFB	FL	32925	USA	321-494-3236	douglas.shull@patrick.af.mil	Attendee
USAF	Silvera, Antonio	2510 Kennedy Circle	311HSW/XPRA	Brooks-City-Base	TX	78235	USA	210-536-3657	antonio.slvera@brooks.af.mil	Attendee
Versar, Inc.	Herrington, John	39 W. Hunter Drive		Enon	OH	45523	USA	937-864-7812	herrington@erinet.com	Speaker
Virginia Tech	Loos, Alfred	204 Flippin Circle		Blacksburg	VA	24060-1326	USA	540-231-4574	aloos@vt.edu	Speaker
Virginia Tech	Sturges, Robert	ISE Department	250 Durham Hall	Blacksburg	VA	24061	USA	540-231-7420	sturges@vt.edu	Attendee
Vought Aircraft Industries, Inc.	Buckholz, Richard E.	1801 E. Airport Road	M/S F16-077	Stuart	FL	3499-4012	USA	772-220-5665	BUCKHRI@voughtaircraft.com	Speaker
West Boeing	Eichinger, Eric	5001 Bolsa Avenue		Huntington Beach	CA	90247	USA	714-372-5197	eric.c.eichinger@Boeing.com	Speaker
Wolverine Tube, Inc	Ng, Chun Man	Suite 1000	200 Clinton Avenue	Huntsville	AL	35801	USA	256-580-3511	cmng@wlv.com	Poster
Wolverine Tube, Inc.	Auchterlonie, Carla	2100 Market St. NE		Decatur	AL	35601	USA	256-580-3954		Exhibitor
Wolverine Tube, Inc.	Horowitz, Dennis	2100 Market St. NE		Decatur	AL	35601	USA	256-580-3954		Exhibitor
Wolverine Tube, Inc.	Kukowski, Rob	2100 Market St. NE		Decatur	AL	35601	USA	256-580-3954		Exhibitor
Wolverine Tube, Inc.	Neshan, Massaud	2100 Market St. NE		Decatur	AL	35601	USA	256-580-3954		Exhibitor
Y-12 National Security Complex	Powell, George L.	298 East Drive		Oak Ridge, TN	TN	37830	USA	865-574-1717	powellgl@y12.doe.gov	Speaker
ZIN Technologies, Inc.	Andrasik, John	300 Aerospace Parkway		Brookpark	OH	44142	USA	216-977-0327	john.andrasik@grc.nasa.gov	Attendee
	Clark, Paul A.	1290 Flint Drive		Christiansburg	VA	24073	USA	540-818-1549	clarkp@megahits.com	Attendee
	Sharp, Sheila									Speaker

Exhibitor	Address 1	Address 2	City	State	Zip	Phone	Staff
3M							Keith Brobst
AGA Chemicals, Inc.	2201 Water Ridge Parkway	Suite 400	Charlotte	NC	28217	704-329-7614	Steve Stagliano
Airtech Advanced Materials	5700 Skylab Road		Huntington Be	CA	92647	714-899-8100	Tom Doty, Scott Patton, Jeff Dahlgren, Peter ____
Alabama A&M University Research Institute	4900 Meridian Street		Normal	AL	35762	256-851-5866	Leslie Evelyn
Alliant Techsystems, Inc.							
American Autoclave Company	7819 Riverside Dr.		Sumner	WA	98309	888-796-3373	Bill Castaneda
Assembly Guidance	315 Littleon Road		Chelmsford	MA	08124	978-244-1166	Scott Blake, Anna Burdo
Brown Precision, Inc.	1103 Putman Drive		Huntsville	AL	35816	256-830-1990	Greg Brown
Correlated Solutions	952 Sunset Blvd.		West Columbia	SC	29169		Hubert W. Schreier, Scott Johnson
DCM Clean Air Products, Inc.	9605 Highway 80 West		Fort Worth	TX	76116	817-654-2829	Ross Cole
Hamilton Precision Metals	1780 Rohrerstown Road		Lancaster	PA	17601-2334	717-569-7061	Michael Campbell, Michael Staab, Robert Crawford, Mark Robinson
Integrated Concepts and Research Corporation	1033 N. Fairfax St.	Suite 400	Alexandria	VA	22314	703-519-9901	Karen Fossett
Joint Group on Pollution Prevention	100 CTC Drive		Johnstown	PA	15904	814-269-2870	Brian Greene, Christina Brown
Lockheed Martin Space Systems Company	13800 Gentilly Road		New Orleands	LA	70129	504-257-4188	Kevin Barre
Marshall Space Flight Center			Huntsville	AL			
Matec Instruments	56 Hudson Street		Northborough	MA	01532	508-393-0155	Ken Bishop, John Cooper, Ed Antolino
Microcare	595 John Downey Drive		New Britain	CT	06051	860-827-0626	Harris Towne
Modern Chemical, Inc.	PO Box 368		Jacksonville	AR	72078	501-988-1311	M.R. Huntley, Nancy Burger, +1
Panametrics	26 Hammond Street		Waltham	MA	02453-3497	781-899-2719	Meindert Wormmeester, Robin Stanton
Petroferm							Carolyn Morrison
Positron Systems	6151 N. Discovery Way		Boise	ID	83713	208-672-1923	Douglas Akers, Curt Rideout
RJ Lee Microsystems							Ellen Martin
Rocketdyne							Ron Daniel
Sandia National Laboratories	PO Box 5800		Albuquerque	NM	87185-0960		Norman DeMeza
Shuttle Program Office							
Surface Optics Corporation	11555 Rancho Bernardo R.		San Diego	CA	92127	858-675-7404	Martin Szczesniak
Sverdrup Technology	Marshall Space Flight Center		Huntsville	AL	35812	256-544-6456	Mike Fisk, Scott Wilson
Touchstone Research Laboratory	The Millenium Center	RR 1, Box 100B	Triadelphia	WV	26059	304-547-5800	
University of New Orleans							Bruce Brailsford
Wolverine Tube, Inc.	2100 Market St. NE		Decatur	AL	35601	256-580-3954	Rob Kukowski, Massaud Neshan, Dennis Horowitz, Carla Auchterlonie

The 5th Conference on Aerospace Materials, Processes, and Environmental Technology was a rousing success!

Check back at this site for information on the next Materials, Processes, and Manufacturing event being planned for September 2004.

- 3 days of learning and networking, complemented by the elegance of the Huntsville Museum of Art and the spacious Von Braun Center

Photo Gallery

- 350 attendees
- 35 exhibitors
- 17 technical sessions with 74 presentations on aerospace materials and processes, environmental replacement technologies, and advanced manufacturing methodologies

Conference Program

- 5 pre-conference tutorials on
  - *Managing Risks in Oxygen Systems*
  - *Space Environmental Effects*
  - *Materials Characterization through Chemical Fingerprinting*
  - *MACT Program Basics: Future of Air Emissions Regulations*
  - *Hot Cities*
- FIRST (For Inspiration and Recognition of Science and Technology) Robotics exposition
- Technology demonstrations on adiabatic compression and thermographic inspection
- 12 posters on
  - *Friction Stir Weld Risk Reduction*
  - *Automatic Ply Verification*
  - *Properties of Solar Sail Materials*
  - *Microdeformation Technology*
  - *Friction Stir Welding using an Adjustable Pin Tool*
  - *Proton Microscopy*
  - *Flammability Igniter Characteristics*
  - *Composite LOX Tank Development*
  - *High Temperature Thermographic Phosphor Coatings*
  - *Correlating Flammability with FTIR Analysis*
  - *Oxygen Compatibility of Composite Materials*
  - *Ammonia Analysis by GC/IRD*

REPORT DOCUMENTATION PAGE

Form Approved
OMB No. 0704-0188

1. AGENCY USE ONLY *(Leave Blank)*	2. REPORT DATE	3. REPORT TYPE AND DATES COVERED
	November 2003	Conference Publication

4. TITLE AND SUBTITLE

5th Conference on Aerospace Materials, Processes, and Environmental Technology

5. FUNDING NUMBERS

6. AUTHORS

M.B. Cook and D. Cross Stanley, Editors

7. PERFORMING ORGANIZATION NAMES(S) AND ADDRESS(ES)

George C. Marshall Space Flight Center
Marshall Space Flight Center, AL 35812

8. PERFORMING ORGANIZATION REPORT NUMBER

M–1096

9. SPONSORING/MONITORING AGENCY NAME(S) AND ADDRESS(ES)

National Aeronautics and Space Administration
Washington, DC 20546–0001

10. SPONSORING/MONITORING AGENCY REPORT NUMBER

NASA/CP—2003–212931

11. SUPPLEMENTARY NOTES

Prepared for Materials, Processes, and Manufacturing Department, Engineering Directorate.
Proceedings of a conference held in Huntsville, AL, September 16–18, 2002.

12a. DISTRIBUTION/AVAILABILITY STATEMENT

Unclassified-Unlimited
Subject Category 23
Availibility: NASA CASI (301)621–0390

12b. DISTRIBUTION CODE

13. ABSTRACT *(Maximum 200 words)*

The next millennium challenges us to produce innovative materials, processes, manufacturing, and environmental technologies that meet low-cost aerospace transportation needs while maintaining U.S. leadership. The pursuit of advanced aerospace materials, manufacturing processes, and environmental technologies supports the development of safer, operational, next-generation, reusable, and expendable aeronautical and space vehicle systems. The Aerospace Materials, Processes, and Environmental Technology Conference provided a forum for manufacturing, environmental, materials, and processes engineers, scientists, and managers to describe, review, and critically assess advances in these key technology areas.

14. SUBJECT TERMS

environment, replacement technology, solvents, propulsions, precision cleaning, coating technology, lessons learned, manufacturing, advanced materials, metal processes, nonmetal processes, ceramic matrix composites, rapid prototyping, pollution prevention, cleanliness verification

15. NUMBER OF PAGES

1620

16. PRICE CODE

17. SECURITY CLASSIFICATION OF REPORT	18. SECURITY CLASSIFICATION OF THIS PAGE	19. SECURITY CLASSIFICATION OF ABSTRACT	20. LIMITATION OF ABSTRACT
Unclassified	Unclassified	Unclassified	Unlimited